Proceedings

of the Third International Workshop on Very Large Floating Structures

VLFS'99

September 22–24, 1999

Honolulu, Hawaii, USA

VOLUME I

EDITED BY R. Cengiz Ertekin and Jang Whan Kim

UNIVERSITY OF HAWAII AT MANOA
SEA GRANT COLLEGE PROGRAM
2525 CORREA ROAD, HIG 238
HONOLULU, HAWAII 96822

UNIHI-SEAGRANT-BB-98-01

The Proceedings of the Third International Workshop on Very Large Floating Structures (VLFS '99)

VOLUME I

Edited by

R. Cengiz Ertekin and Jang Whan Kim

University of Hawaii at Manoa

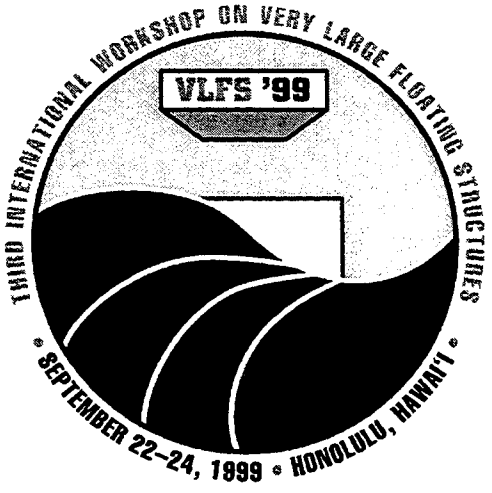

September 22-24, 1999, Honolulu, Hawaii, USA

Citation for this Publication is:

Proceedings of the Third International Workshop on Very large Floating Structures (VLFS '99), Eds. R.C. Ertekin & J.W. Kim, 22-24 September, 1999, Honolulu, Hawaii, 96822, USA (Volume I or II).

SOEST, University of Hawaii at Manoa, 2540 Dole Street, Holmes Hall 402, Honolulu, HI 968222, USA.

Printed in the United States of America by Island Printing Centers, 737 Bishop Street, Suite 149, Honolulu, Hawaii 96813, USA.

This work relates to U.S. Department of the Navy Grant N00014-99-1-0988 issued by the Office of Naval Research.

Additional copies of this publication (as a set) may be available from:

SEA GRANT
HAWAII

Sea Grant Communications Office
2525 Correa Road, HIG 210
Honolulu, HI 96822, USA
Tel: +1 (808) 956-7410
E-Mail: dianen@soest.hawaii.edu

Dedicated to the Honorary Chairs of VLFS '99,

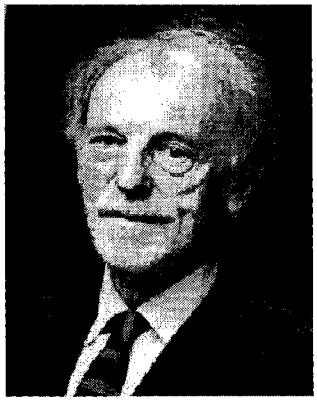

Professor John V. Wehausen
of the University of California at Berkeley,
on the occasion of his eighty sixth birthday

Professor Koichiro Yoshida
of Tokai University, on the occasion of his
retirement from the University of Tokyo

for their teachings and mentorship that we cherish.

Thank you John, thank you Koichiro!

PREFACE

The papers that follow were presented at the Third International Workshop on Very Large Floating Structures (VLFS '99) held in Honolulu, Hawaii, USA from September 22 to 24, 1999. The major sponsor of VLFS '99 was Office of Naval Research, U.S., Department of the Navy.

A number of projects are underway to design very large floating structures for various purposes. The enormous sizes of these floating structures require design and analysis methods that are different from the ones used in conventional floating-structure projects such as oil-drilling platforms. The design of such structures is a complex task of unprecedented proportions (a floating airport will be as long as 5 km long). Consequently, many technical issues must be addressed before a VLFS project can successfully be completed. Some of the more important issues are discussed in this workshop, mainly as they relate to the Mobile Offshore Base (MOB) Project of the U.S. and the Mega-Float Project of Japan; however, more general theoretical and experimental issues on the design and analysis of VLFS are also included.

VLFS '99 is the third international workshop on VLFS and was held jointly with the MOB presentation and workgroup meetings normally held twice a year in Washington, D.C. The first workshop (VLFS '91) was held in Honolulu, Hawaii, and the second workshop (VLFS '96) was held in Hayama, Japan. The main motivation for these meetings is the need to vigorously continue to develop methods that will allow us to have more confidence in the ultimate dynamic load and response predictions for better design through comparative theoretical studies and experimental verification.

The format of the workshop consisted of two keynote lectures, technical paper presentations followed by discussion, and workshop panel discussion sessions. (The summaries of the panel discussion sessions are planned to be included in Volume III of these proceedings and should be available later in 1999.) The two keynote lectures gave overviews of the two major projects being undertaken currently by the United States and Japan on the Mobile Offshore Base and the Mega-Float Programs, respectively. The papers of VLFS '99 contribute significantly to the exponentially growing number of international publications on the subject area in the recent years as evidenced by the publications of the Hydroelasticity in Marine Technology Conference series, International Workshop on Floating Structures in Coastal Zone, ISOPE and OMAE Conferences, and the series of Meetings of the U.S.-Japan Marine Facilities Panel, among others.

Many individuals contributed to the successful completion of VLFS '99, and are listed in the Acknowledgement section. We thank them for their care and tireless efforts, encouragement, and support. Words are not enough to express our appreciation for their help.

It is our pleasure to welcome all participants to VLFS '99 in Honolulu, where we hope you will enjoy the spirit of Aloha!

R. Cengiz Ertekin and Jang Whan Kim
Honolulu, Hawaii
September 1999

INTERNATIONAL ORGANIZING/ADVISORY COMMITTEE

Prof. John V. Wehausen (Honorary Chair), Univ. of California, Berkeley, CA, USA
Prof. Koichiro Yoshida (Honorary Co-Chair), Tokai University, Shimizu-shi, Shizuoka, Japan

Prof. R. Cengiz Ertekin (Chair), Univ. of Hawaii, Honolulu, HI, USA
Dr. Jang Whan Kim (Secretary), Univ. of Hawaii, Honolulu, HI, USA
Mr. Gene Remmers (Co-Chair), Office of Naval Research, Arlington, VA, USA
Prof. H. Ronald Riggs (Co-Chair), Univ. of Hawaii, Honolulu, HI, USA
Mr. Robert Taylor (Co-Chair), Naval Facilities Engineering Service Center, Port Hueneme, CA, USA

Prof. K. June Bai, Seoul National University, Seoul, Korea
Prof. Michael Bernitsas, Univ. of Michigan, Ann Arbor, Michigan, USA
Mr. Ron Brackett, Naval Facilities Engineering Service Center, Port Hueneme, CA, USA
Prof. Sander Calisal, Univ. British Columbia, Vancouver, B.C., Canada
Dr. Subrata K. Chakrabarti, Offshore Structure Analysis, Plainfield, Illinois, USA
Dr. Michael A. Champ, Environmental Systems Development, Inc., Falls Church, Virginia, USA
Prof. Kwok Fai Cheung, Univ. of Hawaii, Honolulu, HI, USA
Dr. Rueybin Chiou, Naval Facilities Engineering Service Center, Port Hueneme, CA, USA
Prof. Rodney Eatock Taylor, Univ. of Oxford, Oxford, U. Kingdom
Prof. Odd M. Faltinsen, Norwegian University of Science & Technology, Trondheim, Norway
Prof. Charles E. Helsley, UH Sea Grant College Program, Honolulu, HI, USA
Mr. Kiyoshi Inoue, Hitachi Zosen Corp., Chiyoda-ku, Tokyo, Japan
Prof. Hiroshi Kagemoto, Univ. of Tokyo, Bunkyo-ku, Tokyo, Japan
Dr. Kentaro Kobayashi, Sumitomo Heavy Industries, Kanagawa, Japan
Prof. Yusaku Kyozuka, Kyushu Univ., Kasuga, Japan
Prof. Hisaaki Maeda, Univ. of Tokyo, Bunkyo-ku, Tokyo, Japan
Prof. Alaa E. Mansour, Univ. of California, Berkeley, CA USA
Dr. Stephen M. Masutani, Hawaii Natural Energy Institute, Honolulu, HI, USA
Mr. Balji Menon, American Bureau of Shipping, Houston, TX, USA
Prof. Choung Mook Lee, Advanced Fluids Eng. Res. Center, POSTECH, Pohang, Korea
Ms. Michele Murdoch, Naval Facilities Engineering Service Center, Port Hueneme, CA, USA
Prof. J.N. Newman, Massachusetts Institute of Technology, Cambridge, MA, USA
Dr. Gerard C. Nihous, Pacific Int. Center for High Technology Research, Honolulu, HI, USA
Dr. Shigeo Ohmatsu, Ship Research Institute, Mitaka, Tokyo, Japan
Dr. Paul Palo, Naval Facilities Engineering Service Center, Port Hueneme, CA, USA
Prof. J.A. Pinkster, Delft University of Technology, Delft, The Netherlands
Dr. Satoru Shiraishi, Port & Harbor Research Institute, Kanagawa, Japan
Dr. Theodore A. Shugar, Naval Facilities Engineering Service Center, Port Hueneme, CA, USA
Prof. Carlos Guedes Soares, Technical Univ. of Lisbon, Lisboa, Portugal
Mr. Hidetoshi Sueoka, Mitsubishi Heavy Industries, Ltd., Yokohama, Japan
Prof. Hideyuki Suzuki, Univ. of Tokyo, Bunkyo-ku, Tokyo, Japan
Prof. Patrick K. Takahashi, Hawaii Natural Energy Institute, Honolulu, HI, USA
Prof. Mikio Takaki, Hiroshima Univ., Higashi-Hiroshima, Japan
Mr. Takeshi Tateyama, Ishikawajima-Harima Heavy Industries Co. Ltd., Koto-ku, Tokyo, Japan
Prof. Marshall P. Tulin, Univ. of California, Santa Barbara, CA, USA
Prof. Shigeru Ueda, Tottori Univ., Tottori, Japan
Dr. C. Linwood Vincent, Office of Naval Research, Arlington, VA, USA
Dr. Yoshiyasu Watanabe, Ship Research Institute, Mitaka, Tokyo, Japan
Prof. William C. Webster, Univ. of California, Berkeley, CA USA
Prof. Ronald W. Yeung, Univ. of California, Berkeley, CA USA
Dr. Robert F. Zueck, Naval Facilities Engineering Service Center, Port Hueneme, CA, USA

SPONSORS

Major Sponsor: Office of Naval Research

Other Sponsors: California Sea Grant College Program
Hawaii Sea Grant College Program, UHM
School of Ocean and Earth Science and Technology, UHM
Ship Research Institute, Japan

ACKNOWLEDGEMENT

We wish to express our thanks to many individuals who have helped us to make this workshop a reality. Gene Remmers of ONR, and Bob Taylor and Ron Brackett of NFESC took the initiative in arranging the workshop, provided generous help in every phase of the preparations, and continuously supported us. Without their encouragement and much appreciated suggestions, VLFS '99 could not have been successful. Koichiro Yoshida of Tokai University and Yoshiyasu Watanabe of Ship Research Institute organized the papers of our colleagues from Japan and were always there when we needed them as good friends. This is the third VLFS workshop that we jointly organize and we look forward to having many more in the future. The Ship Research Institute's sponsorship of the workshop is greatly acknowledged.

The help of our teacher Bill Webster of U.C. Berkeley and our friend Hisaaki Maeda of University of Tokyo in organizing the panel sessions as co-chairs is greatly appreciated. Ron Riggs of University of Hawaii served as the co-chair of the workshop and was always there whenever we needed his advise, support and friendship. The tremendous ideas and support we received from Chuck Helsley, director of the UH Sea Grant Program, is greatly acknowledged. By sponsoring the workshop on the UH side, through the Hawaii Sea Grant Program, he made it all possible. The last minute efforts of Mary Kamiya of the UH Sea Grant Program on putting the proceedings together, again in 1999, is greatly appreciated. Thank you Mary.

The session and panel chairs, panel members, and IOAC members kindly accepted our invitation, and made sure that the paper and panel sessions reached their goals with high quality articles and challenging discussion sessions. We thank them for their tireless efforts in making the workshop the success that it was. Without the countless hours spent by all the authors of the workshop, we could have achieved very little. We thank them for their cooperation in following the rigorous guidelines and meeting the deadlines.

We greatly appreciate the help we received from RCE's graduate students, Bala Padmanabhan, Hari Sundararaghavan, Dingwu Xia and Liqun Yang in handling the proceedings papers and various local organizational matters, and from Prof. H. Ronald Riggs' graduate students Jane Liu and Lin Lin Huang of the CE department, and from Prof. Kwok Fai Cheung's graduate student Amal Phadke of the ORE department at UH who kindly volunteered their time during the workshop.

We thank Jeannie Ross and Alexandra De Visser of NFESC who helped us with the planning as well during the workshop. The talented Brooks Bays of SOEST Publications was the illustrator for the proceedings and conference materials, and Publications Director Diane Henderson provided editorial help with kindness. Associate Dean Lorenz Magaard of SOEST, which is one of the co-sponsoring organizations of VLFS '99, provided the help of his office through Helen Ferrer and her assistant Lori Wakumoto in logistical and fiscal matters. Thank you Helen for your efforts in making sure that our invited guests felt at home. Yvonne Yamashita, the Director of UH Conference Center, and her assistant Jena Tanaka provided excellent organizational help and went beyond the call of duty. Mahalo Yvonne and Jena for everything.

This work relates to U.S. Department of the Navy Grant N00014-99-1-0988 issued by the Office of Naval Research.

CONTENTS

Volume I

Volume II

PROCEEDINGS OF THE THIRD INTERNATIONAL WORKSHOP ON VERY LARGE FLOATING STRUCTURES
(VLFS '99), VOL. I, EDS. R.C. ERTEKIN & J.W. KIM, 22-24 SEPTEMBER 1999, HONOLULU, HAWAII, USA

MOBILE OFFSHORE BASE: A SEABASING OPTION

Gene Remmers
Office of Naval Research*
Robert Taylor, Paul Palo, Ron Brackett
Naval Facilities Engineering Service Center**

ABSTRACT

The United States Office of Naval Research (ONR) is conducting a Science and Technology (S&T) Program to establish the technical feasibility and cost of a Mobile Offshore Base (MOB). A MOB is a very large floating platform comprised of interconnected modules, assembled on-site to provide support for U.S. military activities in areas lacking an adequate basing structure. The unprecedented length (up to 2 kilometers) and the open ocean functions required from a MOB put it well beyond the present industry state-of-practice. Major efforts of this program are to:

- Deliver tools to parametrically quantify performance and construction costs for a wide variety of candidate platform configurations.
- Identify and develop advanced design, analysis, and manufacturing capabilities in a consistent technology development program.
- Quantify fatigue, operational and survival met/ocean (e.g., wind, waves, current) criteria for MOB design.
- Demonstrate the evolving state of practice by advancing a few promising MOB system concepts through preliminary design.

This paper provides a broad overview of the MOB Program, lists program products and provides a framework for the numerous MOB-sponsored developments being reported at this conference.

1. INTRODUCTION

The United States Office of Naval Research (ONR) had been developing and exploring alternatives aimed at establishing the technical feasibility and cost of Mobile Offshore Basing since July 1997. This effort was based on concerns over minimizing, or even eliminating, the dependence on overseas military bases. For example (see [1]), in 1995 the Italian government denied landing access at Aviano to U.S. F-117 aircraft intended to take part in attacks in Serbia. In both 1997 and 1998, the Kuwaiti, Saudi Arabian, and Jordanian governments imposed similar constraints on land-based allied aircraft with respect to operations against Iraq; and as a result, U.S. sea-based assets were required. Even today, there are problems obtaining overflight rights in the Gulf region.

One alternative basing option is a very large floating sea base. In concept, this structure, called a Mobile Offshore Base (MOB), would be positioned tens of miles off the coast and would perform the same functions as a local base. Using a MOB for over-the-horizon, offshore basing of supplies and personnel would reduce the dependence on land bases and neutralize many of the terrorist threats inherent to present forward-deployed facilities. In short, the MOB would support a forward-presence strategy while denying the enemy an opportunity to disrupt a critical line of operations. Forecasts project a continued decline in the number of overseas bases for U.S. military operations.

Not surprisingly, the overall size and configuration of a MOB varies greatly depending on the mission(s). While the requirement to support thousands of troops and their equipment calls for a very large platform, it is the requirement to support conventional take-off and landing (CTOL) cargo aircraft that is most responsible for the unprecedented size of MOB. The size and multiple functions associated with a multi-mission MOB platform lead to several bounding design requirements common to all concepts explored by this program:

- Length of up to 2 kilometers to accommodate CTOL cargo aircraft operations.
- Configured with multiple modules, most likely semi-submersible in hull form (monohulls were not emphasized), allowing for: (a) maximum transit

* 800 N. Quincy St, Arlington VA 22217-5660
** ESC51, 1100 23rd Ave, Port Hueneme, CA 93043-4370

speeds to site, (b) maximum flexibility to evolving missions, and (c) minimal wave-induced runway dynamics. Note that each module will have nominally four times the displacement of a Nimitz-class aircraft carrier.
- Maintainability of 40 years (since each module is too large to be dry-docked in existing facilities).
- Large volume for storage and personnel housing.
- Open ocean, ship-to-MOB, and MOB-to-lighterage cargo transfer.
- Simultaneous inter-service and air-sea operations.

2. CANDIDATE MOB PLATFORMS

This program is advancing the design of four platforms with fundamentally different degrees of module connectivity:

- ***Hinged Semi-submersible Modules.*** Up to five rectangular semi-submersible steel modules, each 305m (1,000 ft) long, hinge-connected with compliant connectors (e.g., collapsible rubber cones). See Fig. 1.

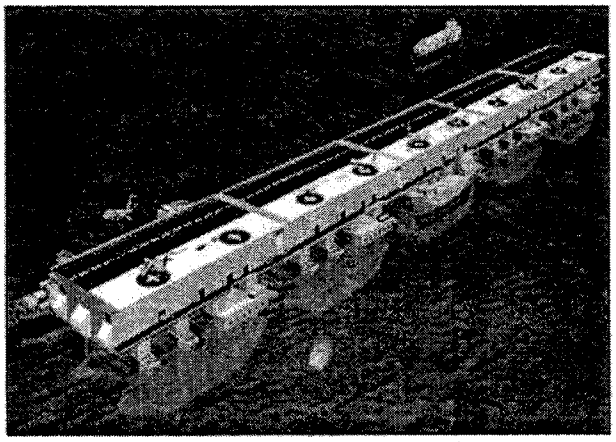

Figure 1. Hinged semi-submersible modules.

- ***Semi-submersible Modules with Flexible Bridges.*** Three rectangular semi-submersible steel modules, each about 220m (725 ft) long, connected by flexible bridges, each about 430m (1,410 ft) long, to form the continuous flight deck. See Fig. 2.
- ***Independent Semi-submersible Modules.*** Three rectangular semi-submersible steel modules, each about 500m (1,650 ft) long. These modules are not structurally connected, but instead, rely on dynamic positioning to maintain overall orientation and relative position between modules. A drawbridge spans the gap to create a continuous airplane runway. See Fig. 3.

The final concept features a material alternative to the all-steel modules:

- ***Concrete Semi-submersible Modules.*** Rectangular semi-submersible modules, each 380m (1,250 ft) long, consisting of a steel deck and concrete hull. A concrete hull may provide a longer life and require less maintenance. Elastomer bearings provide compliant connections between modules. See Fig. 4.

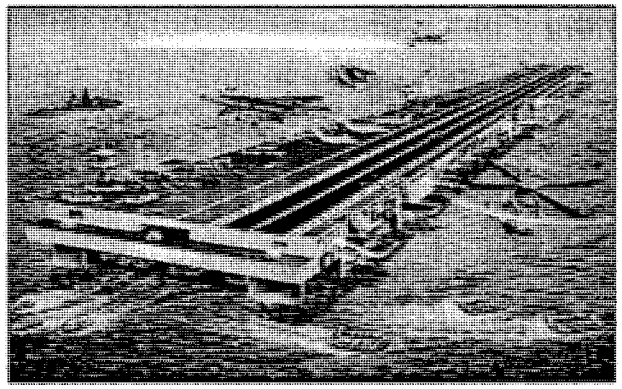

Figure 2. Semi-submersible modules with flexible bridges.

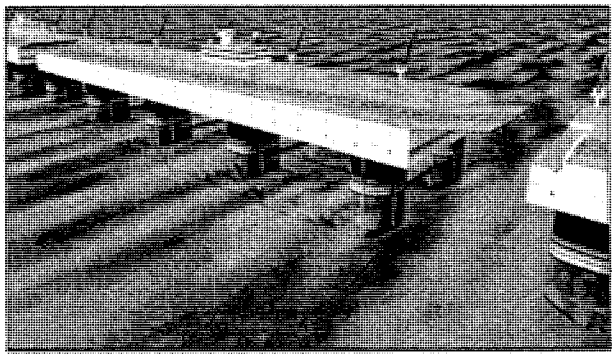

Figure 3. Independent semi-submersible modules.

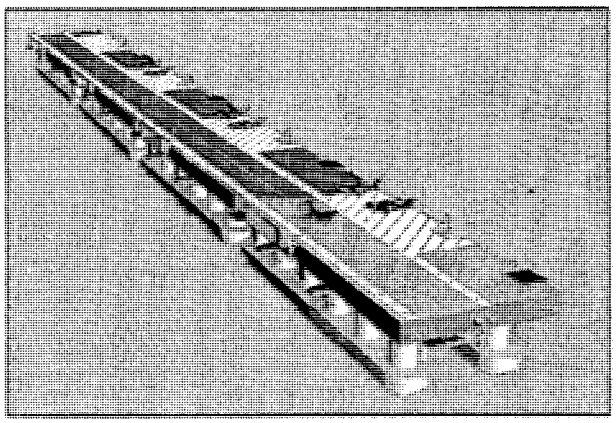

Figure 4. Concrete semi-submersible modules.

Note that this program does not recommend or focus on any one "best" platform concept. Rather, it emphasizes basic technology and cost issues to provide maximum flexibility to future designers for optimizing a MOB configuration relative to the missions and their associated requirements.

3. MOB UNIQUENESS VERSUS OFFSHORE DESIGN PRACTICE

When this Program began, one common opinion was that industry design practice was adequate or easily extrapolated to accommodate the differences between MOB and the state of practice. In many instances, this was proven wrong, rendering the genesis of the many developments fostered by this program.

Many complicated issues were involved in the extrapolation of prior design practice for MOB design:

- Significant increases to the acquisition cost due to large safety factors required to balance the high design uncertainties.
- System performance could be jeopardized without thorough analysis of the known design uncertainties or unrecognized system responses, resulting in the platform failing to fulfill its mission.
- The consequence of failure as related to the large capital cost of the platform, the value of the military equipment stored onboard, and the large number of personnel on board.

All of these factors further reinforced the need for thorough analyses.

4. ONR MOB S&T PROGRAM APPROACH

The initial strategy was driven by:

- Imprecise and evolving missions and mission requirements.
- Numerous technology shortfalls associated with the unprecedented nature of MOB.
- Untested platform concepts.

The technology emerging from this program must be applicable to a range of plausible candidate missions contemplated by future DoD planners. The numerous uncertainties in the state-of-practice required the identification of technology gaps and qualitative prioritization according to their effect on MOB design as well as S&T opportunities. Adapting MOB design to the S&T results continues to be an ongoing process. While each of the fundamental platform concepts (as previously described) has inherent advantages, they are offset by associated disadvantages that are sensitive to mission parameters such as the platform size, wave direction, etc. In other words, while it was important to conclude whether a particular platform concept satisfies any or all MOB missions, it was just as important to establish the limits of its applicability (e.g., maximum platform length and/or environmental conditions) with respect to the mission requirements. The present ONR MOB program used a balance of generic technology and system design studies to best accommodate all of these constraints.

The MOB S&T Program was organized into the following four technical product areas:

- Mission Requirements and Performance Measures.
- Standards and Criteria (MOB Classification Guide).
- Design Tools (validated computer simulation models used in the MOB Classification Guide).
- Alternative Concepts (components and overall system configurations).

Each of the four technical product areas are briefly described in Section 5.

5. MOB TECHNOLOGY AREAS AND ASSOCIATED ACCOMPLISHMENTS

5.1 Mission Requirements and Performance Measures

This product area develops the tools and techniques to enable:

- Conversion of the military mission requirements into quantifiable parameters (e.g. weight, volumes, runway size, etc.).
- Evaluations of how well a conceptual (or in the future, an as-built) MOB platform satisfied the mission requirements at a site of interest.

Information from the first category provided an important *common baseline of required capabilities* for all preliminary designs. Information from the second category directly supported the program objective as a measure of feasibility.

The main accomplishments included:

- Examination of conceptual operations for MOB and quantification of the weight, volume, and other mission requirements.
- Development of an operational availability (Ao) model to allow for relative assessment of performance. This is a time domain based model that correlates hindcasted environmental data with all aspects of MOB at-sea operations to statistically

estimate the long-term effectiveness (e.g., cargo throughput) of a given platform subjected to the wind/waves/current at a given site. This model allows for an objective evaluation of any MOB concept against any set of specific mission requirements for any set of environmental conditions (site and time of year).

- Development of a methodology to assess the rate that cargo can be transferred between the MOB and various types of ships and lighterage over a range of wave conditions (applicable to Ao model above).
- Establishment of the functional requirements for Air Operations (applicable to Ao model above).
- Establishment of the functional requirements and identification of technology gaps for crane related cargo handling (applicable to Ao model above).
- Development of a risk-based numerical model to estimate construction costs, and risk and feasibility of construction.

5.2 Standards and Criteria

The Standards and Criteria and the Design Tools product areas necessarily worked together to provide the three essential requirements of the MOB Classification Guide:

- Design methodology.
- Specialized building blocks (numerical analysis models).
- Validation of the design methodology and the specialized building blocks.

The approach used for the MOB Classification Guide was to modify existing commercial standards, complemented by appropriate military standards. The main products included:

- Draft MOB Classification Guide addressing hydrodynamic/hydroelastic wave loads, survival and fatigue structural responses, stability, constructability, and station keeping. A probabilistic and performance-based approach was developed. The emphasis was on platform integrity, as defined by fatigue, operating, and survival statistics using hindcast data for each site.
- Realistic environmental descriptors for survival, operational, and fatigue analyses. Directional, temporal, spatial, and joint probabilities were included based on a critical examination of known physical ocean processes (e.g., hurricanes, internal waves, and solitons).

A key driver for the environmental description was the recognition that the responses of MOB platforms required knowledge of the spatial coherence of the wave field at a 2-kilometer scale. Since no such information was available, multiple pioneering studies were undertaken and are still underway, ranging from analysis of field wave data to the development and exercising of 3-dimensional wave models.

5.3 Design Tools

The three thrusts in this product area were to:

- Advance hydroelastic modeling.
- Develop a universal interface between the hydroelastic and structural models.
- Generate a comprehensive hydroelastic data set for validation of the models.

A variety of studies were undertaken related to hydroelastic modeling, which at the inception of this program, consisted of two constant source diffraction theory models, both of which were numerically incapable of modeling a full MOB platform, nor adequately validated. There were several motivating factors that drove the coordinated advancement of this modeling capability. The first was uncertainty over elasticity effects due to the extreme length of the individual MOB semi-submersible modules with respect to the connector loads. These loads are vitally important because connectors are the single most critical components in most of the system concepts. The second motivating factor was the need to accurately quantify the wave field under and adjacent to the platform due to its effect on cargo transfer operations.

The main accomplishments included:

- An evaluation of the utility of existing hydrodynamic and hydroelastic models for simulating the wave-induced responses of a representative MOB semi-submersible. Second-order system drift forces on the platform and relative motions and interactions between a cargo vessel(s) and a MOB module were included.
- A new generation, numerically efficient hydroelastic model, which incorporates higher-order (b-spline) diffraction panel elements into an existing hydroelastic model.
- A semi-analytical hydrodynamic (i.e., rigid body) preliminary assessment model to complement the computationally intensive hydroelastic models used for final design.

- A load generator to convert [normalized, frequency domain] hydroelastic excitation and reaction panel pressure forces, along with a stochastic description of a random sea, into pressures for an arbitrary surface element mesh in (time domain) finite element structural models. This approach was based on the assumption that the structural responses may be nonlinear, but that the hydrodynamics remain essentially linear.
- An advanced time-domain, large amplitude response simulation program to account for the instantaneous (rather than incident) free surface; this model was intended for MOB issues such as extreme response, transit draft dynamics, and air gap, validated by model tests.
- A time-domain response simulation program to design and study the unique connect/disconnect operation of the modules of the MOB structure during heavy seas.
- An application of nonlinear system identification techniques to investigate the dynamics and wave field associated with an individual MOB semi-submersible module at transit draft.
- A comprehensive experiment of hydroelastic behavior of floating structures to validate the various analysis models. This experiment simulates the motions of a spring-connected, 5-module, 1,828m (6,000 ft) MOB platform at 1:60 scale using semi-submersible modules specifically constructed to exhibit mild elasticity.

5.4 Alternative Concepts

The two main products were:

- System concept preliminary designs (point designs), that identified the technology issues addressed in this program, in addition to establishing a basis for technical feasibility and cost assessments.
- Subsystems and components critical to MOB system concept feasibility.

Four platform/system concepts (introduced in Section 2) were pursued through preliminary design. These designs represented substantial effort and innovation from all the major contractors. All data and design information generated by each contractor was available to their competitors to minimize duplication of effort, to share knowledge, and to increase the probability of achieving safe and effective designs for MOB.

The four MOB concept designs represent important program products. Their complementary features proved that a solution may indeed exist for satisfying the difficult requirements of MOB.

Some characteristics of each concept are outlined here:

- *Hinged Semi-submersible Modules.* A system which inherently concentrates all loads at a finite position. The connectors release the pitch constraint and allow compliance in other degrees of freedom to reduce the load. Connector material degradation or mechanical fatigue are issues for this concept.
- *Semi-submersible Modules with Flexible Bridges.* A system which acts to distribute the connector loads to minimize the high local stresses and eliminate the slope discontinuity between modules. The flexible bridges essentially decouple the dynamics of adjacent modules. Bridge fatigue life and transit speed are issues for this concept.
- *Independent Semi-submersible Modules.* A system that eliminates connector loads. Collision risk is reduced during connection/disconnection. Fuel consumption and an increased sensitivity to environmental influences are issues for this concept.
- *Concrete Semi-submersible Modules.* An example of a material alternative MOB option. Greatly increased fatigue life over traditional steel construction. The weight of steel in reinforced concrete and steel semi-submersibles is comparable, which lessens the cargo capacity for comparably-sized units.

Other critical subsystems and components of MOB that were investigated within this product area include:

- *Inter-module connectors*: Evaluated the use of nonlinear materials and specific mechanical behavior to reduce dynamic loads and assess limits to manufacturing each type of connector. Currently developing a feasible concept for a nonlinear compliant connector based on collapsible rubber cones.
- *Station-keeping*: Developed a new type of leaderless control Dynamic Positioning System (DPS) with alternative control schemes for holding multiple modules in close relative alignment. Developing design methods for very large suction piles for MOB temporary mooring.

- *Response mitigation methods*: Explored concepts for mitigating the dynamic motions and forces of an ocean platform through active air movement between buoyancy chambers.
- *Alternative marine materials*: Assessed the suitability and limitations of reinforced and prestressed concrete as an alternative hull material. Performing laboratory tests to determine the basic mechanical properties of compliant elastomeric connector materials.
- *Construction and repair methods*: Identified alternative structural material and configurations to achieve significant reductions in weight of platform and bridging decks. Investigated methods and cost of constructing a MOB in conventional U.S. shipyards.
- *Open-sea cargo transfer*: Evaluated methods for berthing ships alongside the MOB in open seas. Examining methods for providing calmer seas around berthed ships.

6. MAJOR DELIVERABLES

Numerous new technologies, information, and special decision making tools were developed that can be used by DOD with confidence to analyze SeaBasing options. Fundamental advancements in offshore technologies, such as the new hydroelastic models, wave spatial coherence, and multi-body dynamic positioning techniques provide the engineering community and industry with tools and techniques necessary for the analysis, design, and construction of a SeaBase. Other significant spin-offs are to ship design and the offshore industry (see [2]).

Some of the many deliverables produced from this program include:

- Higher-order (linear frequency domain) hydroelastic models.
- Large amplitude hydrodynamic models that account for the instantaneous free surface.
- Hydroelastic (model scale, linked, semi-submersible) validation data.
- Hydrodynamic (model scale, single, semi-submersible) validation data (transit, extreme response, and air gap).
- Universal interface to apply diffraction theory pressures to finite element structural models.
- Preliminary characterization of three dimensional ocean wave field coherence.
- Operational Availability model to estimate system performance versus a variety of stochastic variables.
- Various multiple body dynamic positioning studies.
- Open ocean cargo transfer techniques and models.
- Robust connectors.
- Transit dynamics models for high sea conditions.

ONR MOB Program products such as reports, data, and software are available. Additional information can be found on the MOB Internet site [http:// mob.nfesc.navy.mil/].

7. SUMMARY

This program, that began in July 1999, has sponsored a mix of preliminary system concept designs and basic offshore technology advancements, with the objective of establishing feasibility and cost for MOB platforms. Although some technology issues remain, the state of practice at the inception of this program has been advanced significantly as a result of the collaborative efforts of a multidisciplinary team from industry, academia, and government.

Work is ongoing; however, the results to date indicate that a solution does exist to satisfy the difficult requirements of a MOB.

REFERENCES

[1] T. Kilvert-Jones. The Key to Effective Presence, In *Sea*Power Magazine*, May 1999.

[2] R. Zueck, et al. Mobile Offshore Base: Research Spin-Offs. In *Proc. International Offshore and Polar Engineering Conference, Brest, France, 1999.*

PROCEEDINGS OF THE THIRD INTERNATIONAL WORKSHOP ON VERY LARGE FLOATING STRUCTURES
(VLFS '99), VOL. I, EDS. R.C. ERTEKIN & J.W. KIM, 22-24 SEPTEMBER 1999, HONOLULU, HAWAII, USA

Research and Development of Mega-Float

Eiichi Isobe
Technological Research Association of Mega-Float

ABSTRACT

The Technological Research Association of Mega-Float was established in 1995 by seventeen companies with the assistance of the Ministry of Transport. That same year, the Association embarked on its first stage of research into "Research and Development of Very Large Floating Structures" which examined the fundamental technologies of very large floating structures (VLFS) under a three-year program. The target magnitude of floating structures researched consisted of structures several kilometers long VLFS with lifetimes exceeding 100 years. The research was carried out on five practical items, namely, floating structure design technology, floating construction work technology, ultra long service duration technology, operational function ensuring technology, and environmental impact evaluation technology. These studies were carried out using a large floating experimental model 300 m long, 60 m wide and 2 m deep.

The Association started the second stage of research under the theme of "Corroborative Research on the Use of Mega-Float as an Airport" under a schedule of another three years commencing from 1998. This research is focused on application technologies required to support airport functions, with the aim being the realization of a functional floating airport. This phase of the research includes construction of a 1000 m long, 60 m wide (partially 120 m) and 3 m deep experimental model. The model will be used to carry out landing and take-off experiments with small airplanes, to develop simulation programs for larger sized floating airports, and to collect environmental data. This paper summarizes the concept of very large floating structures and the results achieved during the first phase of research before reviewing the content and aims of the second phase of research into the practical application of the Mega-Float structure.

1. INTRODUCTION

As an island nation with limited land resources, utilization of ocean space has contributed greatly to the development of the Japanese economy, and it is expected that demand to use ocean and coastal areas for various facilities, such as harbor facilities, airport facilities, urban function facilities, supplies distribution facilities, to name a few, will increase further in the future. At present, the coast is already highly utilized in Japan, and it is considered necessary in the future to penetrate further offshore or into sea areas with poor subsoil where present utilization is limited. In such sea areas, construction with conventional reclamation techniques might be difficult from both technical and an economic viewpoints. It is this type of situation where use of an ultra large floating structure, namely "Mega-float", might prove most useful in supplementing more traditional reclamation methods. Accompanying research into this method, it is expected that the range of choices thus available for selecting the location and construction method for developing and utilizing ocean spaces will be expanded, and contribute greatly to providing increased infrastructure.

Under such circumstances the Technological Research Association of Mega-float (hereinafter referred to as "TRAM") was organized in April 1995 by seventeen companies for the purpose of commencing research into realizing a Mega-Float with support provided by the Ministry of Transport and The Nippon Foundation. TRAM has aimed its research at achieving a target VLFS structure several kilometers long with a lifetime of more

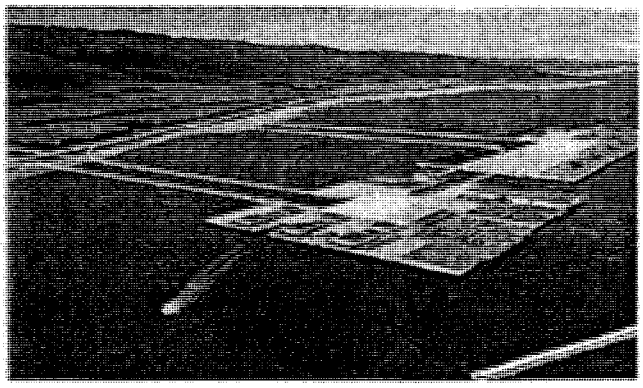

Fig. 1 Integrated Distribution Base

than one hundred years, considering the magnitude as the infrastructure. A conceptual drawing of an Integrated Distribution Base is shown in Fig. 1 as one example of how such a structure may be utilized.

Due to its enormous size, Mega-Float project involves specific technological problems that must be solved from both a theoretical viewpoint as well as through practical demonstrative experiments at sea. The planned research includes an experiment of construction of a large-scale model at sea and establishment and testing of applicable technology through various demonstration experiments in the field using the model.

Although many very large floating structures have been proposed and studied over the past twenty years or so in Japan, none have yet to be materialized. There are several reasons for these plans not being realized, but one major reason is that there are no experience of construction at sea. In this research, a practical experiment at sea was performed using a large model with the expectation that the experimental results could be evaluated as a practical result, even though it was just a model.

Though some comparatively small floating structures could be completed using only shipbuilding technology, generally, a wider variety of technologies is required for a large ocean project. Moreover, cooperation with other areas of industry is indispensable in such technological fields as wave control technology, mooring technology, new materials, technology for evaluating environmental impact, to mention only a few. Given this context, it was expected that this research work would be performed with the participation of experts from many technological fields.

TRAM consists of twelve shipbuilding companies and five steel manufacturing companies. In addition, many experts from national research institutes, universities, related associations and companies from industrial fields other than those of the participants have assisted TRAM in its work, as a national research project, due to the wide range of its research activities.

2. TRANSITION OF MEGA-FLOAT RESEARCH

The initial research of Mega-Float, that is, "Research and Development of VLFS" was started as already described above. At first, TRAM planned a wide range of research activities in order to realize the Mega-Float concept under a three year program and selected a range of research subjects that consisted of basic technologies for application to a variety of purposes. This research was successfully completed with results anticipated at beginning of the research.

Among the many research items comprising the Mega-Float project, one study examined the functions of various facilities that could be used on a VLFS. The study found that the airport function has one of the most difficult requirements to floating structures. Accordingly, a fair amount of time and effort was spent on studying the airport function as part of this research. However, the feasibility of the airport function could not be subjected to corroborative experiments using actual aircraft due to the limited size of the floating model used in this research; it could only be confirmed through simulation calculations or the use of a simulator.

The Ministry of Transport decided to create a Committee for Promoting a Practical Use of Mega-Float under the chairmanship of the Vice-Minister for Technical Affairs in March 1997 to examine ways of realizing the Mega-Float concept. Two subcommittees, the Engineering Development Subcommittee and the Legal Affairs Subcommittee, were created under this committee consisting of director level members of the divisions concerned in each bureau of the ministry, in order to start investigating questions requiring immediate attention. Further, the Airport Utilization Investigating Group was created in May 1997 under the Engineering Development Subcommittee to study problems occurring when the Mega-Float structure is used as an airport. The membership of the Group includes experts gathered from related technical fields.

Hearing concerns about the concept of a floating airport from various aviation interests, prior to holding the Investigating Group, showed that there were many questions about the floating airport. Although an examination of these questions by the Investigating Group showed that a significant portion of them could be resolved using the calculations, or the results of the research, there were views that some of the questions needed to be ensured through corroborative experiments. Since an airport is used by a great number of people, it is essential that safety be ensured.

Under these circumstances, TRAM has proceeded with its research consisting mainly of corroborative

experiments related to airport functions, while working in cooperation with the above-mentioned investigating committees. Support for research of the airport function has been obtained again from the Ministry of Transport and The Nippon Foundation, and mutual agreement to move forward with the research has also been obtained from among the participating companies. As a result, TRAM undertook "Corroborative Research on the Use of Mega-Float as Airport" as the second stage of Mega-Float research. This second stage research is referred to as "Phase II", while contrasted with this, the previous first stage of research is known as "Phase I".

TRAM planned research for realization of a Mega-Float airport under a three year program starting from 1998 and selected research items for the floating airport as a result of studies done by the Airport Utilization Investigating Group. However, the TRAM technology can be applied not only to floating airports but also to many other purposes, such as port facilities, disaster relief bases, distribution bases, as well as amusement and sports facilities. In order to exploit such new projects, TRAM is conducting research in various other types of applications in addition to the airport with its own funds.

3. Phase I Research into Mega-Float

(1) Outline of Research Plan

Construction of the Mega-float structure has already been widely studied, and it is generally considered to raise less technical problems in terms of construction of the structure itself. However, a Mega-float structure has not yet been materialized in spite of the many proposals made thus far, and no actual results have been obtained as already stated above. Although the largest single-body floating structure currently in existence is a floating oil storage base 400 m in length and 97 m in width, all the components comprising the structure were constructed in a building dock using the same methods as those used for building ships, with not a single structure exceeding the size of the dock. The Mega-float structure is larger than a dock and must be assembled at sea afloat. Construction is considered technologically feasible as assembly at sea is also employed in the modification work of ships, and various assembly methods have been studied including actual tests. Even if the method is considered to be technically feasible, however, the technology for large-scale assembly work of high quality, safety and high efficiency yet low in cost has not necessarily been established.

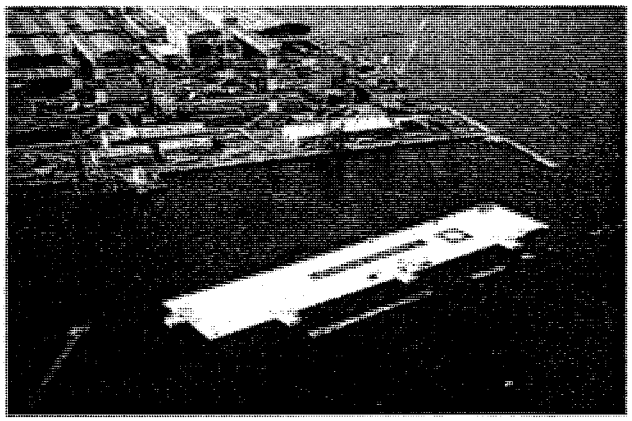

Fig. 2 Phase I Experimental Model

There were many problems other than construction method which needed to be addressed. The method of analyzing ultra large structures several kilometers in length had already been theoretically solved. However, the analytical program had yet to be perfected, because no such requirement actually existed and there were no opportunities for construction of such large structures. Thus, it could not be said that a perfect program which could be applied in the actual analysis of such ultra large structures had already been developed.

Moreover, questions regarding floating structures were also pointed out by potential users to which satisfactory explanations had yet to be made. For instance, sufficient measures for ensuring a long service life exceeding one hundred years, the type of impact that can be expected on the environment due to the existence of a large floating structure, amongst others should be clearly explained. These problems were unavoidable in realizing an actual Mega-float structure, and studies on these problems were included in this research, in addition to design and construction technologies. Therefore, this research not only considered the technology necessary to construct the floating structure itself, but was also extended to wider subjects related to applications of such structures.

Research was conducted with regard to five practical subjects divided into:

(1) floating structure design technology;
(2) floating construction work technology;
(3) ultra long service duration technology;
(4) operational function ensuring technology; and
(5) environmental impact evaluation technology.

A major intent of this research was to establish all of these technologies through actual demonstration tests at sea employing a large experimental model formed by joining nine independent floating units at sea. The final dimensions of the model were:

Length:	300.0 m
Breadth:	60.0 m
Depth:	2.0 m
Draft:	0.5 m
Total area:	1.8 ha

Fig. 2 shows a photograph of the experimental model.

The experiments were carried out in Tokyo Bay off shore from the Yokosuka area.

(2) Timetable

The Phase I research was carried out over a three year period from fiscal 1995 through 1997. Four units of the experimental model (each 100 m x 20 m x 2 m in size) were built by the end of September 1995 and connected to a small model 200 m long, 40 m wide by 2 m high in November 1995. Some verification experiments were performed using this half completed model. Five other units were built by June 1996 and connected to a large model 300 m long, 60m wide by 2 m high in July that same year. The joining work itself was one of the major subjects of research. After completion of the model, various verification tests were carried out using it.

(3) Achievements of Phase I research

The number of research themes considered as part of the Phase I research amounted to nearly two hundred including supplementary areas of research. As it is not possible to review each of these themes of research one by one, an outline of the contents and achievements of five research subjects are summarized and illustrated.

① Floating structure design technology

Ultra-large floating structures are far thinner than conventional floating structures in terms of their ratio of depth per length. Accordingly, elastic response analysis is indispensable to structural analysis and the evaluation of such factors as mooring force, reliability and, of course, floating motions. In order to work out such analytical techniques and the various computer programs needed to perform the analysis in an empirical way, a demonstration test model was used for sea tests of external forces, mooring performance, movement and structural responses, in addition to tank test models.

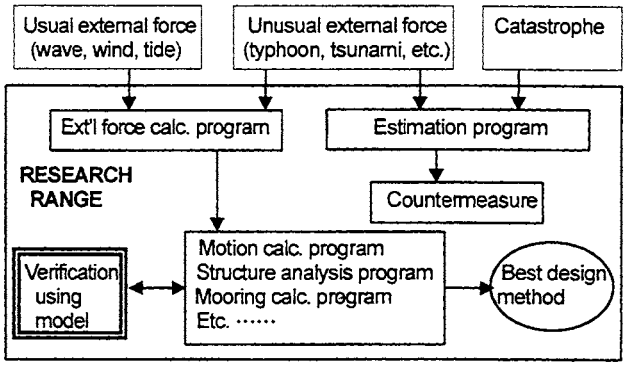

Various calculating programs, which were necessary in the synthesis of the Mega-Float design, were developed, and accurate calculations using these programs will bring safe and economical design.

② Floating construction work technology

Construction of an ultra-large floating structure, which is too large for any building dock to accommodate, requires that work to join the blocks afloat be done at sea. As the blocks are rocked by waves and other external forces, reliable and efficient joining techniques need to be established. To actually carry out the work at sea, various techniques such as those used to pull structures together, or for fastening, offshore joining, as well as underwater welding have to be established that are safe and reliable.

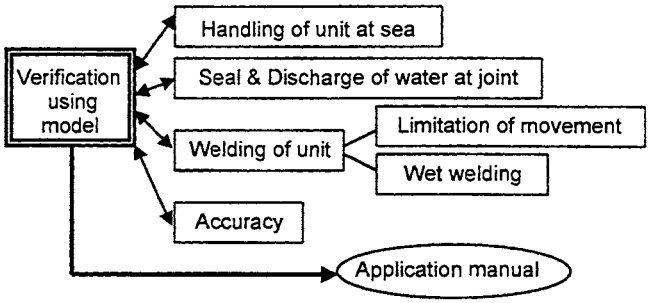

Construction procedures were thus established with verification done by actual joining sections together one by one.

③ Ultra long service duration technology

Various methods are conceivable to make floating structures durable enough to withstand continued use for very long periods, perhaps of even 100 years or more. In this project, research was conducted on applications of new anti-corrosive materials and maintenance techniques involving the combined use of a monitoring system for early detection of damage and a damage repair system.

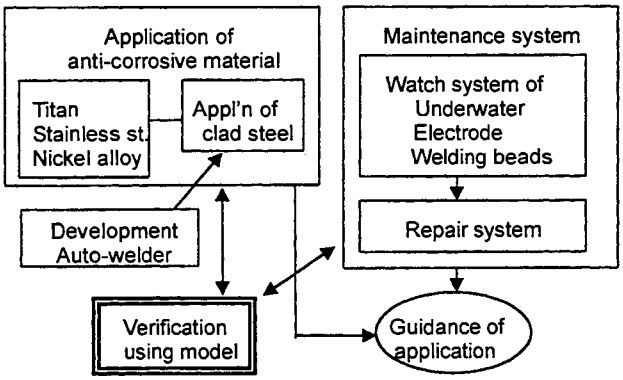

In order to be able to maintain the floating structure for over one hundred years, developments were achieved in methods of applying anti-corrosive material and for the maintenance system of floating steel structures.

④ Operational function ensuring technology

Mega-Float structures intended for use as artificial foundations are required to carry a wide variety of facilities. They must be able to provide the same level of performance as land foundations. Consequently, the floating structures need to be equipped with suitable means to control movement, oscillation, noise and other factors. A number of specific types of facilities were studied as examples, and the functions required for each type were identified. Devices to ensure proper performance of those functions were developed, and demonstration tests using the floating model were conducted to establish systems needed to verify performance.

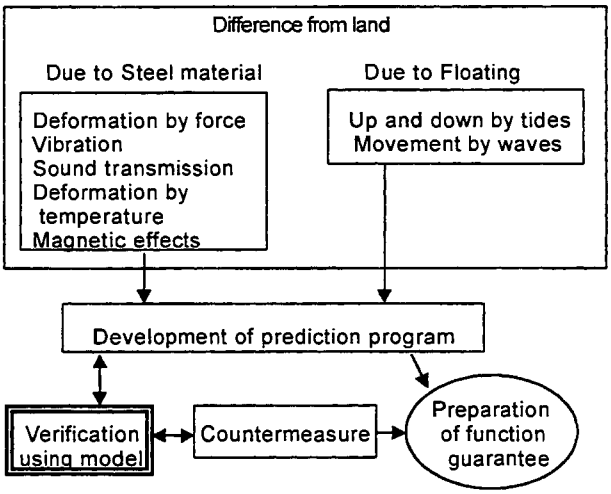

Simulation calculations have been used to predict movement, vibration, noise, temperature deformation, magnetic effects, and the like on floating structures, and some measures prepared to counter the excessive ones.

⑤ Environmental impact assessment technology

Although it is generally thought that floating structures have relatively little impact on the environment, this assumption needs to be verified in order to win public confidence in their use. Such verification requires the development of specific technologies to assess the effect of floating structures on the environment. For example, techniques are needed to predict changes in water flow around floating structures. The impact of large floating structures on the surrounding ecosystem has also to be estimated on the basis of studies conducted using models and demonstration tests at sea.

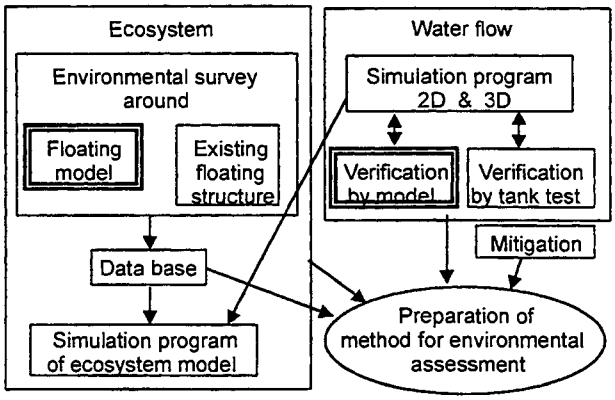

It has been confirmed by the results of environmental examinations of sea areas around the model and existing floating structures that floating structures do not prevent water flow and gives less impact, as its results, on the ecosystem around the floating body. Some methods for environmental assessment have been developed, and various kinds of data have been collected and prepared to assist in such assessments.

4. PHASE II RESEARCH INTO MEGA-FLOAT

(1) Outline of the Research

Phase II of the research into Mega-Float consists of studies of unresolved questions examined by the Airport Utilization Investigating Group mentioned in section 2.

This research consists of corroborative experiments requiring a large-scale model on which aircraft can take-off and land. However, the research also requires that the model be built within a limited budget and that a significant amount of research be undertaken. Although

TRAM expressed concerned about the appropriate size of the model, it finally decided to perform an experiment using a model which is essentially almost the same size as existing small commuter airports.

Dimensions of the airport model are:

Length:	1,000 m
Breadth:	60 m (partially 121 m)
Depth:	3 m
Draft:	1 m
Total area:	8.4 ha
Runway:	900 m x 25 m

A rough sketch of the model is shown in Fig. 3.

Phase II research includes the technical field of airport functions for which the participating companies do not have adequate expertise. Moreover, many kinds of clearances, approvals and licenses are required by various government departments and agencies in order to fly aircraft in corroborative tests. Consequently, Phase II must clear more and higher hurdles than those in Phase I.

(2) Research Schedule

This research was started in April 1998 under a three year schedule. Design work on the airport model was begun immediately followed by construction. The model is scheduled to be completed by the end of September 1999. Experiments regarding landing instruments using aircraft will be carried out from October 1999. Tests of actual take-off and landing of aircraft on the model is scheduled for summer and autumn of the year 2000.

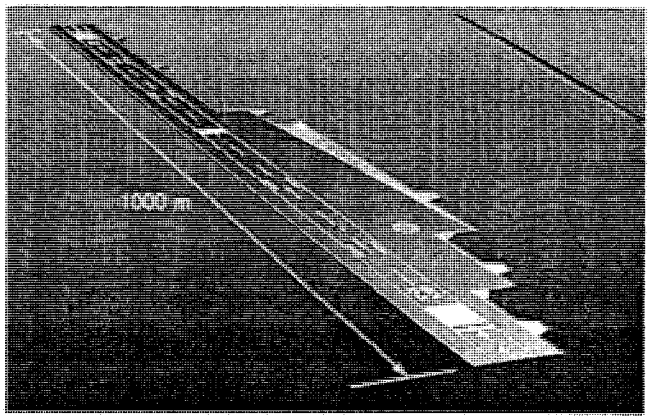

Fig. 3 Rough sketch of experimental model

(3) Contents of the research

The major research utilizes an actual model airport. The content of the research is as described below and is schematically illustrated in Fig. 4.

① Research on airport facilities

The facilities used on the floating airport will be required to have all the functions of a normal airport. To satisfy these requirements, it will be necessary to develop some new facilities. This research aims to develop these facilities and then to confirm their functioning with the airport model or a laboratory model.

② Research on simulation programs

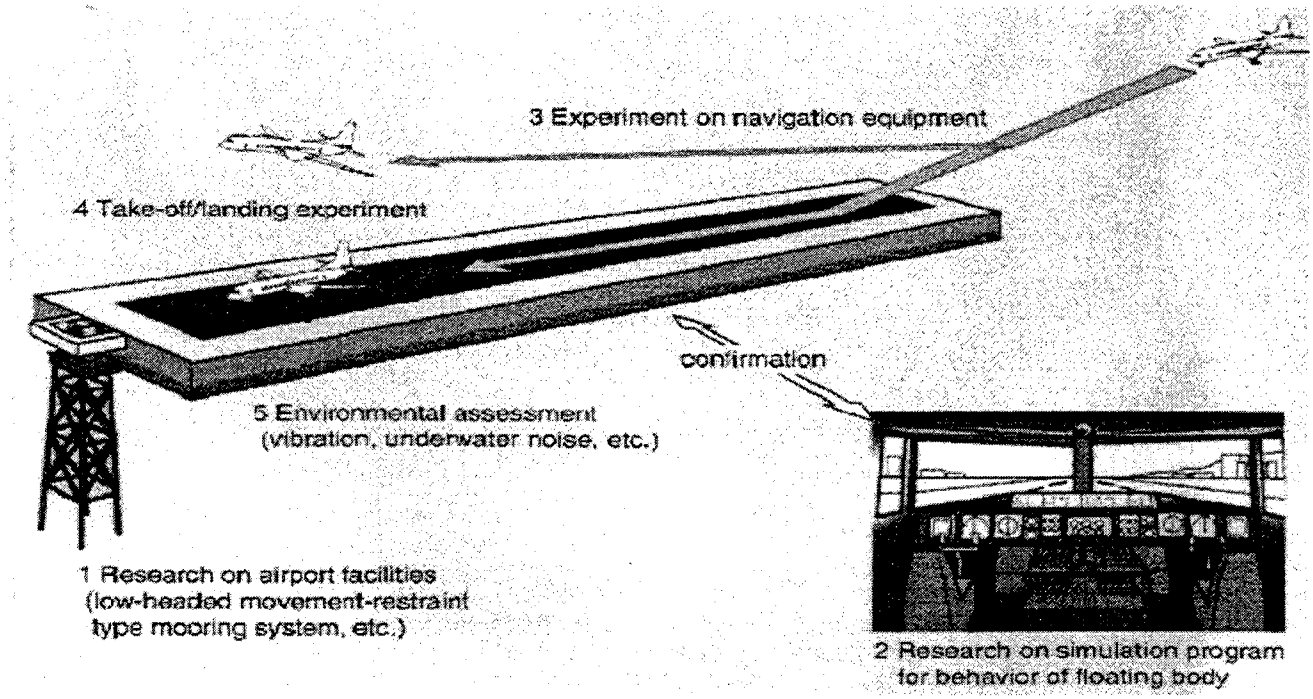

Fig. 4 Illustration of Phase II research

This research consists of developing a computer program capable of simulating the movements of the attached portions of the landing devices on Mega-Float, thereby achieving a simulation which will be accurate no matter how large the Mega-Float airport is. Furthermore, this research will be used to verify whether or not the program thus developed can correctly simulate the airport model of 1,000 m built for this phase of the research.

③ Experiment on navigation equipment for landing

It will be necessary to provide the floating airport with instrumental landing systems for safe operations. When the installation positions of these systems, which instruct an appropriate approach angle to an aircraft, are displaced slightly up and down by deflection or movement of the floating body, the influence due to the angle changing may be unexpectedly greater as distance increases. This research will include corroborative tests to confirm the performance of such devices, which are affected by the behavior of the floating body, while flying an actual aircraft in a low-pass manner, that is, in preparation for actual landing, and then causing the aircraft to climb.

④ Take-off and landing experiments

The behavior of the floating body can be grasped by simulation calculations. Results of calculations thus far suggest that no problems should arise when aircraft take off or land. Thus, this phase of the research will include corroborative take-off and landing tests, verification of the test results obtained, and serve as a basis for gathering necessary data for the actual Mega-Float airport.

⑤ Research on environmental impact assessment

Continuing from Phase I, this phase of the research is intended to obtain and store environmental data on areas surrounding the airport model in order to improve the accuracy of assessments of the impact the airport model on the environment. It will also include research into organisms adhering to the floating structure, and the relationship between the sound generated by the airport and fish in the vicinity.

6. FUTURE DEVELOPMENTS

Although this research project has been allocated a sizeable subsidy, other funds have also been provided from the operating resources of the private companies participating in TRAM despite the severe economic conditions currently prevalent in Japan. Expectations for future development are large, and this phase of research will not be an end the research project itself. All the TRAM participants recognize the importance of linking research with business. Considering that such a Mega-Float structure might perform some role in future shipbuilding and steel manufacturing industries, this research project might come to have a significant bearing on the future of the industry. When considering this point, this association has a large responsibility. However, TRAM has only limited man-power, and it is essential to have continued assistance from related groups including governmental, educational and industrial organizations. From the viewpoint that this research can only obtain full results with the cooperation of related parties, it is important to secure as much cooperation as possible, and TRAM is hoping to achieve good results through such cooperation.

In addition, the way of thinking of the present airport facilities and the standard specification are directed toward onshore-use, so it is important that they also be applied to a floating airport, as well. Accordingly, it will be necessary for the results obtained from Phase II of this research be utilized to set up a new standard. For this reason, it is important that the Japan Civil Aviation Bureau and the International Civil Aviation Organization (ICAO) evaluate the results of the research into Mega-Float.

The airport model of 1,000 m in length will be a giant floating structure and one of the actual results of the Mega-Float project. It will then be expected to serve as a significant towards putting the Mega-Float concept to practical use.

ACKNOWLEGEMENTS

The author would like to take this opportunity to convey his sincere gratitude to the Ministry of Transport and The Nippon Foundation for many kinds of assistance provided by them during the course of this research. At the same time, extensive support has also been received from numerous persons and organizations concerned with the Mega-Float research project. Thank you.

PROCEEDINGS OF THE THIRD INTERNATIONAL WORKSHOP ON VERY LARGE FLOATING STRUCTURES
(VLFS '99), VOL. I, EDS. R.C. ERTEKIN & J.W. KIM, 22-24 SEPTEMBER 1999, HONOLULU, HAWAII, USA

THE RANDOM AND DETERMINISTIC DYNAMICS OF "ROGUE WAVES" IN UNIDIRECTIONAL, DEEP-WATER WAVE TRAINS

A. R. Osborne
*Università di Torino, Italy**

ABSTRACT

"Rogue," "freak" or "giant" sea waves have been reported in a wide variety of contexts and studied from many points of view in recent years. In some sense one might agree that these waves may be "generic" and the availability of an analytical theory to explain their behavior could be quite useful. Here I provide new perspective on the nonlinear wave dynamics for this problem in the particular case of unidirectional wave propagation. My results are based upon the well-known nonlinear Schroedinger equation which governs the space/time dynamics of narrow banded, deep water wave trains to leading order in cubic nonlinearity. I use the nonlinear Fourier formulation of the inverse scattering transform (IST) to provide new insight into the behavior of "rogue" waves which are here assumed to arise due the Benjamin-Feir instability. I give a physical explanation of these phenomena in terms of their deterministic and random dynamics and provide a number of examples of simple "rogue wave" behavior.

1. INTRODUCTION

Rogue waves (also called freak or giant waves) are extreme wave events which have been reported a large number of times in ship's logs and in the scientific and popular literature. Waves of this type have been observed to have many of the following properties [1-3]:

(1) Reports of rogue waves generally occur in rough sea conditions. Their occurrence is likely to be sporadic and they are not likely to be present in many sea states.

(2) Their occurrence is not necessarily governed by the same probability laws which govern "normal" gaussian wave trains [1]. The likelihood of a rogue occurring is evidently rather small in any particular sea state and there is an even smaller likelihood of measuring one at a particular spatial location.

(3) Some sea states tend to have many rogue waves, while others have none at all (which may be the most common situation).

(4) A rogue wave tends to be the largest wave in a packet of (typically) three waves in number.

(5) Rogue waves are occasionally accompanied by "holes", i.e. deep troughs which occur before/after the largest crest. A number of shipboard observers have reported first sailing into deep troughs and then subsequently experienced severe damage as a following immense crest crashed down upon them.

It goes without saying that a list of the type just given may be biased and probably depends strongly on whether a particular observer was on board a ship at the moment when one of these "giant" waves occurred. While these observations are far from being scientifically rigorous or complete, they provide some notion as to what is available in ship's logs and in the literature.

The present paper offers a number of new perspectives which may help focus future research in this interesting frontier area of oceanography and ocean engineering. The present research emphasizes the role of a particular nonlinear water wave equation, the nonlinear Schroedinger equation, and its physical properties. Other areas of rogue wave research based on (for example) caustics and related linear approaches [3] are outside the scope of the present work. The advantage of the method given herein is the explicit analytical prediction of rogue wave dynamics and their properties.

The present work is indicative of a broad attack on the subject of rogue wave dynamics which is being conducted at the Department of Physics at the University of Torino. The areas of research are: (1) *Experimental studies of North Sea surface wave dynamics* in collaboration with a number of offshore industry participants. (2) Experimental studies of rogue waves being conducted in a number of *wave tank facilities* in Europe and in the United States. (3) *Numerical studies* being conducted in both 1 + 1 dimensions and in 2 + 1 dimensions on the nonlinear Schroedinger equation, the

*Dipartimento di Fisica Generale, Università di Torino, Via Pietro Giuria 1, 10126 Torino, Italy. E-Mail: osborne@ph.unito.it

extended order nonlinear Schroedinger equation, the Zakharov equation and the Euler equations. (4) *Theoretical studies*, based upon the inverse scattering transform, for characterization of the behavior of rogue wave dynamics and their integrable behavior. (5) And, finally, the development of *new time series analysis algorithms* for the analysis of measured deep water wave trains; in this approach the rogue wave is only one of many types of nonlinear Fourier components.

Herein I give a number of new mathematical results for the behavior of nonlinear, random wave trains: (1) deep water wave trains may be *spectrally* divided into both *stable* and *unstable* nonlinear modes. (2) The stable modes may be viewed as the *gaussian* or *near gaussian* contribution to the sea state. (3) The "unstable" modes can grow periodically by factors of 2 to 4 in wave height above the gaussian contribution and hence are candidates for "rogue" waves. (4) I provide new analytical solutions for the dynamics of deep water waves and show that the "rogue" solutions are a new kind of wave packet which is "homoclinic" in its mathematical structure. (5) A "rogue" solution normally stays hidden beneath the background gaussian sea state, unobservable to the naked eye, but then occasionally rises up to 3 to 4 times the local H_s, where it remains for awhile, and then subsequently subsides below the background waves; the appearance of these solutions is periodic (or quasi periodic) in time.

There are a number of historical perspectives which lay the groundwork for this paper. The study of nonlinear deep-water wave dynamics has undergone dramatic progress over the last 40 years. In the early 1960s Zabusky and Kruskal [4] discovered the soliton in shallow water numerical simulations. This breakthrough led to the important discovery of the inverse scattering transform (IST), a new method of mathematical physics [5]. Since that time a number of monographs have been written [6-9]. Zakharov [10] discovered the equation which is now named after him and also found a reduced equation which is known as the nonlinear Schroedinger equation (NLS). The NLS equation has received considerable attention by wave researchers due primarily to its simplicity (it contains nonlinear effects only to leading cubic order) and to its integrability using the inverse scattering transform [11].

The major focus of this paper is to discuss an *analytical theory* for certain solutions to the NLS equation using the *periodic* inverse scattering transform [12]. Simple formulas are found for the unstable modes (the "rogue waves") and I discuss how to use these modes to make a nonlinear spectral decomposition of deep water wave trains. The simple mathematical nature of the unstable solutions of the NLS equation has come as a surprise in the present research. I have been tempted to call these solutions "rogue waves" not because they fully describe all oceanic conditions, but because they intriguingly describe so many of the properties often attributed to oceanic rogue waves.

2. THE NLS EQUATION AS A NONLINEAR MODEL OF DEEP WATER WAVE TRAINS

The nonlinear Schroedinger equation is given by [10, 11, 13]:

$$\boxed{i(\psi_t + C_g\psi_x) + \mu\psi_{xx} + \nu|\psi|^2\psi = 0} \qquad (1)$$

For reasons made clear below I call this the *space NLS equation* (sNLS). The constant coefficients are given by:

$$C_g = \frac{1}{2}\frac{\omega_o}{k_o} = \frac{1}{2}\frac{L_o}{T_o}; \qquad \mu = \frac{\omega_o}{8k_o^2}; \qquad \nu = \frac{1}{2}\omega_o k_o^2;$$

The parameter

$$\lambda = \sqrt{\frac{\nu}{2\mu}} = \sqrt{2}k_o^2$$

is important in the inverse scattering transform formulation, which is discussed below. Here the subscript "o" subscripts refer to the *carrier wave* which is modulated by the function $\psi(x,t)$: ω_o is the carrier wave frequency, k_o is the wave number, while L_o, T_o are the carrier wave length and period, respectively. The sNLS equation describes the space/time dynamics of the *complex envelope function*, $\psi(x,t)$, of a deep water wave train which propagates in the $+x$ direction as a function of time, t. This equation solves the *Cauchy problem*, i.e. given the complex envelope at some initial time $t=0$, $\psi(x,0)$, equation (1) evolves the dynamics for all space and time, $\psi(x,t)$. The formulation of the sNLS equation is appropriate for the *space series analysis* of data whose behavior is assumed to be approximated by $\psi(x,0)$. Space series measurements are most appropriately obtained by *remote sensing technology*.

The *sea surface elevation*, $\eta(x,t)$, is computed from the complex envelope function, $\psi(x,t)$, in the following way:

$$\eta(x,t) = \psi(x,t)e^{i(k_o x - \omega_o t)} + c.c.$$

where "c.c." denotes complex conjugate. Thus the carrier $e^{i(k_o x - \omega_o t)}$ is modulated by the complex envelope,

$\psi(x,t)$, as determined by (1) for some chosen initial condition, $\psi(x,0)$.

2.1 The "Time" NLS Equation and its Relation to Physical Experiments

At leading order in nonlinearity in equation (1) we have

$$\psi_t + C_g \psi_x \equiv 0$$

so that $\psi_x \equiv -\psi_t / C_g$ and $\psi_{xx} \equiv \psi_{tt} / C_g^2$. When these are used in the lower order terms in (1) we obtain the *time NLS equation* (tNLS):

$$\boxed{i(\psi_x + C_g' \psi_t) + \mu' \psi_{tt} + \nu' |\psi|^2 \psi = 0} \qquad (2)$$

where

$$C_g' = \frac{1}{C_g} \qquad \mu' = \frac{\mu}{C_g^3} \qquad \nu' = \frac{\nu}{C_g} \qquad (3)$$

The inverse scattering transform parameter has the form:

$$\lambda' = \sqrt{\frac{\nu'}{2\mu'}} = C_g \sqrt{\frac{\nu}{2\mu}} = C_g \lambda \qquad (4)$$

Solutions to tNLS (2) are related to solutions of sNLS (1) by the simple transformation

$$\begin{aligned} &x \to t; \qquad t \to x; \qquad \lambda \to \lambda'; \\ &C_g \to C_g'; \qquad \nu \to \nu'; \qquad \mu \to \mu' \end{aligned} \qquad (5)$$

Thus the space (1) and time (2) NLS equations are related by a simple change of variables and parameters (5). Physically the tNLS equation (2) solves a *boundary value problem*: Given the solution on the boundary, $\psi(0,t)$, the space/time dynamics of (2) determine the solutions over all space and time, $\psi(x,t)$. Equation (2) is thus suitable for the *time series analysis* of measured wave trains presumed to be approximated by the boundary function $\psi(0,t)$. Time series observations are typically obtained by *in situ instrumentation* located at the spatial position $x = 0$.

2.2 An Adimensional Form of the NLS Equation

The simple transformation

$$\begin{aligned} &u = \lambda \psi; \qquad T = \mu t; \\ &X = x - C_g t \end{aligned} \qquad (6)$$

allows (1) to be put into adimensional form. The adimensional *space NLS equation* arises

$$\boxed{iu_T + u_{XX} + 2|u|^2 u = 0} \qquad (7)$$

This simple form of sNLS is often used for mathematical convenience. Note that the field $u(x,t)$ is that "seen" by the inverse scattering transform. It consists of the physical field $\psi(x,t)$ multiplied by λ, thus providing the motivation for emphasizing the important parameter λ in the context of nonlinear Fourier analysis. This observation is essential when applying IST to nonlinearly Fourier analyze measured wave trains.

3. SMALL AMPLITUDE MODULATION OF NLS

Yuen and coworkers [13] studied the NLS equation intensely, together with a number of other wave equations, to improve understanding of deep water wave trains. Their worked focused, in part, on numerical solutions of the NLS equation with periodic boundary conditions. They typically considered a lightly modulated sine (carrier) wave of the form:

$$\begin{aligned} &\eta(x,t) = \\ &= a[1 + \varepsilon \cos(Kx - \Omega t)] \cos\left[k_o x - \omega_o\left(1 + k_o^2 a^2 / 2\right)t\right] \end{aligned}$$

The carrier wave has amplitude a, wave number k_o and frequency ω_o; note the Stokes wave correction to the carrier frequency, $k_o^2 a^2 / 2$. The small modulation amplitude is ε, the modulation wave number is K and its frequency is Ω, with the dispersion relation:

$$\Omega^2 = \frac{\omega_o^2}{8k_o^2}\left(\frac{K^2}{8k_o^2} - k_o^2 a^2\right) K^2$$

This expression shows that the wave train is *unstable* if the modulation wave number K lies in the range

$$0 < K < 2\sqrt{2} k_o^2 a$$

and *stable* if it lies outside this range. Thus the modulated wave train $\eta(x,t)$ can undergo exponential growth provided we choose K in the interval $0 < K < 2\sqrt{2} k_o^2 a$. This was the essence of the early Yuen, et al work, i.e. the experimental and numerical study of the long time evolution of $\eta(x,t)$ for many unstable cases. An example of the simplest case is shown in Fig. 1, where a single unstable mode grows

from a small modulation to a high peak which then disappears, only to reappear periodically in time thereafter. Higher order mode numbers, say N, were found to result in N peaks simultaneously appearing at a particular time, t, in the simulation.

4. NONLINEAR SPECTRAL DECOMPOSITION OF DEEP WATER WAVE TRAINS

I provide in Appendix I a simple overview of the IST *spectral decomposition of deep water wave dynamics.* The following theorem results (in the hyperelliptic function representation of the IST):

Nonlinear Fourier Analysis Theorem: The Nonlinear Spectral Decomposition of Deep Water Wave Trains

All solutions of the NLS equation can be decomposed into two fundamental kind of wave modes, *stable* and *unstable*. The stable modes are *modulationally stable* to perturbations of their envelope functions. The unstable modes are instead *modulationally unstable* in the Benjamin-Feir sense. Formally, the following nonlinear Fourier decomposition holds for all solutions of the sNLS equation:

$$\psi(x,t) = \psi_{stable}(x,t) + \psi_{unstable}(x,t) + \psi_{\substack{Nonlinear \\ Interactions}}(x,t)$$

Note that this is a simple linear superposition law, although the mathematics, and the inclusion of the *nonlinear interaction term*, implies *nonlinear dynamics.* Formally speaking the terms $\psi_{stable}(x,t)$ and $\psi_{unstable}(x,t)$ can be represented as *linear superpositions of stable and unstable modes* of NLS.

Let us look at the significance of this theorem. First, consider the simple *linear limit* for *small wave amplitudes*. In this case the unstable modes and nonlinear interactions disappear, leaving only the stable modes which, in the linear limit, become sine waves. Thus the linear limit of the hyperelliptic function representation reduces to a *linear superposition of sinusoids*. Clearly, the linear limit of the above theorem provides us with familiar linear Fourier analysis. In this way we see that the above *Theorem provides us with a tool for generalizing Fourier analysis to nonlinear wave motions.*

Consistent with the above Theorem we find that a *complex sea state* would normally consist of a *large number of stable modes* which are only "slightly nonlinear" (and presumably described by the Pierson-Moskowitz or JONSWAP power spectra) plus a relatively *small number of unstable modes* which are here described as "rogue waves." It is clear that this perspective provides a scenario in which the *unstable extreme wave events are individual distinct kinds of discrete wave form* which only occasionally rise up out of the near gaussian background periodically (or quasi-periodically) in time. Clearly these "rogues" have different statistical properties than do the background gaussian waves. These conclusions may well be the most important of the present paper. The explicit formulae for "rogue" modes given below, however, are also highly relevant for engineering design purposes.

As noted in the theorem above $\psi_{stable}(x,t)$ and $\psi_{unstable}(x,t)$ are represented as linear superpositions of stable and unstable modes (Appendix I, II). What are these fundamental nonlinear modes of IST? The *stable modes* are ordinary *dn* elliptic functions (small amplitude, modulated Stokes waves) for the wave envelope (I leave their derivation as an exercise to the reader). The *unstable rogue modes* are however substantially more complex, are the major focus of this work, and are discussed in Appendix II and the rest of this paper.

5. FORMULAS FOR ROGUE WAVES

The simplest unstable mode is (as I fondly call them) the *rogue wave solution* to (7) (corresponding to a single, double-point eigenvalue in the IST spectrum) which is given by (see Appendix II):

$$u(X,T) = \\ = a\left[\frac{\cos[\sqrt{2}aX]\mathrm{sech}[2a^2T] + i\sqrt{2}\tanh[2a^2T]}{\sqrt{2} - \cos[\sqrt{2}aX]\mathrm{sech}[2a^2T]}\right]e^{2ia^2T} \quad (8)$$

A mathematician might refer to (8) as a "homoclinic soliton." I am not a mathematician and therefore have a different perspective. I, instead, refer to (8) as the simplest prototypical *rogue wave* because: (1) its dynamics are such that for $t \to -\infty$ the *plane wave behavior*, $u(X,T) = ae^{2ia^2T}$, dominates the motion (see additional perspective below). Thus, far enough back in time the wave is completely hidden beneath the background carrier wave. (2) As $T \to 0$ the solution (8) rises up to its maximum height, $\sim 2.4a$, and then slowly subsides below the carrier again. Fig. 1 shows the space time dynamics of this simple wave solution; here I graph the modulus of (8), $|\psi(x,t)|$, as a function of space and time. Fig. 2 shows a graph of (8) as a function of space, X, shortly before $T = 0$; this result emphasizes the complex nature of the solution. This new type of wave form, a "rogue" wave, lies hidden beneath the carrier wave for most of its entire lifetime and then rises up to its full glory near a particular time

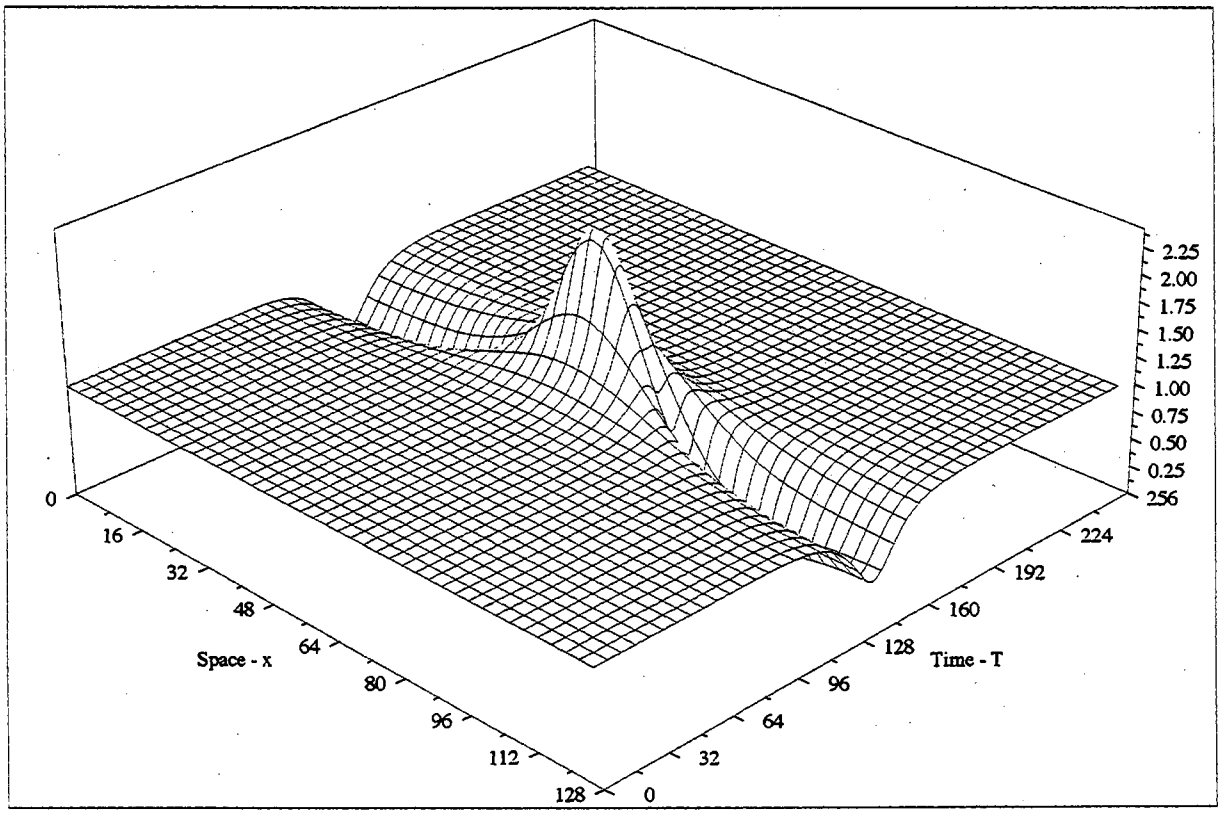

Figure 1. Graph of the modulus of the space/time evolution of the simplest "rogue wave" solution to the sNLS equation given by equation (8).

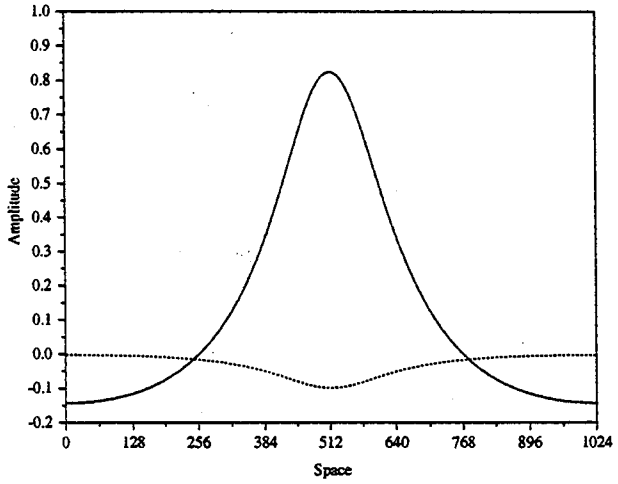

Figure 2. Graph of the simplest "rogue" wave solution (8) of the sNLS equation (7) for a time shortly before the maximum height in the wave evolution. The solid line is the real part of (8) while the dotted line is the imaginary part.

T. It then disappears below the background carrier wave for larger times. There is an infinite class of "sister" solutions to (8), which may be written in terms of Jacobian elliptic functions, that describe other (larger and smaller) "rogue waves"; typically these solutions are characterized by periodic (or quasi periodic) behavior in time and hence have somewhat more complicated behavior than do their simpler counterpart (8): These "generalized rogue waves" remain hidden in the carrier wave background while occasionally rising up to their maximum heights in a temporally periodic (or quasi-periodic) fashion.

5.1 Dimensional Rogue Wave for the Space NLS equation

Use (6) in (8) and set $A = a/\lambda$ to find the *dimensional form of the space rogue wave solution*:

$$\psi(x,t) = A\left[\frac{\cos[\sqrt{2}\lambda A(x-C_g t)]\mathrm{sech}[2\lambda^2 A^2 \mu t] + i\sqrt{2}\tanh[2\lambda^2 A^2 \mu t]}{\sqrt{2} - \cos[\sqrt{2}\lambda A(x-C_g t)]\mathrm{sech}[2\lambda^2 A^2 \mu t]}\right] e^{2i\lambda^2 A^2 \mu t} \tag{9}$$

This is a solution of the *Cauchy problem* so that $\psi(x,0)$ is the fundamental "initial" condition (see discussion below). Eq. (9) is appropriate for comparing to *space series data.*

5.2 Dimensional Rogue Wave for the Time NLS equation

Using (5) in (9) we have the *time rogue wave solution*:

$$\psi(x,t) = A\left[\frac{\cos[\sqrt{2}\lambda A(x-C_g t)]\operatorname{sech}\left[2\frac{\lambda^2A^2\mu}{C_g}x\right]+i\sqrt{2}\tanh\left[2\frac{\lambda^2A^2\mu}{C_g}x\right]}{\sqrt{2}-\cos[\sqrt{2}\lambda A(x-C_g t)]\operatorname{sech}\left[2\frac{\lambda^2A^2\mu}{C_g}x\right]}\right]e^{2i\frac{\lambda^2A^2\mu}{C_t}x} \tag{10}$$

This is a solution of the *boundary value problem* so that $\psi(0,t)$ is the fundamental condition. Eq. (10) is appropriate for the study of *time series data.*

Another way to get (10) is to use $x \cong C_g t$ directly in (9). Eq. (10) is easier to derive in this way, but the derivation given above relates all the parameters to the original space and time equations (1), (2) and hence is useful for nonlinear Fourier analysis purposes.

5.3 Maximum Height of a "Rogue Wave

What is the height of a "rogue wave"? For (8), at $t=0$, we have spatial variation of the wave at its fullest height:

$$u(X,0) = \frac{a\cos[\sqrt{2}aX]}{\sqrt{2}-\cos[\sqrt{2}aX]} \tag{11}$$

Clearly (11) is a periodic function of X. I graph $|u(X,0)|$ in Fig. 3.

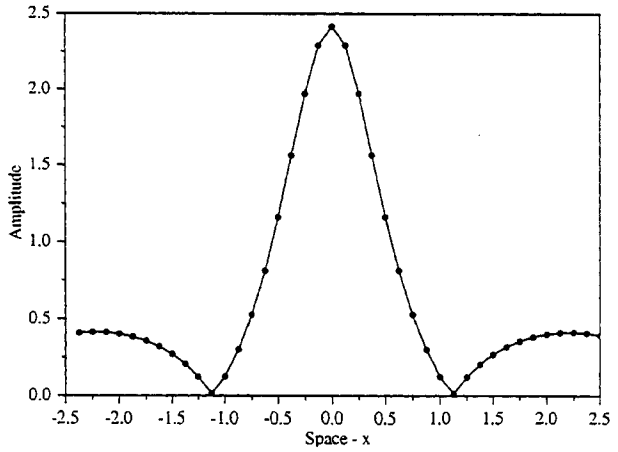

Figure 3. Example of a rogue wave as a periodic function of the spatial variable, X.

Clearly the maximum amplitude of the "rogue" wave is given by

$$u_{\max}(X=0) = \frac{a}{\sqrt{2}-1} \sim 2.42a$$

The *maximum wave height of the modulated carrier wave* is then given by

$$H_{RogueWave} = 2u_{\max} = \frac{2a}{\sqrt{2}-1} \sim 4.83a \tag{12}$$

Therefore, a simple modulated wave train of height $2a$ will have a maximum "rogue" wave height of $\sim 4.83a$ at some particular time ($t=0$ in the present normalization). Thus we have a factor of 2.4 in wave height enhancement (above the height of the background carrier wave) due to the nonlinear dynamics of the Benjamin-Feir instability. As discussed above there are an infinite number of "sister" solutions of (8), some of which can give smaller, others of which can give larger amplitude enhancements. Thus (12) can only be "representative" of the true height enhancement of a particular generalized "rogue wave" mode in the IST spectrum.

5.4 Form of Rogue Waves as $T \to -\infty$

In order to see what all this means, let's take a look at the form of the rogue solution (8) as $T \to -\infty$. For times far in the past note that $\tanh(2a^2T) \sim -1$ and set $\varepsilon = \operatorname{sech}(2a^2T) << 1$, then get

$$u(X, T\to-\infty) = a\left[\frac{\varepsilon\cos[\sqrt{2}aX]-i\sqrt{2}}{\sqrt{2}-\varepsilon\cos[\sqrt{2}aX]}\right]e^{2ia^2T}$$

Expand this in a Taylor series in terms of the small parameter ε and find:

$$u(X,T\to-\infty) \sim -ia\left[1+\frac{\sqrt{2}(1+i)\varepsilon}{2}\cos(\sqrt{2}aX)\right]e^{2ia^2T} \tag{13}$$

This expression is quite instructive from several points of view. First note that the multiplying factor $-i$ is just an arbitrary phase, $\exp[-i\pi/2]$, which can be neglected here (since all solutions of NLS are correct to within an arbitrary constant phase). Equation (13) may be interpreted as a plane wave which is "initially" modulated by the term in square brackets. In this way a single, double-point appears in the IST spectrum provided that one modulates the initial wave train with a small-amplitude wave of the form:

$$1+\frac{\sqrt{2}(1+i)\varepsilon}{2}\cos(\sqrt{2}aX)$$

The modulation amplitude has *equal real and imaginary parts* given by

$$\frac{\sqrt{2}\varepsilon}{2} = \frac{\sqrt{2}\,\mathrm{sech}(2a^2T)}{2}$$

and the wave length of the modulation is given by the formula

$$L = \frac{2\pi}{\sqrt{2}a}$$

The initial modulation amplitude, ε, fixes the time scale of T in the problem and hence determines the time T_{max} at which the maximum in the rogue wave occurs via the relation $\varepsilon = \mathrm{sech}(2a^2T)$. Thus the rogue wave reaches a maximum height at

$$T_{max} = \frac{\mathrm{sech}^{-1}(\varepsilon)}{2a^2}$$

provided that it is modulated initially (for times far in the past) as in (13).

6. CONCLUSIONS

An analytical study of rogue wave properties has been made based upon exact spectral solutions of the NLS equation which describes the nonlinear evolution of deep water wave trains. Future efforts will focus upon a complete characterization of these types of solutions and their incorporation as spectral components in time series analysis algorithms.

Acknowledgment: The Consortium provided valuable financial aid. I thank Tom Swean of the Office of Naval Research for his continued support. I also thank Statoil for its valuable collaboration and supportive efforts. Italian University (CUN) funding also played an important supportive role. I thank Gene Remmers of the Office of Naval Research and Bob Taylor and Paul Palo of the Naval Facilities Engineering Service Center for providing support for research and for trips to MOB Meetings.

Appendix I - Nonlinear Spectral Decomposition Theorem

The solutions to the Cauchy problem for the adimensional sNLS equation (7) are now constructed using the inverse scattering transform for periodic boundary conditions in the hyperelliptic function formulation [12]. It is perhaps best to begin with the *spatial part* of the solution which is found by the following *trace formula*:

$$\partial_x \ln u(x,t) = 2i\left(\sum_{j=1}^{N-1}\mu_j(x,t) - \frac{1}{2}\sum_{k=1}^{2N}E_k\right) \qquad \text{(AI.1)}$$

By abuse of notation I have let $X \to x$ and $T \to t$ in (7).

Thus the spatial derivative of the logarithm of the solution $u(x,t)$ is constructed by the *linear superposition of the hyperelliptic functions*, $\mu_j(x,t)$, which are the nonlinear modes of the sNLS equation, *plus a contribution from the main spectrum eigenvalues*, E_k. This *linear superposition law* is remindful of linear Fourier analysis where one superposes ordinary sine waves. In the present case the hyperelliptic modes, $\mu_j(x,t)$, are fully nonlinear generalizations of sine waves which are the natural basis functions of the NLS equation itself. By itself (AI.1) is not sufficient to solve sNLS. One still needs the corresponding *temporal trace formula*:

$$\begin{aligned}\partial_t \ln u(x,t) &= \\ &= 2i\left(\sum_{j>k}E_jE_k - \frac{3}{4}\left(\sum_{k=1}^{2N}E_k\right)^2\right) \\ &-4i\left[\left(-\frac{1}{2}\sum_{k=1}^{2N}E_k\right)\left(\sum_{j=1}^{N-1}\mu_j\right) + \sum_{j>k}\mu_j\mu_k\right]\end{aligned} \qquad \text{(AI.2)}$$

Now all we need is the machinery to compute the hyperelliptic functions $\mu_j(x,t)$. The space/time evolution of the $\mu_j(x,t)$ is given by the following nonlinear, nonlinearly coupled ordinary differential equations:

$$\begin{aligned}\mu_{jx} &= \frac{-2i\sigma_j\sqrt{\prod_{k=1}^{2N}(\mu_j - E_k)}}{\prod_{m\neq j}(\mu_j - \mu_m)} \\ \mu_{jt} &= -2\left(\sum_{m\neq j}\mu_m - \frac{1}{2}\sum_{k=1}^{2N}E_k\right)\mu_{jx}\end{aligned} \qquad \text{(AI.3)}$$

In these equations the E_k are the *main spectrum eigenvalues* and the σ_j are the *Riemann sheet indices* (both assumed given). One solves (AI.3) for the $\mu_j(x,t)$ and then (AI.1) is used to determine the solution to NLS.

Now integrate (AI.1) over the spatial variable to get

$$\ln u(x,t) =$$

$$= 2i\left(\sum_{j=1}^{N-1}\int_0^x \mu_j(x,t)dx - \frac{1}{2}x\sum_{k=1}^{2N}\lambda_k\right) =$$

$$= 2i\sum_{j=1}^{N-1}\int_0^x \mu_j(x,t)dx - iKx$$

$$K = \sum_{k=1}^{2N} E_k$$

Here the symbol K has been used to represent a "wave number" which is constructed as a summation of the main spectrum eigenvalues. Also set

$$\mu_j'(x,t) = 2\int_0^x \mu_j(x,t)dx$$

so that

$$\ln u(x,t) = i\sum_{j=1}^{N-1}\mu_j'(x,t) - iKx$$

Take the exponential of this and get

$$u(x,t) = e^{-iKx+i\sum_{j=1}^{N-1}\mu_j'(x,t)}$$

$$\mu_j'(x,t) = 2\int_0^x \mu_j(x,t)dx$$

Now suppose the modes are *small in amplitude*. Then this latter expression can be written:

$$u(x,t) = e^{-iKx+i\sum_{j=1}^{N-1}\mu_j'(x,t)} \cong e^{-iKx}\left[1 + i\sum_{j=1}^{N-1}\mu_j'(x,t) + \ldots\right]$$

This looks like a classical superposition law, i.e. the wave field $u(x,t)$ consists of a linear superposition of nonlinear modes. Note that the modes are themselves complex and hence so too is $u(x,t)$.

The general superposition law can be written and interpreted in the following compact shorthand notation:

$$\boxed{u(x,t) = e^{-iKx}\left[1 + i\sum_{j=1}^{N-1}\mu_j'(x,t)\right] + u_{\text{int}}(x,t)}$$

where $u_{\text{int}}(x,t)$ are the interactions among the $\mu_j'(x,t)$ modes. Thus we have, essentially, a linear superposition of the spatially integrated hyperelliptic modes, $\mu_j'(x,t)$, plus their mutual nonlinear interactions, $u_{\text{int}}(x,t)$.

Appendix II - Derivation of Analytical Expression for the Simplest Rogue Wave

Let me now briefly outline the derivation of the rogue wave (8). Please note Fig. A.1, which shows the complex plane. In this plane I assume that the *carrier wave* has the eigenvalues $\pm iA$ (denoted by the black dots in the figure). Furthermore I assume that the main spectrum eigenvalues are given by $E_1 = iE$, $E_2 = iE$, $E_3 = -iE$ and $E_4 = -iE$; the Riemann sheet indices are taken to be $\sigma_1 = +1$, $\sigma_2 = +1$, $\sigma_3 = -1$ and $\sigma_4 = -1$. Note that these eigenvalues are here *degenerate*, i.e. equal for their values above (and below) the real axis. In Fig. A.1 the degenerate eigenvalues are denoted by small x's on the imaginary axis. The x's along the real axis correspond to *stable modes* which do not contribute to the spectrum in the present case, as these components have zero energy (by assumption). In this problem there are *two* hyperelliptic functions $\mu_1(x,t)$, $\mu_2(x,t)$.

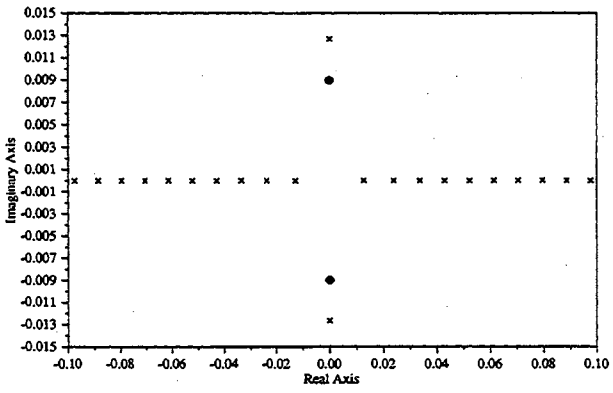

Figure A.1. Main spectrum eigenvalues for the simplest "rogue wave" solution of the sNLS equation.

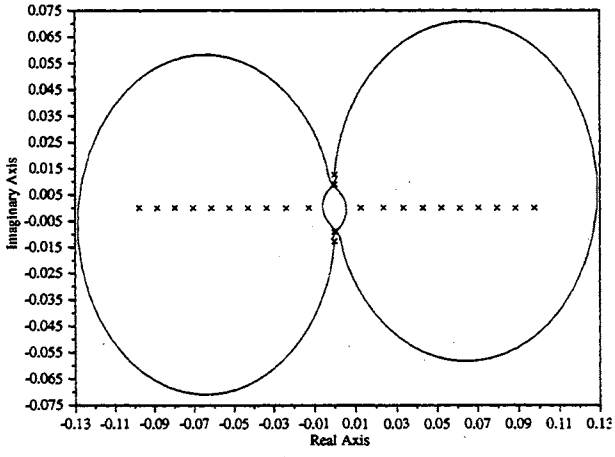

Figure A.2. Main spectrum eigenvalues for the simplest "rogue wave" together with the two hyperelliptic function orbits for the solution of the sNLS equation.

By analytically integrating (AI.3) I find analytic expressions for the hyperelliptic functions: in Fig. A.2 these are the two oval shaped orbits shown in the complex plane. Thus the spectral signature of a rogue wave in the inverse scattering transform spectrum consists of *degenerate imaginary eigenvalues* plus *large oval orbits* for the $\mu_j(x,t)$ variables. These orbital motions, when substituted into (AI.1) and (AI.2) give formula (8) for the simplest rogue wave.

References

[1] Haver, S. and D. Karunakaran, "Probabilistic Description of Crest Heights of Ocean Waves," *Proc. of the 5th Int. Workshop on Wave Hindcasting and Forecasting*, Melbourne, Florida, pp. 451-466, 1998.

[2] Von Bayer, H. C., "Catch the Wave,", The Sciences, May/June, pp. 10-13, 1999.

[3] Fornberg, B. and B. S. White, "On the Chance of Freak Waves at Sea,"*Journal of Fluid Mechanics*, Vol. 355, pp. 113-138, 1998.

[4] Zabusky, N. J. and M. D. Kruskal, "Shallow Water Waves, the Korteweg-deVries Equation and Solitons," Phys. Rev. Lett., Vol. 15, pp. 240-243, 1965.

[5] Gardner, C. S., J. M. Greene, M. D. Kruskal and R. M. Miura, "Method for Solving the Korteweg-deVries Equation," Phys. Rev. Lett., Vol. 19, pp. 1095-1097.

[6] Zakharov, V. E., S. V. Manakov, S. P. Novikov and M. P. Pitayevsky, Theory of solitons. The Method of the Inverse Scattering Problem, Nauka, Moscow, 1980.

[7] Ablowitz, M. J. and H. Segur, Solitons and the Inverse Scattering Transform, SIAM, Philadelphia, 1981.

[8] Dodd, R. K., J. C. Eilbeck, J. D. Gibbon and H. C. Morris, Solitons and Nonlinear Wave Equations, Academic Press, London, 1982.

[9] Newell, A. C., Solitons in Mathematics and Physics, SIAM, Philadelphia, 1985.

[10] Zakharov, V. E., "Stability of Periodic Waves of Finite Amplitude on the Surface of a Deep Fluid," Sov. Phys. J. Appl. Mech. Tech. Phys., Vol. 4, pp. 190-194, 1968.

[11] Zakharov, V. E. and P. B. Shabat, "Exact Thjeory of Two-dimensional Self-focusing and One-dimensional Self-modulation of waves in nonlinear media," Sov. Phys. JETP, Vol. 34, pp. 62-69, 1972.

[12] Kotljarov, V. P. and A. R. Its, Dopovidi Akad. Nauk. UkRSR., Ser. A, Vol. 11, pp 965-968, 1976 (in Ukrainian).

[13] Yuen, Y. C., "Recent Advances in Nonlinear Water Waves. An Overview.," in *Nonlinear Topics in Ocean Physics*, ed. by A. R. Osborne, North Holland (Elsevier), Amsterdam, 1991.

PROCEEDINGS OF THE THIRD INTERNATIONAL WORKSHOP ON VERY LARGE FLOATING STRUCTURES
(VLFS '99), VOL. I, EDS. R.C. ERTEKIN & J.W. KIM, 22-24 SEPTEMBER 1999, HONOLULU, HAWAII, USA

MEASUREMENT OF OCEAN SPATIAL COHERENCE BY SPACEBORNE SYNTHETIC APERTURE RADAR

Frank M. Monaldo
The Johns Hopkins University Applied Physics Laboratory *

ABSTRACT

Proposed Mobile Offshore Bases (MOBs) have dimensions that fall far outside the scope of conventional maritime design experience. There is consequently little experience in the interaction of such structures with the ocean surface waves likely to be encountered. Spaceborne synthetic aperture radar (SAR) offers a unique and rare perspective for the measurement of ocean waves on scales that may interact with these large MOBs. Is this paper we describe techniques that have been developed to measure wave "groupiness" and "long crestedness" using SAR. Results indicate that waves are more groupy and long crested then would be predicted on the basis of linear wave theory.

1. INTRODUCTION

Proposed Mobile Offshore Bases (MOBs) have dimensions that dwarf even aircraft carriers. Due to these large dimensions (1.5 km in length and 300 m in width), there is little experience in the interaction of such structures with the ocean surface waves likely to be experienced. In addition, MOBs will generally not be able outrun or avoid storms, so they may encounter more severe environments than faster and more mobile ships experience. The confident design of such structures requires the specification of wave field characteristics at these long spatial scales.

Ocean surface waves with crest lengths or wavelengths on the order of the MOB dimensions are likely to resonate with the structure. If ocean surface waves were linear phenomena and the phases of the individual wave components were independent and uniformly distributed, the two-dimensional ocean surface wave spectrum would be sufficient to confidently predict the probability of encountering such long waves. However, even weak nonlinearities can act over many cycles of long waves in such a way as to cause the probability of a particularly high or long-crested waves or group of waves to differ from linear predictions.

Two parameters of ocean wave spatial coherence are of particular interest in the design of large structures: wave "long-crestedness" and "groupiness." Long-crestedness is a measure of typical wave crest lengths. Very long-crested waves traveling perpendicular the long axis of an MOB will induce roll motions, while shorter crested waves will introduce torques. Wave groupiness is a measure of the probability that particularly large waves will be bunched together in sequence.

In this paper, we explain the spatial filtering, thresholding, and autocorrelation techniques, developed to measure long-crestedness and groupiness from SAR imagery. Results from the application of these empirical tools are shown. Of particular interest are results obtained from imagery in the vicinity of Hurricane Josephine acquired from a space shuttle-based SAR. We present evidence that waves are significantly more long-crested and "groupy" then would be predicted on the basis of linear wave theory. Quantitative estimates of wave long crestedness and groupiness are presented. In addition, we review prospects for the application of measurement tools to a full inventory of SAR imagery. Such measurements may prove important for the modeling of the interaction of waves with large MOB structures.

2. SAR WAVE MEASUREMENT

Ocean waves are typically measured at a single location as a function of time. However, assessment of the spatial coherence of waves requires measurement of the two-dimensional surface wave field. Spaceborne SARs offer important advantages in measuring spatial coherence:

1. Spaceborne SARs have sufficient resolution (typically from 25 m) to capture ocean wave patterns.

2. Spaceborne SAR image swaths are typically 100 km wide or larger, potentially providing a synoptic view of wave fields and the statistically significant wave parameters.

3. The global coverage of spaceborne SARs allows the acquisition of ocean imagery in the midst of storms.

*11100 Johns Hopkins Road, Laurel, MD 20723, E-Mail: Frank.Monaldo@jhuapl.edu

4. Considerable research over two decades has been devoted to delineating the capabilities and limitations of spaceborne SARs to image waves. There is now a maturity in our understanding of the SAR ocean wave imaging process.

The study of mechanisms for the SAR wave imaging goes back to 1977 with the general description of SAR imagery by Elachi and Brown [1]. Their approach, with a considerable refinement, remains valid today. Additional work by many others has filled in the gaps [2], [3], [4], [5].

According to Bragg scattering theory, the radar cross section in a SAR image is proportional to the roughness on the ocean surface at the radar wavelength projected on the surface. For near-nadir incidence (20° to 25°), the wave imaging is dominated by "tilt modulation" for range (cross-track) traveling waves. Specifically, the wave-induced modulation of radar cross section is proportional to the tilt or slope changes of the long ocean surface waves. There is high confidence in the ability of a SAR to faithfully image range-traveling waves.

The imaging of azimuth-traveling waves is more complex. Azimuth wave imaging is intrinsically tied to how a SAR image is formed [6], [7]. A SAR relies on Doppler information to achieve fine-scale azimuth resolution. As an azimuth-traveling wave propagates it advects the surface so that a component of the periodic wave orbital velocity is moving along the SAR line-of-sight. This causes the apparent azimuth positions of scatterers to be displaced in the SAR image. The periodic ocean wave motion moves scatterers in such a way as to concentrate and dilute the apparent density of the scatterers in the SAR image at the spatial frequency of the long waves. This renders azimuth-traveling waves visible in SAR imagery, and this imaging mechanism is known as "velocity-bunching."

The velocity-bunching effect is proportional to both the orbital velocities of the long waves and to R/V, where R is range from the SAR platform to the surface and V is the radar ground velocity. When the waves grow high and R/V is large, the azimuth shifts can become large enough to smear the image and significantly degrade the azimuth resolution.

The following expression is a useful guide to the magnitude of this effect:

$$\lambda_{\min} = \left[1\frac{\mathrm{m}^{1/2}}{\mathrm{s}}\right]\frac{R}{V}H_{\mathrm{s}}^{1/2} \qquad (1)$$

where $\lambda_{\min}$ is the minimum detectable azimuth wavelength and $H_{\mathrm{s}}^{1/2}$ is the significant wave height. Clearly the higher the sea state and the larger the R/V ratio, the larger the minimum detectable azimuth wavelength.

For a high altitude (800 km) SAR platform like ERS-1/2 or Radarsat, $R/V = 120$ s. The minimum detectable azimuth wavelength varies from 170 m to 380 m for significant wave heights from 2 m to an extreme 10 m. Thus, even under extreme conditions, high-altitude SARs should be able to image azimuth traveling waves at wavelengths that will resonate with MOBs.

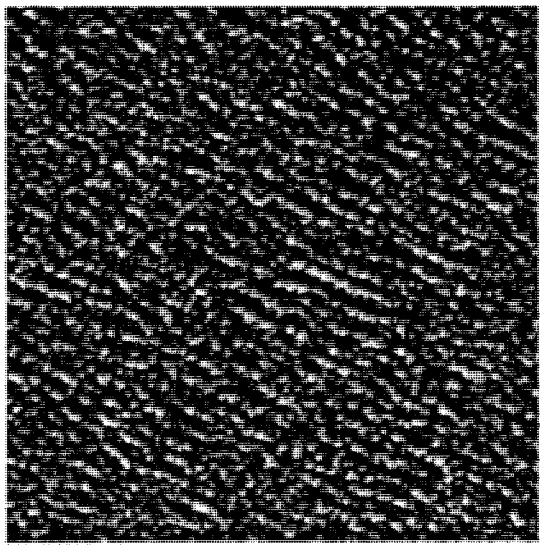

Figure 1: A portion of a SAR image of waves in Hurricane Josephine. The displayed sub-image size is 256 × 256 pixels or 3.2 × 3.2 km

SAR wave imaging at lower altitudes, such as the 200-km shuttle altitude, offer even more fidelity in wave measurement.

3. CREST LENGTH MEASUREMENT

One aspect of wave coherence is wave "long crestedness." To economically assess wave long crestedness requires the development of automated procedures that will produce long-crestedness parameters from image archives with minimal human intervention. Wave long-crestedness is intuitively easy to grasp, but difficult to precisely specify. We all know a long crested-wave when we see one, but can a specific, computer implementable description be agreed upon?

The problem of developing an automated procedure is even more difficult and amorphous when we ask the question "What is meant by long crested?" When does a crest cease to be a crest? What about a wave that has a modest crest length adjacent to another wave crest having the same phase? How close must two crests be to be logically considered as one?

Figure 1 is an example of an image from the SIR-B mission clearly showing the presence of waves.

The challenge of arriving at a statistical description of long wave crests is non-trivial. We present here a rigorous and repeatable procedure for identifying wave crests in imagery that is dependent on the discretionary

selection of only a few key parameters. The procedure allows for the repeatable identification and measurement of crests. Although a unambiguous formal definition of what is meant by long crestedness may exceed our grasp, it is definitely possible to compare observed long-crestedness with the long-crestedness which might be expected if ocean surface waves were purely linear. In this report, we describe a procedure to select and measure long waves, suggest useful parameters for the identification of wave crests, and apply such a procedure to a sample SAR image from the Shuttle Imaging Radar-B (SIR-B) mission.

The extraction of crest length statistics from SAR imagery involves two basic steps: (1) the filtering of a SAR image so that crests are conspicuously identified as separate "blobs," and (2) the measurement of crest length from these blobs.

3.1 Wavenumber Domain Filtering

The first step is to Fourier transform SAR image intensity so that filtering can be applied in the wavenumber domain. Let $I(x, y)$ represent SAR image intensity as a function of range, x, and azimuth, y, position. We represent the Fourier transform of I by $F(k_x, k_y)$ where k_x and k_y are range and azimuth wavenumber, respectively. Specifically, we write

$$F(k_x, k_y) = \mathcal{F}\{I(x, y)\} \tag{2}$$

where $\mathcal{F}\{\}$ represents the Fourier transform operation.

If we let $k_{\min}$ represent the minimum wavenumber at which we want information, we can construct a high-pass filter $H_1(k_x, k_y)$ such that

$$H_1(k_x, k_y) = \begin{cases} 1 & \text{if } k > k_{\min} \\ 0 & \text{otherwise} \end{cases} \tag{3}$$

where $k^2 = k_x^2 + k_y^2$. Essentially long wave components are eliminated. Typically, we set $k_{\min} = 2\pi/1600$ m or 0.00393 r/m.

To remove the remaining noise we threshold based on the values in the image spectrum, $S(k_x, k_y)$, which is defined as

$$S(k_x, k_y) = F(k_x, k_y)F^*(k_x, k_y)\,. \tag{4}$$

The mean and standard deviation of the spectrum are given by

$$\mu_s = \overline{S(k_x, k_y)}\,. \tag{5}$$

and

$$\sigma_s = \{\overline{(S(k_x, k_y) - \mu_s)^2}\}^{\frac{1}{2}}\,, \tag{6}$$

respectively.

We define a threshold level by

$$T_s = \mu_s + A\sigma_s \tag{7}$$

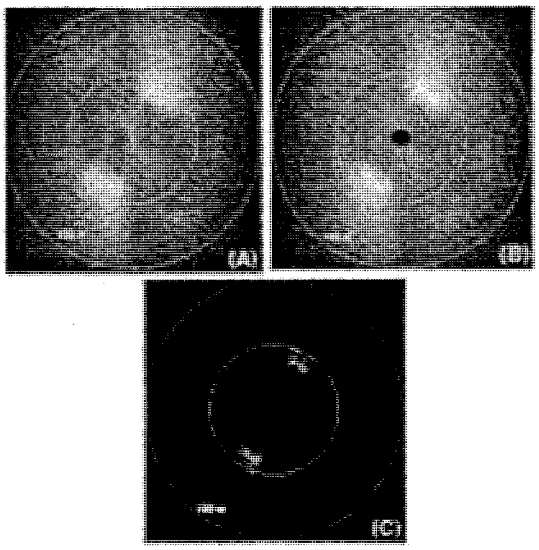

Figure 2: The absolute value of the Fourier transform of the Hurricane Josephine image at various levels of filtering.

where A is an adjustable parameter. Typically we use a value of $A = 3$. This second spectral filter is defined by

$$H_2(k_x, k_y) = \begin{cases} 1 & S(k_x, k_y) > T_s \\ 0 & \text{otherwise} \end{cases} \tag{8}$$

By application of these filters, we generate a new Fourier transform, $F'(k_x, k_y)$ given by

$$F'(k_x, k_y) = H_1(k_x, k_y)H_2(k_x, k_y)F(k_x, k_y) \tag{9}$$

Figure 2 illustrates the application of the frequency domain filters. Figure 2(A) represents the absolute value of the Fourier transform of a 2048 × 2048 pixel (25.6 × 25.6 km) Hurricane Josephine image. The image shown in Figure 1 is included in this larger image. The center of the display is infinite wavelength, the inner circle represents 200 m in wavelength, and outer circle represents 100 m in wavelength.

The Figure 2(B) is the high-passed Fourier transform with the H_1 filter applied, *i.e.* all information at wavelengths longer than 1600 m has been set equal to zero.

The Figure 2(C) represents the fully filtered Fourier transform as given in Equation 9. It is the same as Figure 2(B) except we have set to zero spectral elements that do not reach the preset threshold, T_s.

3.2 Image Domain Filtering

We compute the filtered SAR image by inverse Fourier transforming $F'(k_x, k_y)$, *i.e.*

$$I'(x, y) = \mathcal{F}^{-1}\{F'(k_x, k_y)\}\,. \tag{10}$$

To separate crest from non-crest areas, we applied a threshold to the resulting image. If μ_I is the mean of

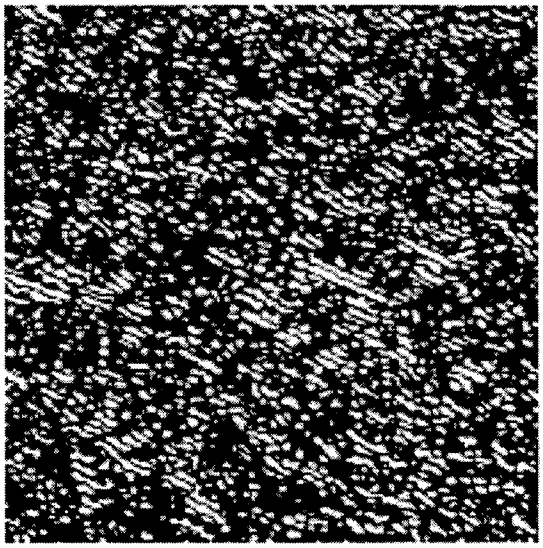

Figure 3: Example of a filtered image that has been thresholded.

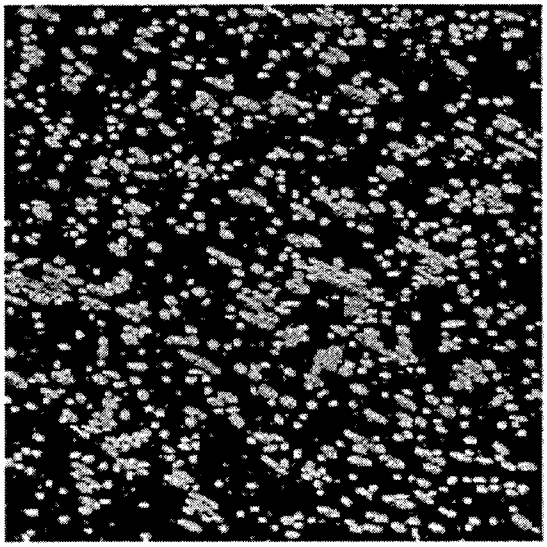

Figure 4: Example of a filtered image that has been thresholded. Ellipses have been fit to the blobs. The blobs are shown in a 50% gray scale. The corresponding ellipses are outlined in white.

$I'(x, y)$ and σ_I its standard deviation, then we define an image threshold level, T_I, by

$$T_I = \mu_I + B\sigma_I \tag{11}$$

where B is an adjustable parameter. We typically use $B = 1.0$. Figure 3 is an example of the thresholding applied to a filtered image. In this image, every pixel either is or is not identified as associated with a crest. Each such crest area is call a "blob." The question now is: what is the size of these blobs?

3.3 Blob Identification and Measurement

There are standard image processing procedures that are able to find contiguous regions or blobs in an image and label them sequentially. For this work we used IDL (Interactive Data Language, by Research Systems Inc., Boulder Colorado) which has a powerful and applicable function that performs this operation. Each blob is thus uniquely identified. To determine the crest lengths lengths we set each value in a blob region to 1 and the values outside the region are set to 0. We fit each such blob to an ellipse. For each such ellipse we determine the semi-major and semi-minor axes, the eccentricity, and the orientation of the ellipse. We retain those ellipses that meet the following criteria:

- The area of the blob from which the ellipse is constructed is larger than 150 m^2.
- No part of the blob intersects the edge of the image.
- The ellipse has an eccentricity exceeding 0.94. This criteria effectively means that the semi-major access must be more than three times greater than the semi minor axis.
- The ellipse is oriented such that the associated wave direction is within $\pm 15°$ of the dominant wave direction determined from the image spectrum.

Figure 4 is an example of an image with crests identifies and ellipses fitted to estimate crest length.

3.4 Sample Image: The Probability of Encountering a Long Wave Crest

We apply the blob identification and measurement procedure to a 2048 × 2048 pixels (25.6 × 25.6 km) area from Hurricane Josephine imagery. After full processing of this image, we obtain a list of all the wave crests in the image and their dimensions.

Wave-wave interactions conspire to bunch waves up and create wave crest lengths which differ from what might be expected if all wave frequency components acted independently. By using a simulation technique, we are able to compare the observed crest length statistics, with similar statistics that would be generated from images having the same spectrum but whose frequency components are independent.

We begin this simulation by using the spectrum computed from observed image. We assume that this spectrum is but one realization of the ensemble mean spectrum which represents the surface. In this single realization, each spectral element is random variable having a χ^2-distribution with two degrees of freedom. The

mean of this distribution is the ensemble mean spectral value. We approximate this ensemble mean spectrum by smoothing the observed spectrum with a 20 × 20-pixel filter. The aim is to produce a new simulated image with the following properties: (1) The ensemble of mean spectrum of similar images equals the ensemble mean of the observed image spectrum and (2) Each spectral component is independent of the others, *i.e.* the phase of each spectral element is independent of all other phases.

To be more mathematically specific, we begin with the spectrum of the observed image, $S(k_x, k_y)$, as defined in Equation 5. We estimate the ensemble mean spectrum by

$$S_{\rm em}(k_x, k_y) = H_3(k_x, k_y) * S(k_x, k_y) \qquad (12)$$

where $H_3(k_x, k_y)$ is the smoothing filter and $*$ represents the convolution process.

We generate a particular, simulated realization of this ensemble mean spectrum, choosing at each particular k_x and k_y value a realization, $S_{\rm r}$ such that $S_{\rm r}$ has a χ^2-distribution with two degrees of freedom. The magnitude of the corresponding Fourier component is given by

$$\mid F_{\rm r}(k_x, k_y) \mid = \sqrt{S_{\rm r}(k_x, k_y)} \qquad (13)$$

while the phase of the component is randomly selected between 0 and 2π. The inverse Fourier transform,

$$I_{\rm r}(x, y) = \mathcal{F}^{-1}\{F_{\rm r}(k_x, k_y)\}\,, \qquad (14)$$

is a single, simulated realization of an image where the individual spectral components are independent. We then treat this simulated image the same way we treated the original observed image to estimate crest lengths.

Results thus far suggest that very long wave crests are more common on the ocean than would be expected if wave components were independent. Figure 5 shows the number of wave crests longer than the abscissa that will be found on average in one square kilometer. The higher curve was computed from the original SAR image, while the lower curves were the result of simulations. From Figure 5, we may infer that in the observed image one is likely to encounter two wave crests longer than 1000 m in a 10 km^2 area. In the simulated images, it is not likely that a single such wave crest would be encountered.

4. WAVE GROUPINESS MEASUREMENT

Wave groupiness is the likelihood that large waves will group together in a series. Any offshore platform will have more difficulty if especially large waves are grouped together possibly setting up a resonance [8].

We suspected that wave groupiness might be apparent in the two-dimensional autocorrelation function.

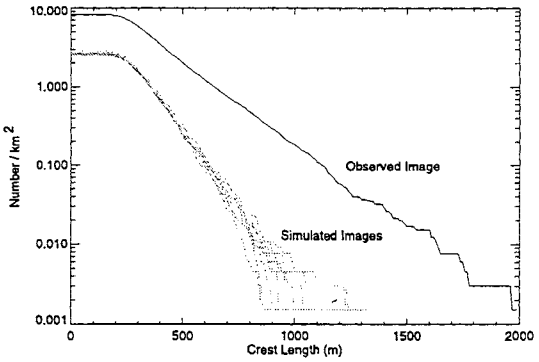

Figure 5: The number of wave crests encountered longer than the abscissa per square kilometer. The two curves represent the observed and simulated images.

Figure 6 represents the two-dimensional autocorrelation function of the image that includes the sub-image shown in Figure 1.

Note at the center, or zero spatial lag, we observed local correlations on scales of a few hundred meters. This corresponds to the existence of ocean waves in the image. Put more simply, a wave crest at any particular position is correlated with other wave crests one, two, or more wavelengths away. The correlation decreases as one moves farther away.

Upon more careful examination of this two-dimensional autocorrelation, groups or packets of waves are visible. This is a consequence of wave groupiness. By rotating the autocorrelation function shown in Figure 6 so that the crests are horizontal and collapsing this two-dimensional representation to one dimension, the groups become more apparent.

Figure 7 is a plot of the one-dimensional autocorrelation function. Again we note the oscillations near zero lag associate with surface waves. The envelope of the oscillations is the signature of groupiness. It has a period of 2.5 km. Hence, for this particular wave field, one would expect especially large groups of waves separated by 2.5 km, about 10 wave periods.

Autocorrelations computed from simulated wave images based on linear theory did not exhibit this groupiness behavior. This is additional evidence that empirical data, rather than linear wave theory is needed to estimate wave groupiness.

5. CONCLUSIONS

Spaceborne SAR images offer the prospect of measuring ocean surface waves on scales and at resolutions necessary to make judgments about the effect of waves on very large offshore platforms. This past year has been occupied developing the repertoire of image processing tools necessary to measure waves coherence properties from SAR images.

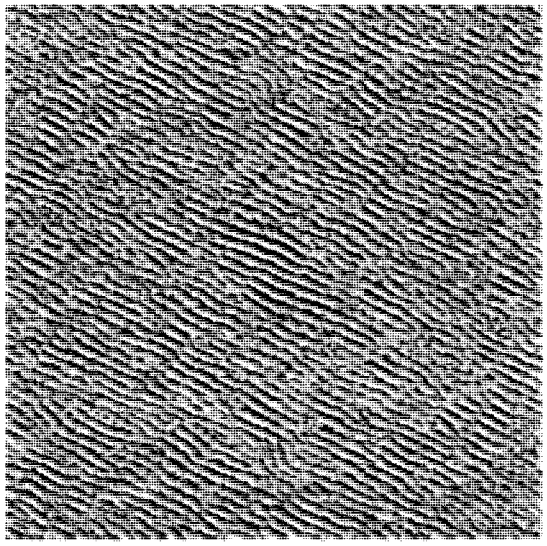

Figure 6: Two-dimensional autocorrelation function of SAR wave image. The image center represents zero spatial lag. The maximum space lag is 7 km.

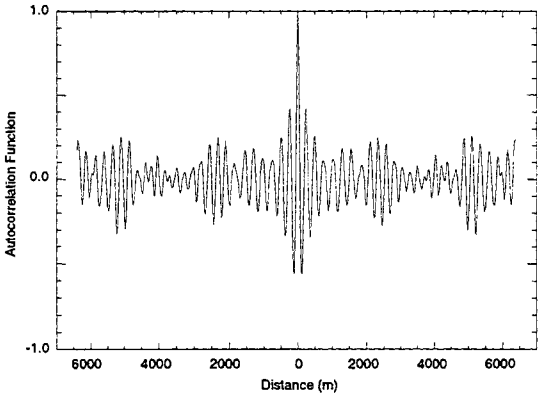

Figure 7: The autocorrelation function along the wave direction of travel.

Preliminary evaluation of imagery in the vicinity of Hurricane Josephine indicates that the waves exhibit both longer crest lengths and more groupiness than would be expect on the basis of linear theory alone. It is clear that wave imagery will be necessary to characterize properties of wave coherence.

At JHU/APL, we have acquired a number of SAR ocean wave data sets, including imagery from Hurricanes Josephine, Bonnie, Danielle, and Edouard. In the coming year we plan to compute the crest length statistics and autocorrelation lengths for these data.

Acknowledgment: The material is based upon work supported by the U.S. Office of Naval Research's MOB Program.

References

[1] C. Elachi and W. Brown Jr. Models of radar imaging of ocean surface waves. *IEEE Trans. Antennas Propag.*, AP-25:84–95, 1977.

[2] W. Alpers, D. Ross, and C. Rufenach. On the detectability of ocean surface waves by real and synthetic aperture radar. *J. Geophys. Res.*, 95:6481–6498, 1981.

[3] R. Beal, F. Monaldo, D. Tilley, D. Irvine, E Walsh, F. Jackson, D. Hancock III, D. Hines, R. Swift, F. Gonzalez, D. Lyzenga, and L. Zambresky. A comparison of SIR-B directional wave spectra with aircraft scanning radar spectra. *Science*, 232:1531–1535, 1986.

[4] K. Hasselmann, R. K. Raney, W. Plant, W. Alpers, W. Shuchman, D. Lyzenga, C. Rufenach, and M. Tucker. Theory of synthetic aperture radar ocean imaging: A MARSEN view. *J. Geophys. Res.*, 90:4659–4686, 1985.

[5] F. Monaldo and D. Lyzenga. On the estimation of wave slope- and height-variance spectra from sar imagery. *IEEE Geosci. Remote Sensing*, GE-24:543–551, 1986.

[6] C. Swift and L. Wilson. Synthetic aperture radar imaging of ocean waves. *IEEE Trans. Antennas Propag.*, AP-27:725–729, 1979.

[7] W. Alpers and C. Rufenach. The effect of orbital velocity motions on the synthetic aperture imagery of ocean waves. *J. Geophys. Res.*, AP-27:685–690, 1979.

[8] F. Monaldo. Estimating wave groupiness using the autocorrelation function. Technical Report JHU/APL SRO–99–03, The Johns Hopkins University Applied Physics Laboratory, Laurel, MD, 1999.

PROCEEDINGS OF THE THIRD INTERNATIONAL WORKSHOP ON VERY LARGE FLOATING STRUCTURES
(VLFS '99), VOL. I, EDS. R.C. ERTEKIN & J.W. KIM, 22-24 SEPTEMBER 1999, HONOLULU, HAWAII, USA

Characterizing Wave Coherence with Satellite-Based Synthetic Aperture Radar

D. T. Walker*, D. R. Lyzenga, & M. Renouf
Earth Sciences Group, ERIM International, Inc.

ABSTRACT

A critical issue in the design of large floating structures, such as those being considered in the Mobile Offshore Base (MOB) effort currently being pursued by the US Navy, is the nature of the ocean-wave field, viewed on scales of 2 km or more. Of prime concern is the ability to assess the spatial 'coherence' of the wave field, or the probability of occurrence of long, unbroken wave crests for various environmental conditions. This paper will describe an effort to use satellite-based synthetic-aperture radar images to determine the crest-length statistics for ocean waves. It summarizes work in determining the appropriate measures to apply to the sea surface, and how they can be applied to SAR data.

1. INTRODUCTION

This study examines the feasibility of using remote sensing data to characterize wave coherence, in order to provide needed environmental data for the design of mobile off-shore bases (MOB). The primary measure of wave coherence used in this study is the crest-length distribution. We first examine the relationship between crest length statistics and wave spectral measures, and then address the question of how well these spectral measures can be estimated from remote sensing data. The remote sensing technologies considered here are satellite-based synthetic-aperture radar (SAR) for observing the spatial pattern of the wave field, and satellite-based microwave altimetry for measuring the significant wave height and wind speed. These satellite-based microwave sensors can 'see through' clouds and operate independent of the weather.

SAR images possess the spatial resolution and area coverage needed to obtain coherence data relevant to these large-scale MOBs, and coincident altimeter observations can provide information on sea state. The main concern in using SAR image data for coherence measures is that some the wave information is lost, or modified, in the SAR imaging process. These SAR imaging effects are most pronounced for short waves; nevertheless, their importance for the large-scale waves of interest in MOB design needs to be considered. The SAR-imaging effects, and how they are manifested in the SAR image spectrum, can be largely determined *a priori*, given knowledge of the significant wave height (obtained from coincident altimeter data), and the sensor viewing geometry. The objective of this study is to determine the range of viewing geometries and significant wave heights which will yield reliable estimates of crest-length statistics, and to quantify the errors introduced by SAR-imaging effects.

2. BACKGROUND

2.1 SAR Imaging of Ocean Waves

A number of radar techniques have been developed to measure ocean wave directional spectra [1]. For the conditions under which most SAR systems operate, the principal radar scattering mechanism from the ocean surface is Bragg scattering, which is controlled by the amplitude or spectral density of surface waves having wavelengths comparable to that of the electromagnetic radiation (typically a few centimeters). These Bragg waves are modulated by their interaction with the orbital velocities associated with longer surface waves, and this produces a variation in backscatter that more or less follows the profile of the long waves. The radar backscatter also varies locally because of the 'tilting' of the surface by the long waves, since the backscatter is a strong function of local incidence angle. This tilting effect produces a backscatter modulation that is approximately proportional to the long-wave slope. The spatial or temporal spectrum of the backscatter is therefore expected to be approximately proportional to the wave spectrum. This relationship is observed experimentally, although the constant of proportionality (the modulation transfer function) tends to be somewhat larger than is predicted using existing hydrodynamic and electromagnetic scattering models [2].

* P.O. Box 134008, Ann Arbor, MI 48113-4008, USA
E-Mail: dwalker@erim-int.com

The motion of the ocean surface influences SAR images because the Doppler shift of the returned signal is used to resolve the surface in the cross-range or azimuthal direction. Random surface motions therefore limit the effective azimuthal resolution of the images. When the image is Fourier transformed in order to estimate the wave spectrum, this results in a loss of information at high wavenumbers, thus limiting the spectral bandwidth of the SAR image spectrum in the azimuthal direction. This loss of information at high azimuthal wavenumbers is called the 'azimuth fall-off' effect. The orbital motions associated with long ocean waves also cause a modulation of the image intensity through the 'velocity-bunching' effect which under some conditions can increase the contrast of the wave images. For large-amplitude waves or large R/V ratios (where R is the range distance and V is the SAR platform velocity), however, this relationship becomes nonlinear, resulting in the generation of harmonics and other image artifacts. This nonlinearity and the 'azimuth fall-off' due to random surface motions constitute the chief difficulties in relating the SAR image spectrum to the wave spectrum [3].

2.2 Anticipated Impact of SAR Imaging Effects on Coherence Measures

The SAR image spectrum differs from the ocean wave spectrum in two significant ways. First, the azimuth fall-off effect removes the high wavenumber waves in the along-track direction. The width of the pass-band depends primarily on the significant wave height and can be estimated, given that information. Secondly, there may be distortions of the spectral shape within the pass-band, due to the wavenumber dependence of the modulation transfer function. For example, the interaction of the tilt, hydrodynamic and velocity-bunching modulations can result in a 'null' in the spectrum along a line passing through the origin of the spectrum, slightly oblique to the look direction [4]. These effects are also largely predictable, given the sensor viewing geometry and the environmental conditions.

The impact of these SAR imaging effects on the resulting coherence estimates may vary, depending upon the direction of the dominant waves relative to the SAR look direction, as well as the wave length and wave height. Knowing the nature and magnitude of these effects allows us to determine when they are significantly influencing the coherence measures. It should be noted that since long-crested seas are potentially more destructive (by inducing large torsional moments in the MOB) than short-crested seas, an overestimate of the coherence length would be considered a conservative error.

2.3 Altimeter Observations of Sea State

Satellite radar altimeters operate by transmitting short pulses of microwave radiation vertically downward toward the ocean surface and measuring the time history of the returned pulses. The time of arrival of the returned pulse is used, along with highly accurate measurements of the satellite position, to obtain the mean surface elevation, from which geostrophic currents and subsurface topography can be inferred. Secondly, the amount of energy in the returned pulse is a measure of the small-scale surface roughness, from which the wind speed can be estimated. Finally, from the rise time or distortion of the returned pulse shape, the large-scale surface elevation variance or significant wave height can be calculated. Measurements of the wave height obtained from altimetry data agree well with *in situ* measurements, but are limited to average values over the surface area intercepted by the incident pulse, which is typically a few tens of kilometers.

2.4 Availability of SAR and Altimeter Data

SAR and altimetry data are available from archival sources as well as from ongoing collections with currently operational sensors. Recent and current SAR sensors include the European Remote Sensing satellites ERS-1 and ERS-2, and the Canadian RADARSAT. The ERS satellites include altimetry as well as SAR data but there is an offset of about 250 km between the side-looking SAR images and the nadir-looking altimeter, which limits the usefulness of the simultaneously collected SAR and altimetry data. Other sources of altimetry data include the Geosat and Topex/Poseidon satellites. Thus, there is a rich source of information that can potentially tapped for this application. Selection of contemporaneous, co-located data sets is a non-trivial task, however.

3. CREST LENGTH STATISTICS

In order to investigate the relationship between crest length statistics and wave spectral measures, surface realizations were constructed for various wave spectra. The realizations were constructed by choosing complex Fourier amplitudes such that the samples are normally distributed with mean values of zero and variances equal to the wave height spectral density at each wavenumber. These amplitudes were then Fourier transformed to obtain surface elevation maps with sample spacings of 12.5 meters, to correspond to the pixel spacings of ERS SAR images. Figure 1a shows a narrow-banded sea surface sea surface generated from a gaussian-shaped spectrum with a directional spread of 0.1 radians, a center frequency of 0.08 Hz and a width of 0.008 Hz.

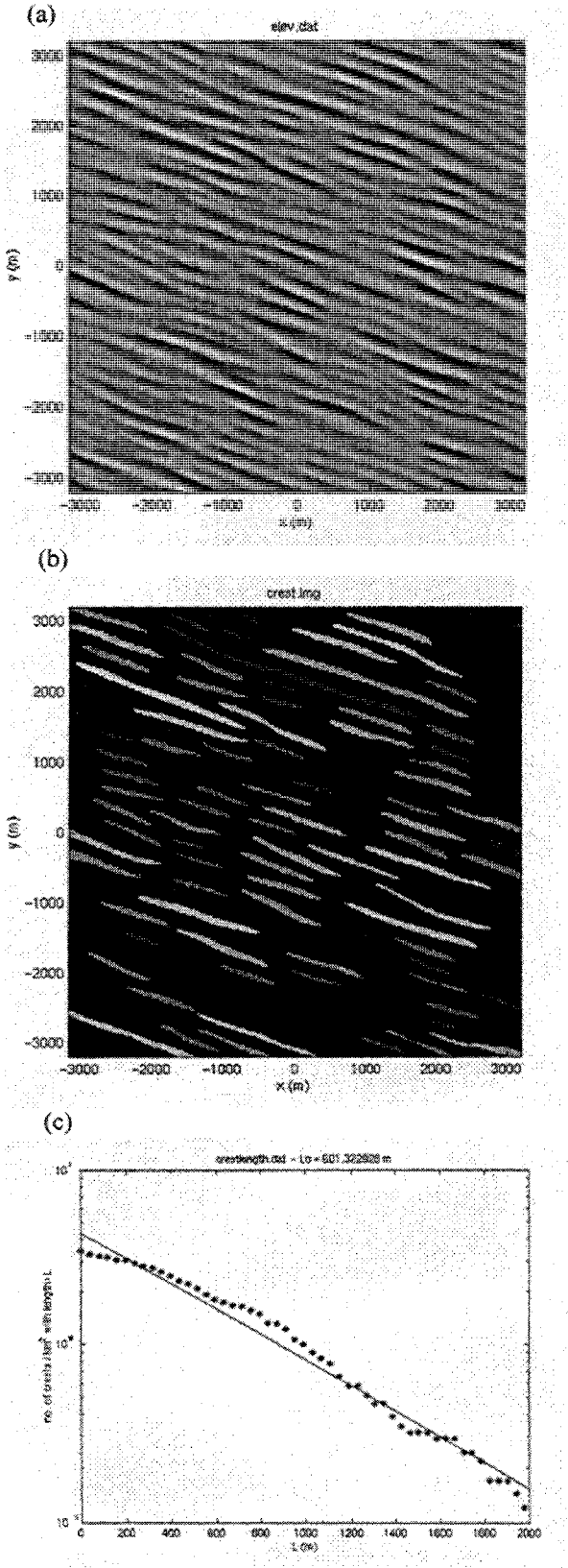

Figure 1: Simulated sea surface and identified crests; a) simulated sea surface, b) wave crests identified in sea surface, and c) crest length distribution.

The resulting elevation maps were processed by passing them through an algorithm that classifies each contiguous set of pixels with elevations greater than one standard deviation as a wave crest. Figure 1b shows the wave crests identified by this procedure, using the elevation map in Figure 1a. The length of each crest was measured and the lengths were binned to form histograms. The histograms were then summed and normalized by the scene area, so as to form an estimate of the number of crests per unit area with lengths greater than L, where L varies from zero to a maximum length that is typically a third or so of the scene length. An example of the resulting crest length distribution, for the surface elevation map in Figure 1a, is shown in Figure 1c. The shape of this distribution function, which is typical of all the cases considered, can be approximated by the equation

$$N(L) = N_o e^{-L/L_o}, \qquad (1)$$

where L is the crest length and N is the number of crests per km^2 with lengths greater than L. The parameters describing this distribution are the scale length (L_o) and the total number of wave crests per km^2 (N_o). It can be seen that L_o is equal to the mean crest length if this equation adequately fits the data. We estimated this parameter by computing a linear least-squares fit to the logarithm of the observed distribution function.

By measuring the crest length distributions for a range of wave spectra, a relationship was found between the mean or characteristic crest length, L_o, the dominant wavelength, λ, and the angular spread of the wave spectrum, $\Delta\phi$. This relationship, as shown in Figure 2, can be approximated by the equation

$$\frac{L_o}{\lambda} \approx \frac{0.35}{\Delta\phi} \qquad (2)$$

where $\Delta\phi$ is defined as the full width of the spectrum at half the maximum value.

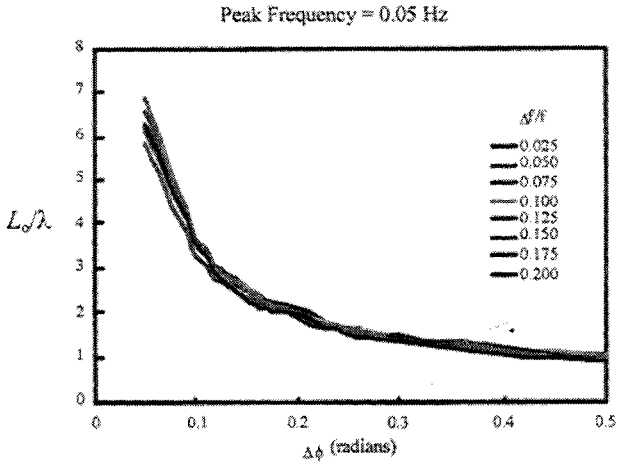

Figure 2: Crest length distributions as a function of directional spread $\Delta\phi$ for various spectral widths $\Delta f/f$ and a peak frequency of 0.05 Hz.

4. SAR IMAGING EFFECTS

To investigate the effects of SAR imaging on wave coherence measures, a series of forward predictions of the SAR image spectrum were carried out using the Hasselmann formulation [5,6]. Simulations were made over a range of significant wave heights (2–10 m), dominant wave frequencies (0.06–0.09 Hz), and SAR look directions relative to the wave propagation direction. The SAR parameters for the simulations were those typical of satellite SAR sensors (specifically the European Space Agency's ERS platform).

Figure 3 shows the apparent directional spread of the SAR spectrum, divided by the directional spread of the actual wave spectrum, as a function of the SAR look direction relative to the dominant wave direction for two significant wave heights. These results are for a narrow wave spectrum ($\Delta\phi$=0.105 rad). The significant wave heights shown are H_s = 2 m, a moderate wave height, and H_s = 10 m, typical of severe weather conditions. The figure shows that for H_s = 2 m, the error in directional spread (and hence in the crest-length distribution) is less than 10%. For H_s = 10 m, the errors are as large as 30% near a relative look angle of 20°. The apparent narrowing of the wave spectrum is due to the narrow azimuth pass band associated with the SAR imaging process, and the resulting modification of the shape of the image spectrum. It should be noted that these errors are conservative in the sense that the directional spread is underestimated, and so the crest lengths are overestimated.

Figure 4 shows similar plots for the same spectral width but a shorter wavelength, λ = 200 m, and wave heights H_s = 2 m, 5 m and 10 m. For H_s = 2 m, the error in apparent directional spread increases with SAR look direction and levels off at about 30% low for angles greater than 20°. For H_s = 5 m the errors are similar for look directions near the wave propagation direction but then the apparent spread increases monotonically for look directions beyond 20°. The apparent widening of the spectrum occurs when the peak of the wave spectrum moves outside of the SAR pass band. For H_s = 10 m the errors become large more rapidly, with the directional spread being overestimated for look directions greater than 20°.

Figure 5 shows the corresponding results for a broader wave spectrum ($\Delta\phi$=0.245 rad) with a 500 m dominant wavelength. The significant wave heights shown are again H_s = 2 m, 5 m and 10 m. For all wave heights, the error increases with look direction and again becomes constant at an apparent directional spread which is about 30–40% low near a relative look angle of 20°. Again, the apparent narrowing of the wave spectrum is due to the narrow azimuth pass band associated with the SAR imaging process, and the consequent distortion of the wave spectrum. The errors for this case are also conservative.

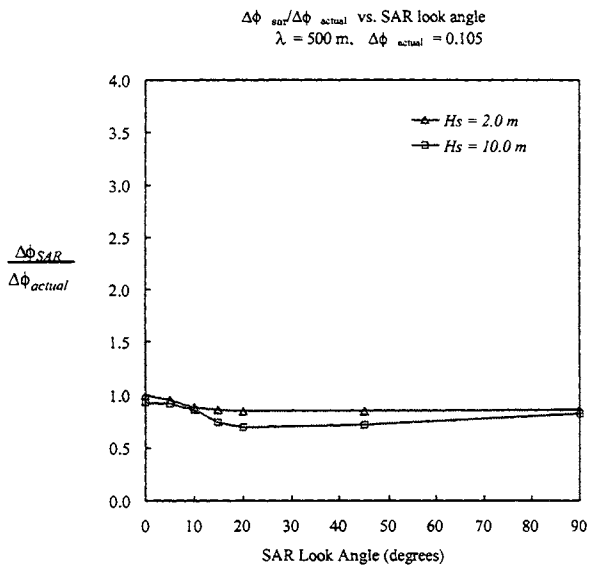

Figure 3: Apparent directional spread $\Delta\phi_{SAR}$ from simulated SAR image, normalized by actual directional spread $\Delta\phi_{Actual}$ = 0.105 for various SAR look directions relative to the dominant wave direction, with H_s = 2.0 m and 10.0 m, and λ = 500 m.

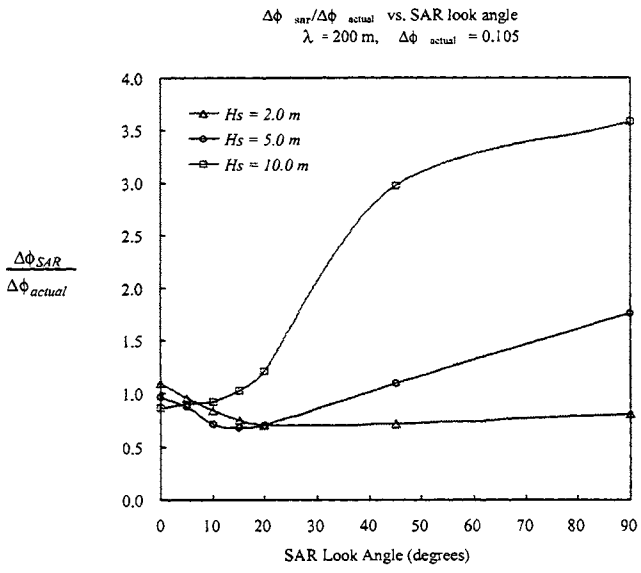

Figure 4: Apparent directional spread $\Delta\phi_{SAR}$ from simulated SAR image, normalized by actual directional spread $\Delta\phi_{Actual}$ = 0.105 for various SAR look directions relative to the dominant wave direction, with H_s = 2.0 m, 5 m and 10.0 m, and λ = 200 m.

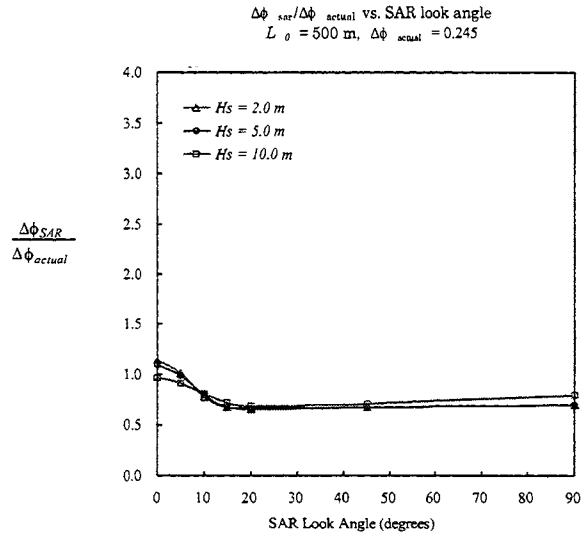

Figure 5: Apparent directional spread $\Delta\phi_{SAR}$ from simulated SAR image, normalized by actual directional spread $\Delta\phi_{Actual} = 0.245$ for various SAR look directions relative to the dominant wave direction, with H_s = 2.0 m, 5 m and 10.0 m, and λ = 500 m.

Similar plots for a shorter wavelength, λ = 200 m, again with the broad spectrum are shown in Figure 6. The results are similar to those shown in figure 4 for the narrow directional spectrum, except that for H_s = 10 m, the directional spread is underestimated for small look directions by more than 40%.

5. ESTIMATING WAVE DIRECTION

From the foregoing, it is clear that the reliability of estimating the directional spread of the wave spectrum from the SAR spectrum depends on the significant wave height, and the look direction of the SAR sensor relative to the wave direction. The significant wave height can be determined form contemporaneous satellite altimeter data. The only available information on the wave direction is in the SAR image data itself. Since the SAR imaging effects modify the shape of the wave spectrum, it is reasonable to expect that the apparent wave direction can differ from the actual wave direction. The accuracy of estimating the wave propagation direction from the SAR image data will now be addressed.

The apparent wave direction can be determined from the location of the peak in the SAR spectrum. Figure 7 shows the apparent wave direction plotted versus SAR look direction for the narrow spectrum conditions of figures 3 and 4, with a wavelength of 500 m. From the figure, it is clear that the wave direction can be estimated within a few percent from the SAR spectrum under all conditions. Similar results for a wavelength of 200 m are shown in figure 8. The errors for this case are slightly larger, but the conclusion is again that the wave direction can be estimated accurately from the SAR spectrum.

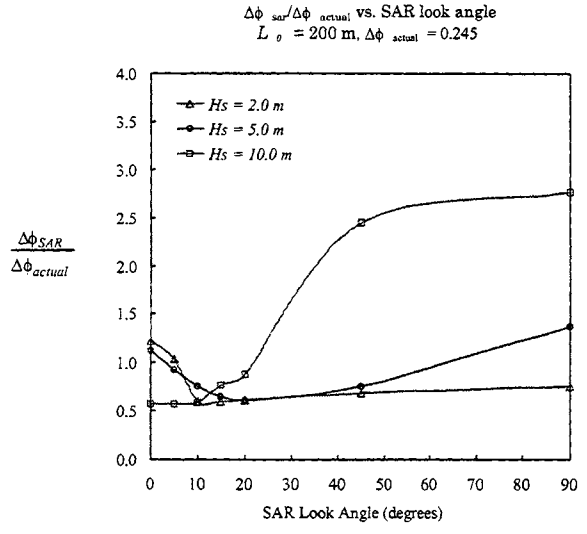

Figure 6: Apparent directional spread $\Delta\phi_{SAR}$ from simulated SAR image, normalized by actual directional spread $\Delta\phi_{Actual} = 0.245$ for various SAR look directions relative to the dominant wave direction, with H_s = 2.0 m, 5 m and 10.0 m, and λ = 200 m.

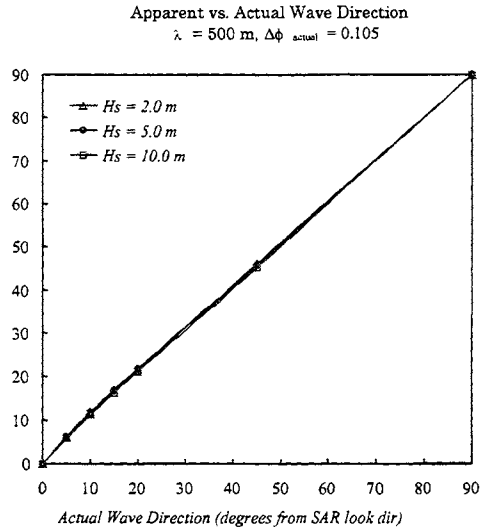

Figure 7: SAR Look Direction vs Apparent Wave direction for $\Delta\phi_{Actual} = 0.105$ vs. SAR look direction with H_s = 2.0 m, 5 m and 10.0 m, and λ = 500 m.

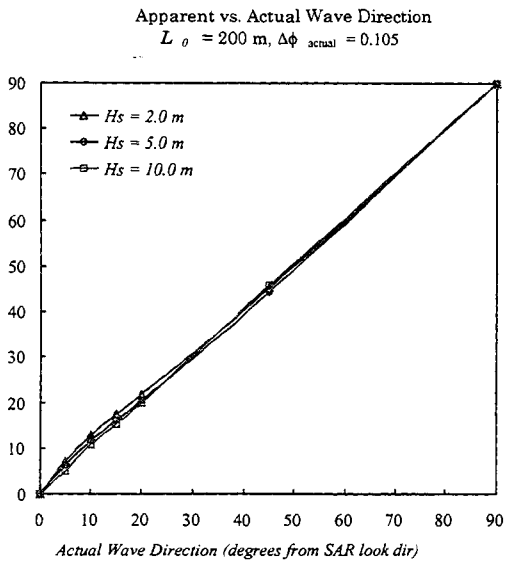

Figure 8: SAR Look Direction vs Apparent Wave direction for $\Delta\phi_{Actual} = 0.105$ vs. SAR look direction for $H_s = 2.0$ m, 5 m and 10.0 m and $\lambda = 200$ m.

6. APPLICATION TO ACTUAL SAR DATA

6.1 Labrador Sea

The methodology described above was applied to two ERS SAR images. Figure 9a shows an ERS image collected on 23 March 1997 over the Labrador Sea, at approximately 57° N and 52° W. The significant wave height, as measured on the nearest Topex/Poseidon altimeter pass was approximately 6.4 m. In order to reduce the effects of low-frequency trends as well as high-frequency speckle noise in the images, a Fourier threshold filter was applied to the data before running the crest recognition algorithm. This filter operates by computing the image spectrum, locating the peak in the spectrum, and zeroing out all Fourier components having a power less than one tenth of the peak value. The resulting crest map is shown in Figure 9b.

The crest length distribution obtained from this data set is shown in Figure 9c. The shape of this distribution is fit quite closely by equation (1) with L_o=360 m and N_o=5 wave crests per km^2. This distribution implies that there are approximately 0.02 wave crests per km^2 with crest lengths greater than 2 km. The dominant wavelength observed in the image spectrum for this case was about 400 m, which translates into a peak period of 16 sec. The directional spreading was relatively broad (about 0.3 rad) for this case, because the region of high winds generating these waves was large and quite near the observation region.

(a)

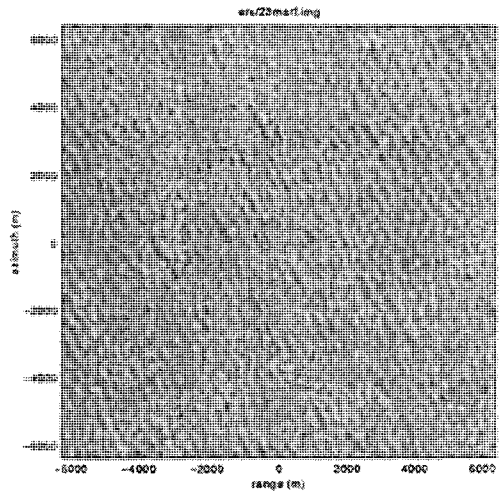

(b)

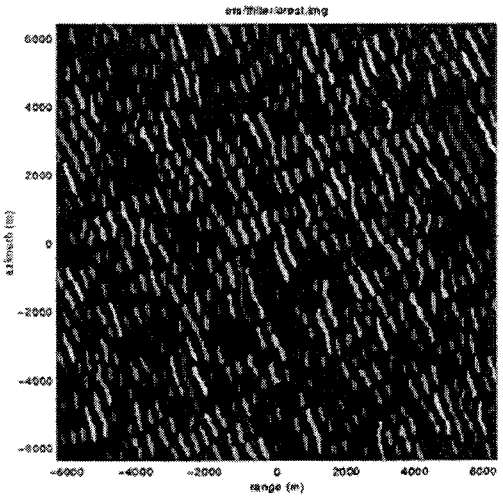

c)

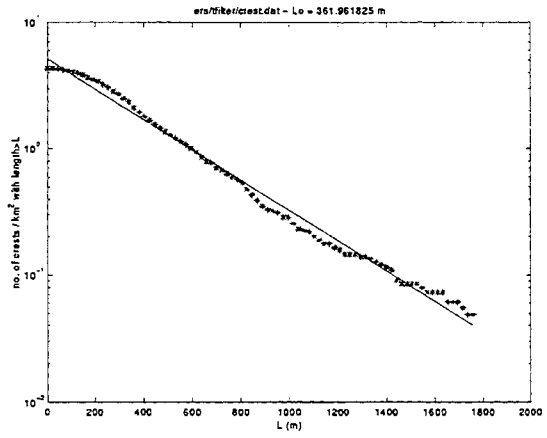

Figure 9: Results for ERS SAR image (©ESA 1997) of waves in the Labrador Sea; a) filtered SAR image, b) wave crests identified in SAR image, and c) crest length distribution.

6.2 Oregon Coast

The second SAR image, shown in Figure 10a, was collected on 24 December 1995 off the coast of Oregon, at approximately 44.5° N and 124.5° W. The significant wave height measured by a nearby NOAA/NDBC buoy was approximately 3.3 m, and the peak period was 16.7 sec. The Fourier threshold filter was applied to this image and the crest recognition algorithm was run on the filtered data, resulting in the crest map shown in Figure 10b.

The crest length distribution for this data, as shown in Figure 10c, is characterized by the parameters L_o=1220 m and N_o=1 per km^2. This distribution implies that the number of wave crests with crest lengths greater than 2 km is approximately 0.2 per km^2, which is an order of magnitude larger than that for the Labrador Sea image. The reason for the larger number of long crests is of course the narrowness of the spectrum, which is related to the distance from the storm generating these waves. The spectral width for this case was estimated to be about 0.1 radians, which is about one third of the width for the Labrador Sea data.

7. CONCLUSIONS

The conclusions of this study are as follows:

1) For 500 m waves, spectral widths derived from SAR are within 20–30%. The errors are conservative (spectral width underestimated, or crest lengths overestimated).

2) For 200 m waves with $H_s < 5$ m, spectral widths derived from SAR are within 20% for wave directions within ~10° of the SAR look direction, and within 40% for wave directions up to 45°. Errors tend to be conservative.

3) For 200 m waves $H_s > 5$ m, spectral widths derived from SAR are within 50% for wave directions within ~20° of the SAR look direction.

4) In all cases, error in the estimated spectral width increases with the actual spectral width.

5) The apparent wave direction can be determined accurately from the SAR-image spectrum for all wave heights.

Acknowledgment: This study was supported by Office of Naval Research Contract No. N00014-98-C-0363, monitored by Dr. C. Linwood Vincent.

(a)

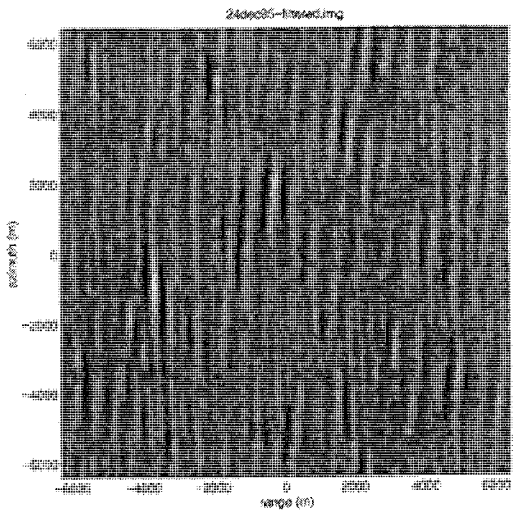

(b)

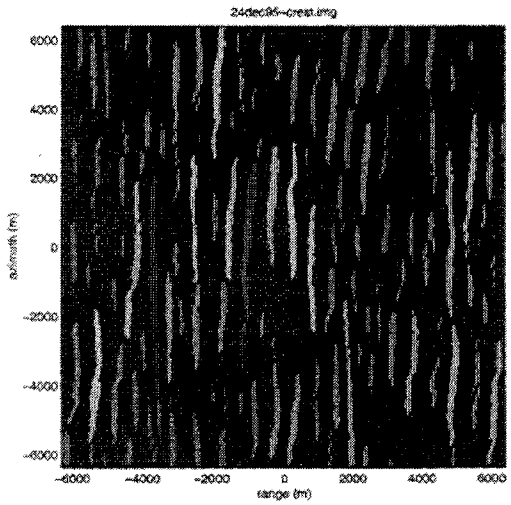

c)

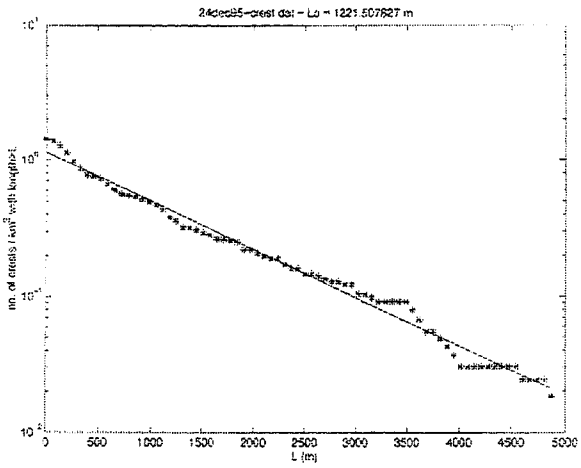

Figure 10: Results for ERS SAR image (©ESA 1995) of waves off the Oregon coast; a) filtered SAR image, b) wave crests identified in SAR image, and c) crest length distribution.

References

[1] Jackson, F.C. and D.R. Lyzenga, "Microwave Techniques for Measuring Directional Wave Spectra," Chapter 14 in *Surface Waves and Fluxes*, ed. by G.L. Geernaert and W.J. Plant, Kluwer Pub. Co., Amsterdam, 1990.

[2] Plant, W.J. and L.M. Zurk, "Dominant wave directions and significant wave heights from synthetic-aperture radar imagery of the ocean," *J. Geophys. Res.* **102**, 3473–3482, 1997.

[3] Lyzenga, D.R. "The Physical Basis for Estimating Wave Energy Spectra from SAR Imagery," *Johns Hopkins APL Technical Digest* **8**, 65-69, 1987.

[4] Bruning, C., W. Alpers, L.F. Zambresky, and D.G. Tilley, "Validation of synthetic-aperture radar ocean wave imaging theory by the Shuttle Imaging Radar–B experiment over the North Sea," *J. Geophys. Res.* **93**, 15 403–15 425, 1988.

[5] Hasselmann, K. and S. Hasselmann, "On the nonlinear mapping of an ocean wave spectrum into a synthetic aperture radar image spectrum and its inversion," *J. Geophys. Res.* **96**, 10 713–10 729, 1991.

[6] Krogstad, H.E., "A simple derivation of Hasselmann's nonlinear ocean-to-synthetic aperture radar transform," *J. Geophys. Res.* **97**, 2421–2425, 1992.

PROCEEDINGS OF THE THIRD INTERNATIONAL WORKSHOP ON VERY LARGE FLOATING STRUCTURES
(VLFS '99), VOL. I, EDS. R.C. ERTEKIN & J.W. KIM, 22-24 SEPTEMBER 1999, HONOLULU, HAWAII, USA

HURRICANE DIRECTIONAL WAVE SPECTRUM MEASUREMENT WITH A SCANNING RADAR ALTIMETER

Charles Wayne Wright, Edward J. Walsh, Douglas C. Vandemark, William B. Krabill
NASA/Goddard Space Flight Center/Wallops Flight Facility[1]

Andrew W. Garcia
Coastal Engineering Research Center, U.S. Army Engineer Waterways Experiment Station[2]

ABSTRACT

The sea surface directional wave spectrum was measured for the first time in all quadrants of a hurricane using the NASA airborne scanning radar altimeter. Waves up to 18 m height were observed and the spatial variation of the wave field was dramatic. At times there were crossing sea and swell with waves at right angles to each other.

1 INTRODUCTION

The data presented here were acquired on 24 August 1998 when Hurricane Bonnie, a Category 1 storm, was east of the Bahamas and moving slowly to the north. This was the first time that the directional wave spectrum was documented in all quadrants of a hurricane.

The Scanning Radar Altimeter (SRA) [1, 2] and its predecessor, the Surface Contour Radar (SCR) [3, 4] were designed primarily to measure the energetic portion of the directional wave spectrum by generating a topographic map of the sea surface. The measurement geometry is shown in Figure 1. The SRA sweeps a radar beam of 1° half-power width (two-way) across the aircraft ground track from -22° (off-nadir to the left side of the aircraft) to +22° (off-nadir to the right side of the aircraft), simultaneously measuring the backscattered power at its 36 GHz (8.3 mm) operating frequency and the range to the sea surface at 64 points spaced across the swath at 0.7° incidence angle intervals. These slant ranges are multiplied by the cosine of the incidence angles (including the effect of aircraft roll attitude) to determine the vertical distance from the aircraft to the sea surface. Subtracting these distances from the aircraft height produces the sea surface height. During the Hurricane Bonnie flight described here, the SRA produced these raster scan lines of wave topography at the rate of about 8 Hz.

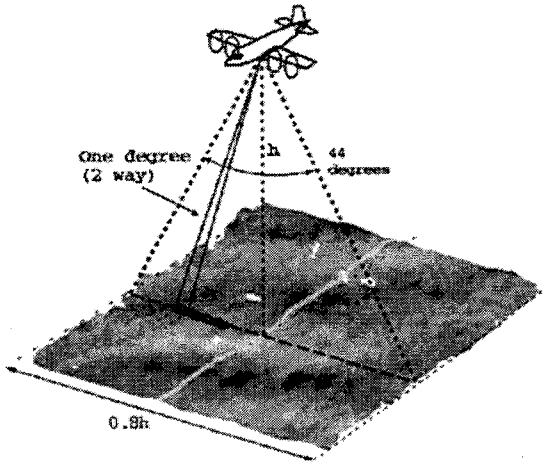

Fig 1. SRA measurement geometry.

2 HURRICANE BONNIE

Figure 2 shows information obtained from the NOAA Atlantic Oceanographic and Meteorology Laboratory (AOML) Hurricane Research Division (http://aoml.noaa.gov) mission summary for Hurricane Bonnie on 24 August 1998. The small dots show the positions at one-minute intervals of NOAA WP-3D

[1]Code 972, Laboratory for Hydrospheric Processes, GSFC/Wallops Flight Facility, Wallops Island, VA 23337: wright@osb.wff.nasa.gov, http://radar.wff.nasa.gov

[2]ATTN: CEWES-CD-P (Andrew Garcia) 3909 Halls Ferry Road, Vicksburg, MS 39180-6199: a.garcia@cerc.wes.army.mil

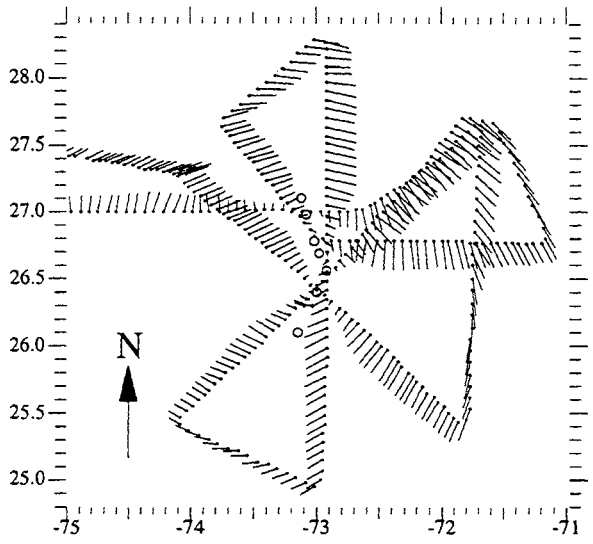

Figure 2. N43RF flight track in Hurricane Bonnie and flight level wind vectors versus latitude and longitude.

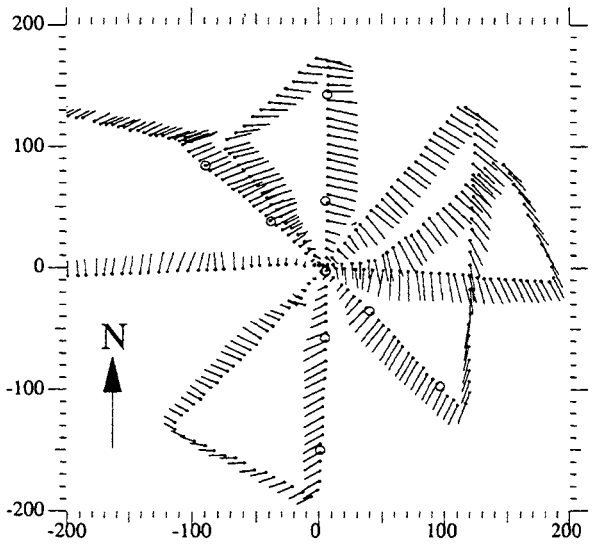

Figure 3. N43RF flight track in Hurricane Bonnie and flight level wind vectors versus distance (km) from eye.

aircraft N43RF, which carried the SRA at 1.5 km altitude, when it was in the vicinity of Hurricane Bonnie. The radial from each dot indicates the flight level wind at that position. The radials extend in the upwind direction and their length is proportional to wind speed, with a scale such that 25 m/s corresponds to 0.1° on the latitude axis.

The seven circles in Figure 2 indicate positions of the eye. The general motion of the eye was to the north at about 4 m/s. The second through sixth positions were determined from the points of closest approach indicated in the mission summaries. The first and last circles are linear extrapolations from the second and third and fifth and sixth positions, respectively.

The motion of the storm toward the north over the period of measurement caused the wind speed and direction to be different each time the same geographic position was reoccupied.

The information in Figure 2 has been replotted in Figure 3 in a relative coordinate system of km distances north and east of the eye. In this reference frame the wind field for the entire flight is perfectly consistent.

3 SRA WAVE TOPOGRAPHY

The left side of Figure 4 shows gray-scale coded wave topography measured by the SRA while traveling toward the southeast on the initial pass through the eye. The data span is centered about 40 km south and 40 km east of the eye, indicated by one of the circles in Figure 3. At 1.5 km altitude, the SRA swath is 1.2 km wide and the along-track distance shown is about 10 km.

The significant wave height (SWH) was 8.6 m and there were crossing wave fields. The image is in proportion and has been rotated about 45° clockwise from its original track orientation. The time sequence of the data progresses from top to bottom on the left side of Figure 4.

The right side of Figure 4 shows a similar span of gray-scale coded wave topography from the ground track passing north through the eye. This span is centered about 145 km north of the eye, also indicated by a circle in Figure 3. The SWH at this location was 11.2 m and the wave field was dominated by swell propagating toward the northwest.

Figure 5 is an enlargement of the central region of the right side of Figure 4. The white line near the center of the enlargement indicates the cross-track position of the 30th elevation measurement from the left side of the swath. The lateral deviations of the line are caused by aircraft roll attitude variations. The white splotches indicate data voids.

Figure 6 shows the surface elevation profile along the white line in Figure 5. The crest of the highest wave is 11 m above mean sea level (msl) and the deepest trough is more than 6.5 m below msl. This 18 m wave was the highest in the sequence shown on the right side of Figure 4, which shows the general spatial variations in wave height which are a function of the spectral width.

4 RESAMPLING SRA DATA

The SRA data points are not uniformly spaced along the sea surface. At 1.5 km altitude, the cross-track spacing is about 20 m, but increases toward the edge of

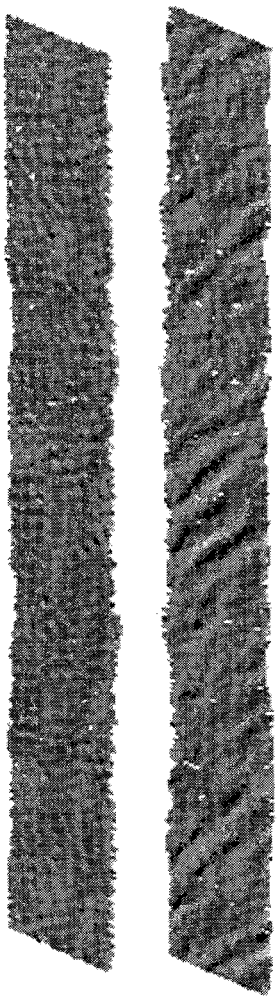

Figure 4. SRA wave topography from southeast (left) and northward (right) flight lines from eye.

the swath because of the fixed 0.7° angular spacing in the cross-track incidence plane. The spacing also varies temporally due to aircraft roll attitude variations. At 120 m/s ground speed and 8 Hz scan rate, the along-track spacing is about 15 m, but this spacing is also nonuniform because of temporal variations of aircraft pitch and ground speed.

The SRA elevations are resampled to a fixed square grid of 7 m spacing with its axes oriented north and east. The grid size is 256 by 256 points (1792 m by 1792 m). These resampled data are then processed with a two-dimensional FFT and the complex amplitudes square to transform them into the encounter directional wave spectrum.

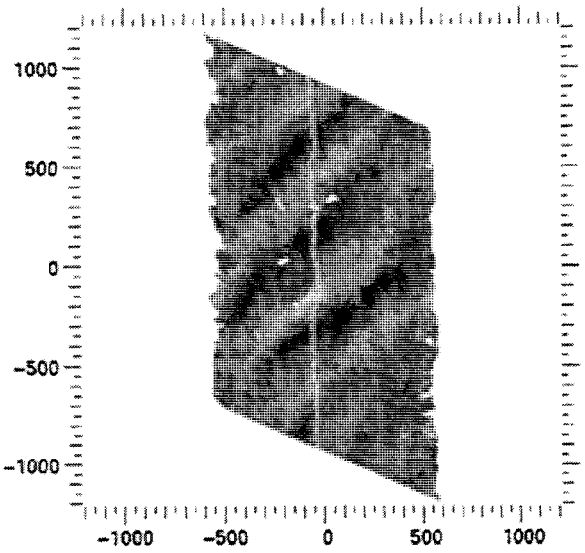

Figure 5. Enlargement of central section of the right side of Figure 4. White line indicates position 30.

5 DOPPLER CORRECTION

The last step in the process is to correct the directional wave spectra for Doppler effects caused by the wave motion. Because the waves move during the measurement interval, those propagating in the direction of flight of the aircraft will appear to have longer wavelengths, while the wavelengths of those propagating in the opposite direction will appear shortened. For most waves there will be apparent changes in both wavelength and direction of propagation.

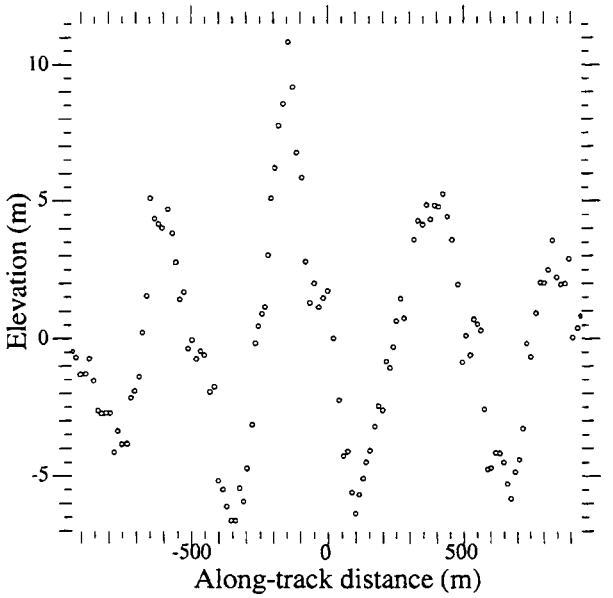

Figure 6. Surface elevation along white line in Figure 5.

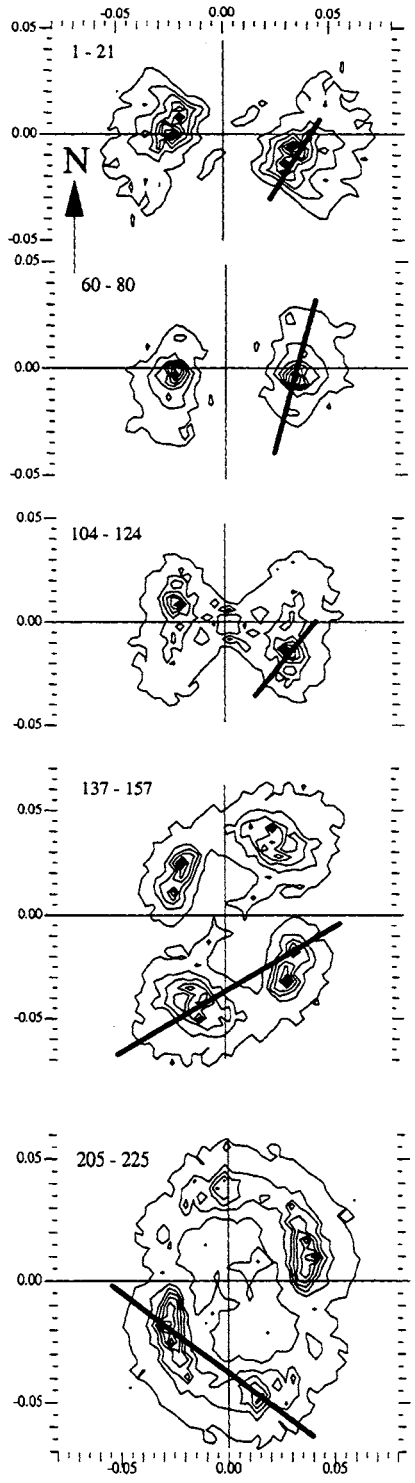

Figure 7. Directional wave spectra from 30 km data spans centered on the five circles located along the northwest to southeast flight line in Figure 3.

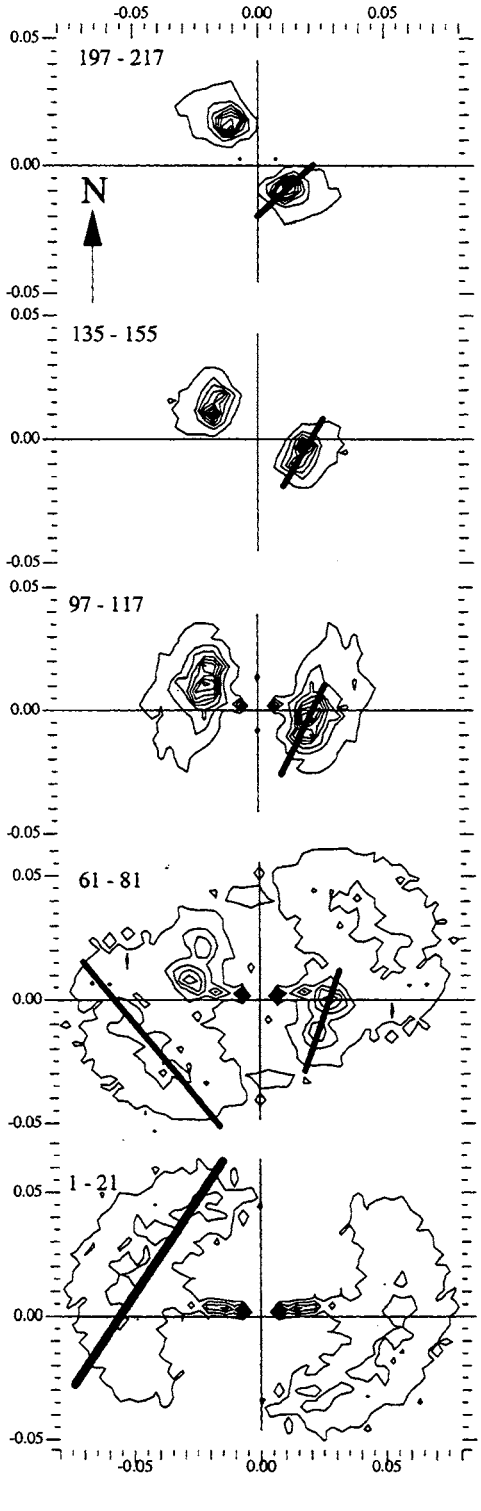

Figure 8. Directional wave spectra from 30 km data spans centered on the five circles located along the south to north flight line through the eye in Figure 3.

Walsh et al. [4] showed that the wave motion affects only the component of the wave number vector parallel to the aircraft ground track, and changes it by an amount equal to the total wave number magnitude times the ratio of wave phase speed to aircraft ground speed. It shifts the encounter wave spectrum in the direction opposite the aircraft flight direction. When the Doppler correction is applied to the encounter wave spectra, it shifts them in the along-track direction.

When elevation data are transformed by an FFT, there is a 180° ambiguity in the direction of propagation. The artifact lobe in the encounter spectrum is perfectly symmetric with the lobe representing the wave propagation direction. When all the spectral components are corrected assuming they are real, the artifact lobes are also shifted in the along-track direction and are no longer symmetric with respect to the true spectral lobes. This asymmetry in the Doppler-corrected spectra allows the true propagation direction of the waves to be determined without a priori information by comparing spectra from different flight lines which cross at angles of about 90° of more. The true lobes in the spectra from different flight lines will register while the artifact lobes will be badly misaligned.

6 SPATIAL VARIATION OF SPECTRA

Individual FFTs were performed on resampled data from groups of 160 scan lines. The center of the scan line groups was only advanced 100 line for each new FFT, so adjacent FFTs were not entirely independent. Figure 7 shows five average spectra from the northwest to southeast flight line through the eye in Figure 3.

Each of the spectra shown in Figure 7 was the average of 21 individual spectra and covered an along-track distance of about 30 km. The spectra have been Doppler-corrected and the artifact lobes have had a line draw through them.

Figure 8 shows five average spectra from the south to north flight line through the eye in Figure 3. Each of these spectra is also the average of 21 individual spectra and covered an along-track distance of about 30 km.

The five average spectra in Figures 7 and 8 are identified with numbers indicating the individual spectra from the flight line that were included in the average. As they are shown in the figures, the most northerly average spectrum is at the top and the most southerly average spectrum is at the bottom.

There is generally low frequency noise in the spectra caused by an imperfect removal of aircraft vertical motion or a consistent cross-track pattern of deviation from msl caused by small scan angle errors. The nine wave number bins surrounding the origin have been zeroed out in the spectra to mitigate this problem, but occasionally the noise is wider than those bins and dominates the contours in Figures 7 and 8 which were normalized to the highest value.

7 CONCLUSIONS

Figure 7 indicates that northwest of the hurricane eye the wave field is dominated by swell propagating to the west (1-21, 60-80), although there is a wind-driven sea propagating to the southwest. In the eye (104-124), the swell component has rotated to about 290°. At about the southeast location of the eyewall (137-157), two components of swell propagating toward the northwest are observed as well as a strong wind-driven sea towards the northeast. Further to the southeast (205-225), the wind-driven sea has rotated towards the east and the swell has rotated towards the north. This quadrant has sea and swell at right angles to each other, which would be quite hazardous to ships.

Figure 8 shows that north of the hurricane (197-217, 135-155), the wave field was dominated by swell propagating toward the northwest. South of the hurricane at about the eyewall position (61-81), there was sea propagating toward the northeast and swell at right angles to it propagating toward the northwest. By 160 km south of the eye (1-21) the wave field wave dominated by a wind-driven sea propagating southeast.

Acknowledgments: The authors thank Drs. Peter Black and Frank Marks of the NOAA/AOML/Hurricane Research Division and the people of the NOAA Aircraft Operation Center for their assistance. This work was supported by the NASA Solid Earth and Natural Hazards Program, the NASA Physical Oceanography Program, and the Office of Naval Research under Document N00014-98-F-0209.

REFERENCES

[1] Walsh, E. J., L. K. Shay, H.C. Graber, A.Guillaume, D. Vandemark, D. E. Hines, R. N. Swift, and J. F. Scott, "Observations of Surface Wave-Current Interaction During SWADE," *The Global Atmosphere and Ocean System*, 5, 99-124, Gordon and Breach Science Publishers SA, 1996.

[2] Parsons, C., and Walsh, E.J., "Off-Nadir Altimetry," *IEEE Trans. Geosci. Remote Sens.*, 27, 215-224, 1989.

[3] Walsh, E. J., D. W. Hancock, D. E. Hines, R. N. Swift, and J. F. Scott, "An Observation of the Directional Wave Spectrum Evolution from Shoreline to Fully Developed," *J. Phys. Oceanogr.*, 19(5), 670-690, 1989.

[4] Walsh, E. J., D. W. Hancock, D. E. Hines, R. N. Swift, and J. F. Scott, "Directional Wave Spectra Measured with the Surface Contour Radar," *J. Phys. Oceanogr.*, 15(5), 566-592, 1985.

PROCEEDINGS OF THE THIRD INTERNATIONAL WORKSHOP ON VERY LARGE FLOATING STRUCTURES
(VLFS '99), VOL. I, EDS. R.C. ERTEKIN & J.W. KIM, 22-24 SEPTEMBER 1999, HONOLULU, HAWAII, USA

ESTIMATION OF WIND LOADS ON VLFS OF SEMISUBMERSIBLE TYPE

Sotaro Masanobu
Koichiro Yoshida
Hideyuki Suzuki
Noriaki Oka
the University of Tokyo, Japan *

ABSTRACT

This paper presents the results of investigation of wind lift force on VLFS of semisubmersible type. In the present study, wind–wave tank experiments on the scale model were also conducted in regular progressive waves. Lift forces and wind pressures were measured as a function of column diameter, unit number, superstructure and wave condition and divided into time averaged mean component and fluctuating component. The importance of lift force, especially at leading edge of deck, was verified in the experimental results. The results showed that fluctuation in lift force which was caused by interaction between wind and wave was significantly large in typhoon conditions. Measured lift forces were lineary related to fluctuation of wind velocity. Lift force model is further proposed for estimation of lift forces on VLFS of semisubmersible type and the effectiveness of this model was confirmed by the present experimental results.

1. INTRODUCTION

VLFS of semisubmersible type is now studied for ocean space utilization such as floating airport, which may be constructed in the near future. For the structure, total wind loads become very large and the local distribution of them may produce local elastic response of the structure. Therefore, it is important to estimate wind loads accurately according to extensive experimental results.

Semisubmersible has deck structure supported on columns above the water surface. In winds, the existence of the obstruction to the air flow passing under deck such as columns and waves produces lift force acting on the deck. For VLFS of semisubmersible type, because of increase of shielding effect of many columns and decrease of the effect of diversion of air flow from the side of structure, the lift force may be larger than that of conventional semisubmersible.

Wind loads are often discussed in connection with typhoon conditions and there always exist waves in such conditions. Large waves induce attack angle of air flow to the deck, which generate potential flow lift forces. They also induce fluctuation of wind velocity and shielding of air flow. The effects may produce significant fluctuation of lift force.

However there are few researches on lift force of VLFS of semisubmersible type. Present authors conducted wind tunnel experiments on the scale model of VLFS of semisubmersible type[1]. In the experiments, measurements in the presence of a solid wavy boundary model which represented wave profile in typhoon conditions were also conducted. Measured lift force was much larger than drag force while lift force is smaller than drag force for conventional semisubmersible. The studies also showed that wind loads, especially lift force, vary with relative position of structure to wavy boundary. It means that significant lift force fluctuation at wave frequency is observed and that the experiments in progressive waves should be conducted.

In the present experiments, wind–wave tank experiments on VLFS of semisubmersible type in regular progressive waves were conducted and the effect of progressive waves on lift force was investigated.

2. WIND–WAVE TANK EXPERIMENT

The present experiments were conducted in the Pulsating Wind Tunnel with Water Tank of the Ship Research Institute of Ministry of Transport of Japan. Test section of wind tunnel of the wind–wave tank is 2m high, 3m wide and water tank is 2m deep, 3m wide.

*7-3-1 Hongo, Bunkyo-ku, Tokyo, Japan

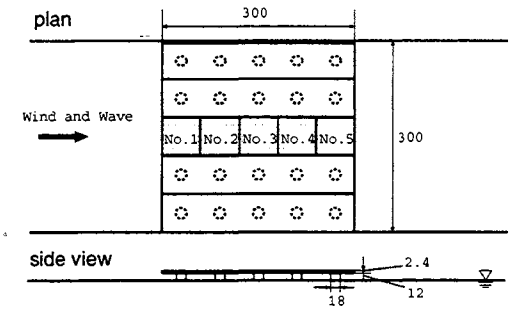

(a) case A (D=18cm; 5units)

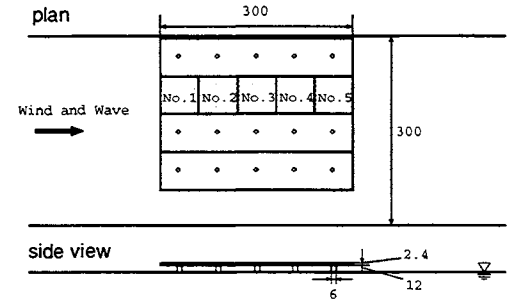

(b) case B (D=6cm; 5units)

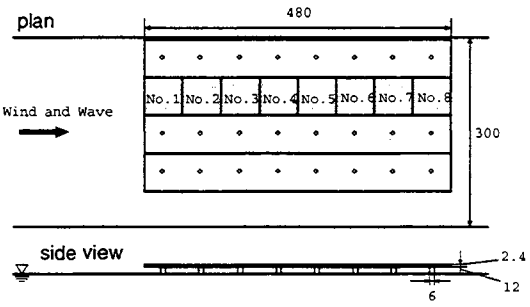

(c) case C (D=6cm; 8units)

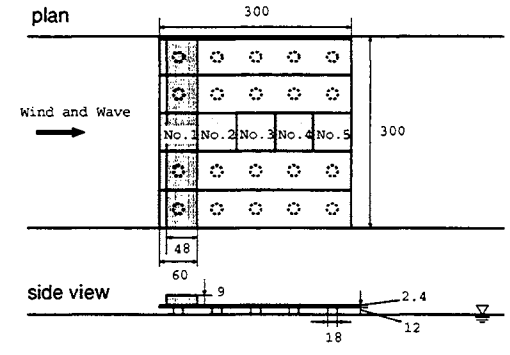

(d) case D (D=18cm; 5units; superstructure)

unit: cm

Figure 1: Experimental models.

2.1 Experimental models

The present experiments were conducted on scale models of medium size floating airports. Dimension of deck is 2200m long, 400m wide and 2m high and the deck was idealized as a flat plate in the experiment. One column supported 50m long and 50m wide unit part of deck, which is hereafter called unit deck. Column diameters used for the experiment are 15m and 5m. In addition, effect of superstructure whose dimensions are 800m long, 40m wide and 7.5m height was also tested in the experiment.

As shown in Fig. 1, case A, case B and case C experimental model respectively consisted of 5, 5 and 8 units in wind direction and column diameters were 18, 6 and 6cm respectively. In case D experiment, superstructure model was placed close to the leading edge of case A model. The experimental models were partial models and scale ratio is 3/250. For convenience each unit has reference number in wind direction as shown in Fig. 1. The distance between deck and the still water level was 12cm and it corresponds to 10m in real scale. Blockage ratios of model to test section of wind tunnel were 2.6% in case A, 1.3% in case B, 1.3% in case C and 6.5% in case D respectively. The correction of blockage effect was not considered in the present experiment. Deck model was made of vinyl chloride and column and superstructure models were made of acrylic and balsa respectively.

2.2 Experimental procedures

In order to investigate the local distribution of lift force, lift force on each unit deck was measured by a load cell installed in each column as shown in Fig. 2 and experimental models were rigidly fixed on water tank.

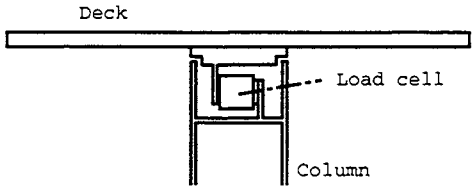

Figure 2: Sketch of load cell set up.

Lift forces were measured along center line of model. Wind pressures on No.1 unit deck which is located at leading edge of model where wind force is predicted to be most significant according to the previous study[1], were measured in case B and case C experiment. Arrangement of pressure sensors is shown in Fig. 3.

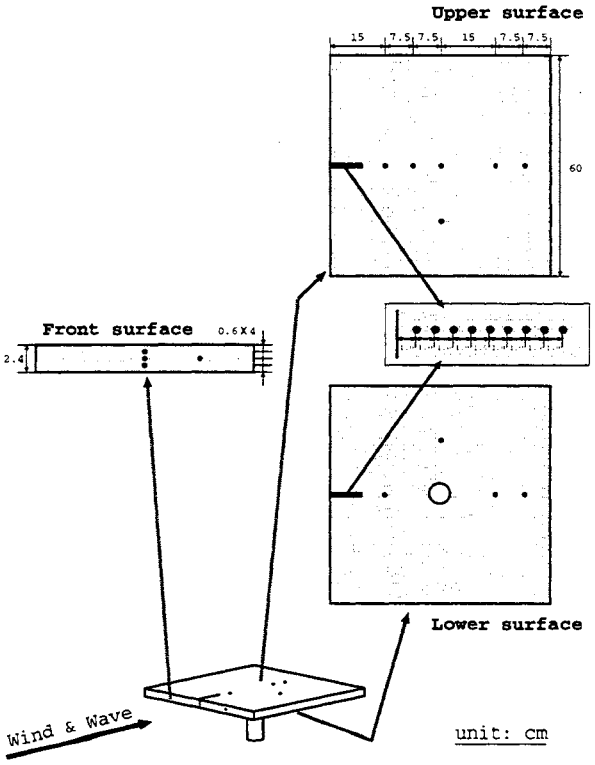

Figure 3: Arrangement of pressure sensors on No.1 deck.

It was assumed that difference in the number of unit in the direction perpendicular to wind had little influence on experimental results.

The wind at the entrance of the test section was uniform flow. Wind velocity at the entrance of the test section, V, was measured by pitot tube. The distance from the entrance to the leading edge of deck model was 4.8m and wind velocity profile in front of the model is similar to that of natural wind. Turbulent intensity was $0.13 \sim 0.15$ and also equal to that of natural wind in typhoon condition. Wind velocity was $3.5 \sim 14.5$m/s. Because of the existence of water surface, Froude number of the present experiment should be equal to that of real structure. When column diameter is selected as representative length, range of Froude number in the experiment is $0.3 \sim 2.1$. Then the wind velocity corresponds to $32 \sim 132$m/s of real structure. The value 132m/s is physical upper limit of natural wind. Reynolds number of the present experiment was $6.0 \times 10^3 \sim 2.4 \times 10^4$ when deck height was selected as representative length and different from that of real structure which is $2.7 \times 10^6 \sim 1.4 \times 10^7$. Flow around deck is hardly affected by Reynolds number and the correction of the difference in Reynolds number was not considered in the present study.

The wave periods used in the experiment were 1.24s, 0.88s and 0.62s.

Wind velocity around experimental model was measured by hot-wire anemometer and wave height was measured by wave probe. Lift forces and pressures were measured as a function of wind velocity, column diameter, unit number, superstructure and wave condition.

2.3 Experimental results

Lift force F_L and wind pressure P are expressed as a sum of time averaged mean component and fluctuating component respectively,

$$F_L = \bar{F}_L + f_L, \quad (1)$$

$$P = \bar{P} + p, \quad (2)$$

where $\bar{F}_L$ and $\bar{P}$ are time averaged components and f_L and p are fluctuating components.

2.3.1 Time averaged component

Time averaged mean lift coefficient $\bar{C}_L$ and mean pressure coefficient $\bar{C}_p$ are given by the following equations,

$$\bar{C}_L = \bar{F}_L \Big/ \frac{1}{2}\rho V_{\mathrm{ref}}^2 S\,, \quad (3)$$

$$\bar{C}_p = \bar{P} \Big/ \frac{1}{2}\rho V_{\mathrm{ref}}^2\,, \quad (4)$$

where $\bar{F}_L$ and $\bar{P}$ are measured mean lift force and mean pressure acting on the unit deck respectively. ρ is density of air, V_{ref} is the reference inflow velocity measured at the height of the upper surface of deck and S is area of the unit deck. Upward lift force is defined positive.

Typical distributions of $\bar{C}_L$ is shown in Fig. 4. Wind velocity V at entrance of test section is 5m/s. $\bar{C}_L$ of No.1 unit deck are large in all cases. $\bar{C}_L$ of No.2 unit deck is much smaller than that of No.1 unit deck and it decrease with distance from leading edge.

Typical distribution in $\bar{C}_p$ of No.1 unit deck in case C experiment is shown in Fig. 5. Measurements were made at wind velocity $V = 15$m/s. Because of flow separation occuring at the leading edge of deck, negative pressure is produced in the vicinity of leading edge of upper surface of deck. Flow reattachment to the surface occurs at leeward about 10cm from the leading edge. These phenomena were recognized by surface tuft method with woolen yarn. On leeward from the reattachment point, pressure is not significant. For lower surface of deck, flow separation occurs and negative

pressure is produced in small region of the leading edge, but the size is small. In other part of lower surface of deck, positive pressure is produced because shielding effect of columns is dominant for $\bar{C}_p$.

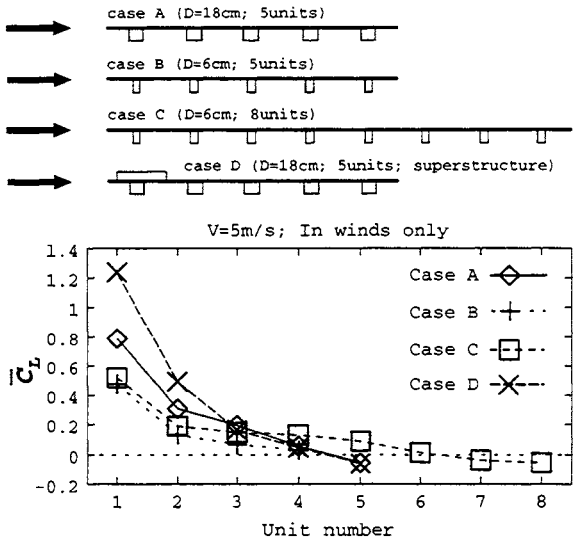

Figure 4: Mean lift coefficient distributions.

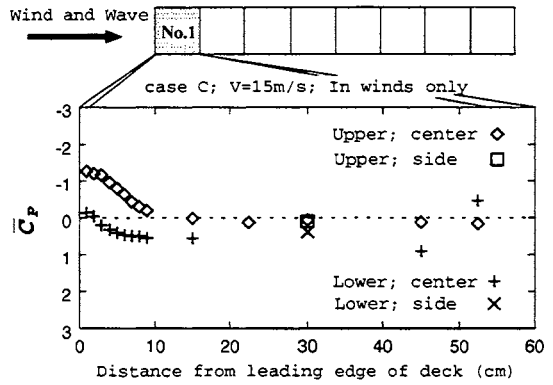

Figure 5: Mean pressure coefficient distribution on No.1.

Table 1: $\bar{C}_{L\,W.D.}$ in winds only.

case A	case B	case C	case D
0.26	0.13	0.12	0.38

Averaging $\bar{C}_p$ for the whole of upper surface of No.1 unit deck, the value becomes about -0.05. However $\bar{C}_L$ of No.1 unit deck is about 0.45, and it shows $\bar{C}_p$ on lower surface of deck is playing an important role in $\bar{C}_L$. This is also valid for the leeward units. Therefore decrease of $\bar{C}_L$ to leeward is largely due to decrease of $\bar{C}_p$ on lower surface to leeward.

The effect of column diameter is significant at windward part of deck. $\bar{C}_L$ of each unit deck increase with length of model.

Table 1 shows mean lift coefficients of the whole deck $\bar{C}_{L\,W.D.}$ which are called lift coefficient generally. These values are large compared with those of the conventional semisubmersibles[2], [3]. Because of the limited air flow diverted from the side of the structure, the phenomena is practically two dimensional. Therefore a two dimensional mean pressure distribution model can predict those of VLFS of semisubmersible type.

In case D experiment, the existence of superstructure has significant influence on $\bar{C}_L$ of No.1 and No.2 unit decks. $\bar{C}_L$ becomes about one and a half times larger compared to that of case A result. Because negative pressure is produced around superstructure and this result is verified by numerical simulation. The result shows that it is neccesary to carefully investigate characteristics of $\bar{C}_L$ when superstructure is constructed on deck.

$\bar{C}_L$ tends to increase with wind velocity and wave height. The observations that $\bar{C}_L$ are linearly related to fluctuation intensity of wind velocity, I_{UH}, is confirmed as shown in Fig. 6.

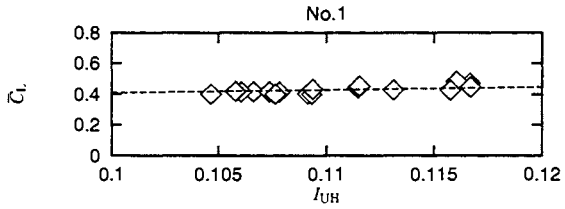

Figure 6: Variations of $\bar{C}_L$ with turbulence intensity.

As discussed above, $\bar{C}_L$ is significant near the leading edge of deck in high winds conditions such as typhoon conditions. For VLFS of semisubmersible type with columns of small diameter, restoring force is small and it is necessary to pay attention to lift force to avoid excessive vertical displacement even when $\bar{C}_L$ is small. And mooring system restraining the vertical displacement must be considered when a real structure is designed based on case C model moored by dolphins. When wind velocity is 50m/s, the leading edge of deck may rise by about 10m.

2.3.2 Fluctuating component

Time histories of F_L measured on No.1 unit deck in waves are shown in Fig. 7. When wave length

is long compared with unit deck length, lift force mainly fluctuates at wave period. At wave period $T = 0.62$s, when wave length equals to unit deck length, fluctuation of lift force at wave period is not noticeable because fluctuation of pressure on unit deck is canceled out each other. But even when wave length is short, the peak frequency of fluctuations is wave frequency. Wave is dominant factor for fluctuation of lift force in regular waves.

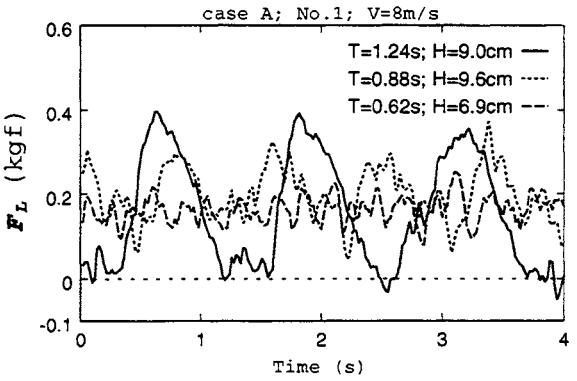

Figure 7: Time histories of lift force.

In the present study, fluctuating lift force f_L and fluctuating pressure p are both characterized by dominant fluctuating component at wave period.

Fluctuating lift coefficient c_L and fluctuating pressure coefficient c_p are given by the following equations,

$$c_L = f_L \Big/ \frac{1}{2}\rho V_{\mathrm{ref}}^2 S\,, \qquad (5)$$

$$c_p = p \Big/ \frac{1}{2}\rho V_{\mathrm{ref}}^2\,, \qquad (6)$$

where f_L and p are measured fluctuating lift force and fluctuating wind pressure acting on the unit deck respectively.

The relationship between $|c_L|$ and wave height are shown in Fig. 8. Experimental conditions for this experiment are V=5m/s for wind velocity and T=1.24s, 0.88s and 0.62s for wave period. 'Model' in Fig. 8 are $|c_L|$ estimated by fluctuating lift force model discussed in the following section. For each unit deck, $|c_L|$ are of equal value in all cases. This result shows that $|c_L|$ is linearly related to wave height and that fluctuating lift force is largely due to wave characteristics. Fig. 9 shows the variation of fluctuating amplitude of wind velocity measured just over the water surface with wave height. Vertical axis shows nondimensional wind velocity, which is fluctuating amplitude of wind velocity v_{wave} divided by mean wind velocity $\bar{V}$. This result shows that c_L is linearly related to fluctuation intensity of wind velocity in the same manner as $\bar{C}_L$. For the leeward unit decks, c_L are negligibly small. As wave length becomes shorter, c_L decrease especially at the windward unit deck owing to the cancel effect of wind pressure mentioned above. As wind velocity V is increased, $|c_L|$ is decreased. It is interpreted that in high winds wave profile is deformed owing to wind pressure and the fluctuation of lift force at wave period is decreased.

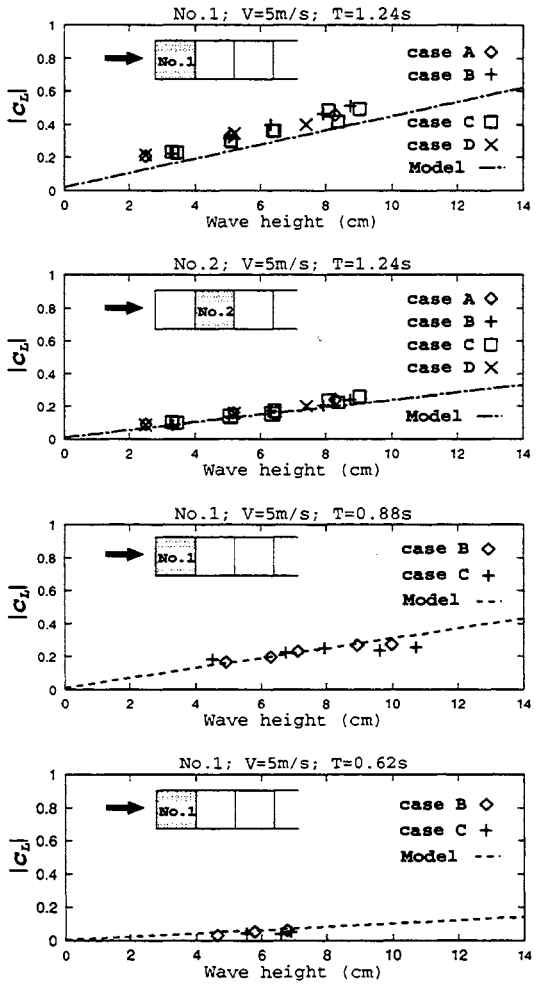

Figure 8: Variations of fluctuating lift coefficient with wave height.

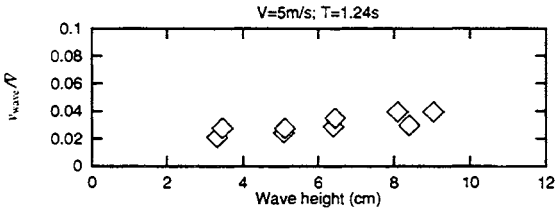

Figure 9: Variation of fluctuating amplitude of wind velocity with wave height.

Phase differences between lift coefficient of windward units and wave are shown in Fig. 10. For example, lift coefficient of No.1 unit deck takes maximum value when the trough of a wave is located under the leading edge of deck.

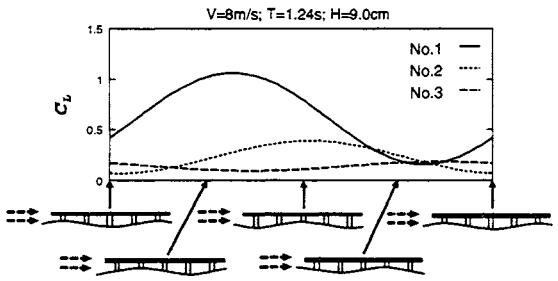

Figure 10: Phase differece between lift coefficient, C_L and wave.

In waves with long wave length and large wave height, c_L may be comparable to $\bar{C}_L$ according to Fig. 8 and lift force becomes comparable to wave force at the leading edge.

Typical distribution of c_p on No.1 unit deck in case C experiment is shown in Fig. 11.

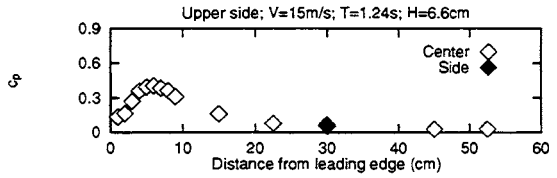

(a) Upper surface

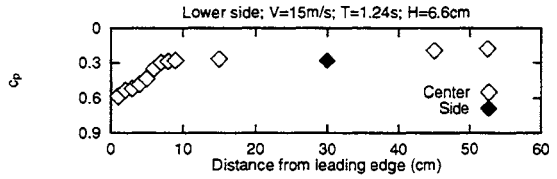

(b) Lower surface

Figure 11: Fluctuating pressure coefficient c_p distribution on No.1 unit deck in winds and waves.

c_p is large at the leading edge on both upper and lower surface. Similar distributions were obtained for other wind velocities. Fig. 12 shows the difference of fluctuating pressure coefficient between upper and lower surface. Where H is wave height and B is distance between deck and the still water level. $|c_p|$ are similarly distributed for all wave periods in experiment.

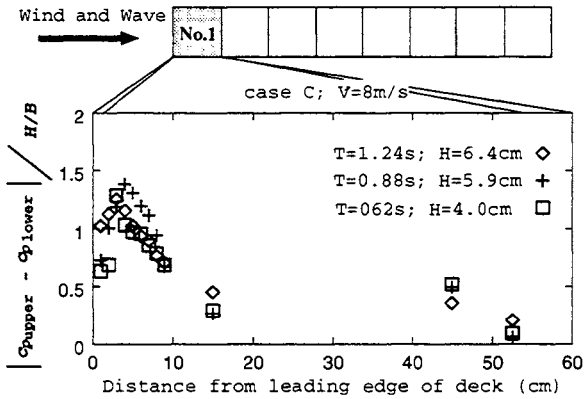

Figure 12: Difference of fluctuating pressure between upper and lower surface.

3. LIFT FORCE MODEL

Lift force model is proposed for estimation of lift forces of VLFS of semisubmersible type according to the experimental results. This model can be applied for lift force on center line of deck.

Lift force is represented by Eq. (1). In the present study, time averaged and fluctuating component are modeled separately.

Lift force models of conventional semisubmersible were proposed by Nishimoto[6] and Arima[3]. Nishimoto showed that the main physical phenomena that could induce lift force are potential flow on flat plate, free surface effect on flat plate and vortex effect produced by appendages. He concluded that lift force due to wake of appendages has considerable value from his experimental results. Arima proposed that the characteristics of $\bar{C}_{Lw.D.}$ can be determined by asymmetry between upper and lower surface of deck. He also proposed that $\bar{C}_{Lw.D.}$ is represented by the product of ratio which represents the asymmetry of structure and mean pressure coefficient on upper surface of the rectangular box placed on a flat surface.

In the present study, Arima's mehod is adopted for lift force model and further, the physical phenomena, i.e., shielding of columns, the effects of water surface and fluctuation intensity of wind velocity are considered according to the experimental results. Mean lift coefficient is represented by the following equation,

$$\bar{C}_L(x) = -\psi(x)\phi(x)\bar{C}_0(x), \quad (7)$$

$\bar{C}_0(x)$: mean pressure coefficient of rectangular box
$\phi(x)$: asymmetry of structure
$\psi(x)$: effects of water surface

When drag force acting on VLFS of semisubmersible type is estimated, a calculation method recommended by a classification society with the assumption that columns can be replaced by box which has same projected area as shown in Fig. 13 agrees with experimental results[4] and the assumption is effective for estimation of lift force of VLFS of semisubmersible type. Therefore asymmetry between upper and lower surface of deck can be represented by solidification factor and the asymmetry parameter is constant $\phi = (Wt + DB)/WH$ according to Fig. 13.

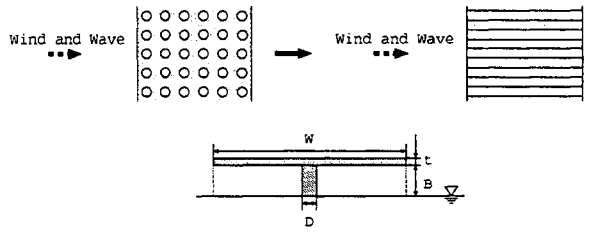

Figure 13: Representaion of shielding effect of columns in lift force model.

Mean pressure coefficient on upper surface of very large rectangular box is adopted as $\bar{C}_0(x)$, which is given by the following equation[5],

$$\bar{C}_0(x) = \begin{cases} f(x) & \text{for } x/R_h < 5, \\ f(5R_h) & \text{for } x/R_h \geq 5, \end{cases} \quad (8)$$

where

$$f(x) = -|\bar{C}_{0p}|(-0.0230 \cdot (x/R_h)^3 + 0.269 \cdot (x/R_h)^2 - 1.048 \cdot x/R_h + 1.810),$$
$$|\bar{C}_{0p}| = 1.85 \cdot I_{UH} + 0.624,$$

R_h is the height of upper surface of rectangular box, I_{UH} is fluctuation intensity of wind velocity.

$\bar{C}_L$ in the case of liquid boundary is different from that of solid boundary because of the effects of water surface. The effects are decrease of wind velocity due to roughness of water surface and depression of water surface due to wind pressure at the windward of the model. Since $\bar{C}_L$ of liquid boundary is 1.5 ~ 2.0 times larger compared with that of solid boundary according to the previous studies, the value of $\psi = 1.5$ fits into the present experimental results.

The distributions of local mean lift coefficient $\bar{C}_L$ are shown in Fig. 14. Estimated $\bar{C}_L$ almost agree with the experimental results.

Total mean lift coefficients of the whole of deck, $\bar{C}_{L\,\text{W.D.}}$, are compared with experimental results and shown in Table 2.

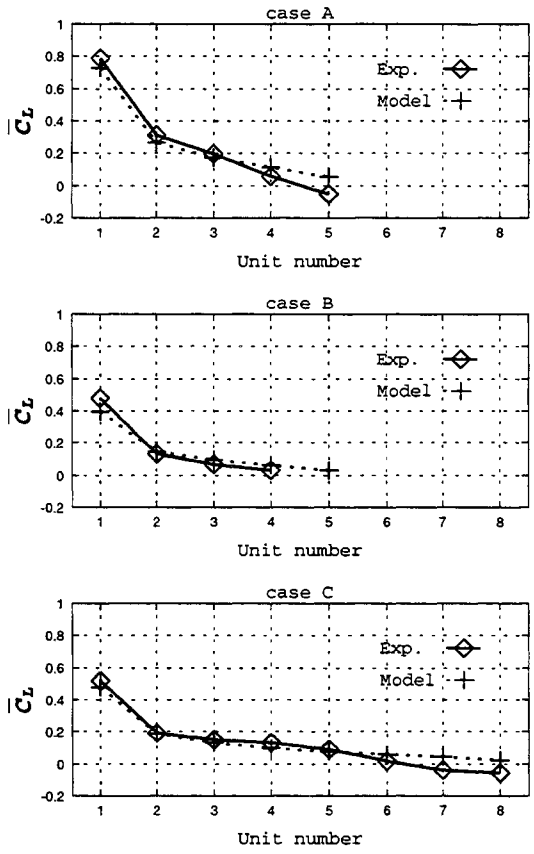

Figure 14: Comparison of model with exp. for the distribution of $\bar{C}_L$.

Table 2: Comparison of estimated $\bar{C}_{L\,W.D.}$ with experimental results.

	case A	case B	case C
model	0.28	0.15	0.14
exp.	0.26	0.13	0.12

	Sedco 700 (1)	Sedco 700 (2)	Kansai International Airport
model	0.09	0.17	0.34
exp.	0.04	0.08	0.35

Table 2 includes the experimental results on Sedco 700–class semisubmersible[2] and VLFS of semisubmersible type that was proposed for the first plan of Kansai International Airport[4]. Schematic diagram and principal dimensions of the both exper-

imental models are shown in Fig. 15. For Sedco 700-class semisubmersible, lift force model overestimates $\bar{C}_L$ because the effect that wind is diverted to the side of structure is not considered. But for VLFS of semisubmersible type, this model estimates appropriate $\bar{C}_L$ and is effective in estimation of lift force.

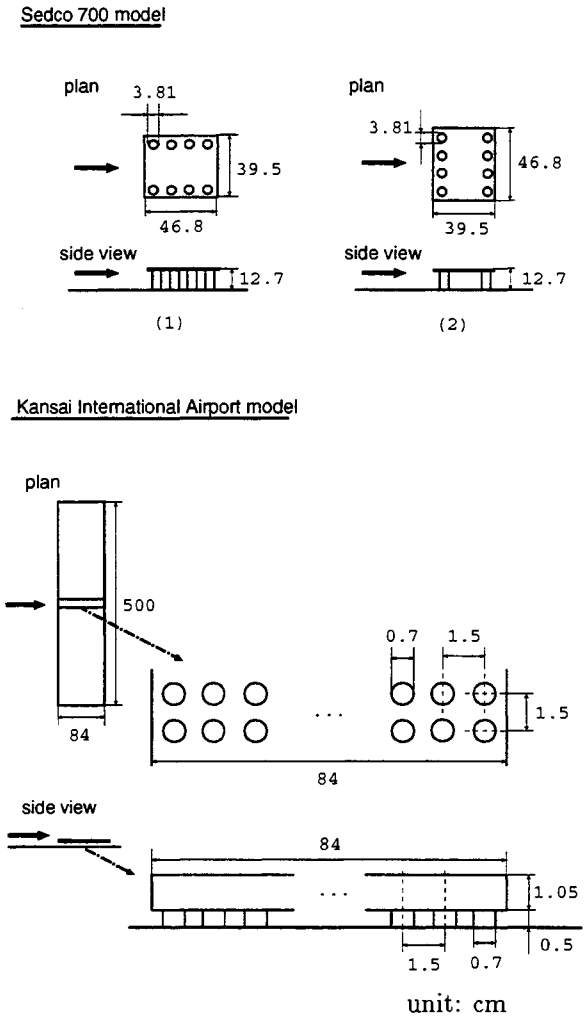

Figure 15: Sketch of experimental models of Sedco 700 and Kansai International Airport.

For fluctuating lift force model, c_L is assumed to be a function of fluctuation intensity of wind velocity according to the present experimental results. Therefore it is assumed that c_L is determined only by fluctuating pressure coefficient of very large rectangular box. Taking the phase difference into account, fluctuating lift coefficient is represented by the following equation,

$$c_L = |c_L| \cos(\omega t + \kappa x_1 + \varepsilon) = \frac{1}{l} \int_{x_1}^{x_1+l} \{c_0(x) \times \cos(\kappa x + \omega t)\} dx, \quad (9)$$

where l, κ and ω are the length of unit deck, wave number and wave circular frequency respectively. x_1 is the distance from the leading edge of No.1 unit deck to the leading edge of unit deck considered.

Fluctuating pressure coefficient on upper surface of very large rectangular box is adopted as $c_0(x)$, which is given by the following equation[5],

$$c_0(x) = \begin{cases} g(x) & \text{for } x/B < 5, \\ g(5R_h) & \text{for } x/B \geq 5, \end{cases} \quad (10)$$

where

$$g(x) = c_{0p} \times (-0.0169 \cdot (x/B)^3 + 0.206 \cdot (x/B)^2 - 0.843 \cdot x/B + 1.637),$$
$$c_{0p} = 1.58 \cdot I_{UH} + 0.0240,$$

Fluctuating pressure coefficient is linearly related to the fluctuation intensity of wind velocity. According to experimental results, it is interpreted that wave height corresponds to fluctuation intensity of wind velocity.

The results are shown in Fig. 8.

This lift force model accurately describe the experimental results and it is shown that this model is effective for estimation of actual lift force distribution of very large semisubmersible.

4. CONCLUSIONS

In the present study, wind-wave tank experiments on VLFS of semisubmersible type were extensively conducted in order to estimate wind lift force on it in coexisted wind and wave typhoon conditions. Lift force model for estimation of lift force acting on a deck of VLFS of semisubmersible type was proposed. The conclusions obtained from the present study were as follows:

1. Lift force is significant at the windward part of deck. Mean lift force can be represented as a function of projected area of VLFS of semisubmersible type.

2. In regular waves, fluctuation of lift force depends mainly on wave characteristics and fluctuates at wave period. Fluctuating lift coefficient is lineary related to wave height and fluctuation intensity of wind velocity.

3. A lift force model proposed for estimation of lift forces of VLFS of semisubmersible type consists of time averaged mean component and fluctuating component. Effectiveness of this model was confirmed by the present experimental results.

Acknowledgment: We thank Dr. S. Ohmatsu and Mr. K. Yago of the Ship Research Institute. Especially thanks are offered to Mr. Yago for experimental support.

References

[1] K. Yoshida, H. Uyama, N. Oka, H. Suzuki, S. Masanobu and M. Naito, Wind Loads of Large Scale Semisubmergible Offshore Structures under Storm Condition. *Proceedings of the 13th Ocean Engineering Symposium*, pp.281–288, 1995 (in Japanese).

[2] J. Michael Macha and Dale F. Reid, Semisubmersible Wind Loads and Wind Effects. *The Society of Naval Architects and Marine Engineers, Transactions, Vol.92*, pp.85–124, 1984.

[3] T. Arima, Estimation of Wind Loads and Motion Response of TLP. *Master's thesis*, the University of Tokyo, 1986 (in Japanese).

[4] N. Takarada, *Bulletin of The Society of Naval Architects of Japan, Vol.640*, pp.574–599, 1982 (in Japanese).

[5] Y. Tamura, H. Marukawa, Y. Uematsu, H. Ueda, H. Seki, O. Nakamura, H. Hayashida, Estimation of Loads on Long Span Structure. *Data of wind-resistant design for structures (Vol.2) - wind dynamic effects and estimation of wind loads* -, Committee on wind loads of Architectural Institute of Japan, pp.85–102, 1991 (in Japanese).

[6] K. Nishimoto, Assessment of Safety Design for Offshore Structures in Ocean Environmental Forces. *Ph.D. thesis*, the University of Tokyo, 1985.

PROCEEDINGS OF THE THIRD INTERNATIONAL WORKSHOP ON VERY LARGE FLOATING STRUCTURES
(VLFS '99), VOL. I, EDS. R.C. ERTEKIN & J.W. KIM, 22-24 SEPTEMBER 1999, HONOLULU, HAWAII, USA

MOBILE OFFSHORE BASE (MOB) DESIGN AND ANALYSIS REQUIREMENTS AND HYDRODYNAMIC TOOLS EVALUATIONS AND MODELING GUIDELINES

C. Chester Wung, Makis Manetas, and Jun Ying
Bechtel National, Inc.*

ABSTRACT

This paper describes the basic analysis requirements for the design of the U.S. Navy Mobile Offshore Base (MOB) structures and the results of evaluations of the computer tools that can be used in the design process. The evaluation emphasizes the tools that employ a linear diffraction/radiation approach for predicting the hydrodynamic loads. General and specific modeling guidelines for hydrodynamic analysis for MOB applications are also provided.

The MOB structure used in this "tool benchmark" analysis has three modules that, when connected, result in a total length of approximately 1500 meters. The benchmark studies included up to three rigid bodies in the analyses.

1. INTRODUCTION

The U. S. Navy is currently in the stages of feasibility and cost studies for developing a very large Mobile Offshore Base (MOB). The MOB is currently envisioned as a 1500-meter long floating base intended to serve as a forward supply point for military operations.

Because of its size and worldwide operability requirement, the MOB design may fall outside the realm of the state-of-practice technology traditionally applied to much smaller semi-submersible vessels. Thus, a study was conducted to verify the readiness of the currently available computer tools for the MOB applications. The study was divided into three major parts: first, identify basic design and analysis procedures and requirements needed for the MOB application; then, survey the associated tools that could fulfill the identified analysis requirements; and, lastly, verify the capabilities of these tools by analyzing practical MOB examples.

Because of the expected large dimensions of the cross sections of the members in the MOB, the study emphasized the hydrodynamic tools that employ a linear diffraction/radiation approach.

2. MOB ANALYSIS REQUIREMENTS

Analysis procedures and requirements in the MOB design were identified for the purpose of assessing the software tools. They were not intended to serve as a MOB design basis.

In general, the design and analysis procedure starts by sizing the MOB to meet basic buoyancy and stability requirements and progresses through analysis for loads, motions, structural response, strength, fatigue and station keeping. Specifically, the overall analysis process to be undertaken during the design of a MOB consists of the following specific analyses:

- Initial sizing
- Hydrostatic stability analysis
- Weight analysis and control
- Global analysis for motions and dynamic loads - deep draft
- Global analysis for motions and dynamic loads - transit draft
- Global analysis for impact
- Global analysis for collision
- Global structural analysis
- Local structural analysis
- Strength and buckling analysis
- Fatigue analysis
- Dynamic positioning

These twelve analysis requirements consider design cases that range from fabrication/erection, laid-up, transit, connected and unconnected, connecting and disconnecting, operational and storm, intact and damaged, and other design scenarios.

* 45 Fremont Street, San Francisco, CA 94119, USA

3. COMPUTER TOOLS SURVEY

A survey was conducted to identify and assess, in a preliminary way, any available software, either commercially available or in the public domain, that can be used to perform the analysis requirements identified above.

The overall survey approach was principally to gather data through the use of a written survey questionnaire sent to a list of more than 50 candidate vendor companies. The vendor list was established through a combination of the experience base within the survey team, internet searches, and networking with other industry and academia experts. The preliminary product evaluation was mainly based on the vendor's provided information, which was cursory in nature, and therefore, the evaluation could not be exhaustive and thorough.

The purpose of the preliminary evaluation was to select key products in each identified analysis category for a further detailed product evaluation to verify their readiness for the MOB applications. The maximum number of products selected in each category was limited to five. The only exception was the deep draft motion and load analysis category, which was considered as a fundamental analysis requirement for the MOB design. A total of 19 distinct products from 16 vendors were selected and are listed below in alphanumerical order:

- Stability - AQWA[1], Autohydro[2], GHS[3], MOSES[4]
- Motions and Loads (Deep Draft) - AQWA, HIPAN[5], HOBEM[6], HYDRAN[7], MORA[8], MOSES, SESAM[9], WAMIT[5]
- Motions and Loads (Transit Draft) - LAMP[10], SWAN[11], USAERO[12]
- Impact - ABAQUS[13], AQWA, CAP[14], MOSES, SESAM
- Collision - ABAQUS, ADINA[15], ASAS[1], COSMOS[16], SESAM
- Global Structural Analysis - ABAQUS, ASAS, MOSES, SESAM, StruCAD[17]
- Local Structural Analysis - ABAQUS, ADINA, ASAS, (other standard FE programs)
- Fatigue - CAP, MOSES, SACS, SESAM, ASAS

The initial sizing and weight analyses involve only simple arithmetic spreadsheet calculations and book-keeping and don't pose any analysis difficulty. Thus, they were excluded from the survey. No product selections were made in the categories of the strength analysis and dynamic positioning system (DPS). Strength analysis was considered as part of the global structural analysis. DPS requires specialized expertise and is principally supported by customized in-house software.

It is noted that, in many respects, this early evaluation process was cursory in nature and cannot be considered an exhaustive thorough review of each software product identified or that the list of products reviewed consists of all the available products. Such a task would be practically impossible.

4. HYDRODYNAMIC TOOLS EVALUATION

No analyses of any kind were performed in the initial evaluation to reach the conclusions made. At this early stage of the project, the evaluation relied primarily on information supplied by vendors, professional opinions and engineering judgment and experience in the analysis and design of offshore structures.

The conclusions reached in this survey should not, under any circumstances, be viewed as an endorsement or approval by BNI of any product. Similarly, they should not be viewed as disapproval. Furthermore, should a particular program exist in the world that may be later found suitable to perform any of the required analysis but was not presently identified, it may be a result of an inherent inability to identify each and every possible program.

Because of project constraints, the detailed product evaluation was limited only to some of the selected hydrodynamic tools that can perform the deep draft motions and loads analysis. Six tools were selected by the US Navy for further evaluation; they were: AQWA, HIPAN, HOBEM, HYDRAN, MORA, and WAMIT. Most of these tools had been used in the development of the different concepts in the MOB project.

4.1 Hydrodynamic Tools Description

The six programs that were benchmarked for their capabilities in wave load and motions analysis all use the diffraction/radiation approach. Among them, four programs, AQWA, HYDRAN, MORA, and WAMIT use a constant panel method, while HIPAN and HOBEM employ a higher-order approach. HIPAN mainly uses B-spline and HOBEM uses quadratic functions as a basis to fit both geometry and potential variation of solutions.

AQWA by WS Atkins can handle single and multiple rigid body analysis but ignores hydrodynamic interactions among different modules. Because AQWA was benchmarked solely by ABS[18], the analysis results from AQWA are not presented here.

HIPAN from MIT is applicable for single or multiple bodies, rigid or flexible modules.

MECAS consisting of HOBEM leased from FCA International, Inc. is limited to solving single rigid body cases only.

HYDRAN by OffCoast, Inc. analyzes a hydrodynamic problem involving single or multiple, rigid or flexible modules. Mean drift wave force and

free surface responses are not available with HYDRAN version 1.11 tested.

MORA by G. J. Garrison possesses the capability for performing single or multiple bodies analysis. For multiple bodies analysis, MORA includes hydrodynamic interaction for adjacent bodies.

WAMIT from MIT handles single or multiple, rigid or flexible modules cases and can compute some of the second-order hydrodynamic loads.

4.2 Benchmark Problem

The benchmark analysis problem created for the hydrodynamic tool evaluation comprised of a three-module MOB structure. In order to cover as wide a range of MOB concepts as possible, models with and without structural connections between adjacent modules were considered.

The three modules utilized were identical, each 485 meters long and 120 meters wide. Each module consisted of two pontoons and 14 columns (see Figure 1) - all rectangular in shape with rounded corners. The total module weight of about 647,000 tonnes produced an operational draft of 35 meters.

Three arrangements of the MOB structure were considered in the analysis. The first arrangement involved a single module case with six rigid body degrees of freedom. The second arrangement considered three modules arranged in series without any structural connection between any two adjacent modules. The third arrangement considered three modules similar to the second arrangement but connected at the deck by hinges allowing relative pitch.

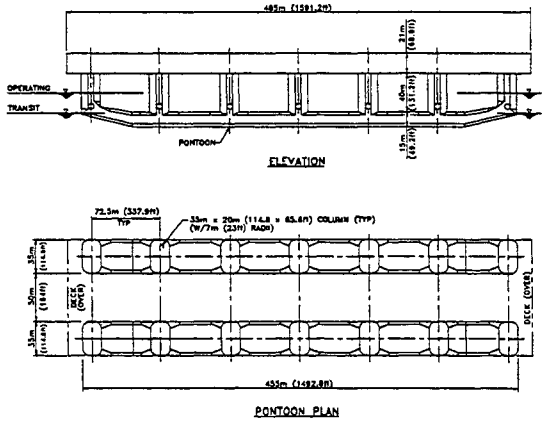

Figure 1: Definition sketch of the physical problem

The analysis parameters included three wave headings – head, quartering, and beam, and 16 wave periods ranging from 4 to 30 seconds. The results of primary interest from the benchmark analysis comparisons included response quantities such as the first order loads and motions, mean wave drift force, free surface elevations (or air gap), and fluid pressures on the wetted surface.

4.3 Model Generation and Convergence Test

MultiSurf [19] was used in the development of all the flat-panel hydrodynamic models. For the higher-order hydrodynamic models, MultiSurf supports HIPAN modeling and was also used for the development of HIPAN models, while MECAS was used for developing HOBEM models.

The adequacy of numerical models created for hydrodynamic load analysis can be determined through a convergence test. The convergence test estimates the hydrodynamic solution errors caused by a simplified mesh model. The convergence test does not determine the errors arising from the use of simplified assumptions made in the diffraction/radiation theory. The latter errors can be estimated only by comparing the analysis data with the data measured in a real-life condition or from model tests.

The convergence test involved hydrodynamic analyses on a set of numerical models with various levels of mesh refinements and sought mess sizes that would produce acceptable hydrodynamic solutions.

The convergence test in this study was conducted only on a single module MOB model and it was divided into two parts for mesh quantitative and qualitative evaluations.

4.3.1 Mesh Quantitative Evaluations

Quantitative evaluations of modeling were performed through a convergence test using seven meshes on a single module model. The seven models basically represented the same geometric structure and differed mainly in their mesh refinement, with numbers of panels used in the full module ranging from 20,112 to 872. The finest and coarsest mesh models are shown in Figure 2. Major horizontal braces were ignored in the coarsest mesh model.

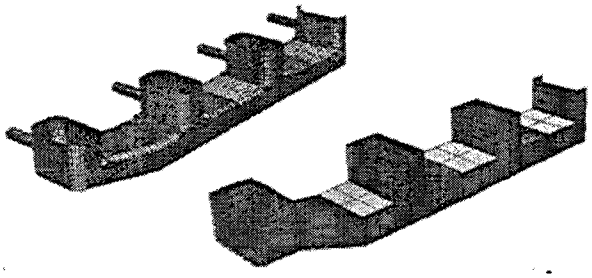

Figure 2: Finest and Coarsest Meshes of One-Quadrant Model (20,112 vs. 872 Panels for Whole Module)

The convergence test for the mesh quantitative evaluations determined the minimum number of the panels required to produce acceptable hydrodynamic solutions.

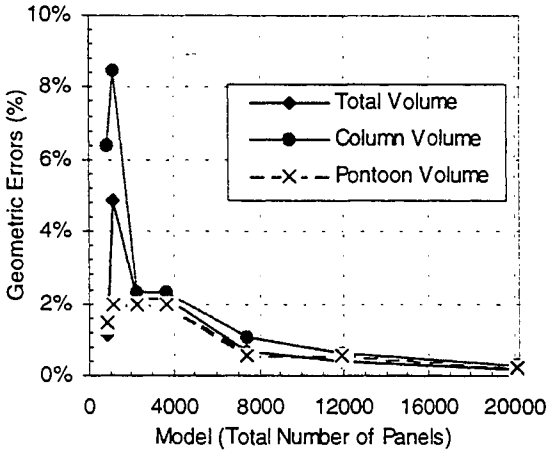

Figure 3: Geometric Errors of Seven Basic Models

Figure 3 shows geometric errors of the seven models from WAMIT calculations. The geometric errors arise from the loss of area and volume in using flat panels to model curved surfaces.

Figures 4 and 5 show the relative differences of basic hydrodynamic solutions from WAMIT calculations. The relative differences refer to the differences of the root mean square (RMS) responses of any model against the finest model. Two sea states were considered in the convergence tests and they have wave spectra with peak periods of 9 and 16 seconds, to effectively cover various design conditions ranging from short to long waves.

Figures 4 and 5 indicate that, using WAMIT, a model with about 3500 panels for a single MOB module (for this specific configuration) can produce basic hydrodynamic results with convergence errors within 3%.

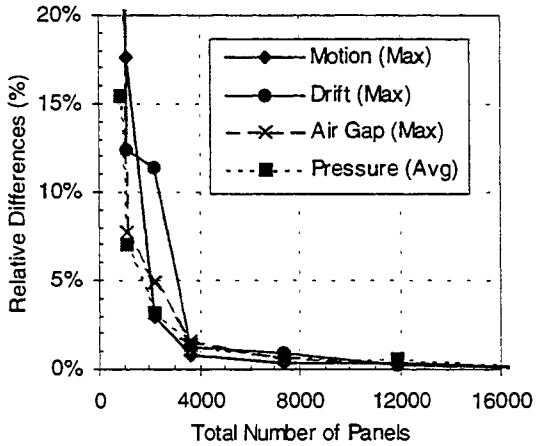

Figure 4: WAMIT Convergence Test Results for 9 sec. Peak Period Waves

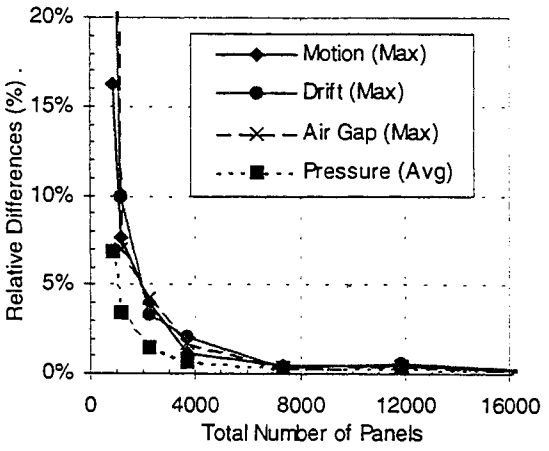

Figure 5: WAMIT Convergence Test Results for 16 sec. Peak Period Waves

The convergence tests were also conducted for the evaluation of AQWA, HYDRAN, and MORA programs that use a flat-panel approach. Because AQWA was benchmarked by ABS, no results from AQWA are shown here. The convergence test results using wave spectra with a peak period of 9 seconds are shown for HYDRAN and MORA in Figures 6 and 7, respectively.

The base model for the comparison of hydrodynamic solutions for HYDRAN and MORA had totals of 11,848 panels and 7,372 panels, respectively. The mean drift force and air gap responses were not available in HYDRAN. The local pressure loads for MORA were not processed.

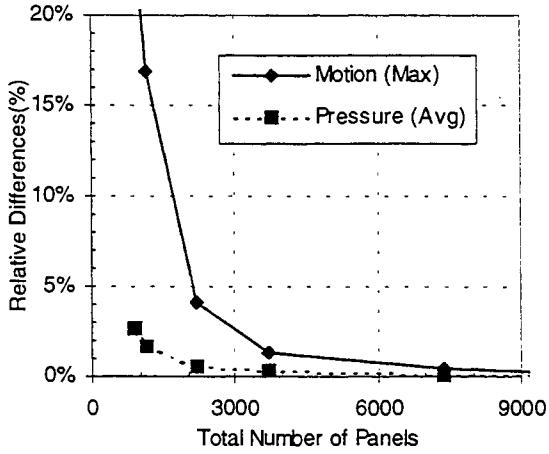

Figure 6: HYDRAN Convergence Test Results for 9 sec. Peak Period Waves

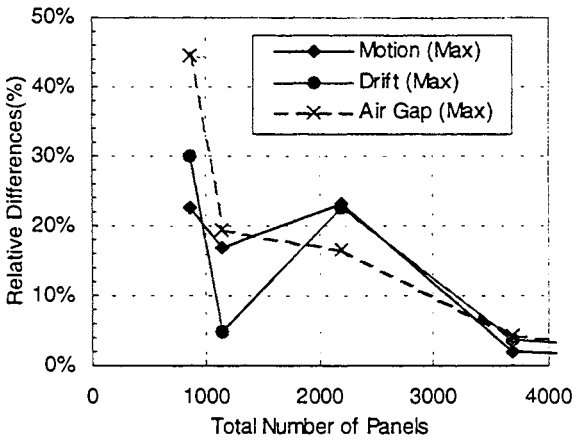

Figure 7: MORA Convergence Test Results for 9 sec. Peak Period Waves

Similar convergence tests were also conducted for the evaluation of HIPAN and HOBEM. Because both programs employ a higher-order panel approach, the models used in HIPAN and HOBEM were not the flat-panel models used by other programs, and new numerical models were created separately for each.

MultiSurf was used to create the HIPAN models that involve B-spline basis functions. Because some surface details, such as on column/pontoon intersection, were expressively modeled, one quadrant of the single module MOB model considered as the base model used 39 patches that were divided into 136 panels (refer to HIPAN manuals for the definitions of patch and panel). The HIPAN convergence test was conducted simply by adjusting parameters of the base model for higher-order numerical calculations that in turn produce more accurate analysis results. The HIPAN convergence test results are expressed in terms of the total number of unknowns used in the analysis and are shown in Figure 8.

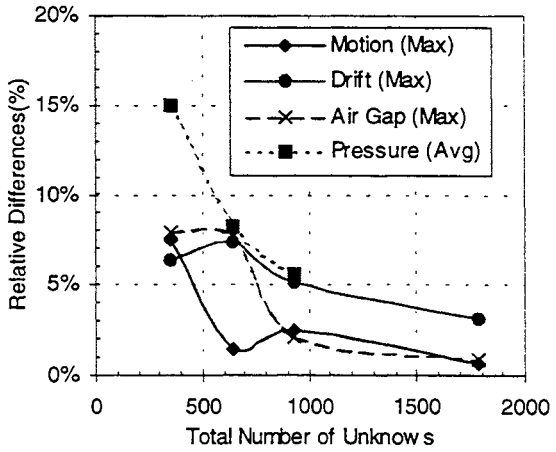

Figure 8: HIPAN Convergence Test Results for 9 sec. Peak Period Waves

MECAS was used to create HOBEM models. HOBEM allows the quadratic variation of potential in the quadratic isoparametric panel. The convergence test can be simply conducted by automatic subdivision of panels into smaller panels, or by adjusting the number of Gaussian integration points used in each panel. The HOBEM convergence test results are shown in Figure 9.

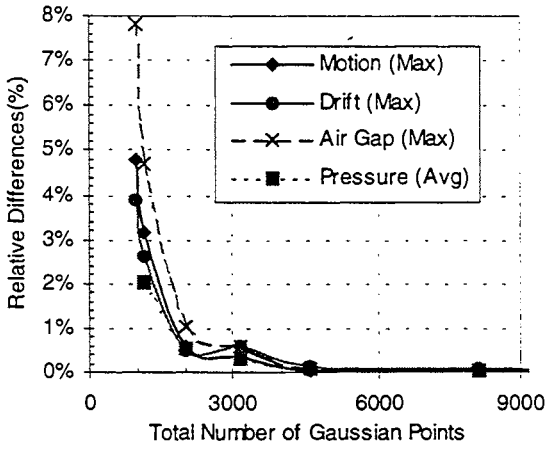

Figure 9: HOBEM Convergence Test Results for 9 sec. Peak Period Waves

4.3.2 Mesh Qualitative Evaluations

Following the quantitative mesh evaluations, where the focus was on the overall size of the mesh, qualitative evaluations were performed to investigate the quality of the mesh refinement in areas that were sensitive to the hydrodynamic solutions. As a result of the mesh qualitative evaluations, an optimized mesh model for efficient computer analysis may be created.

All the models used in the mesh qualitative study were derived from the flat-panel model with a total of 3680 panels. This model was chosen as a base because its hydrodynamic solutions converged very well (within a 2% relative difference) and the analysis times for the models derived from this model were reasonable. Each run, using the option for two planes of symmetry, required approximately one hour of CPU using a Pentium 233 MHz PC for WAMIT analysis.

Considered in this qualitative mesh study were the areas of the horizontal braces, columns close to water surface, column corners, pontoon corners, and brace/column intersections. This study concentrated on one area at a time so that multiple effects would be avoided. The results from the convergence test for the mesh qualitative analysis are now presented.

Exclusion of seven major horizontal braces from the analysis affects global responses, such as first-order motions and mean drift forces, by 5% at most. The braces have greater effect on the relative water surface motion responses because they are close to the water

surface, particularly, for the 9-sec peak period waves.

The mesh close to the water surface requires special attention because the wave energy is larger and the diffraction/radiation solutions pose special numerical difficulties. The results from the waterline mesh study for the 9-sec peak period waves are plotted in Figure 10. For the 16-sec peak period waves, four rows of panels were sufficient to limit the relative difference to 1% (not shown), while seven rows of panels that were used in the base model for the 9-sec peak period waves were required for 2% differences.

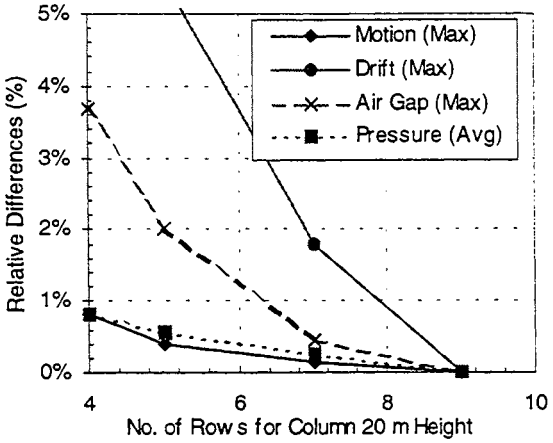

Figure 10: Column Waterline Mesh Study Results For 9 sec. Peak Period Waves

The columns considered in this study are of rectangular section, 35m x 20m, with four rounded corners of 7m radius. The results from the column corner mesh study for the 9-sec peak period waves are plotted in Figure 11. Four arc-wise subdivisions (four panels) for each corner were required to limit the relative differences to 1%.

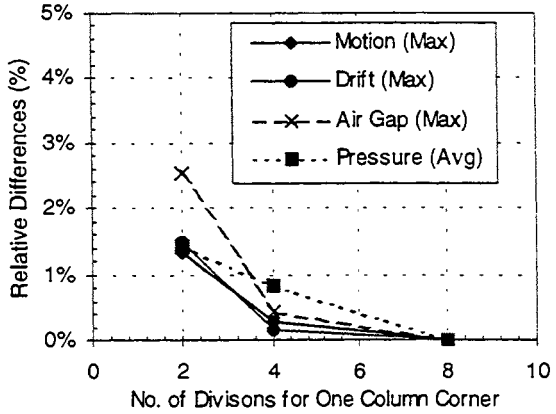

Figure 11: Column Corner Mesh Study Results For 9 sec. Peak Period Waves

The pontoons considered in this study are of rectangular section, 35m x 15m, with four rounded corners of 3m radius. The results from the pontoon corner mesh study for the 9-sec peak period waves are plotted in Figure 12. Two arc-wise subdivisions (two panels) for each corner were required to limit the relative differences to 1%. Because the pontoons were submerged deeper than columns and also because the corners were smaller, a smaller number of divisions was expected.

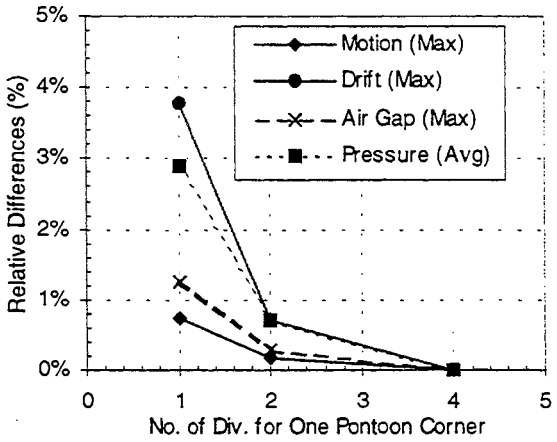

Figure 12: Pontoon Corner Mesh Study Results For 9 sec. Peak Period Waves

Modeling brace and column intersections often requires a substantial effort. The effects on simplified intersection modeling of removing panels near the ends of the seven horizontal braces were studied. The effects on the global motion and mean drift force solutions due to this simplified modeling were found to be less than 1%. However, the maximum relative differences of the local pressure loads around the area close to the removed end panels could be as large as 30%. On the other hand, the local pressure loads in the areas away from the excluded panels were not significantly affected.

4.4 Hydrodynamic Results Comparisons

Comparisons of hydrodynamic solutions from HIPAN, HOBEM, HYDRAN, MORA and WAMIT analyses were made and are presented in this section. Only the results of primary interest are illustrated here.

Figures 13 to 18 show some of the single module responses, while Figures 19 to 20 show the comparisons of primary pitch motions for multiple modules cases.

For the single module case, the results of the finest mesh model analyzed were compared, representing the most accurate solutions from each of the five programs. For the multiple module cases, because of computer limitations, the results were derived from the analyses of coarser mesh models. For HYDRAN, MORA, and WAMIT, the three-module models were all derived

from the single module model with 1144 panels. The HIPAN three-module model was based on the HIPAN single module model but used less computation-intensive parameters.

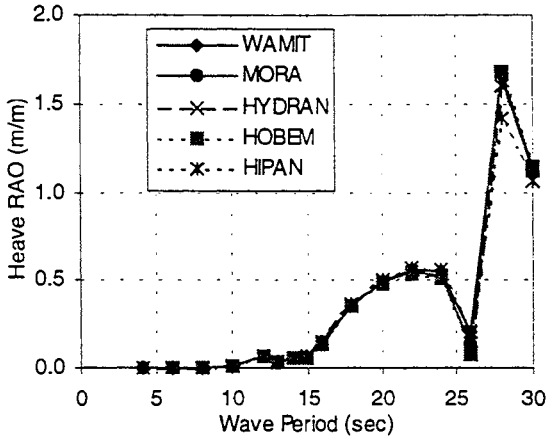

Figure 13: Quartering Sea Heave Motions of Single Module

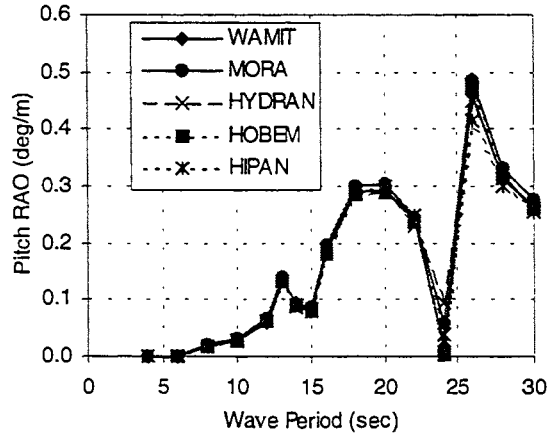

Figure 14: Head Sea Pitch Motions of Single Module

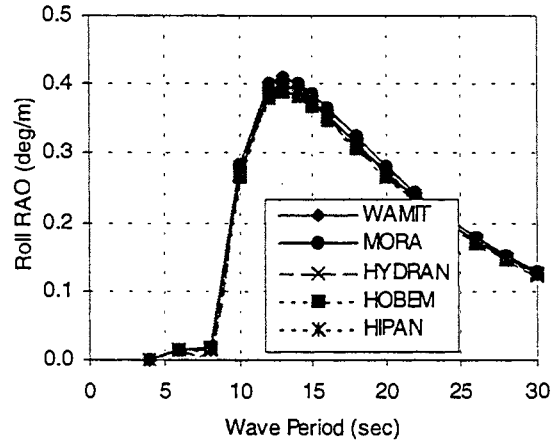

Figure 15: Beam Sea Roll Motions of Single Module

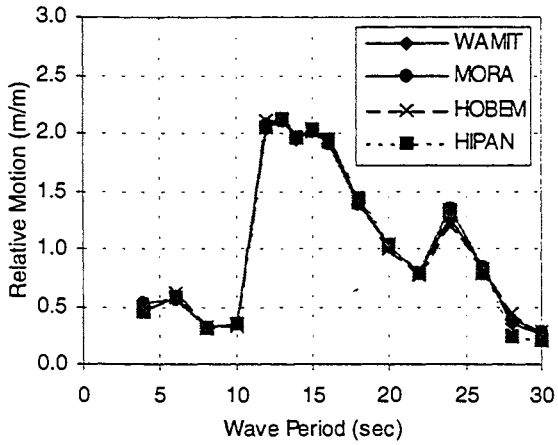

Figure 16: Head Sea Relative Water Surface Amplitudes of Single Module around Stern

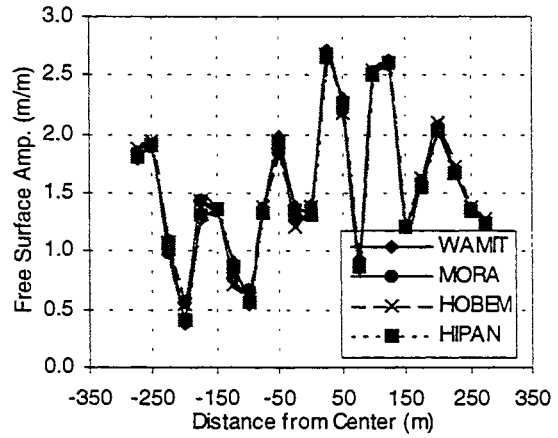

Figure 17: Head Sea Free Water Surface Amplitudes of Single Module at Centerline between Pontoons

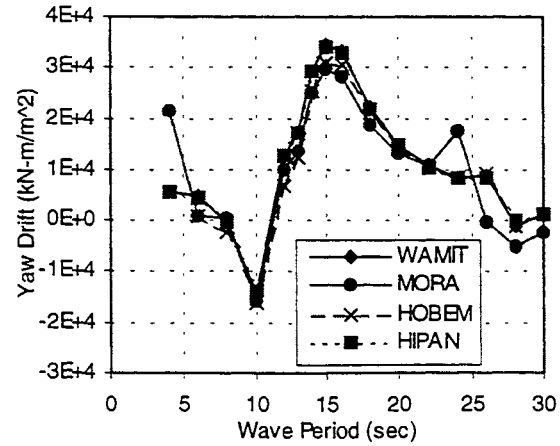

Figure 18: Quartering Sea Mean Drift Yaw Moments of Single Module

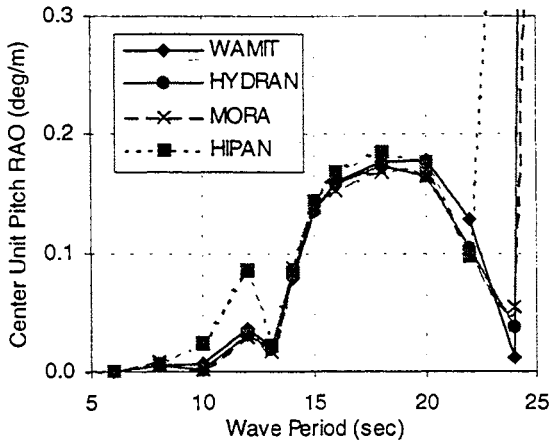

Figure 19: Quartering Sea Center Unit Pitch Motions for Three Inline Unconnected Modules

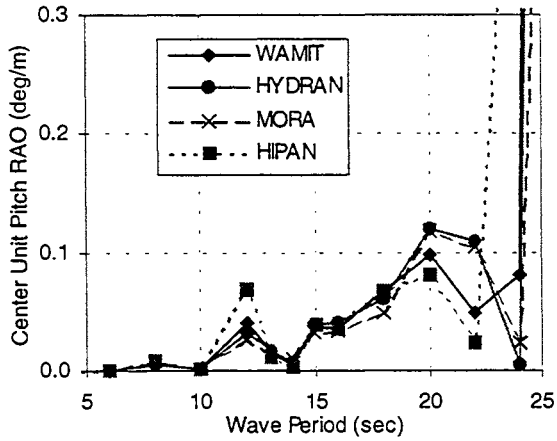

Figure 20: Quartering Sea Center Unit Pitch Motions for Three Hinged Connected Modules

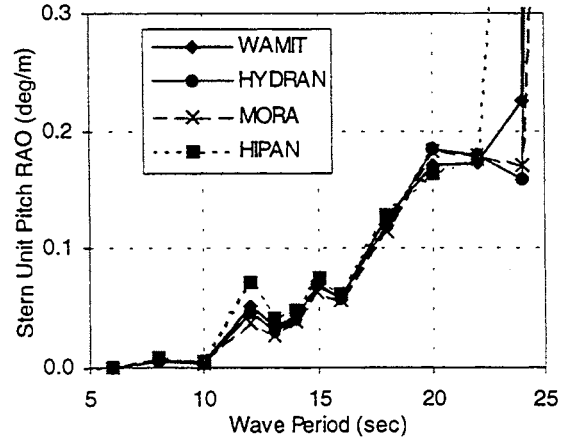

Figure 21: Quartering Sea Stern Unit Pitch Motions for Three Hinged Connected Modules

The comparisons indicate that all of the five programs benchmarked can produce consistent hydrodynamic results for the MOB applications.

5. MODELING GUIDELINES

Modeling guidelines for hydrodynamic analyses that use the diffraction/radiation panel approach were learned in this study. In essence, accurate hydrodynamic solutions rely on proper control of the model geometry and the panel sizes and order of expansion that are used to model the structure. General guidelines are:

- The geometric errors in the model affecting displacement and column waterline cross section should be limited to small values. Any resulting geometric errors translate into convergence errors for the hydrodynamic load and reduce the accuracy of solution.
- A convergence test to estimate the numerical error (convergence error) of modeling is required, particularly, when convergence test data on a similar structure are not available. For accurate estimate of the convergence error, at least three models with significantly different mesh refinements are needed in the convergence test (the quantitative evaluations).
- If analysis speed is an issue, users may want to develop an optimized hydrodynamic model. The optimized model can be developed from a mesh quality study (the qualitative evaluations) on every local important modeling area. In general, finer mesh (i.e., more panels) is required in the areas where rapid change of gradients in the flow are expected, such as areas around the mean water level, corners, and intersections.

Specific modeling guidelines for the MOB applications include:

- Panel sizes should first be determined from the geometric modeling. Errors from displaced volume and heave stiffness calculations should be limited to one half of the maximum allowable convergence error set by the analyst, so that the part of the convergence errors from geometrical errors would not dominate the total convergence errors.
- The magnitude of the maximum allowable convergence error from the convergence test should be smaller than the amount of uncertainty that arises from the analysis in predicting the real life behavior. The continuing study [20] of the hydrodynamic tool evaluations indicates that the difference in the coefficients of variation of results between the MOB hydrodynamic analyses and laboratory test data ranges from 10% to more than 50%. Thus, a maximum allowable convergence error of 5% is believed to be small enough for the convergence test, for the MOB applications.

- For the MOB structure given in this benchmark analysis, a single module model (485 meters long and 120 meters wide) with 3,680 panels is suitable for MOB applications (of a configuration like the one analyzed) limiting convergence errors to within 2%, with WAMIT analyses.

6. CONCLUSIONS

Potential design tools in each of the analysis requirements categories needed for the design of MOB were identified in this study. Even though the readiness of those tools for the MOB applications that involve a structure larger than any existing marine vessel has not been fully verified, most of the MOB analysis requirements were believed to be able to be fulfilled with current technology. However, validation against model test results is necessary [20].

A detailed evaluation was made of the hydrodynamic tools that can perform the deep draft motions and loads analysis. The hydrodynamic tool evaluations indicated that the five hydrodynamic tools examined produce very similar motions, mean drift forces and air gap responses for the single rigid body case. Similar motion responses for three-body motions were also found among HIPAN, HYDRAN, MORA, and WAMIT. This generalization holds true for the hydrodynamic tools that employ a diffraction/radiation approach, provided that the corresponding capabilities for the individual tool are available and that the numerical model (or mesh) used in each analysis is adequate.

A convergence test to determine the hydrodynamic numerical models for the MOB hydrodynamic applications is necessary. Useful modeling guidelines were derived in this study to help MOB analysts in the development of the hydrodynamic numerical models.

Acknowledgement: The material is based upon work supported by the U.S. Office of Naval Research's MOB Program and NFESC.

References:

[1] AQWA and ASAS suites, WS Atkins Engineering Software, Surrey, UK

[2] Autohydro, AUTOSHIP Systems Corporation, Vancouver, Canada

[3] General Hydro Statics, Creative System, Inc., Washington, USA

[4] MOSES, Ultramarine, Inc., Houston, Texas, USA

[5] HIPAN and WAMIT, Department of Ocean Engineering, Massachusetts Institute of Technology, Massachusetts, USA

[6] MECAS/HOBEM, FCA International, Inc., Houston, Texas, USA

[7] HYDRAN, OffCoast, Inc., Kailua, Hawaii, USA

[8] SESAM, Det Norske Veritas, Norway

[9] LAMP, SAIC, Annapolis, Maryland, USA

[10] MORA, C. J. Garrison & Associates, Corvallis, Oregon, USA

[11] SWAN, Boston Marine Consulting, Inc., Boston, Massachusetts, USA

[12] USAERO, Analytical Methods, Inc., Redmond, Washington, USA

[13] ABAQUS, Hibbitt, Karlsson & Sorensen Inc., USA

[14] CAP, Bechtel National, Inc., San Francisco, California, USA

[15] ADINA, Adina R & D, Inc., Watertown, Maryland, USA

[16] COSMOS/M, Structural Research & Analysis, Los Angles, California, USA

[17] STRUCAD*3D, Zentech, Inc., Houston, Texas, USA

[18] American Bureau of Shipping & Affiliated Companies, USA

[19] MultiSurf, AeroHydro, Inc., Southwest harbor, Maine, USA

[20] C. Chester Wung, Makis Manetas, and Jun Ying. Hydrodynamic Computational Tools Validation against MOB Model Testing. *Proc. of Very Large Floating Structures, Hawaii, USA*, 1999.

PROCEEDINGS OF THE THIRD INTERNATIONAL WORKSHOP ON VERY LARGE FLOATING STRUCTURES
(VLFS '99), VOL. I, EDS. R.C. ERTEKIN & J.W. KIM, 22-24 SEPTEMBER 1999, HONOLULU, HAWAII, USA

Mobile Offshore Base Concepts – Hybrid: Concrete Hull and Steel Topsides.

Gunnar Rognaas, Jun Xu, Severin Lindseth, Finn Rosendahl
Aker Maritime ASA[1]

ABSTRACT

This paper describes two different types of concepts for a Mobile Offshore Base (MOB).

The two concepts are hybrids with high strength Light Weight Aggregate Concrete (LWC60) in the hull and steel in the Topside.

One concept is a semi submersible type consisting of 4 identical modules. The MOB is basically 1525m (5000ft.) long.

The second concept is a single structural unit consisting of a central concrete core 890 meter long with a steel cantilever 317 meter long at each end. The total length of the unit is 1525m.

Results from detailed code check of fatigue life for the concrete hull is included. It is concluded that fatigue is a "non-issue" for the concrete hull.

Possible construction methods and schedules are presented.

1. INTRODUCTION

Very Large Floating Structures (VLFS) are characterized by requirements for a long design life (typically 100 years) and low maintenance cost. Durability and fatigue resistance are key words for selection of materials, design and fabrication.

In this paper it will be demonstrated that High Performance Concrete (HPC) fulfils the design and construction requirements of VLFS such as the Mobile Offshore Base.

2. RULES/ FUNCTIONAL REQUIREMENTS

For a semi submersible hull, column stabilized, DnV's "Mobile Offshore Units Classification Rules" are applicable.

For design of concrete structural elements DnV's "Fixed Offshore Installation Rules" are used.

Functional requirements:

Design life	Min. 40 years
Minimum size of the MOB	1525 m x 152.5 m
Runway:	
- minimum size	1525 m x 61 m
- largest airplane	C17 Globemaster
Transit speed	8-10 knots
Storage requirements:	
- material storage	270,000m² (min.) - 837,000 m² (preferably)
- liquid storage	132,400 m³ (fuel)
	9,500 m³ (water)
Minimum draught	15 m - 20 m
Aircraft Operation in Sea State 6; Hs=6m	Maximum pitch between modules 1.5% (.86 degrees)
Survival condition	Hs=15m
Missiles attack	No design requirements
Storage areas (topside)	Minimum effective height is 6.0 m

3. CONCEPT SCREENING

A concept screening was performed focusing on possible concrete concepts.

The following categories of concepts were investigated as possible types for a concrete MOB:

- Dock
- Barge
- Ship
- Catamaran
- Semi- submersible (column- stabilized), Twin hull

[1] Postal address: Tjuvholmen, N-0250, Norway, gunnar.rognaas@akermar.com, jun.xu@akermar.com, severin@lindseth@akermar.com and finn.rosendahl@akermar.com

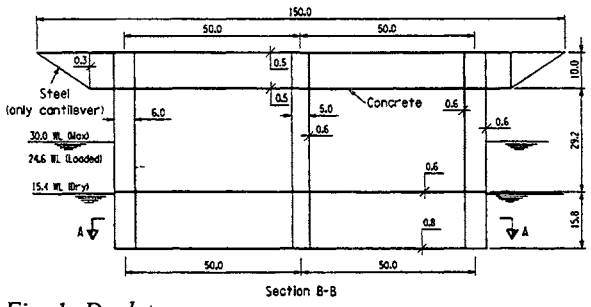

Fig. 1: Dock type

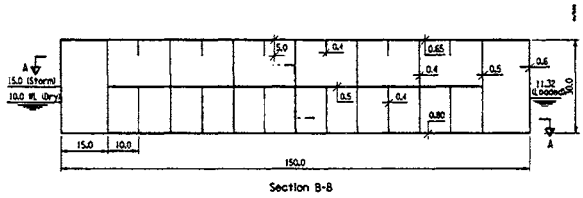

Fig. 2. Barge type. - Cross section

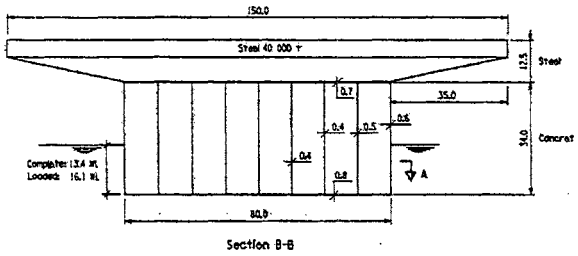

Fig.3: Ship type. - Cross section

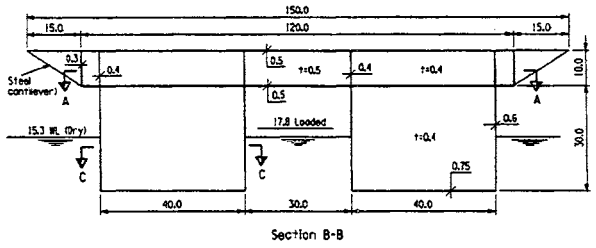

Fig.4: Catamaran type. - Cross section

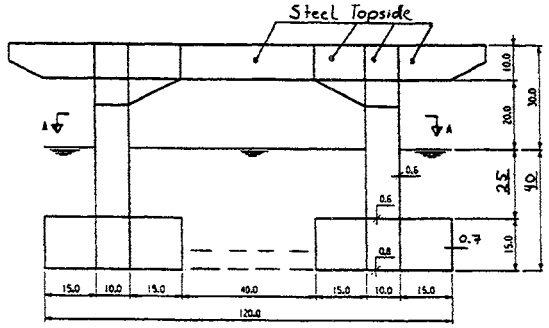

Fig. 5: Semi type/ Twin hull type. – Cross section

The driving parameters were:

- Minimum overall size 1525m x 152.5m
- Draft of about 15 m, (for transit in shallow water)
- Acceptable motions for aircraft operations
- Forces / structural strength for Survival condition
- Transit speed in the range about 10 knots.

A large number of hydrodynamic analyses were run using WADAM program to investigate the behavior of the different concepts for the Operation and Survival conditions.

The following observations were made:

The Dock shaped structure experienced numerical convergence problems in the computer program due to the internal water inside the walls (dock). Probably the concept will experience internal sloshing also in real life. Therefore the concept was abandoned.

The idea of the Dock type concept was to utilize the internal sheltered harbor for on- and off-loading operations of ships.

For *Barge* type structures the natural periods are in the range 11-16 sec. These periods are within the range of frequently occurring waves. This implies that the barges move much more when subjected to waves. A barge will generally follow the wave if the wave length is larger than twice the module length.

The Catamaran and *Ship type structures* behave almost like barges with respect to wave induced motions.

Semi-submergible types and Twin-hull structures with reduced water plane area have a natural periods of more than 30 seconds in roll and pitch.

During the screening period it seemed possible to design a structure with *reduced water plane area* (semi) with a length about 300m, which has a pitch angle less than about 0.8° for aircraft Operations state. It was assumed that by hinging modules together the relative pitch between modules would be acceptable. The pitch will decrease for longer modules. For structural reasons the length of a semi should not be more than 500m.

In order to reduce the pitch to about 0.8° for other types of structures (without reduced water plane area) the length of one module should be at least about 500 - 750 m.

The Semi-submergible hybrid concept with Light Weight Aggregate (LWA) concrete in the hull and with steel Topside deck was selected as the most appropriate concept. The main advantages of a semi structure are:

- A semi type structure with draft in the range of 40m has good motion behavior.
- The concept can be optimized to have relatively high speed at Transit draft.
- Potential for module length in the range of 300 to 500m (plus)
- A steel topside structure is lighter than concrete and is therefore favorable with respect to draft and hydrostatic stability.

The main advantages of using High Performance Concrete (HPC) are:

- superior fatigue resistance,
- ultimate strength,
- low maintenance cost,
- robustness against accidental loading.

For a more thorough description of the screening concepts reference is made to [1].

4. SEMI- SUBMERSIBLE CONCEPT

4.1 General Description

The hybrid semi [3] concept consists of 4 modules of length 381m (1250 feet). Each module is 152.5m (500 feet) wide at the Steel Deck levels. The 4 modules are inter-connected in the Operation condition giving the required 5000 ft long runway.

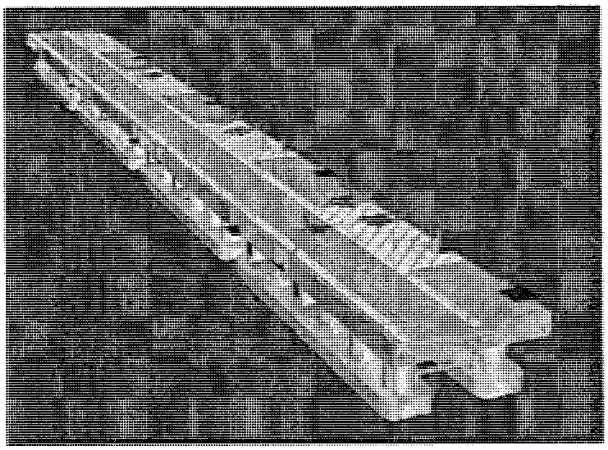

Fig. 6: Hybrid Semi-submersible Concept. Mobile Offshore Base. Length 1525m.

During aircraft Operation the floating draft is 36.5m. During (self-propelled) transportation the Transit draft is 15.7m; i.e. floating on pontoons only.

The 61m wide runway for aircraft landing and take-off is placed on one side of the top deck to allow for parking and loading/ unloading along the other side.

For sea conditions beyond that of Aircraft Operation but below Hs= 7.5m, the modules are disconnected such that each module is operating individually. This is to limit the forces in the connectors.

The connector system between the 4 modules is designed to take axial forces, horizontal- and vertical-shear forces as well as torsion (roll) moments. Both yaw and pitch motions are allowed in the connectors between the modules. In order to reduce the forces on the connectors, the wave directions are limited to ± 45° relative to the longitudinal MOB axis.

The MOB is also equipped with container cranes and pedestal cranes for lifting to and from ships moored alongside the MOB.

8 thrusters of 6 MW each are installed per module to give the required speed of 8 – 10 knots.

The area inside each circular column is one floatation compartment. The area in the pontoons between columns are separated into two compartments. This gives adequate hydrostatic stability both for intact and damage situations.

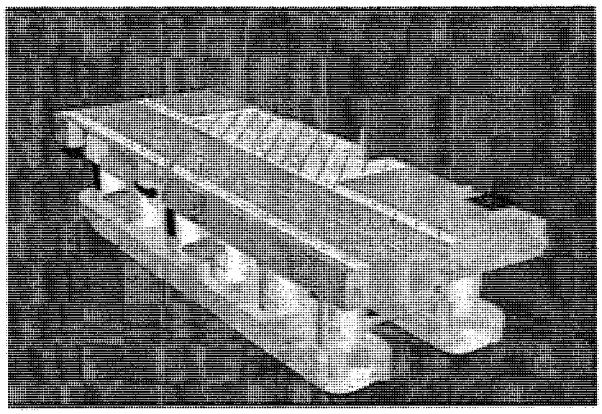

Fig.7: Hybrid Semi. 1 MOB unit. Length 381m.

The modules can go from Operational draft (36.5m) to Transit draft (15.7m) in 31 hours. The reverse operation takes 11 hours.

4.2 Steel Deck - Topside

The geometry of the Steel Deck is given by the overall functional requirements with respect to width and length.

The height of the Steel Topside is given by 3 internal storage decks below the top (flight) deck. Each internal deck has a free height of 6m. The total height of the topside structure is 21.4m.

Inside the structure longitudinal- and transverse-walls are provided in order to give sufficient global shear stiffness.

There are elevators between each deck level and down to sea level for roll off from ships and lift up to appropriate decks in the topside.

4.3 Concrete Hull

The Hull sizing of each module is determined based on the following:

The *Pontoon* length is 365m giving sufficient space between modules to allow for yaw and pitch motions. The pontoon cross-section (47.5m x 16.5m) is based on requirements for buoyancy and speed during Transit. This means that the pontoon top slabs are above water line during Transit which improves transit speed.

The number of *Columns* (12) and column diameter (28m) are based on requirements to stability and strength. Circular columns ("transparent walls"), compared to continuous walls, was selected to reduce the transverse forces between the longitudinal pontoons.

The column height of 45m is based on an assumption that there should be about 20m of still-water above top of the pontoons to cater for the Survival condition. The clearance from still-water to bottom deck of Topsides was set to 25m to avoid severe slamming to the bottom deck.

4.4 Steel Braces

Transverse braces are installed between columns in order to limit forces into the steel deck. The braces are "ball- and socket" connected inside the columns in order to avoid bending moments in the braces.

5. HYDRODYNAMICS

Hydrodynamic analyses, [4] and [5], have been done with the WADAM program in order to investigate motion behavior and wave induced forces on one single module.

The WADAM program utilizes wave diffraction/ radiation theory and operates on panel models.

The first natural periods are given in Table 3, "Basic Configuration".

Short term maxima, for 3 hours storm condition, are calculated by using Pierson Moscowitz wave spectra for wave periods from T_p = 6 sec to 20 sec. The following responses are found, expressed per unit significant wave height (Hs):

Surge (m/m)	0.22
Sway (m/m)	0.40
Heave (m/m)	0.41
Roll (°/m)	0.33
Pitch (°/m)	0.19
Yaw (°/m)	0.11

Table 1: Hydrodynamic responses per m Hs.

An alternative to the Pierson- Moscowitz spectrum is a double peaked spectrum. It may have a more realistic simulation of a storm condition. A brief investigation with double peaked spectrum showed that the Pierson-Moscowitz (PM) spectrum generally is somewhat conservative compared with a double peaked spectrum.

Maximum mid-section moment and forces for Hs=15m are given in Table 5.

6. AIR GAP

Several air gap analyses are performed using WADAM/ SESAM for a single module in Survival condition [5]. These analyses determine the required distance from still water level to the topside structure (i.e. Air Gap at still water). The air gap is calculated based on consideration of radiation/ diffraction effects on the wave surface elevation, i.e. wave enhancement factors are calculated for a range of selected points.

The analyses revealed a need for a larger nominal air gap than initially assumed. The initial air gap was therefore increased from 20m to 25m by increasing the column height from 40m to 45m. *The theoretical calculations must be verified by future model testing.*

The suggested air gap of 25m is a few meters lower than strictly required from WADAM calculations. A slamming design pressure of 70kN/m^2 has been used for the steel bottom deck.

7. STRUCTURAL ANALYSES

A comprehensive Finite Element Analysis (FEA) is performed [6] for one single module of the MOB structure. The FE model comprises the full length of the module.

The total number of elements is nearly 200,000 and the degrees of freedom are in the order of 700,000.

The global FE model is made of shell elements with a relatively fine mesh. Fig. 8.

The wave loads are generated by WADAM and automatically applied to the FE model. Further, the structural responses are calculated by SESTRA. Both WADAM and SESTRA are parts of the SESAM program package, which is widely used in design of offshore structures.

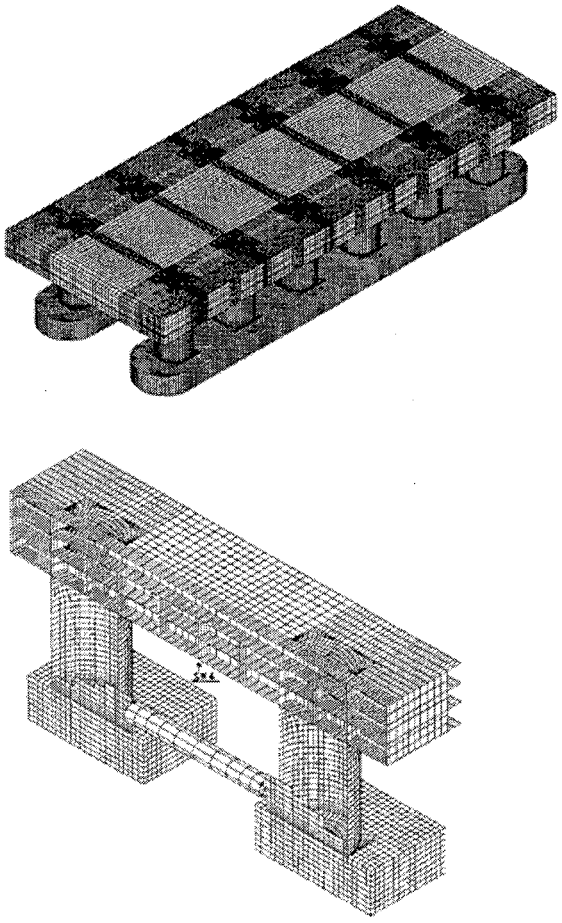

Fig. 8: Finite Element Model

In total 7 different waves are selected for consideration in the global FEA. The wave loads are separated in a real and an imaginary part in order to be able to evaluate all phase angles of the actual wave.

In addition longhand calculations are performed to investigate local loads and moment effects not included in the FEA.

8. STRUCTURAL DESIGN CHECKS

The main objective of the structural analysis and consecutive design has been to demonstrate structural feasibility, and to check realistic dimensions and material quantities. The design checks [6] demonstrate that all structural specifications and requirements, which are assessed to be governing, are fulfilled.

A summary of material quantities are given in Tables 6 and 7, "Basic Configuration".

Maximum intensity of ordinary reinforcement is 3 Ø32 per 200mm. This is a reasonable intensity with respect to constructibility.

The concrete hull has a Fatigue life of 600 years in the anticipated most unfavorable areas. If using a safety factor of 10 for areas without access for inspection, a fatigue design life of 60 years is expected. Fatigue life could be improved if needed.

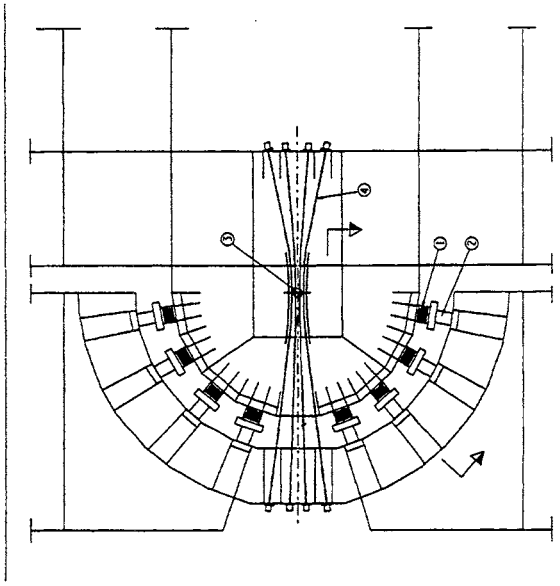

Fig. 10: Detail of Central Connector. Plan view.

9. CONNECTORS

9.1 Connector Arrangement

The design of connectors between modules are based on the following assumptions, Figures 9 –13:

- Relative surge, sway, heave and roll motions between modules are suppressed in the connectors.
- Pitch and yaw motions are allowed.
- Max. wave heading is limited to 45° and Hs≤ 7.5m.
- Technology from the design of the flexible joint ("ball- and socket") bearings on the Troll A offshore project is utilized.
- Steel cables are provided to take axial tensile forces between the modules.

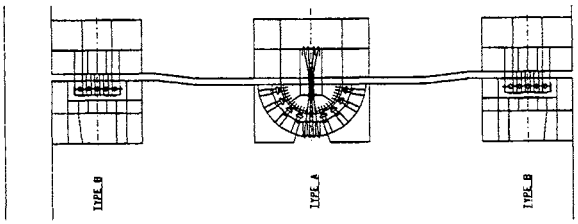

Fig. 9: Connector Arrangement. Plan view.

The design allows for large relative motions during coupling (hook-up) and de-coupling. Vertical relative motions of up to ± 2 meters are acceptable during the start of the coupling operation.

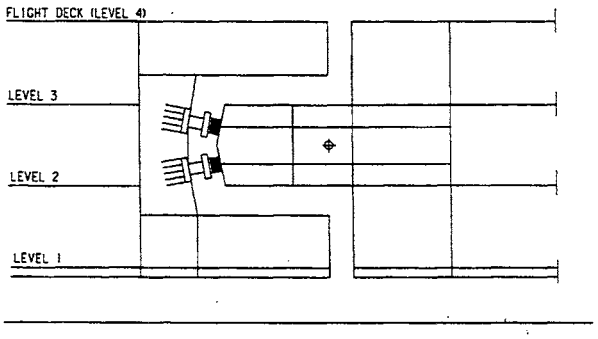

Fig. 11: Section A-A.(fig. 10)

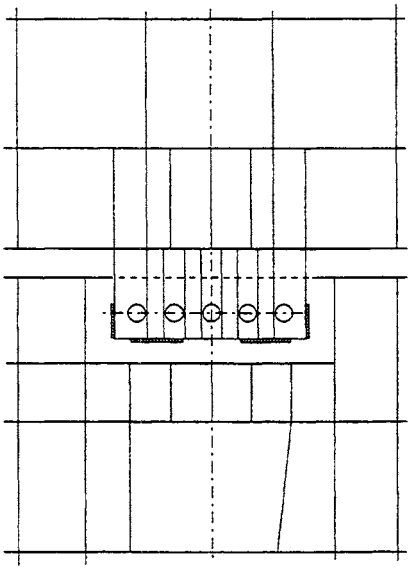

Fig.12: Detail of wing connector. plan view.

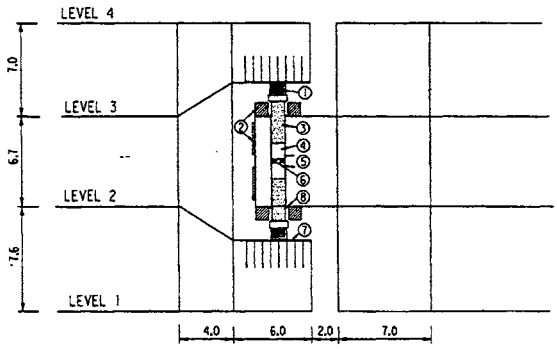

Fig. 13: Vertical/ longitudinal section of Wing Connector.

The design of the connector arrangement is utilizing elastomeric bearings, hydraulic jacks and fenders, which all are commercially available. However, some up-sizing of the components are required.

To activate the elastomeric bearings, a system of hydraulic jacks is used. The jacks are linked together in a the same hydraulic circuit in order to obtain an equal distribution of forces on the different bearings.

The connector arrangement allows a quick de-coupling of the four MOB modules when a critical sea state is forecasted.

During de-coupling the modules will start to move relative to each other. When the movement is increased beyond a certain limit (± 0.15 m in longitudinal direction and ± 1.5 m vertically), the fenders are utilized to reduce impact loading.

For a more thorough description of the connector arrangement reference is made to [7].

9.2 Hydrodynamic Analyses

The computer program SIMO has been used to calculate the relative motions between modules and the connector forces between the modules, [4] and [5].

Input to the SIMO program is data from:

- WAMIT/ WADAM (diffraction/ radiation panel model): added mass, potential damping, wave excitation.
- SEAFLOATER (Morrison beam model): viscous damping coefficients of individual modules. Linear springs are used to simulate the connection system between modules.

Typical simulation time of approximately one hour has been used. Investigations are performed to check the variation in standard deviations related to simulation time.

Relative pitch between modules are plotted in Fig. 14 for Aircraft Operation condition. Wave direction varies between 0° and 45°.

Acceptable pitch angle between modules is obtained for wave periods (T_p) below approximately 16 seconds and for wave heading below 25°. It is also seen that for a reduction of T_p from 17.0 to 10.0 sec, the relative pitch is reduced by a factor of approximately 10.

Connector design forces are obtained for wave heights of H_s = 7.5 m with $T_p \leq 17.4$ sec and maximum wave heading of 45°.

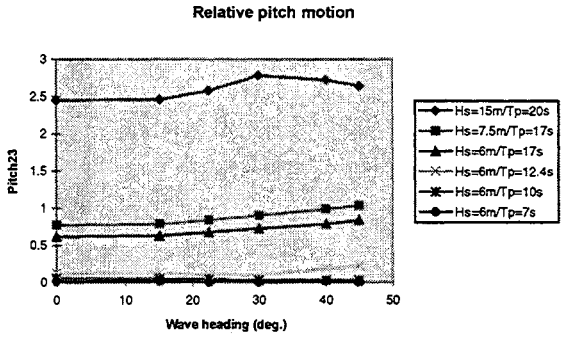

Fig. 14: Relative pitch (degrees) between modules.

Axial force, F_x	135 MN
Horizontal shear, F_y	140 MN
Vertical shear, F_z	150 MN
Torsional moment, Mz	13400 MNm

Table 2: Connector forces for Hs=7.5m and wave heading 45deg.

10. EXTENDED SEMI - 1829 m

10.1 Introduction.

An investigation of extending the MOB hybrid semi from 1525m (5000feet) to 1829m (6000feet) has also been done by extending the 4 modules equally. The main objective was to indicate a correlation between cost and module- length for an hybrid semi-submersible MOB [7].

10.2 Sizing

Each of the 4 modules were modified as follows:

The *steel deck* was increased by 76.2m in length (from 380m to 456.2m).

The *column* height was increased by 2.5m, from 45m to 47.5m, in order to reduce a possible air gap problem from increased module length in combination with pitching motions.

The *pontoon* lengths was kept at an absolute minimum in order to limit the increase of wave loading effects, assumed to increase by the square of the length.

In order to increase buoyancy the pontoon width was increased by 2m from 47.5m to 49.5m. The pontoon length was increased by only 16m from 365m to 381m.

10.3 Hydrodynamics and Structural Design

Hydrodynamic motions and loading for one module

were analyzed almost as for the Basic Configuration.

Natural periods for The Basic and Sensitivity Configurations are given in Table 3.

Mode	Basic Configuration	Sensitivity Configuration
Heave (sec.)	35.7	38.7
Roll (sec)	53.4	113.0
Pitch (sec.)	36.8	42.5

Table 3: Natural periods for the Basic and the Sensitivity Configurations.

The roll period increased from 53.4 sec to 113 sec. The increased roll period can be explained by the reduced transverse GM from 10.1m to 2.8m. This is due to increased Topside steel weight and the elongation of columns by in 2.5m. Furthermore, in the hydrodynamic analysis the Topside storage weight of 86,000 tons was *not* included for the Basic configuration, while a topside storage of 65,000 tons was *included* for the "Sensitivity" case.

From Table 4 one can see that the surge, sway and heave (translations) responses have increased moderately in a Survival condition. The roll, pitch and yaw (rotations) are slightly reduced or unchanged. Based on this it was assumed that the connector motions and forces will change moderately. Multi-body analyses, using SIMO, were therefore not performed in the study of the Sensitivity- case.

Response	Basic	sensitivity
Surge (m)	3.3	4.3
Sway (m)	6.0	7.0
Heave (m)	6.2	6.6
Roll (deg.)	5.0	4.6
Pitch (deg.)	2.9	2.8
Yaw (deg.)	1.6	1.6

Table 4. Motions of a Single Module (Extreme motions at the most critical wave heading for each response). Hs= 15m. Draft 36.5m.

Response	Basic Config	Sensitivity Config	Wave direction
Fx(MN)	390	315	90
Fy(MN)	135	145	60
Fz(MN)	285	309	0
Mx(GNm)	28	35.6	60
My(GNm)	42	43.6	0
Mz(GNm)	16	16.8	70

Table 5: Maximum mid- section forces. Hs=15m.

Material quantities and weight for the Basic and the Sensitivity Configurations are given in Tables 6 and 7.

From Table 6 one can see that the Topside storage capacity is reduced from 86,000 tons to 72,000 tons restricted by the GM of 2m. The storage capacity or GM can be improved, if needed, by tuning the transverse distance between the columns.

The MOB extension from 1524m to 1829m, 20% increase in length, resulted in a cost increase of 11%.

11. CONSTRUCTION METHOD

11.1 Base Case

The evaluation of the construction methods and the temporary marine operations associated with the construction of the MOB structure, are based on Aker Maritime's (Norwegian Contractors) considerable experience from construction of very large concrete offshore platforms over a period of 25 years. No major problems are foreseen in the construction of MOB structures utilizing this experience.

A construction method using a "Construction Assembly Line" technique is suggested [9], ref. Figures 15 and 16. The idea is based on the technique used (e.g.) on the tunnel sections for the Øresund Crossing. See Figures 15 and 16.

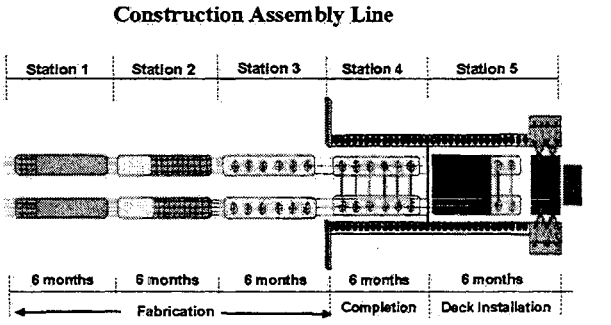

Fig. 15: Construction Assembly Line. Plan view.

Fig. 16: Construction Assembly Line. Elevation view.

The idea is to have an assembly line consisting of 5 workstations. Station 1, 2, 3 and 4 are on the same horizontal level. The 4th and 5th workstations are inside a 2-level dock. Station 4 makes the hull afloat when sea water is pumped into the dock to an elevation above the ocean level, approximately +12m. The hull is subsequently floated to station 5 inside the dock. Station 5 has sufficient depth to make the hull float with water level equal to the sea level.

At stations 1, 2, and 3 civil construction work is carried out. For vertical surfaces such as pontoon walls and columns, the favorable slipforming technique will be used.

The hull is skidded from Stations 1 progressively through 2, 3 and 4 on the same horizontal level.

At Station 4 the transverse permanent and temporary steel braces are installed and the mechanical outfitting

is completed prior to pumping of water into station 4 and 5 in the dock.

When the hull arrives Station 5 , the water level is lowered down to sea level. At Station 5 the Steel Deck is installed in 3 segments per MOB unit. The segments are lifted from barges by cranes placed on the abutments for the outer dock gate. The hull is winched to the exact position under the fixed cranes for installation of the Steel Deck segments.

11.2 Alternative Construction Method

An alternative construction method is also investigated using *graving docks:*

After the construction of the complete concrete hull, installation of transverse braces and a temporary bracing system in the graving dock, the hull is towed to a deep water site in a sheltered area. The hull is ballasted down to a freeboard of approximately 6m. The Topside is installed ("mated") in 3 sections per hull module.

The method requires relatively deep water (about 60m) in sheltered areas close to the graving dock.

12. CONSTRUCTION SCHEDULES

Construction schedules [9] are investigated for the semi- concept 1528m long constructed with the "Assembly Line" method and the alternative "mating" method.

For both methods it is included one year with detail engineering and site preparations prior to start construction. Approximately 24 months construction time is needed for each hull/topsides module prior to installation of the Topside.

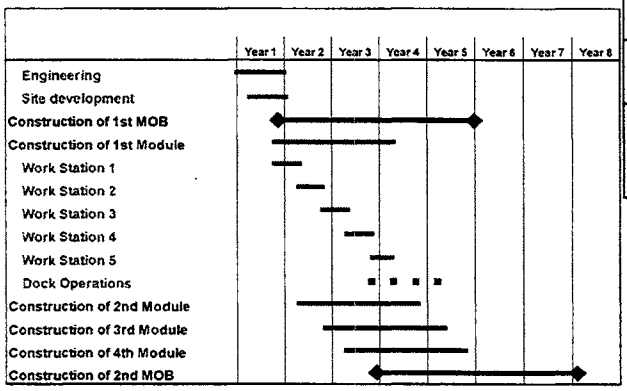

Fig. 17: Construction Assembly Line. Schedule.

The "Assembly Line" method will need approximately 5 years for completion of the first Mobile Offshore Base. The next MOB can be delivered only 2 years after the first one.

If the "mating" method is used with the 4 modules constructed one after the other, total construction time is estimated to 9 years and 6 months. If 2 and 2 modules are constructed in parallel, total construction time is estimated to 5 years and 7 months.

Item	Basic Configuration (t)	Sensitivity Configuration (t)
Concrete	345,000	372,811
Horizontal braces	17,700	17,900
CMO&MMO	2,160	2,592
Topside steel	112,100	137,700
Topside equipment	2,500	2,500
Topside storage	86,000	72,000
Fuel and Fresh water	31,200	31,200
Ballast water	118,400	128,715
Total	***713,760***	***776,5418***

Table 6: Displacement per semi module. Draft 36.5m. Metacentric height 2.0m.

Part	Basic Configuration (380m)	Sensitivity Configuration (456.2m)
Concrete in Pontoons (m^3)	112,000	117,886
Concrete in Columns (m^3)	32,000	32,927
Total concrete volume, Hull (m^3)	144,000	155,338
Ordinary reinforcement (tonnes)	45,840	49,174t
Prestessing cables (tonnes)	13,380	14,287
Steel braces; Hull (tonnes)	17,700	17,900
Topside Structural Steel (tonnes)	112,100	137,700

Table 7: Material Take – off per module

13. ALTERNATIVE CONCEPT – "CONCORE"

13.1 Introduction

Concrete barges have particular benefits due to their robust strength. On the other hand they move more in the waves than the semis. Therefore each module have to be longer to comply with pitch angle requirements between the modules.

The proposed "Concore", concrete core, mono hull concept is an idea evolved from the barge concepts. It is demonstrated that it is possible to design a MOB structure which is 1524m long without connectors.

13.2 General Description

The "Concore" mono-hull [10] concept is 1524m long (5000 feet). It consists of a central concrete box-section. This section forms a 890m long "core" of the MOB. Steel cantilevers are attached at each end of the "core". The cantilevers are 317 m long each. Total MOB length is 1524m (5000ft). See Fig.18.

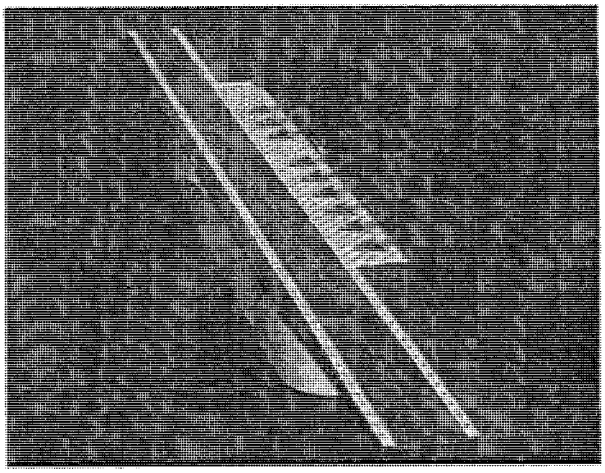

Fig 18: "Concore". Length 1524m.

Minimum draft for this concept is 19.4m.

The transit speed in still water is 12 knots with 173MW of propulsion power. For operation the maximum need of power is 273 MW at wave heading 45 degrees.

13.3 Concrete Hull

The total height of the concrete hull is 100 m. The lower part of the concrete hull is 120 m wide while the upper 8 meters (at deck level) is 152.5m wide.

The hull structure is proposed made of Light Weight Aggregate (LWA) concrete of grade LC60. Total concrete volume is 747,000 m^3.

13.4 Steel Cantilevers

The effective width of the steel cantilevers is 120 m. The height is parabolicly varying from 5 m at the tip to 36.4 m at the connection to the concrete hull. The total weight of one cantilever is 71,600 tonnes.

Maximum vertical Significant Single Amplitude (SSA) velocity is 1.04m/s at the tip of the cantilevers during aircraft Operation, with wave heading less than 45 degrees. Maximum allowable velocity according to the design basis is 1.4 m/s. Maximum vertical acceleration (SSA value) is 0.31 m/s^2.

Most probable maximum vertical acceleration at the tip of the cantilevers in Survival condition is 5.2m/s^2.

14. CONCLUSIONS

It is possible to design and construct a Mobile Offshore Base using High Performance Concrete complying with Det norske Veritas "Mobile Offshore Classification Rules".

Concrete hull is very competitive on acquisition and maintenance cost. Geometry is simple. Durability in marine environment and fatigue resistance is excellent. The concrete structure is robust to impacts from dropped objects, ship impacts etc.

The studies have revealed needs for further works, such as:

- Model testing to confirm theoretical air gap calculations for the semi-submersible concepts.
- Connection arrangements: Relative motions between modules during the time span for de-coupling and assessment of time needed for de-coupling.
- Verification of estimated transit speed against model tests.

15. AKNOWLEDGEMENT

This paper is based upon work performed for US Naval Surface Warfare Center's and Office of Naval Research's MOB Program.

16. REFERENCES

[1]. S. Lindseth: "Concept Screening Report"; Aker Maritime report #9019-ANC-JD-RN-0002 in the Mobile Offshore Base study for Naval Surface Warfare Center, 1999.

[2]. L. Bjerkeli: "High Performance Concrete- An Ideal Material for Large Floating Structures". The 3rd International Workshop on Very Large Floating Structures, Hawaii 1999.

[3]. O. Grøv and G. Rognaas: "Summary Report", Aker Maritime Report #9019-ANC-JD-RN-0003 in the Mobile Offshore Base study for Naval Warfare Center, 1999.

[4]. S. Vedeld: "Global Performance", Aker Maritime Report #9019-ANC-JD-RN-0004 in the Mobile Offshore Base study for Naval Warfare Center, 1999.

[5]. J. Xu: "Hydrodynamic Global Performance. Concrete Semi", Aker Maritime Report #9019-ANC-JD-RN-0022 in the Mobile Offshore Base study for Naval Warfare Center, 1999.

[6]. Ole Grøv and G. Rognaas: "Structural Analysis and Design", Aker Maritime Report #9019-ANC-JD-RN-0023 in the Mobile Offshore Base study for Naval Surface Warfare Center, 1999.

[7]. Per Meaas. "Connection Arrangement", Aker Maritime Report #9019-ANC-JD-RN-0024 in the Mobile Offshore Base study for Naval Surface Warfare Center, 1999.

[8]. J. Xu, S. Åsrud and G. Rognaas: "Hybrid Concrete Semi. Extended from 1524m to 1828m with 4 Modules", Aker Maritime Report #58248-A5 in the Mobile Offshore Base study for the Office of Naval Research, 1999.

[9]. T. Hovda: "Construction Techniques.", Aker Maritime Report #58248-C2 in the Mobile Offshore Base study for the Office of Naval Research, 1999.

[10]. G. Rognaas. "Barge type Concept", Aker Maritime Report #9019-ANC-JD-RN-0031 in the Mobile Offshore Base study for Naval Surface Warfare Center, 1999.

[11].S. Åsrud and J. Munkeby: "Fatigue Life Prediction for Concrete Semi", Aker Maritime Report #58248-A.2.3 in the Mobile Offshore Base study for . Office of Naval Research, 1999.

PROCEEDINGS OF THE THIRD INTERNATIONAL WORKSHOP ON VERY LARGE FLOATING STRUCTURES
(VLFS '99), VOL. I, EDS. R.C. ERTEKIN & J.W. KIM, 22-24 SEPTEMBER 1999, HONOLULU, HAWAII, USA

MODULE LENGTH OPTIMIZATION FOR THE INDEPENDENT MODULE MOBILE OFFSHORE BASE

Robert G. Grant, Richard C. Lundberg & Donald Danmeier

Bechtel National, Inc.*

ABSTRACT

Bechtel conceived and developed a MOB concept consisting of independent semisubmersible modules arranged end-to-end to form an aircraft runway about 1500 m long. The modules are not structurally connected, but are functionally connected by bridges that transfer no loads between modules, accommodate small relative motions and form a continuous aircraft runway. Module relative and absolute position is maintained with a dynamic positioning (DP) system. Since increasing the module length reduces wave-induced motions at the aircraft runway bridges, thus reducing air operations downtime, it is advantageous to make the modules as long as possible. However, strength and stiffness requirements also increase with module length leading to hull steel weight and cost penalties. Early studies suggested that 3 modules, each about 500 m long, constituted a reasonable configuration.

This study investigated some of the costs and benefits of extending module length past 500 m. Three module configurations with lengths equal to 500 m, 605 m & 760 m were developed with sufficient:

- Deck height to pass extreme 30 m waves without impact
- Hull strength to survive 30 m extreme waves
- Flexural stiffness to limit flexural resonant response for fatigue integrity

Then, the module steel weights and costs were calculated to assess cost vs length. Wave motions and flight operations downtime also vary with module length and were calculated.

1. INTRODUCTION

The independent module MOB consists of large semisubmersible modules arranged and held in position end-to-end with a Dynamic Positioning (DP) system.

Structural connectors between the modules are completely eliminated. The small relative wave motions between the modules are accommodated by functional bridges that do not transfer load. The Office of Naval Research (ONR) has sponsored the development of a base case configuration for this MOB concept consisting of three, 500 m long modules. The critical feasibility issues of hydrostatic stability, hull strength & fatigue, wave motions & loads, environmental forces and DP have been successfully addressed.

This MOB concept has many unique advantages. One advantage is that each module's structural independence from the others makes it possible to address many critical issues, including strength, fatigue, steel weight and cost at the module level without consideration to the full length MOB.

There is interest in increasing the module length beyond the 500 m base case to possibly:

- Extend the runway length beyond 1500 m without increasing the number of modules
- Reduce the number of modules while maintaining a 1500 m runway
- Reduce the weather related flight operations downtime by reducing wave-induced motions of the module
- Build one long module first before committing to a full MOB

To have tools for evaluating these options, ONR sponsored this "case study" work to develop modules with 3 lengths, evaluate their wave loads, strength and fatigue resistance, and estimate how module steel weight and cost varies with module length. Wave motions and weather related air operations downtime was also addressed.

2. CONFIGURATION CRITERIA

Three module hull lengths were configured to satisfy the following design criteria:

- *Payload Weight & Volume*: The payload is set at 300,000 MT at deck level for a 1500 m MOB (200 MT/m). The deck cross section dimensions were held constant at 21m x 120m.
- *Hydrostatic Stability:* Minimum operating draft GM was set at 5 m for robust intact and damage stability. At a draft with the pontoon tops awash, the minimum GM was set at 1 m after free surface corrections. Sufficient pontoon buoyancy was provided to operate fully loaded with a 1 m freeboard to the pontoon tops at transit draft.
- *Structural*: High strength (Fy = 50 ksi) steel which is typical in shipbuilding practice was assumed. A working stress design approach with a basic allowable stress of 0.6 times yield was used. For extreme conditions, a one-third increase on this allowable was used.

Figure 1 presents the "base case" 500 m long module configuration. The longer modules were configured by adding column/pontoon bays.

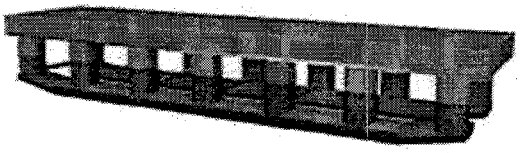

Figure 1: Base Case Module – 500 m

3. WAVE GAP

It is conventional practice to design semisubmersible decks to clear the crests of the highest waves to avoid the huge loads produced by green water impact. The wave gap in storm waves is a superposition of the still water gap, the vertical hull motions and the water surface motions. We found that pitch produces most of the peak vertical hull motion of these long modules at their ends.

Water surface motion is complicated by the MOB's hull that modifies the waves as they pass under the deck. The MOB hull is much larger and less "transparent" to the waves than a conventional drilling semisubmersible hull. Hydrodynamic analysis was performed using the computer program WAMIT and shows that waves are significantly amplified under the deck. Figure 2 is a typical WAMIT result for 12 sec, head waves showing peak amplifications equal to 2.5 under the deck. The figure depicts the module with its 2 rows of 7 columns.

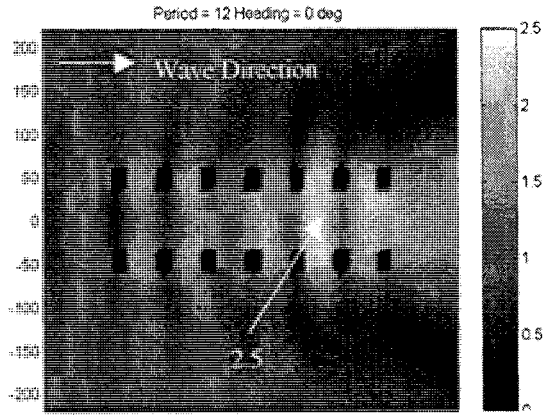

Figure 2: Water Surface Motion RAO Around MOB Module (m/m)

We evaluated many alternative hull forms to reduce this amplification to acceptable levels, and met with no substantial success. We generally found that the pontoons produce most of the amplification at the long storm wave periods, and that increasing their submergence reduced amplification to a limited extent. At shorter wave periods (less than about 8 to 10 sec), the pontoons had little effect, and the columns produced most of the amplification. However, even major changes to hull geometry produced unacceptable amplification as estimated by diffraction analysis.

For a 30 m high survival wave, this suggests 30/2*2.5 = 37.5 m trough and crest amplitudes. With the pontoon tops submerged only 15 m at survival draft, this estimate of trough amplitude will completely expose the pontoon and produce hydrodynamic conditions that clearly violate WAMIT's fundamental assumptions of small wave height. We are not aware of any analysis program that can model the extreme turbulence that develops when a pontoon is exposed in the trough of a large storm wave.

Without an effective analysis tool, we developed engineering approximations for the water surface amplification under the deck. These estimates were combined with calculated hull motions to establish the acceptable still water wave gaps presented on Table 1. These results are applicable to module lengths up to 760 m, and should be confirmed with model tests.

	Operating	Survival
Draft (m)	40	30
Wave Gap (m)	20	30

Table 1: Drafts & Stillwater Wave Gaps

Past experience with physical model tests and field operations of drilling semisubmersibles indicates that resonant pitch and roll will be excited by wave forces that are ignored by conventional calculation procedures. State of the practice methods for calculating these motions are not reliable. However, these motions are limited by damping, and pontoon forms that produce high pitch and roll damping have been found in past model tests to be effective. We therefore re-configured the pontoons with the "semi-elliptical" cross section shown on Figure 3 that provides high pitch/roll damping while maintaining a low profile for horizontal current drag.

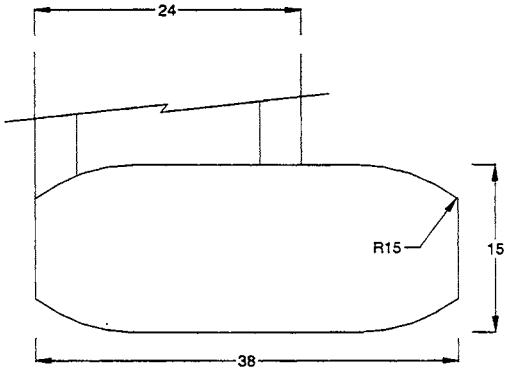

Figure 3: Base Case Pontoon & Column Section

4. CONFIGURATION DEVELOPMENT PROCESS

Each of the three module length configurations were developed in a logical sequence. They were first sized to carry the required payload at various drafts with consideration to buoyancy, stability and wave gap. Steel weights per unit volume were based on past MOB hull designs. Then, a diffraction analysis was performed with WAMIT to calculate the wave loads, the added mass distribution and the wave induced motions. Resonant pitch & roll neglected by linear analysis were accounted for by increasing the wave-frequency motions by 25%. Wave gap was approximated by amplifying the free-field wave amplitude by 1.2. These approximations must be confirmed with physical model tests.

With basic configurations for the 3 module lengths, the structural analysis, design and weight analysis proceeded with the following steps:

1. Using hand calculations, design the principal members for local loads such as deck loads and hydrostatic loads in stillwater conditions (i.e. with no wave loads). This results in a basic framing scheme including plating, stiffeners, beams and frames.

2. Using the plate and stiffener sizes developed in step 1, determine the global member properties and apply them to the stick model of the structure, a typical column-to-column bay of which is shown on Figure 4. The stick model represents the major framing members such as pontoons and columns as single beam elements for analysis purposes.

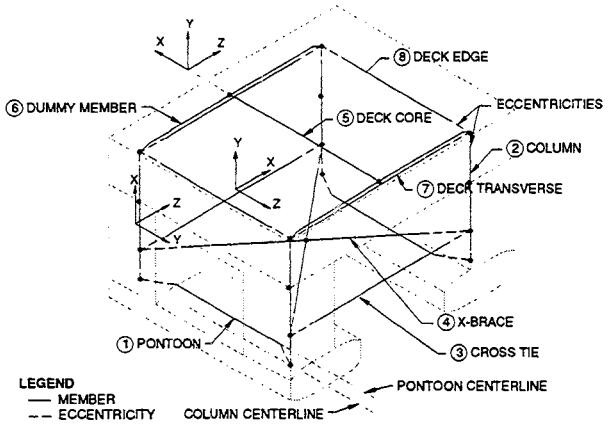

Figure 4: Structural Model – Single Bay

3. Using the computer program MultiSurf, develop a WAMIT panel model for hydrodynamic analysis. Figure 5 shows a panel model for the 760 m module.

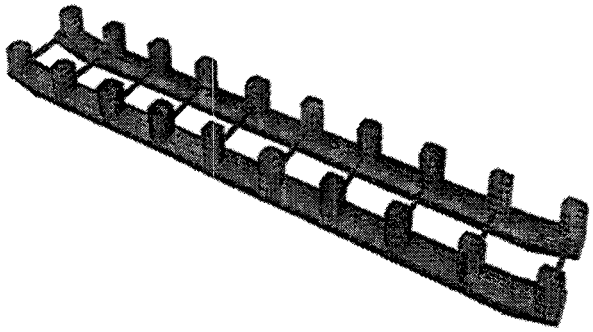

Figure 5: Diffraction Analysis Panel Model 760 m Module

4. Use WAMIT to develop wave loads and hydrodynamic mass characteristics for the model. Wave loads were developed for a range of frequencies and vessel headings. The wave loads and masses were then lumped to the principal nodes of the stick model at each column station as illustrated on Figure 6.

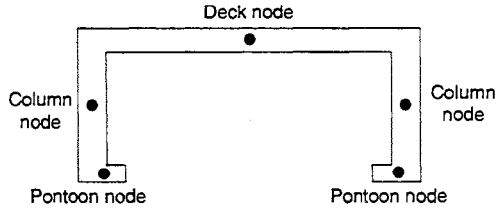

Figure 6: Wave Force, Mass & Added Mass Nodes

5. Apply the masses to the stick model and calculate the resonant mode shapes and periods, and confirm that the model has periods low enough to preclude dynamic resonance due to waves. If this is not true, adjust the structural configurations and member sizes to mitigate the problem.

6. After confirming the structural configuration, execute a static analysis to determine global member forces due to wave loads. The analysis is done for in-phase and out-of-phase waves and the results are postprocessed to determine the maximum member stresses from all the wave directions and frequencies.

7. Add the wave induced global stresses to stillwater condition stresses and check the members for combined stresses. Adjust plate and stiffener sizes to result in acceptable stresses.

8. Finally, for modules that were shown to be dynamically sensitive, adjust the dynamic model for the final member sizes selected to confirm the final resonant periods are acceptable.

9. With final member sizes, calculate weights for typical sections, and volumetric weights (steel densities) for each of the primary element types (pontoon, column, and deck). Then adjust the configuration to provide the required flotation and stability for these revised weights. Table 2 presents these final dimensions and overall weights. All dimensions are in meters and weights are MT.

	Module Length (m)		
	500	605	760
No.of Columns	14	16	20
Op Draft	40	40	40
Survival Draft	30	30	30
Keel to Deck	60	60	60
Pontoon Height	15	15	15
Pontoon Width	36	36	45
Square Column	22.6	25.5	27.2
Steel Weight	229,000	288,000	570,000
Op Draft Displ.	656,000	799,000	1,318,000

Table 2: Module Dimensions & Weights

10. Multiply the final member volumes by the final weight densities to obtain total module steel weight. Then divide by the length to result in a weight per unit length. Finally, compare between module lengths to determine any structural penalty associated with making the module longer.

5. WAVE MOTIONS & WAVE GAP

Wave-induced motions were calculated with WAMIT for wave headings from 0 deg to 90 deg in 22.5 deg increments. Figures 7 and 8 present typical results for heave and pitch in head waves.

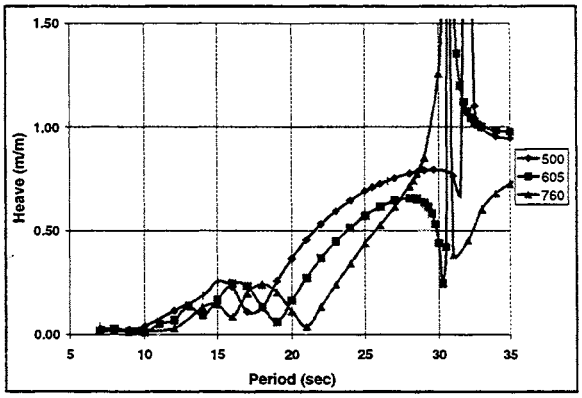

Figure 7: Heave RAOs – Head Waves

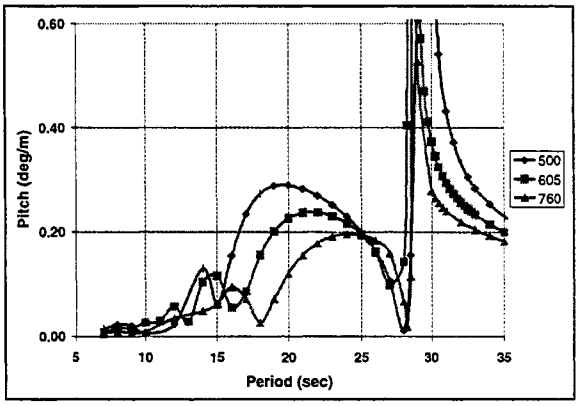

Figure 8: Pitch RAOs – Head Waves

These figures clearly show that increases in module length reduce the wave-induced motions, and move the peaks in the transfer functions to longer, less frequently occurring wave periods.

At the 30 m survival draft, the modules have a nominal air gap of 30 m between the still water level and the deck's underside. This gap is reduced by both the water surface motions and the module motions in storm waves. Table 3 shows how the minimum remaining air gap varies with module length for a seastate with a 30.5m (100 ft) maximum waves. Minimum air gap also varies with the peak period of the wave spectrum. The 605 m module has the lowest air gap equal to 2 m.

Length (m)	Minimum Air Gap(m)		
	T_p=18 s	T_p=20 s	T_p=24 s
500	8	7	6
605	6	5	2
760	8	6	4

Table 3: Minimum Air Gap (m)

6. FLEXURAL DYNAMICS & FATIGUE

Dynamic amplification of resonant flexural hull response can seriously impact its fatigue life. However, it can typically be ignored if the hull's resonant periods are limited to values well below periods that have frequent and significant wave energy. Past experience indicates that it is conservative to limit the flexural resonant periods of the structure to 4 sec and lower.

Thus, the configurations were analyzed to determine their flexural periods, and modified as required to bring the periods down to the target level. The stick model was used for this purpose. The three leading structural responses of the MOB modules were found to be: torsion, vertical bending (hog/sag), and lateral bending.

Modifications were introduced if any flexural resonant period (including beam bending and torsion) was higher than 4 seconds. These modifications included the addition of new structural elements, changes in the geometry of the design, and increasing plate thickness of existing members. The most effective modification that we adopted for all the module lengths was to add horizontal diagonal bracing at the transverse bracing level below the waterline as shown on Figure 9.

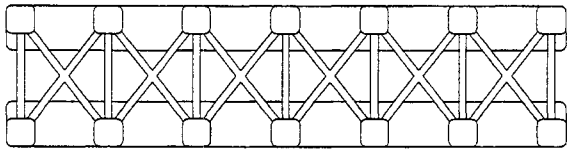

Figure 9: Horizontal Diagonal Bracing

This had a major effect on the torsion period and allowed a reduction in deck steel which was originally relied on to function as a torsion box to resist all the torsion loads. However, it has only a marginal effect on the transverse bending and no effect on vertical bending.

The only other procedure found effective for further reducing the periods was to apply steel weight increases to most of the hull members. The 760 m module's longest flexural period is vertical bending. We hypothesized that reducing the added mass at the pontoon ends by shifting some of the end volume to the center per Figure 10 would be effective in reducing this resonant period. However, the analysis indicted that the stiffness was reduced almost in proportion to the mass resulting in no net change in resonant periods.

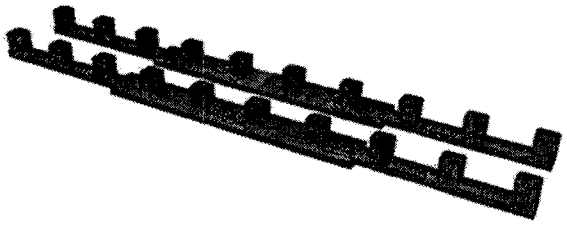

Figure 10: Trial Configuration for 760 m Module

Figure 11 shows how the critical torsion and vertical plane bending resonant periods vary with module length for modules designed only for still water conditions and including horizontal diagonal bracing. Torsion has a higher period than vertical plane bending for module lengths up to about 650m where the periods are relatively short. For longer hulls with longer periods, vertical plane bending has the longest period.

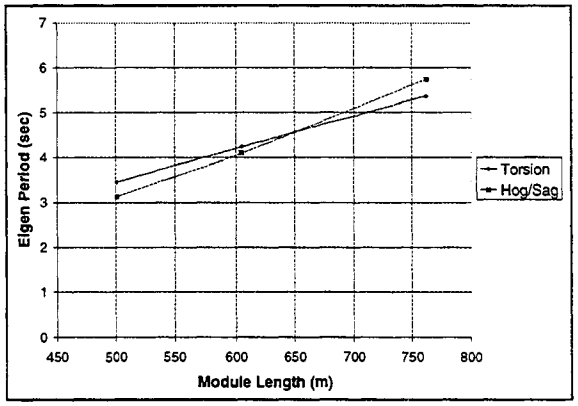

Figure 11: Resonant Flexural Periods (vs) Length

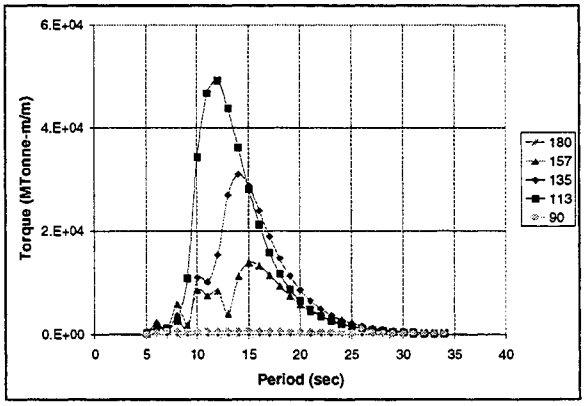

Figure 12: Mid-Ship Torsion RAOs

7. STRENGTH

The 500 m module is the current design and represents the base case. Its design was updated for the revised hull configuration and the resulting structural elements and weights represent the base case for comparison with longer modules. Since the structural arrangement remained nominally the same from length to length with only a nominal difference in the number of bays, local member design and stillwater analysis was performed for the base case only. The results are also applicable to the longer versions.

The general approach was to design the module for local loads and global forces resulting from stillwater conditions first. This is the basic minimum structure. Wave loads were then applied and member sizes increased as required to accommodate the stresses due to wave load. This increase in member size and weight represents the "penalty" imposed by the wave loads in terms of the added steel required to resist these loads. The process was then repeated for the alternate lengths.

The structural analysis proceeded by first calculating the member section loads produced by unit-amplitude waves of various directions and frequencies resulting in member load transfer functions illustrated for torsion at mid-ships by Figure 12.

Then, to limit the height of short period waves, we limited wave steepness to 15:1 per Figure 13, and the maximum wave height to 30.5m (100 ft).

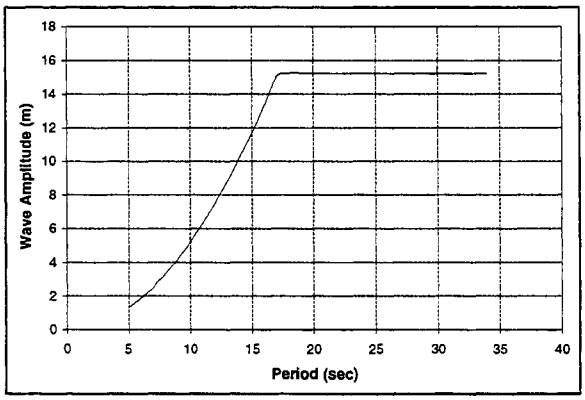

Figure 13: Maximum Wave Height (vs) Period

Figures 12 and 13 were then combined to obtain the variation of maximum member load as a function of design wave period and direction. Figure 14 illustrates this result for the mid-ship torsion wave load, and indicates that the maximum hull torsion is produced by a wave with a period of about 13 sec that is lower than the maximum wave height an approaches from an angle of about 22 ½ deg from broadside.

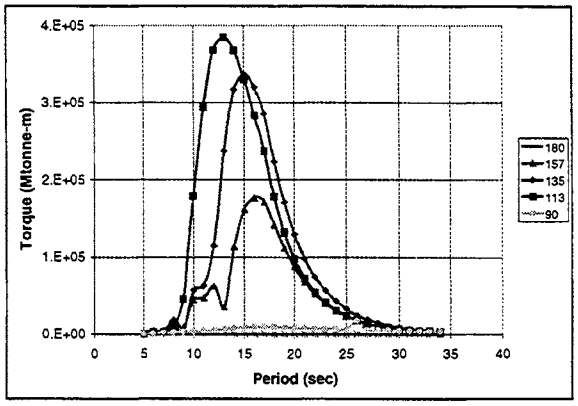

Figure 14: Maximum Design Torsion at Mid-Ship

The analysis results were than used to scale the nominal stillwater condition weights for the various hull elements to bring stresses to allowable values. This was done for each module length. The hull element weights were then distributed on a unit surface area basis. Thus, for any one hull plating the weight typically was assembled by adding the weight of plate, stiffeners, and frames or beams. This weight is based on the actual structural sections required. An allowance was added for miscellaneous detailing parts, welding, mill tolerance and general uncertainty. The allowance used was 15% for the deck and 10% for the pontoons and columns.

For the 605 and 760 m long modules, this factoring process resulted in relatively thick steel sections, and did not develop framing plans or specific stiffened plate arrangements. More engineering is needed to develop these designs with emphasis on practical fabrication issues.

These weights per unit area were multiplied by all the surface areas, and the total weight was divided by the volume to determine the steel density. This was done for one bay length of the deck and pontoons and one column height for the columns. This density was then multiplied by the total volume of the relevant item and the total hull steel weight assembled.

The reference weight is for the 500 m module in stillwater conditions. To include the wave loads and the other module lengths, the individual elements were multiplied by the required factors developed by the strength design and new densities were determined. These densities were then used to compute total steel weights for the various options and divided by the length to arrive at weight per unit length.

In addition to strength considerations, the axial steel areas were increased by the ratios calculated to limit the vertical plane resonant period to either 4 or 5 seconds. The diagonal braces were not increased in this case since they have minimum impact on the vertical plane resonant bending response.

Finally, these weight estimates were normalized to steel weights per unit volume of hull element (deck, columns, pontoons etc.) and then re-cycled through the hull sizing process to calculate final total weights and weight per unit length. This final cycle was needed because the new unit steel weights resulting from the strength and stiffness calculations were different than the unit steel weights used at the start to initially size each hull.

Figure 15 presents the final factors on the stillwater condition steel weight which are needed to satisfy the requirements for strength and both 4 and 5 sec resonant periods. It shows that strength requirements make the steel weight per unit length increase slowly with module length. Steel weight is seen to be much more sensitive to resonant period requirements which begin to control for module lengths in excess of about 625 m for a 4 sec limit. Stretching this limit to 5 sec, the break point extends to module lengths of about 760m.

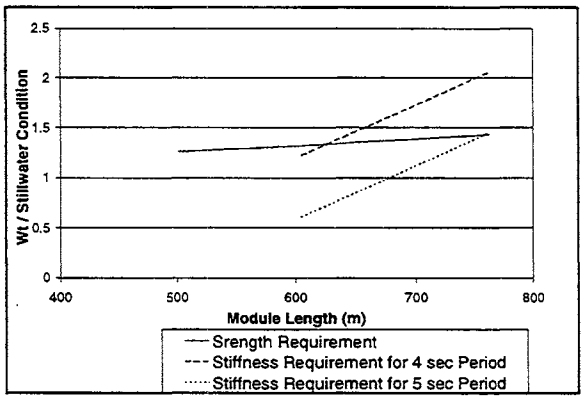

Figure 15: Factors on Sillwater Steel Weight (vs) Module Length

The figure shows that for long modules, the steel weight is very sensitive to the assumed limiting resonant period. We therefore recommend an advanced dynamic fatigue analysis in realistic MOB operating environments to more accurately assess the impact of resonant dynamics.

8. FLIGHT OPERATIONS DOWNTIME

Wave-induced motions, and thus weather-related air operations downtime which is partially controlled by the dynamic runway angle at the module interfaces, will decrease with increasing module length. We simulated the air operations using 2 years of wind and wave history at 4, arbitrarily selected geographic sites. The wave histories consisted of detailed directional wave

spectra and wind speed &direction for 12 hour increments. Boeing designs and builds the C17 cargo planes that will operate on the MOB, and provided maximum allowable runway angles as a function of aircraft speed, weight and whether it is taking off or landing. They also suggested a 40 kt wind limit.

Figure 16 shows the analysis results. The most severe location is the 60 deg N Latitude site in the North Atlantic.

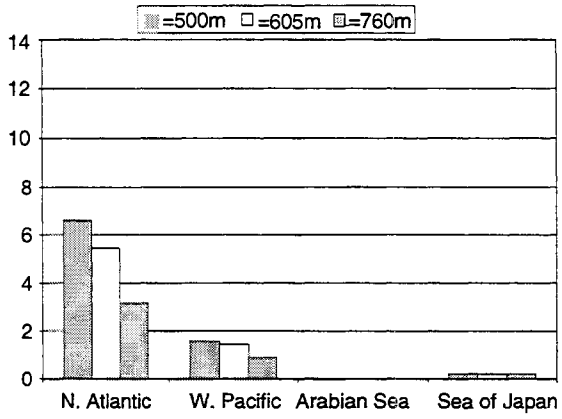

Figure 16: Air Operations Downtime at 4 Geographic Locations for 3 Module Lengths

This analysis assumed that the MOB requires three 500 or 605 m modules, but only two 760 m modules. Downtime due to wave motions is "measurable" at only the N. Atlantic site, and longer modules significantly reduce downtime for two reasons: Longer modules have lower wave motions and in some cases, can reduce the number of bridges an aircraft crosses during take-off from two to one thus reducing risk. Downtime at the W Pacific site is less than 2%. Downtime is negligible at sites with climates typified by the Arabian Sea and the Sea of Japan.

Weather must always be a consideration for any offshore operation, and no offshore facility can function 100% of the time. Weather related downtime is acceptable if it impacts the mission to only a minor extent. We conclude that the independent module MOB can successfully support air operations.

9. COST

A conceptual design of an entire, technically feasible MOB system would need to exist before making an estimate of the cost of the MOB system and its variation with module length. Most of the large cost elements will vary directly with module length. These include most hull outfit items like ballast and bilge piping and mechanical systems, cranes, steel outfit, HVAC, fire fighting systems, salt water systems, lifesaving systems, etc.

Costs that will change if the number of modules changes from 3 to 2 are relatively minor and include module interface systems and DP control & sensor systems.

Hull steel weights can be used to estimate the structural steel cost using a nominal estimated price per unit weight of $6000/MT. Table 4 gives a rough idea of how the steel costs per meter of module length will vary with changes in module length. The options of 4 and 5 sec target resonant periods are shown for the 760m module case.

	Module Length (m)			
	500	605	760 (4 sec)	760 (5 sec)
Steel Wt (MT/m)	456	475	747	524
Cost ($million/m)	2.7	2.8	4.5	3.1
Penalty (%)	-	5	63	15

Table 4: Steel Weight & Cost per Unit Length

Steel weight and cost per unit length increase slowly with increasing module length from the 500 to the 605 m long modules in response to strength requirements. For modules longer than 605 m, stiffness and fatigue requirements begin to control and the rate of increase is rapid.

10. CONCLUSIONS

1. The large hull modifies wave motions under the deck to a great extent. However, there are no analysis programs that can predict it in extreme storm waves, so model tests are recommended.
2. Steel weight (and cost) per unit length increase with increasing module length. Strength controls for lengths in the range of 500 to 600 m, and stiffness/fatigue control for lengths in the range of 600 to 760 m. Advanced dynamic fatigue analysis and design development with consideration to practical fabrication issues related to relatively thick plate are needed to more clearly define these limits. The practical limit to module length is in the range of 600 to 760 m.
3. It is feasible and there is little cost penalty in extending the 3 module independent module MOB's runway length from 5000 to 6000 ft. The module length would change from 500 to 600m.
4. Air operations weather related downtime is significantly effected by module motions making the longer modules with their lower motions beneficial. Modules that are long enough to

eliminate an aircraft runway bridge crossing on take-off will also reduce downtime. The air operations downtime for the independent module MOB concept seems acceptable.

PROCEEDINGS OF THE THIRD INTERNATIONAL WORKSHOP ON VERY LARGE FLOATING STRUCTURES
(VLFS '99), VOL. I, EDS. R.C. ERTEKIN & J.W. KIM, 22-24 SEPTEMBER 1999, HONOLULU, HAWAII, USA

Verification and Validation of Probabilistic Computational Mechanics Methods

Bilal M. Ayyub and Clara Popescu
Department of Civil and Environmental Engineering
University of Maryland at College Park, College Park, MD 20742, USA
ayyub@umail.umd.edu

ABSTRACT

Probabilistic computational mechanics methods can be developed to design very large floating structures (VLFS). Given the complexity of the structures, the verification and validation (V&V) of these methods is an essential step that needs to be added to the design process. The objective of this paper is to adapt and develop quantitative models and measures of various uncertainty types that are suitable for prediction and decision-based design of complex engineering systems. In this paper, a problem definition is provided, and needs and scope are developed. A methodology and work plan are proposed that can be implemented in future studies.

1. INTRODUCTION

Complex engineering systems, such as a mobile offshore base or nuclear plants or space-mission systems, require a systematic modeling and assessment of knowledge or its complement, i.e., ignorance. For example, assessing the safety of a complex system is typically based on various subsystems and components that exhibit uncertainty in performances or anticipated performances on demand, and varying criticality levels to the system. Simulation can be used to deal with this complexity, but there is a need to assess quantitatively the associated uncertainty in order to make relevant and precise decisions that would have the highest and most cost-effective impact on the system.

The objective of this paper is to adapt and develop quantitative models and measures of various uncertainty types that are suitable for prediction and decision-based design of complex engineering systems. This objective can be achieved by performing the following tasks (Figure 1):

1. Definition of a hierarchical taxonomy of ignorance.
2. Association of ignorance taxonomy with phases of modeling and analytically simulating engineering systems.

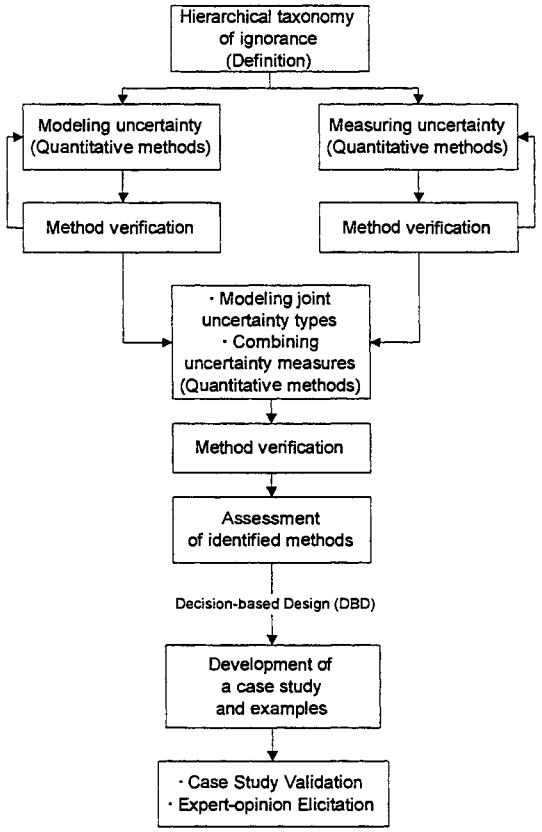

Figure 1. Decision-based Design, Verification, and Validation of Engineering Systems

3. Identification and development of quantitative methods for modeling various uncertainty types. Probabilistic and non-probabilistic methods should be considered in this task to cover ignorance types shown in Figure 2. Verification of developed methods.
4. Identification and development of quantitative methods for measuring various uncertainty types, such as the Hartley-like measures, Shannon-like entropies, fuzziness measures, etc. Probabilistic and non-probabilistic methods such as theory of evidence, generalized fuzzy measures, imprecise

probabilities among others should be considered in this task. Verification of developed methods.

5. Identification and development of quantitative methods for modeling joint uncertainty types and combining uncertainty measures. Verification of developed methods.
6. Assessment of suitability and practicality of using the methods and measures are the product of Tasks 3, 4 and 5 for prediction and decision-based design (DBD) of engineering systems.
7. Development of illustrative examples and a case study. Validation of case study using for example expert opinion elicitation and uncertainty analysis.

In subsequent sections, background materials for performing these tasks are provided.

2. IGNORANCE AND KNOWLEDGE

Modeling and analytically simulating engineering systems, as a process, involves several phases that typically consist of (1) conceptual modeling of a real system, (2) mathematical modeling of the conceptual models, (3) discretization and algorithm selection, (4) computer programming, (5) numerical solution, and (6) representation of the numerical solution (Oberkampf et al 1999). This process can be enhanced by assessing the state of knowledge and ignorance at the various phases. Knowledge regarding some domain of interest may be broadly understood as the body of justified true beliefs pertaining to the domain. It is always defined in the context of humankind experiences, from which it cannot be removed. As a result, knowledge would always reflect the imperfect nature of humans that can be attributed to their reliance on their senses for knowledge acquisition, and mind for extrapolation, creativity and imagination, biasedness, and their preconceived notions due to time asymmetry. An important aspect in dealing with knowledge is non-knowledge or ignorance that need to be examined (see Figure 3), modeled, and measured at the various phases.

Engineering is a practice that often tries to make statements about the future especially in designing new systems. However, Aristotle asserted that contingent statements about the future have no truth value, unlike statements made about the past and present which are determinably either true or false. Events of interest can be viewed to progress in time treelike with fixed branches of the past, and forming branches of the present. However, the future contains branching manifolds of undetermined possibilities. Decision-based design (DBD) would attempt to explore these possibilities in the context of their benefits, costs, uncertainties, and risks. Ayyub (1999) provided a classification of ignorance as shown in Figure 2. Klir and Folger (1988) developed and used various mathematical models and uncertainty measures to analyze and quantify uncertainty. These models are based not only on probability theory, but also on various combinations of fuzzy-set and rough-set theories with evidence theory, possibility theory, imprecise probabilities, and various other theories formulated in terms of non-additive measures. The theories for modeling uncertainty have attributes and bases that make them each uniquely suitable for modeling specific types of Figure 2. Consistent methods of uncertainty measuring and modeling are needed that would allow combining the results from the models.

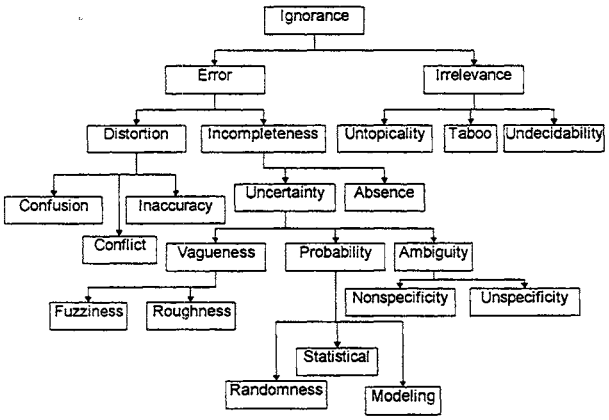

Figure 2. Classification of Ignorance (Ayyub 1999)

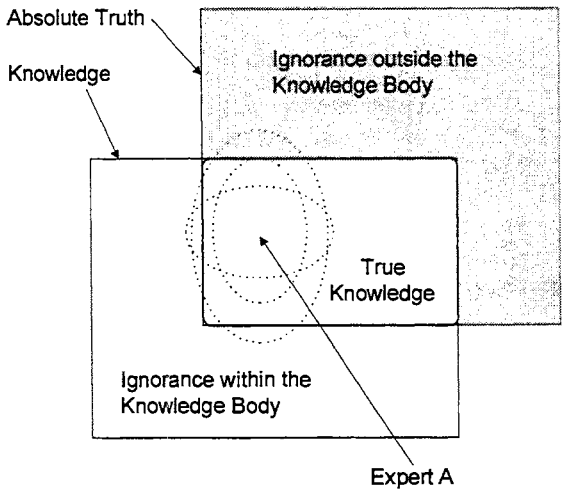

Figure 3. Knowledge and Ignorance (Ayyub 1999)

3. UNCERTAINTY TYPES

Uncertainty modeling and analysis in engineering started with the employment of safety factors using deterministic analysis, then was followed by probabilistic analysis with reliability-based safety factors. Uncertainty in engineering was classified into objective and subjective types. This classification was still deficient in completely covering the complete nature of uncertainty. The difficulty in completely modeling and analyzing uncertainty stems from its

complex nature, and its invasion of almost all epistemological levels of a system by varying degrees which are incompletely comprehended.

Engineers can deal with information for the purpose of system analysis and design. Information in this case is classified, sorted, analyzed, and used to predict system attributes, variables, parameters, and performances. However, it can be more difficult to classify, sort, and analyze the uncertainty in this information, and use it to predict unknown system attributes, variables, parameters, and performances. As a first step, the nature of uncertainty in systems needs to be understood. Then, uncertainty can be classified into types, and different analytical tools can be used for its modeling and analysis.

Uncertainties in engineering systems can be mainly attributed to ambiguity and vagueness in defining the architecture, parameters and governing prediction models for the systems. The ambiguity component is generally due to non-cognitive sources. These sources include (1) physical randomness; (2) statistical uncertainty due to the use of sampled information to estimate the characteristics of these parameters; (3) lack of knowledge; and (4) modeling uncertainty which is due to simplifying assumptions in analytical and prediction models, simplified methods, and idealized representations of real performances. The vagueness-related uncertainty is due to cognitive sources that include (1) the definition of certain parameters, e.g., structural performance (failure or survival), quality, deterioration, skill and experience of construction workers and engineers, environmental impact of projects, conditions of existing structures; (2) other human factors; and (3) defining the inter-relationships among the parameters of the problems, especially for complex systems. Other sources of uncertainty can include conflict in information, and human and organizational errors.

Analysis of engineering systems commonly starts with a definition of a system that can be viewed as an abstraction of the real system. The abstraction is performed at different epistemological levels (Ayyub 1992 and 1994). The resulting model can depend largely on an analyst or engineer; hence the subjective nature of this process. During the process of abstraction, the engineer needs to make decisions regarding what aspects should or should not be included in the model. These aspects include the previously identified uncertainty types. In addition to the abstracted and non-abstracted aspects, unknown aspects of the system can exist, and they are more difficult to deal with because of their unknown nature, sources, extents, and impact on the system.

3.1 Uncertainty in Abstracted Aspects of a System

3.1.1 Non-cognitive Uncertainty Types

Engineers and researchers dealt with the ambiguity types of uncertainty in predicting the behavior and designing engineering systems using the theories of probability and statistics. Probability distributions were used to model system parameters that are uncertain. Probabilistic methods that include reliability methods, probabilistic engineering mechanics, stochastic finite element methods, reliability-based design formats, random vibration, and other methods were developed and used for this purpose. In this treatment, however, a realization was established of the presence of a cognitive type of uncertainty. Subjective probabilities were used to deal with this type that are based on mathematics used for the frequency-type of probability. Uniform and triangular probability distributions were used to model this type of uncertainty for some parameters. The Bayesian techniques were also used, for example, to deal with gaining information about these parameters. The underlying distributions and probabilities were, therefore, updated. Regardless of the nature of the gained information, whether it is cognitive or non-cognitive, the same mathematical assumptions and tools were used.

3.1.2 Cognitive Uncertainty Types

The cognitive types of uncertainty arise from mind-based abstractions of reality. These abstractions are, therefore, subjective, and lack crispness. This vagueness is distinct from ambiguity in source and natural properties. The axioms of probability and statistics are limiting for the proper modeling and analysis of this type and are nor not completely relevant nor completely applicable. The vagueness type of uncertainty in civil engineering systems was previously discussed elsewhere along with applications of fuzzy set theory to such systems (Ayyub 1991).

Fuzzy set theory has been developed by Zadeh (1965, 1968, 1973, 1975, 1987) and used by scientists, researchers and engineers in many fields. Example applications are provided elsewhere (Kaufmann and Gupta 1985, and Kaufmann 1975). In engineering, the theory was proven to be a very useful tool in solving problems that involve the vagueness type of uncertainty. For example, civil engineers and researchers started using fuzzy sets and systems in the early 1970's (Brown 1979 and 1980, and Brown and Yao 1983). To date, many applications of the theory in engineering were developed. The theory has been successfully used in, for example, (1) strength assessment of existing structures and other structural engineering applications; (2) risk analysis and assessment in engineering; (3) analysis of construction failures, scheduling of construction activities, safety

assessment of construction activities, decisions during construction and tender evaluation; (4) the impact assessment of engineering projects on the quality of wildlife habitat; (5) planning of river basins; (6) control of engineering systems; (7) computer vision; and (8) optimization based on soft constraints (Blockley, et al 1975 to 1983, Furuta et al 1985 and 1986, Ishizuka et al 1981 and 1983, Itoh and Itagaki 1989, Kaneyoshi 1990, Shiraishi et al 1983 and 1985, Yao et al 1979, 1980 and 1986).

3.2 Uncertainty in Non-abstracted Aspects of a System

In developing a model, an analyst or engineer needs to decide at the different levels of modeling a system upon the aspects of the system that need to be abstracted, and the aspects that need not to be abstracted. The division between abstracted and non-abstracted aspects can be for convenience or to simplify the model. The resulting division is highly affected by the analyst or engineer, as a result of their knowledge and background, and the general state of knowledge about the system.

The abstracted aspects of a system and their uncertainty models can be developed to account for the non-abstracted aspects of the system to some extent. Generally, this accounting process is incomplete. Therefore, a source of uncertainty exists due to the non-abstracted aspects of the system. The uncertainty types in this case include physical randomness, vagueness, human and organizational errors, and conflict and confusion in information.

The uncertainty types due to the non-abstracted aspects of a system are more difficult to deal with than the uncertainty types due to the abstracted aspects of the system. The difficulty can stem from a lack of knowledge or understanding of the effects of the non-abstracted aspects on the resulting model in terms of its ability to mimic the real system. Poor judgment or human errors about the importance of the non-abstracted aspects of the system can partly contribute to these uncertainty types, in addition to contributing to the next category, uncertainty due to the unknown aspects of a system.

3.3 Uncertainty due to Unknown Aspects of a System

Some engineering failures occurred in the past because of failure modes that were not accounted for in the design stages of these systems. The non-accounting for the failure modes can be due to (1) ignorance, negligence, human or organizational errors; or (2) a general state of knowledge about a system that is incomplete. These unknown aspects depend on the nature of the system under consideration, the knowledge of the analyst, and the state of knowledge about the system in general. The non-accounting of these aspects in the models for the system can result in varying levels of impact on the ability of these models in mimicking the behavior of the systems. Their effects on these models can range from none to significant. In this case, the uncertainty types can include physical randomness, human and organizational errors, and lack of knowledge. Engineers dealt with non-abstracted and unknown aspects of a system by assessing modeling uncertainty which is defined as the ratio of a predicted system's variables or parameter (based on the model) to the value of the parameter in the real system. This ratio, which is called bias, is commonly treated as a random variable that can consist of objective and subjective components. This approach is based on two implied assumptions, (1) the value of the variable or parameter for the real system is known or can be accurately assessed from historical information or expert judgment; and (2) the state of knowledge about the real system is absolutely complete and reliable. For some systems, the first assumption can be approximately examined for its validity. The second assumption cannot be validated because of its absolute strictness.

4. VERIFICATION AND VALIDATION

To better understand the V&V process (see Figure 4), a formal treatment of uncertainty and error is necessary. An error can be due to distortion, which is a recognizable deficiency in any phase of modeling that is not due to lack of knowledge, or to incompleteness. Uncertainty is a type of error that represents a potential deficiency in any phase of modeling due to lack of knowledge. Uncertainty can be mainly attributed to ambiguity and vagueness in defining the architecture, parameters and governing prediction models for the system. Modeling uncertainty arises from using analytical models to predict system behavior. Statistical uncertainty arises from using samples to characterize populations. In this paper expert-opinion elicitation is presented as a solution to deal with uncertainty in selected technical issues related to a system of interest.

4.1 Verification

The verification process deals with the distortion type of error that can be modeled using numerical methods. Verification consists of three stages: conceptual model verification, design verification, and code verification. The verification can be done by comparison and test of agreement between the computational model and solution and results from benchmark (analytical or very accurate numerical solutions) of simplified model problems as shown in Figure 5.

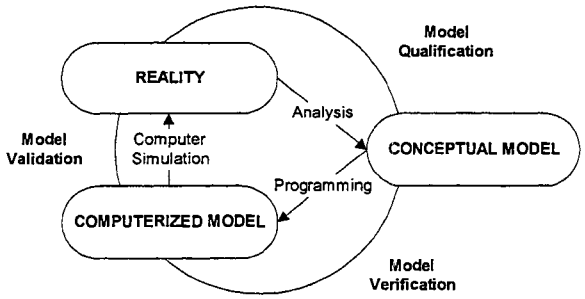

Figure 4. Model Verification and Validation (AIAA 1998)

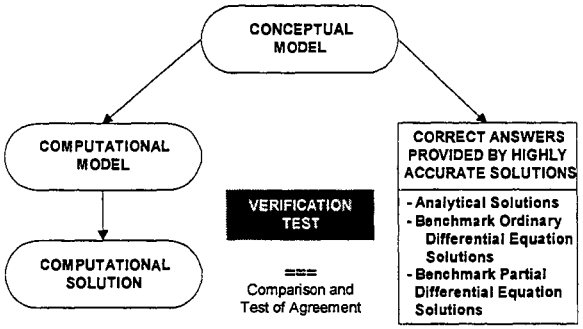

Figure 5. Verification Process (AIAA 1998)

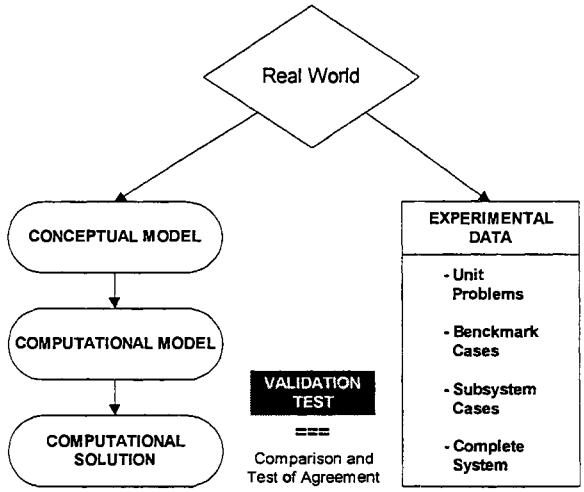

Figure 6. Validation Process (AIAA 1998)

4.2 Validation

The validation process deals with the uncertainty type of error. Validation consists of two stages: conceptual model validation, and results validation that can be done by expert opinion solicitation. To perform the validation of a design, the uncertainty for that system needs to be modeled. The uncertainty can be modeled using fuzzy sets, probability, statistics and numerical methods. The system can be divided into abstracted aspects, non-abstracted aspects, and unknown aspects of the system. Probability distributions are used to model parameters that are uncertain in the abstracted aspects of the system. The vagueness is dealt with by fuzzy sets. The non-abstracted and unknown aspects of the system are treated by assessing modeling uncertainty or bias. Bias is the ratio of predicted variable or parameter (based on the model) to the value of the parameter for the real system. Bias is treated as a random variable. The next section describes expert opinion elicitation, a proposed method for results validation.

4.3 Expert Opinion Elicitation

Expert-opinion elicitation can be defined as a heuristic process of gathering informing and data or answering questions on issues or problems of concern. The expert-opinion elicitation process can be defined as a formal process of obtaining information or answers to specific questions about certain quantities, called issues, such as unsatisfactory-performance rates, unsatisfactory-performance consequences and expected service life. Expert-opinion elicitation should not be used in lieu of rigorous reliability and risk analytical methods, but should be used to supplement them and to prepare for them. The expert-opinion elicitation process proposed in this paper is a variation of the Delphi technique (Helmer 1968) scenario analysis (Kahn and Wiener 1967) based on uncertainty models (Ayyub 1991, 1992 and 1993, Haldar et al 1997, Ayyub et al 1997, Ayyub and Gupta 1997, Ayyub 1998, Cooke 1991), social research (Bailey 1994), USACE studies (Ayyub et al 1996, and Baecher 1998), ignorance, knowledge, and uncertainty defined in the previous sections, nuclear industry recommendations (NRC 1997), Stanford Research Institute protocol (Spetzler and Stael von Holstein 1975).

The Delphi method is by far the most known method for eliciting and synthesizing expert opinions. The RAND corporation developed the Delphi method for the U. S. Air Force in the 1950s. In 1963, Helmer and Gordon used the Delphi method for a highly publicized long-range forecasting study (Helmer 1968). The method was extensively used in a wide variety of applications in the 1960s and 1970s exceeding 10,000 studies in 1974 on primarily technology forecasting and policy analysis (Linstone and Turoff 1975).

The purpose and steps of the Delphi method depend on the nature of use. Primarily the uses can be categorized into (1) technological forecasting, and (2) policy analysis. The technological forecasting relies on a group of experts on a subject matter of interest. The experts should be the most knowledgeable about issues or questions of concern. The issues and/or questions need to be stated by the study facilitators or analysts or monitoring team, and high degree of consensus is sought from the experts. On the other hand, the policy

analysis Delphi method seeks to incorporate the opinions and views of the entire spectrum of stakeholders, and seeks to communicate the spread of opinions to decision-makers. In engineering, we are generally interested in the former type of consensus opinion.

The basic Delphi method consists of the following steps (Helmer 1968):

1. Selection of issues or questions and development of questionnaires.
2. Selection of experts who are most knowledgeable about issues or questions of concern.
3. Issue familiarization of experts by providing sufficient details on the issues on the questionnaires.
4. Elicitation of experts about the issues. The experts generally do not know who the other respondents are.
5. Aggregation and presentation of results in the form of median values and an inter-quartile range (i.e., 25% and 75% percentile values).
6. Review of results by the experts and revision of initial answers by experts. This iterative reexamination of issues would sometimes increase the accuracy of results. Respondents who provide answers outside the inter-quartile range need to provide written justifications or arguments on the second cycle of completing the questionnaires.
7. Revision of results and re-review for another cycle. The process should be repeated until a complete consensus is achieved. Typically, the Delphi method requires three or four cycles or iterations.
8. A summary of the results is prepared with argument summary for out of inter-quartile range values.

The responses on the final iteration usually show less spread in comparison to spreads in earlier iterations. The median values are commonly taken as the best estimates for the issues or questions. Expert-opinion elicitation can be formally performed as provided in Figure 7 (Ayyub 1999).

The NRC (1997) classified issues for expert-opinion elicitation purposes into three complexity degrees (A, B, or C), with four level of study in the expert-opinion elicitation process (I, II, III, and IV) as shown in Table 1. A given issue is assigned a complexity degree and a level of study that depend on (1) the significance of the issue to the final goal of the study, (2) the issue's technical complexity and uncertainty level, (3) the amount of non-technical contention about the issue in the technical community, and (4) important non-technical consideration such as budgetary, regulatory, scheduling, public perception, or other concerns.

Experts can be classified into three types (NRC 1997): (1) proponents, (2) evaluators, (3) resource experts, (4) observers, and (5) peer reviewers. A proponent is an expert who advocates a particular hypothesis or technical position. In science, a proponent evaluates experimental data and professionally offers a hypothesis that would be challenges by the proponent's peers until proven correct or wrong. An evaluator is an expert who has the role of evaluating the relative credibility and plausibility of multiple hypotheses to explain observations. Evaluators consider available data, become familiar with the views of proponents and other evaluators, question the technical bases of data, and challenge the views of proponents. A resource expert is a technical expert with detailed and deep knowledge of particular data, issue aspects, particular methodologies, or use of evaluators. An observer can contribute to the discussion, but cannot provide expert opinion that enters in the aggregated opinion of the experts. A peer reviewer is an expert that can provide an unbiased assessment and critical review of an expert-opinion elicitation process, its technical issues, and results.

The study level as shown in Table 1 involves a technical integrator (TI) or a technical integrator and facilitator (TIF). A TI can be one person or a team (i.e., an entity) that is responsible for developing the composite representation of issues based on informed members and/or sources of related technical communities and experts; explaining and defending composite results to experts and outside experts, peer reviewers, regulators, and policy makers; and obtaining feedback and revising composite results. A TIF can be one person or a team (i.e., an entity) that is responsible for the functions of a TI, and structuring and facilitating the discussions and interactions of experts in the EE process; staging effective interactions among experts; ensuring equity in presented views; eliciting formal evaluations from each expert; and creating conditions for direct, non-controversial integration of expert opinions. The primary difference between the TI and the TIF is in the intellectual responsibility for the study where it lies with only the TI, and the TIF and the experts, respectively. The TIF has also the added responsibility of maintaining the professional integrity of the process and its implementation.

The TI and TIF processes are required to utilize peer reviewers for quality assurance purposes. Peer review can be classified according to peer-review method, and according to peer-review subject. Two methods of peer review can be performed: (1) participatory peer review that would be conducted as an ongoing review throughout all study stages, and (2) late-stage peer review that would be performed as the final stage of the

study. The former method allows for affecting the course of the study, whereas the latter one might not be able to affect the study without a substantial rework of the study. The second classification of peer reviews is by peer-review subject and has two types: (1) technical peer review that focuses on the technical scope, coverage, contents and results, and (2) process peer review that focuses on the structure, format and execution of the expert-opinion elicitation process. A guidance on the use of peer reviewers is provided in Table 2 (NRC 1997).

The expert-opinion elicitation process should preferably be conducted to include a face-to-face meeting of experts that is developed specifically for the issues under consideration. The meeting of the experts should be conducted after communicating to the experts in advance to the meeting background information, objectives, list of issues, and anticipated outcome from the meeting. The expert-opinion elicitation based on the technical integrator and facilitator (IIF) concept can result in consensus or disagreement as shown in Figure 8. Consensus can be of four types as shown in Figure 8 (NRC 1997). Commonly, the expert-opinion elicitation process has the objective of achieving consensus type 4, i.e., experts agree that a particular probability distribution represents the overall scientific community. The TIF plays a major role in building consensus by acting as a facilitator. Disagreement among experts, whether it is intentional or unintentional, requires the TIF to act as an integrator by using equal or non-equal weight factors. Sometimes, expert opinions need to be weighed for appropriateness and relevance rather than strictly weighted by factors in a mathematical aggregation procedure. The suggested steps for an expert-opinion elicitation process depend on the use of a technical integrator (TI) or a technical integrator and facilitator (TIF) as shown in Figure 7 (constructed based on NRC 1997).

4.3.1 Need Identification for Expert-Opinion Elicitation

The primary reason for using expert-opinion elicitation is to deal with uncertainty in selected technical issues related to a system of interest. Issues with significant uncertainty, issues that are controversial and/or contentious, issues that are complex, and/or issues that can have a significant effect on risk are most suited for expert-opinion elicitation. The value of the expert-opinion elicitation comes from its initial intended uses as a heuristic tool, not a scientific tool, for exploring vague and unknown issues that are otherwise inaccessible. It is not a substitute to scientific, rigorous research. The need identification and communication should include the definition of the goal of the study and relevance of issues to this goal.

Table 1. Issue Degrees and Study Levels

Issue Complexity Degree	
Degree	**Description**
A	Non-controversial Insignificant effect on risk
B	Significant uncertainty Significant diversity Controversial Complex
C	Highly contentious Significant effect on risk Highly complex
Study Level	
Level	**Requirements**
I	A technical integrator (TI) evaluates and weighs models based on literature review and experience, and estimates needed quantities.
II	A technical integrator (TI) interacts with proponents & resource experts, asses interpretations, and estimates needed quantities.
III	A technical integrator (TI) brings together proponents & resource experts for debate and interaction. TI focuses the debate, evaluates interpretations, and estimates needed quantities.
IV	A technical integrator (TI) and technical facilitator (TF) (that can be one entity, i.e., ITF) organize a panel of experts to interpret and evaluate, focus discussions, keep the experts debate orderly, summarize and integrate opinions, and estimates needed quantities.

4.3.2 Selection of Study Level and Study Leader

The goal of a study and nature of issues determine the study level as shown in Table 1. The study leader can be either a technical integrator (TI), technical facilitator (TF), or a combined technical integrator and facilitator (TIF). The leader of the study is an entity having managerial and technical responsibility for organizing and executing the project, overseeing all participants, and intellectually *owning* the results.

4.3.3 Selection of Peer Reviewers and Experts

Peer review can be classified according to peer-review method, and according to peer-review subject. Two methods of peer review can be performed: (1) participatory peer review that would be conducted as an ongoing review throughout all study stages, and (2) late-stage peer review that would be performed as the final stage of the study. The second classification of

peer reviews is by peer-review subject and has two types: (1) technical peer review that focuses on the technical scope, coverage, contents and results, and (2) process peer review that focuses on the structure, format and execution of the expert-opinion elicitation process. Peer reviewers are needed for both the TI and TIF processes. Peer reviewers should be selected by the study leader in close consultation with perhaps the study sponsor.

The size of an expert panel should be determined on case by case basis. The size should be large enough to achieve a needed diversity of opinion, credibility, and result reliability. In recent expert-opinion elicitation studies, a nomination process was used to establish a list of candidate experts by consulting archival literature, technical societies, governmental organization, and other knowledgeable experts (Trauth et al 1993). Formal nomination and selection processes should establish appropriate criteria for nomination, selection and removal of experts. One example of selection criteria for experts is presented in detail in NRC 1997 regarding the Yucca Mountain seismic hazard analysis. The panel of experts for an expert-opinion elicitation process should have a balance and broad spectrum of viewpoints, expertise, technical points of view, and organizational representation. The diversity and completeness of the panel of experts is essential for the success of the elicitation process.

Observers can be invited to participate in the elicitation process. Observers can contribute to the discussion, but cannot provide expert opinion that enters in the aggregated opinion of the experts. The observers provide expertise in the elicitation process, probabilistic and statistical analyses, risk analysis and other support areas. The composition and contribution of the observers are essential for the success of this process.

The experts and observers need to receive background materials and information, and description of the process and issues, and anticipated outcomes as defined by Ayyub (1999).

4.3.4 Identification, Selection and Development of Technical Issues

The technical issues of interest should be carefully selected to achieve certain objectives. In these guidelines, the technical issues are related to the quantitative assessment of unsatisfactory-performance probabilities and consequences for selected components, subsystems and systems within a facility. The issues should be selected such that they would have a significant impact on the study results. These issues should be structured in a logical sequence starting by background statement, followed by questions, and then answer selections or answer format and scales. Personnel with risk-analysis background that are familiar with the construction, design, operation, and maintenance of the facility need to define these issues in the form of specific questions. Also, background materials about these issues need to be assembled. The materials will be used to familiarize and train the experts about the issues of interest as described subsequent steps. The guidelines on constructing questions and issues based social research practices are presented in detail in Bailey 1994. Once the issues are developed, they should be pre-tested by administering them a few subjects for the purpose of identifying and correcting flaws. The results of this pre-testing should be used to revise the issues.

Table 2. Guidance on Use of Peer Reviewers (NRC 1997)

Expert-opinion elicitation Process	Peer Review Subject	Peer Review Method	Recom-mendation
Technical integrator and facilitator	Technical	Participat ory	Recom-mended
		Late stage	Can be acceptable
	Process	Participat ory	Strongly recom-mended
		Risky: unlikely to be successful	
Technical integrator	Technical	Strongly recommen ded	
		Risky but can be acceptable	
	Process	Strongly recommen ded	
		Risky but can be acceptable	

4.3.5 Elicitation of Opinions

The elicitation process of opinions should be systematic for all the issues according to the following steps (Ayyub 1999):

1. Issue Familiarization of Experts
2. Training of Experts
3. Elicitation and Collection of Opinions
4. Aggregation and Presentation of Results
5. Group Interaction, Discussion and Revision

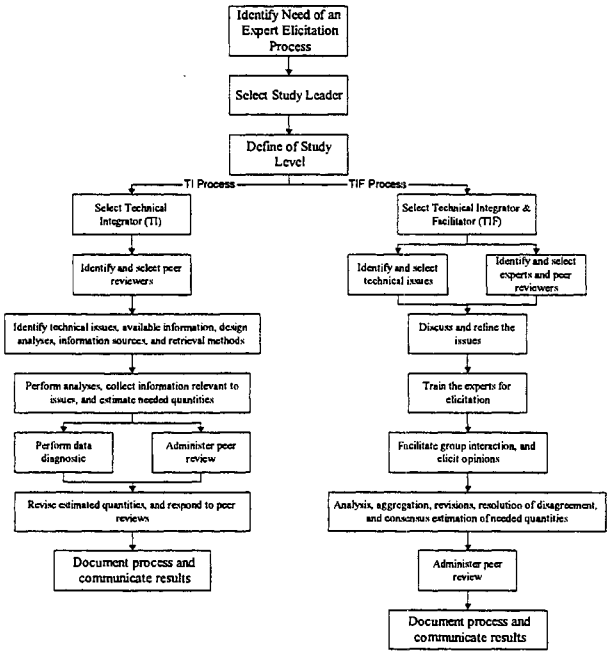

Figure 7. Expert-opinion elicitation Process (Ayyub 1999)

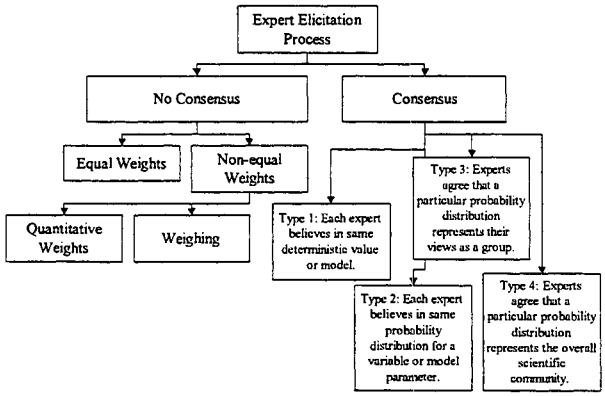

Figure 8. Outcomes of the Expert-opinion elicitation Process (Ayyub 1999)

4.3.6 Documentation and Communication

A comprehensive documentation of the process is essential in order to ensure acceptance and credibility of the results. The document should include complete descriptions of the steps, the initial results, revised results, consensus results, and aggregated results spreads and reliability measures.

4. CONCLUSIONS

This paper adapts and develops quantitative models and measures of various uncertainty types that are suitable for verification, validation, and prediction in decision-based design of complex engineering systems. A problem definition was provided, and needs and scope were developed. A work plan was proposed that could be implemented in future studies.

References

1. AIAA 1998. "Guide for the Verification and Validation of Computational Fluid Dynamics Simulations".
2. Ayyub, B.M 1999. Guidelines on Expert-Opinion Elicitation of Probabilities and Consequences for Corps Facilities, USACE, IWR.
3. Ayyub, B.M., and Chao, R.-J., 1998. "Chapter 1. Uncertainty Modeling in Civil Engineering with Structural and Reliability Applications," in Uncertainty Modeling and Analysis in Civil Engineering, edited by B. Ayyub, CRC Press, 1-32.
4. Ayyub, B. M. 1994. "The Nature of Uncertainty in Structural Engineering," in Uncertainty Modelling and Analysis: Theory and Applications, edited by Ayyub, and Gupta, Elsevier, 195-210.
5. Ayyub, B. M., 1991. "Systems Framework for Fuzzy Sets in Civil Engineering," international journal of FSS, 40(3), 491-508.
6. Ayyub, B. M., 1992. "Generalized Treatment of Uncertainties in Structural Engineering." *Analysis and Management of Uncertainty: Theory and Applications*, Edited by Ayyub and Gupta, Elsevier Science Publisher, NY, 235-246.
7. Ayyub, B. M., 1993. Handbook for Risk-Based Plant Integrity, prepared for Chevron Research and Technology Corporation, Richmond, CA, 1993.
8. Ayyub, B. M., Riley, B. C., and Hoge, M. T., 1996. Expert Elicitation of Unsatisfactory-Performance Probabilities and Consequences for Civil Works Facilities, Technical Report, USACE, PA.
9. Ayyub, B.M., (Editor), 1998, Uncertainty Model. and Analysis in Civil Engineering, CRC Press.
10. Ayyub, B.M., and Gupta, M.M., (Editors), 1997, Uncertainty Analysis in Engineering and the Sciences: Fuzzy Logic, Statistics, and Neural Network Approach, Kluwer Academic Publisher.
11. Ayyub, B.M., Guran, A., and Haldar, A., (Editors), 1997, Uncertainty Modeling in Vibration, Control, and Fuzzy Analysis of Structural Systems, World Scientific, 1997.
12. Bailey, K. D., 1994. *Methods of Social Research.* The Free Press, Maxwell Macmillan, NY.
13. Beacher, G., Expert Elicitation in Geotechnical Risk Assessment, USACE Draft Report, University of Maryland, College Park, MD.
14. Blockley, D. I., 1975, "Predicting the Likelihood of Structural Accidents," *Proceedings*, Institution of Civil Engineers, London, 59, Part 2, 659-668.
15. Blockley, D. I., 1979a, "The Calculations of Uncertainty in Civil Engineering," *Proceedings*, Institution of Civil Engineers, London, England, 67, Part 2, 313-326.
16. Blockley, D. I., 1979b, "The Role of Fuzzy Sets in Civil Engineering," *Fuzzy Sets and Systems*, 2, 267-278.

17. Blockley, D. I., 1980, *The Nature of Structural Design and Safety*, Ellis Horwood, Chichester, UK.
18. Blockley, D. I., Pilsworth, B. W. and Baldwin, J.F., 1983, "Measures of Uncertainty," *Civil Engineering Systems*, 1, 3-9.
19. Brown, C. B. and Yao, J. T. P., 1983, "Fuzzy Sets and Structural Engineering," *Journal of Structural Engineering*, ASCE, 109(5), 1211-1225.
20. Brown, C. B., 1979, "A Fuzzy Safety Measure," *Journal of Engineering Mechanics Division*, ASCE, 105(EM5), 855-872.
21. Brown, C. B., 1980, "The Merging of Fuzzy and Crisp Information," Journal of Engineering Mechanics Division, ASCE, 106(EM1), 123-133.
22. Cooke, R. M., 1991. *Experts in Uncertainty*, Oxford University Press.
23. Furuta, H., Fu, K. S., and Yao, J. T. P., 1985, "Structural Engineering Applications of Expert Systems," Computer Aided Design, 17(9), 410-419.
24. Furuta, H., Shiraishi, N., and Yao, J. T. P., 1986, "An Expert System for Evaluation of Structural Durability," *Proc. of fifth OMAE Symposium*, 1, 11-15.
25. Haldar, A, Guran, A., and Ayyub, B.M., (Editors), 1997, Uncertainty Modeling in Finite Element, Fatigue, and Stability of Systems, World Scientific.
26. Helmer, O., 1968. "Analysis of the Future: The Delphi Method," and "The Delphi Method – An Illustration," Bright (ed.), Techn. Forecasting for Industry and Government, Prentice Hall, NJ.
27. Ishizuka, M., Fu, K. S., and Yao, J. T. P., 1981, "A rule-Inference Method for Damage Assessment," ASCE *Preprint 81-502*, ASCE, Missouri.
28. Ishizuka, M., Fu, K. S., and Yao, J. T. P., 1983, "Rule-Based Damage Assessment System for Existing Structures," *Solid Mechanics Archives*, 8, 99-118.
29. Itoh, S., and Itagaki, H., 1989, "Application of Fuzzy-Bayesian Analysis to Structural Reliability," *the proceedings of the Fifth International Conference on Structural Safety and Reliability*, ICOSSAR, 1771-1774.
30. Kahn, H., and Wiener, A. J., 1967. *The Year 2000: A Framework for Speculation*, Macmillan, NY.
31. Kaneyoshi, M., Tanaka, H., Kamei, M., and Furuta, H., 1990, "Optimum Cable Tension Adjustment Using Fuzzy Regression Analysis," 3rd *IFIP*.
32. Kaufman, A. and Gupta, M. M., 1985, *Introduction to Fuzzy Arithmetic, Theory and Applications*, Van Nostrand Reinhold Co., New York.
33. Kaufmann, A., 1975, *Introduction to the Theory of Fuzzy Subsets*, Academic Press, New York, N.Y., (Translated by D. L. Swanson).
34. Klir, G. J., and Folger, T. A., 1988, *Fuzzy Sets, Uncertainty, and Information*, Prentice Hall, N.J.
35. Linstone H. A., and Turoff, M., 1975. The Delphi Method, Techniques and Applications, Addison Wesley, MA.
36. Nuclear Regulatory Commission, 1997. Recommendations for Probabilistic Seismic Hazard Analysis: Guidance on Uncertainty and Expert Use, prepared by the Senior Seismic Hazard Analysis Committee, NUREG/CR-6372.
37. Oberkampf, W. T., DeLand, S.M., Rutherford, B.M., Diegert, K.V., Alvin, K.F., 1999, "A New Methodology for the Estimation of Total Uncertainty in Computational Simulation," *AIAA Non-Deterministic Approaches Forum*, MO.
38. Shiraishi, N. and Furuta, H., 1983, "Reliability Analysis Based on Fuzzy Probability," *J. of Eng. Mechanics*, ASCE, 109(6), 1445-1459.
39. Shiraishi, N. Furuta, H., and Sugimoto, M., 1985, "Integrity Assessment of Structures Based on Extended Multi-Criteria Analysis, " *Proc. of the fourth ICOSSAR*, Kobe, Japan.
40. Spetzler, C. S., and Stael von Holstein, C.-A. S., 1975. "Probability Encoding in Decision Analysis," Management Science, 22(3).
41. Trauth, K. M., Hora, S. C., and Guzowski, R. V., 1993. Expert Judgement on Markers to Deter Inadvertent Human Intrusion into the Waste Isolation Pilot Plant, Report SAND92-1382, Sandia National Laboratories, Albuquerque, NM.
42. Yao, J. T. P. and Furuta, H., 1986, "Probabilistic Treatment of Fuzzy Events in Civil Engineering," *Probabilistic Engineering Mechanics*, 1(1), 58-64.
43. Yao, J. T. P., 1979, "Damage Assessment and Reliability Evaluation of Existing Structures," *Engineering Structures*, England, 1, 245-251.
44. Yao, J. T. P., 1980, "Damage Assessment of Existing Structures," *Journal of Engineering Mechanics Division*, ASCE, 106(EM4), 785-799.
45. Zadeh, L. A., 1965, "Fuzzy Sets," *Information and Control*, 8, 338-353.
46. Zadeh, L. A., 1968, "Probability Measures of Fuzzy Events," *J. of Math. Analysis*, 23, 421-427.
47. Zadeh, L. A., 1973, "Outline of a New Approach to the Analysis of Complex Systems and Decision Processes," *IEEE Transactions on Systems, Man and Cybernetics*, SMC-3(1), 28-44.
48. Zadeh, L. A., 1975, "The Concept of Linguistic Variable and Its Application to Approximate Reasoning," Parts I, II and III, *Information and Control*, (8), 199-249, 301-357, (9), 43-80.
49. Zadeh, L. A., 1987, "Fuzzy Sets as a Basis for a Theory of Possibility," *FSS*, 1, 3-28.
50. Zadeh, L. A., Fu, K. S., Tanaka, K. and Shimara, J., 1975, *Fuzzy Sets and Their Application to Cognitive and Decision Processes*, Academic Press, New York, N.Y.

PROCEEDINGS OF THE THIRD INTERNATIONAL WORKSHOP ON VERY LARGE FLOATING STRUCTURES
(VLFS '99), VOL. I, EDS. R.C. ERTEKIN & J.W. KIM, 22-24 SEPTEMBER 1999, HONOLULU, HAWAII, USA

ANALYTICAL TOOL FOR EARLY DESIGN OF MEGA-FLOAT STRUCTURE SUBJECT TO WAVE LOADS

Kiyoshi Inoue
Hitachi Zosen Corporation

ABSTRACT

In order to make a structural design of the Mega-Float structure subject to wave loads, it is thought that the two-step method, that is, a dynamic hydroelastic analysis and a static structural analysis, is one of adequate methods from the following reasons:

a) The structural model for stress analysis needs to correspond to the actual structural arrangement as far as possible while dynamic analysis normally applies rather simple model such as uniform plate model.
b) It is better to reduce a burden of the computer by dividing the above-mentioned dynamic and static numerical computation.

This paper presents a simplified method of the second step static analysis by receiving the results of dynamic analysis.

The analysis is based on the grillage modeling. The model includes open structures of which the floating structure is divided into deck and bottom girders, and the effect of local shear bending of such girders are taken into account.

From the results of trial analyses, it has been found that this method could become an effective tool for early design of VLFS.

1. INTRODUCTION

This paper is to propose a practical method of structural analysis for a very large floating structure (VLFS) of which a quasi-static analysis is made by receiving a set of result of a hydroelastic response analysis. The static analysis program (see [1]) developed at the Technological Research Association of Mega-Float (TRAM) is extensively applied for this use.

Although hydroelastic analyses in waves are of essential technology for designing Mega-Float structures, many of various programs including of Nagata (see [2]), Ohmatsu (see [3]) and others give only bending moments and so on compared to ship's longitudinal bending moments. And they are difficult to manage analyses for varying internal structures.

On the other hand, it is essential to handle stresses according to varying internal structures. However, it is difficult to analyze dynamic and structural problems altogether from point of view of computer capacity. The program such as of Seto (see [4]) is rather of exception, of which both of dynamic and structural behavior are treated.

Accordingly, so-called the two-step method becomes a practical method which consists of the first step hydroelastic analysis and the second step quasi-static analysis. Here, a method is applied that the result of the first step analysis is given in the form of fluid dynamic forces and inertia forces: the former consisting of diffraction forces, radiation forces and fluctuating buoyancy; the latter simply induced from the deflection.

2. NECESSITY OF STATIC ANALYSIS

2.1 Advantage and Limitation of Dynamic Hydroelastic and Static Structural Analyses

The followings are comparison between dynamic analysis (D) and static analysis (S):

a) Managing large sized model of some 50 to 100 thousands nodal joints to express varying structure in a whole floating structure:
(D) difficult, (S) easy.
b) Managing varying structural rigidities due to varying deck-bottom plate thickness and other structural arrangement:
(D) difficult, (S) easy.
c) Managing shear and torsional deflections:
(D) difficult, (S) easy.
d) Managing varying internal structural arrangement due to such as hollow structures in bulkheads:
(D) difficult, (S) easy.
e) Solving dynamic behavior due to waves:
(D) easy, (S) difficult.

2.2 Connection of Dynamic and Static Analysis

As itemized in the above, both of dynamic and static analyses are not almighty. Namely, it is difficult to establish an all-in-one program to manage dynamic response and also stress analyses. Accordingly, it is practical to consider so-called the two-step method in the following manner:

a) The two-step method consists of dynamic hydroelastic analysis as the first step, and static structural analysis as the second step.
b) The results of the first step are arranged so as to match the analysis of the second step.
c) Although the results of the first step are normally given in the state of self-equilibrium, there is a possibility that the balance is somewhat disturbed because of differences of analytical models. To meet such situation, adjusting loads to attain equilibrium are added to the original set of loads.

3. METHOD OF ANALYSIS

3.1 General Flow

Fig.1 shows the flow of analysis in which the following functions are incorporated:

a) To receive the result of dynamic analysis in the form of real part and imaginary part.
b) Adjusting calculation is incorporated to maintain equilibrium of the set of loads.
   Fig.2 shows illustrations of uniform, x-directional and y-directional wedge load distributions to adjust possible unbalances raised from the difference between models of static and dynamic analyses. The loads are calculated at each mesh of grillage model surrounded by longitudinal and transverse beam elements.
c) Finally, the amplitudes are calculated to grasp the experienced maximum values of individual items while waves pass through.

3.2 Method to Analyze Hollow Structure by a Grillage Model

Although stress analyses for structures with large openings should be properly made by 3D-FEM, it is often needed to cut the time by taking more shorter check for grasping very approximate stress level and for judging necessity of further detailed examination.

Fig.3 illustrates a typical hollow section, which divide the structure into deck and bottom girders. For such cases, Inoue (see [5]) previously proposed a simplified procedure to be added to the said static analysis program of TRAM.

Fig.4 illustrates the mechanism of deformation of such a structure. The method focused an apparent shear deflection in the plane grillage model composed of local shear bending of deck and bottom girders among other usual bending, shear deflection and axial deformation of a grillage beam element. The trial calculation at this time applies to this.

4. EXAMPE OF CALCULATION

4.1 Calculation Model

Fig.5 shows the calculation model. The analysis at this time uses rather small model although the program can run the model of some 5000 meter long very large floating structure. The outline of the calculation is as follows:

L x B x D x d = 350 x 60 x 5 x 3m
Six (6) lines of longitudinal bulkheads
(see the figure for the distances).
Spacing of transverses: S_T = 5m
Bending rigidity: EI/B = 4.86 x 10^9kgf-m^2/m
Section modulus at deck: Z_d = 0.0974m^3/m
Longitudinal waves: T_w x L_w = 5.79sec x 50m
Wave height: H_w = 2m
Water depth: WD = 15m

4.2 Result of Calculation

Fig.6 shows the results derived from the hydroelastic analyses. The real part and imaginary part are indicated at the left and right columns in the page, respectively.

Fig.7 shows the results of static analyses by the input of the results of the hydroelastic analysis of Fig.6. Deflections, longitudinal stresses of deck, longitudinal stresses of deck girder faces, shear stresses of longitudinal bulkheads are shown from top to bottom.

Fig.8 shows the results of static analyses in the form of amplitude distribution. Shear stresses of deck girder webs are shown instead of deflections.

5. CONSIDERATIONS

5.1 Deflections

Differences of deflections in Fig.7 from those in Fig.6 give some materials to judge the extent that the static analyses can express the results of dynamic ones. The displacements at four corners are of the preset values derived form the dynamic analyses, automatically coinciding those in Fig.6. Accordingly, displacements at other parts of model are checked. The configurations of deflection are very similar to those of dynamic solutions. It is found that each of the peak value coincides with that of dynamic analyses while some differs.

5.2 Longitudinal Stresses of Deck

In Fig.7 (1)-b) and (2)-b), the distributions and values of the stresses of deck are similar to those of dynamic analyses while some points do not coincide. The reason is thought because of the difference of the calculation models such as shear rigidities, with/without hollow structures, etc.

Some disturbances of stresses at the right end of model are found. It is because of the additional preset displacement at the corner to stabilize the torsional deflections at the end, where the value is derived from the dynamic analysis. The treatment of adjusting torsional deformation need to be reinvestigated.

5.3 Longitudinal Stresses of Deck Longitudinal Girder Faces

Longitudinal stresses of deck longitudinal girders are predominantly effected by local shear bending induced by shear forces of grillage elements. The stresses get maximum at the section where shear forces of longitudinal bulkheads get maximum, i.e., the slopes of bending moments get maximum. The stresses reach toward zero at the section where the bending moment get peak. Such characteristics is clearly found in the results. It can be seen that the peak values of deck at the ends of girders need not be added directly to the peak values of bending stresses of deck.

5.4 Shear Stresses of Longitudinal Bulkheads

Shear stresses of longitudinal bulkheads are directly effected by the distance from the neighboring bulkheads as seen in the results in which the values are different each other accordingly. It is noted that the shear forces of each line of longitudinal bulkhead are similar because they are given as the values per unit breadth of the structure.

5.5 Shear Stresses of Deck Longitudinal Girders

Stresses of deck longitudinal girder webs depend on load distributions effected by the relation of rigidities. Consequently, shear stresses of girder webs are different from those of longitudinal bulkheads as seen from the results.

6. CONCLUSIONS

The results of the two-step method connecting dynamic hydroelastic analyses and static stress analyses are summarized as follows:

a) It was found that the two-step method can become a coarse but quick design tool to grasp structural behavior of a whole floating structure.
b) The boundary condition at the static analyses need more consideration from point of view of adjusting load for torsion of a whole structure.
c) It was found that stress analyses for hollow structure give preliminary materials for early check.
d) It is needed to compare stress by using more simple structural model for static analysis without shear deflection and hollow structures.
e) Analyses for oblique waves need to be done to check more complicated behavior.
f) It is expected that the two-step method at this time can be extended to 3D-FEM models and also grillage/FEM combined models.

ACKNOWLEDGMENT

This paper was made as a part of study of the Technological Research Association of Mega-Float. The members of the technical committee of the Association gave useful discussions. The results of hydroelastic analyses were given by Dr. S. Ohmatsu of Ship Research Institute (SRI), Ministry of Transport. The staffs of Hitachi Zosen Information Systems Co., Ltd. (HZS) gave cooperation for computer works. The Author expresses his thanks to all concerned.

REFERENCES

[1] K. Inoue. "Global Static Analysis System for Mega-Float". Proc. of 16th Int. Conf. on Offshore Mechanics and Arctic Engineering (OMAE-97), Yokohama, 1997.
[2] S. Nagata, H. Yoshida, H. Fujita and H. Issiki. "The Analysis of the Wave-Induced Response of an Elastic Floating Plate". Proc. of 16th Int. Conf. on Offshore Mechanics and Arctic Engineering (OMAE-97), Yokohama, 1997.
[3] S. Ohmatsu. "Numerical Calculation of Hydroelastic Behavior of Pontoon Type VLFS in Waves". Proc. of 17th Int. Conf. on Offshore Mechanics and Arctic Engineering (OMAE-98), Lisbon, 1998.
[4] H. Seto and M. Ochi. "A Hybrid Element Approach to Hydroelastic Behavior of a Very Large Floating Structure in Regular Waves". Proc. of 2nd Int. Conf. on Hydroelasticity in Marine Technology, Fukuoka, 1998.
[5] K. Inoue. "A Design Tool for Static Structural Problems of Mega-Float". Proc. of 9th Int. Conf. on Computer Applications in Shipbuilding (ICCAS-97), Yokohama, 1997.

(a) To generate data of grillage beam model for static analysis.

(b) To set nodal restraints:
Three vertical and three horizontal direction.

k=1,2 (k=1: Real, k=2: Imaginary)

(c) To pick up the results of hydroelastic analysis, and divide them into the real part (k=1) and imaginary part (k=2):

i) Pressure
(diffraction + radiation + buoyancy):
$p_{kj}(j=1,2,...,N_j)$

ii) Deflection : $\delta_{kj}(j=1,2,...,N_j)$

Deflections are used only for fixing boundary condition. Static buoyancy is not considered, and only fluctuation of buoyancy due to structural deflection is taken into account.

(d) To convert each p_{kj} into a nodal force F_{kj}:

$F_{kj} = p_{kj} \times A_j (j=1,2,...,N_j)$

A_j = Area covered by the nodal joint j

(e) To calculate the unbalanced force and moments in the whole model, and calculate a set of adjusting loads based on a uniform load, and x-directional and y-directional wedge loads. The loads are combined with the loads of (4)

(f) To run the static analysis program.
Various output curves are obtained for each k.

(k-loop end)

(g) To calculate amplitudes:

$(Amplitude)_j = \sqrt{(\mathrm{Re}al)_j^2 + (\mathrm{Im}aginary)_j^2}$

Output curves are obtained corresponding to those of (6) for deflections, bending stresses, shear stresses, and so on.

Fig.1 General flow of the analysis

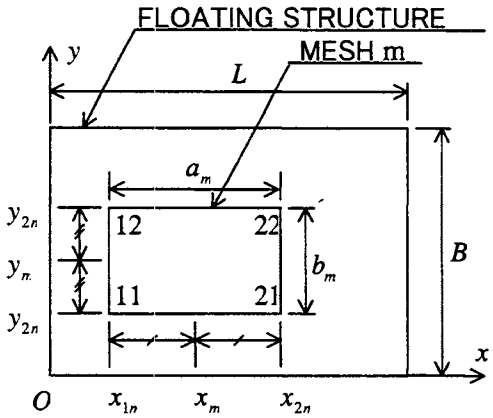

a) Mesh Surrounded by Beam Elements

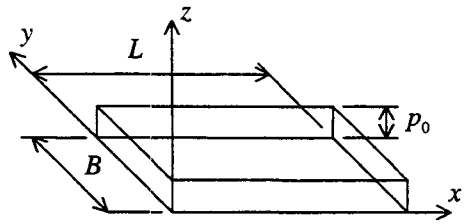

b) Uniform Load Distribution

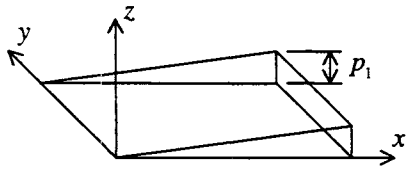

c) x-directional Wedge Load Distribution

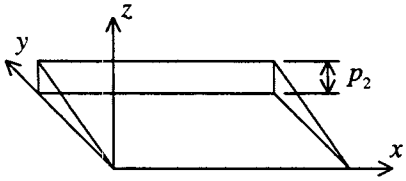

d) y-directional Wedge Load Distribution

Fig.2 Uniform and wedge load distributions for adjusting unbalanced force and moments

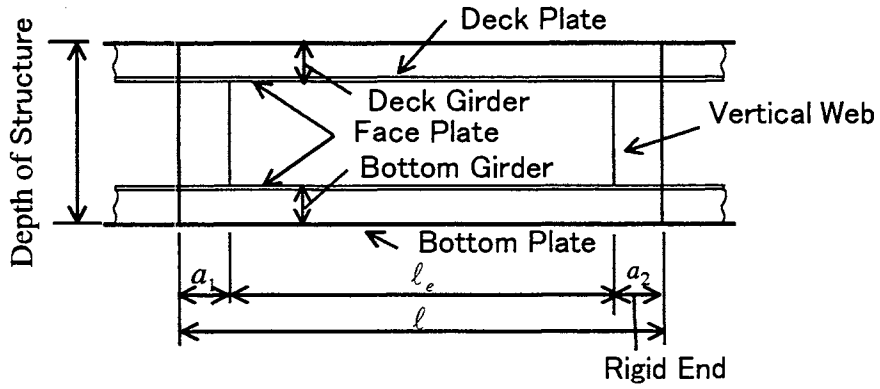

Fig.3 Hollowed structure (see [5])

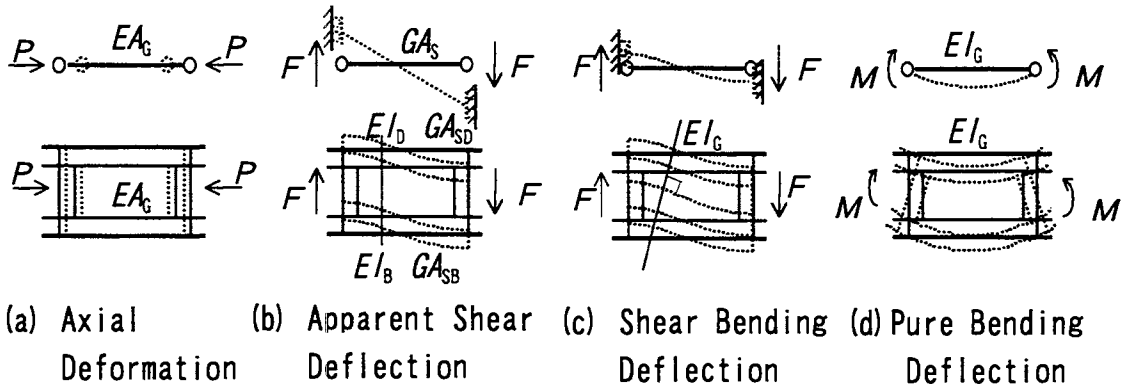

Fig.4 Mechanism of deflection of a hollowed structure (see [5])

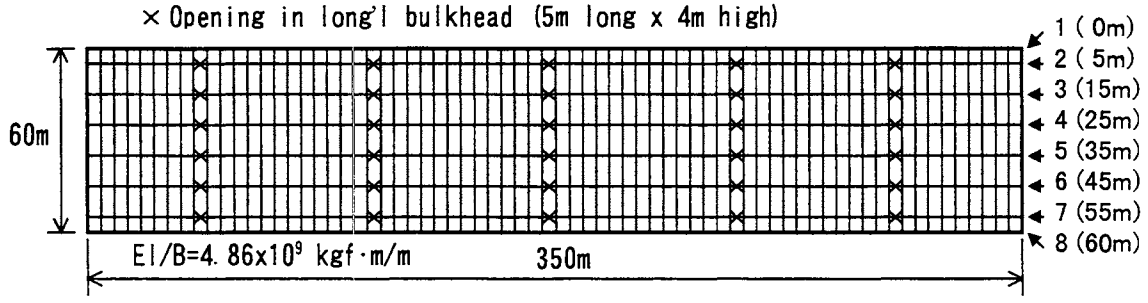

Fig.5 Structural model for analysis of a floating structure

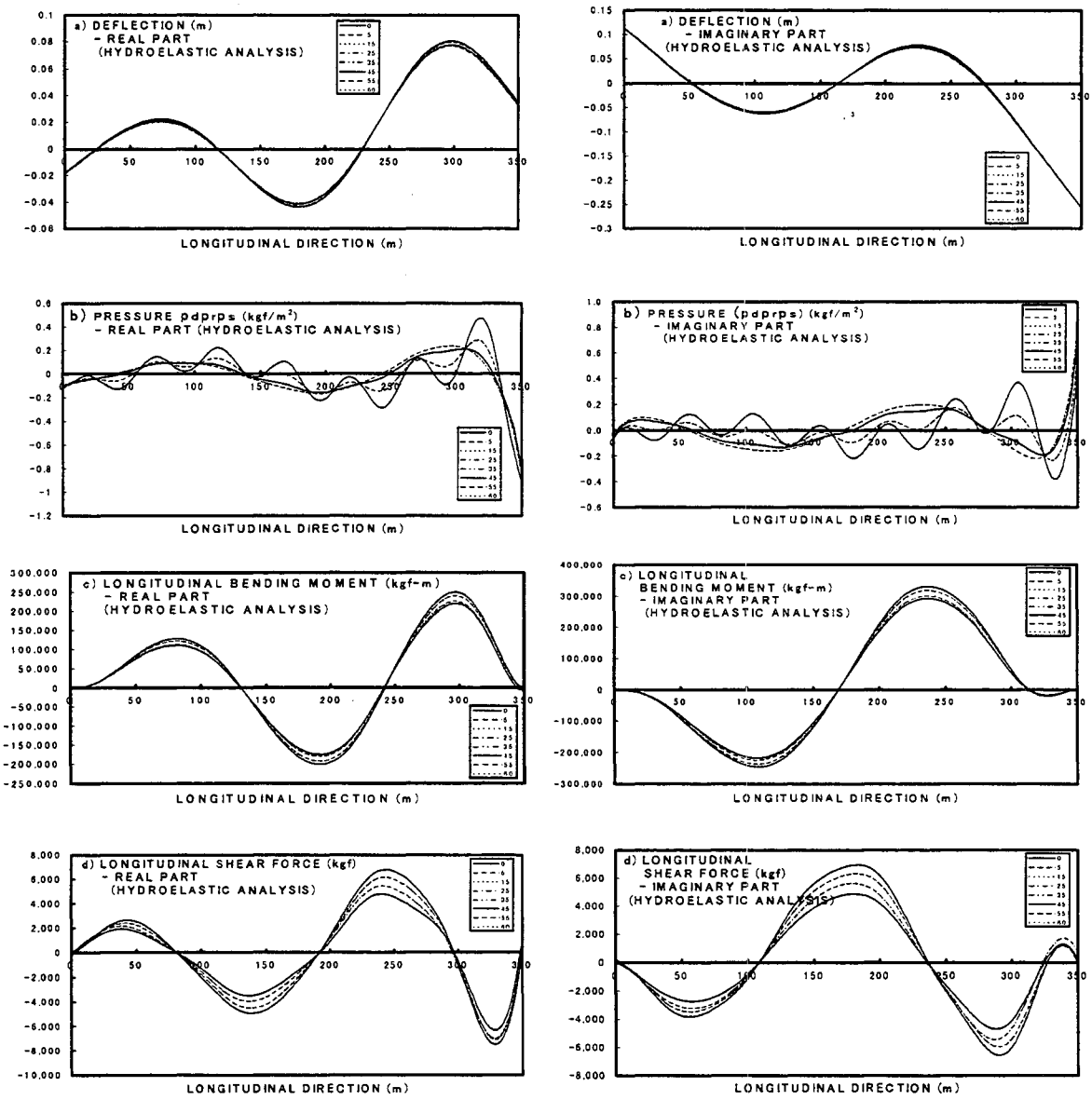

(1) Real part (2) Imaginary part

Fig.6 Given output of the hydroelastic analysis to be used for the static structural analysis

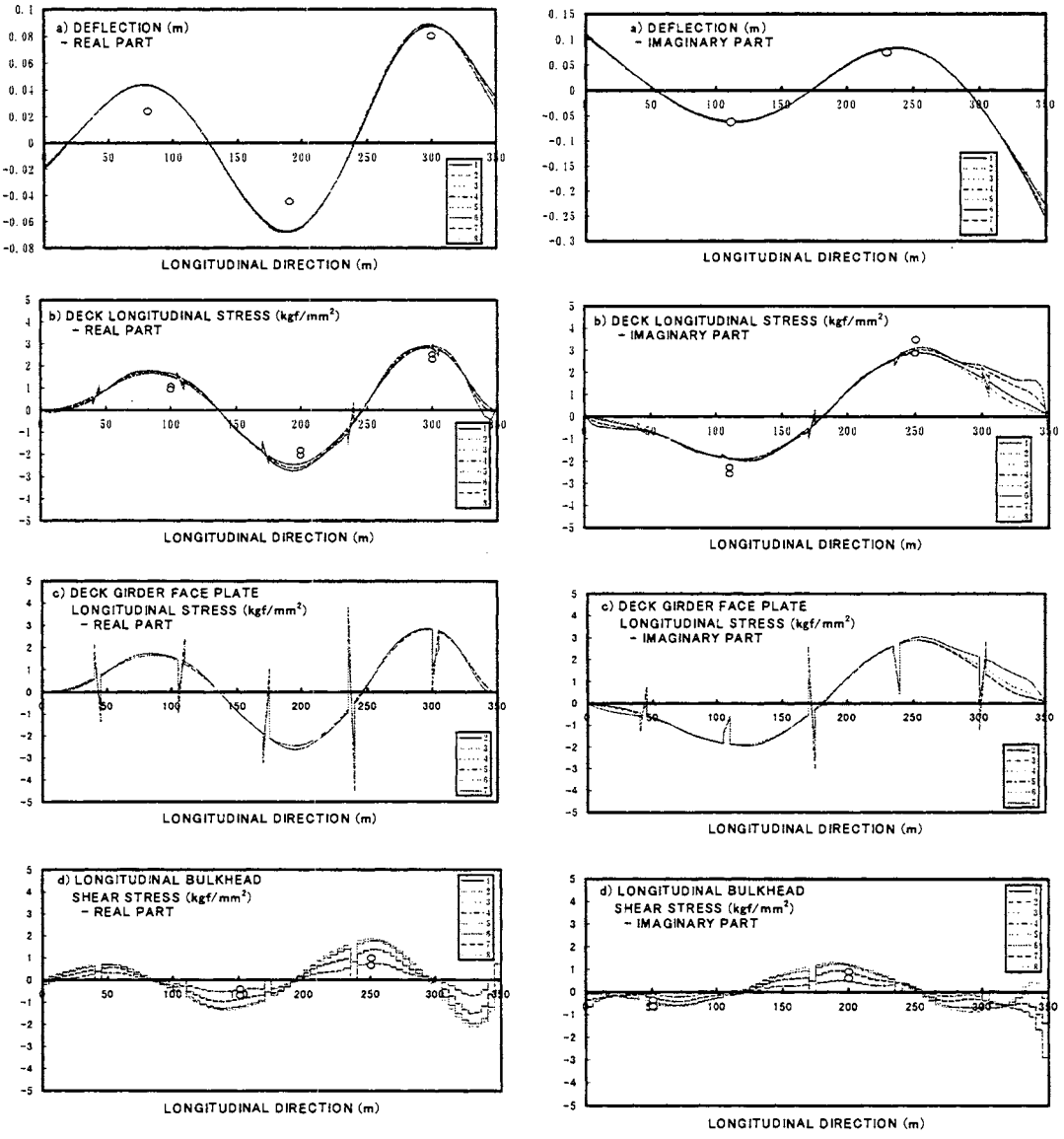

(1) Real part

(2) Imaginary part

Fig.7 Result of the static structural analysis

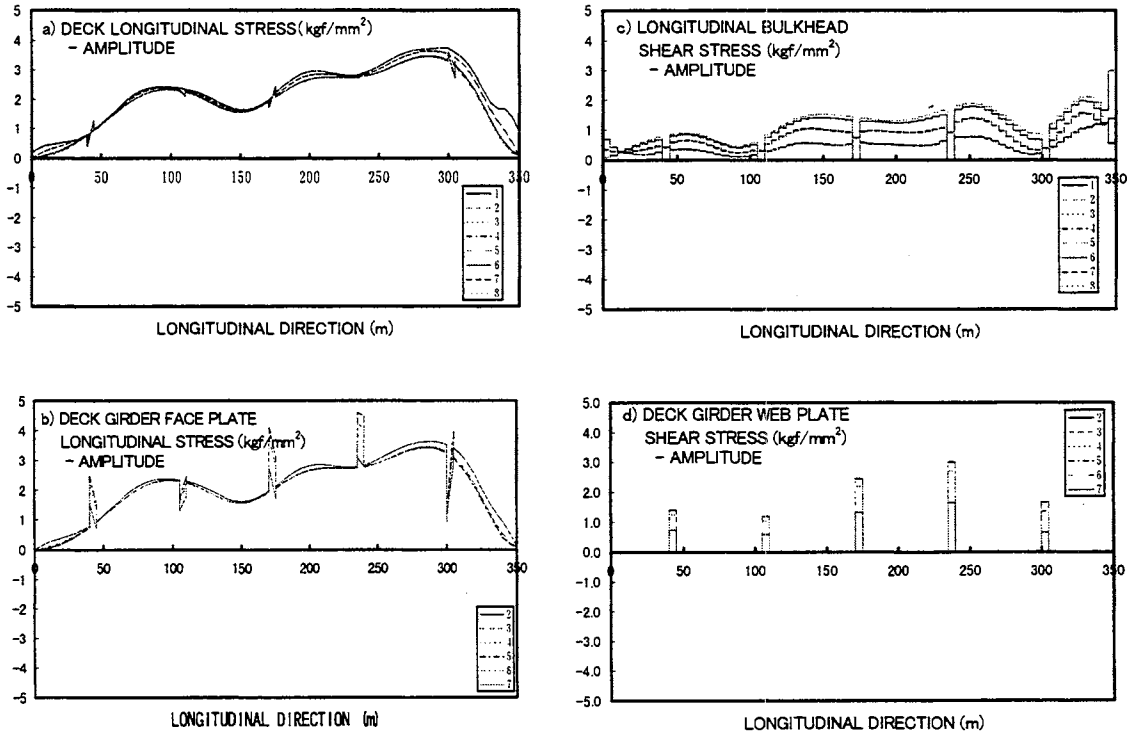

Fig.8 Result of the static analysis in the form of amplitude

PROCEEDINGS OF THE THIRD INTERNATIONAL WORKSHOP ON VERY LARGE FLOATING STRUCTURES
(VLFS '99), VOL. I, EDS. R.C. ERTEKIN & J.W. KIM, 22-24 SEPTEMBER 1999, HONOLULU, HAWAII, USA

A TIME-DOMAIN GREEN FUNCTION METHOD FOR TRANSIENT PROBLEMS OF A PONTOON-TYPE VLFS

Masashi Kashiwagi
Research Institute for Applied Mechanics, Kyushu University *

ABSTRACT

The time-dependent three-dimensional problems of a flexible floating plate are tried to solve by the time-domain Green-function method. Starting from Green's second identity, the integral equation for the time-dependent pressure distribution is derived and the calculation formula for the so-called memory-effect function is presented. Another indirect method for computing the memory-effect function based on the Fourier transform is also summarized, in which only the damping coefficient in the frequency domain is needed.

Despite some efforts to solve the time-dependent integral equation derived, it seems not easy to obtain reasonable results. Thus, considering the numerical burden and relative accuracy, it is concluded in this paper that the indirect method looks more effective. However, for this conclusion to be valid, the frequency-domain computations must be possible up to higher frequencies where the asymptotic fitting in terms of analytical functions can be done with reasonable accuracy.

1. INTRODUCTION

Very large floating structures (VLFSs) are being considered in Japan as a possible floating airport, and its safety and performance in various circumstances are being intensively studied. The preferred configuration of VLFS is of pontoon type, and its size will be 5 km long, 1 km wide, and only a few meters deep. Thus this type of structure is featured in that the flexural rigidity is relatively small and hydroelastic responses are more important than the rigid-body motions.

There could be various excitations to this "sheet-like" structure in a real situation. The most possible and important one is the wave excitation, and hence many studies have been made on the wave-induced hydroelastic responses in regular waves (e.g. a recent review by Kashiwagi [1]). The structure under consideration will also respond flexurally even under moving loads such as those imparted by an aircraft during landing or take-off. A huge-mass impact may occur due to aircraft crash onto the airport, or as Korobkin [2] reported, a VLFS might be used as a platform for the spacecraft launching. These are transient phenomena to be studied for realization of a floating airport. The deterministic prediction of responses to irregular waves is another topic in the time domain.

Watanabe & Utsunomiya [3] studied transient elastic responses at aircraft landing on a circular VLFS, using a commercial-base FEM program. Kim & Webster [4] and Yeung & Kim [5] also studied transient phenomena during the idealized landing and take-off of an aircraft on an infinite elastic runway by means of the double Fourier transform with respect to horizontal spatial variables.

From a practical viewpoint, Endo et al. [6] computed time-dependent responses of an elastic plate to the weight-drop impact or moving load. They computed firstly the impact-response function of the hydrodynamic force using frequency-domain results and then the differential equations for the elastic motion were solved in the time domain. However, enough attention was not paid to the accuracy; for instance, neglect of contributions from the damping coefficient at higher frequencies.

Instead of the impulse-response function of the hydrodynamic force, Ohmatsu [7] considered the impulse- and step-response functions of the elastic deflection according to the problems considered. In his method, the infinite integral with respect to the frequency was also truncated at some finite frequency and contributions from higher frequencies were assumed to be zero. This treatment is questionable for a flexible structure, because the elastic responses are not necessarily small for high frequencies.

The present study started to compute the impulse-response function directly in the time domain. The idea is to adopt the time-domain Green

*6-1 Kasuga-koen, Kasuga, Fukuoka 816-8580, Japan.
E-Mail: kashi@riam.kyushu-u.ac.jp

function in the pressure distribution method, in an analogous manner to the analysis in the frequency domain [8]. In the context of ship hydrodynamics, the time-domain Green function method has been studied (e.g. [9], [10], and [11]). However, few computations based on the time-domain Green function method have been made so far for shallow-draft flexible structures like a floating airport.

In this paper, the integral equation for the time-dependent pressure distribution is derived, which is tried to solve numerically. However, in spite of several efforts, reasonable results are not obtained; which is probably because of highly oscillatory nature of the Green function on the free surface. Instead, the memory-effect function is computed through the Fourier transform using the damping coefficient in the frequency domain. It is noted that the accurate asymptotic fitting to the computed values over higher frequencies is important for reasonable evaluation of the memory-effect function.

2. MATHEMATICAL FORMULATION

Let us consider a shallow-draft pontoon-type structure, which is rectangular in plan with length L and width B. Cartesian coordinates are used with $z = 0$ defined as the plane of the undisturbed free surface and $z = h$ as the horizontal sea bottom. The boundary conditions on the body and free surfaces are linearized and the potential flow is assumed. The draft of VLFS is very small relative to the dimensions in plan and thus it can be regarded as zero in a mathematical sense. Because we are concerned with transient problems, all variables must be understood as time dependent.

It is convenient to describe all quantities in nondimensional form, using the fluid density, ρ, the gravitational acceleration, g, and the half length of the structure, $L/2$, as the characteristic length scale.

In this case, the dynamic and kinematic boundary conditions on the free surface are expressed as

$$p = -\frac{\partial \phi}{\partial t}, \quad \frac{\partial \phi}{\partial z} = \frac{\partial w}{\partial t} \quad \text{on } z = 0 \tag{1}$$

where $p(x, y, z, t)$ is the pressure, $\phi(x, y, z, t)$ is the disturbance velocity potential, and $w(x, y, t)$ is the elevation on the free surface.

Eliminating w from (1), it follows that

$$\frac{\partial \phi}{\partial z} - \frac{\partial^2 \phi}{\partial t^2} = -\frac{\partial p}{\partial t} \quad \text{on } z = 0 \tag{2}$$

As the initial conditions of the velocity potential, the fluid motion is assumed to start from a state of rest at $t = 0_-$, and thus we can write as

$$\phi = \frac{\partial \phi}{\partial t} = 0 \quad \text{at } t = 0_- \tag{3}$$

Note that $p = 0$ on the water surface, whereas $p \neq 0$ beneath the structure because of the disturbance exerted by the motion of the structure.

The motion equation of a structure under consideration can be expressed with the vibration equation of a thin plate, in the form

$$m\frac{\partial^2 w}{\partial t^2} + D\nabla^4 w = -(p + p_E) \tag{4}$$

where $m(x, y)$ is the mass per unit area, D is the flexural rigidity, and $\nabla = (\partial/\partial x, \partial/\partial y)$ is the 2-D differential operator. $p_E(x, y, t)$ on the right-hand side denotes the external load distribution, which may be due to irregular waves, landing and take-off of airplanes, or huge-mass impact onto the structure.

The boundary conditions along the edge of the plate need also to be imposed. In the present case, the bending moment and the equivalent shear force must be zero, which can be written as

$$\frac{\partial^2 w}{\partial n^2} + \nu\frac{\partial^2 w}{\partial s^2} = 0, \quad \frac{\partial^3 w}{\partial n^3} + (2 - \nu)\frac{\partial^3 w}{\partial n \partial s^2} = 0 \tag{5}$$

where n and s denote the normal and tangential directions, respectively, and ν is Poisson's ratio.

In addition, a concentrated force stemming from replacement of the torsional moment with an equivalent shear force must be also zero at four corners of a rectangular plate.

3. BOUNDARY INTEGRAL EQUATION

Let us introduce the time-domain Green function, $G(x - \xi, y - \eta, z, t - \tau)$, which satisfies the followings:

$$\nabla_{3D}^2 G = 0 \qquad \text{for } z \geq 0 \tag{6}$$

$$\frac{\partial G}{\partial z} - \frac{\partial^2 G}{\partial t^2} = \delta(x - \xi)\delta(y - \eta)\delta(t - \tau) \qquad \text{on } z = 0 \tag{7}$$

$$\frac{\partial G}{\partial z} = 0 \qquad \text{on } z = h \tag{8}$$

$$G = \frac{\partial G}{\partial t} = 0 \qquad \text{at } t = \tau + 0_- \tag{9}$$

The explicit form of this function may be obtained using the Fourier transform in x and y and the Laplace transform in t. The result can be found in Wehausen [12] as follows:

$$G(x, y, z, t) = -\frac{1}{2\pi} u(t) \int_0^\infty \sqrt{k \tanh kh} \times \sin(\sqrt{k \tanh kh}\, t) \frac{\cosh k(z - h)}{\sinh kh} J_0(kR)\, dk \tag{10}$$

where $u(t)$ denotes the unit step function, and $J_0(kR)$ the first kind of Bessel function of zero-th order with $R = \sqrt{x^2 + y^2}$.

In the case of infinite water depth ($h \to \infty$), an efficient method for evaluating (10) was developed by Liapis [10] and King [11]. For the special case of $z = 0$ and $h \to \infty$, the Green function can be computed in terms of Bessel functions of fractional order (see [12]), in the form

$$G(x,y,t) = \frac{\pi}{2\sqrt{2}} \frac{\beta^3}{R\sqrt{R}} \times \left\{ J_{\frac{1}{4}}\left(\frac{\beta^2}{2}\right) J_{-\frac{1}{4}}\left(\frac{\beta^2}{2}\right) + J_{\frac{3}{4}}\left(\frac{\beta^2}{2}\right) J_{-\frac{3}{4}}\left(\frac{\beta^2}{2}\right) \right\} \quad (11)$$

where $\beta^2 = t^2/4R$.

Applying Green's second identity to ϕ and G and integrating with respect to τ from 0_- to t_+, we obtain

$$\int_{0_-}^{t} d\tau \iint_{S_F} \left\{ \phi \frac{\partial G}{\partial n} - \frac{\partial \phi}{\partial n} G \right\} d\xi d\eta = 0 \quad (12)$$

where S_F denotes the plane of $z = 0$, which can be reduced to the area of the structure (S_H) because the integral on the water surface becomes eventually zero.

We substitute (2) and (7) into (12) and perform partial integrations with respect to τ with initial conditions taken into account. This procedure gives the following result:

$$\phi(x,y,t) = \int_{0_-}^{t} d\tau \iint_{S_H} \frac{\partial p(\xi,\eta,\tau)}{\partial \tau} G(t-\tau)\, d\xi d\eta \quad (13)$$

where for brevity the spatial arguments of the Green function are not displayed.

Differentiating both sides of (13) with respect to t, substituting the pressure equation given in (1), and considering partial integration once more with initial condition for the pressure, we can obtain the integral equation for the time-dependent pressure in the form

$$p(x,y,t) + \int_{0_-}^{t} d\tau \iint_{S_H} p(\xi,\eta,\tau) \frac{\partial^2 G(t-\tau)}{\partial \tau^2} d\xi d\eta = w(x,y,t) \quad (14)$$

where $w(x,y,0_-) = 0$ has been assumed in the derivation.

In principle, this integral equation can be solved by coupling with the differential equation for the deflection of a structure given by (4). However, this "direct" solution method may be time-consuming for general time-dependent problems.

4. MODE EXPANSION METHOD

As in the analysis in the frequency domain (see [1]), we can decouple (4) and (14) by expressing the structural deflection in the form

$$w(x,y,t) = \sum_{j=1}^{\infty} X_j(t) w_j(x,y) \quad (15)$$

$$= \sum_{m=0}^{\infty} \sum_{n=0}^{\infty} X_{mn}(t) u_m(x) v_n(y) \quad (16)$$

where $w_j(x,y)$ includes modal functions of not only rigid-body motions but also generalized modes to represent elastic deformations.

$u_m(x)$ and $v_n(y)$ in (16) are the natural modes for the bending of a uniform beam with free ends. Specifically, $u_m(x)$ can be written as (see [8])

$$u_0(x) = \frac{1}{2}$$
$$u_{2m}(x) = \frac{1}{2}\left[\frac{\cos \kappa_{2m} x}{\cos \kappa_{2m}} + \frac{\cosh \kappa_{2m} x}{\cosh \kappa_{2m}}\right] \quad (17)$$

$$u_1(x) = \frac{\sqrt{3}}{2} x$$
$$u_{2m+1}(x) = \frac{1}{2}\left[\frac{\sin \kappa_{2m+1} x}{\sin \kappa_{2m+1}} + \frac{\sinh \kappa_{2m+1} x}{\sinh \kappa_{2m+1}}\right] \quad (18)$$

where the factors κ_m denote the positive real roots of the equation

$$(-1)^m \tan \kappa_m + \tanh \kappa_m = 0 \quad (19)$$

These functions are orthogonal and thus the following relation holds:

$$\iint_{S_H} w_i(x,y)\, w_j(x,y)\, dxdy = \frac{b}{4} \delta_{ij} \quad (20)$$

where $b = B/L$ and δ_{ij} is Kroenecker's delta, equal to 1 when $i = j$ and zero otherwise.

From (15) and (16), $w_j(x,y) = u_m(x)\, v_n(y)$. Thus, depending on the combination of odd and even numbers of m and n, the modal functions can be categorized into the following four types:

1) $w_j(x,y) = u_{2m+1}(x) v_{2n}(y)$, which is odd in x and even in y, and is referred to as FX type.

2) $w_j(x,y) = u_{2m}(x) v_{2n+1}(y)$, which is even in x and odd in y, and is referred to as FY type.

3) $w_j(x,y) = u_{2m}(x) v_{2n}(y)$, which is even in both x and y, and is referred to as FZ type.

4) $w_j(x,y) = u_{2m+1}(x) v_{2n+1}(y)$, which is odd in both x and y, and is referred to as FN type.

To avoid complexity, let us consider only the j-th mode in (15) for the moment.

Considering the case of $X_j(-\infty) = 0$, the relation

$$X_j(t) = \int_{-\infty}^{\infty} X_j'(\tau)\, u(t-\tau)\, d\tau \tag{21}$$

holds in general. Therefore we can write

$$X_j(t)\, w_j(x,y) = \int_{-\infty}^{\infty} X_j'(\tau)\Big\{ u(t-\tau) w_j(x,y)\Big\}\, d\tau \tag{22}$$

This implies that, if we can obtain the response (the pressure and the resulting hydrodynamic force) to the step-wise deflection given by $u(t)w_j(x,y)$, we can compute the response to arbitrary time-varying input by means of the convolution integral.

In this step-wise deflection problem, the body boundary condition for the velocity potential is given from (1) as

$$\frac{\partial \phi_j}{\partial z} = \delta(t)\, w_j(x,y) \tag{23}$$

where $\delta(t) = du(t)/dt$ is Dirac's delta function.

The velocity potential for this problem can be constructed in the form

$$\phi_j(x,y,t) = \delta(t)\, \psi_j(x,y) + \varphi_j(x,y,t) \tag{24}$$

Here $\psi_j(x,y)$ is the velocity potential at infinite frequency, satisfying the boundary conditions:

$$\left.\begin{aligned} \frac{\partial \psi_j}{\partial z} &= w_j(x,y) \quad \text{on } z=0,\ |x|<1 \\ \psi_j &= 0 \qquad\quad \text{on } z=0,\ |x|>1 \end{aligned}\right\} \tag{25}$$

The remaining part in (24) represents the fluid motion subsequent to the initial impulse and is related to the so-called memory part.

The pressure in the present case can be expressed as

$$\begin{aligned} p_j^S(x,y,t) = &-\delta'(t)\, \psi_j(x,y) \\ &+ p_j(x,y,t) + u(t)\, w_j(x,y) \end{aligned} \tag{26}$$

where the second term is given from $\varphi_j(x,y,t)$, i.e. $p_j(x,y,t) = -\partial \varphi_j(x,y,t)/\partial t$, and the third term is the hydrostatic pressure due to the step-wise deflection.

The integral equations for $\varphi_j(x,y,t)$ and equivalently for $p_j(x,y,t)$ may be obtained by substituting (24) and (26) into (13) and (14), respectively. Taking only the terms irrespective of $\delta(t)$ function, we obtain from (13) the following equation:

$$\begin{aligned} \varphi_j(x,y,t) = &\int_{0_-}^{t} d\tau \iint_{S_H} \frac{\partial p_j(\xi,\eta,\tau)}{\partial \tau} G(t-\tau)\, d\xi\eta \\ &+ \iint_{S_H} w_j(\xi,\eta)\, G(t)\, d\xi d\eta \\ &- \iint_{S_H} \psi_j(\xi,\eta) \frac{\partial^2 G(t)}{\partial t^2}\, d\xi d\eta \end{aligned} \tag{27}$$

Differentiating this with respect to t and using the relation $p_j = -\partial \varphi/\partial t$, it follows that

$$\begin{aligned} p_j(x,y,t) + &\int_{0_-}^{t} d\tau \iint_{S_H} p_j(\xi,\eta,\tau) \frac{\partial^2 G(t-\tau)}{\partial \tau^2}\, d\xi d\eta \\ &= -\iint_{S_H} w_j(\xi,\eta) \frac{\partial G(t)}{\partial t}\, d\xi d\eta \\ &\quad + \iint_{S_H} \psi_j(\xi,\eta) \frac{\partial^3 G(t)}{\partial t^3}\, d\xi d\eta \end{aligned} \tag{28}$$

These equations may be regarded as the integral equations for the memory part, in terms of the time-domain Green function.

Once the pressure expressed by (26) is determined, the pressure force acting in the i-th direction can be computed as

$$\begin{aligned} F_{ij}(t) &= -\iint_{S_H} p_j^S(x,y,t)\, w_i(x,y)\, dxdy \\ &= -\delta'(t) A_{ij}(\infty) - u(t)\, C_{ij} - K_{ij}(t) \end{aligned} \tag{29}$$

where

$$A_{ij}(\infty) = -\iint_{S_H} \psi_j(x,y)\, w_i(x,y)\, dxdy \tag{30}$$

$$C_{ij} = \iint_{S_H} w_j(x,y)\, w_i(x,y)\, dxdy = \frac{b}{4}\, \delta_{ij} \tag{31}$$

$$K_{ij}(t) = \iint_{S_H} p_j(x,y,t)\, w_i(x,y)\, dxdy \tag{32}$$

Note that $A_{ij}(\infty)$ is the added mass at infinite frequency and C_{ij} is the restoring force coefficient extended to the generalized elastic modes.

Since $F_{ij}(t)$ given by (29) is the force in response to the step-wise deflection, the general force due to arbitrary time-varying deflection can be obtained from (22) and written as

$$\begin{aligned} F_i(t) &= \int_{-\infty}^{t} X_j'(\tau)\, F_{ij}(t-\tau)\, d\tau \\ &= -X_j''(t)\, A_{ij}(\infty) - X_j(t)\, C_{ij} \\ &\quad - \int_{-\infty}^{t} X_j'(\tau)\, K_{ij}(t-\tau)\, d\tau \end{aligned} \tag{33}$$

Here $K_{ij}(t)$ can be understood as the memory-effect function, which is related to the time-dependent added-mass and damping coefficients.

Having completed the hydrodynamic and hydrostatic forces, let us consider next the motion equation given by (4). To get a linear system of simultaneous differential equations for all modes of elastic deflection, we substitute (15) into (4), multiply both sides of the equation by $w_i(x,y)$, and integrate the resultant equation over the bottom of the structure. Writing only the j-th mode, the result of this transformation takes the form

$$\Big\{ M_{ij}+A_{ij}(\infty)\Big\}X_j''(t) + \{ C_{ij} + D\, S_{ij}\}\, X_j(t) + \int_{-\infty}^{t} X_j'(\tau)\, K_{ij}(t-\tau)\, d\tau = E_i(t) \qquad (34)$$

where

$$M_{ij} = \iint_{S_H} m(x,y) w_i(x,y) w_j(x,y)\, dxdy \qquad (35)$$

$$S_{ij} = \iint_{S_H} \nabla^2 w_i(x,y)\, \nabla^2 w_j(x,y)\, dxdy + (1-\nu)\int_{-1}^{1} \Big[\frac{\partial w_i}{\partial x}\frac{\partial^2 w_j}{\partial x \partial y} - \frac{\partial w_i}{\partial y}\frac{\partial^2 w_j}{\partial x^2} \Big]_{-b}^{b} dx + (1-\nu)\int_{-b}^{b} \Big[\frac{\partial w_i}{\partial y}\frac{\partial^2 w_j}{\partial x \partial y} - \frac{\partial w_i}{\partial x}\frac{\partial^2 w_j}{\partial y^2} \Big]_{-1}^{1} dy \qquad (36)$$

$$E_i(t) = -\iint_{S_H} p_E(x,y,t)\, w_i(x,y)\, dxdy \qquad (37)$$

Here (33) has been substituted as the pressure force term in obtaining (34), and the free-edge boundary conditions (5) have been taken into account in obtaining the stiffness matrix S_{ij}.

If the distribution of external load, $p_E(x,y,t)$, is given, (34) can be solved in the time domain with appropriate initial conditions.

5. RELATIONS WITH FREQUENCY DOMAIN ANALYSIS

To derive relations with the added-mass and damping coefficients in the frequency-domain analysis, let us consider a harmonic motion with frequency ω, say $X_j(t) = \overline{X}_j \cos\omega t$.

Substituting this into (33), we obtain

$$F_i(t) = -X_j''(t)\Big\{ A_{ij}(\infty) - \frac{1}{\omega}\int_0^{\infty} K_{ij}(\tau)\sin\omega\tau\, d\tau \Big\} - X_j'(t)\int_0^{\infty} K_{ij}(\tau)\cos\omega\tau\, d\tau - X_j(t)\, C_{ij} \qquad (38)$$

By comparison with the corresponding result in the frequency domain, the following relations can be found:

$$\omega\Big\{ A_{ij}(\omega) - A_{ij}(\infty)\Big\} = -\int_0^{\infty} K_{ij}(t)\sin\omega t\, dt \qquad (39)$$

$$B_{ij}(\omega) = \int_0^{\infty} K_{ij}(t)\cos\omega t\, dt \qquad (40)$$

Next, let us consider the inverse relations by the frequency-domain analysis using the Fourier transform.

Suppose that $X(\omega) = \mathcal{F}\{\, x(t)\,\}$ is the Fourier transform of an arbitrary deflection $x(t)$ and $H_{ij}(\omega) = \mathcal{F}\{\, h_{ij}(t)\,\}$ is the Fourier transform of the pressure force acting in the i-th direction due to harmonic motion of the j-th mode. Then the linear analysis using the Fourier transform gives the relation

$$F_{ij}(t) = \frac{1}{2\pi}\int_{-\infty}^{\infty} X(\omega)\, H_{ij}(\omega)\, e^{i\omega t}\, d\omega \qquad (41)$$

where

$$H_{ij}(\omega) = \omega^2 A_{ij}(\omega) - C_{ij} - i\omega\, B_{ij}(\omega) \equiv H_{ij}^{C}(\omega) + iH_{ij}^{S}(\omega) \qquad (42)$$

$H_{ij}^{C}(\omega) = \omega^2 A_{ij}(\omega) - C_{ij}$ denotes the real part, which is even function in ω. Likewise, $H_{ij}^{S}(\omega) = -\omega B_{ij}(\omega)$ is the imaginary part, which is odd with respect to ω, because $B_{ij}(\omega)$ itself is considered as the even function.

For the unit step deflection,

$$X(\omega) = \mathcal{F}\{\, u(t)\,\} = \pi\delta(\omega) + \frac{1}{i\omega}. \qquad (43)$$

Thus, substitution of this into (41) gives the following:

$$F_{ij}(t) = \frac{1}{2}H_{ij}(0) + \frac{1}{\pi}\int_0^{\infty}\frac{1}{\omega}\Big\{ H_{ij}^{C}(\omega)\sin\omega t + H_{ij}^{S}(\omega)\cos\omega t \Big\}\, d\omega \qquad (44)$$

Utilizing the relation of $H_{ij}(0) = -C_{ij}$ and

$$\frac{1}{\pi}\int_0^{\infty}\frac{\sin\omega t}{\omega}\, d\omega = \frac{1}{2} \quad \text{for } t>0 \qquad (45)$$

$$\frac{1}{\pi}\int_0^{\infty}\omega\sin\omega t\, d\omega = -\delta'(t), \qquad (46)$$

the following expression can be obtained:

$$F_{ij}(t) = -\delta'(t)A_{ij}(\infty) - u(t)\, C_{ij} + \frac{1}{\pi}\int_0^{\infty}\omega\Big\{ A_{ij}(\omega) - A_{ij}(\infty)\Big\}\sin\omega t\, d\omega - \frac{1}{\pi}\int_0^{\infty} B_{ij}(\omega)\cos\omega t\, d\omega \qquad (47)$$

Since this equation must be identical to (29), we can obtain the following expressions:

$$K_{ij}(t) = K_{ij}^{e}(t) + K_{ij}^{o}(t) \qquad (48)$$

where

$$K^e_{ij}(t) = \frac{1}{\pi}\int_0^\infty B_{ij}(\omega)\cos\omega t\, d\omega \tag{49}$$

$$K^o_{ij}(t) = -\frac{1}{\pi}\int_0^\infty \omega\Big\{A_{ij}(\omega) - A_{ij}(\infty)\Big\}\sin\omega t\, d\omega \tag{50}$$

Note that $K^e_{ij}(t)$ is the even function and $K^o_{ij}(t)$ is the odd function with respect to t.

The memory-effect function $K_{ij}(t)$ is causal, i.e. $K_{ij}(t) = 0$ for $t < 0$. Hence for $t > 0$ it follows that $K_{ij}(t) = 2K^e_{ij}(t) = 2K^o_{ij}(t)$. This causality relation gives the desired result in the form

$$\begin{aligned} K_{ij}(t) &= -\frac{2}{\pi}\int_0^\infty \omega\Big\{A_{ij}(\omega) - A_{ij}(\infty)\Big\}\sin\omega t\, d\omega \\ &= \frac{2}{\pi}\int_0^\infty B_{ij}(\omega)\cos\omega t\, d\omega \end{aligned} \tag{51}$$

It should be noted that these are inverse relations of (39) and (40) and either the added mass or the damping coefficient in the frequency domain can give the memory-effect function $K_{ij}(t)$. These are in fact well-established relations in ship hydrodynamics (see [13]).

5. RESULTS AND DISCUSSION

The original intention of this paper was to show numerical results of the memory-effect function, $K_{ij}(t)$, by the direct computation using the time-domain Green-function method. However, in spite of several efforts to solve the integral equation (28), accurate and reasonable results could not be obtained. Presumably the integration with respect to time was not adequate in the computer program for stable computations, because the Green function is highly oscillatory near the free surface. There may still be worth a try for improvement. However, at present, considering the necessary computation time and relative accuracy, the use of (51) looks more effective.

One big problem in (51) is how we estimate the values of $B_{ij}(\omega)$ at high frequencies. The present author [8] developed the so-called B-spline Galerkin scheme for computing hydrodynamic forces on a shallow-draft VLFS in the frequency domain. Although this scheme is fast and accurate, it is still difficult to compute $B_{ij}(\omega)$ up to very high frequencies where the computed values are negligible in the integration of (51).

One example of computed results is shown in Fig. 1, which is for $L/B = 5$ in infinite water depth ($h \to \infty$). The modal shapes considered are the lowest one in (15) and (16), that is, $w_j = u_1 v_0 =$

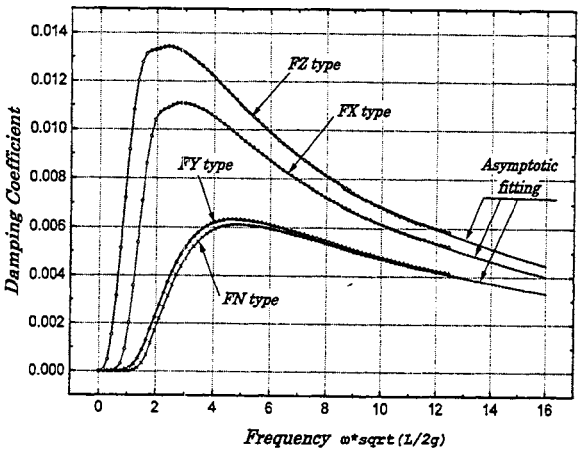

Fig. 1 Damping coefficients obtained by the frequency-domain analysis for $L/B = 5$ in infinite water depth.

$\sqrt{3}x/4$ for FX type, $u_0 v_1 = \sqrt{3}y/4$ for FY type, $u_0 v_0 = 1/4$ for FZ type, and $u_1 v_1 = 3xy/4$ for FN type. The results in Fig. 1 are only for the case of $i = j$, and the highest frequency in the computation corresponds to $L/\lambda = 50$ (where L/λ is equal to ω^2/π).

$B_{ij}(\omega)$ for higher frequencies is approximated by

$$B_{ij}(\omega) = \alpha\, e^{-\beta\omega} \tag{52}$$

where α and β are determined by the least-square method using iterations. The results of fitting using (52) are also shown in Fig. 1.

Numerical integration of (51) is performed by substituting (52) and the result is expressed as

$$\begin{aligned} K_{ij}(t) =& \frac{2}{\pi}\int_0^{\omega_0} B_{ij}(\omega)\cos\omega t\, d\omega \\ &+ \frac{2}{\pi}\frac{\alpha\, e^{-\beta\omega_0}}{\beta^2 + t^2}\Big\{\beta\cos\omega_0 t - t\sin\omega_0 t\Big\} \end{aligned} \tag{53}$$

Here ω_0 is the truncation frequency, and the first term on the right-hand side was numerically evaluated with a Filon-type quadrature.

Figure 2 shows the results of (53). It should be noted that the contributions from the first and second terms on the right-hand side of (53) are more or less the same in order, and thus the details of $K_{ij}(t)$ may be changed depending on the accuracy of the approximation by (52).

At any rate, we can see from Fig. 2 that the memory effect persists only for short duration of time, particularly for the FY and FN types of the mode.

For large values of t, as shown in Newman [9], the memory-effect function is related to the low-

frequency asymptotic behavior of the damping coefficient. The energy-conservation principle gives the following formula (see [8]):

$$B_{jj}(\omega) = \frac{1}{4\pi}\omega^3 \int_0^{2\pi} |H_j(K,\theta)|^2 \, d\theta \qquad (54)$$

where

$$H_j(K,\theta) = \iint_{S_H} p_j(x,y)\, e^{iK(x\cos\theta + y\sin\theta)}\, dxdy \qquad (55)$$

and $K = \omega^2$.

In low frequencies, $p_j(x,y) \sim w_j(x,y) + O(K)$, and hence the leading term of the Kochin function in ω is of the form

$$H_j(K,\theta) \sim b\,\delta_{j0} + O(K) \qquad (56)$$

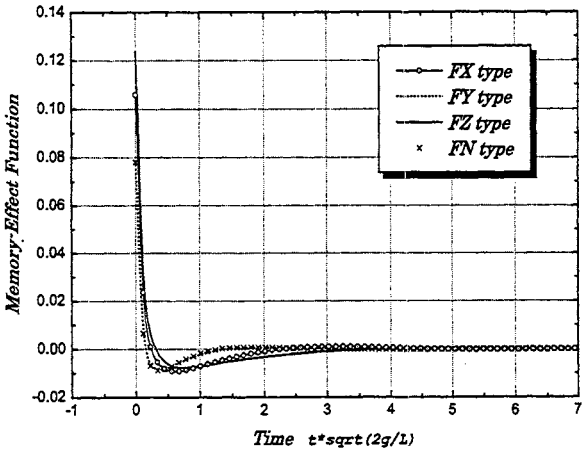

Fig. 2 Memory-effect functions computed using the damping coefficient and analytical fitting ($L/B = 5$ in infinite water depth).

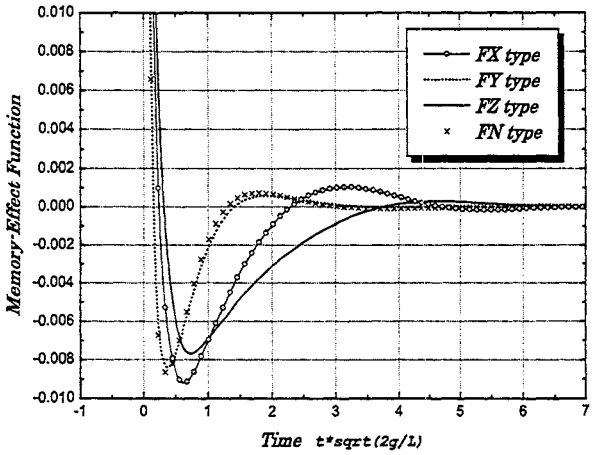

Fig. 3 Memory-effect functions, maginified from Fig. 2 in the ordinate.

for the FZ type. The leading terms in other types are of order of $O(K)$.

Substituting (56) into (54) and then evaluating the integral of (51), we have an asymptotic approximation of the form

$$K_{ij}(t) \sim \frac{2}{\pi}\frac{b^2}{2}\int_0^{\infty} \omega^3 \cos\omega t \, d\omega = \frac{b^2}{\pi}\frac{6}{t^4} \qquad \text{as } t \to \infty \qquad (57)$$

This result seems to be supported approximately by the numerical results shown by Fig. 3 (which is magnified from Fig. 2 to see the details).

According to (39), the added mass can be computed from the memory-effect function. Computed results by (39) are shown in Fig. 4 and compared with corresponding values from the frequency-domain solution. Although slight differences exist in the low frequency region for the FZ type, the overall agreement is acceptable.

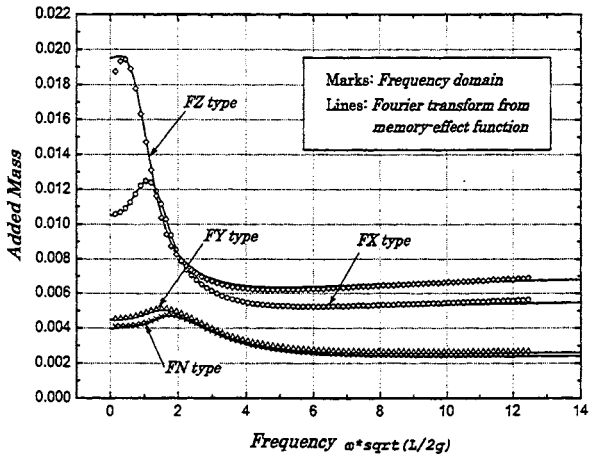

Fig. 4 Added mass computed from the memory-effect function using the Fourier transform ($L/B = 5$ in infinite water depth).

6. CONCLUDING REMARKS

In this paper, the time-domain direct computation method has been studied to use for calculating the memory-effect function. Based on the integral equation (28) (or equivalently (27) for the velocity potential), the computer code has been developed. However, up to now, reasonable results are not obtained, probably because of highly oscillatory nature of the Green function. There still exists a possibility of some bugs in the computer code.

However, considering the necessary computation time and numerical complication to solve the time-domain integral equation, the use of inverse

Fourier transform looks more practical. That is, the memory-effect function for a shallow-draft VLFS had better be computed from the damping coefficient in the frequency-domain solution. Even in that case, the damping coefficient must be computed up to higher frequencies where the asymptotic fitting can be done with reasonable accuracy.

Since most efforts have been consumed to evaluate the memory-effect function, numerical examples of transient hydroelastic phenomena of VLFS could not be demonstrated in this paper. Those are left in another opportunity.

Acknowledgment: This work is supported partly by the Grant-in-Aid for Scientific Research of the Ministry of Education, Science and Culture.

REFERENCES

[1] Kashiwagi, M., "Research on Hydroelastic Responses of VLFS: Recent Progress and Future Work", *Proc. of 9th Int. Offshore and Polar Eng. Conf.*, Brest, Vol. 1, pp. 17–26, 1999.

[2] Korobkin, A., "Unsteady Hydroelasticity of Floating Plates", *Proc. of 2nd Int. Conf. on Hydroelasticity in Marine Tech.*, Fukuoka, pp. 109–117, 1998.

[3] Watanabe, E. and Utsunomiya, T., "Transient Response Analysis of a VLFS at Airplane Landing", *Proc. of Int. Workshop on Very Large Floating Structures*, Hayama, pp. 243–247, 1996.

[4] Kim, J.W. and Webster, W.C., "The Drag of an Airplane Taking Off from a Floating Runway", *Proc. of Int. Workshop on Very Large Floating Structures*, Hayama, pp. 235–241, 1996.

[5] Yeung, R.W. and Kim, J.W., "Structural Drag and Deformation of a Moving Load on a Floating Plate", *Proc. of 2nd Int. Conf. on Hydroelasticity in Marine Tech.*, Fukuoka, pp. 77–88, 1998.

[6] Endo, H., Yago, K. and Chiaki, S., "Elastic Responses of a Floating Platform Stimulated by Dynamic Load", *Proc. of 14th Ocean Engineering Symp.*, Soc. of Nav. Archit. Japan, pp. 411–416, 1998 (in Japanese).

[7] Ohmatsu, S., "Numerical Calculation of Hydroelastic Behavior of VLFS in Time Domain", *Proc. of 2nd Int. Conf. on Hydroelasticity in Marine Tech.*, Fukuoka, pp. 89–97, 1998.

[8] Kashiwagi, M., "A B-Spline Galerkin Scheme for Calculating the Hydroelastic Response of a Very Large Floating Structure in Waves", *J. Marine Sci. and Tech.*, Vol. 3, pp. 37–49, 1998.

[9] Newman, J.N., "Transient Axisymmetric Motion of a Floating Cylinder", *J. Fluid Mech.*, Vol. 157, pp. 17–33, 1985.

[10] Liapis, S.J., *Time-Domain Analysis of Ship Motions*, Ph.D. Thesis, The Univ. of Michigan, 1986.

[11] King, B.K., *Time-Domain Analysis of Wave Exciting Forces on Ships and Bodies*, Ph.D. Thesis, The Univ. of Michigan, 1987.

[12] Wehausen, J.V. and Laitone, E.V., *Surface Waves*, Handbuch der Physik, Vol. 9, pp. 607–609, Springer-Verlag, 1960.

[13] Ogilvie, T.F., "Recent Progress Toward the Understanding and Prediction of Ship Motions", *Proc. of 5th ONR Symp. on Naval Hydrodynamics*, Bergen, pp. 3-128, 1964.

PROCEEDINGS OF THE THIRD INTERNATIONAL WORKSHOP ON VERY LARGE FLOATING STRUCTURES
(VLFS '99), VOL. I, EDS. R.C. ERTEKIN & J.W. KIM, 22-24 SEPTEMBER 1999, HONOLULU, HAWAII, USA

Linear Frequency Domain Hydroelastic Analysis for McDermott's Mobile Offshore Base Using WAMIT

D. Kim, L. Chen, Z. Blaszkowski
J.Ray McDermott Engineering, LLC*

ABSTRACT

Motions and connector forces were calculated for the McDermott's MOB with rigid hinge connectors. The generalized mode feature in WAMIT was used to compute both motions and connector loads in regular and irregular waves. Using rigid hinge and flexible structural modes, WAMIT calculates motions and connector forces including effects of the multiple interacting bodies and structural deformations of the MOB. The effect of structural deformation of the MOB was studied by defining three structural modes (one bending and two torsional) calculated from the finite element analysis. Illustrative computations are presented for both rigid and flexible module MOB with rigid hinge connector.

1. INTRODUCTION

A Mobile Offshore Base (MOB) is a large floating platform that provides a forward-deployable logistics facility for military hardware and personnel. Capable of handling conventional fixed wing aircraft, the MOB will nominally be 1500m (5000ft) long. McDermott's MOB concept consists of self-propelled semi-submersible modules connected near the deck level by rigid and compliant connectors.

Due to its unprecedented size, the MOB poses serious engineering challenges when compared to conventional floating structures. Of the key design consideration for such a huge floating structure are the connector loads and the motions. Since each of the modules is larger than either a typical aircraft carrier or the largest offshore platform, connecting these modules together to form a long runway in waves becomes quite a challenging design task. One of the primary concerns to a design engineer is how to come up with connectors that can be practically constructed using the state-of-the-art technology and yet have a reasonable constraint on relative motions between adjacent modules that will meet the operational criteria of various functional requirements.

To design inter-module connectors that can meet the above requirements, one must first obtain an accurate assessment of the motions and loads experienced by connectors in realistic seas. For most conventional floating structures, this assessment can be accomplished satisfactorily with the currently available state-of-the-art hydrodynamic computer tools and a rigid body dynamic approach. This traditional approach treats a floating structure by considering only its hydrodynamic response in waves, while neglecting any structural deformation due to the hydrodynamic loads. In a traditional integrated hydrodynamic-structural analysis, an engineer is interested in structural loads and stresses in a given seastate, and completes this task in two separate steps. He would first calculate the hydrodynamic loads acting on a floating structure using a hydrodynamic program. He would then use the hydrodynamic loads as external loads and perform a structural analysis (normally using a finite element analysis tool) to obtain a detailed stress distribution on the structure. This traditional approach is normally satisfactory since for most of the floating structures built so far, the coupling between hydrodynamics and structural dynamics is negligible. This however may not always be the case with a huge structure such as a MOB.

The long size of a MOB makes its structure relatively flexible and therefore prone to wave excitation at relatively low frequencies where wave energy is concentrated. To accurately predict the loads and the motions of a MOB in a realistic sea environment, one may sometimes have to consider structural flexibility.

There are a few different ways to account for the effects of structural flexibility in a dynamic analysis. In an earlier study by McDermott engineers (Ref. [1]), a simplified approach was taken to obtain some quick results in the preliminary stage of connector design. In that approach, a frequency domain hydrodynamic computer program WAMIT, developed by the Massachusettes Institute of Technology, was used to obtain hydrodynamic coefficients used in a coupled system of equations for motions and connector loads of

* 801 North Eldridge St. Houston, TX 77079, USA

the connected multi-body system. Structural flexibility was calculated from a detailed finite element analysis (FEA) program. The calculated structural flexibility was then lumped to a connector location by matching the natural vibration periods (or frequencies) of a simplified stick beam lumped mass model with those of the detailed FEA model. This approach is schematically shown in Figure 1.

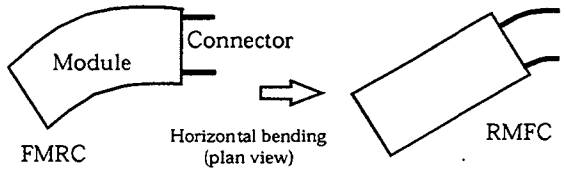

Figure 1: Simplified RMFC model(NBODY approach)

This simplified approach, which we will call "rigid module flexible connector" (RMFC) approach or RMFC model (the terminology, rigid or flexible connector, adopted in this study means hinged connector, which allows free pitch motion), still treats individual modules as completely rigid while modeling the connectors as springs of finite stiffness. Since it is only an approximation to the true hydroelastic phenomenon, we will also call it NBODY approach (for multiple N bodies, as adopted in WAMIT) to differentiate it from a more refined hydroelastic analysis to be described below.

In reality, however, each module of the connected MOB may be much softer than the connectors. Therefore, the true model of the MOB is believed to be closer to "flexible module rigid connector" (FMRC) than to RMFC. To a designer, a natural question is how accurate our RMFC model is and how important the hydroelastic amplitification will be.

In the simplified analysis performed by McDermott engineers using the RMFC model (Ref. [1]), dynamic amplification was found to be quite significant. In fact, the connector loads at some intermediate equivalent connector stiffness (the combined stiffness of the connectors and the modules) were found to be several times that of the infinitely rigid counterpart. Therefore, a more detailed study of the hydroelastic behavior of the MOB is necessary to answer some key questions concerning our load estimate. The analysis procedure may be applied to other MOB concepts, which may have significant hydroelastic amplification.

2. METHODOLOGY

In the current study, a more refined approach was used. This approach uses the generalized mode feature of the hydrodynamic computer program WAMIT that was used before in the simplified RMFC approach. The same McDermott's MOB design as was analyzed before by way of the RMFC approach was considered in a flexible module rigid connector (FMRC) approach.

In the terminology of the generalized modes, rigid body motions as well as flexible body motions and even structural loading can be considered as the so-called generalized modes. By extending the definition of the modes of motion beyond the simple translations and rotations in the three orthogonal directions, one can study effects such as the coupling due to a rigid hinge or local deformation due to structural flexibility. It is important to note that the generalized mode feature offered by WAMIT (Version 5.4PC) is based on a true hydroelastic formulation. That means that the additional modes beyond the traditional are solved from the radiation boundary conditions instead of through post-processing of the coupled system of equations.

For a huge floating structure such as a MOB, the original need for a hydroelastic analysis is based on a concern that structural deformation may not always be small and may play a significant role in motions and connector loads. A detailed description of the generalized mode formulation can be found in Ref. [2].

The hydroelastic analysis was performed for McDermott's Mobile Offshore Base (MOB) which was designed in the preliminary design phase. The principal characteristics of a single unit are detailed in Table 1.

Configuration P1-B			
Upper Hull		Operating Draft	39.0 m
Length	280.0 m	Displacement	337000 mt
Breath	150.0 m	LCG	0
Depth	24.6 m	TCG	0
Lower Hulls		VCG	26.87 m
Length	260.0 m	A_{wp}	3452 m^2
Breadth	38.0 m	VCB	13.1 m
Depth	16.0 m	KM_T	40.1 m
Transverse Spacing	100.0 m	KM_L	66.0 m
Columns		R_x	55.8 m
Length	21.0 m	R_y	93.2 m
Breadth	21.0 m	R_z	97.1 m
Longitudinal Spacing	63.0 m	Hinge Connector Outboard from CL	50.0 m
Transverse Spacing	100.0 m	Hinge Connector Above Baseline	60.0 m
Notes: Radii of gyration based on uniform mass distribution in a LxBxD=300x152x75.6m box with the above VCG. LCG is measured from amidships; TCG is from centerplane; VCG and VCB from baseline.			

Table 1: Principal dimension of the McDermott's MOB

Since the hydroelastic analysis for a MOB using WAMIT requires both hydrodynamic and structural model, it is necessary to perform structural modal analysis to get MOB deflections. In preliminary design

phase, McDermott engineers performed a finite element analysis (FEA) using a structural FEA program developed by ANSYS, Inc. This FEA model employed simple box type geometry to simplify modal analysis and it has different characteristic compared to the hydrodynamic model, which was generated later. However the principal parameters of the FEA model are very similar to those of the hydrodynamic model. With a three-dimensional interpolation, the result from FEA modal analysis can be mapped to derive deflections for the hydrodynamic model. The interpolated deflections for the hydrodynamic model can then be used to calculate the mass matrix or hydrostatic restoring coefficient in WAMIT.

2.1 FEA model

The purpose of the modal analysis is to determine the natural frequencies and mode shapes of a MOB. The natural frequencies and mode shapes are important parameters in the design of a structure for dynamic loading conditions. Only linear behavior of the model was analyzed.

To get proper mass and stiffness distributions a five-module connected MOB was modeled. This coarse 3-D FEA model consists of 6807 nodal points, and 13604 finite elements. The FEA model reflected all major structural components of the MOB including decks, bulkheads, side shells, bottom plates, columns and braces. The material density was adjusted to simulate the total mass of the units. The natural periods were calculated as "in the air" (no added mass or damping was considered). The connector mass was taken into consideration by increasing mass density of the elements used for connector modeling.

Attempt was made to come up with stiffness and mass distribution as realistic as practical at this stage of the MOB design. With this size of the FEA model, the reduced Householder method was used to calculate the solution.

Three basic mode shapes from ANSYS modal analysis, one transverse bending (T_n=6.45 sec) and two torsional (T_n=5.4, 2.5 sec) modes were selected for the hydroelastic analysis. These three dry modes are presented in Figures 2 through 4, respectively.

2.2 Hydrodynamic model

A hydrodynamic analysis was performed using the model constructed in the preliminary design phase. The model has 1120 panels for each unit and a total of 5600 panels (Figure 5). Considering the size of a typical MOB, the number of elements of the hydrodynamic model selected here is relatively small. However it was found that this model was adequate to have good results from intensive numerical tests in the preliminary design phase. Figures 6 through 8 show structural deflection for the hydrodynamic model after three-dimensional mapping from the FEA model.

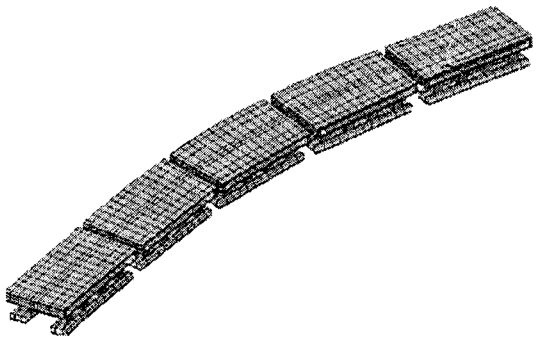

Figure 2: First transverse bending mode (T_n=6.45 sec)

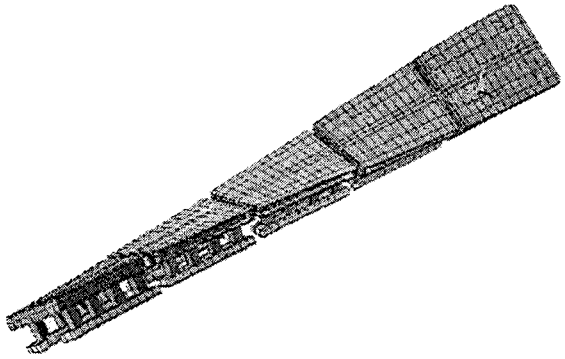

Figure 3: First torsional mode (T_n=5.4 sec)

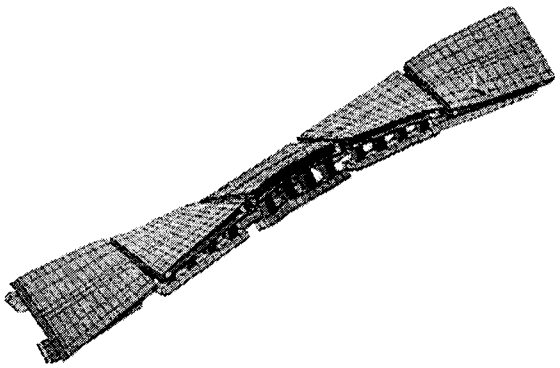

Figure 4: Second torsioinal mode (T_n=2.5 sec)

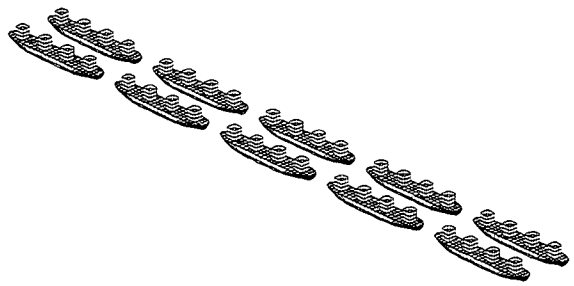

Figure 5: Hydrodynamic model of McDermott's MOB

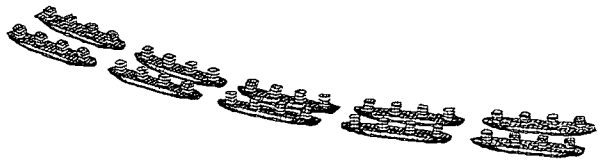

Figure 6: First bending mode for the hydrodynamic model after mapping

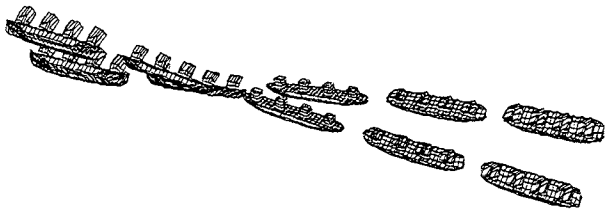

Figure 7: First torsional mode for the hydrodynamic model after mapping

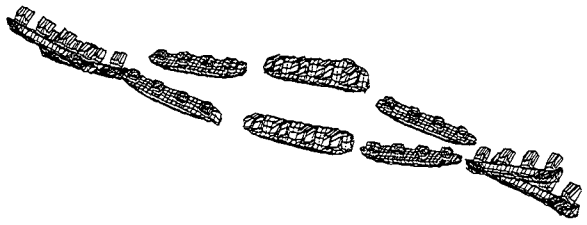

Figure 8: Second torsional mode for the hydrodynamic model after mapping

2.3 Definition of generalized mode

In order to study the hydroelastic behavior for the MOB using WAMIT it is necessary to define generalized modes that represent hinge motions, connector loads and structural deformations. In WAMIT all other modes except the six conventional rigid body modes must be considered as generalized modes and they should be supplied by an external program. Since WAMIT generalized mode approach treats multiple bodies as one global rigid body, the resulting modes of motion of the global body include both rigid modes of the ensemble and discontinuous relative motions between the separated bodies. The resulting motion of each separated body may be defined by a linear superposition of rigid body and hinge motions. In this study 27 generalized modes are defined to describe hinge motions (4 modes), connector loads (20 modes) and structural deformations (3 modes, Figures 6, 7, 8).

A simple rigid hinge connector can be modeled by rotational angle at the center of connector location as defined by Figure 9.

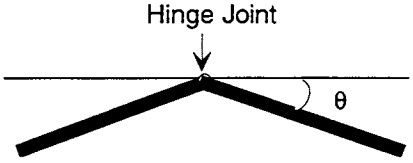

Figure 9: Definition of hinge rotation

With unit rotational angle, the vector shape function can be represented by the following component functions:

$$u = (z-z_c)*sign(x-h),\ v = 0,\ w = -|x-h| \quad (1)$$

where z_c is the vertical distance between the connector and the origin of the global coordinate system (on the free surface) and h is the horizontal hinge location (x-direction) relative to the origin of the local coordinate system. The mode shape functions $\{u, v, w\}$ should be specified for all four hinges and defined relative to the local coordinate system. At each hinge location five fixed modes (surge, sway and heave force, roll and yaw moment) can be defined to describe connector loads. The pitch moment was excluded since it is zero. Table 2, 3 and 4 list mode shape functions defined at each hinge location:

Hinge Mode(Rotation)
$(u_7,v_7,w_7)=((z-z_c)sign(x-h_1),\ 0,\ -\|x-h_1\|)$
$(u_8,v_8,w_8)=((z-z_c)sign(x-h_2),\ 0,\ -\|x-h_2\|)$
$(u_9,v_9,w_9)=((z-z_c)sign(x-h_3),\ 0,\ -\|x-h_3\|)$
$(u_{10},v_{10},w_{10})=((z-z_c)sign(x-h_4),\ 0,\ -\|x-h_4\|)$

Table 2: Four hinge modes

	Hinge #1(h_1>0)	Hinge #2(h_2>0)
F_x	$(u_{11},v_{11},w_{11})=(1,0,0)$	$(u_{14},v_{14},w_{14})=(1,0,0)$
F_y	$(u_{12},v_{12},w_{12})=(0,1,0)$	$(u_{15},v_{15},w_{15})=(0,1,0)$
F_z	$(u_{13},v_{13},w_{13})=(0,0,1)$	$(u_{16},v_{16},w_{16})=(0,0,1)$
	Hinge #3(h_3>0)	Hinge #4(h_4>0)
F_x	$(u_{17},v_{17},w_{17})=(1,0,0)$	$(u_{20},v_{20},w_{20})=(1,0,0)$
F_y	$(u_{18},v_{18},w_{18})=(0,1,0)$	$(u_{21},v_{21},w_{21})=(0,1,0)$
F_z	$(u_{19},v_{19},w_{19})=(0,0,1)$	$(u_{22},v_{22},w_{22})=(0,0,1)$

Table 3: Internal force modes

	M_x
Hinge #1(h_1>0)	$(u_{23},v_{23},w_{23})=(0, -(z-z_c), y)$
Hinge #2(h_2>0)	$(u_{25},v_{25},w_{25})=(0, -(z-z_c), y)$
Hinge #3(h_3>0)	$(u_{27},v_{27},w_{27})=(0, -(z-z_c), y)$
Hinge #4(h_4>0)	$(u_{29},v_{29},w_{29})=(0, -(z-z_c), y)$
	M_z
Hinge #1(h_1>0)	$(u_{24},v_{24},w_{24})=(-y, x-h_1, 0)$
Hinge #2(h_2>0)	$(u_{26},v_{26},w_{26})=(-y, x-h_2, 0)$
Hinge #3(h_3>0)	$(u_{28},v_{28},w_{28})=(-y, x-h_3, 0)$
Hinge #4(h_4>0)	$(u_{30},v_{30},w_{30})=(-y, x-h_4, 0)$

Table 4: Internal moment modes

For three extra structural modes there is no way to define them as explicit functions. In this case structural deformations from FEA model were directly used as mode shapes.

2.4 Generalized matrices

For the generalized mode feature in WAMIT it is also necessary to provide proper mass matrix, hydrostatic stiffness and structural stiffness matrix according to the user-defined generalized modes. The hydrodynamic model used in WAMIT only has the body surface mesh below the free surface. It does not require any geometric data above the free surface and inside the body. The mass property of hydrodynamic model is also defined as a concentrated mass at the center of gravity. Unlike hydrodynamic model the FEA model has super structures and internal structures and it uses simplified geometry like a box. Since ANSYS gives deflections of the body at each nodal point these individual deflections were used directly as mode shape functions for structural modes.

With these discrete mode shape functions and different mesh systems it is very difficult to find out equivalent mass system for the hydrodynamic model. For simplicity, we used hydrodynamic model for mass matrix related to mode 1 to 30. In this case all components of the mass matrix can be calculated for the lumped mass system using the following formula,

$$M_{ij} = \int (u_i u_j + v_i v_j + w_i w_j) dm \qquad (2)$$

where u,v,w are mode shape functions for each mode. For the mass matrix calculation of all components related to modes 31, 32, 33 (eg, $M_{1,31}$, $M_{31,31}$,.....) the FEA model may be used. In this case mode shape functions for all modes are available at the center of each element since ANSYS defines mass property on each element. Once the center point is obtained from four nodal points at each element of FEA model, mode shape functions at each element can be interpolated. The interpolation from n closest point in space can be expressed by

$$f = \frac{[d_2 d_3 .... d_n f_1 + d_1 d_3 .... d_n f_2 + ... d_1 d_2 .... d_{n-1} f_n]}{d_2 d_3 .... d_n + d_1 d_3 .... d_n + ... d_1 d_2 .... d_{n-1}} \qquad (3)$$

d_i = distance from the point of interest to the ith nearest point

f_i=function value at the corresponding point

Then each component of the mass matrices can be calculated from integration of each element over the entire body. This can be expressed by

$$M_{ij} = \int (u_i u_j + v_i v_j + w_i w_j) dm = \sum_m (u_i u_j + v_i v_j + w_i w_j) \cdot \Delta V \cdot \gamma \qquad (4)$$

where m is the total number of elements of the FEA model, ΔV is the volume of the element and γ is the mass density of the element.

The hydrostatic restoring coefficient related to each mode can be calculated from the vertical component of mode shape functions and the area of each element as following.

$$C_{ij} = \rho g \iint n_j (w_i + z D_i) dS = \rho g \sum_m (n_j w_i + z D_i) \cdot \Delta A \qquad (5)$$

Here D_i denotes the divergence of the mode shape function, assumed to be continuous in the vicinity of the body surface. For the mode related to the rigid motion the divergence D_i=0 and C_{ij} is computed by DEFMOD included in WAMIT.

For the structural modes, deflections of the MOB are defined at each nodal point of the FEA model. To evaluate C_{ij} related to structural modes all deflections defined in FEA model are mapped to the hydrodynamic model. In this procedure the same interpolation scheme can be used as defined in mass matrix calculation. In this case the divergence D_i may not be zero and may be calculated for each related mode. DEFMOD in WAMIT does not provide hydrostatic restoring coefficients for structural modes. These are provided by external stiffness matrix in the data file. In this study D_i was computed by a finite difference method by picking up several points near the point where structural deformations are available.

Since three structural modes are modeled in this

study the generalized structural stiffness is needed. The FEA model gives not only structural mode shapes but also structural stiffness matrix. The generalized structural stiffness matrix can be calculated by

$$[K_m]_{MxM} = [\phi]^T_{MxN}[K]_{NxN}[\phi]_{NxM} \quad (6)$$

where K_m is the generalized structural stiffness matrix, ϕ the mode shape displacement vector, ϕ^T a transpose of ϕ, M the number of modes, and N is the total degrees of freedom of the nodal point. Using the above procedure to calculate the generalized structural stiffness requires huge matrix operations and computer memories, and it is very difficult to compute on the personal computer. This procedure however can be simplified by using the generalized mass matrix and the dry natural frequencies of the MOB. The generalized structural stiffness matrix is a diagonal matrix with the diagonals equal to the square of the dry natural frequencies of the corresponding mode. In the WAMIT data file it is necessary to scale the squared frequencies by the generalized mass related to the structural modes

3. NUMERICAL RESULTS

Based on the generalized feature of WAMIT described above, hydroelastic study was conducted on McDermott's MOB whose specifications are given in Table 1.

For a rigidly hinged MOB, the body motion is characterized by the motion of its center of gravity and additional hinge modes. The motion at an arbitrary point can then be calculated from linear superposition of these motion responses. For a flexible body, it is necessary to add the motion due to the structural modes. In addition to the ten rigid modes (from mode 1 to mode 10) the structural deflections due to the three flexible modes are added to the total motions.

The WAMIT generalized mode calculates motion RAOs for the three structural modes related to the mode shape functions. In order to calculate motion at arbitrary points these RAOs are multiplied by the mode shape function at those points. For the flexible mode in this study, the motion at the center of gravity was calculated to compare with the motion of the rigid MOB. Since the center of gravity is usually an internal point of the structure, it is necessary to calculate mode shape for that point using interpolation. The resulting motions may not be accurate if few points are selected as an interpolation base. The connector load RAO was calculated for each connector located at ±50 meters from the center-line. All RAOs were normalized by a unit wave amplitude (m/m, degree/m, Ton/m).

Figures 10 through 15 show sway, roll and yaw response and Figures 16 through 21 show connector force for both the rigid and the flexible MOB. All results presented here are based on a wave heading angle of 85 degrees at which the maximum response was found. The surge, heave and pitch responses are not presented here since they are the same as the rigid MOB case. This means that all the three structural modes mainly contribute to sway, roll and yaw. Comparing to the rigid MOB case, there are some noticeable differences in some wave periods (from 6 to 11 seconds) for both motion and connector force. These results show the effect of the flexibility of the MOB and the presence of the associated natural frequencies of the three structural modes considered in this study. For the connector loads all three components have the same trend as the motions. Relatively different roll and yaw motions were found of the neighboring units (Figure 12 and Figure 14). In the rigid MOB case the roll and yaw motions are the same for the all units (Figure 13 and Figure 15). The flexible modes caused these relative motions between the units.

The extreme values of the motion and connector force in the irregular seas (up to sea state 8+, significant wave height H_s=15.24m, peak spectrum period T_p=20.1s) for the flexible MOB were compared to the results from the rigid module rigid connector (RMRC) and rigid module flexible connector (RMFC) models in Table 5. The results for the rigid module with flexible connector (RMFC) are based on the simplified model with equivalent connector stiffness described in Ref. [1]. Apparently, FMRC model predicts higher motions and connector forces than RMRC model. This trend is mainly due to the resonance by the structural modes considered here. It is noted that the motions are almost the same with RMRC model. The connector forces for the FMRC model are significantly increased by more than 100% compared to the RMRC model. The FMRC model also predicts higher motions and connector forces than the RMFC model. The differences between the two models are mainly due to the slight difference in the dry natural frequencies between the FEA model and the simplified model, since it may change the resonance period and peak values.

	FMRC	RMRC	RMFC
Surge (m)	2.26	2.26	2.808
Sway (m)	8.91	8.478	8.915
Heave (m)	6.72	6.72	6.225
Roll (degree)	4.62	4.60	4.477
Pitch (degree)	3.401	3.401	4.263
Yaw (degree)	0.864	0.707	0.803
Force F_x (Ton)	3.202×10^5	1.334×10^5	2.223×10^5
Force F_y (Ton)	3.738×10^4	1.741×10^4	2.390×10^4
Force F_z (Ton)	9.134×10^4	4.783×10^4	6.720×10^4

Table 5: Maximum motion and connector force for the different MOB configuration in the irregular sea waves

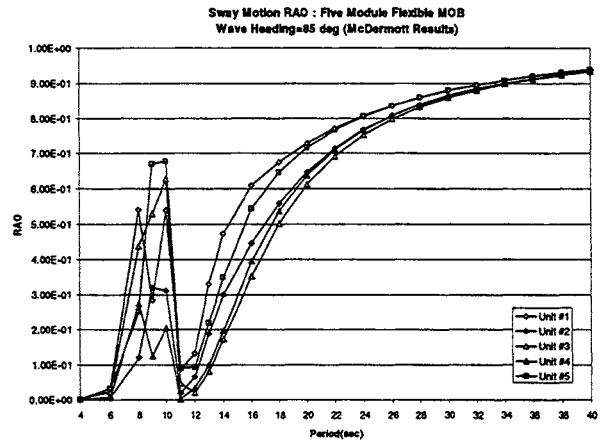

Figure 10 : Sway response for the flexible MOB with 85degree wave heading angle

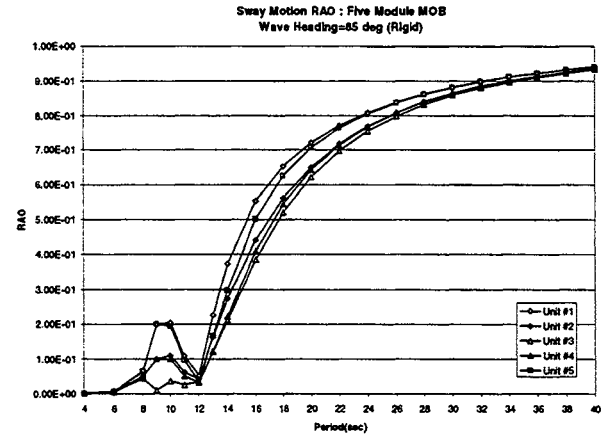

Figure 11 : Sway response for the rigid MOB with 85degree wave heading angle

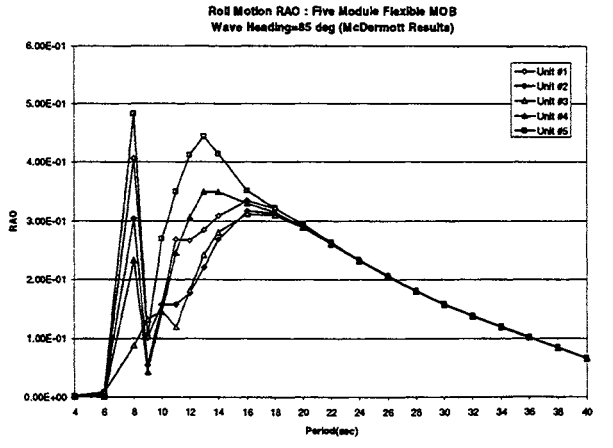

Figure 12 : Roll response for the flexible MOB with 85degree wave heading angle

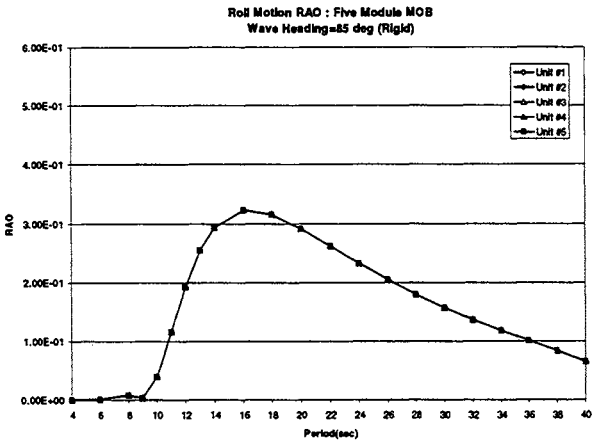

Figure 13 : Roll response for the rigid MOB with 85degree wave heading angle

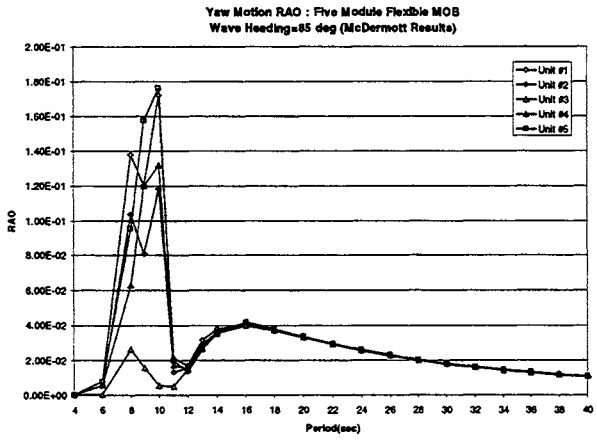

Figure 14 : Yaw response for the flexible MOB with 85degree wave heading angle

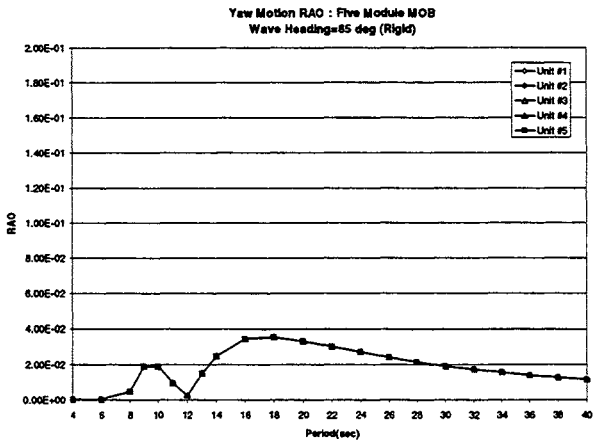

Figure 15 : Yaw response for the rigid MOB with 85degree wave heading angle

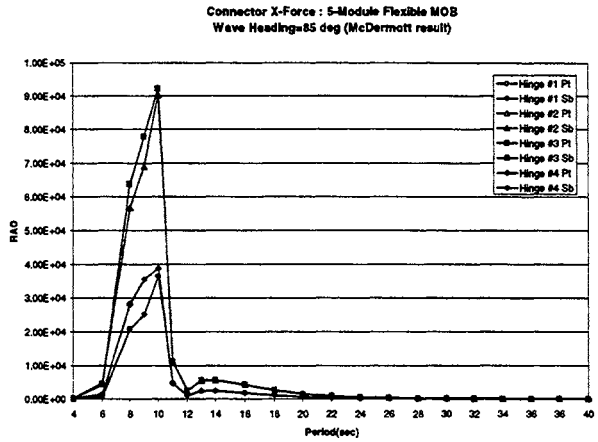

Figure 16 : Connector X-force for the flexible MOB with 85degree wave heading angle

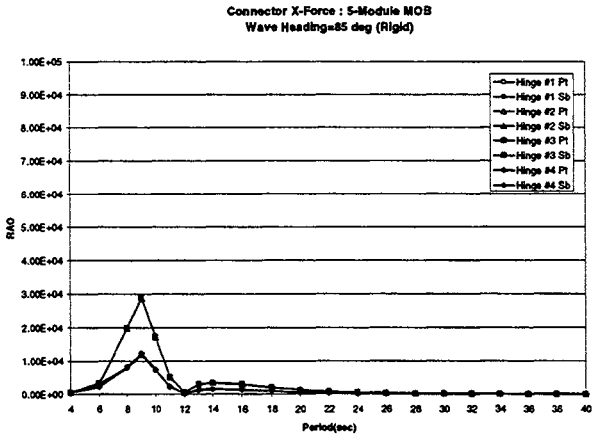

Figure 17 : Connector X-force for the rigid MOB with 85degree wave heading angle

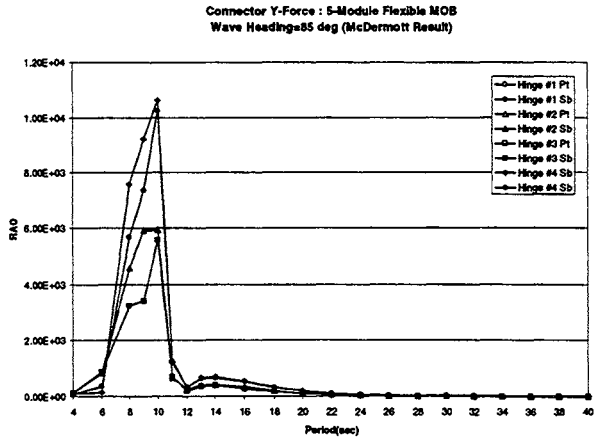

Figure 18 : Connector Y-force for the flexible MOB with 85degree wave heading angle

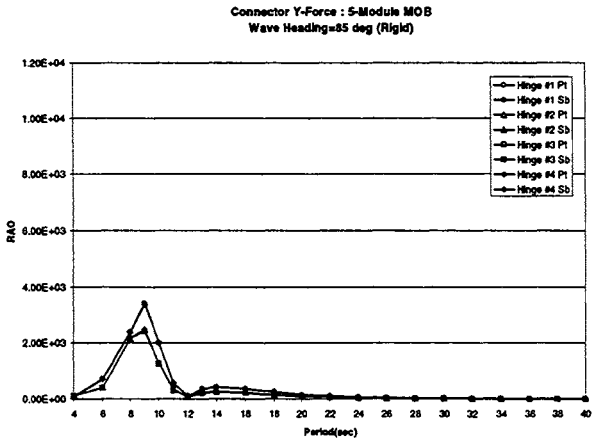

Figure 19 : Connector Y-force for the rigid MOB with 85degree wave heading angle

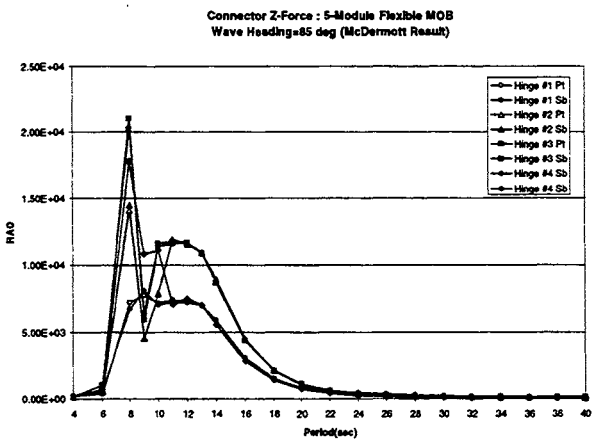

Figure 20 : Connector Z-force for the flexible MOB with 85degree wave heading angle

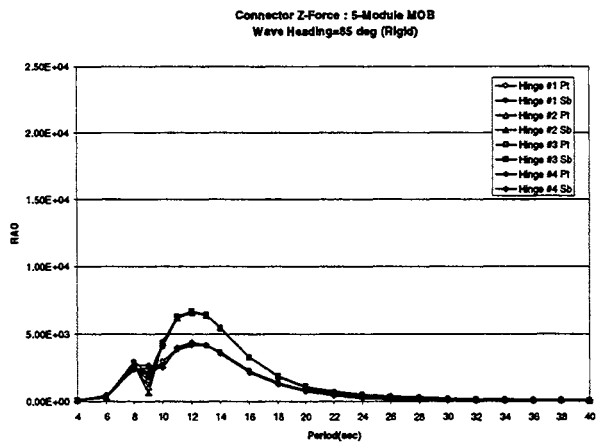

Figure 21 : Connector Z-force for the rigid MOB with 85degree wave heading angle

4. CONCLUSTIONS

A hydroelastic analysis using WAMIT generalized mode was performed for a five-module MOB of the McDermott preliminary design(P1-B). The hydroelastic model was based on a finite element model of the MOB.

In this study, the WAMIT generalized mode approach was successfully applied to both the rigid and flexible five-module MOB with the rigid hinge connector. It was found that continuous deflections (structural modes) of the MOB cause a significant change in the motions (sway, roll and yaw) and the connector forces over certain wave period range. This means that dynamic response of the flexible modes is significant. It is also found that RMFC model based on the simplified model appears to predict the connector force quite well compared to FMRC model based on FEA model.

Acknowledgement: The study is supported by the Office of Naval Research Center. Contract:N00014-98-C-0155. The authors wish to acknowledge helpful contribution from David Raj of McDermott Technology Inc. This work also benefited from a helpful discussion with Robert Taylor, Ray Chiou, Robert Zueck, Ted Shugar, and Billy Karrh of the Naval Facilities Service Engineering Center.

References

[1] MEH., "Mobile Offshore Base (MOB) Preliminary Design Report, Volume II - Connectors, Motions, and Loads," Contract: N00167-95-C-0113, CDRL Sequence No. C009, J.Ray McDermott Engineering Houston, LLC. Sept. 30, 1997

[2] MIT., "WAMIT Version 5.4, A Radiation-Diffraction Panel Program for Wave-Body Interactions," Dept. of Ocean Engineering, Massachusettes Institute of Technology, 1998.

[3] Newman, J.N., "Wave Effects on Deformable Bodies," *Applied Ocean Research*,Vol.16, No. 1, Page 47-59, 1994.

[4] OCI-97-201., "Hydroelastic Analysis of a MOB," Report No. OCI-97-201 , OffCoast, Inc., Kailua, Hi, July 1997.

[5] OCI-99-204., "Hydroelastic Analysis of a MOB Based on a FEA Model," Report No. OCI-99-204 , OffCoast, Inc., Kailua, Hi, May 1999.

[6] Riggs, H.R., "Hydrostatic Stiffness of Floating Structures," *Proc. International Workshop on Very Large Structure*, VLFS '96, Hayama, Japan, pp229-234

[7] Takaki, M. and Tango, Y., "Wave Drifting Forces on Very Large Floating Structures," *International Journal of Offshore and Polar Engineering*, Vol.5, No.3, September 1995.

PROCEEDINGS OF THE THIRD INTERNATIONAL WORKSHOP ON VERY LARGE FLOATING STRUCTURES
(VLFS '99), VOL. I, EDS. R.C. ERTEKIN & J.W. KIM, 22-24 SEPTEMBER 1999, HONOLULU, HAWAII, USA

WAVE-INDUCED MOTION OF AN ELASTIC FLOATING PLATE IN A SEA WITH A BREAKWATER

Shuichi Nagata, Hisafumi Yoshida, Takashi Fujita and Hiroshi Isshiki
Technical Research Institute, Hitachi Zosen Corporation, Osaka, Japan *

ABSTRACT

In this paper, by the method proposed by Nagata et al.([1], [2]), calculated results of wave-induced motions of an elastic mat-like floating structure in a sea with a breakwater are shown. In this method, the method of velocity potential continuation is used for the fluid region and the thin plate theory for an elastic mat-like structure. The deflection of the plate is approximated by an expansion in terms of the natural mode functions for free vibration of a free-free beam. In this paper, calculated results for the vertical deformation of a rectangular floating plate with 1000m in length in a sea with a straight breakwater and the wave elevation distribution around the floating plate and the breakwater are shown.

1. INTRODUCTION

A pontoon type floating structure with 4 to 5 kilometers in length and 5 meters in depth has been studied by The Technological Research Association of Mega-Float in Japan. In this study, reduction of the motion of a floating structure by surrounding it by the breakwater is considered. In order to evaluate the motion of this type of structure, it may be necessary to consider the fluid dynamic force containing the effect of the breakwater and perform analyses on the response of floating structures to waves by taking their elastic deformations into account.

Recently, a number of studies have been made for predicting the behavior of wave-induced motions of very large floating structure. ([3],[4],[5],[6],[7],[8], [9],[10]). However, in these studies, a floating structure only in an open sea is treated. There exist a few studies in regard to the wave-induced elastic motion of the floating structure in a sea with the breakwater.([1],[2],[11],[12])

In this paper, calculated results of wave-induced motions of an elastic rectangular mat-like structure in a sea with a straight breakwater are shown by the method proposed by authors.([1],[2]) The outline of this method is as follows:

(1) Three-dimensional velocity potential continuation method and boundary element method are used to analyze the fluid region [13], [14]. The draft of the floating structure is considered.

(2) The motion of the mat-like structure is assumed to be governed by thin plate theory and the deflection of the plate is approximated by an expansion in terms of the natural mode functions for free vibration of a free-free beam. To solve the motion of the freely floating plate in waves, the variational principle is used. These following conditions are obtained as the natural condition of this variational principle. Namely, the equation of motion of the plate should be satisfied, the bending moment and shear force should vanish at the edges of the plate and the a concentrated force should vanish at the corners of the plate.

(3) Finaly, we can get the solution by solving linear algebraic equations with respect to unknown quantities, potential on the edge of the plate and the coefficients of the function expansion of the plate deflection.

Calculated results for the vertical deformation of a rectangular plate with 1000m in length in a sea with a straight breakwater and the wave elevation distribution around the floating plate and the breakwater are shown for various period and the direction of wave propagation of the incident wave.

*2-11, Funamachi 2-Chome, Taisho-Ku, Osaka 551-0022, JAPAN, E-Mail: nagata@fluid.lab.hitachizosen.co.jp

2. FORMULATION

2.1 Fundamental assumption

As shown in Figure 1, a rectangular floating plate in a sea with a breakwater is considered. The length of the breakwater is finite and the water depth h is constant everywhere. The plan view of the plate is rectangle with length $2a$, width $2b$,and draft qh. With an incident sinusoidal plane wave of frequency σ, amplitude ζ_0 and incident angle ω with respect to x–axis, the floating plate is assumed to be in small motion. We take the origin O of the coordinate system at still water surface, x– and y–axes in horizontal directions and z–axis vertically upwards. For simplicity, we focus on the vertical deformations of the plate. The deflection of the plate is approximated by an expansion in terms of the natural modes of a free-free beam in free vibrations. Therefore, the vertical deformation of the plate $w(x,y)\cdot e^{-i\sigma t}$ is expressed as follows:

$$w(x,y)=\sum_{m=-1}^{M}\sum_{l=-1}^{L}A_{ml}\cdot\mu_m(x)\cdot\psi_l(y) \qquad (1)$$

where

$$\begin{cases}\mu_{-1}(x)=1, & \mu_0(x)=-x,\\ \psi_{-1}(y)=1, & \psi_0(y)=y\end{cases} \qquad (2)$$

$$\begin{cases}\mu_{2m-1}=\dfrac{1}{2}\left(\dfrac{\cos\lambda_{2m-1}^{(1)}x}{\cos\lambda_{2m-1}^{(1)}a}+\dfrac{\cosh\lambda_{2m-1}^{(1)}x}{\cosh\lambda_{2m-1}^{(1)}a}\right)\\ \mu_{2m}=\dfrac{1}{2}\left(\dfrac{\sin\lambda_{2m}^{(1)}x}{\sin\lambda_{2m}^{(1)}a}+\dfrac{\sinh\lambda_{2m}^{(1)}x}{\sinh\lambda_{2m}^{(1)}a}\right)\end{cases} \qquad (3)$$

$$(-1)^{m+1}\tan\lambda_m^{(1)}a+\tanh\lambda_m^{(1)}a=0 \qquad (4)$$

Mode functions ψ_{2l-1} and ψ_{2l} for y direction are given in the same expression of Eq.(3),(4). $A_{-1,-1}, A_{-1,0}, A_{0,-1}$ in Eq.(1) denotes $\zeta^*, \omega_1^*, \omega_2^*$, respectivly.

We assume the fluid motion to be small amplitude potential motion. The velocity potential $\Phi(x,y,z;t)=\Re[\phi(x,y,z)\cdot e^{-i\sigma t}]$ satisfies Laplace equation. As shown in Figure 1, we divide the fluid region into three kinds of regions by the imaginary boundary planes. The region–1 is the outer one which is outside of a closed curved surface D_1, where D_1 consists by breakwater outer surface D_{11} and imaginary boundary D_{12}. The region–2 is the one which is surrounded by D_1 and a boundary plane D_2, which is the cylindrical surface whose cross-section is equal to that of the plate. The region–3 is the inner region below the bottom surface of the plate. The velocity potential ϕ_1 for the region–1, ϕ_2 for the region–2 and ϕ_3 for the region–3 satisfy Laplace equation. ϕ_1 and ϕ_2 satisfy the free surface condition and the sea bottom condition, and the ϕ_3 the condition on the bottom surface of the plate and the sea bottom condition as follows:

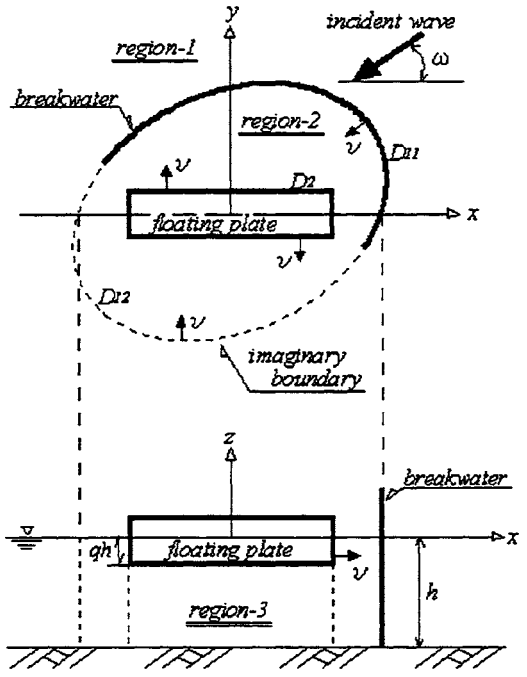

Figure 1: Definition sketch.

$$\phi_1(x,y,z)=\frac{g\zeta_0}{\sigma}\Big[\{f_0(x,y)+f_1(x,y)\}Z_0(z)+\sum_{n=1}^{n^*}f_2^{(n)}(x,y)Z_n(z)\Big] \qquad (5)$$

$$\phi_2(x,y,z)=\frac{g\zeta_0}{\sigma}\Big[f_3(x,y)Z_0(z)+\sum_{n=1}^{n^*}f_4^{(n)}(x,y)Z_n(z)\Big] \qquad (6)$$

$$\phi_3(x,y,z)=\frac{g\zeta_0}{\sigma}\Big[\varphi_0(x,y)+\sum_{s=1}^{s^*}\varphi_s(x,y)S_s(z)$$

$$+\frac{i}{2\overline{q}}\frac{\sigma^2 h}{g}\Big[\Big(-\frac{\zeta^*}{\zeta_0}+\frac{\omega_2^* x}{\zeta_0}-\frac{\omega_1^* y}{\zeta_0}+xy\frac{A_{00}}{\zeta_0}\Big)\Big(1+\frac{z}{h}\Big)^2$$
$$+\Big\{\frac{1}{4}\Big(\frac{2\zeta^*}{\zeta_0}-\frac{\omega_2^* x}{\zeta_0}+\frac{\omega_1^* y}{\zeta_0}\Big)-\frac{xy}{6}\frac{A_{00}}{\zeta_0}\Big\}\Big(\frac{x^2+y^2}{h^2}\Big)\Big]$$
$$-i\frac{\sigma^2 h}{g}H(x,y,z)\Big] \qquad (7)$$

where g is the gravitational acceleration,

$$Z_0(z)=\frac{\cosh k(z+h)}{\cosh kh},\quad Z_n(z)=\frac{\cos k_n(z+h)}{\cos k_n h}, \qquad (8)$$

$$S_s(z)=\cos\overline{S}(z+qh), \qquad (9)$$

$\overline{S}=s\pi/\overline{q}h$, $\overline{q}=1-q$, and wavenumber k,$k_n(n=1,2,\cdots)$ are determined by the following equations:

$$kh\cdot\tanh kh=-k_n h\cdot\tan k_n h=\sigma^2 h/g \qquad (10)$$

$f_0(x,y)$ is a known function which represents an incident wave and given as follows:

$$f_0(x,y)=-i\exp\{-ik(x\cos\omega+y\sin\omega)\} \qquad (11)$$

$H(x,y,z)$ is a particular solution in region–3 derived from the elastic deformation of a floating body, and it's detail is shown in reference [2].

Substituting Eqs.(5), (6) and (7) into Laplace equation, the coefficient functions should satisfy the following equations:

$$\nabla^2 f_j+k^2 f_j=0,\quad j=1,3 \qquad (12)$$

$$\nabla^2 f_j^{(n)}-k_n^2 f_j^{(n)}=0,\quad (n=1,2,3,\cdots),j=2,4 \qquad (13)$$

$$\nabla^2\varphi_0=0,\quad \nabla^2\varphi_s-\overline{S}^2\varphi_s=0\ (s=1,2,3,\cdots) \qquad (14)$$

where

$$\nabla^2=\frac{\partial^2}{\partial x^2}+\frac{\partial^2}{\partial y^2} \qquad (15)$$

2.2 Boundary integral equation

As shown in Figure 1, we denote the boundary of the breakwater, the imaginary boundary and the boundary of the plate by D_{11}, D_{12} and D_2 respectively. D_1 is the sum of D_{11} and D_{12}. We denote the point on the boundary curve D_1 and D_2 by (ξ,η) . We introduce Hankel function of the first kind $H_0^{(1)}(kR)$ as the elementary solution of Eq.(12), where $R=\sqrt{(x-\xi)^2+(y-\eta)^2}$, modified Bessel function $K_0(k_nR)$ as that of Eq.(13), logarithmic function $\log(1/kR)$ as the first equation of Eq.(14), and another modified Bessel function $K_0(\overline{S}R)$ as the second equation of Eq.(14). If the boundary D_1, D_{11}, D_{12} and D_2 are divided into N_1, N_{11}, N_{12} and N_2 pieces of subboundaries, and $f_1, f_2^{(n)}, f_3, f_4^{(n)}, \varphi_0$ and φ_s and their derivatives with respect to the normal are assumed to be constant on the subboundaries, we have the following integral equations from Green's formulas and elementary solutions.

$$\sum_{j=1}^{N_1}\Big[\alpha_{ij}^{(0)}\cdot f_1(j)-A_{ij}\cdot\overline{f}_1(j)\Big]=0 \text{ on } D_1 \qquad (16)$$

$$\sum_{j=1}^{N_1}\Big[\alpha_{ij}^{(n)}\cdot f_2^{(n)}(j)-B_{ij}^{(n)}\cdot\overline{f}_2^{(n)}(j)\Big]=0 \quad \text{on } D_1 \qquad (17)$$

$$\sum_{j=1}^{N^*}\Big[\theta_{ij}^{(0)}\cdot f_3(j)-C_{ij}\cdot\overline{f}_3(j)\Big]=0 \quad \text{on } D_1+D_2 \qquad (18)$$

$$\sum_{j=1}^{N^*}\Big[\theta_{ij}^{(n)}\cdot f_4^{(n)}(j)-D_{ij}^{(n)}\cdot\overline{f}_4^{(n)}(j)\Big]=0 \quad \text{on } D_1+D_2 \qquad (19)$$

$$\sum_{j=1}^{N_2}\Big[\beta_{ij}^{(0)}\cdot\varphi_0(j)-E_{ij}\cdot\overline{\varphi}_0(j)\Big]=0 \text{ on } D_2 \qquad (20)$$

$$\sum_{j=1}^{N_2}\Big[\beta_{ij}^{(s)}\cdot\varphi_s(j)-F_{ij}^{(s)}\cdot\overline{\varphi}_s(j)\Big]=0 \text{ on } D_2 \qquad (21)$$

where

$$N_1=N_{11}+N_{12},N^*=N_1+N_2$$
$$\alpha_{ij}^{(0)}=-\delta_{ij}+\overline{A}_{ij},\qquad \alpha_{ij}^{(n)}=-\delta_{ij}+\overline{B}_{ij}^{(n)}$$
$$\theta_{ij}^{(0)}=\delta_{ij}+\overline{C}_{ij},\qquad \theta_{ij}^{(n)}=\delta_{ij}+\overline{D}_{ij}^{(n)}$$
$$\beta_{ij}^{(0)}=-\delta_{ij}+\overline{E}_{ij},\qquad \beta_{ij}^{(s)}=-\delta_{ij}+\overline{F}_{ij}^{(s)}$$
$$A_{ij}=C_{ij}=\int_{\Delta S_j}\Big\{-\frac{i}{2}H_0^{(1)}(kR_{ij})\Big\}\cdot k\,ds$$
$$\overline{A}_{ij}=\overline{C}_{ij}=\int_{\Delta S_j}\frac{\partial}{\partial\nu}\Big\{-\frac{i}{2}H_0^{(1)}(kR_{ij})\Big\}\,ds$$
$$B_{ij}^{(n)}=D_{ij}^{(n)}=\int_{\Delta S_j}\Big\{-\frac{1}{\pi}K_0(k_nR_{ij})\Big\}\cdot k\,ds$$

$$
\begin{aligned}
&\overline{B}_{ij}^{(n)} = \overline{D}_{ij}^{(n)} = \int_{\Delta S_j} \frac{\partial}{\partial \nu}\left\{-\frac{1}{\pi}K_0(k_n R_{ij})\right\}\, ds \\
&E_{ij} = \int_{\Delta S_j}\left\{-\frac{1}{\pi}\log\left(\frac{1}{kR_{ij}}\right)\right\}\cdot k\, ds \\
&\overline{E}_{ij} = \int_{\Delta S_j} \frac{\partial}{\partial \nu}\left\{-\frac{1}{\pi}\log\left(\frac{1}{kR_{ij}}\right)\right\}\, ds \\
&F_{ij}^{(s)} = \int_{\Delta S_j}\left\{-\frac{1}{\pi}K_0(\overline{S}R_{ij})\right\}\cdot k\, ds \\
&\overline{F}_{ij}^{(s)} = \int_{\Delta S_j} \frac{\partial}{\partial \nu}\left\{-\frac{1}{\pi}K_0(\overline{S}R_{ij})\right\}\, ds \\
&R_{ij} = \sqrt{(\xi_j-\xi_i)^2+(\eta_j-\eta_i)^2} \\
&\overline{f}_1(j) = \frac{\partial f_1(j)}{k\,\partial \nu}, \qquad \overline{f}_2^{(n)}(j) = \frac{\partial f_2^{(n)}(j)}{k\,\partial \nu} \\
&\overline{f}_3(j) = \frac{\partial f_3(j)}{k\,\partial \nu}, \qquad \overline{f}_4^{(n)}(j) = \frac{\partial f_4^{(n)}(j)}{k\,\partial \nu} \\
&\overline{\varphi}_0(j) = \frac{\partial \varphi_0(j)}{k\,\partial \nu}, \qquad \overline{\varphi}_s(j) = \frac{\partial \varphi_s(j)}{k\,\partial \nu}
\end{aligned}
\tag{22}
$$

δ_{ij} is Kronecker's delta. ν is the unit normal vector which has the direction as shown in Figure 1.

2.3 Kinematical boundary condition

On the boundary D_1 and D_2, kinematical condition are given as follows:

a) The condition on the boundary D_1

$$
\left.\begin{aligned}
&\frac{\partial \phi_1}{\partial \nu} = 0, \qquad \frac{\partial \phi_2}{\partial \nu} = 0, \quad (on\ D_{11}) \\
&\frac{\partial \phi_1}{\partial \nu} = \frac{\partial \phi_2}{\partial \nu}, \quad \phi_1 = \phi_2 \quad (on\ D_{12})
\end{aligned}\right\} \tag{23}
$$

b) The condition on the boundary D_2

1) $-qh \le z \le 0$:

$$
\frac{\partial \phi_2}{\partial x} = -i\sigma\omega_2^*(z-\overline{z}_0), \qquad \frac{\partial \phi_2}{\partial y} = i\sigma\omega_1^*(z-\overline{z}_0)
$$

2) $-h \le z \le -qh$:

$$
\frac{\partial \phi_2}{\partial \nu} = \frac{\partial \phi_3}{\partial \nu}, \quad \phi_2 = \phi_3 \qquad \cdots\cdots\cdots\cdots\cdots\cdots\cdots \tag{24}
$$

where $\overline{z}_0$ is the z co-ordinates of the gravity center of the plate.

Substituting Eq.(5) and Eq.(6) into Eq.(23), and Eq.(6) and Eq.(7) into Eq.(24) respectively, then eliminating z from these equation by utilizing the orthogonality of functions $Z_0(z)$ and $Z_n(z)$ in $-h \le z \le 0$, we can get equations represents the relation among $f_1, f_2^{(n)}, f_3, f_4^{(n)}, \varphi_0$ and φ_s and their derivatives with respect to the normal .([2])

2.4 Equation of motion of a plate

The equation of motion and boundary conditions of a rectangular plate which is freely floating can be obtained from the stationarity of the functional

$$
\begin{aligned}
\Pi = \frac{D_p}{2}\int_{-a}^{a}\int_{-b}^{b}\Big[&(\nabla^2 w)^2 \\
&+2(1-\nu)\left\{\left(\frac{\partial^2 w}{\partial x \partial y}\right)^2 - \left(\frac{\partial^2 w}{\partial x^2}\right)\left(\frac{\partial^2 w}{\partial y^2}\right)\right\}\Big] dx dy \\
&-\int_{-a}^{a}\int_{-b}^{b} f w\, dx dy
\end{aligned}
\tag{25}
$$

where $D_p = E\delta_p^3/12(1-\nu^2)$, E is Young's modulus, ν is Poisson's ratio, δ_p is the thickness of the plate and f is a load distributing on the plate. f is given as follows:

$$
f = p - \rho g w + \rho_p \delta_p \sigma^2 w \tag{26}
$$

where $p(x,y)(= i\rho\sigma\phi_3)$ is the dynamic pressure on the bottom of the plate, ρ is the density of a fluid and ρ_p is the mass density of the plate. The variation of f is assumed to be zero. By requiring that the variation of Π vanishes and substituting Eq.(26) into the required equation, we get following equation.

$$
\begin{aligned}
\int_{-a}^{a}\int_{-b}^{b}\Big[&\delta w\left\{-\rho_p\delta_p\sigma^2 w - (p-\rho g w)\right\} \\
&+D_p\Big\{\frac{\partial^2 w}{\partial x^2}\cdot\frac{\partial^2 \delta w}{\partial x^2} + \frac{\partial^2 w}{\partial y^2}\cdot\frac{\partial^2 \delta w}{\partial y^2} \\
&+\nu\Big(\frac{\partial^2 w}{\partial x^2}\cdot\frac{\partial^2 \delta w}{\partial y^2} + \frac{\partial^2 w}{\partial y^2}\cdot\frac{\partial^2 \delta w}{\partial x^2}\Big) \\
&+2(1-\nu)\frac{\partial^2 w}{\partial x \partial y}\cdot\frac{\partial^2 \delta w}{\partial x \partial y}\Big\}\Big] dx dy \\
&= 0
\end{aligned}
\tag{27}
$$

By transforming Eq.(27) into another form, these following conditions are obtained as the natural condittion of this variational principle. Namely, the equation of motion of the plate should be satisfied, the bending moment and shear force should vanish at the edges of the plate and a concentrated

force should vanish at four corners of the rectangular plate.

The velocity potential ϕ_3 for the region–3 is expressed by Eq.(7). $\varphi_0(x,y), \varphi_s(x,y)$ in Eq.(7) are expressed by the values on the boundary D_2. By considering the following equation for Eq.(27),

$$\delta w = 1, \quad x, \quad y, \quad xy, \quad \mu_k(x), \quad y\mu_k(x),$$
$$\psi_n(y), \quad x\psi_n(y), \quad \mu_k(x) \cdot \psi_n(y),$$

the the nine kinds of equations are obtained.

By using the method to calculated a number of the small size matrices instead of a large size matrix, finally, we get the same number of equations as the number of unknowns, $f_3(j)$ and $f_4^{(n)}(j)$ on the boundary D_2 of the plate and the coefficients of the function expansion of the plate, from Eq. (16) $\sim$ (21), Eq. (23),(24) and nine kind of equations obtained from Eq.(27).

3. RESULTS AND DISCUSSIONS

In the privious papar([2]), some calculations were done to show the accuracy of the proposed method. First, calculations for a rectangular floating plate in an open sea were compared with Yago's experiment corresponding to a floating plate of 300m long[4] and Ohta's experiment corresponding to a floating plate of 1200m long[15]. Results of comparison between the calculation and the experiment were shown in [2], and the calculation results obtained by the proposed method showed a good agreement with experimental results. Next, to prove the accuracy of the theoretical treatment of the breakwater, calculation results for motions of a rigid floating body surrounded by the breakwaters in waves were compared with experiments for various configuration of breakwaters[2],[14]. The calculation results agreed well with the experiments, and the validity of the theoretical treatment of the breakwater was shown.

In this paper, in order to investigate the fundamental property for the reduction by the elastic motion of a floating plate in waves by a breakwater, calculations for elastic motion of a floating plate behind a straight breakwater with finite length were carried out. Principal dimensions of the floating plate in the present calculation are shown in table 1. In the present calculation, the length of the breakwater is L_B, the distance between the floating body and the breakwater is C, as shown in Figure 2. The bending rigidity(EI) is 1.5×10^{12}kgf$\cdot m^2$ (E: Young's modulus, I: bending moment of inertia)

Length: L(m)	1000.0
Width: B(m)	200.0
Height: D(m)	7.0
Draft: d(m)	1.5
Water depth: h(m)	60.0

Table 1: Principal dimensions of floating plate

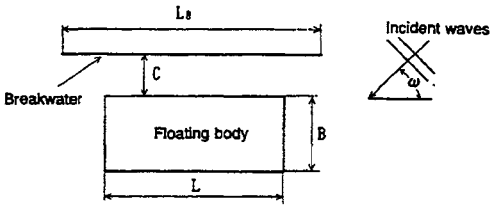

Figure 2: Arragement of the floaing body and the breakwater.

The calculation results of the vertical deformation of the floating plate in a sea with a straight breakwater which is set parallel to the longitudinal direction of the floating plate are shown in Figure 3. When the coordinate system is taken as shown in Figure 1, the floating plate and the breakwater are arranged symmetric with respect to the y axis. In Figure 3, the results for the breakwater with 1400m and 1800m in length are shown. The calculation conditions are: wave period T =10 second, C =200m, ω =90deg. Because the incidence angle of waves is perpendicular to the breakwater, the deformation of the plate in a sea with the breakwater becomes smaller than that in open sea, and the effectiveness of the breakwater to decrease the deformation are shown. The difference of the deformation between the two breakwater length (1400m and 1800m)is small.

Calculation results for oblique wave (ω =45deg.) are shown in Figure 4. For the oblique wave case, effectiveness of the breakwater are not clear for both breakwater lengths compared to the open sea results. However, at the weather side edge of the floating plate, the vertical deformation of the plate in a sea with a breakwater becomes smaller than that in an open sea. And the vertical deformation of the floating plate behind the long breakwater

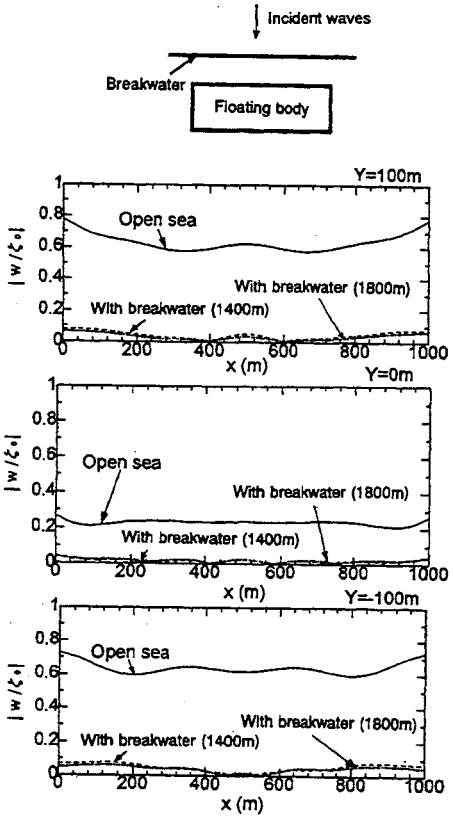

Figure 3: Distribution of the vertical deformation of the plate along the length direction (T =10sec., C =200m, ω =90deg.)

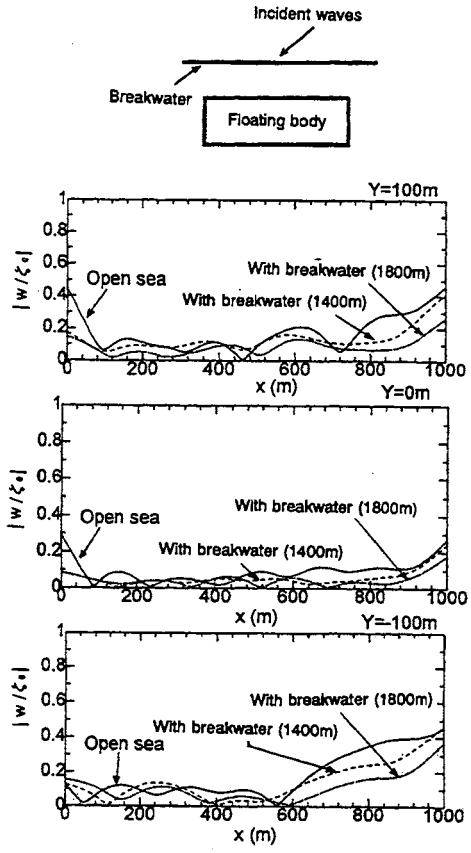

Figure 4: Distribution of the vertical deformation of the plate along the length direction (T =10sec., C =200m, ω =45deg.)

(1800m) is smaller than that behind the shorter one (1400m).

The distribution of the vertical deformation of the plate along the length direction for various wave period (L_B=1400m, C =200m, ω =90deg.) are shown in Figure 5. For the case of long wave period, the deformation of the plate is large, however, as the wave period becomes shorter, the deformation becomes smaller.

The distribution of the vertical deformation of the plate along the length direction for various wave period in oblique wave (L_B=1400m, C =200m, ω =45deg.) are shown in Figure 6. Almost same tendency with Figure 5 are shown about the wave period in this figure.

The distribution of the vertical deformation of the plate in oblique wave along the length direction with three breakwater lengths are shown in Figure 7. In this series calculation, the x-coordinate of the left edge of the breakwater is set equal to the x-coordinate of the left edge of the floating plate. In this case, the vertical deformation of the plate at the right edge of the floating plate becomes smaller as the length of the breakwater increases. However, the vertical deformations of the plate at the left edge of the floating plate is almost same for the three length of the breakwater.

Contour maps of the vertical deformation of the floating plate and wave elevation around the plate and the breakwater at $\sigma t = 0$ are shown in Figure 8 (T=10sec., ω =45deg.) and Figure 9 (T=10sec., ω =90deg.). In these figures, the upper contour maps shows the wave elevation distribution, and the lower contour maps shows the vertical deformations of the plate. The values of the contour for

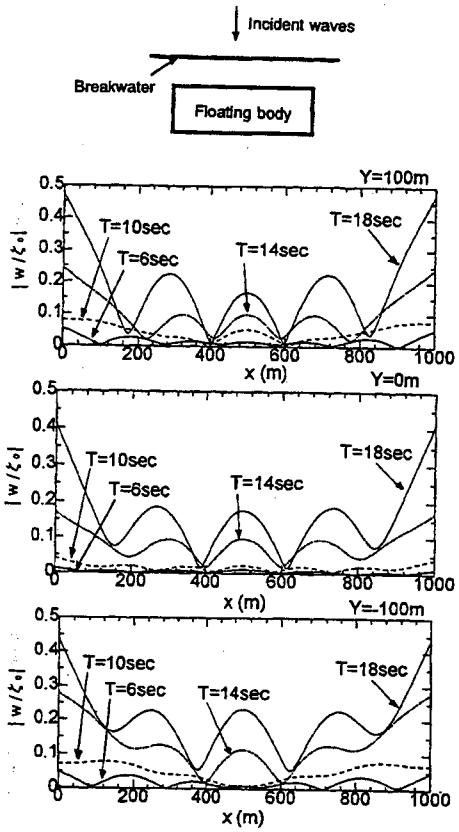

Figure 5: Distribution of the vertical deformation of the plate along the length direction for various wave period (L_B=1400m, C =200m, ω =90deg.).

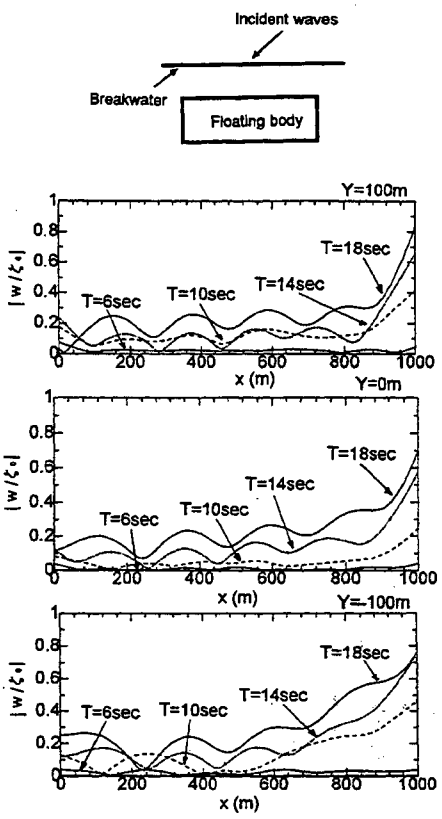

Figure 6: Distribution of the vertical deformation of the plate along the length direction for various wave period (L_B=1400m, C =200m, ω =45deg.).

the wave elevation and the vertical deformations of the plate are that divided by the amplitude of the incident wave. It is clearly seen that the breakwater whose location is properly arranged can reduce incident waves and elastic deformation of the floating plate.

4. CONCLUSIONS

In this paper, calculated results of wave-induced motions of a rectangular elastic floating plate in a sea with a finite straight breakwater are shown by using the method proposed by authors.

As the results of this calculation, it is found that the breakwater whose location is properly arranged can reduce incident waves and elastic deformation of the floating plate.

This study is a part of the work conducted by Technological Research Association of Mega-Float in Japan.

References

[1] S. Nagata, H. Yoshida, T. Fujita, and H. Isshiki. The analysis of wave-induced response of an elastic floating plate in a sea with a breakwater. *Int. Offshore and Polar Eng. Vol.1*, pages 223–230, 1998.

[2] S. Nagata, H. Yoshida, T. Fujita, and H. Isshiki. Reduction of the motion of an elastic flaoting plate in waves by breakwaters. *Proc. of Hydroelasticity'98*, pages 229–237, 1998.

[3] P. Mamidipudi and W. C. Webster. The motions performance of a mat-like floating airport. *Int. Conf. on Hydroelasticity in Marine Technology, Norway*, pages 363–375, 1994.

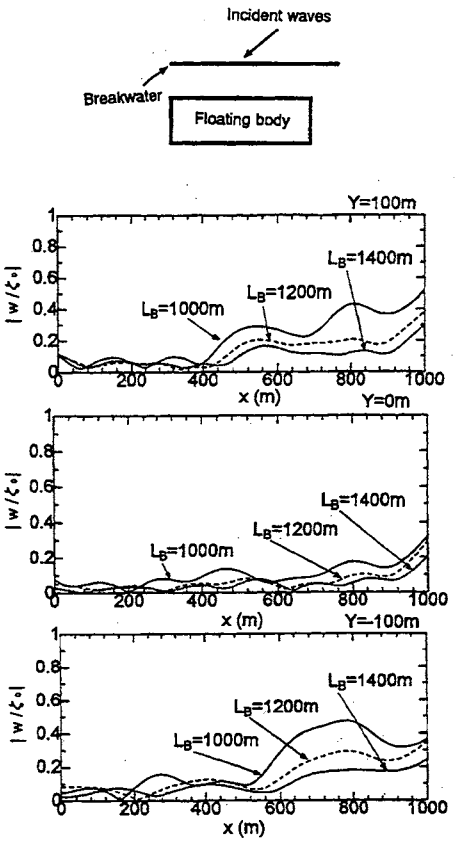

Figure 7: Distribution of the vertical deformation of the plate along the length direction for various breakwater length (T=10sec., C =200m, ω =45deg.).

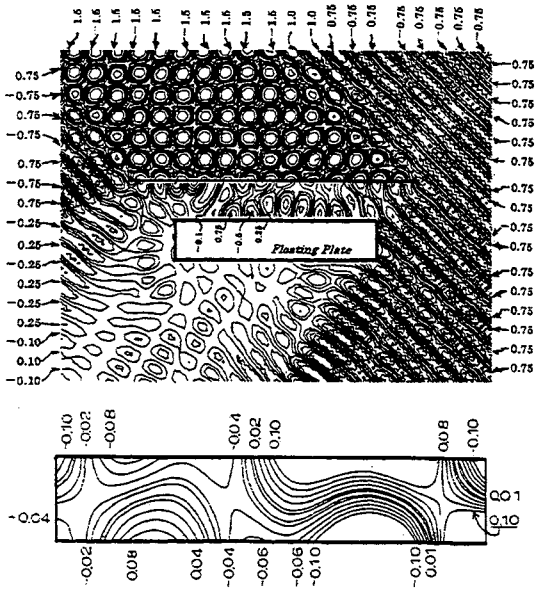

Figure 8: Contour map of the deformation of the plate and wave elevation around the plate at $\sigma t = 0$ (ω =45deg.)

[4] K. Yago and H. Endo. On the hydoroelastic response of box-shaped floating structure with shallow draft. *J. of Soc. of Naval Arch. of Japan, Vol.180 (in Japanese)*, pages 341–352, 1996.

[5] M. Takaki and X. Gu. Motions of a floating elastic plate in waves. *J. of Soc. of Naval Arch. of Japan, Vol.180*, pages 331–339, 1996.

[6] N. Ma, T. Hirayama, and N. Sato. Comparative study of hydroelastic responses of semisubmersible type and pontoon type very large floating structure in waves. *J. of Soc. of Naval Arch. of Japan, Vol.180 (in Japanese)*, pages 353–363, 1996.

[7] H. Maeda, K. Masuda, S. Miyajima, and T. Ikoma. Responses of pontoon type very large floating offshore structures. *J. of Soc. of Naval Arch. of Japan, Vol.180 (in Japanese)*, pages 365–371, 1996.

[8] M. Kashiwagi. A B-spline galerkin scheme for calculating hydroelastic response of a very large floating structure in waves. *J. Marine Science and Technology, Vol.3, No.1*, pages 37–49, 1998.

[9] S. Nägata, H. Yoshida, T. Fujita, and H. Isshiki. The analysis of the wave-induced responses of an elastic floating plate. *OMAE97, Vol.4*, pages 163–169, 1997.

[10] S. Ohmatsu. Numerical calculation of hydroelastic responses of pontoon type VLFS. *J. of Soc. of Naval Arch. of Japan, Vol.182 (in Japanese)*, pages 329–340, 1997.

[11] T. et al Utsunomiya. Wave response analysis of a box-like vlfs close to a breakwater. *Proc. of OMAE'98*, 1998.

[12] H. Seto and M. Ochi. A hybrid element approach to hydroelastic behavior of a very large

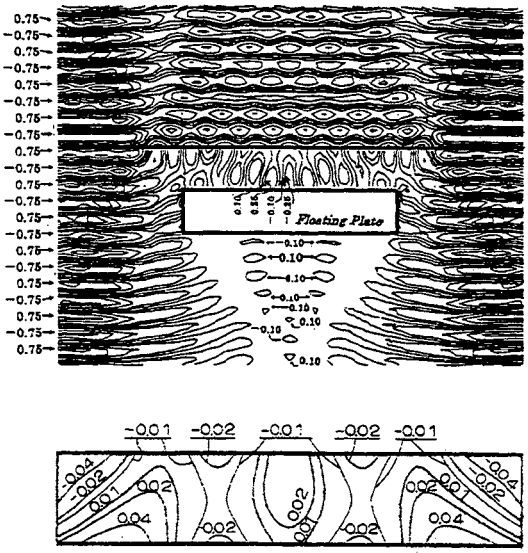

Figure 9: Contour map of the deformation of the plate and wave elevation around the plate at $\sigma t = 0$ (ω =90deg.)

floating structre in regular waves. *Proc. of Hydroelasticity'98*, pages 185–193, 1998.

[13] T. Ijima and A. Yoshida. On the motion of a rectangular or elliptical cylinder in waves of finite water depth. *Memoirs of the Faculty of Engineering Kyushu University, Vol.35, No.2 (in Japanese)*, 1975.

[14] S. Nagata, T. Fujita, S. Miyake, T. Makihata, and K. Oda. Motions of floating bodies in waves, moored by elastic lines in a sea with a breakwater. *Int. Offshore and Polar Eng. Vol.3*, pages 568–575, 1993.

[15] M. Ohta, K. Ikegami, and Y. Yamaguchi. Experimental study on elastic behavior of a huge floating structure in waves. *Trans. of The West-Japan Soc. of Nav. Arch. Vol.95*, pages 99–108, 1997.

PROCEEDINGS OF THE THIRD INTERNATIONAL WORKSHOP ON VERY LARGE FLOATING STRUCTURES
(VLFS '99), VOL. I, EDS. R.C. ERTEKIN & J.W. KIM, 22-24 SEPTEMBER 1999, HONOLULU, HAWAII, USA

Time Domain Analysis of Very Large Floating Structures in Irregular waves

Hisaaki Maeda*, Tomoki Ikoma**, Koichi Masuda*** and Chang-Kyu Rheem**
University of Tokyo*,
UTRC/IIS/University of Tokyo**, Nihon University***

ABSTRACT

Real sea areas where Very Large Floating Structures are installed are random wave fields. Then, it is necessary to analyze the responses in time domain due to arbitrary incident directional waves.

There exist hydroelastic deflections and slow drift motions etc. in the responses of VLFSs in ocean waves. However, it is very time consuming works to solve equation of motion in time domain and these responses due to directional waves. It is unnecessary to solve such equation in time domain if mooring forces can be turn into equivalent linear system.

In this paper, we tried to analyze the responses of time series without solving the equation of motion in time domain. And, the corresponding model test in uni and two-directional irregular waves was carried out. The present method is validated by comparisons between the analytical and measured results of time histories. And moreover, the analytical method of a slowly varying wave drift force is validated too.

1. INTRODUCTION

It is important to develop theoretical methods for an estimation of responses of very large floating structures in ocean waves. In most studies, the responses of very large floating structures have been predicted in frequency domain. However, we would often like to use time series of the responses. Generally speaking, equation of motion must be solved in time domain when it is non-linear, especially due to effects of a mooring system. But, there are a few cases in which the equivalent linear system can be applied to the mooring system. So, the time histories can be estimated from the frequency response functions if it is possible to assume the linear superposition principle to predict the responses.

Ohmatsu (see [1]) showed the estimation method of the elastic responses in time domain. Equation of motion is not solved directly be while an inverse Fourier transformation is used in its method. However, Ohmatsu calculated the elastic responses of the pontoon type VLFS only in long-crested irregular waves of head sea conditions. Ma, et al. (see [2]) predicted experimentally the deflection of the semi-submersible type VLFS in short crested waves based on directional wave spectrum. However, it was analyzed in frequency domain.

By the way, the responses of very large floating structure in ocean waves include not only hydroelastic vertical motions but also horizontal motions and reaction forces of mooring systems. In case of the VLFS, it is supposed that the horizontal motions due to linear wave forces are very small. But, the authors confirmed that the slow drift motions occurred due to non-linear wave forces (see [3]). This non-linear wave forces are the difference frequency component in the second-order wave forces. The motions due to such drifting wave forces cannot be neglected in order to predict the mooring forces. Generally, equation of motion is solved in time domain to calculate the slow drift motions. But, we can calculate them in frequency domain if the equivalent linear system can be applied to the mooring system. Nagai calculated the slow drift motions of a conical floating structure in frequency domain and formulated the second-order mooring force of the moored floating body with linear spring (see [4]).

This paper proposes the formulations of the strict first-order and second-order mooring forces of a linear spring on the VLFS in frequency domain. And, we tried time domain analyses on the responses of the very large floating structure in uni and two directional irregular waves and validated the present method by comparing with the corresponding experimental results. Then, the comparisons were made by time histories. The present analytical method does not use equation of motion in time domain. We expanded Ohmatsu's method to the second-order problem, and the time series of the second-order tether tensions were analyzed.

2. THEORY

*, ** 7-22-1 Roppongi Minato-ku, Tokyo 106-8558, JAPAN
maedah@iis.u-tokyo.ac.jp or tomoki@iis.u-tokyo.ac.jp

In this paper, the hydrodynamic forces and wave exciting forces were analyzed by the pressure distribution method. And, the slowly varying wave drift forces were predicted on basis of the pressure distribution method applying the zero-draft theory. Then, a weak non-linear was assumed in the second-order problem. The analysis of the hydroelastic deflection applied the modal method.

The formulations of the first and second-order mooring forces are shown in frequency domain. And, it is suggested that the analytical method for the time series of the first and second-order components can be derived from the frequency response or transfer functions in this section. The coordinate system is shown in Fig.1.

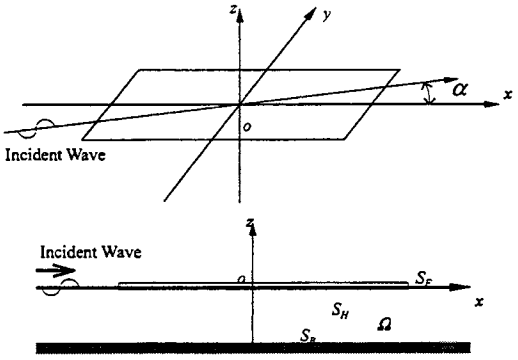

Figure 1 Coordinate system of this study

2.1 Formulation of mooring force

The definitions of the position vector and the displacement vectors are shown in Figs.2 and 3. Where, the mooring tether is assumed as linear sparing. Then, the mooring tension is defined as an axial force of the tether because it is assumed to scalar value. So, the mooring force is determined by the tension and the direction of the tether.

The mooring forces are expanded by perturbation method, and considered up to 2nd-order term. Using the mode shape function $\vec{\eta}_r$ and the principal coordinate q_r, the displacement vector $\vec{\eta}(x,y)$ is expressed as follows:

$$\vec{\eta}(x,y)=\sum_{r=1}^{\infty}\vec{\eta}_r(x,y)q_r, \tag{1}$$

where, q_r is

$$\begin{aligned}\bar{q}_r(t)&=q_r^{(1)}(t)+q_r^{(2)}(t)\\&=\mathrm{Re}\left[\sum_{i=1}^{\infty}q_{ri}^{(1)}e^{-i\omega_i t}+\sum_{i=1}^{\infty}\sum_{j=1}^{\infty}\left(q_{rij}^{+}e^{-i\omega^{+}t}+q_{rij}^{-}e^{-i\omega^{-}t}\right)\right],\end{aligned} \tag{2}$$

and the same mode shape function is used as Kashiwagi did (see [9]). Then, $\omega^{+}=\omega_i+\omega_j$ and $\omega^{-}=\omega_i-\omega_j$ stand for the 2nd-order sum-frequency and difference-frequency respectively. The coordinate system is shown in Fig.2.

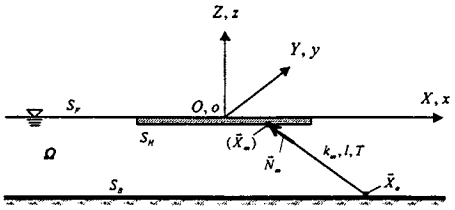

Figure 2 Coordinate system

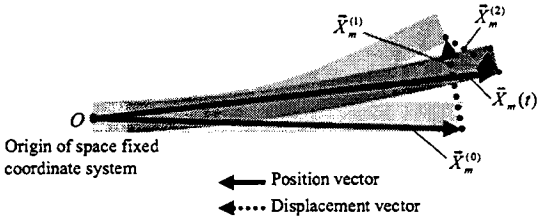

Figure 3 Definition of vector

The first-order and the second-order displacement vector of motion at mooring point are given as follows:

$$\vec{\eta}_m^{(1)}(x_m,y_m,z_m;t)=\sum_r\vec{\eta}_r(x_m,y_m)q_r^{(1)}(t), \tag{3}$$

$$\vec{\eta}_m^{(2)}(x_m,y_m,z_m;t)=\sum_r\vec{\eta}_r(x_m,y_m)q_r^{(2)}(t). \tag{4}$$

By the way, if l indicates the length of the tether and constant coefficient of the spring is k_m, the tension T is obtained by the following equation:

$$T=k_m(l-l^{(0)}), \tag{5}$$

where, $l^{(0)}$ means the initial length of the tether. In addition, the direction vector $\vec{N}_m$ of the mooring tether is defined as follows:

$$\vec{N}_m=\frac{\vec{X}_m-\vec{X}_a}{l}. \tag{6}$$

Using the direction vector and the tension, the mooring force is defined as following equation, where this is defined in right hand term of the motion equation,

$$\vec{F}_m=-T\vec{N}_m. \tag{7}$$

The 1st-order and the 2nd-order tether length and direction vector, etc. are concretely shown on the basis of the definition of the above. The 0th-order means initial value when the model is installed.

Lengths of the mooring tether are expressed as,

$$l^{(0)}=\left|\vec{X}_m^{(0)}-\vec{X}_a\right|, \tag{8}$$

$$l^{(1)}=\vec{\eta}_m^{(1)}\cdot\vec{n}_m, \tag{9}$$

$$l^{(2)}=\vec{\eta}_m^{(2)}\cdot\vec{n}_m+\frac{1}{2l^{(0)}}\left\{\vec{\eta}_m^{(1)}\cdot\vec{\eta}_m^{(1)}-(\vec{\eta}_m^{(1)}\cdot\vec{n}_m)^2\right\}. \tag{10}$$

Where, $\vec{\eta}_m=\vec{X}_m$, and $\vec{X}_a$ is as anchoring point. Direction vectors are:

$$\vec{n}_m=\vec{N}_m^{(0)}=\frac{\vec{X}_0}{l^{(0)}}, \tag{11}$$

$$\vec{N}_m^{(1)}=\frac{\vec{\eta}_m^{(1)}}{l^{(0)}}-\frac{1}{l^{(0)}}(\vec{\eta}_m^{(1)}\cdot\vec{n}_m)\vec{n}_m, \tag{12}$$

$$\vec{N}_m^{(2)} = \frac{\vec{\eta}_m^{(2)}}{l^{(0)}} - \frac{1}{l^{(0)}}\left[(\vec{\eta}_m^{(1)}\cdot\vec{n}_m)\left\{\frac{\vec{\eta}_m^{(1)}}{l^{(0)}} - \frac{1}{l^{(0)}}(\vec{\eta}_m^{(1)}\cdot\vec{n}_m)\vec{n}_m\right\}\right. \quad (13)$$
$$\left. + (\vec{\eta}_m^{(2)}\cdot\vec{n}_m)\vec{n}_m + \frac{1}{2l^{(0)}}\left\{\left|\vec{\eta}_m^{(1)}\right|^2\vec{n}_m - (\vec{\eta}_m^{(1)}\cdot\vec{n}_m)^2\vec{n}_m\right\}\right]$$

2.1.1 *First-order mooring force*

The time term is separated from the variable of mooring force in order to analyze the frequency domain,

$$F_{m,sr}^{(1)}(t) = \mathrm{Re}\left[\sum_{i=1}^{\infty} a_i f_{m,sr,i}^{(1)} e^{-i\omega_i t}\right]. \quad (14)$$

Then, the coefficient of the 1st-order mooring force of the *rs* mode becomes the following equation,

$$f_{msri}^{(1)} = -\vec{\eta}_s \cdot \left[\frac{T^{(0)}}{l^{(0)}}\{\vec{\eta}_r - (\vec{\eta}_r\cdot\vec{n}_m)\vec{n}_m\} + k_m(\vec{\eta}_r\cdot\vec{n}_m)\vec{n}_m\right]. \quad (15)$$

2.1.2 *Second-order mooring force*

Time term separation on the 2nd-order mooring force is similar to the case of the 1st-order as follows:

$$F_{m,sr,ij}^{(2)}(t) = \mathrm{Re}\left[\sum_{i=1}^{\infty}\sum_{j=1}^{\infty}\left\{a_i a_j f_{m,sr,ij}^{+} e^{-i\omega^{+}t} + a_i a_j^{*} f_{m,sr,ij}^{-} e^{-i\omega^{-}t}\right\}\right]. \quad (16)$$

But, the sum-frequency component of 2nd-order problem is ignored here because we are interested only in the slowly varying phenomena. There are two terms, such as Eq.(17), in the 2nd-order mooring force without the time term,

$$f_m^{-} = f_{mp,rs,ij}^{-} + \frac{1}{2}\left(f_{mq,r,ij}^{-} + f_{mq,r,ji}^{-*}\right). \quad (17)$$

Each term is expressed as follows:

$$f_{mprsij}^{-} = \frac{T^{(0)}}{l^{(0)}}\vec{\eta}_r\cdot\{\vec{\eta}_s - (\vec{\eta}_s\cdot\vec{n}_m)\vec{n}_m\} - k_m\vec{\eta}_r\cdot\{(\vec{\eta}_s\cdot\vec{n}_m)\vec{n}_m\}, \quad (18)$$

$$f_{mqrij}^{-} = \vec{\eta}_r\cdot\left[\frac{T^{(0)}}{2l^{(0)^2}}\{(\vec{\eta}_{mi}^{(1)}\cdot\vec{n}_m)\vec{\eta}_{mj}^{(1)} - (\vec{\eta}_{mi}^{(1)}\cdot\vec{n}_m)(\vec{\eta}_{mj}^{(1)}\cdot\vec{n}_m)\vec{n}_m\}\right.$$
$$+\frac{T^{(0)}}{4l^{(0)^2}}\{(\vec{\eta}_{mi}^{(1)}\cdot\vec{\eta}_{mj}^{(1)})\vec{n}_m - (\vec{\eta}_{mi}^{(1)}\cdot\vec{n}_m)(\vec{\eta}_{mj}^{(1)}\cdot\vec{n}_m)\vec{n}_m\}$$
$$-\frac{1}{2}\left\{\frac{k_m}{l^{(0)}}(\vec{\eta}_{mi}^{(1)}\cdot\vec{n}_m)\vec{\eta}_{mj}^{(1)} - \frac{k_m}{l^{(0)}}(\vec{\eta}_{mi}^{(1)}\cdot\vec{n}_m)(\vec{\eta}_{mj}^{(1)}\cdot\vec{n}_m)\vec{n}_m\right\}$$
$$\left.-\frac{k_m}{4l^{(0)}}\{(\vec{\eta}_{mi}^{(1)}\cdot\vec{\eta}_{mj}^{(1)}) - (\vec{\eta}_{mi}^{(1)}\cdot\vec{n}_m)(\vec{\eta}_{mj}^{(1)}\cdot\vec{n}_m)\}\vec{n}_m\right] \quad (19)$$

Equation (19) can be calculated if the 1st-order vertical displacement at the mooring point is given.

2.1.3 *Tensions*

First-order tension is given by

$$T_i^{(1)} = k_m\vec{\eta}_{mi}^{(1)}\cdot\vec{n}_m. \quad (20)$$

And, the 2nd-order tension is expressed by following equations:

$$T^{(2)} = T_p^{(2)} + T_q^{(2)}, \quad (21)$$

$$T_p^{(2)} = \sum_{i=1}\sum_{j=1}\left[a_i a_j T_{pij}^{+} e^{-i\omega^{+}t} + a_i a_j^{*} T_{pij}^{-} e^{-i\omega^{-}t}\right], \quad (22)$$

$$T_{pij}^{-} = k_m\vec{\eta}_{mij}^{-}\cdot\vec{n}_m, \quad (23)$$

$$T_q^{(2)} = \sum_{i=1}\sum_{j=1}\left[a_i a_j T_{qij}^{+} e^{-i\omega^{+}t} + a_i a_j^{*} T_{qij}^{-} e^{-i\omega^{-}t}\right], \quad (24)$$

$$T_{qij}^{-} = \frac{1}{2}\left(t_{qij}^{-} + t_{qji}^{-*}\right), \quad (25)$$

$$t_{qij}^{-} = \frac{k_m}{4l^{(0)}}\left\{\vec{\eta}_{mi}^{(1)}\cdot\vec{\eta}_{mj}^{(1)} - (\vec{\eta}_{mi}^{(1)}\cdot\vec{n}_m)(\vec{\eta}_{mj}^{(1)}\cdot\vec{n}_m)\right\}. \quad (26)$$

2.2 Equation of motion on horizontal modes

The 1st and 2nd-order hydroelastic deflection of out of plane can be calculated by the general modal method with the coefficients of the mooring force. And, the 2nd-order horizontal motion modes can be analyzed in the same way as the calculation of the vertical deflection. I.e., the horizontal motions can be obtained if the beam theory which includes the rigid modes is applied to the equation of motion. Then the mooring forces can be included in the same formulation as equations in preceding section. Where, it is assumed that the motion modes of in-plane and out of plane are independent of each other. This assumption is validated in [5].

By the way, the horizontal motion is induced due only to the 2nd-order wave excitations because there is no 1st-order horizontal wave excitation based on the zero-draft assumption. Then, added mass and wave making damping of the horizontal motion modes become to zero because of zero-draft. The 2nd-order equation of motion of the difference frequency component is expressed as follows:

$$\sum_{r=1}^{4}\left(-\omega^{-2}M_{rs} - i\omega^{-}D_{rs} - f_{mprs}^{-}\right)\cdot q_r^{-} = F_{s,ij}^{-} + f_{mqs,ij}^{-}. \quad (27)$$

Where M_{rs} is generalized mass, $F_{s,ij}^{-}$ is the slowly varying wave drift force of the *s*-th motion mode. D_{rs} means the coefficient of the equivalent linear damping, which consists not only of the wave making damping but also of the coefficients of the friction force. The mode functions are defined as follows:

$\vec{\eta}_1 = (1,0,0)$, (surge)

$\vec{\eta}_2 = \left(-\frac{y}{B/2},0,0\right)$, (*x*-component of yaw)

$\vec{\eta}_3 = (0,1,0)$, (sway)

$\vec{\eta}_4 = \left(0,\frac{x}{L/2},0\right)$. (*y*-component of yaw)

Where, L is length of the body and B is width of the body. Only rigid modes are included on the horizontal motion in this paper.

2.3 Slowly varying wave drift force

The analytical method of the slowly varying wave drift foree has been presented in [6].

When the sum-frequency component of the 2nd-order wave force is neglected, slowly varying wave drift force is expressed as follows:

$$\bar{F}^{(2)}(t)=\mathrm{Re}\left[\sum_{i=1}^{\infty}\sum_{j=1}^{\infty}a_i a_j^{*}F_{ij}^{-}\cdot e^{-i\omega^{-}t}\right], \tag{28}$$

$$F_{ij}^{-}=\frac{1}{2}\left(f_{ij}^{-}+f_{ji}^{-*}\right), \tag{29}$$

$$f_{ij}^{-}=-\frac{\rho g}{2}\iint_{S_H}p_i^{(1)}\cdot\bar{N}_j^{(1)*}dS_H-\frac{\rho g}{4}\int_C\xi_i^{(1)}\xi_j^{(1)*}\cdot\vec{n}dC\,. \tag{30}$$

Where, $\zeta^{(1)}$ means a relative water level on the edge of the structure with the 1st-order elastic motion.

2.4 Tension in two-directional irregular wave

In case of frequency domain analysis, all 2nd-order components of the responses etc. in multi-directional waves are defined by the formulation in the sum of two-component waves. Now, if i component and j component correspond to each direction waves in eq.(29), the interaction of wave frequencies between the wave direction influences to the 2nd-order wave forces. But, the effect of such interaction has only to be considered when the tensions are analyzed. Thus, the 2nd-order tension in multi-directional waves is given by,

$$T^{(2)}(t)=\mathrm{Re}\left[\sum_{i_\theta=1}^{\infty}\sum_{j_\theta=1}^{\infty}\sum_{i=1}^{\infty}\sum_{j=1}^{\infty}a_{i_\theta,i}a_{j_\theta,j}^{*}\left(T_{pi_\theta j_\theta,ij}^{-}+T_{qi_\theta j_\theta,ij}^{-}\right)\cdot e^{-i\omega^{-}t}\right]. \tag{31}$$

Where, the 2nd-order sum frequency component is neglected. And, subscripts i and j indicate the component of the wave frequency. In addition, i_θ and j_θ mean the component of the wave direction. The secondary term with subscript q in right hand side of eq.(31) is defined as following equation,

$$T_{qij}^{-}=\frac{1}{4}\left(t_{qi_\theta j_\theta,ij}^{-}+t_{qi_\theta j_\theta,ji}^{-*}+t_{qj_\theta i_\theta,ij}^{-}+t_{qj_\theta i_\theta,ji}^{-*}\right). \tag{32}$$

2.5 Analysis of time series of responses

After the frequency response functions are given, the time series are calculated by the inverse Fourier transformation.

In case of the 1st-order problem, the time series $r^{(1)}(t)$ can be obtained due to the inverse Fourier transforming the frequency response function $R^{(1)}(\omega)$,

$$r^{(1)}(t)=\mathrm{Re}\left[\frac{1}{2\pi}\int_{-\infty}^{\infty}R^{(1)*}(\omega)a(\omega)\cdot e^{i\omega t}d\omega\right]. \tag{33}$$

In case of the 2nd-order problem, the time series $r^{(2)}(t)$ can be obtained from the frequency response function R^{-},

$$r^{(2)}(t)=\mathrm{Re}\left[\frac{1}{2\pi}\int_{-\infty}^{\infty}H(\omega)\cdot e^{i\omega t}d\omega\right], \tag{34a}$$

where,

$$H(\omega)=2\int_{-\infty}^{\infty}R_{i_\theta j_\theta}^{-*}(\omega+\omega_j)a_{i_\theta}(\omega+\omega_j)a_{j_\theta}^{*}(\omega_j)d\omega_j\,. \tag{34b}$$

In case of multi-directional irregular waves, the total time series is given by the sum of each result due to the direction waves.

$a(\omega)$ is a complex amplitude of the incident wave. If the time history of the incident wave $a'(t)$ is given, $a(\omega)$ can be calculated due to Fourier transformation as follows:

$$a(\omega)=\int_{-\infty}^{\infty}a'(t)\cdot e^{-i\omega t}dt\,. \tag{35}$$

Thus, the time series of the response which includes the 2nd-order response due to arbitrary incident waves can be analyzed. In the real computation, a program code of Fast Fourier Transformation (FFT) is applied to the inverse and normal Fourier transformation.

3. MODEL TEST

The corresponding model tests in irregular waves were carried out. The principal particular of the model is shown in Table 1. And, Fig.4 shows the set-up system. The model is made of styrene foam. The model is moored by four mooring lines, which are a linear spring with the spring constant of 2.0[kgf/m] and the initial tension of 0.247[kgf].

The incident waves were used long-crested irregular waves and two-directional irregular waves, which were head sea, beam sea and oblique sea (20 and 290 degrees) conditions. Then, Bretshneider-Mitsuyasu spectrum was applied.

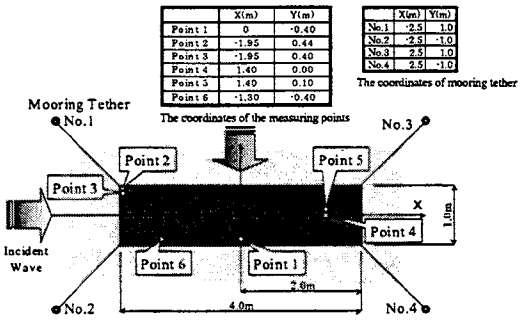

Figure 4 Set-up system of the experiment

Table 1 Principal particular of the model

Length (m)	4.00
Breadth (m)	1.00
Depth (m)	0.03
Young's mod. (kgf/m^2)	0.084×10^7
Displacement (kgf)	2.57(1.6+0.97)
Water depth (m)	2.20

Some of the wave conditions used for the model test are shown in Table 2 (a) and (b). (a) shows the conditions of the uni-directional irregular waves. (b) shows the conditions of the two-directional irregular waves.

Table 2 Conditions of the incident waves

(a) uni-directional waves

Case	1	2	3	4	5
$H_{1/3}$ (m)	0.04	0.06	0.03	0.04	0.06
$T_{1/3}$ (sec)	0.8	0.8	0.8	0.8	0.8
Direction (deg.)	0	0	20	20	20

(b) two-directional waves

Case	A	B
$H_{1/3}$ (m)	0.04+0.04	0.04+0.04
$T_{1/3}$ (sec)	0.8, 0.8	0.8, 0.8
Direction (deg.)	0-270	20-290

4. RESULTS AND DISCUSSIONS

4.1 Frequency response function

Firstly, the amplitudes of the vertical displacement in frequency domain are shown as follows. The experimental results are analyzed from the measured time series in irregular waves. Figures 5~7 show the results of vertical displacement at point 1 and Figs. 8~10 show the results at point 2. The descriptions (0.03m, 0.04m and 0.06m) in the figures mean the significant wave height. And the marks of circle etc. stand for the experimental results, while the solid line is the corresponding calculated results.

The calculation results agree fairly well with the experimental results. From the experimental results, the vertical displacement is just about linear to the wave amplitude. However, it can be found that the experimental results are very widely varied in Fig.10. This case may be due to the low accuracy of the analysis of the measured values.

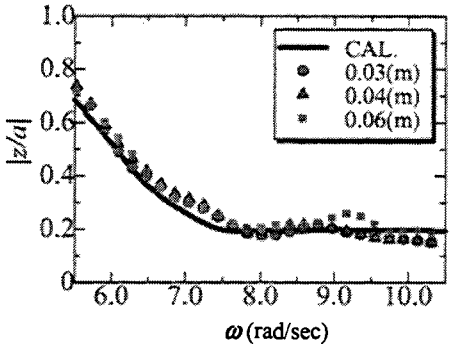

Figure 5 Vertical displacements at point 1 ($T_{1/3}$=0.8sec)

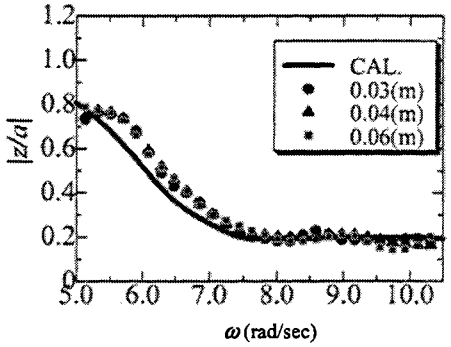

Figure 6 Vertical displacements at point 1 ($T_{1/3}$=0.9sec)

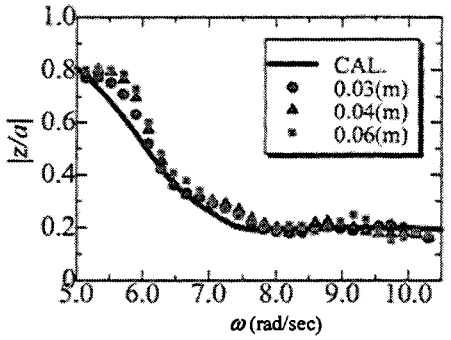

Figure 7 Vertical displacements at point 1 ($T_{1/3}$=1.0sec)

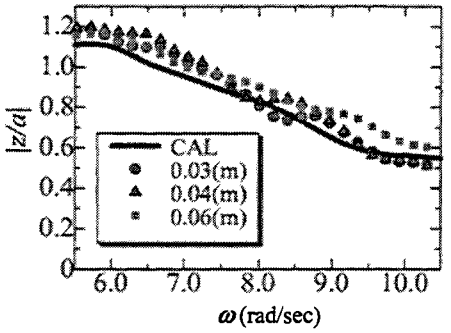

Figure 8 Vertical displacements at point 2 ($T_{1/3}$=0.8sec)

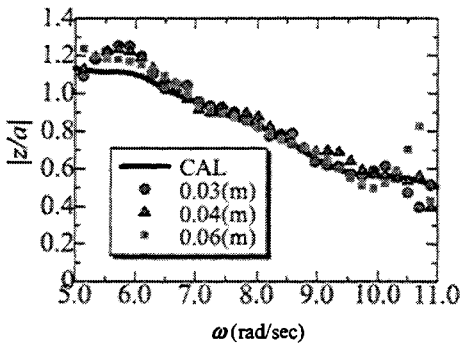

Figure 9 Vertical displacements at point 2 ($T_{1/3}$=0.9sec)

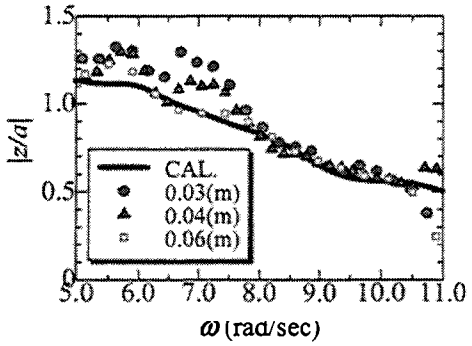

Figure 10 Vertical displacements at point 2 ($T_{1/3}$=1.0sec)

4.2 Time history of vertical displacement

The comparisons of the theoretical results with the measured results of time histories are shown in Figs.11~22. Figures 11~16 show the time series in the uni-directional irregular waves, and Fig.17~22 show the results in two-directional irregular waves. In all figures, both results are in the very good agreement. Thus, the present method and the assumption of the linear superposition theory are sufficiently validated.

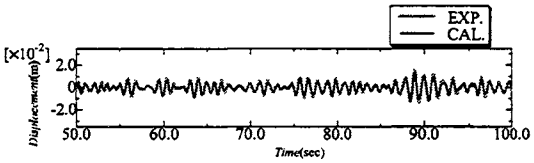

Figure 11 Time histories of vertical displacement at point 1 in Case 2

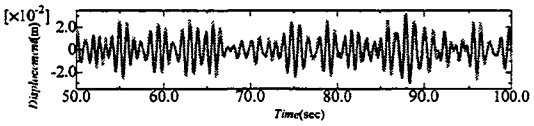

Figure 12 Time histories of vertical displacement at point 2 in Case 2

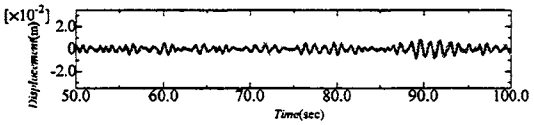

Figure 13 Time histories of vertical displacement at point 4 in Case 2

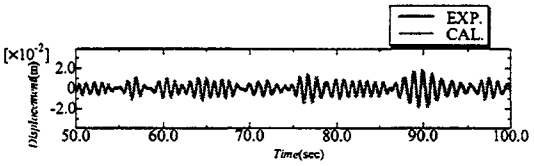

Figure 14 Time histories of vertical displacement at point 1 in Case 5

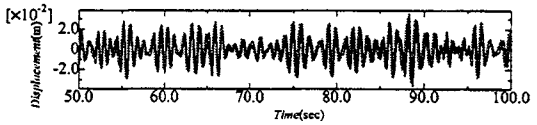

Figure 15 Time histories of vertical displacement at point 2 in Case 5

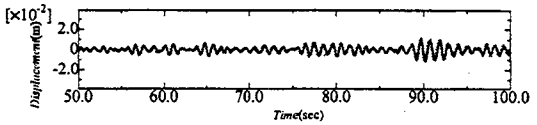

Figure 16 Time histories of vertical displacement at point 4 in Case 5

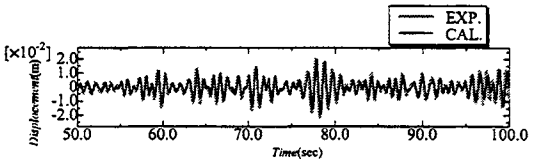

Figure 17 Time histories of vertical displacement at point 1 in Case A

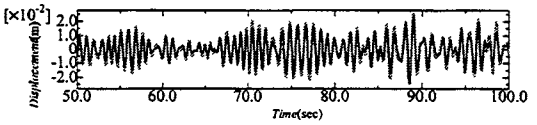

Figure 18 Time histories of vertical displacement at point 2 in Case A

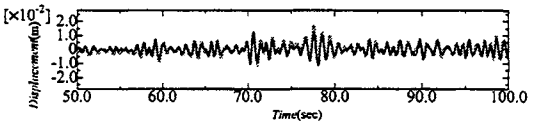

Figure 19 Time histories of vertical displacement at point 4 in Case A

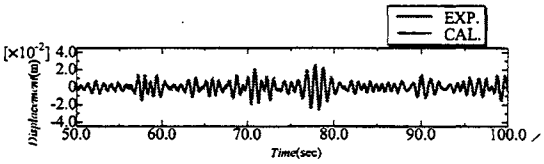

Figure 20 Time histories of vertical displacement at point 1 in Case B

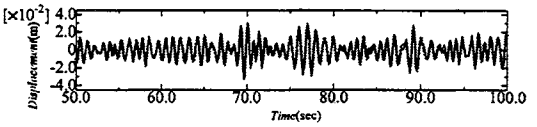

Figure 21 Time histories of vertical displacement at point 2 in Case B

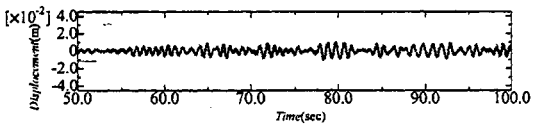

Figure 22 Time histories of vertical displacement at point 4 in Case B

4.3 Time history of tether tension

In this section, the tensions of mooring linear lines on the experimental model are shown as follows. They are comparisons of the calculated results with the measured results of time histories. The coefficients of the linear damping were as follows: D_{11} was 1.25, D_{22} was 0.8, D_{33} was 1.25 and D_{44} was 0.8 in calculations of all frequencies, when equation (27) which is equation of motion in frequency domain in order to predict the 2nd-order horizontal motion modes was solved. The above coefficients were reasonably defined by free oscillation tests. A coefficient of the wave making damping of a surge mode on the model with a draft of 2[mm] was 0.0025 at 4.2[rad./sec] which is a natural frequency of the surge motion. So, the linear damping forces are due to other effects.

4.3.1 *In case of uni-directional irregular waves*

Figures 23~28 show the comparison of the experimental value with theoretical values of the mooring tether tension. The theoretical values of a dark solid line are derived only from the 2nd-order horizontal motion. The dotted lines (total) that are computed one include not only the 2nd-order tension but also the 1st-order tension due to the 1st-order elastic motion of the model. The 1st-order tension due to the 1st-order horizontal motion is neglected in the present analytical method because of zero draft assumption.

We can find that the 2nd-order response is dominant included in the experimental values. And, almost tendency of the time history of the tension is dominated by the 2nd-order effect. However, the experimental values include the high frequency fluctuation, which correspond to components of the incident wave frequencies. So, on No.1 tether tension at weather side, it seems that the effect of the 1st-order response is large.

We think that the analytical results are in fairly good agreement with the experimental time series.

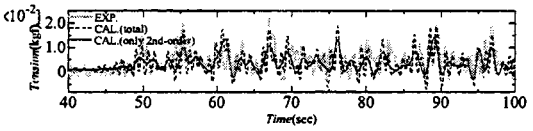

Figure 23 Time histories of tension on No.1 in Case 1

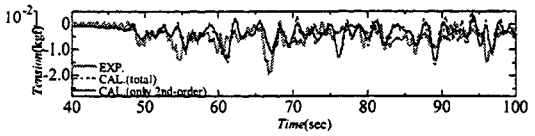

Figure 24 Time histories of tension on No.3 in Case 1

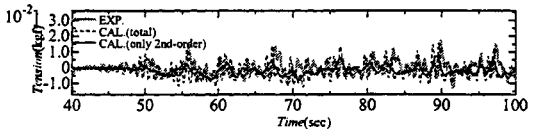

Figure 25 Time histories of tension on No.1 in Case 4

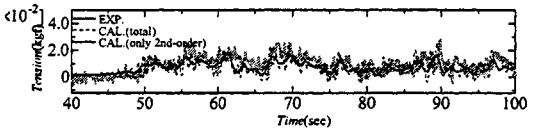

Figure 26 Time histories of tension on No.2 in Case 4

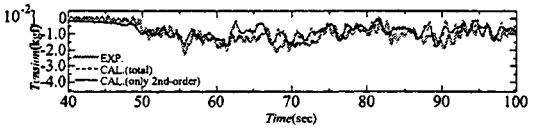

Figure 27 Time histories of tension on No.3 in Case 4

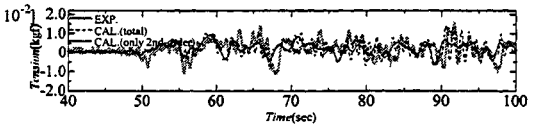

Figure 28 Time histories of tension on No.4 in Case 4

4.3.2 *In case of two-directional irregular waves*

The comparisons between the analytical and measured results of time histories in the two-directional irregular waves are shown in Figs.29~36.

In case of two-directional waves, we can find that the 1st-order response is small in the experimental value and in the calculation results of dotted lines in figures. Thus, there are a little difference between the solid lines and the dotted lines, both of which are calculated one. So, the response of the tension is dominated by the 2nd-order component. Where, the wave height is higher than the case of uni-directional conditions, because of the superposition of 0.04m+0.04m.

In case of A, the theoretical results are very good agreement with the measured values. While the theoretical and experimental values have a little difference, the tendency of the real phenomenon is well predicted.

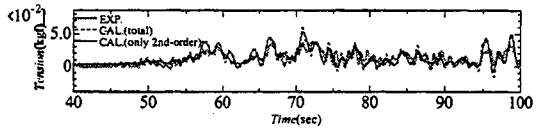

Figure 29 Time histories of tension on No.1 in Case A

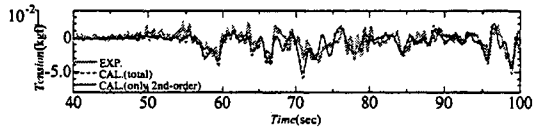

Figure 30 Time histories of tension on No.2 in Case A

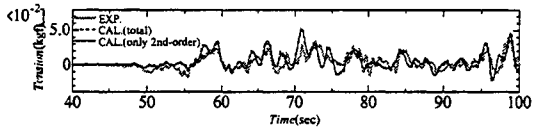

Figure 31 Time histories of tension on No.3 in Case A

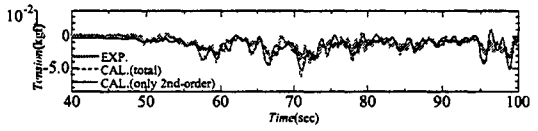

Figure 32 Time histories of tension on No.4 in Case A

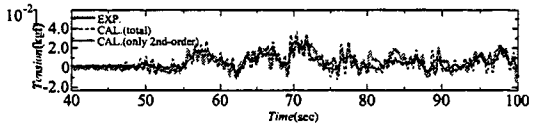

Figure 33 Time histories of tension on No.1 in Case B

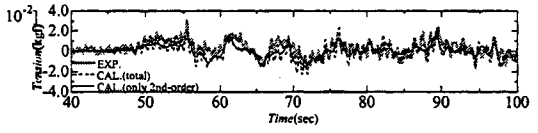

Figure 34 Time histories of tension on No.2 in Case B

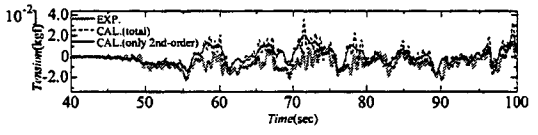

Figure 35 Time histories of tension on No.3 in Case B

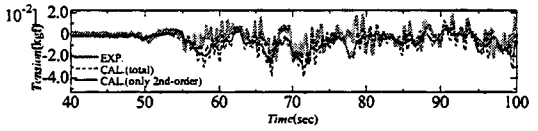

Figure 37 Time histories of tension on No.4 in Case B

4.3.3 *Effect of significant wave height*

The 2nd-order responses are in proportion to the square of the wave amplitude. So, if a significant wave height increases, effects of 2nd-order responses become larger. In this section, the comparisons of the tension in the oblique irregular wave (20 degrees) with the significant wave height of 0.03m with the tension in case of the 0.06m wave height are shown as follows.

Figures 38 and 39 are the results of the tension in case 3, which has 0.03m significant wave height. Figures 40 and 41 show the tension in case 5, which has 0.06m significant wave height. In case 3, as the effect of the 1st-order response are very large, a correlation of the analytical and experimental results is not well. On the other hand, in case 5, the analytical results are approximate agreement with the experiment.

From the above-mentioned results, the estimation method for the 1st-order tension should be reconsidered. I.e., we considered only the vertical deflection in the 1st-order tension. But, effects of the 1st-order horizontal motions should be included to the total tension. On the other hand, the 2nd-order responses must be always considered in order to estimate mooring tensions.

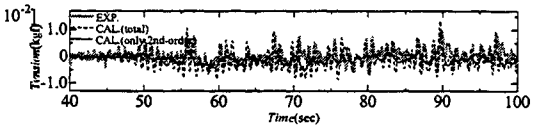

Figure 38 Time histories of tension on No.1 in Case 3

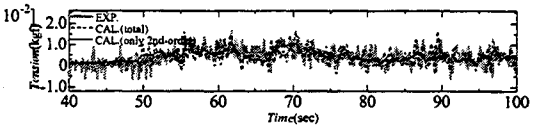

Figure 39 Time histories of tension on No.2 in Case 3

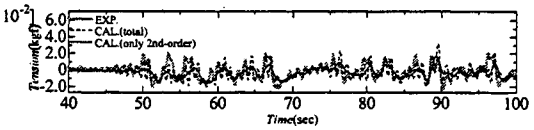

Figure 40 Time histories of tension on No.1 in Case 5

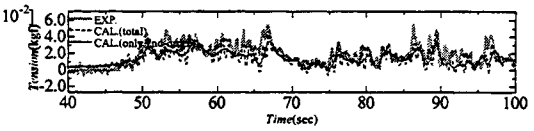

Figure 41 Time histories of tension on No.2 in Case 5

5. CONCLUSIONS

In this study, we validated the estimation method of time series of the responses of a VLFS in uni and two directional irregular waves as long as the equivalent linearization for the mooring line system in held. And, the analytical method for mooring tension was discussed. As a consequence, following information and conclusions are obtained.

1) The assumption of the linear superposition principle in order to predict the elastic responses of the VLFS is effective, not only in uni-directional irregular waves but also in two-directional irregular waves.
2) The time series of the second-order responses can be predicted by the present method if mooring system can be represented by equivalent linear system.
3) The effect of the linear damping forces proportional to the horizontal velocity of the motions is important in order to predict accurate slow drift motions.
4) The total tension on a mooring line is dominated by the second-order responses of the horizontal motions, while the effect of the first-order motions cannot be neglected in irregular waves with smaller significant wave height.
5) The prediction method of the slowly varying wave drift forces is validated in uni and two-directional irregular waves.

REFERENCES

[1] Ohmatsu, S., "Numerical calculation of hydroelastic behavior of VLFS in time domain," *Proc. The 2nd Int. Conference on Hydroelasticity in Marine Tech., Fukuoka, Japan*, pages 89-98, 1998.

[2] Ma, M. and Hirayama, T., "Effect of short-crested irregular waves on response of a very large floating structure," *Proc. 2nd Int. Conference on Hydroelasticity in Marine Tech., Fukuoka, Japan*, pages 99-108, 1998.

[3] Masuda, K., Maeda, H., Ikoma, T., Arita, M., Sano, K. and Suzuki, K., "A Study on Characteristics of Hydro-elastic Responses due to Second-order Long Period Waves for Very Large Floating Structure," *Proc. 14th Ocean Eng. Symposium, Society of Naval Architects of Japan*, pages 453-460, 1998. (in Japanese)

[4] Nagai, T., Masuda, K., Fujisawa, Y. and Ikoma, T., "Study on Second-order Sum and Difference-frequency Responses on Conical Floating Structure," *J. Society of Naval Architects of Japan*, pages 119-130, 1994. (in Japanese)

[5] Maeda, H., Ikoma, T., Rheem, C.K. and Atake, K., "Behavior of Very Large Floating Structure with Mooring System," *Proc. 18th Int. Conference on OMAE, OMAE'99, St. John's, Newfoundland, Canada, ASME*, File No. 3254, 1999.

[6] Maeda, H., Ikoma, T. and Masuda, K., "Wave Drift Forces of a Very Large Flexible Floating Structure," *Proc. 7th Int. Symposium on PRADS, PRADS'98, The Hague, The Nether land*, pages 1037-1043, 1998.

[7] Maeda, H., Masuda, K., Miyajima, S. and Ikoma, T., "Hydroelastic Responses of Pontoon Type Very Large Floating Offshore Structure," *Proc. 15th Int. Conference on OMAE, OMAE'96, Florence, Italy, ASME*, pages 407-414, 1996.

[8] Pinkster, J. A., "Low-frequency second order wave exciting force on floating structures," *Netherlands Ship Model Basin, Publication No.650*, 1980.

[9] Kashiwagi, M. and Furukawa, C., "A MODE-EXPANSION METHOD OF PREDICTING HYDROELASTIC BEHAVIOR OF A SHALLOW-DRAFT VLFS," *Proc. 16th Int. Conference on OMAE, Vol.VI, OMAE'97, Yokohama, Japan, ASME*, pages 179-186, 1997.

PROCEEDINGS OF THE THIRD INTERNATIONAL WORKSHOP ON VERY LARGE FLOATING STRUCTURES
(VLFS '99), VOL. I, EDS. R.C. ERTEKIN & J.W. KIM, 22-24 SEPTEMBER 1999, HONOLULU, HAWAII, USA

EFFECT OF WAVE DRIFT FORCES ON HUGE FLOATING STRUCTURES IN WIND AND WAVES

By Y. Inoue, Islam M. Rafiqul & M. Murai

Graduate School of Engineering, Yokohama National University, Japan

ABSTRACT

The huge floating structure which can be used for as an airport or an offshore city may be as large as several kilometers long and wide. Design procedures of such huge floating structures involves many new areas and special analyses are required to find out their behavior in actual operating conditions. Wave forces as well as wave drift forces and wind forces are very important environmental forces on such a huge floating structures. The precise evaluation of these forces can lead to better prediction of dynamic behavior and design of the structure.

In the present study, 3-D source-sink method has been applied to a arbitrary shaped huge floating object and the hydrodynamic forces in irregular waves and the motion in six degrees of freedom have been calculated. The horizontal drift forces and moments have also been calculated and to allow non-linearity of wave drift forces and wind forces, motion equation in time domain is also numerically solved. As for numerical example, time domain analyses are carried out for a huge box shaped floating structure in various wind and wave conditions. And the amount of the effect of wave drift forces in total environmental forces are discussed.

1. INTRODUCTION

In recent years many researches have been carried out on Very Large Floating Structure (VLFS) in order to utilize the Ocean space effectively as a place to build infrastructure including transport related facilities such as floating airport, floating bridges, artificial floating cities etc. These types of structures are usually several kilometers long and wide in size. The shape of such structures are much more complex than normal sized structures. So more detail analyses are required to find out their actual behavior in ocean environments. The wave induced motion of these structures will be significantly affected. As the structure has vast surface area and large freeboard compared with the shallow draft, so wind forces and its effect on motion should be investigated and at the same time the effect of wave drift forces should be examined to keep the position of the structures. In the case of huge floating structures, the relative stiffness of the structures become softer but in the present analysis is restricted to be based on hydrodynamics of rigid body. Many researches have been done on flexible floating structures; recently Newman[7] (1994) has presented a method of solving three dimensional problems including generalized modes which is an extension of usual six rigid body motion modes. Important other works in hydroelasticity has been carried out by research group of Bishop and Price[1], their effort led to a full 3-D hydroelasticity theory and Inoue et al.[5,6] showed a conceptual design and analyzed the behavior of the structure due to environmental forces. Murai et al.[9] has also given a prediction method of hydroelastic behaviors of a very large floating structures and many researches have been continuing on such a huge floating structures in order to predict in actual environmental condition.

However, in the present study in order to discuss the effect of non-linear wave drift forces and wind forces 3-D source-sink method is applied for evaluation of hydrodynamic forces and linear wave induced rigid body motions and a non-linear time domain simulation has been carried in an irregular sea of ISSC spectrum. The accuracy of the present study is verified through a comparative study.

2. MOTION EQUATIONS

2. 1 Motion equation in frequency domain

To describe the motion of the structure two kinds of co-ordinate systems, one is fixed to the body and another is fixed to the space are introduced. The equation of motion can be expressed by the following matrix relationship :

$$\sum_{j=1}^{6}(M_{kj}+a_{kj})\ddot{X}_j + b_{kj}\dot{X}_j + C_{kj}X_j = F_k \quad \text{.....(1)}$$

$$(k = 1....6)$$

where,

M_{kj} = inertia matrix in k - mode due to the motion in j - mode

a_{kj} = added mass coefficient matrix of kj

b_{kj} = damping coefficient matrix of kj

C_{kj} = hydrostatic restoring force coefficient matrix of kj

F_k = wave exciting force and moments vector in k - mode

X_j = vector containing the three translational and three rotational about the co-ordinate axes in j - mode.

For harmonic motions in waves, the wave exciting forces and the hydrodynamic radiation forces can be formulated separately. The derivation of these quantities in terms of linear potential theory is given in ref[3].

2.2 Equation of motion in time domain

Based on Cummins[2] theory, the equation of motion of the structure in time domain may be written as follows:

$$\sum_{j=1}^{6}(M_{kj}+m_{kj})\ddot{X}_j + \int_{-\infty}^{t} R_{kj}(t-\tau)\dot{X}_j d\tau + B_n\left|\dot{X}_j\right|\dot{X}_j + C_{kj}X_j = F_k(t).....(2)$$

where,

M_{kj} =inertia matrix of kj

m_{kj} = frequency independent added mass matrix of kj

R_{kj} = retardation function matrix of kj

B_n = non-linear damping coefficient matrix of kj

C_{kj} = restoring coefficient matrix of kj

$F_k(t)$ = arbitrary time varying external forces in 'k' mode which contains first order wave forces, forces due to wind and second order mean and slowly varying drift forces. Wave drift forces are computed in the form of frequency domain transfer function based on three dimensional source-sink method and the slowly varying drift forces caused by difference frequency can be written as :

$$F(t) = \sum_{j=1}^{N}\sum_{k=1}^{N} a_j a_k\left[P_{jk}\cos\left\{(\omega_j-\omega_k)t+(\varepsilon_j-\varepsilon_k)\right\} + Q_{jk}\sin\left\{(\omega_j-\omega_k)t+(\varepsilon_j-\varepsilon_k)\right\}\right].....(3)$$

where, the coefficient P_{jk} and Q_{jk} are the phase and out of phase second order transfer function for the difference frequency loads and are the independent of wave amplitude.

$a_j = \sqrt{2S_j(\omega_j)\Delta\omega}$ and ε_j is the random phase angles

ω_j = the wave frequencies

$S_j(\omega_j)$ = spectral density corresponding to wave frequency ω_j

$\Delta\omega$ = frequency width

Newman[8] (1974) proposed that P_{jk} and Q_{jk} can be approximated by P_{jj}, P_{kk}, Q_{jj} and Q_{kk} and this reduces the computer time significantly. Newmans approximation implies that

$P_{jk} = P_{kj} = 0.5(P_{jj}+P_{kk})$

and $Q_{jk} = Q_{kj} = 0$

The wind forces and moments are calculated using Davenport wind spectrum and the method is also derived in ref[4].

Components of m_{kj} and R_{kj} matrices have the following form

$$m_{kj} = a_{kj}(\dot{\omega}) + \frac{1}{\dot{\omega}}\int_0^{\infty} R_{kj}(t)\sin(\dot{\omega}t)dt.....(4)$$

$$R_{kj} = \frac{2}{\pi}\int_0^{\infty} b_{kj}(\omega)\cos(\omega t)d\omega.....(5)$$

Where, a_{kj} and b_{kj} are the frequency -dependent added mass and damping coefficient matrices respectively and $\dot{\omega}$ is the constant frequency which can be chosen arbitrarily.

3. COMPARATIVE STUDY

In order to validate the result of this study, numerical calculation is carried out for the same structure by 3-D separated region method[9] . To compare the present study Fig. 2.2 has been plotted in beam sea condition and it shows the heave motion of the structure, the agreement may be satisfactory with the separated region method which is based on elastic body and in this case the structural rigidity has been taken as 4.945×10^{12} kgf-m which should be considered as almost a rigid body. Fig. 2.3 shows the roll motion of the structure, in this case, the agreement is also may be good. The reason for small differences between these two methods are : numerical program for 3-D source-

sink method is based on rigid body where as the 3-D separated region method is based on hydroelastic body. And the both methods have some numerical errors due to computer abilities and others. So in view of this fact, the result may be acceptable.

4. RESULTS AND DISCUSSIONS

The method described above is applied to a box shaped Very Large Floating Structure which can be used for a Floating Airport. The principal dimensions of the structure is given in Table 1. The responses of such huge floating structure in the conditions of the head sea and beam sea at a water depth of 100 m are calculated. As the structure is very big and due to the computer hardware limitation and also to save computational time smaller meshes are used in longitudinal direction for the head sea condition and course meshes are used in the transverse direction (Fig. 1(a)) and similarly smaller meshes are used in transverse direction during calculation in beam sea condition and course meshes are used in the longitudinal direction (Fig. 1(b)). Figure 1.2 through Fig. 1.3 show the example results of surge, heave and pitch motion of VLFS in head sea condition. From these figures, it is seen that the motion response in surge, heave and pitch mode exhibit peak at λ/B : 0.425, because heave natural period is around 17.5 seconds. Figure 2.1 through Fig. 2.3 describe the motion responses in beam sea condition and Fig. 2.2 and Fig. 2.3 show the comparative motion response in heave and roll in 3-D source-sink method and separated region method where the results show in that two different methods may be acceptable although the results shown are based on two different methods. Figure 3.1 and Fig. 3.2 show the non-dimensional wave drift forces in head and beam sea condition. In order to discuss the effect of the drift forces and moment and also the effect of wind forces a time domain simulation is carried out in an irregular sea of ISSC spectrum density with the significant wave height 10.0 m and mean wave period 10.0 seconds. The simulation results are plotted in Fig. 4.1 through Fig. 4.4. In Fig. 4.2 and Fig. 4.3 second order slow drift surge motion as well as first order wave induced motion are also present in the plotting but the second order slow drift response is not clear, so in order to ensure the effect of slowly varying drift forces power spectral densities are plotted in Fig. 5.1 and Fig. 5.2. In Fig. 5.2 left peak clearly illustrates response for the slowly varying drift force where as in Fig. 5.1 does not dominate that type of peak, because this curve is plotted excluding the effect of wave drift forces and moments. From Fig. 5.2, it is also shown that the effect of second order drift forces is not small as compared with first order wave forces. Figure 6.1 and Fig. 6.2 represent the time history of slowly varying drift forces in head and beam sea conditions respectively.

5. CONCLUSION

The authors here tried to give some idea of the effect of drift forces on such a huge floating structure in the total environmental condition and also from the forgoing discussion, the following conclusion can be drawn:

-The effect of second order wave drift forces is about the same order of the first order wave forces as can be seen from Fig. 5.2, so during design of such huge floating structure one must care of the second order forces.

-As the used meshes are not in equal size in all parts of the structure, so more detail analyses should be required in order to find the convergence of the result and also model testing can lead to better prediction of the behavior of the structure.

Finally, authors recommended that as the structure considered here are stiff and rigid but in practice such a long and wide structures expected to be elastic and also influenced by the bending, torsion and hydro-elastic effects, so these important effects can not be neglected in the total analysis of the system which are outside the scope of this paper and hence more detail studies are required in this field.

Acknowledgment

This research was supported by the grant-in-aid for Scientific Research of the Ministry of Education, Science, Sports and Culture (Monbusho), Japan.

References

1. Bishop, R.E.D and Price W. G (1979) "Hydroelasticity of Ships" Cambridge University Press.
2. Cummins, W.E. (1962) "The impulse response function and ship motions" Schifftechnik, Bd, 101-103.
3. Inoue. Y. and Islam, M. R. (1999) "Comparative Study of Numerical Simulation and the Experimental Results for a Parallely Connected FPSO and LNG in waves" ISOPE-99.
4. Inoue, Y. and Islam, M. R. "Relative motions of Multiple Floating Offshore Structures" OMAE-99
5. Inoue, et al. (1995) " Dynamic behaviors of floating airport and its effect on Ocean current" Proceedings of 5th International Offshore and Polar Engineering Conference (ISOPE), Netherlands.
6. Inoue, et al. (1996) "A study on the hydro-elastic

response of very large floating structure with floating breakwater in waves", JSNAJ, Vol. 180.
7. Newman, J. N. (1994) "Wave effects on deformable bodies" Journal of Applied Ocean Research.
8. Newman, J, N. (1974) "Second order, slowly varying forces on vessels in irregular waves" Proc. Int. Symp. Dynamics of Marine Vehicles and Structures in Waves, ed. R. E. D. Bishop & W. G. Price, pp. 182-6 London: Mechanical Engineering Publications Ltd.
9. Murai, M. , Kagemoto, H. and Fujino, M (1997) "On the predictions of hydroelastic behaviors of a huge floating structure in waves" JSNAJ, Vol. 183, PP 199-210.

Table 1
Principal particulars of the structure

Specification	Dimension
Length (L)	3000 m
Breadth (B)	1000 m
Draft (T)	2.0 m
Depth (D)	4.0 m
Displacement (W)	6114000 (ton)
Water Depth (h)	100 m

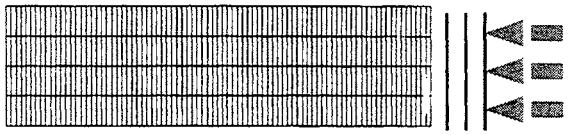

Incident wave

Fig . 1(a) : Mesh considered for the head wave condition

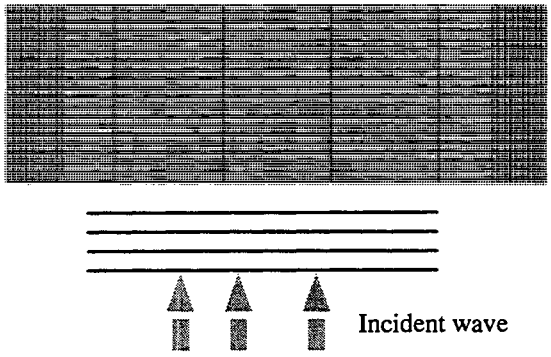

Fig. 1(b) Mesh considered for the beam wave condition

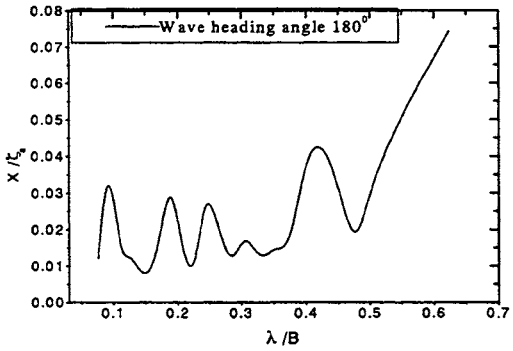

Fig.1.1 Surge motion of the structure

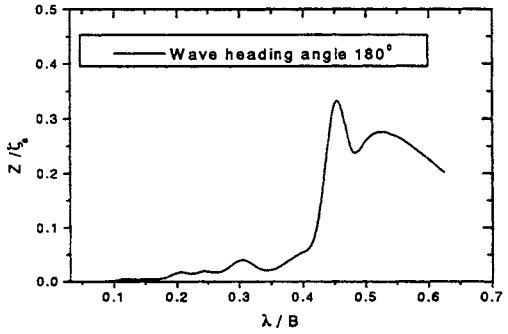

Fig.1.2 Heave motion of the structure

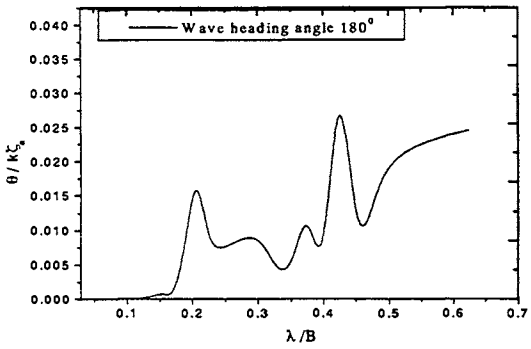

Fig.1.3 Pitch motion of the stucture

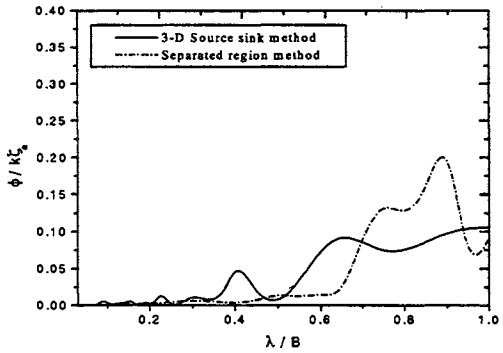

Fig. 2.3 Roll motion of the structure

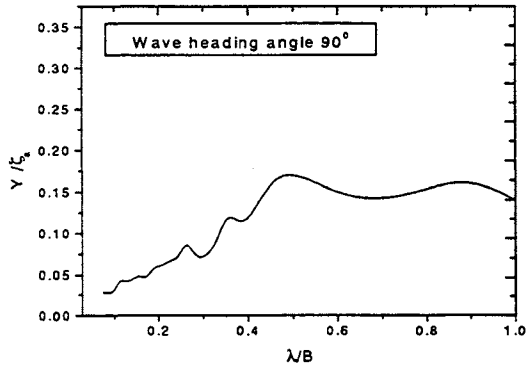

Fig.2.1 Sway motion of the structure

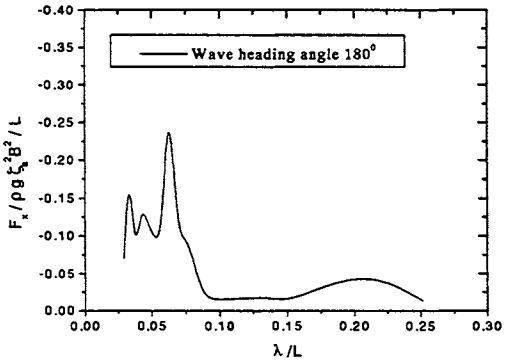

Fig. 3.1 Surge Drift Force

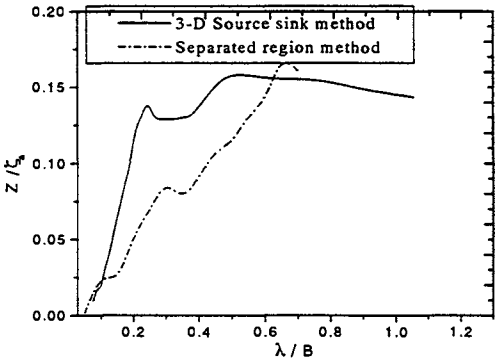

Fig.2.2 Heave motion of the structure
(wave heading angle 90°)

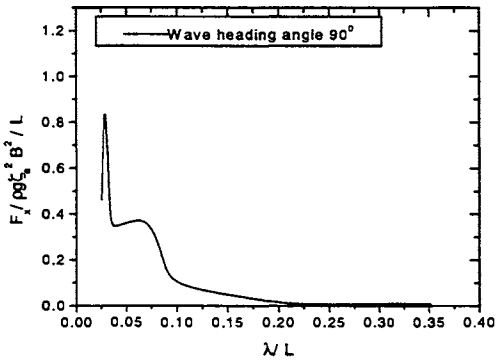

Fig. 3.2 Sway Drift force

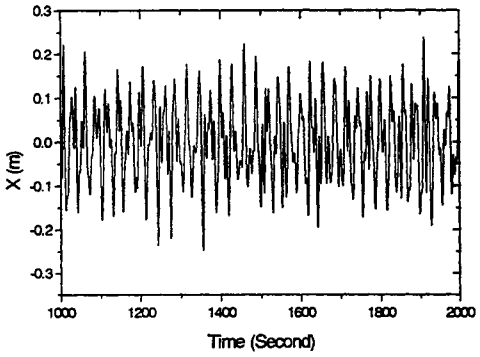

Fig.4.1 Time history of surge motion (excluding the wind and drift forces)

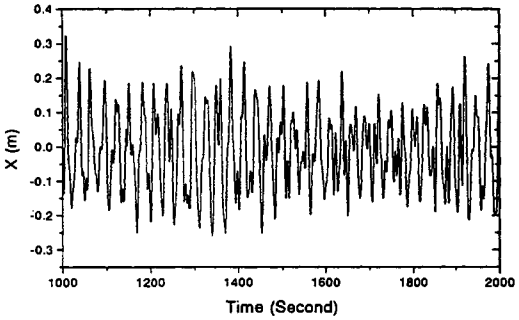

Fig. 4.2 Time history of surge motion (including the drift forces and excluding the wind forcess)

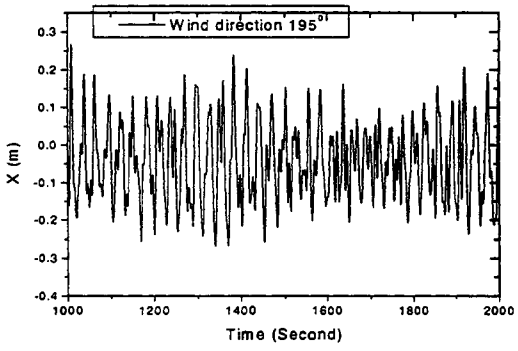

Fig. 4.3 Time history surge motion (including the wind and drift forces)

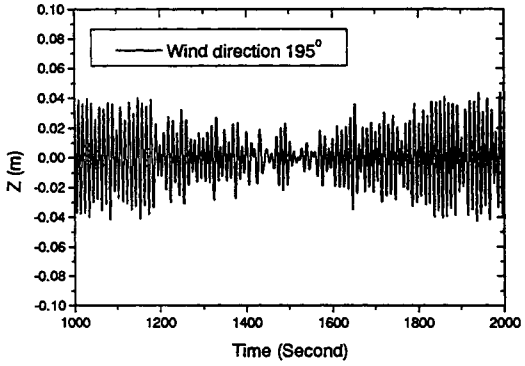

Fig. 4.4 Time history of heave motion

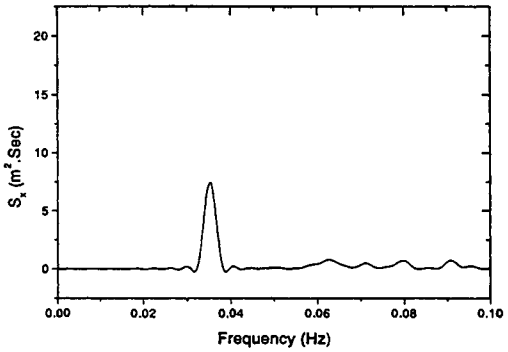

Fig. 5.1 Responses of Spectrum in surge

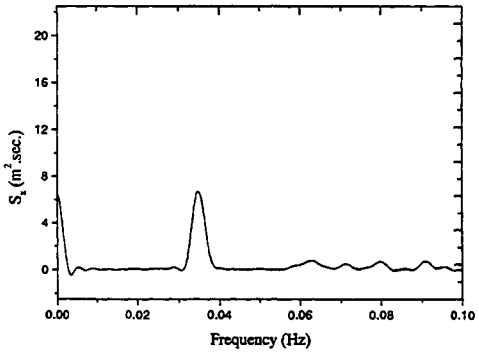

Fig. 5.2 Spectrum of responses in surge including the effect of slowly varying drift forces

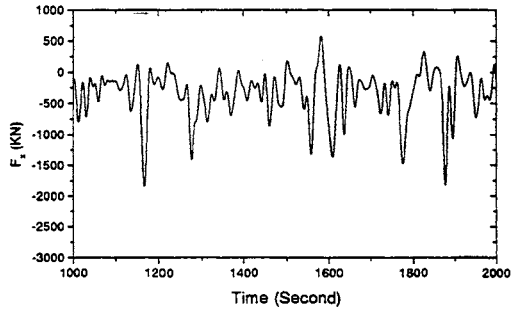

Fig. 6.1 Time history Slowly varying drift force in head sea condition

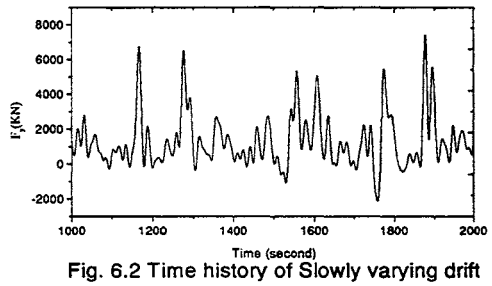

Fig. 6.2 Time history of Slowly varying drift force in beam sea condition

PROCEEDINGS OF THE THIRD INTERNATIONAL WORKSHOP ON VERY LARGE FLOATING STRUCTURES
(VLFS '99), VOL. I, EDS. R.C. ERTEKIN & J.W. KIM, 22-24 SEPTEMBER 1999, HONOLULU, HAWAII, USA

WAVE EFFECTS ON LARGE FLOATING STRUCTURES WITH AIR CUSHIONS

C.-H. Lee and J. N. Newman
MIT *

ABSTRACT

An analysis is made of a VLFS which is partially supported by an air cushion. The interface between the air cushion and the water is considered to be a free surface. The elevation of this surface is represented by an appropriate set of Fourier generalized modes, and extended equations of motion are derived for the rigid-body motions and generalized modes. The dynamic effect of the air is represented by appropriate acoustic added-mass coefficients. The hydrodynamic coefficients are evaluated using the B-spline based panel code HIPAN. Illustrative computations are presented which show significant resonant effects.

1. INTRODUCTION

One of the most important challenges in the design of very large floating structures (VLFS) is to achieve the required overall length without incurring large wave-induced loads. Some designs proposed for floating airports have included massive breakwaters to protect the structure from incident waves. Most concepts for mobile offshore bases consist of several relatively short modules with flexible connections. A design proposed by Norwegian Contractors uses a single hull with long cantilever extensions to achieve the required deck length.

Pinkster *et al.* (1997, 1998) describe an interesting alternative where the structure is supported partially by air cushions. This is achieved by the use of side and end walls extending vertically to a sufficient depth to retain the interior air, which has a positive pressure relative to the atmosphere to provide static support. Assuming a uniform pressure in the air chamber, the wave-induced moments and structural loads will be substantially reduced by comparison to a conventional hull of the same dimensions. The results presented by Pinkster *et al.* include computations of the body motions and air pressure, based on a low-order panel method, as well as supporting experiments. However their results are limited to cases where the length of the vessel is less than 3-4 wavelengths ($L/\lambda < 3-4$). For VLFS applications it is necessary to consider the regime where $L/\lambda > 10$. It is not practical to use the low-order panel method, due to the large number of panels required in this regime, and the assumption of a uniform pressure distribution is questionable.

In this paper we consider the example of a rectangular barge with one pressurized air chamber. The hydrodynamic analysis is performed using the higher-order panel program HIPAN described by Lee (1997). The motion in the air chamber is represented by an eigenfunction expansion. The elevation of the interface is represented by an appropriate set of Fourier generalized modes, with unknown amplitudes. Imposing the condition of pressure continuity across the interface leads to an extended set of 'generalized equations of motion' including the conventional rigid-body motions and the interface Fourier modes.

Since a set of specific generalized modes are prescribed for the elevation of the interface, conventional Neumann conditions specify the normal velocity on the interface. Thus the interface and the submerged body surface can be combined to form one 'global body surface' with the same type of boundary condition. Green's theorem is used to solve for the velocity potential on this global surface. This approach is somewhat indirect from the physical standpoint, and can be contrasted with an approach where the pneumatic pressure is specified directly on the interface. That 'direct' approach leads to a modified integral equation for the unknown potential on the submerged structure surface only.

These two approaches are described further by Lee, Newman & Nielsen (1996) in their analysis of an oscillating water column device for wave-power conversion. The advantages of the indirect approach are (1) it can be implemented numerically without modification of the panel program, which

*Cambridge, MA 02139, USA E-Mail: chlee@rainbow.mit.edu and jnn@mit.edu

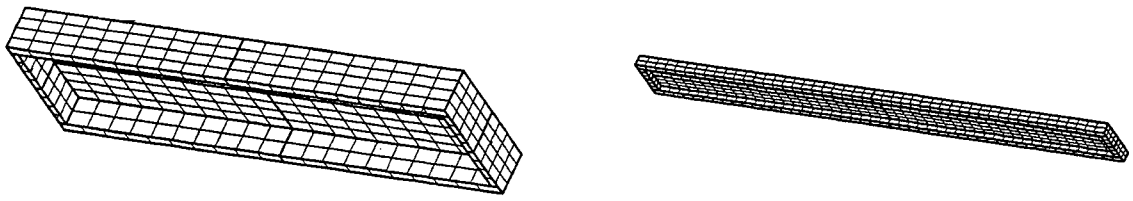

Figure 1: Perspective views of the submerged portions of the model used by Pinkster *et al* (left) and the prototype VLFS (right). The view is from below, with patches outlined by heavy lines and panels by light lines. Part of the air/water interface is visible inside the vertical walls. Pertinent dimensions of the model are length 2.5m, beam 0.78m, and draft 0.15m to the bottom of the walls. The wall thickness is 0.02m at the ends and 0.06m at the sides. The air chamber extends from 0.05m below the exterior free surface to 0.13m above. The corresponding dimensions for the prototype are length 1500m, beam 150m, draft 32m, wall thickness 20m, with the air chamber extending from 16m below the free surface to 20m above.

accepts arbitrary generalized modes; (2) the use of a relatively small number of orthogonal Fourier modes is more efficient computationally than the need to integrate the pressure accurately over the domain of the interface; and (3) poor conditioning of the linear system corresponding to the discretized integral equation, in the vicinity of physically relevant resonances, is transferred to the much smaller system of equations of motion. On the other hand, the direct approach restricts the computational domain of the unknown potential to a smaller boundary surface, and it is more easily understood.

Our method is first applied to the model used by Pinkster *et al* (1998), shown in Figure 1 (left), to permit comparison and verification of the results. We then analyze the prototype barge shown in Figure 1 (right), with a length of 1500m and other dimensions selected to be representative of a mobile offshore base. For this prototype the air cushion supports 55% of the total displacement, and the remainder is provided by the buoyancy of the vertical walls which contain the air chamber.

Two obvious sources of resonance exist for the motions of the air/water interface, sloshing due to standing waves in the water and acoustic standing waves in the air chamber. The resonant frequencies can be estimated easily for a rectangular air chamber with vertical side walls. Since the structure is much longer than the hydrodynamic wavelength, sloshing can be expected for several adjacent wave periods of spectral interest. Acoustic resonance may also occur within the range of relevant wave periods for a structure as large as a VLFS. For periods of 6-9 seconds the acoustic wavelength is 2000-3000m, and the first half-wave resonance will occur in a chamber of length 1000-1500m.

The possible importance of acoustic resonance was one of the motivations for this work, suggested by the analogous 'cobblestone effect' experienced by surface-effect ships. This phenomenon is described by Nakos *et al* (1991) and Ulstein & Faltinsen (1996). The present computational results for the prototype VLFS indicate that the most important resonant response in heave can be predicted in a similar manner as in the simplified analysis of Nakos *et al*, with the inertia force balanced by the sum of the hydrostatic and aerodynamic stiffness coefficients, which are of comparable orders of magnitude. For pitch the most significant resonance is due only to the moment of inertia of the body and the hydrostatic restoring moment, as in the case of a conventional slender ship. The heave resonant frequency is substantially larger than for pitch.

The analysis which follows is based on linearized potential theory. Plane progressive waves of frequency ω move in the longitudinal direction. The unsteady motions of the fluid, structure, and air are oscillatory at the same frequency. The fluid depth is assumed to be infinite. For simplicity we consider only head seas. Thus the rigid-body motions include surge, heave, and pitch, and the Fourier modes are restricted to be symmetrical in the transverse direction. After outlining the method of analysis, computational results will be presented and discussed.

2. FORMULATION

We consider a rigid body floating on the free surface, partially supported by the pressure in a rectangular air chamber ($-a < x < a, -b < y < b, z_1 < z < z_2$). Here $2a$ is the length, $2b$ the width, and $z_2 - z_1$ the height of the air chamber, $z = 0$ is the plane of the undisturbed free surface outside the body, and $z = z_1 < 0$ is the mean position of the interface. The static pressure in the chamber is $p_0 = -\rho_w g z_1 > 0$, where ρ_w is the density of water and g denotes gravity. The subscripts a and w are used to designate the air/water densities, respectively. For other parameters and variables upper/lower case symbols are used. The sides, ends, and top of the chamber are fixed with respect to the body.

The fixed surface of the air chamber is denoted by S_c and the wetted surface of the body by S_b. The air/water interface is S_i. The complete closed surface bounding the air chamber is $S_a = S_c + S_i$. The complete boundary surface of the water is $S_w = S_b + S_i$, and the free surface outside the body.

The motions of the air and water are represented by the velocity potentials

$$\mathrm{Re}\{\Phi(x,y,z)\,\mathrm{e}^{i\omega t}\} \quad \text{and} \quad \mathrm{Re}\{\phi(x,y,z)\,\mathrm{e}^{i\omega t}\} \tag{1}$$

The time-dependent factor $\mathrm{e}^{i\omega t}$ is assumed implicitly hereafter. These potentials are governed by the Helmholtz and Laplace equations,

$$\nabla^2\Phi + K^2\Phi = 0 \quad \text{and} \quad \nabla^2\phi = 0 \tag{2}$$

which are valid throughout the corresponding physical domains. Here $K = \omega/c_0$ is the acoustic wavenumber and c_0 is the velocity of linearized sound waves. From the linearized Bernoulli equation the pressures are

$$P(x,y,z) = -\mathrm{i}\rho_a\omega\Phi(x,y,z) \tag{3}$$

$$p(x,y,z) = -\mathrm{i}\rho_w\omega\phi(x,y,z) - \rho_w g(z+c-d) \tag{4}$$

The aerostatic pressure $-\rho_a g(z+c-d)$ is neglected on the assumption that $c_0 >> g/\omega$.

The elevation of the interface can be represented by the superposition of the following modes: (a) uniform vertical motion with amplitude equal to the heaving motion of the body, (b) the vertical component of the rigid-body rotations in roll and pitch, and (c) a complete set of orthogonal Fourier modes

$$\zeta_{mn}(x,y) = \begin{pmatrix}\cos u_m x \\ \sin u_m x\end{pmatrix}\begin{pmatrix}\cos v_n y \\ \sin v_n y\end{pmatrix} \tag{5}$$

where

$$u_m = \frac{m\pi}{2a}, \quad v_n = \frac{n\pi}{2b} \tag{6}$$

and the integers m and n are even or odd, respectively, for the modes proportional to the cosine or sine. Each Fourier mode is associated with a corresponding pair of velocity potentials ϕ_j and Φ_j ($j \geq 7$) which are appended to the six radiation potentials ($j = 1-6$) for the rigid-body motions. The explicit relationship between (m,n) and j is not important, as long as the expansion is complete. Thus, for $7 \leq j \leq \infty$ we require that all combinations of m and n are represented in the ranges $0 \leq m \leq \infty$, $0 \leq n \leq \infty$. (In the numerical implementation to follow, the upper limits of these ranges are truncated at sufficiently large finite values to demonstrate convergence of the results.) It is convenient to use the notation ζ_j in place of ζ_{mn}. The elevation of the interface, relative to its static level, is

$$\zeta = \sum_{j=1}^{\infty} \xi_j \zeta_j \tag{7}$$

The potentials can be expanded in the forms

$$\Phi = i\omega \sum_{j=1}^{\infty} \xi_j \Phi_j \tag{8}$$

$$\phi = \phi_D + i\omega \sum_{j=1}^{\infty} \xi_j \phi_j \tag{9}$$

Here ξ_j ($j = 1-6$) are the amplitudes of the six rigid-body motions and ξ_j ($j \geq 7$) are the amplitudes of the Fourier modes for the interface elevation. The kinematic boundary conditions on S_a for $j = 1-6$ are

$$\Phi_{jn} = N_j \quad \text{on} \quad S_a \tag{10}$$

where $(N_1, N_2, N_3) = \mathbf{N}$ is the unit normal vector pointing out of the air chamber, and $(N_4, N_5, N_6) = \mathbf{x} \times \mathbf{N}$. For the generalized modes ($j \geq 7$) we define

$$N_j = -\zeta_j(x,y) \quad \text{on} \quad S_i, \quad N_j = 0 \quad \text{on} \quad S_c \tag{11}$$

Similarly for the fluid domain,

$$\phi_{jn} = n_j \quad \text{on} \quad S_w \tag{12}$$

where

$$(n_1, n_2, n_3) = \mathbf{n} \tag{13}$$

$$(n_4, n_5, n_6) = \mathbf{x} \times \mathbf{n} \tag{14}$$

and, for $j \geq 7$,

$$n_j = \zeta_j(x,y) \quad \text{on} \quad S_i, \quad n_j = 0 \quad \text{on} \quad S_b. \tag{15}$$

The potential ϕ_D is the solution of the diffraction problem where incident waves are present and there is no motion of the body or interface. Thus

$$\phi_{Dn} = 0 \quad \text{on} \quad S_w \tag{16}$$

Note that this is *not* the complete solution of the physical diffraction problem, where the interface is free to move; that solution will include appropriate contributions from the modes $j \geq 7$.

Equating the air and water pressures on the interface gives the dynamic boundary condition

$$-i\rho_w\omega\phi - \rho_w g\zeta = -i\rho_a\omega\Phi \qquad (17)$$

After using the kinematic condition $\phi_z = \mathrm{i}\omega\zeta$ to eliminate ζ, in the same manner as for a conventional free surface, it follows that

$$\rho_w(\omega^2\phi - g\phi_z) = \rho_a\omega^2\Phi \quad \text{on} \quad S_i \qquad (18)$$

This is analogous to the modified free-surface condition which is applicable when an oscillatory pressure is imposed on the free surface (cf. Wehausen & Laitone, 1960, equation 21.2).

On the free surface outside the body the conventional free-surface condition is applicable, equivalent to the homogeneous form of (18). In addition to these boundary conditions, each potential ϕ_j and the scattering component of ϕ_D satisfy the radiation condition of outgoing waves in the far field, and vanish at large depths.

3. EXTENDED EQUATIONS OF MOTION

The conventional equations of motion stipulate that the six components of the force and moment due to the air and water pressures should be equal to the inertial force and moment of the body. The integrated pressure force and moment acting on the body will include contributions from the hydrodynamic pressure acting on S_b, and from the air pressure acting on S_c. It is convenient to add the total hydrodynamic pressure force and moment acting on S_i, and the corresponding air pressure force or moment on the same surface, since these are equal and opposite. This permits us to define force coefficients which are consistent with the extended normal vectors n_i and N_i.

The six hydrodynamic contributions are

$$f_i = \int_{S_w} n_i p dS = X_i + \sum_{j=1}^{\infty} \xi_j(\omega^2 a_{ij} - i\omega b_{ij} - c_{ij}) \qquad (19)$$

where $i = 1,2,3,4,5,6$ and the coefficients in this equation are defined as follows:

$$X_i = -i\omega\rho_w \int_{S_w} n_i \phi_D dS \qquad (20)$$

$$a_{ij} - (i/\omega)b_{ij} = \rho_w \int_{S_w} n_i \phi_j dS \qquad (21)$$

and

$$c_{ij} = \rho_w g \int_{S_w} n_i n_j dS \quad (i = 3,4,5) \qquad (22)$$

These are, respectively, the coefficients of the exciting force, added mass, damping, and hydrostatic restoring force (and moment).

The analogous expressions for the aerodynamic force and moment are

$$F_i = \int_{S_a} N_i P dS = \omega^2 \sum_{j=1}^{\infty} a_j A_{ij} \qquad (23)$$

where

$$A_{ij} = \rho_a \int_{S_a} N_i \Phi_j dS \qquad (24)$$

is the acoustic added-mass coefficient. (As will be shown in the Appendix, the acoustic potentials are real and there is no analogous damping coefficient. This can be anticipated physically by noting that the air chamber is closed, with no energy radiation or dissipation.

Assuming the body is free to respond in each mode of rigid-body motion, with the body mass distribution represented by an inertia matrix M_{ij}, six conventional equations of motion follow in the form

$$\sum_{j=1}^{\infty} \xi_j \left[-\omega^2(a_{ij} + A_{ij} + M_{ij}) + i\omega b_{ij} + c_{ij})\right] = X_i \qquad (25)$$

for $(i = 1 - 6)$.

An extended set of equations of motion including the generalized modes is derived from the dynamic boundary condition on the interface. If this condition is multiplied by $\phi_{in} = n_i$ $(i \geq 7)$, and integrated over the interface, a set of linear equations for the modal amplitudes ξ_j follow in the form

$$\sum_{j=1}^{\infty} \xi_j \left[-\omega^2(a_{ij} + A_{ij}) + i\omega b_{ij} + c_{ij})\right] = X_i \qquad (26)$$

for $(i \geq 7)$. The definitions of these coefficients are unchanged, except for the extended range of the index i.

The generalized equations of motion, including (27) and (28), can be solved by truncation and standard linear algebra to obtain the modal amplitudes ξ_j. The hydrodynamic force coefficients in this linear system can be evaluated by a panel method such as WAMIT or HIPAN. The only non-standard coefficients required are the added-mass coefficients A_{ij}. These are derived in the Appendix.

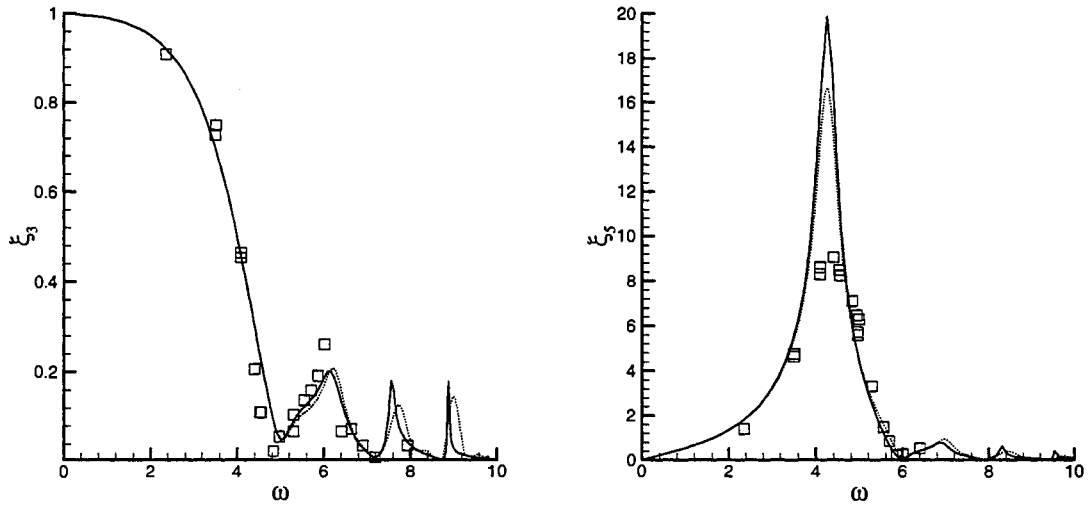

Figure 2: Normalized heave (left) and pitch (right) response amplitude operators of the model used by Pinkster *et al* (1998). The solid lines are the computational results from the present analysis. The dotted lines and square symbols are the computational and experimental results of Pinkster *et al* (1998). ξ_3 is normalized by the incident wave amplitude A, and ξ_5 is normalized by A/L.

4. COMPUTATIONAL RESULTS

Our computations are based on the higher-order B-spline code HIPAN, described by Lee (1997). One quadrant of S_w is represented by six rectangular patches on S_b and one patch on S_i. The geometry is described exactly. Cubic B-splines are used to represent the velocity potential on each patch. The patches are subdivided into panels, with B-spline knots at the intersections of adjacent panels.

We first consider the model with one air chamber used by Pinkster *et al* (1998) for their free-floating model tests, with the dimensions indicated in the caption of Figure 1. The water depth is 2.5m, the center of gravity is at $(0, 0, 0.15)$ and the pitch radius of gyration about this point is 0.751 meters. The total number of panels used in these computations is 150 and the corresponding number of unknowns (i.e. the number of B-spline coefficients) is 441. The elevation of the interface is represented by 16 Fourier modes in the longitudinal direction and 2 symmetric Fourier modes in the transverse direction. The computational results are estimated to converge to two significant digits. Figure 2 shows the heave and pitch response computed by the present method, at 100 closely-spaced frequencies, and comparisons with the numerical and experimental results of Pinkster *et al.* The computational results agree quite well, except for relatively small differences in the vicinity of the resonant peaks. These are assumed to be caused by the limitations of the low-order panel method used by Pinkster *et al* (1998).

Next we consider the prototype barge described in Figure 1. The center of gravity is located at $(0, 0, 0)$ and the radius of gyration for pitch is assumed to be 400m. The patch definition and B-spline order are the same as in the paragraph above, but the number of panels is increased to 182 and the corresponding number of unknowns is 596. The number of Fourier modes in the longitudinal direction is increased to 64. A total of 225 wave frequencies are used to define the oscillatory features of the results.

The heave and pitch RAO's are shown in Figure 3, and compared with a conventional barge with the same horizontal dimensions and displacement. For the low-frequency (long-wave) limit, the air-cushion barge maintains static equilibrium relative to the incident wave and it behaves as if the body and the air chamber are a single rigid structure without motion of the interior free surface relative to the body. Thus the heave and pitch RAO's approach to the amplitude and the slope, respectively, of the incident wave. For intermediate frequencies the RAO's are oscillatory in a similar manner for both vessels, but the peaks are amplified by sloshing in the case of the air-cushion barge.

Significant resonant responses are indicated in

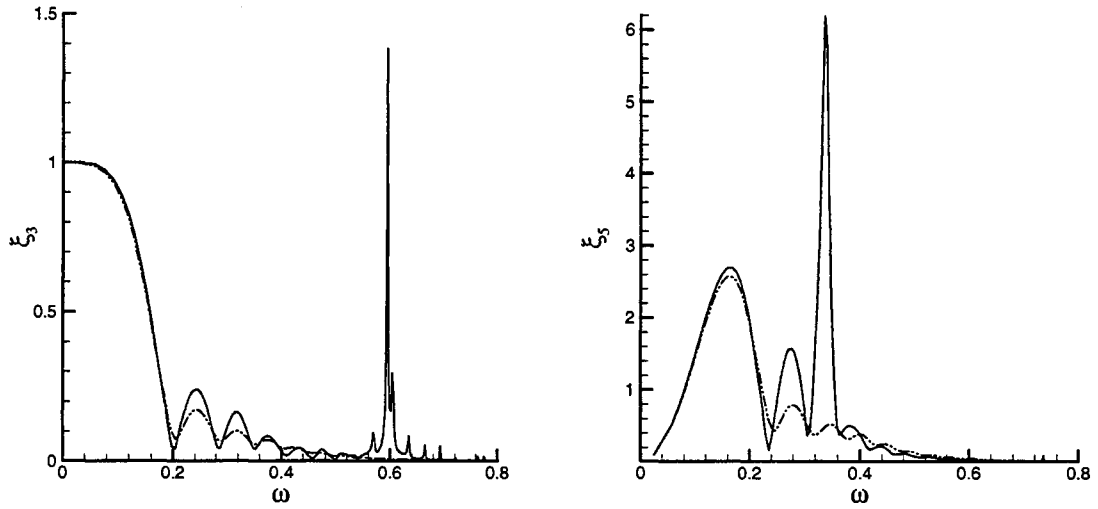

Figure 3: Heave (left) and pitch (right) response amplitude operators for two barges of length 1500m and beam 150m, normalized as in Figure 1. The solid lines are for the prototype with air chamber, and the dashed lines are for a conventional rigid barge with the same displacement.

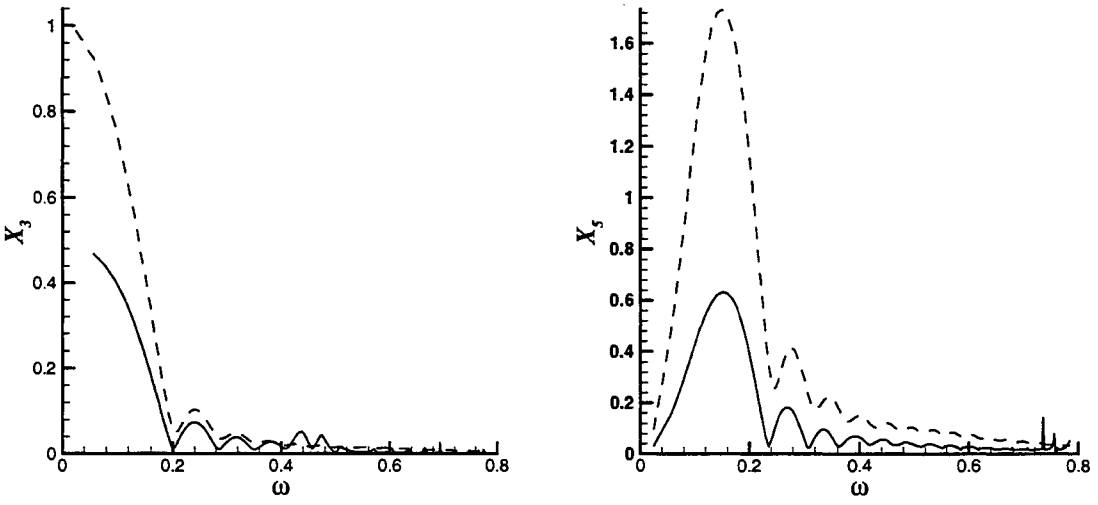

Figure 4: Heave exciting force (left) and pitch moment (right) for the two barges in Figure 3. These results are normalized by the hydrostatic limit $\rho gALB$ and by $\rho gAL^2B/12$ where L =length and B =beam.

Figure 3, for heave at $\omega = 0.595$ (period 10.6 seconds) and for pitch at $\omega = 0.336$ (period 18.7 seconds). These resonances can be explained by noting that, since the walls are relatively thin and deep, the dominant pitch moments are due to the body inertia and to the hydrostatic restoring coefficient associated with the walls. This is essentially the same as for a conventional slender floating body, except that the body inertia is about 2.2 times the displaced volume of the walls (due to the hydrostatic support of the air cushion). Thus the natural frequency can be approximated from the simple equation $\omega_n = (g/2.2T)^{1/2} = 0.37$ where T is the draft of the walls. The error in this estimate can be attributed primarily to neglect of the added moment of inertia due to the walls, and to the small motions of the interface. For heave the hydrostatic restoring coefficient is augmented by the effective stiffness of the air chamber, and the natural frequency is increased relative to pitch. This explanation is not complete, however, since there is substantial vertical motion of the interface relative to the body, and it is necessary to consider the coupled two-degree-of-freedom system $j = 3$ and $j = 7$ in order to confirm the heave resonance. (At the heave resonant condition, the RAO for the mode $j = 7$ is almost twice as large as for $j = 3$, and with opposite phase.)

Figure 4 shows the heave exciting forces and pitch moments for the both vessels. The low-frequency limits of the exciting force and moment are reduced by the air cushion, relative to the conventional barge. At intermediate frequencies the force and moment are oscillatory in a similar manner for both vessels, due to diffraction. The oscillations of the RAO's in Figure 3 are correlated with these diffraction effects. A small local peak is noticeable in the pitch exciting moment at the half-wave acoustic resonant frequency $\omega = 0.74$, but this does not have a significant effect on the pitch RAO.

The elevation of the interface is shown in Figures 5 and 6, plotted as a function of ω at six fixed points in Figure 5 and conversely in Figure 6. The first two frequencies shown in Figure 6 correspond to the resonant peaks of heave and pitch in Figure 3, and the others correspond to the three highest peaks of Figure 5. Only the symmetric modes are relevant at $x = 0$, as indicated in the bottom curve of Figure 5 which includes only half of the peaks shown in the other curves. The normalized elevation approaches 1 for long waves, and peaks are obvious at the resonant frequencies for sloshing modes. The elevations for the three higher frequencies shown in Figure 6 are clearly similar to standing waves.

5. CONCLUSIONS

We have analyzed the motions of a prototype barge with dimensions similar to a VLFS, and with partial support from an air cushion. The method is based on matching of acoustic modes in the air chamber with the hydrodynamic solution below the air/water interface. The acoustic problem is solved in the rectangular air chamber by the method of separation of variables. In the fluid, the three-dimensional higher-order panel program HIPAN is used. The displacement at the interface between the air and water is expanded in Fourier modes whose coefficients are obtained from the kinematic and dynamic conditions at the interface.

For the relatively small vessel analyzed by Pinkster *et al* (1998) our computational results are consistent. This favorable comparison, together with their experimental results, support the validity of the present computational methodology. For the prototype vessel with dimensions more relevant to a VLFS convergent results have been obtained which account for both the short-wavelength effects of the water wave diffraction and radiation, and for nonuniform acoustic pressures in the air chamber. The former effects are qualitatively similar to those associated with a conventional rigid barge of the same horizontal dimensions and displacement, but the occurrence of sloshing modes in the water below the air chamber amplify the frequency-dependent variations in the RAO's and exciting forces.

The initial motivation for this work was the possible importance of the half-wave acoustic resonance, which occurs for the very long VLFS within the practical range periods of ocean waves. The computational results do show this effect as a small resonant peak of the pitch exciting moment, but there is no significant effect on the pitch amplitude due to the relatively high frequency. The lack of a strong resonance in this mode can be attributed to the large discrepancy between the wavelengths of the acoustic and wave waves.

The most significant resonant peaks in heave and pitch are primarily due to the balance between the body inertia, hydrostatic restoring, and the stiffness associated with the change of volume in the air chamber. The oscillatory air pressure only affects the heave response, in a manner analogous to that of cobblestone oscillations for air-cushion vehicles. At these resonant frequencies the hydrodynamic damping is small, and the large amplitudes of response are cause for practical concern. Viscous damping may help to attenuate these peaks, but probably not sufficiently to overcome their practical consequences. Further developments including the

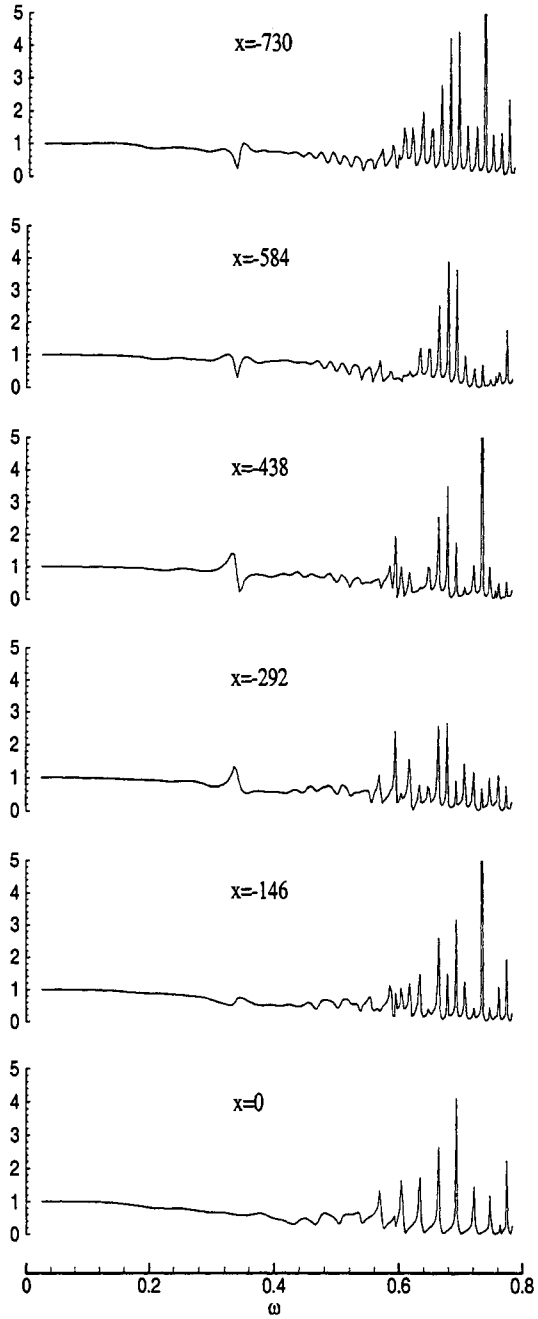

Figure 5: Amplitude of the air/water interface elevation normalized by the incident wave amplitude A. Six positions along the centerline are shown, with values of the longitudinal coordinate x in meters.

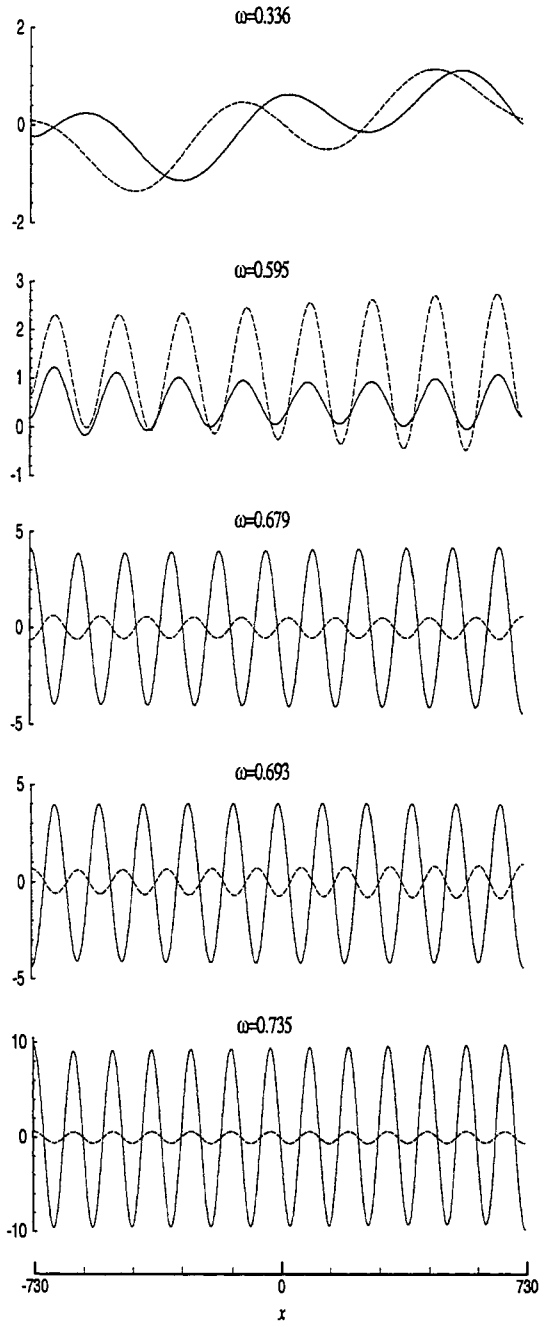

Figure 6: Real (solid lines) and imaginary (dashed) parts of the elevation along the centerline of the interface at the indicated wave frequencies ω.

considerations of passive and active damping may be useful in this context. Except for these peaks the motions of the air-cushion barge are substantially the same as for a conventional rigid monohull, and the structural loads are expected to be relatively small. It remains to compare the structural loads themselves, which requires a straightforward extension of our analysis.

From the practical design point of view, it may be necessary to compartmentalize the air chamber to increase the static stability in pitch and roll. The extension to two compartments with a longitudinal subdivision is included in the work of Pinkster *et al* (1998). It is straightforward to extend the present method to this configuration. With increased subdivision the structural wave loading will be greater, unless some type of pneumatic control system is introduced to partially equalize the pressures in different chambers. An important consequence of subdivision is that pitch motions will be accompanied by (antisymmetric) changes in the volume of the air chambers, and thus the pitch response will be more similar to that of heave.

Another practical concern is the large amplitude of resonant sloshing modes at the air/water interface. An amplification factor of 10 is indicated by the bottom curves in Figure 6, at a wave period of 8.5 seconds where significant wave energy can be expected. Viscous effects may attenuate this resonance somewhat, but it may be necessary to use special hydrodynamic or pneumatic dampers to keep the resonant modes within acceptable levels.

The concept of a VLFS which is partially supported by air cushions is a very interesting alternative to others which have been considered more extensively. Extensions of the present analysis would be appropriate to provide a more complete and practical appraisal of this concept.

ACKNOWLEDGMENT

This work was supported by the Office of Naval Research, Grant N00014-97-1-0827, under the direction of the Naval Facilities Engineering Service Center. The development of HIPAN was supported by a Consortium including the Chevron Petroleum Technology Company, David Taylor Research Center, Exxon Production Research, Mobil Oil Company, Norsk Hydro, Offshore Technology Research Center, Petrobrás, Saga Petroleum, Shell Development Company, Statoil, and Det Norske Veritas. Professor Pinkster kindly provided data files for the results shown in Figure 1.

REFERENCES

Lee C.-H. 1997, 'Wave interactions with huge floating structures,' *8th International Conference on the Behaviour of Offshore Structures*, Delft, The Netherlands, **2**, 253-265.

Nakos, D. E., Nestegard, A., Ulstein, T., and Sclavounos, P. D. 1991, 'Seakeeping analysis of surface effect ships,' *FAST'91 Conference*, Trondheim, Norway.

Lee, C.-H., Newman, J. N. & Nielsen, F. G. 1996. 'Wave interactions with an oscillating water column,' *International Offshore and Polar Engineering Conference (ISOPE-96)*, Los Angeles.

Pinkster, J. A., 1997. 'The effect of air cushions under floating offshore structures,' *8th International Conference on the Behaviour of Offshore Structures*, Delft, The Netherlands, **2** 143-158.

Pinkster, J. A., Fauzi, A., Inoue, Y. & Tabeta, S., 1998. 'The behaviour of large air cushion supported structures in waves,' *2nd International Conference on Hydroelasticity in Marine Technology,* Fukuoka, Japan, pp. 497-505.

Ulstein, T., & Faltinsen, O. M., 1996. 'Cobblestone effect on surface effect ships,' *Schiffstechnik / Ship Technology Research* **43**, 78-90.

Wehausen, J. V., and Laitone, E. V., 1960. 'Surface waves', *Encyclopedia of Physics* **9**, 446-778.

APPENDIX – Added-mass coefficients A_{ij}

The acoustic added-mass coefficients (26) are derived from the appropriate solutions of the Helmholtz equation which satisfy the boundary conditions (10). Since the domain is rectangular, the method of separation of variables can be used.

For the rigid-body modes ($i \le 6$, $j \le 6$) it is convenient to use an indicial notation in conjunction with a coordinate system $\hat{x}_i$ where the origin is at the centroid of the air chamber. Thus

$$\hat{x}_i = (x, y, z - z_2 + c) \tag{27}$$

where $z_2 - z_1 = 2c$ is the height of the chamber. In addition we define the parameters

$$a_i = (a, b, c) \tag{28}$$

$$\alpha_i(n) = \frac{n\pi}{2a_i} \tag{29}$$

$$k_i(n) = \sqrt{K^2 - \alpha_i(n)^2} \tag{30}$$

where $(i = 1,2,3)$ in all cases and the cyclic convention applies. The explicit dependence of α_i and k_i on n will be implied hereafter.

For $i = j = 1,2,3$ the potentials and added-mass coefficients are easily derived in the forms

$$\Phi_i = \frac{\sin Kx_i}{K \cos Ka_i} \tag{31}$$

$$A_{ii} = 8\rho_a a_{i+1} a_{i-1} \frac{\tan Ka_i}{K} \tag{32}$$

The potentials for the rotational modes are more complicated. To satisfy the boundary condition (10) it is helpful to replace $\hat{x}_i$ in (12) by $a_i q$, where the normalized variable q is in $(-1,1)$, and to use the Fourier series

$$q = \frac{8}{\pi^2} \sum_{\substack{n=1 \\ (n \text{ odd})}}^{\infty} \frac{s_n}{n^2} \sin\left(\frac{n\pi q}{2}\right) \tag{33}$$

where $s_n = \sin(n\pi/2)$. The potentials (Φ_4, Φ_5, Φ_6) then can be derived in the form

$$\Phi_{i+3} = \frac{8}{\pi^2} \sum_{\substack{n=1 \\ (n \text{ odd})}}^{\infty} \frac{s_n}{n^2} \left(\frac{a_{i+1} \sin \alpha_{i+1} \hat{x}_{i+1} \sin k_{i+1} \hat{x}_{i-1}}{k_{i+1} \cos k_{i+1} a_{i-1}} - \frac{a_{i-1} \sin \alpha_{i-1} \hat{x}_{i-1} \sin k_{i-1} \hat{x}_{i+1}}{k_{i-1} \cos k_{i-1} a_{i+1}} \right) \tag{34}$$

and the corresponding added-moment coefficients in the $\hat{x}_i$ reference frame are

$$\hat{A}_{i+3,i+3} = \frac{64}{\pi^2} \rho_a abc \sum_{\substack{n=1 \\ (n \text{ odd})}}^{\infty} \frac{1}{n^2} \left[\frac{1}{k_{i+1}^2} + \left(\frac{1}{\alpha_{i+1}^2} - \frac{1}{k_{i+1}^2} \right) \frac{\tan k_{i+1} a_{i-1}}{k_{i+1} a_{i-1}} + \frac{1}{k_{i-1}^2} + \left(\frac{1}{\alpha_{i-1}^2} - \frac{1}{k_{i-1}^2} \right) \frac{\tan k_{i-1} a_{i+1}}{k_{i-1} a_{i+1}} \right] \tag{35}$$

For the generalized modes $(j \geq 7)$ the potentials satisfy the boundary conditions $\Phi_{jN} = 0$ on S_c and $\Phi_{jz} = \zeta_j(x,y)$ on S_i, where ζ_j is defined by (5). The appropriate solutions are

$$\Phi_j(x,y,z) = \zeta_j(x,y) \frac{\cos w_j(z_2 - z)}{w_j \sin 2w_j c} \tag{36}$$

where

$$w_j = \sqrt{K^2 - u_m^2 - v_n^2} \tag{37}$$

For the 'pumping mode' $(j = 7)$, $m = n = 0$ and the acoustic pressure is independent of the horizontal coordinates. If $Kc << 1$ this pressure is equivalent to the time-varying air pressure in the analysis of Pinkster et al. The solutions for $j \geq 8$ represent acoustic standing waves in the chamber.

For $(i \geq 7)$ and $(j \geq 7)$ the only contributions to the added-mass coefficients are from the interface S_i. Since the functions ζ_j are orthogonal, the only nonzero coefficients are

$$A_{ii} = -\rho_a \frac{\cot 2w_i c}{w_i} \int_{S_i} \zeta_i^2 dS = -\rho_a \frac{\cot 2w_i c}{w_i} ab\epsilon_m \epsilon_n \tag{38}$$

Here $\epsilon_0 = 2$ and $\epsilon_m = 1 \quad (m \geq 1)$, and the indices m, n correspond to the Fourier modes (5).

For $(i \leq 6)$ and $(j \geq 7)$ the added-mass coefficients can be evaluated by integration of the potentials (38) over the surface S_a. For the surge force $(i = 1)$ the only contributions are from the modes where m is odd and $n = 0$:

$$A_{1j} = \frac{4\rho_a b}{w_j^2} s_m \delta_{n0} \tag{39}$$

where δ_{mn} is the Kroenecker delta function. Similarly for the sway force $i = 2$ the only contributions are from the modes where $m = 0$ and n is odd:

$$A_{2j} = \frac{4\rho_a a}{w_j^2} s_n \delta_{m0} \tag{40}$$

The only contribution to the heave force is from the pumping mode:

$$A_{37} = 4\rho_a ab \frac{\tan Kc}{K} = \tfrac{1}{2} \hat{A}_{33} \tag{41}$$

The moments are

$$A_{4j} = -\frac{4\rho_a a}{w_j^2} s_n \left[z_1 + \frac{\tan w_j c}{w_j} \left(1 - \frac{w_j^2}{v_n^2} \right) \right] \delta_{m0} \tag{42}$$

$$A_{5j} = -\frac{4\rho_a b}{w_j^2} s_m \left[z_1 + \frac{\tan w_j c}{w_j} \left(1 - \frac{w_j^2}{u_m^2} \right) \right] \delta_{n0} \tag{43}$$

$$A_{6j} = \frac{4\rho_a}{w_j^2} s_m s_n \left(\frac{1}{u_m^2} - \frac{1}{v_n^2} \right) \tag{44}$$

The remaining elements $(i \geq 7)$ and $(j \leq 6)$ can be evaluated directly, but it is simpler to use the symmetry relations $A_{ij} = A_{ji}$. Except for the coefficients A_{ij} which are explicitly evaluated above, and the reciprocal coefficients A_{ji}, the off-diagonal elements A_{ij} $(i \neq j)$ are equal to zero when $i \geq 7$ and/or $j \geq 7$. In all cases the potentials and added-mass coefficients are real.

PROCEEDINGS OF THE THIRD INTERNATIONAL WORKSHOP ON VERY LARGE FLOATING STRUCTURES
(VLFS '99), VOL. I, EDS. R.C. ERTEKIN & J.W. KIM, 22-24 SEPTEMBER 1999, HONOLULU, HAWAII, USA

A STUDY ON ESTIMATION OF WAVE EXCITING FORCES ON FLOATING STRUCTURE UNDER TSUNAMI

Koichi Masuda and Tsuyoshi Miyazaki
College of Science & Technology, Nihon University at Funabashi*

ABSTRACT

Tsunami is brought about an earthquake in the bottom of the sea. Tsunami's wave height becomes higher in shallower sea. Under that condition, Tsunami is considered as shallow water long period wave. Wave load from Tsunami has much influenced to the motions and mooring tensions of a floating structure in offshore area. For this reason, wave load from Tsunami is essential to planning protection against calamities. Since, an estimation method on Tsunami wave exciting forces in the stage of basic design of floating structure has been presented in this study. Summaries of this study are shown as follows;

A concept of solitary wave corresponding to Tsunami has been proposed. Tsunami wave exciting forces can be calculated with lessor labor.

1. INTRODUCTION

Tsunami is brought about an earthquake in the bottom of the sea. Tsunami is long period wave and spreads all directions. And Tsunami's wave height become higher in shallower sea. Wave load from Tsunami has much influenced to the motions and mooring tensions of a floating structure in offshore area. For this reason, wave load from Tsunami is essential to planning protection against calamities.

As studies about responses of floating structure in Tsunami, wave load of MEGAFLOAT floating structure has been reported by Tabete et al. (see [1]) On this report, Tsunami wave load has been calculated by estimation method based upon shallow sea long wave theorem. But it seems that this method need much calculation time and labor. On the other hand, previous report about responses of rectangular floating structure under Tsunami has existed that has made by Miyazaki et al. In this study, a numerical estimation method with responses of floating body under solitary wave supposed that it is Tsunami was developed, and Floating structure under solitary wave has shown characteristic of motions that Amplitudes of surge motions are about four times as incidental wave height from computational results and experimental results (see [2]). And another numerical estimation with responses of floating body under Tsunami has been carried out by Ikeno et al (see [3]).

The present paper has presented the practical estimation method for Tsunami wave exciting forces with lessor labor with some calculation sample. And using this present method results, Tsunami's effect in the point of view that the maximum values of mooring tensions with floating structure have been considered comparing the case floating structure under survival condition wind wave.

2. ANALYSIS METHOD FOR WAVE EXCITING FORCE OF TSUNAMI

In this chapter, an estimation method for Tsunami wave exciting forces on floating structures has been presented.

The first stage of floating structure design has been kept in mind with this estimation method. In the first stage of floating structure, some basic assumptions have been presence. Those assumptions have been shown as follows;

1) Floating structure has been set up on open sea coastal area that 40m deeper water depth. Generally, some points of advantage of floating structure have been arisen to reclaimed lands in this water depth.

2) Practical estimation with maximum value of Tsunami wave exciting forces has been aimed in this method. So, Tsunami wave elevation has been assumed that solitary wave.

Under these assumptions, tsunami wave exciting forces can be calculated with lessor labor.

In this study, practical method with estimation of Tsunami wave exciting forces has been presented. In this method, Tsunami wave elevations have been replaced with solitary wave using the parameters of tip wave of Tsunami that wave height and wave length.

* 7-24-1, Narashinodai, Funabashi-shi, Chiba, 2748501, JAPAN

The flow of this method has been shown as follows;

1) Initial wave height of Tsunami correspond to earthquake magnitude number.
2) Estimation of wave height of Tsunami in the set up point of floating structure.
3) Estimation of wave length of Tsunami in the set up point of floating structure.
4) Determination of the Equivalence solitary wave to Tsunami.
5) Calculation of Tsunami exciting forces using the Equivalence solitary wave.

2.1 Initial wave height of Tsunami correspond to earthquake magnitude number

In this method, initial Tsunami wave height has been given by data base of Tsunami wave height that had been calculated beforehand used Mansinha's method (see [4]).

Characteristics of sea bed's faults has been described as 6 parameters those length, width, displacement, angle of inclination, angle of slip and depth of fault. This calculation method assumed that based upon 2 dimensional area. Since, fault's length is constant. And, in this Practical method, Tsunami wave height has been calculated considered about only the effect of fault's width. Other 5 parameters have been looked upon constant. Using fault' length L and magnitude of earthquake M, Fault's width W has given as;

$$\log LW = M - 4.07 \quad (1)$$

(see [1]).

An example of fault's parameters using Tsunami initial wave height calculation has been shown as Table 1.

Table 1 parameter of fault

width of fault	W=10M-4.07/L
Depth of fault	2
Displacement	4
Angle of inclination	60
Angle of slip	30

Initial Tsunami wave height calculated by presented method has been shown as Fig.2.1. In this figure, Tsunami wave height has become higher when magnitude of earthquake has become larger.

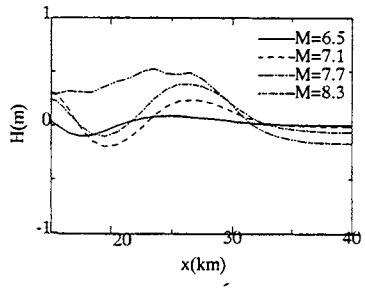

Fig. 2.1 Initial water height of Tsunami

From the point of view increasing magnitude of earthquake, initial Tsunami wave height has been shown as Fig.2.2. Using this figure, estimation of Tsunami wave height corresponding earthquake magnitude has been enabled.

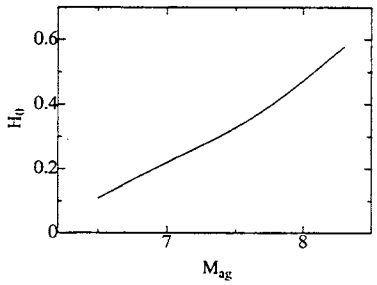

Fig. 2.2 Tsunami Wave height with magnitude

2.2 Estimation of wave height of Tsunami in the set up point of floating structure

In this section, the method of estimation with Tsunami wave height in the set up point of floating structure has been shown.

Green's equation (see [5]) shown as

$$\frac{H}{H_0} = \left(\frac{B_0}{B}\right)^{1/2}\left(\frac{h_0}{h}\right)^{1/4} \quad (2)$$

has been used for equation of Tsunami wave height. Here, H is wave height of the point, those water depth is h and breadth is B, H_0 is initial wave height, those water depth is h_0, and breadth is B_0.

In shallow water sea, Tsunami wave height may be calculated by Kishi's theorem (see [5]) as follows;

$$\frac{h}{h_0} = \left(\frac{\sqrt{1+\bar{\eta}_0}-1}{\sqrt{1+\bar{\eta}}-1}\right)^{4/5}\left(\frac{6\sqrt{1+\bar{\eta}_0}-1}{6\sqrt{1+\bar{\eta}}-1}\right)^{6/5} \quad (3)$$

$\bar{\eta}$: $\bar{\eta} = \eta/h$

η : wave height on the point of floating body

η_0 : wave height on the point of wave source

h : water depth on the point of floating body

h_0 : water depth on the point of wave source.

2.3 Estimation of wave length of Tsunami in the point of floating structure

Tsunami wave length and Tsunami wave height may be important parameter that determine characteristics of Tsunami. In this method, Tsunami wave length has been estimated based upon Tsunami wave height, water depth and slope of sea bed. Here, Tsunami wave length has determined as tip wave length of Tsunami by zero-up-cross method. For estimation of wave length, preparation calculations have been carried out. From these calculations' results, Fig.2.3 has been given. In Fig.2.3, 1/10 and 1/5 means the sea bed's slope.

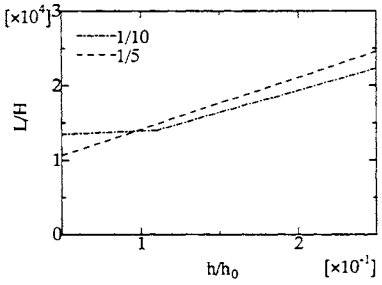

Fig. 2.3 Wave length of Tsunami with water depth

Using Fig.2.3, Tsunami wave length has been given.

2.4 Determination of the Equivalence solitary wave to Tsunami

In this presented method, Tsunami has been represented as solitary wave that has been thought that have same energy to Tsunami. In this report, these solitary waves determine the Equivalence Solitary Wave. The equivalence solitary wave has been determined by wave height and wave length. Here, wave length L of solitary wave has been determined as Fig.2.4 (η'/η =1/100).

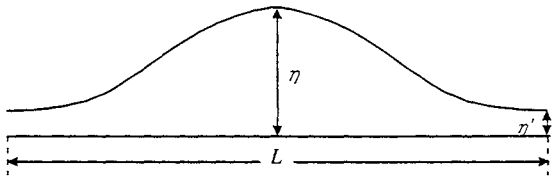

Fig. 2.4 Solitary wave length

2.5 Calculation of Tsunami exciting forces using the Equivalence solitary wave

Tsunami wave exciting forces has been estimated using the equivalence solitary wave. In this calculation, water depth near the floating body is assumed that is constant.

2.5.1 BASIC EQUATIONS

This method is based upon some assumptions as follows;

1) Fluid is assumed to be incompressible and inviscid.
2) Fluid motions are irrotational.

Under these assumptions, existence of velocity potential $\Phi(x,z;t)$ is assurance.

Thus, basic equation in fluid region is defined as follows;

$$\nabla^2\Phi = 0 \qquad (4)$$

This is the Laplace equation of hydrodynamics. As shown in Fig.2.5, a 2 dimensional space fixed coordinate system (X, Z) are used in this numerical computation.

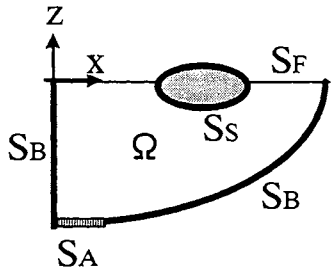

Fig.2.5 Coordinate system of fluid field

2.5.2 BOUNDARY CONDITIONS

a) Wave making boundary S_A

Boundary condition of wave making boundary is velocity of motion $v(x,z;t)$ condition. This boundary condition as follows is given.

$$\frac{\partial\Phi}{\partial n} = v(x,z;t)\cdot\vec{n} \qquad \text{on } S_A \quad (5)$$

$\vec{n}$ is outward normal vector on boundary.

b) Bottom surface S_B and body surface S_S

Boundary condition of bottom and body surface is

$$\frac{\partial\Phi}{\partial n} = 0 \qquad \text{on } S_B,\ S_S \quad (6)$$

without boundary transformation and normal fluid velocity on boundary.

c) Free surface S_F

This method is time domain analytical method. Boundary condition of free surface is considered as kinematic condition from free surface shape and dynamic condition from Bernoulli's theorem.

Kinematic condition of free surface has been left to

$$\frac{\partial\Phi}{\partial z} = \frac{\partial\eta}{\partial t} + \frac{\partial\Phi}{\partial x}\frac{\partial\eta}{\partial x} \qquad \text{on } S_F \quad (7)$$

from shape of free surface wave. η is displacement of free surface at normal direction. Dynamic condition of free surface is

$$\frac{\partial\eta}{\partial t} + g\eta + \frac{1}{2}(\nabla\Phi)^2 = 0 \qquad \text{on } S_F \quad (8)$$

in case of standard on the atmosphere pressure.

2.5.3 BOUNDARY INTEGRAL EQUATIONS

Boundary integral equation has been given

$$\frac{1}{2}\Phi(P) = \int_s \frac{\partial \Phi}{\partial n}\Phi^* ds - \int_s \Phi(Q)\frac{\partial \Phi^*}{\partial n} ds \quad (9)$$

. Equation (6) is equivalent boundary problem shown as 2.5.2. Here, P is observation point and Q is source point. Φ^* is basic resolution. In this method, this boundary integral equation has been divided and simultaneous equations dealing with velocity potential has been lead. In two-dimensional space, fundamental resolution Φ^* is

$$\Phi^*(P,Q) = \frac{1}{2\pi}\log\frac{1}{r} \quad (10)$$

. r is distance P to Q.

Transition of given velocity potential has been analyzed by time increment method. Velocity potential Φ and displacement of free surface η in time domain has been given

$$\Phi_{t+\Delta t} = \Phi_{t-\Delta t} + 2\Delta t\left(\frac{D\Phi}{Dt}\right)_t \quad (11)$$

$$\eta_{t+\Delta t} = \eta_{t-\Delta t} + 2\Delta t\left(\frac{D\eta}{Dt}\right)_t \quad (12)$$

. In these equations, higher order Δt^3 has been ignored. $D\Phi/Dt, D\eta/Dt$ have been defined as follows

$$\frac{D\Phi}{Dt} = -g\eta + \frac{1}{2}(\nabla\Phi)^2 \quad (13)$$

$$\frac{D\eta}{Dt} = \frac{\partial \Phi}{\partial z} \quad (14)$$

under boundary conditions of free surface. Since, equation (13) and (14) has been transformed as follows

$$\Phi_{t+\Delta t} = \Phi_{t-\Delta t} + 2\Delta t\left\{-g\eta + \frac{1}{2}\left(\nabla\Phi^2\right)\right\}_t \quad (15)$$

$$\eta_{t+\Delta t} = \eta_{t-\Delta t} + 2\Delta t\left(\frac{\partial \Phi}{\partial z}\right)_t \quad (16)$$

2.5.4 HYDRODYNAMIC FORCE

Thus velocity potential has been given, pressure $p(x,y;t)$ on body surface is given by Bernoulli's theorem.

$$p = -\rho\frac{\partial \Phi}{\partial t} - \frac{1}{2}\rho(\nabla\Phi)^2 \quad (17)$$

ρ is density of fluid. t is time. Wave exciting force FE on each direction of body's motion is given by integration of pressure p on under water line of floating body.

3. APPLICATION

In this report, examples of application of this present method have been shown. First, the results of calculation have been shown that floating structure supposed Japan's Mini Float project thought as the station for protection against calamities that specifications given as its length is several hundreds of meter. Second, the results of calculation have been shown that structure supposed Japan's MEGA FLOAT project. Third, calculation results has been compared the case in Tsunami with the case in the survival condition of wind wave for Mini Float structure.

3.1 Tsunami wave exciting forces with floating structure

Using presented estimation metod, Tsunami wave exciting forces have been calculated. Floating structure's specifications are given as B =48.0m, L=100.0m, D=6.0m (supposed that Mini Float projects in Japan). Water depth of the set up point of floating structure is supposed 40.0m. And, the earthquake magnitude number M supposed is M=7.7. The site plan of the floating is shown as Fig.3.1.

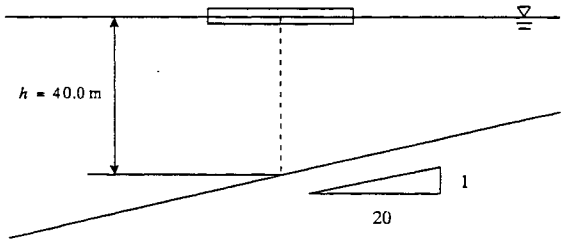

Fig. 3.1 simulation model

In this case, the time series of the equivalence solitary wave that has been calculated is shown as Fig.3.2.

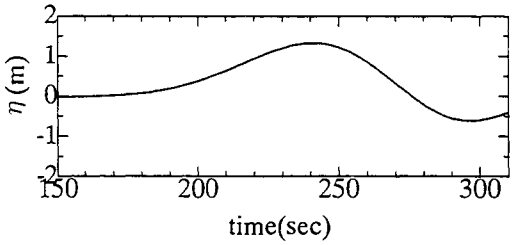

Fig. 3.2 Time series of wave height

The time histories of Tsunami wave exciting forces that have been estimated using the solitary wave are shown as Fig.3.3 to Fig.3.5.

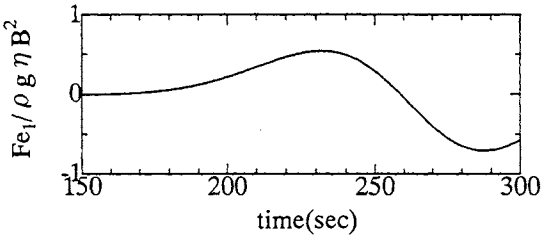

Fig. 3.3 Wave exciting force (surge)

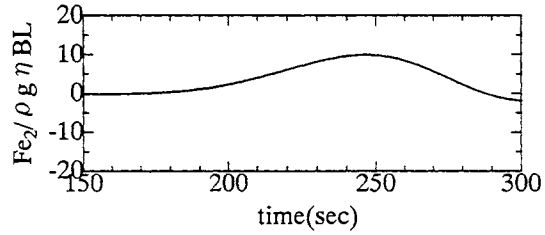

Fig. 3.4 Wave exciting force (heave)

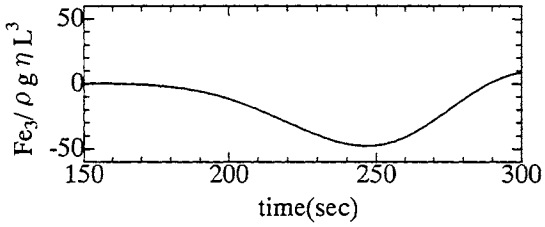

Fig. 3.5 Wave exciting force (pitch)

3.2 Tsunami wave exciting forces with Very Large Floating Structure

Using presented method, Tsunami wave exciting forces have been calculated. This case, the calculations have been carried out that supposed very large floating structure.

Calculation model is same of the former case. Water depth is 40.0m. Structure's specifications are given as L=1000.0m, B=100.0m, D=1.0m. Time series of Tsunami wave height is shown as Fig.3.6.

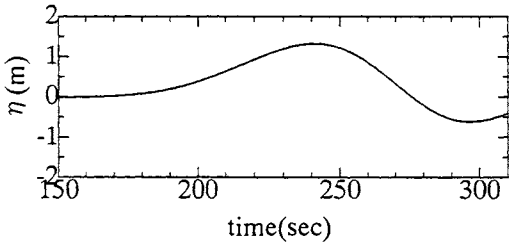

Fig. 3.6 Time series of wave height

And, time series of Tsunami wave exciting forces are shown as fig.3.7 to 3.9.

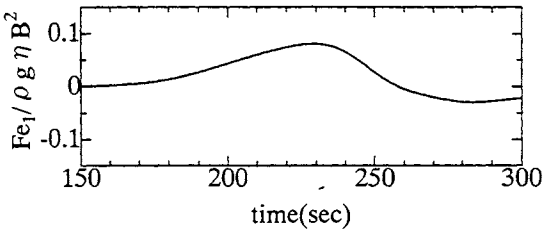

Fig. 3.7 Wave exciting force (surge)

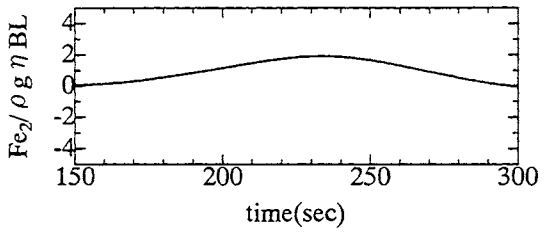

Fig. 3.8 Wave exciting force (heave)

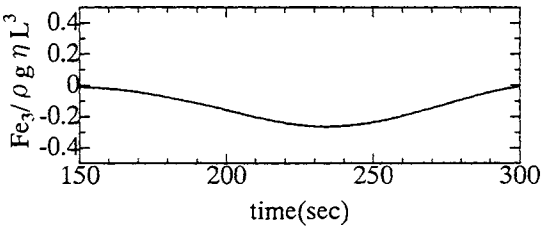

Fig. 3.9 Wave exciting force (pitch)

From these calculation results, it seems that Tsunami wave exciting forces with very large floating structure can relatively be smaller than wave exciting forces with normal size floating structure in non-dimensional values.

But, It seems that these characteristics of Tsunami wave exciting forces with very large floating structure have been due to its specifications of structure size. Its draft is too small (=1.0m) to its length (=1000.0m). Since, wave exciting force in surge motion may become small in non-domensional value. And its length is too long, since, the effect of wave slope have become lessor. For this reason, pitch directional wave exciting force has become small in non-dimensional value. Off cause, these values are large in .dimensional values.

On the other hand, heave directional wave exciting force have been due to bottom area of floating structure. For this reason, heave directional wave exciting force is larger than other directional wave exciting forces.

From these results, Tsunami exciting force can be calculated by this presented method. But, more detailed examination should be carried out for Tsunami's effect

to very large floating structures (in the point of view that its elasticity, fluid viscous, its elastic displacement, its stress on the part of floating body).

3.3 Mooring Tension responses with Mini Float Structure

Using Tsunami wave exciting forces that have been calculated, motion and mooring tension responses with Mini float structure have been estimated. Here, mini float structure assumed that has slackly moored. Mooring tendon characteristics shown as Table 2. In this calculation, an existing method has been used (see [2]).This case, Water depth is 40.0m.

Table 2 Tendon characteristics

Chain	Steel chain (ϕ =130)
Unit weight in water	333.09kgf/m
Yang's modulus	8.0×10^9
Section area	$0.0265m^2$
Initial tension	90.0tf

And calculation motion and tension responses in survival conditions wind wave have been carried out due to comparison with the results of the case in Tsunami. In this calculation, an existing method has been used (see [5]). Incident wave of this calculation assumed as Table 3.

Table 3 Incident wave conditions

Significant wave height	6.6m, 7.4m
Significant wave period	8.0sec,14.0sec

Calculation results with maximum values of mooring tensions shows as Fig.3.10.

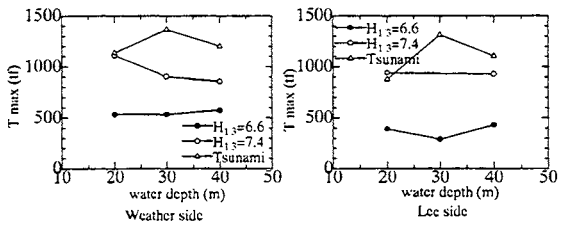

Fig.3.10 maximum value of mooring tension

Compared mooring tensions in Tsunami with in survival condition wind wave, same order mooring tensions has been occur in Tsunami to survival wind wave conditions. For this reason, Tsunami's effect on the design of mooring systems could not be ignored. On the other hand, in the point of view that the first stage of floating structure's design, maximum values of mooring tensions has been given us important data for the mooring design.

4. CONCLUSIONS

In this report, A concept of solitary wave corresponding to Tsunami has been proposed. Tsunami wave exciting forces can be calculated with lessor labor.

Using presented method, Tsunami wave exciting forces have been estimated in the case of normal size floating structure (Mini Float structure) and very large floating structure. From these computational results, using the presented method, Tsunami exciting forces with floating structures can be calculated lessor labor. But, more detailed examination should be carried out for Tsunami's effect to very large floating structures.

And, in the point of view that maximum values of tensions, Tunami effects to floating structures has been made clear in the case of Mini Float structure compared with the case under survival condition wind waves. In this case, mooring tensions have been occurred near the same order under survival condition wind waves.

Acknowledgement: The present paper is based upon work supported by the subsidy of scientific research of the Ministry of Education, Japan.

References

[1] S. Tabeta, Y. Inoue, S. Kimura, H. Makino. *Numerical Calculation of Forces on Very Large Floating Structure by Tsunami.* Journal of the Society of naval architects of Japan, vol.184, pages 307-313

[2] T. Miyazaki, K. Masuda, H. Takamura. *Estimation on Dynamic Response of Moored Floating Structure under Tsunami,* Proc. of the 17th International Offshore Mechanics and Arctic Engineering Symposium, ASME,1998.

[3] M. Ikeno, M. Matsuyama.. *Nonlinear Analysis of Floating Structure under Tsunami,,* Proc. of Coastal Engineering, Vol. 43(2),JSCE, 1996

[4] Mansinha,L.et al, *The displacement field of incind faults,* Bull. Seism. Soc. Amer., 61, 1971

[5] *Hydraulic formulas*, Japan Society of Civil Engineers, 1986

[6] K. Masuda, H. Osawa, *Prediction of Motions and Tension in Mooring Lines on Slack-moored Floating Oceanic Architectual Building in Coastal Zones.* Proc. of the 11th International Offshore Mechanics and Arctic Engineering Symposium Vol. 1-A, ASME,1995

PROCEEDINGS OF THE THIRD INTERNATIONAL WORKSHOP ON VERY LARGE FLOATING STRUCTURES
(VLFS '99), VOL. I, EDS. R.C. ERTEKIN & J.W. KIM, 22-24 SEPTEMBER 1999, HONOLULU, HAWAII, USA

Non-linear Time-domain Response of Connected Mobile Offshore Base Units Using Linear Frequency Domain Hydrodynamic Forces

Michael J. Edwards and David Raj
McDermott Technology, Inc.*

ABSTRACT

Analyses of Mobile Offshore Base (MOB) designs indicate that the use of non-linear connectors is desirable in high sea states. To fully assess the response of these non-linear connectors requires the use of time-domain structural analysis. Under the Navy contract "Design Technologies for Mobile Offshore Base", McDermott Technology, Inc. has developed the methodology and software tools to couple linear, frequency-domain hydrodynamic analyses using MIT's HIPAN code to non-linear, time-domain structural analysis using ABAQUS by Hibbitt, Karlsson & Sorensen, inc.

This paper describes a methodology for performing time-domain structural analysis using linear hydrodynamics, without hydroelasticity. This methodology is used to predict connector forces under a severe sea state for a MOB using non-linear connectors and consisting of five Single Base Units (SBUs). These time-domain results are compared to two other models. The first model uses linear connectors, while the second model uses the same non-linear connectors, but with constant values of added mass and radiation damping.

1. INTRODUCTION

A Mobile Offshore Base (MOB) is a self-propelled, floating base deployable to an area of national defense interest. It provides worldwide logistic support of unequaled proportions in military, humanitarian, and nonmilitary (commercial) uses. A MOB can accept cargo from Air Force C-17s and Container ships, and provides over 3 million square feet of reconfigurable internal storage. With a size on the order of 1 mile long by 500 feet wide, it is an ocean-going megastructure.

*1562 Beeson Street, Alliance, Ohio 44601, USA
eMail: mike.j.edwards@mcdermott.com
david.raj@mcdermott.com

Various MOB concepts have been proposed by a number of companies and agencies. The analysis and evaluation of these designs has been challenging. Because of their unprecedented size and nature, these MOB concepts often exceed the limits and assumptions of traditional analysis methods. Analyses must account for the large scale of these structures, the application of novel features (such as non-linear connectors), and the need for long term reliability and operability over a wide range of conditions.

Traditional methods to predict hydrodynamic loading on hulls and the resulting structural loads/ship motions (rigid body and resonant responses) employ frequency domain, three-dimensional, linear hydrodynamic theory. Hull structural analysis is accomplished by post-processing the hydrodynamic results and applying them to a more detailed structural model (typically FEA), still in the frequency domain. These methods have proven to be powerful tools for prediction of ship responses under a wide range of conditions. The assumption of additive response permits ready consideration of regular and irregular waves and virtually any wave spectra, plus calculation of extreme responses based on probabilistic (risk-based) methods.

However, only linear hydrodynamics and linear structural response can be treated in the frequency domain, precluding consideration of non-linear structural effects such as plasticity or energy absorption through inelastic members. In order to design with and take advantage of non-linear structural members (e.g. advanced MOB connector designs), a time domain approach is required. While time domain structural analysis programs are available that can correctly treat non-linear behavior, time domain hydrodynamic analysis methods which can consider non-linear hydrodynamic effects are in development and are not sufficiently mature for most analysis applications.

McDermott Technology Inc. (MTI), under the Navy contract "Design Technologies for Mobile Offshore Base", has developed the methodology and software tools (MOB-HyLoads) to couple linear, frequency domain hydrodynamic analysis to non-linear, time-domain structural analysis. HIPAN is used for the hydrodynamic analyses, while ABAQUS is used for the non-linear time-domain structural analyses (see [1], [2]). The developed methodology allows the hydrodynamic loads to be applied to the structural model as either distributed loads along the structure, or as point forces at the centers of gravity of an N-Body problem. This paper describes and demonstrates this later methodology for the analysis of non-linear connectors in a MOB consisting of five Single Base Units (SBUs).

2. METHODOLOGY

The methodology employed assumes exact linear hydrodynamics, without hydroelasticity. HIPAN's N-Body solution technique is used to determine the hydrodynamic diffraction forces and the hydrodynamic coefficients (added mass and radiation damping) for the SBUs. Diffraction forces and radiation coefficients are calculated for a range of periods and headings that cover the sea state of interest. The diffraction forces are known apriori, and thus the structural analysis time-domain diffraction loading is directly applied. However, the radiation forces depend on the structural response of the SBUs. Since the non-linear connectors influence the motions of the SBUs, these forces must be coupled with the time-domain responses. The finite element program ABAQUS is used to calculate the time-domain structural response of the MOB. Since the radiation forces for a MOB depend on the current response, they are calculated iteratively within ABAQUS through the use of a general-purpose user-defined element (ABAQUS user written subroutine UEL). This calculation is based on the motion history and impulse response functions derived from the HIPAN radiation solution.

The program MOB-HyLoads is used to apply linear, frequency domain hydrodynamic loads to a non-linear, time-domain structural analysis. MOB-HyLoads provides hydrodynamic loading as either distributed loads, or as point forces at the CGs of each SBU. Since hydroelasticity is not being considered in this paper, a simplified lumped mass structural model is used, and the hydrodynamic loads are applied as point forces at the SBU CGs.

MTI has developed an ABAQUS user written element (UEL subroutine) which is used to apply the hydrodynamic loads. Input to this subroutine is supplied by MOB-HyLoads in the form of a diffraction force time history and impulse response functions. This data is used by the ABAQUS user subroutine to apply the motion dependent hydrodynamic forces. For each time step, equations of motion being solved by ABAQUS are:

$$[M]\{\ddot{x}\} + [C]\{\dot{x}\} + [K]\{x\} = \{F\} \qquad (1)$$

where the forcing function, {F} is:

$$\underset{\text{Forcing Function}}{\{F\}} = \underset{\text{Diffraction}}{\{F_D\}} + \underset{\text{Radiation}}{\{F_R\}} \qquad (2)$$

The diffraction force $\{F_D\}$ is known apriori from the HIPAN diffraction solution for different wave periods and wave headings. A sea state is then simulated by scaling these forces with wave spectrum and spreading functions, where the contributions from the different wave periods and headings are added with random phases.

The radiation force $\{F_R\}$ depends on the current displacement of the structure and, hence, has to be calculated iteratively until a converged solution is obtained.

If we assume that there are "N" bodies in the N-Body analysis, and each body has 6 degrees of freedom, then there are a total of 6N degrees of freedom for the model. Hence, 6N radiation forces have to be calculated. The radiation force for a degree of freedom "i" is obtained from the infinite frequency added mass and impulse response functions as follows:

$$(F_R)_i = -\sum_{j=1}^{6N}\left[\{m(\infty)\}_{ij}\,\ddot{x}_j + \int_0^t K_{ij}(t-\tau)\,\dot{x}_j(\tau)\,d\tau\right] \qquad (3)$$

where :

- $i = 1, 2, 3, \ldots\ldots, 6N$
- $m(\infty)_{ij}$ infinite frequency added mass of dof "i" due to acceleration of dof "j"
- x_j displacement for mode "j"
- $K_{ij}(t)$ wave portion of impulse response function

The impulse response functions are calculated from the radiation damping coefficients $b(\omega)$ as follows:

$$K_{ij}(t) = \frac{2}{\pi}\int_0^\infty b_{ij}(\omega)\,\text{Cos}\;\omega t\;d\omega \qquad (4)$$

The hydrodynamic forces on the model are applied with a general user-defined element (UEL), which is defined using the CG nodes of the SBUs. This user element permits access to the displacements, velocities,

and accelerations of its nodes at each time step and iteration within the time step. These values are used to define motion dependent forces during the solution process. For each time step three forces are applied to the model – the diffraction force, the force due to the infinite frequency added mass and the force due to the wave component of the radiation solution.

3. ANALYSIS DESCRIPTION

MOB-HyLoads is used to analyze a MOB consisting of five rigid SBUs, shown in Figure 1. The connection between the SBUs is assumed to be with a ball joint amidships and non-linear springs outboard, as shown in Figure 2. Three different cases were examined, spanning the range of non-linear structural assumptions. The first case is a linear system, with linear connectors between the SBUs. The second case uses non-linear connectors, but assumes a constant value of added mass and radiation damping. The final case contains the same non-linear connectors, but uses the convolution theorem to include the effect of frequency dependent added mass and radiation damping.

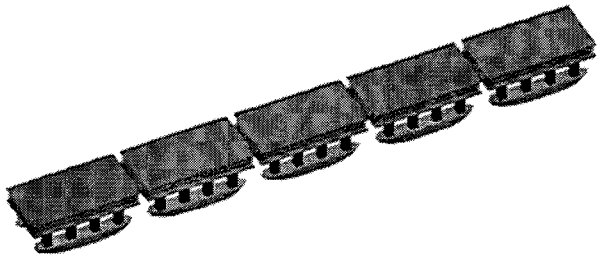

Figure 1. McDermott MOB Design

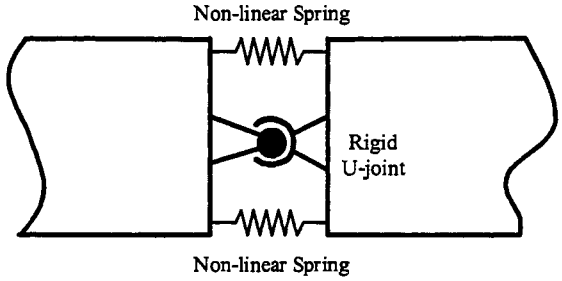

Figure 2. SBU Connectors – Plan View

The hydrodynamic program HIPAN was used to calculate the hydrodynamic response of the MOB. The hydrodynamic model used HIPAN's N-Body option. The five SBUs of the MOB were assumed to be rigid, and were modeled in an unconnected state. A convergence study was performed on one SBU to assure the use of a valid hydrodynamic model. This model was then extensively exercised to characterize the response of the MOB over a wide range of frequencies and headings.

The finite element program ABAQUS is used for structural modeling. The structural model consists of a simplified lumped mass model of the MOB. A plan view of a SBU model is presented in Figure 3. Five SBU models are strung together to form the MOB model. The major feature of the MOB model is the inclusion of a user defined element whose nodes are the CG nodes of the SBUs. This user element permits the hydrodynamic forces to be applied to the model.

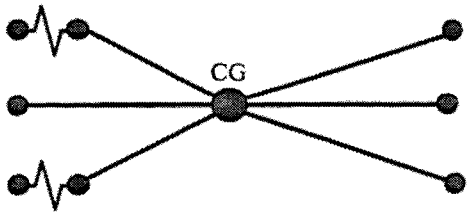

Figure 3. SBU Structural Model – Plan View

Each SBU is modeled with the mass lumped at its CG, with rigid beams attaching the connectors to the CG. Table 1 lists the mass properties of each SBU.

Table 1. SBU Mass Matrix (Kg)

Mx – Surge	3.626E+8
My – Sway	3.626E+8
Mz – Heave	3.626E+8
Ixx – Roll	1.129E+12
Iyy – Pitch	3.149E+12
Izz – Yaw	3.418E+12

The hydrostatic stiffness of each SBU is modeled as springs between the CG and ground, using an ABAQUS JOINT element. The properties of these springs are presented in Table 2.

Table 2. SBU Hydrostatic Stiffness (N/m)

Kx - Surge	0.000
Ky - Sway	0.000
Kz - Heave	3.400E+7
Kxx - Roll	4.007E+10
Kyy - Pitch	1.244E+11
Kzz - Yaw	0.000

The connectors were modeled with both linear and non-linear springs in the outboard position, as shown in Figure 2. Linear springs are used in Case 1, with a stiffness of 2.0E7 N/m. Cases 2 and 3 used non-linear springs. Figure 4 plots the force-displacement curve for these springs. Note that these springs are not representative of any actual MOB design, but were selected only for illustration.

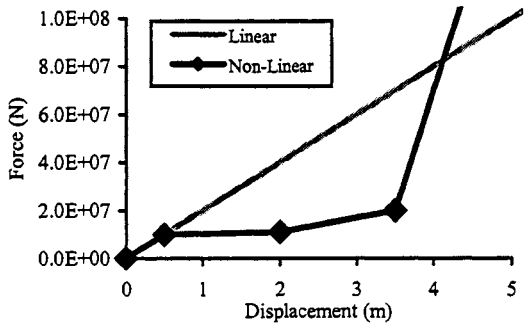

Figure 4. Spring Characteristics

Case 2 differs from Cases 1 and 3 in the calculation of added mass and radiation damping. Case 2 assumes a constant value of added mass and radiation damping. Constant added mass was modeled with a mass element at the CG, while constant radiation damping was modeled using dashpots between the CG and ground. Properties of these elements are presented in Tables 3 and 4 respectively. Cases 1 and 3 use the complete methodology described in section 2, above. This method uses an ABAQUS user written element to calculate the motion dependent radiation forces based on impulse response functions.

Table 3. Constant Added Mass

M11 – Surge	4.117E+8
M22 – Sway	5.752E+8
M33 – Heave	8.508E+8
M24 = M42	1.855E+9
M44 – Roll	2.735E+12
M15 = M51	1.935E+9
M55 – Pitch	5.186E+12
M66 – Yaw	4.539E+12

Table 4. Constant Radiation Damping

Cx - Surge	8.427E+6
Cy - Sway	3.042E+7
Cz - Heave	5.990E+7
Cxx - Roll	1.748E+11
Cyy - Pitch	2.591E+11
Czz - Yaw	2.524E+10

4. ANALYSIS RESULTS

The analysis procedure used by MOB-HyLoads has three basic steps:

1. Calculate the hydrodynamic response of the MOB with unconnected SBUs.

2. MOB-HyLoads is used to calculate the hydrodynamic loads. The radiation damping coefficients are used to calculate the impulse response functions. The hydrodynamic diffraction results are scaled with spreading and spectrum functions to create a diffraction load time history.

3. Perform the structural analysis, using the calculated diffraction load time history and impulse response functions.

4.1 Hydrodynamic Analysis

In order to fully characterize the hydrodynamic response of the MOB a large range of headings and periods were analyzed. This analysis was especially detailed over the frequency range. Approximately 400 different periods ranging from 1 to 1000 seconds were investigated.

Figure 5 shows the diffraction forces for the surge motion of the first SBU in head seas. The HIPAN non-dimensionalized diffraction amplitude is plotted versus period. Results for the remaining degrees of freedom (30 total) and for other headings were also obtained.

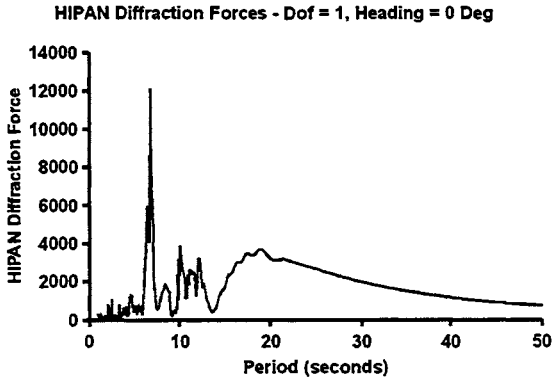

Figure 5. HIPAN Diffraction Forces vs Period

Sample radiation results are presented in Figures 6 and 7. These figures plot the non-dimensionalized radiation added mass and damping coefficients respectively, versus period for mode 1,1 (surge of SBU 1 on surge of SBU 1). A total of 900 added mass and 900 damping coefficients (30x30 matrix) were calculated.

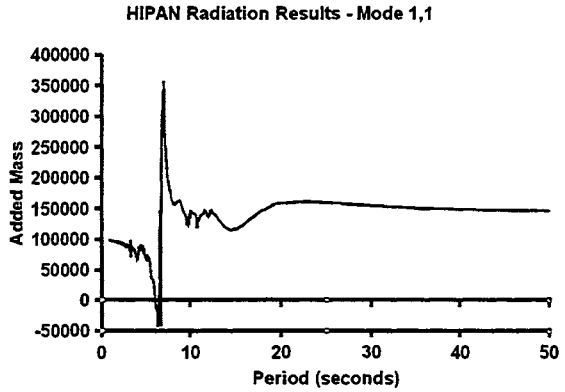

Figure 6. HIPAN Added Mass vs Period

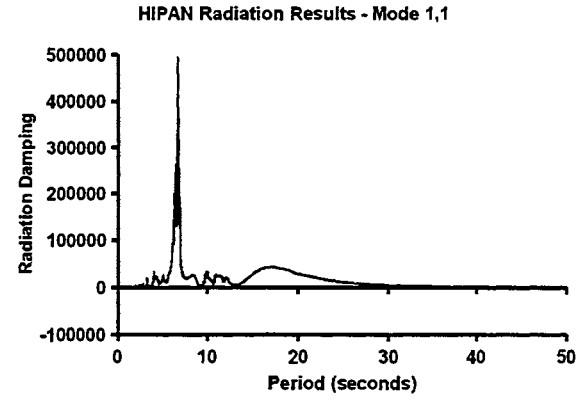

Figure 7. HIPAN Radiation Damping vs Period

4.2 MOB-HyLoads Analysis

MOB-HyLoads uses the results from HIPAN hydrodynamic analyses to calculate impulse response functions and a diffraction load time history for subsequent use in a structural analysis.

Figure 8 shows the impulse response function for mode 1,1. This function was calculated at intervals of 0.2 seconds, and extends to nearly 500 seconds. All 900 impulse response functions were calculated, although many of them have zero amplitude.

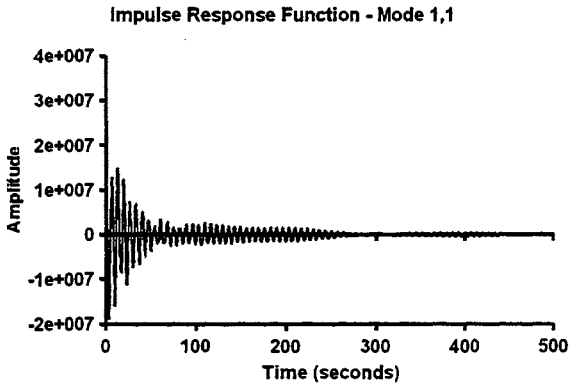

Figure 8. Impulse Response Function

Extreme sea conditions were selected for the diffraction load time history (Sea State 9). A Bretschneider spectrum with a significant wave height, Hs, of 15.24m and a peak period, Tp, of 20.10 seconds was used to scale the diffraction forces. The wave heading was 30 degrees with no spreading. Figure 9 shows the resulting diffraction load time history for the surge force of the first SBU.

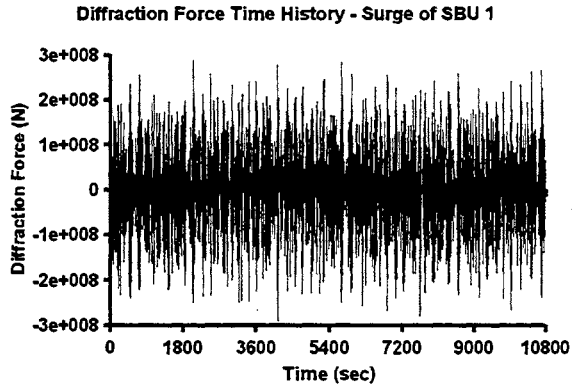

Figure 9. Diffraction Force Time History

4.3 Structural Analysis

Prior to running the three connected MOB cases, a case to verify the structural model was analyzed. An unconnected MOB was analyzed using the calculated impulse response functions. The diffraction force time history was for a unit amplitude, single period wave (19.947 sec), with a heading of 30 degrees. For this linear model the RAOs calculated by ABAQUS can be directly compared to the RAOs calculated by HIPAN, as seen in Table 5. This good comparison confirms the accuracy of the calculated impulse response functions.

Table 5. RAO Comparison – Unconnected SBUs

SBU 1	ABAQUS	HIPAN
Surge	0.546	0.539
Sway	0.313	0.312
Heave	0.624	0.627
Roll	0.00251	0.00254
Pitch	0.00293	0.00297
Yaw	0.00105	0.00104

Three separate cases were analyzed, representing three different MOB connector configurations. These cases differ in the connector stiffness and in the calculation of added mass and radiation damping forces. Table 6 summarizes these cases.

Table 6. MOB Analysis Cases

Case	Connector	Radiation Forces
1	Linear	Impulse response function
2	Non-linear	Linear added mass & damping
3	Non-linear	Impulse response function

Figure 10 shows results from Case 1. It plots the force history for one side of the connector between SBU 1 and SBU 2. The maximum connector force is approximately 8.0E7 N, which corresponds to about 4m connector displacements.

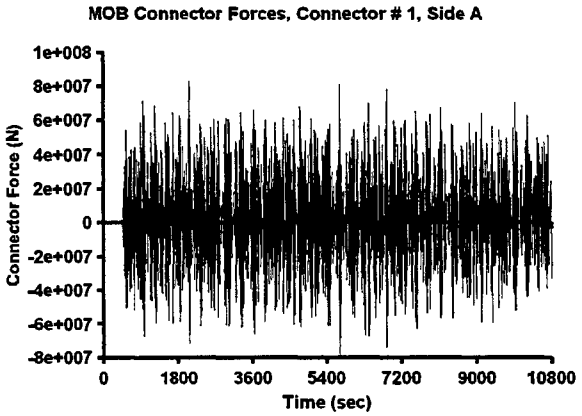

Figure 10. Connector Forces – Case 1

Figure 11 shows results from Case 2. It plots the force history for the same connector location as in Figure 10, but with a non-linear connector. The maximum connector force is significantly reduced to approximately 1.0E7 N, which corresponds to about 2m connector displacements.

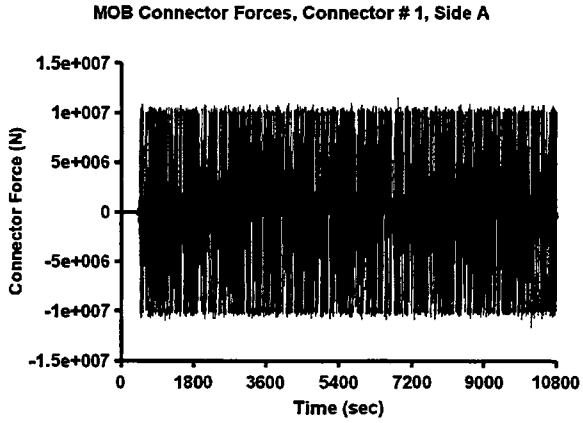

Figure 11. Connector Forces – Case 2

Figure 12 shows results from Case 3. It plots the force history for the same connector location as in Figures 10 and 11. The maximum connector force of approximately 2.0E7 N (about 3.5m connector displacements) is significantly lower than Case 1, yet double that of Case 2.

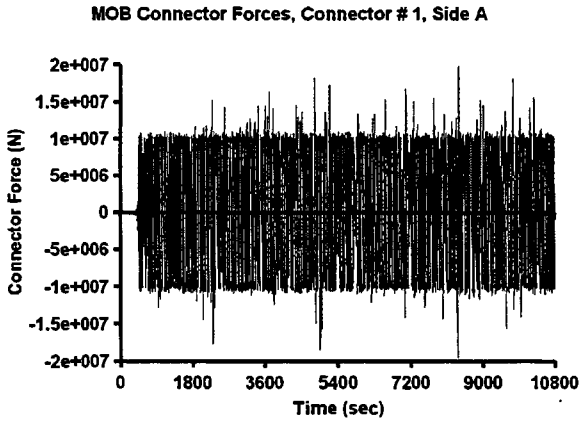

Figure 12. Connector Forces – Case 3

5. CONCLUSION

The use of advanced connector concepts for a MOB, such as non-linear connectors, requires the use of time domain structural analysis. MOB-HyLoads has been developed by McDermott Technology, Inc. to provide the software tools and methodologies to couple frequency-domain hydrodynamics with time-domain structural analysis.

The methodology to use linear, frequency-domain hydrodynamics for non-linear, time-domain structural analysis has been demonstrated. For linear structural models, the calculated force and motion RAOs compare well with those calculated by linear frequency dependent hydrodynamics.

Analyses of non-linear MOB connectors show a need for these tools. Predicted force and motion RAOs for the linear cases (Case 1 and 2), are significantly different from the fully non-linear example (Case 3).

Finally, it should be acknowledged that the use of these advanced tools must be validated against experimental data. While comparison to linear, frequency-domain hydrodynamics is excellent, validation of the non-linear capabilities of MOB-HyLoads is needed.

REFERENCES

[1] Lee, C.H. and Newman, J.N., HIPAN 2.0.2 User's Manual, "A Radiation-Diffraction Panel Program for Wave-Body Interactions", Massachusetts Institute of Technology, 1998.

[2] Hibbitt, Karlsson & Sorensen, Inc., ABAQUS User's Manual Version 5.8, Hibbitt, Karlsson & Sorensen, Inc., 1998

Acknowledgment: This material is based on work supported by the U.S. Office of Naval Research's MOB Program, ONR Contract N00014-97-C-0410, "Design Technologies for Mobile Offshore Base".

PROCEEDINGS OF THE THIRD INTERNATIONAL WORKSHOP ON VERY LARGE FLOATING STRUCTURES
(VLFS '99), VOL. I, EDS. R.C. ERTEKIN & J.W. KIM, 22-24 SEPTEMBER 1999, HONOLULU, HAWAII, USA

A Numerical Study of Nonlinear Wave Interaction in Regular and Irregular Seas: Irrotational Green-Naghdi Model

Jang Whan Kim and R. Cengiz Ertekin
University of Hawaii at Manoa*

ABSTRACT

The Irrotational Green-Naghdi model for nonlinear wave propagation in deep water is developed to simulate the irregular sea surface of a given directional wave spectrum. The model is derived from Hamilton's principle with a depthwise approximation to the flow field. The nonlinear boundary conditions are exactly satisfied on the actual free surface, and the continuity equation is satisfied exactly within the fluid domain. The "Level" of approximation in the depthwise direction is optimally chosen to simulate a given wave spectrum accurately with minimum computational effort. Several numerical techniques also are introduced to cut the computational cost further. Numerical results for two-dimensional nonlinear waves are presented.

1. INTRODUCTION

The sea surface in a storm area is usually treated as a 'short-crested' irregular surface, which can be described by a directional wave spectrum. However, there have been many observed occasions where the waves with extreme heights and long crests arise from short-crested surfaces. With their extreme heights and slopes, they have been called 'freak waves', 'rogue waves', 'episodic waves' or simply 'wall of water' (see, e.g., [1], [2]). It has been pointed out that this coherent structure of waves should be considered as an important environmental factor in the operations of a MOB (Mobile Offshore Base) in open seas (see [3]).

Recently, there have been two major approaches to explaining this phenomenon. One is based on the interaction between the waves and current, and the other is on the nonlinear interaction between waves themselves. White and Fornberg [4] showed that waves in a variable current can be focused to generate a 'freak wave' using the ray-tracing technique. In the other approach, Trulsen and Dysthe [5] used a modified nonlinear Schrodinger (MNLS) equation to explain the phenomenon. A number of relevant references on these two approaches can be found in these two papers.

Since we are more interested in waves in the open ocean, where a MOB will operate and where there are no strong currents, as there would be in a coastal region, the wave-wave interaction seems to be the more important phenomenon to be considered. Weakly nonlinear models, such as the NLS and MNLS models, have been tried in this line of approach, with few successes. Since the analyses of nonlinear wave-wave interaction have been made under the assumption that the nonlinearity and/or dispersion is weak, the full nonlinear interaction in a wide-band spectrum has yet to be made. This may be the reason of some recent failures in generating freak waves by nonlinear wave-wave interaction. The final conclusion should not be made until we can simulate nonlinear waves fully with a wide-band spectrum.

One of the possible approaches to understanding the phenomenon is by the direct numerical simulation of irregular waves with full account of nonlinear and three-dimensional features. There are a number of numerical methods developed that can be used for this purpose. To name a few, the panel, finite-difference, finite-element and spectral methods, and the Green-Naghdi model, are among the available methods. But only a few of them can be employed if one considers the huge size of the computational domain to be included. Suppose that we are simulating a two kilometer by two kilometer area of the ocean and that the waves of interest have lengths longer than 100 meters. To maintain only ten panels in one wavelength, we need about 40,000 panels on the horizontal plane, which is an impracticably large number for most of the numerical methods, except for the spectral method and the Green-Naghdi model. If one restricts the choice of the model further by requiring the full consideration of nonlinearity, we have only one remaining model,

* 2540 Dole St., Holmes Hall 402, Honolulu,
HI 96822, USA. E-mail: kjw@oceaneng.eng.hawaii.edu

namely the Green-Naghdi model, which will be used here.

In this paper, we introduce the Irrotational Green-Naghdi (IGN) equations to study the nonlinear wave-wave interaction in irregular seas. The GN equation was originally developed by A.E. Green & P.M. Naghdi in 1974 to analyze some nonlinear free-surface flows. After the successful application of the method to nonlinear ship wave-making problems by, for example, Ertekin et al. [6], the method has been applied to many nonlinear water-wave problems. Later, the model has been extended to deep water waves by Webster & Kim [7] and Xu et al. [8] in two and three dimensions, respectively. The new model to be used here can be derived by integrating the GN equations through the transformation between the Lagrangian and Eulerian variables as shown by Kim et al. [9]. The new model shares the same linear equations and the conservation laws with the old model, but does not permit a vortical flow which was acceptable in the old model. The elimination of the vorticity simplify the structure of the model equations considerably. In the new model, it is rather easy to extend the theory to an arbitrary level, as will be shown in one of the numerical results in this paper. We will refer to the new model as the IGN (Irrotational Green-Naghdi) model.

In the present IGN equations, we do not make any assumptions on the magnitude of waves or velocity field within the assumptions of incompressible and inviscid fluid, and irrotational flow, and non-breaking waves. We simply assume that the velocity field can be approximated by a finite number of interpolation functions in the vertical direction. The number of interpolations, which we refer as the Level of the IGN model, determines the dispersion properties of the model. As a result, nonlinearity is strongly considered and the dispersion (or Level) can optimally be chosen to simulate a given wave spectrum accurately with minimum computational effort.

In the numerical implementation of the IGN equations, several techniques are employed here to improve the computational efficiency further. The new model is successfully applied to the nonlinear evolution of both regular and irregular waves in two dimensions and the extension to three dimensions is ongoing. In this paper, we present the results in two dimensions after presenting the general formulation of the model.

2. IGN (Irrotational Green-Naghdi) EQUATIONS

The derivation of the equations is based on Hamilton's principle, which has been widely used in the development of approximate theories for water waves (e.g., [9], [10]). Let *Oxyz* be the Cartesian coordinate system with *z* axis pointing against the gravity. Then the Lagrangian density of the inviscid and incompressible fluid of density ρ, occupying the volume under the free surface $z=\zeta(x,y,t)$ can be written as

$$L=\rho\phi(\zeta_t-w+\mathbf{u}\cdot\nabla\zeta)+\rho\int_{-\infty}^{\zeta}\left(\mathbf{u}\cdot\mathbf{u}+w^2\right)dz-\frac{\rho g}{2}\zeta^2, \quad (1)$$

where g is the gravitational constant, and $\mathbf{u}=\mathbf{u}(x,y,z,t)$ and $w=w(x,y,z,t)$ denote the horizontal velocity vector and the vertical velocity component of fluid particle, respectively, and $\phi=\phi(x,y,t)$ denote the velocity potential on the free surface. The velocity field should satisfy the continuity equation as a kinematic constraint:

$$\nabla\cdot\mathbf{u}+\frac{\partial w}{\partial z}=0, \quad -\infty<z<\zeta. \quad (2)$$

In the *M*-th Level of the IGN theory, we interpolate the velocity field in the vertical direction using *M* interpolation functions, say, $\{f_1(z), f_2(z), \ldots, f_M(z)\}$. The velocity field that satisfies the continuity equation (2) can be given as

$$\begin{aligned}\mathbf{u}&=\sum_m f'_m(z-\zeta)\psi_m(x,y,t),\\ w&=-\sum_m \nabla\cdot\{f_m(z-\zeta)\psi_m(x,y,t)\},\end{aligned} \quad (3)$$

where the vector potentials $\{\psi_1(x,y,t), \psi_2(x,y,t), \ldots, \psi_M(x,y,t)\}$ are the unknown functions to be solved, and prime indicates differential with respect to the argument. Substituting Eq. (3) into Eq. (1), we obtain the Lagrangian as

$$\begin{aligned}L=&\rho\phi\left\{\zeta_t+\sum_m f_m(0)\nabla\cdot\psi_m\right\}\\ &+\frac{\rho}{2}\sum_{m,n}\{A_{mn}(\nabla\cdot\psi_m)(\nabla\cdot\psi_n)+B_{mn}\psi_m\psi_n\}\\ &+\rho\sum_{m,n}\left\{\frac{1}{2}B_{mn}\nabla\phi\cdot\nabla\zeta\psi_m\cdot\psi_n\right.\\ &\left.-D_{mn}(\nabla\cdot\psi_m)(\nabla\zeta\cdot\phi_n)\right\}-\frac{\rho g}{2}\zeta^2,\end{aligned} \quad (4)$$

where the tensors A_{mn}, B_{mn} and D_{mn} are defined as

$$A_{mn} = \int_{-\infty}^{0} f_m(z) f_n(z) dz,$$
$$B_{mn} = \int_{-\infty}^{0} f'_m(z) f'_n(z) dz, \quad (5)$$
$$D_{mn} = \int_{-\infty}^{0} f_m(z) f'_n(z) dz$$

Taking the variations of the action integral $\iiint L\, dxdydt$ with respect to ϕ, ζ and ψ_m, successively, we obtain

$$\zeta_t + \sum_m f_m(0) \nabla \cdot \psi_m = 0, \quad (6)$$

$$\phi_t + g\zeta - \sum_{m,n} \{D_{mn} \nabla \cdot (\psi_n \nabla \cdot \psi_m) + B_{mn} \nabla \cdot (\nabla \zeta \psi_m \cdot \psi_n)\} = 0, \quad (7)$$

$$\sum_n \{A_{mn} \nabla(\nabla \cdot \psi_n) + D_{mn} \nabla(\nabla \zeta \cdot \psi_n) - D_{nm} \nabla \zeta \nabla \cdot \psi_n - \left(1 + |\nabla \zeta|^2\right) B_{mn} \psi_n\} = -f_m(0) \nabla \phi, \quad m = 1, \ldots, M, \quad (8)$$

where Eqs. (6) and (7) are the evolution equations for the two canonical variables ζ and ϕ, which are the wave elevation and the free-surface potential, respectively, and Eq. (8) relates ϕ and the two-dimensional vector potentials, ψ_m.

3. NUMERICAL APPROXIMATIONS

3.1 Vertical Interpolation

For the vertical interpolation, Webster & Kim [7] and Xu et al. [8] used specific polynomials with an exponential weight:

$$f_m(z) = z^{m-1} \exp(az), \quad (9)$$

where the parameter a is chosen such that it is tuned to the wave number of the peak frequency. In a recent application of the GN equations to capillary-gravity waves by Kim & Webster [11], it has been found that more general expressions for the interpolation is necessary when there is a substantial variation in the wave-length scale between the wave components under consideration. And, as a result, the following type of interpolation was used:

$$f_m(z) = z^{p_m} \exp(a_m z), \quad (10)$$

where both the order of the polynomial, p_m, and exponents of the weight, a_m, are allowed to vary. We shall show later the accuracy of the dispersion of the IGN model by changing the order of the polynomial and number of exponents.

If the vertical interpolation functions were chosen from an orthogonal set, Eqs. (7) and (8) could be written in a simpler form. As a matter of fact, we can always construct an orthogonal set from the interpolation-function set as long as the functions are linearly independent. The new orthogonal set $\{\bar{f}_1(z), \bar{f}_2(z), \ldots, \bar{f}_M(z)\}$ can be obtained as

$$\bar{f}_m(z) = \sum_{n,l=1}^{M} E_{nm} A_{nl} f_l(z),$$

where E_{mn} is the eigenmatrix, each column of which consists of the eigenvectors of a matrix eigenvalue problem, $\mathbf{Be} = \lambda \mathbf{Ae}$, where $\mathbf{A} = [A_{mn}]$ and $\mathbf{B} = [B_{mn}]$. We can use the new orthogonal set as the interpolation functions to rewrite Eqs. (7) and (8) as

$$\phi_t + g\zeta - \sum_m \lambda_m \nabla \cdot (\nabla \zeta \psi_m \cdot \psi_m) - \sum_{m,n} D_{mn} \nabla \cdot (\psi_n \nabla \cdot \psi_m) = 0, \quad (11)$$

and

$$\nabla(\nabla \cdot \psi_m) - \lambda_m \left(1 + |\nabla \zeta|^2\right) \psi_m + \sum_n \{D_{mn} \nabla(\nabla \zeta \cdot \psi_n) - D_{nm} \nabla \zeta \nabla \cdot \psi_n\} = -\bar{f}_m(0) \nabla \phi, \quad m = 1,2,\ldots,M, \quad (12)$$

where $\lambda_1, \lambda_2, \ldots, \lambda_M$ are the eigenvalues of the eigenvalue problem $\mathbf{Be} = \lambda \mathbf{Ae}$.

3.2 Approximation in the horizontal plane

We shall, in general, use a pseudo-spectral method in the xy-plane. For a given square domain of length L, the surface elevation and the potentials are expanded in Fourier series:

$$\zeta(x,y,t) = \sum_{p,q=-N}^{N} Z_{pq}(t) e^{i(k_p x + k_q y)},$$

$$\phi(x,y,t)=\sum_{p,q=-N}^{N}\Phi_{pq}(t)e^{i(k_p x+k_q y)}, \qquad (13)$$
$$\psi_m(x,y,t)=\sum_{p,q=-N}^{N}\Psi_{mpq}(t)e^{i(k_p x+k_q y)},$$

where $Z_{pq}(t), \Phi_{pq}(t)$ and $\Psi_{mpq}(t)=\left(\Psi^x_{mpq}(t), \Psi^y_{mpq}(t)\right)$ are time-dependent Fourier coefficients of the surface elevation, surface potential and the vector potential, respectively, and the discrete wave numbers k_p and k_q are defined as

$$k_p=\frac{2\pi p}{L},\ k_q=\frac{2\pi q}{L}.$$

The spatial derivatives are evaluated in the Fourier space and the nonlinear terms are evaluated in the physical space. The transformation between the Fourier space and the physical space can effectively be made using the FFT algorithm, i.e.,

$$\dot{Z}_{pq}=-i\sum_m f_m(0)\mathbf{k}_{pq}\cdot\Psi_{mpq}, \qquad (14)$$

$$\dot{\Phi}_{pq}=-gZ_{pq}+F_{pq}\left[\sum_m \lambda_m\nabla\cdot(\nabla\zeta\psi_m\cdot\psi_m)-\sum_{m,n}D_{mn}\nabla\cdot(\psi_n\nabla\cdot\psi_m)\right]=0, \qquad (15)$$

$$\mathbf{k}_{pq}(\mathbf{k}_{pq}\cdot\Psi_{mpq})+\lambda_m\Psi_{mpq}= if_m(0)\mathbf{k}_{pq}\Phi_{pq}-\lambda_m F_{pq}\left[|\nabla\zeta|^2\psi_m\right]+F_{pq}\left[\sum_n\{D_{mn}\nabla(\nabla\zeta\cdot\psi_n)-D_{nm}\nabla\zeta\nabla\cdot\psi_n\}\right], \qquad (16)$$

for $m=1,\ldots,M; p,q=1,\ldots,N$, and where $\mathbf{k}_{pq}=(k_p,k_q)$ and the linear operator $F_{pq}[\cdots]$ denotes the Fourier component of a function in the bracket, i.e.,

$$F_{pq}[f(x,y)]=\frac{1}{4N^2}\sum_{r,s=0}^{2N-1}f(rk_r,sk_s)e^{-i(prk_p+qsk_s)},$$

which can be efficiently evaluated using the FFT method.

The linear part of Eq. (16) is a set of simple linear algebraic equations without any coupling within the set and can easily be inverted. When nonlinearity is weak, we can solve Eq. (16) by a fixed point iteration, where the nonlinear terms are evaluated from the results of the previous iteration. When nonlinearity is not weak and the fixed point iteration converges slowly, we will use the conjugate gradient method with preconditioning by using inversion of the linear operator. Since $\lambda_1,\lambda_2,\ldots,\lambda_M$ are the eigenvalues of the symmetric positive definite matrices A_{mn} and B_{mn}, they all are positive real numbers. As a result, we can expect that fixed point iteration will converge fast in most of the cases we study. Note that the one-dimensional version of the equations of this section are used in this work.

3.3 Initial conditions

We need initial conditions for the surface elevation and the corresponding velocity potential on the free surface from a given directional spectrum to initiate the evolution of the IGN model. Unfortunately, however, there is no available model for fully nonlinear waves. We will, thus, use the linear solution as the initial condition. Since the linear solution cannot fully satisfy the nonlinear model, substantial non-physical distortion of the spectrum may occur when wave amplitude is high. For a given directional wave spectrum, in general, we can construct a wave spectrum, $F(k_x,k_y)$ in the wave number space, such that

$$|F(k_x,k_y)|^2\Delta k_x\Delta k_y \qquad (17)$$

defines the spectral energy density of the wave components around (k_x,k_y) within the square region $\Delta k_x\Delta k_y$ in the wavenumber space. At t = 0, we can use the linear theory for the realization of the wave field:

$$Z_{mn}(0)=\frac{2\pi e^{i\delta_{mn}}}{L}|F(k_m,k_n)|,$$
$$\Phi_{mn}(0)=\frac{-2\pi i\sqrt{g}e^{i\delta_{mn}}}{L(k_m^2+k_n^2)^{1/4}}|F(k_m,k_n)| \qquad (18)$$

where δ_{mn} are randomly generated numbers between 0 and 2π. Note that the two-dimensional versions of Eqs. (17) and (18) are used in the results given later.

4. NUMERICAL RESULTS

The new IGN model is applied to simulate long-crested random seas for a given one-dimensional wave spectrum. Before we simulate random waves, we performed several numerical tests to validate the new model. First, the linear and nonlinear dispersion properties of the periodic wave solution are studied and compared with the known exact solutions. And then, Su's [12] experiments on the nonlinear evolution of a wave packet is simulated by use of the method developed here and then compared with the experimental and theoretical results of others.

4.1. Periodic wave of permanent form

In the present IGN model, the nonlinearities are fully considered without any order consideration within the assumption that the surface elevation can be given as a single-valued function. However, there is an approximation in the dispersion relation since we use a finite number of interpolation functions. As we increase the level of approximation, we can expect more accurate dispersion, at the expense of an increase in computational time. The accuracy also depends on the type of the interpolation function we choose. In the following examples, we will show how the shape and number of interpolation functions affect the accuracy in the dispersion of the periodic wave of permanent form. First, we investigate the linear dispersion of an infinitesimal wave in the following.

4.1.1 Linear dispersion of infinitesimal waves

There are two ways to increase the accuracy: one is to increase the order of the polynomial for a given exponent as in Eq. (9), the other is to use multiple values of the exponent in Eq. (10). In Figs. 1 and 2, the dispersion relations from the two approaches are compared with the exact linear relation in deep water:

$$\omega^2 = gk\,. \qquad (19)$$

In these figures, the top figures are for $0 \le k/a \le 1.0$, to show the details at low k/a values.

In Fig. 1, we used the interpolation function given in Eq. (9). The dispersion relation is exact at $k = a$ and the order of accuracy increases as we increase the order of the polynomial. In Fig. 2, we used Eq. (10) with $p_m = 0$ and exponentially increasing exponents, i.e., $a_1 = 1, a_2 = 2, a_3 = 4, \ldots$. Hereafter, we will use the same interpolation for the IGN equation unless otherwise stated. As can be seen in Fig 2, the dispersion relation is exact at the given exponents. The accuracy for long waves improves more slowly than the first approach. On the other hand, the applicable range of the approximation is wider than the first approach.

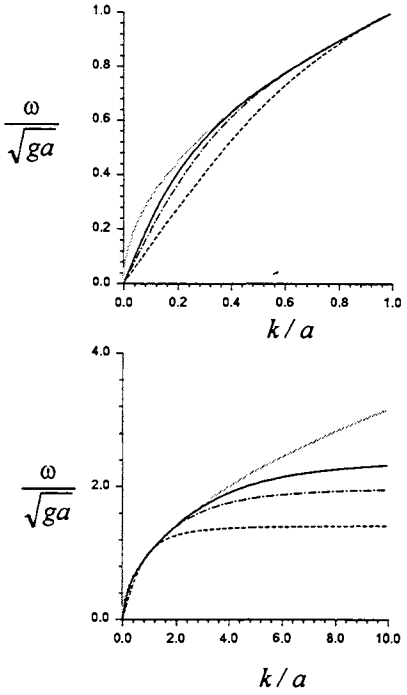

Fig. 1 Dispersion relation of the GN Level I, II and III models. ——— : Exact, ----- : Level I, —·—·— : Level II, ——— : Level III.

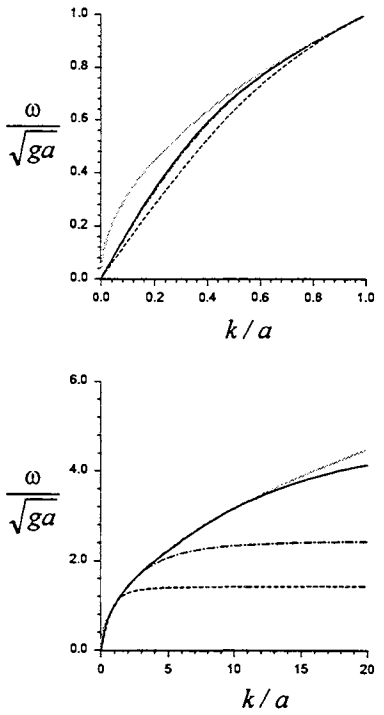

Fig. 2 Dispersion relation of the IGN model with interpolation function given in Eq. (10), with $p_m = 0, a_1 = 1, a_2 = 2, a_3 = 4$. ——— : Exact, ----------: Level I, —·—· : Level II, ———: Level III.

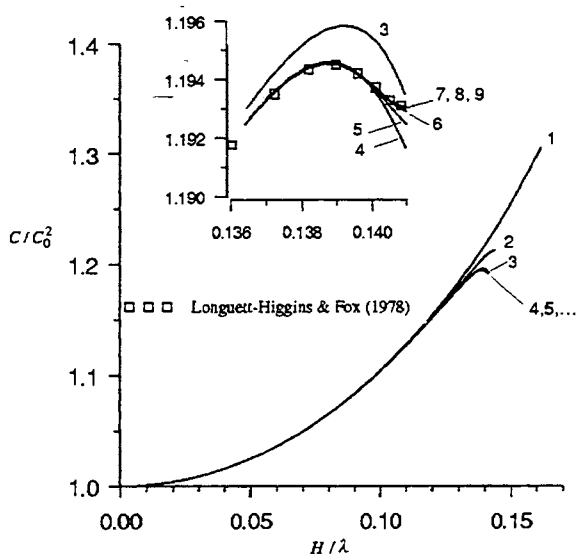

Fig. 3 Nonlinear dispersion of periodic waves in deep water predicted by the IGN model. The numbers on the results denote the Level.

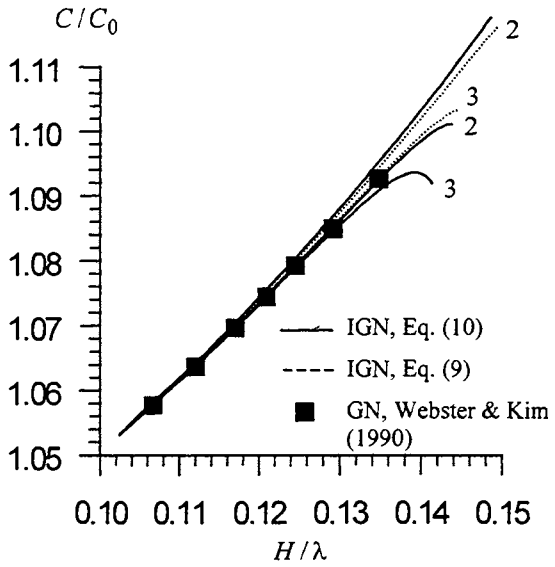

Fig. 4 Nonlinear dispersion of periodic waves in deep water predicted by the IGN model, with interpolation functions given by Eq. (10) and Eq. (9), and compared with the GN results of Webster & Kim [7]. The numbers on results denote the Level.

When we apply the IGN model to nonlinear irregular waves, we determine the number of interpolations based on the bandwidth and number of modes of the wave spectrum. The number of modes will be considered by the number of exponents to be used and the order of polynomials will be decided based on the bandwidth of the spectrum. When the band is quite wide such that we need to consider wave numbers which are greater than two times of the peak frequency, we will use multiple exponents.

It should also be noted that the frequency approximated by the GN and IGN models gives the lower bound of the exact one. The numerical stability of a numerical method is dependent on the eigenvalue (frequency) of the shortest wave component in the numerical solution. Since the dispersion error is inevitable for the short-wave components, it is desirable that the approximate solution gives the lower values of eigenvalues to make the numerical solution more stable, as in the GN and IGN models.

4.2.2 Large amplitude wave of permanent form

When the amplitude of the periodic wave is not small, the celerity of the wave is also dependent on the amplitude. We studied the nonlinear dispersion of periodic waves and compared the results with the numerically exact solutions of Longuett-Higgins & Fox [13] and Cokelet [15], and also with the solution of the original GN model given in Webster & Kim [7]. The numerical solution is obtained in the coordinate system moving with the wave, following the method described in Webster & Kim [7].

Level	H/λ	C^2/C_0^2
1	0.16168	1.3059
2	0.14382	1.2124
3	0.14133	1.1919
4	0.14120	1.1910
5	0.14121	1.1922
6	0.14118	1.1929
7	0.14113	1.1931
8	0.14110	1.1931
10	0.14107	1.1931
12	0.14106	1.1931
Schwartz [13]	0.1412	
Cokelet [14]	0.141065	

Table 1 Steepness and celerity of the highest wave obtained from the IGN model and other theoretical results.

The relation between wave steepness, defined as the ratio of wave height, H, and wavelength, λ, and celerity, C, is shown in Fig. 3. The celerity is normalized by its linear value, i.e., $C_0 = \sqrt{g\lambda/2\pi}$. The maximum error in celerity is seen to be less than 0.1% in Level III, and it is seen that the results of Levels 6-9 agree well with Longuett-Higgins & Fox's [13] results.

In Fig 4, the nonlinear dispersion obtained from the

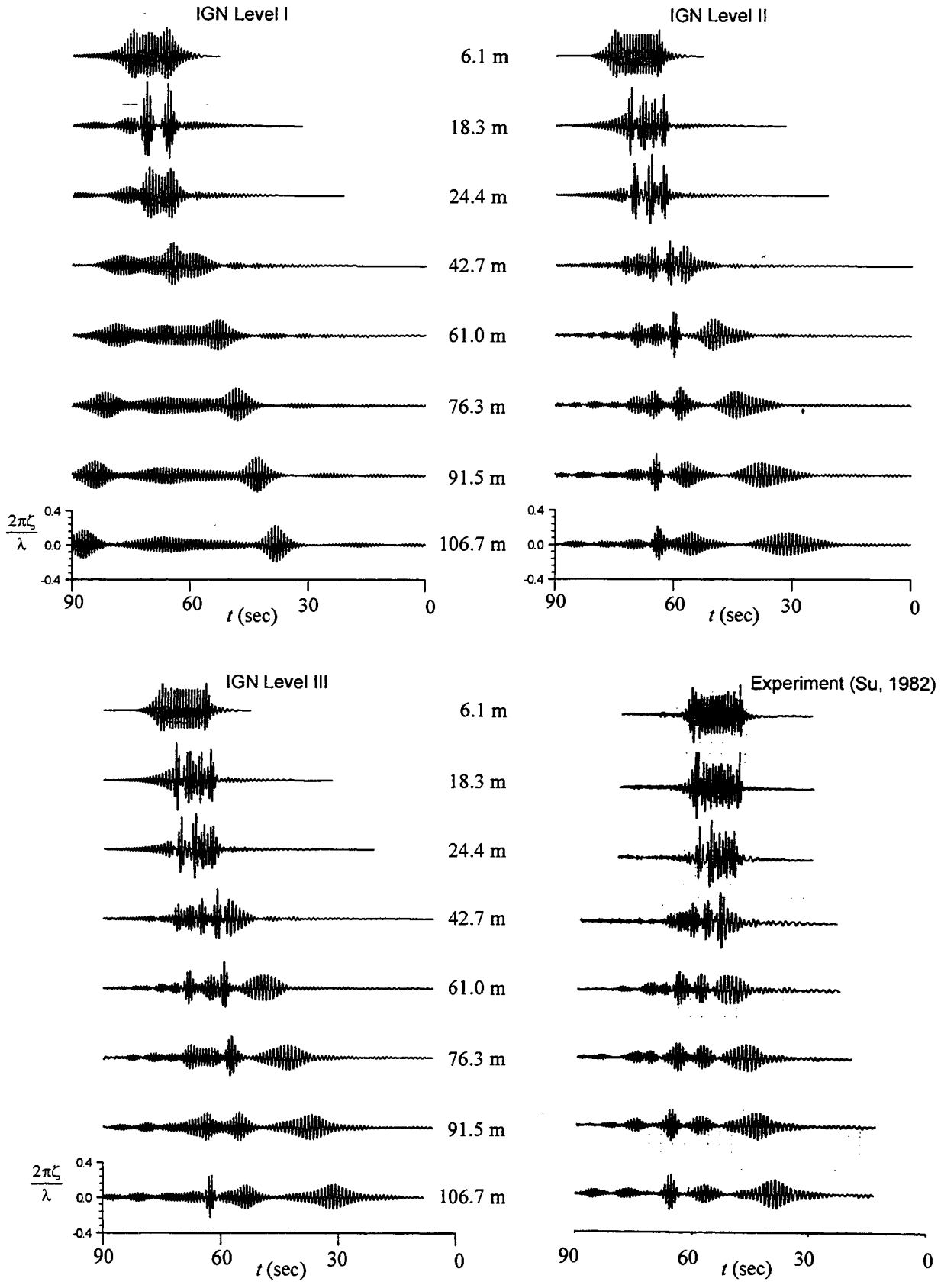

Fig. 5 Computed versus experimentally measured free-surface elevations at eight different wave gauges. Numbers between the figures denote the distance from the wavemaker.

IGN model and the original GN Level III model, taken from Webster & Kim [7], is compared. We can see that the IGN Level II provides almost the same accuracy as the GN Level III. In all fairness, we also compare the results of the IGN model with the same interpolation functions used in the GN model. It can be seen that the GN and IGN models provide almost identical results. We believe that the GN model can provide more accuracy if the new interpolation functions are used.

In Table 1, the wave height and celerity of the highest wave obtained from the IGN model is given for Levels 1 to 12. We found that the IGN solution converges to the known exact value of Cokelet [15] rapidly.

Based on these results, we can conclude that the Level III model of the IGN equations predicts the periodic waves quite well up to the maximum wave height, and the Level II model shows good agreement for wave steepnesses up to 0.13, which cover most of the practical range of wave steepnesses.

4.3 Disintegration of a wave packet

The field experiments of Su [12] is simulated and compared with the measurements. Su's experiments cover two important features of nonlinear interaction among waves, namely, Type I and Type II instabilities. In the numerical tests we conducted, the capability of the new model to capture the Type I instability (the side-band instability and downshifting in carrier frequency) is tested. Fig. 5 shows the wave elevations at eight different wave gauge locations, obtained from the Level I, II and III IGN models and Su's measurements when the frequency of the carrier wave is 1.34 Hz and steepness, a_0k_0, is 0.22 (Fig 4 of [12]). There are 10 waves in the wave train, which give 20 peaks in the wave gauge signal, since group velocity is two times slower than the phase velocity. To consider the energy dissipation due to wave breaking, smoothing of the surface elevation and potential are made using the ideal filter described in Dommermuth and Yue [16].

Surprisingly, the Level II model can show most features of nonlinear interaction found in the field experiments. We can observe the development of a side-band instability at the earlier stages of evolution at the first two wave gauges, and the disintegration of the wave train into a finite number of envelope solitons at the farther gauges. Shifting of the peak frequency and wave number in the energy spectrum are also observed. The number of solitons in the IGN model is 6, whereas 5 solitons are found in the measurements. Better agreement is expected when we use the three-dimensional model. The Level III results show further refinement such as the shape of the envelope soliton at the gauges located farther than x = 61.0 m. It also is of interest to note that the predictions from the Level I model is very similar to those from the Cubic Nonlinear Schrodinger equation, which shows a symmetric envelope evolution.

4.4 Modulation of Stokes waves

Dommermuth and Yue [16] carried out extensive numerical experiments on the evolution of wave packets using the Higher-Order Spectral (HOS) method. We noted one of their results showing a possible freak wave developed from a regular wave train and attempted to reproduce their results.

The initial condition is given as the linear sum of a Stokes wave with steepness, H/λ = 0.04, as a carrier wave, and the two dominant side-band instabilities added to modulate the carrier wave. More details can be found in [16]. Fig. 6 shows the wave profiles at t/T = 57, where T denotes the period of the carrier wave, by the IGN Level II model and the 4th-order HOS. Both models predict the occurrence of a peak at around x/λ = -1.25. The local wave steepness is measured as 0.9, which is about 2.3 times of the initial steepness. In irregular seas, single waves of height exceeding the significant wave height by a factor 2.2 has been called a "freak wave" (see [5]). If we interpret the initial steepness as the significant wave height normalized by the wave length, the peak wave in Fig. 6 can qualify as a freak wave.

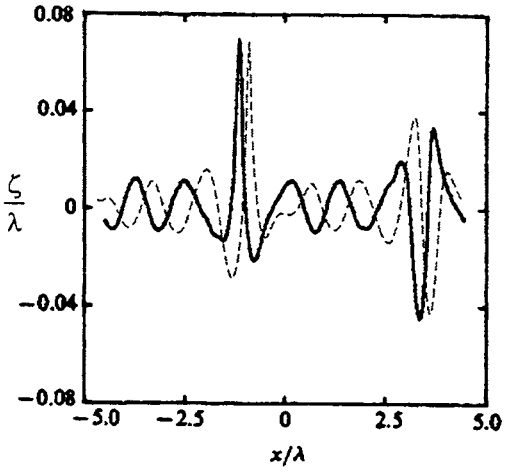

Fig. 6 Wave elevation of modulated Stokes wave at t/T = 57. —— : HOS, Dommermuth & Yue (1987); ------ : IGN Level II.

4.5 Long-crested irregular waves

It has been noted that extreme waves, with wave heights greater than twice the significant wave height, can also be observed in two-dimensional irregular wave trains ([17]). Yasuda et al. [18] have made two-dimensional simulations based on the 3rd-order HOS

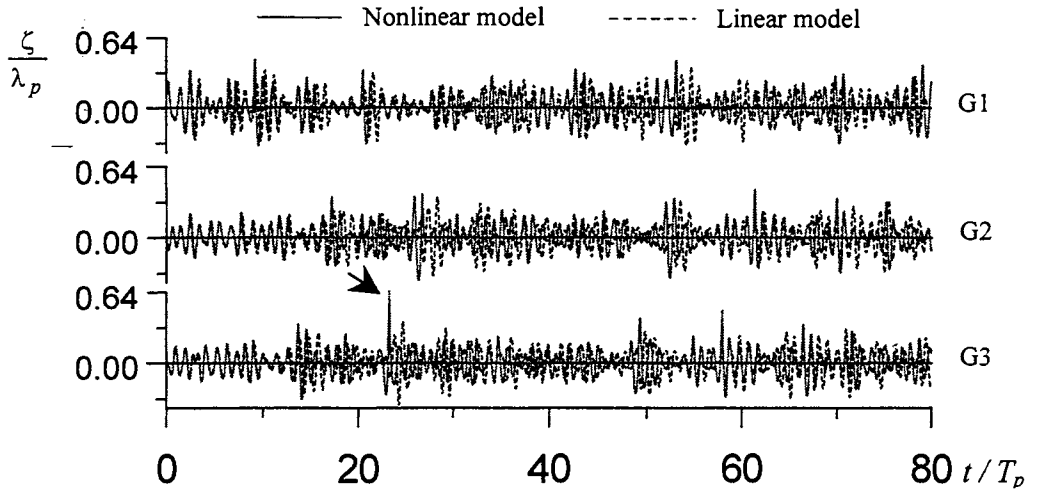

Fig. 7 Time history of surface elevation at three different numerical wave gauges. The IGN Level II model is used.

and noted the existence of freak waves. We used the same wave spectrum of Yasuda et al. [18] and performed simulations based on the IGN Level II and III models. In most simulations, we could observe extreme waves with heights greater than two times the significant wave height. Fig. 7 shows one of the results. The significant wave height, $H_{1/3}$, is such that $H_{1/3}/\lambda_p = 0.04$ where λ_p denotes the wavelength at the peak frequency of the spectrum. The length of the computational domain is 18 times the wavelength, and the time step is 1/100th of the wave period, T_p. Total of 512 Fourier modes are used to simulate the wave field. The wave elevation is measured at 6 different locations with a uniform distance of $3\lambda_p$, and are denoted by G1, G2, ..., G6. At G3, an extreme wave

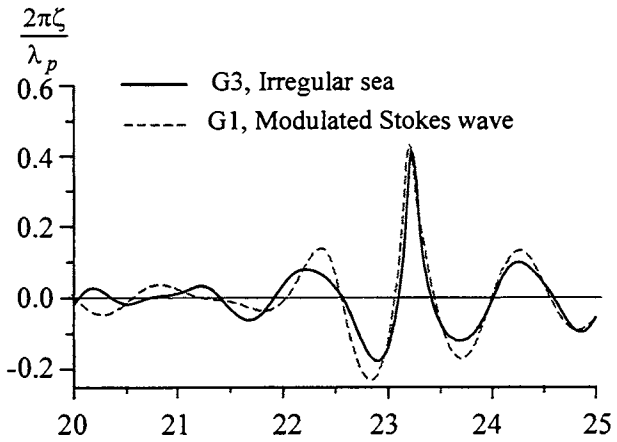

Fig. 8 Wave profile around extreme waves.

height, $H = 2.1H_{1/3}$ was observed at $t \approx 22T_p$. Also presented is the wave elevation computed by the use of linearized IGN Level II equations, which use the same initial conditions, but show no extreme waves.

During the simulations, we observed that the wave profiles around the extreme wave elevation, developed from regular and irregular wave trains, are similar to each other. In Fig. 8, the extreme wave in Stokes wave train, shown in Fig. 6, and that in the irregular wave train in Fig. 7 are put together. The free-surface shapes around the crest are quite similar to each other. The regular wave train troughs show a little more depression than the one from irregular waves. We observed similar wave profiles for different initial values of the significant wave height and bandwidth of the spectrum.

The extreme waves simulated in two-dimensional *irregular seas* in the present study cannot fulfill the criterion of "freak waves". It is also noted that the life duration of these extreme waves is very short - less than half period in time and space. However, one may also expect that nonlinear wave-wave interaction in three-dimensions can bring a larger, and more stable, wave structure than in two dimensions.

5. CONCLUSIONS

A new Green-Naghdi model for irrotational flows (the IGN model) for an arbitrary Level is developed to study the role of nonlinear interaction in the coherent structure of an irregular ocean surface. The new model is applied to two-dimensional waves in both regular and irregular seas. We have shown numerically that the new model converges to the known exact solutions of maximum height as the Level of the model increases. Other than the highest wave, the Level II model could describe the most important features of nonlinear interaction in wave packets and narrow-band irregular waves. One of the important features of the coherent wave structure - the extreme wave height - was

simulated successfully using the new model in two dimensions. The other feature - the crest length problem - will be addressed soon in the numerical simulations of the IGN model in three dimensions.

Acknowledgment: This material is based upon work supported by the Office of Naval Research, Mobile Offshore Base Program, under the direction of Dr. C. Linwood Vincent.

References

[1] Bascom, W. *Waves and Beaches*, Anchor Books, Garden City, New York, 1980.

[2] Doneal, M. Research needs for better wave forecasting: LEWEX panel discussion. *Directional Ocean Wave Spectra* (Edited by Beam, R.C.), Johns Hopkins Univ. Press, pp.196-204, 1991.

[3] Vincent, C. L. (Eds.) Spatial Coherence of Wave Phenomena: Information for Mobile Offshore Base Design, *Report of an Office of Naval Research Workshop*, Arlington, Virginia, 19-20 August, 1997.

[4] White, B.S. and Fornberg, B. On the chance of freak waves at sea. *J. Fluid Mech.*, Vol. 355, pp.113-138, 1998.

[5] Trulsen, K and Dysthe, K.B. Freak waves: a 3-D wave simulation. *Proc. 21st Int. Symp. on Naval Hydrodyn.*, Trondheim, Norway, 1997.

[6] Ertekin, R.C., Webster, W.C. and Wehausen, J.V. Waves caused by a moving disturbance in a shallow channel of finite width. *J. of Fluid Mech.*, Vol. 169, pp.272-292, 1986.

[7] Webster, W.C. and Kim, D.Y. The dispersion of large-amplitude gravity waves in deep water. *Proc. 18th Symp. On Naval Hydrodyn.*, pp. 397-415, 1990.

[8] Xu, Q., Pawlowski, J.W. and Baddour, R.E. Development of Green-Naghdi models with a wave-absorbing beach for nonlinear, irregular wave propagation. *J. of Marine Sci. & Tech.*, pp.21-34, 1997

[9] Kim, J. W., Bai, K.J., Ertekin, R.C. and Webster, W.C. A derivation of the Green-Naghdi equations for irrotational flows, To appear in *J. Engineering Mathematics*, 1999.

[10] Miles, J. W. and Salmon, R. Weakly dispersive, nonlinear gravity waves *J. Fluid Mech.*, Vol.157, pp. 519-531, 1985.

[11] Kim, J. W. and Webster, W. C. A Numerical Computation of Gravity-Capillary Waves in Deep Water," The 11th International Workshop on Water Waves and Floating Bodies, Hamburg, Germany, 1996.

[12] Su, M. -Y. Evolution of Groups of Gravity Waves with Moderate to High Steepness. *Phys. Fluids*, Vol. 25, pp. 2167-2174, 1982.

[13] Longuett-Higgins, M. S. and Fox, M. J. H. Theory of the Almost Highest Wave II: Matching and Analytic Extensions, *J. Fluid Mech.*, Vol. 85, pp. 769-786, 1978.

[14] Schwartz, L. W. Computer Extension and Analytic Continuation of Stokes' Expansion for Gravity Waves, *J. Fluid Mech.*, Vol. 62, pp. 553-578, 1974.

[15] Cokelet, E. D. Steep Gravity Waves in Water of Arbitrary Uniform Depth, *Phil. Trans. R. Soc. London*, A 286, pp. 183-230, 1977.

[16] Dommermuth, D. G. and Yue, D. K. P. A High-Order Spectral Method for the Study of Nonlinear Gravity Waves, *J. Fluid Mech.*, Vol. 184, pp. 267-288, 1987.

[17] Stansberg, C. T. Extreme Waves in Laboratory Generated Irregular Wave Trains, In *Water Wave Kinematics*, A. Torum & O. T. Gudmestad (Eds.), pp. 573-589, Kluwer, 1990.

[18] Yasuda, T., Mori, N. and Ito, K. Freak Waves in Unidirectional Wave Trains and their Properties, *Proc. 23rd Int. Conf. On Coastal Engineering*, pp. 751-765, 1992.

PROCEEDINGS OF THE THIRD INTERNATIONAL WORKSHOP ON VERY LARGE FLOATING STRUCTURES
(VLFS '99), VOL. I, EDS. R.C. ERTEKIN & J.W. KIM, 22-24 SEPTEMBER 1999, HONOLULU, HAWAII, USA

ENVIRONMENTAL SPECIFICATION FOR THE MOBILE OFFSHORE BASE (MOB)

Stuart F. Pawsey and Makis Manetas
Bechtel National, Inc.*

ABSTRACT

The Mobile Offshore Base (MOB) will be designed for deployment in one or more fixed locations and for transit to and from these sites. Long term wind, wave and current data were obtained for the design process for 4 deployment sites and 21 sites along transit routes.

The primary data are about 20 years of wind from a climatology database and global wave and current hindcasts. For a potential deployment site in the Northwest Pacific, these data were supplemented by dedicated typhoon wind, wave and current hindcasts for 22 of the most intense typhoons in the last 50 years. In addition to these data, other metocean events such as internal waves and ocean and atmospheric fronts were included because of possible importance due to the length of the MOB.

Finally, an assessment was made of the accuracy of the wind, wave and current data selected.

1. INTRODUCTION

The MOB is currently envisioned to be a floating base somewhat more than 5,000 ft (1,500 m) long, which is intended to serve as a forward supply point for military operations [1]. Currently, the MOB program is in the concept development stage with several contractors developing alternative concepts with the intent of proving its feasibility and identifying issues requiring further development. In order to evaluate or design alternative concepts on a consistent basis, or carry a single concept to final design, a detailed description is needed of the environment to which the MOB will be exposed during its lifetime. The development of this environmental data was funded by the Office of Naval Research and is described in the Environmental Specification report to the Naval Facilities Engineering Service Center [2], and is summarized in this paper.

The primary issues that distinguish a MOB from a conventional floating structure, such as a semi-submersible platform, relate to its size. Semi-submersibles are quite short relative to important wavelengths, so that variations of wind, waves and current across or along the platform are not important. However, with dimensions of the order of 5,000 ft, there may be significant variations over the length of the MOB inducing responses not experienced by smaller structures. For instance, non-uniform wind, waves or currents will exert differential forces along the length of the MOB, resulting in connection forces or dynamic positioning requirements that are quite different from those found from more uniform conditions.

The final design of the MOB will be based on a reliability method. There are a number of important inter-related environmental parameters that affect the MOB, and it is not possible to choose design values of these without knowing the characteristics of the structure. Therefore, these data consist of statistical or historical information on the environment to which the MOB will be subjected, rather than a set of discrete design seastates and it will be the responsibility of the designer to use this information in a manner that assures that the responses of his/her particular structure have the appropriate reliability.

For a projected design life of 40 years, statistics covering several decades are desirable, but seldom available. Often high-accuracy data are available for only several years. As a result, a balance must frequently be sought between accuracy and duration of available data.

Based partly on geo-political reasons and partly on the environmental severity of the sites, the Navy specified the following possible sites for the deployment of the MOB:

- North Atlantic
- Northwest Pacific
- Arabian Sea
- Sea of Japan

Of these four sites, the North Atlantic and the Northwest Pacific sites have the most severe conditions. A map showing these locations and transit

* 45 Fremont St, P.O. Box 193965, San Francisco, CA 94119-3965

routes between them and to a home base in the U.S. is shown in Figure 1.

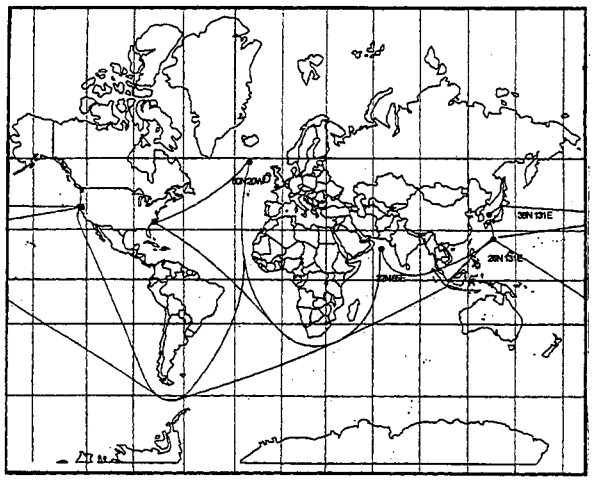

Figure 1: MOB Deployment Sites and Transit Routes

The MOB will operate at these sites during part of its life, either with its modules connected or unconnected, and will spend a part of its life transiting between these sites and to and from its home base, where it will be laid up, presumably in protected waters in the U.S. Estimates from the Navy for the proportion of time in each of these situations are:

1.	Operating, unconnected	35%
2.	Operating, connected	35%
3.	Laid up	25%
4.	Transit	5%

Since it is not known where the MOB will operate, the design will have to assume it is deployed at the worst site for any particular response being studied.

2. RELIABILITY METHODOLOGY

The MOB will be a floating structure far larger than any previously built floating structure. Because of its size and configuration there is less historical information on performance than for ships and other ocean platforms, and it has been decided that the final design should be carried out using a reliability methodology. [3] In this procedure, the failure probability of the structure is required to be less than some pre-determined value. The process is as follows:

A set of design cases are identified representing various situations that could result in structural failure, instability or exceedance of operational criteria (such as excessive motions). If a single parameter could be used to describe the loading (say wave height), it would be possible to identify a sufficiently unlikely level of this parameter (say the level corresponding to a 100 year return period) and use this to determine the applied load. If the return period is chosen appropriately, the desired probability of failure can be realized. With dependency on several parameters (such as wind and current speed), using the 100 year value (say) for all parameters would result in a conservative design unless these parameters are closely correlated. Further, the structure loading may depend on a number of metocean parameters, for which the return period has no relevance (for instance wave spectral peak period, or wave direction). The reliability method attempts to overcome these problems.

A relationship is first established between the failure criterion (say, stress greater than an allowable value), the parameters that cause the loading (say, wave height, period and direction) and the parameters that contribute to the resistance (say, cross section dimensions of a beam if examining the failure of some beam in the structure). Then the statistics of the loading and resistance parameters are identified (for instance, the probability distributions of the wave heights, periods and directions, the uncertainty in these parameters and the uncertainty in the beam dimensions, in this example). For correlated parameters, joint probabilities of these data should be made available. Finally load and resistance parameters are sought that satisfy the failure criterion, and result in the desired probability of failure.

It is seen that, in this process, design values of the environmental parameters cannot be specified without knowing the details of the structure being studied. For this reason, no design values of any metocean parameters were given in the Environmental Specification, and instead, data that allows statistical descriptions of these parameters were given.

3. PRIMARY METOCEAN DATA

Two basic types of data were assembled. The first, referred to as global data, are records of wind, wave and current recorded continuously over about 20 years. The second, the typhoon data, were gathered only for the NW Pacific site and consist of data during the passage of selected typhoons. These sources of data are now described.

3.1 Hindcasting

Metocean data can be obtained either from field measurements or from the results of numerical modeling of the wind, waves and currents, known as hindcasting. The oceans are divided up into grid points at appropriate spacing and wind records are assembled at each grid point. In hindcast models, the winds are then used to drive numerical models of the waves and/or currents (independently), with algorithms defining the driving of waves and currents by the wind, and their propagation and decay as they move away

from the regions where they are created. The accuracy of the modeling depends first on the accuracy of the wind fields used to drive the models. The accuracy also depends on the time step size being small enough relative to the important rates of change of wind speeds and directions, and the grid point spacing being fine enough relative to the spatial structure of the important winds being modeled.

Considerable development in the technology of wave hindcasting has taken place in the last few decades and the numerical models are considered quite mature, and have been used for design of offshore platforms for many years. Hindcasting of currents is somewhat more recent in its development.

The following lists a few advantages of hindcast metocean data.

- Because ships try to avoid storms, there is a natural low bias in much of the data from ships, that has to be removed by estimating the bias.
- Data can be determined at any site of interest, and are not subject to availability of records.
- Few measured records in the past have included wave directions, while these come automatically with hindcast data.
- Very little measured data are available in the intense regions of tropical storms.
- Although measurements of currents in coastal and estuarine waters have been made for many years, relatively few deep ocean sites have long-term current data, due to the difficulty and expense of such measurements.
- Long-term hindcasts over many decades can be made with relative ease.

For these reasons, it was decided to collect wave, current and some wind data from hindcast modeling. These data were provided at the 4 deployment sites and 21 sites on the transit routes. The long-term wind data was from a climatology, which is basically measured data. The output from hindcast models is a history of the wind, wave or current during the period of the modeling. These data can be used to compute statistics of any one parameter output, or the joint statistics of more than one parameter.

3.1.1 Global and Local Models

Global models include large regions of the ocean's surface, in this case all the major oceans of the world. A global model, with time spacing of six hours and grid point spacing of a degree or so (approximately 100 km) will not accurately model the detail of the waves caused by a cold front, or a typhoon, both of which have space and time scales considerably less than these values. If these events are important, separate models have to be used. The most severe winds at the North Atlantic deployment site are principally due to large scale wind systems and can generally be modeled adequately by global models.

Typhoons consist of circular winds with radii to the peak winds that can be of the order of 100 km, and can produce extreme wind, wave and current conditions,. Recorded typhoon data typically suffer from there being very few measurements of the extreme winds, due to the rather few times that a typhoon has scored a direct hit on an instrumented site, and due to failure of such instruments, generally, when it does. The only way to capture the details of the wind and hence the wave and current fields in a typhoon is to model the region around the typhoon with a local model during the period when the typhoon is in the vicinity, and calculate the wind, waves and currents.

3.2 Wind Data

Wind data came from two separate sources, one for the long-term winds, and one to estimate the winds in typhoons at the Northwest Pacific site.

3.2.1 Global Wind Data

The primary wind data are from the NCEP/NCAR CDAS/Reanalysis Project climatology. (NCEP is the National Centers for Environmental Prediction; NCAR is National Center for Atmospheric Research; CDAS is Climate Data Assimilation System. (See [4]).

Until recently, the meteorological community had to use analyses for weather forecasting that were very inhomogeneous in time as there have been big improvements in the data assimilation systems. NCEP and NCAR cooperated in a project (denoted "Reanalysis") to produce a 40-year record of global analyses of atmospheric fields. This effort involved the recovery of land surface, ship, rawinsonde (balloon), pibal (also balloon), aircraft, satellite and other data, quality controlling and assimilating these data with a data assimilation over the reanalysis period 1957 through 1996. This eliminates perceived climate jumps associated with changes in the data assimilation system. The database was enhanced with many sources of observations not available in real time for operations, provided by different countries and organizations. Wind data are available at 6-hour intervals for an elevation of 10 m.

These data were obtained by Oceanweather for the years 1974-1996, and used in their wave analyses. A grid spacing of 1.25° in latitude by 2.5° in longitude was used. Data were provided to the project at the four deployment sites and at the 21 transit sites. It consists of wind speeds and directions.

As mentioned previously, this wind data does not give accurate information on events characterized by rapid changes in time, or small scale spatial structures. In particular it will not give accurate representation of

events such as cold fronts and typhoons. In tropical regions where typhoons (hurricanes, etc) are present and produce the extreme values of the data, attempts to use these data will result in considerable inaccuracies. The statistics of extreme events should be assembled from the dedicated typhoon data described below.

Typhoon Wind Data

Three of the deployment sites (not the N. Atlantic) are in tropical regions that encounter typhoons (known in other parts of the world as cyclones or hurricanes). In the Arabian Sea, typhoons exist but are not as severe as in the NW Pacific. The Sea of Japan experiences much the same set of typhoons as the NW Pacific site, but it is sheltered by the island of Japan. As a result, it can be assumed that typhoons at the NW Pacific site will be the most severe, and typhoon data was modeled for this site only.

Typhoon wind fields were determined at the Northwest Pacific site by Oceanweather, Inc. These typhoons were chosen as the 22 most intense during 50 years, that passed within a 2° box around the site. Working from available historical data sources including aircraft reconnaissance data, ship and buoy reports, weather maps, and annual cyclone reports produced by various agencies the following cyclone parameters were developed:

- Storm track
- Time history of central pressure, peripheral pressure and ambient pressure gradient
- Radius to maximum wind

The storm track of typhoon Ruby is shown in Figure 2.

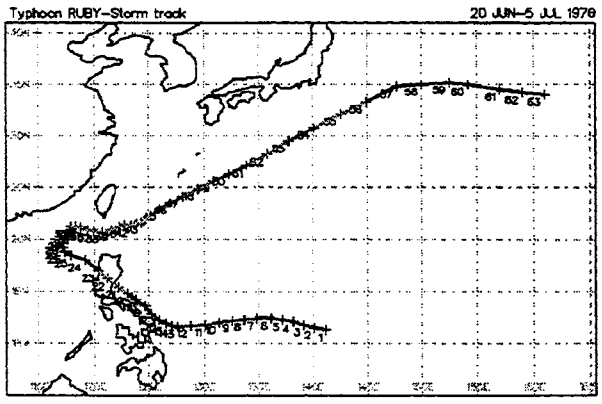

Figure 2: Track of Typhoon Ruby

The track is typical of typhoons in this area, coming out of the Pacific in a generally NW directions, and veering clockwise to a NE direction.

From the selected typhoon parameters, the wind fields at hourly intervals were developed within a 25^0 region around the site. Figure 3 shows part of this wind field for typhoon Ruby. Wind speeds and directions were archived at 1-hour intervals.

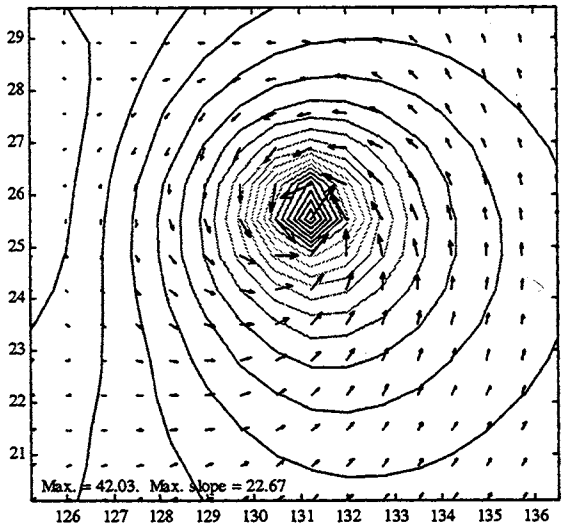

Figure 3: Wind Speeds and Directions for Typhoon Ruby

One of the problems of a dedicated typhoon hindcasting study is that typhoons vary greatly in intensity and of course in the track followed. A large number of typhoons models are therefore needed to capture the distributions of both intensity and track location. From a study of the typhoon geographical distribution at the NW Pacific site, it was found that typhoons passing within about 2° of the site had very similar intensity distributions, there being no preferential routes. It was therefore possible to assert that the distribution of typhoon intensity and path were independent. So, one can characterize the randomized tracks of the 22 typhoons by selecting the locations for the computation of metocean data randomly within this box. This essentially expands the 22 modeled typhoons to a represent a rather larger number that pass through the region with random intensity and path.

Wave Data

Wave data are from two separate hindcasts. The first is a global hindcast that was used for long-term information at all sites, and the second was from a set of typhoon hindcasts at the Northwest Pacific site.

Global Wave Data

A global wave hindcast was performed by Oceanweather Inc., using the so-called ODGP2 spectral wave model. The grid spacing of 1.25° in latitude by 2.5° in longitude was used. Figure 4 shows a typical set of significant wave heights and peak spectral periods from this model.

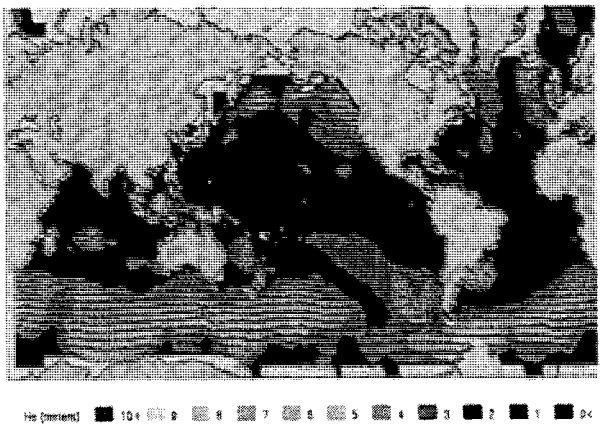

Figure 4: Wave Hindcast Model Results

The model uses a directional wave spectrum consisting of 24 directions and 15 frequencies. Wind fields were derived from the NCEP/NCAR CDAS/Reanalysis Project climatology updated at 6-hourly intervals. The years covered are from 1974 through 1996. Data were provided to the project at the four deployment and 21 transit sites.

To reduce the amount of archived data to a manageable amount, the 24 x 15 matrix representing the directional wave spectrum at any location was converted to a reduced set of parameters. With these parameters the waves can be described in various ways, including significant height, peak spectral period and direction of the dominant waves, or the same parameters defining three wave trains, the first representing the waves generated by the local winds, and the second and third two swell trains that have traveled into the region from distant storms.

Typhoon Wave Data

These hindcasts were made using the wind fields described in Section 3.2.2. The same wave model was again used by Oceanweather, Inc. to run these hindcasts. Results were archived at 1-hour intervals. A typical wave field is shown in Figure 5 for typhoon Ruby.

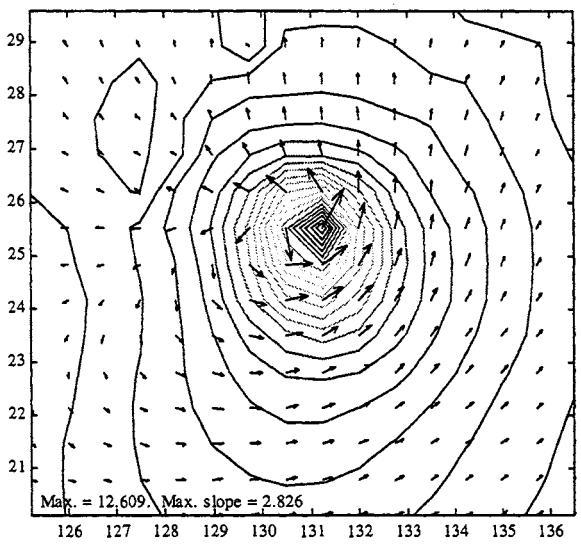

Figure 5: Wave Significant Heights and Directions for Typhoon Ruby

3.4 Current Data

Current data came from two independent hindcasts, each hindcast contributing data not available in the others. The first is a global current hindcast, the second a local wind-driven currents hindcast.

3.4.1 Global Current Data

The global hindcast was provided by the Oceanography Division of the Naval Research Laboratory (NRL) from a global numerical model. The model uses winds to compute the shear forces on the ocean surface and hence, from dynamic equations of equilibrium, the currents in the ocean. The model used was driven by winds from the European Center for Medium Range Weather Forecasts (ECMWF). The model assumes constant density, and there are no mixed layer effects included. However, it is sophisticated enough to resolve the effects of large eddies in the ocean.

The model covers all the oceans of the world with a $^1/_{16}$ degree grid spacing, and was run over the years 1979 to 1996. The model has six layers in the vertical direction, but as the MOB has a draft of only about 30 m, the information relevant to the MOB is in the upper layer, which is typically 100 m in thickness. The current speed and direction were archived at 3.0 day spacing, at the grid points nearest to the four deployment sites and the 21 transit sites. In addition, to enable comparisons between the hindcast currents and measurements at deep ocean buoys, current data were obtained at another 8 sites at various locations around the world.

These current data were supplemented by local wind-driven currents computed by BNI using winds from the NCEP/NCAR CDAS/Reanalysis Project at 6-hourly intervals, as described in the next section.

3.4.2 Local Wind-driven Currents

The NRL global current model, covering all the oceans, provides modeling of large-scale processes, such as the effects of winds that blow over long periods of time and produce currents that move thousands of miles. The time step size of 3.0 days allows the effects that occur over many days or months to be modeled, but events with shorter time scales will be missed, or modeled poorly. One such effect is the effect of local winds on currents, and this should be added to the currents from the global model.

Local winds will generate currents that increase with the length of exposure to these winds, and these currents rotate clockwise (counterclockwise) in the northern (southern hemisphere) as they develop. A conceptual model of this current would be of an ocean where the surface mixed layer is free to move relative to the interior, essentially "sliding" over the interior at the bottom of the mixed layer. The wind-driven flow speed is inversely proportional to the mixed layer depth so we need to know the depth of the mixed layer to model these currents. The rotational period is 0.5/sin(latitude) days, so everywhere poleward of about 8^0 this period is shorter than 3.0 days, and so these currents would not be modeled at all by the global current model.

Two mathematical models were used. The first was used in predicting currents at all sites from global winds. The mixed layer depths were estimated for each month from oceanographic data in the World Ocean Atlas 94, and the appropriate constant values were used in solving the equations. The wind input was the wind data archived by Oceanweather for the global hindcast.

The second model was used for typhoon-driven winds at the Northwest Pacific site. During the late summer and fall, this site has quite a shallow mixed layer, but, during typhoons, it gets stirred up by the high shear stress at the bottom of the layer, and by the large waves that accompany the high winds. As a result, the mixed layer becomes considerably deeper during typhoons, a characteristic that is not modeled by the first model This model, referred to as the PWP model, [5] has been verified against observations and adapted by the U.S. Navy for predicting the penetration depth of the diurnal mixed layer and sea surface temperatures. The program allows the depth of the mixed layer to change as a result of the mixing process and accepts a heat flux into the water at the air/sea interface, which was set to zero on account of the rapid passage of the typhoons. It uses a temperature and salinity profile with depth to initiate the computations. From these profiles the mixing calculations are performed, and the mixed layer depth and current strength and direction are computed by the program at each time step.

The total current was then assumed to be the sum of the currents from these two models. An example of these currents is given in Figure 6, showing the low and high frequency content or each contribution.

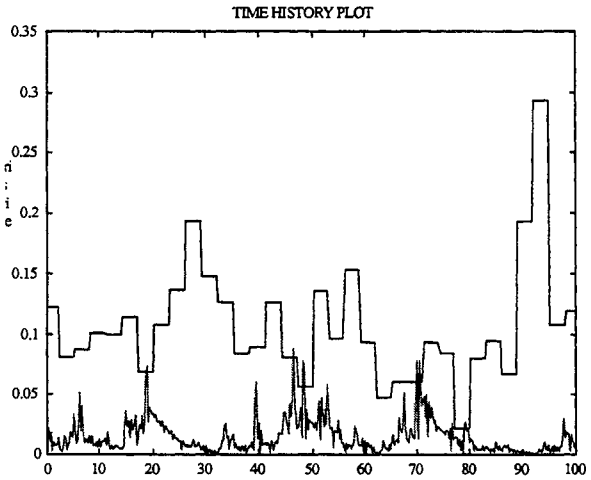

Figure 6: Typical Global and Local Wind-driven Currents

3.5 Summary of Data at Deployment Sites

The data assembled for the Environmental Specification allow a variety of statistical information to be computed. An example is given in Figure 7 showing a histogram of the relative occurrences of significant wave height and dominant wave direction for the North Atlantic deployment site. Units are in m and sec.

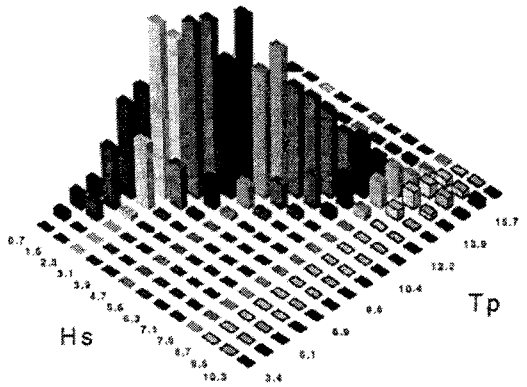

Figure 7: Joint Distribution of Significant Wave Height

and Dominant Wave Direction for North Atlantic Site

The Northwest Pacific and North Atlantic sites are the most severe deployment sites in terms of winds and waves, and it is instructive to look at the conditions at both, since they are likely to govern the design of the MOB both for strength and fatigue. Figure 8 shows the significant wave height distributions for the two sites from the global hindcasts.

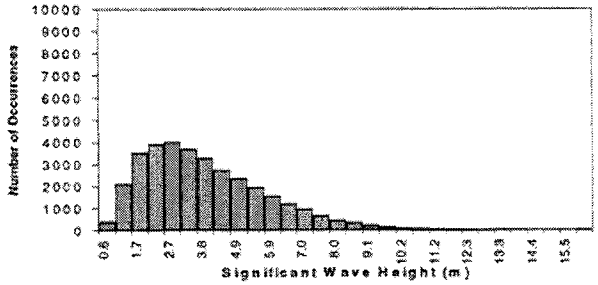

(a) North Atlantic

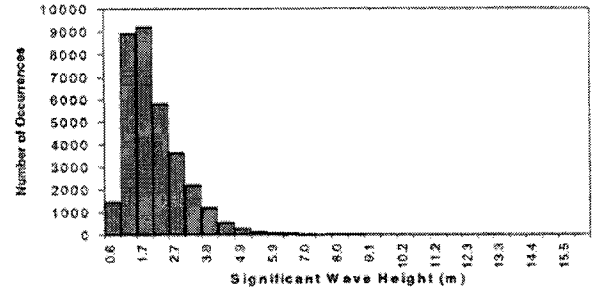

(b) Northwest Pacific

Figure 8: Significant Height Distributions

From the positions of the centroids of these distributions, it can be seen that the most commonly occurring waves are almost twice as large at the North Atlantic site as at the Northwest Pacific. The effect of this is almost certainly that the North Atlantic site will be more critical for fatigue. By comparing the 100 year significant wave heights at these two sites (from the global model data at the N. Atlantic and the typhoon data at the NW Pacific it is found that these waves are slightly higher at the NW Pacific site. Table 1 compares these data at the two sites.

Site	N Atlantic	NW Pacific
100 year significant wave height	18 m	19 m
Mean significant wave height	3.8 m	2.0 m

Table 1 Wave Heights at two Principal Sites

4. UNCERTAINTY IN THE DATA

To use the metocean data for design, within a reliability framework, a knowledge of their accuracy is needed. Figure 9 shows schematically load and resistance distributions.

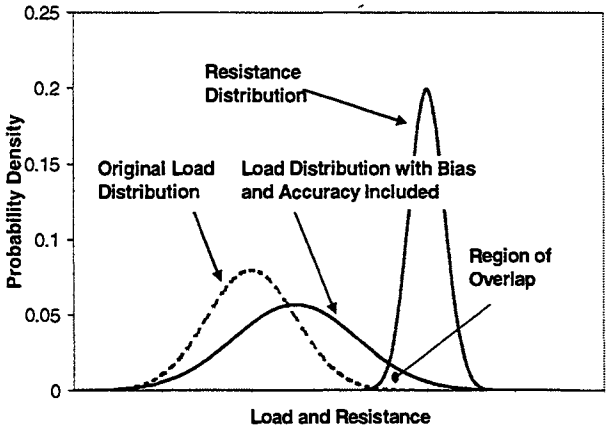

Figure 9: Load and Resistance Distributions

The overlapping region of the load and resistance curves is related to the probability of failure. The figure shows how increased mean load (shift to the right) and increased uncertainty of the load (flattening and widening) both result in an increase in this overlap, and hence an increase in the probability of failure.

A section of the Environmental Specification is devoted to estimating the uncertainties in the wind, wave and current data. However, determining the accuracy of this data is often quite difficult to do and hard statistical data are sometimes supplemented by estimates from experts.

Estimates of uncertainty and bias in wind and wave hindcasts came from a somewhat cursory study of the technical literature. These are currently being improved by more thorough research. Estimates of the accuracy of the current hindcasts were made by hindcasting the currents at several sites where current meters have been installed in the open ocean (see list of references in Appendix 6 of [1]) and comparing the hindcast currents with measured data.

Looking at global winds first, the accuracy of the mean of the 6-hour mean wind speeds may be as good as 5% and the standard deviation of the scatter of individual values is probably about 10% to 15%. It is more difficult to estimate the uncertainty of the winds in the intense part of a typhoon, due to the almost total

lack of such data. Uncertainties are estimated at 15% or 20%.

It is generally recognized that good wave hindcast models create wave fields whose accuracy depends largely on the winds that drive them. Estimates of the uncertainty are that the mean error in wave height is less than 0.5m in extra-tropical areas, and the scatter of individual values (standard deviation) is about 25%. The mean error in peak period is less than 0.5 sec, and the scatter is estimated as 35%.

Estimates of the global current accuracy suggest that the currents are probably biased about 35% low, with considerable scatter.

5. INCLUSION OF EFFECTS NOT PRESENT IN HINDCAST DATA

The hindcast data described in Section 3 are expected to give reliable long-term statistics that can be used in the design of the MOB. However, considerable detail in both time and space is missing from these data due to the limited number of parameters in the data. To complete the environmental description, a number of detailed environmental characteristics are provided. These vary from including turbulent variations of wind speeds, defining the spectral shape for wave spectra and providing the vertical current profile. In addition metocean events, such as solitons and ocean fronts, are described quantitatively that are not included in the wind, wave or current database.

5.1 Wind

Various items were included by which more detailed modeling of the wind can be included. These include the following:

- the variation of mean wind speed with averaging period, needed to compute mean wind speeds for elements with short natural periods
- variation of mean wind speed with elevation above the water; a logarithmic variation is recommended
- horizontal variation of mean wind speed; it is recommended that constant value be used for the open ocean
- cold fronts; very approximate estimates due to lack of hard data
- thunderstorms and waterspouts; very approximate estimates due to lack of hard data
- spectral description of time variations of wind speed
- turbulence scales and coherence of fluctuations of speed with spatial separation of points

5.2 Waves

Items included for waves are:

- spectral shape;
- directional spreading of wind seas and swell
- nonlinearities; although it is recognized that nonlinearities of water particle kinematics with respect to wave height may play an important role in the design of the MOB, at the moment there is not enough knowledge of the role of nonlinearities across distances of the order of a mile to give any useful guidance. The issue is currently being studied in several projects sponsored by the Office of Naval Research, and these projects are being reported in papers at this Conference.

5.3 Currents

Issues discussed in the Specification are:

- variation with depth; likely to be small in the open ocean
- variation with horizontal position; likely to be small in the open ocean
- turbulence in currents; ocean eddies have space scales far more than a mile, and time scales far more than 3 days, so can be ignored
- ocean fronts; like cold fronts in the atmosphere, an ocean front is a mass of water moving in the ocean relative to the stationary water it passes through. Quite rapid spatial changes in current velocity are possible, and the effect of these on the MOB is, like solitons, to attempt to separate the modules from each other. An estimate of the magnitude of currents and rate of change of current speeds is given in the Specification.

5.4 Solitons

Solitons are highly nonlinear waves that propagate along a horizontal surface in the ocean where there is a rapid change in density due to change in temperature and salinity (the thermocline). They look rather like upside down solitary waves, and typically have short wavelengths (100 – 300 m) and can have currents as high as 1 m/sec. Figure 10 shows a typical cross section through a solitary wave, showing the disturbance at the thermocline and little effect at the surface.

Because of the rather small crest widths, solitons will tend to separate the modules of the MOB, causing loads on the connectors, or requiring the dynamic positioning system to respond if the modules are not connected. They have been observed in the major oceans of the world. Formulas were provided for the calculation of the variation of currents with time and space, for what is considered a worst-case soliton.

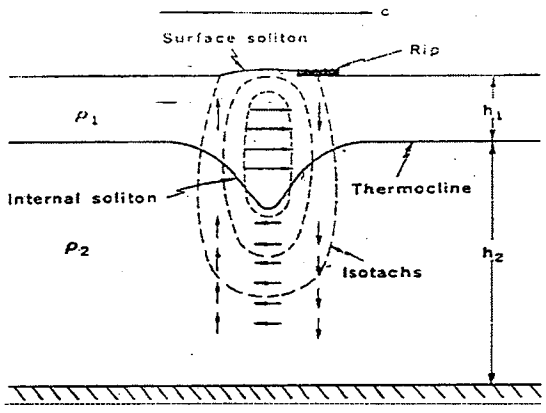

Figure 10: Cross-section of Typical Soliton

Acknowledgements

The work was supported by the U.S. Office of Naval Research's MOB Program and Naval Facilities Engineering Service Center.

The work was executed by Bechtel National, Inc., with the assistance of the following:

- Leon Borgman, University of Wyoming, Laramie
- C. Allin Cornell, Stanford University
- Mark Donelan, University of Miami
- Robert Pinkel, University of California, San Diego
- Emil Simiu, National Institute of Standards and Technology
- Robert Weller, Woods Hole Oceanographic Institution
- Yi-kwei Wen, University of Illinois, Urbana-Champaign
- Jun Zhang, Texas A&M University
- Oceanweather Inc., Connecticut
- Naval Research Laboratory, Oceanographic Division.

References

[1] Remmers, G., Taylor, R., Palo, P., & Brackett, R. "Mobile Offshore Base Science and Technology Program." *Proc. of 3rd International Workshop on Very Large Floating Structures*, Honolulu, Hawaii, U.S.A., 1999.

[2] Bechtel National Inc., "Mobile Offshore Base (MOB) Environmental Specification," Technical Report, Contract No. N47408-93-D-7001, D.O. 22, CDRL A005, Naval Facilities Engineering Service Center, Port Hueneme, California, March 1999.

[3] ABS Americas, "Draft MOB Classification Guide," Technical Report to Naval Facilities Engineering Service Center, Port Hueneme, California, 1999.

[4] Kalnay, E., Manamitsu, M., Kistler, R., Collins, W., Deaven, D., et al., "The NCEP/NCAR 40-Year Reanalysis Project," *Bulletin of the American Meteorological Society*, March 1996.

[5] Price, J. F., R. A. Weller, and R. Pinkel, "Diurnal cycling: observations and models of upper ocean response to diurnal heating, cooling, and wind mixing," *Journal of Geophysical Research*, 91, pp 8411-8427, 1986.

PROCEEDINGS OF THE THIRD INTERNATIONAL WORKSHOP ON VERY LARGE FLOATING STRUCTURES
(VLFS '99), VOL. I, EDS. R.C. ERTEKIN & J.W. KIM, 22-24 SEPTEMBER 1999, HONOLULU, HAWAII, USA

STORM WAVE TOPOGRAPHY: CREATING A DESIGN ENGINEER'S ATLAS OF REALISTIC SEA SURFACE FEATURES FROM SRA MEASUREMENTS

Leon E. Borgman
L.E. Borgman, Inc.*

Ronald W. Marrs and Samantha L. Reif
University of Wyoming †

Edward J. Walsh
NASA Goddard Space Flight Center ‡

ABSTRACT

An atlas of measured storm wave topography is being prepared as an aid to engineers designing very large floating structures. Water elevations from scanning radar altimeter measurements (Walsh [3,4]) are being processed to obtain various statistical representations of the sea surface. The first year of the study, completed this spring, consisted of developing methodology and algorithms, and writing related software. Although most of the data processing is planned for the second year, a moderate amount of pre-existing measurements and one section of Hurricane Bonnie data (1998) were analyzed for this presentation.

The Bonnie data contains large wave crests and troughs, exceeding 1600 meters in length (the length of a MOB) with heights up to 16 meters (Fig. 1). A normal probability plot of the cumulative distribution function of the elevations in Hurricane Bonnie lie almost exactly on a straight line (up to the 99.74 percentile) supporting the conjecture that linear statistical wave theory will give a good approximation to the spatial statistical structure in Bonnie.

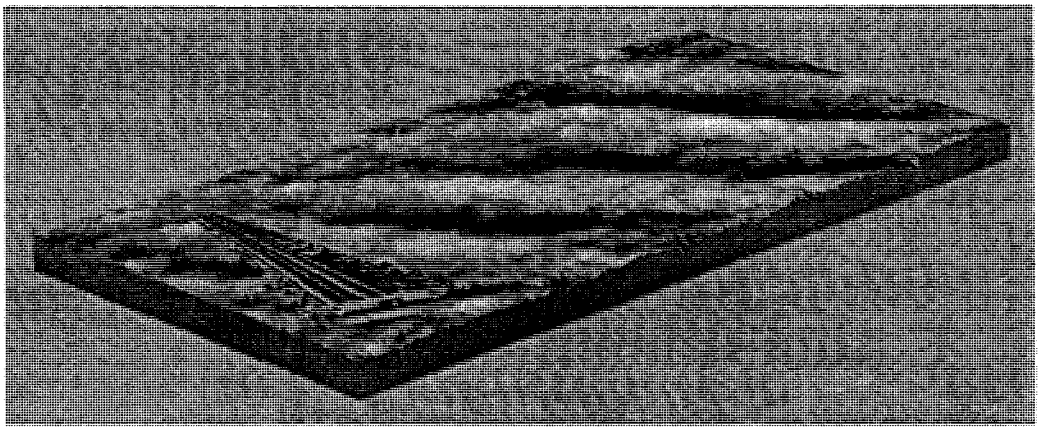

Figure 1: Perspective view of sea surface during hurricane Bonnie. Large floating structure approximately 1 kilometer shown for comparison.

*2526 Park Avenue, Laramie, WY 82070, USA. E-Mail: borgman@cyberhighway.net or borgman@uwyo.edu
†Department of Geology and Geophysics, Laramie, WY 82071. E-Mail: rwmarrs@uwyo.edu
‡1505 Mapleton Avenue, Boulder, CO 80304, USA. E-Mail: walsh@osb.wff.nasa.gov

1. INTRODUCTION

Lack of *in situ* ocean data is a major difficulty for MOB design. Many frustrations and uncertainties would disappear if adequate data on the proper spatial scale were available to serve as a basis for selection of design criteria.

Some key questions are:

1. Can the MOB be impacted broadside with a long-crested wave extending the full length in typical storm seas?

2. How nonlinear are the large wave systems?

3. Does linear, directional, statistical theory provide an adequate approximation (say an 85% solution) for engineering design?

4. Do spatial coherencies predicted by linear statistical theory agree reasonably well with observations?

5. To what extent are wave fields stationary? Is there a sort of local stationarity, but a general nonstationarity over large areas?

6. Can a storm wave system be approximated by separate "packets" of waves (not at regularly-spaced, FFT, frequencies) interfering with one another?

2. SCANNING RADAR ALTIMETER (SRA) DATA

SRA measurements made by NASA personnel provide one source of data for answering some of these questions. Ed Walsh has recorded SRA data in flights over storm wave systems near Australia and is in the process of collecting data for Atlantic storms (1998 and 1999 hurricane seasons). These data are being organized into a graphically presented "design engineer's atlas of storm wave measurements". The atlas includes summaries of various studies that address the questions mentioned above.

3. NONLINEAR/LINEAR BALANCE

Irregular ocean wave systems with large amplitudes clearly have nonlinear features. Despite this fact, design computations used in the offshore petroleum industry have typically been based on linear, directional, statistical wave theory, as combined with certain *ad hoc* "stretching" of wave kinematics away from MWL up to crest and down to troughs (Ried-Wheeler stretch) (Borgman [1], p. 152). This provides a sort of 85% approximation that explains many structural responses, but requires cross-checking for the strength of nonlinearities.

Commonly observed "wave grouping" in storm seas does not require nonlinearity. Suppositions of linear waves with a narrow spectral density will produce waves which group into "beats" of high waves. Figure 2 shows a histogram of frequency of number of waves per group in SRA data and the theoretical histogram from simulations with linear wave theory and the same spectral density (Borgman *et al.* [2]). The difference indicates at most, a weak nonlinearity in wave groupings.

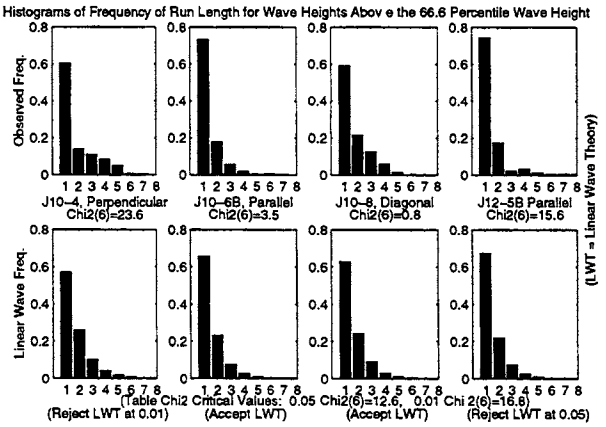

Figure 2: Histograms of frequency of run length for wave heights above the 66.6 percentile wave height.

If it turns out that linear statistical wave theory is a satisfactory "85%" approximation for statistical features on a larger, one-mile scale, this will have a considerable impact on future methods of MOB design. Methods for computations with linear statistical theory are reasonably well known. The SIMBAT software package developed by the Navy (NCEL, now NFESC) facilitates simulations of wave kinematics in combination with measured data. Reliability determinations are relatively easy to make if the waves are Gaussian (as is the case in statistical wave theory).

On the other hand, nonlinear computations can become very complicated in the methods that are currently available. For some nonlinear wave modeling problems, no methods are currently known. This is not to say that nonlinear computations can be avoided. But if linear statistical theory works well enough for many critical design purposes, the nonlinear methods can be reserved for cross-checks on accuracy of approximation and for cases requiring a full nonlinear treatment.

4. BONNIE DATA

The project from which the results reported here evolved, was planned as a two-year study. The first year (May 98–May 99) was devoted to developing methods and software for studies of spatial coherence in SRA data. The second year (scheduled to start this summer) will make detailed analyses of SRA data collected in Atlantic storms in the 1998 and 1999 hurricane seasons. Preliminary to this effort, one SRA flight line from hurricane Bonnie, consisting of a swath about 16,000 meters long and about 1,000 meters wide, was rushed through the data correction and quality assurance procedures, so that some results from Hurricane Bonnie could be presented here. Conclusions drawn from this one segment of hurricane data must be considered very preliminary and certainly need to be cross-checked against additional data.

The results obtained thus far are quite intriguing and seem to support the conjecture that the storm wave systems in Bonnie were very nearly Gaussian, and that linear statistical theory will give a fair approximation to the spatial patterns observed on a one-mile scale.

5. STEPS IN BONNIE DATA REDUCTION

A number of steps were involved in the generation of the data presented here for Bonnie. These include:

A considerable number of data calibrations, reviews, cross-checks, and corrections at NASA to reduce the SRA data to a list $\{x(j), y(j), z(j); j = 1, J\}$ for $J = 64 * 1024 = 65,536$, giving (x, y) locations and z elevations for 1024 sweeps across the swath, each with 64 measurements of elevation. The measurements were made in the midst of a storm, with rains, wind turbulence, and other disruptions, so clearly some of the values along a sweep will be in error. This is particularly true along the outer edges.

An estimate of the standard deviation of the main data population was made by ranking the 65,536 values and selecting one-half the difference between the 84.13 percentile and the 15.87 percentile as a (very approximate) rank-based estimate, $\hat{s}_1$. Measurements exceeding 12 times $\hat{s}_1$ were deemed inconsistent with the dominant population. Figure 3 shows the cdf of the values less than $12 * \hat{s}_1$.

The gap in Fig. 3 between 23 and 36 meters is not physically consistent, and elevations in excess of 36 meters are, by engineering judgment, out of line with most of the data; consequently, measurements exceeding 25 meters were taken as being "noise" outliers. Next, the values between 11 and 25 meters were examined one-by-one with a scatter plot of the type shown in Fig. 4. The circles are at the position of the measurement and the color (shown here as gray) gives the elevation according to the color bar at the right. It is obvious that the value at (2900, 334,700) is extremely discontinuous (15 meters different) from all its surrounding neighbors. Hence, it can be classified as a noise outlier.

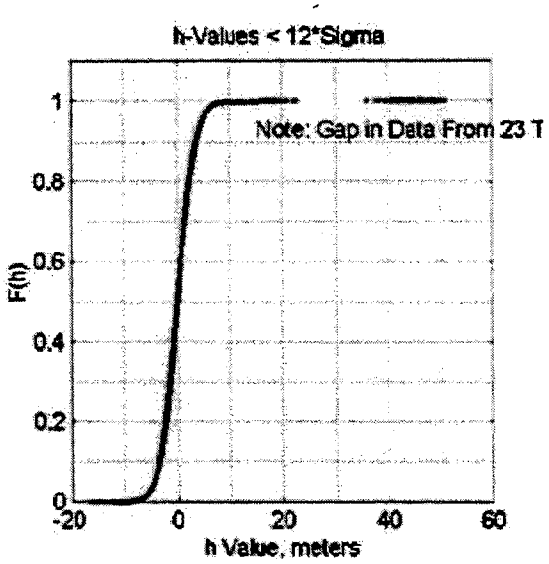

Figure 3

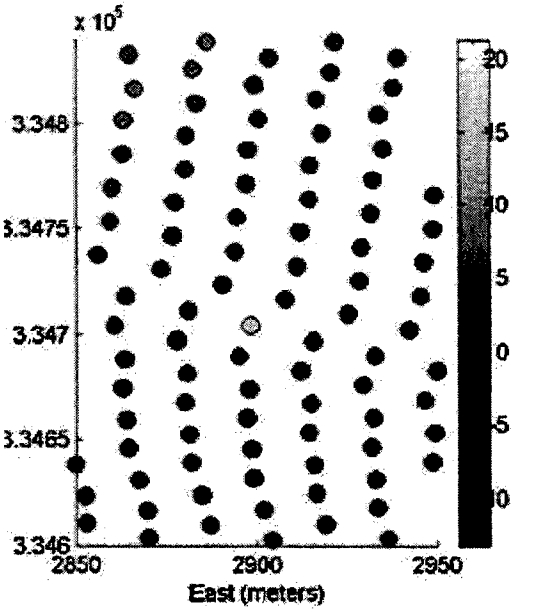

Figure 4

Every value between 11 meters and 25 meters turned out to be fairly obvious discontinuities. By similar reasoning, a few very negative elevations were also eliminated. This left the measurements between −9 meters and 11 meters as not being obviously out of line. The cdf of these values on standard straight-line normal probability paper is shown in Fig. 5. The plot of the screened data lies almost exactly on the line, except for the top 0.25% of values.

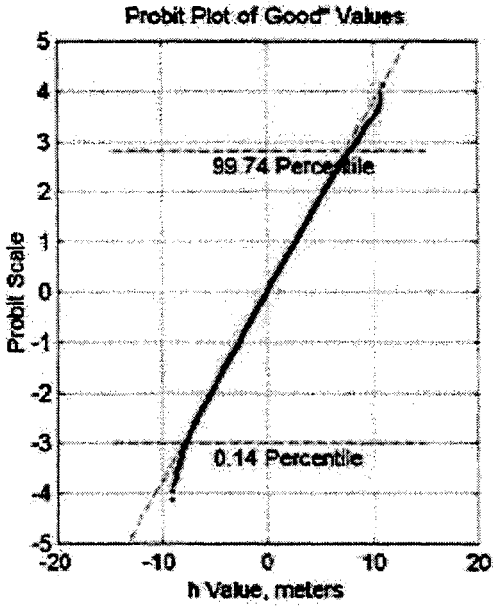

Figure 5

The almost straight line normal graph supports the conjecture that the storm seas in Bonnie are a Gaussian process, which is certainly consistent with linear statistical wave theory. Of course this is just one analysis, and further confirmation from other hurricane data will be needed to confirm or disprove this conclusion. Indeed, future data may show that this plot is not general behavior, but a statistical fluke.

6. CREST AND TROUGH LENGTH STATISTICS FOR BONNIE

A section of the contoured elevations for Bonnie is shown in Fig. 6. Wave crests and troughs extend nearly across the strip which is about 1100 meters wide (Fig. 7). The crests and troughs are diagonal (about 45°) to the flight direction. Thus, a crest with a 45° orientation would have a length about $\sqrt{2}$ times 1100 meters, or about 1540 meters. This is very nearly the length of a one-mile long MOB.

The data from Bonnie (Fig. 6), thus, demonstrates that a, more or less, continuous large wave crest stretching the full length of the MOB can develop in even an intermediate Hurricane such as Bonnie. The trough-to-crest height at the most severe wave is about 16 meters or 52 feet. The waves in the data set are believed to be among the larger sea states in Bonnie, although there may be other sections of unanalyzed data which are more extreme.

7. CREST AND TROUGH LENGTH STATISTICS

Before the statistics for crest and trough lengths in a two-dimensional wave field can be compiled, it is necessary to develop a definition of what constitutes a crest line or trough line. No definition is perfect, but the following formulation seems to work reasonably well for flights in the direction of wave travel.

1. Each of the 64 grid lines in the direction of flight are searched for all elevations which are larger than the preceding and succeeding elevations along the line, and which are in the upper p-fractile of the elevations. The values 0.20 or 0.25 seemed to work pretty good for p. The restriction to the larger elevations kept out many insignificant maxima from low wave activity.

2. Each maxima from Step #1 was grouped with any other such maxima lying within a distance of "PixelSep". This produced clusters of maxima which were reasonably contiguous with each other. A value of 3, 4, or 5 seemed to work for "PixelSep", depending on the pixel separation distance.

3. Finally, a straight line was fit through each cluster and terminated at each end at the outermost projection of the cluster elements onto the line. This line segment was defined to be a crest line.

The trough lines were similarly defined using minima. A scatter plot of the crest line and trough line length and orientation in the Bonnie data, on polar coordinates, is given in Fig. 8. The outer circle radius scale of 1600 meter is very nearly the MOB length of one mile.

A few other modes of presentation for the SRA data are shown in Figs. 9, 10, and 11. Shift plots of Australian data are shown in Figs. 9 and 10 and a mesh plot is given in Fig. 11.

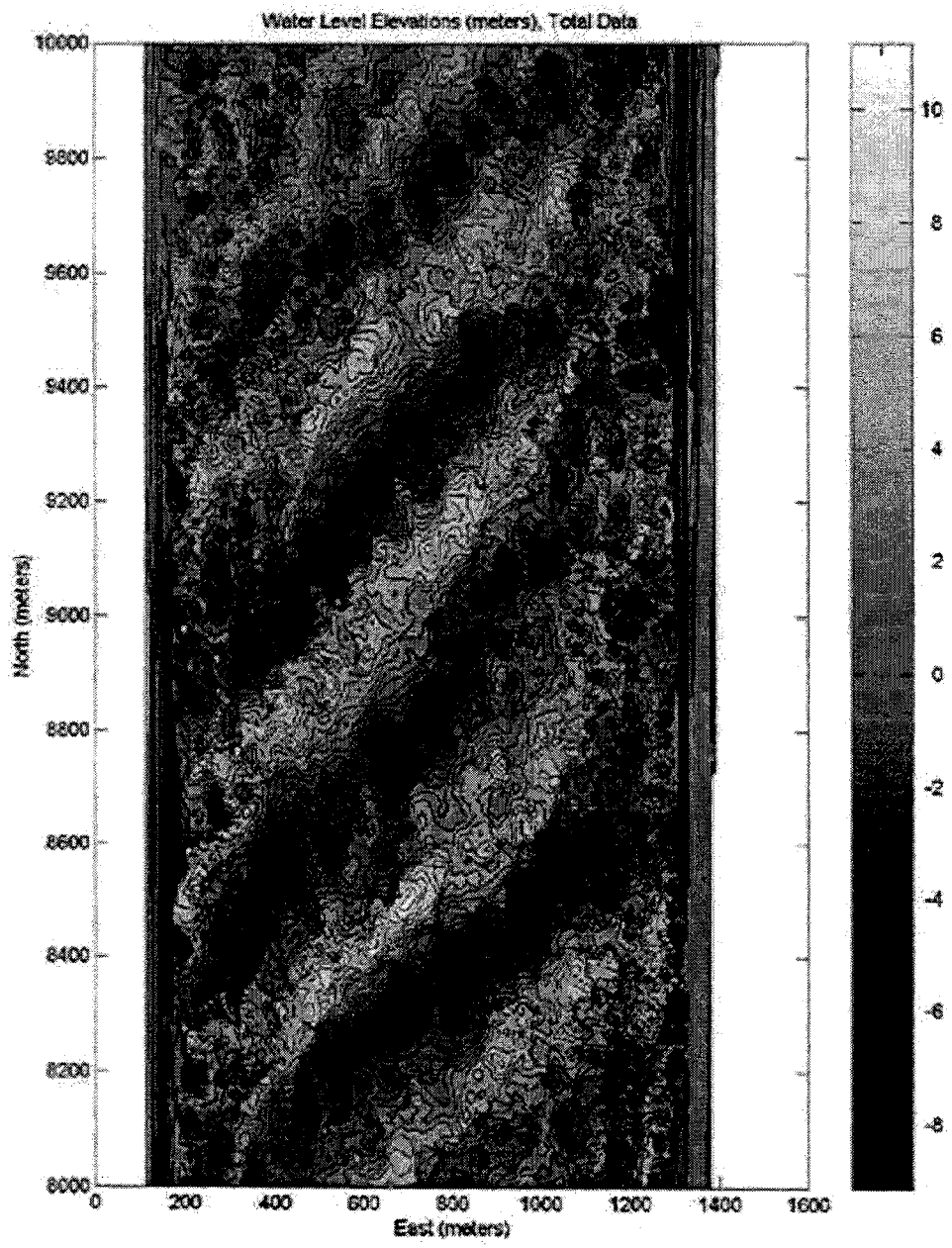
Water Level Elevations (meters), Total Data
North (meters)
East (meters)
10000
9800
9600
9400
9200
9000
8800
8600
8400
8200
8000
0
200
400
600
800
1000
1200
1400
1600
10
8
6
4
2
0
-2
-4
-6
-8

Figure 6

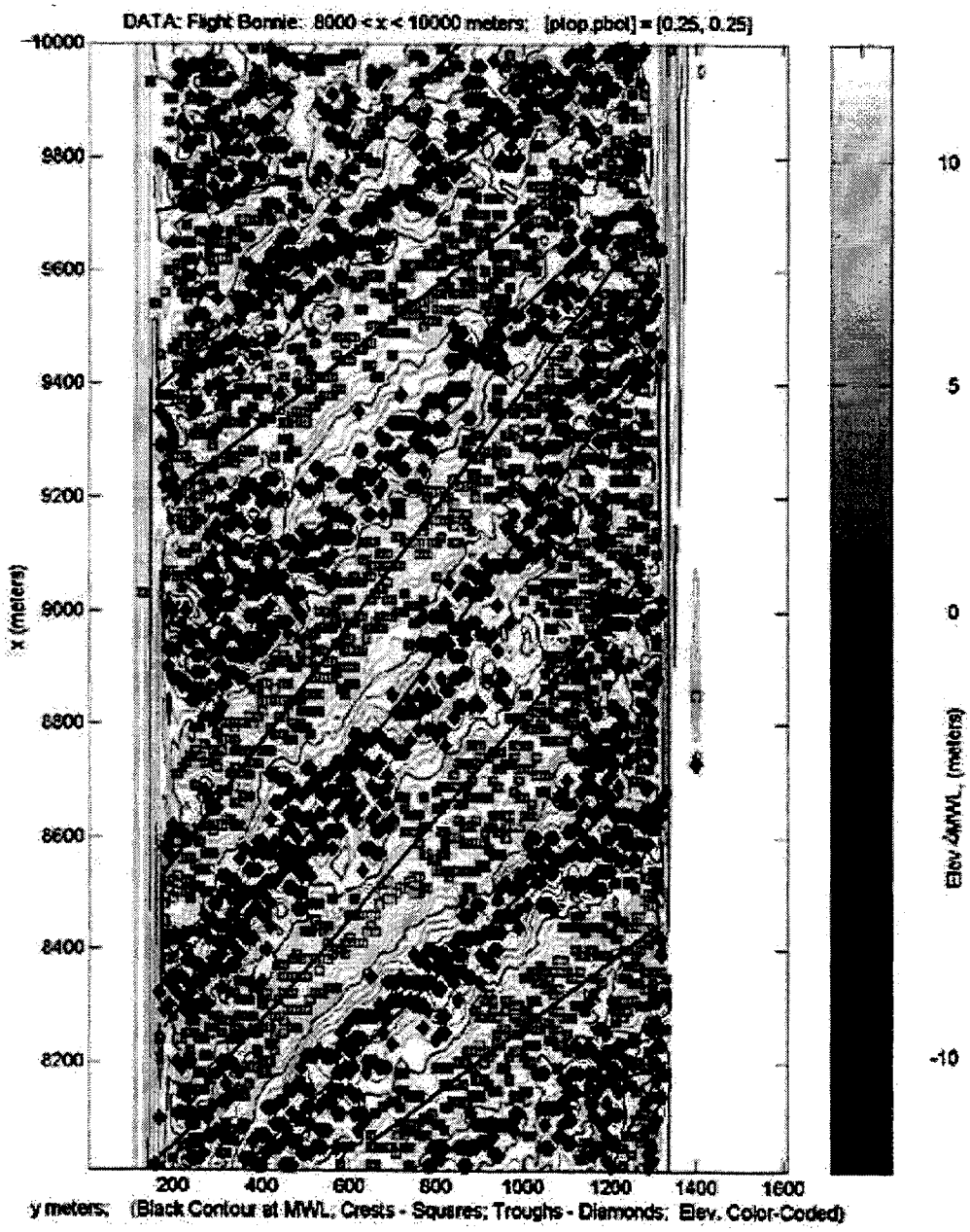
DATA: Flight Bonnie: 8000 < x < 10000 meters; [plop,pbot] = [0.25, 0.25]
10000
9800
9600
9400
9200
9000
8800
8600
8400
8200
x (meters)
200
400
600
800
1000
1200
1400
1600
y meters; (Black Contour at MWL, Crests - Squares; Troughs - Diamonds; Elev. Color-Coded)
10
5
0
-10
Elev AMWL (meters)

Figure 7

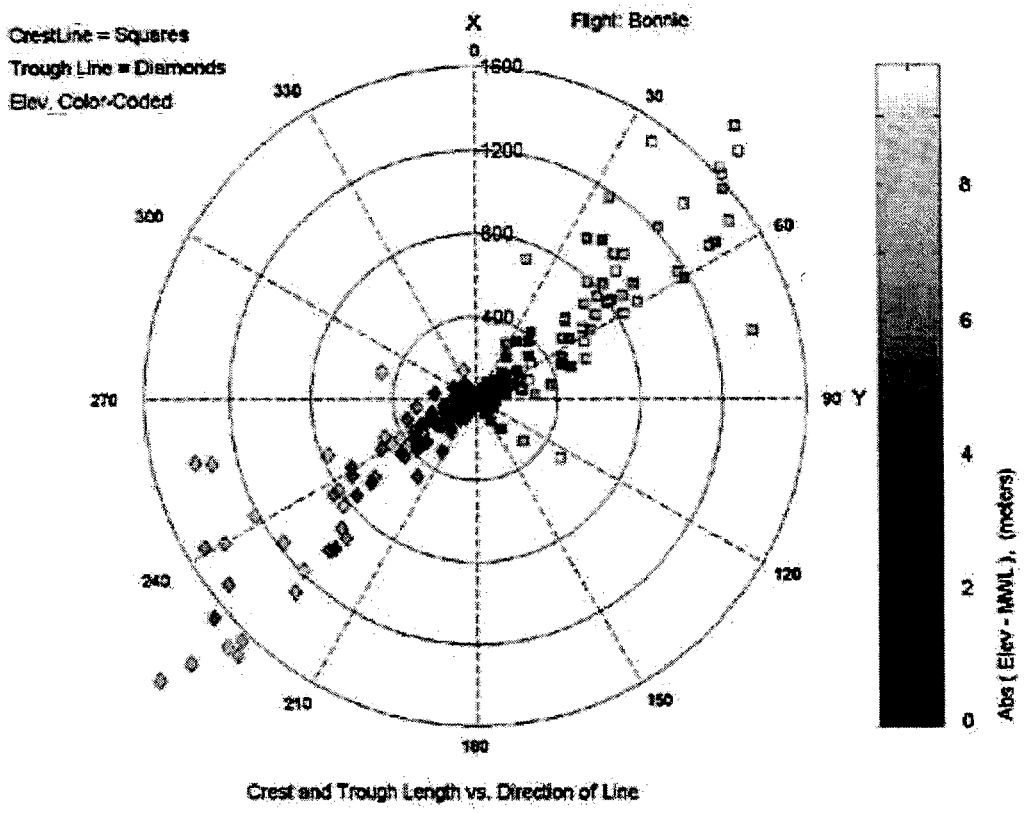

Figure 8

8. CONCLUSIONS

1. The wave topography has been developed and studied for a reasonable amount of SRA data measured near Australia and one section of 1998 data from Hurricane Bonnie.

2. There exist large waves in the Bonnie data which have crest and trough lengths about the length of proposed MOB structures, with heights from 10 to 17 meters.

3. The cumulative distribution function for the elevations in Hurricane Bonnie plot almost exactly on a straight line on normal probit paper (from the 0.14 percentile up to the 99.74 percentile). This supports the conjecture that the sea surface in Bonnie is Gaussian and that linear statistical wave theory will yield a reasonable approximation for spatial correlations in engineering design. It also supports the use of linear statistical wave software, such as SIMBAT, for MOB design work. *However*, this is a very preliminary finding since it is only based on one piece of hurricane data. Considerably more data segments need to be analyzed before this conclusion can be trusted.

4. If the conjecture that hurricane waves behave, at least locally, approximately as a Gaussian process can be verified, it will have a major effect on future MOB design practices. The substantial methodology from linear statistical wave theory used by many engineers in the petroleum industry, could be carried over to the MOB-scale structures, with some assurance of validity.

REFERENCES

[1] L. E. Borgman. Irregular waves: Kinematics and forces. *Ocean Engineering Science*, **9(a)** (Le Mehaute and Hanes, eds.), Wiley Interscience, pages 121–168, 1990.

[2] L. E. Borgman, R. W. Marrs, E. J. Walsh, S. L. Reif, and M. A. Andrews. Clustering of ocean waves. *Shore & Beach*, **67(1)**, pages 66–69, January 1999.

[3] E. J. Walsh. Spatial coherence of nonlinear, nonstationary, non-gaussian ocean waves on a one-mile scale from scanning radar altimeter

data. *ONR Report, Contract N00014-98-C-0206*, 58 pages, September 9, 1998.

[4] E. J. Walsh, L. K. Shay, H. C. Graber, A. Guilaume, D. Vandemark, D. E. Hines, R. N. Swift, and J. F. Scott. Observations of surface wave-current interactions during Swade. *The Global Atmosphere and Ocean System*, **5**, pages 99–124, 1996.

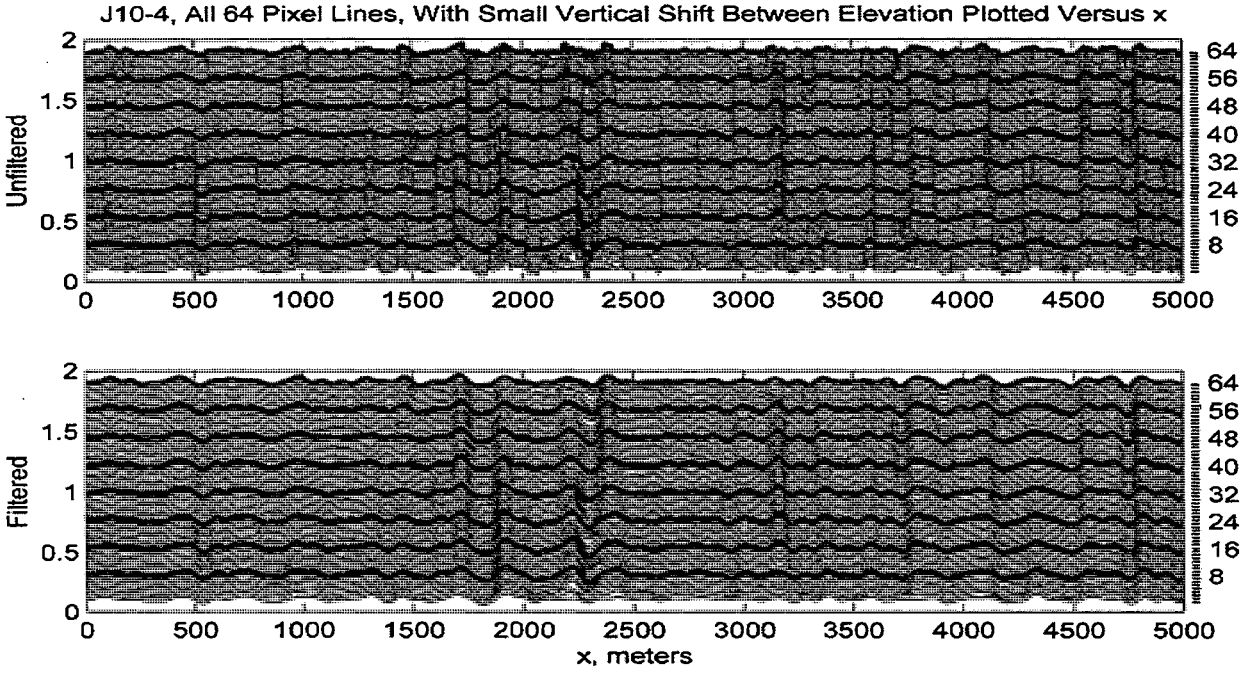

Figure 9: Shift Plot

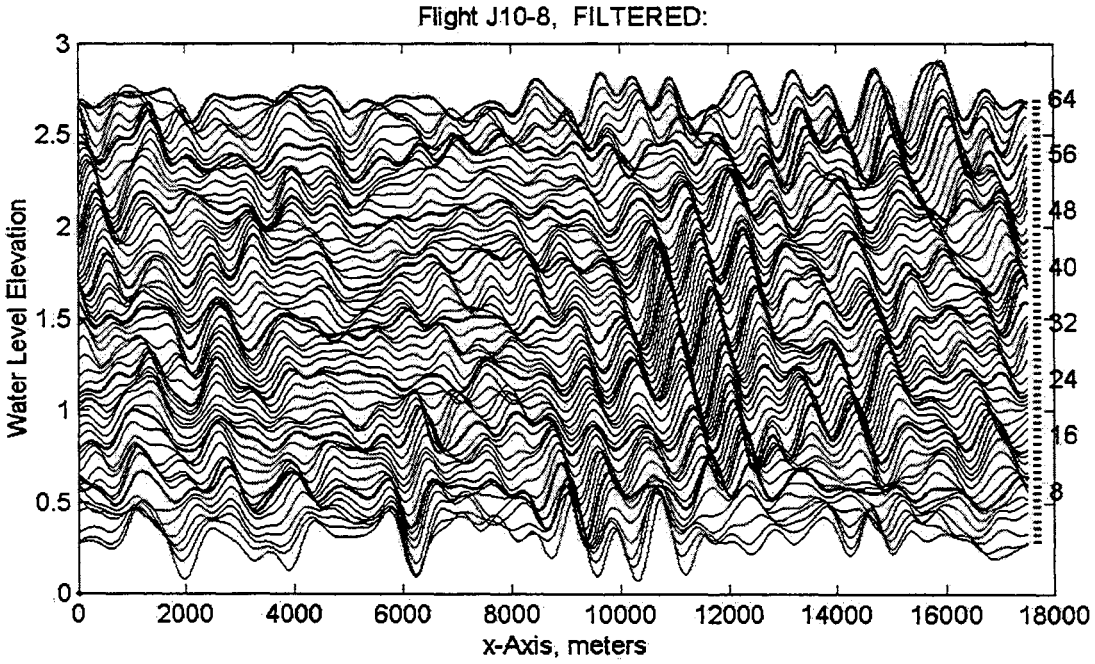

Figure 10: Shift Plot

Figure 11: Mesh Plot

PROCEEDINGS OF THE THIRD INTERNATIONAL WORKSHOP ON VERY LARGE FLOATING STRUCTURES
(VLFS '99), VOL. I, EDS. R.C. ERTEKIN & J.W. KIM, 22-24 SEPTEMBER 1999, HONOLULU, HAWAII, USA

WAVE CHARACTERIZATION FOR SMALL BOAT LOADING AT A MOBILE OFFSHORE BASE (MOB)

Richard C. Lundberg and Robert G. Grant
Bechtel National, Inc.

ABSTRACT

A Mobile Offshore Base (MOB), a new platform concept, is intended to serve as a floating base for conducting military and peacetime operations at various deployment sites worldwide. A critical mission for the MOB will be to offload supplies and equipment to small vessels for transport to shore. These vessels are intended to operate up through seastate 3. Relative motion between the vessels and MOB will determine whether operations can be conducted as required.

Experience to date in analyzing the MOB for large waves indicates that the large hulls and columns of the MOB semi-submersible shape significantly modify the wave surface in the immediate region of the MOB. This paper summarizes work which evaluates the wave climate in the vessel lee and how this may be modified by changing the MOB hull form or by adding deployable breakwater elements.

In all cases the work consists of passing waves of varying frequencies through the MOB structure from various directions and determining the water surface profile around the MOB. The results indicate the amplification or deamplification of the waves due to the MOB structure. The wave surface results are then used to select the most promising location for small vessel loading and vessel motions are then determined and compared to those in the unmodified sea condition.

1. WAVE CRITERIA

The basic criteria for loading and unloading landing craft is that the operations should be able to take place through seastate 3. Seastate 3 includes significant wave heights through 1.25 m. The statistics of spectral period were developed from oceanographic data available at the four sites identified as typical operating sites for the MOB (North Atlantic, Northwest Pacific, Sea of Japan, and Arabian Sea). Figure 1 shows the resulting exceedence diagram of the peak spectral period for seastates with a significant wave height of 1.25 m. This indicates that the mean period is 8 seconds, periods greater than 6 seconds occur 80% of the time and periods greater than 10 seconds occur 20% of the time. Based on these results, waves with periods of 6 to 13 seconds were used for comparing wave surface characteristics. For vessel motions calculations this was expanded to a range of 3.1 to 31 seconds.

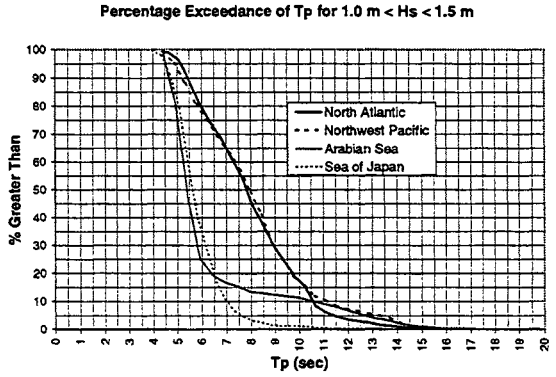

Figure 1: Spectral Period Exceedences for High Seastate 3 (H_s = 1.25 m)

2. WAVE CHARACTERIZATION

2.1 Analysis Procedure

Relative wave surface elevations were determined from a diffraction analysis of a single MOB module. The program MultiSurf was used to generate a panel model for analysis by the diffraction program WAMIT. One output available from WAMIT is amplitude at selected points. In this case, points were selected on a 10 m grid for an area up to 200 m from the module. The procedure used was to run waves from 6 to 13 second periods at 1 second increments from headings which varied from 0 to 90° at 10° increments through the module and obtain maximum wave amplitudes at the grid points. The 0° heading is from the bow. Since the waves run through the module are unit waves, results less than 1.0 indicate deamplification of the waves or quieting of the seas. Results greater than 1.0 indicate wave amplification. Once numerical results were available, the program MATLAB was used to plot the results as contours for

easy visualization. A typical black and white version of the plot is shown in Figure 2 although color plots were used for easier visualizaiton. A separate plot was made for each frequency and heading and the results were compared visually.

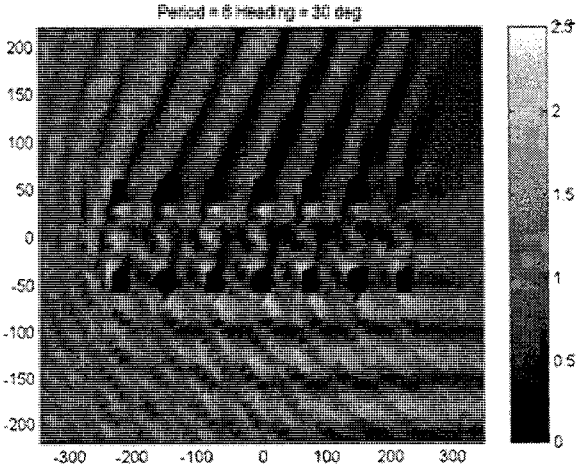

Figure 2: Typical Water Surface Contour Plot (Base Case - 6 Second Waves - 30 Heading)

2.2 Wave Surface Contours

2.2.1 Base Case – Existing Module Configuration

The base case is the module for the current configuration for the Independent Module Concept as described in reference [1] and shown in Figure 3. It consists of seven columns per side, each 24 m square with rounded corners. The pontoon tops are 25 m below the surface and are nominally elliptical shaped,15 m deep by 38 m wide.

Wave surface contours were produced for each heading and frequency combination. The principle conclusion from looking at these results is that they are very frequency dependent and that there is no well defined trend. For example, for the 30° heading at 6 seconds there are significant bands of de-amplification well spread along the module, while at 7 seconds these bands have largely disappeared and some amplification is starting to appear. At 8 seconds the bands of amplification continue to develop. At 9 seconds the de-amplification is again strong but at 10 seconds it starts to break down again. From 12 to 13 seconds the waves amplify substantially, presumably because of the long period waves interacting with the pontoons. The variability of these results is typical for all directions.

Just as the results vary dramatically as frequency changes, they also vary by direction. Due to the varying shielding and relative geometry this variation is to be expected, but it is not always clear why the wave surface is behaving the way it is. For example, for 8 second waves at 0° heading, the results are bands of de-amplification which grow stronger towards the aft end of the module. As the heading swings around to 10° the reduction largely disappears and amplification is evident close in to the side where loading operations would occur. At 20° amplification is consistent along the side. For 30° through 50° the results are mixed with some amplification and some de-amplification, but in narrow bands. At 60° the de-amplification starts to develop and is well spread at 70°. However, at 80° this is largely lost and amplification is starting to appear at the forward end. Broadside at 90° there is some slight de-amplification, but the averaged results indicate essentially no protection. With the exception of 70° where the columns are essentially staggered on the two rows, effectively blocking the waves, there are no easily detectable causes and effects. In general, the high amplification between the rows of columns would seem to indicate a high degree of reflection and reverberation under the module.

The results of this analysis indicate that for selected directions and periods there is substantial reduction in wave height on the lee side. Unfortunately the reverse is also true and there are also combinations which result in substantial wave amplification. There is no one direction that provides a consistent level of reduction. No patterns of results were evident which would indicate which direction to go in modifying the module geometry to affect the problem.

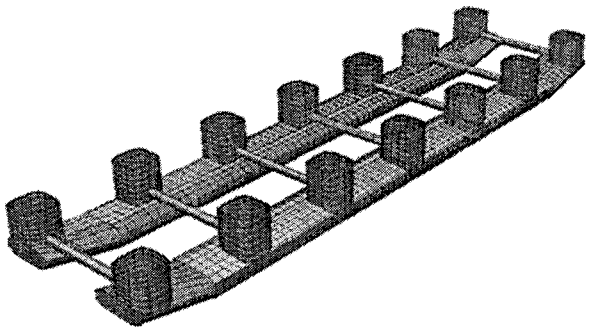

Figure 3: Base Case Configuration

1.1.1 Alternate 1 – Round Columns

The first alternate considered was to change the columns from square to an equivalent 26.6 m diameter round. The resulting wave surface elevation plots were compared visually with the base case and were found to be essentially identical. This confirms that the radius selected to smooth the columns in the development of the base case provides the desired results of smoothing the flow.

1.1.2 Alternate 2 – 21 Columns

The second alternate considered was to change the number of columns from 7 per side to 21, equally distributed along the hull as shown in Figure 4. The resulting 13.3 m columns are at 22.3 m on center. The 21 smaller columns effectively create a wall which provides a very high level of deamplification for all headings and frequencies. While these results are very encouraging from the standpoint of local reduction in wave surface elevation, they show that the closely spaced columns effectively act as a wall, which implies that global loads on the module will be high. This was confirmed, as discussed below, and the wave drift forces become several times higher which would seriously impact dynamic positioning requirements.

Thus, the continuous closely spaced columns do not appear to be a reasonable solution. However, if the columns were closely spaced in only a limited region, it could be that the local reduction might be less, although still acceptable and the global impact much less severe. Therefore, it was decided to pursue a similar solution with closely spaced columns in two bays only.

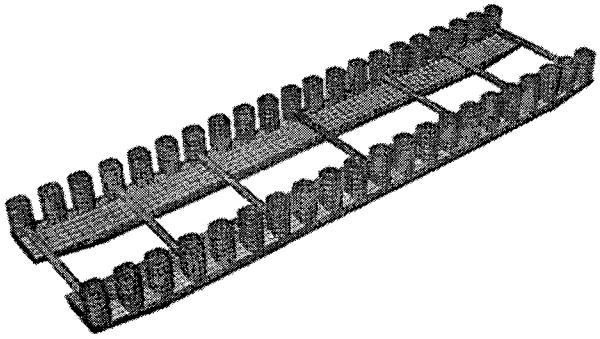

Figure 4: 21 Column Configuration

1.1.3 Alternate 3 – Two Bays With Closely Spaced Columns

In this option seven columns were substituted for the three columns in the two middle bays as shown in Figure 5. The resulting column spacing and sizes are similar to the 21 column case in the center two bays. In this case the middle columns end up 15.7 m square while the outside columns remain at 24 m square. Unexpectedly this configuration provides hardly any of the protection provided by the 21 column solution. While there is some de-amplification for selected periods and headings, these results are generally very limited. Since even for the cases where wave surface reduction does apply, it is over a limited area, this configuration does not seem to be attractive.

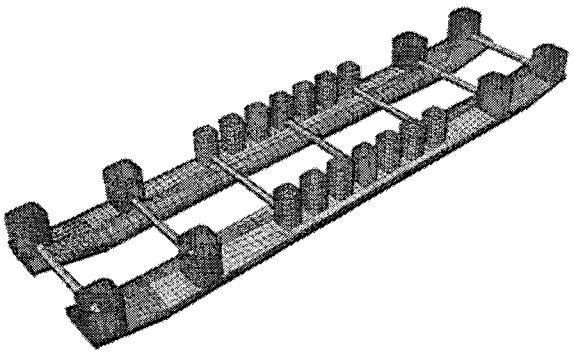

Figure 5: Two Bays with Closely Spaced Columns

1.1.4 Alternate 4 – 14 Columns

In an effort to get a more wide spread reduction and gain some benefit as seen in the 21 column case, a final configuration with 14 equally spaced columns as shown in Figure 6 was considered. In this case, the columns are 17 m square. The results for this configuration are mixed. In some cases it produces worst results than the base case and in some an improvement. Just as in the base case, the results vary dramatically with frequency and direction although the actual magnitudes and locations are different than the base case. Since there is no clear trend, further data interpretation and comparison was done as described below.

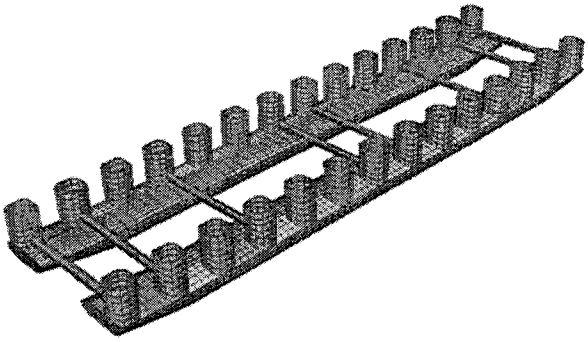

Figure 6: 14 Column Configuration
14 Column Option

2.3 Impact on MOB Functionality

Since the 21 column case showed dramatic shielding and quiet water consistently on the lee side, the implication is that there is most likely a large net force on the module. To evaluate this, the mean drift force normalized by mean height squared was calculated and is plotted in Figure 7 for all the concepts considered. The 21 column case results in wave drift forces about four times as large as any of the other concepts. This has unacceptable implications for the dynamic positioning system which must resist these forces.

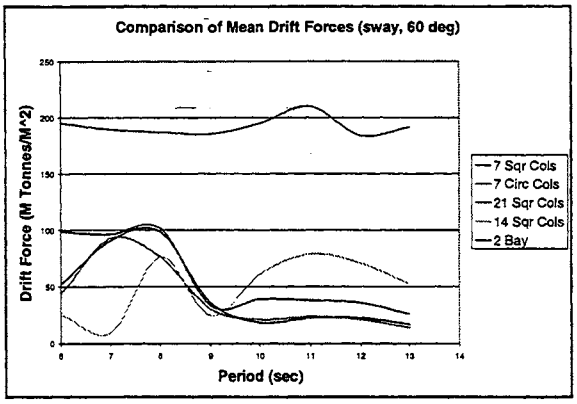

Figure 7: Mean Drift Force Comparison

2.4 Configuration and Loading Site Selection

Since the results were so mixed and there was no clear trend evident from visual examination of the wave surface plots, the numerical results were averaged over proposed loading sites and then numerically compared. The sites are defined in Figure 8. The results of this numerical evaluation suggested that the base case, seven column solution was marginally better than the others and that site 4 near the aft end is the most protected site. This configuration and site were then used for vessel motions analysis.

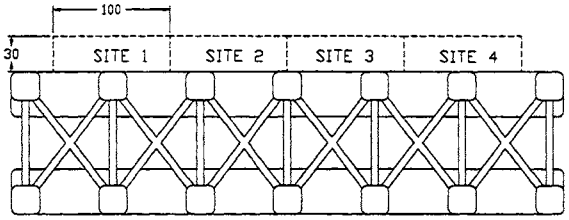

Figure 8: Loading Site Definitions

3. LANDING CRAFT MOTIONS

3.1 Landing Craft Descriptions

Motions were computed for two landing craft; the LSV and the LCU-2000. Vessel characteristics are summarized as follows:

	LCU-2000	LSV
Length Overall	53.0 m (174')	83 m (272' 9")
Length Between Perpendiculars	47.6 m (156')	78 m (256')
Width	12.8 m (42')	18.3 m (60')
Draft	2.4 m (8')	3.7 m (12')
Displacement	1147 m^3	4148 m^3
Center of gravity above the keel (KG)	6.6 m	6.0 m
Ramp length (scaled)	5.7 m	13 m

3.2 Analysis Procedures

WAMIT models were assembled for the two landing craft. Each landing craft was then placed in position next to the module and a two body analysis performed. Since the focus is on the module being nominally headed into the seas, it was assumed that the landing craft was parallel to the module for all runs. Twenty waves were run through the system with circular frequencies from 0.2 to 2.0 (periods from 3.14 to 31.4 seconds). Response amplitude operators (RAOs) were then plotted for heave, pitch and roll at the center of gravity of the vessel. Relative motions as defined in Figure 9 were calculated by transferring the motions from the two vessel's centers of gravity to the points in question and then calculating the difference.

Finally, since seastate 3 has a wide range of spectral periods, three representative seastates were passed through the transfer functions to determine relative heave and ramp angle vs. vessel heading.

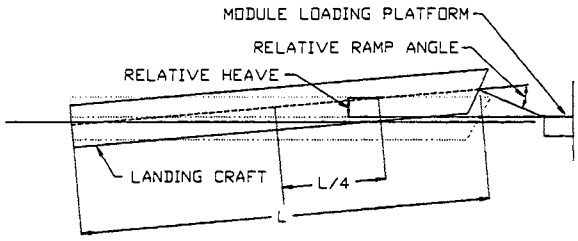

Figure 9: Relative Motions Definitions

3.3 Vessel Motions

Representative results in the form of relative ramp angle RAOs for the LCU-2000 for various headings are shown in Figure 10. It is clear from this that the results vary dramatically with heading and frequency. The relative heave RAOs are very similar in shape and characteristics for all headings, and the RAOs for the LSV are similar to the LCU-2000 except for magnitude. The RAOs were then combined with sea spectra to calculate the maximum values. Since the range of periods is large, three separate seastates were considered with spectral periods of 6, 8 and 10 seconds. H_s was 1.25 m in all cases. The maximum values of relative heave and ramp angle were calculated from these spectral results and are summarized in Table 1 and Table 2. The maximum heave is double amplitude, since for loading with a crane, the total motion of the deck is the desired quantity. The maximum ramp angle is single amplitude, since for rolling stock it is the maximum angle that causes vehicles to bottom out that is of interest.

The LSV produces less relative heave than the LCU-2000, especially for the shorter period seas. The difference in ramp angles is much more

pronounced, with the angles for the LCU-2000 being two to three times those for the LSV for the shorter period seas. This is to be expected since the LCU-2000 is shorter and lighter than the LSV. The LSV ramp is also much longer than the LCU, minimizing ramp angle. Since there is no specified operating criteria, it is unclear how the results compare to what is required for operations. However, they represent a point of comparison in evaluating other wave mitigation concepts.

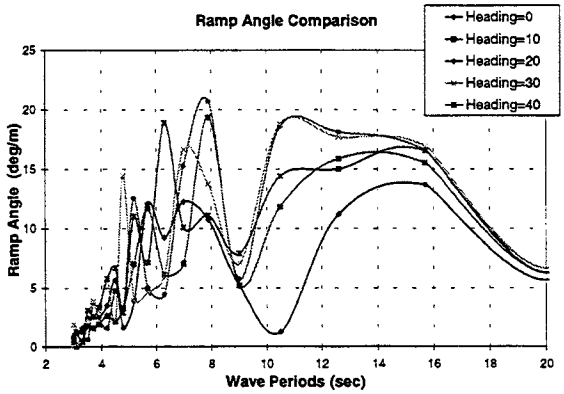

Figure 10: Ramp Angle RAO for LCU-2000

Heading (degrees)	Spectral Period (seconds)	LCU-2000	LSV
0	6	0.93	0.52
0	8	1.26	0.82
0	10	1.26	0.93
20	6	0.90	0.59
20	8	1.64	1.12
20	10	1.97	1.71

Table 1: Maximum Relative Heave (meters)

Heading (degrees)	Spectral Period (seconds)	LCU-2000	LSV
0	6	8.5	2.4
0	8	9.3	3.0
0	10	9.7	3.9
20	6	9.3	3.2
20	8	14.2	6.3
20	10	16.8	9.3

Table 2: Maximum Ramp Angle (degrees)

4. WAVE MODIFICATION

4.1 Candidate Solutions

Since the goal of this task was to develop a system which would provide sheltered conditions for loading operations, reference was made to breakwater type structures. However, although the MOB and the breakwater are trying to produce the same nominal results, the situations are quite different in many respects. For example comparing the breakwater to the MOB some issues are:

- Shallow water vs. deep water
- Difficult seafloor attachment (foundations and mooring issues) vs. solid structure to support the barrier
- Use of compliant objects to limit loads vs. minimum load sensitivity
- Need to provide an enclosed area vs. limited protection (a single lee side)
- Reflected waves generally an issue vs. not an issue
- Large vs. small design waves (assuming that the wall is readily removable).

As a result of a literature search and internal brainstorming sessions, several possibilities for wave mitigation were proposed. Of these the most direct and most promising is the use of walls between the columns. These walls could be of varying depths and located on different column lines.

4.2 Transverse Walls

The first configuration studied was the use of 10 m deep transverse walls between each pair of columns as shown in Figure 11. The thought was that for near head seas, the successive walls would each one reduce the flow from the one before, resulting in protected areas after the first two or three walls. However, the walls tend to trap the waves causing reverberation and wave amplification between the walls. This amplification then spills out to the lee side and there is no benefit derived from the transverse walls.

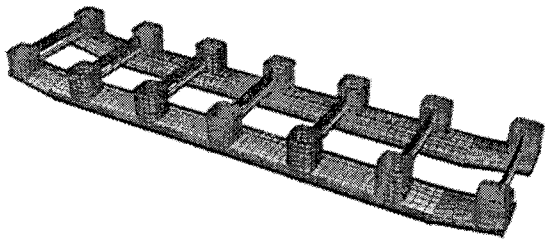

Figure 11: Transverse Walls

4.3 Walls of Varying Depths

The next solution studied was the use of walls between the columns on the weather side. This was investigated for varying wall depths. The arrangements are shown in Figure 12. The full depth wall extends from the surface to the pontoon 25 m below. Other options studied were for 20 m, 15 m and 10 m deep walls with a gap above the pontoon. As expected, based on the 21 column module solution, the addition of walls significantly reduced the wave transmission. As is to be expected, the deeper the wall, the more the protection. Thus, for maximum protection the 25 m deep walls which extend to the top of the pontoons were selected.

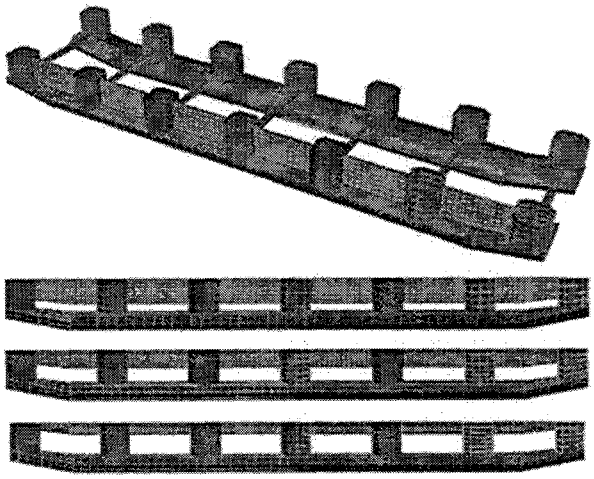

Figure 12: Longitudinal Wall Options

4.4 Wall Configurations

After the wall depth was selected, varying horizontal arrangements of walls were considered. These included three cases as shown in Figure 13. Of these, based on visual examination of wave surface contours, Case 2 produced the most promising results.

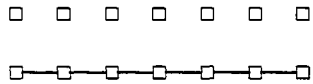

Case 1: Single longitudinal wall on the weather side

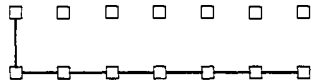

Case 2: Case 1 with a single transverse wall at the bow

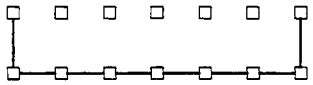

Case 3: Case 1 with a single transverse wall at the bow and stern

Figure 13: Vertical Wall Arrangements

4.5 Sea Surface Comparisons

As was the case for the wave comparisons of module configuration options, the differences in sea surface are sensitive to frequency and direction and often subtle, making identification of the preferred option difficult. In this case a slightly different approach was used to identify the preferred solution and loading site. As before, the wave surface elevations were averaged within a site perimeter. However, in this case the averaged values for each frequency were squared and multiplied by the incoming spectra. This results in an averaged spectra for the site. Example incoming and sheltered spectra are shown in Figure 14. Significant wave heights were then computed from these spectra and the ratio of sheltered to incoming significant wave height calculated. These values of spectral transmission coefficient are summarized in Table 3 and Table 4 for the base case with no walls and Case 2 with 25 m deep walls. The table shows that Case 2 always produces the best results although for the 0° heading the difference is small. Based on these results, site 4 for the configuration in Case 2 was selected to perform motions analysis for the landing craft.

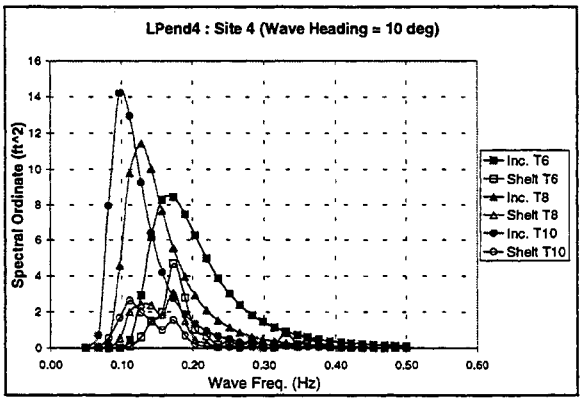

Figure 14: Comparison of Incoming and Sheltered Spectra

	Site	1	2	3	4
To=6	0 deg	0.92	0.76	0.67	0.59
	10 deg	0.87	0.79	0.70	0.63
	20 deg	0.85	0.77	0.69	0.65
To=8	0 deg	0.91	0.79	0.68	0.55
	10 deg	0.90	0.84	0.76	0.70
	20 deg	0.92	0.90	0.87	0.85
To=10	0 deg	0.91	0.81	0.70	0.60
	10 deg	0.97	0.91	0.84	0.85
	20 deg	1.03	1.04	1.04	1.08
ave		*0.92*	*0.85*	*0.77*	*0.72*

Table 3: Spectral Transmission Coefficient No Walls

	Site	1	2	3	4
To=6	0 deg	0.90	0.73	0.61	0.53
	10 deg	0.77	0.53	0.44	0.39
	20 deg	0.66	0.49	0.41	0.39
To=8	0 deg	0.86	0.72	0.60	0.52
	10 deg	0.73	0.57	0.48	0.43
	20 deg	0.67	0.55	0.43	0.42
To=10	0 deg	0.87	0.76	0.64	0.57
	10 deg	0.76	0.64	0.53	0.49
	20 deg	0.71	0.60	0.49	0.48
ave		*0.77*	*0.62*	*0.51*	*0.47*

Table 4: Spectral Transmission Coefficient - Case 2

4.6 Vessel Motions

The two landing craft were placed at site 4 as before and motions analysis performed for the Case 2 configuration. The results are compared with the base case in Table 5 and Table 6. In general, the

motions are about equal or slightly worse for the 0° heading. This is because, with the wall in place and the vessel close in, the waves that radiate from the vessel reverberate against the wall and cause some additional motion. For the 20° heading the results are essentially unchanged for the 6 second spectral period, but for the 8 and 10 second spectral period the motions are reduced by about half. This is a considerable improvement.

If the MOB is operated broadside to the waves, the protection is more complete and relative motions improve further. However, this would require mooring the landing craft headed perpendicular to the MOB to minimize roll and, while this would be better for roll-on/roll-off loading, it would most likely not be viable for lift-on/lift-off loading due to the requirement for long crane reaches. Also, a broadside heading for the MOB is contrary to that desired for air operations.

Maximum Heave (meters)					
Heading (deg)	Spectral Period (sec)	LCU-2000		LSV	
		Base Case	Case 2	Base Case	Case 2
0	6	0.93	0.76	0.52	0.50
0	8	1.26	1.17	0.82	0.88
0	10	1.26	1.31	0.93	1.13
20	6	0.90	0.84	0.59	0.64
20	8	1.64	0.96	1.12	0.77
20	10	1.97	0.97	1.71	0.85

Table 5: Maximum Heave Comparison

Maximum Ramp Angle (degrees)					
Heading (deg)	Spectral Period (sec)	LCU-2000		LSV	
		Base Case	Case 2	Base Case	Case 2
0	6	8.5	7.6	2.4	2.7
0	8	9.3	10.3	3.0	3.9
0	10	9.7	9.5	3.9	4.3
20	6	9.3	8.3	3.2	3.1
20	8	14.2	8.9	6.3	3.9
20	10	16.8	8.3	9.3	4.3

Table 6: Maximum Ramp Angle Comparison

4.7 Wall Feasibility

The feasibility of providing the walls was briefly investigated and it appears that providing walls for low seastate environments is feasible. The walls must span between columns, a distance of 50.5 m (166 feet) and be deployable. The solution adopted is a triangular truss with one face plated in and oriented vertically to form the wall. The truss slides up and down in grooves in the column as shown in Figure 15. Two wall elements, upper and lower, are shown for each location to minimize size and weight of individual deployable elements. Each wall element weighs about 250 metric tons and is raised and lowered with chain jacks or windlasses. When in the raised position, the plated side of the truss is stored facing up towards the deck, with the tubular truss hanging below. The tubular truss is largely wave transparent, so the stored truss will have only a small effect on wave load on the MOB from the very large storm waves that reach to near the deck.

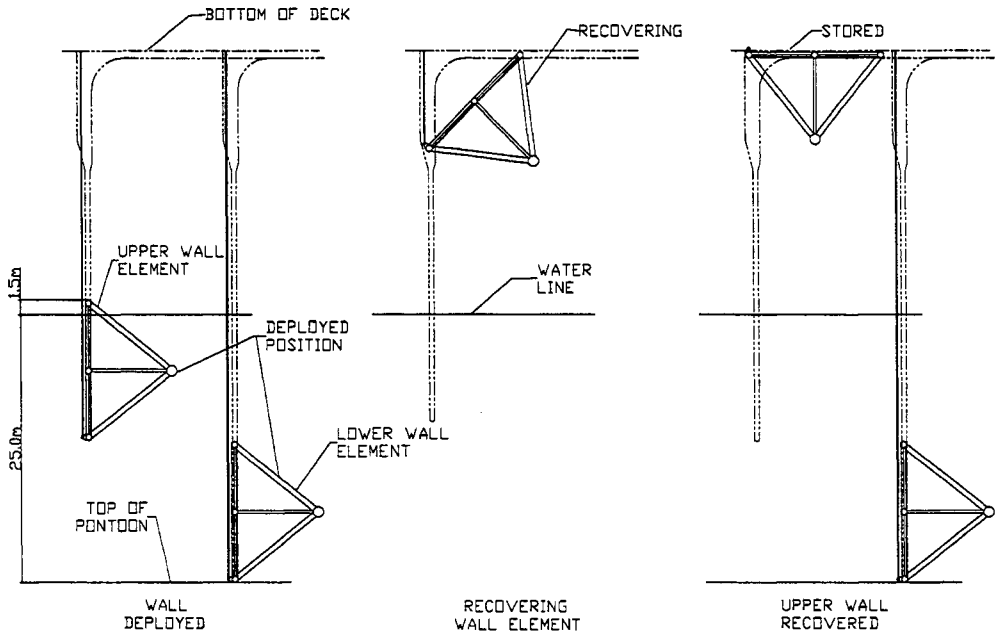

Figure 15: Wall Recovery Sequence

5. CONCLUSIONS

The principal conclusions from this study are as follows:

- Since any improvements in sea conditions due to MOB configuration changes are minimal, ignore this aspect and configure the MOB for optimal structural, naval architectural and operational characteristics.
- Use deployable vertical walls to mitigate sea conditions on the lee side.

6. REFERENCES

[1] Bechtel National Inc., Multi-Module Dynamic Positioning System - Refinement of Independent Module MOB Concept - Module Cost vs. Length, June 1999.

PROCEEDINGS OF THE THIRD INTERNATIONAL WORKSHOP ON VERY LARGE FLOATING STRUCTURES
(VLFS '99), VOL. I, EDS. R.C. ERTEKIN & J.W. KIM, 22-24 SEPTEMBER 1999, HONOLULU, HAWAII, USA

THE USE OF DESIGN SYNTHESIS TOOLS FOR CONDUCTING TRADE AND COST STUDIES FOR VERY LARGE FLOATING STRUCTURES

Daniel G. Bagnell and Brian G. Forstell
Band, Lavis & Associates, Inc.*
A CDI Marine Group Company

ABSTRACT

Traditional synthesis models use empirical algorithms that are based on historical databases. This paper describes the development of a first-principles based design synthesis tool that includes a fully integrated acquisition and life-cycle cost module. Only first-principles can be used with any level of confidence when extrapolating as far beyond the bounds of existing data as is necessary for very large structures. The Parametric Assessment of Ship Systems (PASS) design synthesis tool has been under development for three years and draws on experience gained from 20 years of development of design synthesis programs. PASS is actually a compilation of separately developed synthesis tools for monohulls, catamarans, SWATH, semi-SWATH and wave-piercing catamarans. The key feature of PASS is that structural, hydrostatic and hydrodynamic calculations are based on first-principles. The use of first-principles allows the extrapolation to new technology that are outside the bounds of current technology. This paper addresses the problems associated with the extension of the current design algorithms used by PASS to very large monohulls and multi-hull structures. Included in this paper is a discussion of the acquisition and life-cycle cost model and how it is fully integrated into the engineering calculations, allowing the evaluation of cost changes for every input variation.

1. DESIGN SYNTHESIS MODELING

Band, Lavis & Associates, Inc. (BLA) has developed and has continuously upgraded and validated, over a period of more than 20 years, a range of Whole-Ship Design Synthesis Models. Models specialized for the following types of hullform have been available at BLA:

- Planing Monohulls (MDSM)
- Surface Combatant Displacement Monohulls (MONODSM)
- Catamarans (CDSM) that includes Semi-SWATH
- Air Cushion Vehicles (ADSM)
- Surface Effect Ships (SDSM).

These models share a common general architecture which reproduces the naval architectural design spiral (Figure 1-1) in order to produce, for a given set of design and operational requirements, a balanced design for which all of the important interactions between subsystem characteristics (weight, volume, performance and cost), have been accounted for.

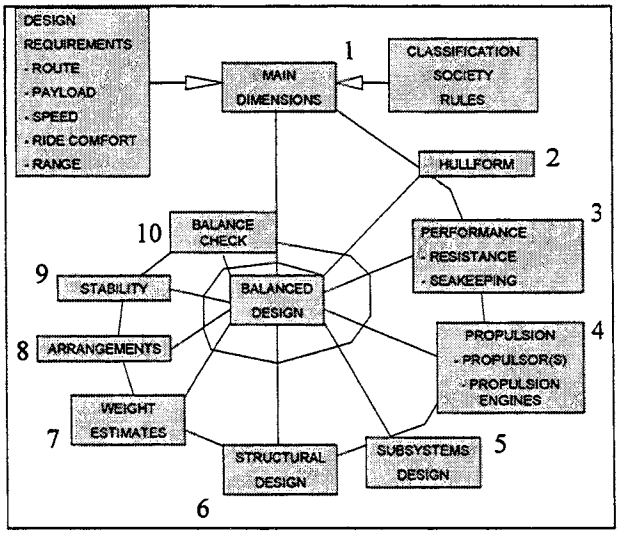

Figure 1-1. Naval Architectural Design Spiral

All models share several generic routines which design and predict the performance and size of subsystems such as engines and propulsors. Such routines rely, for the most part, on analytical algorithms that are based on first-principle physics and have been extensively correlated with the characteristics of actual systems. In all cases, a considerable effort has been continually made to develop and improve the routines from

*900 Ritchie Highway, Suite 203, Severna Park, MD 21146, USA; dbagnell@cdicorp.com & bforstell@cdicorp.com

first-principles rather than to rely exclusively upon empirical relationships.

Over the past three years, BLA has been developing a new generation of a design synthesis model known as PASS (Parametric Analysis of Ship Systems). The PASS model has been funded by ONR via a Small Business Innovative Research (SBIR) contract and incorporates many of the design routines and lessons learned from all prior development of design synthesis models that have been completed at BLA. A primary emphasis in the PASS development was to further develop design routines based on first-principle physics and provide entry points into the various systems and subsystem design modules so that the user could provide the physical characteristics of new or emerging technologies (e.g., specific weight, specific power, specific fuel consumption, material properties) for use in the process of design synthesis. In doing so, PASS has become an ideal tool for assessing new technologies or conceptual ship designs which are very large departures from the current state-of-the-art.

Typical uses include those in which the impact of changing operational requirements are easily examined and those in which design to cost trade-offs are conducted for determining the preferred selection of ship size and subsystem choices including the choice of hullform geometry, hull structural material, powerplant and propulsor type and arrangement, with either acquisition cost or life-cycle cost as the selection criterion. Choices are also made within set limits of stability, seakeeping and state-of-the-art restrictions on feasible geometry.

Upon initiating a design, the designer will generally be interested in investigating a variety of issues, including:

- Quick optimization of ship characteristics.
- Rapid response to changing end-user needs ("what if" questions, concerning cost versus requirements).
- Minimization of acquisition cost, life-cycle cost, vessel displacement or installed power for a given set of requirements.
- Subsystem trade-off and selection.
- Comparison of ship types for a given set of requirements.

In order to more easily understand the results of the parametric analysis, it is beneficial to gain a general understanding of what the PASS program does.

Figure 1-1 provides a graphical depiction of the standard design spiral that every design process follows. The design process starts with a set of a total of 360 design requirements which includes items such as:

- Maximum Payload Weight
- Required Payload Volume
- Range at Cruise Speed
- Cruise Speed
- Speed/Time Operating Profile.

At Step 1, Main Dimensions (see Figure 1-1), the main dimensions of a particular point design are set. The dimensions include:

- Length on the waterline (LWL).
- Beam on the waterline which is set through a user specified length-to-beam (L/B) ratio.
- Maximum length of super-structure expressed as a percentage of the LWL.
- Maximum breadth of super-structure expressed as a percentage of overall beam.

At Step 2, the user specified dimensional information from Step 1 is combined with other (up to 28) non-dimensional user specified hullform characteristics to establish an initial estimate of the hullform. This hullform includes a simplified 3-D wireframe of the entire ship's hull from baseline up to the main deck level. In order to do this, it is necessary to make an estimate of the full-load displacement on the first iteration around the design spiral. Subsequent iterations around the design spiral will use the calculated full-load displacement from the previous iteration for hullform development.

Some of the primary output from this step includes: (1) the number of decks in the ships hull and (2) total volume available in the ship's hull and total area available on each deck.

At Step 3, Performance, the resistance and seakeeping of the hullform which was established in Step 2, are calculated. This evaluation is done for up to eight different user specified speed/sea state conditions.

At Step 4, Propulsion, the entire propulsion system is designed. This includes the design of the propulsor(s), the power transmission, the propulsion prime mover(s) and associated systems. The propulsion system can be either a mechanical-drive or electric-drive system. The propulsion machinery is sized to match the most demanding speed/sea state case from Step 3. Subsequently, the propulsion system characteristics (power consumed, fuel flow, rpm, etc.) are evaluated at the remaining "off-design" speed/sea state conditions specified by the user.

The electrical systems, auxiliary system and outfitting are designed in Step 5. Note that the ship's command and control system (SWBS Group 400) and armament system (SWBS Group 700) are user specified input and are not calculated or designed by PASS. In order to design the electrical system, a complete electrical loads analysis is conducted by the program along the lines of NAVSEA Design Data Sheet (DDS) 300.

The ship's structure is designed in Step 6.

The calculation of global structural loads for very large ships becomes a potentially difficult area. This arises from the fact that the standard formulation for the

calculation of a design wave length for subsequent use in calculating the design bending moment can yield a wave length which will not physically occur in nature. One solution to this problem is to employ a statistical approach to the determination of the largest expected combination of wave height and wave length that the ship is expected to experience in the ship's design life and use the results of this statistical analysis for the calculation of design bending moments.

At Step 7, Weight Estimates, the calculated weights of all the ship's systems and subsystems are added together to establish a calculated lightship weight. Subsequently, all ship's loads are calculated and summed together. Note that ship's fuel is calculated using one of two possible methods. In the first method, the cruise speed and specified range are used in conjunction with the fuel consumption rate that was calculated for the cruise condition in Step 4, to calculate the fuel required to transit the required distance. In the second method, the user specified speed/time operating profile is used in conjunction with the associated propulsion system characteristics to establish the total fuel load which is required to complete the speed/time profile that was specified for the ship. The fuel load calculated by these two methods are compared together, and the largest value of fuel weight is added together with the other calculated loads to establish the design value for ship's loads. These loads are then added to the calculated lightweight of the ship and required margins are applied to establish a calculated full-load displacement.

The ship arrangements are organized in Step 8. The required deck area and volume necessary to support all of the ship's systems and loads are calculated and compared with the volume that is available in the ship's hull. If the ship's hull does not contain sufficient volume to satisfy the volume demand, the volume deficit is made up by increasing the size of the super-structure until the sum of the volume available in the ship's hull and super-structure equals the total volume requirement.

User specified super-structure length and breadth constraints play a significant role in PASS design synthesis in as much as PASS will initially establish a one deck super-structure and increase the dimensions of the super-structure in an effort to balance the volume requirements until the super-structure length and breadth constant are encountered. If additional super-structure volume is necessary to satisfy the super-structure requirements, PASS will then add super-structure decks until such time as the sum of super-structure volume plus hull volume equals total volume required. This use of super-structure to satisfy volume requirements will often raise the vertical center of gravity which, in turn, has a significant impact on the stability of the ship.

At Step 9, Stability, the intact stability of the PASS generated point design is assessed. This analysis uses the 3-D wireframe developed in Step 2 to evaluate the righting arm throughout the heel angle range of 0 to 90 degrees at three different weights. These weights are: (1) full-load design weight, (2) minimum operating weight, and (3) end of service life weight. The area ratios and metacentric height calculated in the stability analysis are compared with the corresponding standards in NAVSEA DDS 079 to determine if the point design CFRs have adequate intact stability.

Step 10 determines if a balanced point design has been reached. Here, the full-load weight that was used to establish the hullform in Step 2 is compared with the full-load weight that was calculated in Step 7. If these two weights differ by more than 0.5%, then another cycle around the complete design spiral is performed, wherein, the hullform calculations are performed using the full-load gross weight calculated in the previous cycle. This iterative process is repeated until such time as the calculated full-load displacement at the end of a cycle is within 0.5% of the full-load displacement that was used at the start of the same cycle.

Once the balanced point design has been established, the cost module discussed in the remainder of this paper is run, the leading particulars of the design point are stored and printed, and, if PASS is running a parametric analysis, the next set of user specified dimensions are analyzed.

2. COST MODULE

2.1 Introduction

Band, Lavis & Associates, Inc. (BLA) has developed a ship acquisition and life-cycle cost model for use in early stage design to support trade-off studies. This model is an integral part of PASS.

The need for cost-based optimization has been stressed in the last decade, due to budget constraints, which have placed greater emphasis on affordability, both first cost and life-cycle cost. By incorporating a cost module into PASS, every configuration studied automatically has an acquisition and life-cycle cost associated with it. This allows the user to evaluate the cost of various operations and configurations starting with the very first feasibility study undertaken. The data can be examined from a traditional approach, i.e., evaluating the cost of various options, or the data can be used in a "cost-as-an-independent-variable" (CAIV) approach to determine what capabilities can be achieved for a fixed budget.

The key feature of any cost estimating model is the Cost Estimating Relationships (CERs). The CERs represent the dollars-per-ton, production rates, labor rates, hourly operating costs, yearly maintenance costs, etc., associated with a particular design. As will be shown, the CERs are key to the cost model and since they are controlled by many variables, such as inflation and yard

efficiency, they need to be continually updated to reflect current construction trends and/or the characteristics of individual shipyards and operating scenarios.

The PASS cost module consists of two parts. The first part covers the basic ship construction cost and its associated programmatic costs. The second part, covers the life-cycle costs of the ship, i.e., how much the ship will cost to operate, both on a yearly basis and over the life of the ship.

2.2 Basic Ship Construction

The cost module provides an estimate for the basic construction cost of a ship based on a set of CERs. The CERs have been derived from a large database of cost estimates and actual as-built costs for a number of ships. Special adjustments can be made to reflect the specific production capability of a particular yard.

The cost is calculated based on the U.S. Navy's Ship Work Breakdown System (SWBS) and includes the following:

Structure	SWBS 100
Propulsion Plant	SWBS 200
Electrical Plant	SWBS 300
Command and Surveillance	SWBS 400
Auxiliary Systems	SWBS 500
Outfit and Furnishing	SWBS 600
Armament (for Military Ships)	SWBS 700
Integration and Engineering	SWBS 800
Ship Assy & Support Services	SWBS 900.

The following costs are also accounted for:

- Spares and Documentation
- Programmatic Costs (Program Management, Change Orders, etc.)
- Profit
- Program Margin.

2.3 Life-Cycle Cost

Life-cycle costs cover three basic areas: cost of development, investment costs, and operation and support costs for the ship class. The disposal of the ship at the end of its service life has not been included although this may very well be a significant cost issue which should be addressed.

2.3.1 Development Costs

Development costs reflect the costs incurred to develop a ship's design from feasibility studies to the award of the lead ship's construction contract. These costs include design studies and the engineering required to perform trade-off studies, to analyze performance, to develop ship-maintenance and training plans, and to develop the shipbuilding specifications and guidance drawings. The costs also include the support of subcontractors.

The pre-award period represents the time between the formal completion of contract design and the award of the contract to build the lead ship. During this period, negotiations with the shipbuilder often require changes to drawings and specifications and other additional engineering work. These costs are also included in the development cost.

The cost to develop and to certify components and technologies that are not currently approved for production may significantly effect the RDT&E costs of "High Tech" designs. However, because the R&D may be funded separately or may be shared with other projects, these costs are not included in the estimates of development costs.

2.3.2 Investment Costs

Investment costs reflect the cost of ship construction, owner furnished equipment, outfitting and post delivery work.

Ship construction costs include funds normally paid to the shipbuilder. These funds cover the major categories of Plan Costs, Basic Construction, Change Orders and Escalation.

Plan costs include the costs of detail design; construction plans; engineering specifications; and the preparation of manuals, damage control books, general information books, and other software deliverables associated with a ship. Plan costs are assumed only to occur with the lead ship. The costs of incremental changes, that are made to a design as a class is built, are covered by change orders.

Basic construction costs include the costs of labor, material, overhead, and profit to build a ship in a private shipyard. This category includes the cost to install owner furnished equipment, but not the cost of the equipment itself. Estimates for follow-on ships reflect productivity improvements resulting from applying learning-curve theory to the lead ship's labor costs. No quantity reductions were applied to the material portion of the estimate for the lead ship. All ships are assumed to be built in a single yard.

Change-Order costs are those associated with changes to a shipbuilding contract during a ship's construction.

Escalation cost is an allowance to cover shipbuilding costs that are expected to increase during the construction period due to economic factors beyond the control of the shipbuilder.

Payload cost includes the cost of all mission electronics, armament, and information supplied to the shipbuilder by the owner. Payload does not include the cost of embarked helicopters and expendable ordnance for military ships.

Other miscellaneous costs and reserves include the costs of planning to maintain and to service a ship's subsystems; owner-furnished engineering support services; transportation; the commissioning ceremony; and the project manager's growth reserve.

Outfitting costs include costs for government-furnished outfitting material. Post delivery cost is an allowance for work items on the worklist approved by the project manager for the correction of defects and deficiencies and for work deferred while a ship is under construction.

2.3.3 Operating and Support Costs

Operating and support costs cover a number of areas such as personnel costs, operations costs, fuel, maintenance, overhaul, and repair.

Operating costs cover direct personnel costs which includes labor and allowances for the ship's crew and temporary additional duty pay (TAD). TAD is the cost of travel for training, administrative purposes, and crew rotation.

Direct operations cost is composed of the costs for repair parts, supplies, training expendable stores, and purchased services, but not fuel costs. Repair parts cover the cost of repair parts used by a ship's crew in maintaining the ship and installed equipment. Supplies include the costs of consumables that are not classified as repair parts and of repair material used by the ship's crew during overhauls. Training expendable stores for military vessels covers the cost of ammunition, training missiles, and pyrotechnics expended by the ship in non-tactical operations and training exercises. Purchased services covers the cost for the ship to buy printing services and publications not carried in the company or Government's standard stock; to rent automatic data processing equipment and related services; and to pay for rents, utilities, long distance-telephone services, postal charges, and other miscellaneous services which are not provided by owner.

Fuel cost is composed of the cost of fossil fuel; and other petroleum, oil, and lubricants (POL). Fossil fuel is the cost of fuel consumed each year by the propulsion plant and by the electric plant. The cost of fuel is a direct computation of the estimated fuel used each year and the cost per ton to buy, store, and deliver fuel. The price of fuel used in the estimate includes the purchase price of the fuel, storage and a delivery charge. Other POL is the cost of fuel for portable self-powered equipment, lubricants, and hydraulic oil.

Direct maintenance cost is the material and labor expended by a tender, repair ship or an ashore facility to repair, or alter, a ship. Depot maintenance covers the cost of work done in a shipyard to maintain and modernize a ship, to overhaul ordnance and equipment that are removed from the ship and sent to depots for repair, to pay for the design services, and to purchase material that the owner supplies to shipyards without charge.

Recurring investment cost is the repair of repairable parts which a ship draws from a supply system, and the cost to replenish spares stocks as a result of condemning repairable parts as being beyond economic repair, or for other reasons.

Indirect costs cover other services and items that are required during the service life of the ship, but not directly relatable to a particular ship, such as: training; publications; engineering and technical services; and ammunition handling.

2.4 Input Options

Via the PASS input file, the user can select those options that impact the selection of the proper CERs. Some of these are:

The construction standards and types of operation:

- Commercial
- Paramilitary (USCG, etc.)
- Military.

Hull Material:

- Steel
- Aluminum
- Structural Concept
- Composite.

Propulsion Plant:

- Diesel
- Gas Turbine
- CODOG/CODAG
- Diesel/Gas Turbine Electric
- Fixed and Variable Pitch Propellers
- Waterjets
- Mixed and Axial Flow
- Podded Propulsors.

Crew:

- Size
- Mix of Officers, CPOs, and Enlisted or Rated and Non-Rated for Commercial Crews
- Military or Commercial Operations

Fleet:

- Number of Ships in Fleet
- Service Life.

Additionally, there are overrides in the input file that allow the user to utilize any CER information that is unique to a particular program or shipyard so that costs can be customized for any shipyard or program.

2.5 Model Description

The cost model is configured to develop a basic ship construction cost and life-cycle cost for each solution developed by PASS. This permits the user to not only evaluate a particular solution based on its technical merits, but also its basic construction cost and life-cycle costs. The cost module in PASS is intended for first-order, ROM estimates.

As already mentioned, cost estimates are dependent on the fidelity of the CERs used for those estimates. PASS utilizes a database of nominal CERs. The estimates developed will represent an average cost for con-

struction in the U.S. Since labor rates and automation and production techniques vary widely from one shipyard to the next, so will the estimates. Thus, an estimate for one design could vary by as much as 25%.

However, if a shipyard can provide real cost data for ships it has built, then CERs can be developed for that specific yard. In cases like this, cost estimates developed by PASS have been shown to be within 10% of those developed for a specific yard.

2.5.1 Acquisition Cost

Acquisition costs are estimated on a dollars per ton and manhours per ton basis. Additionally, propulsion plant and electric plant costs are augmented using dollars per horsepower or dollars per kilowatt.

Typical algorithms have the following structure:

Cost = (Weight * Dollars Per Ton) + (Weight * Manhours Per Ton * Dollars Per Hr)

For propulsion plant and electrical plant costs, the algorithms have the following structure:

Cost = (Weight * Dollars Per Ton) + (Weight * Manhours Per Ton*Dollars Per Hr) + (Kilowatts * Dollars Per Kilowatt)

Costs for weapons and electronics on warships are input. Algorithms have not been developed for these items since each one is so unique. However, based on their estimated weights, an installation cost is estimated.

Ship integration and assembly costs as well as spares and documentation costs are based on a percentage of the lightship costs and labor hours.

2.5.2 Life-Cycle Costs

The life-cycle cost items outlined in the previous section have been simplified in the following manner:

- **Life-Cycle Cost** = Design Cost + Basic Construction Cost + Operations Cost + Personnel Costs
- **Design Cost** = f (Preliminary, Contract and Detail Design Costs)
- **Basic Construction Cost** = Construction Cost, See 2.5.1
- **Operations Cost** = f (Maintenance, Overhaul, Replacement, Fuel)
- **Personnel Costs** = f (Rating, Quantity, Number of Hours and Labor Rate.

In this simplified structure, the CERs can be broken down into simple, easily defined quantities such as:

- Hours of Operation/Year
- Maintenance Hours/Hours of Operation
- Meantime Between Overhaul
- Cost/Overhaul
- Meantime Between Replacement
- Hours/Overhaul or Replacement
- Fuel Consumption/Item
- Labor Rates.

3. PROBLEMS WITH ESTIMATING COST OF VERY LARGE STRUCTURES

3.1 Structure

One of the first problems encountered with large structures is the estimate of structural loads and the structural arrangement. Typical estimates at the parametric level start with a longitúdinal bending moment that is based on the ship straddling a wave with a height equal to $1.1\sqrt{L}$, where L is the waterline length of the ship. For very large ships this could result in a longitudinal bending moment being developed for a wave/sea condition that may never exist. This could result in an overly conservative estimate for bending. Another important issue that needs consideration in determining structural loads is ship heading relative to the sea. Larger structures may not be as maneuverable as more conventional ships and less likely to change headings to reduce wave loads in severe storms.

3.2 Construction and Productivity

Large vessels may lead to the use of larger than normal construction blocks which will provide larger areas to work in that will be more conducive to automated construction processes. This tends to reduce construction time and construction cost. The end result is a less costly ship or structure. However, other issues come into play which may offset some or all of the savings, such as:

- Large blocks require heavy lifting capacity in which a shipyard may have to invest.
- Large structure usually mean excessive drafts which can lead to added costs for dredging.
- If dredging is required, there are environmental issues to be dealt with for the dredging operation. Although this may or may not be a substantial cost compared to the cost of the whole program, permits and environmental impact issues could cause delays that will substantially affect the cost.
- Large structures require large drydocking facilities. This could limit competition which, in turn, could drive up the cost.
- Large structures require thicker plating, or possibly, ferrocement for the structure. Either or both of these materials can be costly to procure. Labor hours associated with welding thicker structures and material handling of heavier, thicker plate, will increase. Lack of, or limited experience with new materials, will add cost due to learning curve issues.

Issues such as these must be addressed from the very outset of feasibility studies. Discussions with yards and material suppliers, as well as owners and program managers are imperative if reasonable designs and cost estimates or trends are to be developed.

3.3 Manning, Automation and Maintenance

Large ships will have limited access to ports and will tend to be "underway" much longer than may currently by the norm. This will mean that crew transfer will have to be via aircraft or shuttle boat. This will be a costly operation with longer times "underway". An alternative approach may be larger crew sizes to increase the number of on-duty/off-duty cycles before crew transfer is needed. Along with this will come an increase in recreational facilities onboard. This could also mean that it will require higher pay to induce crews to sign-on for longer tours. It could also mean an increase in training costs due to lower retention rates.

Even with automation, larger crew sizes may be required to conduct routine inspections. Larger ships will also, generally, mean that damage control issues will be on a much larger scale. Larger, heavier structural members, piping, etc., will require more effort to repair. Thus, it might be expected that, even with automation, the trend of crew size reduction (i.e., number of crew per ton) may reverse.

Even though the trend today is to minimize onboard maintenance and repair, a shift to very large structures may also necessitate a reversal of this trend. Large structures lead to large compartments and large pieces of equipment which, in turn, can lead to large components that may be manpower intensive to move around and repair. Deep draft ships will have limited or no options to drydock for maintenance and repair due to lack of facilities. Thus, the low-manning/automation trend may have to be reversed here also to increase the onboard crew to maintain the vessel. Another costly solution is to ferry shore-based maintenance crews, via ship or aircraft, to the ship to facilitate the repair. However, for large structures unique equipment may be required that is portable (such as lathes) which will have to be transported to the ship, or the ship will have to have fully equipped shops.

Not being able to drydock a ship requires unique and new technologies for exterior hull maintenance. How will the bottom be preserved? Will special paints, special underwater cleaning and repairing equipment be needed, or will the ship be built with extra thick plating that is designed to last the life of the ship? Again, when figuring the life-cycle cost of this, the up-front construction expense must be factored in.

The owners, designers and users must sit down and deal with these issues and the different approaches to these problems that are going to be considered before the design process begins. All of these factors can be accounted for in a first-principles based synthesis model.

3.4 Auxiliary Systems

One unique feature of large structures will be the size and the length of distributive systems. Piping runs with long runs will tend to have larger diameters to minimize losses over the longer runs and/or boost pumps. This will not be treated properly with conventional empirical algorithms and may even require modifications to first-principle algorithms. Savings due to large structures may be outweighed by the extra cost to manufacture larger than normal piping systems for shipboard use. Standard off-the-shelf fittings for such marine piping may not exist.

On large "stationary" structures such as rig type structures, auxiliary systems, such as thrusters, will tend to get "over worked" compared to conventional ship practice, whereas propulsion systems, if they exist, may get "under worked". The biggest impact associated with this will be the maintenance cycle for this equipment and its effects on life-cycle costs.

3.5 Propulsion Plant

Due to the sheer size of very large vessels, propulsion plants, if required, will have to utilize newer technologies for gas turbine engines and even low speed diesels. Propellers and combining gears will probably be pushed to newer limits. This will require considerable development costs to bring this new technology or the extension of technology into production.

A current example of this is the Fast Ship Atlantic project. This project not only requires new cargo handling equipment, both onboard ship and shoreside, but also in gas turbine and waterjet technology. Waterjet and gas turbine technologies are not new, but there are added development costs because these technologies are being pushed to new limits.

4.0 SUMMARY

Experience utilizing design synthesis models both empirically based and first-principle based, has shown that two key factors standout when dealing with large ships; (1) first-principle based synthesis models are the only way to deal with ship/structures that are far outside the bounds of current and past practice; and (2) it is imperative that designers, owners, operators, and the shipyard review and discuss the new design and how it is planned to be built, operated and maintained. Furthermore, many of the standardized approaches that are used to calculate design loads need to be reviewed and structured when being applied to the design of a very large ship. Such review is necessary to ensure that ship structures are neither over designed, which leads to unnecessary growths in cost, nor inadvertently under designed which could result in catastrophic failures.

This is one area where additional research and even dedicated subscale model testing is warranted. It is only through open discussions and the exchange of ideas throughout the design process that effective trade studies can be conducted.

PROCEEDINGS OF THE THIRD INTERNATIONAL WORKSHOP ON VERY LARGE FLOATING STRUCTURES
(VLFS '99), VOL. I, EDS. R.C. ERTEKIN & J.W. KIM, 22-24 SEPTEMBER 1999, HONOLULU, HAWAII, USA

Airfield Operational Requirements for a Mobile Offshore Base

J. N. Polky*
The Boeing Company
Seattle, WA

ABSTRACT

This paper discusses an airport concept for a Mobile Offshore Base. Insight into basic MOB requirements is established through the use of the airport design process. The layout is based on previously defined MOB support missions, which specify the number and type of aircraft to be used. Using the largest aircraft type, the airport functions are allocated to a typical MOB configuration. Specific details are given for runway/taxiway areas, cargo loading areas, maintenance areas, and aircraft support areas An airport layout is developed using established standards and practices for a constrained environment. Safety analysis methods are described, with results shown for missed ILS approaches, and runway overrun and excursion events. These preliminary results suggest that a reasonable MOB airport design may be achieved, which can be operated within acceptable safety levels for large transport aircraft.

1.0 INTRODUCTION

A draft Mission Needs Statement (MNS) was developed in 1995 intending to serve as a broad statement of the expected features of a Mobile Offshore Base (MOB) in support of the National Military Strategy. However, the MNS was written as a high level description of the general characteristics of a MOB, which is open to a wide range of interpretation. In order to assess the feasibility of aircraft operations on a MOB, a set of airfield functional requirements are needed.

The airfield functional requirements were developed based on a hierarchical decomposition of the MNS into a Concept of Operations (CONOPS). The CONOPS includes the mix for four support missions: logistics, tactical air, operational maneuver from the sea, Special operation. The type and quantity of the aircraft for these missions were used to define a conceptual airport design in order to establish overall MOB feasibility. The airport requirements presented in this paper are generally independent of any specific MOB concept.

The deign requirements for any airport will generally be influence by the largest aircraft required to operate from the base. In our case this is the US Airforce's new C-17 Globemaster-III transport. Other aircraft types will influence the layout primarily via requirements for support services and parking space. A secondary driver is throughput based on the mission needs.

A baseline airport layout is first developed using the FAA standards for air operations involving C-17 transport. Next the airport dimension are adjusted to conform to the limited deck area suggested by the ONR MOB Science & Technology Program [1]. Finally the requirements are evaluation based on safety for aircraft operations. It should be noted that these results are not final. They represent recommendations which could be used as a starting point for any future detailed design of a MOB.

2.0 BASIC AIRPORT DESIGN

Federal Aviation Administration (FAA) airport design standards and practices were used to develop an airport configuration for a MOB. The airport design standards are contained in the FAA Advisory Circular [2]. The standards are based on the FAA act of 1958 which seeks to "regulate air commerce in a manner as to best promote its development and safety". Since the standards do not regulate the operation of aircraft, deviations can be made on a case by case basis usually related to safety. Later in this discussion we will see how this is done for a MOB.

The process of designing (or planning) an airport is complicated by many factor. For our study we will simplify it to a set of essential parameters. Any airport design first requires selection of the Airport Reference Code (ARC), The ARC is derived from the Aircraft Approach Category and the Aircraft Design Group, which are defined for a range of aircraft wing spans and a range of approach speeds. Usually the largest aircraft

* john.n.polky@boeing.com

expected to operate from the airport is used in the initial planning.

Precision approach minimums may also be chosen by the airport planner based on the desire to provide Instrument Landing System (ILS) capability for the airport. This is mainly driven by a requirement to meet a particular mission related throughput for the airport. Throughout may be define by a variety of metrics such as: quantity of cargo, number aircraft sorties, number passengers, etc.

2.1 Definitions

A standard airport is made up of the basic elements shown in Figure 1. The following definitions are used to explain these areas [2]:

- Runway (Rnwy) - A defined rectangular surface on an airport prepared or suitable for landing or takeoff of aircraft
- Runway Shoulder - An area adjacent to the edge of the runway providing a visual transition between the runway and other surfaces.
- Runway Safety Area (RSA) - A defined surface surrounding the runway prepared or suitable for reducing the risk of damage to airplanes in the event of an undershoot, overshoot, or excursion from the runway
- Runway Objet Free Area (ROFA)- An area on the ground entered on a runway provided to enhance safety of aircraft operations by having the area free of objects except for air navigation or aircraft ground maneuvering purposes.
- Primary Surface (PS)- A clear area centered on the runway extending beyond the runway end, and having a width greater than the runway. This extra width is used to establish general operational airspace protection for landing aircraft relative to parked aircraft.
- Runway Threshold - The beginning of that portion of the runway available for landing.

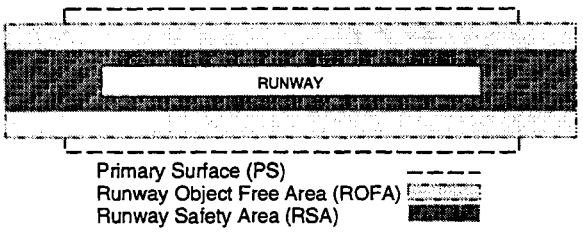

Figure 1 Basic Airport Elements

2.2 Aircraft Operational Parameters

For the C-17, the airport will be classified as *ARC-D-IV*. This code corresponds to an approach speed of greater than 141 knots and less than 166 knots (*D*), with a wing span from 118 feet (36 m) to less than 171 feet (52 m) (*IV*).

Other important aircraft specific data are the landing and takeoff distances. Unfortunately unlike the Design Group there is no single set of values that correspond to an aircraft like the C-17. Figures 2 represents an example of how much the takeoff distances can vary based on simple weather conditions, such as atmospheric pressure and air temperature. A similar chart exists for landing. The chart also illustrates how gross weight can be used as a variable to accommodate a fixed field length relative to variable weather conditions.

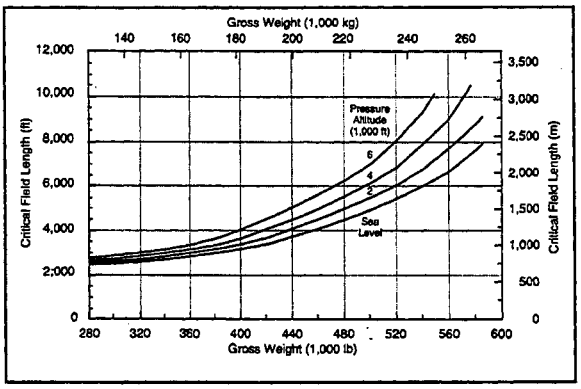

Figure 2 C-17 Critical Field Lengths

Since the MOB will be nearly at sea level, the family of curve will collapse into a single curve. For planning purposes one might chose a tropical day temperature and select a gross weight consistent with a given MOB field length. Similarly, if any mission requires a maximum gross weight capable aircraft, then this would lead to a specific length requirement for the MOB.

Another important operational condition for the airport is the ILS Category needed to support a specific mission capability. This will be driven by the need to continue airport operation during degraded weather conditions. For our study we assumed a Category-II ILS capable airport. Category-II translates into a runway visibility range of less than 1,600 feet (448 m) but greater than 1,200 feet (366 m), and a decision height of less than 200 feet (61 m) but greater than 100 feet (30 m). The decision height is the distance above the airport threshold when the pilot can visually land the aircraft. The MOB will need to be equipped to a suitable glide slope and localizer antenna system. Table II summarizes the aircraft operational parameters.

Table 1- Summary of the aircraft operational parameters

Approach Condition	Category-II ILS
Approach Speed	Category-D-141-161knots
Glide Slope	3 degrees
Wing Span	170 ft (52 m)
Decision Height	115 ft (35 m)
Decision Range	0.3 miles (0.48 Km)

2.3 FAA Standard Airport

Given the preceding choice of aircraft operational parameters, the FAA Advisory Circular specifies the dimensions of a standard airport configuration [2]. Figure 3 illustrates what the general layout of standard airport might look like for C-17 operations. The Figure does not include parking areas for cargo loading operations. These areas would be added to the overall airport lateral dimensions. The Advisory Circular includes a procedure to calculate the setback distance, however we will not include it in this discussion.

The runway length value is not shown because it is established by the specific operation capabilities of the pacing aircraft. As we have seen in the previous discussion, the C-17 can operate over a wide range of runway lengths. For example if we were to specify an gross weight of 480,000 lbs., then the takeoff runway requirement would be 4500 feet (1372 m) for a dry tropical conditions. For wet runway conditions the length might increase to approximately 5800 feet (1768 m).

The main item to note from the Figure is that a standard FAA airport for C-17's might cover an area as large as 8000 feet (2438 m) by 1000 feet (300 m), excluding aircraft parking areas. Clearly these dimensions are significantly larger than the nominal MOB dimensions of 5000 feet (1524 m) by 561 feet (171 m).

2.4 MOB Airport Functional Layout

The function layout for a MOB airport is developed by first considering the basic needs of the mission aircraft. These include runway, taxiway, parking, maintenance. air traffic control, and ground support. A important consideration is to maintain adequate separation between the air operations and the deck operations. This is primarily guided by safety relative to aircraft obstacle collision. However, good inter-function flow must be maintained for efficient airport operation.

Figure 4 illustrates an example of a MOB airport concept. Function separation is achieved by moving the runway and airport support functions to opposite sides of the deck. The taxiway runway separation standard is achieved by eliminating the taxiway. The runway can provide taxiway function by time sharing the three aircraft actions of landing, takeoff, and taxi The arrival/departure rates would have to be adjusted proportional to the transit time to a parking space. Future airport operational analysis must be conducted to understand the impact of such a choice on throughput.

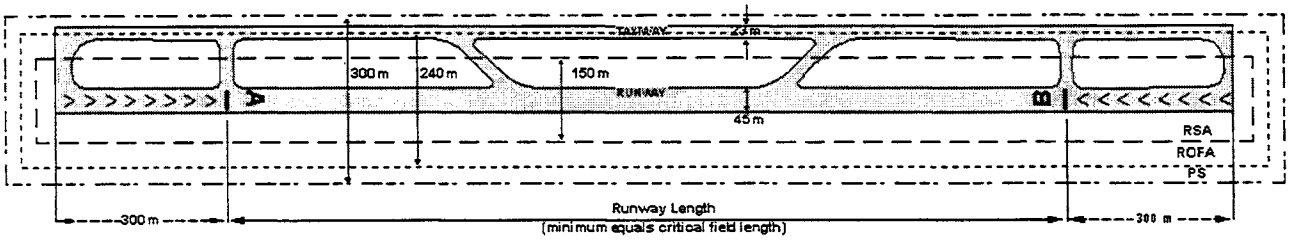

Figure 3 Standard FAA Airport Layout and Dimension

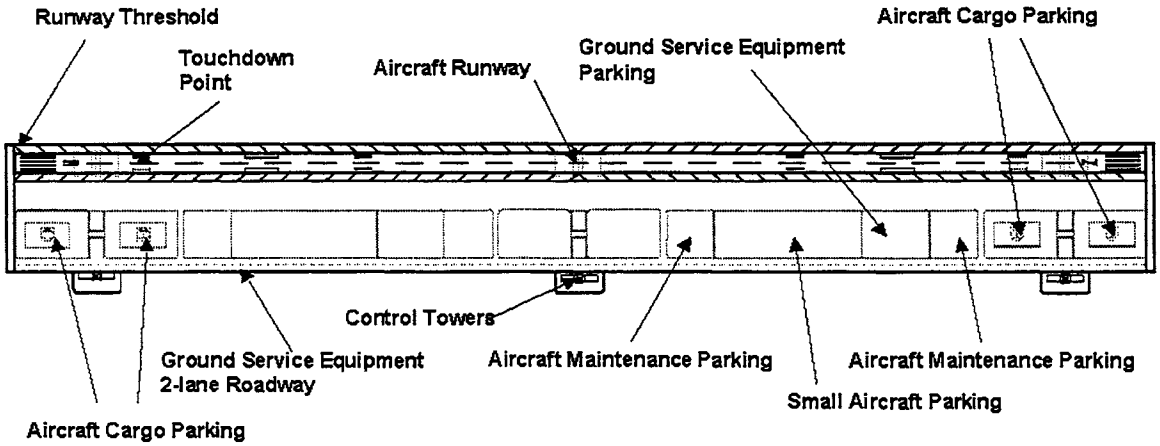

Figure 4 MOB Conceptual Airport Functional Allocations

Aircraft parking areas are determined by the size of the C-17 and the space needed for ground support equipment (GSE). For the C-17 this turns out be about 6364 m^2. The orientation of the parking area is driven by the need to keep the 55 ft high tail as far away from the runway as possible, and allow for efficient cargo loading. For a rear loading C-17 it is felt that a tail-to-tail arrangement would be desirable, and the aircraft centerline parallel to the runway. Additional park spaces are needed for long term maintenance of a C-17. In this case the aircraft centerline can be oriented perpendicular to the runway with the tail facing outboard. This will achieved the greatest tail separation from the runway and allow the engine blast to face overboard during testing. The specific location of the maintenance areas is an example of one possible arrangement. The remaining space was allocated to smaller aircraft parking and GSE storage. A two lane GSE roadway runs continuously along the outboard deck edge to allow rolling stock and cargo hauling to occur without interference with the parked aircraft.

An air traffic control tower is place half way down the runway and at the deck. This minimizes the probability of collision during aircraft takeoff and landing. Three tower positions are indicate in the Figure, however they all are not needed to operate the airport. They are shown to illustrate to desire for commonality between the MOB modules. The towers could be permanent or erected on station. The FAA recommends that the tower be in a position to see all arriving and departing aircraft.

The MOB airport looks somewhat different that the standard FAA airport, especially the separation distances.

2.5 Airport Declared Distances for MOB

In order to resolve these dimensional differences we appeal to Appendix 14 of the FAA Advisory Circular. Appendix 14 defines the alternate design methodology of *Declared Distances*. The use of declared distances is allowed for special cases of constrained airports where it is impractical to provide the runway safety area, runway object free area, and primary surface dimension listed in the AC design tables. They are chosen in coordination with the aircraft operating rules and aircraft certified performance capability. The use of Declared Distance follows a process of choosing dimensions as close as possible to the design tables and then by analysis showing that aircraft operational safety is maintained. In the next section we will discuss our results of such a safety analysis.

Table 2 lists the dimensional differences between a conceptual MOB airport and a FAA standard airport. We have reviewed the Department of Defense standards and found them to be similar to the FAA (some times greater). The dimension are listed for the distance from the runway center line. Since the MOB runway is shifted to one side of the flight deck area, these numbers refer to the inboard direction toward the parking spaces.

Table 2 - Dimensional differences between a standard versus a MOB airport.

	FAA Standard	MOB Concept
Rnwy-1/2width	75 ft (23 m)	45 ft (14 m)
Rnwy-Shoulder	25 ft (7.5 m)	37 ft (11 m)
RSA-length	1000 (300 m)ft	0
RSA-1/2width	240 ft (72 m)	82 ft (25 m)
ROFA-1/2width	400 ft (120 m)	140 ft (43 m)
PS-1/2width	500 ft (150 m)	140 ft (43 m)

3.0 AIRPORT OPERATIONAL SAFETY

The use of Declared Distances is dependant on the ability of the airport design to enable the safe operation of all aircraft. For this study we look at two areas: collision risk for missed ILS approaches, and estimated runway overrun and excursion rates.

3.1 Aircraft Collision Risk on Landing

Collision risk is defined in terms of the probability of collision with a stationary object on a missed ILS approach. The International Civil Aviation Organization (ICAO) has developed a Collision Risk Model (CRM) which can be used to quantify the level of risk associated with missed approaches [3]. Independent parameters in this model include: aircraft wing span, approach speed, glide slope ILS antenna locations; ILS approach category, size and location of fixed obstacles, parked aircraft location, etc.. The CRM statistically predicts the position of the landing aircraft trajectory and calculates the probability of collision with airport obstacles.

The software tool calculates the risk for the precision segment of the approach. The calculation covers the flight segment from the obstacle clearance height (OCH) (i.e. decision height), to the missed approach altitude or a missed approach turn point. The CRM does not cover the risk for visual decent below the decision height, the landing maneuver, or rollout after landing. In the next safety section we will discuss events dealing with ground maneuver and rollout.

The CRM output gives the collision risk for each obstacle as well as the total risk for all obstacles. The model assumes that the obstacles are independent and that the total risk is simply the sum of each obstacle risk. Care must be taken when defining the obstacle models so as to maintain this independence. The obstacle Clearance Panel of ICAO has established a target level of safety for airport operation as one

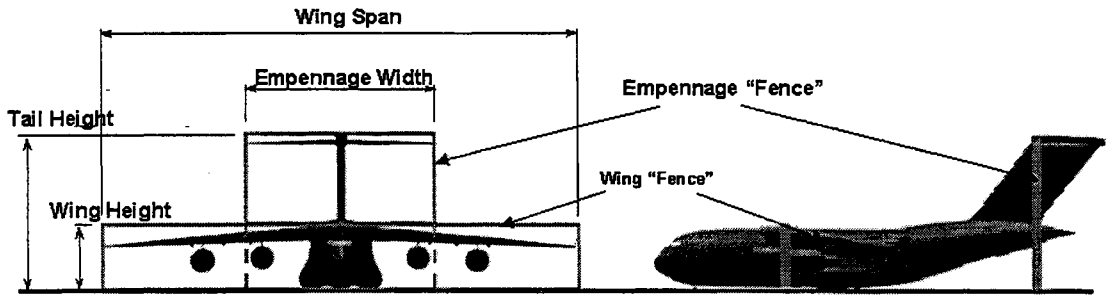

Figure 5 C-17 Obstacle Model for CRM Analysis

accident per 10 million approaches. The CRM also calculates a collision risk for the runway surface, which is used to gauge the lower bound in comparison with the obstacles.

Obstacle models are define using combinations of fence and spike primitives. A fence primitive has height, width and zero depth oriented perpendicular to the runway centerline. A spike primitive has only height.

Three types of obstacle were used in our analysis: parked aircraft, control towers, and miscellaneous obstacles. The control tower was modeled as fence 10m wide by 30 m high. Miscellaneous obstacles were assumed to be cargo containers, aircraft check stands, or large GSE, and they were modeled as a 3 m spike.

The C-17 aircraft were models using combinations of one or two fences depending on their relative to the runway center line. Since the aircraft are relatively complex, a variety of modeling approaches may be taken, however we chose to keep them simple for now. Figure 5 illustrates a two fence model for C-17 in the cargo loading position. The maintenance parked aircraft were represented by a single fence along the aircraft centerline.

The total arrangement of the spike and fence models are shown in Figure 6. The miscellaneous spike obstacles are placed at the corner of each parking area. This was done to represent the possibility of the deck crew to push these items to the extreme edge of the parking space.

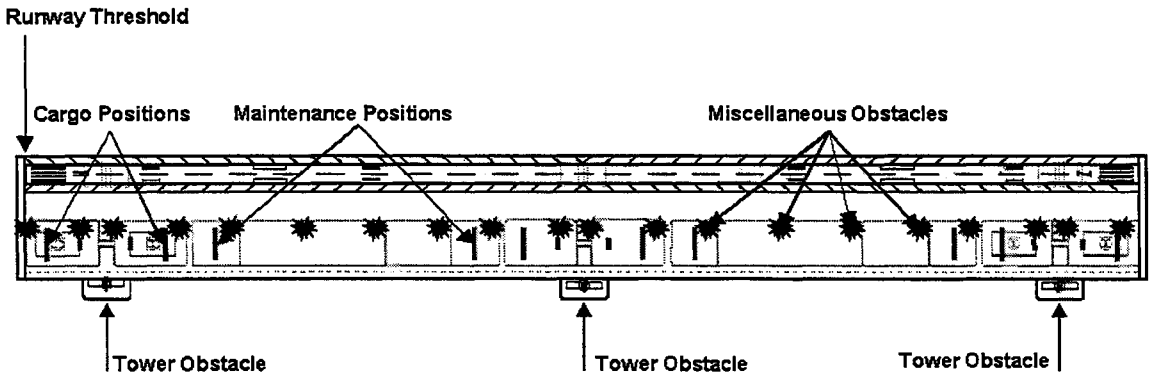

Figure 6 Location of obstacles models on MOB airport

The analysis results are show in Figure 7. The only significant obstacles are those which lie between the upper and lower bounding risk levels. The lower bound of 9.0E-10 represents the risk of hitting the runway. The upper bound is the Target Level of Safety, 1.0E-07. The lower risk obstacles, below the runway risk, would be important only if in total they added significantly to the overall risk. The most significant obstacles are the parked aircraft near the runway threshold and the center control tower. The total risk for this configuration is 6.5E-08, well below the Target Level of Safety set by the ICAO committee.

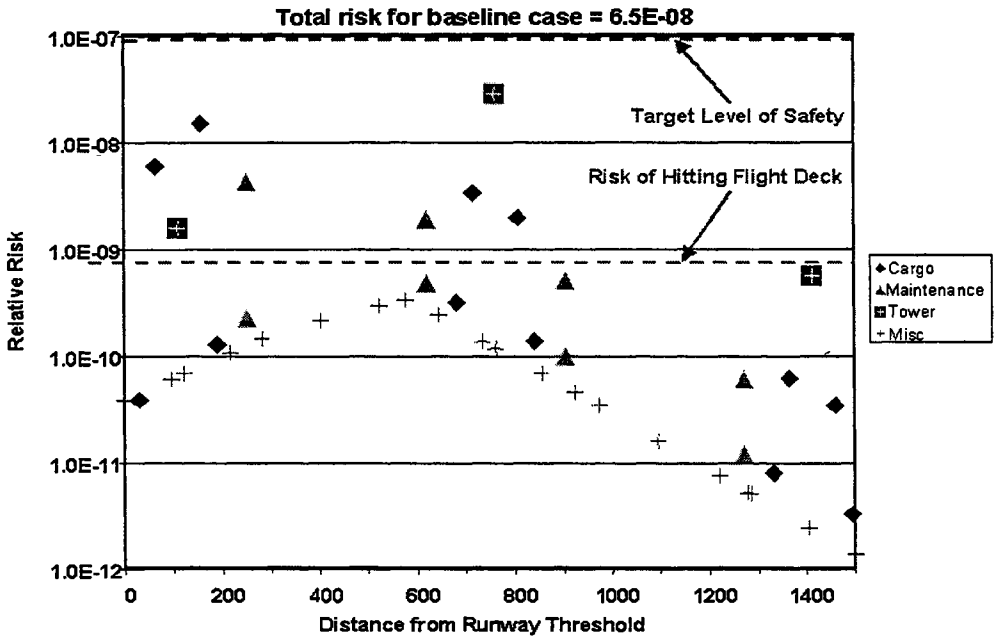

Figure 7 Collision risk for MOB airport obstacles

3.2 Aircraft Overboard Risk

For land based airports the consequences of runway excursion and overrun may not necessarily result in a hull loss. For an MOB it may always be catastrophic. A survey was conducted of commercial airports in order to begin to understand the potential overboard risk for a MOB.

The data was based on world wide event records for a 10 year period beginning in mid 1989, for all standard commercial aircraft [4]. During the same period of time the approximate number of arrivals and departures totaled 160 million.

Table 3 - Event rates for landing and takeoff

	Overrun	Offside
Landing	1.0E-06	6.7E-07
Takeoff	1.6E-07	1.4E-07

We can see by these results that aircraft landings are the most significant. For the constrained environment of a MOB excursion could result in collision with parked aircraft on the inboard side, and hull loss on the outboard side. Even though the overrun event rate appears relatively low, is based commercial runway lengths which are at least twice as long an a nominal MOB. In many cases weather influences the events. Usually a gusting cross wind condition may influence an offside event, while wet runway condition may influence an overrun. An overrun can also occur during an engine failure during takeoff when the pilot chooses to abort the takeoff.

CONCLUSIONS

The operational requirements for a MOB airport have been discussed for a basic MOB geometry. By using a FAA *Declared Distance* approach, a MOB airport may be designed to operate safely for large transports such as the C-17. A preliminary safety analysis suggests that an acceptable safety levels can be achieved, even in a constrained MOB. Further work is needed to resolve some issues such overrun and offside risk reduction. However, the overall conclusion is that there are enough variables available to successfully manage the flight operations risk. We feel that it is feasible to consider large aircraft operations from a MOB.

Acknowledgement: The material is based upon work supported by the U.S. Office of Naval Research's MOB Program. Kvaerner Maritime for technical data about their flexible bridge concept.

References

[1] G. Remmers, et. al., *Proc. Int. Offshore and Polar Engineering Conf.*, Montreal, Canada, 1998

[2] Federal Aviation Administration, AC 150/5300-13, *Airport Design*, Sept 1989, Washington. D.C.

[3] International Civil Aviation Organization, *Manual on the Use of the Collision Risk Model (CRM) for ILS Operations*, 1980, Montreal, Canada.

[4] Boeing Company Data

PROCEEDINGS OF THE THIRD INTERNATIONAL WORKSHOP ON VERY LARGE FLOATING STRUCTURES
(VLFS '99), VOL. I, EDS. R.C. ERTEKIN & J.W. KIM, 22-24 SEPTEMBER 1999, HONOLULU, HAWAII, USA

THE BEHAVIOR OF AN AIRPLANE TAKING OFF FROM AND LANDING ON A VLFS IN ROUGH SEA CONDITION

Hisayoshi Endo
Ship Research Institute*

ABSTRACT

The concern of the paper is a transient behavior of a VLFS subjected to dynamic load induced by airplane landing and takeoff. A time-domain analysis method is applied to the hydroelasticity problems for this purpose. The method is based on FEM scheme to treat structure and on Wilson's θ method to pursuit time step procedure taking advantage of the memory effect function for hydrodynamic effects. The effectiveness of the method is verified through comparing the obtained results with frequency domain analysis and tank experiment.

The present calculation method is applied to the hydroelastic response analysis of a floating runway on which an airplane is supposed to take off or land. MF-300 which was designed as the first Mega-Float prototype structure is adopted as an example VLFS runway. Then the runway is supposed to be subjected simultaneously to incident wave and to takeoff/landing load. The combined action due to moving load and wave load is investigated, then the magnitude of the drag force on the airplane which is induced by the deformed runway is evaluated through example studies.

1. INTRODUCTION

VLFS has been a attention focussing research/development project in Japan since 1977 when the first stage project to construct Kansai International Airport started and a preliminary design of VLFS type of airport was proposed. Since then VLFS is expected to be utilized as a floating airport considering its advantage to realize large space near urban area.

It has been recognized that dynamic behavior of VLFS is entirely based on hydro-elasticity phenomena and that larger size of structure requires more degrees of freedom in the analysis. Up to this day much effort has been paid to the development of analysis method to treat wave-induced behavior. Unfortunately most of them are inclined to frequency domain analysis.

When considering functional requirement of VLFS not only environmental but also functional load should be taken into account at the design stage. Since takeoff and landing of airplane is considered most severe functional requirement for a floating runway the study on the hydroelastic transient response of runway is quite important. Though most of all research works have been forwarded to wave-induced behavior there have been some research works to treat this kind of transient phenomena.

Watanabe & Utsunomiya[1], Technological Research Association of Mega-Float[2] and Imai & Ataka[3] investigated into the airplane landing and takeoff by using the time domain method. However, their calculation model is too much simplified in treatment of structure and/or fluid. Endo [4] and Endo et al.[5] carried out a series of model tests in which the pontoon-type model is subjected to moving load and vertical impact load which idealizes airplane landing and takeoff. He also developed a time-domain analysis method in which the structure is modeled by many segmented panels with hundreds of d.o.f. and hydrodynamic effect is evaluated using the memory effect function. The analysis method was verified by comparing its results with tests and was found to show good agreement. Ohmatsu[6] also developed another kind of time-domain analysis method in which the structural response is obtained from the convolution integral of frequency response function and impulse response function. He also demonstrated the effectiveness of his analysis method by comparing its results with the test results of moving load and vertical impact load[5]. Kim and Webster[7] and Yeung and Kim[8] presented analytical method to obtain the response of VLFS runway subjected to moving load. They derived not only the structural response but also the magnitude of the added drag on airplane. They also demonstrated a very interesting phenomena that the hydroelastic wave goes first then the airplane follows after that.

6-38-1 Shinkawa, Mitaka, JAPAN 181-0004
E-mail : endo@srimot.go.jp

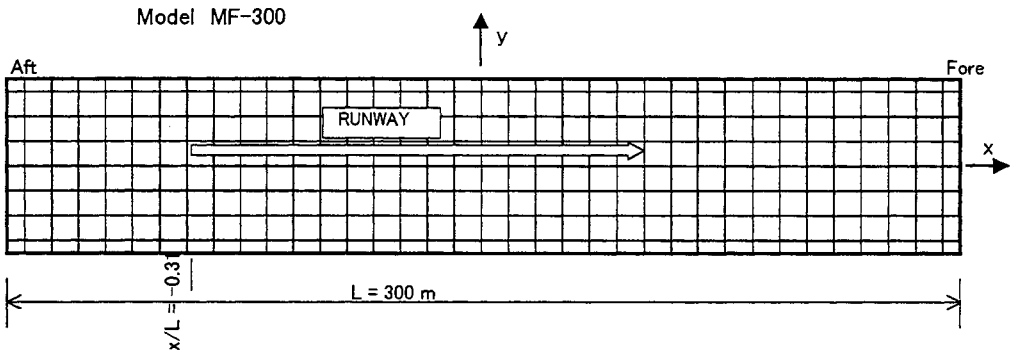

Figure 1: Plan view of MF-300

Though there have been a lot of contributions in the research activities related to airplane landing and takeoff, their mathematical models involve idealization and simplification to some extent in them. It is still doubtful that they can treat the real situation of airplane landing and takeoff. The author would like to present the simulation of airplane landing and takeoff taking account of the combined action of incident wave.

2. MODEL STRUCTURE

Here adopted as an example VLFS is MF-300 which was constructed as the first prototype Mega-Float and had been tested at sea by Technological Research Association of Mega-Float for three years from 1995 to 1998. MF-300 is a pontoon-type square plate-like structure the particulars of which are listed in Table 1. It is assumed to be used as a runway for a small airplane. Though the structure of MF-300 is wide and strong enough for the use of landing and takeoff of a small airplane, it had never experienced airplane landing in reality.

The plan view of MF-300 is shown in Fig.1 in which the location of the assumed runway is illustrated.

Table 1 Particulars of MF-300

L × B × D	300 × 60 × 2 m
Draft	0.5 m
Water Depth	8 m
EI (Bending Stiffness)	4.78×10^8 KN-m^2

3. ANALYSIS METHOD

3.1 Equation of Motion

Following Ogilvie[10] the equation of motion at time t is expressed in the time-domain as follows,

$$(M+A)\ddot{x}_t + \int_{-\infty}^{t} S(t-\tau)\dot{x}_t d\tau + Kx_t = p_t$$

$$S(t) = \frac{2}{\pi}\int_0^{\infty} N(\omega)\cos(\omega t)d\omega \qquad (1)$$

where

M : Structural mass matrix

A : Added mass matrix

$S(t)$: Memory effect function.

$N(\omega)$: Wave making damping matrix with respect to circular frequency ω

K : Structural stiffness and static restoring force coefficient matrix

p : External force vector

Added mass, A, and damping, N, have to be evaluated from a frequency-domain calculation before time-domain procedure. They are obtained through the direct method in which the pressure distribution is calculated based on BEM. The mathematical procedure of the direct method is described in detail in [9].

3.2 Calculation Method

The equation of motion is solved by using FEM for the structure and Wilson's θ method to pursuit time step procedure. The calculation method developed is explained in detail in the previous papers[4,5].

There exist some difficulties in carrying out the time-domain calculation to obtain hydroelastic behavior of VLFS. The major difficulties are as follows,

1) The structure model is composed of many small panels that have tremendously large d.o.f. This requires large CPU time and memory size of the computer.
2) The memory effect function requires the infinite integral with respect to the frequency. The integration range must be truncated at some high frequency range.

3) The memory effect function is composed of hydrodynamic damping terms which usually requires full matrix size. Large memory and CPU time is needed.
4) The added mass which corresponds to the added mass with respect to infinite frequency, $\omega = \infty$, must be evaluated before time-step calculation.

These difficulties give restriction to the mathematical modeling. But it can be overcome to some extent by refining the numerical treatment as described in [4].

3.3 Verification of the Calculation

Since there exists restrictions to some unknown extent in the analysis method, verification of the accuracy is indispensable. The verification will be carried out for the load cases of regular wave condition and of moving load condition respectively.

The response of the vertical displacement to incident regular wave with wave length $\lambda/L = 0.1$ and $\lambda/L = 0.2$ is calculated by using the time-domain procedure. The vertical displacement obtained is confirmed to be stable and periodic after the time step of more than four times the wave period. Thus the vertical displacement amplitude was determined from the first harmonic term of Fourier transform after the time step of four times the wave period. The distribution of vertical displacement amplitude obtained are shown in Fig. 2. The author et al. carried out the model experiment and the frequency-domain analysis for the same loading case. The experimental model structure, VL-10, was so designed as similar to MF-300 on the basis of the law of similitude. The detail is presented in [9]. The results obtained from the present method, TD, and from the experiment, EXP, and from the frequency-domain analysis, FD, are comparatively shown in Fig. 2. As far as the range of the wave length is $\lambda/L \geqq 0.1$, the present method is found to keep sufficient accuracy.

The moving load experiment was also carried out on the same model with a movable weight which weighs 6.9 Kg. In the experiment the weight was translated on the runway from x/L=-0.31 to 0.4 (see Fig.1) with almost constant velocity, 0.61 m/sec (12.2 Km/h in the scale of MF-300). The detail of the experiment is presented in [4]. The time history of the vertical displacements obtained from the present method, CAL, and from the experiment, EXP, are comparatively shown in Fig.3. Though the velocity is very low as compared with airplane, the calculated results are found to show a reasonable agreement with the experiment.

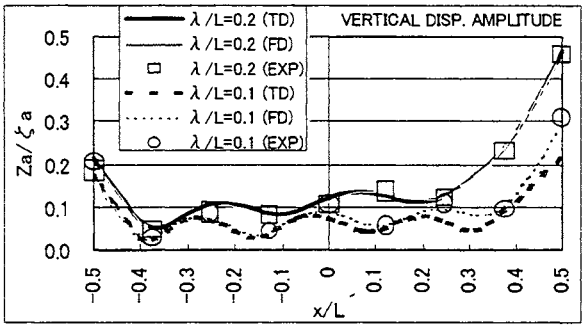

Figure 2: Distribution of vertical displacement amplitude in regular waves

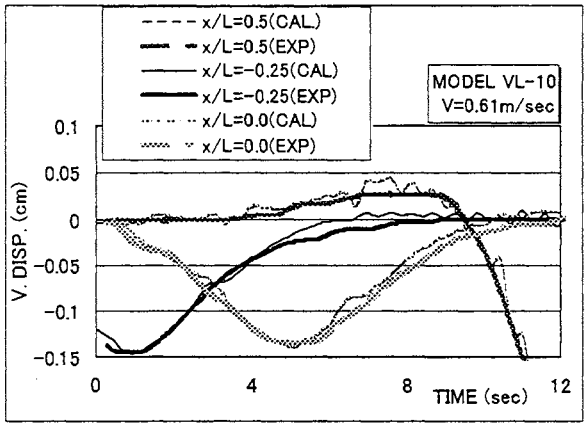

Figure 3: Time history of vertical displacements in the moving load test

4. MATHEMATICAL MODEL

4.1 Floating Structure

Coordinate system and FEM mesh subdivision are illustrated in Fig.1. The structure is subdivided into 36 $\times$ 8 flat shell elements and 37 $\times$ 9 nodes in FEM scheme. Thus the total d.o.f. of the structure model is 999 (=3$\times$37$\times$9).

The runway is assumed to lie parallel to and 3.3 m apart from the centerline. The landing and takeoff always starts from the position x/L=-0.31 unless otherwise stated.

4.2 Incident Wave

The incident wave assumed is a regular wave with.

length : λ = 30 m (λ/L = 0.1)
period : T_W = 4.4 sec
height : H_W = 1.0 m (ζ_a = 0.5 m)
incident angle : head sea .

This wave condition represents rough sea condition MF-300 would encounter.

After the magnitude and the phase angle of the

diffraction force is obtained from the frequency-domain analysis they are converted to the time varying cyclic load. Then the time step loads which will be used as the wave exciting force in the time-domain analysis are prepared.

When handling the regular wave the time increment in the calculation is set to $T_W/32$.

4.3 Airplane

The particulars and the performance of the model airplane are assumed as follows,

Weight : Δ = 3 tons (always)
Landing Performance
Landing velocity : V_L = 150 Km/h
Run acceleration : A_L = -5.79 m/sec^2 (constant)
Run distance : X_L = 150 m
Elapsed time : T_L = 7.2 sec

Takeoff Performance
Takeoff velocity : V_T = 150 Km/h
Run distance : 150 m
Run acceleration : A_T = 5.79 m/sec^2 (constant)
Run distance : X_T = 150 m
Elapsed time : T_T = 7.2 sec

The action of the airplane to the runway is also simplified as follows,

1) Airplane is treated as a moving weight which exerts vertical force to the runway.
2) The vertical force exerted is reduced by the lift force which is proportional to the second power of the moving velocity.
3) The fluctuation of the vertical force induced by the vertical motion of the airplane is negligible.
4) The vertical force is idealized as the point load which is distributed to the adjacent four nodal points.

When following assumption 3) no coupling effect between the airplane and the runway might be induced. The adequacy of assumption 3) will be discussed after carrying out simulation calculation.

5. SIMULATION

5.1 Landing

As above-mentioned the acceleration of the airplane is assumed constant during run. The airplane is supposed to touch the runway at x/L=-0.31 then to stop at x/L=0.19. The load induced by the weight of the airplane is evaluated from its current velocity. Thus the time step load applied to the nodal point is as shown in Fig.4. The load applied to the nodal point i is denoted as $p(x_i)$ where x_0 is the starting point, then the load moves to the node x_1, node x_2, node x_3, ...

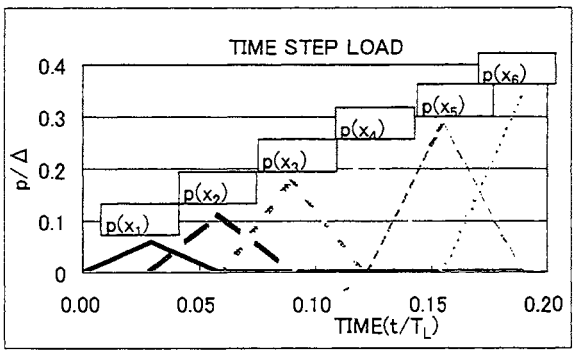

Figure 4: Time step load applied to the nodal points during landing

5.1.1 Landing in still water condition

The deformed profiles of the runway during run are shown in Fig.5A and 5B. The location of the airplane is indicated with circles. The airplane completes landing run in 7.2 sec.

The figures tell us that the deformed shape of the runway is close to the current static equilibrium configuration. The elastic vibration is transmitted ahead and behind of the airplane though the magnitude of it is small. The airplane seems always to stay at the bottom of the dent which continues to descend during the landing run. The vertical displacement of the runway is very small all over the length though it reaches the maximum just after the airplane. The vertical displacement is always less than 0.1 cm and the inclination angle at the foot of the airplane is less than $tan^{-1}(0.00001)$.

5.1.2 Landing in the regular wave condition

In the treatment of time step procedure the time history of the loading is divided to two stages. The regular wave comes first then the landing load arrives later by four cycles of the wave period. The airplane is supposed to land heading toward the wave from the aft side of the runway.

The deformed profiles of the runway during the landing are shown together with the location of the airplane in Fig.6A to 6C. The trajectory of the airplane run on the runway is indicated in Fig.6C. It can be seen that the magnitude of the vertical displacement is about a hundred times the one in the still water condition. This means the wave load is far dominant as compared with the landing load. Then the vertical movement of the airplane depends largely on the structural wave propagation which is induced by the incident wave. Fig.6C shows that the airplane encounters two and a half of structural waves within 7.2 sec during landing run whereas the wave period is 4.4 sec.

The vertical displacement of the runway is almost equivalent to the elevation of the structural wave even

just under the airplane. The magnitude of the displacement is within 6 cm and the inclination angle is less than $tan^{-1}(\pm 0.002)$ at the foot of the airplane.

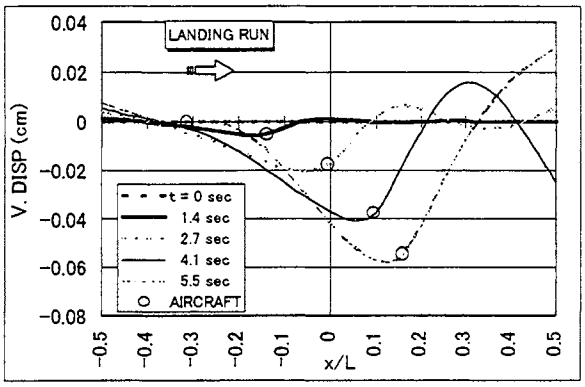

Figure 5A: Deformed profile of the runway subjected to landing load ($t/T_L = 0 \sim 0.76$)

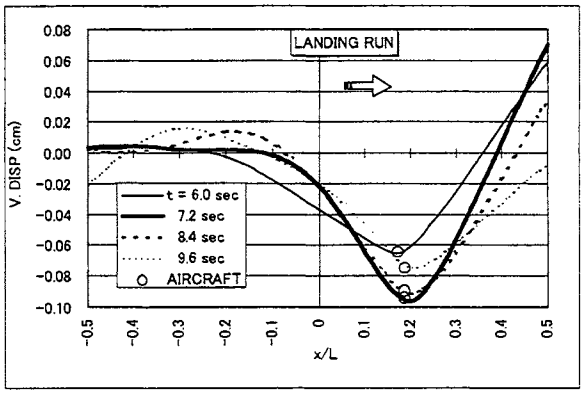

Figure 5B: Deformed profile of the runway subjected to landing load ($t/T_L = 0.83 \sim 1.33$)

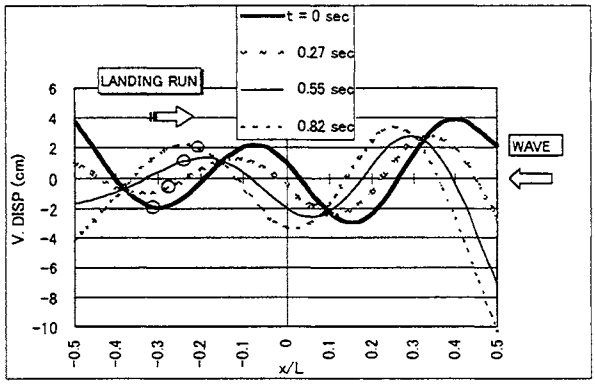

Figure 6A: Deformed profile of the runway subjected to wave and landing load ($t/T_L = 0 \sim 0.11$)

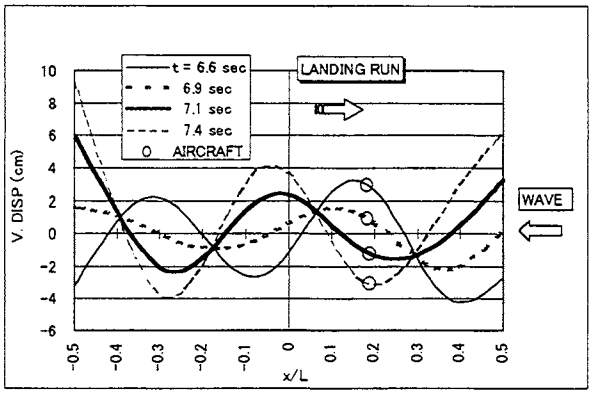

Figure 6B: Deformed profile of the runway subjected to wave and landing load ($t/T_L = 0.91 \sim 1.03$)

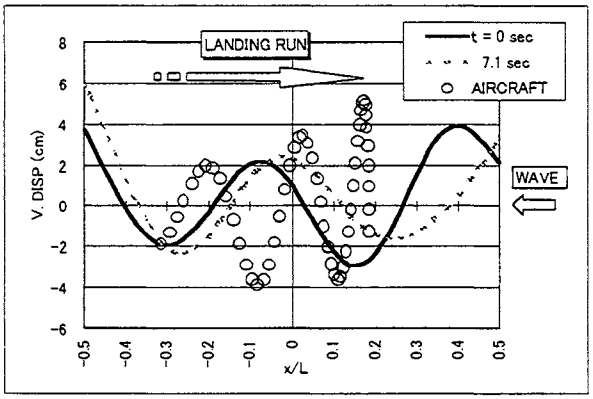

Figure 6C: Deformed profile of the runway and the trajectory of the airplane run ($t/T_L = 0 \sim 1.0$)

5.2 Takeoff

The acceleration of the airplane is assumed constant during run . Before starting the airplane stays put at the starting point x/L=-0.31 keeping static equilibrium condition. Then it suddenly starts from the rest then completes the takeoff at x/L=0.19 in 7.2 sec. The load induced by the airplane weight is evaluated from its current velocity. Thus the time step load applied to the nodal point is as shown in Fig.7.

5.2.1 Takeoff in still water condition

The deformed profiles of the runway during the takeoff run are shown in Fig.8A to 8C. The location of the airplane is also indicated with circles. The airplane completes its takeoff in 7.2 sec.

The deformed shape of the runway is close to the current static equilibrium configuration. The tendency of the dynamic behavior is similar to the case of landing. The airplane seems always to stay at the bottom of the dent which continues to ascend during the landing run. The vertical displacement of the runway is very small also in this case. The vertical

displacement is always less than its static equilibrium configuration and stays within 0.07 cm. The inclination angle at the foot of the airplane is less than $tan^{-1}(0.000004)$.

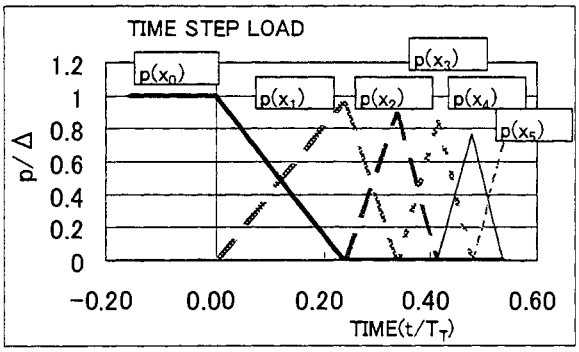

Figure 7: Time step load applied to the nodal points during takeoff run

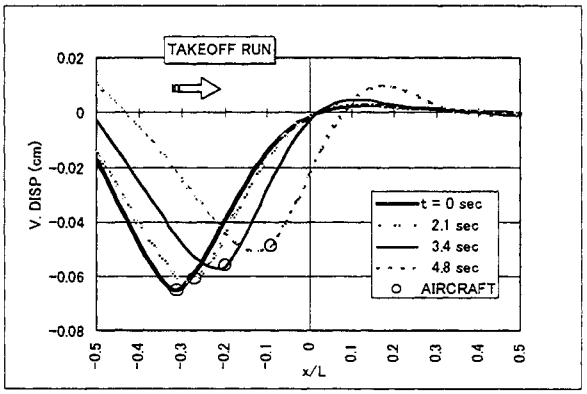

Figure 8A: Deformed profile of the runway subjected to takeoff load ($t/T_T = 0 \sim 0.67$)

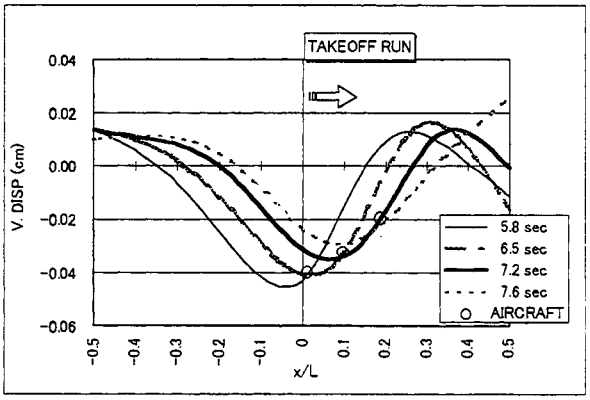

Figure 8B: Deformed profile of the runway subjected to takeoff load ($t/T_T = 0.81 \sim 1.06$)

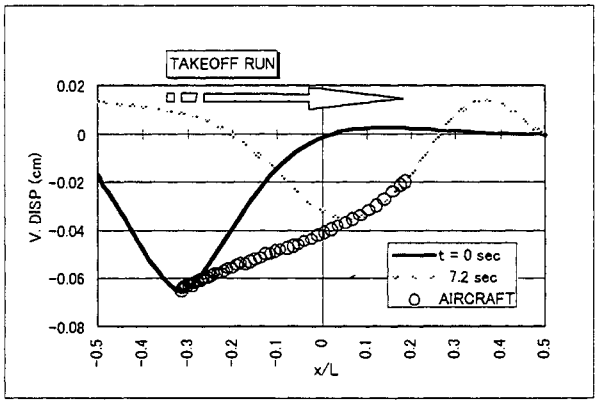

Figure 8C: Deformed profile of the runway and the trajectory of the airplane run ($t/T_T = 0 \sim 1.0$)

5.2.2 Takeoff in the regular wave condition

In the treatment of the calculation the regular wave comes first then the landing load arrives later by four cycles of the wave period. The airplane is supposed to take off heading toward the wave from the aft side.

The deformed profiles of the runway during the run are shown together with the location of the airplane in Fig.9A to 9C. The trajectory of the airplane run on the runway is also indicated in Fig.9C. It can be seen that the magnitude of the vertical displacement is more than a hundred times the one in the still water. The action of the wave load is far dominant as compared with the takeoff load just like in the case of landing load. Then the vertical movement of the airplane depends largely on the structural wave propagation which is induced by the incident wave. Fig.9C shows that the airplane encounters two and a half of structural waves within 7.1 sec during the run.

The vertical displacement of the runway is almost equivalent to the elevation of the structural wave. The magnitude of the displacement is about 4 cm and the inclination angle at the foot of the airplane stays within $tan^{-1}(\pm 0.002)$.

5.2.3 Takeoff in the following sea condition

For the purpose of comparison the run direction is reversed to a following sea condition. The trajectory of the airplane run on the runway is shown in Fig.10. Comparing the results shown in Fig.9C and Fig.10 it can be seen that the fluctuation of vertical displacement is nearly the same at the beginning of run but it changes abruptly in its magnitude and phase after the run gains velocity. At the final stage of the run the velocity of the airplane becomes very near to the velocity of structural wave. Then the airplane goes into surfing condition where it advances together with the structural wave.

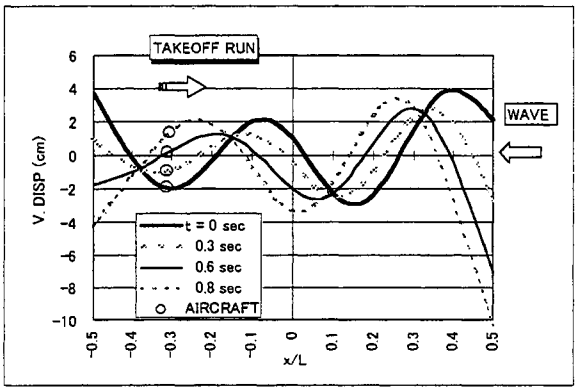

Figure 9A: Deformed profile of the runway subjected to wave and takeoff load ($t/T_T = 0 \sim 0.11$)

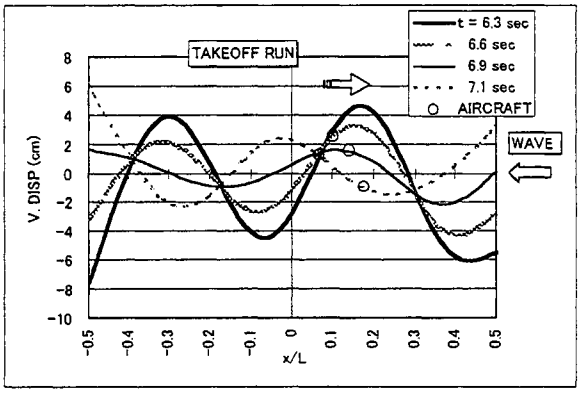

Figure 9B: Deformed profile of the runway subjected to wave and takeoff load ($t/T_T = 0.88 \sim 1.0$)

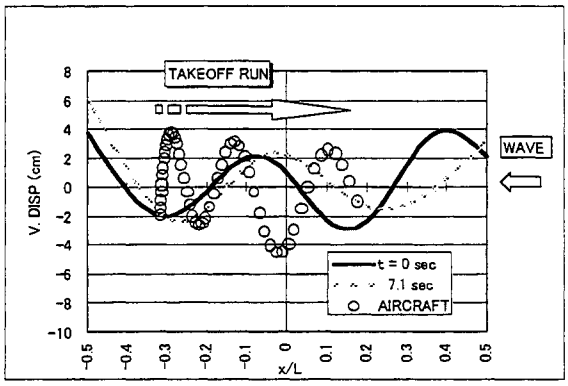

Figure 9C: Deformed profile of the runway and the trajectory of the airplane run ($t/T_T = 0 \sim 1.0$)

5.2.4 Discussion

The airplane moves up and down riding on the structural waves during run. Thus the structural wave plays a significant role on the behavior of the airplane. It is well known that the characteristics of the structural wave is governed by the following dispersion relation (see [11] and [12]).

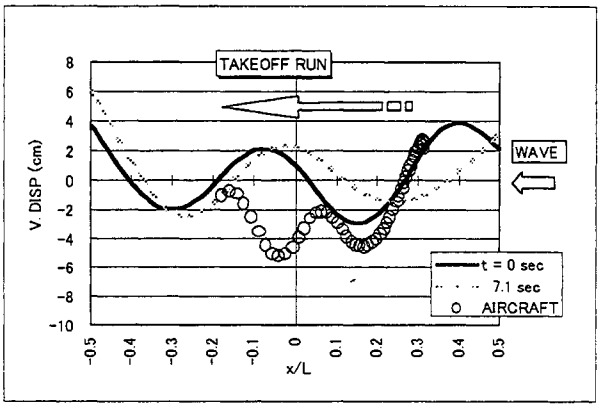

Figure 10: Deformed profile of the runway and the trajectory of the airplane run in the following sea condition

$$\omega^2 = \frac{Dk^4 + \rho g}{\rho d + \dfrac{\rho}{k \tanh kh}} \qquad (2)$$

where ω : circular frequency
D : bending stiffness rigidity
ρ : density of water
k : wave number of the structural wave
h : water depth
λ_s : length of the structural wave

The characteristics of the structural wave in the water wave with $\lambda/L = 0.1$ is determined by using Eq.(2).

$\lambda_s = 148.3$ m ($\lambda_s / L = 0.494$)
V_s (propagation velocity) = 33.8 m/sec (3)

The propagation velocity of the structural wave is 4.94 times the one of the water wave.

The velocity of run varies from 0 to 41.7 m/sec during takeoff run. Thus in the case of head sea condition the airplane encounters the structural wave coming up very fast and on the contrary in the case of following sea condition it rather runs together with the wave. In the case illustrated in Fig.10 the wave passes by at the beginning and then the airplane overtakes the wave at last.

The undulation of the runway causes the drag on the airplane. Following Kim and Webster [7] the drag force, D, is represented by the following equation.

$$D = \Delta \frac{dz}{dx} \qquad (4)$$

z : vertical displacement of the runway

The drag induced on the airplane during takeoff run is estimated for the cases of 5.2.2 and 5.2.3. The results are shown in Fig.11. The trend of the time history of the drag is keenly related to the propagation of the structural wave. The magnitude of the drag is less than $0.002\,\Delta$ and it fluctuates between positive and negative.

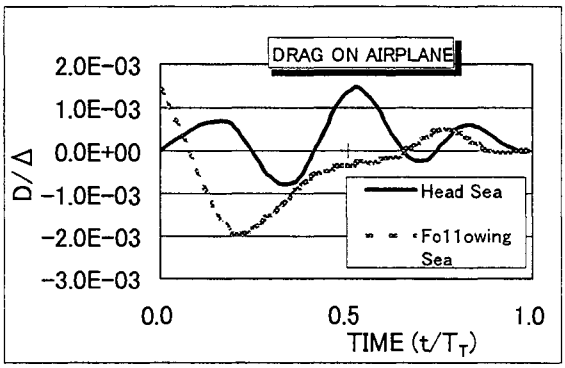

Figure 11: Time history of the drag during takeoff run

6. CONCLUSIONS

In the simulation of takeoff run and landing run the following facts have been confirmed.

1) The airplane makes a V-shaped valley on the runway staying at its bottom and dragging it. Small elastic vibrations induced by the plane are transmitted from the valley to the hill.
2) In the wave condition the magnitude of the vertical displacement of the runway is far greater than that induced by the plane.
3) The airplane moves up and down during the run riding on the very fast structural wave. In the following sea condition the plane may experience kind of surfing after it gains speed just before takeoff.
4) The vertical motion of the airplane induced by the motion of the runway is very small even in the wave condition. The magnitudes of vertical displacement and acceleration at its foot are within 0.06 m and 0.32 m/sec^2 in the case of the regular wave with length λ =30 m and height H_W= 1 m .
5) The structural wave plays a significant role on adding the drag on the airplane. But the magnitude of the drag is very small.

References

[1] E. Watanabe and T. Utsunomiya, "Transient Response Analysis of a VLFS at Airplane Landing", *Proc. Int. Workshop on Very Large Floating Structures*, VLFS'96 Hayama, pp.243-247, 1996.

[2] Technological Research Association of Mega-Float, " Very Large Floating Structure (Mega-Float)", Technical Report Abstract, pp.215-217, 1998.

[3] S. Imai and K. Ataka, "Elastic Response of a Floating Airport During Airplane Landing and Takeoff", Graduate Thesis of Univ. of Tokyo, 1997.

[4] H. Endo and K. Yago, "Time History Response of a Large Floating Structure Subjected to Dynamic Load", to appear *in J. of Soc. Nav. Archit. Japan*, 1999.

[5] H. Endo, K. Yago and S. Chiaki, "Elastic Response of a Floating Platform Stimulated by Dynamic Load", *Proc. of 14th Ocean Engineering Symposium*, Soc. Nav. Archit. Japan, pp.411-416, 1998.

[6] S. Ohmatsu, "Time Domain Analysis of Hydroelastic Behavior of VLFS", *J. of Soc. Nav. Archit. Japan*, Vol 184, pp.223-230, 1999.

[7] J. W. Kim and W.C. Webster, "The Drag of an Airplane Taking Off from a Floating Runway", *Proc. of Int. Workshop on Very Large Floating Structures*, VLFS'96 Hayama, pp.235-241, 1996.

[8] R. W. Yeung and J. W. Kim. "Structural Drag and Deformation of a Moving Load on a Floating Plate", *Proc. of 2nd Intl. Conf. on Hydroelasticity in Marine Technology*, RIAM, Kyushu Univ,. Fukuoka, pp.77-88, 1998

[9] K. Yago and H. Endo, "On the Hydroelastic Response of Box-Shaped Floating Structure with Shallow Draft (Tank Test with Large Scale Model)", *J. of Soc. Nav. Archit. Japan*, Vol 180, pp.341-352, 1996

[10] T. F. Ogilvie, "Recent Progress Toward the Understanding and Prediction of Ship Motions", *5th ONR Symp. on Naval Hydrodynamics*, 1964

[11] T. Tsubogo and H. Okada, "A Basic Investigation on Deflection Wave Propagation and Strength of Very Large Floating Structures", *J. of Soc. Nav. Archit. Japan*, Vol 181, pp.299-307, 1997

[12] Y. Iwahashi, S. Ohmatsu and T. Tsubogo, "Hydroelastic Response Characteristics of a Pontoon Type VLFS in Waves", *J. of Soc. Nav. Archit. Japan*, Vol 183, pp.211-218, 1998

PROCEEDINGS OF THE THIRD INTERNATIONAL WORKSHOP ON VERY LARGE FLOATING STRUCTURES
(VLFS '99), VOL. I, EDS. R.C. ERTEKIN & J.W. KIM, 22-24 SEPTEMBER 1999, HONOLULU, HAWAII, USA

MOB STABILITY ASSESSMENT*

Biswajit Bandyopadhyay and Balji Menon
American Bureau of Shipping*

ABSTRACT

The difficulty in the stability assessment of a novel multiple connected floating structure such as the Mobile Offshore Base (MOB) arises out of the inherent complex motion responses of one module in relation to its adjacent one(s) as well as with respect to the whole structure. It is therefore imperative that MOB stability evaluation be performed through analysis of the motion responses of the connected structure under the environmental conditions that are determined by the MOB operational requirements. This paper outlines the analyses that will be required for the classification of the novel structure with American Bureau of Shipping, as currently envisaged. This paper is not aimed at providing complete stability analysis procedures, rather a glimpse of what has been accomplished thus far from the perspective of Draft MOB Classification Guide development. It is expected that new findings will unfold as the analysis effort continues during the next phase of Guide development.

1 INTRODUCTION

Various multiple module concepts for the MOB are under consideration of U.S. Navy. The stability assessment of the concepts, which involve mechanical connections (through connectors) between adjacent modules, poses new challenges that should be addressed from the perspective of motion response dynamics of the connected structures.

The stability of a single MOB module (referred to as SBU in MOB literature) as well as of a connected MOB should address not only its capsize but also keeping its motions within the limits that are determined by the MOB operational requirements (Table 1). The static stability of one SBU can be evaluated by the conventional quasi-static method through proven commercial computer software. The motion response based stability assessment of one SBU and of the connected MOB is best achieved through first identifying the critical responses in frequency domain by examining the response amplitude operators (RAO). These critical cases are then analyzed in time domain through scrutiny of the behavior of the motion trajectories in time series as well as phase plane plots.

The static stability assessment of one SBU is the basic check for the inherent stability of the floating structure in calm water without which response based stability analysis is extraneous. The motion response based stability assessment of SBU/MOB provides a measure of its capability to meet the MOB operational motion limits (Table 1) when the deployed MOB configuration includes one or more SBUs. It also evaluates the danger of transient capsize under severe environmental conditions.

The motion response based stability assessment of the connected MOB necessitates evaluation of relative motions (translational and angular displacements, velocities and accelerations) between the adjacent SBUs. This exercise is necessary to check if the relative motions exceed the MOB operational limits outlined in Table 1 (details are provided in ABS Draft MOB Classification Guide [1]). These limits pertain to Sea State 7 with head and bow seas and with MOB speed between 0 and 15 knots. The operational limits

* The views expressed in this paper are those of the authors and not necessarily those of American Bureau of Shipping.

* 16855 Northchase Drive, Houston, TX 77060, USA. E-Mail: bbandyopadhyay@eagle.org

are given in terms of significant single amplitude values.

The inherent linearity assumption in the frequency domain analysis forbids appropriate predictions of large motions. Nevertheless, the analysis provides a prudent guidelines for detecting the critical motion RAOs that warrant in-depth analysis for revealing the possible danger of loss of stability due to large motions. The responses of the structure are then parametrically analyzed for these critical cases in time domain considering various combinations of environmental and vessel parameters. The responses in time domain can be effectively summarized in the form of time series and phase plane plots of motion trajectories. Judicious scrutiny reveals the stability or instability of motion responses. A divergent trajectory in the phase plane indicates instability.

MOB Motion or Displacement	Limit
Pitch motions (depending on operations)	1°-2°
Roll motions (depending on operations)	2°-4°
Vertical velocity at touchdown spots	2.1 m/s
Runway surface discontinuity for landing	1.5°
Vertical acceleration at touchdown spots	0.5 g
Runway surface waviness tolerance (height/distance)	1/100

Table 1 : MOB operational requirements [1]

2 FORMULATION OF THE PROBLEM

The problem formulation is based on the respective analysis software as mentioned in Section 3.3. The theoretical backgrounds are not reproduced in this paper to keep its length within the limit. For background material, User's Manuals of the respective software may be referred to.

3 APPLICATION

This section describes the details and limitations of the stability analyses performed to generate a standard for the stability assessment procedures for ABS classification of MOB.

3.1 Scope

The scope of the analyses was limited to the capability of the analysis software, as well as to the simplifications due to the lack of pertinent data, required by the software, at this stage of concept development. These simplifications are briefly discussed in the respective sections that follow.

The principal aim of this paper is to demonstrate the procedure, as currently envisaged, for MOB stability assessment with regard to its classification with ABS. The validity of the motion response results and consequently the stability assessments, presented in the following sections, should therefore be interpreted qualitatively within the aforementioned scope.

3.2 Case study

For brevity, the cases, briefly described in this section, are intended to exemplify the procedure that MOB designers will be expected to follow for ABS certification of its stability, as currently envisioned. The analysis results are presented for the cases that have been worked on so far.

The cases primarily pertain to two stability analysis categories namely the static and the motion response based. Intact and damaged cases were analyzed for static stability of one SBU. Only intact cases for one SBU as well as connected MOB have been analyzed so far for motion response based stability.

The selection of model and the computer software mentioned hereafter does not in any way express preference and/or prejudice from American Bureau of Shipping (ABS).

3.3 Software used

The commercial computer software GHS version 3.0 for Windows, marketed by Created Systems Inc., was used to perform the static stability analysis of an SBU. A quasi-static approach was adopted for the analysis.

The motion responses of one SBU as well as of the connected MOB were obtained by using AQWA suite of programs of W.S. Atkins, Inc., U.K. ABS has proprietary licenses for the above mentioned software that have pre- and post-processors integrated into the system.

3.4 SBU/MOB model

The SBU/MOB model used in this study is the concept developed by McDermott Technology, Inc. (McMOB). The selection was based on the availability of sufficient model details for ABS to start global response and stability analyses. McMOB model consists of five (5) identical semisubmersibles modules (McSBU) connected through compliant mechanical connectors. The principal particulars of module (McSBU) are given in Table 2 and its AQWA model is shown in Figure 1.

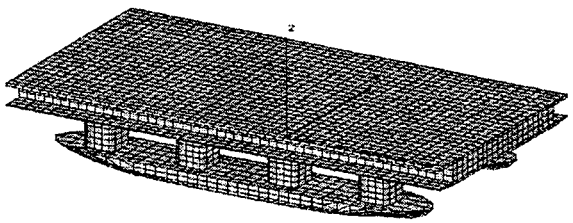

Figure 1: AQWA model of McSBU

Table 2: Principal particulars of McSBU

Upper hull dimensions (meter)	280x 150x 24.6
Lower hull dimensions (meter)	260 x 38 x 6
Column dimensions (meter)	21 x 21
Operating draft (meter)	39.0
Displacement (tonnes)	337,000
LCG from midship (meter)	0
TCG from centerline (meter)	0
VCG above base (meter)	26.87
Trans. metacenter from baseline (meter)	40.1
Long. metacenter from midship (meter)	66.0
Roll radius of gyration (meter)	55.8
Pitch radius of gyration (meter)	93.2
Yaw radius of gyration (meter)	97.1

3.5 Analyses procedures

The static stability of McSBU was evaluated through GHS. The righting arms in calm water and sinusoid waves are calculated through quasi-static analysis of the restoration forces and moments arising due to balance/imbalance between gravitational and buoyancy forces and moments. The buoyancy effects in waves are evaluated for the immersed hull for different positions of the wave crest with respect to the structure center of gravity.

The motion responses to regular waves are evaluated using the AQWA suite of programs. The AWQA LINE module was first used to generate the hydrodynamic (added mass and damping) coefficients and the responses (motion, velocity and acceleration) in all six modes of motions per unit amplitude of wave (RAO).

The RAOs are then scrutinized to identify the wave frequency range that result in high responses. Time domain simulations through the AQWA NAUT module were then obtained for the above mentioned regular wave frequencies (periods), and for wave amplitudes that SBU/MOB will encounter during its deployment at four selected sites around the globe and while in transit between the sites (for SBU only).

The responses were then analyzed using the AQWA graphical post processor AGS in the form of time series as well as phase plane plots in relevant modes of motions. The time series graphs included plots of position of the center of gravity (CG), the velocity and the acceleration at the CG. For one McSBU, the phase plane plots included the graphs of the position of and velocity at the center of gravity as time progresses. For connected MOB, the phase plane plots depict the positions of CG of two adjacent structures relative to one another, in addition to the aforesaid McSBU phase plane plots for each structure.

The behavior of the motion trajectories in the aforesaid plots as time progresses was scrutinized to assess the stability of motion responses. A divergent or unbounded trajectory in the phase plane indicates instability that may lead to capsize whereas a convergent trajectory demonstrates decay of motions and thereby assures stability. A bounded but non-convergent trajectory does not warrant any danger of capsize but may represent instability from the perspective of MOB operational motion limits as outlined in Table 1. The phase plane plots are intended to help the analysts to judge stability as described above.

4 RESULTS

For brevity, the analysis results are presented for the draft and loading condition that pertain to the fully loaded operating condition of an intact McSBU and McMOB.

4.1 Static Intact Stability

The critical inclination axis, about which the righting capability of a floating structure is the least, was found to be the pure roll axis, i.e. the fore and aft longitudinal axis of McSBU [2] that has length to breadth ratio of 2:1. However, if the said ratio reduces, the critical axis may be different from the pure roll axis.

The static stability characteristics of an intact SBU in calm water are summarized in Figure 2 in the form of its righting arm (GZ). The wind inclining moment shown in the plot corresponds to a steady wind velocity of 70 knots measured at a height of 10 meters above the calm waterline. It is evident from Figure 2 that McSBU has sufficient intact static stability in calm water under the specified loading and wind conditions. The selected wind speed of 70 knots corresponds to Hurricane condition (Beaufort sea 12) of Sea State 9. The wind forces and moments were in accordance with the results of wind tunnel tests at NSWC/CD.

The righting arm calculations take into account the additional buoyancy due to partial immersion of the completely watertight boxed-deck atop in inclined conditions. It is realized that complete watertight integrity for very large means of closure around the boxed-deck for loading/unloading of military vehicles and supplies into/from MOB, may not be achievable in practice. Reference [2] provides supporting documentation for this consideration.

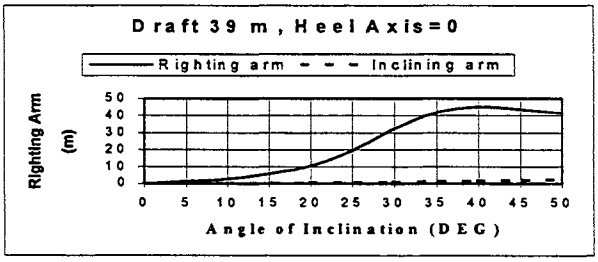

Figure 2: McSBU intact righting arm in calm water

Figure 3 depicts the McSBU static stability characteristics in regular sinusoid waves for different positions of the wave crest with respect to the center of gravity of McSBU. The selection of wave height and period, wind speed pertains to the worst environmental condition amongst what McSBU is likely to encounter at its four designated deployment sites around the globe and during its transit between sites.

It is evident from Figure 3 that based on the considerations stated above, the righting capability of McSBU far exceeds the external effects, and therefore, the stability of McSBU against capsize is not warranted under the environmental conditions considered.

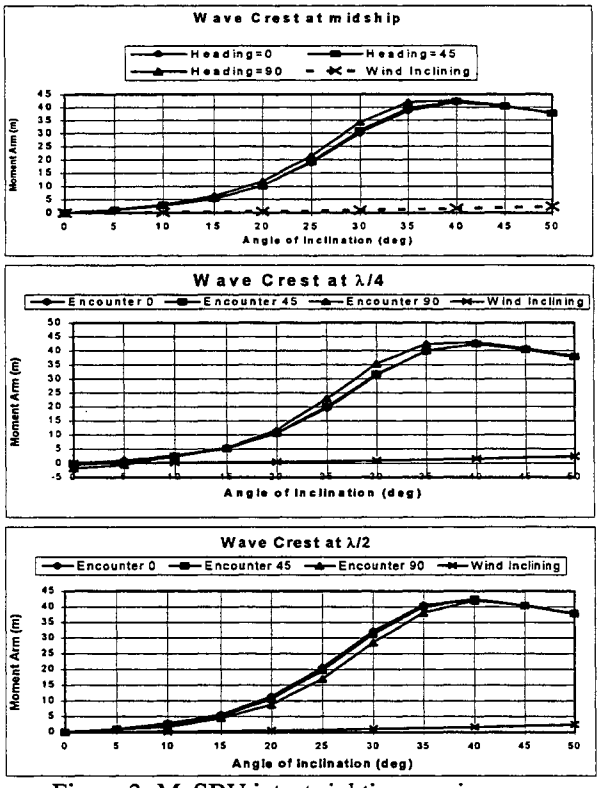

Figure 3: McSBU intact righting arm in waves

4.2 Static Damage Stability

The static damage stability assessments were performed with various damage scenarios. As before, the draft loading conditions pertain to the intact SBU fully loaded operational case. The results for only one selected case with complete loss of one corner column are presented in Figure 4 and Figure 5.

4.3 Motion Response Based Intact Stability

The selection of the wave parameters for motion response analyses is based on the identification of the frequencies that result in high response of the floating structure.

First AQWA LINE run was performed for a range of wave frequencies and headings to produce RAOs for motion, velocity and acceleration. For conciseness, only the motion RAOs are presented in Section 4.3.1.

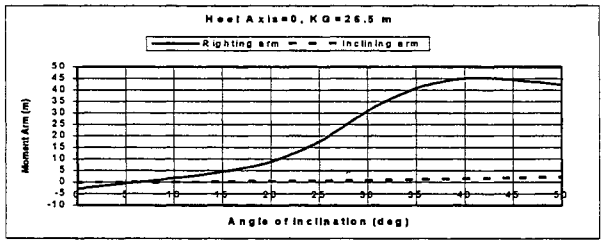

Figure 4: McSBU damage righting arm in calm water

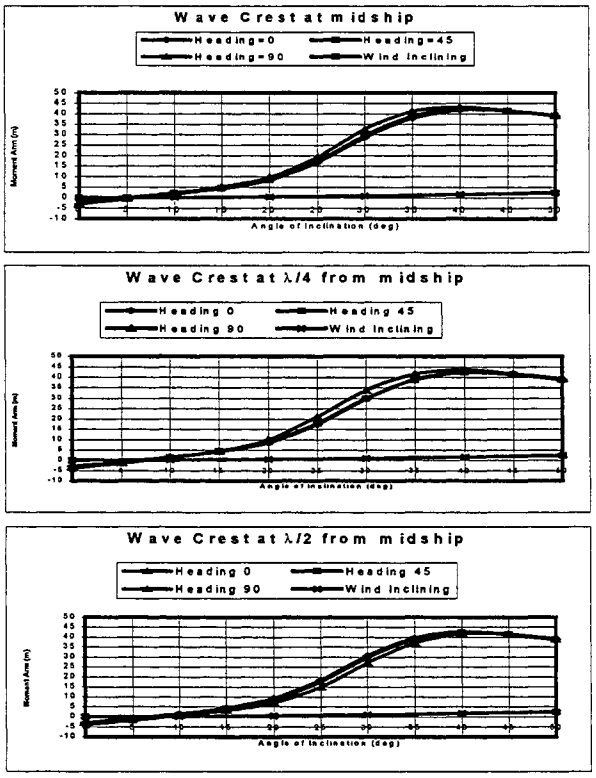

Figure 5: McSBU damage righting arm in regular sinusoid waves

Scrutiny of these motion-RAOs determines the range of wave frequencies and headings that are likely to produce large McSBU responses. Time domain simulations of motion responses for the aforesaid range were then performed through AQWA NAUT module. The simulation results were then analyzed for examining stability of McSBU motion responses. The results of these analyses are presented in Section 4.3.2

The motion response based stability assessment of a single McSBU was followed by similar analyses for a connected MOB. As mentioned earlier, these analyses are primarily aimed at stability of the motions of one

SBU relative to its adjacent one(s). The results of these analyses for two hinged McSBUs are presented in Section 4.3.3

The results in the following sections are based on the simplifications listed below:

- No viscous effects in the form of hull drag, viscous damping effects were considered. AQWA suite of programs can account for hull drag in the form of current drag with zero current velocity. But it requires current force coefficients in the form of force per unit velocity squared in the selected directions. These coefficients were not available.
- Current or wind effects are not considered. The time domain simulation module AQWA NAUT requires relevant coefficients in the aforementioned form. These coefficients were not available.
- No thruster forces and moments were considered because of lack of information.

4.3.1 McSBU motion RAO

The AQWA model of McSBU is shown in Figure 1. The x-axis is aligned with the fore and aft direction, the y-axis represents the transverse direction, and the z-axis is directed vertically upwards. The axis system follows the right hand rule.

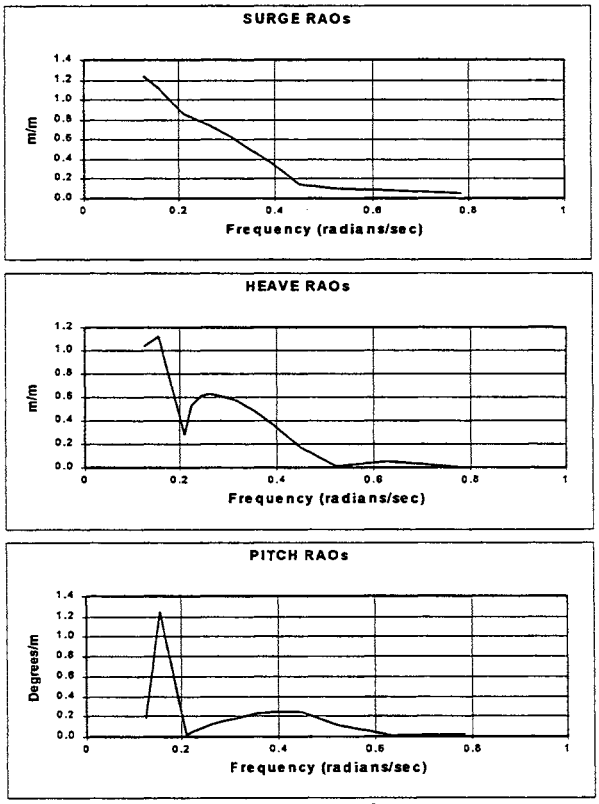

Figure 6: McSBU RAO for 0° Wave Heading

Figure 6 - Figure 8 depict the significant RAOs in different modes of motions for wave heading of 0°, 45° and 90°. These figures illustrate the need of further motion response analyses in large waves in time domain for wave frequencies ranging from 0.5 radian/sec and smaller that translate to wave periods of 12.5 seconds and higher.

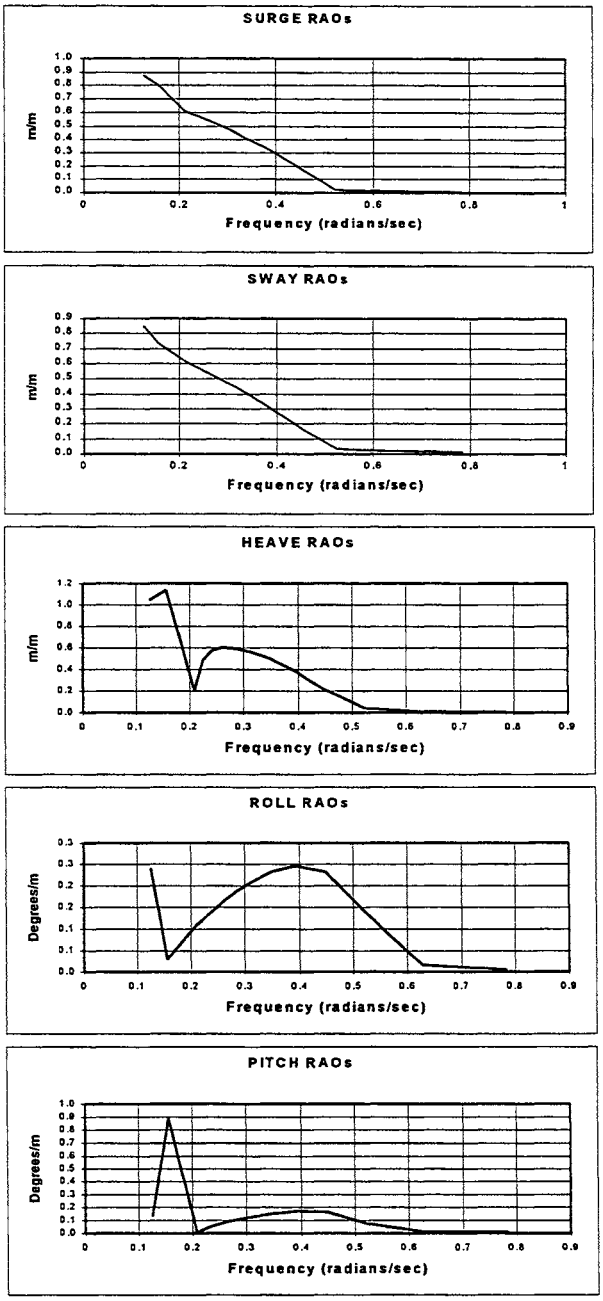

Figure 7: McSBU RAO for 45° Wave Heading

4.3.2 McSBU motion stability

The time domain simulation results for wave period of 40 seconds, wave amplitude of 7 meters, and wave headings of 0, 30, 60 and 90 degrees are presented in the forms of time series and phase plane plots in Figure

9through Figure 12. To limit computer time and also for initial insight, simulation time was limited to 450 seconds. Only selected graphs are accommodated for illustrations. The purpose of this exemplification is to explain the methodology and not to restrict the analysts from performing further studies. The results should be interpreted qualitatively because of the simplification mentioned in Section 4.3.

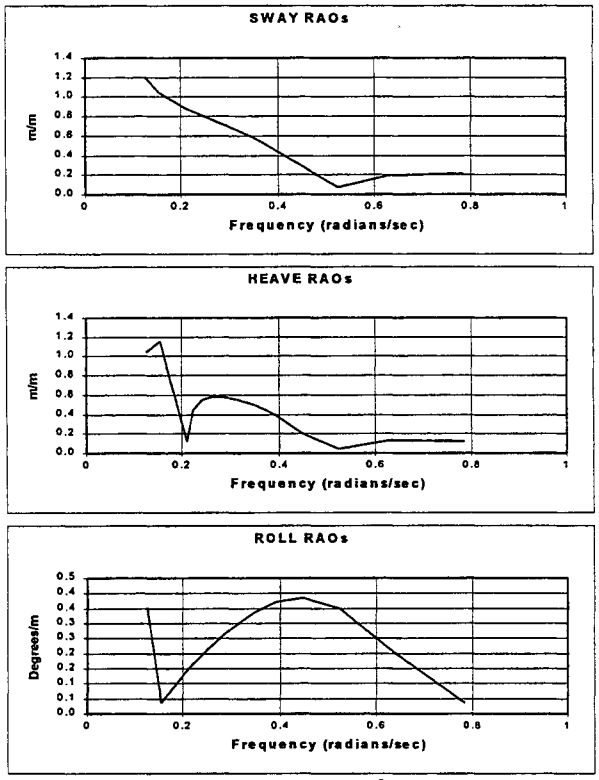

Figure 8: McSBU RAO for 90° Wave Heading

The following observations are pertinent to the stability of the structure:

- The time series plot of the position of the center of gravity in x-direction in Figure 9 depicts a steady drift over time. This drift may be attributed to the neglect of hull drag forces and thruster contributions. This drift does not warrant any danger to McSBU stability.
- The time series plots of the heave velocity and acceleration display that although these do not warrant instability, the peak vertical velocity and acceleration in Figure 9 exceed MOB operational limits (Table 1). Therefore, this may be interpreted as instability with regard to the specific MOB operations as detailed in Draft MOB Guide. [1]
- The time series and the phase plane (angle versus velocity) plots of the pitch motion at the center of gravity in Figure 9 - Figure 12 depict stable bounded motions. However, the peak pitch motion exceeds the MOB operational limits (Table 1). Therefore, this may be interpreted as instability with regard to the specific MOB operations as detailed in Draft MOB Guide. [1]
- The time series and the phase plane plots depict bounded roll motions in the case of wave heading of 30 and 90 degrees. These responses indicate no danger of capsize and show operational stability. However, the phase plane plot for the wave heading of 60 degrees depicts sudden divergence of trajectory within the simulation time and signals instability due to large roll motions. It should be noted that over longer simulation time, the phase plane trajectory may reveal bounded behavior.

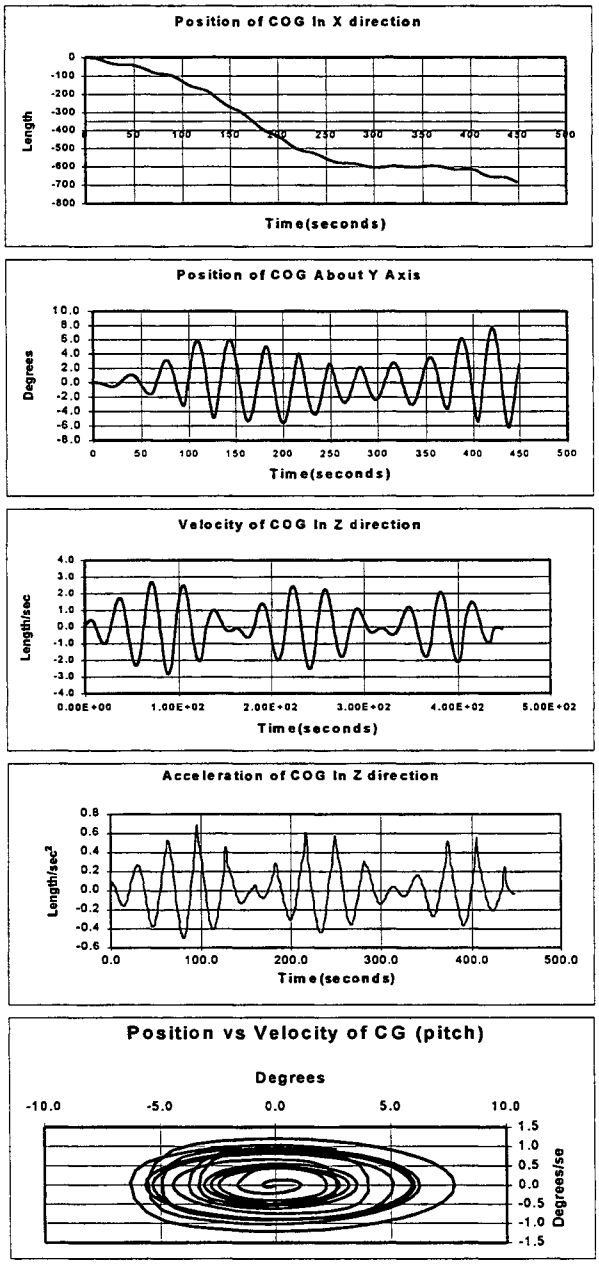

Figure 9: McSBU responses for 0° wave heading

The following inferences are drawn on the basis of the aforementioned observations:

- The circular/elliptical trajectories in phase plane plots of Figure 9 - Figure 12 indicate that McBSU responses generally remained bounded over time in the modes of motions depicted.
- A bounded trajectory in phase plane negates the possibility of capsize due to loss of stability. However, it does not necessarily signify response based stability from the perspective of MOB operational limts outlined in Table 1.
- Scrutiny of the trajectories in time series and phase plane plots reveals a better insight into the motion response based stability of floating structures.

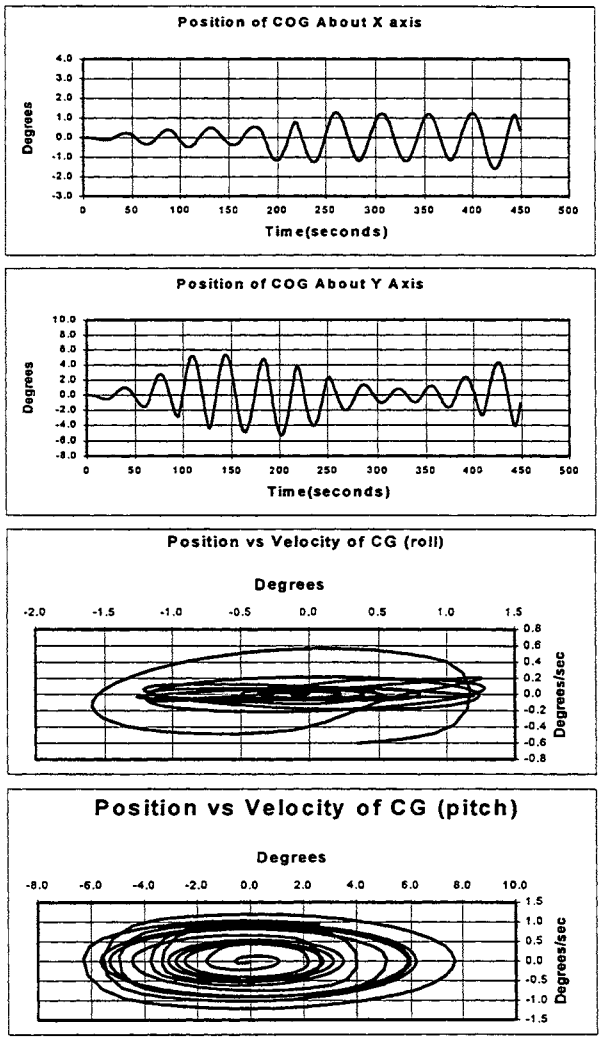

Figure 10: McSBU responses for 30° wave heading

4.3.3 Connected McMOB motion stability

To gain a first understanding of the stability of relative motion responses and also to limit computer time for simulations, the connected McMOB stability was performed for two hinged McSBUs. The model is displayed in Figure 13.

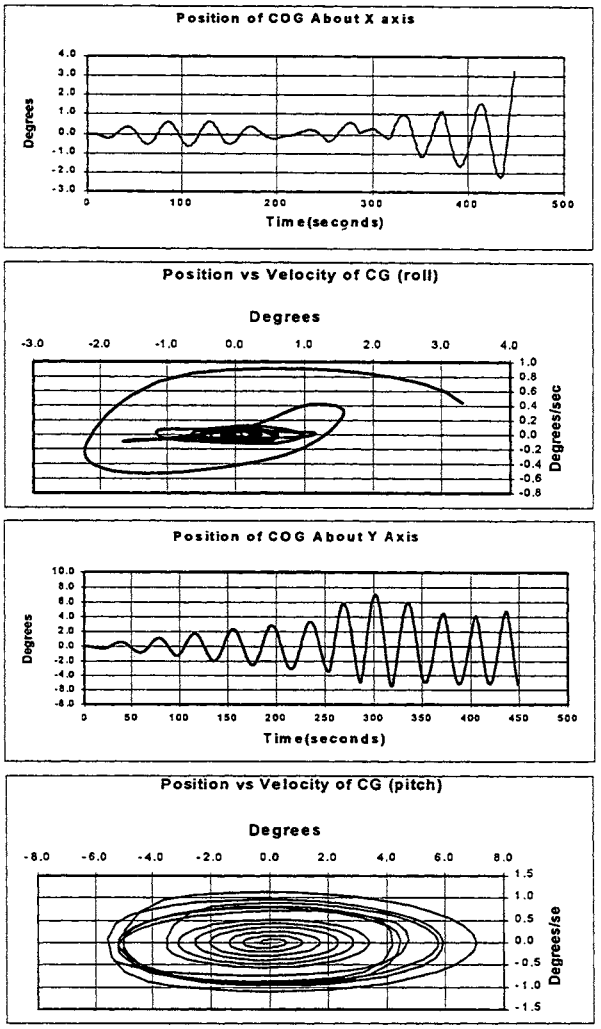

Figure 11: McSBU responses for 60° wave heading

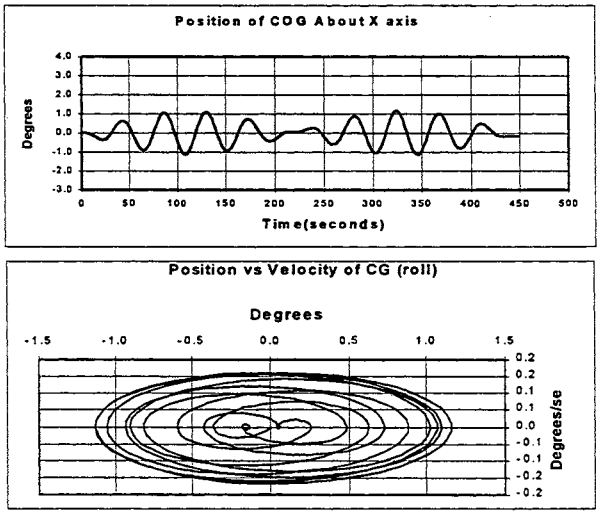

Figure 12: McSBU responses for 90° wave heading

In addition to the time series and phase plane plots of the responses of each McSBU similar to those provided in Section 4.3.2, significant responses of one McSBU relative to the other are also included for the stability assessment of relative motion responses. The aforesaid plots are presented in Figure 14 - Figure 16. For brevity, discussions will be focussed on the relative motions between the McSBUs.

For wave heading of 0 degree, the peak amplitude of heave oscillation (about 16 meters) of each McSBU in the connected configuration, in Figure 14, is quite similar to that of an individual module (Not Shown). The plots of relative vertical oscillations of CG of two McSBUs in Figure 14 reveal that for 0 degree wave heading, although the relative positions remain bounded, the peak difference (approximately 20 meter in the time series plot) over time may not be conducive to MOB operational limits. The phase plane plots of pitch motions of each module show bounded motions. However, the time series plot of the relative pitch motion reveals that at around 200 seconds, the motion peaks at approximately 8 degrees. Such high relative pitch warrants MOB operational stability.

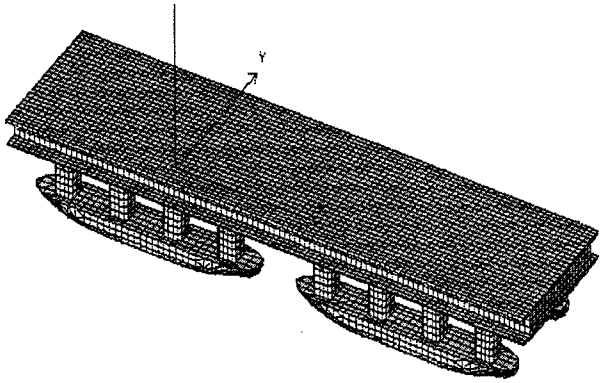

Figure 13: Connected (hinged) McMOB model

For 60 degrees wave heading, the phase plane plots depict that the pitch response of the second McSBU remained bounded, but that of the first shows signs of divergence of trajectory. Longer time simulations are required to verify if this divergence leads to unbounded motions and finally to instability. The time series plot of relative pitch motions clearly reflects the aforesaid divergence and so does the phase plane plot through the expansion along its diagonal.

The phase plane plots in roll for each McSBU in the case of 90 degree wave heading depict completely bounded motions with a maximum roll angle of about 1.1 degree that ascertains roll stability within operational limits. The straight-line phase plane plot of the relative roll is indicative of perfect agreement between the roll motions of the two hinged McSBUs.

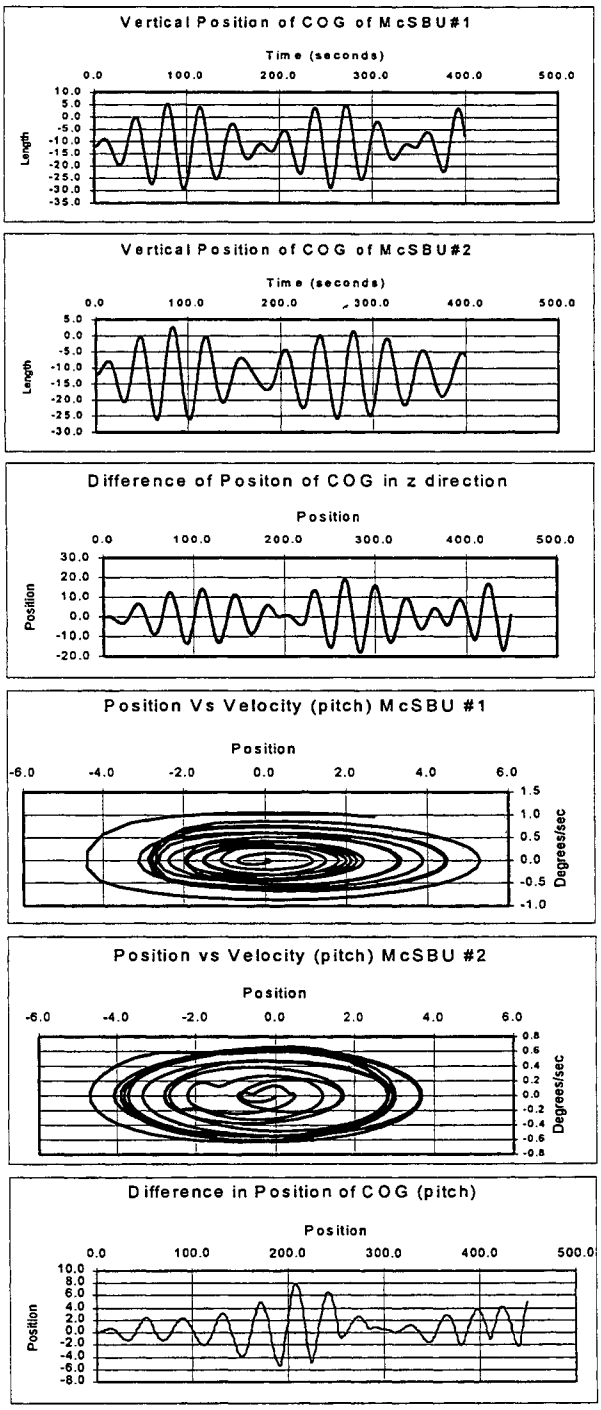

Figure 14: McMOB responses for 0° heading

5 CONCLUSION

The illustrations presented in this paper establishes the importance of motion response based stability analyses of a multi module connected floating structure such as MOB, over and above the conventional static stability assessments. The usefulness of phase plane plots, in addition to the time series plots, in revealing

the latent problem of motion dynamics, is emphasized. The exemplification forms the groundwork for the procedure to be adopted for ABS classification of MOB stability.

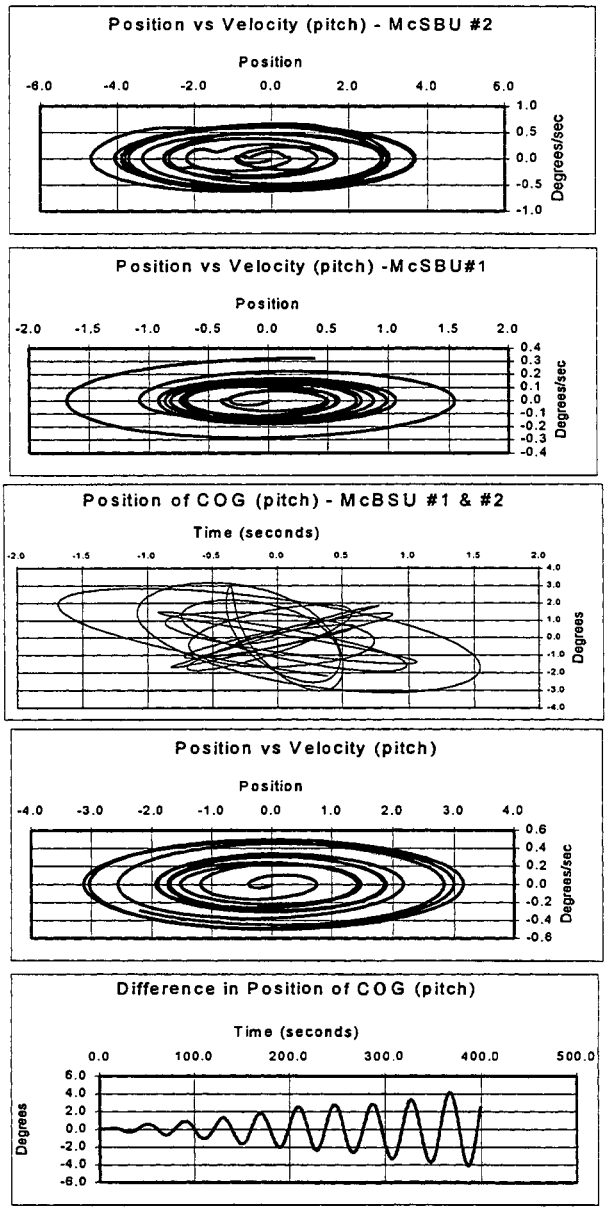

Figure 15: McMOB responses for 60° heading

ACKNOWLEDGEMENT

The authors wish to thank the Office of Naval Research for sponsoring the project the objective of which is the development of a MOB Classification Guide. Oversight of this project is provided by the MOB Standard & Criteria Working Group under the chairmanship of Dr. Theodore Shugar of Naval Facilities Engineering Service Center, Port Hueneme, California.

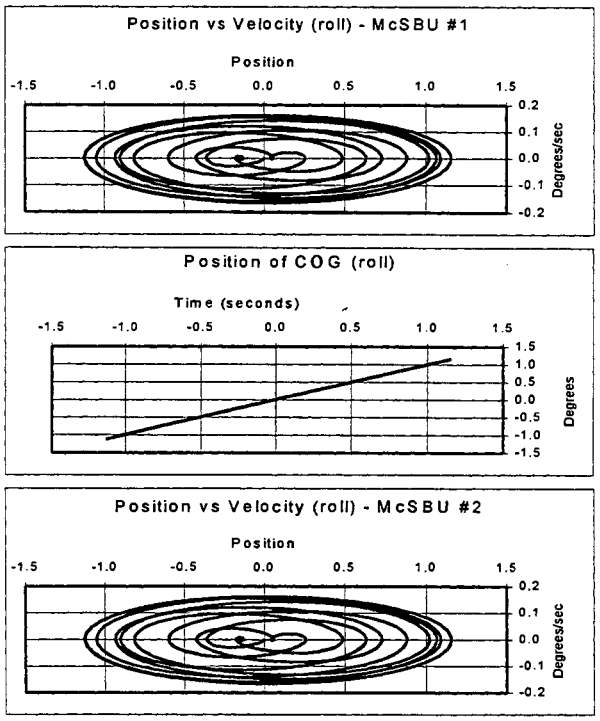

Figure 16: McMOB responses for 90° wave heading

Acknowledgement is due to Mr. Maciej Wdziekonski, a student-trainee from University of Michigan, for judiciously creating the AQWA model of McSBU, for performing AQWA runs, and for the active participation in the preparation of this manuscript. The authors also appreciate the dedicated effort of Ms. Claire Smith and Mr. Corey Brown, student-trainees from Memorial University of Newfoundland, Canada, for creating GHS models and performing static stability analyses of McSBU using the software.

REFERENCES

[1] Basu, R. et al, "Draft MOB Classification Guide", American Bureau of Shipping September, 1999.

[2] Basu, R. et al, "Commentary to Draft MOB Classification Guide", American Bureau of Shipping September, 1999.

[3] "Mobile Offshore Base Preliminary Drawings and Trim and Stability Booklet", McDermott Technology, Inc., Revision 1, October 1997.

[4] "User's manual of General Hydrostatics (GHS)", Creative Systems, Inc., February, 1997.

[5] "AQWA User's Manuals", WS Atkins Engineering Software, UK, 1995.

[6] "AQWA Reference Manual", WS Atkins Engineering Software, UK, 1997.

PROCEEDINGS OF THE THIRD INTERNATIONAL WORKSHOP ON VERY LARGE FLOATING STRUCTURES
(VLFS '99), VOL. I, EDS. R.C. ERTEKIN & J.W. KIM, 22-24 SEPTEMBER 1999, HONOLULU, HAWAII, USA

SIMULATION AS A TOOL FOR CARGO RATE DETERMINATION

M. Ken Cybulsky[1] and Richard Currie[2]
McDermott Technology, Inc.

ABSTRACT

One of the major mission requirements for a mobile offshore base (MOB) is the transfer of cargo to and from auxiliary ships on the high seas. In fact, given the common wisdom that more than 90% of all cargo required for any given military deployment will arrive by ship, this transfer is arguably the most important operational parameter for measuring mission effectiveness.

The usual method for determining cargo transfer is to assume that if the maximum relative movements for a given environmental condition exceed transfer equipment limits, then no cargo transfer will occur at those conditions. This is a very conservative assumption and may result in ignoring significant "windows of opportunity" when movements are well below the maximums and below the equipment limits. There is no analytically robust understanding of degraded operations. The best way to account for these opportunities in rate estimation is to use a detailed discrete-event simulation model of the transfer process and run analyses of a ship unloading or loading sequence against predicted random wave excitations, gathering statistics on rates of transfer against the random wave motions.

This paper describes such a model that has been developed to act as an evaluation tool for various designs of MOB cargo transfer systems. It integrates information from designers of cargo transfer systems, designs of MOB and auxiliary ship vessels, and environmental models of waves and motions in a system that models the likely cargo movement activities of an operational MOB. It permits a more realistic estimate of cargo transfer rates as a function of auxiliary ship type, wave environment, and heading. It also is useful as a tool to identify weaknesses in a given design and to suggest areas where redesign can have the largest overall impact on mission.

1. 1562 Beeson St., Alliance, OH 44601; ken.cybulsky@mcdermott.com
2. Rt. 726, Mt. Athos Rd., Lynchburg, VA 24506; richard.l.currie@mcdermott.com

1. INTRODUCTION

Cargo transfer to and from an MOB presents a unique set of circumstances when contrasted with two other types of sea cargo handling commonly used in current practice:

- At-dock loading and unloading
- Underway replenishment

Compared to at-dock transfers, MOB handling is characterized by substantial environmental forces (wave-induced motions) on the supply vessel. This may result in large relative displacements and velocities. On the other hand, compared to underway replenishment, MOB handling provides one platform (the MOB itself) that is very stable against these forces, while the supply vessel continues to be strongly affected by environmental forces. Methods commonly used to estimate or determine transfer rates for these two conditions may therefore not be directly applicable to the MOB situation.

Figure 1 shows a sketch of the cargo transfer environment on the MOB. At sea with a container ship berthed alongside the MOB, each vessel, including all single-base units (SBUs) of the MOB and the ship, are affected by random wave motions. Assuming that the vessels are rigid bodies, we can characterize their motions in the six degrees of freedom about their centers of gravity.

Our primary concern for cargo transfer is the relative motion between the crane hooks and the top of the container being moved at critical times during the movement process. The relative motion at each point of time in the transfer process depends on the location of the container being moved, the relative motions of the vessels, and their physical relationship to each other (shown in Figure 1).

A significant portion of the Office of Naval Research's (ONR's) MOB research budget to date has been devoted to developing better methods to accurately predict the wave-induced motions of vessels the size of an MOB and ships berthed alongside under different ocean conditions. These research programs have provided the basic wave-induced motion data needed as input to a new analytical tool to analyze the

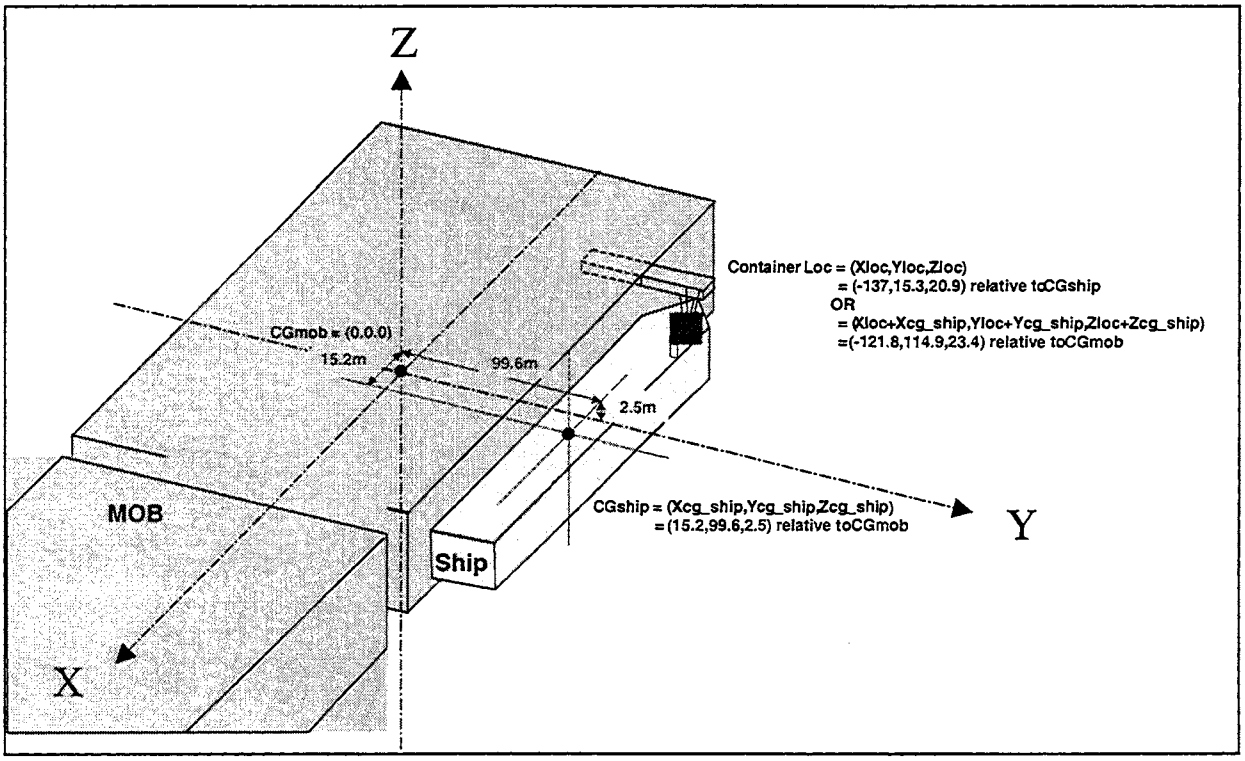

Figure 1: Container cargo transfer environment of Mobile Offshore Base

MOB cargo transfer process — **discrete-event simulation**.

There are two types of sea-based cargo that play an important role in military sustainment — lift on/lift off (Lo/Lo) and roll on/roll off (Ro/Ro). Both types of cargo have been analyzed in this work, but for purposes of clarity, only the Lo/Lo containerized cargo portion of the work is reported here

2. MODEL DESIGN

A discrete-event simulation model is a model of discrete events occurring in time. It accounts for resource utilization and queue buildups whenever an event is scheduled that requires a specific resource that is busy. This modeling approach fits perfectly in a container transfer situation, where the primary resources are the cranes and the entities that trigger the events are the containers. The key information to drive the simulation is an ordered entity arrival list. In this case, that is simply a listing of all of the containers on the ship being modeled, sorted in the order that they are to be unloaded, and identified with exact location on the ship.

The model described here includes only one crane, based on the assumption that the overall MOB transfer rate will be a multiple of the single-crane transfer times number of cranes incorporated in the design. This assumes that each crane will operate independently of the others and that each crane's cargo area will not overlap the others.

2.1 Container Transfer Steps

The container transfer model breaks the process down into nine specific steps beginning right after the previous container is released:

1. Lift crane to travel position
2. Move to target
3. Focus on target
4. Latch
5. Lift to travel position
6. Move to unload point
7. Drop to MOB deck
8. Unlatch
9. Store container on MOB

These steps are shown in Figure 2. The simulation proceeds by stepping through these steps for each container, in turn, calculating the time to execute the step and pausing as required by conditions (see Section 2.2). It is important to observe that after Step 8 is complete, the crane can proceed to start Step 1 for the next container in parallel with the storage of the just unloaded box.

Steps 3 and 5 contain additional substeps whenever the container is located below deck in cell guides. In

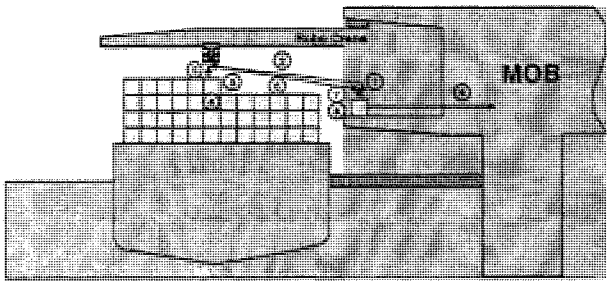

Figure 2: Process steps for container model

these cases, Step 3 includes additional substeps to insert the spreader bar into the cell guide and to lower the spreader bar in to the cell guide; Step 5 also includes a substep to lift the container to the top of the cell guide.

The simulated process time for each of these steps is calculated by the model based on the characteristics of the crane design and the physical distances traveled. For instance, the times for Steps, 1, 2, 5, 6, and 7 are based on the distance moved divided by the crane's travel speed in that direction. All of these design factors are user-changeable inputs to the model, allowing for analysis of alternative crane designs or alternative ship configurations.

2.2 Program Logic

The key feature that makes the MOB cargo transfer model unique compared to typical cargo transfer simulation models is the inclusion of wave-induced motion logic. By reading from a file of vessel motions over time (produced using state-of-the-art engineering codes such as WAMIT, HIPAN, MOSES, and ABAQUS), we can translate the vessel motions into relative motions at the point in space and time where and when the cargo transfer process step is occurring. For convenience, we produce motion information at 1-second intervals in this work.

2.2.1 Gate Logic

Key cargo transfer process steps, such as focusing on the target, inserting the spreader bar into the cell guide, and lowering and lifting in the cell guide are motion dependent — they take more time to perform as the relative motion between the ship and the MOB increases. These process times are determined based on user-input crane characteristics.

The most important characteristic of these steps, however, is that they may also become nonperformable when the relative motions reach a limiting value or "gate." The fundamental premise of our approach is that even though a gate is hit during the cargo transfer process, this does not mean that cargo transfer must be stopped until the sea state subsides. Our assumption is that the process step need only be delayed until the limiting condition has passed and that cargo transfer may proceed from that point.

In actual operation, such a strategy would involve the operator making a judgement based on current relative motions and observations of sea conditions that a "window of opportunity" will exist for the time required to proceed through the next step in cargo movement. In the model, we have elected to model "perfect foresight" — the step does not start unless the window is, in fact, there. This represents an upper bound on the opportunistic cargo transfer rate.

2.2.2 "Perfect Foresight" Implementation

Because the model is a discrete-event simulation with a number of active entities moving in parallel, we cannot simply jump ahead in time to find a string of consecutive seconds where the relative motions fall within the gate limits. The simulation model instead delays each entity currently at a gate delay one second at a time, checking the appropriate motion characteristic against the gate value during that second. If the value falls within the gate limit, the remaining time for that operation is decremented by one second and the process repeated until the remaining time reaches zero. If the value falls outside the gate limit, the remaining time is reset to the originally calculated process time and process is initiated again. In effect, the program finds a "valley" in the graph of motion over time where the motion characteristic being followed does not exceed the gate for a period of time equal to the calculated operation time.

Some gates are multiple. One example is the focus-on-target (Step 3) operation, where there are gates for both relative velocity and tilt angle. These are handled in the same way; only the check is simply on multiple parameters at each time interval.

When a gate is exceeded, the program records a delay time and an identification of the source of the delay (the gate exceeded). This permits statistical evaluation of the nature of environmental effects on transfer rates and can identify which steps in the cargo handling operation offer the most potential for performance improvement.

The gate values as well as the crane operation times are inputs from the user to compare alternative equipment, operating philosophies, personnel policies, etc.

2.3 Data Interfaces

Figure 3 summarizes the general organization of the MOB cargo transfer modules.

Four input files describe the auxiliary ship, its cargo load, the MOB cargo-handling equipment, and the motions of the MOB and auxiliary ship at a given sea condition.

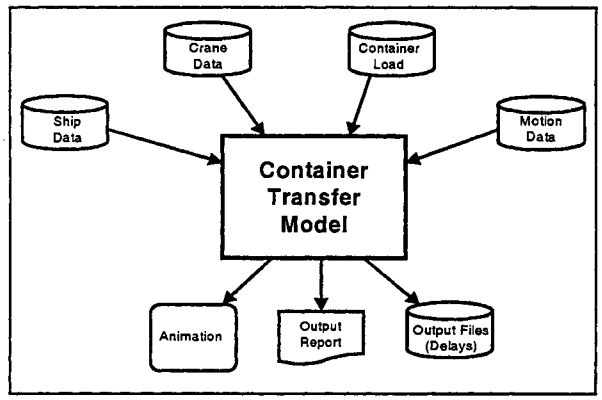

Figure 3: Data interfaces for cargo transfer model

Outputs of the model include:

- An animation of the ship unloading process
- A standard simulation output report that quantifies key scenario results such as the average transfer rate, delay times, and counts of the number of each type of delay encountered
- Output files that provide a detailed history of every delay encountered during the scenario run. (This last file may be used for in-depth postprocessing analysis.)

A sample output report is shown in Figure 4.

3. APPLICATION RESULTS

Although we are still in the process of soliciting feedback from industry experts on the validity of the cargo transfer model, we have performed some preliminary analyses that have produced some useful insights.

3.1 Container Transfer Rate over Time

Our initial runs of the model were focused on determining how long it would take for the model transfer rate to converge to a meaningful value. By plotting the transfer rate over time as each container completes its transfer cycle, we found that the container model converges to its final average value after about three holds, or about 396 containers.

Taking a closer look at the plots provided us with an in-depth understanding of the dynamics of transfer rate computations for container ships. Figure 5 provides such a look at the first 9 hours of a container model simulation run and shows how the overall model transfer rate relates to the individual container transfer rates.

The unloading sequence used for this simulation was to remove all containers at a given level or tier, starting with those closest to the MOB and proceeding across the beam. When all tiers in all cells of a given hatch are removed, the crane steps to the next hatch and starts over. The plot shows scallops caused by the differences in crane time required to collect and to retrieve containers as they are removed across the ship's deck.

The line labeled TRate is a plot of the individual container transfer rate computed as the inverse of the container's cycle time in hours. It includes the crane operation time and the time to transfer the container to the MOB hold. As can be seen, this rate is low for the first container in each new hold because the crane movement time to the new hold is also included in the first container's cycle time. Since container ships are unloaded from the dockside first, the closer containers in each tier are unloaded faster, producing the saw-tooth pattern in the Trate plot.

The top four tiers in our example container ship are above deck, showing identical transfer rate patterns for the individual containers across each tier. After reaching the first tier of containers below deck, the individual container transfer rates diminish with each tier removed. This is due to the fact that the containers below deck are in cell guides that require additional crane time to pass through as each new lower tier is uncovered.

The transfer rate that we are interested in our analysis is the overall transfer rate of the MOB, computed as the total number of containers stored divided by the simulation time in hours. Recall that the crane is free to begin picking up the next container once it delivers the current container to the MOB deck. Therefore, there is an overlap in the sequential container cycle times, which amplifies the model transfer rate above the individual container transfer rates. For the case shown, where we have assumed an average storage time on the MOB of 2 minutes and we are averaging a crane cycle time of approximately 2 minutes, the multiplier is near ((2+2)/2) = 2.

3.2 Automotion Compensation Versus Manual

One of the major features of the MOB cargo transfer model is the ability to model different crane designs through the crane data input file. Our initial analysis runs were to model the capabilities of a motion-compensated crane design compared to a manually operated crane. The motion-compensated crane design tested is the MOB RoboCrane designed by the National Institute of Standards and Technology (NIST) [3].

Our analysis to date has shown that the focus velocity gate is the most significant limiting factor for container transfer. The normal gate settings for the other gated operations, like the 2 degree focus angle gate and the 2 degree cell guide angle gates were never exceed in any of the analyses done to date. For the RoboCrane, sensors and computerized control mechanisms automatically focus on its target at relative speeds of up to 0.5 m/sec in any direction. Based on

MOB CONTAINER TRANSFER MODEL RESULTS
Wed Mar 10 12:05:30 1999

Run ended at time: 36755.0 Seconds - or - 10 Hrs 12 Minutes in Simulated time

TALLY VARIABLES

Identifier	Average	Half Width	Minimum	Maximum	Observations
10_Cycle Time	136.53	(Insuf)	69.000	219.33	262
20_Focus Time	19.928	(Insuf)	8.0000	35.000	266
21_Focus w Gates	19.928	(Insuf)	8.0000	35.000	266
30_CG Down Time	14.848	(Insuf)	3.0000	27.000	158
31_CG Down w Gate	14.848	(Insuf)	3.0000	27.000	158
40_Wait for Wave Peak	.05263	(Insuf)	.00000	2.0000	266
50_CG Up Time	12.848	(Insuf)	1.0000	25.000	158
51_CG Up w Gate	12.848	(Insuf)	1.0000	25.000	158

OUTPUT VARIABLES

Identifier	Value
01 Avg.Transfer Rate	25.563
02 Tot Minutes Delay	.23333
10 Focus Angle Gate	2.0000
11 Focus Angle Delays	.00000
12 Num Focus Ang Delay	.00000
20 Focus Velocity Gate	.50000
21 Min Focus Vel Delay	.00000
22 Num Focus Vel Delay	.00000
25 Total Focus Delays	.00000
30 CG Down Angle Gate	2.0000
31 Min Down Ang Delays	.00000
32 Num Down Ang Delays	.00000
40 Wave Peak Vel Gate	.25000
41 Min Wave Peak Delay	.23333
42 Num Wave Peak Delay	10.000
50 CG Up Angle Gate	2.0000
51 Min Up Angle Delays	.00000
52 Num Up Angle Delays	.00000

COUNTERS

Identifier	Count	Limit
Containers_Unloaded	262	Infinite

Simulation run time: 1.95 minutes.
Simulation run complete.

Figure 4: Sample container model output report

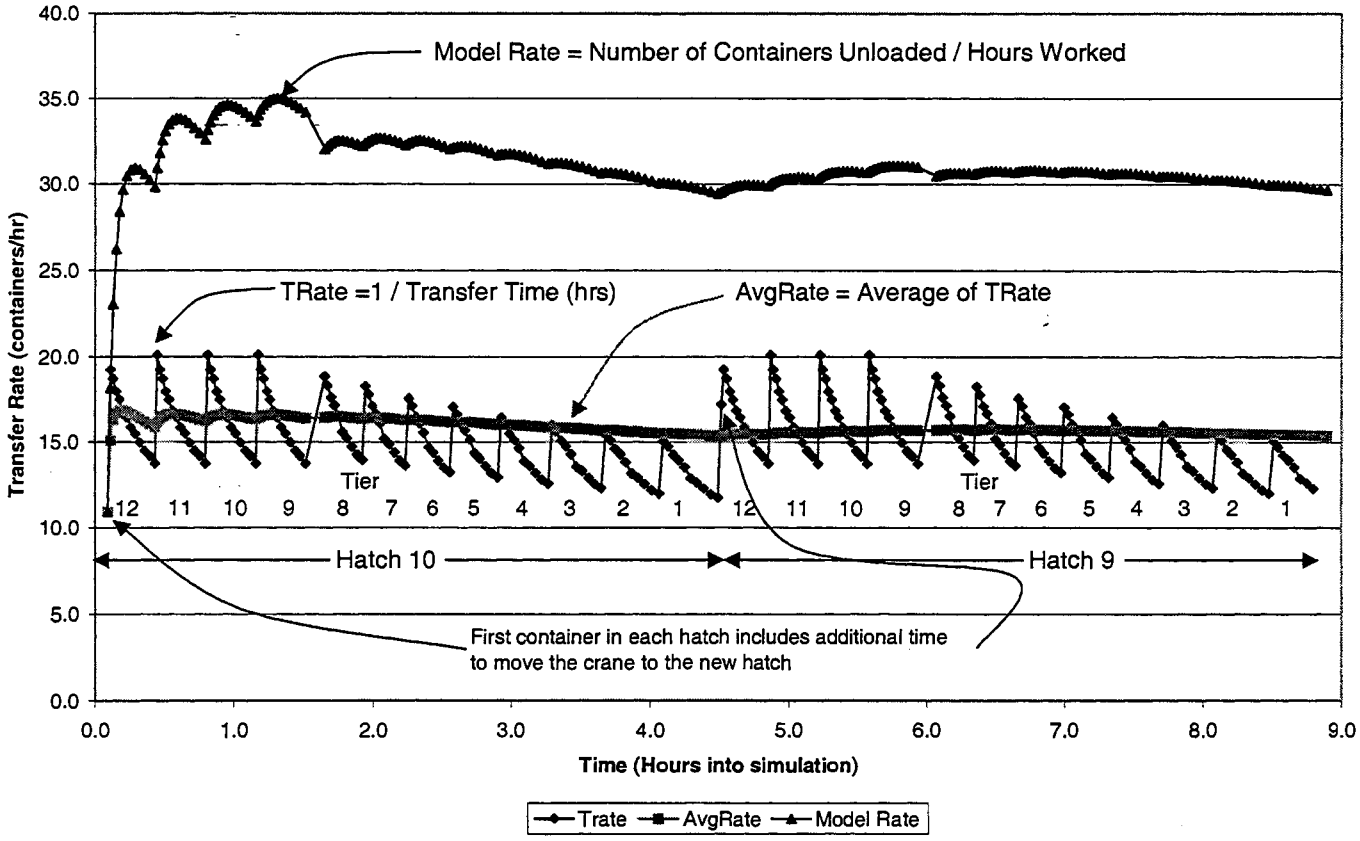

Figure 5: Container model transfer rate over time

discussions with crane experts, we originally selected a value of 0.10m/sec as the focus velocity gate for manual operations. This resulted in an inability to unload a complete ship in Sea State 3, so we increased the gate to 0.11 m/sec based on the sensitivity analysis discussed in Section 3.3.

A partial listing of the preliminary analysis results to date is shown in Table 1.

Table 1: Sample of preliminary results

Sea State	*Heading*	*Manual Comp Rate*	*Auto Comp Rate*
3	0 °	25.9 ctrs/hr	29.3 ctrs/hr
3	+45 °	22.8 ctrs/hr	29.3 ctrs/hr
3	- 45 °	n/a	29.3 ctrs/hr
4	0 °	n/a	29.3 ctrs/hr
4	+45 °	n/a	29.3 ctrs/hr
4	- 45 °	n/a	29.3 ctrs/hr

These results indicate that a motion-compensated crane will be required to move cargo at Sea State 3 or higher. We have also concluded that a container transfer rate of approximately 29 containers per hour per crane is the maximum rate that may be obtained with either type of motion compensation, as long as conditions permit. As you will note from the table, the manually operated crane could only complete a ship unloading at the 0° and +45° headings at Sea State 3. The "n/a" entries in Table1 indicate that the simulation did not complete the full ship unloading process for the other manually operated scenarios.

You may also note that the automotion-compensated scenarios all resulted with the same transfer rate of 29.3 containers per hour. This is due to the fact that the simulations showed no motion-induced delays at all at Sea State 3 and only minimal delays at Sea State 4. We did not request motion data for sea states beyond Sea State 4, so we cannot proceed further with the analysis at the current time. These results indicate that container transfer may be possible beyond Sea State 4 using the RoboCrane design.

3.3 Sensitivity to Focus Velocity Gate

Discrete-event simulation analysis provides the ability to perform sensitivity analysis on any input variable that may not be known precisely or may be difficult to determine. The focus velocity gate in the MOB cargo transfer simulation model is just such a variable. Therefore, we performed sensitivity analysis

on the focus velocity gate for both designs considered in our analysis so far.

Figure 6 shows the results of the analysis for the MOB rail crane using the RoboCrane motion compensation system in Sea State 4. The graph plots both the transfer rate and total motion-induced delay time during the unloading of a half of a complete ship as the focus velocity gate varies from 0.3 m/sec. to 0.5 m/sec. As can be seen, the transfer rate increases rapidly as the focus velocity gate increases. At the same time, motion-induced delay time decreases.

Figure 7 shows the results of a similar analysis for the same rail crane using manual motion compensation at Sea State 3. (The manual system failed to complete the transfers at Sea State 4.) As can be seen in the graphs, they have very similar shapes only at different scales on the axis.

In fact, as noted earlier, at a focus velocity gate of 0.1 m/sec, no transfers occurred. Thus, a 10% change in the anticipated operator performance (0.11 m/sec to 0.10 m/sec) resulted in a drop from a 20% degradation in performance to complete failure. This indicates that for manual crane operations, the onset of problems and compete failure are very near neighbors. The concept that there is a sharp limit to cargo transfers for manual cranes, a fact observed in Joint Logistics Over The Shore (JLOTS) operational exercises, is also observed in the simulated operation[4].

3.4 Maximum Velocity by Hatch

Another useful insight discovered during the preliminary cargo transfer analysis is that there may be a means to transfer extremely critical cargo during normally limiting sea conditions by positioning it amidships.

For example, we found that even in the case of manual crane operation in Sea State 4, at least a few holds near the center of the vessel could be unloaded. This is due to the fact, obvious to a naval architect, that the relative motion of a point on a vessel in waves increases with its distance from the vessel's center of gravity. Although other factors may refute this option, we simply note that it may be possible to unload high-priority cargo in near-limiting conditions by being careful where on the supply vessel the item is located.

The graph shown in Figure 8 shows the maximum relative velocity (x, y, or z) of the most distant container from the MOB in three different hatches along the example ship for a representative portion of the Sea State 4 motion data file. Hatch 10 is amidships, Hatch 1 is at the bow, and Hatch 5 is midway between them. As can be seen, the maximum relative motions for these containers exceeds the 0.11 velocity gate for manually operated cranes for nearly the complete span of time shown. But it rarely exceeds the RoboCrane limiting velocity gate of 0.5.

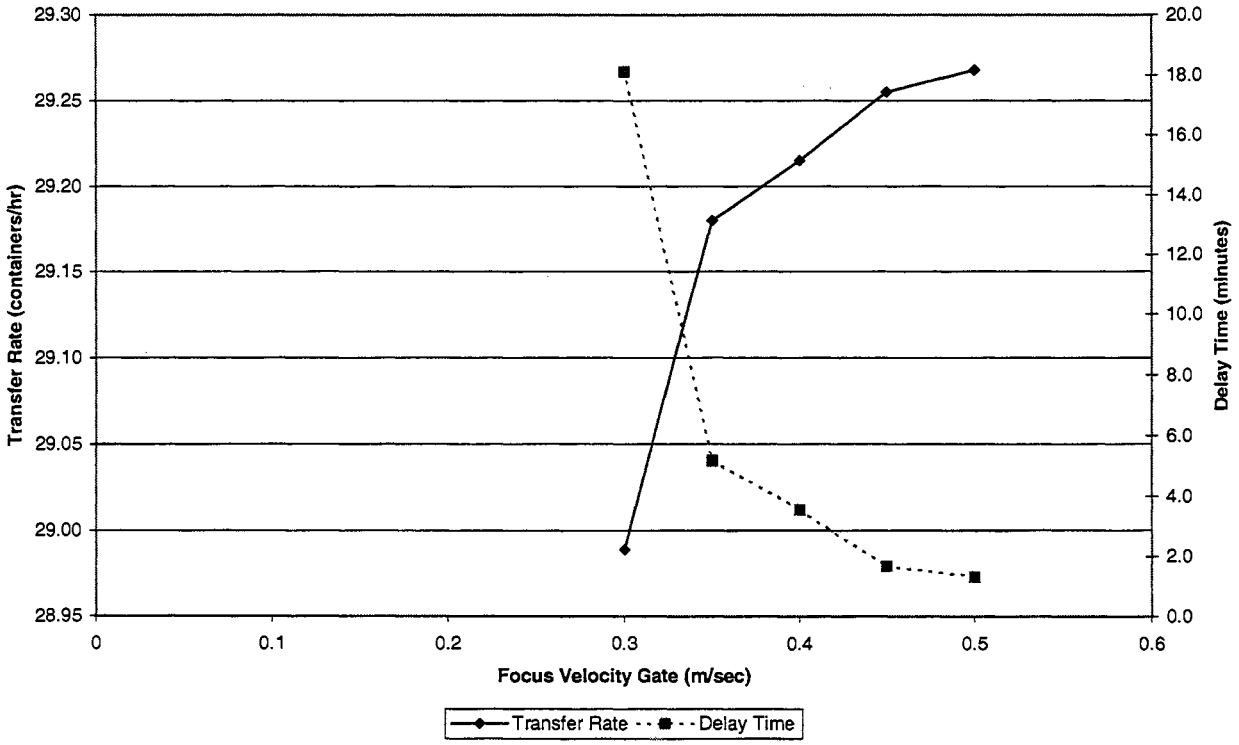

Figure 6: Sensitivity analysis with automotion compensation; Sea State 4, H 45, latch fail = 5%

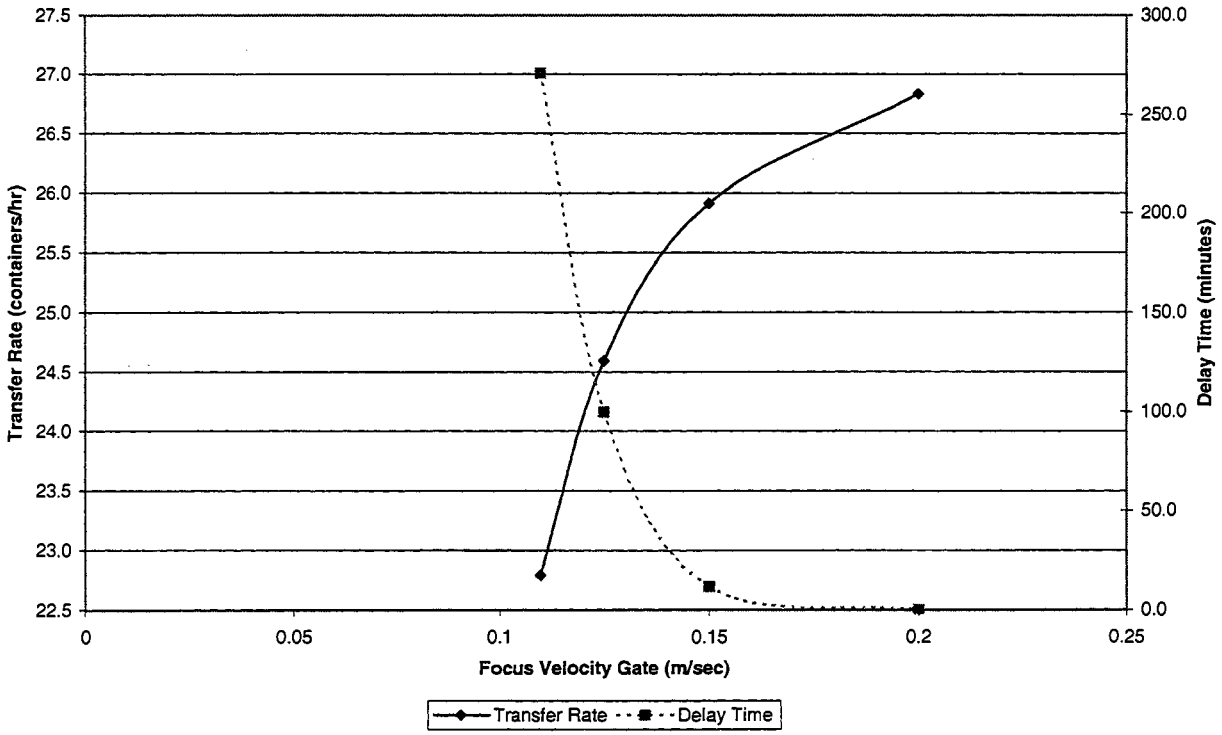

Figure 7: Sensitivity analysis with manual motion compensation; Sea State 3, H 45, latch fail = 5%

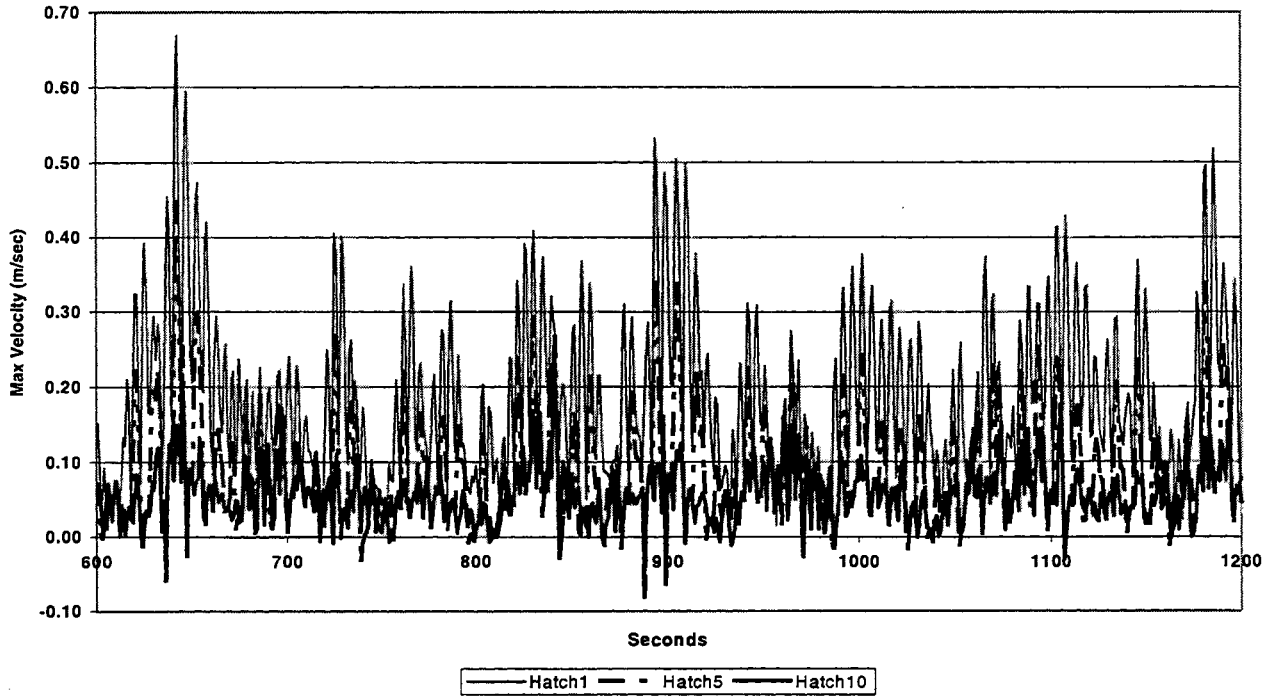

Figure 8: Maximum relative velocity by hatch Sea State 4

3. CONCLUSIONS

The primary observations of the preliminary analyses performed with the MOB container transfer model are that:

- In calm seas, we can expect to move a maximum of 29 containers per hour per crane using either the RoboCrane automatic motion compensation system or with manual motion compensation. In fact, the model has been tuned to produce this value for non-delayed operation because it is the expected performance of such cranes at dockside.
- The RoboCrane can transfer container cargo at its maximum capacity at Sea States 3 and 4 due to its superior motion-compensating capability. Indications are that it may be usable at even higher sea states.
- Manually compensated cranes are not likely to be used in the MOB, since they cannot transfer cargo beyond amidships holds in Sea State 3. However, manual operations do represent a fallback position for the automated cranes in the event of a failure in the compensation control system.
- The model predicts that performance deteriorates quickly as the velocity limit for acquiring the target container is approached. Therefore, the focus velocity capability of the crane should be central to the design of its motion-compensating system and to testing programs for crane prototypes.
- Because of this sensitivity, it will be important to design hardware with a lot of margin versus expected environmentally induced motions.
- Current motion-predicting mechanisms indicate that that "hang-up" in guides due to angular misalignment is unlikely up to Sea State 4.

References

[1] M.K. Cybulsky and R.L Currie. *Generalized Sea Cargo Transfer Model & Manual - Beta Release of Software and Documentation.* McDermott Technology, Alliance, Ohio, March 24, 1999.

[2] M.K. Cybulsky and R.L Currie. *Generalized Sea Cargo Transfer Models – Application of Models and Statistical Analysis.* McDermott Technology, Alliance, Ohio, June 18, 1999.

[3] K. Goodwin and R. Bostelman. *Final Report MOB RoboCrane.* Intelligent Systems Division, National Institute of Standards and Technology, Gaithersburg, Maryland, Jan. 17, 1997.

[4] T.G. Vaughters and M.F. Mardiros. *Joint Logistics Over the Shore Operations in Rough Seas.* Naval Engineer Journal, May 1997, pp. 385-396.

[5] W.A. Wood, Principal Investigator. *Preliminary Design of Mobile Offshore Base Ship Interfaces,* Seaworthy Systems, Inc. Centerbrook, Connecticut, Sept. 30,1997.

Acknowledgement: This material is based on work supported by the U.S. Office of Naval Research's MOB Program, Contract No. N0014-97-C-0410.

PROCEEDINGS OF THE THIRD INTERNATIONAL WORKSHOP ON VERY LARGE FLOATING STRUCTURES
(VLFS '99), VOL. I, EDS. R.C. ERTEKIN & J.W. KIM, 22-24 SEPTEMBER 1999, HONOLULU, HAWAII, USA

PERFORMANCE ASSESSMENT OF MOBILE OFFSHORE BASES: OPERATIONAL AVAILABILITY AND PROBABILITY OF MISSION SUCCESS EVALUATION

A. K. Jha, L-C Lee and R. C. Lundberg
Bechtel*

ABSTRACT

This paper describes a computer model developed to assess the performance of Mobile Offshore Bases (MOBs). A MOB is intended to serve as a floating base for conducting military and peacetime operations at various deployment sites worldwide. A floating structure of this size, about 5000 feet, does not exist yet and feasibility assessment studies of these novel concepts have required advancement in various technology areas unique to the MOB. The operational availability (Ao) and probability of mission success (Ps) analysis in the model provides for a quantitative assessment of new platforms like MOBs and allows assessment or evaluation of the new technologies being developed to make a MOB feasible.

Ao represents the expected percentage of time that a MOB will be ready to perform satisfactorily in a mission and Ps represents the probability of successfully performing the mission itself.

The model adopts a reliability block diagram approach connecting the various MOB systems and capabilities based on their cross-functional relationships. The analysis methodology is to simulate the specified mission scenario of the MOB and keep track of statistics of Ao and Ps during the simulations. The model addresses reliability (failure and repairs) of the systems involved, motion or response characteristics of the various MOB components (e.g., module motion, bridge motion, and connector loads) and the availability of resources required in the mission.

1. INTRODUCTION

A Mobile Offshore Base (MOB), a new platform concept, is intended to serve as a floating base for conducting military and peacetime operations at various deployment sites worldwide (see Figure 1 for a proposed MOB concept). In accordance with the varied mission requirements, the MOB is to have a deck length of about 5000 feet long to support fixed-wing air operations. A floating structure of this size does not exist yet and feasibility assessment studies of these novel concepts have required advancement in various technology areas unique to the MOB. The operational availability (Ao) analysis provides for a quantitative assessment of new platforms like MOBs and allows assessment of the new technologies being developed to make a MOB feasible.

Operational availability [1] represents the expected percentage of time that a weapon system or individual component will be ready to perform satisfactorily in an operating environment when called for at any random point in time. This handbook also states: "It is Navy policy that Ao shall be the primary measure of material readiness for weapon systems and equipment." Bechtel was contracted to develop a program capable of performing an Ao analysis of any MOB concept, based on the Navy's requirement. The development of the assessment model has the following potential benefits for MOBs:

- Promote a better understanding of the MOB missions, functional requirements, required subsystems and operations
- Assess the relative performance of subsystems within a MOB concept when limited data is available and absolute performance when all necessary data is available
- Assess the performance of different systems within a given MOB concept to help identify weak links for that concept
- Provide guidance to the MOB Science and Technology Program
  - Permit cost-benefit sensitivity analyses
  - Identify gaps in available reliability data and MOB technology to permit quantitative performance assessment

The mission needs statement (MNS) developed by the Navy in 1995 for the MOB was used as a guide to develop the initial features of the model. Some of the

* 50 Beale Street, San Francisco, CA 94105-1895, USA

main objectives defined in the MNS that were used as a guide are:

1. Provide an advanced base from which air, land, and naval expeditionary forces can conduct operations
2. Provide an in-theater command and control (C2) center and operation facility, providing command, control, communication, and computers [intelligence] (C4I) capabilities
3. Provide a tactical aviation operations and support base for conventional takeoff and landing (CTOL), short takeoff and landing (STOL), vertical/short takeoff and landing (VSTOL), and rotary wing aircraft, including Joint Advanced Strike Technology (JAST) aircraft.
4. Provide an inter-theater and intra-theater logistics node, supporting movement of both pre-positioned and deployed equipment and supplies via both sealift and airlift
5. Provide a transportation node capable of supporting routine movement of combat and transportation assets including commercial and military air and sea transports
6. Provide an in-theater maintenance and repair facility supporting deployed air, sea, and land systems

Each of these mission objectives requires that the MOB possess particular operational as well as functional capabilities. These were considered when developing the computer model for assessing the performance of MOBs. The simulation program Extend [2] was used for this purpose.

2. BACKGROUND

This section provides some background on the definitions of Ao and Ps used in this paper. Ao is the fraction of time the MOB is available for conducting mission operations as mentioned earlier. This definition applies to both MOB systems and components. Given a time history of the operational state (up or down), Ao can be written as

$$Ao = \frac{\text{Uptime}}{\text{Uptime} + \text{Downtime}} = \frac{\text{Uptime}}{\text{Total time}} \quad (1)$$

Figure 2 shows an example of the availability states of a component in a total mission time T_M. The component is up or available for operation during the times T_{F1}, T_{F2}, and T_{F3} shown by the hatched boxes. The component is down or unavailable for operation during the times T_{R1}, T_{R2}, and T_{R3}. When the component goes into a down or a failed mode, the component is considered to be undergoing repairs. Failure, here, may be an actual mechanical failure of the component or simply the inability of the component to meet a certain target performance level (for example, excessive motions of the MOB beyond a tolerance level). When failure is the mechanical failure of the component, repair includes the time required to order parts and the time to repair the component after obtaining the parts. When failure is performance below a tolerance level, repair includes the time for performance to come back above acceptable levels so operations can be resumed.

Based on the above, Ao is then given as

$$Ao = \frac{T_{F1} + T_{F2} + T_{F3}}{T_M} \quad (2)$$

T_F and T_R are, in general, random times that are specified by a distribution and it's associated parameters. For example, T_F and T_R can be exponentially distributed with means denoted as MTBF (Mean Operating Time Between Failures) and MTTR (Mean Time To Repair), respectively.

Regardless of the distribution types of T_F and T_R, it can be shown easily that

$$Ao = \frac{MTBF}{MTBF + MTTR} \quad (3)$$

(As a side note, the third repair time T_{R3} has been arbitrarily assumed to end when the mission ends at T_M for explanation purposes here.)

The above equations can be generalized for M failures of a component as

$$Ao = \sum_{i=1}^{M} \frac{T_{Fi}}{T_M};\ MTBF = \sum_{i=1}^{M} \frac{T_{Fi}}{N};\ MTTR = \sum_{i=1}^{M} \frac{T_{Ri}}{N} \quad (4)$$

Here, Σ indicates a summation.

For system of N independent components in series, it can be easily shown that the system availability Ao_S is

$$Ao_S = \prod_{i=1}^{N} Ao_i \quad (5)$$

Here, Π indicates a product and the subscript i denotes the value for the i^{th} component. For exponentially distributed T_F and T_R, the system $MTBF_S$ is.

$$\frac{1}{MTBF_S} = \sum_{i=1}^{N} \frac{1}{MTBF_i} \quad (6)$$

Given Ao_S and $MTBF_S$, the MTTR of the system can be found from Eqn. 3.

For a system with N independent components in parallel,

$$Ao_S = 1 - \prod_{i=1}^{N} (1 - Ao_i) \quad (7)$$

For components with T_F and T_R distributed exponentially, in parallel-components system

$$\frac{1}{MTTR_S} = \sum_{i=1}^{N} \frac{1}{MTTR_i} \qquad (8)$$

and $MTBF_S$ can be found again from Eqn. 3.

For MOBs, the model contains complex combinations of components in series and parallel and so the system Ao, MTBF and MTTR are found using simulation since simple formulas are difficult to develop. Multiple simulations can be performed to get statistics such as mean and standard deviation of the parameters of interest.

The probability of success Ps is based on the time required to achieve a certain task in the simulation of a MOB mission versus the time allocated or scheduled for this task. Examples of mission tasks to be done in a specified amount of time include (a) move a specified amount of cargo using sea operations, (b) transit a certain distance, or (c) perform a set of sub-tasks (that include transit or cargo transfer). When N simulations are performed and only in N_S simulations success of an event is found then P_S for that event is given as N_S/N.

3. ASSESSMENT METHODOLOGY

This section describes the assessment methodology adopted for analyzing the performance of a MOB in a mission. Given the eventual complexity of the modes of operation onboard a MOB, mission to be performed and complex cross-dependencies among various MOB systems, a reliability block diagram approach was adopted to develop the MOB performance assessment tool (MPAT). In MPAT the mission-critical operations (e.g., air, sea operations, stationkeeping) and systems (e.g., ballast, control, sensor systems) are connected to reflect the logical dependencies among them. Due to the complexity of the tool (model), the systems will not necessarily be independent and so an analytical calculation of the Ao statistics or P_S is extremely difficult. (The Ao statistics include MTBF, MTTR, and Ao for the individual capabilities and systems as well as for the overall MOB.) It was much easier to develop a simulation-based model to calculate these statistics. This approach can be applied to analyze both the on-site missions and the transit modes of the MOB operations.

In the tool, the MOB systems and capabilities that were identified to be critical for MOB missions were implemented in the model. Each mission-critical capability or system is modeled as a "block" in Extend (the simulation program used for this purpose, see [2]). A block simulates the time history of availability state (up or down) in the simulation analysis. If a block modeling a capability or system is described by its sub-capabilities or sub-systems, then it (the block containing the sub-systems) is called a hierarchical block. Every attempt has been made to make the blocks as general as possible to facilitate application to different MOB concepts and missions. In the model, the blocks are connected to reflect downtime effects of one block (system/capability) on another. Based on the mission specified, the model is used to simulate and analyze the MOB mission operations required. The simulation is performed at regular time steps (increments) from the start to end of the mission. Each block calculates the state of its capability or system at each time step, and propagates the net operational readiness state (i.e., whether block is up or down) of all the blocks connected before it in the chain. This way the availability state of each block (system/capability) and of the entire system is assessed at each time step. Multiple simulations can also be performed to get estimates of the Ao statistics.

The availability states of the blocks modeled using probability distributions of T_F and T_R are simulated using the distributions specified. An up state is simulated using the T_F distribution followed by a down state simulated using the T_R distribution. The block is unavailable during the down state. In the blocks modeling other performance measures or the weather-affected responses, the standard deviation or the root-mean square (rms) values are calculated using the weather data and response analysis results (developed outside of this model and provided as input to this model). The rms values are checked against specified threshold values to see if these are acceptable. The block is available for operations if the rms value is acceptable and unavailable otherwise.

Similarly, weather parameters (e.g., Hs, wind speed) can also be monitored to determine when threshold limits have been exceeded.

4. MODEL FEATURES AND CAPABILITIES

The following points describe the major features and capabilities of MPAT.

- MPAT permits a quantified performance assessment of MOBs including both the inherent (mechanical) performance and mission performance (in presence of weather effects).
- MOBs with up to six modules can be analyzed and the MOB can optionally have structural connectors between the modules.
- MPAT permits analysis of simple to very complex MOB missions. For example, a simple mission could be one module performing air operations on one deployment site. An example of a complex mission (see Figure 4) could be three modules performing onsite operations (e.g., cargo transfer by air or sea) at site A and simultaneously the two remaining modules (for a five-module MOB) perform onsite operations at site B. They transit at different times to site C where they connect to form a full (connected) MOB. The MOB then performs onsite operations followed by a transit to a fourth site D to perform

onsite operations there. In general, the model is extremely flexible in terms of the missions that can be analyzed.

- The model addresses downtime due to the following effects:
  - **Mechanical/electrical/structural reliability effects**: failure (or repair) modes of mechanical (e.g., ballast system) or structural (e.g., hull) components.
  - **Weather effects**: weather effects at the site cause loads on the connectors, environmental loads on the dynamic positioning (DP) system or motions of modules. Excessive response values of these beyond acceptable levels may halt mission operations.
  - **Inventory limits**: when the inventory levels exceed the maximum capacity or fall below zero (no inventory available) then mission operations have to stop. For example, if the MOB fuel runs dry then stationkeeping operations cannot be performed. Eight types of "inventory" are currently tracked in the model and these are personnel, roll-on/roll-off cargo, containers, aircraft, lighters, fuel, water, and pallets.
- The model has access to 23 years (1974-96) of weather data at each of the 22 sites worldwide (see Ref. 4 for more details). The data exists in the form of weather conditions of six-hour durations called a seastate. A seastate is described by a directional wave spectrum, mean wind speed and direction, current speed and direction. This data is used to calculate all weather-affected responses and any resulting downtime.
- The major operations/capabilities modeled in MPAT include air operations (inventory transfer by air), sea operations (inventory transfer by sea), and stationkeeping or propulsion operations.
- The major reliability (failure/repair based on T_F and T_R statistics) issues address the hull, personnel support functions, auxiliary support systems, and command, control, communication, computers and intelligence among others.
- MPAT allows analysis of a what-if scenario (what is the performance of the MOB in, say, February 1996 at a given site?) and also allows statistical analysis of MOB performance (performance in, say, an arbitrary February at a given site).
- Three major types of output are generated from this model: (a) mean and standard deviation of Ao, MTBF, MTTR, number of up states, number of down states for all relevant blocks, (b) mean and standard deviation of start time, end time, duration and the probability of success of each task in the mission, and (c) detailed time histories of several important parameters (e.g., weather, response rms values, MOB fuel level) to help understand the Ao and Ps results.

5. DESCRIPTION OF THE MODEL

This section describes the major parts of the model and the details can be found in Reference [3] and follow-on reports to be published soon.

5.1 Overall Model

Figure 5 shows the first screen of MPAT and as an example shows a three-module MOB to be analyzed. The arrows allow the user to follow the model from specifying input to running the simulation to checking the output. The organization of the model facilitates easy input of all required data in the first few portions of the model. This data is then applied to the last portion where the actual logic diagram of the MOB systems and capabilities are programmed for simulation analysis. A detailed discussion of the entire model is not possible in this paper and so only a brief description of each portion (separated by arrows) is provided below followed by details of some of the major blocks in the model.

MOB Configuration Block: This block allows the user to specify the reliability properties of the MOB mechanical systems or capabilities whose availability states have been defined using failure and repair times chosen from a library of distribution types built into the model. The library includes Normal, Lognormal, Exponential, Weibull and Uniform distribution types.

For all weather-affected responses, the block allows the user to specify the transfer functions or response amplitude operators (RAOs), that is, functions that relate the weather parameters to the response of interest. The user specifies the number of modules and whether connectors exist in the MOB between modules. The hardware and behavior properties specified here are applied in the next portion of the model labeled MOB Hardware and Behavior Properties.

MOB Hardware and Behavior Properties: Properties specified in the MOB Configuration Block are applied identically to each module and this portion of the model allows the user a chance to change the properties across different modules. For example, the pitch motion RAOs could be specified as different from the first to the last module due to shielding effects.

Check MOB Block: This block simply checks and displays whether the properties specified in the MOB Configuration Block and applied in the MOB Hardware and Behavior Properties portion were used or changed by the user.

Mission Profile Block: This block lets the user specify

a time schedule of the different mission operations on board MOB and defines the module modes (site location and time windows for modules), and events for air and sea operations (time windows for performing cargo transfer operations and cargo amounts to be moved). More details of this block are discussed in Section 5.2.

Operation Thresholds Block: Here the user specifies all the thresholds for the weather-affected responses in the model. These thresholds define limits beyond which the corresponding response is considered to be unacceptable for the task being performed. Specifically, the thresholds for the standard deviation or the rms values of all responses modeled in MPAT are to be specified in this block. The user also specifies the wind speed threshold values that would terminate air operations in the mission to be analyzed.

Apply Block: This block gathers the input parameters specified in the MOB Configuration Block, MOB Hardware and Behavior Properties, and Operations Threshold Block and applies it to the Transit and Onsite blocks of the individual modules and the full MOB, as these are the blocks that perform the actual simulation analysis of the mission.

Onsite and Transit Blocks: The last portion of the model, as mentioned earlier, contains the programmed logic connecting the MOB systems and capabilities for the full MOB and all individual modules. Since the model described is for a three module MOB, Figure 5 shows one block for full MOB transit, three blocks for the three individual module transit, one block for full MOB onsite, and three blocks for the three individual module onsite operations. Depending on the scheduled modes at any given simulation time step, these blocks are exercised to simulate the corresponding mode for mission analysis. More details of these blocks are discussed in Sections 5.3 and 5.4.

5.2 Mission Profile Block

As mentioned in the previous section, this block allows the user to specify the overall mission requirements and detailed time schedules of the module modes and of all the events (tasks) to be performed by air or sea operations. The onsite mode of either a module or a full MOB comprises of events (tasks) by air or sea operations. For example, cargo (one of the eight inventory types) is to be moved off the MOB or on to the MOB using one of the three types of air operations or any one of the three types of sea operations. These include, for air operations, (a) CTOL, (b) short takeoff and landing STOL, and (c) vertical takeoff and landing VTOL, and for sea operations (a) large ships, (b) medium ships, and (c) small ships. The distinction made between these different types of air or sea operations is in regards to the module motion thresholds that can be tolerated. For example, smaller ships can tolerate smaller relative motion alongside the MOB versus large ships. The user specifies the actual values of the thresholds in the Operation Thresholds Block.

The paragraphs below provide the major features of the Mission Profile Block.

The user specifies the overall mission duration, the number of simulations to be analyzed, the time resolution (time step) in the simulation and the calendar time at which the mission should start. The available calendar times are any day of the 23-year data set.

The user specifies time schedules of the modes of each individual module and of the full MOB. The input includes the start and end times of each mode. If the mode for a module or full MOB is onsite then the user specifies the deployment site location, which can be one of the site numbers as shown in Figure 3, or can be the latitude and longitude of any site worldwide. In the later, case the model uses the weather data of the nearest available site (one of the 22 sites) for simulating weather at this arbitrary site. In case the mode is transit, the user specifies the transit route as a series of sites across the world using any of the 22 sites at which data is available. The user is permitted to begin and end the transit at arbitrary sites for which the latitude and longitude are to be provided. This transit information will be used by the Transit Blocks (see Section 5.4) to calculate distances along the great circle connecting two neighboring sites.

The user specifies the details of each event for each of modes defined above. For single module modes, cargo transfer operations by air or sea are permitted and additionally for full MOB an inter-module cargo transfer event can also be specified. A user-specified inter-module cargo transfer rate as a function of the significant wave height Hs is used to model the time required to redistribute a specified target amount of cargo to model the operational time required to redistribute cargo between the modules after the modules have been mated to form a full MOB. The user also specifies the scheduled start and end time of this event. For air and sea operations, the user specifies (a) the module (a specific individual module or the full MOB) being used, (b) the scheduled start and end time, (c) the sortie rate of aircraft or ship being used for sealift or airlift operations, (d) the type of inventory (any one of the eight permitted) to be moved, (e) amount of inventory to be moved on or off the MOB, and (f) the type of operation within air (CTOL, STOL, VTOL) or sea (large, medium or small ship) being used.

In order to model the sequence of modes or events, the user also specifies whether to permit taking

advantage of any schedule slack in the simulation. For example, if the mission for a module is to perform onsite operations until a certain end time and then begin transit operations. If taking advantage of slack is permitted then as soon as the onsite operations end, the transit operations will begin, otherwise the transit operation will begin at the scheduled start time even if the previous onsite operation ends earlier than scheduled. This feature has been added to the model to allow flexibility in analyzing a mission scenario where taking advantage of any slack in the schedule may not be desirable if the activities on a MOB are tied to activities of other entities in the overall war scenario.

Based on the mission details specified, the model simulates the modes and events appropriately. The block starts each mode or event based on the slack type chosen and uses the last portion of the model (Transit and Onsite Blocks of individual modules and full MOB) to track the amount of inventory being moved and check at what time the cargo targets were met. This information is used to track the simulated start time, end time and durations of each mode and event. Mean and standard deviation of each of these times are reported for each of the modes and events in the mission.

The block also calculates the probability of (mission) success for each mode and event. The user is permitted to choose any one of the four definitions of success (for each mode and event) (1) simulated duration is less than or equal to the scheduled duration, (2) simulated start time is less than or equal to the scheduled start time, (3) simulated end time is less than or equal to the scheduled end time, and (4) both (2) and (3) are true. Again, these definitions have been included to provide the user with the freedom to define success in a way that suits the overall war (mission) scenario being analyzed.

5.3 Onsite Full MOB

Figure 6 shows the model layout for the onsite analysis of the full MOB. The MOB systems and capabilities in this portion of the model have been placed left to right to reflect the downtime effects of the systems on the left to those on the right. For example, Air Operations is affected by Hull downtime effects and not the other way around. The model for the individual module differs slightly from the Onsite Full MOB Block (see discussion at end of this section). In the Onsite Block (for full MOB), the MOB systems and capabilities are connected in a logical fashion reflecting all the functional interdependencies. The following are the major tasks performed within this portion of the model:

1. when onsite full MOB mode is scheduled by the Mission Profile Block, get the appropriate weather data as simulation proceeds based on the present calendar time and the site at which the operation is to be performed
2. simulate the availability state of each of the MOB systems and capabilities addressed in this block
3. calculate the Ao statistics of the MOB systems and capabilities addressed in this portion of the model
4. perform cargo (inventory) transfer operations when the system is available for operations and when the mission schedule permits doing so
5. keep track of time histories of data that could be useful in understanding output results.

The major blocks in this Onsite Block (Figure 6) are described below:

5.3.1 Onsite Weather

This block communicates with the weather database to access the appropriate data needed at the different time steps in the simulation.

5.3.2 MOB Heading

This block finds the optimum heading of the MOB at the site at the different time steps in the simulation. The optimum heading is that orientation of the MOB (with respect to the North direction) which maximizes the availability of the MOB for air and sea operations while minimizing the structural loads on the MOB. The optimum heading found here is needed to calculate all the weather-affected responses in this portion of the model. For example, module motions are calculated using this optimum heading to orient the MOB in a multidirectional sea (wave spectrum) and then to appropriately multiply the directional RAOs of these motions.

5.3.3 Hull

This block models the reliability properties of the hull of the MOB and simulates the up (repaired) or down (failed) state of the hull components. The hull components include (a) lower structure, (b) lower bulkheads, (c) column flats, and (d) upper deck. The reliability properties are assumed to include the frequency of failure or mission inoperation due to accidents (e.g., fire, aircraft impact), fatigue, and ultimate strength failure. The hull components are connected in series meaning if any one of these components is down then the Hull Block is down. The Hull state information is sent through the right connector of the block to the rest of the Onsite Block. This block and the remaining such reliability blocks have been laid out according to the Ship Works Breakdown Structure (SWBS) nomenclature [7] so that the model is easily understood by users in the Navy.

5.3.4 Maintenance, Personnel Support Function
These blocks model the reliability properties of the maintenance operations both organic and inorganic maintenance on the MOB, and the personnel support functions on the MOB, respectively. These blocks are defined only in a high-level manner at this stage.

5.3.5 C4I
This models the reliability properties of the system for command, control, communication, computers and intelligence on board the MOB. This block has been further modeled by its SWBS sub-components (further details can be found in the report to be soon published). The reliability properties required here reflect the frequency of failures for C4I that halt the overall MOB mission.

5.3.6 Other Systems
This includes the mission-critical reliability properties of ballast systems, weapons storage and handing, auxiliary systems (500 SWBS category), and outfit and furnishings (600 SWBS category).

5.3.7 Stationkeeping
A detailed model of the stationkeeping capability was developed to address the reliability properties of the systems involved and to address the MOB capacity to resist the environmental loads. Figure 7 shows the details of the stationkeeping block. The three connectors of the Stationkeeping Block in Figure 6 (shown as small square blocks on the perimeter of this block) correspond to the three variables shown in the square boxes in Figure 7. The stationkeeping hierarchical block is modeled by four blocks addressing the different reliability components. These are the electric plant system, sensor system, control system, and the propulsion system. These again follow the SWBS nomenclature.

The Thruster System is a major block within the Stationkeeping Block. It calculates the environmental loads based on the weather conditions in the present seastate in the simulation and also calculates the available stationkeeping capacity at the current time step. Based on a comparison of the stationkeeping loads and capacity, the block decides whether the MOB can remain on station or not, or should the full MOB be disconnected into its individual modules. The block also keeps track of when modules can be reconnected if they had to be disconnected.

The environment loads include loads from mean wave drift, wind and current in surge, sway and yaw directions. The block requires specification of the corresponding RAOs for loads calculation. The stationkeeping capacity is calculated based on the number of thrusters and power-generating turbines that are available for operation at the present simulation time step. The user specifies the reliability properties of the thrusters and the turbines. There are two types of power management logic implemented in MPAT and these are the connected power-plants logic and the isolated power-plants logic assumed to reflect peacetime and wartime power management logic, respectively (see References 3 and 5 for more details).

Based on the net environmental loads on a MOB module (in a connected configuration or independent module), the thrust for each thruster that is up or available for operation is based on the thruster allocation logic detailed in Ref. 6. The Stationkeeping Block also calculates the fuel required or the fuel demand for stationkeeping and compares it against the fuel supply in the MOB inventory. If the fuel is unavailable the mission is halted. The connector loads are also monitored in case these are present in the MOB concept being analyzed. If the connector loads exceed a user-specified threshold then the MOB modules in a full MOB are required to be disconnected. Finally, prior to disconnecting the MOB based on the stationkeeping loads, the model lets the user specify that the MOB can drift a certain specified distance before it is to be disconnected. The Systems Analysis Block calculates the Ao statistics of the system within the hierarchical block where it is placed.

5.3.8 Air Operations
The Air Operations capability in Figure 6 has been modeled as a hierarchical block and details are shown in Figure 8. The first three blocks on the left model the reliability properties of the aircraft handling system, aircraft hangaring system and air traffic control. These three are required to be in an up state for CTOL, STOL and VTOL operations to be performed. The CTOL is a hierarchical block and in turn is comprised of blocks that monitor (a) wind speed, (b) motions of each of the two bridges between the MOB modules in a full MOB, and (c) pitch, roll and yaw motions of each of MOB modules in a full MOB. Recall that the thresholds at which CTOL, STOL and VTOL operations need to be halted may be different. The availability state of each of these motion types is required in the Check Inventory Block that simulates the cargo transfer operations (see details below).

5.3.9 Sea Operations
The Sea Operations in Figure 6 is a hierarchical block modeling availability state of sea operations and Figure 9 shows the details. The first three blocks model the reliability properties of the cargo traffic system, cargo handing system, and berthing facility. The next block monitors the tension in the mooring lines of ships alongside the MOB. The tension is calculated from the specified RAOs and when it exceeds the specified threshold, the sea operations are halted. The next three

blocks model the availability of the operations using large, medium and small ships. The significant wave height is tracked in each of these three blocks and when the threshold is exceeded in any one block, the corresponding operation is halted. The availability state information for each of three sea operation types is sent to the Check Inventory Block as in the case of the Air Operations Block.

5.3.10 Check Inventory

This block simulates the cargo (inventory) transfer operations. Based on the air or operation specified, the block tracks the transfer the of the desired inventory type during the simulation. The user-specified transfer rates as a function of weather parameters are used to calculate the transfer rate in the present seastate. This rate is used to calculate the amount of cargo transferred in this simulation time step if (a) the corresponding air or sea operation type required in the mission is available for operations, (b) inventory level for the cargo type being transferred is within permitted limits, and (c) the aircraft or ship being used in this cargo transfer can be accommodated on the MOB. The sortie rate specified in the Mission Profile Block is used to simulate a uniform arrival rate of aircraft or ships being used in the mission event.

The major differences for the Onsite Block for an individual module are

- In the individual module, the stationkeeping logic applies only to one module. Disconnection of modules is not relevant here.
- For the individual module, CTOL is disabled in air operations since the assumption is that CTOL requires more than one module for operation.

5.4 Transit Full MOB

The Transit Full MOB (see Figure 10) simulates the transit portion of the mission and does not permit any air or sea operations to be scheduled while in transit other than refueling operations of the MOB in case the fuel runs below a specified threshold level. The major tasks performed by this block are:

- access the appropriate weather data along the transit route
- calculate the transit speed of the MOB in the present seastate in the simulation and then calculate the distance covered along the route
- the MOB transit operations are halted if any of the systems modeled are not available for operation
- the MOB transit is halted and the MOB ballasted down in case weather conditions become too severe.

The following sections discuss the blocks that perform the above major tasks in the Transit Block.

5.4.1 Transit Weather

This block gets the weather data from the database based on present calendar time during the simulation. The block gets information on the present distance along the route from the Check Distance Block (see Section 5.4.6) and uses this to find the nearest site in the database. The data corresponding to the present calendar time is retrieved from this site.

5.4.2 Weather Parameters

This block converts the weather into a moving reference frame. Due to the MOB moving along the transit route, the weather data will appear in a relative direction or with an encounter speed. The block converts the wave directional spectrum, wind speed and direction and current speed and direction to reflect the present speed and direction of the MOB. On doing so, the RAOs for the weather-affected responses can be easily applied on the encountered weather data to arrive at the responses of the MOB while in motion.

5.4.3 Speed Calculator

The user specifies, in an input table, the MOB transit speed as a function of up to four variables – the significant wave height, the wave spectral peak period, the current speed, and the head wind speed. Linear interpolation is used to find the speed corresponding to the present weather conditions in the simulation.

The model allows the user to specify two reduction factors to the transit speed calculated above. One reduction factor is intended to model the impact of instability while in transit on the MOB or module speed and the second factor is intended to model the effect of motions on operations critical while in transit. For each of these two issues, the user specifies RAOs using which rms values are calculated during the simulation. The user also specifies the speed reduction factor as a function of these rms values.

5.4.4 Ballast Block

The transit speed calculated by the Speed Calculator is reduced to zero if Hs exceeds a user-specified threshold indicating that the weather is severe enough that the MOB should be ballasted down. The block models the time required in ballasting down and then when the Hs drops below a second lower threshold, a deballasting operational delay is simulated. During the process of ballasting down, and deballasting the transit speed is reduced to zero, i.e., the MOB is assumed to have halted its transit operations.

5.4.5 Propulsion System & Other Reliability Blocks

The propulsion system is identical to the Stationkeeping Block in the Onsite Block in functionality with minor exceptions (e.g., drifting of MOB not permitted and fuel demand includes fuel

required for transit purposes). The other reliability blocks are also identical to the Onsite Block and these include Hull, Maintenance, Personnel Support Function, C4I, and Other Systems. All of these systems are required to be up (available for operation) in order for the MOB to move along its transit route. In this context, the reliability properties in the blocks here reflect the frequency of failures of those events that cause the MOB to terminate its transit operations.

5.4.6 Check Distance

When all the required systems and capabilities modeled are available for operation, then the MOB is simulated to move at the transit speed calculated by the Speed Calculator. This speed is multiplied by the simulation time step to arrive at the distance moved in this time step. The distance information is then used by the Transit Weather Block to decide which site data should be used for the next simulation time step.

The major difference for the Transit Block for an individual module is that the propulsion logic applies only to one module. Disconnection of modules is not relevant here.

6. SUMMARY AND FUTURE WORK

The following lists the summary of the work described in this paper:

- The simulation-based model MPAT permits a quantitative assessment of the performance of different MOB concepts under a variety of mission scenarios and environmental conditions. The performance measures include the statistics of Ao and Ps for the different mission tasks.
- Simple to complex missions can be analyzed using individual modules or the full MOB in transit or onsite
- The major features of the model include ability to model reliability properties of the several MOB systems categorized using the SWBS nomenclature and include the ability to model the availability of stationkeeping/propulsion, sea operations, and air operations.
- The downtime analysis addresses three major types of concerns: weather effects (e.g., motions, wind speeds), reliability effects (e.g., failure and repair frequencies of major systems, and inventory limits (e.g., availability of fuel, or water).
- The major benefits of applying this methodology include:
  - Doing this analysis complies with Navy policy of using Ao to measure performance of new warfare systems
  - Permits integration of the different aspects of the MOB program
    - force definition of interface of information
    - identify data or technology needs
    - allow Ao/Ps trade-off studies with cost/technology trade-offs
  - Ability to identify MOB systems and capabilities in order of criticality for a MOB mission
  - Ability to provide valuable feedback to concept developers and mission planners
  - Evaluate relative performance of different MOB concepts under identical mission conditions

Some of major items for future work include:

- The model should be updated when new information on any MOB technology that is considered mission-critical becomes available.
- The model should be applied to available MOB concepts to demonstrate the usefulness of the model and to robustly test the implemented features in the model.

Acknowledgement: The material is based on work supported by the U.S. Office of Naval Research's MOB Program.

References

[1] OPNAVINST 3000.12. *Operational availability handbook.* 1987

[2] ImageThat Inc. *Extend – Simulation software for the next millenium.* Ver. 4.1.2, San Jose, California, 1999.

[3] Bechtel National Inc, *Preliminary operational availability assessment model – Interim report,* 1998.

[4] S.F. Pawsey and M. Manetas, *Environmental specification of metocean conditions for design of the MOB,* VLFS 1999, Honolulu, 1999.

[5] Bechtel National Inc, *Multi-module dynamic positioning system – Propulsion system hardware characterization,* Nov. 1998.

[6] Bechtel National Inc, *Mobile Offshore Base dynamic positioning system configuration study,* Feb. 1999.

[7] Naval Sea Systems Command (NAVSEA), *Expanded Ship Work Breakdown Structure for all Ships and Ship/Combat Systems,* Washington, D.C.: Naval Sea Systems Command, 1985

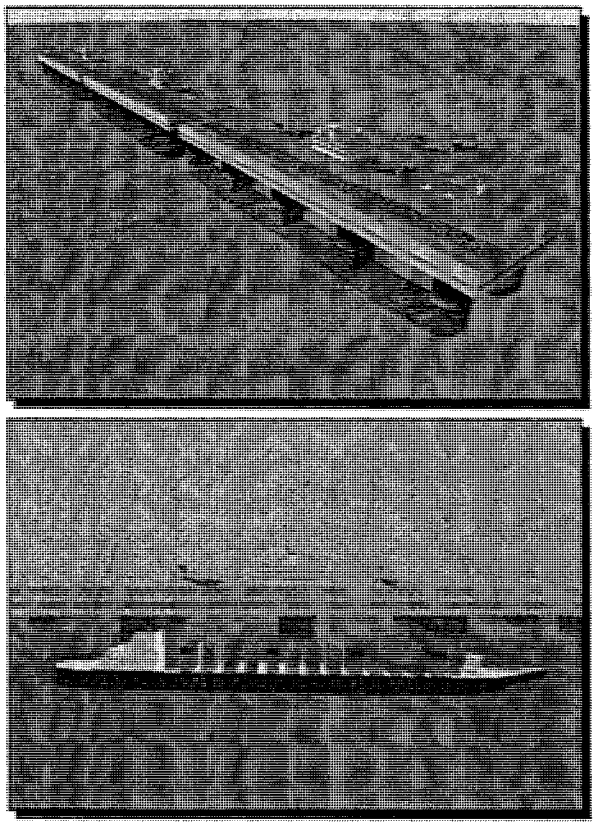

Figure 1: Complexity of operations on MOB

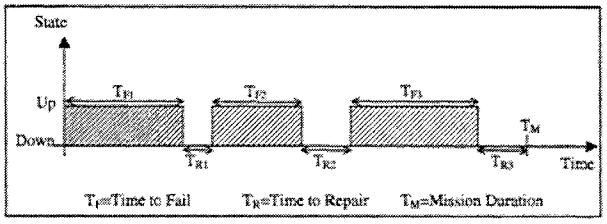

Figure 2: Availability state of a component

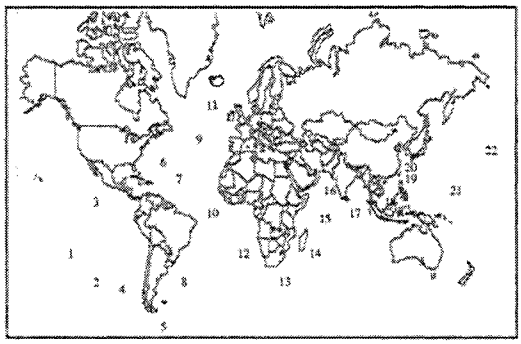

Figure 3: Sites at which weather data is available

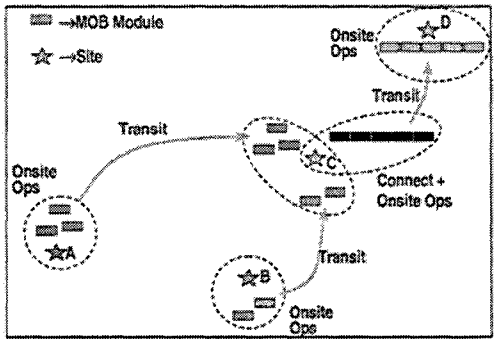

Figure 4: Example mission scenario of MOB

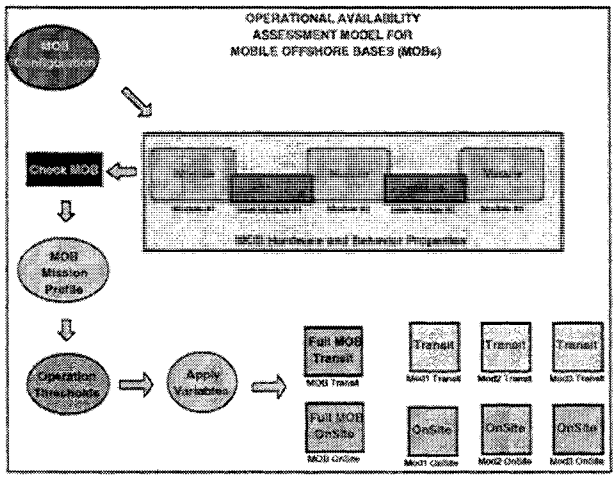

Figure 5: Operational availability model for MOBs

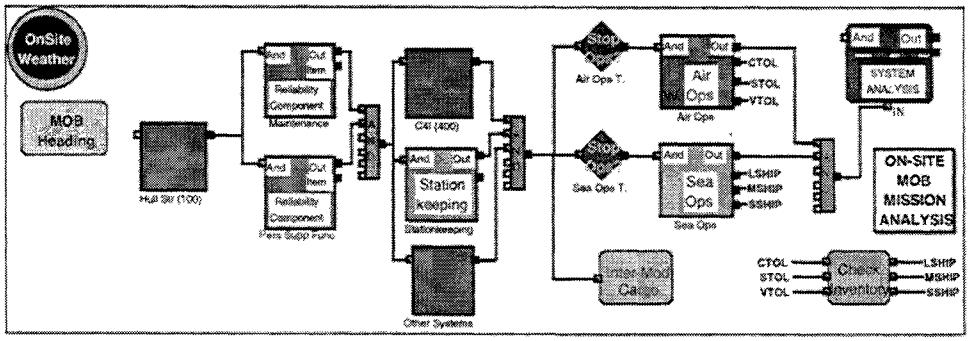

Figure 6: Onsite analysis block

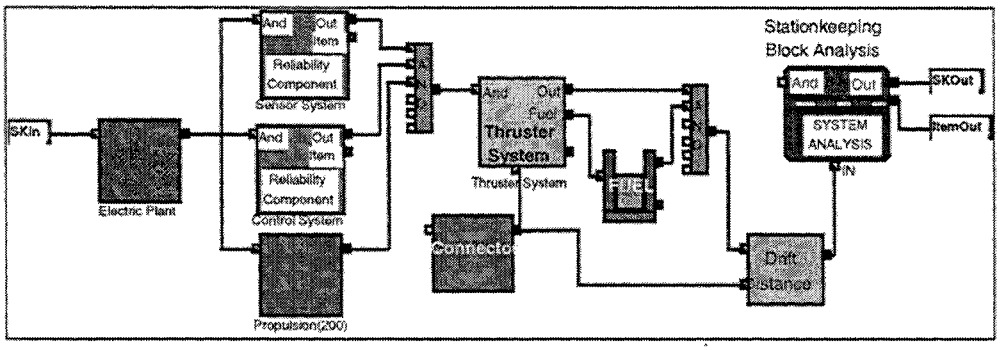

Figure 7: Stationkeeping analysis block

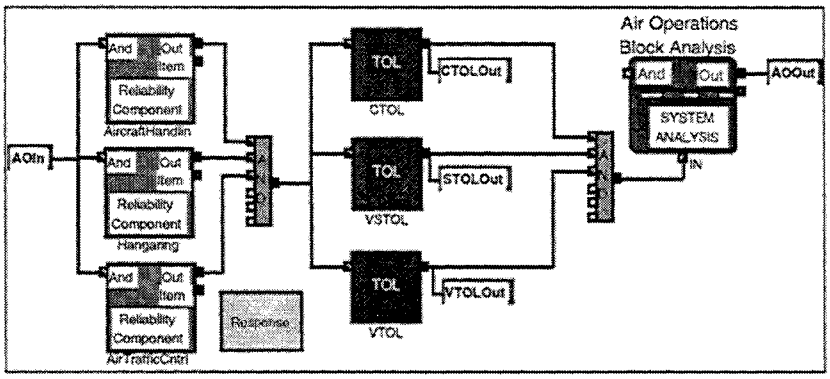

Figure 8: Air operations analysis block

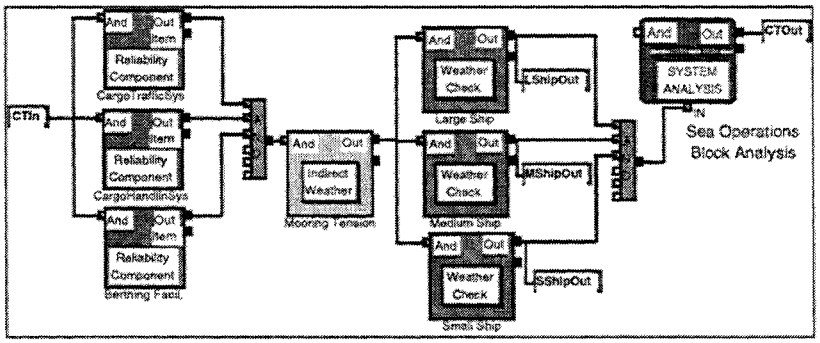

Figure 9: Sea operations analysis block

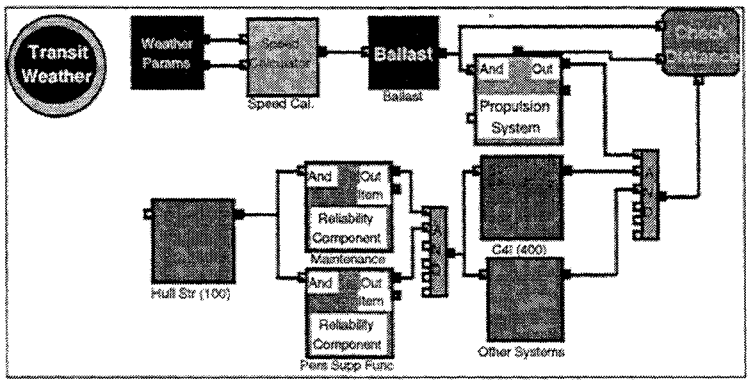

Figure 10: Transit analysis block

PROCEEDINGS OF THE THIRD INTERNATIONAL WORKSHOP ON VERY LARGE FLOATING STRUCTURES
(VLFS '99), VOL. I, EDS. R.C. ERTEKIN & J.W. KIM, 22-24 SEPTEMBER 1999, HONOLULU, HAWAII, USA

STRUCTURAL DESIGN METHODOLOGY OF VLFS FROM THE VIEWPOINT OF DYNAMIC RESPONSE CHARACTERISTICS

K.Iijima, H.Suzuki and K.Yoshida
The University of Tokyo*

ABSTRACT

We studied response characteristics of various types of VLFS through numerical analysis. Hydroelasticity and hydrodynamic interactions are fully considered in the numerical method. First, four types of VLFS were taken up. The results were explained with a help of some important parameters that were derived from analytical method where the structure is modeled as a beam on elastic foundation. Tank test was also carried out for verification at the University of Tokyo. In order to clarify furthermore the relation between the parameters and response characteristics, additional parametric studies were conducted. We showed how the response is influenced by the parameters and which parameter is the most dominant. We finally discussed design methodology of VLFS, especially of semisubmersible type.

1. INTRODUCTION

The authors have been studying dynamic response of VLFS of semisubmersible type in waves. At the beginning of our research, numerical analysis method was developed especially for semi submersible VLFS (see[1]). Hydroelasticity and hydrodynamic interactions are fully considered in the numerical method. The method was first applied to several types of semisubmersible structures (see[2]).

While development of numerical analysis method is of great importance, interpretation of the response and understanding of the mechanism are also necessary for the design. In this context, the authors have proposed analytical method (see [3]), in which the structure is modeled as a beam on elastic foundation. The advantage of the analytical method is that it can describe the response of the whole structure by a few parameters and the obtained solution has an easy form to discuss the response characteristics with.

In the present study, we apply the numerical method to four types of structures including pontoon type structure. It turned out that the numerical method is applicable even to pontoon type structures as well. One of other types of the structures is column supported type structure. Tank test was carried for confirmation of its response characteristics as well as for validation of numerical method. These calculated results are explained by use of the analytical method. Additional parametric studies were carried out for discussion of the optimum structural configuration.

2. NUMERICAL METHOD

The present method (see [1]) is an extension of Goo's Method (see [4]), with sub-structure method and group body concept newly employed. Structure is divided into multiple sub-structures. Each sub-structure is assumed to be supported on group bodies, each of which is composed of several numbers of bodies. Group body is a unit that can be treated as if one body. By introducing the group body concept, the number of bodies is virtually reduced. In the following sections, the word 'body' can be replaced by 'group body'.

2.1 Fluid domain formulation

The fluid is assumed incompressible and inviscid, and fluid motion irrotational with respect to particle motion of small amplitude. Linearized free surface is infinite toward all directions and the water depth uniform. N oscillating rigid bodies of arbitrary shape are considered. The total scattering from i-th body isexpressed as follows.

$$\phi_{si} = \phi_{di} + \sum_{l=1}^{6}(-i\varpi\eta_{li}\phi_{Rli}) = \{A_i\}^T\{\psi_i^D\} + \sum_{l=1}^{6}(-i\varpi\eta_{li})\{R_i\}^T\{\psi_i^D\} \qquad (1)$$

A_i is the coefficient vector related to diffraction and ψ_i^D is the vector of diffracted cylindrical partial waves written in terms of Bessel functions in the local coordinate system of body i. The first term represents diffraction term with the A_i vector unknown and the second radiation terms. Kagemoto et. al (See [5]) have used

* 7-3-1 Hongo, Bunkyo-ku, Tokyo 113-0033, Japan

diffraction transfer matrix $[B_i]$ to obtain the vectors and consequently final stationary state. $[B_i]$ depends upon wave frequency and isolated body shape. Goo has employed Singularity Distribution Method to obtain the matrix of a body of arbitrary shape. A_i *(i=1..N)* must satisfy the following equations (see [5])

$$\{A_i\} = [B_i]\left(\{a_i\} + \sum_{\substack{j=1 \\ i\neq j}}^{N}\left([T_{ji}]^T\{A_j\} + \sum_{l=1}^{6}(-i\varpi\eta_{li})[T_{ji}]^T\{R_{li}\}\right)\right) \quad (i = 1\ldots N) \tag{2}$$

where a_i represents incident plane wave and T_{ji} transformation matrix with respect to coordinate system from the j-th body to the i-th body. With $\{A_i\}$ replaced by $[B_i]\{D_i\}$, we obtain the next equations. D_i is interpreted as total incident wave to the i-th body while A_i as diffraction from the i-th body.

$$\{D_i\} = \left(\{a_i\} + \sum_{i=1}^{N}\left([T_{ji}]^T[B_j]\{D_i\} + \sum_{l=1}^{6}(-i\varpi\eta_{li})[T_{ji}]^T\{R_{li}\}\right)\right) \quad (i = 1\ldots N) \tag{3}$$

2.2 Hydrodynamic force expression

An elementary force vector at a node where a part of the i-th body is attached to can be written as follows employing linearized Bernoulli's theory.

$$\{f_w\} = -i\rho\omega\iint_{S_p}(\phi_0 + \sum_{\substack{j=1 \\ j\neq i}}^{N}\phi_{sj} + \phi_{si}) \tag{4}$$

Though we omit writing the derivation of the final expression here, however, the final form can be formally written as follows.

$$\{f_w\} = -\varpi^2[\mu]\{\eta\} - i\varpi[\nu]\{\eta\} - i\rho\varpi\{D_i\}\times\{f_{el}\} \tag{5}$$

In this equation added mass matrix $[\mu]$, damping force matrix $[\nu]$ and $\{f_{el}\}$ are already obtained when computing singularity distribution around isolated body i.

2.3 Structural domain formulation

The equation of motion including elasticity of the structure is written as in Eq. (6) following the FEM procedure. In this equation, M represents mass matrix of structure, M_a added mass related to $\{\mu\}$, C_f damping matrix due to wave making which is related to $\{\nu\}$, C_s structural damping matrix, K_r restoring force coefficient due to hydrostatic force, K_s stiffness matrix of the structure and F_w wave exciting force written in terms of vector $\{D_i\}$.

$$\left(-\varpi^2([M]+[M_a]) - i\varpi([C_f]+[C_s]) + ([K_r]+[K_s])\right)\{\eta\} = \{F_w\} \tag{6}$$

In this process, sub-structure method is actually employed to reduce the number of unknowns related to nodal displacement without making any approximations or assumptions.

2.4 Final system of equations

$\{\eta\}$ and $\{D\}$ are solved simultaneously using Eq.(3) and Eq.(6). From these solutions, deflection shapes, member forces, dynamic pressure distribution, steady drifting forces, etc. are obtained.

3. ANALYTICAL METHOD

Some important characteristics are derived from the analytical method. The structure is modeled as a beam on elastic foundation (Fig. 1). Its dynamic response is expressed by Eq. 7 neglecting damping effects.

$$m\ddot{w} + EI\frac{\partial^4 w}{\partial x^4} + k_c w = f\sin(kx - \varpi t) \tag{7}$$

m represents mass including added mass per unit length, EI bending rigidity, k_c restoring force coefficient per unit length and f vertical wave force amplitude per unit length. Wave force is assumed to be periodic in lengthwise. Wave force amplitude f should be asymptotically equal k_c when only Froude-Kriloff force is considered.

The analytical solution is obtained as a summation of a particular solution and homogenous solutions. Except at the parts around ends of the structure, responses are dominantly expressed by the particular solution. The particular solution is written as in Eq.(8). It includes no mass force effects as the effect is small compared with other terms in low frequency domain and these equations are going to be mainly used for discussion in that domain. In Fig. 2 and Fig. 3, frequency response curve of vertical displacement at the center of the structure and that of bending moment at the center which is subsequently obtained are respectively shown according to Eq.(8) and Eq.(9). These solutions are characterizing fundamental response.

$$w(x,t) = \frac{f(\approx k_c)}{k_c + EIk^4}\sin(kx - \varpi t) \tag{8}$$

$$|M| = EI\left|\frac{\partial}{\partial x^2}w(x,t)\right| = \frac{k_c k^2}{k_c + EIk^4} \tag{9}$$

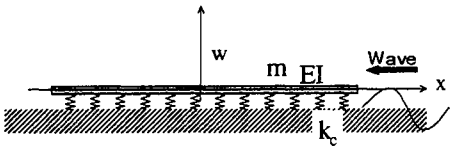

Figure 1:modeling of VLFS by analytical method

From this Eq. (9), we can obtain that the maximum bending moment M_{max} appears at characteristic wave number k_s.

$$k_s = \sqrt[4]{\frac{k_c}{EI}} \quad (10) \qquad M_{\max} = \frac{\sqrt{EIk_c}}{2} \quad (11)$$

At the characteristic frequency ϖ_s corresponding to k_s, where a relation as $\varpi_s^2 = kg\tanh(kh)$ exists in case of finite water depth (=h) case, the deflection amplitude is half of incident wave amplitude in Eq.(8). In this sense, the characteristic frequency ϖ_s is an important parameter which dominates the motion response as well as structural response.

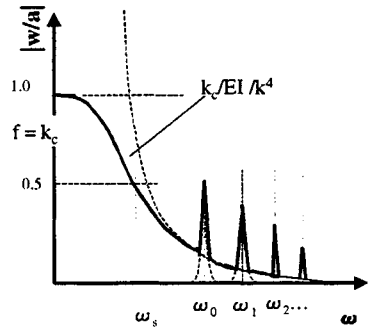

Figure 2: Schematic of frequency response curve of vertical displacement at the center of VLFS

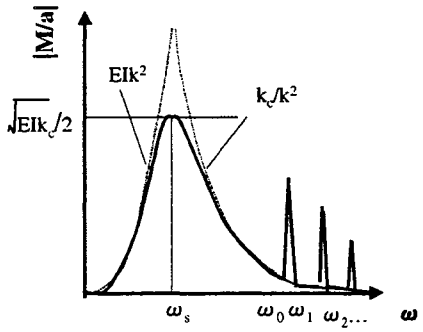

Figure 3: Schematic of frequency response curve of bending moment at the center of VLFS

Though these results contains no resonant response of elastic mode, elastic resonance frequencies are obtained by combining particular solution and homogeneous solution together with appropriate boundary conditions. Then the frequencies ϖ_n (n=1...) are given,

$$\varpi_n = \varpi_0\sqrt{1+\left(\frac{1+2n}{4}\right)^4\left(\frac{\lambda_s}{L}\right)^4} \quad (12)$$

where $\varpi_0 = \sqrt{k_c/m}$ is heave resonance frequency, λ_s is characteristic length defined as $2\pi/k_s$ and L is structure's length. From Eq.(12), it is understood that all the resonance frequency of elastic mode is above the heave resonance frequency. Heave resonance frequency ϖ_0 is another important parameter for dynamic response characteristics.

4. RESPONSE OF VARIOUS TYPE OF VLFS

In this section, four types of structures are analyzed by use of the numerical method and compared in their response characteristics. Main particulars of the four structures are summarized in Table 1. Important dynamic response characteristic parameters which are derived from the above analytical method are calculated and shown in the same table. In this report, wave incident angle is fixed as head sea condition.

Table 1: structure types and their characteristic parameters in real scale

	Type1	Type2	Type3	Type4
$L\times B$ (m)	914× 56	500×120	3000× 400	300×60
EI/B (Nm)	A 4.0E12 B 1.4E10	1.1E11	1.3E11	8.2E9
k_c (N/m³)	500	2000	2000	9800
λ_s (m)	1800 450	540	560	190
ϖ_s (rad/sec)	0.18 0.37	0.34	0.33	0.55
ϖ_s (rad/sec)	0.25	1.0	0.7	2.6

Type1: MOB type, Type2: Column supported,
Type3: Pontoon supported, Type4: pontoon type

4.1 MOB type structure (columns lower hull supported type)

MOB type structure consists of multiple unit structures, each of which has a dimension of usual semi-submersible rig. Units are connected at deck and/or lower hulls (Fig. 4). We call these two models as Model A and Model B, respectively. These structures are characterized by small restoring force coefficient, low heave resonant frequency and high rigidity in case of Model A.

In Fig. 5 and Fig. 6, these two models are compared with respect to response of vertical displacement and strain in deck. Responses are amplified by elastic resonant mode although the fundamental response expressed by Eq. (8) is small. Resonance responses are dominant for these types of structure.

In case of Model B, as it has smaller rigidity, the fundamental response is larger. This is consistent with the discussion in the last section. In addition, much larger resonant response appears in certain frequencies. The large resonant responses are excited when the wave length is long enough compared to the length between nodes of resonant mode. When the wave length is small compared to structure's length, only small resonant response appears.

It should be noted that though these calculations are made under head sea condition, according to the results calculated in oblique sea condition, the horizontal bending responses are too large, resulting in the lack of strength of these types of slender structures (see [2]).

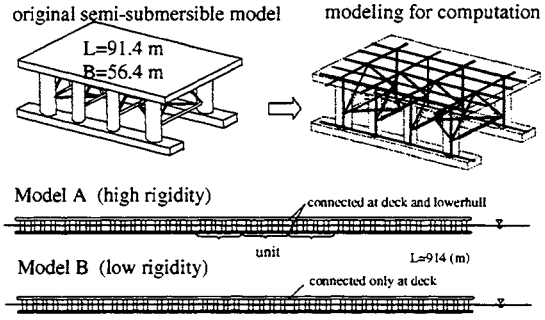

Figure 3: MOB type structure

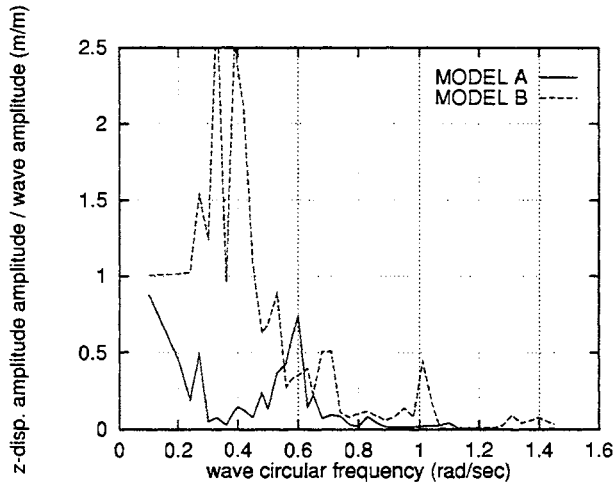

Figure 4: Vertical displacement at the center of MOB type structures

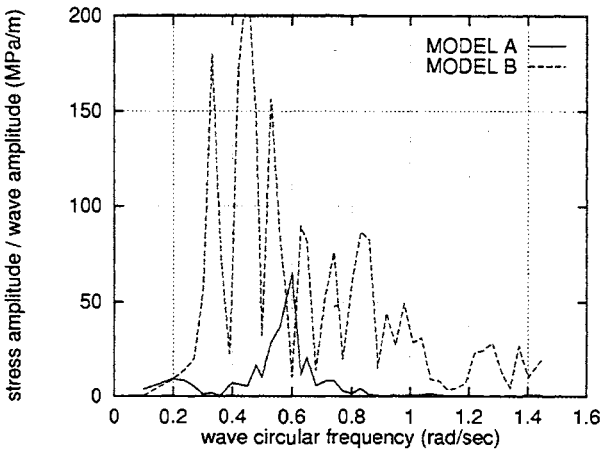

Figure 5: Stress in the upper deck at the center of MOB type structures

4.2 Column supported type structure

A deck structure which is supported on many columns is treated. Such a structure is called column supported type structure here. One of the example is that proposed for Kansai 1st International airport project. This structure is characterized by comparatively large restoring force coefficient. The present model is shown in Fig. 6. Although the values are written in experimental model scale in this figure, results are converted into real scale.

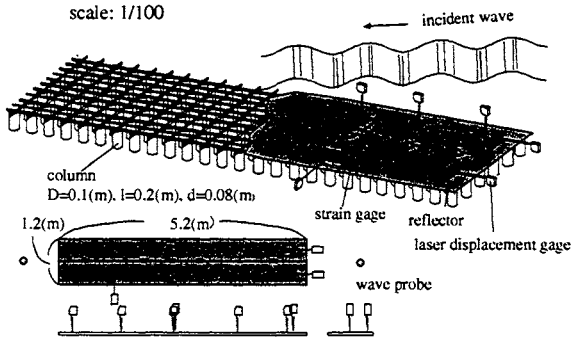

Figure 6: Column supported structure and experimental setup

In Fig. 7 and Fig. 8, frequency response curves of vertical motion and stress at the center of structure are shown with experimental results. The tank test was conducted at the University of Tokyo. The values are converted into the real scale ones both in abscissa and vertical axis. The calculated results show good agreements with the experimental results.

In case of column supported type structure, the most important response is explained by Eq.(9). That is, the resonant response at wave circular frequency 1.0 (rad/sec) is moderate.

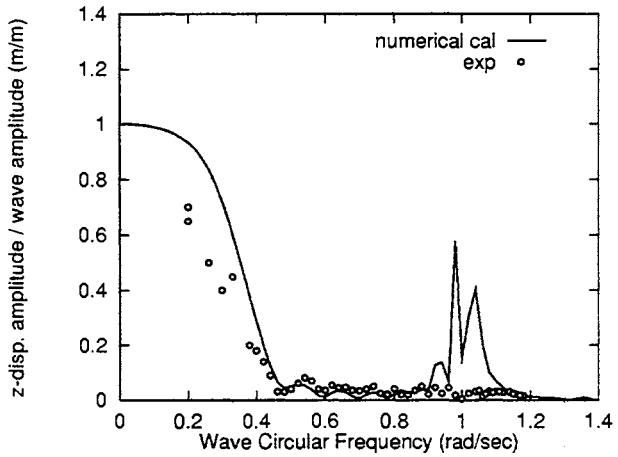

Figure 7: Vertical displacement at the center of column supported type model.

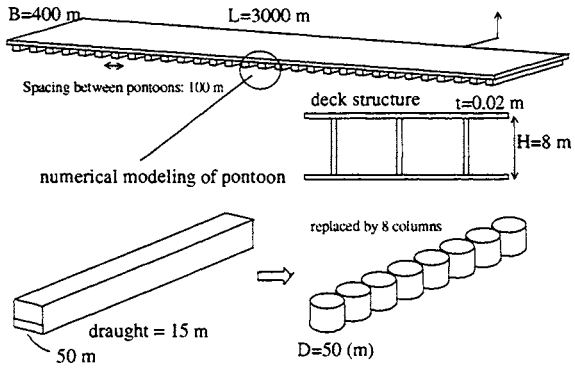

Figure 9: pontoon supported type structure

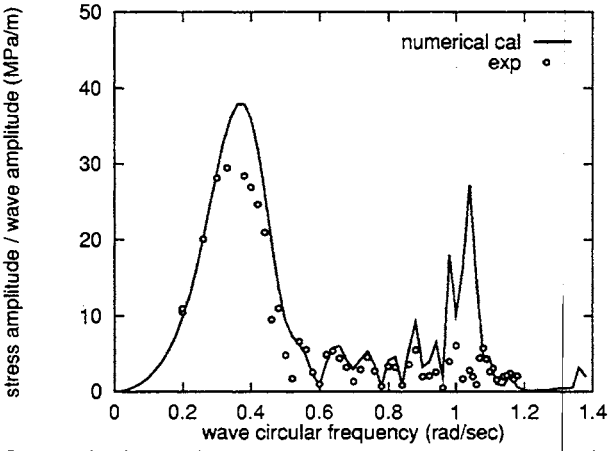

Figure 8: Stress in the upper deck at the center of clumn supported type model

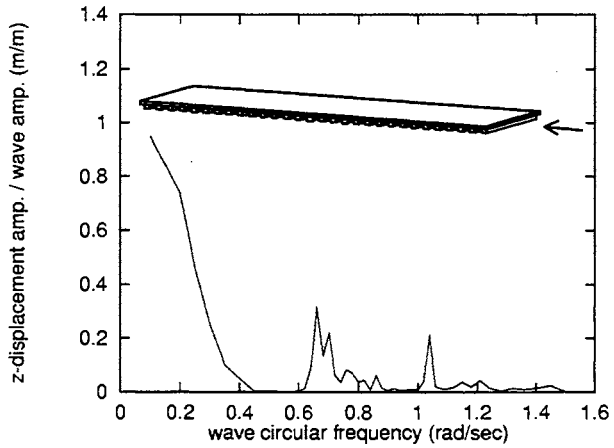

Figure 10: Vertical displacement at the center of pontoon supported type model

4.3 Pontoon supported type structure

A deck structure which is partially supported by multiple pontoon structures or pontoon supported type structure is discussed. The pontoons are hydrodynamically modeled as a set of several numbers of column (Fig. 9). The parameter k_c is almost the same as that of column supported type structure. In a sense, this type can be classified into the same category as column supported type structure, but of different column array configurations. The same response characteristics are expected as that of column supported type structure. However, this type is expected to be advantageous in terms of construction. Semi-submersible type VLFS has been concluded to be too expensive to be an alternative of reclamation, however, such ideas may reduce the cost of its construction.

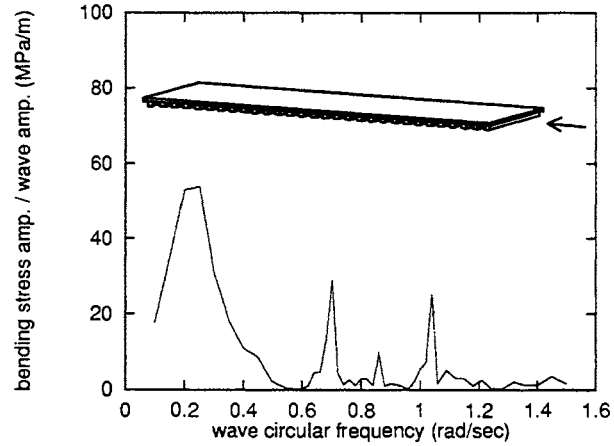

Figure 11: Stress in the upper deck at the center of pontoon supported type structure

Frequency response curves are shown in Fig.10 and Fig. 11, vertical displacement and stress, respectively. The response characteristics are almost the same as that of column supported type. The important response is fundamental response expressed by Eq.(9) and only small resonant responses appear though resonance frequencies exist in the curves. As the mass per unit area is larger that that of the calculated column supported type structure, the resonance frequencies have shifted to the lower frequency (Fig. 7, Fig. 8). The characteristic frequency shifts to the lower frequency as the bending rigidity EI is large due to large structure depth.

4.4 Pontoon type structure

Pontoon type structure or mat-like structure is now popular structure for study after the proposal by Mega float Technological Research Association. This type is characterized by large restoring force coefficient. The structure is 300 m long, 60 m wide, 2 m structure depth, with 0.5 m draught. Calculated results are compared with experimental results (See [6]) in Fig. 12 and Fig. 13. Note that both of the response are shown in model scale in these figure. The present numerical method holds good accuracy even if applied to pontoon type structure though 'imaginary cylinder assumption' is partially violated in an exact sense (see [4]).

In Fig. 13 and Fig. 14, the frequency response curves are shown. Though the exciting force expression in the analytical method may not be accurate anymore, however, it still gives a good insight to understanding of the response characteristics. The heave resonance frequency falls into high frequency (> 2.0rad/sec). As the characteristic frequency is also high, large fundamental response governs both responses. The displacement is over 0.1 even at wave period 6 sec.

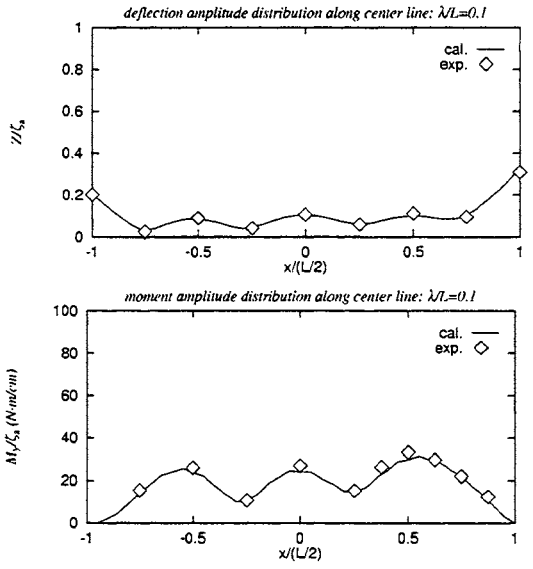

Figure 12: Distribution of vertical displacement amplitude and bending moment amplitude (See [6]).

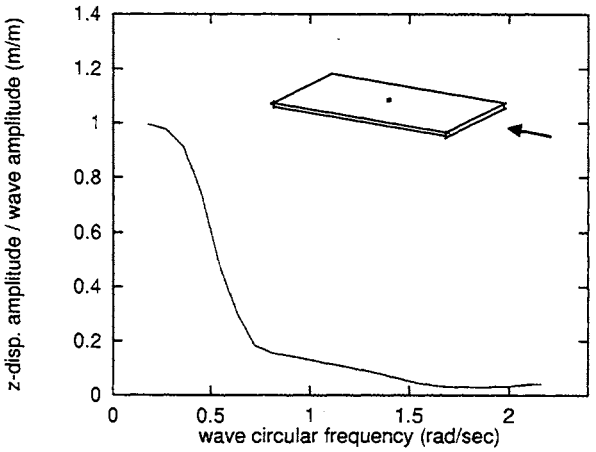

Figure 13: Vertical displacement at the center of pontoon type structure

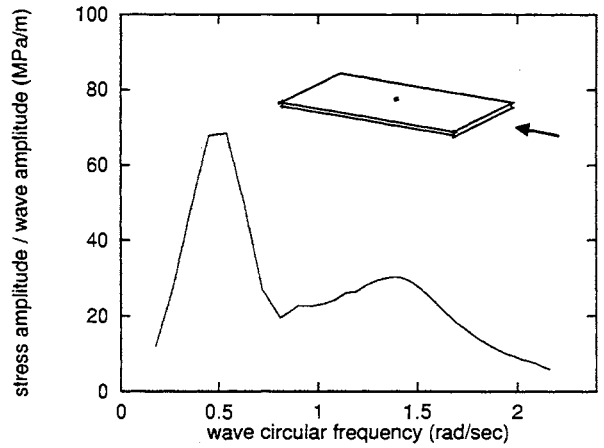

Figure 14: Stress in the upper deck at the center of pontoon type structure

5. PARAMETRIC STUDIES AND DISCUSSION

In the last sections, four types of floating structures were compared in terms of response. Column supported type structure showed good response characteristics. In this section, parametric studies focusing on column supported type are carried out to find out the important parameters governing the response and explain the response characteristics more clearly. Numerical method is used and results are evaluated quantitatively by calculating significant values in a certain wave spectrum as $H_{1/3}$ =10 m and T_{01}=12 sec.

The specifications are given as L=1000m, B=360 m, weight including structural weight per unit area 20000 N/m^2, structural depth of the deck H =6 m, plate thickness t = 0.025 m, column diameter D = 15 m and spacing between two adjacent columns l = 30 m. The deck rigidity per unit width EI_0/B = 1.0×10^{11} Nm^2/m and restoring force coefficient per unit area k_c/B =2000 N/m/m^2. The draught d is calculated 10 m.

In the first series, only deck rigidities are changed.

The structural depth is changed as H= 4.2, 6.0, 8.5, 13.5 m with plate thickness fixed. As a consequence deck rigidity EI_0 is multiplied by 0.5, 1.0, 2.0, 5.0 . In the next series, only column diameter is changed as D =7.5, 10, 15, 20 m. The restoring force coefficient is changed in accordance by the relation $k_c/B=\pi/4\left(D/l\right)^2 \rho g$. k_c/B is 500, 900, 2000, 3400 N/m/m^2 (Fig. 15). In order to support the fixed weight per unit area, draught d is also changed to 40, 22, 10, 6 m, respectively. In the last series, only spacing l is changed as 20, 30, 40, 50 m with the ratio of D to l unchanged. The value of deck rigidity and restoring force coefficient are fixed.

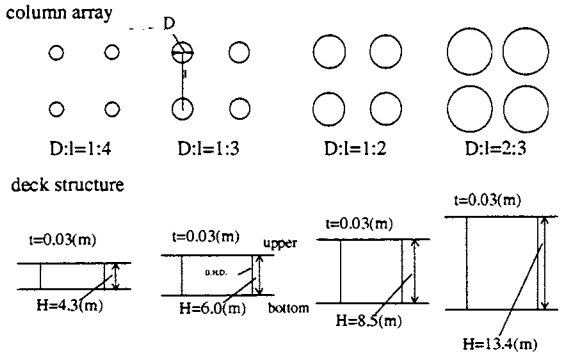

Figure 15: Two main parameters in the numerical experiment

5.1 Change of deck rigidity

In Fig. 16, frequency response curves of verical displacement of structures of various deck rigidities are presented. It is clearly shown that the response is reduced with the increase of deck rigidity. This tendency is explained by use of Eq.(11). That is, in higher frequency than the characteristic frequency, vertical displacement response is approximately in inverse proportion to deck rigidity EI. The characteristic frequency it self decreases as well. As a result, curves shift to the left or to the lower frequency range.

In Fig. 17, strain response characteristic changes are shown. Though the characteristic frequency becomes lower with the increase of deck rigidity, the maximum response is almost the same. This is explained by use of Eq.(11) together with the fact that I/B is approximately expressed by $H^2t/2$. The maximum strain value in the upper deck at the characteristic frequency is proportional to $\sqrt{k_c/t}$. The value does not depend on deck structural depth H. In this sense, the effect of deck rigidity increase is limited on the response improvement.

The resonance frequency at 0.8 (rad/sec) does not vary with the deck rigidity increase. Increase of deck rigidity gives little effects on the resonance.

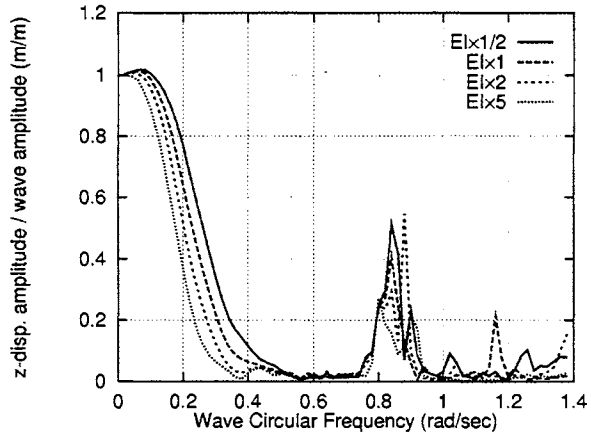

Figure 16: Frequency response curves of vertical displacement at the center of the structure for various deck rigidities.

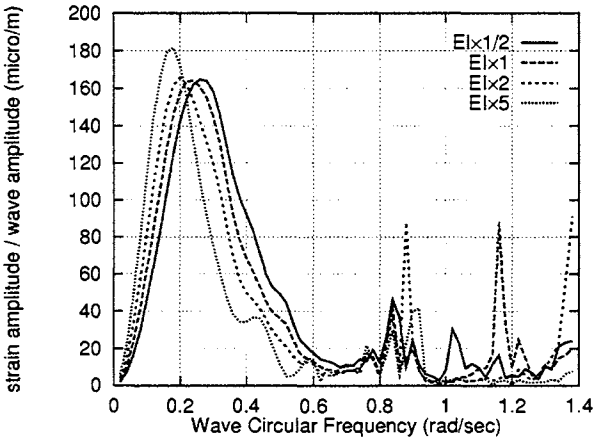

Figure 17: Frequency response curves of strain in the upper deck at the center of the structure for various deck rigidities.

5.2 Change of restoring force coefficient

Frequency response curves of vertical displacement are shown in Fig. 18. The decrease of restoring force coefficient has the same effects on the response characteristic change as the increase of deck rigidity. The vertical response basically increases in proportion to restoring force coefficient k_c as is explained from Eq.(8).

Another effect comes from change of resonance frequencies. The resonance frequencies are expressed by Eq.(12). In this equation, ϖ_0 or k_c has a strong effect while the contribution from the term in the radical sign is small as the structure's length is far larger than the characteristic length.

Fig. 19 shows frequency response curves of strain in the upper deck. The strain due to the maximum bending moment at the characteristic frequency and the characteristic frequency itself increases in accordance with the increase of restoring force coefficient as is predicted by Eq.(10) and Eq.(11).

It is concluded that restoring force coefficient dominates the response characteristics as it has two strong effects. One is fundamental response change represented by Eq.(8) and (9). The other comes from resonance frequency change as in Eq.(12).

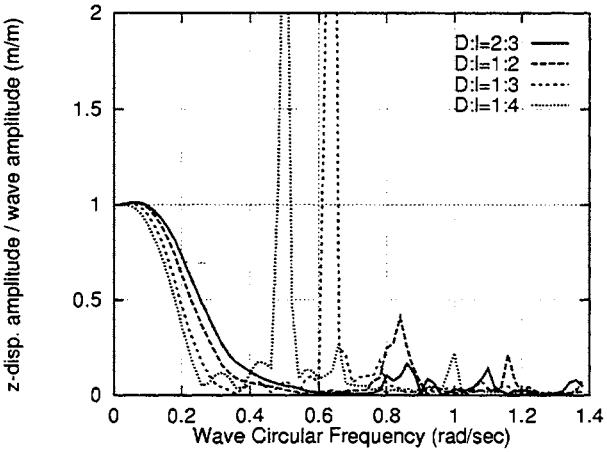

Figure 18: Frequency response curves of vertical displacement at the center of the structure for various restoring force coefficients.

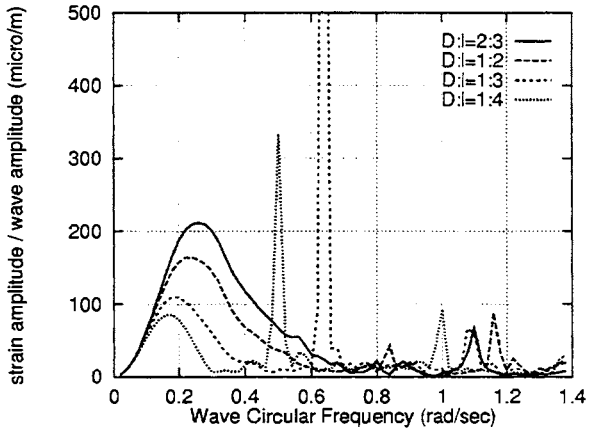

Figure 19: Frequency response curves of strain in the upper deck at the center of the structure for various restoring force coefficients.

5.3 Change of column spacing

In Fig. 20, strain responses are shown for various column spacing l. As the dominant parameter k_c or second dominant parameter EI keep the same value in these cases, the fundamental response explained by Eq.(8) or Eq.(9) does not vary. The outstanding change is shift of sharp peaks to the lower frequency as the column spacing increases. These peaks are not explained by resonance frequency of elastic mode but explained by hydrodynamic resonance frequency where a particular standing wave occurs. Incident wave length at these frequency coincides with twice the length between two diagonally adjacent columns, or $\lambda = 2\sqrt{2}l$ (see [7]).

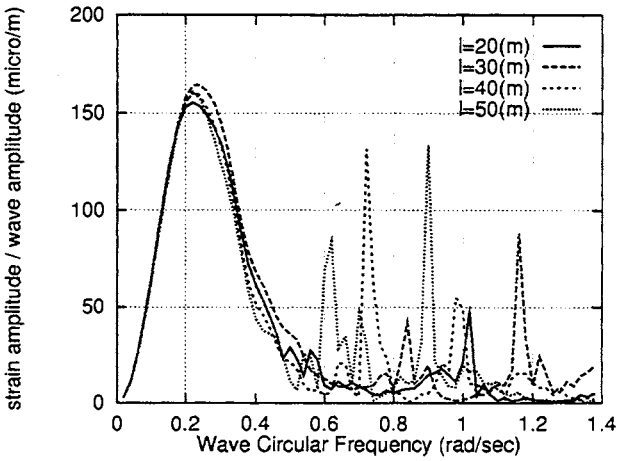

Figure 20: Frequency response curves of strain in the upper deck at the center of structure for various column spacings.

5.4 Discussion

When designing VLFS, the response must be discussed with environmental condition or wave spectrum taken into account. In this study, wave spectrum of $H_{1/3}$=10m, T_{01}=12 sec is used, supposed that the structure is set up in open sea. All the responses are compared in the significant value as shown in Table 2 and Table 3. The responses become small as the deck rigidity increases at the ratio D:l=1:2 or 2:3. Such tendency that the response becomes small when deck rigidity is either high or low at the ratio D:l=1:3 or 1:4 can be seen in Table 3.

Table 2: Comparison of significant value of vertical displacement in wave spectrum $H_{1/3}$ =10m, T_{01} =12 sec; EI_0/B = 1.0×10^{11} (Nm^2/m).

	0.5× EI_0	1.0× EI_0	2.0× EI_0	5.0×EI_0
D:l =2:3	0.91m	0.61 m	0.39 m	0.22 m
D:l =1:2	0.67m	0.44 m	0.35 m	0.24 m
D:l= 1:3	1.85m	4.56 m	9.03 m	2.34 m
D:l= 1:4	4.34m	3.98 m	2.63 m	2.17 m

Table 3: Comparison of significant value of strain in the upper deck in wave spectrum $H_{1/3}$ =10m, T_{01} =12 sec; EI_0/B = 1.0×10^{11} (Nm^2/m).

	0.5× EI_0	1.0× EI_0	2.0× EI_0	5.0×EI_0
D:l =2:3	580μ	310μ	410μ	290μ
D:l =1:2	380μ	360μ	240μ	160μ
D:l= 1:3	220μ	400μ	1200μ	270μ
D:l= 1:4	360μ	500μ	250μ	130μ

Generally, we need to consider the relative position of response frequency response curve to wave spectrum curve in the horizontal axis as well as in the vertical axis for minimize the significant value. So far, there have been two kinds of important responses discussed. One is fundamental response represented by Eq.(8) and (9). And the other is resonant response represented by Eq. (12). In other words, two frequencies ω_s and ω_n are key parameters, both of which are well influenced by the parameter k_c.

According to the results in the tables, there seems to be two choices for VLFS to be realized. One is to settle ω_s in the lower frequency to the wave spectrum and ω_n in higher frequency. The other is to settle both ω_s and ω_n in the lower frequency. In case of structures of $D:l$=1:2 or 2:3, ω_n are in high frequency as ω_0 is comparatively high. These correspond to colmun supported type. In case of structures of $D:l$=1:3 or 1:4 with large deck rigidity EI, ω_n are high. As a result, no large resonant responses appear and the responses become small. At the same $D:l$ ratio and low deck rigidity EI, ω_n shifts the lower of the wave spectrum. However, according to Eq.(12), the structure must be generally long enough compared to the characteristic length for this to be realized. These correspond to column lower-hull supported type

It can be seen that the good response is obtained when the ratio $D:l$ is 1:2. This is explained as follows. The fundamental response which is governed by quasi-static response expressed by Eq. (8) and (9) becomes smaller when k_c is smaller. However, to avoid large resonant response k_c must be large enough. The k_c at the ratio $D:l$=1:2, calculated 2000 (N/m/m^2), falls into just the mid-point of these two regimes.

As to the methodology of design of VLFS, the choice of heave resonant frequency ϖ_0 should be set up at first. The restoring force coefficient k_c is subsequently decided. Deck rigidity EI is decided by considering fundamental response. The increase of deck rigidities generally drecreases the response. Column spacing l gives only small influence on response characteristics.

5 CONCLUSIONS

We studied response characteristics of various types of VLFS. First, four types of VLFS were analyzed by use of numerical method, analytical method and tank test. In order to clarify furthermore the characteristics, additional numerical experiments were conducted. We have made the following conclusions.

(1) Response characteristics of four types of structures are almost explained by use of analytical method. In this method, the whole structure is modeled as a beam on elastic foundation.

(2) The most important parameter that governs the response characteristics has proved to be restoring force coefficient k_c. The increase of the parameter leads to the shift of frequency response curves to the higher both in vertical axis and horizontal axis. It also strongly influences the resonance frequencies. The second important is deck bending rigidity EI. The increase of it shifts the frequency response curves to the lower, however, the change of maximum stress response in the upper deck does not occur as it is dependent on deck plate thickness t but independent of EI.

(3) The present analysis method which was originally developed for semi-submersible type VLFS has proved to be valid even for pontoon-type structure.

As to structural design of VLFS, we have concluded.

(4) There are two choices for VLFS in open sea. One is column supported type and the other is MOB type or column and lower-hull supported type structure.

(5) The decision of structural configuration parameters k_c, EI, l, should be made in the order named. Here, k_c is the restoring force coefficient, EI deck rigidity and l column spacing.

We especially studied column supported type structure.

(6) The smaller restoring force coefficient k_c is favorable from the view point of fundamental response while the larger k_c is expected in order to avoid the large resonant response. The most advantageous response characteristics are obtained at the best trade off point between these two effects. In the present results, such point was realized when the ratio of column spacing length to the column diameter was 2.0 which corresponded to restoring force coefficient per unit area of 2000 (N/m/m^2).

Acknowledgement: The tank test at the University of Tokyo was carried out with help of Mr. Ohashi and Mr. Odaira. The authors would like to express their thanks.

References

[1] K.Iijima, K.Yoshida and H.Suzuki *Hydrodynamic and Hydroelastic Analyses of Very Large Floating Structures in Wave. OMAE'97, Vol.VI*, 1997

[2] K.Iijima, K.Yoshida and H.Suzuki *Structural Response Characteristics of Semi-submersible V.L.F.S. in Waves and Fundamental Guideline to the Stuructural Design. J. of SNAJ, Vol.183 (in Japanese)*, 1998

n[3] H. Suzuki and K.Yoshida *A Consideration on the Dynamic Behavior of Large Scale Floating Structures. J. of SNAJ Vol.178 (in Japanese)*, 1995

[4] J.S.Goo and K.Yoshida *A numerical Method for Huge Semisubmersible Response in Waves. SNAME Transactions, Vol.98*, 1990

[5] H.Kagemoto and Dick K.P.Yue *Interactions among Multiple Three-Dimensional Bodies in Water Waves.J.Fluid Mech.Vol.166*, 1986

[6] K. Yago and H. Endo *Proc. Model Experiment and Numerical Calculation of the Hydrodynamic Behavior of Mat-like VLFS. Int. Workshop on Very Large Floating Structures, VLFS '96, Hayama.* Ship Research Institute, Japan, 1996.

[7] K.Yoshida *et.al Hydrodynamic Interaction Effects on Wave Exciting Force in Large Floating Structures (2nd Report). J. of SNAJ, VOL176 (in Japanese)*, 1994

PROCEEDINGS OF THE THIRD INTERNATIONAL WORKSHOP ON VERY LARGE FLOATING STRUCTURES
(VLFS '99), VOL. I, EDS. R.C. ERTEKIN & J.W. KIM, 22-24 SEPTEMBER 1999, HONOLULU, HAWAII, USA

CONCEPTUAL DESIGN AND HYDROELASTIC BEHAVIOR OF A 4000-M SEMI-SUBMERSIBLE TYPE VLFS

Kentaro Kobayashi
Sumitomo Heavy Industries, Ltd.*

Katsunori Shimazaki
NKK Corporation**

Koichiro Yoshida and Kazuhiro Iijima
University of Tokyo***

ABSTRACT

A conceptual design for a 4000-meter-class floating airport supported by a great number of columns is proposed. With dimensions of 4000 meter long and 650 meter wide, the proposed semi-submersible type VLFS has approximately 2800 columns. For the hydroelastic analysis in waves, a numerical computation method which has been developed by part of the authors since 1997 are adopted. The whole structure is modeled and analyzed as three-dimensional frame with full considerations of structural hydroelasticity and hydrodynamic interactions among columns. The result shows the applicability of the computational method for very large floating structures with numerous columns and also shows that the semi-submersible type is feasible for a 4000-m-class VLFS as well as the pontoon type.

1. INTRODUCTION

Very large floating structures have a wide variety of applications in view of ocean space utilization, such as floating airports, harbor terminals, energy-related facilities, and so on. Particularly, a floating airport might be a challenging and possible application of VLFS in future.

Representatively, there are two types of VLFS; a pontoon type and a semi-submersible type. The pontoon type VLFS has been eagerly investigated in the "Mega-Float" project in Japan. A number of studies have been carried out both on the theoretical estimation of hydroelastic responses and on the experimental research with the large floating model(300 x 60 x 2 meters) on the real sea.

The semi-submersible type VLFS consists of a large number of columns and a relatively thin upper deck structure mainly. Some kind of semi-submersible type VLFS may contain lower hull structures connecting columns.

In view of construction cost and maintenance cost, the pontoon type VLFS is advantageous comparing with the semi-submersible type due to the simplicity of the structure. However, considering the proven good seaworthiness of semi-submersible offshore platforms, the semi-submersible type VLFS can be a powerful alternative for the pontoon type VLFS especially for applications which should be placed in fierce sea condition.

On the contrary, the pontoon type VLFS should suffer large exciting forces and drift forces due to waves. Therefore, as possible solutions, it is said that pontoon type VLFSs are suitable for rather calm sea or bay. If necessary breakwaters should be constructed to reduce the severe wave condition. In the case of deep sea, open to ocean, the construction of breakwaters should be very difficult and highly costly.

In this paper, considering these conditions, a conceptual design is carried out for semi-submersible type VLFS as a 4000-m-class airport which might be placed in deeper depth and rather severe sea. Using the new calculation method for column-supported type VLFSs, hydroelastic responses in waves are computed and its dynamic characteristics is investigated. The results are briefly compared with those of the pontoon type VLFS.

* 19 Natsushima, Yokosuka 237-8555, Japan
** 1 Kumozukokan-cho, Tsu, Mie 514-0393, Japan
*** 7-3-1 Hongo, Bunkyo-ku, Tokyo 113-0033, Japan

2. CONCEPTUAL DESIGN

One possible application of VLFS in near future is said to be a floating airport in Japan. As an example, therefore, a conceptual design for a semi-submersible type VLFS has been made on a 4000-m-class floating airport.

Fig. 1 shows the conceptual design and layout of floating airport with a runway length of 3500 meters. It consists of a floating runway part and a terminal part. The dimensions of the floating runway structure are about 4000 m in length, 650 m in breadth. The terminal area is to be 2000 m x 700 m approximately.

Because the terminal buildings and other airport facilities on the terminal area could be massive and heavy, a column-supported structure might not be suitable for the terminal structure. A pontoon type structure or a reclamation may be adopted for the terminal part. Therefore, for the first step, only the runway part has been designed separately as the column-supported semi-submersible type VLFS.

Fig. 2 shows the column and deck structure size of the runway part. The thin deck with depth of 4 m is supported by equally-spaced columns. The columns have dimensions of 9.5 m in diameter, 13 m in draft, and are placed 30 m apart from each other. A simple cylinder shape is selected for columns in order to simplify hydrodynamic calculations, and construction too. Number of columns in the lengthwise side is assumed 132, and 21 in the breadthwise side. This amounts to 132 x 21 = 2772 columns in total. The dimensions of VLFS with 132 rows and 21 lines of columns become 3960 meter in length, 630 m in breadth. The air gap under the deck structure is only 4m, which might be relatively small and minimum for actual design. However this value can be modified easily and scarcely influence dynamic responses of the VLFS.

The rigidity and the depth of deck structure are also designed on the minimum design basis, so as to reduce the construction cost. The bending rigidity of the 4m-depth deck with 20mm-thick deck plates is estimated as $EI/B = 3.55E09\ kgfm^2/m$.

The total displacement of 2772 columns is about 2.6 million tons. The hull steel weight is estimated to be 2.1 million tons. It can be said therefore that this displacement is sufficient to support the hull steel weight plus the weight of pavement with asphalt or concrete.

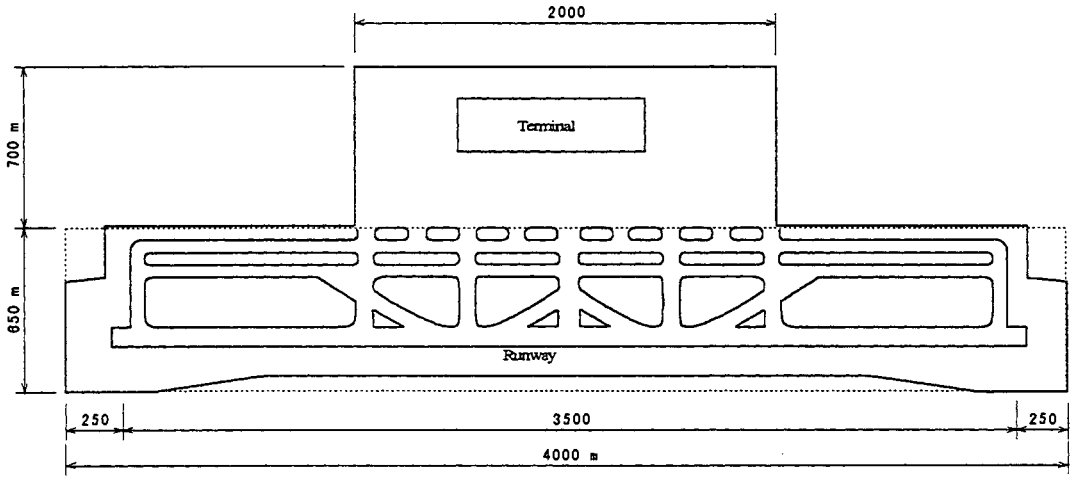

Fig.1 Conceptual design of a 4000-m-class floating airport

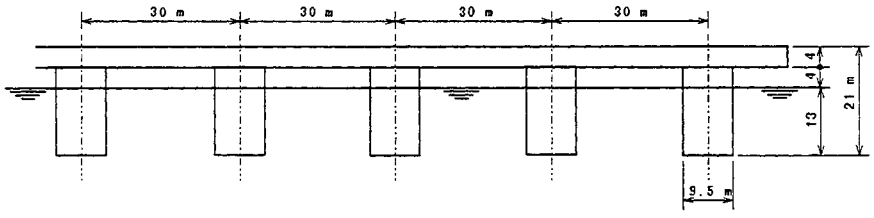

Fig. 2 Conceptual design of the runway part as a semi-submersible type

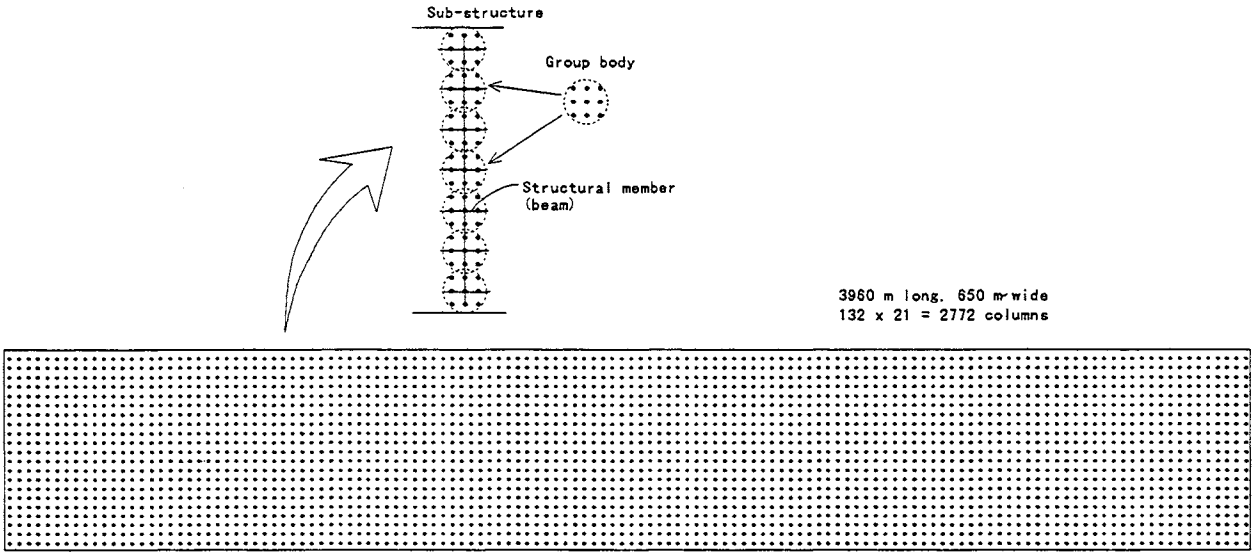

Fig. 3 Calculated model with 2772 columns and definition of sub-structure and group body

3. NUMERICAL ANALYSIS METHOD

The numerical analysis code, which is applied to this study, is based on the theory which has been developed by a part of the present authors[1]. The theory employs "sub-structure" method and "group body" concept newly introduced in an extension of Goo ' s method[2]. Although the theory itself is developed especially for large scale floating structures, it has almost no limitations on the shape or configuration of the structure in application. In other words, it can be well applied to almost all kinds of floating structures, such as semi-submersible rigs, TLP, barge type floating structures, MOB like semi-submersible structures, etc.

The present method assumes the group body as a rigid body hydrodynamically, which means that radiation problem of group body due to its elastic motion is not considered. However, the present method has the significant advantage of that it can model the structure as three dimensional frame. Comparing with another methods which calculate only the vertical force as external forces and model the structure as a plate, the present method can consider all degrees of forces and moments including axial force, horizontal force, vertical force, axial torsion, horizontal moment and vertical moment.

As a consequence, member forces of all degrees are directly obtained, which is necessary for the zoom-up analysis in the next stage of structural design. Nodal displacements, deflection shape of the whole structure, member force, dynamic pressure distribution, steady drifting force and wave elevation distribution can also be computed by this numerical code.

Fig.3 illustrates the calculated model of the conceptual design with 2772 columns, and also shows the sub-structure and the group body adopted for the present calculation.

Table 1 Principal particulars of the semi-submersible type and pontoon type VLFS

	Semi-submersible type	Pontoon type
L (m)	3960	3960
B (m)	650	650
D (m)	4 (w/o column)	7
d (m)	13	2
Displacement (ton)	2618000	5330000
Diameter of column (m)	9.5	—
Number of columns	2772	—
Air gap (m)	4	—
EI/B ($kgfm^2/m$)	3.55E09	8.54E09

4. DYNAMIC RESPONSES IN WAVES

Computations were executed on wave-induced hydroelastic responses of the designed 4000-m-class column-supported VLFS using the above mentioned numerical code. The breadth is slightly extended from 630 m to 650 m. To make a comparison between the semi-submersible type and a pontoon type VLFS, responses of a corresponding pontoon type VLFS which has the same horizontal dimensions(3960 m x 650 m) were also carried out. As the numerical analysis code

for the pontoon type VLFS, Ohmatsu's method[3] was adopted. Structural properties of the both VLFSs are summarized in Table 1.

4.1 Vertical displacement distribution

Some of calculated results of vertical displacement due to the hydroelastic response in regular waves are shown in Fig.4. The wave direction is assumed to be 0 degree, which corresponds to head waves propagating along the longitudinal side of the structure.

From these figures, we can generally find very small vertical displacements of the semi-submersible type VLFS along its center line. Except at both ends(leading and trailing edges) of the structure and the case of T=8 second, response amplitude ratios to the unit wave amplitude are no more than 0.05.

Responses of the corresponding pontoon type VLFS are shown in the same figures by dotted lines for comparison. In most cases except T=8 second, the pontoon type shows larger responses than the semi-submersible type, with the ordinate level of 0.2 in middle part of the structure.

4.2 Vertical displacement RAO

Response amplitude operators of vertical displacement at midship and at front end of the VLFSs are plotted in Fig.5 vs. wave period. Curves with marks are showing responses of the semi-submersible type and others the pontoon type. From this figure, again, vertical displacements of the semi-submersible type are found to be much smaller than that of the pontoon type except around particular wave frequency; T=8 second.

This wave period corresponds to the natural period of heave motion of the conceptual design. In the case of pontoon type, the heave natural period becomes long enough due to the enormous hydrodynamic added-mass. However, the column-supported semi-submersible type, which has relatively small added-mass due to columns, may have heave natural period around existing wave period in the ocean.

At the natural period, the magnitude of responses depends on the damping. In the present calculation, only wave damping and small viscous damping were taken into account. Although the estimated responses at this period are larger than those of the pontoon type, the magnitude at around midship is comparable with the pontoon type. In general, it can be said that the column-supported semi-submersible type VLFS has a excellent property about hydroelastic behavior in waves.

4.3. Responses in oblique waves and structural response

The instantaneous displacement distribution in an oblique wave, for instance T=7 second and wave direction=45 degree case, is shown in Fig.6 together with that in a head wave. The responses in oblique waves are also found to be small.

As an example of the structural responses in oblique waves, vertical bending moments acting on structural members along center line, port and starboard lines are shown in Fig.7.

5. CONCLUSIONS

The proposed column-supported semi-submersible type VLFS is a preliminary concept design for a 4000-m-class floating airport. With about 2800 simple columns and a 4-m-depth deck, a 3960 m x 650 m runway part was designed under the minimum requirement basis which implies smaller number of columns, lesser deck thickness, sufficient displacement, and minimum air gap. Undoubtedly there should be an optimum design for these parameters and further study should be made. However, as the preliminary study for this kind of problem, the dynamic behavior of the designed VLFS in waves was investigated using the hydroelastic numerical analysis considering large number of columns, its interactions, and 3-D frame structural responses.

From the calculated responses and comparing with those of the corresponding pontoon type VLFS, the following conclusions are made.

(1) The column-supported semi-submersible type VLFS shows very small hydroelastic responses(vertical displacement) in waves. Except the case of heave resonance, response amplitude ratios are no more than 0.05 at middle most part of the structure. On the other hand, the corresponding pontoon type VLFS shows much larger responses even at middle part than the semi-submersible type.

(2) The column-supported semi-submersible type VLFS may have a heave natural period within the existing wave period range. In the case of resonance, the vertical displacements can be significant. However the magnitudes in the middle part of VLFS are expected to be roughly on a equal level with that of the pontoon type.

(3) The column-supported semi-submersible type VLFS can be one of good alternatives for pontoon type VLFSs especially in view of dynamic responses in waves.

REFERENCES

[1] K. Iijima, K. Yoshida and H. Suzuki. "Structural Analyses of Very Large Semi-submersibles in Waves". Journal of the Society of Naval Architects of Japan, No.181, pp.281-288, 1990

[2] J. S. Goo and K. Yoshida. "A Numerical Method for

Huge Semi-submersible Responses in Waves". SNAME Transactions, Vol.98, 1990

[3] S. Ohmatsu. "Numerical Calculation of Hydroelastic Behavior of Pontoon Type VLFS in Waves". Proc. of 17th Int. Conf. on OMAE, Lisbon, 1998

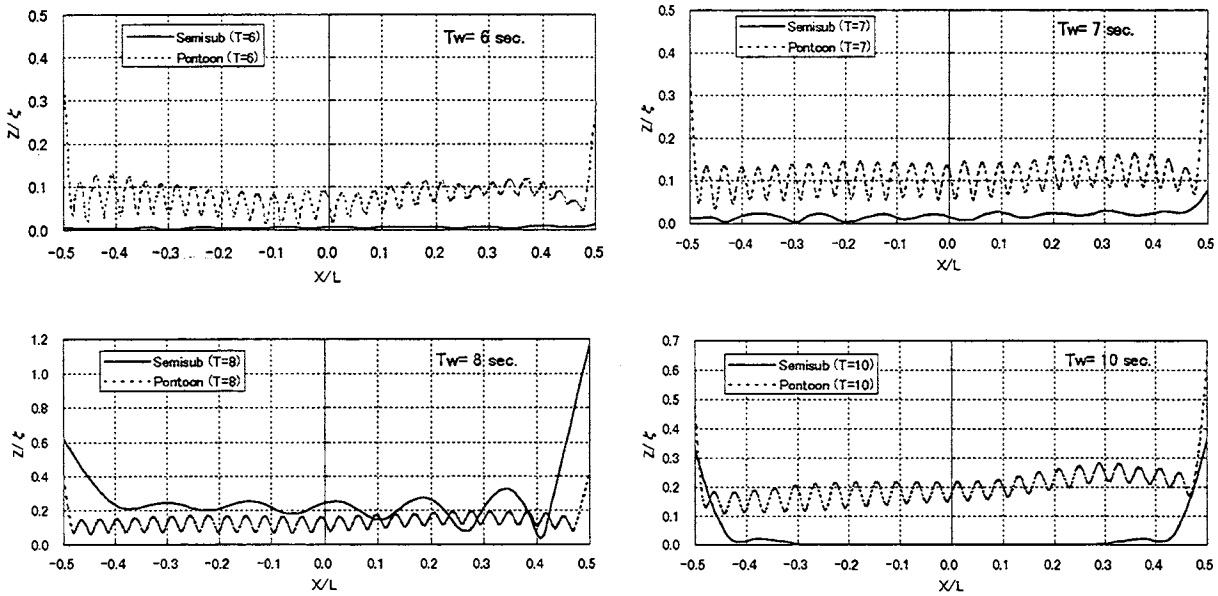

Fig.4 Amplitude distributions of vertical displacements at centerline in head waves

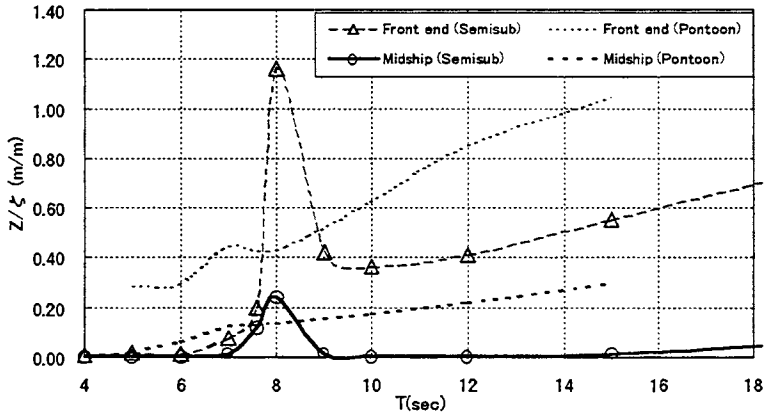

Fig.5 RAO of vertical displacements at midship and front end in head waves

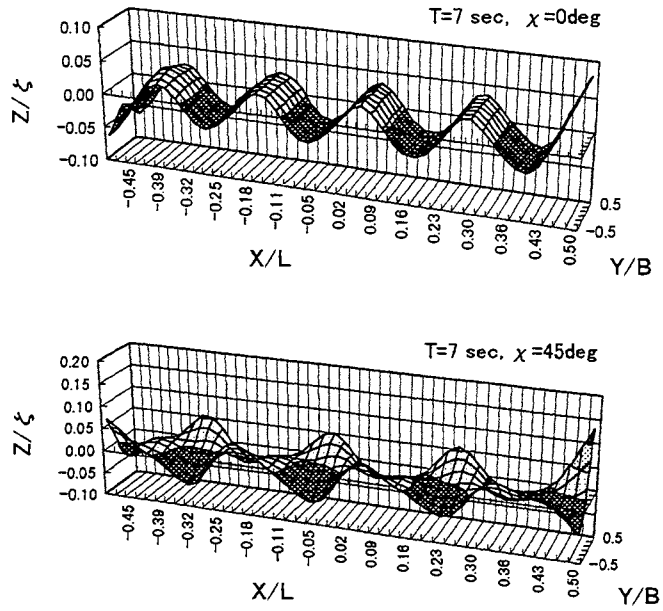

Fig.6 Instantaneous displacement distribution of the semi-submersible type in head and oblique waves

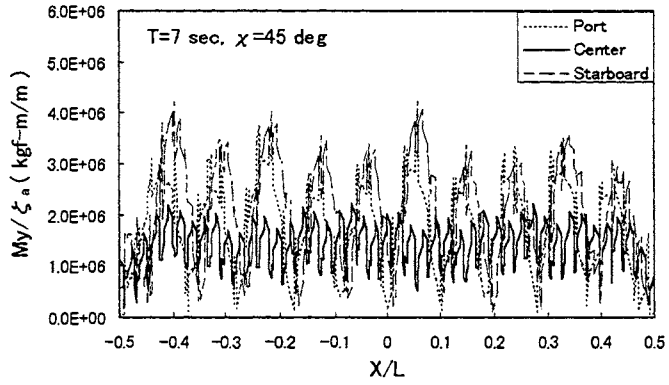

Fig.7 Vertical bending moment acting on structural members of the deck of semi-submersible type

PROCEEDINGS OF THE THIRD INTERNATIONAL WORKSHOP ON VERY LARGE FLOATING STRUCTURES
(VLFS '99), VOL. I, EDS. R.C. ERTEKIN & J.W. KIM, 22-24 SEPTEMBER 1999, HONOLULU, HAWAII, USA

EFFECT OF ATTACHMENT OF A HORIZONTAL/VERTICAL PLATE ON THE WAVE RESPONSE OF A VLFS

Hidemi Ohta, Tadashi Torii, Nobuyuki Hayashi Nippon Steel Corporation*, Japan
Eiichi Watanabe, Tomoaki Utsunomiya Kyoto University, Japan
Kinji Sekita, Shunji Sunahara Tokai University, Japan

ABSTRACT

Recently, in the study on the very large floating structure(VLFS), the tendency has been clarified that elastic deformation predominates in the vertical displacement of the structure due to waves and that displacement is more pronounced at edges than at the interior of the structure. The present concept for displacement reduction is to construct breakwaters around the structure. However, depending on the conditions involved, breakwater construction can be both difficult and costly. Furthermore, breakwater construction can cause environmental problems such as disturbing tidal current. Accordingly, the authors proposed the attachment of a horizontal/vertical plate and investigated its effect at an edge of the floating structure. As a result, it has been clarified that the attachment of these devices can reduce the vertical displacement of the floating structure.

1. INTRODUCTION

When a very large floating structure is to be constructed in a bay, the basic concept is that breakwaters are constructed and a pontoon type floating structure is set afloat in a calm sea area behind the breakwaters and moored with dolphins. This method is economical so far as it is constructed within a bay. However, the displacement of a VLFS due to waves is characterized in that the elastic response predominates and the vertical response at both ends is comparatively larger than that in the interior of the structure. If breakwaters with high wave transmission are adopted in consideration of environmental protection, the response at the ends may become an obstacle to the operation of the facilities mounted on the floating structure. When constructing a VLFS on a coast facing the open sea, such cases may occur in which the construction of breakwaters with great wave dissipation effect is uneconomical. It is, therefore, necessary to develop a vertical displacement reduction method which can be applied to such cases where the wave dissipation effect of breakwaters is small or there are no breakwaters constructed. Accordingly, for reduction of vertical displacement of the structure at its ends and in its interior, study has been made on various methods to be applied to the ends of floating structure. In the present paper, two methods, one employing a horizontal plate, and the other employing a vertical plate, which have proved effective in experiment are described.

2. EXPERIMENT

The present paper describes the results of experiment on vertical plate which was conducted in Nippon Steel's wave tank and the results of experiment on horizontal plate which was undertaken in Tokai University's wave tank.

2.1 Experimental model

To simulate a VLFS of about 5m in height and 1,000m in length which is of steel structure, the scale of experimental model was set to 1:100 in consideration of the performance of wave generator and others. Fig.1 schematically shows the model used and Table 1 gives the principal particulars of the model. The model was constructed by pasting 40 mm thick polyurethane foam (specific gravity: 0.027) to the bottom of 15 mm thick vinyl chloride foam (Young's modulus: 13,000kgf/cm^2, specific gravity: 0.7) as a structural material and arranging 1.21kgf/m chains in four lines on the vinyl chloride foam for draft adjustment.

Fig.2 shows the model in more detail. Three vinyl chloride plates were pasted together using a solvent. The polyurethane foam cut to 80mm long pieces was attached with a clearance of about 2 mm. To reduce the effect of this clearance on the fluid, 0.5mm thick vinyl chloride film was pasted to one side of the polyurethane foam so as to cover the clearance. The side where the displacement reducing device was bolted was reinforced with aluminum plate. In the center, a jig for mooring was installed.

* Mail: 6-3 Otemachi 2-Chome, Chiyoda-ku, Tokyo, 100-8071 E-mail: hayashi.nobuyuki1@eng.nsc.co.jp

As shown in Fig.3, the mooring device consists of a steel plate (36mm wide) and a supporting base made of aluminum (50mm wide) which are installed in such a manner that rotation and vertical displacement are not restrained. This mooring device was installed in the center of the floating model (in 2 places – one each on the left and right sides).

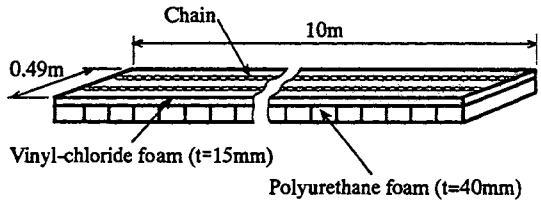

Fig.1 Schematic view of the model

Table.1 Principal particulars of the model

	Full scale	1/100 Model
Length	1000 (m)	1000 (cm)
Width	49 (m)	49 (cm)
Depth	5.5 (m)	5.5 (cm)
Draft	2.6 (m)	2.6 (cm)
Stiffness (EI/Width)	3.66×10^{6} (tf·m^2)	3.66×10^{3} (kgf·cm^2)

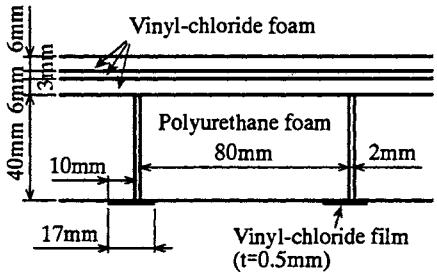

Fig.2 Cross section of the model

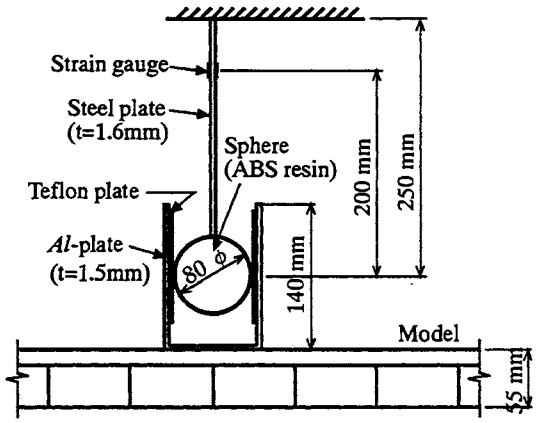

Fig.3 Cross section of the mooring device

2.2 Type of experiment

The experimental conditions are shown in Table 2. For regular incident waves, the wave period was changed from 5 to 19 sec simulating the actual sea conditions.

For reduction of displacement, the horizontal plate attached to the model(attached horizontal plate), horizontal plate fixed on the tank bottom(fixed horizontal plate) and plate installed vertically (attached vertical plate) which are shown in Fig.4 were used. For the fixed type, the plate which was supported from the bottom of the tank independently from the floating model was prepared. The attached horizontal plate was of such construction in which the attaching jig made of aluminum (40mm wide, 1.5mm thick) was bolted to the end of the floating model and the polypropylene plate (5mm thick, specific gravity: 0.9) was bolted to that jig. The buoyancy was adjusted by attaching lead plates to the polypropylene plate. For the attached vertical plate, the polypropylene plate (6mm thick) was bolted to the top surface at the end of the wave incident side of the model. Horizontal plates of four different lengths (B=19, 38, 57 and 76cm) were prepared and installed at three different depths of water (d=8, 15 and 22cm). Two types of vertical plates (d=15 and 30cm) were prepared. As shown in Fig.5, they were installed at three locations, i.e., a location where one end of the plate projected from the structure by 1/2 of its length (Type-A), a location where the ends of both the plate and the structure were aligned (Type-B), and a location where one end of the plate was inside of the structure by 1/2 of its length (Type-C).

Table.2 Experimental conditions

	Period (sec)	Wave height (m)
Regular wave	0.5, 0.6, 0.7, 0.8, 0.9, 1.0, 1.1, 1.3, 1.5, 1.7, 1.9	1.5~3.0

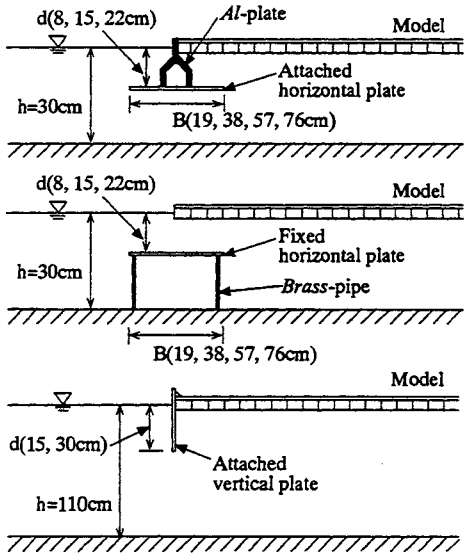

Fig.4 Schematic view of the displacement reducing device

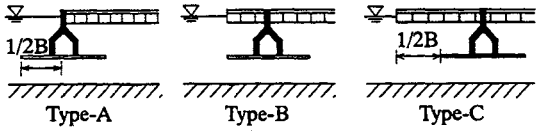

Fig.5 Horizontal location of the horizontal plate

2.3 Measuring method

Fig.6 shows the model installed in the tank. The two-dimensional wave tank at Nippon Steel's Sagamihara Research & Engineering Center is 70m in overall length, 2.5m in width and 1.1 m in depth of water. The tank at Tokai University is 38m in overall length, 1.0m in width and 0.3m in depth of water. To meet the size of the model used, a partition wall was set in both tanks to form an experimental channel of 0.5m in width. The model was installed nearly in the center of the channel.

The distribution of vertical displacement and the mooring force of the model were measured. For the measurement of vertical displacement, 21 laser displacement meters installed on the center line of the model at a pitch of 0.5m were used. The mooring force was measured by strain gauges attached to both sides of the steel plate (see Fig.3). The wave height was measured by the capacity-type wave height gauge. The data was collected during the period from the time the waves arrived at the stern of the model and the displacement of the model reached a steady condition to the time the reflected waves returned to the stern of the model.

3. NUMERICAL ANALYSIS

The method of wave response analysis of a VLFS to which the horizontal plate was attached is shown in appendix.

4. EFFCT OF HORIZONTAL PLATE

4.1 Displacement reducing effect

The 38cm long plate which was installed at Type-A position and at a depth of 22cm showed the greatest displacement reducing effect. Fig.7 shows the vertical response distribution of this plate for each wave period. The ordinate represents the dimensionless values obtained by dividing the amplitude Za(x) of vertical displacement on the center line of the model by the amplitude ζ a of the incident wave, while the abscissa represents the position of measuring points in the longitudinal direction of the model. The wave propagates from left to right.

First, the experimental results will be compared. It will be seen that the displacement at the bow, center and stern of the model to which a horizontal plate is attached is reduced compared with the basic model (model to which the displacement reducing device is not added). Fig.8 shows changes in displacement of the model with horizontal plate depending on the ratio of model length to wave length (L/λ in which L is the model length and λ is the wave length) at three representative points, i.e., bow, center and stern, in comparison with the basic model. Relationship between L/λ and period are shown in Table 3. The reduction in displacement at the bow is pronounced, i.e., displacement at this end is reduced to less than 25% at $L/\lambda > 7.3$ (actual period: less than 10sec). The displacement reducing effect is decreased as L/λ decreases.

In the numerical results for the basic model which are shown in Fig.7, the maximal and minimal values are clearly seen. However, the maximal and minimal values of experimental results are not so clear and are somewhat smaller than those of the numerical results. The probable reason is the decrease in wave height due to the friction between the water and the bottom and sides of the tank or the structural damping of the model itself which are not taken into account in the numerical analysis. The numerical results of the model with horizontal plate do not agree exactly with the results of

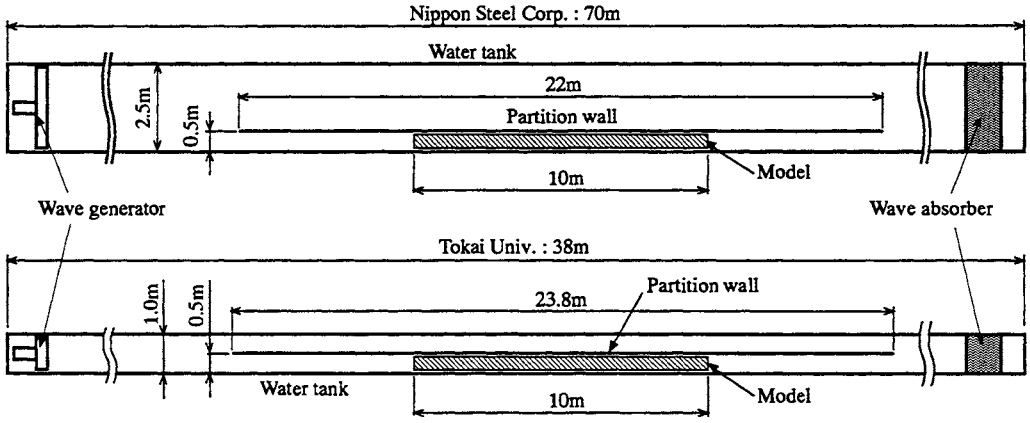

Fig.6 Plan view of experimental setup

experiment. If the difference in condition between calculation and experiment is taken into account, however, it may be said that the tendency of displacement could have been nearly clarified.

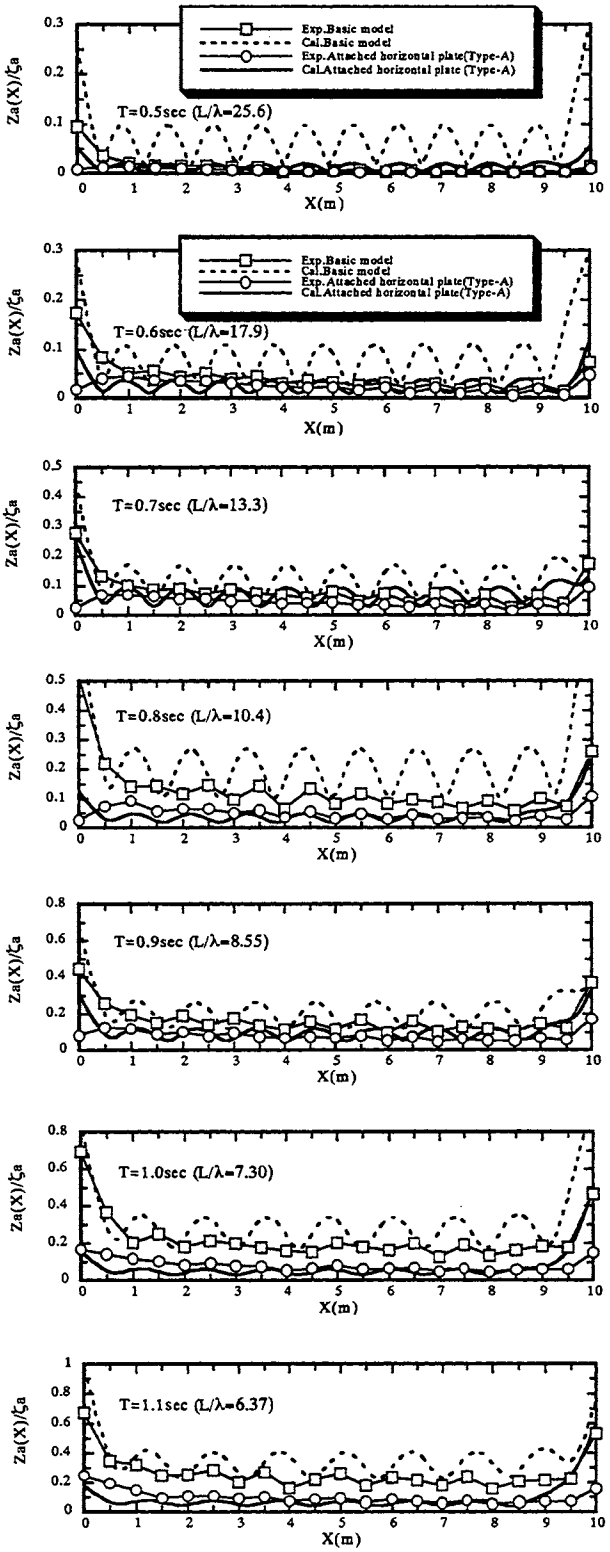

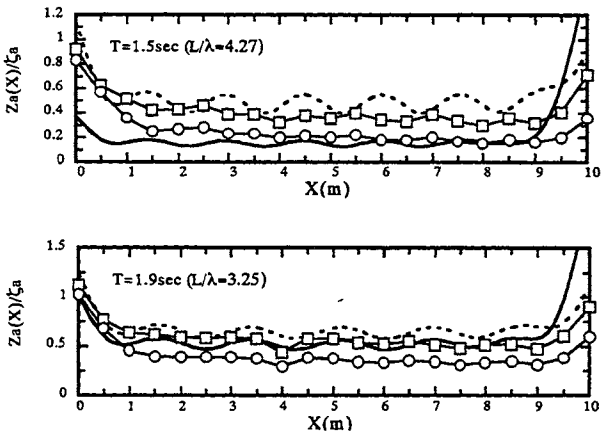

Fig.7 Distributions of displacement of the model with attached horizontal plate (B=38cm,d=22cm,Type-A).

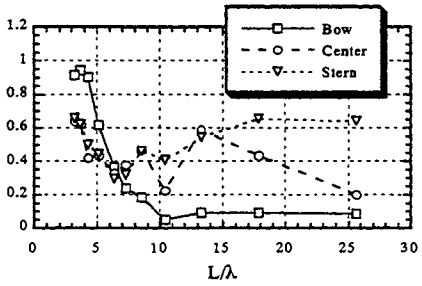

Fig.8 Ratio of displacement of the model with attached horizontal plate (B=38cm,d=22cm,Type-A) to that of the basic model.

Table.3 Relationship between L/λ and wave period

Period (sec)	0.5	0.6	0.7	0.8	0.9	1.0
λ (cm)	39	56	75	96	117	137
L/λ	25.6	17.9	13.3	10.4	8.55	7.30

Period (sec)	1.1	1.3	1.5	1.7	1.9
λ (cm)	157	196	234	271	308
L/λ	6.37	5.10	4.27	3.69	3.25

4.2 Effects of horizontal position and the depth of installation

It will be seen from Fig.7 that the displacement of the whole model can be nearly estimated from the displacement at the bow, center and stern. Figs.9, 10 and 11 show changes in vertical response depending on L/ λ at the bow, center and stern of the model, respectively. The experimental parameters are the horizontal position of the horizontal plate and the depth of installation. The length of the horizontal plate is 38 cm. To determine the influence of the wave energy dissipation effect of the horizontal plate on displacement reduction, experiment was also conducted

using the fixed horizontal plate. The results of experiment conducted using the fixed horizontal plate at Type-A position are described below.

According to the experimental results at the bow which are shown in Fig.9, the horizontal plate at Type-A position showed the greatest displacement reducing effect. The plate at Type-B position exhibits its effect as the depth of installation increases. On the other hand, the displacement of the fixed horizontal plate at a depth of 8 cm was reduced at a certain range of L/λ, but noticeable differences are not observed between the basic model and the model with fixed horizontal plates at depths of 15 and 22cm. In comparison between experimental results and the numerical results, the experimental results of the model with horizontal plate at Type-A position agree with the numerical results fairly well.

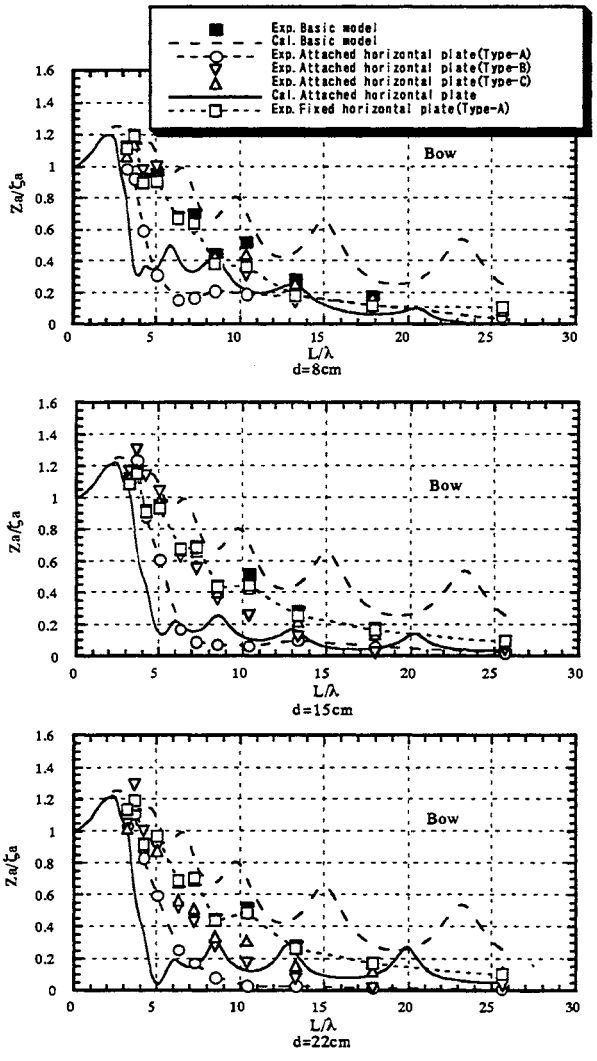

Fig.9 Displacement of the model with different types of horizontal plate for different L/λ at the bow.

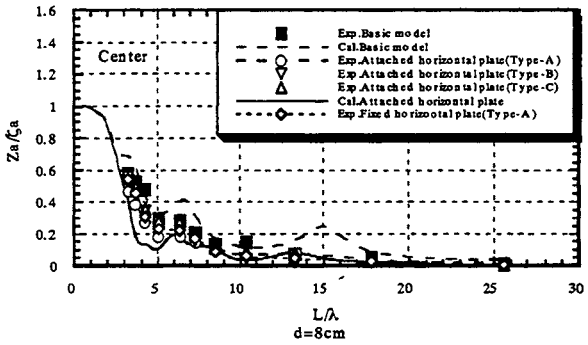

Fig.10 Displacement of the model with different types of horizontal plate for different L/λ at the center.

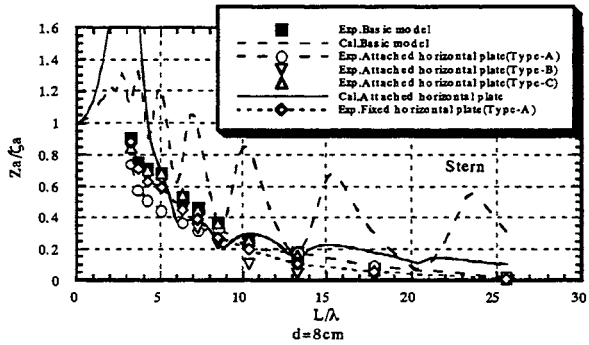

Fig.11 Displacement of the model with different types of horizontal plate for different L/λ at the stern.

The results obtained at the center and stern of the model installed at a depth of 8cm are shown in Figs.10 and 11 respectively. For the center, both the experimental results and the numerical results showed the similar tendency as that of the results at the bow. The results at the stern are nearly the same, but the experimental results do not agree well with the numerical results. The fixed horizontal plate showed nearly the same effect as that of the attached horizontal plate at the center and stern.

Based on the results described above, it may be said that the displacement reducing effect becomes greater if the horizontal plate is installed so that it protrudes from the end of the floating structure. In our experiment, the plate installed at the greatest depth of 22cm showed greater effect. In the comparison between experimental results and the numerical results, the horizontal plate at Type-A position showed comparatively good agreement (at the bow in particular). The probable reason is that the plate used for experiment has a free water surface over the half of its length and this condition is similar to the condition used for the numerical analysis (see Appendix). Moreover, the jig for attaching the horizontal plate is at the end of the

model in the case of Type-A position and this condition is the same as the condition used for the numerical analysis.

The effect of the fixed horizontal plate installed at a depth of 8cm was small at the bow, but the effect of this plate at the center and stern is nearly the same as that of attached horizontal plate. As reference data, the numerical results of transmission coefficient in cases where the fixed horizontal plate only is installed are shown in Appendix. The effect of this plate increases with decreasing depth of installation. When the plate is installed at a depth of 8cm, the plate shows a wave energy dissipation effect of about 30% max. This is one of the factors causing displacement reduction. Furthermore, the effect of increase in added mass of the model due to the reduction in depth of water may be one of the factors causing displacement reduction.

Based on the results described above, it may be said that the radiation force resulting from the vertical displacement of horizontal plate is one of the factors for displacement reduction at the bow, center and stern. As described in 4.1, however, experimental results do not agree exactly with the numerical results. Accordingly, it will be necessary to conduct numerical analysis under the boundary conditions which are closer to the actual conditions, and to consider the effect of non-linear hydrodynamic force, such as eddy-making damping.

4.3 Effect of changes in length

Fig.12 shows changes in vertical response depending on L/λ at the bow. The experimental parameter is the length of horizontal plate (19, 38, 57 and 76cm). The horizontal position of the plate is at Type-B position and the depth of installation is 15cm.

According to the experiment, the 38 and 76cm long plates exhibit a great displacement reducing effect at $L/\lambda > 13.3$ (actual period: less than 7sec) and at $L/\lambda < 6.37$ (actual period: more than 11sec), respectively. At $6.37 \leqq L/\lambda \leqq 13.3$, however, the 57cm long plate has a great effect. According to the numerical results, the displacement reducing effect of 38cm long plate is great. When the plate length is other than 38cm, however, the order of effectiveness of the plates is changed depending on L/λ.

The experimental results at the center and stern showed nearly the same tendency as that at the bow. It will be seen from the experimental results described above that the longer plate becomes effective as the wave length increases and that an optimum installation shape exists for the expected effect.

4.4 Effect of the horizontal plates installed both at the bow and stern of the model

Fig.13 shows changes in vertical response depending on L/λ at the bow and stern. The experimental

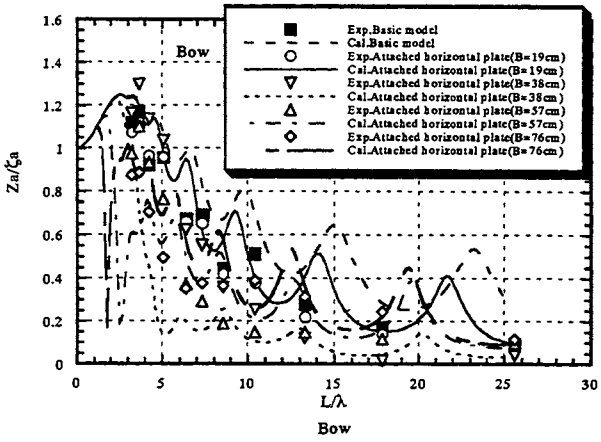

Fig.12 Displacement of the models with attached horizontal plates of different length for different L/λ at the bow.

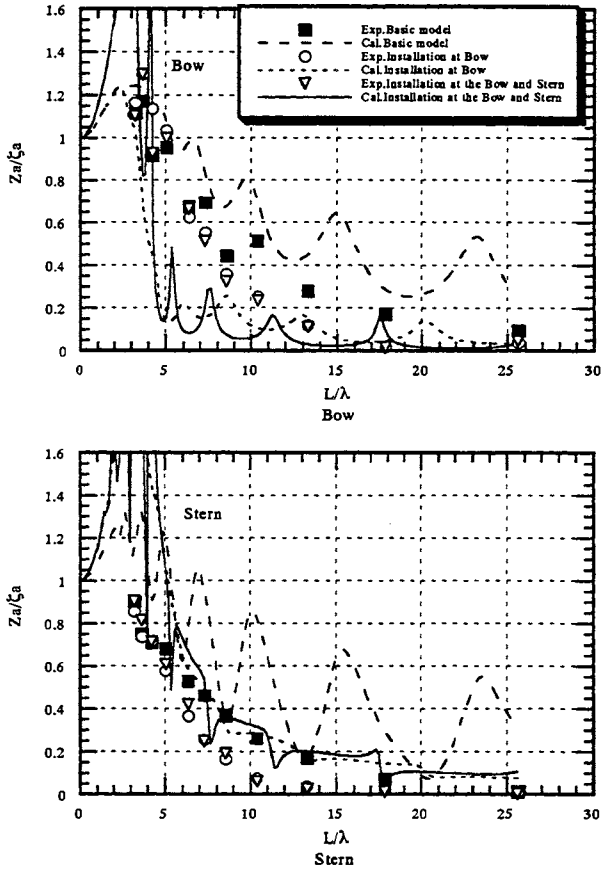

Fig.13 Displacement of the model with attached horizontal plates both at the bow and stern for different L/λ.

parameter is the installation of the horizontal plate both at the bow and stern and the installation at one end only (bow). The horizontal position is Type-B and the depth of installation is 15 cm.

According to the experimental results, significant differences in effect are not seen at the bow, center and stern between the case where the plate is installed at the bow and the case where the plates are installed at the bow and stern. The comparison of the numerical results obtained in the both cases shows nearly the same tendency but the positions and magnitudes of the maximal and minimal values vary.

In the future, it will be necessary to confirm the effect of the plates installed at the bow and stern of the model so as to protrude from the ends of the model as these plates are expected to produce greater displacement reducing effect.

5. EFECT OF VERTICAL PLATE

Fig.14 shows changes in the distribution of vertical response when the vertical plate was attached at two different depths, while Fig.15 shows changes in the maximum vertical response with changes in L/λ. At $5.3 \leqq L/\lambda \leqq 25.6$ (actual period: 5~11sec), the displacement was reduced both at the bow and center of the model with vertical plate. Apparently, the plate installed at a greater depth (30cm) is more effective. At $L/\lambda \leqq 3.8$ (actual period: more than 13sec), however, the displacement is not reduced and the ratio of water depth to wave length becomes small. It may be, therefore, said that the wave energy passes through the model under the bottom of the vertical plate. When the depth of attachment is 30cm, the ratio of displacement of the model with vertical plate to that of the basic model is decreased to about 10 ~ 30% at $6.4 \leqq L/\lambda \leqq 25.6$ (actual period: 5~10sec)

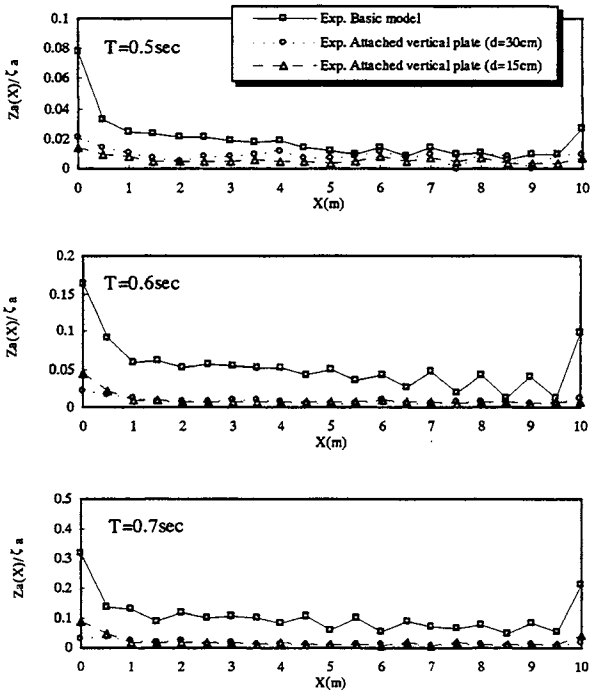

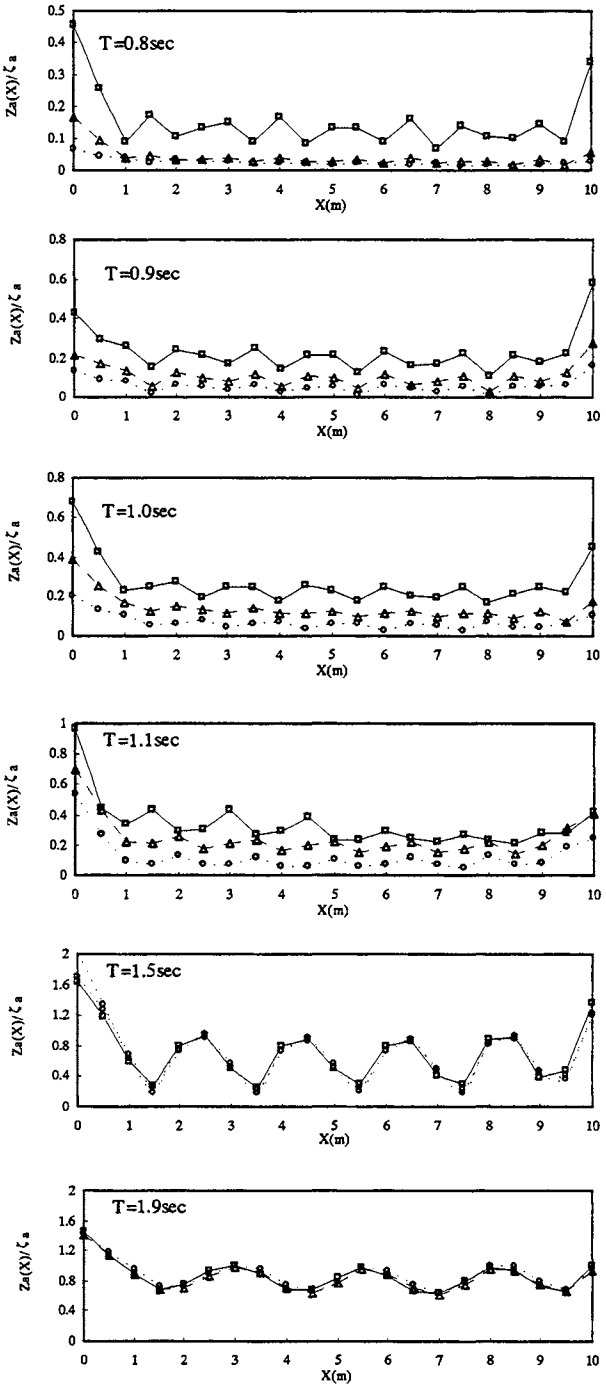

Fig.14 Distributions of displacement of the model with attached vertical plate (d=15, 30cm).

The reduction in displacement by the vertical plate occurs as the reflected waves are increased and the waves passing through under the model are correspondingly decreased. This is the same as the wave energy dissipation effect of curtain type breakwater. This effect increases with decreasing wave period. Fig.16 shows changes in the amplitude of the horizontal wave force with changes in wave period in comparison with the basic model. The ordinate represents the values obtained by dividing the amplitude of horizontal wave force $F_h a$ by the product of the amplitude of incident wave height ζa and the width of model. As is apparent from Fig.16, the force of horizontal wave increases with increasing wave period. In the study of practical application of floating structure, therefore, the displacement reducing effect should be studied in consideration of the effect on mooring force.

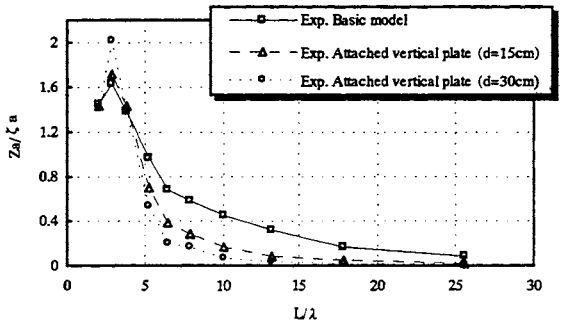

Fig.15 Maximum displacement of the model with attached vertical plate for different L/λ .

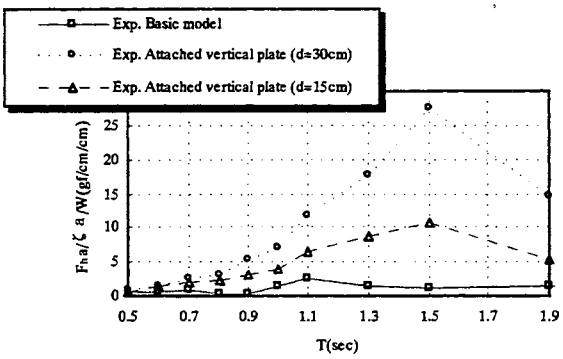

Fig.16 Horizontal wave force acting on the model with attached vertical plate for different wave periods.

6. CONCLUSIONS

The displacement reducing effect of the structure with horizontal or vertical plate was confirmed by our study. It was found that it would be possible to eliminate the construction of breakwaters in a bay where waves are comparatively small. For the horizontal plate, the following findings were obtained.

(1) It is effective to attach the plate in such a manner that it protrudes from one end of the floating structure.

(2) The attachment of longer horizontal plate at greater depth is not necessarily effective. An optimum shape of attachment exists for the expected effect.

(3) When the plate is attached at greater depth, the influence of wave energy dissipation effect on displacement reduction is smaller than that of radiation force.

For the displacement reducing effect of the vertical plate, the following conclusions were drawn.

(4) The displacement reducing effect is increased with increasing depth of attachment in the water and decreasing wave period.

(5) It is necessary to study the effect of the vertical plate on mooring force.

References

[1] K. Yago, S. Ohmatsu and H. Endo. On the hydroelastic response of box-shaped floating structure with shallow draft. *Journal of The Society of Naval Architects of Japan,* No.182, 307-317, 1997.

[2] K. Tanimoto, Y. Yoshimoto and S. Takahashi. Irregular wave experiments on hydroulic performances of new types of deep-water breakwaters a study on development of deep-water breakwaters (Part 1), *Technical Note of The Port and Harbour Research Institute,* No.516, 17-23, 1985

[3] M. Takagi, and T. Kawasaki. Experimental study on breakwater performance of a submerged horizontal plate, *The 8th Ocean Engineering Symposium, The Society of Naval Architects of Japan,* 259-266, 1988

APPENDIX: THE METHOD OF ANALYSIS

In this appendix section, the method of analysis, numerical results by which are presented in the main part of the paper, is summarized. In order to account for the effect of the attached horizontal plates, we have first calculated the radiation forces due to heaving of the isolated horizontal plate in a two-dimensional wave tank, and then the calculated added mass has been given at the fore-end (or at each end) of the elastic floating plate as an attached mass. The attached mass is treated as a complex value in order to account for the radiation damping force (imaginary part) together with the added mass force (real part).

The diffraction/radiation forces for a horizontal flat plate can be calculated by utilizing eigenfunction expansions within the assumptions of the linear potential theory; we have employed here the method given by McIver [1]. Figure A1 shows the configuration of the analytical model for the horizontal plate and the regions of separate eigenfunctions.

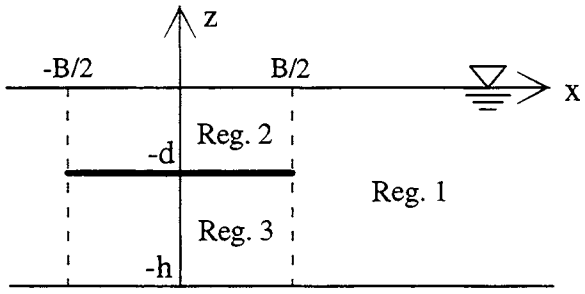

Figure A1: Configuration for the horizontal plate.

Figure A2 shows the variation of the transmission coefficient, $|T|$, of the fixed horizontal plate with non-dimensional wavenumber, kh. It is seen that except b-type around kh=1.5 the transmission coefficient is close to 1.0 and thus most of the incident wave energy will transmit along the horizontal plate. With this observation, we consider that the cause of the response reduction of the elastic floating plate would mainly be due to the radiation effect.

Figure A3 shows the variation of the non-dimensional added mass and the radiation damping coefficients with kh for heaving of the horizontal plate. Although the non-dim. added mass coefficients vary with the oscillating frequency (kh), the ratios of a/h and d/h, they are roughly equal to π, which is the non-dim. added mass coefficient for a flat plate in an unbounded fluid domain. From the comparison among b, c, and d-type plates, it is recognized that as the plate position becomes closer to the water bottom, the added mass becomes larger in the high frequency region. Although the non-dim. added-mass coefficients are similar among e, f, and g-type plates in the high frequency region, it should be reminded that the dimensional added mass is proportional to the square of the plate length, and thus the g-type plate has actually about sixteen times added mass of the e-type plate for the same water depth.

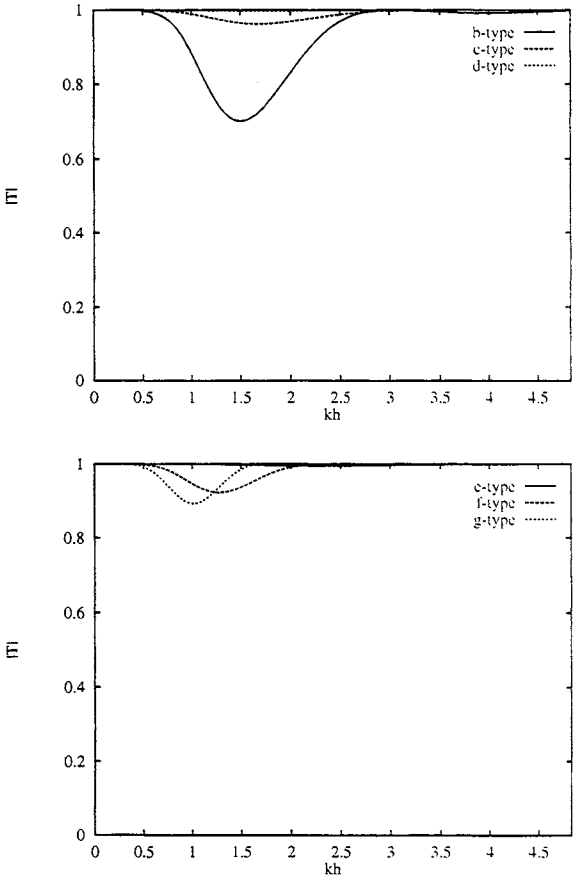

Figure A2: The transmission coefficient of the fixed horizontal plates. b-type: B/h=1.267, d/h=0.267; c-type: B/h=1.267, d/h=0.5; d-type: B/h=1.267. d/h=0.733; e-type: B/h=0.633, d/h=0.5; f-type: B/h=1.9, d/h=0.5; g-type: B/h=2.533, d/h=0.5.

Subsequently, the wave-induced response of the elastic floating plate is analyzed, where the added-mass and radiation damping of the horizontal plate are considered as an attached complex-valued mass at the fore-end (or at each end) of the floating plate. The method employed is again an eigenfunction expansion method [2], where the structural motion is expanded by modal functions including the rigid body motions (heave and pitch) and the bending modes.

Although most part of the formulations are the same as in [2], some modifications are needed. In [2], the eigenfunctions of a free-free beam is employed as the modal functions, which always have zero shear-force at their each end. Unfortunately, the boundary condition

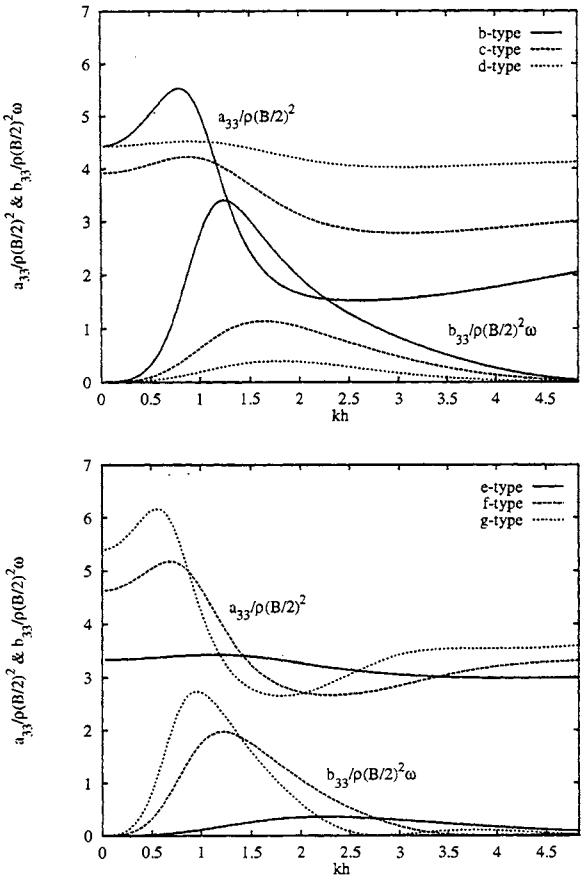

Figure A3: The added mass and the radiation damping coefficients for heaving of the horizontal plates.

at the position of the attached mass, where the shear force must be in equilibrium with the inertial force of the attached mass, can not be satisfied by any combinations of the free-free beam eigenfunctions.

Therefore, we have employed here the trigonometric functions, which express the elastic modes, superposed on the linear function corresponding to the heave and pitch modes. Such a combination for a floating elastic body was firstly used in [3]. By use of the trigonometric functions, the boundary conditions for the moment and the shear force can be satisfied as a sense of the minimization of the sum of the potential and the kinetic energies.

The modal functions employed are

$$f_l^S = \begin{cases} 1/\sqrt{2} & \text{for } l=0 \\ \cos(\mu_l^S x/b) & \text{for } l=1,2,\ldots \end{cases} \quad (1)$$

$$f_l^A = \begin{cases} \sqrt{6}x/2b & \text{for } l=0 \\ \sin(\mu_l^A x/b) & \text{for } l=1,2,\ldots \end{cases} \quad (2)$$

where $\mu_l^S = (2l-1)\pi/2$; $\mu_l^A = l\pi$, and b is the half length of the elastic floating plate.

The corresponding inhomogeneous solutions are

$$\phi_{0R}^S = -\frac{1}{2\sqrt{2}h}[(z+h)^2 - x^2] \quad (3)$$

$$\phi_{0R}^A = -\frac{\sqrt{6}}{2b}\frac{[3x(z+h)^2 - x^3]}{6h} \quad (4)$$

$$\phi_{lR}^S = -\frac{b}{\mu_l^S}\cos(\mu_l^S x/b)\frac{\cosh(\mu_l^S(z+h)/b)}{\sinh(\mu_l^S h/b)} \quad (5)$$

$$\phi_{lR}^A = -\frac{b}{\mu_l^A}\sin(\mu_l^A x/b)\frac{\cosh(\mu_l^A(z+h)/b)}{\sinh(\mu_l^A h/b)} \quad (6)$$

Applying the Hamilton's principle, the equations of motion in the modal coordinates ζ_j are obtained for the floating plate having an attached mass of m at the fore-end:

$$\sum_{j=0}^{N}[-\omega^2(M_{ij}^S + M_{aij}^S + A_{ij}^S) + K_{ij}^S]\zeta_j^S - m\omega^2\sum_{j=0}^{N} f_i^S(-b)f_j^A(-b)\zeta_j^A = F_j^S \quad (7)$$

$$\sum_{j=0}^{N}[-\omega^2(M_{ij}^A + M_{aij}^A + A_{ij}^A) + K_{ij}^A]\zeta_j^A - m\omega^2\sum_{j=0}^{N} f_i^A(-b)f_j^S(-b)\zeta_j^S = F_j^A \quad (8)$$

where $A_{ij}^S = mf_j^S(-b)f_i^S(-b)$, $A_{ij}^A = mf_j^A(-b)f_i^A(-b)$. and for other parameters reference should be made in [2]. Solving Eqs. (7) and (8), the deflection of the plate $w(x)$ can finally be obtained by

$$w(x) = \sum_{j=0}^{N}\zeta_j^S f_j^S(x) + \sum_{j=0}^{N}\zeta_j^A f_j^A(x) \quad (9)$$

References for the Appendix

[1] M. McIver. Diffraction of water waves by a moored, horizontal, flat plate. *J. Engng Maths* **19**, 297-319, 1985.

[2] C. Wu, E. Watanabe and T. Utsunomiya. An eigenfunction expansion-matching method for analyzing the wave-induced responses of an elastic floating plate. *Appl. Ocean Res.* **17**, 301-310, 1995.

[3] R. Eatock Taylor and M. Ohkusu. Green functions for hydroelastic analysis of vibrating free-free beams and plates. 1998. (in preparation)

PROCEEDINGS OF THE THIRD INTERNATIONAL WORKSHOP ON VERY LARGE FLOATING STRUCTURES
(VLFS '99), VOL. I, EDS. R.C. ERTEKIN & J.W. KIM, 22-24 SEPTEMBER 1999, HONOLULU, HAWAII, USA

OBSERVATION OF VERTICAL HEAT TRANSFER THROUGH A MEGA-FLOAT MODEL IN TOKYO BAY

Hiroshi Irie, Takaharu Hamada, Yusaku Kyozuka
Kyushu University *

ABSTRACT

The Very Large Floating Structure (VLFS) covers a wide area of the sea surface, making it important to evaluate the influence of the structure on sunlight interception at the surface. Particularly it is important to predict how the VLFS suppresses the transport of heat. Recordings of temperature, humidity and heat flux on the pontoon-type floating structure were thus conducted in summer and winter, and the measured data were compared with the typical equations used in the architecture. The effect of the pontoon-type structure on the heat budget at the sea surface is discussed by comparison with heat flux through the open sea surface.

1. INTRODUCTION

The Very Large Floating Structure(VLFS) covers a wide area of the sea surface, shielding the surface from solar radiation, and suppressing the sensible and latent heat transfer. It also absorbs and emits heat, and thus may alter the ocean environment surrounding it. Consequently, it is necessary to know the characteristics of VLFS as they affect heat transfer, and to be able to predict change in the heat budget through the sea surface. Heat transfer of a floating structure was discussed to estimate the deformation and stress distribution of the structure (for instance, Ando *et al*[1]), but the effect of such structure on the energy transport through the sea surface has not been discussed.

Although, the numerical simulation is thought to be very useful to evaluate the influence of a floating structure, it is not clear how to parameterize the characteristics of heat transfer of VLFS. Fujino *et al.*[2] treated VLFS as an insulator for simplicity.

The main aim of this study was to evaluate its influence of VLFS on the heat transport through the sea surface. In a compartment of the Mega-Float experimental model, temperature, humidity, and heat flux on the ceiling and floor were observed for several days in summer and winter.

We then estimated the heat flux and heat budget of Mega-Float using the typical equations of heat transfer in the architecture, and the heat flux observed was compared with that through the open sea surface. Influence of the floating structure on the heat budget of the seawater was then discussed.

2. MEASURING ARRANGEMENT

The Mega-Float experimental model was a pontoon-type floating structure of L=300m, B=60m, and D=2m placed offshore at Oppama, Yokosuka, Japan. [1]

The structure had many compartments separated by partitions. Thermometers, a hygrometer, heat flux sensors were placed in one of these compartments and the values shown are as follows. In the following description, CH * means channel number of data logger. The arrangement of sensors is shown in Figs. 1 and 2.

- Air temperature (CHs 1-5): Thermometers were placed vertically at intervals of 0.45m.
- Temperature of the ceiling and the floor(CHs 6,7): Thermometers were placed on the ceiling and floor.
- Humidity(CH 9): A hygrometer was placed 1.30m above the floor.
- Air temperature (CH 10): The hygrometer installed could also measure the temperature.
- Heat flux of the ceiling and the floor (CHs 11,12): The heat flux sensors were placed on the ceiling and floor to record the vertical heat flux in the structure.

Observations were made in 1998 from Aug. 4 to 8, and from Nov. 30 to Dec. 3. The data were recorded automatically by the data logger every 10 minutes. Removal of drops of moisture formed on

*6-1 Kasuga-koen, Kasuga-city, Fukuoka 816-8580, Japan. E-Mail: hamada@esst.kyushu-u.ac.jp

[1] In the Phase II experiment, the model is being expanded to L=1000m, B=60-121m, and D=3m .

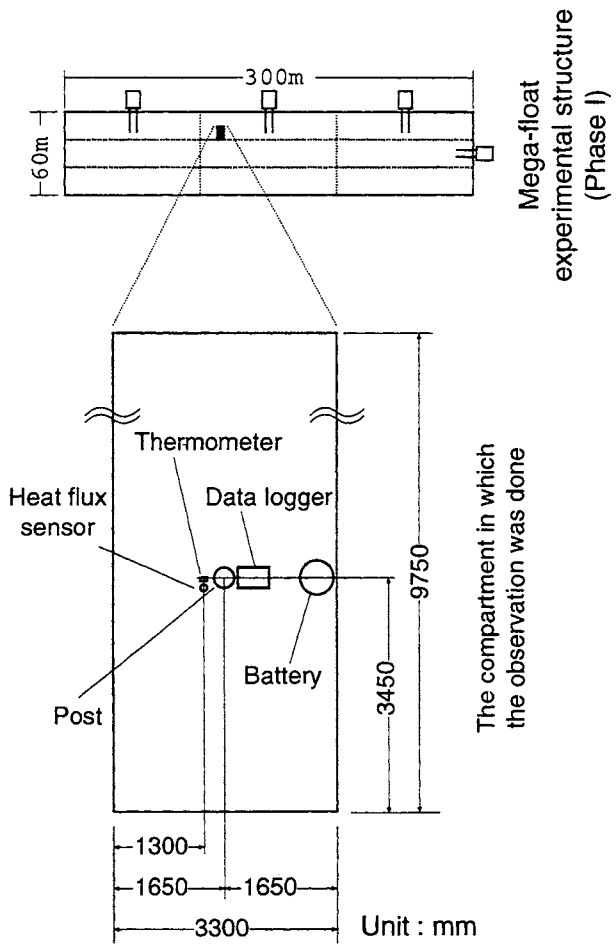

Figure 1: Location of the experimental compartment in the Mega-Float model and horizontal arrangement of the devices

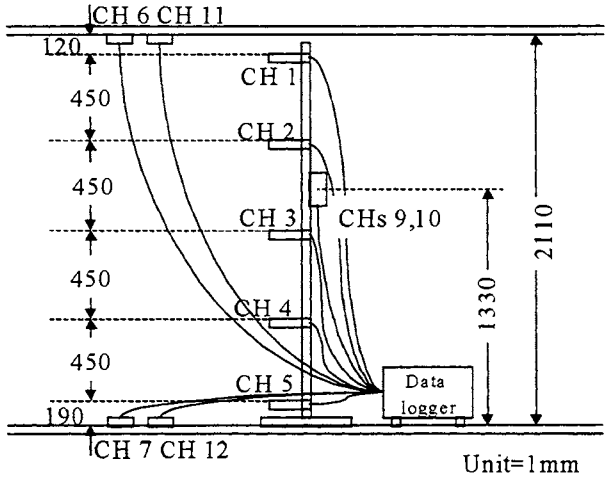

Figure 2: Vertical arrangement of the devices

the ceiling and floor in the compartment and recovery of data were done once a day.

3. FORMULAS FOR ESTIMATING HEAT TRANSFER

The equations of heat transfer and thermal storage used in the architecture follow.

3.1 Formulas of heat flux

It is assumed that heat transfer at the ceiling and floor surfaces of the compartment is mainly due to radiation and convection. (Heat of evaporation and condensation is assumed to be small enough to be neglected.)

The radiative heat transfer on the surface (Q_r)is described as follows:

$$Q_r = \alpha_r(\theta_i - \sum_{j=1}^{3} g_{ij}\theta_j) \quad (1)$$

$$\alpha_r = 4\varepsilon_i \sigma T_m^3 \quad (2)$$

where suffixes i, j, and k indicate walls: suffix 1 means ceiling, 2 sidewall, and 3 floor, respectively, and ε_i is emittance, θ_i temperature of the surface, σ Stefan-Boltzmann constant(= $5.670 \times 10^{-8}[W/m^2K^4]$), T_m average of temperature in the compartment, and g_{ij} absorption factor, respectively.

The temperature of the sidewall (θ_2) was not recorded in this observation, and we assume θ_2 as $(\theta_1 + \theta_3)/2$. We use the temperature recorded at CH 9 as T_m.

The convective heat transfer on the surface(Q_c) is described as follows:

$$Q_c = \alpha_c(\theta_a - \theta_s) \quad (3)$$

where α_c is convective heat transfer coefficient, and we assume α_c =6$[W/m^2]$ when the heat flows upwards, and α_c = 2$[W/m^2]$ when the heat flows downwards. θ_a is air temperature[K]. (Value of CH 1 is used for the ceiling and that of CH 5 is used for the floor.) θ_s is temperature of the surface of ceiling or floor.

3.2 Formula of thermal storage

The amount of heat stored per unit time and unit area of the floating structure is given by the difference of the measured heat flux at the ceiling of the structure (Q_1) and at the floor (Q_2) as follows:

$$\Delta Q = (Q_1 - Q_2) \quad (4)$$

It is also expressed by the change of the temperature in the compartment(ΔT) as follows (Q_{TMP}):

$$\Delta Q_{TMP} = \int_V \rho C_p \Delta T dV \quad (5)$$

where ρ is density $[kg/m^3]$, C_p specific heat capacity $[J/K \times kg]$, and V the volume of the compartment. In this study we assume C_p of air = 1.006, C_p of water = 4.1816, ρ of air = 1.205, ρ of water = 998.2. (these are values at 20°C). In the room, there is a small condensation of water in the room which has an average depth of about $1cm$. We take the this "pool" into account when we estimate ΔQ by using Eq.5.

4. SUMMER OBSERVATIONS

4.1 Daily variations of temperature, humidity and heat flux in a day

Figure 3 shows variation of recorded temperature, humidity and heat flux on Aug. 5, 1998. There was a lack of data from 10:20 to 11:10 because the sensors were being serviced.

Comparison of the surface temperature(CHs 6 and 7) in Fig. 3(a), shows that the temperature at the ceilng is higher than that at the floor during the daytime.This fact suggests that the heat flows downwards. During the night, however, the temperature at the ceiling is lower than that at the floor during the night,suggesting that the heat flows upwards.

Figure 3(a) also shows temperature stratification during the daytime, while at night it is vertically homogeneous, except near the ceiling and the floor. This suggests that the air is cooled down from the top at night, and then is well mixed by the convection.

Figure 3(b) is the daily variation of humidity. In the daytime, the humidity falls to about 65%, however, it rises in the evening, and retains its highest value from midnight to 5:00. This is explained by the change in saturation vapor pressure due to the change of temperature.

Because of the small pool of water condensation mentioned earlier, we estimated the effect of latent heat flux in the room to the heat budget of the floating structure. The maximum amount of vapor per $1m^2$ was 65.3g and the minimum was 47.0g on Aug. 5. If we assume that the difference between the maximum and minimum amount of vapor occurred over 6 hours, we can estimate the latent heat energy due to evaporation to be $4.6[W/m^2]$. This is much smaller than the total heat budget of the compartment. We estimated the latent heat energy in winter in the same manner and found that the effect of the evaporation was also minimal in that season.

Figure 3(c) shows the heat flux at the ceiling and floor. (Positive value denotes the downward heat flux.) The heat flows downwards at the ceiling and

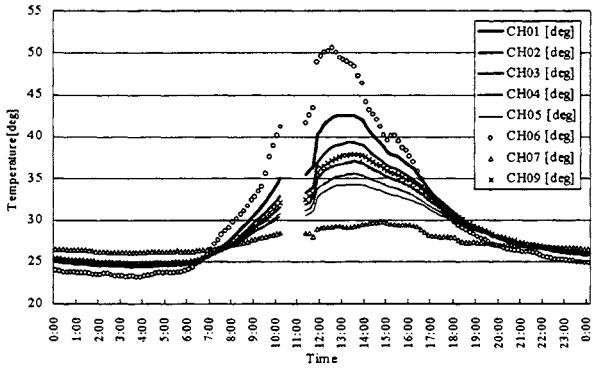

(a)

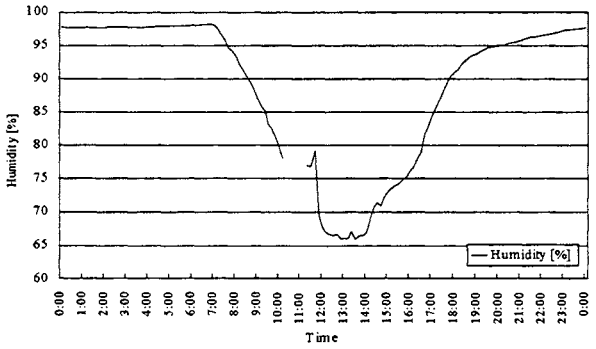

(b)

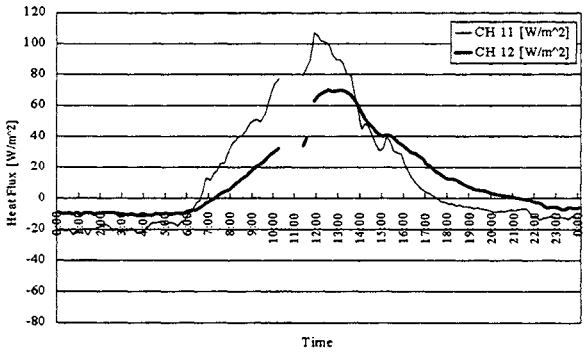

(c)

Figure 3: Time series of (a)temperature, (b)humidity and (c)heat flux measured on Aug. 5.

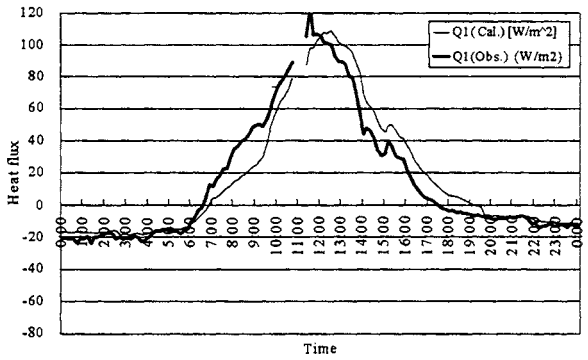

(a)

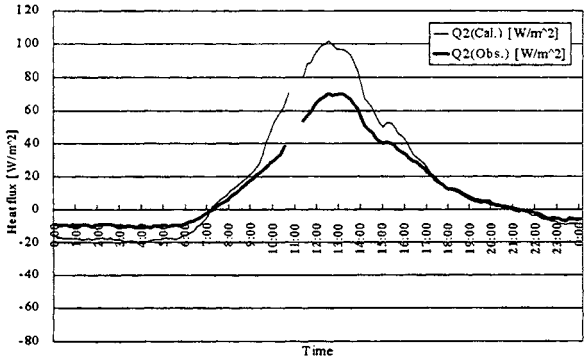

(b)

Figure 4: Comparison of observed heat flux with calculated heat flux on Aug. 5. (a)at ceiling, (b)at floor

floor during the daytime. Maximal downward flux appeared at about 12:00 in CH 11 and had a value of almost $110[W/m^2]$. In CH 12 it appeared at about 13:00 and the value was almost $70[W/m^2]$.

Throughout the night, the heat flows upwards. The value of heat flux at CH 11,12 did not change significantly during the night, and there was no remarkable peak shown in Fig. 3(c).

The difference between the value of CH 1 and CH 2 represents the heat storage per unit time of the compartment. The heat flows from outside to inside in the daytime, and from inside to outside at night.

4.2 Estimation of heat flux and storage

4.2.1 Heat flux

Figure 4 shows the heat flux on Aug. 5, 1998 and the calculated heat flux described in section 3.1. At the ceiling (a) the observed and calculated values correspond well except for the presence of a small

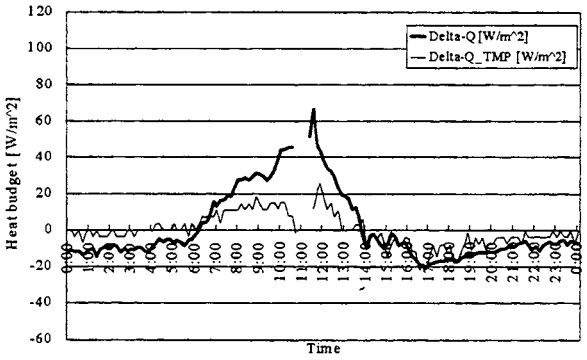

Figure 5: Comparison of observed and calculated thermal storage on Aug. 5.

phase difference. At the floor, however, the maximum difference is almost $30[W/m^2]$. Observed and calculated values does not correspond well, and yet, the shapes of the graphs are similar. The reason the difference between the observed and calculated values at the floor is larger than that at the ceiling is not clear. It may be due to the presence of the condensation pool on the floor, or the influence of heat flow through the sidewall, frame etc.

4.2.2 Heat storage

Figure 5 shows the heat budget ΔQ and heat storage per unit time ΔQ_{TMP} (described by Eq. 5). Positive value denotes inflow to the compartment. The two curves correspond well except for the underestimation of ΔQ_{TMP} in the daytime. This result shows that the formula of thermal storage is applicable for estimation of the heat budget of the floating structure in summer.

5. WINTER OBSERVATIONS

5.1 Daily variations of temperature, humidity and heat flux

Figure 6 shows the daily variations of the observed temperature, humidity and heat flux on Dec. 3. Small peaks appearing around 11:00 were caused by our entering the room to service the equipment.

Figure 6(a) shows that the temperature at the ceiling was lower than that at the floor,and no temperature stratification was not found all day, suggesting that the heat flows upwards in the compartment, and that the air in the compartment was well mixed by convection. These characteristics were similar to that of a summer night.

On Dec. 1, however showed the temperature stratification in the daytime (not shown in figure). The difference of these results may be due to the

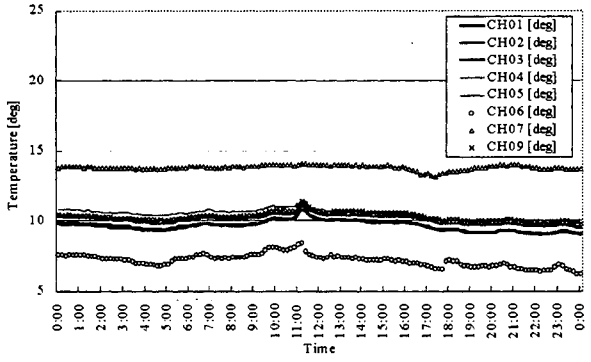

(a)

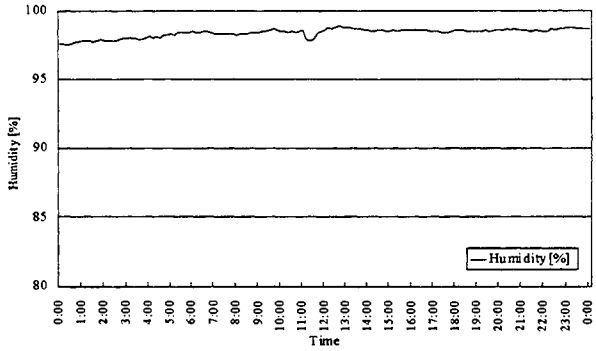

(b)

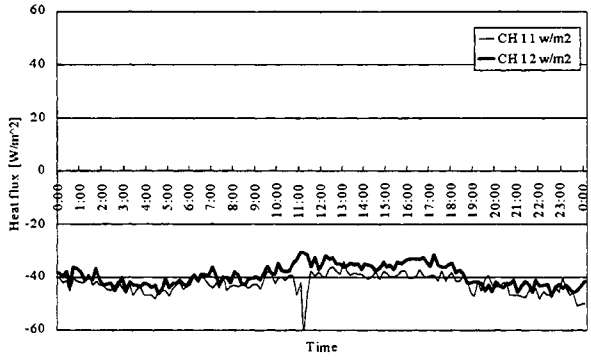

(c)

Figure 6: Results of observation on Dec. 3, (a)temperature, (b)humidity, (c)heat flux

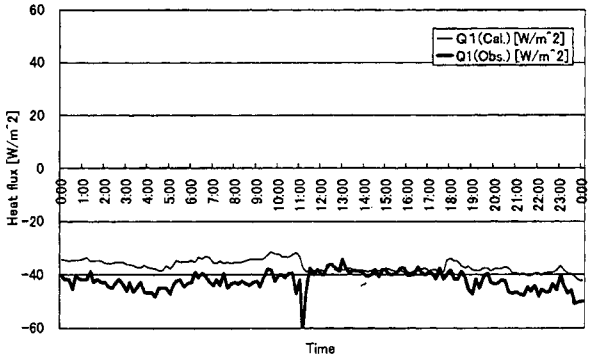

(a)

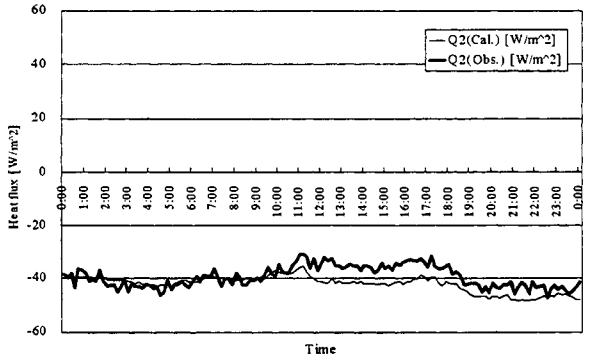

(b)

Figure 7: Comparison of observed heat flux and calculated heat flux on Dec. 3. (a)at ceiling, (b)at floor

weather conditions: the weather was fine on Dec. 1, and the global radiation was greater than that on Dec. 3 (a cloudy day), thus the floating structure was heated from the top which may have been the cause of the stratification.

Figure 6(b) shows the daily variation of humidity. We can see that the humidity was almost saturated during the observation period.

Figure 6(c) shows the daily variations of heat flux at the ceiling and floor of the compartment. The heat flows upwards both on the ceiling and floor and their values are almost the same during the period observed.

5.2 Estimation of heat flux and storage

5.2.1 Heat flux

Figure 7 shows the recorded heat flux on Dec. 3, and the heat flux calculated by the method described in Section 3.1. These correspond well except for some outlying values.

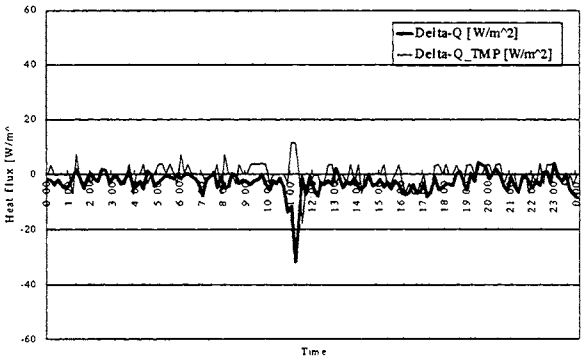

Figure 8: Comparison of observed heat thermal storage and calculated thermal storage on Dec. 3

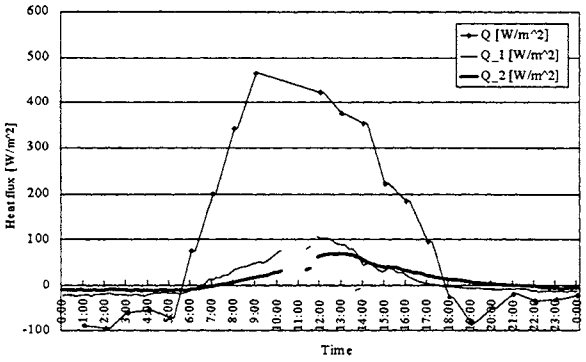

Figure 9: Comparison of heat flux through the sea surface and heat flux through the structure in Aug. 3,1998

5.3 Heat storage

The heat budget ΔQ and the heat storage per unit time ΔQ_{TMP} is shown in Fig. 8. Though the difference between them reaches about $10[W/m^2]$, the shapes of the curves are similar.

Consequently, we concluded that the calculated heat storage using the observed temperature corresponds well to the heat budget in winter.

6. HEAT FLUX WITH/WITHOUT A FLOATING STRUCTURE

To discuss the effect of floating structure on the heat budget through the sea surface, we estimate the heat flux through the open sea surface and compare it with the vertical heat flux observed on the floating structure.

6.1 Formulas of heat flux

The heat flux through the sea surface is described as follows:

$$Q = Q_s - (Q_b + Q_h + Q_e) \tag{6}$$

where Q_s is solar radiation flux, Q_b longwave radiation flux, Q_h sensible heat flux, and Q_e latent heat flux.

Q_s is calculated by the following equation[3]:

$$\begin{aligned} Q_s &= I_0 \sin H\{b_0 + b_1\left(\frac{CC}{10}\right) + b_2\left(\frac{CC}{10}\right)^2 \\ &\quad + b_3\Delta T + b_4\Psi\}(1-\alpha_s) \end{aligned} \tag{7}$$

where I_0, H, CC and α_s are solar radiation at the top of the air, solar height, amount of cloudiness, and albedo at the sea surface, respectively. In this study, we used $\alpha_s = 0.09$. $b_0 - b_4$ are considered as a function of location and are given by 0.5774, 0.3232, -0.5143, 0.0221 and -0.0035, respectively.

ΔT is the difference in temperature from 6:00 to 12:00, and we use the rise of sea surface temperature as ΔT. Humidity observed by the Yokohama Local Meteorological Observatory is used as the value of Ψ.

We calculated the longwave radiation Q_b by the following equation[4]:

$$\begin{aligned} Q_b &= \varepsilon\theta_s^4(0.254 - 0.00495e_a)(1-\delta C) \\ &\quad + 4\varepsilon\sigma\theta_a^3(T_s - T_a) \end{aligned} \tag{8}$$

where ε,σ,θ_a,e_a,δ,T_s,T_a are the emissivity of the sea surface(=0.97),the Stefan-Boltzmann constant, air temperature in K, vapor pressure, cloud coefficient which is a function of latitude, sea surface temperature, and air temperature respectively.

Sensitive heat flux(Q_h) and latent heat flux (Q_e)are given by the bulk aerodynamic method as follows:

$$Q_h = \rho_a c_a C_H (T_s - T_a) W \tag{9}$$

$$Q_e = \rho_a L C_E (T_s - T_a) W \tag{10}$$

where ρ_a is density of the air, c_a specific heat of the air, W wind speed, L latent heat of vaporization, q_s saturated specific humidity at the sea surface, and q specific humidity. We assumed that $C_H = C_E = 1.2\times10^2$.

6.2 Comparison of heat flux through the sea surface and that through the structure

The net heat flux through the sea surface (Q), the observed heat flux at the ceiling of the structure(Q_1) and that at the floor(Q_2) are shown in Fig. 9. Although Q_2 is smaller than Q in the daytime, we cannot regard the floating structure as an adiabatic body.

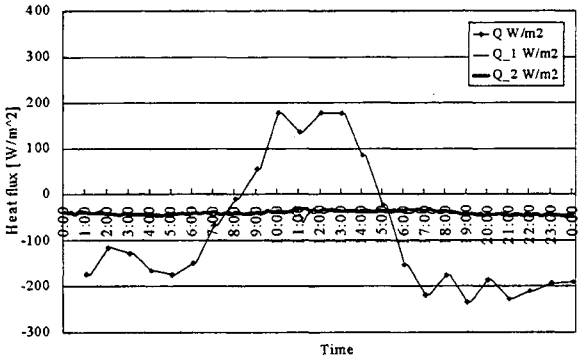

Figure 10: Comparison of heat flux through the sea surface and heat flux through the structure in Dec. 3,1998

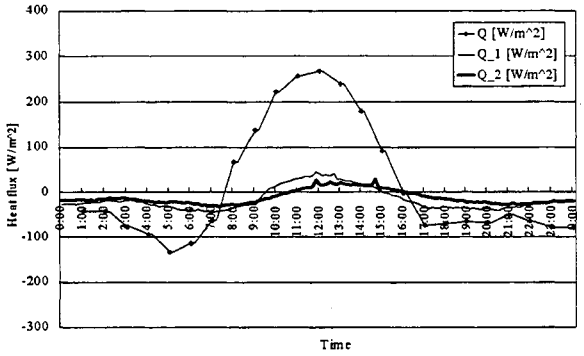

Figure 11: Comparison of heat flux through the sea surface and heat flux through the structure in Dec. 1,1998

It is interesting that Q, Q_1, and Q_2 were correlated with a small phase difference, and that Q_1 and Q_2 delayed from Q in Fig. 9. In winter, there was no correlation between Q, Q_1 and Q_2 on the cloudy day of Dec. 3 in Fig. 10. On the fine day of Dec. 1, on the other hand, Q, Q_1, and Q_2 correlated with each other like Q,Q_1 and Q_2 on Aug. 5 did (Fig. 11).

6.3 Daily mean of heat budget

Table. 1 shows the mean of heat budget for each day.

The average of heat flux $\overline{Q_2}$ in summer flows downwards and is about 10 % of the average of heat flux through the sea surface.

In winter, although it was difficult to estimate it because of the scattering of data, the direction of heat flux was substantially upward. Moreover, the heat flux through the sea surface was almost 0 in fine weather, and the direction of heat flux was upwards under cloudy condition.

Table 1: Heat Budget(daily mean)

	Aug.			
	4	5	6	7
$\overline{Q}[W/m^2]$	144	87	134	145
$\overline{Q_1}[W/m^2]$	-	11	15	-
$\overline{Q_2}[W/m^2]$	-	11	14	-

(a)Summer

	Nov.	Dec.			
	30	1	2	3	4
$\overline{Q}[W/m^2]$	4	3	-32	-128	-52
$\overline{Q_1}[W/m^2]$	-	-16	-27	-42	-
$\overline{Q_2}[W/m^2]$	-	-12	-22	-39	-

(b)Winter

7. CONCLUSION

To discuss the effect of Mega-Float on the heat budget of the surrounding sea, temperature, humidity and vertical heat flux were recorded in the compartment of the pontoon-type floating structure. The heat flux and heat budget of Mega-Float were estimated by the typical equations used in the architecture and were validated by the recorded data. Finally, the vertical heat flux through the structure was compared with the heat flux of the open sea surface, and effect of the structure on the heat budget were evaluated.

The conclusions of this study are summarized as follows:

1. In summer, the vertical heat flux through the structure flows from top of the structure to the bottom in the daytime. It changes greatly during this period, with a maximum value of about 20% of the maximum value of heat flux through the sea surface. During the night, the heat flows from the bottom to the top constantly.

2. In winter, the direction of heat flux changes depending on the weather conditions. In fine weather, the tendency is similar to that in summer, while on a cloudy day, the heat flows from the bottom to the top.

3. The vertical heat flux at the ceiling is well explained by the equations of heat transfer, and the calculation of heat storage ratio per unit time corresponds well to the heat budget of the compartment.

Acknowledgments: The authors wish to thank the Technological Research Association of Mega-Float for permission to observe the Mega-Float experimental model structure. They also thank Associate Professor Yuji Ryu, Kyushu University, for his helpful comments. Sumitomo Heavy Industries, Ltd. gave generous assistance during the observation. The meteorological data was provided by the Yokohama Local Meteorological Observatory and the Technological Research Association of Mega-Float.

References

[1] Sadao Ando, Kunihiro Hoshino, and Naoto Yamagishi. The field tests of proto-type floating offshore structure part 2. on the distribution of temperature by solar radiation for experimental structure. *J. Soc. Naval Arch. Japan Vol. 167*, 1990.

[2] Masataka Fujino, Hiroshi Kagemoto, and Takaharu Hamada. On the sea-covering effect of a huge floating structure on the surrounding water. *J. Soc. Naval Arch. Japan, Vol. 180*, 1996.

[3] Cui Limin, You Matsuo, and Akihiro Nagata. Statistics and analysis of weather data for estimation of solar radiation. *Summaries of technical papers of annual meeting,Architectural Institute of Japan*, 1995.

[4] Young-seup Kim. *Estimate of heat transport across the sea surface near Japan with bulk methods.* PhD thesis, The University of Tokyo, 1992.

PROCEEDINGS OF THE THIRD INTERNATIONAL WORKSHOP ON VERY LARGE FLOATING STRUCTURES
(VLFS '99), VOL. I, EDS. R.C. ERTEKIN & J.W. KIM, 22-24 SEPTEMBER 1999, HONOLULU, HAWAII, USA

ENVIRONMENTAL CONSIDERATIONS FOR DESIGN AND ACQUISITION OF A MOBILE OFFSHORE BASE

Gilbert Jones, Steve Evans, Daniel Kelley, Gary Rahl
Booz•Allen & Hamilton Inc.*

ABSTRACT

The Mobile Offshore Base (MOB) will have to be designed, constructed, and tested to operate worldwide while maintaining compliance with an ever-increasing array of environmental laws, regulations and requirements. Additionally, a MOB will face imperatives to provide a safe and healthful work environment for the personnel stationed on board. Experience has shown that establishment at program initiation of an environmental safety and health (ESH) management program encompassing comprehensive ESH responsibilities can offer significant benefits. Early planning can make compliance with ESH requirements achievable without unnecessary cost and/or schedule impacts. Additionally, advance planning for ESH requirements can ensure that necessary resources are programmed and budgeted, which minimizes the danger of program delays caused by reprogramming resources in response to an unforeseen ESH crisis. A sound program to address ESH requirements can potentially eliminate some of those hurdles.

1. INTRODUCTION

Assumptions

The use of the DoD 5000.2R as a requirement driving the ESH aspects of the MOB assumes that the MOB will be procured as a DoD Acquisition Category I Program. Further, even if the procurement is done in another manner, the following ESH strategy is still beneficial for use by the MOB designers, maintainers, and ultimate disposal personnel.

To facilitate life cycle ESH compliance for a MOB, rigorous analysis and planning should be initiated at the earliest possible phase in the design that considers the entire life cycle of the MOB.

*1725 Jefferson Davis HWY, Crystal Square 2, Suite 1100, Arlington VA, 22202, USA, Email: jones_gilbert@bah.com

To operate effectively in the 21st Century, DoD weapons systems must consider ESH issues as an integral part of the design, construction, operation and disposal. During the initial acquisition phase, ESH requirements need to be put on the same plateau with other important design drivers such as cost, space, weight, risk, etc. With proper emphasis and attention applied to ESH issues, the MOB Program will be in a position to begin the process of successful ESH integration into the entire system that will become the MOB.

2.0 BACKGROUND

Weapons systems were previously designed, constructed, operated, and disposed of without pertinent ESH issues being considered in the initial design activities. The DoD weapons system design teams did not consider the integration of ESH issues crucial to the overall success of the program. ESH issues were typically not addressed until one or more such issues significantly threatened progress within the program. This retroactive approach has been expensive and time consuming for the programs and personnel involved.

The life cycle ESH considerations for the MOB will be a complex process involving a multitude of participants and ESH requirements, and must yield a product that will be used in a harsh environment and may be placed in harm's way. Since the operating environment that the MOB will be placed in is unforgiving, any ESH decisions considered must include a complete understanding of the operating requirements and the overall mission of the MOB. This understanding of the operational mission requirements partnered with an understanding of the ESH requirements will provide a solid foundation for the life cycle management of MOB ESH issues.

ESH requirements in the United States (US) and abroad have evolved substantially in the last 50 years. Along with the expansion of requirements is the increase in the level of scrutiny given to DoD systems,

in the US as well as abroad where US DoD systems are deployed.

US DoD acquisition requirements state the Program Manager shall initiate the ESH evaluation at the earliest possible time in support of a program initiation decision, and shall maintain an updated evaluation throughout the life cycle of the program. The ESH evaluation describes the Program Manager's strategy for meeting ESH requirements, establishes responsibilities, and identifies how progress will be tracked.[1] In addition, SECNAVINST 5000.2B requires that all programs, regardless of size and type, conduct a programmatic ESH evaluation. A well-organized and comprehensive strategy will give the MOB Program Manager(s) detailed guidance for meeting current as well as the future ESH requirements.

Another often ignored issue associated with proper ESH analysis is the political climate at the location where the weapon system may be deployed. The MOB (as proposed) will be a daunting site as well as a symbol of American military and political presence. To mitigate the potential ESH aspects of the MOB, a comprehensive ESH program is recommended. The following sections will address some of the actions and recommendations for a successful MOB ESH program.

3.0 PROGRAM IMPLEMENTATION

One of the best methods for implementing ESH requirements into the life cycle of a program is to ensure that applicable ESH language is in the Operational Requirements Document (ORD) *or the document that serves the purpose of the ORD.* The generation of these requirements for the ORD should provide explicit guidance in the following areas:

- Compliance
- Pollution Prevention
- Pollution Control
- Hazardous Material
- Safety and Health.

This guidance will provide the basis for all future ESH activities in the MOB Program. In addition if specific ESH language is contained in the ORD it is much more likely that program participants will have greater acceptance of the ESH language when it is presented in various design, solicitation and contract documents. With the requirements for the MOB set in place the program is in the position to plan and budget for the implementation of a proactive ESH management system.

To ensure that all ESH guidance depicted in the ORD is properly coordinated the MOB Program Manager(s) should take the following steps:

- Appoint a *(full time)* ESH Manager
- Establish a comprehensive ESH Program
- Develop an ESH Management Plan.

3.1 ESH Stewardship

The MOB Program Manager(s) can provide responsible ESH stewardship by promoting a proactive ESH policy throughout the program including involvement by the industry teams. At the earliest possible stage, a proactive ESH policy statement will place ESH requirements from the ORD on the same level as cost, space, weight, affordability, and other similar factors.

Two examples of aggressive but achievable ESH policy statements are those developed by the Virginia Class Submarine and the DD 21 Program Offices. The programs both issued very aggressive policy statements for the program participants to follow when considering ESH life cycle aspects of the respective systems. This stewardship is allowing the Virginia Class Submarine and the DD 21 Program Offices to effectively integrate ESH considerations into all decisions affecting their systems.

The duties of any Acquisition Program Manager are numerous. To execute and adjudicate the multiple aspects of a program, managers are appointed for issues such as risk, research and development, logistics and cost. For a program as daunting as the MOB, it would be logical and prudent to appoint a full time ESH Manager to execute and fulfill the intent of the Program Manager's ESH policy statement and to ensure the requirements set forth in the ORD are addressed and coordinated effectively in all appropriate contracting documentation.

3.2 MOB ESH Manager

The MOB ESH Manager should be responsible for the establishment, implementation, and maintenance of the ESH program. The key function of the ESH Manager would be to integrate ESH issues into the systems engineering process meeting all requirements of DoD Regulation 5000.2-R. Based on our experience with acquisition programs, to adequately meet the exit criteria required by the Milestone Decision Authority, the MOB Manager(s) should develop an ESH acquisition strategy that meets the intent of 5000.2-R. At a minimum, it is recommended the ESH Manager:

- Develop, execute and maintain a comprehensive ESH Management Plan
- Maintain and update the Programmatic Environmental Safety and Health Evaluation (PESHE)
- Develop and execute ESH requirements (compliance, pollution prevention, hazardous material, safety and health and pollution control) based on the guidance stated in the ORD
- Develop consistent achievable ESH metrics for MOB participants to use as guidance

- Assist the various MOB Program/Project Managers in the identification of actions that require National Environmental Policy Act analysis documentation
- Develop and execute an ESH training program that provides guidance on identification and mitigation actions for meeting applicable MOB ESH requirements
- Provide guidance to the industry team(s) on the ORD ESH requirements in the MOB Program
- Project ESH program budget and resource requirements.

To ensure consistency between MOB program office and industry team personnel, the ESH Manager must also ensure the industry team(s) include, at a minimum, the following aspects of ESH into the acquisition program at the earliest stage:

- Integrate ESH requirements into the total MOB systems engineering approach in the same manner as cost, logistics, and maintenance
- Ensure system trade-off analysis adequately considers ESH requirements
- Identify and interpret current and proposed ESH policy that may affect their construction facility and that of their major sub-contractors
- Determine the ESH impacts anticipated during the construction and throughout the lifetime operation of the MOB
- Implement an environmental risk reduction approach pertaining to cost and schedule through early identification, planning, and compliance with ESH requirements.

It should also be noted that the industry teams as well as their vendors should be responsible for upholding the ESH goals of the MOB Program. Every effort should be made by the MOB ESH Manager to ensure that major program activities such as contracting, planning, decision-making and budgeting reflect the ESH goals and objectives of the MOB program. This will ensure that adequate resources, staff and equipment are available when required.

4.0 ESH MANAGEMENT PLAN FOR THE MOB

The ESH Management Plan for the MOB should provide guidance and pertinent information relating to ESH responsibilities, requirements and provide an anticipated program objective and milestone (timeline) schedule of events. In addition, the ESH Plan should show the responsibilities and requirements for the MOB ESH Program as they relate to the ORD requirements. The environmental program should include all actions necessary to support the MOB environmental strategy.

The major components of the ESH Management Plan should include:

- Pollution Prevention
- ESH Compliance
- National Environmental Policy Act (NEPA) and Executive Order (EO) 12114 Environmental Effects Abroad of Major Federal Actions
- Hazardous Material Control & Management
- ESH Training
- Safety and Health
- Environmental Life Cycle Cost Analysis
- ESH Technical Advisory Group
- Documentation Management.

4.1 Pollution Prevention

The concept of pollution prevention is to prevent the generation of pollutants during the entire life cycle of the MOB. Potential ESH impacts associated with all MOB system and sub-systems will need to be identified and assessed in an effort to minimize the generation of pollution. As a minimum, for each system evaluated, the following areas should be considered:

- Use of natural resources and raw materials
- Solid and hazardous waste management
- Source reduction
- Liquid discharges
- Air emissions
- Federal, State, Local, National and International environmental requirements.

To manage this aspect of the MOB ESH program, it is recommended that the program develop a Pollution Prevention Strategy. The purpose of the subject strategy should be to establish actions and procedures to bring together pollution prevention requirements called for in directives and instructions on system acquisition.[2] The activities defined will facilitate life cycle product and process requirements for priority materials/issues.

4.2 ESH Compliance

Federal, State, Local and International ESH regulations provide a source of external program drivers to the life cycle of the MOB. While these rules and regulations frequently change, the initial minimum requirements that the MOB will adhere to are discussed in the MOB Classification Guide (DRAFT), Section 15A, dated April 1999. To minimize the risk to cost and schedule that ever-changing ESH regulations may cause, new ESH regulations should be regularly reviewed and potential impacts to cost, schedule, and performance evaluated.

The requirements for meeting the regulations should be divided into: (1) current requirements, (2) MOB thresholds and (3) MOB projected goals. Current requirements would be those that the MOB or similar platforms currently meet. MOB thresholds should be based on compliance with current ESH requirements as modified by near term changes that are likely known and projected to be in effect by to a specific point in time and beyond. The projected goals are the desired

ESH performance standards, which would be selected to ensure the MOB faces no operational restrictions over its life cycle.

It would also show prudent business sense to have industry monitor new ESH requirements that may effect their facilities and potentially impact the systems and subsystems of the MOB. To ensure that the MOB will be able to operate and perform its designated mission anywhere in the world, MOB Classification Guide (DRAFT), Section 15A, dated April 1999, recommends reviewing the environmental requirements of three countries. It is recommended that these three countries have the most stringent ESH requirements. Designing to the strictest requirements will ensure the MOB can be deployed anywhere, anytime.

4.3 National Environmental Policy Act and Executive Order 12114

The NEPA process is intended to help public officials make decisions that are based on the understanding of environmental consequences and take actions that protects restore and enhance the environment.[3] The MOB program must ensure total compliance with NEPA and EO 12114. These requirements are expected to be encountered at various stages in the life cycle of the MOB. As stated in the MOB Classification Guide (DRAFT) Section 15A dated April 1999, "NEPA will be applicable for construction, testing or operation of MOBs located in waters of the United States, its territories or possessions." Of all the major ESH requirements, failure to comply with the requirements of NEPA and EO 12114 can place the entire program schedule at risk.

4.4 Hazardous Material Control & Management

MOB must be designed to incorporate pollution prevention principles including minimal use of hazardous or toxic materials, which will serve to further reduce the cost of operation throughout the vessel's life from construction to disposal. Eliminating the use of environmentally harmful chemicals, such as toxic hydraulic fluids, certain types of solvents, cleaners, lubricants and paints, ozone-depleting substances, and other hazardous materials, would be the preferred method for reducing most potential problems. Substitution or replacement of hazardous chemicals with less hazardous substitute materials (i.e., environmentally preferable lubricants and bioenzymatic cleaners) for most military applications will serve to reduce hazardous waste management, disposal costs, and diminish the exposure to personnel of potentially dangerous substances.

It is recommended the program establish an aggressive hazardous material control and management (HMC&M) program. The program should strive to eliminate, reduce or substitute hazardous materials whenever feasible and properly manage the remaining hazardous materials. It is recommended that a hazardous material avoidance list be developed and maintained throughout the life cycle of the MOB. This list can be developed from sources such as:

- Environmental Protection Agency list of 17 Toxic Chemicals
- Extremely Hazardous Substances (40 CFR 355, Appendix A)
- Listed Carcinogens under the National Toxicology Program
- RCRA Characteristics and Listed Hazardous waste (40 CFR 261)
- OSHA Toxic and Hazardous Substances (29 CFR 1910.1000)
- NSSN List of 70 Hazardous Substances.

The MOB team should explore a number of other solutions to comprehensively address hazardous material related problems. These include extensively reviewing all potential hazardous material source reduction opportunities, such as commercially available pollution prevention technologies and equipment that utilize less hazardous substitute materials thereby reducing hazardous material waste streams; process modifications that will meet or sustain operation, maintenance, housekeeping and disposal requirements; and medical waste management alternatives.

The HMC&M program should also provide an interactive methodology that will allow the designer, builder, operator, as well as maintenance and disposal personnel to know where all hazardous material is stored and designed into the MOB.

Acquisition programs conducted by DoD components also require the weapon system contractor to implement a Hazardous Materials Management Program (HMMP). One way to accomplish this is to use the National Aerospace Standard (NAS 411). The purpose of the HMMP, as stated in the NAS 411, is to ensure that "adequate consideration is given to the elimination or reduction of hazardous materials used or generated by the system being analyzed throughout its life cycle."

4.5 ESH Training

The MOB ESH Manager should initiate an interactive and proactive ESH training program. The training program should be designed around the particular events of the MOB's life cycle phases. This training program should not be designed to convert MOB participants into ESH experts but emphasize the goals and objectives of the ESH Program. The training should provide the basic knowledge necessary to recognize actions, materials, and requirements that may have potential negative ESH impacts during the life cycle of the MOB. This training should also be made available to the major contractors involved.

The following is representative of the issues that should be presented:

- Identification, selection and approval for use of major hazardous materials
- Programmatic planning for inclusion of pollution prevention in life cycle cost estimates
- Inclusion of ESH language into the request for proposal, statement of work, source selection criteria and other contract provisions
- Emerging ESH requirements that may affect the MOB.

4.6 Safety and Health

As requirements and performance specifications are determined, system safety and health hazards should be identified and evaluated. All identified health hazards as well as the associated risk that may impact the MOB during design, construction, testing, operation, maintenance, and disposal should be integrated into the MOB design. One model for this system safety program is MIL-STD 882-C.

Several acquisition programs have coordinated these efforts through the establishment of a Human Systems Integration Team or a "Safety and Industrial Hygiene Team" as stated in the MOB Classification Guide (DRAFT) Section 15A dated April 1999. This team should provide the MOB ESH Manager with the necessary tools for identifying system safety and occupational safety and health requirements of the MOB and associated systems and subsystems.

4.7 Environmental Life Cycle Cost Analysis

One of the major questions facing program managers today is: during the development of the overall cost for a major weapon system, what is the best way to account for the environmental cost over the life cycle of the weapon system? Environmental life cycle costing analysis would attempt to provide the MOB Program Manager(s) with a defensible method for making sound environmental decisions on processes and material selections while not sacrificing operating or survivability characteristics of the MOB. Additionally, good foresight tells the MOB Program Manager(s) that in order to field and maintain the MOB, it must also be affordable to the sustainment community. If environmental cost information remains hidden and unaccounted for in the decision-making process, well-informed decisions on ESH management and sound pollution prevention investments cannot be made by the MOB Program Manager(s).

Environmental life cycle cost estimating methodology should simply be part of the overall evaluation to assist the MOB Program Manager(s) in making sound design and business decisions on processes or material selection aspects over the life cycle of the program.

An overall evaluation should include answering several questions such as:

- What are the significant environmental impacts and costs associated with similar fielded programs?
- What processes/operations/materials will create the most significant environmental impacts throughout the life cycle of the MOB?
- What is the root cause of the impacts and costs? (military specification/standard, existing or proposed Federal State or Local International ESH regulations, etc.)
- What can be changed (now for fielded systems and during design of new systems) to minimized environmental impacts and costs?
- What are the expected effects on cost, environment, operations and performance of the subject change?

While there are voluminous tools available for this type of activity, it is recommended that the MOB ESH Manager look incrementally at the MOB system and subsystems for a tool that is not burdensome to the program.

4.8 ESH Technical Advisory Group

To facilitate the inclusion of a total life cycle perspective, it is recommended that the MOB ESH Manager establish an ESH Technical Advisory Group (TAG). The MOB ESH TAG should be composed of personnel associated with the various aspects of the MOB life cycle.

The ESH TAG should be matrixed into the entire MOB program. Their primary goal should be to ensure the incorporation of ESH issues into working government and industry teams who will provide oversight and leadership in the development of strategies for evaluation of all alternatives, logistics, and cost performance trade-offs. Potential members might include:

- MOB ESH Manager
- Industry Team ESH Manager
- Legal Policy and Regulatory Affairs
- System/Worker Safety
- MOB Design and Engineering
- Facilities
- Mission Specific Users
- Research Development
- Environmental Specialist (i.e. Marine Biologist)
- Test and Evaluation
- Joint Services Representatives
- Media Specific Specialist
- Consultants.

4.9 Documentation Management

Competent defensible information pertaining to the ESH philosophy is necessary to ensure the MOB ESH

program can accomplish its goals and comply with applicable Federal, State, Local and International ESH requirements.

A Programmatic ESH evaluation (PESHE) or update will need to be assembled and submitted as part of the MOB Program Acquisition Strategy at each program milestone or representative event. At a minimum, the PESHE should be supported by the following documentation:

- ESH Management Plan
- Hazardous and Non Hazardous Material Studies
- Hazardous Material Management Program Plan
- NEPA Documents
- System Safety and Health
- ESH Life cycle Cost Estimates and Analysis
- ESH Trade-off Analysis
- ESH Awareness Training
- Design Alternative ESH Evaluations
- Pollution Prevention Strategy
- Lessons Learned from other Acquisition Programs.

5.0 MAJOR WEAPON SYSTEM INTEGRATION

The MOB will be a staging area for troops, airplanes, tracked vehicles, electronic assets and ships. While the MOB program cannot completely control the ESH concerns that these systems may bring to the MOB, it is imperative that the designers request input from all military and commercial components to determine the potential ESH impacts their systems may present.

Representative wastes from ships, aircraft, tracked vehicles, crew and troops consists of:

- Graywater
- Blackwater
- Hazardous material
- Sealants/solvents
- Engine emissions
- Noise
- Medical waste
- Inorganic and anti-foul coatings
- Paints
- Glycol coolants
- Petroleum oils/lubricants/hydraulic fluids
- Batteries
- Paper products
- Food wastes
- Metals
- Plastics
- Glass
- Rags.

6.0 RESEARCH AND DEVELOPMENT

A strong set of ESH requirements in the ORD can assist with scoping out potential research and developments needs for the MOB. ESH research and development needs should focus on demonstrating technologies and processes in which the required ESH attribute are attainable. Relevant research and development the MOB ESH Manager may propose for implementation are:

- Detailed pollution prevention research necessary to identify alternatives to replace hazardous materials
- Research required for satisfying impending future ESH requirements associated with construction, manufacturing, operation, maintaining or disposing the MOB
- Engineering studies to assess the most practical means to manage and mitigate liquid, solid and/or special system waste or byproducts.

7.0 CONCLUSION

The MOB must be capable of operating worldwide unconstrained by ESH regulations. MOB should be designed and constructed to comply with all applicable Federal, State, Local and International ESH laws, regulations, agreements and treaties. These include but are not limited to the Clean Air Act, Clean Water Act, the Resource Conservation Recovery Act, the Act to Prevent Pollution from Ships, the Marine Mammal Protection Act, the Montreal Protocol, the Uniform National Discharge Standard and the International Convention for the Prevention of Pollution from Ships (MARPOL 73/78).

With ESH requirements, management and planning functions incorporated into the MOB acquisition program, the MOB Program Manager(s) will be fully prepared to pursue the numerous ESH activities needed for successful fielding of the MOB system.

Acknowledgement

This paper was completed under Government Contract N00174-98-D-0005.

References

[1] *Department Defense 5000.2-R Acquisition Policy Regulation. Mandatory Procedures for Major Defense Acquisition Programs and Major Automated Information System Acquisition Programs.* US Department of Defense, 1998.

[2] *Pollution Prevention Strategy for the New Attack Submarine Program.* Program Executive Office Submarines, US Navy, 1996.

[3] *40 CFR § 1500.1 (c) 1978.*

PROCEEDINGS OF THE THIRD INTERNATIONAL WORKSHOP ON VERY LARGE FLOATING STRUCTURES
(VLFS '99), VOL. I, EDS. R.C. ERTEKIN & J.W. KIM, 22-24 SEPTEMBER 1999, HONOLULU, HAWAII, USA

THE NUMERICAL SIMULATION OF WATER MASS SURROUNDING THE VERY LARGE FLOATING STRUCTURE WITH THE WATER PARTICLES TRACING METHOD

Takaharu Hamada*and Masataka Fujino†
*Kyushu University
†The University of Tokyo

ABSTRACT

In order to evaluate the influence of very large floating structure on marine environment, it is necessary to know the effects of the floating structure on the water circulation around it and in particular important to evaluate the water exchange process under the floating structure. In order to investigate this, numerical experiments of water exchange process around the floating structure which is placed at the center of rectangular bay were performed by using the water particle tracing method. Through these experiments, it was found that water exchange around the center of the bay is promoted in the presence of the floating structure. It is also found that althogh thereis no remarkable differnece between the temporal variation of remnant fuction in summer and that in winter, threre are large differences between the spatial distributions of water particles at the final state of the experiments in summer and those in winter. Moreover, there is a differnece between the temporal vatiation of remnant function in the cases that between the daily variation of solar raidiation is included and not. This result indicates that it is neccesarry to consider daily variation of solar radiation in the simulation of the water circulation around a very large floating structure.

1. INTRODUCTION

The very large floating structure (VLFS) is now coming into the spotlight for large scale utilization of ocean space (e.g. floating airport etc.), since the environmental impact of VLFS is considered to be small. However, it is not well-known that how much impact does the VLFS cause the environment of coastal ocean, and in particluar how does the VLFS changes the circulation of water and the water exchange process.

In order to disscuss the environment of coastal ocean, the idea of "water mass exchange" is important as disscussed in Kashiwai[1]. For evaluating this, Imasato and Awaji[2] developed the method of numerical simulation to trace the movement of water particles.

In this study, we performed the numerical experiments by using the water particle tracing method to evaluate the effects of the floating structure on the water exchange process of surrounding water and discussed the seasonal variation of water exchange processes. We also discussed the effects of daily variation of solar radiation on the water mass exchange processes.

2. METHOD OF NUMERICAL SIMULATION

2.1 Calculation of velocity field

In this section, we describe the method of the velocity field calculation. It is essentially the same as in Tabeta et al.[3] and Fujino et al.[4].

2.1.1 Governing equations and thier discretizations

The governing equations are the traditional hydrodynamic equations for conservation of mass, momentum, temperature, and salinity with right-handed Cartesian coordinates (see Fig. 1). The momentum equations with f-plane, Boussinesq and hydrostatic approximations are as follows :

*6-1 Kasuga-koen, Kasuga, Fukuoka 816-8580, Japan. E-Mail: hamada@esst.kyushu-u.ac.jp
†7-3-1 Hongo, Bunkyo-ku, Tokyo 113-0033, Japan. E-Mail: fujino@k.u-tokyo.ac.jp

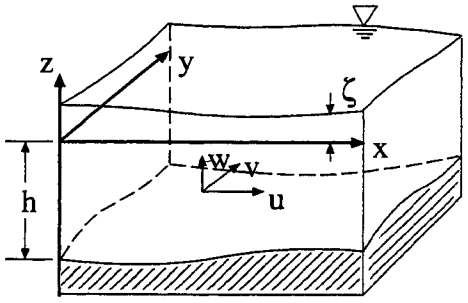

Figure 1: Coordinate System for numerical simulation.

$$\frac{Du}{Dt} = -\frac{1}{\rho_0}\frac{\partial p}{\partial x} + fv + A_M\left(\frac{\partial^2 u}{\partial x^2} + \frac{\partial^2 u}{\partial y^2}\right) + \frac{\partial}{\partial z}\left(K_M\frac{\partial u}{\partial z}\right) \quad (1)$$

$$\frac{Dv}{Dt} = -\frac{1}{\rho_0}\frac{\partial p}{\partial y} - fu + A_M\left(\frac{\partial^2 v}{\partial x^2} + \frac{\partial^2 v}{\partial y^2}\right) + \frac{\partial}{\partial z}\left(K_M\frac{\partial v}{\partial z}\right) \quad (2)$$

$$0 = -\frac{1}{\rho}\frac{\partial p}{\partial z} - g \quad (3)$$

where, u, v, w, ρ_0, A_M, K_M, p, f and g are x, y, z components of velocity, reference density, horizontal and vertical eddy viscousity, pressure, coriolis parameter and acceralation of gravity, respectively. In this study, coriolis parameter, f is set to zero for simplicity.

In the limit of incompressibility, the equation of conservation of mass becomes the continuity equation as follows :

$$\frac{\partial u}{\partial x} + \frac{\partial v}{\partial y} + \frac{\partial w}{\partial z} = 0 \quad (4)$$

The equations for temperature and salinity are as follows :

$$\frac{DT}{Dt} = A_C\left(\frac{\partial^2 T}{\partial x^2} + \frac{\partial^2 T}{\partial y^2}\right) + \frac{1}{\delta}\frac{\partial}{\partial z}\left(K_C\frac{\partial T}{\partial z}\right) \quad (5)$$

$$\frac{DS}{Dt} = A_C\left(\frac{\partial^2 S}{\partial x^2} + \frac{\partial^2 S}{\partial y^2}\right) + \frac{1}{\delta}\frac{\partial}{\partial z}\left(K_C\frac{\partial S}{\partial z}\right) \quad (6)$$

where, T, S, A_C, K_C and δ are water temperature, salinity, horizontal and vertical eddy diffusivity and the parameter of convective adjustment. We apply the stratification function to determin K_M and K_C[5].

Boundary conditions at sea floor are described as follows:

$$u\frac{\partial h}{\partial x} + v\frac{\partial h}{\partial y} + w = 0 \quad (7)$$

$$K_M\frac{\partial u}{\partial z} = \frac{\tau_{xB}}{\rho_0} \quad (8)$$

$$K_M\frac{\partial v}{\partial z} = \frac{\tau_{yB}}{\rho_0} \quad (9)$$

where, h denotes water depth and the bottom stress is described as follows: which are described as follows:

$$\tau_{xB} = \gamma^2\rho_0 u\sqrt{u^2+v^2} \quad (10)$$

$$\tau_{yB} = \gamma^2\rho_0 v\sqrt{u^2+v^2} \quad (11)$$

where, τ_{xB} and τ_{yB} denote x and y components of bottom stress, respectively and γ represents the bottom friction coefficient.

Boundary conditions at sea surface are as follows:

$$-\frac{\partial \zeta}{\partial t} - u\frac{\partial \zeta}{\partial x} - v\frac{\partial \zeta}{\partial y} + w = 0 \quad (12)$$

$$K_C\frac{\partial T}{\partial z} = \frac{Q_T}{\rho_0 C} \quad (13)$$

$$K_C\frac{\partial S}{\partial z} = \frac{Q_S}{\rho_0} \quad (14)$$

where C is specific heat, Q_T and Q_S are flux of heat and salinity.

The equation of sea surface elevation is obtained by integrating Eq.(4) from the sea bottom($z = -h$) to the sea surface($z = \zeta$) under the boundary condition Eqs. (7) and (12).

Pressure is obtained by integrating Eq.(3) from sea surface as:

$$p = p_0 + \int_z^\zeta \rho g dz \quad (15)$$

where p_0 is the atmospheric pressure on the sea surface.

The governing equations with their boundary conditions are solved by finite difference techniques with staggard arrengement of grid points and a leap frog scheme. Variables u,v,ζ, S, and T are solved by the discretized forms Eqs. (1), (2), (5), and (6) explicitly, and w and p are calculated by the discretized forms Eqs.(4) and (15) using u,v,ρ at each time step.

2.1.2 Expression of floating structure

In order to calculate the motion of floating structure, the dynamical equations of the motion of floating structure and the hydrodynamic equations of fluid motion must be solved simultaneously.

However, if the assumption is made that the vertical movement of floating structure is not restricted and the movement of it is vely slow, these equations can be transformed to the equation as follows :

$$p = p_0 + \rho g(\zeta' - Z) \quad (16)$$

where ζ' denotes imaginary sea surface,which is defined so as to satisfy following equation

$$\zeta' - Z = d \quad (17)$$

where, Z is the vertical displacement of the bottom of floating structure, d is the draft of the structure. Eq. (16) is the same form of the equation of the hydrostatic balance and threfore the pressure under the structure is easily calculated by the same algolythm used at the free-surface. For more detail, see the reference[4] et al.

2.2 Total flux of heat and salinity

In this study, heat flux through the sea surface Q_T is expressed as,

$$Q_T = (1 - \mathrm{ref})S^{\downarrow} - \varepsilon(\sigma\theta_s^4 - L^{\downarrow}) - H - \iota E. \quad (18)$$

where, $S^{\downarrow}$ is global solar radiation, ref is albedo, ε is emittance, σ is Stefan-Boltzman constant, θ_s is water temperature at sea surface, $L^{\downarrow}$ is downward longwave radiation, H is sensible heat flux, ι is latent heat of vaporization, and E is water flux by evapolation. In this study,floating structure is assumed to be insulator($Q_T = 0$).

$S^{\downarrow}$ is calculated by using the Suzuki&Aratani's equation[6]. If weather condition would not change, $L^{\downarrow}$ could be assumed to be constant. Thus, we approximate $L^{\downarrow}$ by an average of experimental value, $L^{\downarrow}_{df}$. $L^{\downarrow}_{df}$ is described as follows:

$$L^{\downarrow}{}_{df} = (0.74 + 0.19x + 0.07x^2)\sigma\theta_a^4 \quad (19)$$

$$x = \log_{10} w_{TOP}{}^{*} \quad (20)$$

where w^*_{TOP} is effective water vapor amount.

Equations for H and E are described by use of bulk aerodynamic method as follows :

$$E = \rho_a C_E U(q_{SAT,S} - q) \quad (21)$$

$$H = C_p \rho_a C_H U(T_s - T_a) \quad (22)$$

where C_H and C_E are bulk constant, ρ_a is density of air, U is wind velocity, q is specific humidity, $q_{SAT,S}$ is specific humidity of sea water, C_p is specific heat, T_S is water temperature at sea surface, and T_a is air temperature.

Salinity flux through the sea surface is calculated approximately as follows :

$$Q_S = SE = S\rho_a C_E U(q_{SAT,S} - q) \quad (23)$$

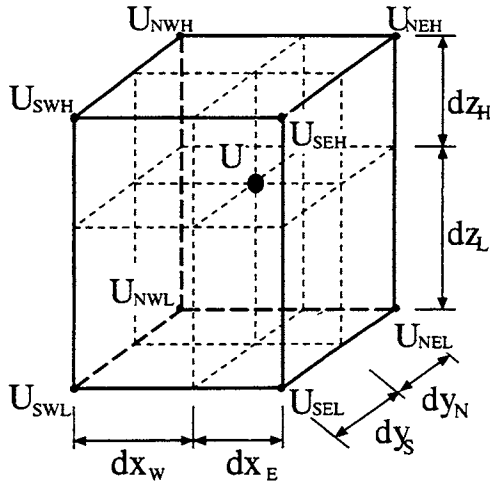

Figure 2: Scheme of interpolation for velocity.

since vaporized water mass is much smaller than the mass of sea water.

2.3 Calculation of trajectories of water particles

The position of a water particle at $m+1$ time step is written as follows[2]:

$$\mathbf{X}(t^{m+1}) = \mathbf{X}(t^m) + \int_{t^m}^{t^{m+1}} \mathbf{U}(\mathbf{X}(t^m), t)dt + \int_{t^m}^{t^{m+1}} \int_{t^m}^{t} \mathbf{U}(\mathbf{X}(t^m), t')dt' \cdot \nabla\mathbf{U}(\mathbf{X}(t^m), t)dt \quad (24)$$

where, $U(X(t), t)$ denotes eularian velocity of water at time t, which is interpolated from velocities calculated at 8 grid points around the particle. For example, u and $\partial u/\partial x$ in the descrete form is described as follows(for description of the symbols such as SWL etc., see Fig. 2),

$$\begin{aligned} u = {} & (((U_{SWL} \cdot dx_E + U_{SEL} \cdot dx_W) \cdot dy_N \\ & + (U_{NWL} \cdot dx_E + U_{NEL} \cdot dx_W) \cdot dy_S) \cdot dz_H \\ & + ((U_{SWH} \cdot dx_E + U_{SEH} \cdot dx_W) \cdot dy_N \\ & + (U_{NWH} \cdot dx_E + U_{NEH} \cdot dx_W) \cdot dy_S) \cdot dz_L) \\ & /(dx \cdot dy \cdot dz) \end{aligned} \quad (25)$$

$$\frac{\partial u}{\partial x} = ((U_{SWL} + U_{NWL} + U_{SWH} + U_{NWH}) - (U_{SEL} + U_{NEL} + U_{SEH} + U_{NEH}))/(4 \cdot dx) \quad (26)$$

3. MODEL BASIN AND CALCULATION CONDITION

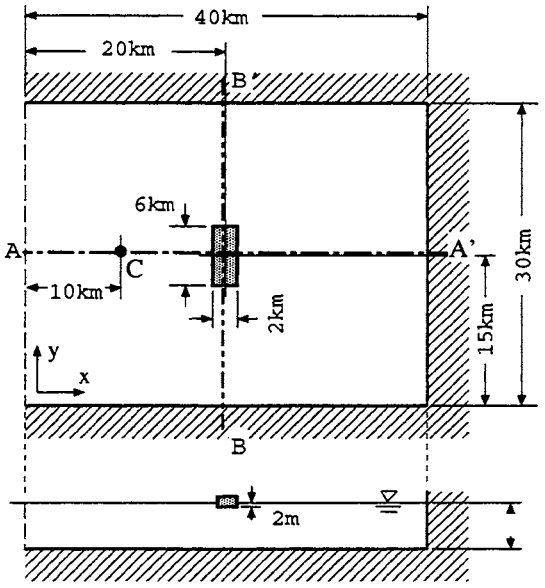

Figure 3: Model sea area used in numerical simulation.

A simple rectangular bay is adopted as a model basin as shown in Fig. 3. At the center of the model basin, a pontoon-type floating structure of B=2km,L=6km and D=2m is placed. The model basin has an open boundary at its western boundary. At the open boundary, non-reflection scheme which is developed by Hino[7] is adopted and semi-diurnal tidal elevation is given as that the amplitude of which at the center of the bay may be 0.5m. In order to discuss the effects of the the seasonal variation of the meteorological condition and water properties (temperature and salinity), different values of which in summer (July) and winter (January) are adopted (See Table 1).

Under these conditions, calculation is performed in 9 cases which are summarized in Table 2.

The distributions of water particle at the initial state are same in Cases 1-8 as shown in Fig. 4 and the number of particle is $432(=4\times12\times9)$. In order to evaluate the effects of the number of particles at an initial state of the results of the calculation, we performed the additional experiment of which the number of particles at an ititial state were increased as 150 times as large as Cases 1-8 (five times in x and y-directions, and six times in z-direction). This experiment is called Case 9.

The periods of calculation are 7 days(14 periods of semi-diurnal tide). The first day of calculation is for the approach time to the quasi-steady state, and another 6 days are for the tracing of particles.

4. RESULTS

Table 1: Parameters for calculation.

Parameters for all seasons			
dx,dy	1.0	[km]	Horizontal mesh size
dz	4.0	[m]	Vertical mesh size
Δt	10	[sec]	Calculation interval
Parameters for summer (Jul.)			
ref	0.06		Albedo of sea surface
p_a	1007.3	[HPa]	Air pressure
T_a	29.9	[℃]	Air temperature
e	26.1	[HPa]	Vapor pressure
U	3.8	[m/sec]	Wind velocity
T_0	20.3	[℃]	Initial condition of temperature
S_0	27.29	[PSU]	Initial condition of salinity
Parameters for winter (Jan.)			
ref	0.10		Albedo of sea surface
p_a	1018.9	[HPa]	Air pressure
T_a	6.1	[℃]	Air temperature
e	5.8	[HPa]	Vapor pressure
U	3.4	[m/sec]	Wind velocity
T_0	10.66	[℃]	Initial condition of temperature
S_0	30.86	[PSU]	Initial condition of salinity

Table 2: Condition of calculations.

Case	Floating Structure	Solar radiation	Season	Number of particles
1	exists	variable	summer	432
2	not exist	variable	summer	432
3	exists	constant	summer	432
4	not exist	constant	summer	432
5	exists	variable	winter	432
6	not exist	variable	winter	432
7	exists	constant	winter	432
8	not exist	constant	winter	432
9	exists	variable	summer	64800

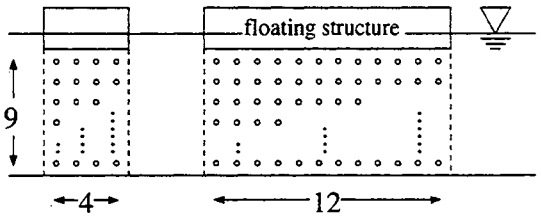

Figure 4: Initial distribution of particles.

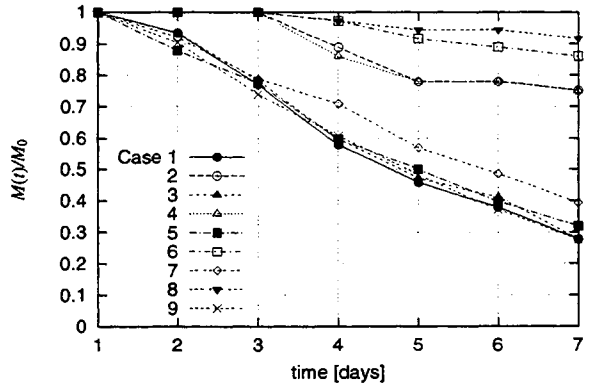

Figure 5: Temporal variations of remnant function.

The remnant functions of the water under the structure for each case are shown in Fig. 5.

In this study the remnant function $R(t)$ is defined to the water mass under the structure, and its expression is as follows:

$$R(t) = M(t)/M(0) \tag{27}$$

where $M(0)$ is the number of particles which exists under the structure in initial state and $M(t)$ is the number of particles which remains under the structure at the time t.

4.1 Improvement of water mas exchange in the presence of the floating structure

Comparing the remnant functions between case 1 and 2, it shows that the floating structure improves water mass exchange. Figs. 6 and 7 show the distributions of particles after 6 days from the start time of tracing of particle in case 1 and 2.

In Case 2 (Fig. 7), the distribution of particles is not disturbed and is not quite different from initial state. On the other hand, Fig. 6 (Case 1) shows that the particle shifts 7 km away from the center of the structure. It shows that the area that water exchange occurs in Case 1 is wider than that in Case 2.

In Fig. 5, we can see that the remnant functions of case 1 and 9 are very similar. Thus, we consider that the number of the particles at an initial state does not affect the results of the calculation.

4.2 Seasonal variation

Comparing the remnant functions in Cases 5 and 6 in Fig. 5, we find no significant difference between remnant functions in winter as same as in summer. However, the spatial distributions of particles are quite different between the cases in summer and winter. Fig.6 and 8). Fig. 8 shows the spatial distributions of particles in Case 5 at the time six days

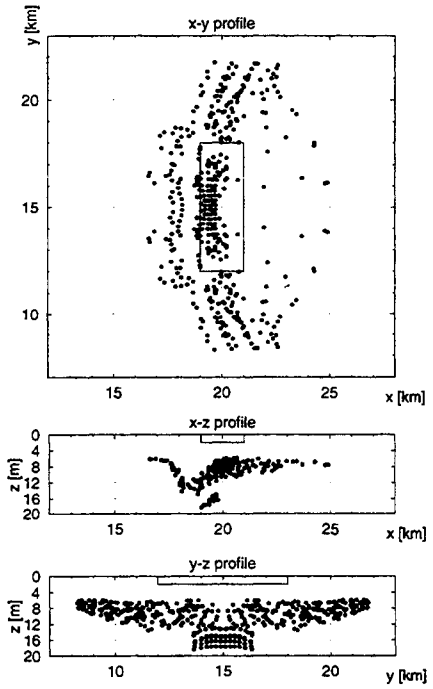

Figure 6: Distributions of particles at the end of calculation; Case 1 (Summer, without floating structure).

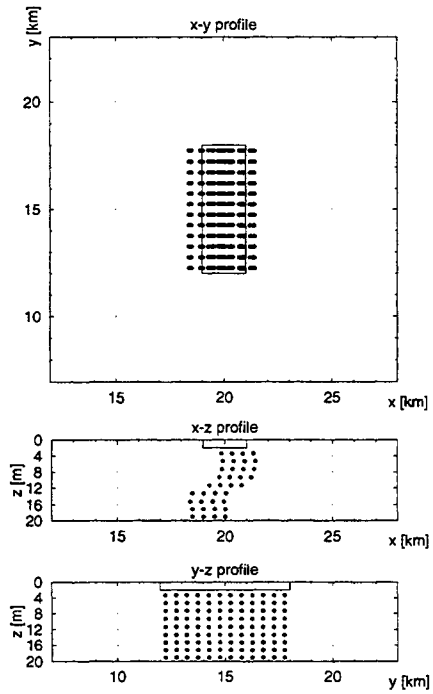

Figure 7: Distributions of particles at the end of calculation; Case 2 (Summer, with floating structure).

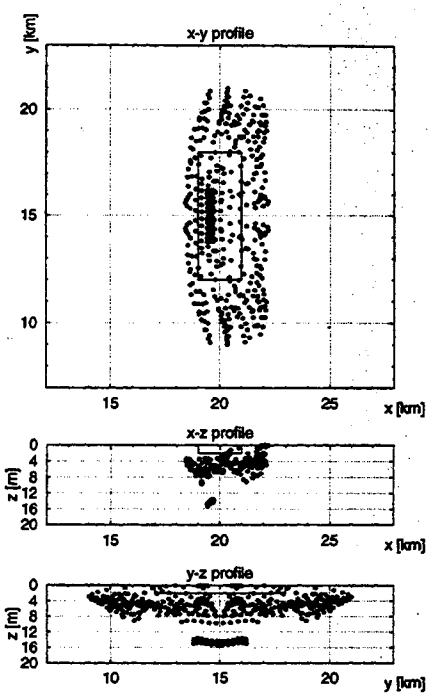

Figure 8: Distributions of particles at the end of calculation; Case 5(Winter, with floating structure).

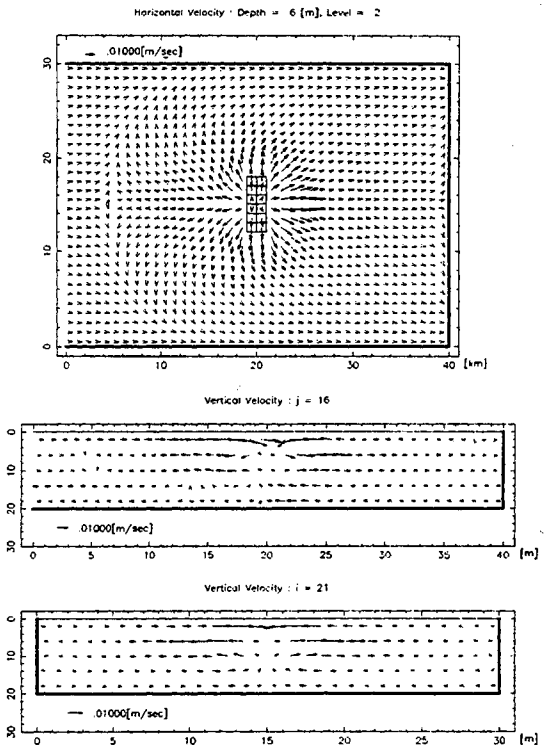

Figure 9: Horizontal and vertical profiles of residual flow; Case 1 (Summer, with floating structure).

after from the initial time. Campared with Fig. 6, it seems that the water mass under the structure quickly exchanges the surrounding waters, but does not move so far from the structure. On the other hand, in Fig. 6 we found that there is no water particles above a 4-m deep and they concentrates in the layer between 4-m and 8-m deep in Case 1.

Figs.9 and 10 show the distribution of tidal residual current of case 1 and 5, respectively.

It shows that the effects of the structure on the residual flow reaches so far from the structure in Case 1 than in Case 5 and the pattern of the residual flow in the upper layer (from 0-m to 4-m deep) in Case 1 differs from that in Case 5. It seems that difference of distribution of particles correspond to these differences of residual flow pattern.

4.3 Effect of daily variation of solar radiation

To discuss the effect of daily variation of solar radiation, the calculation with constant solar radiation condition was done and compared with that with variable solar radiation. In the Cases 3,4,7, and 8, the meteorological conditions are the same as in the Cases 1,2,5 and 6, except that the solar radiation does not change. Figs. 11 and 12 show the distribution of particles at the final state of calculations in Cases 3 and 7, respectively.

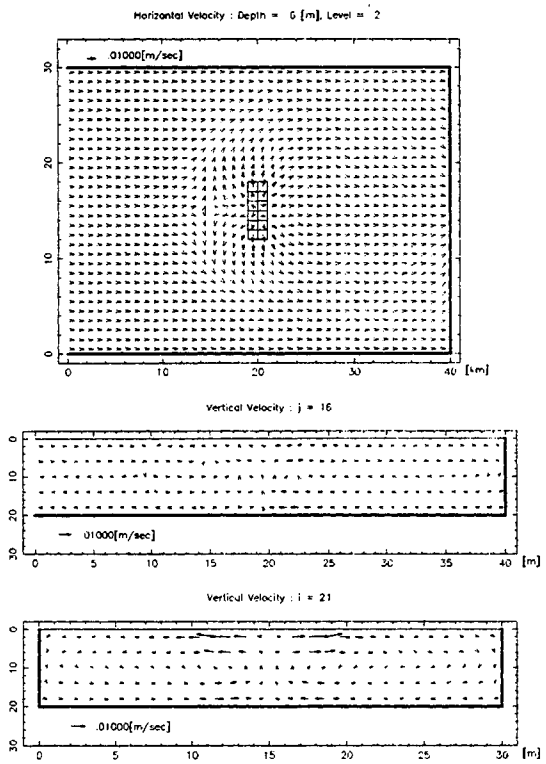

Figure 10: Horizontal and vertical profiles of residual flow; Case 5 (Winter, with floating structure).

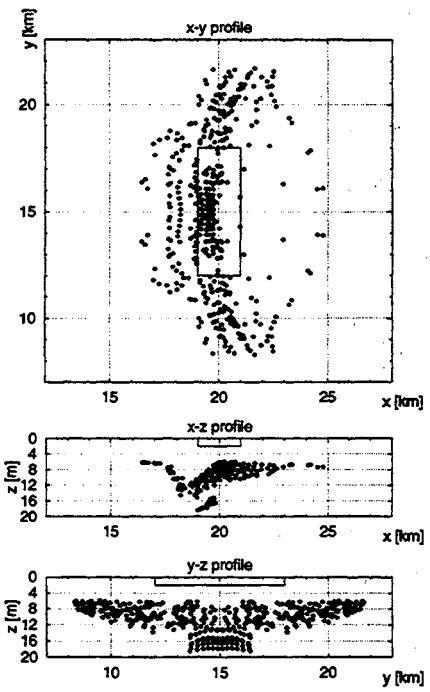

Figure 11: Distributions of particles at the end of calculation; Case 3 (Summer, with floating structure, constant solar radiation).

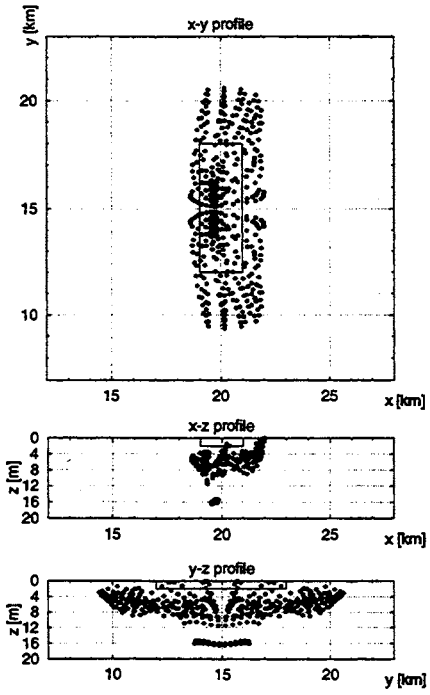

Figure 12: Distributions of particles at the end of calculation; Case 7 (Winter, with floating structure, constant solar radiation).

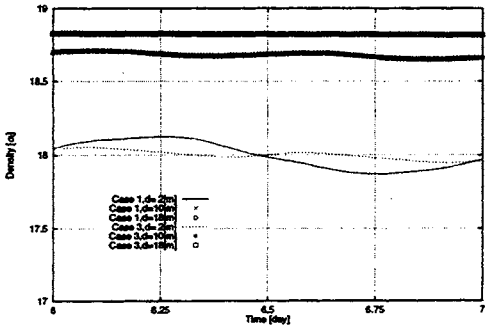

Figure 13: Temporal variations of density at point C in Case 1,3.

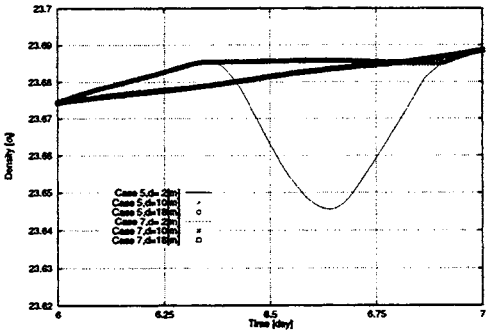

Figure 14: Temporal variations of density at point C in Case 5,7.

Distribution of particles in Case 1 (Fig. 6) is similar to that of Case 3,and distribution of particles in Case 5 (Fig. 8) is similar to that of Case 7. In Fig. 5, it seems that there is no remarkable difference whether the daily variation of solar radiation is taken into account or not in summer. In winter, however, the daily variation of solar radiations affects the water circulation around the floating structure, and consequently, the remnant function.

Temporal variations of density at the point C in Cases 1 and 3 are shown in Fig. 13. Whether an account of the daily variation of solar condition is taken or not, density stratification is found at point C throughout the period of calculation in summer.

In winter, however, Fig.14 shows that if daily variation of solar varidation is taken into account, density stratification is found in the daytime, but if not, there is no stratification throughout a day.

That may be the reason why the daily variation of solar radiation have greater effects in winter than in summer.

5. CONCLUSION

In this study, we simulated the movement of water mass under the floating structure by tracing water particle in a rectangular bay with a pontoon-type floating structure. and the results are summarized as follows :

1. The presence of the floating structure advances water exchange under the structure in summer and winter.

2. There is no remarkable difference between temporal varations of remnant function in summer and those in winter. However, significant differences are found between the spatial distributions of water particles at the final state of caculation in summer and in those in winter. These results correspond well to the velocity fields of the tidal residual currents in summer and winter.

3. In winter, the temporal variations of remnant functions vary depending on whether the daily variation of solar radiation is included or not. This result indicated that it is important to consider the daily variation of solar radiation in the simulation of water circulation around the VLFS.

Acknowledgments: The authors are grateful to Professor Yusaku Kyozuka, and Assistant Professor Atsuhiko Isobe, for their helpful comments. We also thank to the member of Laboratory of Coastal Environment Research, Department of Earth System Sciences and Technology,Interdisciplinary Graduate School of Engineering Sciences, Kyushu University.

References

[1] Makoto Kashiwai. The concept of tidal exchange and the tidal exchange ratio. *J. Oceanogr. Soc. Japan, Vol.40*, 1986.

[2] Norihisa Imasato, Toshiyuki Awaji, and Hideaki Kunishi. Tidal exchange through naruto, akashi and kitan straits. *J. Oceanogr. Soc. Japan*, 1980.

[3] Shigeru Tabeta and Masataka Fujino. Numerical simulation of currents and density variation in tokyo bay by means of multi-level model. *J. Soc. Naval Arch. Japan Vol.176*, 1994.

[4] Masataka Fujino, Hiroshi Kagemoto, and Takaharu Hamada. On the sea-covering effect of a huge floating structure on the surrounding water. *J. Soc. Naval Arch. Japan, Vol. 180*, 1996.

[5] Keiji Nakatsuji, Jae-Yeong Huh, and Akira Murota. Numerical experiments of three-dimensional buoyant surface discharges. *Japan Soc. Civil Engr., No.434*, 1991.

[6] Kenzo Suzuki and Noboru Aratani. The development of equations in the calculation of solar radiation. *Trans. Arch. Inst. Japan, No.279*, 1979.

[7] Mikio Hino. A very simple numerical scheme of non-reflection and complete transmission condition of waves for open boundaries. Technical report, Dept. Civil Engr., Tokyo Inst. of Techno., 1987.

PROCEEDINGS OF THE THIRD INTERNATIONAL WORKSHOP ON VERY LARGE FLOATING STRUCTURES
(VLFS '99), VOL. I, EDS. R.C. ERTEKIN & J.W. KIM, 22-24 SEPTEMBER 1999, HONOLULU, HAWAII, USA

A STUDY ON THE EFFECTS OF A VERY LARGE FLOATING STRUCTURE ON MARINE ENVIRONMENT

Daisuke Kitazawa and Masataka Fujino
University of Tokyo*

ABSTRACT

To realize a very large floating structure (VLFS) such as an artificial airport, it is indispensable to examine various effects on marine environment around a VLFS. For an assessment in the physical, chemical and biological aspects, a numerical study by means of an ecohydrodynamic model, which is an ecological-physical coupled model, has been performed. After verifying the ecohydrodynamic model, the effects of an imaginary VLFS on the surrounding environment are examined in two cases; the VLFS is installed in the sea area off Yokosuka or off Haneda in Tokyo Bay. As a result of some computations, it is concluded that the impacts of the VLFS on marine environment are localized in Tokyo Bay as a whole, however the extent of the effects is large in the sea area, where photosynthesis actively occurrs and residual current is slow.

1. INTRODUCTION

It is a common knowledge that the supply of land space has become more and more important with the development of human activities. As one of the solutions of this problem, a project on constructing a very large floating structure (VLFS) for ocean space utilization is now being conducted. A VLFS is said to have less effects on marine environment than a reclaimed island, however it is important to examine the impacts on the surrounding environment around a VLFS. For this examination, numerical simulation by means of the multilevel model is expected to be one of the useful tools. From a physical viewpoint, several numerical simulations for environmental impact assessment (EIA) of a VLFS has been conducted and it is found that the impacts are expected to be very small. In the meantime, discussion from the chemical and biological aspects is necessary for comprehensive EIA. Kyozuka et al. [1] and Nakagawa et al. [2] extended the multilevel model to simulate the distributions of organic and inorganic matters by means of the ecohydrodynamic model, which is an ecological-hydrodynamic coupled model developed by Nakata [3]. They represented that a VLFS may not have a large impact on the marine environment of Tokyo Bay.

In the present paper, the authors simulate the marine environment of Tokyo Bay using the ecohydrodynamic model and the results are compared with the observation data or existing computations. After that, the impacts of an imaginary VLFS on the surrounding environment are examined in two cases. In one case, an imaginary VLFS is installed in the sea area where residual current is fast and primary production is not active in Tokyo Bay, and in another case, an imaginary VLFS is installed in the sea area where residual current is slow and photosynthesis actively occurs. Then the difference between the effects in two cases is discussed.

2. NUMERICAL MODEL

2.1 Hydrodynamic model

2.1.1 Basic equations

Cartesian coordinate system in which the horizontal x-y plane is placed on the mean sea level and the z axis is positive upward is used in the present study. The equations of fluid motions and continuity with the assumptions of f-plain, Boussinesq and hydrostatic approximation are as follows [3];

$$\frac{Du}{Dt} = -\frac{1}{\rho_0}\frac{\partial p}{\partial x} + fv + A_M \nabla_H^2 u + \frac{\partial}{\partial z}\left(K_M \frac{\partial u}{\partial z}\right) \quad (1)$$

$$\frac{Dv}{Dt} = -\frac{1}{\rho_0}\frac{\partial p}{\partial y} - fu + A_M \nabla_H^2 v + \frac{\partial}{\partial z}\left(K_M \frac{\partial v}{\partial z}\right) \quad (2)$$

$$0 = -\frac{1}{\rho}\frac{\partial p}{\partial z} - g \quad (3)$$

$$\frac{\partial u}{\partial x} + \frac{\partial v}{\partial y} + \frac{\partial w}{\partial z} = 0 \quad (4)$$

where u, v, and w are velocity components in the direction of the x, y, and z axis, respectively, t time, p the pressure, f the Coriolis parameter, ρ the density of sea water, ρ_0 a constant reference density, g the

* 7-3-1 Hongo, Bunkyo-ku, Tokyo, 113-8656, JAPAN

acceleration of gravity, A_M the horizontal eddy viscosity coefficient, K_M the vertical eddy viscosity coefficient, and ∇^2_H the two-dimensional Laplacian defined in the horizontal x-y plane. Similarly, variations of water temperature T and salinity S can be written

$$\frac{DT}{Dt} = A_C \nabla_H^2 T + \frac{1}{\delta}\frac{\partial}{\partial z}\left(K_C \frac{\partial T}{\partial z}\right) \tag{5}$$

$$\frac{DS}{Dt} = A_C \nabla_H^2 S + \frac{1}{\delta}\frac{\partial}{\partial z}\left(K_C \frac{\partial S}{\partial z}\right) + \Delta R \tag{6}$$

where A_C and K_C are horizontal and vertical eddy diffusivity coefficient, respectively. ΔR is the term of river's inflow and is set to be zero in dealing with the sea area other than the estuary. The case of dealing with the region adjacent to the river mouse is shown later. The parameter δ in Eqs.(5) and (6) is defined by

$$\delta = \begin{cases} 0 & (\partial\rho/\partial z > 0) \\ 1 & (\partial\rho/\partial z \le 0) \end{cases} \tag{7}$$

This indicates that when $\partial\rho/\partial z$ is positive, water mass in upper and lower layers are mixed instantaneously. The water density is assumed to be a function of temperature and salinity [4];

$$\rho = 1028.14 - 0.0735T - 0.00469T^2 + (0.802 - 0.002T)(S - 35.0) \tag{8}$$

When the sea water stratifies, the density gradients suppress the vertical turbulent transportation of momentum, heat and salinity fluxes. To take this effect into consideration, the following formulae are used for evaluating vertical eddy viscosity and diffusivity coefficients.

$$\frac{K_M}{K_{M0}} = (1 + 5.2R_i)^{-1}, \frac{K_C}{K_{C0}} = \left(1 + \frac{10}{3}R_i\right)^{-1.5} \tag{9}$$

where K_{M0} and K_{C0} indicate the K_M and K_C values under homogenous condition, and R_i is the Richardson Number defined by

$$R_i = -\frac{g \cdot \partial\rho/\partial z}{\rho(\partial U/\partial z)^2} \tag{10}$$

where U is velocity in the horizontal direction.

These equations are transformed to finite-difference equations by means of staggered mesh in the horizontal direction and by the multilevel model in the vertical direction.

2.1.2 Boundary conditions

At the coastline, the no-slip condition is applied, and the heat and salinity fluxes through the boundary are assumed to be zero. At the open boundary, which is treated as the non-reflecting boundary, the sea level and, both temperature and salinity of sea water are fixed to those of the outer sea, and gradients of current velocity is assumed to be zero.

In the estuary, ΔR in Eq.(6) is defined by

$$\Delta R = -\frac{RS}{V_R} \tag{11}$$

where R is river inflow per unit time that flows into the volume V_R, which is taken to be the volume of the sea area adjacent to the river mouse.

The boundary conditions at the sea bottom (z=-h; h is depth) are as follows;

$$u\frac{\partial h}{\partial x} + v\frac{\partial h}{\partial y} + w = 0 \tag{12}$$

$$K_M \frac{\partial u}{\partial z} = \frac{\tau_{xB}}{\rho_0}, \quad \tau_{xB} = \gamma^2 \rho_0 u\sqrt{u^2 + v^2} \tag{13}$$

$$K_M \frac{\partial v}{\partial z} = \frac{\tau_{yB}}{\rho_0}, \quad \tau_{yB} = \gamma^2 \rho_0 v\sqrt{u^2 + v^2} \tag{14}$$

where τ_{xB} and τ_{yB} denote the bottom frictions, and γ^2 is the drag coefficient of the sea bottom. The heat and salinity fluxes through the sea bottom are assumed to be zero.

The boundary conditions at the sea surface (z=ζ; ζ is sea level) are as follows;

$$p = p_a \tag{15}$$

$$-\frac{\partial \zeta}{\partial t} - u\frac{\partial \zeta}{\partial x} - v\frac{\partial \zeta}{\partial y} + w = 0 \tag{16}$$

$$K_M \frac{\partial u}{\partial z} = \frac{\tau_{xW}}{\rho_0}, \quad \tau_{xW} = \rho_a C_d W_x \sqrt{W_x^2 + W_y^2} \tag{17}$$

$$K_M \frac{\partial v}{\partial z} = \frac{\tau_{yW}}{\rho_0}, \quad \tau_{yW} = \rho_a C_d W_y \sqrt{W_x^2 + W_y^2} \tag{18}$$

$$-K_C \frac{\partial T}{\partial z} = \frac{Q_T}{\rho_0 C_p}, \quad Q_T = Q_r - Q_b - Q_e - Q_h \tag{19}$$

$$-K_C \frac{\partial S}{\partial z} = \frac{Q_S}{\rho_0}, \quad Q_S = S(E_{vap} - P_r) \tag{20}$$

where p_a is the atmospheric pressure at the sea surface, τ_{xW} and τ_{yW} the wind stresses, ρ_a the air density, C_d the drag coefficient of the sea surface, and W_x and W_y the

wind velocities. Q_T and Q_S are downward heat and salinity fluxes per unit time per unit area, respectively, C_p the specific heat of sea water, Q_r global solar radiation, Q_b long wave radiation from the sea, Q_e latent heat transport by evaporation, Q_h sensible heat transport by convection and conduction, E_{vap} evaporation rate at the sea surface, and P_r precipitation rate. Each of Q_r, Q_b, Q_e, Q_h, and E_{vap} is calculated by the so-called bulk formulae of transport [5].

The principal parameters used in the numerical model are shown in Table 1.

2.2 Ecological model

A simplified ecological model [6] based on primary production is adopted and eight compartments are taken into account; phytoplankton (*P*), zooplankton (*Z*), particulate organic matter (*POM*), dissolved organic matter (*DOM*), dissolved inorganic phosphorous (*DIP*), dissolved inorganic nitrogen (*DIN*), dissolved oxygen (*DO*), and chemical oxygen demand (*COD*). Interactions among the compartments in terms of carbon in the marine ecosystem are shown in Fig.1 [3]. The roles of microbe, benthos, and fish cannot be explicitly included in the present model, however they can be implicitly included by tuning zooplankton mortality, oxygen comsumption, and so forth.

Time evolution of these compartments (B) are described with differential equations which are composed of advection terms, diffusion terms, and biological source term;

$$\frac{DB}{Dt} = A_C \nabla_H^2 B + \frac{1}{\delta}\frac{\partial}{\partial z}\left(K_C \frac{\partial T}{\partial z}\right) + \left(\frac{\partial B}{\partial t}\right) \qquad (21)$$

where the variable B indicates P, Z, POC, and other compartments. Each of biological source terms is modeled below.

2.2.1 *Phytoplankton(P_i)*

Several groups of phytoplankton should be considered and each of them has its own characteristic. The differential equation of P_i measured in conversion of carbon (mgC/m^3) is given by

$$\left(\frac{\partial P_i}{\partial t}\right) = B_{1,i} - B_{2,i} - B_{3,i} - \sum_{j=1}^{N_Z} B^j_{4,i} - B_{5,i} - B_{6,i} \qquad (22)$$

where $B_{1,i}$ is production by photosynthesis, $B_{2,i}$ extracellular release, $B_{3,i}$ respiration, $B^j_{4,i}$ grazed phytoplankton by zooplankton which belongs to group j, $B_{5,i}$ mortality, and $B_{6,i}$ sinking. In the present paper, we take only one group of phytoplankton into account (N_P=1).

Table 1: Principal parameters used in numerical model

Symbol	Value	Symbol	Value
g(m/s^2)	9.807	A_C (m^2/s)	10.0 (for 1000m grid)
f(rad/s)	8.42×10^5		
ρ_0 (kg/m^3)	1020.0	K_{C0} (m^2/s)	0.0001
A_M (m^2/s)	50.0 (for 1000m grid)	γ^2	0.0026
		C_d	0.0015
K_{M0} (m^2/s)	0.0001	ρ_a (kg/m^3)	1.147
		C_p (J/kg/K)	3.930×10^3

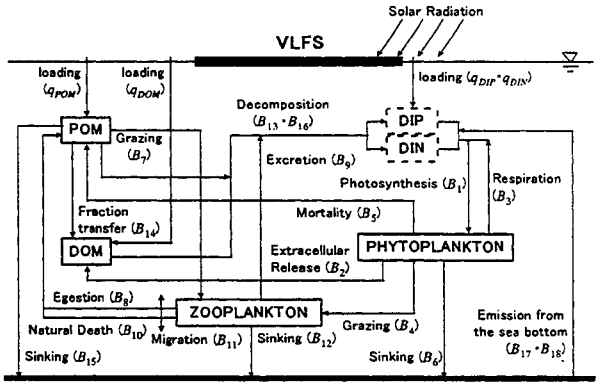

Figure 1: Interactions among the compartments in the marine ecosystem. Boxes with the solid line represent organic matters, those with the dashed line represent nutrients, and arrows represent carbon flow.

2.2.2 *Zooplankton(Z_j)*

Several groups of zooplankton should be also considered and size distribution of zooplankton with their growth is neglected. The differential equation of Z_j measured in conversion of carbon (mgC/m^3) is given by

$$\left(\frac{\partial Z_j}{\partial t}\right) = \sum_{i=1}^{N_P} B^i_{4,j} + B_{7,j} - B_{8,j} - B_{9,j} - B_{10,j} \pm B_{11,j} - B_{12,j} \qquad (23)$$

where $B^i_{4,j}$ is grazed phytoplankton which belongs to group i, $B_{7,j}$ feeding of detritus, $B_{8,j}$ egestion, $B_{9,j}$ excretion, $B_{10,i}$ natural death, $B_{11,i}$ migration, and $B_{12,i}$ sinking. In the present paper, we also take only one group of zooplankton into account (N_z=1).

2.2.3 *Particulate organic matter (POM)*

POM is calculated in the conversion of *POC* (mgC/m^3), and particulate organic phosphorus (*POP*) and nitrogen (*PON*) are calculated by converting *POC* using *P/C* and *N/C* ratio, respectively. The differential

equation of *POC* is given by

$$\left(\frac{\partial POC}{\partial t}\right)=\sum_{i=1}^{N_P}B_5^i+\sum_{j=1}^{N_Z}\left(-B_7^j+B_8^j+B_{10}^j\right) -B_{13}-B_{14}-B_{15}+q_{POC} \tag{24}$$

where B_{13} is bacterial decomposition of *POC*, B_{14} fraction transfer to *DOC*, B_{15} sinking of *POC*, and q_{POC} loading.

2.2.4 Dissolved organic matter (DOM)

DOM is also calculated in the conversion of *DOC* (mgC/m^3), and dissolved organic phosphorus (*DOP*) and nitrogen (*DON*) are calculated by converting *DOC* using *P/C* and *N/C* ratio, respectively. The differential equation of *DOC* is given by

$$\left(\frac{\partial DOC}{\partial t}\right)=\sum_{i=1}^{N_P}B_2^i+B_{14}-B_{16}+q_{DOC} \tag{25}$$

where B_{16} is bacterial decomposition of *DOC*, and q_{DOC} loading.

2.2.5 Dissolved inorganic phosphorous (DIP)

The differential equation of *DIP* (mgP/m^3) is given by

$$\left(\frac{\partial DIP}{\partial t}\right)=\sum_{i=1}^{N_P}[P_h:C_P]_i\left(-B_1^i+B_3^i\right)+\sum_{j=1}^{N_Z}[P_h:C_Z]_jB_9^j +[P_h:C_{POM}]B_{13}+[P_h:C_{DOM}]B_{16}+B_{17}+q_{DIP} \tag{26}$$

where $[P_h{:}C_P]_i$, $[P_h{:}C_Z]_j$, $[P_h{:}C_{POM}]$, and $[P_h{:}C_{DOM}]$ are composition ratios of phosphorus to *P*, *Z*, *POC*, and *DOC*, respectively. B_{17} is emission of *DIP* from the sea bottom, and q_{DIP} loading.

2.2.6 Dissolved inorganic nitrogen (DIN)

The differential equation of *DIN* (mgN/m^3) is given by

$$\left(\frac{\partial DIN}{\partial t}\right)=\sum_{i=1}^{N_P}[N:C_P]_i\left(-B_1^i+B_3^i\right)+\sum_{j=1}^{N_Z}[N:C_Z]_jB_9^j +[N:C_{POM}]B_{13}+[N:C_{DOM}]B_{16}+B_{18}+q_{DIN} \tag{27}$$

where $[N{:}C_P]_i$, $[N{:}C_Z]_j$, $[N{:}C_{POM}]$, and $[N{:}C_{DOM}]$ are composition ratios of nitrogen to *P*, *Z*, *POC*, and *DOC*, respectively. B_{18} is emission of *DIN* from the sea bottom, and q_{DIN} loading.

2.2.7 Dissolved oxygen (DO)

To take oxygen circulation in the marine ecosystem into account, the differential equation of *DO*(mg/l) is given by

$$\left(\frac{\partial DO}{\partial t}\right)=D_1-D_2-D_3-D_4-D_5-D_6+D_7+q_{DO} \tag{28}$$

where D_1 is supply by photosynthesis, D_2 consumption by phytoplankton, D_3 consumption by zooplankton, D_4 consumption by *POM* decomposition, D_5 consumption by *DOM* decomposition, D_6 consumption at the sea bottom, and D_7 re-aeration.

2.2.8 Chemical oxygen demand (COD)

Chemical oxygen demand has been used as an index of water quality in Japan. It is calculated using the organic matters; phytoplankton, zooplankton, *POM*, and *DOM*. The differential equation of *COD*(mg/l) is given by

$$\left(\frac{\partial COD}{\partial t}\right)=\sum_{i=1}^{N_P}[C:C_P]_i\left(\frac{\partial P_i}{\partial t}\right)+\sum_{j=1}^{N_Z}[C:C_Z]_j\left(\frac{\partial Z_j}{\partial t}\right) +[C:C_{POM}]\left(\frac{\partial POC}{\partial t}\right)+[C:C_{DOM}]\left(\frac{\partial DOC}{\partial t}\right)+q_{COD} \tag{29}$$

where $[C{:}C_P]_i$, $[C{:}C_Z]_j$, $[C{:}C_{POM}]$, and $[C{:}C_{DOM}]$ are composition ratios of COD to *P*, *Z*, *POC*, and *DOC*, respectively.

For further details on modeling of each process and numerical values of parameters, refer to Nakata [6].

3. RESULTS AND DISCUSSION

3.1 Numerical conditions

Figure 2 shows the modeling of Tokyo Bay. To get detailed knowledge on the variation of current speed, water temperature, water salinity, and ecological compartments around a VLFS, much finer grids are adopted in the sea area adjacent to a VLFS. In the present numerical simulation, three kinds of square-grid are used; 200m (Rank 3), 600m (Rank 2), and 1800m (Rank 1). The region in Tokyo Bay is called Rank 1, that enclosed by the solid line is called Rank 2, and that enclosed by the dashed line is called Rank 3. The finest grids of 200m are used to cover the sea area adjacent to a VLFS off Yokosuka where residual current is fast, and off Haneda where residual current is slow, respectively. The values of horizontal eddy viscosity and horizontal eddy diffusivity should be varied depending on the grid size in accordance with the Richardson's 4/3 power law. In the vertical direction, the multilevel model with 10 layers is adopted.

As for the initial and boundary conditions, initial conditions are shown in Table 2 and boundary conditions at open boundary are shown in Table 3. Six large rivers are taken into account and the loading rates of organic matters, nutrients, and others are shown in Table 4.

Numerical conditions are as follows;

- Case 1: Applying the finest square-grid to the sea area adjacent to an imaginary VLFS off Yokosuka, numerical simulation is conducted in two cases, where the VLFS is assumed not to exist and where the VLFS is assumed to exist, respectively.
- Case 2: Applying the finest square-grid to the sea area adjacent to an imaginary VLFS off Haneda, numerical simulation is conducted in two cases, where the VLFS is assumed not to exist and where the VLFS is assumed to exist, respectively.

An imaginary VLFS (5km in length, 1km in width, and 0m in draft) is assumed to impede wind stress, and heat and salinity fluxes, and exchange of oxygen through the sea surface. The effects of the VLFS on the surrounding marine environment are examined from comparison of the result when the VLFS is assumed not to exist with that when the VLFS is assumed to exist.

Time step is set to 6sec. in Case 1, and 8sec. in Case 2. The simulation is conducted for 20 days.

Table 2 Initial values

Level	1	2-3	4-5	6-10
T(℃)	24.84	23.96	22.48	20.06
S(psu)	30.2	31.84	32.54	33.83
P(mgC/m^3)	500	500	300	200
Z(mgC/m^3)	50	50	30	20
POC(mgC/m^3)	600	600	200	100
DOC(mgC/m^3)	1500	1000	300	200
DIP(mgP/m^3)	124	124	93	62
DIN(mgN/m^3)	140	140	112	70
DO(mg/l)	8.0	8.0	6.0	4.5
COD(mg/l)	5.5	4.5	1.0	0.5

Table 3 Values at open boundary

Level	1	2-3	4-5	6-10
T(℃)	24.56	23.72	23.28	21.27
S(psu)	32.76	33.23	33.61	33.92
P(mgC/m^3)	500	500	300	200
Z(mgC/m^3)	50	50	30	20
POC(mgC/m^3)	600	600	200	100
DOC(mgC/m^3)	1500	1000	300	200
DIP(mgP/m^3)	20.15	20.15	17.05	12.4
DIN(mgN/m^3)	50.4	50.4	50.4	42
DO(mg/l)	8.0	8.0	6.0	4.5
COD(mg/l)	3.5	3.5	1.0	0.5

Table 4 Loading rate of rivers

River	Edo	Naka	Ara	Sumida	Tama	Tsurumi
R(m^3/s)	115.7	66.4	100.8	40.5	33.4	9.8
T(℃)	26.3	26.5	26.5	26.5	26.6	27.0
S(psu)	5.0	5.0	5.0	5.0	5.0	5.0
POC(mg/l)	2.14	2.35	2.45	2.82	1.90	2.58
DOC(mg/l)	3.1	3.4	3.5	4.1	2.7	3.7
DIP(mg/l)	0.120	0.216	0.227	0.577	0.329	0.404
DIN(mg/l)	2.380	2.449	3.028	7.431	5.194	5.811
DO(mg/l)	5.7	4.3	5.8	2.7	7.8	6.2
COD(mg/l)	6.3	6.9	7.2	8.3	5.6	7.6

3.2 Results and discussion

3.1.1 Comparisons with observation data

The horizontal distributions mentioned below are those of the averaged values in 20th day after commencement of computation. They are the distributions in Tokyo Bay (Rank 1) or at the mooring site of a VLFS (Rank 3). Figure 3(a) shows the horizontal distribution of residual current at 1m below the sea surface in Tokyo Bay. Figure 3(a) agrees with the result by Nakagawa et al.[2] and it is clear from Fig.3(a) that residual current in the sea area off Haneda is slow, compared with the current in the sea area off Yokosuka. Figure 3(b) shows the horizontal distribution

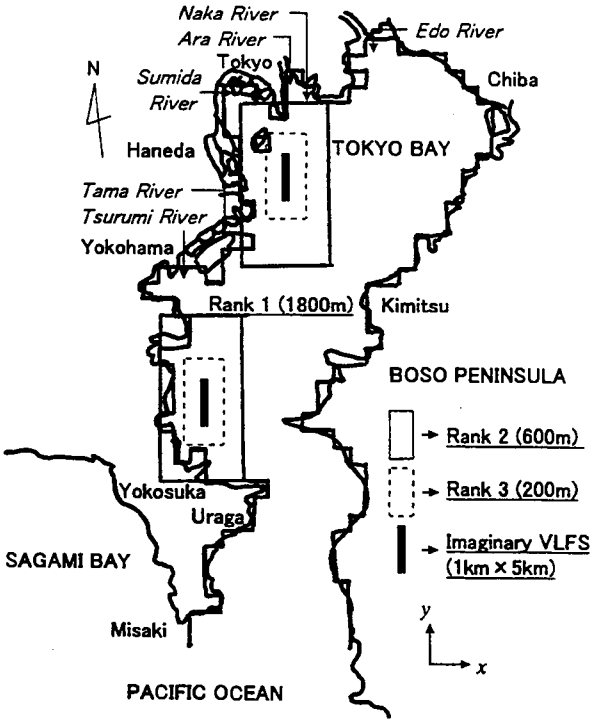

Figure 2: Modeling of Tokyo Bay. The region in Tokyo Bay is called Rank 1, that enclosed by the solid line is called Rank 2, and that enclosed by the dashed line is called Rank 3

of water temperature, and reproduces some characteristics of distribution. For instance, water temperature is relatively high along the west coast to the head of the bay and is getting lower and lower to the opening of the bay.

In Fig.4, the result of calculating COD is compared with the averaged observation data, which were measured at 31 points of Tokyo Bay in the summer of 1988 [6]. As is shown in Fig.4(a), the values of COD are large in the sea area along the west coast to the head of the bay due to increase in phytoplankton by photosynthesis, due to increase in zooplankton by grazing phytoplankton, and due to increase in POM and DOM which consist of dead bodies of plankton. As shown in Fig.4(b), the distribution of observed COD is predicted well. Figure 5 shows the present simulation result of phytoplankton together with the prediction by Kyozuka et al. [1]. Both predictions agree well with each other; the high concentration of above 1800 mgC/m^3 is obtained in the head of the bay, where supply of nutrients from several rivers is large.

Figure 6 shows the horizontal distributions of DIP and DO. Similarly, the amounts of them are large in the head of the bay because of sufficient supply of nutrients from the rivers, and because of large production of oxygen by photosynthesis, respectively.

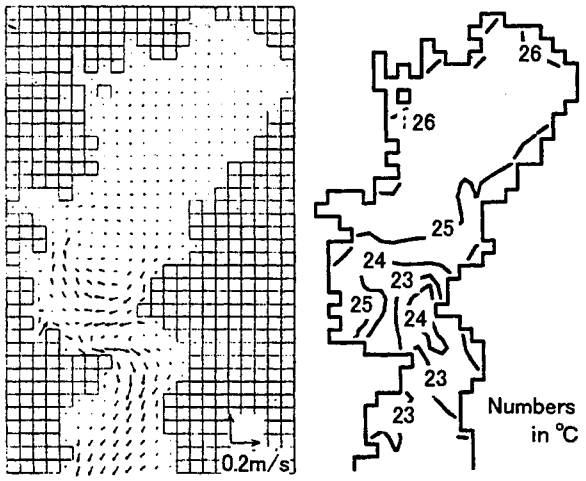

(a) Residual current (b) Water temperature

Figure 3: Predicted distributions of residual current and water temperature at 1m below sea surface in Tokyo Bay

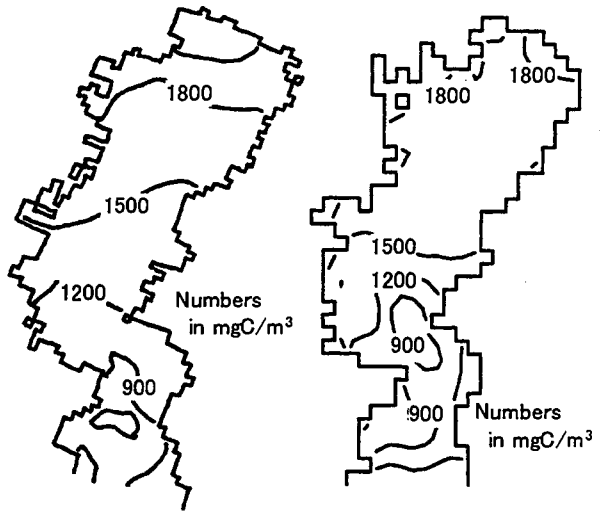

(a) by Kyozuka et al. (b) The present result

Figure 5: Predicted distribution of phyplankton at 1m below the sea surface in Tokyo Bay

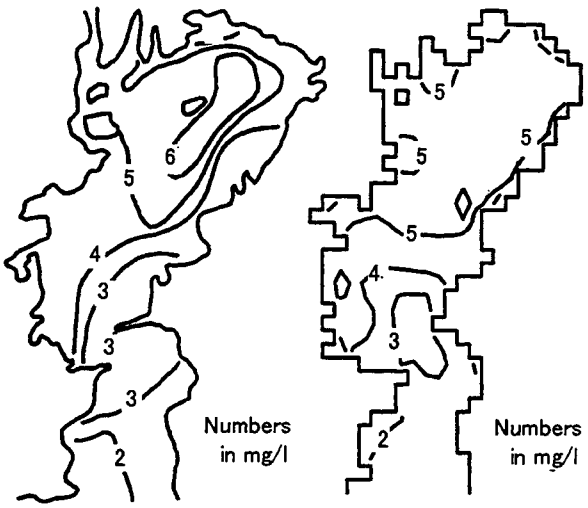

(a) Observation data (b) The present result

Figure 4: Distribution of COD at 1m below the sea surface in Tokyo Bay.

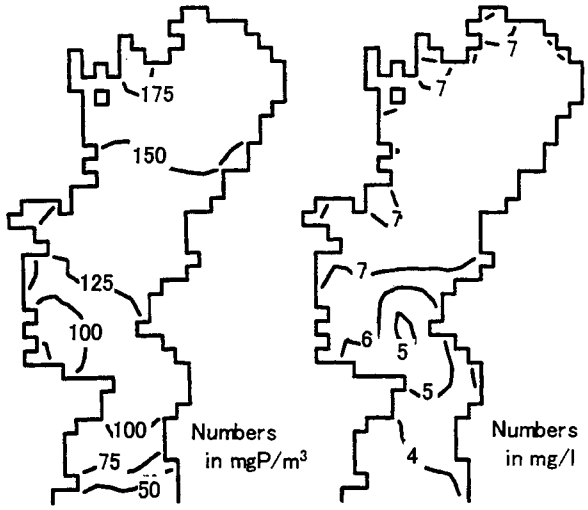

(a) DIP (b) DO

Figure 6: Predicted distributions of DIP and DO at 1m below sea surface in Tokyo Bay

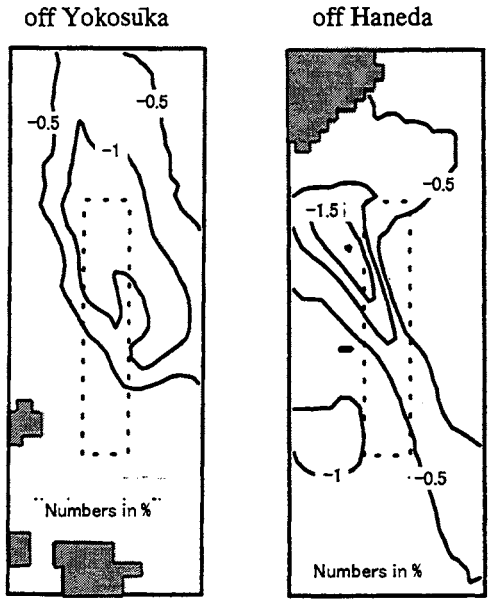

(a) Case 1 (b) Case 2

Figure 7: Distributions of water temperature variation at 1m below the sea surface at the site of a VLFS

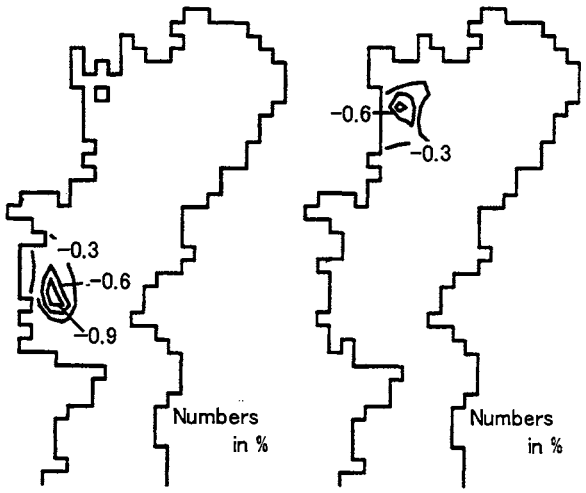

(a) Case 1 (b) Case 2

Figure 8: Distributions of water temperature variation at 1m below the sea surface in Tokyo Bay

3.2.2 Effects of a VLFS on marine environment

Several results of numerical simulation are shown in the form of horizontal distribution of difference in predicted values; which is defined by subtracting the values predicted when a VLFS is assumed to exist from those predicted when it is not assumed to exist. Positive and negative values denote increase and decrease of the variables, respectively. Further, the numbers shown in the figures mentioned later indicates the variation in terms of percentage.

First, the impact of a VLFS on oceanophysical environment is examined. Figures 7 and 8 show the horizontal distributions of water temperature at 1m below the sea surface at the mooring site of a VLFS and in Tokyo Bay, respectively. The drops of water temperature due to impediment of heat flux by a VLFS are shown at the site of the VLFS. Maximum decrease of about 1.5% in Case 2 (where a VLFS is installed in the area off Haneda) is larger than that of about 1% in Case 1 (where a VLFS is installed in the area off Yokosuka). The sea area with water temperature drop of more than 0.6% is much smaller in Case 2 than in Case 1. It can be said that the effect of a VLFS on water temperature is more localized in the area off Haneda because residual current is slow and sea water in the area adjacent to the VLFS is less exchanged.

The horizontal distributions of phytoplankton variation at 1m below the sea surface at the site of the VLFS are shown in Fig.9. The amount of phytoplankton decreases around a VLFS in both cases

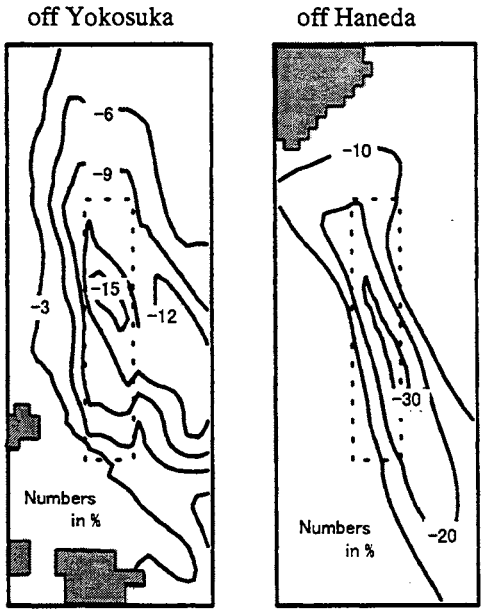

(a) Case 1 (b) Case 2

Figure 9: Distributions of phytoplankton variation at 1m below the sea surface at the site of a VLFS

because photosynthesis is prevented due to the impediment of solar radiation by the VLFS. At this point, it should be noted that photosynthesis actively occurs off Haneda due to the abundance in nutrients from the rivers, and therefore the effects of impediment of photosynthesis is emphasized off Haneda rather than

in other areas. This seems the reason why a VLFS installed off Haneda may have more pronounced effect on the surrounding phytoplankton concentration. In addition to this, it should be mentioned that the sea water flows slowly in the area off Haneda, so that the effects of impediment of photosynthesis may be much localized when a VLFS is installed off Haneda. However, in order to make more clear statement on the effects of a VLFS on the surrounding sea water, more investigation is needed: for example, difference in the impact of the VLFS should be investigated in the various different conditions with the residual current speed being kept unchanged.

Figures 10 and 11 show the horizontal distributions of

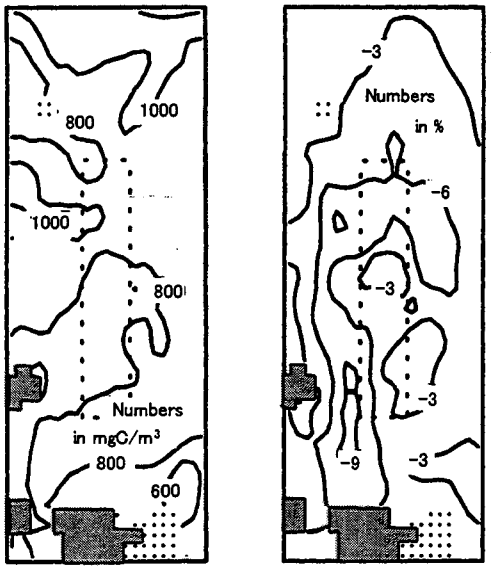

(a) Phytoplankton (b) Variation

Figure 10: Distributions of phytoplankton and its variation at 5m below the sea surface at the site of a VLFS off Yokosuka

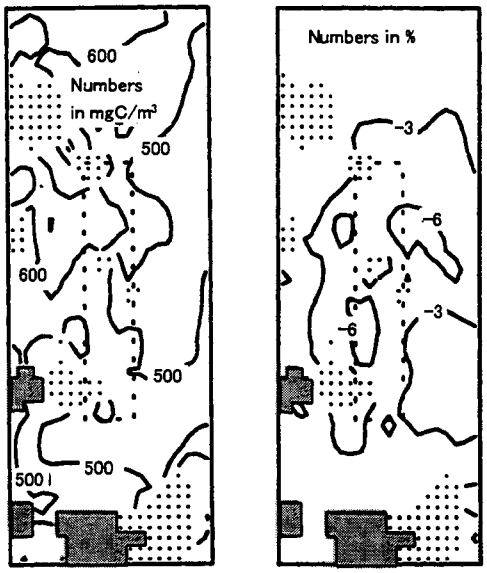

(a) Phytoplankton (b) Variation

Figure 11: Distributions of phytoplankton and its variation at 10.5m below the sea surface at the site of a VLFS off Yokosuka

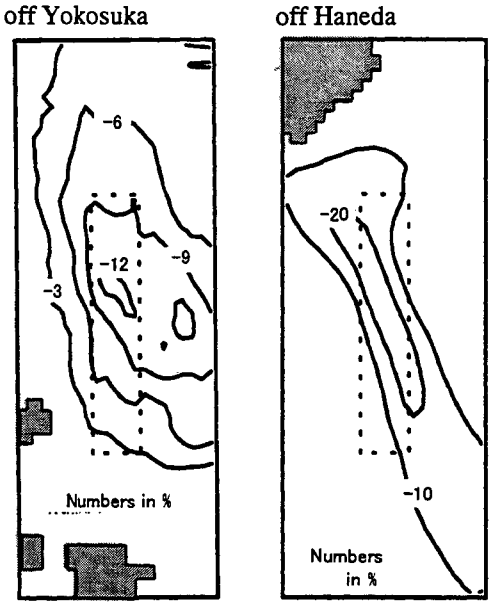

(a) Case 1 (b) Case 2

Figure 12: Distributions of COD variation at 1m below the sea surface at the site of a VLFS

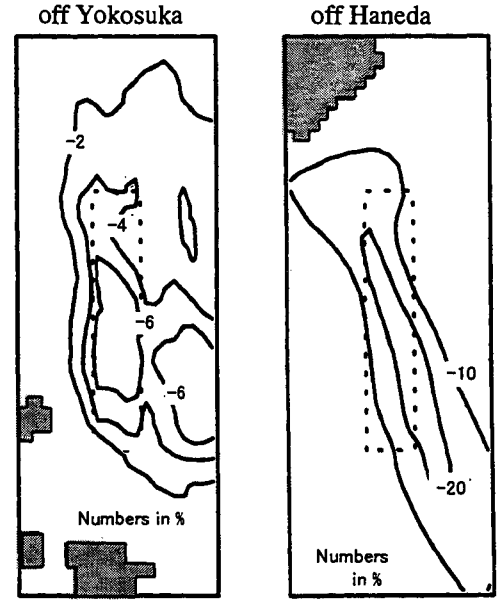

(a) Case 1 (b) Case 2

Figure 13: Distributions of DO variation at 1m below the sea surface at the site of a VLFS

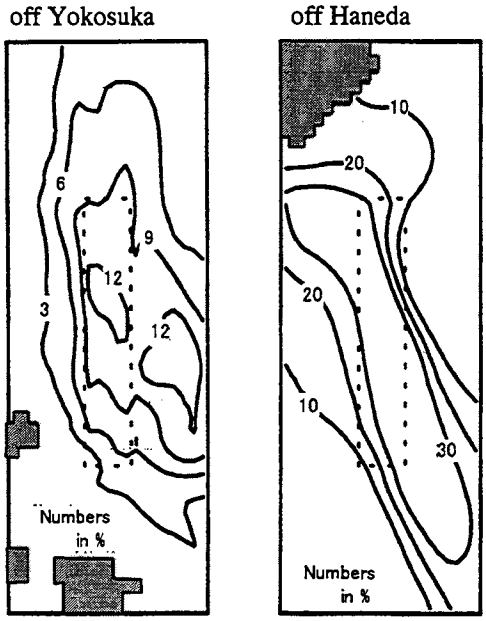

(a) Case 1 (b) Case 2

Figure 14: Distributions of DIP variation at 1m below the sea surface at the site of a VLFS

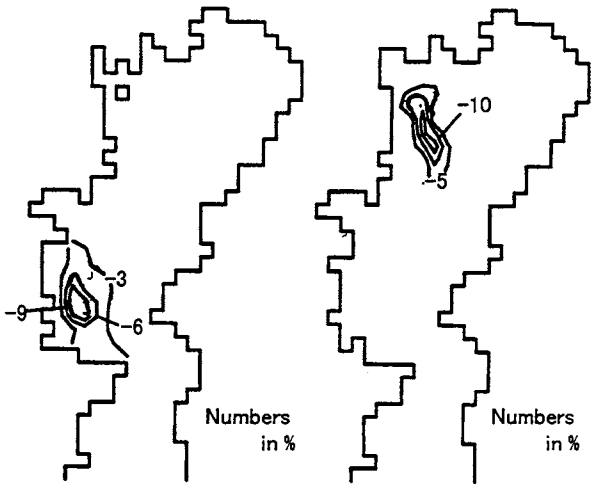

(a) Case 1 (b) Case 2

Figure 15: Distributions of phytoplankton variation at 1m below the sea surface in Tokyo Bay

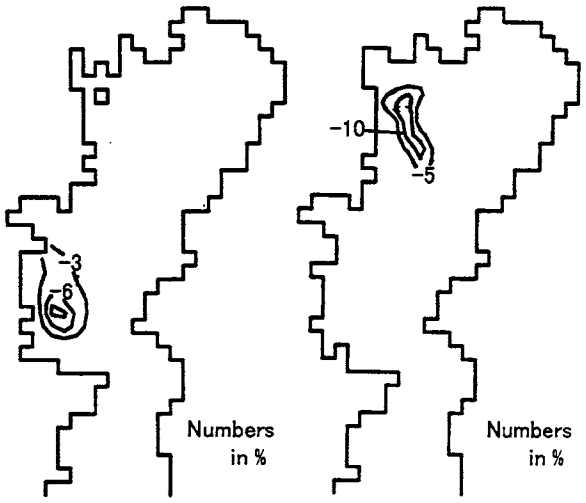

(a) Case 1 (b) Case 2

Figure 16: Distributions of COD variation at 1m below the sea surface in Tokyo Bay

phytoplankton and its variation at 5m and 10.5m below the sea surface at the site of a VLFS, respectively. The left-hand side figure shows the phytoplankton distribution predicted when a VLFS is assumed not to exist, and the right-hand side shows the phytoplankton variation caused by installing the VLFS off Yokosuka. From these figures, it can be observed that the effects of a VLFS decreases as the distance from the sea surface increases.

Phytoplankton variation has effects on the distributions of other components. Figures 12, 13, and 14 show the horizontal distributions of COD, DO, and DIP variation, respectively, at 1m below the sea surface in the sea area off Yokosuka and in the sea area off Haneda. The concentration of COD decreases because phytoplankton decreases due to impediment of photosynthesis and it leads to decreases of other organic matters. The concentration of DO also decreases due to the decrease of oxygen production by photosynthesis. On the contrary, the concentration of DIP increases because the amount of consuming nutrients by photosynthesis decreases. The effects of a VLFS on the concentration of COD, DO, and DIP are the same as those on phytoplankton: a VLFS may have more pronounced effects when the VLFS is installed off Haneda rather than when it is installed off Yokosuka. Further, those effects of a VLFS also decreases as the distance from the sea surface increases.

Figures 15, 16, 17, and 18 show the horizontal distributions of phytoplankton, zooplankton, DIP, and DO variations at 1m below the sea surface in Tokyo Bay. As is obvious at a glance, the effect is quite localized around a VLFS in Tokyo Bay as a whole.

4. CONCLUSIONS

The conclusions of this paper are as follows;

1. The results of predicting marine environment using the ecohydrodynamic model agree well with the observation data or existing computations. For further verification, collecting observation data of marine environment, and the comparison of numerical results with them are necessary.
2. The impacts of a VLFS on marine environment are localized in Tokyo Bay as a whole. However the extent of those impacts at the site of a VLFS is larger when a VLFS is installed in the sea area where residual flow is slow and photosynthesis is actively occurred. Therefore when a VLFS is intended to be installed in the sea, the position of installing a VLFS should be decided with sufficient caution.

It is important to take other ecological processes, for example, benthic environment and microbial food web into account for future study of EIA.

References

[1] Y. Kyozuka, C. HU, H. Hasemi, H. Nakagawa and A. Hikai. *An Ecohydrodynamic Model for Environmental Assessment of a Mega-Float in a Bay,* OMAE-Volume VI, Ocean Space Utilization, 1996.

[2] H. Nakagawa, H. Omori, A. Hikai, K. Nakagawa and K. Uchino, *On the prediction of the flow and water quality change due to a Mega-Float installation*. 14th Ocean Engineering Symposium, The Society of Naval Architects of Japan, 1998, (in Japanese).

[3] K. Nakata, *Ecosystem; its formulation and estimation method for unknown rate parameters*, J. Adv. Tech. Conf., Vol.8, pages 99-138 1993, (in Japanese).

[4] T. Yanagi. *Coastal Oceanography,* Kouseisya-Kouseikaku Inc., 1989, (in Japanese).

[5] J. Kondo, *Meteorology in water surroundings*, Asakura Syoten, 1994, (in Japaneses).

[6] K. Nakata, *Simulation model in coastal bay estuary, Marine Environmental Simulation* (Edit. N. Yokoyama), Hakua Syobo, 1993, (in Japanese).

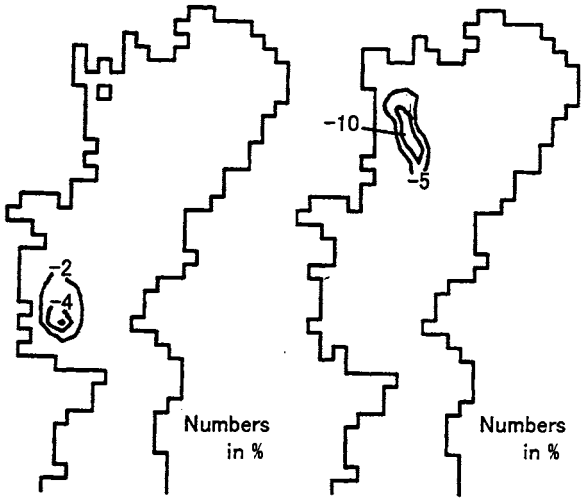

(a) Case 1 (b) Case 2

Figure 17: Distributions of DIP variation at 1m below the sea surface in Tokyo Bay

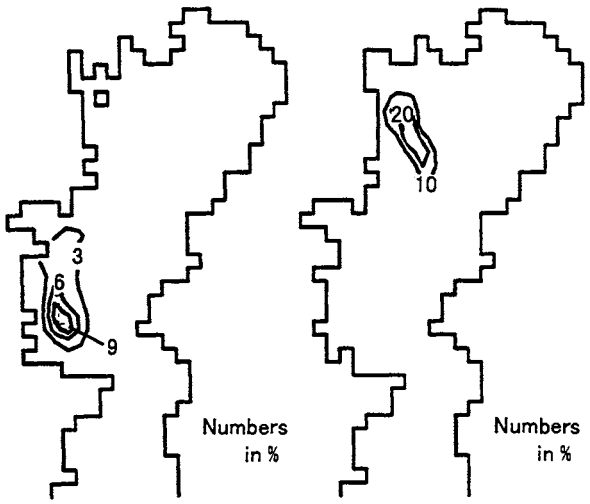

(a) Case 1 (b) Case 2

Figure 18: Distributions of DO variation at 1m below the sea surface in Tokyo Bay

PROCEEDINGS OF THE THIRD INTERNATIONAL WORKSHOP ON VERY LARGE FLOATING STRUCTURES
(VLFS '99), VOL. I, EDS. R.C. ERTEKIN & J.W. KIM, 22-24 SEPTEMBER 1999, HONOLULU, HAWAII, USA

DEVELOPMENT OF A SAFETY GUIDE FOR ARTIFICIAL FIXED FLOATING BASE STRUCTURES

Susumu Harada
Offshore Technology Division, Nippon Kaiji Kyokai*

ABSTRACT

Floating structures are widely used in various types of facilities, such as petroleum storage / oil drilling / production units, floating piers, and the like. However, there is no example of a floating structure constructed as a replacement for facilities on land - especially a massive structure spanning several kilometers in length. Since reclamation of deep-water offshore areas is difficult compared to conventional reclamation methods in Japan, consideration is being given to the utilization of very large floating structures (VLFS). To this end, a technical association made up of seventeen shipbuilders and steel manufacturers, known as Technological Research Association of Mega-Float (TRAM) ,has been established to carry out joint research and development into the creation of a large-scale floating structure. In view of the lack of relevant data related to such structures, TRAM constructed large experimental model of the floating structure (300m × 60m × 2m) for the purpose of carrying out demonstration tests and research over a three year period starting from 1995. Further, it has also begun conducting tests using a larger model (1,000m × 120m/60m × 3m) from 1998 in order to examine its potential for use as a floating airport.

A VLFS is a structure that can be used for many different applications such as a base for airports, container yards, and so on, provided that the facilities to support such functions are built on the structure. A VLFS is intended to be used in a similar manner as a foundation built on land. However, not being fixed structures, they are more readily affected by the dynamic motions of their environment (waves and wind) and as such are prone to not having the degree of rigidity necessary to support such large facilities with a sufficient degree of safety. Thus, the construction of an Artificial Fixed Floating Base Structures (AFFBS) is proposed in this paper as a means of addressing this problem. However, at present, there are no existing standards, guides, or rules, which can be applied to an AFFBS.

This paper examines the basic concept behind the development of suitable safety guidelines which can be applicable to an AFFBS based on the experiments and research outlined above.

1. INTRODUCTION

An AFFBS is an integrated structural system which consists of a VLFS, station keeping systems, suitable buildings, and facilities provided for specific support purposes, means of access such as bridges and tunnels, as well as a breakwater to mitigate and protect the structure from varying sea conditions, to name a few. Figure 1 shows a sketch of the structural system of an AFFBS.

A VLFS plays a role in supporting suitable buildings and facilities for various purposes. A VLFS is moored to a specific place at sea by a station keeping system. In this sense, a AFFBS resembles land in its role and characteristics. Dr. Norihisa Yokouchi, et. al presented their ideas regarding the major characteristics that comprise the concept of land at the 14th Ocean Engineering Symposium[1] as follows.

(1) Land has the characteristic of being "immobile" and "perpetual (invariable)".
(2) The role of land include such functions as being used "to support loads", "as a space for refuse" and "as a sanctuary from disasters".
(3) Functions of land also include its being used as a base for "producing food, provisions, etc." and for "preserving or improving the environment".

On the other hand, a VLFS, which is the main structural element of an AFFBS, moves up and down due to the ebb and flow of the water upon which it sits, and has a limited life span because of its being an artificial object. However, it is possible for such a structure to be regarded as being "immobile" in terms of geography and as being "perpetual", if it is designed for a sufficiently long-life and its structure is suitably maintained during its life. Therefore, it is essential that an AFFBS maintain the conditions, characteristics, and functions which are as similar to those of land as possible. The concept of a safety guide for an AFFBS is aimed at setting forth guidelines for facilitating the retention of such characteristics and conditions to the greatest extent and as safely as possible. In particular, an AFFBS is primarily comprised of several through conceivably up to several hundred VLFS units which are the main structural elements of the system. The dimensions of the VLFS is basically limited only by the size of the shipyard or factory where they are constructed and the technical limitations that can be overcome in achieving safe construction of the structure as a whole. The main structure of the ABBFS, that is

* 4-7 Kioi-cho, Chiyoda-ku, Tokyo, 102-8567, Japan

the VLFS, is constructed by joining and welding individual units together at sea. The structure is designed to support buildings and facilities for specific purposes together with wide ranging uses by many people. Hence, in order to discuss the safety of an AFFBS, it is necessary to first consider the safety of a VLFS. Discussion regarding requirements for the breakwater and other elements comprising the AFFBS which support the VLFS, etc., will be considered separately.

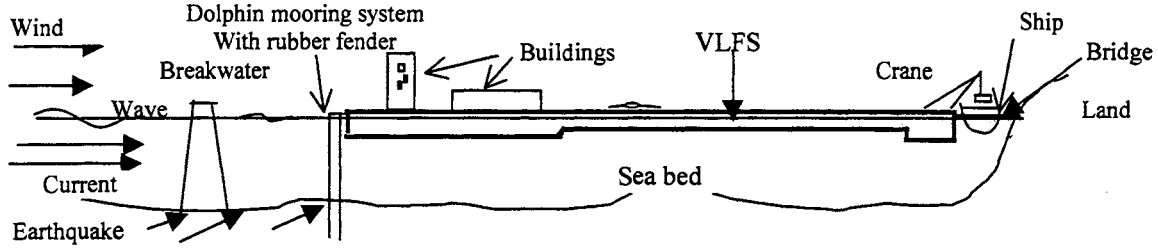

Fig 1 Sketch of an AFFBS

Safety includes the safety of life, and property (structures) as well as preserving the environment,. There are two concepts of safety regarding the safety of life. One depends on the safety of structures while the other concerns the protection of human lives against accidents such as fire, explosion, and similar dangers. This paper only explores the concept of the safety aspect of structures and does not include the concept of the safety of human life and environmental impact.

The most important aspect for safety of a VLFS to prevent the occurrence of fatal events such as sinking, capsizing, total collapse or breaking, or drifting, as well as preventing damage to ships and other offshore floating structures. Once a VLFS is able to avoid such fatal events, it is considered that the characteristics of the AFFBS satisfy the concept of "immobility" which is an important characteristic of land.

ClassNK examined the drawings and related documents of the Mega-Float Phase II Model (hereafter referred to as "Phase II model") considering the safety concept described above and surveyed the structure during its construction. This paper looks at the concept of safety guidelines for such structures based on the experience gained from examining the safety design and construction of the Phase II model.

2. Phase II Model

2.1 Summary

The Phase II model consists of a very large pontoon-type floating structure, which is owned by TRAM, used for various structural and functional tests. Figure 2 shows an illustration of the structure while Table 1 gives the principal dimensions of units.

Table 1 Principal Dimensions and Shapes of Units

Unit	Dimensions(L*B*D)	Shape
A*	383m*61m*3m	Rectangular
B	258m*61m*3m	Rectangular
C*	359m*61m*3m	Rectangular
D	300m*60m*3m	Rectangular
E	64m*(31.3m – 34.5m)*3m	Trapezoid
F	100m*29.7m*3m	Rectangular

* This unit is towed from other places far from several hundred kilometers to the experimental sea area.

The Phase II model is being constructed so that many tests related to airport functions can be carried out. Construction will be completed by the end of September 1999. This floating structure consists of six units which are constructed on the shipways of several shipyards. They are then towed from the shipyards to the experimental sea area, where they are welded to other units there. The welding procedure is as follows (letters represent the various units shown in Fig.2).

$$(1)\,D+E \rightarrow (2)\,F+(DE) \rightarrow (3)\,B+(DEF) \rightarrow$$
$$(4)\,A+(BDEF) \rightarrow (5)\,C+(ABDEF)$$

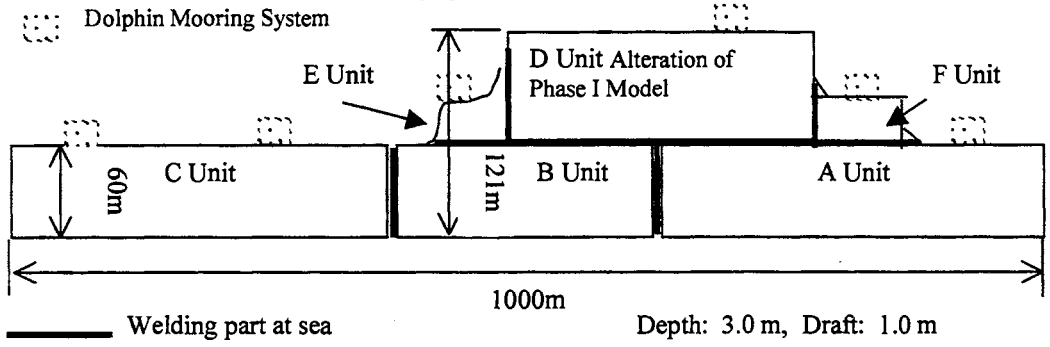

Fig. 2 Illustration of Phase II Model

2.2 Examination of Floatability and Stability

One of the most important aspects of the use of any large scale floating structure is its stability in the water. This was one of major themes of research done with the Mega-Float Phase I Model (hereinafter referred to as the "Phase I model"), the results of which have been applied to tests of the Phase II model. The Phase I model was constructed in 1996 for the purpose of verifying the design and construction technologies of the structure, together with other supporting technology developed based on various tests conducted using the model. The Phase I model was 300 m in length, 60 m wide, 2 m deep, and had a draft of 0.5 m. The Phase I model was a very thin floating structure, and although its length and width were the same as that of a VLCC, its depth was less than 0.1 times that of a VLCC. If the Phase I model is assumed to be a rigid body, its GZ-lever would be about 100 times that of a VLCC. Thus, a one degree inclination of the Phase I model, for example, would result in the edge of the structure being displaced by only about 0.5 m. This is equivalent to saying that a load of about 3000 tons is shifted from the center of the structure to the side of the Phase I model. If the model is assumed to be a cantilever beam, then when a concentrated load of 3000 tons acts on the end of it, the end will be deformed by about 2 m. Very rough calculations show that although such a thin structure with sufficient width would be very stable, the effects of elastic deformation of the structure on stability cannot be neglected. Figure 3 shows the results of experiments in which the compartment tanks of the structure were alternately filled with 2000 tons of water under different arrangements (basically two compartments at a time) in order to examine the elastic deformation and overall strength of the structure.[2]

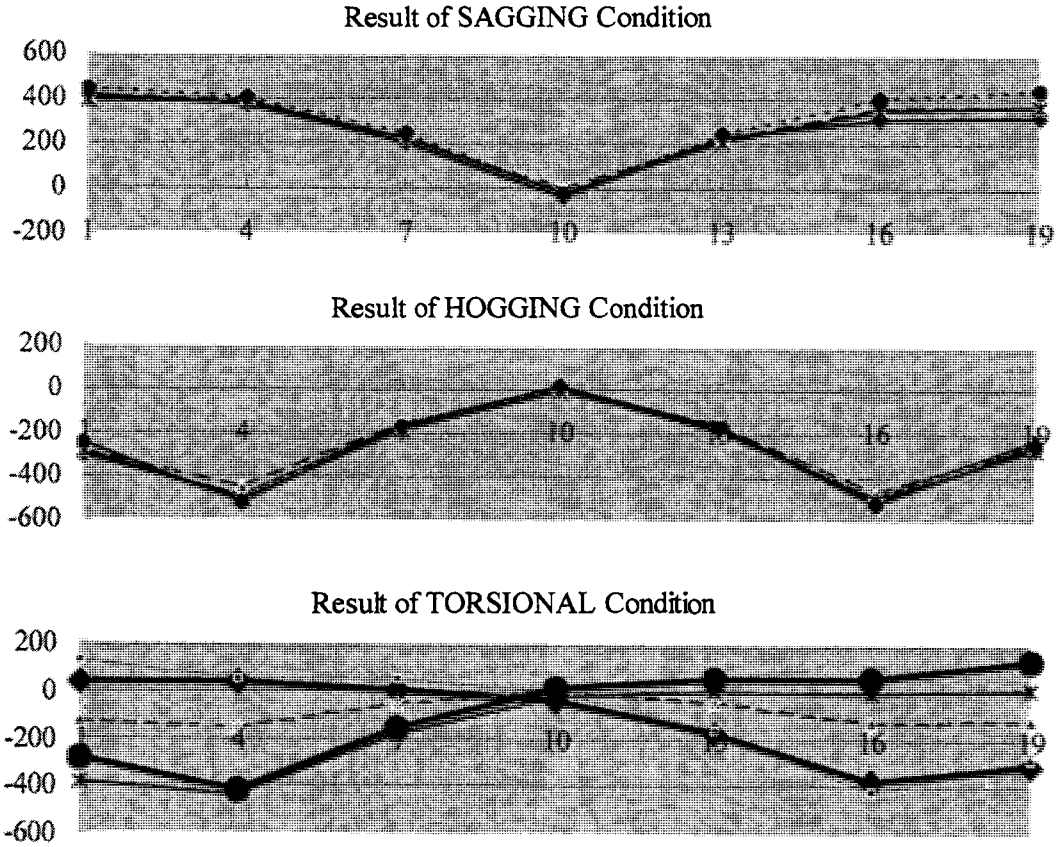

Fig. 3 Result of Experiment of Phase I Model

In this figure, the zero point is the point of maximum downward deformation. This result shows that the maximum deformation is about 500 mm (i.e. about the one fourth of the depth of the model) in the case of a load of 2000 tons regardless of the distribution of the load. If this model were assumed to be a rigid body, this weight would make the entire structure uniformly sink by about 110 mm. However, since it is not a rigid body, the structure does not deform uniformly, and its deformation was found to be about four times what it would be if the structure were assumed to be a rigid body. From these results, it is clear that it is neither reasonable nor practicable to expect to apply the same intact stability criteria required of ships and more traditional offshore floating structures to such a very thin but broad structure as it is not a rigid body. In the

damaged condition, especially assuming extensive compartment flooding, the elastic deformation of a very thin structure would be significantly larger than that for a ship of the same size.

Thus, if sufficient attention is paid to the size, arrangement and strength of the watertight bulkheads of the watertight compartments, elastic deformation in the flooded condition due to damage to the structure will be limited and progressive flooding can be prevented. From these tests, it was also possible to verify the accuracy of the analytical program used to design the Phase I model to determine the elastic behavior of such a very thin structure, as the calculated results could be compared with the results of this test.

From the above results obtained from the Phase I model, tentative criteria regarding the stability and floatability of the Phase II model were developed as outlined below.

(1) Intact stability criteria

Intact stability need not be considered in the case of calm seas because the Phase II model has sufficient GZ-lever compared with that of ships or offshore floating structures to remain stable.

(2) Damage stability criteria

(a) Any two compartments are assumed to be damaged the same as that required for a passenger ship.

(b) Calculations of elastic behavior of the structure in a damaged condition are carried out using a verified analytical program.

(c) In addition to condition (b) above, blue water is never to break over the top of the structure under maximum wave conditions assumed for the one-year return period, and the bottom is never become exposed to the air.

(d) Tests are to be conducted to measure the elastic deformation and total strength of the structure.

(3) Other criteria

(a) Air pipes of compartments installed topside

Requirements regarding height and closing devices for air pipes are not necessary because the model satisfies the criteria in (2)(c) above. (Criteria are still need to be defined for suitable measures against rain, etc.)

(b) Hand rails

Hand rails required on ships by related laws are not necessary because any sloping or tilting of the model is either very minimal or is limited to local sloping.

(c) Bilge system

Although a fixed bilge system is not necessary, portable pumps with sufficient capacity to drain the water of two flooded compartments are equipped on board.

When a VLFS satisfies the criteria described above, it becomes difficult for such fatal events as sinking or capsizing to occur. Since a VLFS has a huge area, however, it is necessary for rainwater to be stored in the VLFS because it can not be discharged directly off the structure. Therefore, the pump system needs to have sufficient capacity to discharge any water topside due either to flooding or rainwater.

2.3 Structural strength and station keeping system

2.3.1 Strength of Phase II model and dolphin mooring system

-1 Environmental conditions

The Phase II model has a very short life span of only about one year because it is used for tests to verify the feasibility of airport functions. The life span of ships and offshore structures is not always clear, but it is generally considered to be about twenty years for design purposes. The strength of a ship is required to withstand the maximum loads expected to occur during a return period of about twenty years, which is the same length of time as its life span because a ship can avoid encountering harsh storms. In the case of offshore structures, the strength of a structure is required to withstand the maximum loads expected to occur during a return period of about 50 to 100 years, which is three to five times that of its expected life span because the structure cannot avoid encountering harsh storms. Since the Phase II model is a type of offshore structure, the maximum environmental condition is to be considered a return period of three to five times its expected life span, i.e., a return period of 3 to 5 years. However, this period is considered as being too short. The maximum environmental condition corresponding to a return period of about 10 years may be considered for a temporary dwelling or structure built under laws relating to construction in Japan. Hence, the maximum environmental condition of the Phase II model is taken to correspond to a return period of 10 years. However, the maximum environmental condition expected during the 10 year return period is considered to be a small value compared with the design conditions for ordinary offshore structures, because it is quite possible to exceed this value based on statistical data for structures in typhoons. Thus, the maximum environmental condition expected during a return period of 100 years is considered for caution's sake.

The environmental condition is determined from the data measured over a 50 year period at and near the place where the Phase II model is installed and close to the place where the environmental data was measured in detail when tests of the Phase I model were carried out over a period of two years.

-2 Assessment of structural strength

(1) Phase II model

Environmental loads due to the environmental condition determined in sub-section –1 above, static loads, and variable loads other than environmental loads acting on the Phase II model are calculated using an appropriate program. Structural analysis when these loads act on the Phase I model is then carried out. The stresses of the structural elements calculated are assessed based on the following criteria, and structural strength is confirmed.

(a) Stresses of structural elements calculated for

environmental loads with a return period of 10 years acting on the model do not exceed a set allowable stress ($0.8\sigma_y$ or $0.8\sigma_{critical}$), where σ_y is yield strength of the material used.

(b) Stresses of structural elements calculated for environmental loads with a return period of 100 years acting on the model do not exceed a set allowable stress (σ_y or $\sigma_{critical}$)

(c) Stresses of structural elements calculated for damaged condition in the case of flooding in two compartments do not exceed a set allowable stress ($0.8\sigma_y$ or $0.8\sigma_{critical}$).

(d) Fatigue strength is calculated assuming a life span for the model of 10 years. Criteria for fatigue strength do not exceed a cumulative fatigue damage ratio of 1.0. Structural elements critical to fatigue strength not only consist of areas of stress concentration but also consist of the parts joined together between units welded at sea where welding procedures and conditions differ from those at a shipyard or factory.

(e) The requirements required with respect to ship strength are applied to the strength and local strength of the structure.

(f) The corrosion margin is 1.0mm due to the short life of the structure. However, a corrosion protection system has been employed which consists of painting the parts exposed to air and attaching anodes to the structure underwater.

Design loads of the Phase II model are considered small compared with those of existing offshore structures because the return period is determined as being 10 years. However, strength checks were also carried out against design loads for an assumed return period of 100 years. Therefore, it is considered that the Phase II model has sufficient strength to withstand the loads that it is expected to encounter under the environmental conditions.

(2) Dolphin mooring system

The Phase II model is kept in its specific position by six dolphin mooring system with rubber fenders. Dolphin mooring systems with rubber fenders are not only very important structures for keeping a floating structure in a specific position, but also act to prevent floating structures from drifting, which is the most fatal event that can befall such structures. The strength of the structural elements and the characteristics of pulling and pushing of piles from the sea bed are applied to the criteria or rules most usually used in civil engineering. The compression strength of the rubber fender is also applied. The following points are examined.

(a) The stresses of the structural elements acting on the dolphin due to environmental conditions for a 10 year return period are not to exceed a set allowable stress ($0.8\sigma_y$ or $0.8\sigma_{critical}$), and safety factors of pulling and pushing forces acting on the dolphin are not to be less than 1.2.

(b) Stresses of structural elements of the dolphin calculated for the environmental conditions for a 10 year return period acting on the model and dolphin do not exceed a set allowable stress (σ_y or $\sigma_{critical}$), and safety factors of pulling and pushing forces are not to be less than 1.0.

(c) Deformation of the rubber fender due to the compression force of environmental conditions for a 100 year return period is not to be less than a set allowable stress (σ_y or $\sigma_{critical}$), and safety factors of pulling and pushing forces are not to be less than 1.0. It is necessary to confirm that progressive collapse cannot occur due to the failure or loss of any one system.

(d) The corrosion margin is to be 1.0 mm due to the short life span of the structure.

Based on the above-mentioned factors, it was confirmed that the Phase II model is securely moored and will not be able to drift.

2.3.2 Arrangement of dolphin mooring system, etc.

It is necessary that the floating structure and dolphin mooring system should be designed so as to avoid any obstruction to the landing and taking off of an airplane, because the Phase II model is designed and constructed for the purpose of carrying out experiments to confirm its function as an airport. Thus, special consideration is given to the height and top shape of the dolphin mooring system and to the arrangement of all topside structures, including the control tower and the like.

2.3.3 Construction work

-1 Welding work

The Phase II model consists of six units each having a configuration resembling that of the double bottom of a ship. Welding work is done at sea to connect the units together. It is no problem to construct the units themselves because they are constructed at a shipyard or a factory. Therefore, surveys during construction are carried out in the same manner as those for a ship. However, the following matters regarding welding work at sea differ from those of welding work on land.

(1) The parts being joined are continually moving slightly during welding due to motion of the unit induced by waves.

(2) Welding work of the bottom of the structure is carried out in conditions of high moisture because it is done in seawater.

(3) The second and subsequent passes during welding cools rapidly because the welded parts are exposed to the water on the reverse side if the welded part is kept watertight after the first pass is completed.

(4) For, the Phase II model, the structure has a draft of about 0.5 m, and the wet welding method is not used. Thus, water around the parts being welded

must be discharged before welding work is begun. The method used to discharge water consists of blowing the target area with air that has a pressure higher than the water head corresponding to the draft. Consequently, welding work is carried out under high air pressure.

(5) Units become deformed as a result of differences in temperature between the top of the unit and the bottom of the unit. Therefore, it is possible for joined parts to become misalign.

Hence, welding qualification tests are carried out to verify the effectiveness of the welding method.

-2 Non-destructive tests

Non-destructive tests are required for all welded structures. Non destructive tests are carried out as specified in Table 3.

Table 2 The rate of non-destructive test

	Top & Side	Bottom
Unit	0.5 %	1 %
At Sea	2.5%	5%

Internal members: 1%

For units constructed at a ship yard or a factory, the sampling rate is the same as that for a ship because each unit has a simple configuration such as a double bottom. For welding work at sea, the sampling rate is more severe than that for a ship because the method of welding is different, as mentioned above.

3. Concept of Structural Safety for an AFFBS

The concept of structural safety for the AFFBS may be tentatively considered as being an extension of the criteria used for the structural safety applied to the Phase II model.

An AFFBS integrates some structural elements, which mainly consist of a VLFS, and several to many mooring systems, as shown in Fig. 1. It is necessary for the strength of all structural elements to withstand static loads including the weights of all fixed facilities, buildings, and such installed thereon, as well as resulting hydrostatic pressures, variable loads such as consumables on board, the weight of movable objects, and environmental loads due to the wind, waves, earthquakes, and the like. It is also important for a VLFS not to experience fatal events such as sinking, capsizing, or drifting. With regard to the sinking and capsizing of a VLFS, it is considered sufficient that prescriptive rules may be applied. In addition, a ship should also be required as a safe means of escape in the event of an emergency. Further, it is also considered sufficient that prescriptive rules be applied with regards to the strength of the structure including those used for ships, where applicable. Prescriptive rules have certain advantages which include their being:[3]

(1) somewhat ambiguous thereby permitting suitable interpretation to account for local conditions;

(2) straightforward to use and easy to check; and

(3) based on a broad base of experience such as past damage and the like.

Since most prescriptive rules are based on a history of successful use and are changed only in small increments, they implicitly embody the current state of knowledge. The scope of prescriptive rules, however, is based on the assumption that the floating structure is a rigid body. Therefore, given the elastic nature of the VLFS, it is neither reasonable nor practicable for prescriptive rules to be applied to a VLFS in their entirety. Prescriptive rules have certain shortcomings with respect to assessing the strength of a VLFS, however, due to the lack of sufficient data concerning past results of construction and the VLFS being used for longer periods of time than ordinary floating structures. Such disadvantages include:

(1) difficulty in assessing structures which are beyond the scope of prescriptive rules;

(2) difficulty in calculating environmental loads;

(3) difficulty in determining how much environmental load a VLFS can withstand safely.

Further, if prescriptive rules are applied to a VLFS which is considered to have variable configurations and size, there is a danger that the degree of freedom in design will be restricted, and improvements in design, construction, equipment, and development of analysis program will be hindered. Consequently, assessing the safety of the novel structures requires rules which correspond to the limit states of design, performance based design or risk based design. The basic elements of such rules would be as follows:

(1) Requirements would be a qualitative expression of performance goals for safety.

(2) Performance goals for safety would be set which the designer would be required to meet. It would be acceptable to meet the safety goals by any suitable approach.

(3) Evaluation would be carried out based on specific qualitative analysis or tests.

(4) The designer would specify the criteria used and their evaluation.

It is clear that more work would be required of designers and greater engineering expertise required of the surveyor or inspector under a performance oriented design approach than with traditional design approach using prescriptive methods. However, since the qualitative expression of safety goal is set, it is easy for people with a minimal level of engineering knowledge to understand the safety requirements and conditions of the structure being designed. Specific structures such a VLFS could then be designed more reasonably so that new technologies and advanced analytical methods could be more readily reflected in their design.

However, it would be difficult to design all structural elements of a VLFS using a performance oriented design method because the configuration of the VLFS now considered resembles that of a double bottom structure to which prescriptive rules can be applied. This being said, however, it is necessary for the structure of a VLFS to be designed as a whole using

a performance standard because it is not possible to neglect the elastic behavior of the structure. Still, it seems easier to design the structural elements of the units and local structures using prescriptive methods according to their structural configuration. Hence, it is desirable that the design approach taken for a VLFS consist of a hybrid method which includes both a performance standard and a prescriptive method.

In general, performance standards are based on assessments of reliability. The key elements of any reliability based methodology adopted for a VLFS should include the following:[3]

(1) definition of failure modes and limit states;
(2) target reliability;
(3) load combination; as well as
(4) load, resistance and model uncertainties.

For structural elements of units and local members, the design needs to incorporate an allowable stress method or consist of load and resistance factor design. The limit state design approach should be applied to the overall structure as a whole. The failure modes normally considered for general offshore engineering structures consist of the following.[4]

(1) Ultimate limit state (ULS)
This is a criterion corresponding to the maximum resistance to applied action. Examples of ultimate limit states include:
(a) loss of static equilibrium of the structure, or of a part of the structure, considered as a rigid body (e.g. overturning, capsizing, sinking)
(b) failure of critical components of the structure caused by exceeding the ultimate strength (in some cases reduced by repeated actions) or the ultimate deformation of the components,
(c) transformation of the structure into a mechanism (collapse or excessive deformation),
(d) loss of structural stability (plastic buckling, etc.),
(e) loss of station keeping (free drifting)

(2) Serviceability limit state (SLS)
This corresponds to the criteria governing normal functional use. Examples of serviceability limit states include:
(a) deformations or movements that affect the efficient use of structural components,
(b) excessive vibrations producing discomfort or affecting non-structural component or equipment,
(c) local damage (including cracking) that reduces the durability of a structure or affects the use of structural or non-structural components,
(d) corrosion that reduces the durability of the structure and affects the properties and geometrical parameters of structural and non-structural components,
(e) motions that exceed the limitation of equipment.

(3) Fatigue limit state (FLS)
This is criteria corresponding to the accumulated effect of repeated actions. Fatigue limit states refer to cumulative damage due to repeated actions.

(4) Accidental damage limit state (ALS)
This is a criterion corresponding to the situation where damage to components has occurred due to an accidental event. The accidental damage limit states check ensures the local damage or flooding does not lead to complete loss of integrity or performance of the structure.

While the above limit states can to a large extent also be applied to the design of a VLFS, a number of these states differ for such types of structures due to their unique configuration. Additional limit states with respect to the serviceability of the structure need to be considered, in particular. Most notables of these would include:

(a) excessive elastic deformation due to the elastic nature of the structure
(b) deformation due to differentials in temperature across the structure
(c) breaking up of the structure due to excessive plastic deformation or inadequate structural integrity
(d) greater susceptibility to the impact of fatigue stress due to greater variations in the distribution of stress and strain over the entire structure

Careful consideration needs to be given to various loads such as static loads, variable loads other than environmental loads, environmental loads, as well as accidental loads for each limit state in design bearing in mind the special characteristics of the structure. Particular attention should be given to variations in environmental loads based on values for the rate of probable incidence of occurrence during the lifetime of the structure and degree of potential severity assigned accordingly. For this purpose, environmental loads are divided into three classes as follows:

(1) Normal environmental condition (Class 0 condition)
This condition is frequently encountered during the lifetime of the structure. Generally speaking, it represents a frequency of incidence in which the return period for a given maximum condition is one year.

(2) Maximum environmental condition (Class 1 condition)
This indicates a condition that may be encountered at least once during the lifetime of the structure. Generally speaking, the return period of a given maximum environmental condition is defined as being 2 to 5 times the lifetime of the structure.

(3) Incidental environmental condition (Class 2 condition)
This indicates a condition that is rarely encountered during the lifetime of the structure. Generally speaking, the return period of a given maximum environmental condition in this case is defined as being 100 or more times the lifetime of the structure.

Large-scale accidental loads such as collision with a ship is regarded as being a Class 2 condition. Small-scale accidental loads such as a fire at a small

compartment would be regarded as Class 1 conditions.

The combination of loads corresponding to each limit state is given in Table 3

Table 3 Combination of loads corresponding to each limit state

Limit State	Combination of loads				
	Static Loads	Variable loads	Environ-mental loads*1	Environ-mental loads*2	Acci-dental loads
ULS	X	X	Class 2	----	----
	X	X	Class 0	Class 2	----
	X	X	Class 0	----	Class 2
SLS	X	X	Class 1	----	----
	X	X	Class 0	Class 1	----
	X	X	Class 0	----	Class 1
FLS	X	Frequency	Frequency	----	----
ALS	X	X	Class 0	----	----

Notes

*1 Loads due to such phenomena as waves, wind, currents, etc. occur on a regular basis.

*2 Loads due to such phenomena as earthquakes, tsunami, etc. occur only very rarely.

Safety checks with respect to ULS and SLS are carried out in order to ensure that load effect (Sd) is not less than the resistance of the structure (Rd), where Sd and Rd is calculated from the following formula:

$$S_d = \sum_{i=1}^{n} (\gamma_{fi} S_{ki}) \quad (1)$$

$$R_d = R_k / \gamma_m \quad (2)$$

Where,

Ski = Nominal load effect

γ_{fi} = Load coefficient

Rk = Nominal resistance

γ_m = Material factor

4. Basic concept for future development for a Safety Guidance of an AFFBS

It is reasonable and reliable for the safety assessment of the strength of a VLFS to be being carried out using the hybrid method mentioned above. However, the AFFBS itself is integrated structural system which consists of a VLFS, numerous station keeping systems, as well as a breakwater. For example, a breakwater is installed to mitigate design wave conditions or to increase the working ratio by calming the waters of a specific site when general sea conditions are rough. In this case, the wave conditions used in the structural design of a VLFS and its associated station keeping systems are determined based on the assumption that the function of the breakwater is always performed effectively. If any part or the entire function of the breakwater ceases to work effectively for any reason, the VLFS will be subjected to waves which could quite conceivably exceed the design parameters of the structure with a corresponding increase in risk to safety. Thus, it is not enough for only the safety of the VLFS and its station keeping systems to be assessed, but attention must be given to each element comprising the AFFBS as a whole. With regard to safety of an integrated structural system such as an AFFBS, it is very important for redundancy within the system to be discussed.

For this purpose, it is felt that a risk assessment approach would be effective. Therefore, the basic concept for future development of a safety guidance for an AFFBS is thus the adoption of a risk assessment approach. This would include such considerations as:

(1) Setting of quantitative safety levels considering the following:
   (a) social and environmental risks;
   (b) risk to life and property;
   (c) cost benefit; as well as
   (d) passive risk.

Details of these risks are introduced in a separate paper by Dr. Hideyuki Suzuki.[5]

(2) Identification and modeling of hazards (modes of failure)
   (a) modeling of limit states with respect to each mode of failure;
   (b) modeling of probability distribution functions against the parameters of limit of state;
   (c) calculation of reliability for each mode of failure using reliability based approach, etc.;
   (d) quantitative evaluation of risk; as well as
   (e) assessment of risk levels compared with quantitative safety levels described in item (a) above.

In general, the safety level of a VLFS is also considered with reference to the safety levels of other structures such as ships, offshore structures for oil or natural gas industry, airplanes, automobiles, railways, buildings, bridges, dams, etc. However, since a VLFS of the large-scale size being considered has never existed in the world before, it is very difficult to determine quantitative risk levels due to a lack of data related to design and construction.

5. CONCLUSION

Examination of the drawings and documents of the Phase II model and surveys during its construction have already been carried out. Based on this experience, it is becoming easier to consider a possible framework for the development of a suitable guideline for an AFFBS, including a VLFS, in the future. The concept for such a guideline would consist of the following:

(1) Stability and floatabilty
   The requirements for ships or offshore structures are available considering the elastic behavior of an VLFS.

(2) Structural strength
   Adoption of a hybrid method of approach, which combines the allowable stress approach and limit state approach, is considered reasonable, practical

and effective. The criteria such an approach would be based upon the reliability approach.

(3) System redundancy
A risk assessment approach is thought to be an effective means of designing system redundancy. However, it is first necessary to develop suitable methods and analytical programs to address the current lack of data.

In closing, it is essential that consideration be given to assessing the environmental impact of installing an AFFBS. Similarly, it is very important to establish suitable maintenance technologies, including repair and inspection technologies, in order to maintain the structural soundness of such systems over their life spans. Although this aspect is not covered in this paper due to a lack of space, it is another area of concern in which further study needs to be undertaken in the future.

References

[1] N. Yokouchi, O. Saijo, & T. Okada. "Study on the Legal System of Very Large Floating Structures(Mega Float) Aiming at Construction", the 14th Ocean Engineering Symposium, Tokyo, Japan, 1998.

[2] S. Harada, Lecture of Research Institute of Nippon Kaiji Kyokai, 1997

[3] R.I. Basu, "The Development of a Classification Guide for the Mobile Offshore Base"

[4] International Standard ISO 13819-1, Petroleum and natural gas industries – Offshore structures – Part 1: General requirements

[5] H. Suzuki, "Safety Target of Very Large Floating Structure Used for Floating Airport"

PROCEEDINGS OF THE THIRD INTERNATIONAL WORKSHOP ON VERY LARGE FLOATING STRUCTURES
(VLFS '99), VOL. I, EDS. R.C. ERTEKIN & J.W. KIM, 22-24 SEPTEMBER 1999, HONOLULU, HAWAII, USA

High Performance Concrete – An Ideal Material for Large Floating Structures

Lars Bjerkeli, Jan Munkeby and Finn Rosendahl
Aker Maritime ASA *

ABSTRACT

Reinforced high performance concrete fulfils the key material requirements for Very Large Floating Structures (VLFS), namely a 100 years design life, superior fatigue resistance and ultimate strength, low maintenance cost and robustness against accidental loading. These characteristics are documented through in service experience from offshore concrete structures that are comparable to VLFS's in both size and complexity.

1. INTRODUCTION

Very Large Floating Structures (VLFS) are characterized by requirements for a long design life (typically 100 years) and low maintenance costs, and they have to be designed for a variety of loading situations. Durability and fatigue resistance are key requirements for selection of materials for fabrication of such structures.

Even though VLFS's will be unique by their huge size, corresponding design requirements have been applied to existing structures that are operating in a comparable environment. Typical examples are coastal bridges and offshore structures for the oil industry. In this paper it will be demonstrated that High Performance Concrete (HPC) fulfils the material requirements for VLFS's. The statement is illustrated by some case histories.

2. GENERAL CHARACTERISTICS OF HIGH PERFORMANCE CONCRETE

2.1 High Performance Concrete characteristics

Durability, strength and constructability are the key characteristics for an HPC and are obtained by careful selection of constituent materials and mix proportions. In addition, strict quality assurance and quality control are required during concrete production to obtain a uniform and predictable material.

2.2 Durability

The durability of concrete in a marine environment has been documented through 25 years of experience with concrete structures for the exploitation of oil and gas in the North Sea. A review and status of the in-service experience with these structures can be found in [1]. It is concluded that the structures are in remarkable good condition. The success parameters for the mix design of the concretes for the North Sea platforms have been a dense concrete with 380 to 430 kg of cement pr. m^3, appropriate cover to the reinforcement, sulfate resisting cement and non-reactive aggregates, simple geometry and high standard of workmanship and supervision.

The most serious, and probably most frequent type of deterioration of marine concrete structures in general is reinforcement corrosion caused by penetration of chloride ions to the reinforcement. This corrosion is prevented by the alkaline nature of the surrounding concrete. This protection may be reduced by the ingress of chlorides, causing a too high concentration of chlorides ions. Sufficient cover of dense concrete with low permeability prevents chloride concentration from becoming critical. To monitor the risk of corrosion, chloride profiles can be established from drilled core samples, ref. Fig. 1. Theoretical models to predict the remaining service life based on this information has been developed and verified. By applying this model on results from core samples from five exisitng offshore structures a service life of more than one hundred years have been predicted for all of them [2].

* Postal address: Tjuvholmen, N-0250 Oslo, Norway
e-mail; lars.bjerkeli@akermar.com, jan.munkeby@akermar.com, finn.rosendahl@akermar.com

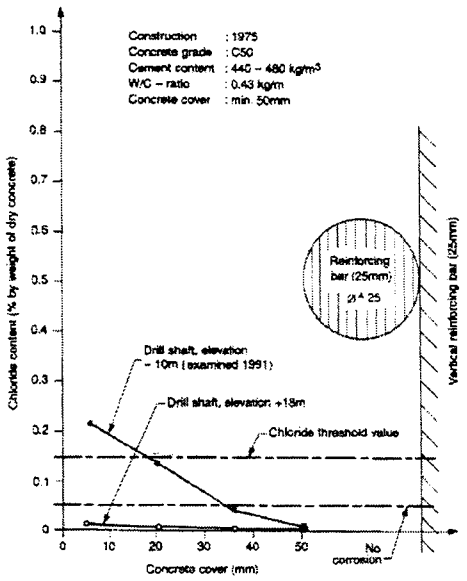

Fig. 1 Chloride profile, splash zone of a 16 years old concrete gravity base structure (GBS) [1]

The Troll A Gravity Base Structure (GBS), which is situated in 300 m water depth in the North Sea, has been designed for a service life of 70 years [3], ref Fig. 2. It was taken into operation in 1995. Concrete floating bridges and submerged concrete tunnels are designed for a service life of 100 years [4] and [5].

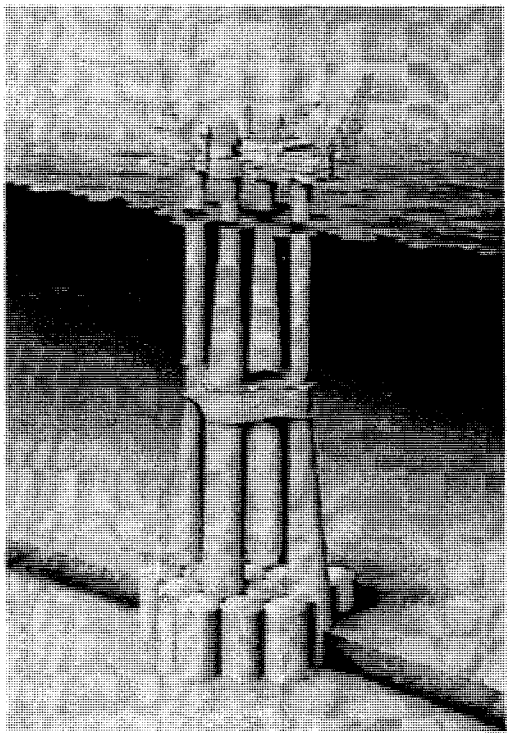

Fig 2 The Troll A GBS

2.3 Fatigue properties

The design for fatigue is an important issue for structures that have a long service life and are subjected to dynamic loading. Offshore concrete structures in the North Sea are subjected to severe dynamic loading from environmental loads. The Norwegian concrete code NS 3473 offers a complete set of fatigue design rules for such structures [6]. This code has been used for the fatigue design of most offshore concrete structures.

Reinforced concrete has superior fatigue resistance when subjected to compression–compression loading. Post-tensioned cables are therefore extensively used to keep the concrete members in membrane compression during the majority of the load cycles. By following this design approach, the fatigue design is rarely governing for the selection of section thickness of the concrete or ordinary reinforcement quantities.

Even for the slender and dynamically sensitive Troll A platform at 300 m of water depth, the fatigue requirements were not the governing design issue for the shafts. According to [1], no fatigue damage has been reported in structural concrete of North Sea structures, since their introduction 25 years ago.

2.4 Concrete material properties

Contrary to steel, the main design parameters of concrete structures may be varied. The modulus of elasticity, the density and the compressive strength can be tailored to fit a specific design requirement. This may for example be a maximum weight requirement for draft restrictions of the construction dock or related to the dynamic behaviour of the structure.

The density may vary from 1.9 t/m^3 for Light Weight Aggregate Concrete (LWAC) to about 2.4 t/m^3 for Normal Density Concrete (NDC). Correspondingly, the modulus of elasticity may vary from about 22 GPa to 36 GPa depending of the type of aggregates used. The range of compressive strength may be even wider, from about 45 MPa up to 80 MPa, which is close to the upper limit for large-scale production with today's technology. Grinded faces from core samples of different concrete types are shown in Fig 3.

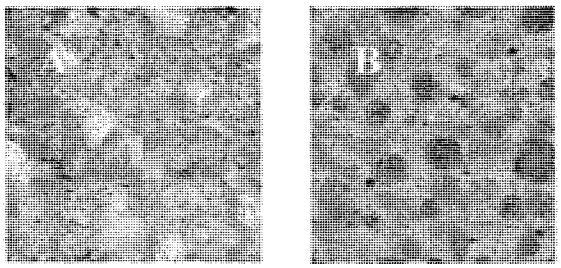

Fig 3 Examples of A) Normal Density and B) Light Weight Aggregate Concrete

Concrete also provides excellent fire resistance against hydrocarbon fire. This quality is particularly relevant for VLFS's, which often will have storage facilities for different kinds of fuel.

3 DESIGN REQUIREMENTS TYPICAL FOR CONCRETE STRUCTURES

General design principles for marine structures may be found in ABS or DNV Classification rules. Some design topics that are related to concrete structures only are addressed in the following. The design of offshore concrete structures is performed according to recognized codes and regulations, for example [6], [7] or [8].

Crack width limitations:

The ultimate capacity of a concrete section assumes yielding of the reinforcement. Consequently, the concrete will crack in tension to allow the steel to yield. For durability reasons concrete codes limit the allowable crack widths during service conditions. Crack widths are also restricted if liquid tightness is required. The means to control crackwidths are to specify an adequate compression stress applied by post-tensioned cables, as well as a minimum amount of well distributed ordinary reinforcement.

Imposed deformations

Creep and shrinkage induce volume changes in a concrete material. This may subsequently cause imposed deformations. The magnitude of these deformations is well established and is taken care of in the design in a similar way as temperature deformations.

Water pressure in cracks

As concrete is allowed to crack in tension, water will penetrate the cracks. In particular for deep water, water pressure in a crack will influence the load situation of the different concrete sections. Well established procedures describe the way of incorporating this effect in the design [9].

Other particularly concrete related design aspects, such as in-plane forces and design of discontinuity regions, are also described in [6] and [9].

Concrete structures offer smooth interior faces ideal for liquid and fuel storage and make inspections easy to perform. Significant resistance to collision loads from supply boats or similar traffic can be accounted for in the design. For practical purposes, there are no restrictions on section thickness as often is the case for welded steel structures. Up to 2 meters of thickness have been used in offshore structures.

4. INSPECTION, MAINTENANCE AND REPAIR

All loadbearing structures with a significant design life require a planned condition monitoring. Offshore structures in the Norwegian sector of the North Sea are subjected to legal requirements stated in [10]. Periodic framework programs running for 4 years with annual assessments is the main requirement in [10]. A typical inspection program for a large offshore concrete structure includes visual inspection of both submerged and atmospheric areas. Submerged parts are normally inspected by Remotely Operated Vehicles (ROV's). Observations from the visual inspection may require closer investigations such as drilling of core samples for laboratory testing, electrochemical measurements for corrosion assessment or closer visual inspection. An outline of a typical inspection program may be found in [11].

The conclusion from inspections of the many North Sea concrete platforms is that they are in remarkably good condition [1]. Compared to the huge area of exposed concrete (more than 1 km^2) the number of repairs that have been reported are insignificant. The few major repairs have been caused by accidental incidents such as ship impact and dropped objects. Some maintenance repairs have been required due to insufficient cover to the reinforcement or porous concrete. No maintenance repair has been necessary on submerged parts of the platforms.

For a service life of 100 years or more the use of a protective coating on the exterior concrete surface above the waterline will improve the durability and reduce the maintenance costs [12].

5. HIGH PERFORMANCE CONCRETE USED IN OFFSHORE STRUCTURES

In the following, some examples of large concrete structures are presented. In weight and volume, some of these structures are among the largest structures ever built by man and subsequently moved.

The Troll A platform has already been presented in Fig. 2. The displacement during tow to field in 1995 was 1,028,000 tonnes. The total height of the substructure is 369.4 meters and it contains 245,000 m^3 of concrete.

The Hibernia platform is another concrete giant of impressive dimension. With a displacement of 600,000 tonnes during towout and concrete volume of 167,000 m^3 this platform is designed to resist icebergs up to one million tonnes with a speed of up to 2.5 knots. The platform is show in Fig. 4.

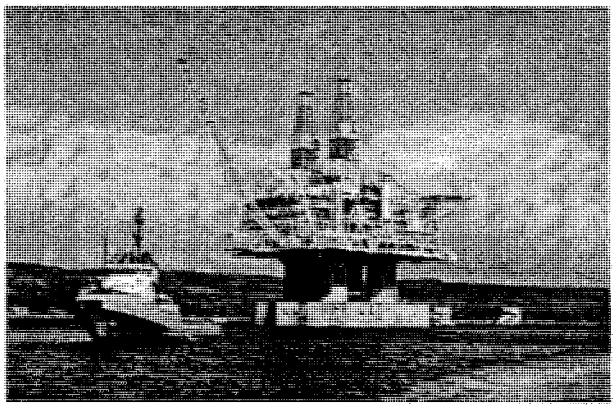

Fig 4 The Hibernia platform during tow to Grand Banks off Newfoundland

While the two previous platforms are fixed structures in operation, the Heidrun Tension Leg Platform (TLP) is the first concrete floater built for oil production. It was installed in 1995 in 345 meters water depth and has a displacement of 285,000 tonnes. Heidrun has the highest load-bearing capacity of all offshore platforms in the world, about 80,000 tonnes. The hull is constructed using LWAC. The platform is shown in Fig 5.

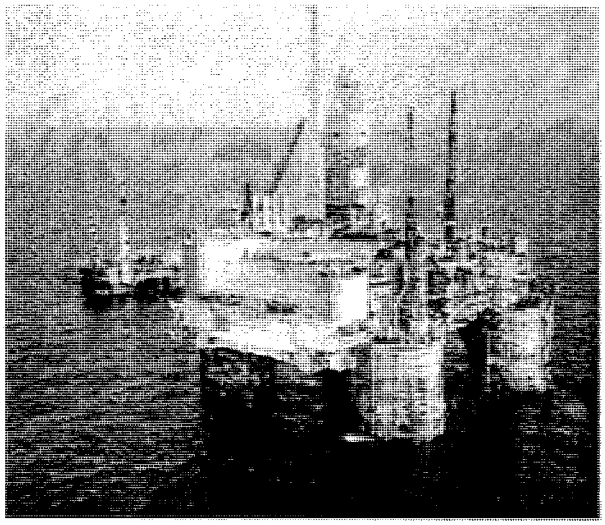

Fig. 5 The Heidrun TLP in operation in the North Sea

In Fig 6 the NKossa oil production barge is presented. This rectangular barge, 220 m long, 46 m wide and 16 m deep has an operating displacement of 110.000 tonnes. It is producing oil from the NKossa field located 60 km off the Congo coast. The platform has been in production since June 1996.

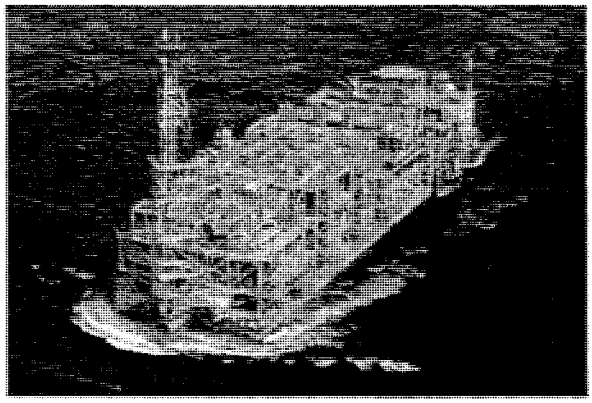

Fig 6 The NKossa barge offshore Congo (Photo courtesy of Elf)

The platforms presented above represents only a fraction of the close to 40 oil related offshore concrete structures in operation world wide. Still the examples demonstrate the variety of concepts and climatic conditions for which concrete has been considered the preferred material.

Aker Maritime has developed a concept for a hybrid Mobile Offshore Base (MOB) with a steel deck and a concrete hull for the Office of Naval Research (ONR). What particularly attracted the ONR by this concept was the durability aspects, the superior fatigue resistance, the adaptability to different climates and the low maintenance cost. The MOB concept is presented in another paper on this work shop [13]. The concept is shown in Fig 7.

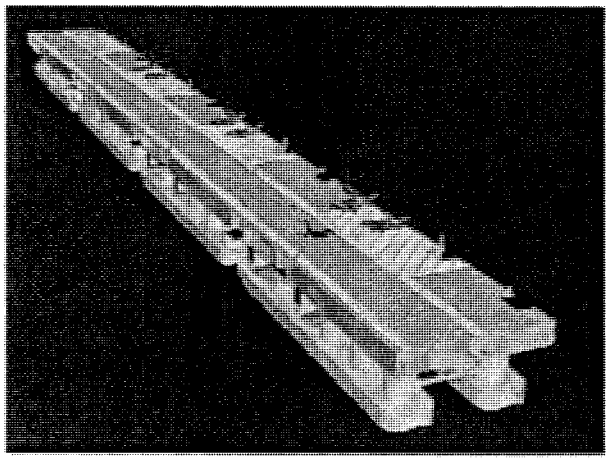

Fig 7 Concrete/steel hybrid concept for a Mobile Offshore Base

6. CONCLUSION

It can be concluded that it has been documented through in-service experience that properly designed and constructed concrete structures have a service life of more than a 100 years. Surplus capacity with respect

to fatigue resistance is to be expected even with this long service life. Concrete also offers a range of material densities and stiffness that can be favorably utilized in design. In addition, reinforced concrete is very resistant to accidental loadings such as fire and impact loads. Smooth faces make in-service inspection easy and maintenance costs are documented to be low. Fuel or other liquid storage can easily be incorporated into the structure, practically without additional cost for the structure. These features make concrete a very attractive material for use in Very Large Floating Structures.

7. ACKNOWLEDGEMENT:

This paper is based upon work supported by the U.S. Office of Naval Research's MOB Program.

8. REFERENCES

[1] Durability of concrete structures in the North Sea. FIP State of the Art Report. Nov. 1998

[2] S.Helland and L.Bjerkeli: Service life of offshore structures. Offshore West Africa '99, Abidjan, Ivory Coast

[3] Lindseth, Lassessen, Syvertsen and Moen: Troll A Gas production platform – Implications of 50-70 years life span. OTC-paper 8412. Offshore Technology Conference, Houston 1997.

[4] G.Moan: Design philosophy of floating bridges with emphasis on ways to ensure long life. International workshop on Very Large Floating Structures, Japan 1996.

[5] W.Janssen, S.Lykke and U.Kjær: Øresund link, durability aspects for the concrete. Proceeding of the 13th FIP congress on challenges for concrete in the next millennium. Amsterdam May 1998.

[6] NS 3473. Norwegian Standard NS 3473 E. Concrete Structures. Design Rules. 3rd edition, 1989

[7] DNV Rules, Det norske Veritas. Rules for the design construction and inspection of offshore structures, App. D: Design of concrete structures

[8] British Standard BS8110, Structural Use of Concrete

[9] J.Munkeby: Overall description of the detail design process. Aker Maritime report A1 in the Mobile Offshore Base study performed for ONR, 1999.

[10] Norwegian Petroleum Directorate (NPD): "Acts, regulations and provisions for the petroleum activity". 1.1.97.

[11] Liodden and Rindarøy: Condition monitoring and maintenance of offshore structures. Proceedings at the second international conference on concrete under severe conditions, CONSEC –98, Tromsø, Norway.

[12] R.Aarstein, O.E.Rindarøy, O.Liodden, B.W.Jensen: Effect of coatings on chloride penetration into offshore concrete structures. Proceedings at the second international conference on concrete under severe conditions, CONSEC – 98, Tromsø, Norway.

[13] G.Rognaas: Mobile Offshore Base Concepts – Hybrid: Concrete hull and steel topsides. International workshop on Very Large Floating Structures, Hawaii 1999.

PROCEEDINGS OF THE THIRD INTERNATIONAL WORKSHOP ON VERY LARGE FLOATING STRUCTURES
(VLFS '99), VOL. I, EDS. R.C. ERTEKIN & J.W. KIM, 22-24 SEPTEMBER 1999, HONOLULU, HAWAII, USA

LIGHTWEIGHT COMPOSITE TRUSS SECTION DECKING

Mr. Richard T. Brown*
Atlantic Research Corporation
and
Professor Abdul-Hamid Zureick
Georgia Institute of Technology

ABSTRACT

An all fiberglass decking panel has been designed to the requirements of the Trilateral Code for Military Bridging and the Circular of Requirements for New Construction Strategic Sealift Ships. The truss structure provides a lightweight fiber reinforced plastic (FRP) module that can be rapidly installed as decking for floating structures or military causeways. The edge supported composite deck can span up to 3 meters by 9 meters at a weight less than 100-kg/per square meter (20 pounds/sq. ft.)

Triangular elements are fabricated using a single, thick ply of 3D-braided fiberglass textile drawn through a pultrusion die. The triangular pultrusions are bonded together with face sheets, using Plexus adhesive, to form the deck modules. The assembly is optimum weight for a plate over a span because the triangles carry the load with truss action and the face sheets carry the load in beam (EI) bending.

1. INTRODUCTION

The Defense Advanced Research Projects Administration (DARPA) funded the development of a lightweight, all fiberglass, modular deck for application to the Landing Ship Quay/Causeway (LSQ/C) and Mobile Offshore Base (MOB) programs. The Atlantic Research Corporation (ARC) is the prime contractor and has applied a truss deck concept developed by the Georgia Institute of Technology. The Georgia Institute of Technology, under Federal Highway Administration (FHWA) funding, developed and optimized the FRP deck to meet the standards of AASHTO HS 20-44.

* 5945 Wellington Rd., Gainesville, VA 20155, USA
E-mail dbrown@arc-ag.com or zureick@ce.gatech.edu

The deck modules, developed for the LSQ/C application are 3.05 meters (10 ft) long in the traffic direction and 9.15 meters (30 ft) wide. A module is supported only at the edges for ease of assembly with the causeway superstructure. The 97.6 km/sq.m (20 lb/sq. ft.) deck consists of pultruded vinylester resin/3D braided fabric trusses and surface plates constructed from engineered fiberglass knits and vinylester using standard marine lay-up practice.

A 3 meter by 3-meter test module was loaded to 635 kN (140 kips) with a measured deflection of 1.78 cm (0.7 in.).

2. LOADING CONDITIONS

The Landing Ship Quay/Causeway (LSQ/C), as envisioned by DARPA, consists of a large, ocean-going ship, prefabricated material, and cranes, capable of installing a causeway for ship-to-shore cargo movement. At a predetermined site, the vessel is grounded in sufficiently deep water to form a pier head for ship mooring. The on-board causeway sections, Figure 1, are deployed inshore past the surf zone. The causeway consists of separate sections 45 meters in length and 9 meters wide. The FRP deck provides a road surface for two lanes of military traffic. The deck, Figure 2, is comprised of discrete modules 3 meters long in the traffic direction and spanning the causeway width. Deck modules are connected to the causeway superstructure only at the edges and can be individually removed and replaced as necessary.

Loading conditions and design requirements are taken from the Trilateral Design and Test Code for Military Bridging and the Circular of Requirements for New Construction Sealift Ships [1],[2].

Specific load factors for a military Class 70 bridge are:

- Track Load (M1 Tank) = 0.126 MPa (18.3 psi)
- Wheel Load = 10,886 kilograms (24 kips) per axle
- Cargo Truck (fork lift) = 63,504 kilograms (140 kips) per axle
- Dynamic load factor = 1.15.

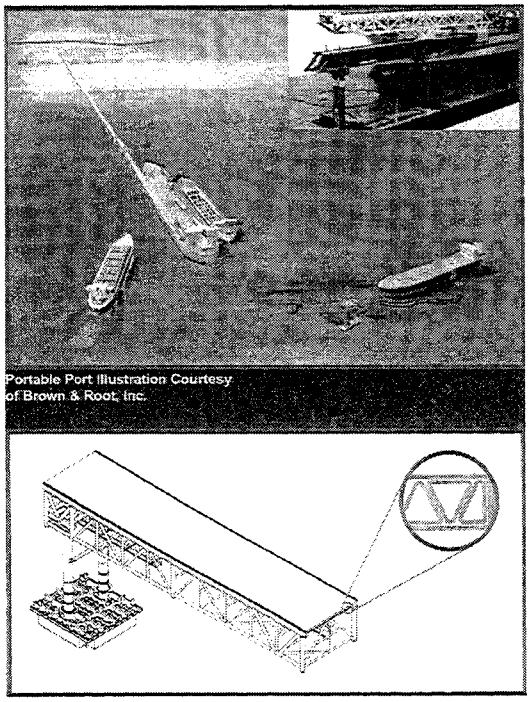

Figure 1. LSQ/C Causeway Structure

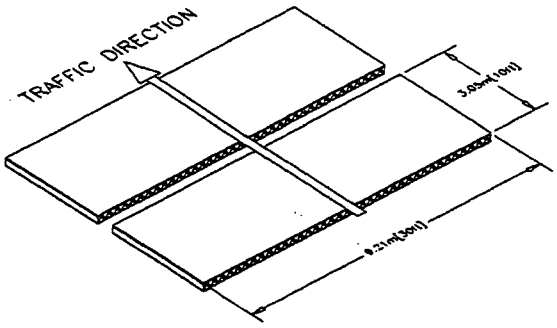

Figure 2. Modular FRP Causeway Decking System

Design criteria were:

- Dead Load not to exceed 100 kg/sq. meter
- Allowable fiber strain = 50% of minimum tested strain at failure
- Multi-axial stress = 1.5 factor of safety using Tsai-Wu criteria
- Fatigue Life = 1.8 design life
- Buckling = 2.0 factor of safety
- Gross Deflection not to exceed 0.89 cm (0.35 in) at over test load of 1.33 design load.

3. DESIGN AND ANALYSIS

Prior research by the Georgia Institute of Technology established the triangular truss configuration as the weight optimum solution for minimum deflections given the span under consideration [3]. The deck was designed to be constructed from top and bottom plates bonded to the triangulated multi-cell trusses. The reinforcement scheme oriented the plate fibers parallel to the truss long axis (parallel to the traffic direction) and the majority of the truss fibers perpendicular to the truss axis. The lamination was:

- Top plate: 14 layers stacked [90/90/90/+45/-45/0/0]s
- Triangular component: 10 layers stacked [0/0/-45/+45/90]s
- Bottom plate: 10 layers stacked [90/90/+45/-45/0]s.

Truss dimensions and principle material directions are illustrated in Figure 3.

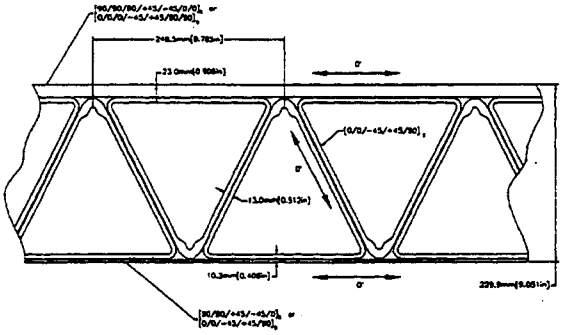

Figure 3. Truss Configuration

Layer properties were derived using Classical Laminate Theory and the following fiberglass lamina properties:

Strength	Modulus
f_{1t}=827 MPa	E_{11}=31 GPa
f_{1c}=827 MPa	E_{22}=8.3 GPa
f_{2t}=27.6 MPa	G_{12}=4.0 GPa
f_{2c}=137 MPa	nu_{12}=0.25
f_s =41.4 MPa	

The FRP deck was analyzed using the ABAQUS finite element computer program. The model used a four nodded shell element with reduced integration and five degrees of freedom per node (ABAQUS element S4R5). Simply supported boundary conditions were used in the model and loading footprints were applied at three critical locations:

- On the top plate between two adjacent webs - controls plate thickness
- Directly on a web apex - controls web thickness
- On a web apex and on a supporting girder - controls buckling strength.

Un-deformed and deformed finite element models for the M1 tank track loads are shown in Figure 4.

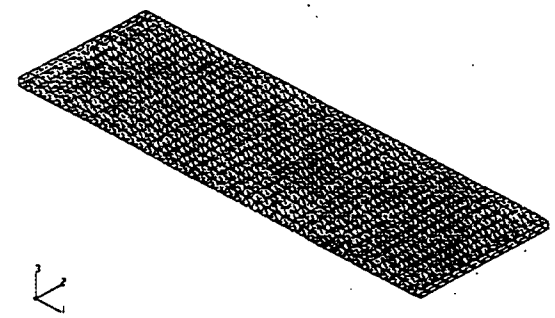

(a)

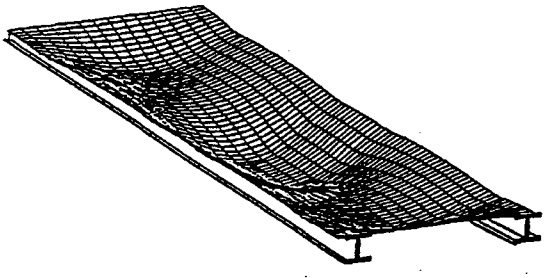

(b)

Figure 4. Finite Element Grids -- (a) Undeformed; (b) Deformed

Typical results for two web thicknesses are given in Table 1 for the loading condition of dead weight plus two passing tanks (with a dynamic factor of 1.15). The top plate thickness was 1.9 cm.

Table 1. Analysis Results for M1 Tank Loading

Web and Bottom Plate Thickness (cm)	Dead Weight (Pa)	Tsai-Wu Safety Factor	Maximum Deflection (cm)
0.635	766	5.5	0.49
0.953	958	8.6	0.39

Mechanically, the design carries the plate loads from edge to edge using truss action and across the traffic direction span by beam bending (EI). The plate reinforcement has the highest stiffness in that direction and hence the highest EI. Special consideration was given to the forklift loading footprint of 0.89 MPa. While a web thickness of 0.635 cm was acceptable for the M1 tank load, concentrated loading on the triangle apex could buckle the web, see Figure 5. Table 2 gives local deflection, Tsai-Wu factor of safety, and buckling Eigenvalue for forklift loads.

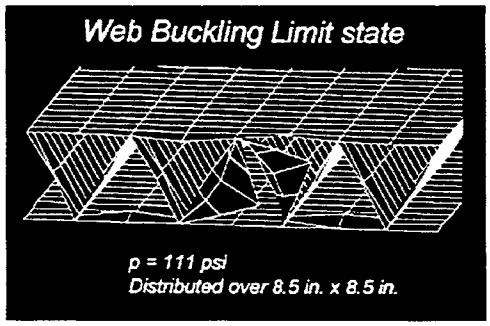

Figure 5. Web Buckling Limit State

Table 2. Analysis Results for Cargo Truck (Fork Lift) Loading

Web and Bottom Plate Thickness (cm)	Max. Deflection (cm)	Tsai-Wu Safety Factor	Buckling Safety Factor
0.635	0.89	2.0	1.15
0.953	0.66	2.8	2.80

Based on the results in Table 2, the selected design consisted of a 1.9 cm top plate and web and bottom plate thickness of 0.935 cm. The results of beam bending tests ultimately resulted in increasing the bottom plate thickness to 1.43 cm.

4. FABRICATION

The top and bottom plates were fabricated by wet lay-up at Structural Composites, Inc. Melbourne, Florida. Plates were fabricated, with 42% fiber volume, using multiply knitted fabric supplied by Johnston Industries and Inter Plastic CORVE - 8110 vinylester. This approach eliminated the ply by ply lay-up sequence associated with exact implementation of the lamination plan. E-glass PPG Hybon 2002 was knitted into 4-ply textiles with fiber orientations and distribution approximating the lamination, although thickness build up required stacking fabric in a series of 0/-45/90/45 layers instead of a symmetrical pattern. The manufacturing advantage is that rolls of the fabric can be run though an impregnator and laid up in multiple passes using standard marine practice. The engineered knits had the following fiber orientations and distributions:

Top Plate	Bottom Plate
Fabric - EQX 4500	Fabric - EQT 5200
0° - 29.2%	0° - 12%
+-45° - 27.8%	+-45° - 21%
90° - 43.0%	90° - 67%

The triangular truss elements were formed using 3D Through-the-Thickness® braided fabric, produced by Atlantic Research [4]. Initially knitted fabric was proposed for the trusses but the built-up plies consistently delaminated at the corners. Figure 6 demonstrates that the three dimensionally intertwined braid eliminated the process-induced delaminations.

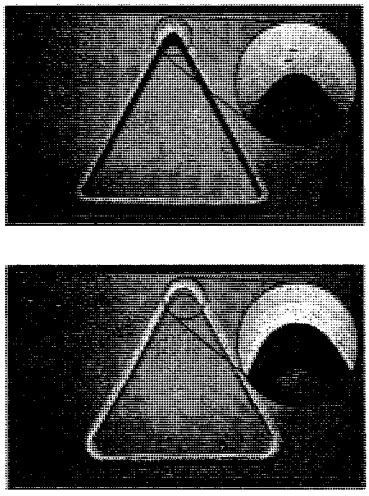

Figure 6. Detail of Triangle Element – (a) Knitted Fabric; (b) 3D Braided Fabric

Since braids have only three axis of orientation, 0+-θ°[1], a new fiber balance, 0° -17% and +-75° - 83%, was selected by closely matching the predicted moduli for the design lamination. The fabric areal weight was 5187 gms[2]. The 3D braiding equipment was modified to cut a tubular braid into a flat fabric, which was then rolled up for shipment as shown in Figure 7.

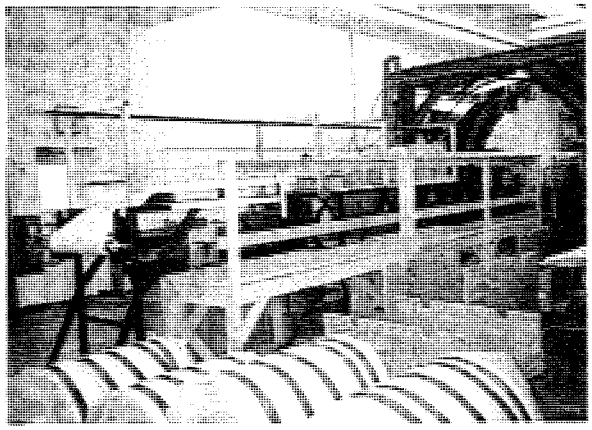

Figure 7. 3D Braiding Machine Producing Flat Fabric

The braided fabric was formed into hollow, triangular elements by Creative Pultrusions Alum Bank, Pennsylvania, using Reichhold ATLAC 850-05 modified vinylester resin with anti-flammability additives, see Figure 8. Creative Pultrusions successfully matured a process for pulling, without distortion, preforms with approximately 80% of the fiber oriented off-axis and with a fiber volume of 41%. The triangular pultrusion die folded the flat braided textile into the triangular geometry with overlapping edges at the apex.

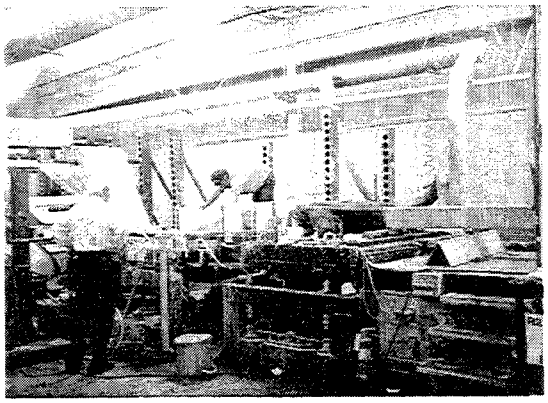

Figure 8. Truss Section Pultrusion

[1] 0° degree braid orientation is in the long axis of the triangle in contrast to laminate notation

[2] gms is a textile term denoting grams/m^2

The triangle truss elements and plates were bonded into deck assemblies using Plexus MA555 adhesive and activator. Truss sections were first bonded in groups of six triangles in a vertical fixture shown in Figure 9. Bottom and top plates were, in turn, bonded to the truss assemblies using a pneumatic press, Figure 10. Closeout channels were laid-up from knitted fabric and bonded over the edges of the deck modules. Two completed three by six-meter (10 ft. by 20 ft.) decks are shown in Figure 11.

Figure 9. Truss Bonding

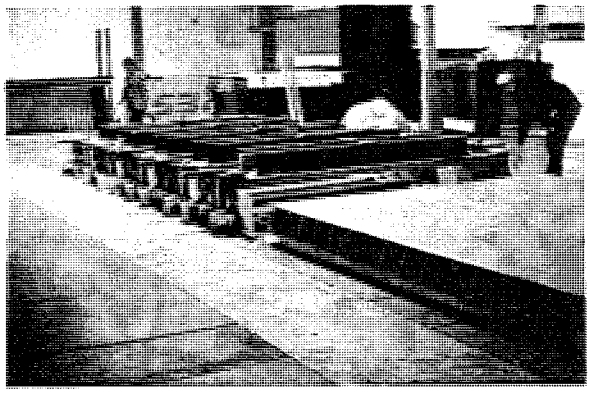

Figure 10. Deck Assembly

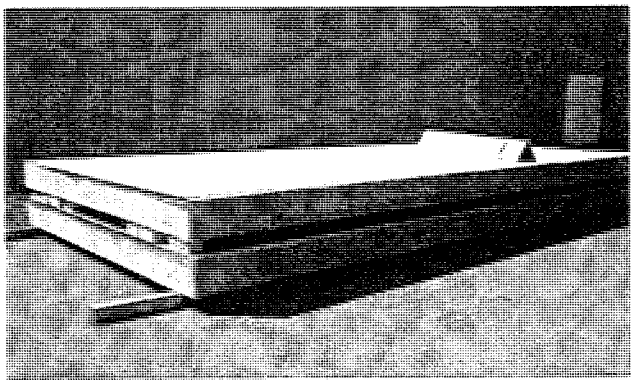

Figure 11. Completed Deck Modules

5. MATERIAL AND COMPONENT TESTING

Predicted mechanical properties for the various knitted fabrics and braids are listed in Table 3. Material specimens and structural components at all levels of assembly were tested at the Georgia Institute of Technology. This "building block" allowed a continuous reappraisal of fabric properties, molding technique, bonding adhesives, and wall thickness.

Table 3. Predicted Laminate Properties[3]

Fabric/ Properties[4]	EQX5200 (bottom plate)	EQX4500 (top plate)	3D Braid (triangles)
areal weight	1777.95 gms	1531.94 gms	5187.38 gms
E_1	11.08 GPa	13.11 GPa	11.11 GPa
E_2	23.85 GPa	16.98 GPa	20.74 GPa
nu_{12}	0.259	0.190	0.237
G_{12}	4.98 GPa	5.34 GPa	4.53 GPa

[3] Assuming a fiber volume of 45%

[4] Notation - 1 perpendicular to triangle axis, 2 parallel to triangle long axis and traffic direction

Representative material properties from coupons excised from the plates and triangles are summarized in Table 4. One outcome of the coupon testing was the observation that the mechanical properties of the pultruded triangles could be improved by post cure at 140C. Presumably the matrix is not fully reacted as it leaves the die and post cure maximizes the resin performance. The average knockdown factor for 150 freeze/thaw cycles of the un-post cured pultrusion specimens was 5%.

Table 4. Representative Measured Properties

Specimen/ Measured Properties	Top Plate	Bottom Plate	Triangle	Post Cured Triangle (140°C)
E_{1t} (GPa)	15.3	12.7	11.9	13.6
E_{2t}	17.7	17.7	16.6	16.1
E_{1c}	15.4	13.8	12.7	12.8
E_{2c}	17.7	17.3	17.9	18.1
F_{1t} (MPa)	N/A[5]	204	133	120
F_{2t}	N/A	300	64	101
F_{1c}	N/A	253	136	225
F_{2c}	N/A	312	76	113

4-point bending tests were performed on the pultruded triangular sections. The loading fixture at the Georgia Institute of Technology laboratory allowed measurement of vertical, horizontal, and rotational displacements of the triangles during loading, as illustrated in Figure 12.

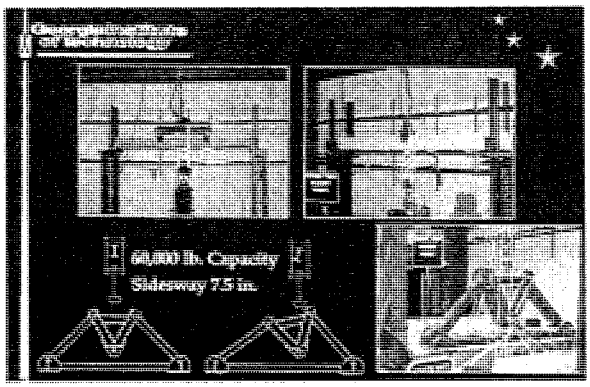

Figure 12. Sidesway Capable 4-Point Bend Fixture

[5] Tension test to failure were not performed due to load cell limitations with the thick top sheet

Rotation and out-of-plane distortion is an indication of material and dimensional non-uniformity. The braided/pultruded triangles show minimal lateral displacement and rotation as shown in Figure 13. Figure 14 reports the apparent flexural modulus for the triangle element bending tests. Two braided and pultruded fabrics were evaluated, Beam A had an areal weight of 4746.6 gms and Beam B had a weight of 5187.4 gms. The braid for Beam B was carried into production and coupon test data was reported previously in Table 4.

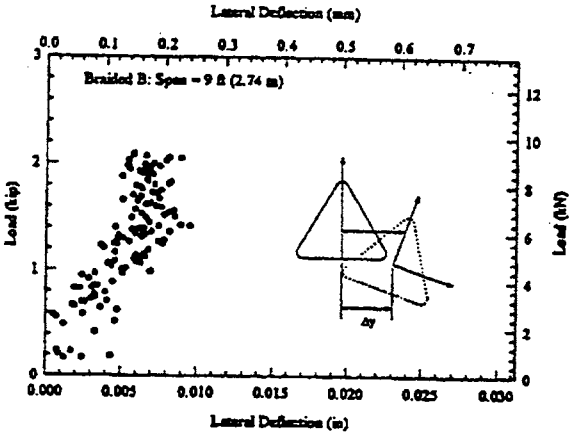

(a)

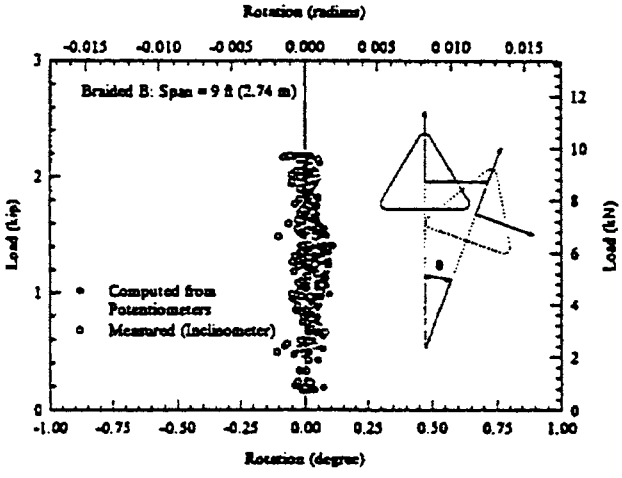

(b)

Figure 13. Lateral Displacement and Rotation during Triangle Bending Tests

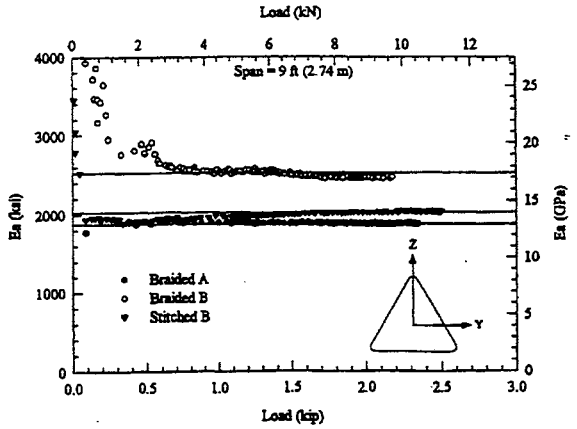

Figure 14. Apparent Flexural Moduli for Triangular Beams

Following the completion of coupon and single triangle tests, the response to loading on truss assemblies was investigated. Three, five, and seventeen cell trusses were tested in bending and shear.

The first assembly test was conducted without the top and bottom plates to determine bond quality and truss rigidity in bending. A 2.29meter (7.5 ft) span, three cell truss was tested in 3-point bending with results as shown in Figure 15.

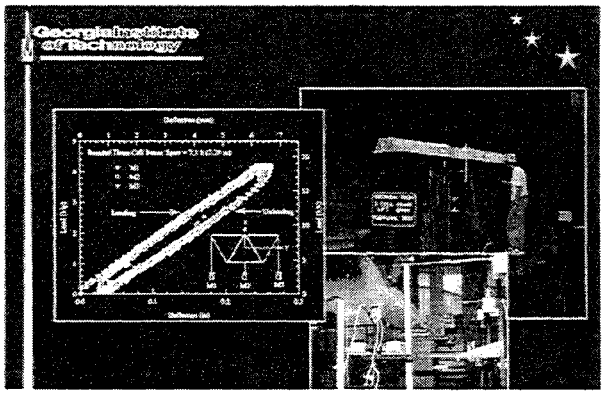

Figure 15. 3-Cell Beam Bending Test

A patch load test, Figures 16 and 17, was performed on a three-cell assembly with top and bottom plates. Loading was applied on the truss apex distributing 7.75 MPa (1,125 psi) over an area of 413 sq. cm. (64 sq. in.). The failure load of 320 kN (73 kips) corresponded to a local pressure of 786 MPa (1,140 psi).

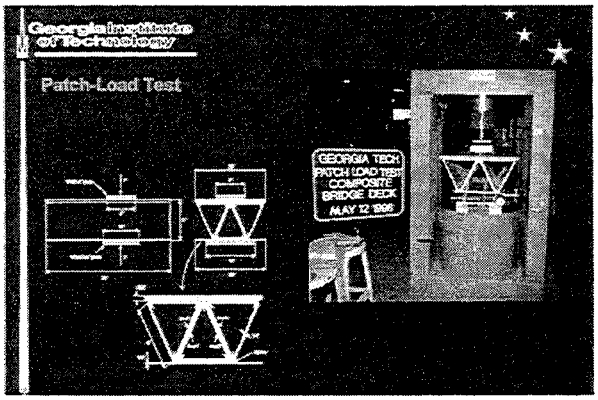

Figure 16. Patch Load Test Set-up

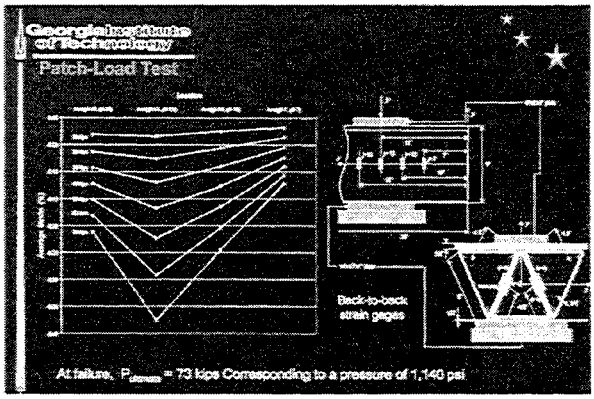

Figure 17. Patch Load Results

A one meter wide by seventeen cell truss was tested in 3-point bending, as shown in Figure 18, to determine how well load was transferred across the span though the web sections. Unidirectional fiber top and bottom plates of equal thickness were used instead of the optimized plates in order to remove that experimental variable. The strain results, plotted in the figure, show identical values from gages on either side of the span, indicating efficient truss action.

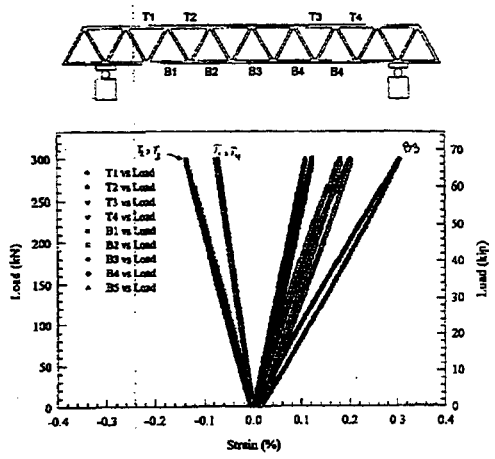

Figure 18. Truss Beam Test Results

A five-cell assembly was tested in three point bending over a 3 meter span. The deck section loaded to failure without cracking or load drop off until the bottom plate failed in tension at 425 kN, as shown in Figure 19. No debonding was observed between the deck components.

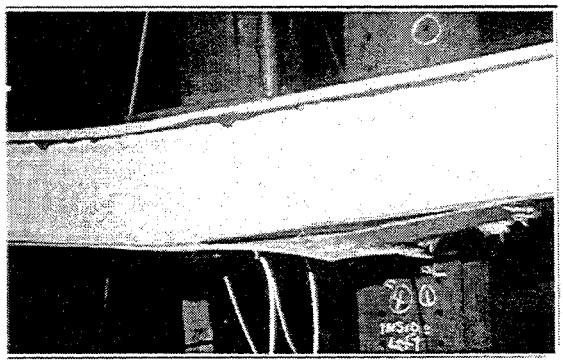

Figure 19. Tension Failure of 5-Cell Assembly

Loads versus deflection results are plotted in Figure 20. The waviness seen in the curves is due to problems with the loading piston. The 7 cm deflection at failure was slightly higher than anticipated. Using flexural moduli backed out from the test results, the original analysis using the tank track loads would result in a deflection higher than the design goal. As a result, the bottom plate thickness was increased by 0.48 cm and a higher percentage of fibers were oriented in the traffic direction. The data in Table 3 reflects this change.

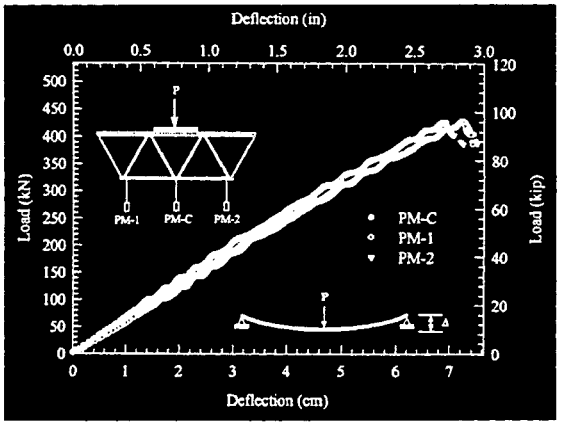

(a)

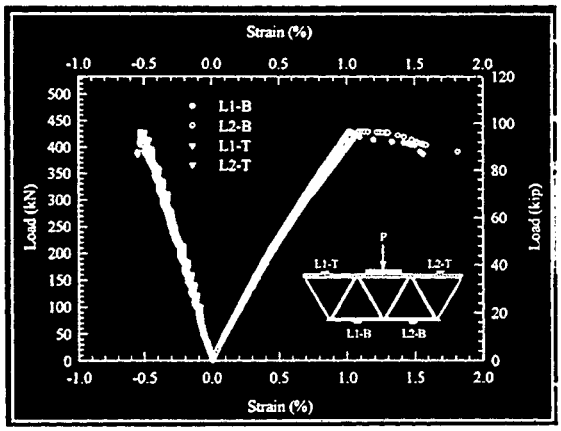

(b)

Figure 20. 5-Cell Beam Bending Test Results -- (a) Load versus Deflection; (b) Strain versus Deflection

Full-scale test sections were fabricated in 3 and 6-meter widths (traffic direction) by 3 meters long. The 3 by 3 panels were tested in simply supported plate bending. Load was applied up to 635 kN (140 kips) without failure. Measured deflection was 1.78 cm (0.7 in.) accounting for deflection of the elastomeric bearing pads. At a service loading of 180 kN (40 kips) the expected plate deflection is 0.5 cm (0.2 in.), well within the design goal. Test results are shown in Figure 21. The full-scale sections had a measured weight of 97 kilograms per square meter (20 pounds per square foot) without the sand epoxy wear surface.

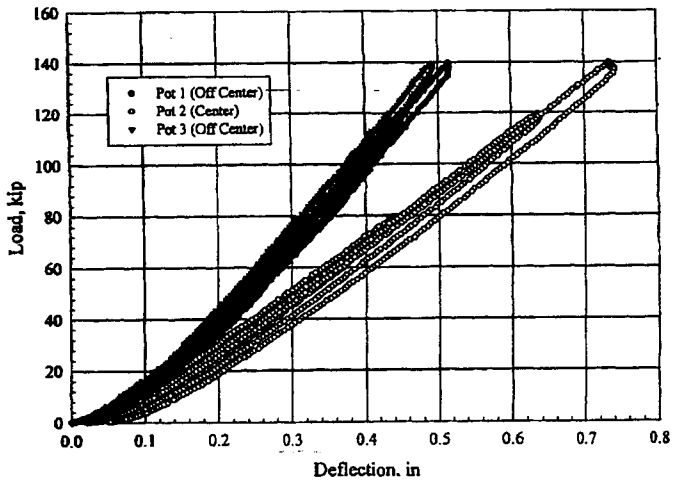

(a)

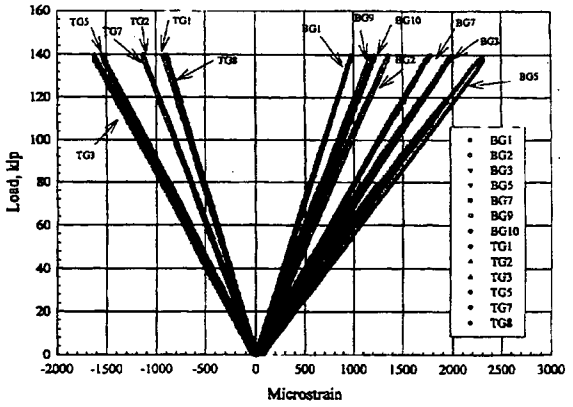

(b)

Figure 21. 3 Meter by 3 Meter Plate Bending -- (a) Load versus Deflection; (b) Strain versus Deflection

6. CONCLUSIONS

The conduct of the program demonstrates the benefits of guiding the design and fabrication effort by analysis and test. Comparison of test data to predictions, during all phases of the program, resulted in improved design and manufacturing approaches.

Truss elements are fabricated using a single, thick ply of 3D-braided fiberglass textile drawn through a die while being impregnated and rigidized with vinylester resin. The triangular pultrusions are bonded together with top and bottom faceplates, using Plexus adhesive, to form the deck modules. Fiber balance in the plates is oriented along the long (pultrusion) axis of the triangle elements. Fiber balance in the pultruted triangles is oriented perpendicular to the pultrusion axis.

This product form is unusual for pultrusion because the majority of the 2,000 fibers in the preform are oriented over 65 degrees from the direction of pull. This results in a product with balanced strength and stiffness in all directions. Through the thickness fibers eliminate ply debonding at the sharp corners and provide sufficient strength to allow pultrusion of the thick, multi-directional textile. The fabrication process is continuous and automated, which assures uniform fiber placement.

A significant difference between the design of the optimized truss and other FRP decking structures is that the truss deck is designed to carry plate loads with only edge support. This is a consequence of the military causeway requirement for attachment to a 3 meter by 9.15 meter (10 ft. by 30 ft.) space frame, as illustrated in Figure 2. The demonstrated minimum 3 meter stringer spacing minimizes dead weight through the elimination of supporting beams and simplifies installation.

The Georgia Institute of Technology, School of Civil Engineering, designed the truss configuration and tested the deck materials and structure. The Virginia Department of Transportation (VDOT) will conduct a durability demonstration of the composite deck at a site on Interstate 81 near Roanoke, Virginia.

The test site is an excavated section of pavement adjacent to a "weigh in motion" scales. Traffic will consist solely of tractor-trailers moving at approximately 40 mph. Two 3 meter by 6 meter (10 ft. by 20 ft.) deck sections will be edge supported by concrete foundations over the 6 meter wide excavation. The deck is instrumented with fiber optic strain gages built into the top and bottom plates and at the truss to plate bond. Strain versus traffic loads (weight and speed) will be recorded. Durability results will validate the deck for military traffic and are completely applicable to civilian bridge decking applications.

Acknowledgement: Design and test of the causeway deck was funded by the Defense Advanced Research Projects Administration administered by the Mobile Offshore Base Project Office at the Office of Naval Research. The Contract is managed by Dr. Jo Wen Lin, Code 5040, Naval Surface Weapons Center, Carderock.

REFERENCES

[1] *Trilateral Design and Test Code for Military Bridging and Gap Crossing Equipment*, US Army Tank Automotive & Armaments Command, AMSTA-TR-R(MS-21), Warren, MI, (1966).

[2] *Circular of Requirements for New Construction Strategic Sealift Ships*, Naval Sea Systems Command, CSP/S-24, (1992).

[3] A. Zureick, "Fiber-Reinforced Polymeric Bridge Decks", *The National Seminar on Advanced Composite Bridges, FHWA, (1997).*

[4] R. Brown, "Automatic Through-the-Thickness® Braiding", *37th International SAMPE Symposium and Exhibition, 37, 832, (1992).*

PROCEEDINGS OF THE THIRD INTERNATIONAL WORKSHOP ON VERY LARGE FLOATING STRUCTURES
(VLFS '99), VOL. I, EDS. R.C. ERTEKIN & J.W. KIM, 22-24 SEPTEMBER 1999, HONOLULU, HAWAII, USA

Non-Linear Time-Domain Structural Finite Element Analysis of a Mobile Offshore Base Using Distributed Hydrodynamic Loads

David Raj and Michael J. Edwards
McDermott Technology Inc.*

ABSTRACT

Current methods for predicting the response of large offshore structures utilize linear hydrodynamic theory and linear structural response analysis methods. The analysis is typically performed in the frequency-domain, precluding the use of highly non-linear structural members (e.g. advanced MOB connector designs). In order to design with and take advantage of such members, a time domain approach is required. This paper discusses a methodology that has been developed for utilizing the frequency domain hydrodynamic results (diffraction and radiation forces) from a linear hydrodynamics code, such as HIPAN, and applying them to an ABAQUS non-linear finite-element structural model in the time domain. The finite element model is a shell model, with the hydrodynamic forces treated as external loads and applied as distributed pressures. These pressures are applied using a user element within ABAQUS. The effect of hydro-elasticity is included. To demonstrate the approach, this methodology is applied to a simple cylinder model and then to a more complex MOB model.

1. INTRODUCTION

The Mobile Offshore Base (MOB) is a large floating structure consisting of multiple connected semi-submersible units. The connector systems being considered vary from simple hinges to more sophisticated non-linear connector systems. State-of-the-art methods to predict hydrodynamic hull loads and the resulting structural response employ frequency domain, three-dimensional, linear hydrodynamic theory. Hull structural analysis is accomplished by applying the hydrodynamic results to a structural model (typically FEA), still in the frequency domain. These methods have proven to be powerful tools for the prediction of ship responses under a wide range of conditions. However, only linear hydrodynamics and linear structural response can be treated in the frequency domain, precluding consideration of non-linear structural effects such as plasticity or energy absorption through inelastic members. In order to design with and take advantage of non-linear structural members (e.g. advanced MOB connector designs), a time domain approach is required.

Finite element methods for solving non-linear structural problems in the time-domain are mature and codes such as ABAQUS [1] are routinely used for solving these problems. In addition, the assumption of linear hydrodynamics for calculating diffraction loads is generally accepted to be valid for large structures. Since, a fully coupled non-linear hydrodynamics/ structural analysis code that can be used routinely for design is currently in the research phase and very computationally intensive, the coupling of a linear hydrodynamic code with a non-linear structural analysis code is desirable. In the following, we discuss a methodology that has been developed for utilizing the frequency domain hydrodynamic results (diffraction and radiation forces) from a linear hydrodynamics code, such as HIPAN [2], and applying them to an ABAQUS non-linear finite-element structural model in the time domain. The finite element model is a shell model, with hydrodynamic forces applied as distributed pressures, so that the structural model is loaded exactly. The effect of hydro-elasticity is included by using

* 1562 Beeson Street, Alliance, OH 44601, U.S.A.
eMail: david.raj@mcdermott.com
mike.j.edwards@mcdermott.com

generalized modes of the structure to evaluate the radiation forces. The radiation forces are obtained from the convolution integral of the impulse response function with the modal velocities. These forces are treated as external forces (pressures) and are applied to the structure. The diffraction forces are directly applied as pressures on the structures. A dynamic analysis of the non-linear structure subjected to the hydrodynamic wave forces is performed using ABAQUS. At each time step, the deformed shape of the structure is decomposed into its modal contributions and the appropriate loads applied to the model. The problem is then iteratively solved at each time step, since the radiation forces depend on the current deformation of the body.

An assumption inherent in this method is that the hydrodynamic loads on the structure can be accurately predicted using linear hydrodynamics. All other effects such as structural non-linearities, frequency dependent added mass and radiation damping, and hydro-elasticity are accurately modeled. Loads and stresses are calculated during the motion analysis, eliminating the need for additional stress analyses. This methodology is demonstrated on a cylinder model. Results of the analysis are presented here. Work on applying this methodology to a MOB is currently in progress.

2. METHODOLOGY

The methodology assumes linear, frequency-domain hydrodynamics (including hydro-elasticity) and employs non-linear, time-domain structural analysis. HIPAN's generalized modes solution technique is used to determine the diffraction forces (pressures) and the hydrodynamic coefficients (added mass and radiation damping) for the MOB. Diffraction forces are calculated for a range of periods and headings that cover the sea state of interest. The hydrodynamic coefficients are calculated over a large range of periods, to properly characterize the impulse response functions. However, in order to minimize the number of impulse response functions, the radiation forces are calculated as modal quantities and distributed over the wetted surface as pressures. The diffraction forces are known apriori, and thus the structural analysis time-domain diffraction loading is directly applied. However, the radiation forces depend on the structural response of the MOB and must be coupled with the time-domain responses. The finite element program ABAQUS is used to calculate the time-domain structural response of the MOB. Since the radiation forces for a MOB depend on the instantaneous response, they are calculated within ABAQUS, using a general-purpose user-defined element (ABAQUS user written subroutine UEL). This calculation is based on the motion history and the impulse response functions derived from the HIPAN radiation solution.

The analysis procedure used by MOB-HyLoads has three basic steps:

1. Calculate the hydrodynamic loads (diffraction forces and hydrodynamic coefficients) of the MOB using HIPAN's generalized modes solution.
2. Use MOB-HyLoads to map frequency-domain hydrodynamic loads to time-domain structural loads. The hydrodynamic diffraction results are scaled with spreading and spectrum functions to create a diffraction load time history. The radiation damping coefficients are used to calculate the impulse response functions.
3. Perform the structural analysis using the ABAQUS UEL subroutine to apply the hydrodynamic loads.

2.1 Hydrodynamic Analysis

The hydrodynamic analysis is performed using the generalized modes option of HIPAN. In this option, the user provides the mode shapes of the generalized modes to be included in the analysis. These modes are in addition to the 6 rigid body modes that the program automatically includes in the analysis. A convergence study is performed to determine the analysis refinement required to obtain a desired accuracy. Next, the periods and headings for the analysis are selected. The periods and headings selected for the analysis should cover the ranges required for the diffraction and radiation solutions. The HIPAN results of interest are the diffraction forces (pressures) and the hydrodynamic coefficients. For each period and heading, there are N diffraction forces, where N is the total number of modes (rigid body + generalized modes) used in the analysis. In addition, there are NxN added mass and radiation damping terms for each analysis period. A separate HIPAN run is required to obtain the NxN infinite frequency added mass coefficients.

2.2 MOB-HyLoads execution

MOB-HyLoads reads the HIPAN diffraction forces (pressures) and hydrodynamic coefficients and stores the results in a random access database. The diffraction pressures are needed at specific integration point locations of the structural finite element model. Since, HIPAN does not provide these pressures directly, a special utility, HIP2FEA, developed by AeroHydro is used to extract this information from the HIPAN results [3]. Then, after the sea state is defined (wave spectrum and spreading), MOB-HyLoads scales the diffraction pressures based on the wave spectrum and spreading and uses random phases to generate diffraction force time histories. The radiation damping results are used

to generate the NxN impulse response functions. The diffraction pressures, infinite frequency added mass and the impulse response functions (IRF) are provided to the ABAQUS UEL subroutine for the calculation of the diffraction and radiation pressures at each time step.

2.3 Structural Analysis

MTI has developed an ABAQUS user written element (UEL subroutine) which is used to apply the hydrodynamic loads. The user element is a four-node, fully integrated element, shown in Figure 1. This element only applies forces to the nodes. It has no stiffness. These elements are applied on top of the structural elements of the wetted surface, sharing the same nodes. The structural elements model the mass and stiffness, while the user elements apply the hydrodynamic forces.

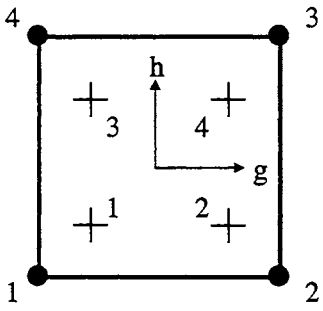

Figure 1 Hydrodynamic Loading Element

The hydrodynamic results from HIPAN are diffraction forces (pressures) and hydrodynamic coefficients as a function of frequency and heading. This data is used by the ABAQUS user subroutine to apply the motion dependent hydrodynamic forces. The time domain equations of motion being solved by ABAQUS are:

$$[M]\{\ddot{x}\}+[C]\{\dot{x}\}+[K]\{x\}=\{F\} \quad [1]$$

where the forcing function, {F} is:

$$\underset{\text{Forcing Function}}{\{F\}} = \underset{\text{Diffraction}}{\{F_D\}} + \underset{\text{Radiation}}{\{F_R\}} \quad [2]$$

The radiation force $\{F_R\}$ depends on the instantaneous displacement of the structure and, hence, has to be calculated iteratively until a converged solution is obtained.

The hydrodynamic loading element applies the forcing function to the ABAQUS model. The diffraction forces are calculated on a local basis, using HIPAN diffraction forces scaled by spreading and spectrum functions. The radiation forces (added mass and radiation damping effects) are calculated on a modal basis and then distributed over the surface. The execution procedure of this ABAQUS UEL is outlined below:

1. Start of analysis
   a. Read & initialize the hydrodynamic data.
2. Start of time step (increment)
   a. Predict modal acceleration & velocities based on previous values
   b. Calculate modal radiation force – added mass & radiation damping effect
   c. Calculate local pressures
      i. Diffraction pressure
      ii. Distribute modal radiation forces
   d. Calculate nodal forces from local pressures
3. Iterations during time step
   a. Apply nodal forces
   b. Update local accelerations & velocities
4. End of time step (increment)
   a. Calculate modal acceleration & velocities, based on local accelerations & velocities

2.3.1 Start of Analysis

Input to this subroutine is supplied by MOB-HyLoads in the form of diffraction pressure time histories, impulse response functions, and model constants (mode shapes and surface normals). This data is read by the UEL at the beginning of the analysis.

2.3.2 Start of Time Step

At the beginning of each time step the ABAQUS UEL calculates the diffraction and radiation forces to apply to the nodes of the hydrodynamic loading elements for this time increment.

The modal acceleration, A, is taken from the end of the previous time step, while the modal velocity at the present time, V, is calculated as:

$$V = A\,dt + V_0 \quad [3]$$

where: V_0 = Previous modal velocity
dt = Current time step

Modal Force Calculations

The radiation forces (added mass and damping effects) are calculated on a modal basis. These forces are subsequently distributed over the wetted surface area as pressures. The radiation force for mode "i" is

obtained from the infinite frequency added mass and impulse response functions as follows:

$$(F_R)_i = -\sum_{j=1}^{N}\left[\{m(\infty)\}_{ij}\,\ddot{x}_j + \int_0^t K_{ij}(t-\tau)\,\dot{x}_j(\tau)\,d\tau\right] \quad [4]$$

where :

i = 1, 2, 3, ..., N
$m(\infty)_{ij}$ = infinite frequency added mass of mode "i" due to acceleration of mode "j"
x_j = displacement for mode "j"
$K_{ij}(t)$ = wave portion of impulse response function

The impulse response functions are calculated from the radiation damping coefficients b(ω) as follows:

$$K_{ij}(t) = \frac{2}{\pi}\int_o^\infty b_{ij}(\omega)\,\mathrm{Cos}\,\omega t\,d\omega \quad [5]$$

Local Pressure Calculations

The diffraction force, F_D, and the radiation force, F_R, are applied to the hydrodynamic loading elements at the integration points, see Figure 1.

The diffraction force at each integration point is known apriori from the HIPAN diffraction solution for the different wave periods and wave headings. A sea state is then simulated by scaling these forces with wave spectrum and spreading functions, where the contributions from the different wave periods and headings are added with random phases.

The modal radiation forces, F_R, are distributed to the hydrodynamic loading elements as pressures. The normal component of this pressure, $p_N(x)$, is assumed to be a linear combination of the mode shapes:

$$p_N(x) = a_n\varphi_n \quad [6]$$

where:

a_n = modal pressure factor
ϕ_n = mode shape

Multiplying by the mode shape and integrating over the surface:

$$\int_S p_N(x)\,\varphi_i(x)\,ds = \int_S a_n\varphi_n(x)\,\varphi_i(x)\,ds \quad [7]$$

Note that the first term is the definition of the modal force, F_i:

$$F_i = \int_S p_N(x)\,\varphi_i(x)\,ds \quad [8]$$

Defining:

$$\alpha_{ni} = \int_S \varphi_n(x)\,\varphi_i(x)\,ds \quad [9]$$

Equation [7] can then be written as:

$$F_i = \alpha_{ni}a_n \quad [10]$$

Solving for a_n and substituting into equation [6] we obtain the normal pressure as a function of modal force:

$$p_N(x) = \alpha_{ni}^{-1}\varphi_n F_i \quad [11]$$

Nodal Forces

The element forces within the ABAQUS UEL are distributed to the nodes as forces. The isoparametric interpolation function used by the four-node hydrodynamic loading element, shown in Figure 1, follows:

$$u = \begin{Bmatrix} \frac{1}{4}(1-g)(1-h)\,u_1 + \\ \frac{1}{4}(1+g)(1-h)\,u_2 + \\ \frac{1}{4}(1+g)(1+h)\,u_3 + \\ \frac{1}{4}(1-g)(1+h)\,u_4 \end{Bmatrix} \quad [12]$$

2.3.3 Iterations During Time Step

The nodal forces calculated at the beginning of the time step are applied as external forces. These forces are held constant throughout the step.

The acceleration and velocity normal to the element surface is calculated for each integration point. These values are interpolated from the nodal quantities using the element shape functions and are updated each iteration.

2.3.4 End of Time Step

The local surface normal accelerations and velocities are used to calculate the modal accelerations and velocities at the end of each time step. The methodology used to calculate the modal acceleration follows. A similar technique is used to calculate the modal velocities.

Modal Acceleration

The normal component of the acceleration field, $a_N(x)$, is assumed to be a sum of the modal acceleration times the mode shape:

$$a_N(x) = A_n \varphi_n \qquad [13]$$

where:

A_n = modal acceleration

ϕ_n = mode shape

Multiplying by the mode shape and integrating over the surface:

$$\int_S a_N(x)\,\varphi_i(x)\,ds = \int_S A_n \varphi_n(x)\,\varphi_i(x)\,ds \qquad [14]$$

Defining:

$$\alpha_{ni} = \int_S \varphi_n(x)\,\varphi_i(x)\,ds \qquad [15]$$

Equation [14] can then be written as:

$$\int_S a_N(x)\,\varphi_i(x)\,ds = \alpha_{ni} A_n \qquad [16]$$

Solving for A_n:

$$A_n = \alpha_{ni}^{-1} \int_S a_N(x)\,\varphi_i(x)\,ds \qquad [17]$$

At the end of each time step the modal acceleration, A_n, is calculated from the surface accelerations, $a_N(x)$.

The application of the diffraction and radiation forces (pressures) by the UEL is the unique feature of the structural analysis. The dynamic analysis utilizes ABAQUS' standard DYNAMIC procedure. All the modeling and analysis features supported by ABAQUS are also available for use for the analysis. Component stresses can be calculated and output during the analysis, eliminating the need for performing a separate stress analysis run.

3. SINGLE CYLINDER EXAMPLE

The methodology described in this paper was first applied to a single rigid cylinder to verify that the user element subroutine and the necessary procedures performed as planned. A rigid cylinder of 100m radius and 100m height is floating vertically with a 50m draft. The cylinder is subjected to unidirectional unit amplitude (1m) waves with a 10-second period. The motion of this cylinder was calculated in the time domain using ABAQUS and the UEL subroutine for applying the diffraction and radiation forces. The motions were also calculated in the frequency-domain using HIPAN and the results were then compared.

3.1 Hydrodynamic Analysis

The hydrodynamic analysis for this case consisted of HIPAN analyses performed at 200 periods and a single heading of 0 degrees. Even though the diffraction forces are only needed at a single period (10 seconds), the radiation damping coefficients are needed for a large number of periods so that accurate impulse response functions can be calculated. Since, the cylinder was assumed to be rigid, only the 6 rigid body modes are needed, and no additional generalized modes were defined. The symmetry of the cylinder was exploited by defining only one-quarter of the model. Three patches were used to define the geometry including a patch at the free surface required to remove irregular frequency effects. Convergence studies were performed to optimize the analysis refinement such that accurate results were obtained down to a period of 1 to 2 seconds. This resulted in 540 unknowns for the cylinder. Figure 2 shows the HIPAN model of the cylinder. Only the wetted surface of the cylinder is modeled.

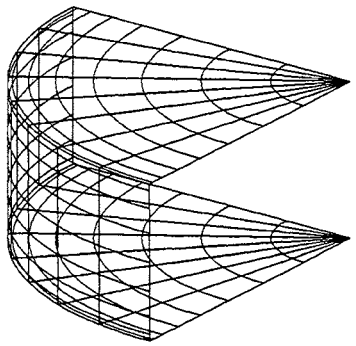

Figure 2 HIPAN Model of Cylinder

3.2 Mob-HyLoads Execution

Prior to executing MOB-HyLoads, a points file containing the x, y, and z-coordinates of all the structural model element integration points must be generated. This points file is then used by the utility HIP2FEA to extract all the diffraction pressures at these locations from the HIPAN pressure output file. MOB-HyLoads then reads all these diffraction pressures and the hydrodynamic coefficients (6x6 per period x 200 periods) into a random access data file. MOB-HyLoads also reads in the infinite frequency added mass from the HIPAN infinite frequency analysis results file. The radiation damping coefficients are used to calculate the impulse response functions (6x6). The impulse

response functions (IRFs) and the infinite frequency added masses are stored in a file and provided to the ABAQUS UEL subroutine during the structural analysis.

3.3 Structural Analysis

The ABAQUS structural model of the cylinder is shown in Figure 3. A total of 360 4-noded shell elements are used to model the full cylinder. The center of gravity (CG) is located at the center of the cylinder. BEAM MPCs (multi-point constraints) are used to connect all the shell nodes to the center of gravity (CG) so as to prevent deformation of the cylinder. Hydrostatic pressure is applied to the 180 wetted elements (lower half of the cylinder) so that we can correctly account for the hydrostatic forces. Soft springs are applied in the surge, sway and yaw directions (using an ABAQUS JOINT element) to prevent the model from "drifting" away during the dynamic analysis.

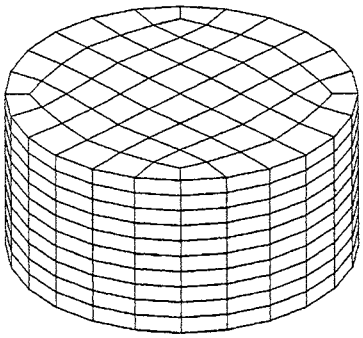

Figure 3 ABAQUS Structural Model of Cylinder

A second set of 4-noded user elements (UEL) is placed on the 180 wetted elements. These UELs are used to apply the diffraction and radiation forces on the model. The UEL subroutine reads the IRF file (which contains the IRFs and the infinite frequency added masses), the diffraction force file (which contains the diffraction forces to be applied), and a surface definition database file (which contains information on the element surface normals). These files are generated by MOB-HyLoads. When non-rigid body modes are included, MOB-HyLoads also reads the mode shape file (used to define the generalized modes for the HIPAN analysis; this file was not used for the cylinder example since there were no additional generalized modes).

The DYNAMIC procedure of ABAQUS was used to calculate the cylinder motion as a function of time when subjected to unidirectional 10-second waves of unit amplitude. The wave forces are ramped up over a 500-second period to prevent impulsive loading on the structure. The CG displacements of the cylinder were saved at each time step.

3.4 Comparison of Results

The problem of a cylinder with soft springs is a linear problem and, hence, HIPAN can be used to predict the cylinder motion. Since, the ABAQUS solution utilizes the HIPAN hydrodynamic results, both HIPAN and ABAQUS should give exactly the same results. Any errors in the theoretical formulations, the UEL subroutine coding and in MOB-HyLoads will result in poor comparison between the two results. The HIPAN RAO results are compared to the ABAQUS results in Table 1. In the table, the ABAQUS results are for the case where the radiation forces are applied over the wetted surface using the UEL subroutine. The diffraction forces, however, were applied directly to the CG and not distributed over the wetted surface (because of compatibility issues between HIP2FEA and the version of HIPAN used for this analysis, which are currently being resolved). Table 1 shows excellent agreement between the results obtained using HIPAN and ABAQUS. The good agreement confirms the validity of the methodology and procedures used to analyze a structure in the time-domain using distributed hydrodynamic loads that are obtained from a linear frequency-domain hydrodynamic code (HIPAN).

Table 1 Comparison of ABAQUS and HIPAN Results

	ABAQUS	HIPAN
Surge (m/m)	8.33E-02	8.37E-02
Sway (m/m)	3.62E-08	0.00E+00
Heave (m/m)	8.21E-03	8.24E-03
Roll (rad/m)	4.36E-08	0.00E+00
Pitch (rad/m)	1.20E-04	1.21E-04
Yaw (rad/m)	4.90E-11	0.00E+00

4. APPLICATION TO MOB

The methodology is next applied to a more complex structure, a preliminary McDermott MOB design, shown in Figure 4, that consists of 5 SBUs connected using hinge connectors. These connectors only allow relative pitch motions between the SBUs. For this example, each SBU is assumed to be flexible.

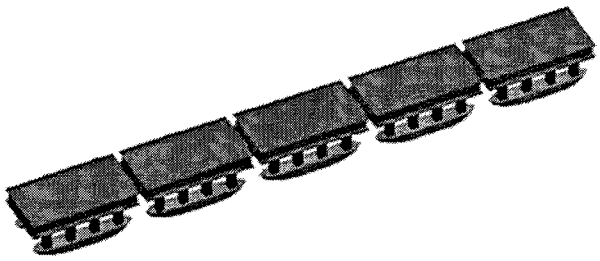

Figure 4 McDermott 5-SBU MOB Design

4.1 Hydrodynamic Analysis

The hydrodynamic models required for HIPAN consist of the definition of the surface geometries of the wetted surfaces of the MOB. The wetted surfaces are divided into large patches, and each patch is defined as a B-spline surface. The program MultiSurf [4] was used to generate the B-spline surfaces for the MOB. The HIPAN geometry model of the MOB is shown in Figure 5. A total of 310 (62 patches/SBU x 5 SBUs) patches were used to define the wetted surface. Convergence studies were performed on a single SBU to optimize the analysis refinement so that accurate results are obtained down to a period of 1 to 2 seconds. This resulted in 1960 unknowns for each SBU or a total of 9800 unknowns for the MOB.

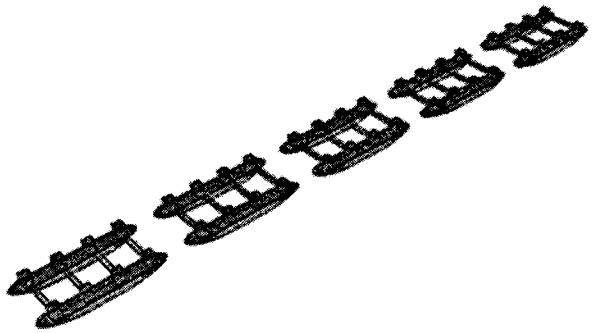

Figure 5 HIPAN Model of 5-SBU MOB

The flexibility of the MOB required that the generalized option of HIPAN be used for the hydrodynamic analysis. The first four modes are the rigid body hinge modes as shown in Figure 6. These modes can be easily defined analytically. The flexural modes are more complex and ABAQUS was used to calculate these mode shapes. Hence, for this case, the structural model had to be built before the hydrodynamic analysis could proceed. The structural model developed for the structural analysis was also used to calculate the mode shapes. A total of 10 flexural modes were calculated. Figures 7 to 9 show the first three of the 10 flexural modes. It should be noted that the mode shapes calculated are the dry modes. Ideally, the wet modes are desired, since fewer wet modes are required to define an arbitrary deformed shape of the body. However, the dry modes are not significantly different from the wet modes and can be used. In cases where the dry and wet mode shapes are very different, convergence can be achieved by increasing the number of dry modes selected.

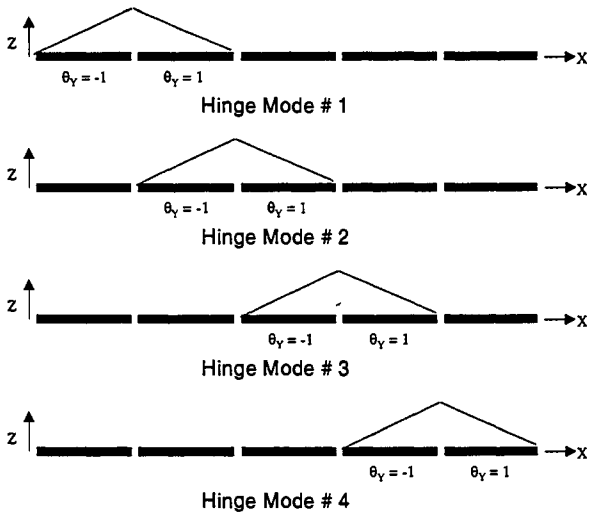

Figure 6 Four Hinge Modes of the MOB

Figure 7 Mode #1 of 5-SBU MOB (1st Torsion Mode)

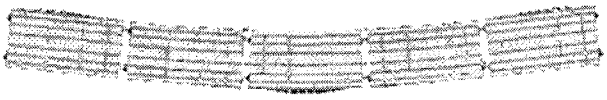

Figure 8 Mode #2 of 5-SBU MOB (1st Bending Mode)

Figure 9 Mode #3 of 5-SBU MOB (2nd Torsion Mode)

The generalized modes option of HIPAN was used to calculate the diffraction forces (pressures) and hydrodynamic coefficients for the 20 modes (6 rigid body + 4 hinge + 10 flexural). These calculations were performed at 50 periods and 5 headings with the option of increasing the number of periods if it was found that the resulting impulse response functions did not produce accurate results.

4.2 Mob-HyLoads Execution

After the HIPAN analyses are completed, the first step prior to executing MOB-HyLoads is to create a points file. The points file contains the coordinates of

all the integration points of all the wetted structural shell elements. HIP2FEA uses the points file to extract the diffraction pressures at these points from the HIPAN pressure output file. MOB-HyLoads then reads the diffraction pressures and hydrodynamic coefficients and stores them in a random access database. Once the sea state is defined, MOB-HyLoads scales the unit amplitude pressure results in the database using the wave spectrum and spreading function and combines the pressures with random phases to generate the pressure time histories. This information is stored in a file and provided to the UEL subroutine. The radiation damping coefficients are used to calculate the impulse response functions (20x20). The impulse response functions along with the infinite frequency added masses are stored in a separate file and also provided to the ABAQUS UEL subroutine during the structural analysis.

Two other files are needed by the UEL. The mode shape file used for the generalized mode HIPAN analysis (this should include the rigid body modes also) and a surface definition database file. The surface definition database file is a file containing information on the structural shell elements including the surface normals. This database file is created by MOB-HyLoads. Only the surface normals of the wetted shell elements are used by the UEL subroutine.

4.3 Structural Analysis

The structural model of the 5-SBU MOB is shown in Figure 10. The only requirement of the model is that the wetted surfaces (and other surfaces where pressure loads are applied) be covered with shell elements so that pressure loads can be applied.

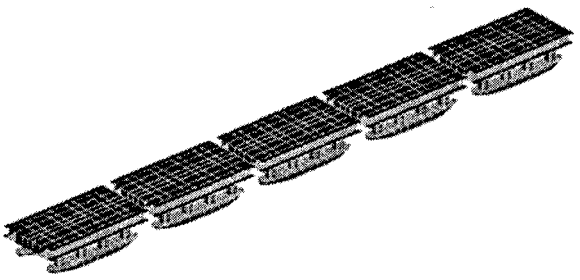

Figure 10 ABAQUS Structural Model of 5-SBU MOB

Since the run times are expected to be long, it is desirable to use as few elements as possible. To that end, a significant effort was expended to minimize the number of elements but maintain the same mass, stiffness characteristics as the MOB. This was achieved by starting with a very detailed model of a SBU and determining the mass and stiffness characteristics of the various sub-components. The natural frequencies and mode shapes were also calculated. The properties of a coarser model were then adjusted such that its components had the same mass and stiffness as those of the detailed model. In addition, the natural frequencies were also matched to within 10 percent. This resulted in a "coarse" model of a SBU having approximately 1000 elements while the 5-SBU MOB has approximately 5000 elements.

5. CONCLUSIONS

The structural analysis of the MOB has not been completed at the time of the writing of this paper. The UEL subroutine has been verified using the cylinder model, and the methodology is expected to work for the hinged MOB. The results of this analysis will be compared with the response predicted by HIPAN. Good agreement is expected since the model is linear. The final step is to repeat the analyses after replacing the hinge connectors with non-linear connectors, more typical of the latest McDermott MOB design.

REFERENCES

[1] Lee, C.H. and Newman, J.N., HIPAN 2.0.2 User's Manual, "A Radiation-Diffraction Panel Program for Wave-Body Interactions", Massachusetts Institute of Technology, 1998.

[2] Hibbitt, Karlsson & Sorensen, Inc., ABAQUS User's Manual Version 5.8, Hibbitt, Karlsson & Sorensen, Inc., 1998

[3] Letcher, J. S., "HIP2FEA, XYZ2NUV User Documentation," AeroHydro, Inc., April 15, 1998.

[4] MultiSurf, General Reference Version 4.0, AeroHydro Inc., December 1998.

Acknowledgment: This material is based on work supported by the U.S. Office of Naval Research's MOB Program, ONR Contract N00014-97-C-0410, "Design Technologies for Mobile Offshore Base".

PROCEEDINGS OF THE THIRD INTERNATIONAL WORKSHOP ON VERY LARGE FLOATING STRUCTURES
(VLFS '99), VOL. I, EDS. R.C. ERTEKIN & J.W. KIM, 22-24 SEPTEMBER 1999, HONOLULU, HAWAII, USA

Application of the Large Amplitude Motion Program (LAMP) for Design and Operation of A Mobile Offshore Base (MOB)

Kenneth Weems, Woei-Min Lin, Sheguang Zhang, and Thomas Treakle
Ship Technology Division, Science Applications International Corporation*

ABSTRACT

The Large Amplitude Motion Program (LAMP) is a physics-based seakeeping and wave load program that is currently being used for design and operation studies of the Mobile Offshore Base (MOB). LAMP solves the three-dimensional time-domain nonlinear motion and load problems using a potential-flow boundary-element method including body-nonlinear effects and a linear or nonlinear solution of the local free surface. Under the MOB Program, LAMP has been used to compute detailed local free surface elevations for air-gap evaluation and for predictions of motions and loads for a MOB geometry in both operating and transient conditions. A description of the LAMP system, computational results for a candidate MOB geometry including of nonlinear effects, and a discussion of other application areas for the LAMP code to very large floating structures are presented.

1 INTRODUCTION

The feasibility of using a Mobile Offshore Base (MOB) for military purposes has been intensively studied in recent years. A MOB consists of multiple modules and can be as long as 2 kilometer in operating condition. Because of its enormous size and unique mission requirements, there are design considerations that may be very different from conventional floating platforms. One important design consideration for a MOB is the air gap between the wave surface and the upper deck. The prediction of air gap involves several components including the incident waves, the diffraction waves, the radiation waves, and the motion of the upper deck itself. Other important design considerations include nonlinear motions and nonlinear wave loads for a MOB in both operating and transit conditions. The motions and loads in transit conditions are especially tricky, because the MOB is floating very close to the top of the pontoons and nonlinear effects may be prominent. This paper documents the effort to apply the LAMP code to these design issues.

2 THE LAMP SYSTEM

The LAMP (Large Amplitude Motion Program) System has been under development as a multi-level physics-based time-domain simulation system for the prediction of motions, loads, and structural response for ships operating in extreme wave conditions. As shown in Figure 1, the LAMP System consists of three closely integrated modules. The first module is for the calculation of ship motions and wave-frequency loads. The second module is for the slamming impact computation. The third module is for computing whipping responses using a non-uniform-section dynamic beam method. In addition, the LAMP System includes an interface to provide loading information for finite element analysis [1]. The present study used only the ship motion calculation module, which includes the calculation of body surface pressure distribution, local free surface elevations, and the rigid-body motion and loads.

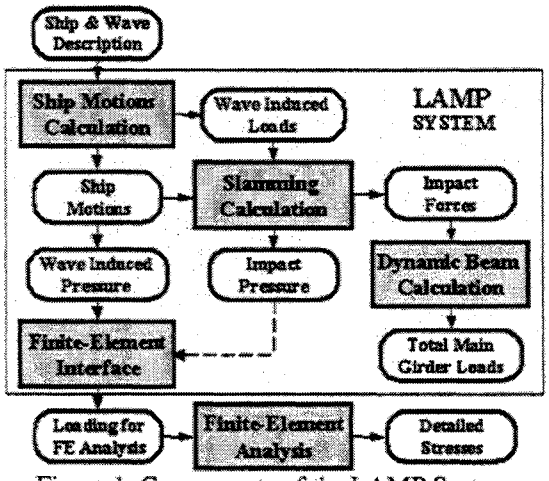

Figure 1: Components of the LAMP System

While developed for ship applications, several features of the LAMP system make it well suited for large floating structures as well. LAMP's numerical model is general, three-dimensional and physics-based. The body-nonlinear and approximate body-nonlinear solution techniques allow significant nonlinear effects

*134 Holiday Ct. Suite 318, Annapolis, MD 21401,USA

of the wave-body problem, which will be of considerable importance in the transit condition, to be modeled. The mixed-source formulation allows complex body geometry to be modeled efficiently. The solution of the 6-DOF equations of motion in the time domain allows arbitrary non-pressure force models, such as mooring or position keeping systems, to be applied. Finally, the explicit solution of the local free surface boundary conditions as part of the body-wave interaction problem allows for the detailed evaluation of local wave field including diffracted and radiated waves and for the implementation of nonlinear free surface boundary conditions.

2.1 Hydrodynamic Calculation

LAMP solves the three-dimensional time-domain nonlinear motion and load problems using a potential-flow boundary-element method. The hydrodynamics problem is solved in the time domain by a 3-D boundary element method using a transient free-surface Green function singularity distribution. A so-called "body-nonlinear" approach is used [2,3,4]. In contrast to the linear approach in which the body boundary condition is satisfied on the portion of the hull under the mean water surface, the body-nonlinear approach satisfies the body boundary condition exactly on the portion of the instantaneous body surface below the incident wave. It is assumed that both the radiation and diffraction waves are small compared to the incident wave so that the free surface boundary conditions can be linearized with respect to the incident wave surface. Note that with this formulation, both the body motions and the incident waves can be large relative to the draft of the ship.

Several variations of Lin and Yue's original "body-nonlinear" approach have been developed and are currently available in the LAMP System. LAMP-4 satisfies the free surface boundary condition on the incident wave surface, provides 3-D large-amplitude hydrodynamics, and calculates nonlinear hydrostatic restoring and Froude-Krylov wave forces. LAMP-2 satisfies the free surface boundary condition on the mean wave surface, provides 3-D linear hydrodynamics, and calculates nonlinear hydrostatic restoring and Froude-Krylov wave forces. LAMP-1 differs from LAMP-2 only in that it calculates linear hydrostatic restoring and Froude-Krylov wave forces.

2.2 Mixed Source Formulation

In Lin and Yue's original formulation, the transient Green functions are distributed over the hull surface. While effective for most conventional ships, this implementation proved to have significant numerical stability problems for severely non-wall-sided ships.

For this reason, a hybrid numerical approach (referred to as the "mixed source formulation" in LAMP) has been implemented [5] which is a combination of the transient Green function (*e.g.* [4]) and the Rankine source (*e.g.* [6]). In the mixed source formulation, the fluid domain is divided into an inner domain (I) and an outer domain (II) by a matching surface S_m, as shown in Figure 2. In the inner domain, Rankine sources are distributed on the entire inner domain boundary S_I, including the body surface S_b, the local free surface S_f, and the matching surface S_m. The outer domain boundary S_{II} consists of the matching surface S_m, the remaining free surface, and an imaginary surface S_∞ at infinity. In the outer domain, the transient Green function singularities are distributed only on the matching surface S_m because the transient Green function satisfies both the linearized free-surface boundary conditions and the radiation condition.

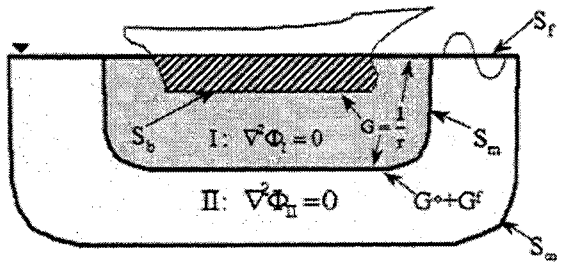

Figure 2: Mixed Source Formulation

In the inner domain, the total disturbance velocity potential Φ_I satisfies Laplace's equation. The nonlinear body boundary condition is satisfied on the wetted body surface S_b under the undisturbed incident wave surface. The linearized free surface boundary conditions are satisfied on the part of the free surface S_f between the body surface and the matching surface. The boundary integral equation in terms of the Rankine source distribution on S_I can be written as

$$2\pi\Phi_I + \int_{S_I} (\Phi_I G_n - \Phi_{In} G) dS = 0 \qquad (1)$$

where $G = 1/|\vec{p} - \vec{q}|$, with $\vec{p}$ and $\vec{q}$ denoting the field point and source point, respectively. The subscript n denotes the directional derivative with respect to the outward normal $\vec{n}$ on the boundary of the inner domain.

In the outer domain, the total disturbance velocity potential Φ_{II} satisfies Laplace's equation and the linearized free surface boundary conditions. With transient Green function distribution on the matching surface, the boundary integral equation can be written as

$$2\pi\Phi_{II} + \int_{S_m} (\Phi_{II} G_n^0 - \Phi_{IIn} G^0) dS = M(\vec{p}, t) \qquad (2)$$

The function $M(\vec{p},t)$ is defined as

$$M(\vec{p},t)=\int_0^t d\tau\{\int_{S_m}\left(\Phi_{II}G_{\vec{n}}^f-\Phi_{IIn}G_\tau^f\right)dS + \frac{1}{g}\int_{\Gamma_m}\left(\Phi_{II}G_{\tau\tau}^f-\Phi_{II}G_\tau^f\right)V_N dL\} \quad (3)$$

where Γ_m is the waterline of the matching surface, V_N is the outward normal velocity of Γ_m relative to domain I, $\vec{N}$ is the unit normal to the waterline on the free surface, t is time, and G^0 and G^f are the infinite frequency and memory function part of the transient Green function [2]. The matching surface S_m is treated as a control surface. This control surface can be stationary in the case of zero or small horizontal body motions, or it can move with the body in cases where the body has horizontal motion. On S_m, the matching conditions are imposed, requiring that the disturbance velocity potentials and their normal derivatives in the inner and outer domains be continuous. These conditions together with the integral equations for Φ_I, Φ_{II} and their normal derivatives form a coupled equation system for the velocity potential Φ_I on S_b, Φ_{In} on S_f, or Φ_I and Φ_{In} on S_m. The solution is obtained at each time step with given Φ_{In} on S_b and Φ_I on S_f. The free surface boundary conditions on S_f are used to update the disturbance velocity potential and the disturbance free surface elevation in time. The time integration is performed using the fourth order Adams-Bashforth-Moulton formula

This numerical solution technique, which was originally developed to avoid stability problems associated with non-wall-sided ships, has several very powerful advantages for MOB assessment. One is that the use of the relatively inexpensive Rankine singularities on the hull surface means that a large number of panels can be used to define complex geometries like the MOB and an accurate, detailed 3-D pressure distribution can be computed. The surface pressure distribution can then be used to develop load sets for structural analysis.

A second advantage of the numerical solution technique is that the direct solution of the local free surface solution allows the local wave disturbance, including diffracted and radiated waves, to be computed as part of the solution. For most solution techniques using complex Green functions in either the time or frequency domain, free surface elevation calculations are often expensive, inaccurate, or both. The direct local solution of the free surface boundary condition also greatly simplifies the implementation of nonlinear free surface boundary conditions.

2.3 Time Domain Motions and Loads

In order to calculate the time-domain six-degree-of-freedom coupled motions for any ship heading and speed, LAMP also includes nonlinear models for non-pressure forces including viscous roll damping, propeller thrust, bilge keels, rudder and anti-rolling fins, etc. For oblique seas cases, a PID (Proportional, Integral, and Derivative) course keeping rudder control algorithm and rudder servo model are implemented. Other non-pressure force models, including models for mooring systems, position keeping thrusters, viscous drift forces, etc., could be added to the LAMP simulation. Because of LAMP's general time-domain approach, these models could include nonlinear dependency on the state variables and active or active control. Once a complete set of hydrodynamic, hydrostatic and non-pressure forces have been computed, the general 6-DOF equations of motions are solved using a 4th order Runge-Kutta or Predictor-Corrector scheme.

In addition to motion simulations, LAMP calculates the time-domain wave-induced global loads, including the vertical and lateral bending and torsional moments and shear forces, at any cross-section along the length of the ship. Furthermore, at each time step, LAMP calculates the relative motion of the ship and the wave as well as the hydrodynamic pressure distribution over the instantaneous wetted hull surface below the incident wave surface. The relative motion information can also be used as input for the impact load calculations. The mapped pressure distribution may then be used to derive input for finite element structural analysis.

2.4 Nonlinear Free Surface Model

The original LAMP development was mainly for accurate prediction of platform motions and wave loads, especially in extreme sea conditions. For this purpose, the original LAMP formulation, in which the free surface solution is linearized about the mean (LAMP-1) or incident wave (LAMP-4) surface, is adequate. However, one of the design concerns for MOB is the "air gap," which is the distance between the wave surface and the bottom of the platform's lower deck. In order to predict the air gap accurately, it is necessary to accurately predict both the motion of the platform and the local wave elevations (including both radiation and diffraction waves).

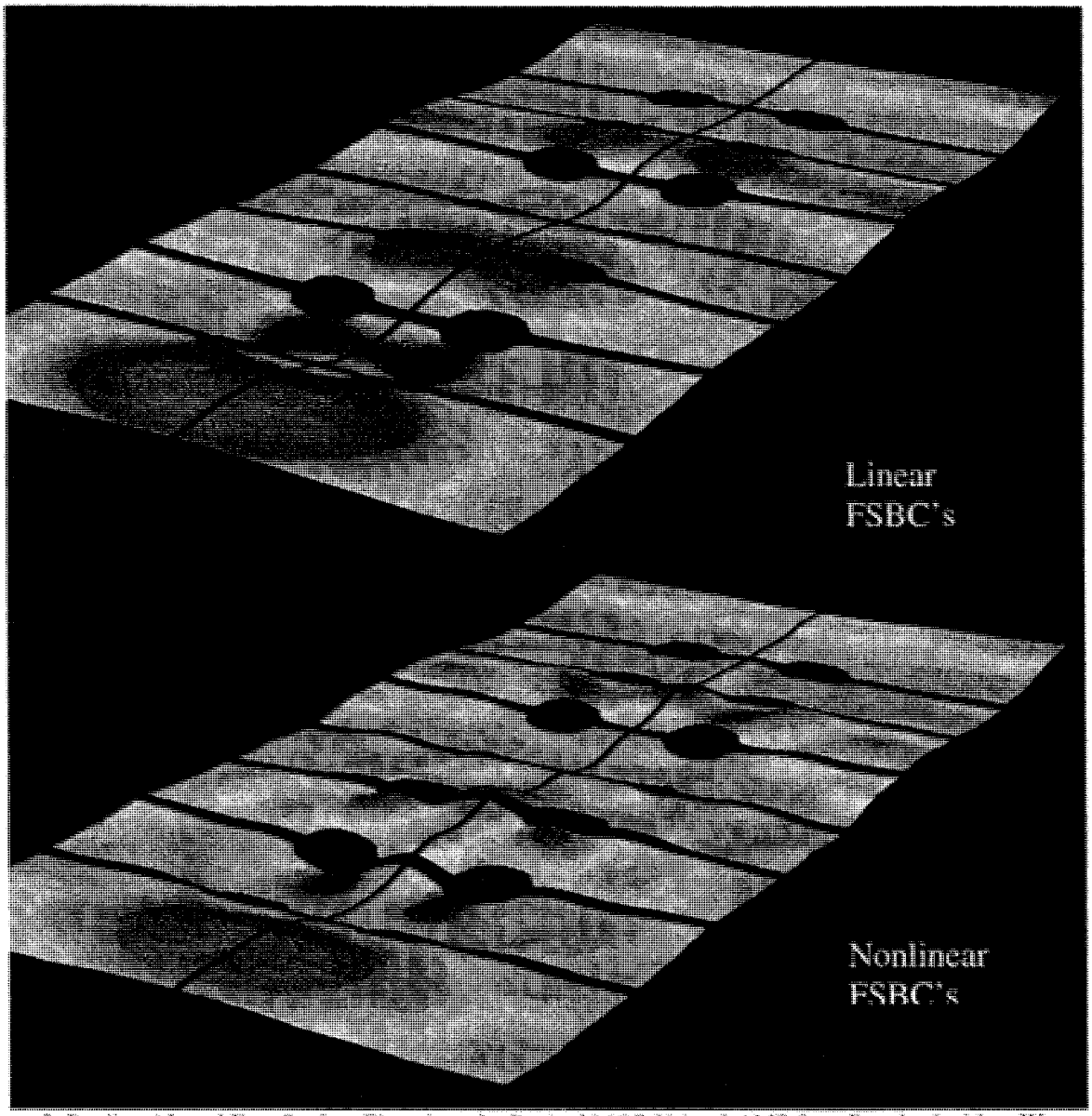

Figure 3. Predicted Local Free Surface Elevations for Bechtel MOB Using LAMP for a Regular Incident Wave with 12.0 Second Period and 1.0 Meter Amplitude

While LAMP's prediction of the platform motions was felt to be more than adequate, it was felt that nonlinear free-surface boundary conditions are required to predict the local wave disturbance with sufficient accuracy. Under the support of the MOB project, the second-order nonlinear free surface boundary conditions were incorporated into the LAMP formulation and a series of calculations were made for a MOB design developed by Bechtel [7].

To include the nonlinear free surface boundary condition effects, LAMP uses a perturbation method to transform the fully nonlinear problem into separate linear problems. In the perturbation method, the quantities related to the velocity potential, the free surface elevation, and the body motions are expanded as perturbation series with respect to a small perturbation parameter. Substituting the perturbation series into the governing equation, body boundary condition, and free surface boundary conditions, the original nonlinear problem due to nonlinear free surface conditions can be recast as separate linear problems to different orders of the perturbation parameter. The linearized free surface boundary conditions can further be expressed with respect to the undisturbed free surface at z=0 using the Taylor's expansion. LAMP solves the perturbed problem up to the second order. It is straightforward for LAMP to solve the first order perturbation problem. While solving the first order solution, LAMP also calculates and stores the nonlinear contribution to the second order problem due to the first

order perturbation. Once the calculation of the first order solution is completed, LAMP starts to solve the second order problem, which is still linear but contains nonlinear contribution from the first order problem. After the second order solution is finished, the total solutions for the velocity potential, free surface elevation, and body motions are obtained by adding together the first and second order solutions. The solution including non-linear effects typically contains a great deal more detail in the wave field as shown in Figure 3.

3 NUMERICAL RESULTS

3.1 Validation of the Nonlinear Free-Surface Boundary Condition

In order to validate the nonlinear free surface boundary condition, a series of test runs were made for an axisymmetric flared body undergoing forced large-amplitude motions. This body, which has a maximum flare of 45°, was extensively tested at the University of Michigan in order to provide validation data for very non-wall-sided where non-linear body and free surface effects are important [8]. The time history of the radiation wave elevations at a point about 0.1D (diameter) away from the body, as computed by both linear and nonlinear methods, are plotted in Figure 4. A distinctive nonlinear pattern in wave elevation can be observed.

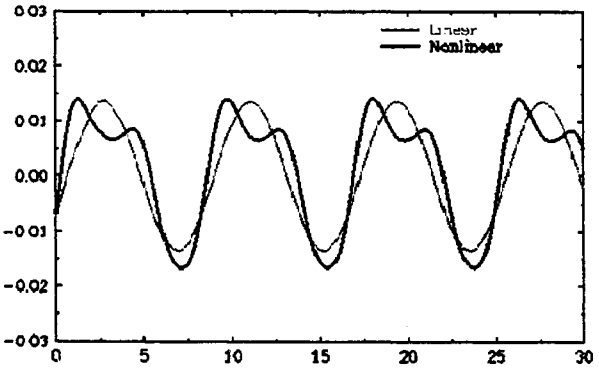

Figure 4: Time History of Wave Elevation at a Point

The time history of the hydrodynamic forces acting on the flared body using linear, second-order nonlinear, and fully nonlinear methods are shown in Figure 5. The linear result is obtained using LAMP's body-linear formulation, LAMP-1, with the body boundary condition satisfied on the mean body position and the linearized free surface boundary conditions satisfied on the mean free surface. The second-order nonlinear result is obtained by the newly developed method with the body boundary condition satisfied on the exact location of the body boundary and the second-order free surface boundary conditions satisfied on the mean free surface. The fully nonlinear result is obtained using the fully nonlinear "Mixed Eulerian Lagrangian" method developed by Professor Dick Yue at MIT. As can be seen, the result from the second-order nonlinear method compares extremely well with the fully nonlinear predictions.

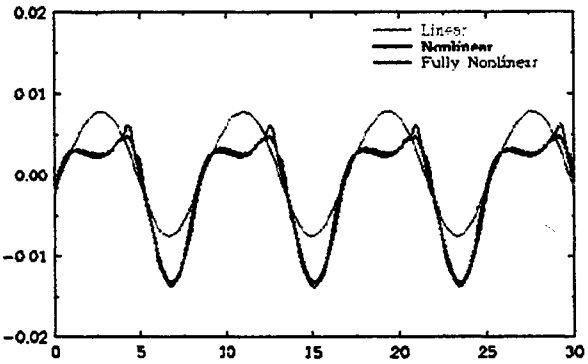

Figure 5: Time History of Hydrodynamic Forces Acting on the Flared Body

3.2 Free Surface Elevations for MOB Air Gap Evaluation

As discussed earlier, the "air gap" is an important design consideration for the MOB project. A series of LAMP calculations were performed for a Bechtel MOB design in order to compute the complete local wave field for air gap evaluation. Linear and nonlinear free-surface LAMP calculations were conducted and the effects of including body motions were also investigated. Linear free surface LAMP calculations for the air-gap region compared favorably to results supplied for other linear potential flow codes.

It should be noted that the results presented here are the local free surface elevations rather than the air gap itself, which would be the relative motion between a point or points on the underside of the upper part of the MOB and would include both the free surface elevation and the motion of the platform. Such a quantity could easily be computed from the LAMP solution by combining the local free surface elevations with the computed platform motion. This study, however, concentrated on the calculation of the local free surface.

The LAMP panel model, including body, matching, and local free surface grids, is shown in Figure 6. A body-fitted free-surface grid was used for all the computations presented in this section.

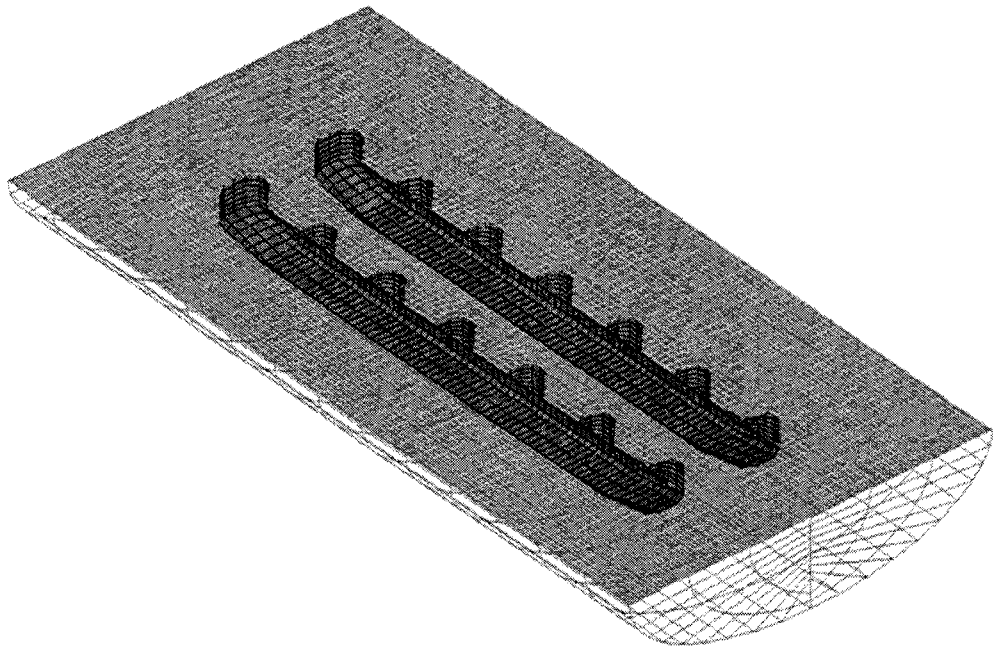

Figure 6. LAMP Panel Model for Bechtel MOB Design

Figure 7 compares the maximum wave elevation near the centerline using the linear and nonlinear free-surface formulations in LAMP for an 18-second 1.0-meter wave in head seas. The incident wave is coming from a direction consistent with the left-hand-side of the figure, and the body is free to pitch and heave. The linear free surface formulation has a very "regular" behavior while the nonlinear formulation has several more pronounced humps and valleys. The X location of the highest peak is in a different region for the two formulations, and the nonlinear peak is noticeably higher than the linear result.

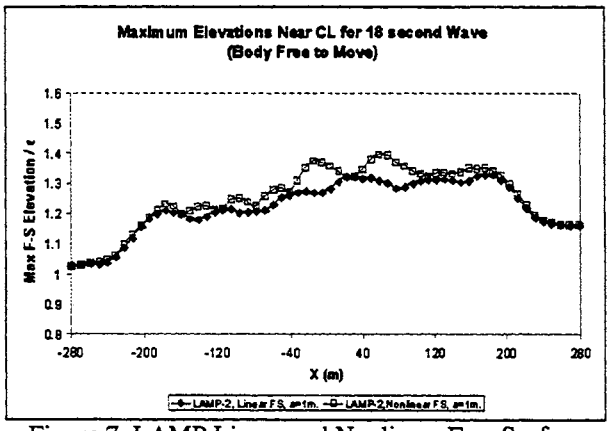

Figure 7. LAMP Linear and Nonlinear Free Surface Comparison for Head Sea, 18-Second Wave

Figure 8 shows maximum centerline elevations for an 18-second head wave as predicted by LAMP's linear and nonlinear free surface formulations. This figure shows that not only is there a significant difference between the linear and nonlinear formulations, but the nonlinearity depends strongly on the incident wave elevation. The linear free surface formulation curves for both the 1.0 and 3.0 meter waves collapse on one another when the incident wave amplitude divides the maximum free-surface elevation. This suggests that the linear free surface elevation is independent of incident wave amplitude, which is consistent with linear theory. The nonlinear formulation curves do not collapse, and the X location and the magnitude of the peaks are varied. This trend shows that the free-surface elevation is a function of the incident wave amplitude, which corresponds more closely to the behavior of waves in nature.

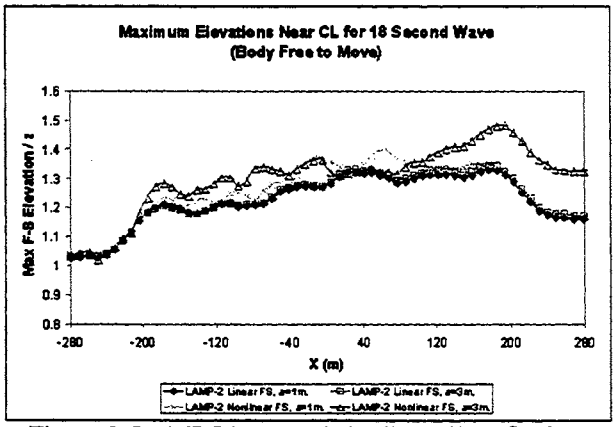

Figure 8. LAMP Linear and Nonlinear Free Surface Comparison for Head Sea, 18-Second Wave

Figure 9 compares LAMP results for a regular, head wave with a period of 12 Seconds and an amplitude of 1.0 meters. Of the wave periods and headings that were examined, the head 12-second condition showed the largest wave amplification (the ratio of the maximum total wave elevation to the incident wave amplitude) and the most noticeable effect of the radiated waves caused by the body motion.

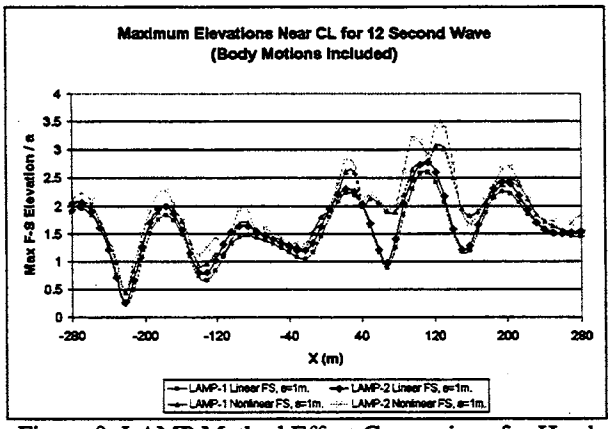

Figure 9: LAMP Method Effect Comparison for Head Sea, 12-Second Wave

As before, the maximum free surface elevations along the centerline are plotted. Results are shown with both the linear and nonlinear free surface models and with the body-linear (LAMP-1) and approximate body-nonlinear (LAMP-2) models. Calculations using the body nonlinear (LAMP-4) calculations were not performed as it was felt that the approximate nonlinear method would capture the most important body nonlinear effects. Note that the body formulation can be selected independently of the linear *vs.* nonlinear free surface solution without compromising either formulation.

As expected, there are small but noticeable differences between the LAMP-1 and the LAMP-2 results, which appears to result from larger pitch motion, and corresponding larger radiated wave, in the LAMP-2 results. Several interesting phenomena can be observed from Figure 9. First, the wave amplification is much larger for the 12 second incident wave compared to the 18 second wave shown previously. Secondly, the nonlinear free surface model has a much more significant effect on the predicted elevation, especially in the peak region where the interaction between the incident, diffracted, and radiated waves is most important. Such a large wave amplification factor can potentially be significant for the MOB platform design. Further study and experimental verification are necessary in this area.

3.3 Motions and Loads at Operating Condition

LAMP motion and load calculations were performed using the Bechtel MOB design at both operating (deep draft) and transit (shallow draft) conditions. Sample computations for the operating draft were done using head incident waves with 8 to 18 second wave periods and varying wave amplitudes. The calculation for each wave condition involved a 216-second time-domain simulation. Selected LAMP results are presented in Figure 10. For a 3-meter amplitude incident wave, the maximum heave and pitch responses are about 1.068 meters and 0.866 degrees, respectively. The results from the air-gap study showed that the nonlinear free surface model had only a small effect on the predicted body motions. Therefore, these results were generated using the approximate body nonlinear (LAMP-2) calculations with the linear free surface model. The current computations were done to establish the procedure for using LAMP with this type of geometry and computation. No difficulty was encountered.

Incident Wave Period (s)	Wave Amplitude (m)	Max. Heave Motion (m)	Max. Pitch Motion (deg)
8	3.00	0.039	0.015
12	3.00	0.499	0.358
14	3.00	0.944	0.143
18	3.00	1.068	0.866

Figure 10: LAMP-2 Calculations for the Bechtel MOB, Operating Condition in Head Seas

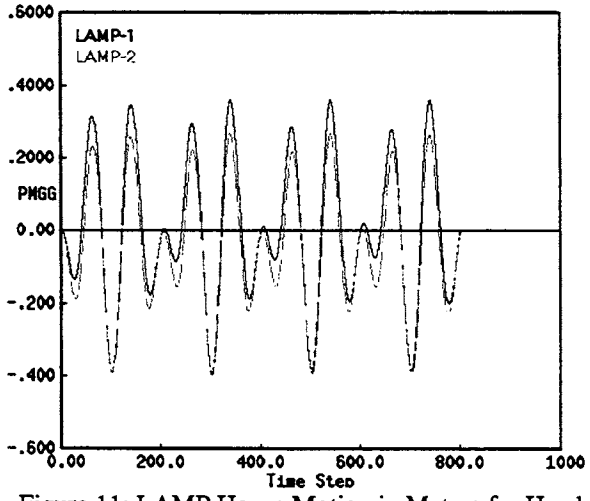

Figure 11: LAMP Heave Motion in Meters for Head Sea, 18-Second 1.0-Meter Wave

Figure 11 and Figure 12 present the LAMP predictions from a 216-second simulation for heave and pitch in the 18-second head sea wave. Figure 11 shows that there is a slight difference in the heave motion predicted for the LAMP-1 and the LAMP-2 calculations, while Figure 12 shows that the pitch

motion is virtually identical. This result is not surprising considering the "wall-sided-ness" of the MOB in the operating condition and the modest wave height as compared to the submergence of the lower pontoon at this draft.

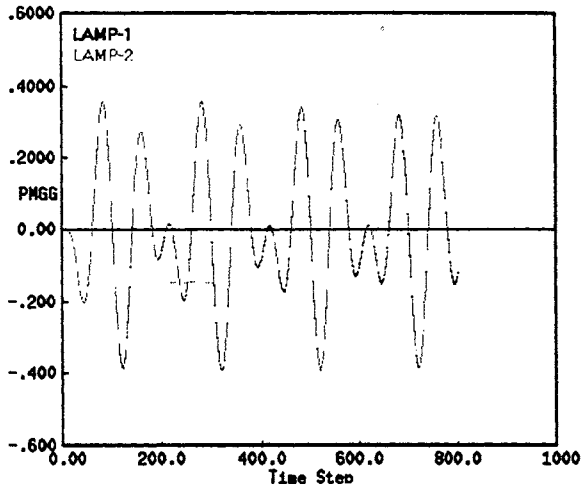

Figure 12. LAMP Pitch Motion in Degrees for Head Sea, 18-Second 1.0-Meter Wave

3.4 Extreme Responses in Transit Condition

LAMP calculations have also been performed to determine what enhancements are needed for extreme response calculations of a MOB in transit conditions. Once again, the Bechtel geometry was used for this test. The predicted motions in transit conditions were evaluated in a very preliminary manner. Three LAMP calculations of this condition have been completed: two head sea cases and one beam sea case. Figure 13 compares the LAMP-1 linear calculation and the LAMP-2 nonlinear calculation for the Bechtel MOB in a head sea condition. The heave response shows how the nonlinear condition in the LAMP-2 calculation causes a noticeable variation in the motion history. The hydrostatic force and Froude-Krylov wave excitation forces are included up to the incident wave surface in LAMP-2 calculations. This means that the LAMP-2 case accounts for the weight of the water on top of the pontoons that will affect the heave motion for this transit condition.

The response of the Bechtel MOB in a LAMP-2 calculation for a beam sea condition is shown in Figure 14. The heave and roll responses also have a noticeably nonlinear time history. No difficulty was found in the LAMP-1 or –2 calculations for the MOB geometry. Careful study of the motions in the beam sea condition is important since the buoyancy force can be very nonlinear and cause some stability problems.

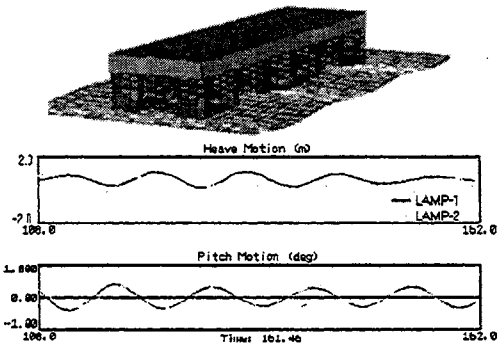

Figure 13: LAMP-1 and LAMP-2 Calculations of Bechtel MOB in Transit Head Sea Condition with 3.0-Meter Incident Wave Amplitude

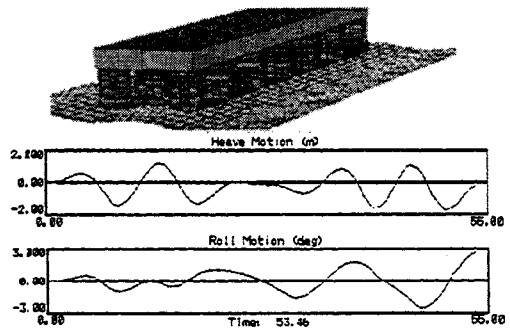

Figure 14: LAMP-2 Calculation of Bechtel MOB in Transit Beam Sea Condition with 3.0-Meter Incident Wave Amplitude

4 OTHER VLFS APPLICATION AREAS

While the present effort has focused on the air gap and intact motions problem, LAMP can potentially be applied to many other areas for very large floating structures such as MOB. LAMP's non-pressure force modeling capability can be used for including mooring or position keeping system models or models of nonlinear forces due to vortex shedding and other viscous effects. These models could be developed from empirical data or large scale viscous flow (e.g. RANS) calculations. In addition, LAMP's general 3-D hydrodynamic model makes it well suited for evaluating damaged conditions.

In the load area, LAMP can currently compute the "main girder" loads at longitudinal cut plans using a rigid body or non-uniform beam calculation. The procedure could be extended to include transverse or local sectional loads as well. In addition, LAMP surface pressure interface module can be used to generate Finite-Element surface load data for detailed structural analysis. In principle, complete hydroelastic effects could be modeled by running concurrent hydrodynamics and structural analysis and feeding the computed body deformations to a body nonlinear (LAMP-4) calculation.

While LAMP's impact force and whipping response modules are probably too ship-specific for use on a MOB, the procedure could be adapted to compute relative motion and impact loads on local platform elements such as the pontoons.

Another area in which LAMP can potentially be applied to large structures such as MOB is the interaction between multiple platforms or ship and platforms. A multiple body capability has been implemented into LAMP and successfully demonstrated in a sample platform-barge calculation. However, some continued development and validation of this capability is required before it can confidently be applied to design problems.

Other potential development areas for the LAMP program include the calculation of slow drift damping forces and the implementation of a nonlinear incident wave specification for a more realistic representation of large sea conditions.

5 SUMMARY

Over the last year, the LAMP System has been successfully applied to key hydrodynamic design problems facing the MOB project, including the air gap problem and platform motions and loads in extreme sea conditions. A nonlinear free surface boundary condition has been implemented into LAMP and a series of calculations have been made to evaluate the effects of body motion, platform configuration, free surface topology, and nonlinear free surface on predictions of motions and local wave fields including radiation and diffraction effects. A comparison of linear free surface LAMP results with other linear computations shows good agreement between the different computational methods.

Calculations demonstrate LAMP's ability to predict motions and loads for the MOB at both operating and transit conditions. A full validation has not been possible due to a lack of relevant experimental data.

With the enhancements and validations conducted under the MOB project over the last year, we feel that LAMP is fast becoming an effective physics-based dynamics simulation tool for assessment of design and operation for large offshore platforms such as those under consideration for the MOB. Ongoing development of the LAMP System and validation with good experimental data for MOB-like systems, as it becomes available, will continue to improve its applicability to VLFS design.

ACKNOWLEDGEMENTS

The current work is supported by the U.S. Office of Naval Research's MOB Program, managed by Mr. Gene Remmers. The authors are indebted to Mr. Bob Taylor, Dr. Paul Paolo, and Dr. Rueybin Chiou of the Naval Facilities Engineering Service Center for their encouragement and support of this work. The development of the LAMP System has been supported by DARPA, the U.S. Coast Guard, Naval Sea System Command (NAVSEA), Office of Naval Research (ONR), American Bureau of Shipping (ABS), and SAIC.

REFERENCES

[1] Weems, K., S. Zhang, W.M. Lin, Y.S. Shin, and J. Bennett, "Structural Dynamic Loadings Due to Impact and Whipping," *Proceedings of the Seventh International Symposium on Practical Design of Ships and Mobile Units, The Hague, The Netherlands,* 1998.

[2] Lin, W.M., and D.K.P. Yue, "Numerical Solutions for Large-Amplitude Ship Motions in the Time-Domain," *Proceedings of the Eighteenth Symposium of Naval Hydrodynamics*, The University of Michigan, U.S.A., 1990.

[3] Lin, W.M., and D.K.P. Yue, "Time-Domain Analysis for Floating Bodies in Mild-Slope Waves of Large Amplitude," *Proceedings of the Eighth International Workshop on Water Waves and Floating Bodies*, Newfoundland, Canada, 1993.

[4] Lin, W.M., M.J. Meinhold, N. Salvesen, and D.K.P. Yue, "Large-Amplitude Ship Motions and Wave Loads for Ship Design," *Proceedings of the Twentieth Symposium of Naval Hydrodynamics*, The University of California, U.S.A., 1994.

[5] Lin, W.M., S. Zhang, K. Weems, and D.K.P. Yue, "A Mixed Source Formulation for Nonlinear Ship-Motion and Wave-Load Simulation," *Proceedings of the Seventh International Conference on Numerical Ship Hydrodynamics*, Nantes, France, 1999.

[6] Nakos, D.E., D. Kring, and P.D. Sclavounos, "Rankine Panel Methods for Transient Free-Surface Flows," *Proceedings 16th Symposium of Naval Hydrodynamics*, Iowa, U.S.A. 1993.

[7] Wung, C., "Design Tool Benchmark Study," *The Fourth Mobile Offshore Base Technology Exchange Conference*, Rosslyn, Virginia, March 1999.

[8] Troesch, A., and M. Wang, "An Experimental Study for Slamming Flow and Green Water on Deck," Technical Report, 327, Department of Naval Architecture and Marine Engineering, University of Michigan, 1994.

PROCEEDINGS OF THE THIRD INTERNATIONAL WORKSHOP ON VERY LARGE FLOATING STRUCTURES
(VLFS '99), VOL. I, EDS. R.C. ERTEKIN & J.W. KIM, 22-24 SEPTEMBER 1999, HONOLULU, HAWAII, USA

Analyzing Mobile Offshore Bases using Accelerated Boundary-Element Methods

D. Kring, T. Korsmeyer, J. Singer, and J. White
Research Laboratory of Electronics, Massachusetts Institute of Technology *

ABSTRACT

In this paper we describe the application of the precorrected-FFT accelerated boundary-element method to linear, frequency-domain and nonlinear time-domain seakeeping analyses for a complete MOB. Acceleration reduces the computational runtime and memory cost for these boundary-element methods from order $O(N^2)$ to order $O(N \log N)$, where N represents the number of computational elements. In the MOB examples considered, exploiting accelerated methods reduced CPU time by nearly two orders of magnitude and memory by nearly an order of magnitude.

1. INTRODUCTION

Limited experience and high construction cost have made the computational analysis of seakeeping a key design tool for the Mobile Offshore Base. However, existing analysis programs are too slow and use too much memory to handle a MOB which may have fifty or more distinct components. Attempting to use existing seakeeping methods on a single unit of the MOB and then extrapolating to the entire structure is simply too dangerous for this new concept. With no prior history of design, construction, and operation, more reliance must be placed on a complete numerical simulation for the whole structure in the MOB design process.

Besides the numerical challenge, MOB seakeeping is further complicated by new physical issues that need to be considered. While linear theory should be sufficient for the vast majority of design needs, this assumptions must be validated for the MOB concept. For example, linear theory may under or over predict wave-runup along the semisub columns and the size of the air-gap below the superstructure. Other examples where there can be nonlinear effects are mating and offloading procedures or in the analysis of local loads.

Clearly, new tools must be developed which can analyze an entire MOB and, in addition, can include nonlinear effects. In this paper we show that the precorrected-FFT accelerated boundary-element methods, originally developed for electromagnetics problems, can be used to meet both of these goals. In the next section we briefly describe why traditional boundary element methods are too slow and too memory inefficient to analyze the MOB, and then in section 3 we describe the accelerated approach. In section 4 and 5 we describe applying acceleration to linear frequency-domain and nonlinear time-domain analysis. Conclusions follow in Section 6.

2. INTEGRAL FORMULATION DIFFICULTIES

For many problems in seakeeping, it is possible to determine sufficiently accurate structural loads and ocean wave heights using a potential flow model. All such potential flow models require the solution of Laplace's equation in three space dimensions,

$$\nabla^2 \phi(x) = 0 \quad \text{in} V, \tag{1}$$

where the domain V is the ocean surrounding the structure of interest. The boundary of the domain, denoted S, includes the structure's wet surface and the ocean-air interface. Depending on the analysis performed, S may also include the ocean floor and a truncation boundary distant from the structure. Boundary conditions on S depend on the specific boundary, but are always in the form

$$\beta(x)\phi(x) + \gamma(x)\hat{n}(x) \cdot \nabla\phi(x) = f(x), \tag{2}$$

where $\hat{n}$ is the unit vector normal to S and directed out of V.

Since the Laplace's equation is space-invariant, and the quantities of interest in seakeeping are always on S, the most commonly used approach to solving (1) is to reformulate (1) as an integral equation. In particular, Green's Second Identity is used to derive an equation which relates the potential on

*Cambridge, MA 02139, USA. e-mail kring@rle-vlsi.mit.edu

the surface to its normal derivative as in

$$\alpha(x)\phi(x) + \int_S \phi(x')\hat{n}(x') \cdot \nabla G(x,x')da' \qquad (3)$$

$$- \int_S \hat{n}(x') \cdot \nabla\phi(x')G(x,x')da' = 0. \qquad (4)$$

where x is a point on the surface S, $\alpha(x)$ is the solid angle formed by S at x ($\alpha = 2\pi$ if S is C^2 at x). Given (3), and (2) the surface potential and its normal derivative can be determined uniquely.

The classical approaches for numerically solving (3), such as traditional boundary-element methods (BEM), generate dense linear systems of equations that are usually solved, at great cost, with some variant of Gaussian elimination. More precisely, if N elements are used to numerically discretize the surface S in a given problem, then traditional methods require order N^2 storage and order N^3 operations to determine ϕ and its normal derivative. For MOB problems, where nearly 100,000 elements are needed to represent the complete structure, traditional boundary element methods would require at least 40 gigabytes of memory and months of computer time.

3. ACCELERATION METHODS

If the discretization of equation (3) is sufficiently well conditioned, iterative methods such as GMRES [1] can be used to reduce the problem solution time from order N^3 to order N^2. Switching from Gaussian elimination to an iterative method like GMRES has an added benefit that makes further acceleration possible. GMRES replaces Gaussian elimination's detailed manipulation of matrix elements with matrix-vector products. This implies that when GMRES is used, the matrix is not explicitly required.

To see how to further accelerate solving the discretized version of (3), consider the commonly used discretization in which the potential and its normal derivative on the surface S are approximated by N small constant-strength panels. Given this discretization, evaluating the potential

$$\int_S \phi(x')\hat{n}(x') \cdot \nabla G(x,x')da' \qquad (5)$$

at N test points located at the centroids of the N panels is equivalent to computing the matrix-vector product

$$d = D\Phi \qquad (6)$$

where Φ is the an N-length vector of panel potentials and D is an $N \times N$ matrix given by

$$D_{i,j} = \int_{panel_j} \hat{n}(x') \cdot \nabla G(centroid_j, x')da'. \qquad (7)$$

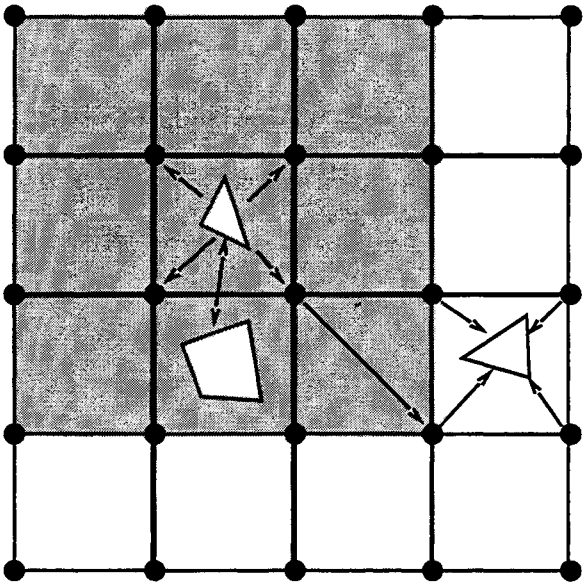

Figure 1: 2-D representation of the steps of the precorrected-FFT (pFFT) algorithm. For the triangular element at the upper left, its influence on nearby elements (any in the grey area) is computed directly and precorrected, its influence on distant elements is computed via the FFT on the uniform grid.

As D is a dense matrix, forming $D\Phi$ requires N^2 operations. However, $D\Phi$ can be accurately approximated in nearly order N operations by separating D into two parts. D_{near}, associated with nearby panel-centroid pairs, is represent explicitly. Note that D_{near} is sparse, having only order N nonzero entries. The distant contribution to the potential, $d_{far} = (D - D_{near})\Phi$, is approximated. There are a wide variety of methods for rapidly computing d_{far}, though the most commonly used programs are based on fast-multipole schemes [2] or fast Fourier transform (FFT) based methods [3].

In the FFT-based methods, which allow for general Green's functions, d_{far} is approximated by representing distant panels with point singularities which reside on a uniform grid. The fact that all the point singularities are on a uniform grid makes it possible to rapidly calculate potentials due to those point singularities using the FFT. Below we give a brief overview of one such FFT-based algorithm, the precorrected-FFT approach [3].

Figure 1 is a schematic of the steps in the algorithm to compute d. Instead of computing all interactions directly, there is a series of steps as follows:

Grid set-up: Overlay the problem geometry

with a uniform right-parallelepiped grid and sort the elements into the cells formed by the grid. The nearby elements of a given element are those elements in the 27 cells that share a vertex with the given element's cell. Set point singularities on the grid at at least the cell vertices (grid-order = 2), or at half the spacing of the vertices (grid-order = 3), *etc*, as desired for accuracy.

Projection operators: Numerically evaluate the operator that can replace the set of element singularity distributions in each cell with an equivalent set of point singularities on the grid. These are matrices deduced from a collocation problem for each cell that matches, at a set of test points, the potential due to the singularities at the points on the grid with the potential due to the singularity distributions on the elements. The essential idea in this step is that the operator is based on the fundamental solution of the Laplace equation, not the particular Green function for the problem. That is, we seek the grid point source strengths q_i in

$$\sum_{i=1}^{I} q_i \frac{1}{||r_j - r_i||} = \sum_{k=1}^{K} \sigma_k \int_k dr_k \frac{1}{||r_j - r_k||}, \qquad \text{j=1,J}$$

for I grid points, J projection collocation points, and K elements in the cube with source distributions. The expression for replacing dipole distributions with grid point sources is similar.

Interpolation operators: Numerically evaluate the interpolation operator that provides the potential at each collocation point given the potentials at a set of grid points. This operator is the transpose of the complementary projection operator for point sources, not element distributions, as we are using a collocation method. That is, we use the transpose of the operator implied by

$$\sum_{i=1}^{I} \phi_i \frac{1}{||r_j - r_i||} = \sum_{k=1}^{K} \phi_k \frac{1}{||r_j - r_k||}, \quad j = 1, J$$

for K element collocation points. Again, it is important to note that only the fundamental solution of the Laplace equation appears in the definition of these operators.

Direct interaction and precorrection: Directly compute the small number of nearby influences for each element using the same algorithms that would be used in a conventional approach. Use the projection operators, the Green function, and the interpolation operators to precompute and subtract from these nearby influences the grid-based influences for these same nearby elements that will be included inaccurately when the far influences are added from the potential interpolated off the grid.

Projection: Project the element singularity distributions to point singularities on the uniform grid by applying the projection operator to the element singularity distributions.

Convolution: Compute the potentials at the grid points due to the singularities at the grid points using FFT-accelerated convolution [4]. Note that the problem-specific Green's function must be used.

Interpolation: Interpolate the grid point potentials onto the elements by applying the interpolation operator to the grid potentials, and then adding the results to the precorrected direct influences.

Note that in the above process it is necessary to evaluate the Green function (8) order-N times, so efficient and robust algorithms are required. We use those described in [5] for the Rankine part of (8) in the calculation of the nearby influences and those in [6] for the wave-like part in the calculation of both the nearby and grid-point influences.

4. LINEAR FREQUENCY DOMAIN

The linear, low-order element, frequency-domain analysis code WAMIT®has been extended to include the precorrected-FFT algorithm, and the extended program has been named FastWAMIT. WAMIT and FastWAMIT solve (3). In this case, the surface S is only the structure's wet surface and the Green function is given by

$$G(x,\xi,\omega) = \frac{1}{r} + \frac{1}{r'} + \frac{2k}{\pi} \int_0^\infty d\nu \frac{e^{k(x_3+\xi_3)}}{\nu - k} J_0(\nu R), \tag{8}$$

where ω is the wave frequency, r is the Euclidean distance $r = ||x - \xi||$, $r' = ||x - \xi + (0,0,2\xi_3)||$, $R = ||(x_1,x_2) - (\xi_1,\xi_2)||$, and $J_0(x)$ is the zeroth-order Bessel function. The above Green's function insures that the solution satisfies

$$-\omega^2 \phi(x) + g\phi_{x_3}(x) = 0 \qquad x_3 = 0 \tag{9}$$

on the ocean surface.

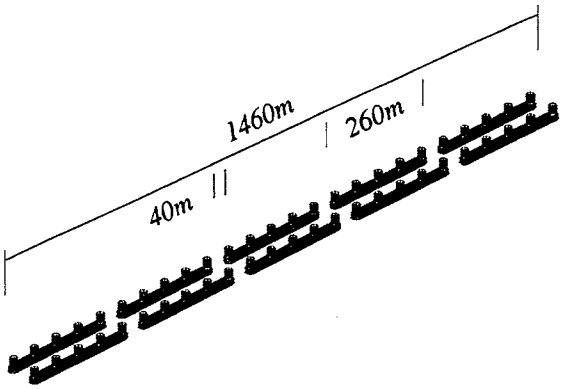

Figure 2: The five-unit MOB configuration.

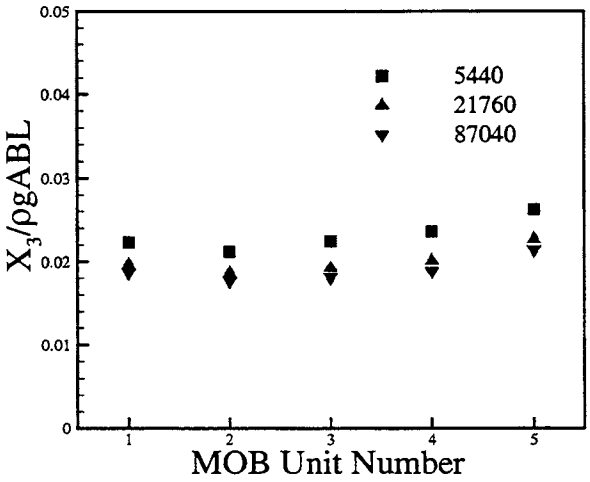

Figure 3: Heave exciting force magnitude on each unit of the 5-unit MOB in head seas with period 12 seconds. The numbers in the legend denote the number of elements on the entire MOB structure.

To validate the precorrected-FFT accelerated BEM approach for computing wave loads, solutions computed using the accelerated algorithm have been compared to the results obtained using classical techniques [7]. In those experiments, it was shown that the accelerated algorithm agreed with the classical approach to at least three significant digits. In addition, it was shown that Fast-WAMIT can easily handle problems with as many as 100,000 panels.

The importance of analyzing a complete MOB, rather than an isolated unit, can be seen by examining the diffraction force for the MOB in Figure 2. Figure 3 shows the converging results for the heave exciting force on each of the units for the entire MOB in head seas. Here, there is a clearly interference that could not be predicted by analyzing a single unit alone.

For the calculation in Figure 3, 87040 elements where required to achieve sufficient accuracy. As shown in the table below, for this MOB example the precorrected-FFT algorithm was two orders of magnitude faster, and used an order of magnitude less memory, than classical techniques. It should be noted that in this comparison, two planes of symmetry were exploited in the classical techniques but not in the precorrected-FFT algorithm. Such symmetry optimizations would be eliminated if a ship were moored next to the MOB, and then classical techniques would be even slower.

The efficiency of the precorrected-FFT algorithm presented in [7] has been improved by exploiting the frequency-independence of many of the algorithm's steps. Only the "Direct Interaction and Precorrection" and the "Convolution" steps are *frequency dependent.* This means that in a sweep of frequencies for radiation and diffraction analysis, the *frequency independent* set-up steps of the algorithm may be performed once and re-used at each frequency. In addition, as the frequency-dependent part of the Green function (8) is smoothly dependent on distance, there is no need to separate nearby and distant interactions. This makes it possible to use the grid alone to represent the frequency-dependent part. The result is that the "Direct Interaction and Precorrection" steps become frequency independent, further improving efficiency.

Figure 4 shows a comparison of the RAO's for a floating cylinder with a draft equal to half its radius. The solutions computed by including the frequency-dependent part of the Green function in the nearby interactions are indistinguishable from the solutions computed by representing the frequency-dependent part with the grid alone. In the table below it is shown that by using the grid representation for the frequency-dependent part of the Green function, one achieves speed improvements of at least a factor of three.

5. NONLINEAR TIME DOMAIN

Precorrected-FFT acceleration has also been applied to a high-order, nonlinear, time-domain, Rankine BEM called AEGIR, which was first introduced in [8]. For large, complicated structures such as the MOB, computationally demanding nonlinear wave-body simulations are simply not feasible without BEM acceleration.

Ele's	Acc %	Time (min)		
		pFFT	pFFT grid	WAMIT
5440	25	5	2	14
21760	5	29	11	(215)
87040	1	(150)	50	(3440)

Ele's	Acc %	Memory (Mbyte)	
		pFFT	WAMIT
5440	25	40	38
21760	5	230	(600)
87040	1	870	(9,600)

Table 1: Computational resources required for a diffraction calculation for a 5-unit MOB at 16 frequencies. "Ele's" indicates the number of elements in the discretization; "Acc %" indicates an estimate of the percent error in the result; "pFFT" indicates a precorrected-FFT accelerated solution with the wave part of the Green function included in the direct interactions; "pFFT grid" indicates a precorrected-FFT accelerated solution with the wave part of the Green function included in the grid-based acceleration only; "WAMIT" indicates the conventional solution technique including the exploitation of geometric symmetries; "Time" indicates cpu time in minutes on a DEC alpha workstation driven at 433MHz; "Memory" indicates allocated memory in megabytes; parentheses indicate estimated values.

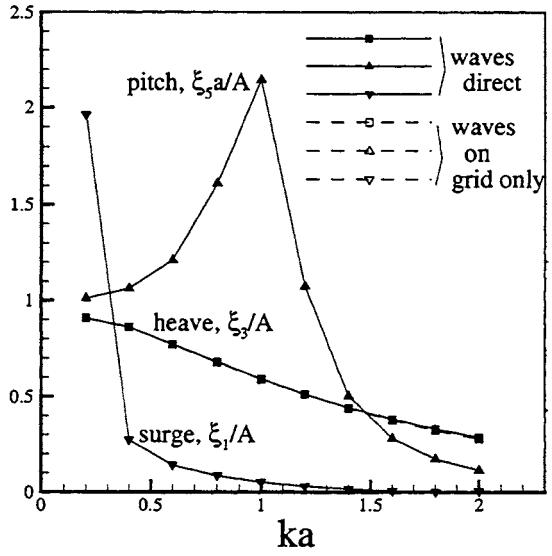

Figure 4: Surge, heave, and pitch RAOs for a truncated cylinder. Comparison of the solution with the wave part of the Green function included in the direct precorrection (solid lines) and on the grid only (dashed lines).

Linear theory may be valid for most MOB seakeeping and structural analyses. However, nonlinear theory is critical for MOB analysis for two reasons. First, nonlinear theory can help validate and define linear assumptions. Second, some important features in MOB analysis such as air-gap [9], wave run-up, offloading, and mating may have significant nonlinear effects.

For the validation of linear theory, experimental studies have traditionally been used. However, the MOB is a complicated structure with little experimental and no operation experience. In the case of a radical departure from previous designs, nonlinear theory is very useful to help define the applicability of traditional, linear seakeeping. This need for more capable models to substitute for experience is seen in the study of advanced marine vehicles that depart from traditional ship concepts [10].

A practical, nonlinear seakeeping method requires a stable discretization scheme and an accelerated BEM. A stable, efficient implementation of the the body-exact and fully-nonlinear time-domain wave-body formulations is described below. Precorrected-FFT acceleration is adapted to this discretization, which is based o high-order, Rankine BEM.

Instead of the frequency-domain, wave Green function (8) this time-domain Rankine approaches uses a Green function,

$$G(x,\xi) = \frac{1}{r} \tag{10}$$

that only satisfies the governing Laplace equation. To satisfy the free-surface conditions, elements must now be placed on the free-surface and the body. A stable, numerical scheme integrates the free-surface conditions in time on the discretized free-surface. This temporal integration requires the solution of the mixed boundary-integral equation with β non-zero on the free surface and γ non-zero on the body in (2).

Although there are more unknowns in the Rankine approach than the wave Green function approach, the Rankine method has some important advantages. First, the time-domain problem can be solved without resorting to the expensive convolution integrals needed for a time-domain wave Green function approach. Second, the evolution of the free-surface can be modeled with either linearized or exact nonlinear free-surface conditions. The wave Green function methods are inherently linear.

In this method, a nonlinear formulation for the free-surface conditions has been implemented using a variation on the Zakharov formulation. The kinematic and dynamic free-surface conditions are expressed, respectively, as,

$$\left[\frac{\partial}{\partial t} - (W + \frac{\partial x}{\partial t}) \cdot \nabla\right] \zeta = (1 + \nabla\zeta \cdot \nabla\zeta)\phi_{x_3} - \nabla\varphi \cdot \nabla\zeta, \quad \text{on } x_3 = \zeta, \tag{11}$$

$$\left[\frac{\partial}{\partial t} - (W + \frac{\partial x}{\partial t}) \cdot \nabla\right] \varphi = -g\zeta - \frac{1}{2}\nabla\varphi \cdot \nabla\varphi + \frac{1}{2}(1 + \nabla\zeta \cdot \nabla\zeta)\phi_{x_3}^2, \quad \text{on } x_3 = \zeta. \tag{12}$$

Here, W represents a steady forward speed, $\frac{\partial x}{\partial t}$ allows a waterline that changes shape in time, ζ is the wave elevation, ϕ_{x_3} the vertical velocity of the fluid, and φ is the Zakharov surface potential.

Together with the exact-body boundary conditions (no-flux imposed on the instantaneous position of the body), this leads to the so-called "fully-nonlinear" formulation. The "body-exact" formulation has also been implemented in which the exact-body boundary condition is used with a linearized version of (11) and (12).

AEGIR uses a high-order, geometry-independent BEM where arbitrary-order B-splines are used to discretize the unknown wave flow. The choice of the geometry description is not linked to this flow representation and can be defined by the user to be analytic or based on a CAD representation, for instance. This improves local accuracy and eases transfer of the results to structural FEM codes.

To apply precorrected-FFT acceleration, the high-order surface is decomposed into a large collection of flat subpanels. The number of subpanels for each high-order element has been determined through numerical testing. For instance, nine subpanels (three along each direction on the surface) have similar truncation error as a single bi-quadratic element for typical geometries. The problem is solved with the accelerated technique, and the results are interpolated back to the original B-spline basis. Acceleration schemes that treat high-order discretizations directly are also being developed.

The high-order scheme is necessary for the Rankine time-domain problem since it allows a numerically stable integration for the free-surface. A low-order approximation of the free-surface conditions creates numerical instability that requires unacceptable numerical damping. Acceleration, with the interpolation procedure for the high-order BEM, has only been implemented for the "body-exact" formulation. Further work is necessary to accelerate the "fully-nonlinear" method where a pure, high-order acceleration scheme may be necessary.

Without acceleration, the fully-nonlinear formulation can only be applied to simple cases such as the heaving cylinder represented in Figure 5. This case-study is important to the MOB, however, since it illustrates the failure of linear analysis to model wave run-up. The nonlinear over-predicted the linear analysis by 80 percent. This raises some concerns for the MOB design. This sensitivity of wave run-up to nonlinearity is confirmed by the analysis of [11] and the experiments of [12].

Stepping beyond this simple problem, acceleration can be used to examine the more complicated geometries of the MOB. Figure 6 shows the convergence of the method for a single semi-sub in heave with 17000, 36000, and 63000 subpanels. Although the coarse grid is adequate for the global heave force, the wave elevation, a local quantity, is much more sensitive and needs a finer grid for convergence within a one percent tolerance.

Finally, a MOB can be simulated in the time-domain using acceleration. In Figure 7, a body-exact simulation of the MOB heaving with a period of 6 seconds is shown. The snapshot of the

wave-pattern was taken 6 cycles after an impulsive start-up. The dark lines represent the boundary of the numerical B-spline patches that define the free surface. For this run, 61000 subpanels were used.

It is with this large MOB discretization that the need for acceleration becomes evident. The simulation over 6 heave cycles (360 time steps) took 42 hours on a 433 Mhz DEC ALPHA and required 750 Megabytes of memory. A traditional dense solution of this problem would have required 2.5 months of run-time and 6 Gigabytes of memory.

6. CONCLUSIONS

The precorrected-FFT acceleration method presented in this paper makes the analysis of MOB seakeeping practical. The precorrected-FFT acceleration scheme has been chosen not only for its computational efficiency, but also for its flexibility.

For the linear frequency-domain problem, acceleration led to savings of a factor of 20 in run-time and 10 in memory over traditional approaches. By evaluating the wave Green function on the FFT grid, the time savings was increased to a factor of 60. Since linear analysis is typically performed for a wide range of design parameters, total design evaluation can be reduced from months to hours. Nonlinear time-domain analysis is much more computationally demanding than linear analysis, and is only practical using acceleration. Useful nonlinear results can now be obtained in two days instead of two months. Finally, the order of magnitude memory reductions make workstation-based analysis possible.

Acknowledgment: This research was supported by an ONR Grant under the direction of NFESC, a DARPA MURI contract, and by the industry consortium: Numerical Analysis of Wave Loads on Offshore Structures, with participants Chevron, DNV-Software, Exxon, Mobil, Norsk-Hydro, NSWC-CD, OTRC, Petrobras, Saga, Shell, and Statoil.

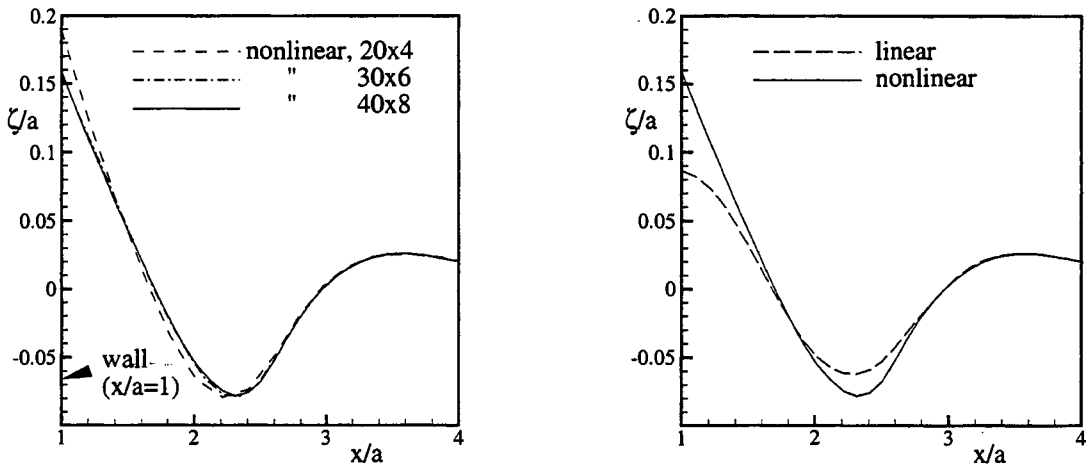

Figure 5: Wave run-up and elevation along a radial cut for a truncated column in heave. The wall of the truncated column is at $x/a = 1$.

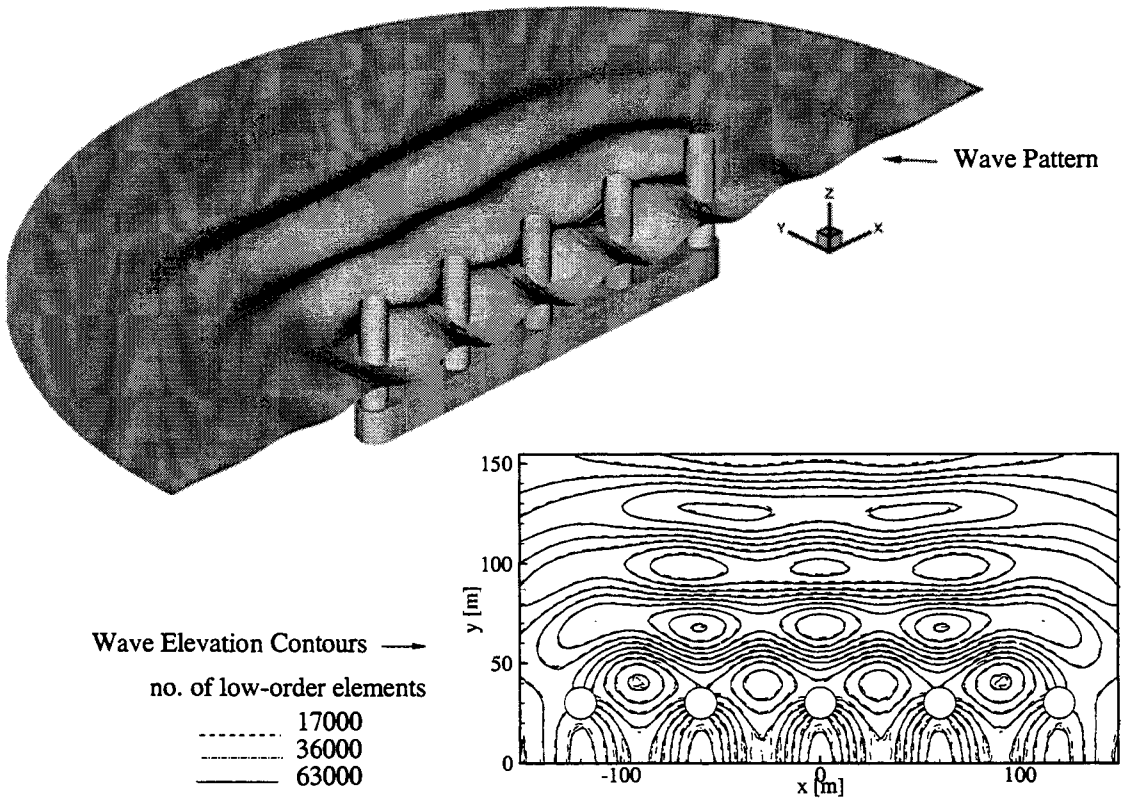

Figure 6: Body-nonlinear wave pattern and wave elevation contours for a MOB semi-sub heaving at period, $T = 6$ sec. Vertical scale x2.

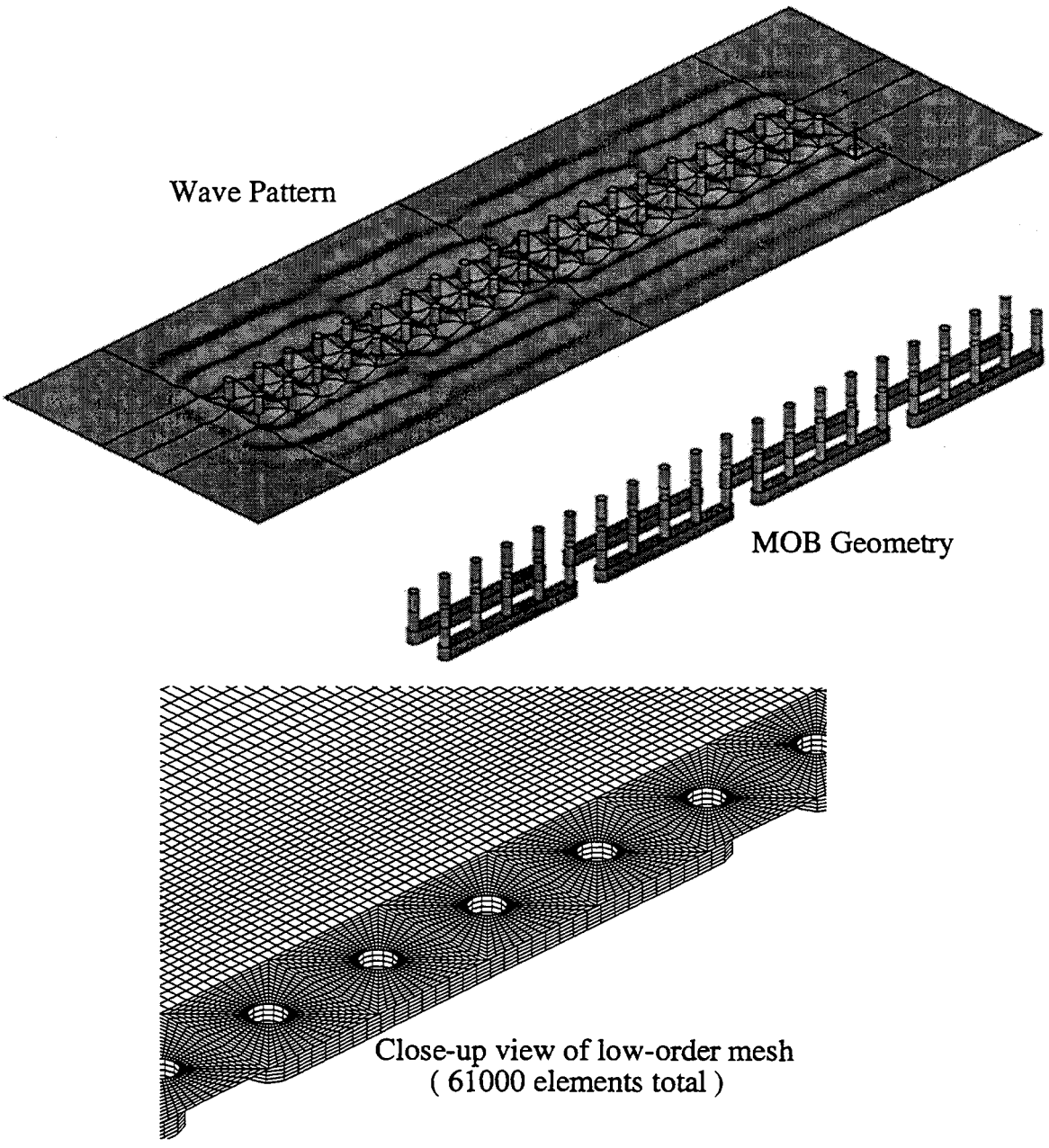

Figure 7: Body-nonlinear heave wave pattern, 4-unit MOB geometry, and computational mesh. MOB heaving at 6 second period with a 5m amplitude. Vertical scale x2.

References

[1] Y. Saad and M. H. Schultz. GMRES: A generalized minimal residual algorithm for solving nonsymmetric linear systems. *SIAM J. Sci. Stat. Comp.*, 7(3):856–869, July 1986.

[2] K. Nabors, F. T. Korsmeyer, F. T. Leighton, and J. White. Preconditioned, adaptive, multipole-accelerated iterative methods for three-dimensional first-kind integral equations of potential theory. *SIAM J. Sci. Comp.*, 15(3):713–735, 1994.

[3] J. R. Phillips and J. K. White. A precorrected-FFT method for electrostatic analysis of complicated 3-d structures. *IEEE Trans. on Computer-Aided Design*, 16(10):1059–1072, 1997.

[4] C. Van Loan. *Computational Frameworks for the Fast Fourier Transform.* SIAM, Philadelphia, 1992.

[5] J. N. Newman. Distribution of sources and normal dipoles over a quadralateral panel. *J. of Engineering Mathematics.*, 20:113–126, 1986.

[6] J. N. Newman. The approximation of free-surface Green functions. In P. A. Martin and G. R. Wickham, editors, *Wave Asymptotics*, pages 107–135. Cambridge University Press, 1992.

[7] T. Korsmeyer, T. Klemas, J. Phillips, and J. White. Fast hydrodynamic analysis of large offshore structures. In *ISOPE'99*, Brest, 1999.

[8] D. C. Kring, F.T. Korsmeyer, J. Singer, , D. Danmeier, and J. White. Accelerated nonlinear wave simulations for large structures. In *7th Intl. Conf. on Numerical Ship Hydrodynamics*, Nantes, 1999.

[9] W. M. Lin, S. Zhang, K. Weems, and D. K. P. Yue. A mixed source formulation for nonlinear ship motions and wave-induced loads. In *7th Intl. Conf. on Numerical Ship Hydrodynamics*, Nantes, 1999.

[10] D. C. Kring, D. A. Mantzaris, G. B. Tcheou, and P. D. Sclavounos. A time-domain seakeeping simulation for fast ships. In *7th Intl. Conf. on Fast Sea Transportation*, Sydney Australia, 1997. FAST97.

[11] B. Buchmann, J. Skourup, and K. F. Cheung. Run-up on a structure due to second-order waves and a current in a numerical wave tank. *Applied Ocean Research*, 20:297–308, 1998.

[12] D. L. Kriebel. Nonlinear wave interaction with a vertical circular cylinder, part ii: Wave run-up. *Ocean Engineering*, 19:75–99, 1992.

PROCEEDINGS OF THE THIRD INTERNATIONAL WORKSHOP ON VERY LARGE FLOATING STRUCTURES
(VLFS '99), VOL. I, EDS. R.C. ERTEKIN & J.W. KIM, 22-24 SEPTEMBER 1999, HONOLULU, HAWAII, USA

MOTIONS OF A MOVABLE FLOATING BRIDGE IN WAVES

Shuichi Nagata, Seijiro Miyake, Takashi Fujita, Hisafumi Yoshida, Hiroshi Tanaka,
Hitachi Zosen Corporation*, Osaka, JAPAN

Tadaaki Maruyama
Osaka Municipal Government, Osaka, JAPAN

and

Shigeru Ueda
Tottori University, Tottori, JAPAN

ABSTRACT

A new movable floating bridge supported on two pontoons is under construction in a channel of about 400m in width in Port of Osaka. The dynamic responses induced by the waves and winds during typhoon are one of the important aspects in the design of the floating bridge. Hydraulic model test is carried out under the design environmental conditions corresponding to the 100-year storm. From this model test, the distribution of wave height in a channel, the motions of the floating bridge and the deflection of the rubber fender which are useful for the design are obtained. A non-linear simulation calculation for motions of the floating bridge is carried out at the same time. From the comparison the numerical results with the experimental results, it is found that the numerical results for the motions of the floating bridge and deflection of the rubber fender agree well with the experiments.

1. INTRODUCTION

A new movable floating bridge is under construction in a channel between Yumeshima and Maishima in Port of Osaka in Japan. The width of this channel is about 400m. This bridge is supported by two floating steel pontoons (58m × 58m × 8m) as shown in Fig. 1. This bridge is with 410m in length and 32m in width. To prevent this floating bridge from drifting, the mooring system is equipped. This mooring system consists of dolphins, reaction walls and rubber fenders. The reaction walls are located on the fixed dolphins with sheet pile foundation in the seabed and are usually in the standing-position to moor the bridge. The bridge is rotated about an inserted pivot axis after the reaction walls are turned down. As this bridge is the first swinging floating bridge in the world, it is necessary to make a full investigation in designing. Especially, the estimation of the behavior of the bridge and the deflection and reaction force of the rubber fenders are important for the design of the mooring, the transitional bridges which are installed at the both ends of the floating bridge to connect the approach bridges supported on the grounds and the running performance of cars. In our study, hydraulic model tests for a moored floating bridge under the design wind and wave conditions corresponding to the 100- year storm and the traffic regulation due to wind are carried out. In these tests, the distribution of wave height in the channel, the motions of the floating bridge and the deflection of

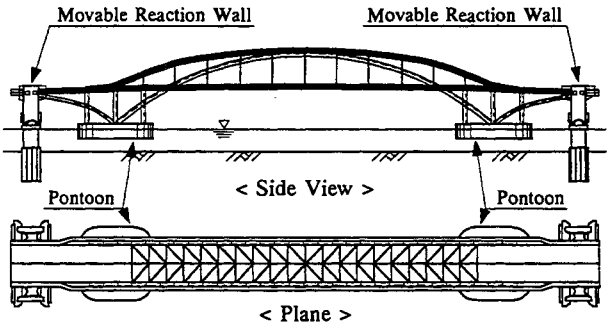

Fig. 1 Movable floating bridge

* Technical Research Institute,
2-11, Funamachi 2-Chome, Taisho-Ku, Osaka, 551-0022, JAPAN.
E-mail: *nagata@fluid.lab.hitachizosen.co.jp*

the rubber fender are measured. The experiments are carried out for two cases. One is the case in which a breakwater is set up in the Maishima side of the entrance of the channel supposing the construction of the breakwater for the yacht harbor in future. The other is the case in which floating breakwaters are set up in front of the pontoons of the floating bridge in order to decrease the motion of the floating bridge. A non-linear simulation calculations for motions of the floating bridge and deflection of the rubber fender are carried out, and the calculation results are compared with the experimental results.

2. EXPERIMENT

2.1 Model

The experiments were carried out in a three-dimensional wave tank with 50m in length, 40m in width and 1.5m in depth at Tetra Co., Ltd. Model scales are 1/80 considering the ability of the wave generator and the size of the wave tank. In experiments, the channel between Maishima and Yumeshima is reproduced in the wave tank including a Yumeshima side breakwater and the Maishima side promenade exactly as shown in Fig.2. The wave-guide plates are set up from the wave generator to the entrance of the channel. The water depth in the channel is constant.

The model of the floating bridge is a rigid bode made of aluminum as shown in Fig. 3. The pontoons are made geometrically similar to the prototype but the rigidity of the parts of the model above water surface is larger than that of a model scaled down from the prototype by similarity law. The displacement, draught, height of the center of gravity, radius of gyration etc. of the model are similar to the prototype. The characteristics of the model of a floating bridge are shown in Table 1.

The prototype floating bridge is moored by rubber fenders with 2500 mm in height. The number of the rubber fender is 24. These rubber fenders have remarkable non-linear and hysteresis characteristics as shown in Fig. 4. However, as it is difficult to make the model of rubber fenders that have such characteristics, the fender devices that consists of two leaf springs and counter-weight are made. The broken line in Fig.4 shows the characteristic of reaction of this device. In our experiments, these mooring devices are arranged as shown in Fig. 5. A mooring device corresponds to the two rubber fenders in prototype.

As shown in Fig. 6, the models of floating breakwaters used in the experiment are air-controlled

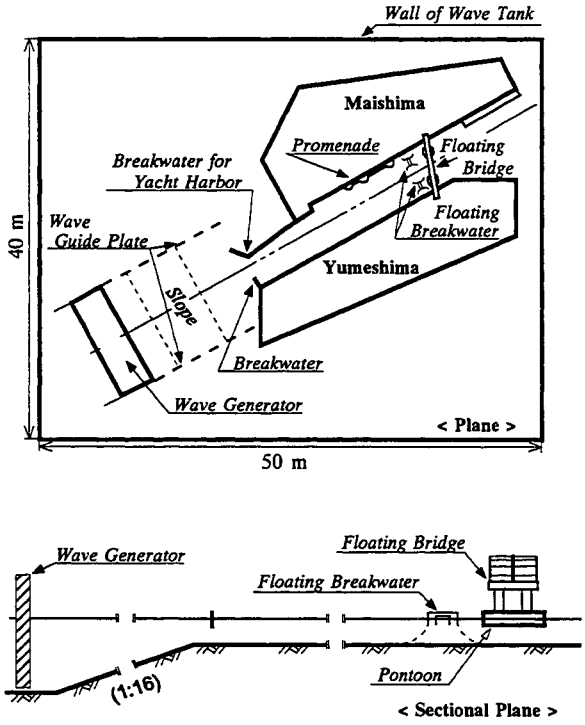

Fig. 2 Layout of a floating bridge and a geographical model in basin

Table 1 Characteristics of the floating bridge

		Model	Prototype
Length	(m)	5.125	410.00
Draught	(m)	0.054	4.35
Displacement	(kgf, tf)	55.640	28,490
Length of Pontoon	(m)	0.725	58.00
Depth of Pontoon	(m)	0.100	8.00
Center of Gravity (KG)	(m)	0.319	25.51
Radius of Gyration: roll	(m)	0.250	19.68

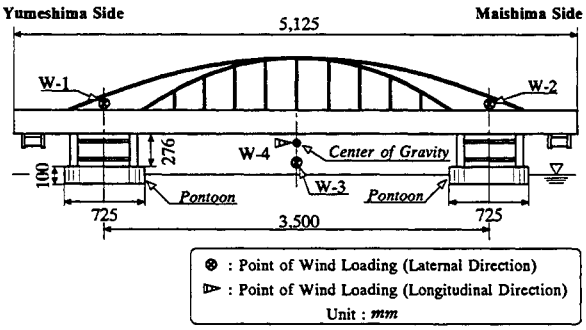

Fig. 3 Floating bridge model and acting points of wind load

type floating breakwater and are set up in front of the two pontoons of the floating bridge.([1]) These are moored by chain. The floating breakwater model shows a lower wave transmission coefficient obtained from another two- and three-dimensional experimental results. The characteristics of the floating breakwaters used in our experiments are shown in Table 2.

2.2 Wind force loading device

When we are trying to apply wind to the floating bridge model, it is necessary to have a wind tunnel which contains the whole channel in the test section, and it is difficult to do such an experiment practically. Therefore in this experiment, the force corresponding to the wind force is applied to the floating bridge by an actuator. As the effects of the wind forces are dominant in the surge, sway, roll and yaw mode of the floating bridge, four actuators are used. As shown in Fig. 7, wind force loading system is composed of an actuator, a controller, wire and a load cell. In this system, firstly, the time sequence of the wind velocity is generated from Davenport spectrum. And the time sequences of the wind force for four mode motions about the center of gravity are made from the sequence of the wind velocity and the drag coefficient obtained by wind tunnel test.([2]) Next, time sequences of wind forces at four points where the wind forces are applied are calculated by considering the distance between the center of gravity and the four points and are inputted to the controller. The controller receives a signal proportional the wind force measured with the load cell which is attached at the point of application of wind force and keeps the wind force by a feedback control equal to the inputted wind force data. The outline of this system is shown in Fig.7.

Table 2 Characteristics of the floating breakwater

		Yumeshima Side		Maishima Side	
		Model	Prototype	Model	Prototype
Length	(m)	1.06	85.00	1.44	115.00
Width	(m)	0.25	20.00	0.25	20.00
Depth	(m)	0.10	8.00	0.10	8.00
Draught	(m)	0.81	6.50	0.08	6.50
Displacement	(kgf, tf)	3.31	1,694	5.27	2,188

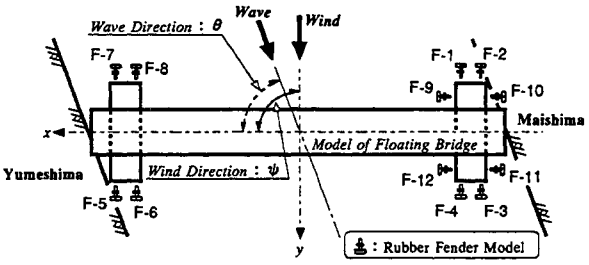

Fig. 5 Layout of the rubber fender model

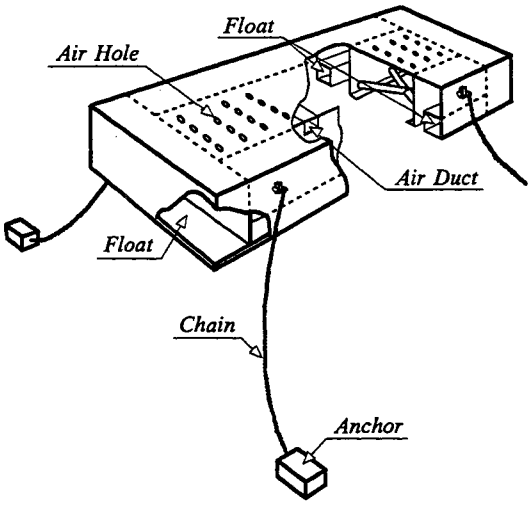

Fig. 6 Air-controlled type floating breakwater

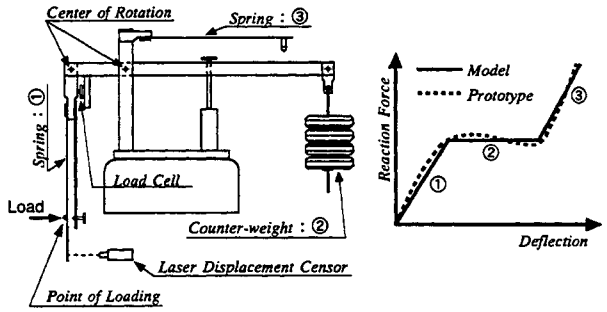

Fig. 4 Model of rubber fender and it's characteristic curve

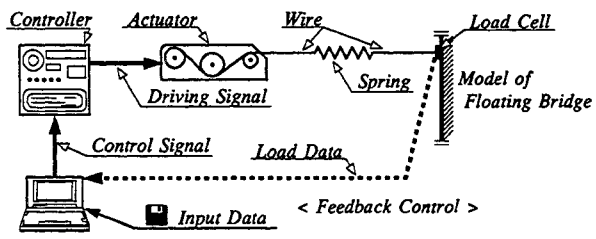

Fig. 7 Method of wind force loading

2.3 Measurements

In our experiments, the free surface displacement, wind load, motions of the floating body, the deflection of the rubber fender and reaction force of the rubber fender are measured. Capacitance-type wave probes and servo-type wave probes are used to measure the free surface displacement. The wind load is measured by the load cell where is placed between the floating bridge model and the wire as shown in Fig. 7.

The motions about the center of gravity of the floating bridge model are obtained by calculating the measured values of the displacement by eight laser displacement censors as shown in Fig. 8. The calculation is based on the geometrical relations between the displacement of the measured points and motions about the center of gravity of the floating bridge model. These relations on the measured point B-i (i=1,2,$\cdots$,8) can be expressed as follow:

$$D_1 = X_3 + [z_1 \cdot \tan(X_4/2) + y_1] \cdot \tan X_4 + [z_1 \cdot \tan(X_5/2) - x_1] \cdot \tan X_5 \quad (1)$$

$$D_2 = X_3 + [z_1 \cdot \tan(X_4/2) + y_2] \cdot \tan X_4 + [z_2 \cdot \tan(X_5/2) - x_2] \cdot \tan X_5 \quad (2)$$

$$D_3 = X_3 + [z_3 \cdot \tan(X_4/2) + y_3] \cdot \tan X_4 + [z_3 \cdot \tan(X_5/2) - x_3] \cdot \tan X_5 \quad (3)$$

$$D_4 = X_2 + [y_4 \cdot \tan(X_4/2) - z_4] \cdot \tan X_4 + [y_4 \cdot \tan(X_6/2) + x_4] \cdot \tan X_6 \quad (4)$$

$$D_5 = X_2 + [y_5 \cdot \tan(X_4/2) - z_5] \cdot \tan X_4 + [y_5 \cdot \tan(X_6/2) + x_5] \cdot \tan X_6 \quad (5)$$

$$D_6 = X_2 + [y_6 \cdot \tan(X_4/2) - z_6] \cdot \tan X_4 + [y_6 \cdot \tan(X_6/2) + x_6] \cdot \tan X_6 \quad (6)$$

$$D_7 = X_1 + [x_7 \cdot \tan(X_5/2) + z_7] \cdot \tan X_5 + [x_7 \cdot \tan(X_6/2) - y_7] \cdot \tan X_6 \quad (7)$$

$$D_8 = X_1 + [x_8 \cdot \tan(X_5/2) + z_8] \cdot \tan X_5 + [x_8 \cdot \tan(X_6/2) - y_8] \cdot \tan X_6 \quad (8)$$

where (x_i, y_i, z_i) is the co-ordinates of the measuring point when the floating bridge model is at rest. D_i refers to the difference between the measured value by laser displacement censor at rest and that in motion. X_i (i=1 $\sim$ 6) are the six-degree motions of the floating bridge as shown in Fig. 8. In Eq.(1)$\sim$(8), if an equation is subtracted from another equation in the same plane, eight equations can be obtained. For example, we can obtain a following equation from Eq. (1) and Eq. (3).

$$D_1 - D_3 = (y_1 - y_3) \cdot \tan X_4 + (-x_1 + x_3) \cdot \tan X_5 \quad (9)$$

By using the method of least squares for these eight equations, the time sequences of the six-degree motions of the floating bridge model are obtained.

The deflection of rubber fenders is measured at the point of loading shown in Fig. 4 by the laser displacement censor. The reaction force of rubber fender is obtained by correcting the data measured by the load cell as shown in Fig. 4.

2.4 External force

The condition of wind and wave in experiments is shown in Table 3. Case-1 is the condition under traffic regulation due to wind. The other cases are the condition during a typhoon. In this figure, θ and ψ are the angle of incident wave and the wind direction angle with respect to the axis of the floating bridge model, respectively as shown in Fig.5. The

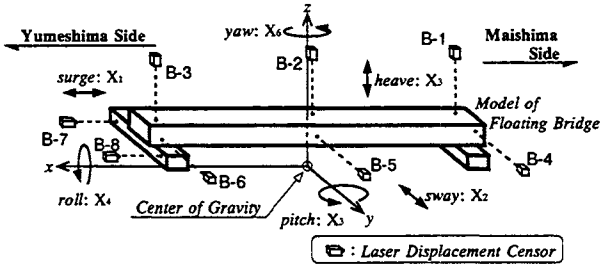

Fig. 8 Measuring point of the displacement of the floating bridge and definition of the motions

Table 3 Condition of the external force

Case	Wave			Wind	
	$H_{1/3}$ (m)	$T_{1/3}$ (s)	θ (deg)	U_{10} (m/s)	ψ (deg)
case-1	2.0	5.5	73.0	20.0	90.0
case-2	4.4	6.4	73.0	43.0	90.0
case-3	5.0	6.7	73.0	50.0	90.0
case-4	4.4	7.0	73.0	43.0	90.0
case-5	4.4	8.0	73.0	43.0	90.0
case-6	4.4	9.0	73.0	43.0	90.0

experiments in regular waves which correspond to the swell and those for other wind direction angles also carried out.

Bretschneider-Mitsuyasu spectrum is used as the irregular wave spectrum. The wind force is applied by the wind force loading device as explained in 2.2.

2.5 Type of experiments

In experiments, two kinds of experiments are carried out. One is the experiment for measuring the wave height in the channel without the floating bridge. The other is the experiment for measuring the motions of floating bridge in waves and wind. The purpose of experiment for measuring the wave height is to investigate the wave height distribution in the channel, especially at the place where the floating bridge model will be set up. Experiments for measuring the motions of floating bridge in waves and wind include the measurements the deflection of rubber fender etc. The two kind of experiments are carried out for two cases with a breakwater in the Maishima side of the entrance of the channel and with floating breakwaters in front of the pontoons of the floating bridge, respectively.

3. RESULTS OF THE EXPERIMENTS OF WAVE HEIGHT

First, the experiments of wave height in the state of present channel without a breakwater in the Maishima side of the entrance of channel and floating breakwaters are carried out.

Fig. 9 shows the wave height distribution of the irregular incident wave along the line which passes at the horizontal center of the Yumeshima side pontoon and is perpendicular to the axis of the channel. In this figure, the ordinate means the significant wave height divided by that the incident wave. And Yumeshima side's breakwater refers to the breakwater at the Yumeshima side's entrance of channel. From this figure, we can understand that the Yumeshima side's breakwater is very useful to decrease the wave height at the position where the Yumeshima side's pontoon of floating bridge is set up and wave height changes remarkably in the transverse direction of the channel.

Fig. 10 and Fig. 11 show measured wave spectrum at positions corresponding to both positions of pontoons of the floating bridge for a case with the breakwater for the yacht harbor and for a case with the floating breakwaters. The wave height is measured at the center and four edges of each pontoon. From these figures, it is found that the change of wave height inside each pontoon is very big.

However, it is important to obtain a relation between the typical wave height at the pontoon of the floating bridge and the incident wave height. Fig. 12 shows the average value of measured five wave heights at the position of the Maishima side's pontoon divided by the incident wave height. The abscissa is the significant wave period of incident wave. In this figure, the experimental results for three cases, that is, Ⅰ) for the present channel without breakwater for yacht harbor and floating breakwater, Ⅱ) with the breakwater for yacht harbor, Ⅲ) with floating breakwaters, are shown. With respect to the effect of the floating breakwater, the average value at the pontoon of the floating bridge is 0.39 ~ 0.49 times wave height measured in front of floating breakwater. This value is close to the estimated value from another fundamental three-dimensional experiments in which the two floating breakwaters are set up between the parallel channel walls. ([3])

4. COMPARISON OF THE EXPERIMENTAL RESULTS WITH CALCULATED ONES FOR MOTIONS OF THE FLOATING BRIDGE

4.1 Numerical calculation

The non-linear simulation calculations of the motions of the floating bridge are conducted by using following equations. ([4])

$$\sum_{j=1}^{6}\left[(M_{ij}+\mu_{ij})\ddot{X}_j+\lambda_{ij}\dot{X}_j+C_{ij}\dot{X}_j\left|\dot{X}_j\right|+B_{ij}X_j\right] = D_i(t)+F_{W_i}(t)+F_{D_i}(t)+F_{A_i}(t)+F_{C_i}(t) \quad (10)$$

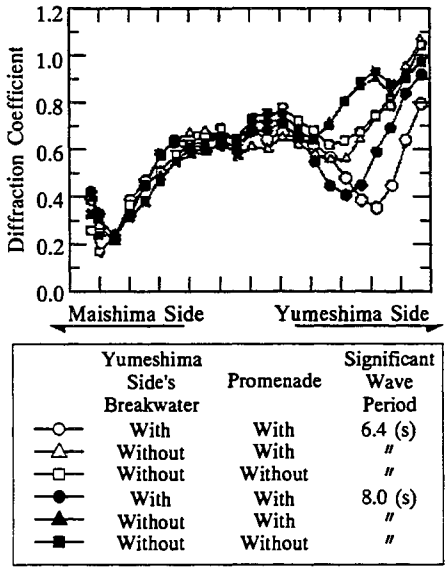

Fig. 9 Distribution of wave height in the channel

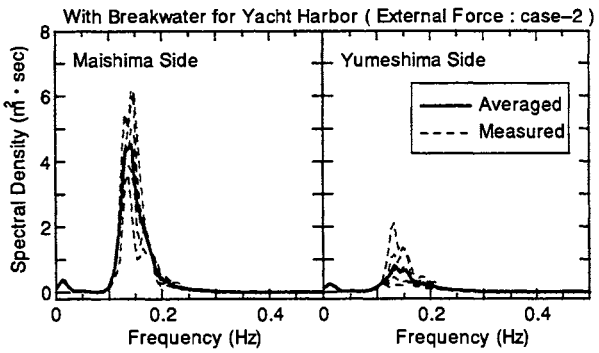

Fig. 10 Measured wave spectrum

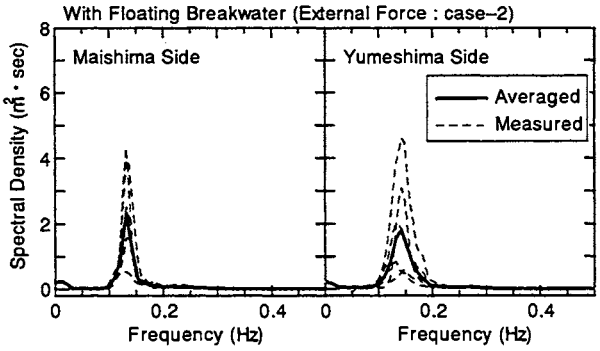

Fig. 11 Measured wave spectrum

where i=1 ~ 6 and

X_j : *displacement vector of a floating bridge*
M_{ij} : *mass matrix*
μ_{ij} : *added mass coefficients*
λ_{ij} : *wave damping coefficients*
C_{ij} : *non-linear damping coefficients*
B_{ij} : *hydrostatic restoring force matrix*
$D_i(t)$: *mooring force vector*
$F_{W_i}(t)$: *wave exciting force vector*
$F_{D_i}(t)$: *wave drift force vector*
$F_{A_i}(t)$: *wind force vector*
$F_{C_i}(t)$: *tidal current force vector*

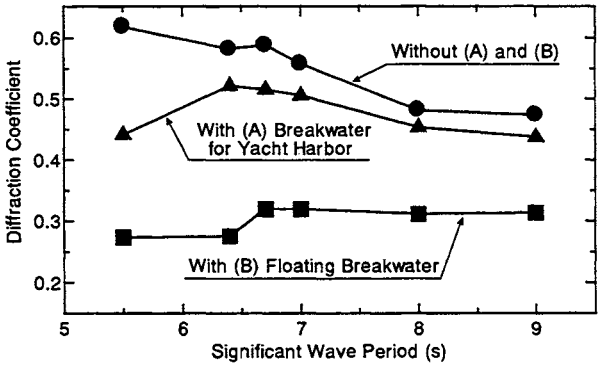

Fig. 12 Diffraction coefficient at the position of the Maishima-side pontoon

The radiation and diffraction forces are calculated for two pontoons in an open sea by using source distribution method. As for the added mass coefficients and wave damping coefficients used in Eq.(10), at the first step, the values at the period corresponding to the significant wave period of the incident wave are used. From the second step, the values at the average period which is obtained from the previous calculation of Eq.(10) are used. This operation is repeated until the average period obtained as the results of the calculation of Eq.(10) converges. The wave drift damping is calculated by Hsu's method.

The other calculation conditions are given as follows:

Ⅰ) As for the mooring force, the relation between the deflection and the reaction force in the mooring device model is used.

Ⅱ) The time sequence of the wind force used in the experiment is used for the wind force in the calculation.

Ⅲ) Average wave spectrum measured at five points inside the region corresponding to each pontoon, such as the wave spectrum in Fig.10 and Fig.11, is used for the calculation.

Ⅳ) The time sequence of the wave exciting force which is applied to the floating bridge is calculated as follows:

① The wave exciting force applied to each pontoon is calculated in frequency domain.

② The time sequence of the wave exciting force applied to each pontoon is calculated from wave exciting force obtained from ① and the average measured wave spectrum at the position of each pontoon obtained by the experiment.

③ The time sequence of the wave exciting force for the floating bridge is obtained by adding the time sequence of the wave exciting force for each pontoon.

4.2 Results and consideration

(1) In order to confirm whether prescribed wind force is applied to the floating bridge correctly, signal in wind force loading device is compared with the wind force which is measured by a load cell shown in Fig. 7. Fig. 13 shows the comparison of the input time sequence with the measured one for the wind load at loading point W-1 in case-2. The values in this figure, which are shown from now on, are for prototype. Fig. 14 shows the comparison for the spectrum obtained from input and measured time sequence of the wind load. From Fig. 13 and Fig. 14, it was found that prescribed wind force is applied to the floating bridge correctly. The same results as this case are obtained for the other loading points and experimental cases.

(2) The numerical results for the motion of the floating bridge are compared with measured ones when only the wind force is applied to the floating bridge. Fig. 15 is a comparison of the measured and calculated time sequence of the displacement of the floating bridge at the measuring point B-6 in case-2 in which only the wind force is applied to the floating bridge. As the displacement of the floating bridge are measured at eight points directly as shown in Fig.8, these measured displacement are used for the comparison with the numerical results. The calculated time sequence is good agreement with the measured ones.

(3) The numerical results for the motion of the floating bridge are compared with measured ones when both the wind force and wave force are applied to the floating bridge. Fig. 16 is the comparison of the measured and calculated average values for sway and roll motions of the floating bridge when both the wind force and wave force are applied to the floating bridge. In this figure, the results for the two cases, with the breakwater for the yacht harbor and with the floating breakwaters, are shown. These average values of sway and roll motions are mainly depend on the wind force. Fig. 17(a)～(c) are the comparison of the measured and calculated significant values for double amplitude of sway, heave and roll motions. In these figures, it is found that the difference between numerical results and measured ones is within about 20%. Fig. 18 (a), (b) are the comparison of the measured and calculated deflection in F-3 and F-5 fender. The deflection of fender is the sum of the average values and the amplitude of the deflection. In these figures, it is found that the difference between numerical results and measured ones is within about 20% same as the motion of the floating body.

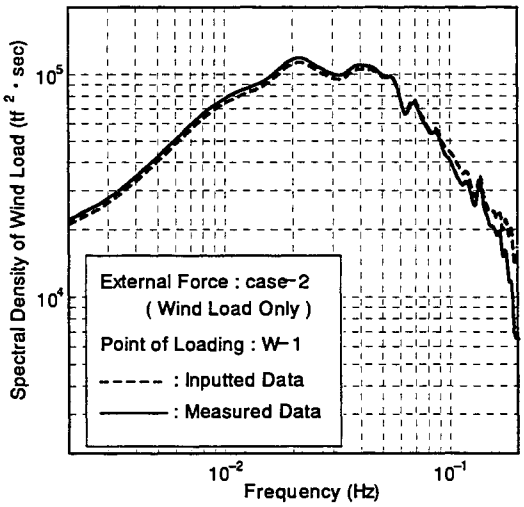

Fig. 14 Inputted and measured wind load spectrum

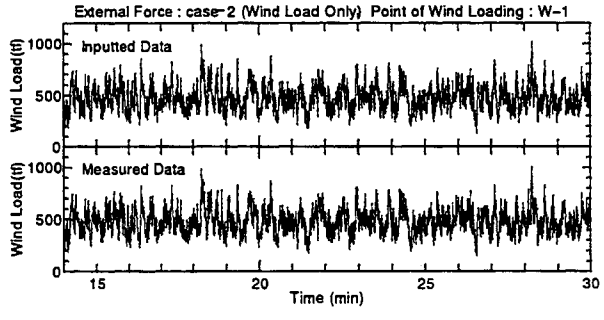

Fig. 13 Inputted and measured time history of the wind load

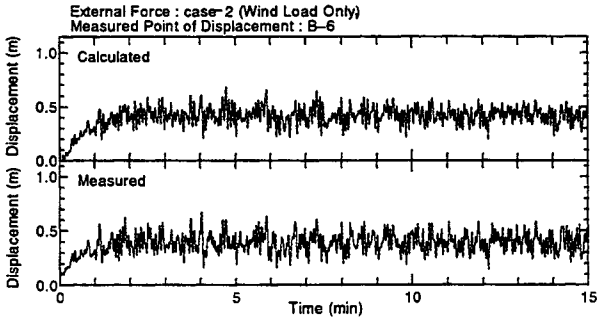

Fig. 15 Measured and calculated time history of the displacement of bridge (B-6)

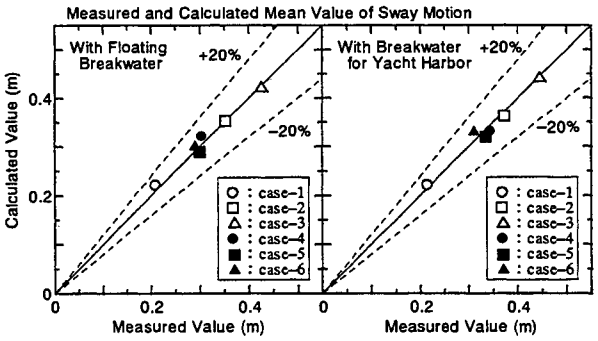

Fig. 16(a) Measured and calculated mean value of sway motion

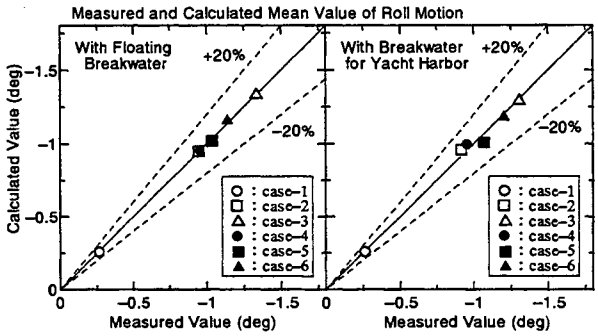

Fig. 16(b) Measured and calculated mean value of roll motion

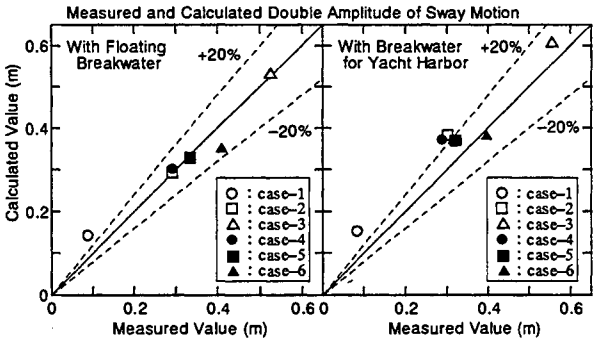

Fig. 17(a) Measured and calculated double amplitude of sway motion

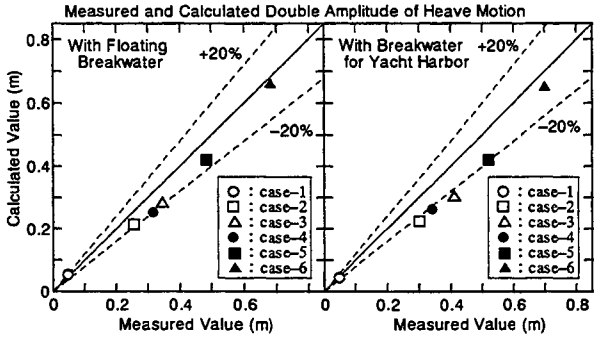

Fig. 17(b) Measured and calculated double amplitude of heave motion

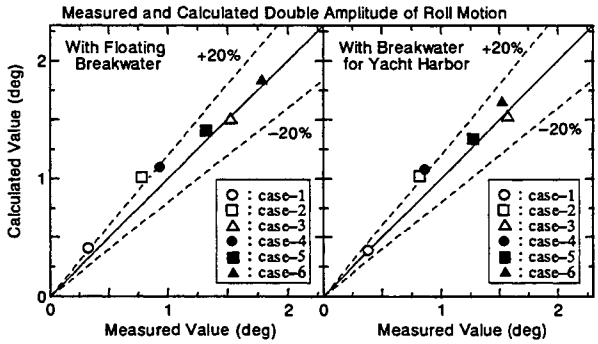

Fig. 17(c) Measured and calculated double amplitude of roll motion

5. CONCLUSION

The results of the hydraulic model tests for a moored floating bridge under design environmental conditions corresponding to the 100-year storm and the traffic regulation due to wind and non-linear simulation calculations corresponding to the experiments is summarized as follows:

(1) From the experiments of wave height in the channel, the distribution of the wave height in the channel are confirmed. From these experiments, the wave spectrum at the positions corresponding to the pontoons of the floating bridge is obtained. This wave spectrum is used in the numerical calculation of the motions of floating bridge and be applied in design.

(2) From the hydraulic model tests, data which are useful for the design, such as the motions of the floating bridge and the deflection of the fender etc., are obtained.

(3) From the results of the comparison of the measured results and calculated results for the motions of the floating bridge and the deflection of the fender etc., it is found that the numerical calculation method has a sufficient accuracy for the estimation of the motions of the floating bridge when the external force is wind force alone. When the external forces are wind force and wave

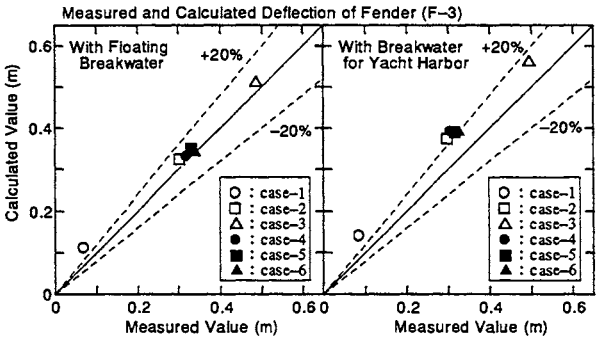

Fig. 18(a) Measured and calculated deflection of fender (F-3)

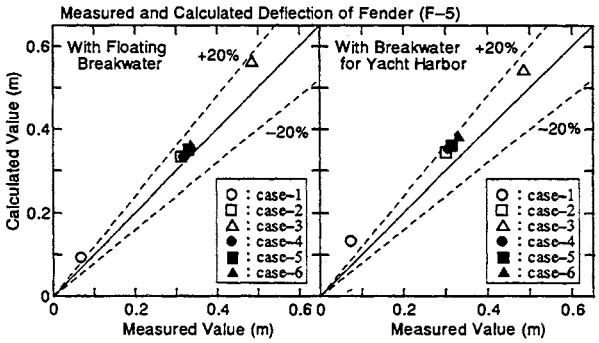

Fig. 18(b) Measured and calculated deflection of fender (F-5)

force, it is found that the difference between experimental results and calculated results is within about 20%.

(4) The rubber fender in prototype has a remarkable non-linear and hysteresis characteristics. In our experiments, the fender device whose reaction & deformation curve is shown as the broken line without the hysteresis characteristics is used. And this reaction & deformation curve is also used in numerical calculation. Therefore, the availability of the numerical calculation for prototype is not shown perfectly. The non-linear model which contain hysteresis characteristics of rubber fender is used in the numerical calculation which corresponds to the prototype of the floating bridge. The availability of this non-linear model for fender is shown by comparison between a numerical calculation and a hybrid simulation([5]). The hybrid simulation is composed of a computer, tri-axis compression test equipment and models of real rubber fenders. In hybrid simulation, numerical simulation for a two dimensional motion of the floating bridge is carried out. The instantaneous reaction force of the rubber fender which is the input for the numerical simulation is obtained by the compression test of the model of the rubber fender carried out simultaneously.

Incidentally the floating breakwaters in front of the pontoons of the floating bridge were not applied because it is found that the stability and safety of the floating bridge are sufficient if the floating breakwaters are not installed from the results of these experimental studies.

Acknowledgment: The writers wish to express their sincere appreciation to the members of the Committee of the Movable Floating Bridge (chairman: Prof. Eiichi Watanabe of Kyoto university) and the Special Committee of the Dynamic Motion (chairman: Prof. Kazuki Oda of Osaka City University).

References

[1] Hosogaya,K., Nekado,Y., Nagata,S., Fujita,T., Kadono,A. and Miyakawa,Y.: Development of New Floating Breakwater, Hitachi Zosen Technical Review, Vol.54, No.2,1993.

[2] Maruyama,T., Agawa,K. and Shimodoi,H.: Wind-tunnel test for the Maishima-Yumeshima Bridge, J. of Wind Engineering, JAWE, No.63, 1995.

[3] Nagata,S., Fujita,T., Oda,K., Maruyama,T., Takeda,S., Tanaka,H.: Development of Air-Controlled Type Floating Breakwater for Movable Floating Bridge, TECHNO-OCEAN'98, Kobe Japan,1998.

[4] Makihata,T., Yoguchi,M., Nagata,S., Miyake,S., Endo,H., Fujita,T. and Kato,E.: The Characteristics of Motion of Oil Storage Barges Moored in the Sea Confined by the Breakwater, Hitachi Zosen Technical Review, Vol.55,No.4,1995.

[5] Maruyama,T.,Kawamura,Y.,Takeda,S., Nagata,S., Yoshida,H. and Yamase,S.: Validation of mathematical fender model by hybrid simulation method, Proceedings of Coastal Engineering, JSCE,1990(in Japanese).

PROCEEDINGS OF THE THIRD INTERNATIONAL WORKSHOP ON VERY LARGE FLOATING STRUCTURES
(VLFS '99), VOL. I, EDS. R.C. ERTEKIN & J.W. KIM, 22-24 SEPTEMBER 1999, HONOLULU, HAWAII, USA

RELIABILITY ANALYSIS OF FRACTURE-BASED FATIGUE LIFE FOR MOBILE OFFSHORE BASE CONNECTORS

D.V. Ramsamooj, Professor, California State University, Fullerton
T. A. Shugar, Research Structural Engineer, NFESC, Port Hueneme, Ca.

ABSTRACT

A reliability analysis of the fracture-based fatigue life of proposed mobile offshore base (MOB) connectors is demonstrated. A performance function is defined in terms of nominal stress range, inherent defect or starter crack, and appropriate material properties, which are considered random variables. The reliability analysis is performed for a sea state 1-8 random loading having a Gumbel distribution. Where possible, uncertainty data for the random variables are obtained from published data relating to fatigue of steels. Otherwise, judgmental coefficients of variation are prescribed for purposes of demonstration. The fatigue life is assumed to follow the Weibull distribution. The reliability function is defined in terms of the mean fatigue life and the total uncertainty in the fatigue life.

Preliminary reliability calculations suggest that current design stress levels be reduced to meet the current fatigue life target reliability level for MOB connectors. Modest reductions appear to result in substantial increases in fatigue life, so that reliable fatigue design may be feasible.

1. INTRODUCTION

The MOB Standards and Criteria Working Group has chosen a reliability-based approach to the structural design of MOB in the *MOB Classification Guide and Commentary* [1]. The approach follows a recent trend towards risk-based technology in rule making. In addressing sources of uncertainty directly, it has the advantage of promoting uniform decision making by the structural design engineer.

There are two kinds of uncertainty in structural reliability, that due to randomness and that due to imperfect estimation procedures. The first pertains to the uncertainty of some load and resistance variables, such as stochastic wave fields and variations in yield strength, plate thickness, etc., due to manufacturing and/or corrosion. This leads to inherent uncertainty in both demand and capacity of a MOB structure regardless of the accuracy of the estimation and simulation procedures used. The second uncertainty is introduced via simplifications in the modeling or simulation procedures themselves, such as linearizations in hydrodynamic and structural analysis codes. Consideration of both types is an implied requirement of the reliability-based *Guide*.

Fatigue design at the structural component level for MOB is appropriately approached by an empirical SN-curve method cast within a reliability framework (e.g., Ang, et al. [3]). However, MOB connectors are a key technology issue by virtue of their importance, uniqueness and high estimated cost, which is roughly estimated at $80 million per module interface for one particular concept. The *Guide* currently specifies a life time target reliability of 0.9999 for fatigue design of connectors. Further, it has been estimated by the MOB Connector Working Group that a reasonable design life for connectors is five to ten years (Brown & Root [5]).

Fundamental approaches to MOB connector design are therefore warranted. Moreover, there are no SN-curve data in existence for large monolithic connector concepts, which currently involve plate thicknesses of 4-1/2 inches or greater. Thus, a fracture mechanics-based approach to fatigue design has been recommended by the MOB Standards and Criteria Working Group, and prescribed in the *Guide*.

Linear elastic fracture mechanics (LEFM) is a rational theory for failure analysis, which is founded in the theory of elasticity. A newly developed LEFM method for fatigue design of MOB connectors has been proposed by Ramsamooj [8]. In the present paper, this fracture-based method is cast within a direct reliability-based design procedure. Section 2 describes the corresponding theoretical development. Section 3 discusses uncertainty parameters and their values. Section 4 presents an example of the reliability method for connectors. Section 5 discusses reliability calculation results, and Section 6 presents a summary and conclusions.

2. THEORY

2.1 Fracture-Based Fatigue Life

Fatigue life N_f can be obtained by integrating a crack growth rate law, in this case derived by Ramsamooj [8],

$$\frac{dc}{dN} = \frac{8}{3\pi^2(1+n)}\frac{C}{EY}(\Delta K_I - \Delta K_{th})^2 \frac{K_{Ic}^2}{K_{Ic}^2 - K_I^2}$$

In this equation, c is the crack length, N is the number of cycles, C (equal to 0.63) is a non-dimensional constant, n is the strain hardening exponent, E is the modulus of elasticity, Y is the yield stress, K_I is the mode 1 stress intensity factor (SIF), ΔK_I is the SIF range for the cyclic stress field (tension and compression), ΔK_{th} is the threshold SIF range, and K_{Ic} is the fracture toughness. A similar crack growth rate equation has also been proposed which includes the effects of a marine environment. (See also, Ramsamooj and Shugar [9].)

Fatigue life is obtained by integrating over the crack length from an initial crack size c_0 to a final or failure crack size c_f as follows,

$$N_f = \int_{c_0}^{c_f} \frac{1}{dc/dN} dc$$

This integral may not be evaluated analytically for the subject crack growth rate law. Thus, it is evaluated numerically to produce fatigue life calculations.

Nonetheless, it is instructive to briefly illustrate the process with an analytical expression for N_f. To that end, a central crack of length 2c is considered in an unbounded elastic domain for which it may be assumed that ΔK_I can be replaced by $\Delta\sigma\sqrt{\pi c}$, where $\Delta\sigma$ is a range for load-induced, free field stress normal to the crack. Further, assume that no material strain hardening exists, and that crack growth occurs for all levels of stress range (i.e., n = 0 and ΔK_{th} = 0). Then, the integral for N_f becomes tractable as follows,

$$N_f = \int_{c_0}^{c_f} \frac{5.875EY[K_{Ic}^2 - (\sigma\sqrt{c\pi})^2]}{K_{Ic}^2(\Delta\sigma)^2 c\pi} dc$$

or,

$$N_f = \frac{5.875EY}{\pi(\Delta\sigma)^2}(\ln c_f - \ln c_0) - \frac{5.875EY\sigma^2}{(\Delta\sigma)^2 K_{Ic}^2}(c_f - c_0)$$

This fatigue life is proportional to the product EY and inversely proportional to the range of load-induced stress squared. For an infinite fracture toughness K_{Ic}, the fatigue life apparently remains finite using this simple version of the crack growth rate law.

Moreover, it is clear that an LEFM-based fatigue life calculation is independent of structural details, unlike an SN-curve approach that relies on families of curves peculiar to specific structural details. That is, LEFM is directly applicable to real structures provided only that they are manufactured of the same material used in laboratory test specimens to measure material properties such as K_{Ic}, Y, and E.

2.2 Reliability of Fracture-Based Fatigue Life

Ang [2] presented the following concepts. Due to its high variability, fatigue life N_f is considered a random variable. A reliability measure would be a function of the design variables. Accordingly, a performance function of multiple random variables Z is defined, in this case as,

$$Z \equiv N_f = g(\Delta\sigma, c_0, K_{Ic}, \Delta K_{th}, Y, E)$$

It is noted that the constant C, the material parameter n, and the failure crack size c_f, are treated deterministically.

Let μ_Z and σ_Z be the mean and standard deviation of Z, respectively. Then,

$$\mu_Z = N_f(\mu_{\Delta\sigma}, \mu_{c_0}, \mu_{K_{Ic}}, \mu_{\Delta K_{th}}, \mu_Y, \mu_E)$$

where μ_X represents mean values of the respective variables in subscripts.

Then, to a first order approximation, the standard deviation of Z is,

$$\sigma_Z^2 = \sum_{i=1}^{6} c_i^2 \sigma_{Xi}^2 + \sum_{i=1}^{6}\sum_{i=1}^{6} \rho_{ij} c_i c_j \sigma_{Xi}\sigma_X$$

where,

$$c_1 = \frac{\partial N_f}{\partial \Delta\sigma}, \quad c_2 = \frac{\partial N_f}{\partial c_0}, \quad c_3 = \frac{\partial N_f}{\partial K_{Ic}}$$

$$c_4 = \frac{\partial N_f}{\partial \Delta K_{th}}, \quad c_5 = \frac{\partial N_f}{\partial Y}, \quad c_6 = \frac{\partial N_f}{\partial E}$$

and where, $\sigma_{X1} = \sigma_{\Delta\sigma}$, $\sigma_{X2} = \sigma_{c_0}$, etc. That is, corresponding σ_x-terms exist for K_{Ic}, ΔK_{th}, Y, and E. The term $\rho_{12} = \rho_{21}$, for example, is the correlation between $\Delta\sigma$ and c_0. Explicit expressions for all the derivatives are available for the aforementioned simplification, but for the subject crack growth rate law

they are in general evaluated numerically.

Since there is no correlation between load-induced stress range $\Delta\sigma$ and the starter crack length c_0, ρ_{12} is zero. Similarly, ρ_{ij} equals zero for all i and j. Therefore,

$$\sigma_Z^2 = \sum_{i=1}^{6} c_i^2 \sigma_{Xi}^2$$

The total uncertainty in the stress range is,

$$\Omega_{\Delta\sigma} = \frac{\sigma_{\Delta\sigma}}{\mu_{\Delta\sigma}} = \sqrt{\delta_{\Delta\sigma}^2 + \Delta_{\Delta\sigma}^2}$$

where $\delta_{\Delta\sigma}$ and $\Delta_{\Delta\sigma}$ are the scatter of the stress range data and the coefficient of variation (CoV) representing the uncertainty in the estimated values of the means, respectively. Similar total uncertainty terms may be written for the variables c_0, K_{1c}, ΔK_{th}, Y, and E.

The total uncertainty in fatigue life is expressed as,

$$\Omega_Z^2 = \Omega_g^2 + \frac{1}{\mu_Z^2}(c_1^2\sigma_{\Delta\sigma}^2 + c_2^2\sigma_{c0}^2 + c_3^2\sigma_{K_{1c}}^2 + c_4^2\sigma_{\Delta K_{th}}^2 + c_5^2\sigma_Y^2 + c_6^2\sigma_E^2)$$

$$= \Omega_g^2 + \sum_{i=1}^{6} c_i^2 \Omega_{Xi}^2$$

where $\Omega_g^2 = \delta_g^2 + \Delta_g^2$, and δ_g and Δ_g are, respectively, the scatter in the model validation data, and the uncertainty in the predicted mean life associated with imperfection in the theory of the fatigue life model.

The distribution of fatigue life under a constant stress range follows the Weibull distribution as described by Ang [2]. In a fracture mechanics setting, this distribution is a monotonically increasing function consistent with the idea of cumulative fatigue crack growth. The resulting reliability function (i.e., probability of no fatigue failure) can be shown to be

$$L(N_f) = \exp\left\{-\left(\frac{N_f}{\overline{N}_f}\right)\Gamma(1+\Omega_Z^{1.08})\right\}^{\Omega_Z^{-1.08}}$$

where $\overline{N}_f$ is the deterministic or mean fatigue life predicted by the crack growth rate model (in contrast to the probabilistic fatigue life N_f), $\Gamma()$ is the gamma function, and Ω_Z is the total uncertainty in the fatigue life, assuming that the minimum performance level is zero. (See also, Ang et al., [3])

3. UNCERTAINTY IN FATIGUE LIFE VARIABLES

The reliability parameters consisting of the means and standard deviations are given in Table 1 and discussed below. Due to the huge monetary investment that a MOB implies, the cost of developing uncertainty data beyond usual standards should be evaluated against the extra cost incurred due to uncertainty. This is particularly true for parameters such as $\Delta\sigma$, c_0, K_{1c} and ΔK_{th}.

3.1 Wave Load-Induced Stress Range, $\Omega_{\Delta\sigma}$

Wave loads have significant uncertainty. They are developed from random environmental force input data, and computed by imperfect hydrodynamic computer programs. Stresses are, in turn, computed by imperfect finite element computer programs. The resulting uncertainty in nominal stress range can be very substantial.

Sea state data in this study were proposed standard conditions for the North Sea and were taken from Schutz and Pook [11]. They are reproduced here in Table 2. The relative occurrence of sea states within small intervals of significant wave height, $H_{1/3}$, was proposed for use in calculating fatigue loads on tubular members for fixed and moored floating platforms. Another motivation for proposed sea state standards is for uniform comparison of alternative fatigue life models.

Although more applicable to fixed platforms than to floaters, it is assumed that wave loads are linearly proportional to wave heights. In this case, average wave heights are computed for each sea state from the $H_{1/3}$ values in Table 2. Further, a common assumption is that MOB modules are to be disconnected in SS7 or SS8, freeing the connectors from SS9 and greater load-induced stresses. The maximum hot-spot stress is correlated with the average $H_{1/3}$ value for the highest applicable sea state (SS8), 25.7 feet.

It is commonly assumed that $H_{1/3}$ waves for SS7 or SS8, are less damaging than waves in mid range sea states. That is, for high cycle fatigue, a relatively few very high waves are not as critical to fatigue life. However, this assumption depends on the SIF and the lower bound specification for damage, i.e., the threshold SIF, ΔK_{th}. Similarly, it is assumed that for high cycle fatigue the effects of loading sequence in random loading is negligible.

Preliminary comparisons of predictions to experimental data for assessment of linearized hydrodynamic computer programs for MOB application have been completed (Bechtel National, Inc., [4]). The

results suggest CoV's from 10% to 20% for prediction of motion response of five connected MOB single base units in regular waves. However, physical modeling testing that includes hydroelastic behavior is needed to assess this uncertainty.

Uncertainty in the load-induced stress is largely obviated if it may be assumed that conditions leading to crack growth are being continuously monitored, and that crack growth is controlled through manual intervention. This strategy was assumed for demonstration purposes, and a rather low CoV of 5% was selected for load-induced stress range.

3.2 Starter Crack, Ω_{c0}

Knowledge of maximum crack sizes is critical to the success of LEFM applications in both design and maintenance of MOB connectors. Recent improvement in performance of NDE methods, such as magnetic particle and eddy-current methods, allow detection of cracks as small as 0.1 mm, with high confidence. This relates to precision of measurement and thus to scatter or variability in the starter crack size, and that in turn relates to total uncertainty in starter crack size, c_0.

Measured starter crack sizes will have random distribution. As in Jiao and Moan [6], it is assumed the initial crack size distribution will be determined from measurements by appropriate NDE methods during production of MOB connectors. Further, the crack size distribution is considered a normal distribution with a mean of $c_0/2$ and a CoV of 50%. For polished surfaces, the largest value of c_0 is assumed to be 0.008 inches.

Similar procedures may likely form the basis of in-service inspection procedures for MOB connectors. Application of fracture mechanics has the advantage of incorporating structural inspection results into the fatigue model for updating the degree of fatigue damage accumulation.

It is assumed that during the connected mode of operation for MOB, cyclic strain in connectors will be continuously recorded. Further, the progress of cracks will be periodically determined by inspection. These data may be used for condition assessment of connectors, and for reassessment of the reliability-based fatigue life for connectors. While this has no direct bearing on the uncertainty of starter crack size during the design stage, it does speak to design-for-maintenance strategies such as fail-safe and damage-tolerant design. These strategies, which have been successful in the aircraft industry, can provide updated estimates of fatigue life reliability and confidence in controlling the fatigue problem of MOB connectors.

3.3 Fracture Toughness, Ω_{K1c}

Fracture toughness is a random material property having fundamental uncertainty. In a study by Rosenfield and Marschall [10] for Oak Ridge National Laboratory, many cases of failure were reviewed and analytically investigated using fracture mechanics. About half of these failures were ascribed to fatigue, with weld defects the second leading cause of failure. The result of the study was that SIF's at failure (from post mortem calculations) correlated poorly with book values of fracture toughness.

In a related previous study, these authors reported that in 60% of the cases the calculated SIF's were accurate to within 10%, and in 15% of the remaining cases the SIF's were conservative. In 25% of the cases, the method of fracture mechanics analysis was in fact non-conservative. Further, no significant improvement was noted in the accuracy of post mortem LEFM analyses during the 12 years since the previous study leading up to their report.

The method of LEFM analysis itself was deemed accurate in theory. However, it was concluded that specification of inaccurate input data during the design process, particularly an improper value of fracture toughness (too often only an approximation), was the main reason for the poor correlation.

The material assumed in the present study is A533B-1 steel, a common steel in the nuclear power industry and a widely used steel for structures in general. The book value for the mean K_{1c} is 200 ksi-in$^{1/2}$. A CoV of 9.0% in the fracture toughness values of low to high strength steel and aluminum was reported in the aforementioned study, and it is used here for demonstration purposes.

3.4 Threshold Stress Intensity Factor, $\Omega_{\Delta Kth,0}$

As the value of SIF range ΔK_1 approaches ΔK_{th} from above, the fatigue life approaches infinity asymptotically. This means that for ΔK_1 below the mean value of threshold SIF, the fatigue life is infinite. The discontinuity caused by this produces numerical problems in the calculation of the mean fatigue life. Consequently, the CoV is currently not handled in the usual manner. The uncertainty is indirectly accounted for by reducing the mean value of the threshold SIF by an amount equal to what otherwise would be the CoV, in this case 20%. This procedure essentially treats ΔK_{th} deterministically, so that $\Omega_{\Delta Kth,0}$ is in effect zero. This strategy is believe to produce a conservative result. A representative mean value of 7.6 ksi-in$^{0.5}$ was taken from Paris et al. [7].

3.5 Yield Strength, Ω_Y

A CoV of 3% was used in this study for the yield strength of A533B-1 steel. However, it could be somewhat higher in practice, even assuming very good laboratory measurement of yield strength.

3.6 Young's Modulus, Ω_E

A CoV of 2% for Young's modulus can be expected assuming good laboratory testing. Uncertainties in this range may be considered almost negligible in comparison to sources elsewhere in the formulation.

3.7 Fatigue Life Model, Ω_g [8]

The fatigue life model is regarded as imperfect having a fundamental prediction uncertainty. The bias of model predictions for 38 cases of published crack propagation data was better than 0.95, so that the uncertainty in mean fatigue life prediction Δ_g is set equal to 5%. The scatter δ_g is equal to about 10%. Thus, the total uncertainty in model prediction is 11.2%.

4. RELIABILITY ANALYSIS EXAMPLE

The design procedure developed so far calculates reliability as a function of the variables stress range and fatigue life. It is embodied in a computer program called MOBYDICK featuring the subject crack growth rate law, and developed to provide a framework for fatigue analysis of MOB connectors [8]. Currently, it is restricted to connector systems based on monolithic thick tubes. If necessary, it should be relatively straightforward to extend this program to other connector systems, and to calculate any one of the three principal variables given the other two, as was done in [3]. The computer program might then be more forthcoming in a design environment.

The mean and standard deviation, μ_X and σ_X respectively, are required input data for the following variables: connector load-induced stress range, $\Delta\sigma$; size of the starter defect, c_0; fracture toughness, K_{1c}; threshold SIF, ΔK_{th}; yield strength, Y; and Young's modulus, E.

One proposed MOB connector concept comprises a 20 foot diameter steel tube having a wall thickness of 6 inches, and a 12 foot diameter thick-walled shear pin. It is depicted in Figure 1 along with the assumed loads and crack growth pattern, which is discussed elsewhere [9]. This connector concept is the subject for illustrating the proposed reliability-based design process.

Consistent with LEFM, a brittle fracture mode is assumed for failure of the connector. The appropriate SIF equations are coded in MOBYDICK for the subject connector [8,9]. In this case there are two phases to the fracture. The first is complete fracture through the thickness of the thick-walled tube, starting from a quarter-circle surface crack. The second is continued fracture along the circumference of the tube until the limit state is violated and failure occurs.

4.1 Connector Loads

The following connector loads are used in this demonstration to define the combined load (Brown & Root [5]):

Loads	
Axial: 100,000 tonnes	(75 ksi)
Vertical: 36,000 tonnes	(27 ksi)
Transverse: 12,000 tonnes	(9 ksi)

The axial force is a tension force. Corresponding hot-spot stresses are shown in parentheses. The latter two values are simple-products of 75 ksi and the ratio of the loads to the largest load. A finite element analysis of the stresses in the subject connector was reported by Brown & Root [5]. The stress component data were not given, but the maximum Von Mises stress was observed to be 75 ksi for an axial load of 100,000 tonnes. This may be considered a hot-spot stress in the connector.

4.2 Limit State Equation

For combined loading, the norm (Euclidean) of these three stresses is used to compute the maximum combined hot-spot stress, 83.2 ksi. The axial, vertical, and transverse stresses are also used to calculate the SIF's for the three modes of fracture K_1, K_2, and K_3, respectively, in MOBYDICK, as shown in [8]. An equivalent SIF, K_{1eq}, is then formed from the norm of these three SIF's. It is then compared with fracture toughness K_{1c}, leading to the limit state equation,

$$K_{1eq} - K_{1c} = 0$$

in the proposed fracture-based fatigue design process.

4.3 Fatigue Crack Initiation Criterion

The crack initiation criterion is given by

$$\frac{\Delta K_{1eq}}{\sqrt{\rho}} = 10\sqrt{Y}$$

where ρ is the crack tip radius equal to 0.008 inches and Y is the yield stress. It is discussed in [8,9].

4.4 Material Properties

For A533B-1 steel, the following material properties are appropriate and were prescribed in MOBYDICK.

Material Properties
Fracture Toughness, K_{1c} = 200 ksi-in$^{0.5}$
Threshold SIF, $\Delta K_{th,0}$ = 7.6 ksi- in$^{0.5}$
Yield Strength, Y = 70 ksi
Young's Modulus, E = 29,600 ksi
Strain hardening exponent, n = 0.2

The last parameter represents an engineering correction in LEFM for the effect of strain hardening at a crack tip in an elastic-plastic material.

When LEFM is applied to fatigue, a stress ratio R is used to characterize the cyclic stress field associated with ΔK_1. It is the ratio of minimum to maximum stress in a single excursion of the stress-time history. It appears reasonable to assume a stress ratio of R equal to -0.9 for stresses induced by oscillating wave action. It comes into play in the calculation of ΔK_{th} as follows,

$$\Delta K_{th} = \Delta K_{th,0}\sqrt{\frac{1-R}{1+R}}$$

where $\Delta K_{th,0}$ is the measured threshold SIF.

5. RESULTS OF RELIABILITY CALCULATION

The computer program MOBYDICK was used to compute the mean fatigue life as a function of maximum combined hot-spot stress for a number of different trial alloys. Corresponding to the maximum hot-spot stress in this example, the highest mean fatigue life, $11.2(10)^6$ cycles, was given by an A533B-1 steel connector. It is noted that crack growth initiation occurred in SS7 during this calculation. Further, no allowance for marine stress corrosion was made. (See reference [9] for these results.)

Then, reliability as a function of fatigue life, i.e., $L(N_f)$, was computed for the subject connector by MOBYDICK. The results are shown in Figure 2 for two maximum hot-spot stress levels, 75 ksi (517 MPa), and 83.2 ksi (574 MPa), the latter being the combined hot-spot stress for the subject connector, and the former an assumed lower level combined hot-spot stress for comparison.

For a reliability of 0.99 with a maximum hot-spot stress of 83.2 ksi, the fatigue life N_f for an A533B-1 connector is only about $1.6(10)^6$ cycles. However, for a reliability of 0.99 with a reduced maximum hot-spot stress of 75 ksi, the fatigue life N_f of an A533B-1 connector is about $17.5(10)^6$ cycles. A reduction in maximum hot spot stress of about 10% produces a one order magnitude increase in fatigue life, so the sensitivity of fatigue life to maximum hot-spot stress is considerable at this stress level. Further, N_f equal to $1.6(10)^6$ cycles is also nearly an order magnitude below the mean value, and indicates the relative cost of the total uncertainty.

Assuming MOB connectors are exposed to a 10s average wave period over their life span, the calculated fatigue life is 5.6 years at a maximum hot-spot stress level and reliability of 75 ksi and 0.99, respectively. For 83.2 ksi, the calculated fatigue life is only one-half year. MOB design life is specified at 40 years, although, according to some connector designers, it might be reasonable to assume that connectors will be replaced every five to ten years. However, the life time target reliability for MOB connectors is currently specified to be much greater than 0.99 in the *MOB Classification Guide and Commentary* [1]

Nonetheless, the result of this reliability-based design demonstration is that the subject connector design would be deemed wholly unacceptable at the given maximum hot-spot stress level, 83.2 ksi, and reliability, 0.99. However, due to the sensitivity of fatigue life to the level of hot-spot stress, significant reductions in the maximum hot-spot stress could result in connector designs with reliable fatigue resistance.

6. SUMMARY AND CONCLUSIONS

A preliminary, direct reliability based fatigue design procedure has been outlined and demonstrated for large monolithic steel components typical of MOB inter-module connector systems. The reliability methodology itself has been adapted from a method proposed elsewhere for MOB structural components other than connectors. Aside from this methodology, the physical basis used for addressing fatigue is a fundamental approach based in LEFM. Moreover, it employs a new analytical model for crack propagation, which is well validated and believed to be a substantial improvement over existing models.

There remain issues in handling uncertainty for the load-induced stress range and threshold stress intensity factor range variables, and the preliminary version of the fatigue design computer program needs to be generalized. However, the framework of the reliability-based fatigue life model is in place.

Assuming that design life spans for connectors are five to ten years, preliminary structural reliability calculations suggest that design stress levels for monolithic MOB connector concepts will have to be reduced to achieve current life-time target reliabilities. However, this should be feasible because fatigue life appears to increase substantially with reasonable reductions in current design stress levels.

ACKNOWLEDGEMENT

This work was sponsored by the Office of Naval Research MOB Science and Technology Program. The authors would like to express their appreciation to Prof. Al Ang, University of California at Irvine, Dr. Max Cheung, MCA Engineers, Inc., and Dr. Richard Yee, ABS Americas, for their interest.

REFERENCES

[1] ABS (1999). "MOB Classification Guide and Commentary," Revision 10, ABS Americas, Houston, September 1999.

[2] Ang, A. H-S. (1974). "A Comprehensive Basis for Reliability Analysis and Design," Japan-U.S.A. Joint Seminar on Reliability Approach in Structural Engineering, Marzuen, Co. Ltd., Tokyo, pp. 29-47.

[3] Ang, A. H-S, M. C. Chueng, T. A. Shugar and J. Fernie (1999). "Reliability-Based Fatigue Analysis and Design of Floating Structures," Third International Workshop on Very Large Floating Structures, Honolulu, 22-24 September 1999.

[4] Bechtel National, Inc. (1999). "Mobile Offshore Base (MOB) Design Tools and Procedures - Draft Validation Summary Report," Contract No. N47408-93-D-7001, San Francisco, June 1999.

[5] Brown & Root (1999). "Mobile Offshore Base (MOB) Connector System Study," Final Report No. CM-0031, Brown & Root, Inc., Houston, June 1999.

[6] Jiao, G. and T. Moan (1992). "Reliability-Based Fatigue and Fracture Design Criteria for Welded Offshore Structures," Engineering Fracture Mechanics, Vol. 41, No. 2, pp. 271-282, 1992.

[7] Paris, P. C., R. J. Buck, W. G. Weasel, and T. R. Merger (1971). "Extensive Study of Low Fatigue Crack Growth Rates in A533 and A508 Steels," ASTM Stress Analysis and Growth of Cracks, Proceedings of the National Symposium on Fracture Mechanics, Part I, STP, 196-217.

[8] Ramsamooj, D. V. (1999). "Fracture Mechanics Fatigue Design for Mobile Offshore Base Connectors," MCA Engineers, Inc., Costa Mesa, Ca. August 1999.

[9] Ramsamooj, D. V. and T. A. Shugar (1999). "Prediction of Fracture-Based Fatigue Life of Connectors for the Mobile Offshore Base," Third International Workshop on Very Large Floating Structures, Honolulu, 22-24 September 1999.

[10] Rosenfield, A. R. and C. W. Marschall, (1993). "Fracture-mechanics based failure analysis," Engineering Fracture Mechanics, Vol. 45, No. 3, pp. 333-338.

[11] Schutz, W. and L. P. Pook (1987). "WASH (Wave Action Standard History) - A Standardized Stress Time History," Steel in Marine Structures, Eds., C. Noordhoek and J. de Back, Elsevier Science Publishers, BV, Amsterdam, 1987.

Table 1. Reliability Parameters

	Mean, μ_X	Standard Deviation, σ_X
Starter Crack	0.004 in.	0.002 in
Maximum Hot Spot Stress	75 ksi 83.2 ksi	3.75 ksi 4.16 ksi
Fracture Toughness	200 ksi-in$^{1/2}$	18 ksi-in$^{1/2}$
Threshold SIF R = 0	7.6 ksi-in$^{1/2}$	0
Yield Strength	70 ksi	3.5 ksi
Young's Modulus	29,600 ksi	600 ksi
Fatigue Life Model scatter, $\delta_g = 0.10$ uncertainty, $\Delta_g = 0.05$		

Table 2. Approximation of Sea State Data for the North Sea

Sea State	$H_{1/3}$ m*	Range m	Wave Period, s	Time %
0	1.75	0.00-1.95	5.9	38.5
1	2.55	1.95-2.85	6.6	28.5
2	3.40	2.85-3.80	6.9	17.5
3	4.15	3.80-4.45	7.3	7.18
4	4.80	4.50-5.10	7.7	3.40
5	5.40	5.10-5.75	8.0	2.16
6	6.15	5.75-6.55	8.4	1.31
7	6.90	6.55-7.35	8.7	0.678
8	7.80	7.35-8.30	9.1	0.334
9	8.80	8.30-9.40	9.5	0.156
10	10.35	9.40-12.55	10.2	0.0797
11	13.60	12.55-	11.5	0.0043

*One meter equals 3.281 feet.

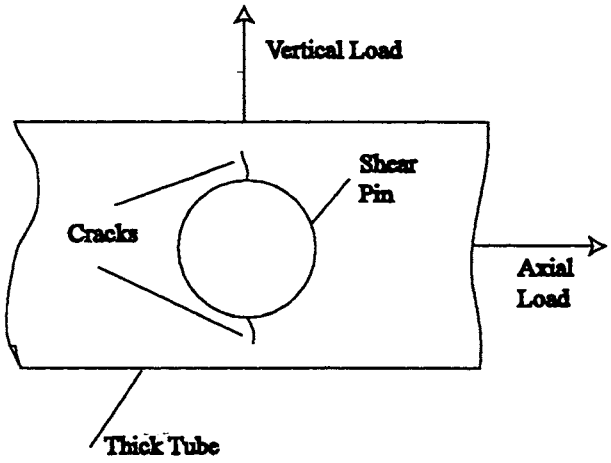

Figure 1. Crack Pattern in Monolithic Steel Connector

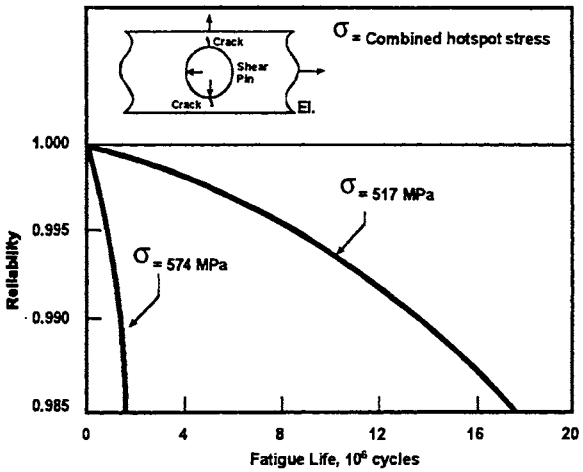

Figure 2. Reliability versus Fatigue Life for A533B-1 Steel Connectors (1 MPa = 0.145 ksi)

PROCEEDINGS OF THE THIRD INTERNATIONAL WORKSHOP ON VERY LARGE FLOATING STRUCTURES
(VLFS '99), VOL. I, EDS. R.C. ERTEKIN & J.W. KIM, 22-24 SEPTEMBER 1999, HONOLULU, HAWAII, USA

RELIABILITY-BASED FATIGUE ANALYSIS AND DESIGN OF FLOATING STRUCTURES

A.-H. Ang[1], M.C. Cheung[2], T.A. Shugar[3] and J.D. Fernie[4]

1 Research Professor, University of California, Irvine, CA
2 President, MCA Engineers, Inc., Costa Mesa, CA
3 Research Structural Engineer, Naval Facility Engineering Service Center, Port Hueneme, CA
4 Manager, LNG Marine Operations, Marathon Oil Company, Houston, TX

Abstract

Floating structures are more susceptible to fatigue damages than land-based structures. Due to the large uncertainty occurring in a number of key parameters, fatigue life may be modeled as a random variable, and thus safety against fatigue failures can be systematically evaluated in terms of probability.

A technical procedure for a reliability-based approach to fatigue analysis and fatigue-resistant design has been developed. It assumes that random loading can be modeled with beta distribution and fatigue is characterized by a SN relationship. Weibull distribution is adopted for formulating the reliability function representing the probability of a failure-free life.

The procedure was applied to the stress-range data measured on an existing LNG tanker and to the analytical model of a newly designed double hull tanker with ABS's DLA rating. In both cases, the level of reliability is about 0.85. Ironically, this range of reliability is significantly lower than that used in conventional Civil Engineering for land-based buildings.

1.0 Introduction:

Metal structures are generally susceptible to fatigue damage that accumulates with repeated cyclic loadings. Such damages invariably occur at locations of welded joints or where there is high stress concentration. The physical process of fatigue is rather complex. For practical purposes, engineering consideration of fatigue resistance has relied on the use of SN relationships that are developed from tests of specific welded joints under constant amplitude cyclic loadings, and invoking the linear Miner's cumulative damage rule when variable or random loadings are involved. However, even under constant-amplitude loadings, very large scatter in the fatigue life can be observed; consequently, there is considerable uncertainty in the prediction of fatigue life of a welded joint in any metallic structure. There is, of course, also uncertainty in the cyclic loadings that tend to induce fatigue damage. In light of these uncertainties, fatigue life of a structure or of a welded joint may be predicted only in terms of reliability (i.e., probability of no fatigue failure within a given life).

Proposed herein is a practical procedure for assessing the reliability of a fatigue life, as well as for determining the allowable stress-range for design within specified target reliability. It is applicable to structural components of floating structures, such as the proposed Mobile Offshore Base. The same procedure has been proposed and used in bridge structures (Ref. 1) and available for ship structures in a Ship Structures Committee Report (Ref. 2). Other equivalent reliability–based methods for fatigue analyses are available (e.g. Ref. 3). All such methods are also based on the same physics of fatigue; i.e. the SN relationships and Miner's damage rule; however, the reliability formulations are based on different assumptions.

Section 2 of this paper details the theoretical development. Section 3 explains the Hull Monitoring System that collects the stress range data on board of a LNG tanker. The recorded stress-range data is used to calibrate the reliability level of such construction with the observed fatigue life at cracked locations. Section 4 discusses the results from this procedure when applied to a new double hull tanker designed to DLA notation. Sensitivity analysis of the reliability to several c.o.v.s was performed and is presented at the end of Section 4. Some conclusions were drawn in Section 5.

2.0 Reliability Analysis:

Analysis of Reliability against Fatigue – As fatigue is a process of cumulative damage, the conditional probability that failure will occur in the next loading cycle should monotonically be increasing with the

life spent; i.e., the *hazard function* should be monotonically increasing (Ref. 4). A probability distribution with this property is the Weibull distribution, whose hazard function is

$$h(n) = \frac{k}{w-\varepsilon}\left(\frac{n-\varepsilon}{w-\varepsilon}\right)^{k-1}; \quad k > 1.0 \qquad (1)$$

The corresponding reliability function is (Ref. 5),

$$L(n) = exp\left[-\int_0^n h(n)dn\right] = \exp\left[-\left(\frac{n-\varepsilon}{w-\varepsilon}\right)^k\right] \qquad (2)$$

Where: w = the most probable life;
ε = the minimum life
k = the shape parameter.

With a conservative assumption of a zero minimum life, i.e.

$$\varepsilon = 0$$

the remaining two parameters, w and k, are related to the mean and standard deviation of the fatigue life as follows:

$$\overline{n} = w\Gamma\left(1+\frac{1}{k}\right) \qquad (3)$$

and,

$$\sigma_N = w\left[\Gamma\left(1+\frac{2}{k}\right) - \Gamma^2\left(1+\frac{1}{k}\right)\right]^{1/2} \qquad (4)$$

from which the c.o.v. becomes,

$$\Omega_N = \sigma_N / \overline{n} \cong k^{1.08} \quad \textit{(numerically fitted)}$$

Therefore,

$$k = \Omega^{-1.08} \qquad (5)$$

And thus, the reliability function, Eq. 2, becomes,

$$L(n) = exp\left[-\left\{\frac{n}{\overline{n}}\Gamma\left(1+\Omega^{1.08}\right)\right\}^{\Omega^{-1.08}}\right] \qquad (6)$$

Physical Basis of Fatigue – As alluded to earlier, a practical approach to fatigue may be based on available SN relationships for the type of welded joints under consideration. In this respect, fatigue failure is defined also consistent with that underlying the construction of the SN relationships, which means the occurrence of observable cracks in the weld material or weld-affected zones.

Under constant-amplitude stress-range, the SN relationship represents the regression equation of available test data, given as

$$ln\ \overline{n} = c - m \cdot ln\ s$$

or

$$\overline{n} = c/s^m$$

Whereas under variable or random stress-ranges, the Miner's linear damage rule may be invoked, which says that the total damage under variable loadings is

$$D = \sum_{all\ i} \frac{n_i}{\overline{n}(s_i)}$$

and fatigue failure will occur when

$$E(D) = E\left[\sum \frac{n_i}{\overline{n}(s_i)}\right] = 1.0.$$

For random stress-range S with a PDF (probability density function), f(s),

$$E(D) = \int_0^\infty \frac{\overline{n} f_S(s)\,ds}{\overline{n}(s)} = \overline{n}\int_0^\infty \frac{s^m}{c} f_S(s)ds = 1.0$$

from which,

$$\overline{n} = \frac{c}{\int_0^\infty s^m f_S(s)ds} = \frac{c}{E(S^m)} \qquad (3a)$$

where, $S^m = m^{th}$ *moment of S (Ref. 5).*

Therefore, under a random stress-range with PDF, $f_S(s)$, the m^{th} moment of S can be evaluated, and the reliability at life n can be assessed through Eq. 6.

Fatigue Loading – Theoretically, all loading amplitudes above a minimum threshold can cause fatigue damage. Therefore, in considering fatigue reliability of structures, the probability distribution (PDF) of all applied stress-ranges is important. On the other hand, it is reasonable to assume an upper limit stress-range (e.g., the yield stress of the material) when considering fatigue loading. With these considerations, the *beta* distribution is suitable to model fatigue loadings; this distribution has finite lower and upper limits, and is quite versatile (can have any unimodal shape depending on the values of its two parameters) for fitting any histogram of stress-range data.

The PDF of the beta distribution with lower bound = 0 and upper bound = S_0 is

$$f_S(s) = \frac{1}{B(q,r)} \frac{s^{q-1}(s_o - s)^{r-1}}{s_o^{q+r-1}}; \quad 0 \le s \le s_o$$

Where,

$$B(q,r) = \text{beta function} = \frac{\Gamma(q)\Gamma(r)}{\Gamma(q+r)}$$

q,r = parameters *of distribution, which are related to the mean and c.o.v. of the applied stress - range as follows:*

$$q = \frac{\mu}{s_o}\left[\Omega^{-2}\left(\frac{s_o}{\mu}-1\right)-1\right]$$

$$r = \left(\frac{s_o}{\mu}-1\right)q$$

With the above beta distribution, the m^{th} moment of S becomes (Ref. 5),

$$E(S^m) = s_o^m \frac{\Gamma(m+q)\Gamma(q+r)}{\Gamma(q)\Gamma(m+q+r)} \qquad (7)$$

Reliability-Based Design for Fatigue Resistance – The reliability basis for fatigue resistant design requires the determination of the allowable stress-range to design a welded joint or structural detail so as to insure a design life n_o with a target reliability $L(n_o)$. Therefore, equating Eq. 6 to the target reliability,

$$L(n) = L(n_o) = 1 - p_F(n_o)$$

in which, $p_F(n_o)$ = the probability of failure within life n_o. Then, inverting Eq. 6 and using the approximation

$$ln[1 - p_F(n_o)] \cong -p_F(n_o)$$

yields the required mean life,

$$\bar{n} = n_o \frac{\Gamma(1+\Omega^{1.08})}{(p_F)^{\Omega^{1.08}}} = n_o \cdot \gamma_F \qquad (8)$$

where, γ_F is the "scatter factor".

For constant-amplitude loadings, the allowable stress-range for design is:

$$s_c = \left(\frac{c}{\bar{n}}\right)^{1/m} = \left(\frac{c}{n_o \gamma_F}\right)$$

Whereas for beta-distributed random loadings, the allowable upper bound stress-range for design would be (Ref 5 & Ref 1):

$$s_o = \left(\frac{c}{\bar{n}}\right)^{1/m}\left[\frac{\Gamma(q)\Gamma(m+q+r)}{\Gamma(m+q)\Gamma(q+r)}\right]^{1/m} \qquad (9)$$

Eq. 9 can be rewritten as,

$$s_o = s_c \cdot \zeta$$

where, ζ *is the "random stress factor".*

3.0 Hull Monitoring Data Evaluation:

Since 1995, Marathon Oil Company has installed the Hull Monitoring System on two sister LNG tankers (87,500 m^3) that trade in designated routes between Kenai, Alaska and Yokohama, Japan. Figure 1 shows the deployment of sensors including: accelerometer, bottom pressure, pitch and roll motions and strain-gauges at mid ship. For the purpose of this paper, we limit the discussion on the strain-gauge and the data it generated. Figure 2 shows that the strain-gauge has a 2-meter long rod, which is clamped fixed to the deck on one end, and is connected to a displacement potentiometer at the other end. This arrangement filters out the stress components from all directions, but retains only the longitudinal hull-girder bending stress.

The system electronically polls the stress signal at 10HZ and the records are stored in an optical disc. Upon completion of one round trip (approximately 20 days), the data were analyzed. The digital stress data were reconstructed for stress-range cycle count by using Rain-Flow analysis. Table 1 summarizes the accumulated two-year results from one ship collected between May 24, 1995 to May 29, 1997. The stress-range was divided at 1-kg/mm^2 intervals into 15 categories as listed in the first column of Table 1. The second column shows the total number of cycles experienced by each stress-range level. The large number of cycles between 0 to 1 kg/mm^2 was because of the calm ocean during the summer months, accentuated by extremely short period of noise. These responses do not produce any structural fatigue and therefore can be ignored. The last two columns represent the "Cumulative Damage Ratio" (CDR) interpolated from the SN curves "C" and "D" defined by UK's DOE (Ref. 6). The bottom row in Table 1 is the summary of total number of cycles experienced in two years of services and the corresponding total CDR for "C" and "D" type of structural details, after applying the Miner's law of linear superpositioning of the damage profiles.

It is interesting to note that the most fatigue damage (marked with "*") does not come from the highest stress-range group because the number of cycles is low, nor from the lower end because the stress-range is not high enough to cause significant damage. It is the mid-range (6-7 kg/mm^2 for "C" and 5-6 kg/mm^2 for "D") that causes most of the damage. The total

damage for the two years is logged in as 0.00330 for "C" curve and 0.01716 for "D" curve. The inverse of the damage will be their respective fatigue lives of 303 years and 116 years. This represents the life at the point of the strain-gauge is much longer than the traditional design life of 20 to 30 years. However, at other points of the hull where high stress concentration is involved, the stress range could be much higher. In turn, the respective fatigue life is much shorter. From finite element analysis or other equivalent methods, one can relate the stress-range at other locations to the stress-range at the measured location. The ratio of these stress-ranges can be expressed as "STF" Stress Transfer Factor. In general, where the SN curve has a slope of m=3, the fatigue life is reduced by a factor of 8, if the stress-range is increased by a factor of 2, subjected to minor corrections for bilinear SN curve at low stress-range. Table 2 illustrates the relationship between the STF and the HMS measured fatigue lives, using "D" curve projection. These life expectancies are in general agreement with what is observed in real operation. It was observed that after 3 years of service, no fracture was found with STF less than 3.7. Higher STF values result in fractures earlier than three years. These values will be used to calibrate the reliability level to be discussed next.

The probability density function of the measured stress-range from Table 1 is presented in Figure 3 in the form of a histogram. Following the procedure outlined in the previous Section, this fatigue loading is fitted with a Beta distribution curve with lower bound = 0 and the upper bound (s_0) = 15 kg/mm^2. The c.o.v. for the loading distribution was estimated to be 0.49079, and the mean stress to be 2.0496 kg/mm^2; from which q = 3.44755 and r = 21.78296. After these parameters are determined, the m^{th} moment of S can be calculated from Eq. (7), the mean fatigue life from Eq. (3a), the reliability at life n can be assessed through Eq. (6) and the allowable stress from Eq. (4).

To complete the reliability evaluation, some assumptions of the fatigue c.o.v.s must be made. For comparison, Table 3 tabulates four c.o.v. components from three sources (Refs. 1, 7 and 8). Values from Ref. 1 are used in this paper. It should be noted that both C_{sn} and C_s are much smaller in Ref. 1 than the other sources. This could lead to a higher reliability level for the same fatigue life estimation. Table 4 summarizes the fatigue lives with reliability levels from 0.8 to 0.999, assuming the loading profile of the Beta curve obtained from the previous paragraph. From the range of STFs, it is consistent that the realistic reliability level should be between 0.8 and 0.9 when compared with Table 2. If c.o.v. from Refs. 7 or 8 are used, the reliability level would be less than 0.8.

4.0 Spectral Fatigue Analysis vs. Reliability Fatigue Analysis:

Finite Element Analysis (FEA) was broadly used to analyze ship structures during the past two decades. The results in identifying hot-spot stresses are remarkably accurate. The success of FEA approach together with the prolific advancement of the PC computer soon extends the application of FEA into Spectral Fatigue Analysis (SFA). Typical procedures can be found in reports such as Ref. 9. Strictly adhering to the SN curve and Miner's Law, these SFA can predict fatigue life with some degree of accuracy. However, fatigue prediction cannot be precise due to the inherent scatter of material properties, loading patterns and the repeatability of key parameters. It is time to bring the fatigue analysis in the framework of Reliability Analysis as illustrated in Section 2 of this report. The purpose of this section is to calibrate the traditional SFA with the present proposed Reliability Analysis through a recently designed double-hull tanker that meets the ABS's DLA standard.

The FEA model presented here is a part of the deck structure, intersecting with the transverse oil-tight bulkhead. There is a total of nearly 20,000 plate and solid elements in the model. Calculated by SFA, the fatigue lives of a group of five elements near one hot-spot are summarized in Table 5. To compare with the Reliability Analysis, Table 6 summarizes the fatigue lives of the same model when evaluated with various reliability levels. It should be clear that the results from SFA lie in between reliability levels of 0.8 and 0.9 when comparing Tables 5 and 6.

As demonstrated in Tables 5 and 6, the Reliability and Fatigue Life estimates vary greatly according to the values of the total c.o.v. (C_N) assumed. For this demonstration, (C_N) is composed of four components, where three of them carry the same weight but the forth (C_S) is magnified by the slope m of the SN curve. With a nominal value of m=3, the influence from (C_S) equals to the sum of influences from all the three other components. Table 7 summarizes the effect of varying C_N from 0.5 to 0.9 at 0.1 intervals, with Reliability level set at 0.9. Comparing with the FEA result shown in Table 5, it could be concluded that c.o.v. of slightly over 0.5 at reliability level of 0.9 would yield fatigue life close to what is predicted by the FEA method.

5.0 Conclusion:

A concise and practical reliability analysis procedure is outlined in this report. The analysis can be used to calculate the level of reliability, allowable stress-range and fatigue life, if two of the three parameters are known. To further demonstrate how the theory checks with reality, the fatigue lives of an existing LNG tanker and a newly designed double hull tanker are compared with those calculated by the proposed reliability analysis. Examples from two years ship board measured data indicated that the fatigue life of stress hot spots have reliability levels between 0.8 and 0.9. Another example of a newly designed double hull tanker that satisfies ABS's DLA designation also shows that the observed fatigue life at stress hot spots have similar reliability levels. It is surprising that the existing ship building practice accepts below 0.9 reliability level, as opposed to routine land-based structures, where the acceptable reliability levels are usually above 0.9. This indicates that the current ship building practice may require shorter inspection periods and should expect some amount of repairs if long service life is required. Nonetheless, most of the uncertainties in the ship structures are from the environmental loading. Even when two ships are identical, their fatigue life could be significantly different, depending upon what kind of weather they encounter. On the other hand, it may be very time consuming to design and expensive to build a ship with the same level of reliability as a land-based structure.

6.0 References:

1. Ang, A.H.S., and Munse, W.H., "Practical Reliability Basis for Structural Fatigue", Preprint 2494, ASCE National Structural Engineering Conference, April 1975.

2. Munse, W.H., et. al, "Fatigue Characterization of Fabricated Ship Details for Design", SSC-318, 1983.

3. Wirsching, P.H., "Probability-based Fatigue Design Criteria for Offshore Structures", API PRAC Report No. 81-15, 1983

4. Freudenthal, A.M., "Prediction of Fatigue Life", J. of Applied Physics, Vol. 31, Dec. 1960, pp. 2196-2198

5. Ang, A.H.S.,"Bases for Reliability Approach to Structural Fatigue", Proc. ICOSSAR '77, Munich, Sept. 1977, pp. 97-114

6. UK, DOE, "Offshore Installations: Guidance on Design, Construction and Certification", Appendix A21.2.13, Forth edition, January 1990.

7. Mansour, A., "An Introduction to Structural Reliability Theory", SSC-351, 1990

8. Mansour, A. et al, "Assessment of Reliability of Ship Structures", SSC-398, 1997

9. Sucharski, D., and Cheung, Maxwell, "Applications of Spectral Fatigue Analysis to the ARCO 190 MDWT Tankers", SSC-M-1, Ship Structures Symposium '93.

Acknowledgement:

The authors wish to thank the Office of Naval Research, MOB Science and Technology Program, for the support of the research. We also would like to thank Marathon Oil Company and ARCO Marine, Inc. for allowing us to use their data. The authors also wish to thank Dr. John Lien and Mr. Arne Stenseng for their technical support as well as Mr. Sal Herrera and Mrs. Kristi LePore for their editing assistance.

FIGURE 1: HULL MONITORING SYSTEM LAYOUT

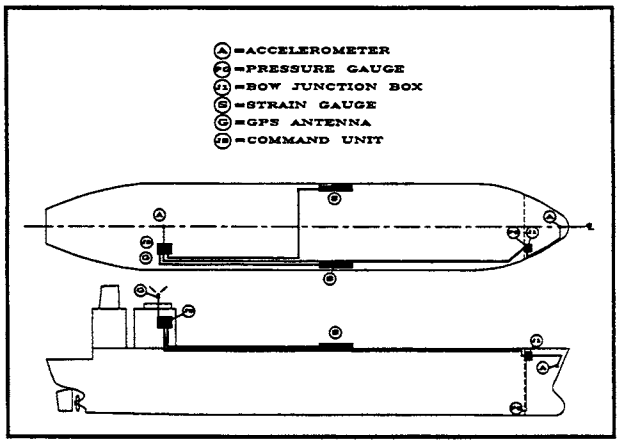

FIGURE 2: LONG BASE STRAIN GAGE

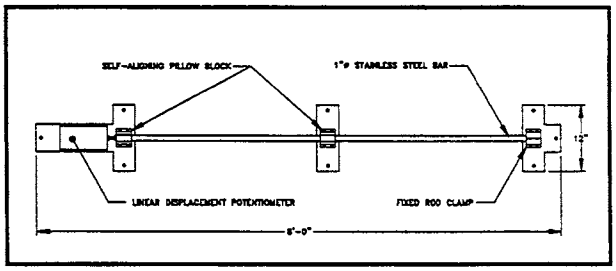

FIGURE 3: PROBABILITY DENSITY FUNCTION OF THE MEASURED STRESS RANGES

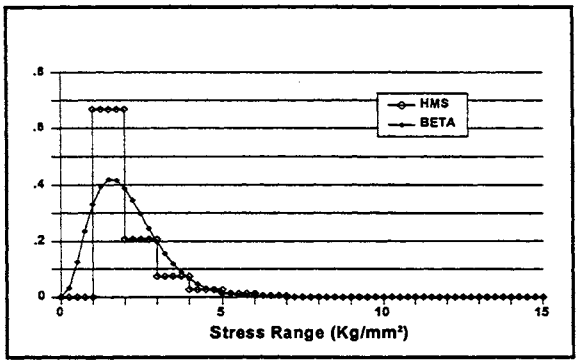

TABLE 1: STRESS RANGE HISTORY OF THE LNG TANKER (Period from 5/24/95 to 5/29/97)

Stress Range	No. Cycles	CDR "C"	CDR "D"
0 – 1 kg/mm2	78,961,760	.00000	.00000
1 – 2	1,786,015	.00000	.00027
2 – 3	557,416	.00008	.00110
3 – 4	200,056	.00020	.00207
4 – 5	72,117	.00029	.00267
5 – 6	35,198	.00044	.00341 *
6 – 7	15,214	.00047 *	.00251
7 – 8	6,466	.00045	.00167
8 – 9	3,098	.00038	.00117
9 – 10	1,345	.00024	.00071
10 – 11	579	.00015	.00042
11 – 12	248	.00009	.00024
12 – 13	91	.00005	.00012
13 – 14	30	.00002	.00006
>14	65	.00045	.00073
TOTAL	81,639,633	.00330	.01716

TABLE 2: FATIGUE LIFE ESTIMATES BY MEASURED DATA ON LNG(C.O.V.=0.585)

STF	FATIGUE LIFE (YR)
1	116.55
2	9.78
3	2.65
4	1.08
5	0.54

TABLE 3: COEFFICIENT OF VARIATION (C.O.V.)

Variables	Descriptions	Sources Ref. 7	Ref. 8	Ref. 1
Cmr	Strength Modeling Miner's Rule	0.15	0.3	0.15
Cc	Workmanship Fabrication	0.4	-	0.4
Csn	S-N Data		@ 0.50	
		0.62	(D) 0.51	0.37 (Ave.)
Cs	Stress Modeling Error	0.1	@ 0.05	@ 0.05
Cn	Total Effect "C"	0.66	@ 0.60	@ 0.592
	Total Effect "D"	0.5	(D) 0.75	(D) 0.565

Note: $C_N = [\, C_{mr}^2 + C_c^2 + C_{sn}^2 + m^2 C_s^2 \,]^{1/2}$

TABLE 4: FATIGUE LIFE ESTIMATES BY SPECTRAL FATIGUE ANALYSIS ON DOUBLE HULL TANKER

	RELIABILITY LEVELS			
STF	0.8	0.9	0.99	0.999
1.0	97.90	64.2	17.2	4.72
2.0	12.2	8.03	2.15	0.59
3.0	3.62	2.38	0.64	0.18
4.0	1.53	1	0.27	0.07
5.0	0.78	0.51	0.14	0.04

TABLE 5: FATIGUE LIFE ESTIMATES BY SPECTRAL FATIGUE ANALYSIS ON DOUBLE HULL TANKERS

ELEMENT	S-N CURVE	FATIGUE LIFE (YRS)
14644	D	200.09
13124	C	38.32
17287	D	18.8
17093	C	16.97
16788	C	14.27

Note: Table shows Fatigue Life in years.

TABLE 6: FATIGUE LIFE ESTIMATES BY RELIABILITY ANALYSIS ON DOUBLE HULL TANKERS

	S-N	RELIABILITY LEVELS			
ELEMENT	CURVE	0.8	0.9	0.99	0.999
14644	D	251.6	164.37	43.34	11.71
13124	C	43.96	28.68	7.74	2.13
17287	D	23.56	15.39	4.06	1.1
17093	C	19.47	12.79	3.43	0.94
16788	C	16.39	10.76	2.89	0.79

Note: Table shows Fatigue Life in years.

TABLE 7: SENSITIVITY OF FATIGUE LIFE TO C.O.V.

	C.O.V.				
ELEMENT	0.5	0.6	0.7	0.8	0.9
14644	204.27	161.05	125.38	96.46	73.39
13124	35.29	27.82	21.66	16.66	12.68
17287	19.13	15.08	11.74	9.03	6.87
17093	15.63	12.32	9.59	7.38	5.61
16788	13.15	10.37	8.07	6.21	4.73

Note: Table shows Fatigue Life in years with Reliability of 0.9.

PROCEEDINGS OF THE THIRD INTERNATIONAL WORKSHOP ON VERY LARGE FLOATING STRUCTURES
(VLFS '99), VOL. I, EDS. R.C. ERTEKIN & J.W. KIM, 22-24 SEPTEMBER 1999, HONOLULU, HAWAII, USA

COMBINING LOW AND HIGH FREQUENCY LOADS ACTING ON LARGE FLOATING STRUCTURES

By
Alaa E. Mansour

University of California, Berkeley
Mechanical Engineering Department
6171 Etcheverry Hall, MC 1740
Berkeley, CA 94720
Alaa@uclink4.berkeley.edu

ABSTRACT

Loads acting on large floating structures usually consist of high frequency and low frequency loads. The high frequency loads are associated with the hydroelastic behavior of the structure and excitation of the natural frequency modes. The low frequency loads are associated with the body motion of the structure and the wave profile. In design analysis, extreme values of these loads must be combined taking into consideration the correlation between them. This paper discusses a methodology for combining the extreme loads, and proposes a simple formulation suitable for use in reliability analysis. A proposed load combination factor K was found to depend on the correlation coefficient of the two loads, the ratio of their standard deviations and the frequency content of the processes from which the loads are determined. The correlation coefficient was found to depend on the complex frequency response functions of the loads and the input wave spectrum. The paper also discusses characteristic extreme values of slightly nonlinear loads acting on large floating structures.

Extreme loads may be based on a storm condition with a specified return period. Since very large floating structures are expected to have a long operational lifetime, the return period must be selected carefully. The paper discusses a method for selecting return periods based on the expected operational life of the structure and encounter probability.

1. INTRODUCTION

A designer of a large floating structure is usually faced with the important problem of computing the total response from individual components which are calculated using separate procedures and computer programs. For example, several computer programs exist for calculating the stillwater loads using a static balance procedure. Other programs and tools are available for computing the low frequency loads acting on the structure. These loads usually consist of vertical, horizontal and torsion loads. Secondary response due to hydrostatic pressure acting on portions of the hull is computed using other tools and procedures. Similarly, the hydroelastic loads and vibrational response of the structure are calculated taking into consideration the flexibility of the structure.

If all these loads/response components were static in nature, the problem would have been simple, because only the magnitude and direction of each load/response component would be necessary to obtain the total response. If the total response involves dynamic cyclic individual responses, the problem becomes a little more complicated since attention must be given to the phase relation between the different response components. However, the actual problem that faces the designer involves dynamic random individual responses that require the additional complication of determining the degree of correlation between the different components and the method of combining them which is the subject of this paper.

2. COMBINING EXTREME LOADS

A large floating structure encountering oblique irregular waves can be considered as a multiple system with the ocean waves presenting a common input to the system. Over a short period of time the waves can be represented as a stationary random process in the wide sense. The sum of the outputs y(t) of this multiple system represents the combined response, e.g., motion, acceleration or stress.
For linear systems, the output in time domain is given by the convolution integral:

$$y(t) = \sum_{i=1}^{n} a_i \int_o^{\infty} h_i(\tau) x(t-\tau) dz \qquad (1)$$

where $h_i(.)$ are the impulse response functions of the individual components and x(.) is the common input, i.e. a time history of wave surface elevation.

Since $x(t)$ is a common input to all terms of equation (1), and since the integration and summation signs can be exchanged in this case, a composite impulse response function can be defined as:

$$h_c(t) = \sum_{i=1}^{n} a_i \, h_i(t) \qquad (2)$$

In a frequency domain, a composite frequency response function $H_c(\omega)$ of the system can be defined as:

$$H_c(\omega) = \sum_{i=1}^{n} a_i \, H_i(\omega) \qquad (3)$$

where $H_c(\omega)$ is the frequency response function for each component, defined by the Fourier transform of $h_i(t)$, i.e.

$$H_c(\omega) = \int_0^{\infty} h_c(t) e^{-j\omega} dt$$

The relation between the input spectrum $S_x(\omega)$ and the output (response) spectrum $S_y(\omega)$ for the composite system can be written in the form:

$$S_y(\omega) = H_c(\omega) H_c^*(\omega) S_x(\omega)$$

$$= S_x(\omega) \sum_{i=1}^{n} \sum_{j=1}^{n} a_i a_j H_i(\omega) H_j^*(\omega)$$

$$= S_x(\omega) \sum_{i=1}^{n} a_i^2 |H_i(\omega)|^2$$

$$+ S_x(\omega) \sum_{i=1}^{n} \sum_{j=1}^{n} a_i a_j H_i(\omega) H_j^*(\omega) \qquad (4)$$

where $|H_i(\omega)|$ are the modula of the individual frequency response functions and the double summation terms in equation (4) represent the cross spectra terms. The second term of the equation, which can be either positive or negative, is a corrective term that reflects the correlation between the load components.

The variance of the combined output response is given by the zero moment of the output spectrum, i.e.

$$\sigma_c^2 = m_0 = \int_0^{\infty} S_y(\omega) d\omega$$

$$= \sum_{i=1}^{n} a_i^2 \int_0^{\infty} |H_i(\omega)|^2 S_x(\omega) d\omega$$

$$+ \sum_{\substack{i=1 \\ i \neq j}}^{n} \sum_{j=1}^{n} a_i a_j \int_0^{\infty} H_i(\omega) H_j^*(\omega) S_x(\omega) d\omega \qquad (5)$$

Equation 5 can be written in a different form that makes it easier to define the correlation coefficient between the different response components.

$$\sigma_c^2 = \sum_{i=1}^{n} a_i^2 \sigma_i^2 + \sum_{\substack{i=1 \\ i \neq j}}^{n} \sum_{j=1}^{n} a_i a_j \rho_{ij} \sigma_i \sigma_j \qquad (6)$$

where σ_i are variances of the individual components

$$\sigma_i^2 = \int_0^{\infty} |H_i(\omega)|^2 \, S_x(\omega) d\omega \qquad (7)$$

and ρ_{ij} are correlation coefficients between individual components

$$\rho_{ij} = \frac{1}{\sigma_i \sigma_j} \int_0^{\infty} \mathrm{Re}\left[H_i(\omega) H_j^*(\omega)\right] S_x(\omega) d\omega \qquad (8)$$

The above results can be generalized to the case of short crested waves where the sea spectrum is defined in terms of frequency and waves spreading angle μ. For a heading angle α, the combined response variance given by (6) is valid but with equations 7 and 8 replaced by:

$$\sigma_i^2 = \int_{-\Pi/2}^{\Pi/2} \int_0^{\infty} |H_i(\omega, a-\mu)|^2 S_x(\omega, \mu) d\omega \, d\mu \qquad (9)$$

and

$$\rho_{ij} = \frac{1}{\sigma_i \sigma_j} \int_{-\Pi/2}^{\Pi/2} \int_0^{\infty} \mathrm{Re}\{H_i(\omega, \alpha-\mu) H_j^*(\omega, \alpha-\mu)\} S_x(\omega, \mu) d\omega \, d\mu \qquad (10)$$

Re(.) indicates the real part of the function and $H_j^*(.)$ is the conjugate of the complex frequency response function.

If the response components are uncorrelated, i.e., if ρ_{ij} =0, the second term equation 6 drops out and combined variance is simply the sum of the individual variances modified by the factors.

On the other hand, if the response components are perfectly correlated, i.e., ρ_{ij} will approach plus or minus 1, and the effects of the second term in equation 7 on the combined variance can be substantial.

Considering a Gaussian seaway as common input, the output of the multiple system is also Gaussian. The probability density function of the output peaks for a general-Gaussian process with bandwidth parameter ε is given by [1]:

$$f(\zeta)= \frac{1}{\sqrt{2?\ m_0}} \left\{ \varepsilon\, e^{-\xi^2/2\varepsilon^2 m_0} + \sqrt{\frac{2\Pi(1-\varepsilon^2)}{m_0}}\,\zeta e^{-\zeta^{2/2m_0}}\, \Phi\left(\frac{\sqrt{1-\varepsilon^2}}{\varepsilon}\cdot\frac{\xi}{\sqrt{m_0}}\right)\right\} \quad (10)$$

where

$$\varepsilon^{\,2}=1-\frac{m_2^2}{m_0 m_4};\ m_n=\int_0^\infty \omega^n S_y(\omega)d\omega;\ n=0,2,4$$

$$\Phi(u)_-= \int_{-\infty}^{u}\frac{1}{\sqrt{2\Pi}}e^{-2^2/2}dz$$

When ε =0 , i.e. a narrow-band process, equation 10 reduces to the Rayleigh distribution. If ε = 1, i.e., a wide-band output spectrum, equation 10 reduces to the normal distribution, that is, it reduces to the distribution of the process itself. Extreme values of the peaks of the combined response can be estimated from equation 10 using order statistics, out-crossing analysis, or Gumbel asymptotic distribution (see for example [2].

Although the approach outlined above can be used to determine the extreme value of the combined response, equation 10 and associated extreme values are not suitable for direct use in design. A simplified format is sought.

The following format for the combined response is simple and particularly suitable for reliability analysis. For two correlated loads, the combined extreme response can be written as:

$$f_c = f_1 + Kf_2 \qquad f_1 > f_2 \qquad (11)$$

Where K is a load combination factor and f_1 and f_2 are individual extreme responses (e.g. characteristic extreme values of stresses).
The characteristic design values f_1 and f_2 are usually determined from extreme value theory. For example, the expected extreme stress peak in N_i peaks in a Gaussian sea state is given by:

$$f_i = E[f_{i\max}] = \alpha_i \sigma_i \qquad (12)$$

where σ_i is the standard deviation of the stress process and α_i is the a multiplier that depends on the number of peaks and the bandwidth parameter given by:

$$\alpha_i=[2\ln(1-\varepsilon_i^{\,2})^{1/2}N_i]^{1/2}+0.2886[2\ln(1-\varepsilon_i^{\,2})^{1/2}N_i]^{-1/2} \quad (13)$$

If the most probable extreme value (mode) instead of the expected extreme value (mean) is used as a characteristic (design) value, then the equation 12 still holds but with α_i given by the first term only of equation 13.

Equations 12 and 13 are valid for the combined response f_c as well, since the process of the combined response is also Gaussian. Therefore equation 11 can be solved for the load combination factor K in terms of the variances:

$$\mathrm{K}=\frac{f_c-f_1}{f_2}=\frac{\alpha_c\sigma_c-\alpha_1\sigma_1}{\alpha_2\sigma_2} \qquad (14)$$

If the most probable extreme values are used as the characteristic values, the coefficients α_i in equation 14 are given by:

$$\alpha_i=\sqrt{2\ln(1-\varepsilon_i^{\,2})^{1/2}N_i} \qquad i=1,2,\mathrm{c} \quad (15)$$

Using equation 6 and 14, and for α_i=1, the load combination factor is determined as:

$$\mathrm{K}=\frac{m_r}{r}[m_c(1+r^2+2pr)^{1/2}-1] \qquad (16)$$

Where

$$\mathrm{r}=\frac{\sigma_2}{\sigma_1},\ m_r=\sqrt{\frac{\ln(1-\varepsilon_1^{\,2})^{1/2}N_1}{\ln(1-\varepsilon_2^{\,2})^{1/2}N_2}}\ \text{and}$$

$$m_c=\sqrt{\frac{\ln(1-\varepsilon_c^{\,2})^{1/2}N_c}{\ln(1-\varepsilon_1^{\,2})^{1/2}N_1}} \quad (17)$$

ρ is the correlation coefficient between the two rms stress components given by equation (8) for long crested waves or (10) for short crested waves.
It is seen that the load combination factor depends not only on the correlation coefficient but also on the ratio of the stresses standard deviations and the frequency ratio factors m_r and m_c. Notice that even

if the correlation coefficient ρ is zero the load combination factor will have a nonzero value (see equation 16).

This indicates that presence of a second load will always contribute to the combined response even if the two loads were uncorrelated.

The above analysis can be extended to the case of three correlated loads in a straightfoward manner (see [13]).

2. SLIGHTLY NONLINEAR EXTREME LOADS

A slightly nonlinear (non-Gaussian) reponse process M(t) of a large floating structure can be expressed in a stationary sea in the form of an N-term Hermite series of a standard Gaussian process [4,5]:

$$\frac{M(t)-\mu}{\sigma} = M_0(t) = k[U(t) + \sum_{n=3}^{N} c_n He_{n-1}(U(t))] \quad (18)$$

where $k = k(c_n)$ is a scaling factor to ensure that $M_0(t)$ has a unit variance, and the coefficients c_n control shape of the standardized distribution. Expanding equation (18) up to N=4, one obtains

$$M=\mu + k\sigma[U + c_3(U^2-1) + c_4(U^3-3U)] \quad (19)$$

The argument t is omitted for brevity.

Equivalently, a polynomial in the standard Gaussian process U(t) can be used to model M(t):

$$M = a_0 + \sum_{i=1}^{3} a_i U^i \quad (20)$$

One advantage of using the cubic Hermite series (18) is that the response is expressed explicitly in terms of the mean μ and standard deviation σ of the reponse, and that the coefficients c_3 and c_4 can be approximately related to the skewness α and the kurtosis β of the response using Gram-Charlier series and a coefficient matching procedue [4]:

$$\alpha \cong 6c_3(1+6c_4) \quad (21)$$

and

$$\beta \cong \frac{2}{3}[18c_4+1)^2-1]+3 \quad (22)$$

This means that the response process M(t) is expressed explicitly, though approximately by the first four statistical moments (means, standard deviation, skewness and kurtotsis).

The polynomial representation of the response given by equation (20) can be made equivalent to the Hermite representation given by equation (19) by matching the coefficients of the two series, i.e.,

$$c_3 = a_2(a_1+3a_3)^{-1}$$
$$c_4 = a_3(a_1+3a_3)^{-1} \quad (23)$$
$$k\sigma = a_1 + 3a_3$$
$$\mu = a_0 + a_2$$

and the variance σ^2 is given by [5]:

$$\sigma^2 = a_1^2 + 2a_2^2 + 15a_3^3 + 6a_1a_3 \quad (24)$$

From the four lowest statistical moments, the a_i can be determined using equation 21,22 and 23. The standardized moment process can be written in terms of the coefficients a_i as:

$$\frac{M-\mu}{\sigma} = kU[1 + \frac{a_2}{a_1+3a_3}\frac{(U^2-1)}{U} + \frac{a_3}{a_1+3a_3}(U^2-3)] \quad (25)$$

The probability distributions of the response process, its peaks, and its extreme peak in time duration T can be thus determined from the transformation given by equation 19 and the fact that U(t) is a standard normal process. From the probability distribution of the extreme peak in time duration T, one may determine the most probable extreme value (MPEV) as well as other extreme values associated with prescribed probability levels in the usual way.

The MPEV of the Gaussian process U(t) is:

$$\text{MPEV of U(T)} = \sqrt{2\ln \nu_o T} \quad (26)$$

Inserting equation 26 in 25 and using equations 21,22 and 23 to obtain the coefficients a_i in terms of skewness α and the kurosis β, the MPEV of M(t), denoted f, can be cast in the form:

$$f = \delta\,\sigma\sqrt{2\ln \nu_o T} \quad (27)$$

Where the mean μ was taken to be zero (without loss of generality) and δ is a nonlinearity parameter defined by:

$$\delta = k\left\{1 + \frac{\alpha(2\ln \nu_0 T - 1)}{(6+2\gamma)\sqrt{2\ln \nu_0 T}} + \frac{\gamma}{18}(2\ln \nu_o T - 3)\right\} \quad (28)$$

and

$$\gamma = [1 + 1.5(\beta - 3]^{1/2} - 1$$

$$k = [1 + \frac{1}{2}(\frac{\alpha}{\gamma + 3})^2 + \frac{\gamma^2}{54}]^{1/2} \qquad (29)$$

Equation 27 is similar to equation 12 or 26 for the linear case except for the nonlinearity parameter δ. It can be easily verified that equation 27 converges to the linear case when the skewness α is zero and the kurtosis β is 3. Other characteristic values, beside the MPEV, can be approximately determined using an equation similar to equation 27. An extreme value f_2 associated with exceedance probability η can be determined by replacing ν_0 with $\nu_{0\eta}$, i.e.

$$f_\eta = \delta\, \sigma \sqrt{2 \ln \nu_{0\eta} T} \qquad (30)$$

where

$$\nu_{0\eta} \cong \frac{\nu_0}{\ln(1-\eta)^{-1}} \qquad (31)$$

The MPEV is associated with an exceedance probability 2=1-1/e = 0.6321. It's easy to verify that, in this special case $\nu_{0\eta} = \nu_0$ and equation 30 reduces to equation 27 for the most probable extreme value. The above equations apply to narrow-band response spectra. An approximation for the wide-band case is possible for the MPEV if one uses in equation 27:

$$\nu_0 T = \sqrt{(1-\varepsilon^2)N}$$

N is the number of peaks and ε is the spectrum bandwidth parameter.

According to reference [6], an extreme value associated with probability η becomes independent of ε as η approaches zero, and therefore, equation 30 may be used to approximately estimate f_η with $\nu_0 T$ = N= number of peaks of the wideband process for small values of η.

3. RETURN PERIODS AND EXTREME VALUES

Return periods and the associated extreme values are not sufficient to develop criteria for the design of large floating structures. In addition, it is important to determine the probability of the structure encountering a design storm that has a specified return period. This probability of encounter will depend on the lifetime of the structure, i.e., on how long the structure will remain at the location where the return period and the associated wave height are calculated. If the structure's life is long, the probability of encounter will be higher. This is particularly important for large floating structures since their operational life is expected to be long.

For a stationary large floating structure, the useful life of the structure can be estimated, and the corresponding encounter probability can be determined. For a mobile large floating structure, however, the estimation of the encounter probabilities is more complicated because of their mobility, and because of the fact that different regions (zones) in the oceans have different wave severity and wave statistics.

This section presents a procedure for calculating encounter probabilities which can be used as a basis for establishing design criteria for mobile large floating structures. The encounter probabilities can provide better and more meaningful criteria for design, since they involve the life of the structure, as well as wave statistics, in the region of operation. Return periods reflect wave statistics only, and therefore are less meaningful as a basis for developing design criteria.

The relationship between the non-encounter probability and the return period R_i is [7,8]

$$P_{ne_i} = (1 - R_i^{-1})^{L_i} \qquad (32)$$

and by definition:

$$P_{e_i} = 1 - (1 - R_i^{-1})^{L_i} \qquad (33)$$

where P_{e_i} is the probability of encounter.

The probability of a mobile large floating structure encountering a severe storm (or the design sea state) will depend on its route and the wave statistics in the zones along the route. Wave statistics in different zones of the oceans are available from sources such as *Global Wave Statistics* [9] and can be used to determine return periods and encounter probabilities in each zone. The operation time in each zone is important in order to determine L_i.

In order to determine the probability of encountering a wave height (or a storm condition) along the route, we will consider the zones as members in a series system. A series system is defined as a system in which a state of encounter occurs if an encounter occurs in any of its members. That is, for the system encounter probability to be realized, it is sufficient that the large floating structure encounters the sea state in any one zone. Similarly, the system non-encounter probability P_{ne} can be realized only if mutual non-encounter takes place in all zones, i.e.,

$$P_{ne} = P\left[\bigcap_{i=1}^{n} A_i\right] \tag{34}$$

where A_i is the event of no encounter in zone i, i.e., $P[A_i] = P_{ne_i}$ and the symbol $\bigcap$ indicates the intersection or mutual occurrence of the events A_i. n is the total number of zones. The system (overall) probability of encounter P_e is simply given by

$$P_e = 1 - P_{ne} \tag{35}$$

First-order bounds on the non-encounter probability given by eqn. (34) can be determined. Corresponding bounds can also be determined for the encounter probability given by eqn. (35). The upper and lower bounds on P_e are determined by assuming statistically independent or fully correlated wave conditions in the zones along the route, respectively.

If A_i are assumed statistically independent, then

$$P_{ne} = \prod_{i=1}^{n} P(A_i) = \prod_{i=1}^{n} P_{ne_i} \tag{36}$$

and

$$P_e = 1 - \prod_{i=1}^{n} P_{ne_i} \tag{37}$$

on the other hand, if A_i are assumed perfectly correlated, then

$$\begin{aligned} P_e &= \max_i [1 - P(A_i)] \\ &= 1 - \min_i P(A_i) = 1 - \min_i P_{ne_i} \end{aligned} \tag{38}$$

Thus, the bounds on the system encounter probability P_e are [10]:

$$1 - \min_i (P_{ne_i}) \le P_e \le 1 - \prod_{i=1}^{n} P_{ne_i} \tag{39}$$

These bounds are tight if the non-encounter probability in any of the zones is dominant.

Instead of determining upper and lower bounds on P_e or P_{ne}, one can determine the 'exact' value of either under certain assumptions. If the members of a series system are equally correlated, then the system probability of encounter is:

$$P_e(\rho) = 1 - \int_{-\infty}^{\infty} \prod_{i=1}^{n} \Phi\left[\frac{\beta_1 + \sqrt{\rho}t}{\sqrt{1-\rho}}\right] \varphi(t)dt \tag{40}$$

where β_i can be calculated from:

$$\beta_i = -\Phi^{-1}(P_{e_i}) = -\Phi^{-1}(1 - P_{ne_i}) \tag{41}$$

Φ and φ denote the standard Gaussian distribution and density functions, respectively, and ρ is the correlation coefficient. When $\rho = 0$, eqn. (40) converges to the upper bound of eqn. (39). Equation (40) is not valid for the specific case when $\rho = 1.0$.

4. SUMMARY AND CONCLUSION

A simple model suitable for design analysis has been presented for combining extreme correlated loads and the associated stresses. The case of two correlated loads has been modeled in a format suitable for use either in the usual deterministic design analysis or in probabilistic and reliability analysis.

The model is based on developing a composite frequency and impulse response functions of multiple linear systems subjected to common input (ocean waves). The requirement for the applicability of the model is the satisfaction of the stationarity condition of the common wave input and the linearity of the multiple system. The stationarity of the wave input implies short-term analysis, and the linearity assumption allows the use of the superposition principle but decreases the accuracy in high sea states.

The load combination factor K was found to depend not only on the correlation coefficient but also on the ratio of the standard deviations and frequency dependent factors.

An equation suitable for preliminary estimation of the extreme value of a slightly nonlinear response is presented. The equation contains a newly defined nonlinearity parameter that is a function of the response process skewness and kurtosis. The equation is consistent with the linear theory of extremes, and in fact reduces to the linear theory prediction as a special case when the nonlinearity parameter is equal to one.

A procedure has been developed for estimating encounter probabilities which can be used as a basis for formulating design criteria for large floating structures. The encounter probabilities provide better

and more meaningful criteria for design than wave return periods, since they involve the life of the structure as well as the wave statistics in the region of operation. This is particularly important for large floating structures because their operational life is expected to be long.

The encounter probabilities in any specific ocean zone were first determined as a function of the operation time in the zones as well as the return period. The return period depends on the selected wave height. The overall encounter probability along any given route was modeled as a 'system probability' and first-order bounds were determined. In addition, the encounter probability as a function of the correlation coefficient of the wave conditions in the different zones was determined assuming equal correlation coefficients between the zones.

References

[1] Rice, S. O. Mathematical analysis of random noise. *Bell System Technical Journal,* pages 23, 24. 1994, 1995.

[2] Mansour, A.E. *Extreme value distributions for linear systems and applications to marine structures.* Fourth International Marine Systems Design Conference, Kobe, Japan. 1991.

[3] Mansour, A. E. *Extreme loads and load combinations.* Journal of Ship Research, 39, 1, pages 53-61. 1995.

[4] Winterstein, S.R. *Nonlinear vibration models for extremes and fatigue.* Journal of Engineering Mechanics, 114, 10, pages 1172-1790. 1994

[5] Jensen, J. J. *Dynamic amplification of offshore steel platform responses due to non-Gaussian wave loads.* Marine Structures, 7, pages 91-105. 1994

[6] Silvaria, W. A. and Brillinger, D. R. *On the maximum wave heights in severe seas.* Proceedings, Offshore Technology Conference Paper no. 3232, Houston, Texas. 1978

[7] Borgman, L.E. *Extreme statistics, risk, and reliability.* Report, University of Wyoming.

[8] Mansour, A. E. and Preston, D. B. *Return Period and encounter probabilities.* Applied Ocean Research 17. Pages 127-136. 1995.

[9] Hogben, N., Dacunha, N.M. & Oliver, G.F. *Global Wave Statistics.* British Maritime Technology Ltd, Middlesex, UK. 1986.

[10] Ang, A. H.-S. & Tang, W. H. *Probability Concepts in Engineering Planning and Design Vol. II.* Decision, Risk and Reliability. John Wiley, New York, 1984.

PROCEEDINGS OF THE THIRD INTERNATIONAL WORKSHOP ON VERY LARGE FLOATING STRUCTURES
(VLFS '99), VOL. I, EDS. R.C. ERTEKIN & J.W. KIM, 22-24 SEPTEMBER 1999, HONOLULU, HAWAII, USA

RELIABILITY-BASED DESIGN FOR FATIGUE OF MARINE STRUCTURES

Ibrahim A. Assakkaf, Ph.D. and Bilal M. Ayyub, Ph.D., P.E.
University of Maryland, College Park*

ABSTRACT

Marine and offshore structures are subjected to fatigue primarily due to the action of seawater waves and the sea environment in general. The load cycles in such an environment can be in the order of million cycles per year.

The objective of this paper is to develop design methods for fatigue of structural details for conventional displacement type surface monohull ships. The methods are based on structural reliability theory and can be either as direct reliability-based design or in a load and resistance factor design (LRFD) format. The resulting design methods are to be referred to as the LRFD fatigue rules for marine structures. They were developed according to the following requirements: (1) spectral analysis of wave loads, (2) building on conventional codes, (3) nominal strength and load values, and (4) achieving target reliability levels. The first-order reliability method (FORM) was used to demonstrate the development of partial safety factors for selected limit states.

1. INTRODUCTION

In recent years, a great deal of attention has been focused on general fatigue cracking of ship structural details because the phenomenon is so vital that structural engineers must consider fatigue strength in their designs, especially for those structural components that are exposed to cyclic loading. The term "fatigue" is commonly used in engineering to describe repeated-load phenomena and their effect on the strength of a structural member. The exact mechanism of a fatigue failure is complex and is not completely understood. Failure by fatigue is a progressive cracking and unless it is detected this cracking can lead to a catastrophic rupture. When a repeated load is large enough to cause a fatigue crack, the crack will start at the point of maximum stress. This maximum stress is usually due a stress concentration (stress raiser). After a fatigue crack is initiated at some microscopic or macroscopic level of stress concentration, the crack itself can act as an additional stress raiser causing crack propagation. The crack grows with each repetition of the load until the effective cross section is reduced to such an extent that the remaining portion will fail with the next application of the load. For a fatigue crack to grow to such an extent to cause rupture, it usually takes thousands or even millions applications of the stress, depending on the magnitude of the load, type of the material used, and on other related factors. A detailed bibliography for fatigue of welds was developed by the University of Tennessee (1985). However, this bibliography does not cover work beyond 1985.

Fatigue must be considered in the design of all-structural and machine components that are subjected to repeated or fluctuating loads. During the useful life of a structural member, the number of loading cycles, which may expected, varies tremendously. For example, a beam supporting a crane may be loaded as many as 2,000,000 times in 25 years to failure, while an automobile crankshaft might be loaded 5,000,000 times for rupture to occur, if the automobile is driven 200,000 miles (Beer and Johnston, 1981). The number of loading cycles required to cause failure of a structural component through cyclic successive loading and reverse loading may be determined experimentally for any given maximum stress level. One common test used to evaluate the fatigue properties of a material is a rotating-beam test (Byars and Snyder, 1975). In this test, the number of completely reversed cycles of bending stress required to cause failure is measured at different stress levels. In one complete cycle, the stress goes from maximum tensile stress, to zero, to maximum compressive stress of the same magnitude as the maximum tensile stress, and then back to the original maximum stress passing the zero stress level. If a series of tests are conducted in this case, using different maximum stress ranges, the resulting data can be plotted as an *S-N* curve. For each test, the maximum stress range S is plotted against the number of cycles N. These test data are usually plotted on semi-log paper,

* 0305 Engineering Classroom Building, Civil Engineering Department, University of Maryland, College Park, MD 20742, USA, Tel: (301) 405-8385, E-mail: ayyub@umail.umd.edu.

and the resulting plot is referred to as an *S-N* curve. Figure 1 shows typical curves for various materials. It is to be noted that from these curves, as the magnitude of the maximum stress range decreases, the number of cycles required causing rupture increases. Also these curves tend to be approximately horizontal lines as a lower limit. When the stress level for a specimen reaches this limit, the specimen does not fail and it is said to have reached the endurance limit (fatigue limit). The endurance limit is then defined as the stress for which failure does not take place (Beer and Johnston, 1981) even for an indefinitely large number of loading cycles. The endurance limit for most engineering material is less than the yield strength. For a low carbon structural steel, the endurance limit is about half of the ultimate strength of the steel.

Fatigue properties for materials are usually determined at high temperatures and also in various corrosive environments. Temperature and environment can play a drastic role in influencing the fatigue properties. For example, in applications in or near seawater, or in other applications where high level of corrosion is expected, a reduction up to 50% in the endurance limit may be anticipated. Also, since fatigue failure may be initiated at any crack or imperfection, the service condition of a specimen has a vital effect on the value of the endurance limit obtained in the test.

The inherent nature of fatigue tests gives rise to a great deal of scatter in the data. For example, if several specimens that have carefully machined and polished, are tested at the same stress level, it certainly not unusual to have a variation of 10 to 20 percent in their fatigue life measured in terms of the number of loading cycles at which the specimen ruptures (Byars and Snyder, 1975). It therefore requires a few tests to correctly identify an S-N curve for a material.

Fatigue cracking of structural details in ship and offshore steel structures due cyclic loading has gained considerable attention in the past few years. Numerous research studies have been conducted in this field on both the theoretical and practical aspects. Consequently, a great deal of papers has been published resulting in various topics relating to fatigue assessment and prediction. In these papers, the macroscopic behavior of materials as well as models for its description is investigated. Due to the extreme complexity in modeling the process of material cracking at the microscopic level, solutions from the microscopic aspect are rarely available or not practically feasible. This is mainly due to the complexity of the damaging process under cyclic loading and the scatter of material properties. Ship and offshore structures are subjected to fatigue primarily due to the action of seawater waves (Byers et al, 1997) and the sea environment in general. The load cycles in such an environment can be in the order of million

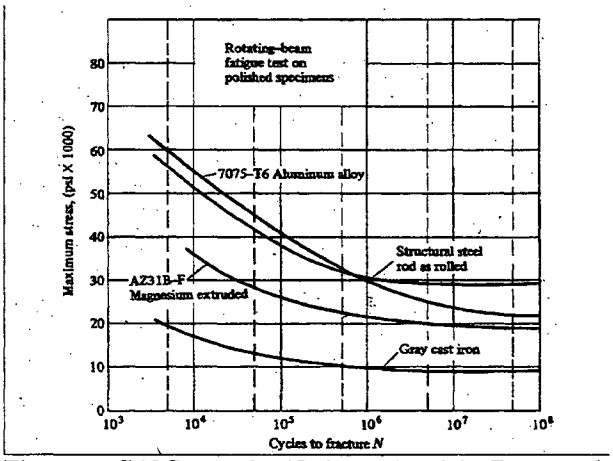

Figure 1. *S-N* Curves for Various Materials (Byars and Snyder, 1975)

cycles per year. Fatigue failures in ship and offshore structures can take place at sites of high stress concentration that can be classified into two major categories: (1) baseplate and (2) weldments. The former includes locations of high stress concentration such as openings, sharp re-entry corners, and plate edges. In general, the mechanisms behind these failures are described by the general approaches to fatigue life prediction as discussed in this paper. There are two major approaches for evaluating fatigue life prediction: (1) the *S-N* curve approach and (2) the fracture mechanic (FM) approach. The *S-N* approach is based on experimental measurement of fatigue life in terms of cycles to failure for different loading levels as discussed previously. On the other hand, the fracture mechanic (FM) approach is based on the existence of an initial crack in a stress-free structure. Only the *S-N* approach is emphasized in this paper.

2. FATIGUE ANALYSES AND DESIGN APPROACHES

There are two major technical approaches for fatigue analysis and design of welded joints: (1) the fracture mechanics approach and (2) the characteristic *S-N* approach. Both of these approaches are discussed briefly in the subsequent sections with the emphases on the former approach.

2.1 The Fracture Mechanics Approach

The fracture mechanics approach is based on crack growth data. For welded joints it is assumed that the initiation phase is negligible and that life can be predicted using the fracture mechanics method. The fracture mechanics approach is more detailed and it involves examining crack growth and determining the number of load cycles that are needed for small initial defects to grow into cracks large enough to cause fracture. The growth rate is proportional to the stress

range. It is expressed in terms of a stress intensity factor K, which accounts for the magnitude of the stress, current crack size, and weld and joint details. The basic equation that governs crack growth is given by

$$\frac{da}{dN} = C\Delta K^m \qquad (1)$$

where a = crack size, N = number of fatigue cycles, ΔK = range of stress intensity factor, and C and m are crack propagation parameters that come from fracture mechanics. The range of the stress intensity factor is given by Broek (1986) as

$$\Delta K = SY(a)\sqrt{\pi a} \qquad (2)$$

in which $Y(a)$ is a function of crack geometry. When the crack size a reaches some critical crack size a_{cr}, failure is assumed to have occurred. Although most laboratory testing is typically performed with constant amplitude stress ranges, Eq. 1 is always applied to variable stress range models that ignore sequence effects (Byers et al 1997). Rearranging the variables in Eq. 1, the number of cycles can be computed from

$$N = \frac{1}{CS^m}\int_{a_0}^{a}\frac{da}{Y^m} \qquad (3)$$

Eqs. 1 and 3 involve a variety of sources of uncertainty (Harris 1995). The crack propagation parameter C in both equations is treated as a random variable (Madsen 1983). However, in more sophisticated models, Eq. 1 is treated as a stochastic differential equation and C is allowed to vary during the crack growth process (Ortiz 1985 and Byers et al 1997). Lin and Yang (1983) treat the crack growth as Markov process, while Ditlevsen (1986) treats it as a first-passage problem.

2.2 The Characteristic *S-N* Approach

The Characteristic *S-N* approach is based on fatigue test data (*S-N* curves) as described in Section 1 and on the assumption that fatigue damage accumulation is a linear phenomenon (Miner's rule). According to Miner's rule, the total fatigue life under a variety of stress ranges is the weighted sum of the individual lives at constant stress S as given by the *S-N* curves, with each being weighted according to fractional exposure to that level of stress range (Hughes 1988). Upon crack initiation, cracks propagate based on the fracture mechanics concept as shown in Figure 2.

The fatigue behavior of different types of structural details is generally evaluated in constant-cycle fatigue tests and the results are presented in terms of the nominal applied stresses and the number of cycles of loading that produce failure. The resulting *S-N* curves are usually presented as straight lines on a log-log paper as shown in Figure 3. The basic equation that represents the *S-N* curve is given by

$$N = \frac{A}{S^m} \qquad (4)$$

where N = number of cycles to fatigue initiation (failure), A = the intercept of the *S-N* curve at S equals to one, S =constant amplitude stress range at N, and m = slope of the *S-N* curve. Eq. 4 can also be expressed as

$$\log N = \log A - m\log S \qquad (5)$$

where log is to the base 10. The fatigue strength can be computed over a range of lives covered by the straight line if the slope of the line and one point on the line are known. However, only one type of stress cycle and one detail are represented on an individual *S-N* curve (Munse et al 1983). In general, a least-squares analysis of log N given S is used to produce the *S-N* curve.

Uncertainty in fatigue strength is evidenced by the large scatter in fatigue *S-N* data. The scatter of the data about the mean fatigue line is not the only uncertainty involved in the *S-N* analysis (White and Ayyub 1987).

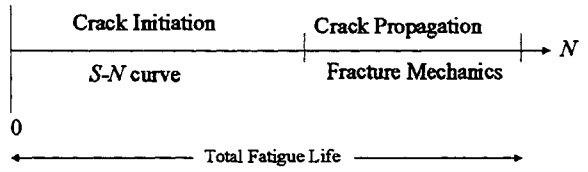

Figure 2. Comparison Between the Characteristic *S-N* Curve and Fracture Mechanic Approach

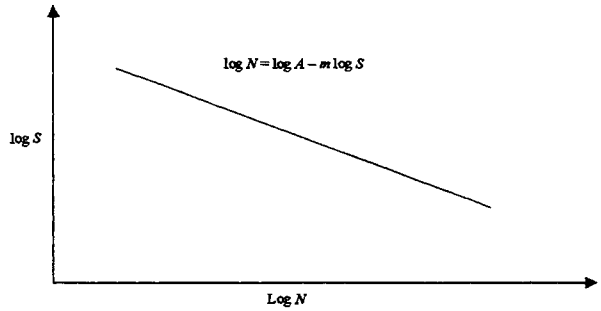

Figure 3. *S-N* Relationship for Fatigue

For this reason, a measure of the total uncertainty in the form of a coefficient of variation (*COV*) in fatigue life is usually developed to include the uncertainty in data, errors in fatigue model, and any uncertainty in the individual stresses and stress effects. According to Ang and Munse (1975), the total coefficient of variation (*COV*) in terms of fatigue life can be given by

$$\delta_N = \sqrt{\delta_f^2 + \delta_A^2 + m^2 \delta_S^2} \qquad (6)$$

where

δ_N = total *COV* in terms of cycles to failure

δ_f = variation (*COV*) due to errors in fatigue model and utilization of Miner's rule

δ_A = uncertainty (*COV*) in mean intercept of the regression line including effects of fabrication, workmanship, and uncertainty in slope

δ_S = uncertainty (*COV*) in equivalent stress range including effects of error in stress analysis

m = slope of mean *S-N* regression line

Values for δ_N and m are obtainable from sets of *S-N* curves for the type of detail under consideration. Munse et al (1983) has managed to tabulate such values. Typical values for δ_S, δ_A, and δ_f are 0.1, 0.4, and 0.15, respectively.

Other researchers such as Wirsching (1984) and Ayyub et al (1998) have tackled the same source of uncertainty in a slightly different way. For example, Wirsching (1984) introduces the random variable B to represent a bias factor and the random variable Δ to denote fatigue damage at failure. The bias factor B is assumed to account for the stress modeling error, while the fatigue damage at failure Δ is to quantify the modeling error associated with Miner's rule, which is presented in the next section. He also suggests that uncertainty in fatigue strength can be accounted for by considering the intercept of the *S-N* curve (A) as a random variable with the slope of the same *S-N* curve (m) taking as a constant. Uncertainty in B, as described by Wirsching (1984), is assumed to stem from five sources: (1) fabrication and assembly operations, (2) seastate description, (3) wave load prediction, (4) nominal member loads, and (5) estimation of hot spot stress concentration factor.

Ayyub et al (1998), in assessing the fatigue reliability of miter gates components for the U.S. Army Corps of Engineers (USACE), chose to look at the same sources of uncertainty in a slightly different way. He introduces the random variables ε' and k_s to account respectively for the uncertainty in the *S-N* relationship and fatigue stresses. He also uses a factor Δ similar to that of Wirsching (1984) to account for the uncertainty

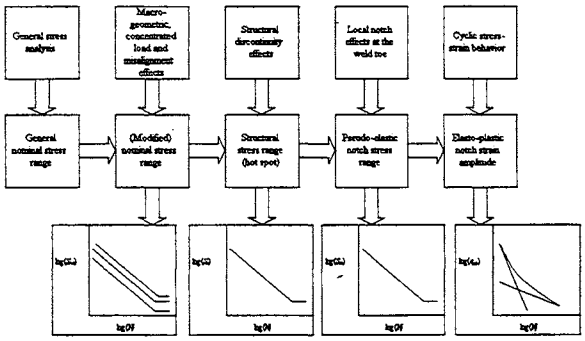

Figure 4. *S-N* Approaches for Fatigue Strength Assessment (Niemi 1995)

due to the utilization of linear cumulative damage of Miner's rule. A full coverage of fatigue parameter uncertainties is presented in Section 7.5 (Basic Random Variables) of Assakkaf (1998).

The choice of appropriate stress history is an important factor in reliability-based design and analysis for fatigue. The question is not really how to determine the stress history, rather, what constitutes an appropriate stress history. According to Moan and Berge (1997) and based on the terminology adapted by the International Institute of Welding (IIW) in 1996, the following four different approaches are classified for stress determination for fatigue design and analysis: (1) the nominal stress approach, (2) the hot spot stress approach, (3) the notch stress approach, and (4) the notch strain approach. Figure 4 shows a schematic of these approaches. Except for the nominal stress approach, the rest are commonly called local stress approach. Probably the most common approaches for determining fatigue stresses in marine industry are the nominal stress and the hot spot approaches. These methods are discussed in the next section. For more detailed description of the notch stress and notch strain approaches, Section 2 (Fatigue and Fracture) of Moan and Berge (1997) provides such a description.

2.2.1 Nominal Stress Versus Hot Spot stress

The nominal stress approach is the simplest one among the others approaches. In this approach, the stress is represented by an average loading of the whole structural detail under study. The nominal stress is the maximum stress due to sectional forces or moments or the combination of the two at the location of possible cracking site in the detail. In this approach, neither the weld toe nor the properties of the material constitutive relations are taken into consideration (Moan and Berge 1997). The *S-N* curve resulting from this analysis is unique to the structural detail for which it is established. It is possible to use one such curve to be

applied for a range of similar details if there is insignificant variation in their geometry. Most design codes nowadays divide various structural details into different classes and provide standard *S-N* curve for each class. For example, the British Standards (BS 1980) and Norwegian Standards (NS 1984) have nine classifications as shown in Table 1. However, for a more rigorous analysis, each detail must be identified with a specific curve in the menu.

The hot spot stress is defined as the fatigue stress at the toe of the weld, where the stress concentration is the highest and where fatigue cracking is likely to initiate (Mansour et al 1995). The hot spot stress is comprised of membrane and bending shell stress parts, which are linearly distributed over the plate thickness. The hot spot stress analysis takes into account two factors (Moan and Berge 1997): (1) the local increase in membrane stress due to complex structural geometry of welded joint and (2) the information of shell bending stress due to eccentricity. The exact weld toe geometry and nonlinear stress peak due to local notch at the weld toe are disregarded. The hot spot stress is an average nominal stress of the stresses near the weld. The advantage of the hot spot stress method is that only one universal *S-N* curve is required to define fatigue strength for all welds, if such curve exists. The disadvantage is that this approach may require finite element analysis to determine the hot spot stress

3. RELIABILITY-BASED DESIGN METHODS

3.1 Direct-Reliability-Based Design

A direct reliability-based design requires performing spectral analysis for the loads. The spectral analysis shall be used to develop lifetime fatigue loads spectra by considering the operational conditions and the characteristics of a ship in the sea. The operational conditions are divided into different operation modes according to the combinations of ship speeds, ship headings, and wave heights. The ship characteristics include the length between perpendicular (*LBP*), beam (*B*), and the bow form as shown in Figure 4-1. With the proper identification of the hull girder section modulus (*Z*), the bending moment histograms (moment range versus number of cycles) shall be converted to mean stress range spectra to compute the equivalent stress range $\bar{S}_e$ according to the following equation:

$$\bar{S}_e = \sqrt[m]{\sum_{i=1}^{n_b} f_i S_i^m} \qquad (7)$$

where

$\bar{S}_e$ = Miner's mean equivalent stress range
S_i = stress in the i^{th} bolck
f_i = fraction of cycles in the i^{th} stress block
m = slope of *S-N* curve
n_b = number of stress blocks in a stress (loading) histogram

Table 1. Description of Joint Details (BS 1980, NS bbb 1984, and Mansour et al 1995)

Class	Description
B	Plain steel in the as-rolled condition, or with cleaned surfaces, but with no flame cut edges or re-entrant corners. Full penetration butt welds, parallel to the direction of applied stress, with the weld overfill dressed flush with the surface and finish-machined in the direction of stress, and with the weld proved free from significant defects by non-destructive examination
C	Butt or fillet welds, parallel to the direction of applied stress, with the welds made by an automatic submerged or open arc process and with no stop-start positions within the length. Transverse butt welds with the weld overfill dressed flush with the surface and with the weld proved free from significant defects by non-destructive examination.
D	Transverse butt welds with the welds made in the shop either manually or by an automatic process other than submerged arc, provided all runs are made in the flat position.
E	Transverse butt welds that are not class C or D.
F	Load-carrying fillet welds with the joint made with full penetration welds with any undercutting at the corners of the member dressed out by local grinding.
F2	Load-carrying fillet welds with the joint made with partial penetration or fillet welds with any undercutting at the corners of the member dressed out by local grinding.
G	Parent metal at the ends of load-carrying fillet welds which are essentially parallel to the direction of applied stress.
W	Weld metal in load-carrying joints made with fillet or partial penetration welds, with the welds either transverse or parallel to the direction of applied stress (based on nominal shear stress on weld throat area).

The direct reliability-based design for fatigue requires the probabilistic characteristics of the random variables in the performance function equation. It also requires specifying target reliability index β_0 to be compared with a computed β resulting from reliability assessment methods such as first-order reliability method (FORM). The general form for reliability checking used in the rules is given by

$$\beta \geq \beta_0 \tag{8}$$

The performance function for fatigue is given by either one of the following two expressions:

$$g_1 = \frac{\Delta A}{k_s^m \bar{S}_e^m} - N_t \tag{9}$$

or

$$g_2 = \log(A) + \log(\Delta) - m\log(\bar{S}_e) - m\log(k_s) - \log(N_t) \tag{10}$$

where

Δ = fatigue damage ratio
A = intercept of the *S-N* curve
m = slope of the *S-N* curve
$\bar{S}_e$ = Miner's mean equivalent stress
k_s = fatigue stress uncertainty factor
N_t = number of loading cycles expected during the life of a structural detail.

The N_t variable is a deterministic quantity that is commonly assigned a value of 10^8 cycles.

3.2 The Load and Resistance Factor Design (LRFD)

An alternative approach for reliability-based design is the use of partial safety factors (PSF's) using a load and resistance factor (LRFD) design format. The PSF's are for both strength and load variables. They are commonly termed strength reduction and load amplification factors. The structural detail or joint element of a ship is to meet one of the following performance functions:

$$\gamma_{S_e} S_e \leq \left[\frac{(\phi_\Delta \Delta)(\phi_A A)}{\gamma_{k_s}^m k_s^m N_t} \right]^{\frac{1}{m}} \tag{11}$$

$$\log(\gamma_{S_e} S_e) = \frac{\log(\phi_A A) + \log(\phi_\Delta \Delta) - m\log(\gamma_{k_s} k_s)}{m} - \frac{\log(N_t)}{m} \tag{12}$$

where

$$S_e = \sqrt[m]{\sum_{i=1}^{n_b} f_i S_i^m} \tag{13}$$

S_e = Miner's equivalent stress range
ϕ_Δ = reduction safety factor corresponds to fatigue damage ratio Δ
ϕ_A = reduction safety factor corresponds to the intercept of the *S-N* curve
γ_{k_s} = amplification safety factor for fatigue stress uncertainty
γ_{S_e} = amplification safety factor for Miner's rule equivalent stress range

It is to be noted that the nominal S_e is the best estimate resulting from spectral analysis. The nominal (i.e., design) values of the fatigue variables shall satisfy these formats in order to achieve specified target reliability levels. The probabilistic characteristics and nominal values for the strength and load components were determined based on statistical analysis, recommended values from other specifications, and by professional judgment. These factors are determined using structural reliability methods based on the probabilistic characteristics of the basic random variables for fatigue including statistical and modeling (or prediction) uncertainties. The factors are determined to meet target reliability levels that were selected based on assessing previous designs. This process of developing reliability-based LRFD rules based on implicit reliability levels in current practices is called code calibration.

4. LRFD APPROACH FOR FATIGUE OF MARINE STRUCTURES

As mentioned earlier, the load and resistance factor (LRFD) approach consists of the requirement that a factored (reduced) strength of a structural component is larger than a linear combination of factored (magnified) load effects. In this approach, load effects are increased, and strength is reduced, by multiplying the corresponding characteristic (nominal) values with factors, which are called strength (resistance) and load factors, respectively, or partial safety factors (PSF's). The characteristic value of some quantity is the value that is used in current design practice, and it is usually

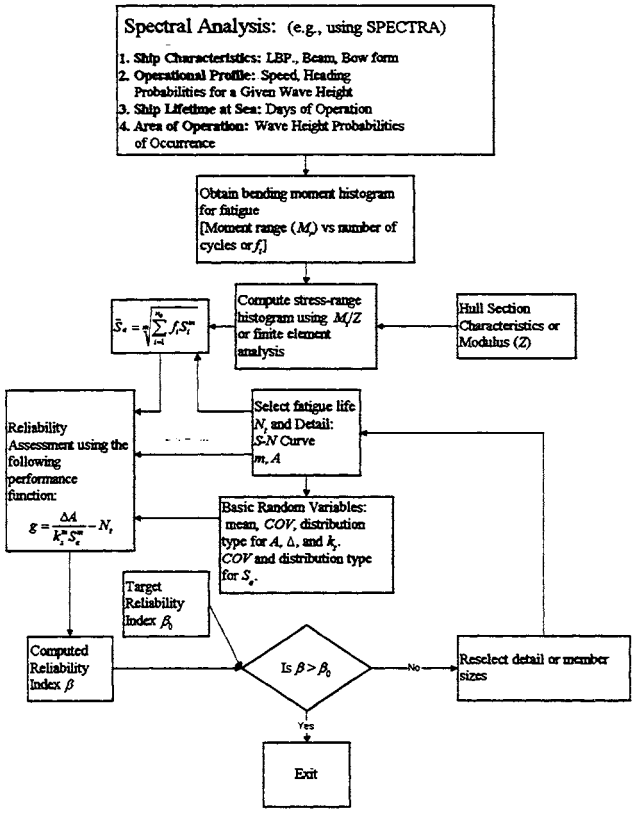

Figure 5. Direct Reliability-based Design and Analysis for Fatigue (Assakkaf 1998)

equal to a certain percentile of the probability distribution of that quantity. The load and strength factors are different for each type of load and strength. The higher the uncertainty associated with a load, the higher the corresponding load factor. These factors are determined probabilistically so that they correspond to a prescribed level of safety. Designers can use the load and resistance factors in limit-state equations to account for uncertainties that might not be considered properly by deterministic methods without explicitly performing probabilistic analysis.

Calculation of partial safety factors (PSF's) for fatigue variables in the limit state function can be accomplished using the first-order reliability methods (FORM). The partial safety factors are defined as the ratio of the value of a variable in a limit state at its most probable failure point (MPFP).

The generalized FORM approach was selected to calculate the partial safety factors due to the existence of non-normal basic random variables in the corresponding limit states for fatigue. Reliability-based design formats for fatigue can be expressed in the following form:

$$g(\Delta, A, k_s, S_e, N_t) = \frac{\Delta A}{k_s^m S_e^m} - N_t \quad (14)$$

where

$$\overline{S}_e = \sqrt[m]{\sum_{i=1}^{n_b} f_i S_i^m} \quad (15)$$

Δ = fatigue damage ratio, A = intercept of the S-N curve, m = slope of the S-N curve, $\overline{S}_e$ = Miner's mean equivalent stress, k_s = fatigue stress uncertainty factor, N_t = number of loading cycles expected during the life of a structural detail, n_b = number of stress blocks in a stress (loading) histogram, f_i = fraction of cycles in the i^{th} stress block, and S_i = stress in the i^{th} block. By equating the reliability index, β, with the target reliability index, β_O, the partial safety factors are computed. The strength variables in the limit-state at the design point (MPFP) is given by

$$S_e^* = \left[\frac{\Delta^* A^*}{k_s^{m*} N_t}\right]^{\frac{1}{m}} \quad (16)$$

By treating S_e, Δ, A, and k_s as random variables, the partial safety factors are computed as follows:

$$\phi_{S_e} = \frac{S_e^*}{S_{e_n}} \quad (17)$$

$$\gamma_\Delta = \frac{\Delta^*}{\Delta_n} \quad (18)$$

$$\gamma_A = \frac{A^*}{A_n} \quad (19)$$

$$\gamma_{k_s} = \frac{k_s^*}{k_{s_n}} \quad (20)$$

where the subscript n means nominal value. The variable N_t was treated as a deterministic quantity. However, it can be treated as a random variable, and its partial safety factor can be evaluated accordingly. The uncertainty in A can be attributed to the regression standard error.

4.1 Example 1: Partial Safety Factors for Fatigue

In this example, partial safety factors calculations for two classes of structural detail are illustrated. The probabilistic characteristics of the random variables pertaining to these details are shown in Tables 2 and 3. The first-order reliability method (FORM) was used to develop the partial safety factors. The following performance function is used as defined by Eq. 14:

$$g = \frac{\Delta A}{k_s^m S_e^m} - N_t \qquad (21)$$

where A, S_e, Δ, and k_s are random variables, m =slope of S-N curve (deterministic), and $N_t = 10^5$. The partial safety factors are defined as the ratio of the value of a variable in the performance function at its most probable failure point (MPFP) to the nominal value. Summary of the partial safety factors for details B and W of the British standards are shown in Tables 4 and 5, respectively.

Table 2. Statistics of Random Variables (Category B of the British Standards(BS 5400, 1980)

Random Variable	Mean	*COV*	Distribution Type
S_e	27.54 ksi	0.1	Lognormal
Δ	1.0	0.48	Lognormal
A	4.47 E11	0.44	Lognormal
k_s	1.0	0.1	Normal
m	4.0	n/a	n/a
N_t	10^5	n/a	n/a

Table 3. Statistics of Random Variables (Category W of the British Standards, BS 5400)

Random Variable	Mean	*COV*	Distribution Type
S_e	8.21 ksi	0.1	Lognormal
Δ	1.0	0.48	Lognormal
A	2.88 E08	0.44	Lognormal
k_s	1.0	0.1	Normal
m	3.0	n/a	n/a
N_t	10^5	n/a	n/a

Table 4. Partial Safety Factors for Category B of the British Standards (BS 5400)

β	ϕ_Δ	ϕ_A	γ_{ks}	γ_S
2.0	0.55	0.60	1.09	1.10
2.5	0.48	0.53	1.11	1.12
3.0	0.42	0.48	1.13	1.15
3.5	0.37	0.43	1.15	1.18
4.0	0.32	0.38	1.17	1.21

Table 5. Partial Safety Factors for Category W of the British Standards (BS 5400, 1980)

β	ϕ_Δ	ϕ_A	γ_{ks}	γ_S
2.0	0.52	0.57	1.07	1.08
2.5	0.45	0.50	1.09	1.10
3.0	0.39	0.45	1.11	1.12
3.5	0.34	0.40	1.13	1.15
4.0	0.29	0.35	1.14	1.17

5. DIRECT RELIABILITY-BASED DESIGN AND ANALYSIS APPROACHES FOR FATIGUE OF MARINE STRUCTURES

As mentioned earlier, the direct reliability-based design requires performing spectral analysis for the loads as described in Section 3.1. The spectral analysis is used to develop lifetime fatigue loads spectra by considering the operational conditions and the characteristics of a ship in the sea. The operational conditions are divided into different operation modes according to the combinations of ship speeds, ship headings, and wave heights. The ship characteristics include the length between perpendicular (*LBP*), beam (*B*), and the bow form as. In performing such spectral analysis, it is possible to generate bending moment histograms (moment range versus number of cycles). With the proper identification of the hull girder section modulus, these moment range spectra can be easily converted to stress range spectra. The stress range spectra are used to compute the equivalent stress range S_e as given by Eq. 15.

The reliability-based design and analysis for fatigue requires the probabilistic characteristics of the random variables in the performance function equation. It also requires specifying target reliability index β_0 to be compared with a computed β resulting from reliability assessment methods such as FORM. The performance function for fatigue is given by the following expression:

$$g_1 = \frac{\Delta A}{k_s^m \bar{S}_e^m} - N_t \qquad (22)$$

where

$$\bar{S}_e = \sqrt[m]{\sum_{i=1}^{n_b} f_i S_i^m} \qquad (23)$$

and Δ = fatigue damage ratio, A= intercept of the S-N curve, m = slope of the S-N curve, $\bar{S}_e$ = Miner's mean equivalent stress , k_s = fatigue stress uncertainty factor, N_t = number of loading cycles expected during the life of a structural detail, n_b = number of stress blocks in a stress (loading) histogram, f_i = fraction of cycles in the

i^{th} stress block, and S_i = stress in the i^{th} block. With this information at hand, it is possible to develop a methodology for reliability checking expressions and design procedures for fatigue details. This methodology is presented in the next two sections. The methodology consists of two parts: (1) reliability checking, and (2) reliability-based design stress procedure.

5.1 Reliability Checking Procedure

The following steps summarize the procedure needed to perform reliability checking on an existing ship structural fatigue detail (see Figure 5):

1. For given ship characteristics (i.e., LBP, Beam, hull section modulus, etc.), operational profiles (i.e., speed, heading), ship lifetime at sea, and area of operation, stress range spectra can be generated using for example the program SPECTRA (Assakkaf 1998).
2. With the generation of stress range spectra, the Miner's mean equivalent stress range $\bar{S}_e$ can be computed using Eq. 23.
3. At this stage, a target reliability index β_0, a ship structural detail, and design life N_t should be selected.
4. The probabilistic characteristics of fatigue variables (Δ, A, k_s) in the performance function of equation Eq. 22 are evaluated in this step. Also, the COV of S_e and its distribution type are needed in this step. Section 7.5 of Assakkaf (1998) can be consulted for guidance.
5. Once all the variables are identified and computed in steps 1 through 4, the first-order reliability method (FORM) is used to compute the safety (reliability) index β.

The safety index β computed in step 5 is compared with the target reliability index β_0. If β is greater than β_0, this mean the structural detail under study is adequate, otherwise steps 3 to 6 should be repeated.

5.2 Reliability-Based Design Stress

The following steps provide a procedure for computing the design stress for a ship structural detail:

1. A target reliability index β_0, a ship structural detail, and design life N_t should be selected.
2. The probabilistic characteristics of fatigue variables (Δ, A, k_s) in the performance function equation (Eq. 22) are evaluated in this step.
3. For the selected target reliability index β_0, probability distributions and statistics (means COV's) of the fatigue variables (Δ, A, k_s), and the coefficient of variation of the stress range S_e, the mean value of S_e (i.e., $\bar{S}_e$) is computed based on the iterative solution of FORM. The mean stress value ($\bar{S}_e$) is the design stress.

5.3 Example 2: Direct Reliability-Based Design for Fatigue of Marine Structures

In this example, a direct reliability-based procedure is used. This procedure is used to perform safety checking by evaluating the reliability indices based on selected pairs of m and A that correspond to certain fatigue details of interest, and identifying the details that meet or exceed the specified target reliability of 2.5. The performance function as defined in Eq. 22 is used in this example, where Δ, A, k_s, and S_e are random variables, and $N_t = 10^5$. The probabilistic characteristics of the random variables that are used for each detail in this example are provided in Tables 6 through 9. Summaries of the results based on this approach are shown in Table 10. An alternative procedure is to determine the design stress (mean of S_e) for each detail as outlined in Section 5.2. For target reliability β_0 of 2.5, probabilistic distributions and statistics of fatigue random variables for each detail, and the coefficient of variation of S_e, the mean design stress can be evaluated for each detail. The results based on this approach are summarized in Table 11.

Table 6. Probabilistic Characteristics of Random Variables for Detail No. 5 of Munse (1983)

Random Variable	Mean	COV	Distribution Type
S_e	6.96 ksi	0.10	Lognormal
Δ	1.0	0.48	Lognormal
A	4.47 E09	0.40	Lognormal
k_s	1.0	0.10	Normal
m	3.278	na	na
β	2.5	na	na

na = not applicable

Table 7. Probabilistic Characteristics of Random Variables for Detail No. 7(P) of Munse (1983)

Random Variable	Mean	COV	Distribution Type
S_e	7.95 ksi	0.10	Lognormal
Δ	1.0	0.48	Lognormal
A	2.88 E11	0.40	Lognormal
k_s	1.0	0.10	Normal
m	4.172	na	na
β	2.5	na	na

na = not applicable

Table 8. Probabilistic Characteristics of Random Variables for Detail # 27(S) of Munse (1983)

Random Variable	Mean	*COV*	Distribution Type
S_e	9.13 ksi	0.10	Lognormal
Δ	1.0	0.48	Lognormal
A	1.15 E12	0.40	Lognormal
k_s	1.0	0.10	Normal
m	5.277	na	na
β	2.5	na	na

na = not applicable

Table 9. Probabilistic Characteristics of Random Variables for Class B Detail (BS)

Random Variable	Mean	*COV*	Distribution Type
S_e	27.54 ksi	0.10	Lognormal
Δ	1.0	0.48	Lognormal
A	4.47 E11	0.44	Lognormal
k_s	1.0	0.10	Normal
m	4.0	na	na
β	2.5	na	na

na = not applicable

Table 10. Results of Reliability Checking for Fatigue Design (Target $\beta = 2.5$)

Detail No.	m	Mean A $(\overline{A})$	$\overline{S}_e$	Computed β	Reliability Checking
5	3.28	4.47 E09	6.96	5.6	acceptable
7(P)	4.17	2.88 E11	7.95	7.5	acceptable
27(S)	5.28	1.15 E12	9.13	4.8	acceptable
Class B	4.0	4.47 E11	27.5	2.3	unacceptable

na = not applicable

Table 11. Results Using Direct Reliability-Based Fatigue Design (Target $\beta = 2.5$)

Selected Detail	Computed Mean Value of S_e $(\overline{S}_e)$
5	14.10
7(P)	20.71
27(S)	13.57
Class B	26.27

6. REFRENCES

[1] Ang, A. H-S. and Munse, W. H., 1975. "Practical Reliability Basis for Structural Fatigue." ASCE National Structural Engineering Conference, April 14-18, Preprint No. 2494.

[2] Assakkaf, I. A., 1998. "Reliability-based Design of Panels and Fatigue Details of Ship Structures," A Ph.D. Dissertation submitted to the Faculty of the Graduate School of the University of Maryland, College Park in partial fulfillment of the requirements for the degree of Doctor of Philosophy.

[3] Ayyub, B.M., Patev, R.C., and Leggett, M.A., 1998. "Chapter 17: Fatigue Reliability Assessment of Miter Gate Components at Navigation Locks," in Uncertainty Modeling and Analysis in Civil Engineering, edited by B. Ayyub, CRC Press, 321-336.

[4] Beer, F. P., and Hohnston, E. R., 1981. "Mechanics of Materials," McCraw-Hill, Inc., 41-42.

[5] Broek, D., 1986. "Elementary Engineering Fracture Mechanics." 4th Edition, Martinus Nijhoff Publishers, Dordrecht, The Netherlands.

[6] BS 5400 (British Standards), 1980. "Steel, Concrete, and Composite Bridges; Code of Practice for Fatigue,".

[7] Byars, E. F., and Snyder, R. D., 1975. "Engineering Mechanics of Deformable Bodies," Third Edition, Thomas Y. Crowell Company Inc., 427-430.

[8] Byers, W. G., Marley, M. J., Mohammadi, J., Nielsen, R. J., and Sarkani, S., 1997. "Fatigue Reliability Reassessment Procedures: State-OF- The-Art Paper." Journal of Structural.

[9] Ditlevsen, O., 1986. "Random Fatigue Crack Growth – a first-passage problem." Engineering Fracture Mechanics, 23, 467-477.

[10] Harris, D. O., 1995. "Probabilistic Fracture Mechanics." Probabilistic Fracture Mechanics handbook, Sundarajan, ed., Chapman and Hall, New York, N.Y.

[11] Hughes, O. F., 1988. "Ship Structural Design, A rationally-Based, Computer-Aided Optimization Approach," The Society of Naval Architects and Marine Engineers, Jersey City, New Jersey.

[12] International Institute of Welding (IIW), 1996. "Recommendations on Fatigue of Welded Components," Abington Publishing, Cambridge.

[13] Lin, Y. K., and Yang, J. N., 1983. "On Statistical Moments of Fatigue Crack Propagation." Engrg. Fracture Mechanics, 18(2), 243-256.

[14] Madsen, H. O., 1983. "Probabilistic and Deterministic Models for Predicting Damage Accumulation due to Time Varying Loading." DIALOG 5-82, Danish Engrg., Acad., Lyngby, Denmark.

[15] Mansour, A. E., Wirsching, P. H., White, G., and Ayyub, B. M., 1995. "Probability-Based Ship Design: Implementation of Design Guidelines," SSC 392, NTIS, Washington, D.C., 200 pages.

[16] Moan, T. and Berge, S., 1997. "Fatigue and Fracture," Committee III.2, Proceedings of the 13th International Ship and Offshore Structures Congress, Norwegian University of Science and Technology, Trondheim, Norway, 292-294.

[17] Munse, W. H., Wilbur, T. W., Tellalian, M. L., Nicoll, K., and Wilson, K., 1983. "Fatigue Characterization of Fabricated Ship Details for Design,"SSC-318, Washington, D.C.

[18] Niemi, E., 1995. "Stress Determination for Fatigue Analysis of Welded Components," Abington Publishing, Cambridge.

[19] NS 3472 (Norwegian Standards), 1984. "Design Rules for Steel Structures,".

[20] Ortiz, K., 1985. "On the Stochastic Modeling of Fatigue Crack Growth," PhD dissertation, Stanford University, Stanford, California.

[21] University of Tennessee, Welding Research and Engineering, 1985. "Bibliography on Fatigue of Welds," Research Report.

[22] White, G. and Ayyub B., 1987. "Reliability-Based Fatigue Design for Ship Structures." Naval Engineers Journal, May.

[23] Wirsching, P. H., 1984. "Fatigue Reliability for Offshore Structures." Journal of Structural Engineering, Vol. 110, No. 10, Paper No. 19235, ASCE.

PROCEEDINGS OF THE THIRD INTERNATIONAL WORKSHOP ON VERY LARGE FLOATING STRUCTURES
(VLFS '99), VOL. I, EDS. R.C. ERTEKIN & J.W. KIM, 22-24 SEPTEMBER 1999, HONOLULU, HAWAII, USA

Developing Target Reliability for Novel Structures: the Case of the Mobile Offshore Base*

Baidurya Bhattacharya[1], Kai-tung Ma and Roger Basu
American Bureau of Shipping, Houston, TX 77060

ABSTRACT

Target reliabilities are usually calibrated to existing structures (of the same class) having a history of successful service. However, as the offshore industry continues to witness innovations, some novel structures clearly exceed the scope of existing design standards. A reliability-based design is attractive in such cases, but the calibration exercise is not entirely feasible for such novel structures and target reliabilities need to be derived from more fundamental considerations.

The US Navy's Mobile Offshore Base (MOB) is conceived as a unique offshore structure in terms of function and size, and no precedence or industry standard exists for such a structure. The American Bureau of Shipping is developing a reliability-based MOB Classification Guide. This paper describes how significant MOB limit states (at the component as well as system levels) are identified and corresponding target reliabilities are derived. Reliabilities of various existing structures and available analytical methods for determining target reliabilities are surveyed. Careful consideration is given to failure consequences --- tangible and intangible, and reliability of intact as well as damaged structures is considered. The methodology is general and may be adopted for other types of structures.

1. INTRODUCTION

The objective of every structural design is to develop a structure that is able to perform its function in a cost-effective manner while meeting the constraints of safety. A reliability-based design can address the issue of safety in a transparent and quantitative manner, by specifying the maximum permissible probabilities of failure (or non-compliance) in all modes that are relevant to the given kind of structure. The target reliability, which is the complement of the maximum permissible failure probability, should ideally depend on the consequence of the type of failure in question. A well-designed structure should be safe enough against every failure mode, but just so, if it has to be economical as well.

The question, 'How safe is safe enough?', needs to be asked when setting the reliability target for a structure. Conventional structures that have a history of successful service, such as concrete buildings, highway bridges and steel vessels, can be deemed sufficiently safe, and their calculated reliability levels may be used as the targets for new structures of the same kind. This, in principle, is done when a new reliability-based code is developed for a given class of structures having a successful history of use and a wide knowledge-base about their performance [1]. The objective is to produce more uniform levels of safety and more optimal structures.

1.1 The Case for Novel Structures

The offshore industry is continuing to witness innovations in structural concepts and designs. Some of these new concepts clearly exceed the domain of applicability of existing codes and structures. The rational decision for such structures is to adopt a reliability-based design (e.g., [2]).

However, calibration of the above sort is difficult or even impossible, if the structure is novel with no history of use or if the pace of innovation in the industry is relatively fast. The target reliability (and partial safety factors if an LRFD format is desired) required in the reliability-based design of such novel structures therefore needs to be derived from more fundamental considerations. A variety of methods, analytical as well as subjective, can be employed to relate the value of this novel structure and consequences of its failure to its target reliability.

---

* The views expressed in this paper are those of the authors and not necessarily those of the American Bureau of Shipping.

[1] Corresponding author. Telephone: 281 877 6127. Email:bbhattacharya@eagle.org. Fax: 281 877 5931.

1.2 The Mobile Offshore Base

The US Navy's Mobile Offshore Base (MOB) is currently undergoing feasibility studies under a Science and Technology Program administered by the Office of Naval Research. The MOB is intended to be a mile-long, multi-module, sea-borne forward-deployable logistics facility combining the attributes of aircraft carriers, troop transports, cargo vessels and offshore semi-submersible platforms [3]. It will be a unique marine structure in terms of function and size. Needless to say, there is no precedence, no validated design capability, no fabrication or operational experience, and no industry standard for such a structure.

The American Bureau of Shipping (ABS) is developing a reliability-based Classification Guide for the MOB [4]. A rigorous process is being followed in establishing what the appropriate MOB target reliabilities should be. Careful consideration is given to the failure consequences, including loss of lives and structure, including socio-political factors like national prestige.

The process, which is a mix of quantitative and qualitative approaches, has yielded target reliabilities of the level presented in Section 4 of this paper. Some of these are significantly higher than those typical of the commercial offshore industry. Studies are currently underway to establish their practical impact on structural designs, and it may be necessary as a consequence of this exercise to adjust target reliabilities such that the conflicting demands of safety, economy and other requirements are met in a balanced fashion.

Setting target reliabilities for high-value novel structures is not an engineering decision alone: active involvement on the part of the owners and policy-makers is also required. With this paper we therefore hope to continue the discussion within the interested community.

This paper summarizes a representative set of target reliabilities in various existing codes and structures (Section 2), and then lists some of the available analytical methods for deriving target reliabilities (Section 3). In Section 4, we demonstrate how target reliabilities for different MOB limit states are derived.

2. EXISTING RELIABILITY LEVELS

This section compiles target reliability levels, explicit or implicit, in existing codes and structures. It should be noted that some cases listed here report annual target reliability, and others report life-time target reliability. Also note that comparison between these values may be difficult as failure may be defined differently (i.e., limit states may be set up differently) in the various codes and projects. For example, some codes may define failure as the onset of yielding while others consider full plasticity.

Table 1: P_f and generalized reliability index, β

P_f	10^{-1}	10^{-2}	10^{-3}	10^{-4}	10^{-5}	10^{-6}	10^{-7}	10^{-8}
β	1.28	2.32	3.09	3.71	4.25	4.75	5.20	5.60

In this paper, the terms "reliability" and "failure probability" are used interchangeably. The relation between reliability (L) and failure probability (P_f) is:

$$L = 1 - P_f \tag{1}$$

The probability of failure, P_f, can equivalently be expressed in terms of the generalized reliability index $\beta = \Phi^{-1}(1-P_f)$, where Φ is the normal distribution function. For convenience, relation between the two is listed in Table 1.

2.1 Reliability Levels in Existing Rules/Standards

2.1.1 ABS Rules for Ship Structures

Mansour calculated the safety index for existing ships the design of which were based on ABS Rules [5]. The limit state was of hull girder bending against still-water and wave-induce bending moments. It is found that the life-time failure probabilities implied in ABS Rules ranged from 10^{-6} to 10^{-3}.

2.1.2 API Codes for Offshore Structures

The average annual failure probability in API RP 2A LRFD code has been estimated as 4×10^{-4} [6]. See also Section 2.2.3 and 2.2.5.

2.1.3 CSA Codes for Offshore Structures

The Canadian Standards Association [7] defines two safety classes and one serviceability class for the verification of the safety of the structure or any of its structural elements (Table 2).

2.1.4 DNV Rules for Offshore Structures

DNV suggests that minimum values of target reliabilities should be calibrated against well-established cases that are known to have adequate safety [8]. If, however, it is not possible to establish target reliability by calibration against similar structures, then the minimum target reliability values may be based upon accepted decision analysis techniques, or taken in accordance with Table 3.

2.1.5 AISC and other Structural Codes

β values for various structural design codes are summarized in Table 4, taken from [9]. Note that these values correspond to component failure and not collapse of the structure.

Table 2: CSA's annual target P_f [7]

Safety class	Consequence of failure	Annual target P_f
Safety Class 1	Great risk to life or high potential for environmental pollution or damage	10^{-5}
Safety Class 2	Small risk to life or low potential for environmental pollution or damage	10^{-3}
Serviceability	Impaired function and none of the above	10^{-1}

Table 3: DNV's annual target reliability [8]

Type of structural failure	Less serious consequence	Serious consequence
I – Redundant structure	10^{-3}	10^{-4}
II – Significant warning before the occurrence of failure in a non-redundant structure	10^{-4}	10^{-5}
III – No warning before the occurrence of failure in a non-redundant structure	10^{-5}	10^{-6}

Table 4: Life-time β's in structural standards [9]

Standard	Remarks	β
AISC LRFD 1984, ANSI A58.1 1982	gravity loads (dead, snow and live loads)	3.0
	gravity + wind	2.5
	gravity + earthquake	1.75
Canadian codes for steel, concrete buildings, bridges	30-year lifetime	3.5
Eurocode	normal construction	3.5
Nordic Code (Denmark, Finland, Iceland, Norway & Sweden)		4.3

2.2 Target/Recommended Reliabilities in Existing Structures

2.2.1 Design Criteria for Confederation Bridge

Design of the Confederation Bridge (Northumberland, Canada) required that load and resistance factors be calibrated to "a β of 4.0 for ultimate limit states, for a 100 year life" [10].

2.2.2 Existing Ship Structures

Mansour et al [11] analyzed the reliabilities of two military and two commercial vessels (Table 5). Two kinds of loading situations were considered: short term and long term. The failure modes were: (i) primary (initial yield), (ii) primary (ultimate strength),

Table 5: Critical β's for 4 ships in 4 limit states [11]

Limit state	Cruiser 1	Cruiser 2	SL-7	Tanker
Initial yield	7.40	4.54	4.20	3.31
Ultimate	4.09	3.09	2.67	0.81
Secondary	3.75	1.73	2.11	0.04
Tertiary	3.71	2.39	3.58	2.30

Table 6: Recommended life-time target β's [11]

Limit state	Commercial ships	Naval ships
Initial yield	5.0	6.0
Ultimate	3.5	4.0
Secondary	2.5	3.0
Tertiary	2.0	2.5
Fatigue -minor	1.0	1.5
-significant	2.5	3.0
-severe	3.0	3.5

(iii) secondary (gross panel buckling in deck or bottom of ship), and (iv) tertiary (buckling of a single stiffened panel), each of which was applicable to hogging and sagging modes.

Based on their analyses, survey and professional judgment, Mansour et al [11] recommended a set of life-time target reliability levels for naval and commercial ship structures (Table 6).

2.2.3 Jacket Structures and Jackup Rigs

The implicit reliability levels in two reliability-based codes -- the API RP2A for fixed jackets and the SNAME T&R Bulletin 5-5A for jack-ups -- were determined by analyzing two representative structures (a jacket and a jack-up respectively in the UK sector of the North Sea) built to the two standards [12]. The P_f of the jacket was found to be 5.9×10^{-5} at the component level and 4.2×10^{-6} at the system level. The corresponding values for the jack-up were 1.1×10^{-3} for component and 4.5×10^{-5} for the system.

2.2.4 Floating Production Systems

A specialist panel of the 13th ISSC [13] presented a set of recommended target system reliability levels for floating production systems which are listed in Table 7. These are based on expert opinions and judgments. Corresponding component reliabilities are about an order of magnitude higher.

2.2.5 Miscellaneous Floating Structure

Another specialist panel of the 13th ISSC [6] also compiled a set of reliabilities implicit in the design of various floating structural components and systems (Table 8).

Table 7: Recommended FPS target reliability [13]

Unit		Failure probability
Monohulls		10^{-5} to 10^{-3}
Semi-submersibles	-Hulls	10^{-4} to 10^{-3}
	-Moorings	$2x10^{-3}$ to 10^{-2}
TLPs:	-Hull	10^{-4} to 10^{-3}
	-Tethers	10^{-5} to 10^{-4}

Table 8: Annual P_f in existing structures [6]

Type of Structure	Relevant code	Area of operation	Annual P_f
Production ship	"current codes"	North sea Tropics	10^{-4} $<10^{-4}$
Merchant vessels	"current codes"	North sea	10^{-3}
Floating steel:			
- platform hulls	NPD/DNV,	unknown	10^{-6} to 10^{-4}
-cylindrical shells	API RP2T	unknown	10^{-5} to $5x10^{-4}$
- stiff. flat plates		unknown	$10^{-5}$to $5x10^{-4}$
- stiff. panels	API RP2T,	unknown	10^{-4}
- shell plates	RCC/ API		10^{-3}
- stiff. shell bays	Bul-2U		$3x10^{-4}$
Fixed offshore structures	API RP2A LRFD	unknown	$4x10^{-4}$
	CSA S471	unknown	10^{-5} to 10^{-4}

2.2.6 Highway Bridges

The following reliability requirements have been suggested to ensure adequate redundancy of a highway bridge structure [14]:

$$\beta_u - \beta_1 \geq 0.85, \quad \beta_f - \beta_1 \geq 0.25, \quad \beta_d - \beta_1 \geq -2.7 \qquad (2)$$

The subscripts 1, *f*, *u* and *d* refer, respectively, to first member failure, functionality limit state, ultimate state and damaged condition limit state.

2.2.7 Aircraft Structures

The international Civil Aviation Organization has set the maximum probability of collision with a stationary object during aircraft landing at 10^{-7} [15].

3. AVAILABLE METHODS

The techniques of evaluating risk and reliability continue to mature, and there are several methods available for determining target reliability rationally. Some of the methods are summarized in this section.

3.1 Risk-based Approach

In a probabilistic context, risk is defined as

$$\text{Risk} = p \times C \qquad (3)$$

where C is the consequence of an event (in terms of dollars, lives lost etc) and p is the probability (or likelihood) of the event occurring. Figure 1, based on [16] and [17] describes the risk levels in different industries. The failure probabilities are based on historical rates of accidents. The consequences are based on monetary costs (actual costs, insurance payments and judicial awards) and fatalities that have been associated with failures. The two straight lines indicate acceptable and marginal combinations of likelihoods and consequences.

Initial estimates suggest that the cost of a MOB is of the order of 10 billion US dollars. Assuming that the acceptable level of risk for a MOB is comparable to that shown in Figure 1, the acceptable annual P_f of a MOB is of the order of 10^{-6}.

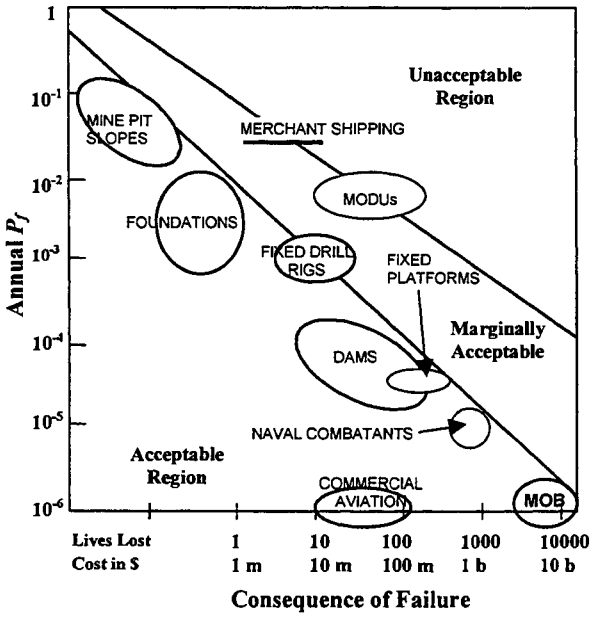

Figure 1: Risk diagram

3.2 Life Cycle Cost Analysis

Target reliabilities can be chosen to minimize the expected total cost over the service life of the system. In a simple way the expected total cost, C_T, is:

$$C_T = C_I + C_F p \qquad (4)$$

where C_I, C_F and p are, respectively, initial cost, failure cost and failure probability. C_I and the expected failure cost $C_F p$ can be approximated as:

$$C_I = a(1 + b\beta) \tag{5}$$

$$C_F p = C_F \Phi(-\beta) \cong C_F c \exp\left(-\frac{\beta}{d}\right) \tag{6}$$

where a and b are constants for the structure; c and d are constants that relate β to p. Note that there are other formulations for modeling C_I and C_F p [18]. The reliability index β_t that minimizes C_T is given by:

$$C_F = \frac{abd}{c} \exp\left(\frac{\beta_t}{d}\right) \tag{7}$$

This provides a formal approach to estimating target reliability. However, constants a and b can be difficult to determine for a unique structure such as the MOB.

3.3 Code Calibration

As mentioned earlier, calibration of reliabilities and partial factors is suitable for generic structures with a history of successful service. Consequently, this is not applicable to a novel structure such as a MOB.

3.4 Professional Judgment

Safety factors have traditionally been based on experience and subjective judgment. If an activity fails to provide a tolerable balance of risks and benefits, then targets and standards are modified. The failure of bulk carriers in the recent past shows an example where codes/rules were enhanced after a series of casualties.

For novel and innovative systems, a professional committee may select reasonable design criteria based on best available information, which need to be subsequently approved by regulatory agencies.

Table 9: Society's general reaction to risk [19]

Probability	Society Reaction
10^{-3}	This level is unacceptable to everyone. When risks approach this level, immediate action should be taken to reduce the hazard.
10^{-4}	People are willing to spend public money to control hazards at this level. Safety slogans popularized for accidents in this category show an element of fear (e.g., the life you save may be your own).
10^{-5}	Though rare, people still recognize these hazards, warn children (e.g., drowning, poisoning). Some accept inconvenience to avoid such hazards (e.g., avoid air travel).
10^{-6}	Not of great concern to the average person. People are aware of these hazards, but feel "it can never happen to me" -- a sense of resignation if they do (e.g., an act of God).

3.5 Social Criteria

Keese and Barton [19] related numerical probabilities to qualitative statements of society's general reaction to perceived levels of risk (Table 9).

3.5.1 Flint's Approach

Flint developed an empirical formula in [20] for setting the annual target failure probability, p_t, as

$$p_t = \frac{K_s}{n_r} p' \tag{8}$$

where:

p' = basic annual probability of death accepted by an individual member of society. Typical value used in the UK is 10^{-4}.

K_s = social criterion factor. If activity on a structure is hazardous and voluntary, a person may be willing to increase his exposure by a factor of K_s, whose typical value is 5.

n_r = aversion factor defined as the number of people involved. Public reaction to an accident is assumed to be in direct proportion to the number of people involved.

However, this method does not include the loss of the structure and properties in the consequence of failure, but only considers loss of lives.

To set the target reliability for MOB, assume there are total 5000 personnel onboard the connected modules in operational mode. Use the typical value of 5 for the social criterion factor. This yields a target annual failure probability of 10^{-7} as shown below:

$$p_t = \frac{K_s}{n_r} p' = \frac{5}{5000} 10^{-4} = 10^{-7} \tag{9}$$

The value of p_t should be lower if economic costs of failure are taken into consideration. On the other hand, military structures may be governed by a different set of parameters p' and K_s.

3.5.2 Allen's Approach

Allen [21] proposed a somewhat different formula:

$$p_t = \frac{A}{W\sqrt{n_r}} 10^{-5} \tag{10}$$

where, n_r = aversion factor,
A = activity factor, and
W = warning factor.

Allen's approach uses $1/\sqrt{n_r}$ rather than $1/n_r$. This suggests the influence of utility theory notions in which the rate of risk aversion decreases with the number of fatalities [22].

To set the target reliability for MOB, assume there are 5000 personnel onboard. Use 10.0 and 0.1 for A and W, respectively. This yields the annual target:

Table 10: Typical values of activity factor [21]

Type of Activity		A
Post-disaster activity		0.3
Normal activities	-buildings	1.0
	-bridges	3.0
High exposure structures (construction, offshore)		10.0

Table 11: Typical values of warning factor [21]

Nature of Warning	W
Fail-safe condition	0.01
General failure with some warning likely	0.1
Gradual failure hidden from view	0.3
sudden failure without Previous warning	1.0

$$p_t = \frac{10}{0.1\sqrt{5000}} 10^{-5} = 1.4 \cdot 10^{-5} \qquad (11)$$

3.5.3 Fatal Accident Rate

Fatal accident rate (FAR) is defined as the number of fatalities per 1000 people working 2500 hrs a year and having working lives of 40 years each:

$$\mathrm{FAR} = 10^8 P[F] / T_h \qquad (12)$$

where $P[F]$ is probability of fatality, and T_h is the exposure time in person-hours [23]. Typical values of FAR in the UK ranges from 5 (chemical processing industry) to 67 (construction industry). However, it is difficult to ascertain what an acceptable FAR should be for activities related to a MOB.

4. MOB TARGET RELIABILITIES

MOB target reliabilities for different limit states are developed in this section. These are based on the material presented in Sections 2 and 3, as well as on the deliberations in the MOB Standards and Criteria Working Group formed as part of the MOB Science and Technology Program.

4.1 Definitions of Structural Categories

Current MOB concepts variously envision the MOB to be composed of 3 to 6 modules connected in series. Each of these modules, which typically have a semi-submersible form, is also capable of operating and transiting individually. Like any complex structural system, a MOB is composed of various structural subsystems, which is turn are composed of numerous elements and assemblies. It is important to precisely define these structural categories since the consequence of exceedance of a particular class of limit state depends on the type of structure involved, its accessibility, redundancy and so on.

Structural Element: A structural element is the simplest structural unit, such as a tubular member, a longitudinal, a stiffener or a connection.

Structural Assembly: A structural assembly is a collection of elements structurally connected, such as a stiffened plate panel or a bulkhead. Several structural elements constitute a structural assembly.

Structural Sub-system: A sub-system refers to a major constituent of an SBU, such as deck, pontoon or column. Several structural elements and assemblies constitute a structural sub-system.

Structural System: The structural system refers to the entire MOB in its connected state, and to an individual SBU (module) when disconnected. Several structural sub-systems constitute the structural system.

Connector: Due to the uniqueness of the intermodule connectors and the wide differences in their concept designs, inter-module connectors (structures/devices which physically or functionally connect two adjacent MOB modules) have been placed in a separate category, but are equivalent to a structural subsystem in importance.

4.2 Limit States

Four classes of limit states are considered for the MOB:

1. Serviceability/operability
2. Fatigue
3. Ultimate
4. Global failure/survivability.

These are defined in Table 12.

The first three are essentially element-level (or sometimes subsystem level) limit states, while the last one pertains only to the entire system. Exceedance of an element-level limit state may have different consequences depending on the position and function of the element, the degree of structural redundancy etc. For a complex structure such as a MOB, it is therefore necessary to assign different consequences to the exceedance of a given class of limit state, since any rational assignment of target reliability will need to take into account the consequences of limit state violation. Levels of consequence are discussed next.

4.3 Consequences of Failure

Depending on the scale of structural involvement in the exceedance a given class of limit state, more than one consequences of failure are possible. Five levels of failure consequence, in increasing magnitude, are possible for a MOB:

Table 12: MOB structural limit states

Limit State	Scale of Structural Participation	Definition of Limit State
Serviceability/ Operability	Mostly elements/ assemblies, sometimes subsystem and system	Disruption of normal use (including military operations) due to excessive deflection or deformation, wear, local yielding or vibration.
Fatigue	Element/assemblies, inter-module connectors	Critical level of cumulative fatigue damage or critical crack size determined by functional considerations, fracture toughness, and/or static strength.
Strength	Element/assemblies, inter-module connectors	Local failure such as rupture, instability, plastic mechanism, and buckling.
Global Failure /Survivability	Entire system (fully connected MOB, or single module when disconnected)	Loss of entire structure (i.e., capsizing, sinking, loss of stationkeeping) (i) as a result of *progressive collapse*, or (ii) in *damaged condition* after sustaining severe damage in a subsystem. Includes non-structural initiating events such as fire, explosion, failure of other systems such as dynamic positioning or power generation.

Table 13: Possible consequences of limit state exceedance and scale of structural involvement

Limit state	Consequence				
	Minor	**Moderate**	**Serious**	**Critical**	**Catastrophic**
Serviceability	element/ assembly	subsystem, system			
Fatigue	element/ assembly (redundant & accessible)	element/ assembly (redundant but inaccessible)	element/assembly (nonredundant)	assembly (nonredundant), subsystem	
			intermodule connector (redundant design)	intermodule connector (nonredundant design)	
Strength		element (redundant)	element/assembly (redundant)	element/ assembly (non-redundant), subsystem	
			intermodule connector (redundant design)	intermodule connector (nonredundant design)	
Global failure					system

1. *Minor*: Inconvenience.
2. *Moderate*: Interference with operation, no immediate threat to structural integrity or life.
3. *Serious*: Impaired operation/ threat to structural integrity and life.
4. *Critical*: Impaired mission/ loss of structural integrity and life.
5. *Catastrophic*: Loss of mission, lives, module/ MOB.

The successive levels differ by one order of magnitude.

Exceedance of serviceability limit states can only lead to minor or moderate consequences. Exceedance of fatigue limit states, depending on structural scale, accessibility and redundancy, can have any of the first four levels of consequence. Exceedance of strength limit states cannot have a minor consequence, but depending on structural scale and redundancy, can have moderate, serious or critical consequences. Finally, the catastrophic consequence is reserved for the global failure limit state. The possible consequences of limit state exceedance and scale of structural involvement are provided in Table 13.

4.4 Proposed Target Reliabilities for Different Limit States

The target reliability of each class of limit state as applied to an element/assembly, a subsystem or the system should take into account the consequence of its violation.

The MOB global failure limit state has the most severe consequence, and the target reliability for this limit state is selected first (Section 4.4.1).

The target reliabilities for the element-level limit states are then fixed on a uniform risk basis (Section

4.4.2). Since a MOB is required to fulfill mission requirements in addition to having structural integrity, operational availability numbers are also incorporated in target reliabilities where appropriate.

Finally, a MOB is expected to encounter a range of accidental loads (occurring from collision, grounding, accidental explosions etc.), and weapons effects. Section 4.4.3 discusses target reliabilities against these events.

MOB target reliabilities are specified as life-time targets (based on a 40-year life), instead of annual targets that are sometimes provided for floating structures. Life-time targets are preferred as they implicitly take into account structural degradation due to operational and service conditions. This is particularly relevant in view of the MOB's maintainability options, namely, long time-intervals between scheduled maintenance, and lack of dry-dock inspection/repair during its entire life.

4.4.1 Target Reliability of the Structural System

While determining the target system reliability for a MOB, we note that (i) there is no truly comparable floating structure (in terms of cost and complexity) that could provide a benchmark, and (ii) there are possible "intangible" consequences of MOB failure (like mission failure and loss of national prestige) that are difficult to be assigned dollar or loss-of-life values (which are required in risk or cost analyses). On the other hand, a balance needs to be found so that a very high reliability does not come in the way of performance and efficiency.

The following qualitative observations can be made about MOB reliability:

1. The MOB system reliability should exceed those of all commercial floating structures such as merchant ships, jacket platforms, jack-up rigs etc.
2. The MOB system reliability should be greater than building structures, and its component reliabilities should be greater than those of building structure components.
3. The reliability of MOB should be greater than other naval vessels taking into account its value and strategic importance.

Table 14 lists various estimates based on which MOB target reliability may be assigned.

For example, a value of 10^{-7} per year may be selected for MOB system P_f. However, Table 14 does not take into account intangible consequences of failure, and we therefore introduce a factor of 2 to account for such additional consequences. The desired target annual P_f that produces the same level of risk is then 5×10^{-8}. Based on a 40 year life, the target life-time failure probability is 2×10^{-6}.

Table 14: Comparative estimates of target P_f

Method	Allowable system failure probability
Risk analysis (Figure 1)	10^{-6} per year
CSA - Safety Class 1 (Table 2)	10^{-5} per year
DNV - serious consequence, non-redundant (Table 3)	10^{-6} per year
Professional recommendations - naval ships, ultimate strength (Table 6, Table 7)	10^{-5} life time
Social criteria (Eqs 9, 11)	10^{-7} to 10^{-5} per year
Existing structures (Sections 2.1.1, 2.1.2, 2.1.5, 2.2.3, 2.2.5, Table 4, Table 7, Table 8)	10^{-6} to 10^{-3} per year

In general, let us denote the target life-time failure probability by q^* (row 4b in Table 15). The consequence of the loss of one module is roughly an order of magnitude lower than that of the entire MOB, and the life-time target P_f of one module is set at $10q^*$ (row 4b in Table 15).

The proposed life-time target P_f's for all limit states and structural categories are presented in Table 15. The column of maximum permissible P_f's pertains only to structural integrity and not to other systems such as dynamic positioning, etc. Unless otherwise noted, these are unconditional life-time probabilities.

4.4.2 Target Reliability of Elements/Assemblies, Subsystems and Connectors

The reliability of elements/assemblies, connectors and subsystems are assigned according to Table 13 on a uniform risk basis. Recall that risk is defined as the product of consequence and probability of occurrence. Rows 1a through 3f of Table 15 list target reliabilities for these structural categories under serviceability, fatigue and strength limit states. These values assume that $q^* < 10^{-5}$, which in turn is based on the assumption that there is an order of magnitude difference between successive levels of consequence.

Note that rows 1b, 2d, 2f, 3c and 3e incorporate operational availability requirements as well. Values A_1, A_2 are expected to be provided by the Department of Defense.

4.4.3 Target Reliability Against Accidents and Weapons Effects

It is likely that during its service-life a MOB will be subject to accidents and weapons effects. However, unlike environmental loads and dead & live loads, probabilistic characterization of accidents and weapons effects is generally not practical. A full

Table 15: Proposed life-time target reliability levels (40-year life)

Class Of Limit State	No.	Consequence	Scale of Participating Structure	Maximum Permissible Life-time P_f
Serviceability/ Operability	**1a**	minor	Structural element or assembly	$10^5\, q^*$
	1b	moderate	Structural sub-system or SBU or fully connected MOB	$\min(10^4\, q^*, 1\text{-}A_1)$
Fatigue	**2a**	minor	Structural element/ assembly (redundant & accessible)	$10^5\, q^*$
	2b	moderate	Structural element/ assembly (redundant but inaccessible)	$10^4\, q^*$
	2c	serious	Structural element/assembly (non-redundant)	$10^3\, q^*$
	2d	serious	Intermodule connector (redundant design)	$\min(10^3\, q^*, 1\text{-}A_2)$
	2e	critical	Structural element/assembly (non-redundant) or subsystem	$10^2\, q^*$
	2f	critical	Intermodule connector (non-redundant design)	$\min(10^4\, q^*, 1\text{-}A_2)$
Strength	**3a**	moderate	Structural element (redundant)	$10^4\, q^*$
	3b	serious	Structural element/ assembly (redundant)	$10^3\, q^*$
	3c	serious	Intermodule connector (redundant design)	$\min(10^3\, q^*, 1\text{-}A_2)$
	3d	critical	Structural element/ assembly (non-redundant) or sub-system	$10^2\, q^*$
	3e	critical	Intermodule connector (non-redundant design)	$\min(10^2\, q^*, 1\text{-}A_2)$
	3f	critical	Structural sub-system subject to weapons effect / accident of specified magnitudes	$10^4\, q^*$ (conditional)
Global Failure / survivability				
(i) Progressive Collapse	**4a**	catastrophic: loss of one module	One module	$10\, q^*$
	4b	catastrophic: loss of all modules	Fully connected MOB	q^*
(ii) Damaged Condition	**4c**	catastrophic: loss of one module	One module after loss of one subsystem	$10^5\, q^*$ (conditional)

q^* = life-time target failure probability of entire MOB, assumed less than 10^{-5}.
A_1 = minimum permissible availability of one module, A_2 = minimum permissible availability of connector.

reliability analysis is therefore not feasible under these types of loading and corresponding target reliabilities are prescribed in a conditional format:

The subsystem target reliability under weapons effect (row 3f of Table 15) is conditional on an MCE (minimum credible event) weapons load or a specified accidental event. This event occurs at any potential location within the subsystem and is expected to cause substantial local structural damage at the element/assembly level.

The damaged condition limit states represent global failure occurring after the MOB sustains severe damage in a structural sub-system. Such damage may be the result of accidents (e.g., grounding, collision, fire) or weapons effects (explosions, shock waves etc.), and is quantified by removal of a structural sub-system at a time. Consequently, irrespective of how the damage occurs, row 4c of Table 15 prescribes the target reliability conditional on the damage.

5. CONCLUSIONS

This paper addresses the problem of setting design criteria for structures for which there is no direct experience; the subject structure in this case is the Mobile Offshore Base. As discussed in the paper a reliability-based framework is considered the most appropriate for MOB, and in this context design criteria are expressed in terms of target reliabilities.

In the absence of past history "calibration", the most common method used for setting target reliabilities, is not an option in the case of MOB particularly for global levels of response. This paper discusses the various methods available for establishing target reliabilities, and also presents existing data on reliability for large engineered structures. This data provides a useful basis upon which to base MOB reliability levels.

A risk-based approach is employed to develop a hierarchy of reliability levels which takes into account the failure mode considered and the consequence of failure. A key parameter in this hierarchy of reliability levels is the extent of participation of the structure in the failure mode in question.

Studies investigating the application of the reliability methodology to MOB are currently underway. The objective of these studies is to ensure that the framework is consistent and that the resulting designs strike a balance between the competing claims of safety, economy, etc.

Acknowledgement

The authors wish to thank the Office of Naval Research for sponsoring this work as part of the MOB Science & Technology Program. Oversight of this project is provided by the Standards and Criteria Working Group chaired by Dr. Theodore Shugar of Naval Facilities Engineering Service Center, Port Hueneme, CA.

References

[1] Ellingwood, B. and Galambos, T. V. "Probability-Based Criteria for Structural Design", *Structural Safety,* vol. 1, pp. 15-26. 1982.

[2] Moan, T. "Current Trends in the Safety of Offshore Structures", vol. IV, *Proceedings of the Eighth International Offshore and Polar Engineering Conference*, Honolulu, 1997.

[3] Remmers, G., Zueck, R., Palo, P. and Taylor, R. "Mobile Offshore Base", *Proceedings of the 8th International Offshore and Polar Engineering Conference,* Montreal, Canada, 1998.

[4] ABS. *Draft Mobile Offshore Base Classification Guide*, Proprietary Publication subject to restricted distribution, Houston, TX, 1999.

[5] Mansour, A. E. *An Introduction to Structural Reliability Theory*, Ship Structure Committee Report 351, 1990.

[6] Committee IV.1, "Design Principles and Criteria", *Proceedings 13th International Ship and Offshore Structures Congress*, Trondheim, Norway, 1997.

[7] CSA, *General Requirements, Design Criteria, the Environment, and Loads*, A National Standard of Canada, CAN/CSA-S471-92, 1992.

[8] DNV, *Structural Reliability Analysis of Marine Structures*, Classification Notes No. 30.6, 1992.

[9] Galambos, T. V. "Design Codes", *Engineering Safety,* ed. D. Blockley, McGraw Hill, 1992.

[10] MacGregor, J. G. et al. "Design Criteria and Load and Resistance Factors for the Confederation Bridge", *Canadian J. of Civil Engineering*, vol. 24, pp. 882-897, 1997.

[11] Mansour, A. et al. *Assessment of Reliability of Existing Ship Structures,* Ship Structure Committee Report No. SSC-398. Washington DC, 1997.

[12] MSL Engineers Limited. *Reliability of Fixed and Jack-up Structures,* Draft Final Report. 1996.

[13] Committee V.6, "Structural Design of Floating Production Systems", *Proceedings 13th International Ship and Offshore Structures Congress*, Trondheim, Norway, 1997.

[14] Ghosn, M. and Moses, F. *Redundancy in Highway Bridge Superstructures,* Report 406, Transportation Research Board, National Academy Press, Washington, DC. 1998.

[15] Polky, J. N. and Held, J. T. "Analysis of the Collision Risk for Aircraft Operation on a Mobile Offshore Airfield", *Proceedings, 22nd UJNR Marine Facilities Panel Meeting,* Arlington, VA, 1998.

[16] Whitman, R., "Evaluating Calculated Risk in Geotechnical Engineering," *J. of Geotechnical Engineering,* ASCE, Vol. 110, No. 2, 1984.

[17] Cullen, H. N. *The Public Inquiry into the Piper Alpha Disaster,* Technical Report, The Parliament by the Secretary of the State for Energy, 1990.

[18] Bea, R. G., *Reliability Based Design Criteria for Coastal and Ocean Structures*, The Institution of Engineers, Australia, 1990.

[19] Keese, D. L. and Barton, W.R., "Risk Assessment and its Application to Flight Safety Analysis", Sandia National Laboratories, SAND89, 1982.

[20] CIRIA, "Rationalization of Safety and Serviceability Factors in Structural Codes", Report No. 63, Construction Industry Research and Information Association, London, 1977.

[21] Allen, D. E., "Criteria for Design Safety Factors and Quality Assurance Expenditure," *Structural Safety and Reliability*, Elsevier, pp. 667-678, 1981.

[22] Melchers, R. E. *Structural Reliability Analysis and Prediction,* Ellis Horwood. 1987.

[23] Mander, J. B. and Elms, D. G. "Quantitative Risk Assessment of Large Structural Systems", *Proceedings,* ICOSSAR, 1993.

PROCEEDINGS OF THE THIRD INTERNATIONAL WORKSHOP ON VERY LARGE FLOATING STRUCTURES
(VLFS '99), VOL. I, EDS. R.C. ERTEKIN & J.W. KIM, 22-24 SEPTEMBER 1999, HONOLULU, HAWAII, USA

MOBILE OFFSHORE BASE (MOB) TACTICAL AIR OPERATIONS CREDIBLE WORST CASE

Donald R. Bouchoux and John M. Lillard
Whitney, Bradley & Brown
1604 Spring Hill Road
Vienna, VA

Abstract

The Mobile Offshore Base (MOB) concept reflects the U.S. requirement to support aircraft conducting military operations in areas of the globe where adequate host-nation support is either limited, unavailable or not desirable. The operations of these aircraft would occur in a variety of conditions and aircraft configurations. The length of the runway associated with the MOB that is required to conduct tactical aircraft operations is a function of these considerations. This requirement will tend to increase as environmental conditions worsen and as the configuration of the aircraft differs from optimal flight configurations. The purpose of this paper is to assess a variety of these conditions and configurations in order to derive a "credible worst case", those conditions which are beyond normal operating parameters, but not to the degree that the requirement would be overstated.

Study Objective and Outline

The objective of this paper will be to identify that combination of parameters that would define a "reasonable worst case" for tactical aircraft operations. For the purposes of this paper, tactical aircraft are defined as high-performance, jet or turbo-prop aircraft that perform tactical missions for the United States Air Force, United States Navy and United States Marine Corps. The combinations of these parameters would include both environmental aspects and operational constraints (aircraft weights and configurations). Once these parameters have been established, this will compare landing and takeoff distances computed for various types of aircraft operating under these constraints in order to derive a "credible worst case" requirement for runway length.

This study will first identify environmental parameters for MOB operations matched with the location where these would be measured. Then, the study will identify aircraft-related operational parameters, specifically in the following flight regimes:

- takeoff
- landing
- on deck operations

Finally, we will identify differences in land-based and sea-based aircraft operating procedures between the USAF and the US Navy. The USAF and US Navy have fundamental differences in operating procedures; the object of this section will be to identify which of these will drive the requirement for MOB runway length.

Background

As part of the background for the definition of the credible worst case, a few items related to the general operation of tactical aircraft may be in order. The criticality for the takeoff at the beginning of a mission and the landing at the end are often different. In a combat situation, with coordinated strike planning and the use of joint forces, the timing of a takeoff may be critical. The timing of many of the missions envisioned in the MOB Concept of Operations (CONOPS) for the operation of tactical aircraft, however, does not approach this degree of criticality. Specifically, takeoffs:

- Have mission driven parameters that are determined before takeoff and can be adjusted based on prevailing conditions

- Weight may be adjusted by downloading fuel and/or payload
- Aircraft failures are more likely to be determined during pre-flight operations
  - control surface failures
  - some engine malfunctions
- However, some malfunctions occur during takeoff roll. These are the underpinnings of refusal distances
- Some delay may be possible before beginning a takeoff, specifically waiting until after the most serious condition has mitigated (e.g., squall)

The same amount of flexibility, however, does not apply to the landing evolution. Specifically, landings:

- Have limited capability to adjust weight due to factors such as hung ordnance (ordnance that has not separated from the aircraft after trigger pull) and a reluctance to jettison fuel
- There is no control over aircraft failures, specifically common failure modes such as
  - engine malfunctions or failures
  - control surface failures
- The available delay of the landing evolution is limited to condition of aircraft and fuel on board
  - The use of a divert field if available may be an option, however, the aircraft may not be able to outlast most severe condition.

The U S Navy has conducted significant research into the combination of aircraft failures under differing mission conditions in support of determining the requirement for wind over the deck. Wind over the deck is typically a function of both the speed of the an aircraft operating ship (aircraft carrier or large deck amphibious operations ship), which yields self generated wind and ambient (natural) wind. As the possibility exists for ambient wind = 0, the top speed the aircraft carrier is capable of making is a key parameter in determining the requirement for wind over the deck. Individual aircraft failure/weight combinations are evaluated, and based on the probability of occurrence are determined to be either within the requirement for an arrested landing or outside the requirement. In those cases, three options exist (in order of preference):

- divert to a field ashore
- barricade arrestment
- controlled ejection/bailout

The aircraft's airspeed will be function of

- weight
- aerodynamic configuration
- environment

The acceptable arresting speed for the aircraft for a give weight equals the airspeed minus the wind over the deck (WOD). However, there are some cases that are unrecoverable with any reasonable amount of wind. This has been translated into determining the requirement for aircraft carrier speed by determining necessary wind over the deck based on formula, determining likelihood of occurrence and finally determining other possible options.

The significant implications here for the credible worst case for tactical aircraft operations from the MOB is that some cases will always exist that will require a runway length beyond stated requirement. The goal is to seek cost-effective balance between requirement as driven by the possible cases and probability of occurrence. Operating conditions and geographic area can mitigate requirement if divert field is available and
if emergency gear (barricade/arresting gear) is available on the MOB.

Environmental Considerations

In absence of aircraft performance parameters, environmental factors that affect takeoff and landing distances will include:

- temperature
- relative humidity
- atmospheric pressure
- runway condition (wet, dry, icy)
- wind

The first three can be combined to determine pressure altitude. However, as the MOB will always operating at sea level, this will help mitigate some effects of the above. The combinations that would most severely degrade performance *may not occur simultaneously.* For example, the extreme precipitation associated with the heaviest rains will not occur simultaneously with highest temperatures and low/no wind conditions. Some environmental combinations, however, preclude operations. As a specific example, US Navy aircraft carriers do not operate under all environmental conditions. In many cases, the Navy will maneuver its ships to avoid the most severe conditions, however, conditions of extreme winds, sea state, reduced visibility, icing or large deck movements will cause a cessation of flight operations.

Some environmental conditions do not affect aircraft takeoff or landing distances *per se*, but will affect periodicity of those events. These factors include

- visibility
- cloud coverage

Wind direction may not be a factor if the MOB can orient itself into the prevailing wind. High wind speed is a beneficial effect if it is aligned with the takeoff heading, however, crosswinds (winds beyond 45 degrees of the takeoff or landing heading) are detrimental to aircraft landing and takeoff performance.

A critical factor for the determination of takeoff and landing rollout distances is density altitude. Air Density decreases:

- With Air Temperature Increase
- With Altitude Increase (not applicable)
- With Humidity Increase
- With Barometric Pressure Decrease

With lower air density:

- The engine develops less thrust
- The wings produce less lift

This results in:

- Longer takeoff run
- Poorer climb performance
- Longer landing distance

The following table characterizes the environmental conditions for a credible worst case:

Items in Bold Affect RWY Length	Standard	Credible Worst	Incredible Worst	
Pressure Altitude	29.92	29.70	29.30	
Temperature	59F/15C	0F(LOW)/10 0F(HIGH)	10F(LOW)/1 10F(HIGH)	
Rel. Humidity (%)	0	90	99	
Visibility	5NM	0.5NM	0NM	
Wind Speed				
- Head/Tail/Cross	10	0	0	
- Gusting/Steady	Steady	N/A	N/A	
Cloud Cover	50%	100%	100%	
Ceiling	3000	200	0	
Sea State	3	6	8 or above	
Runway Condition (RCR)	Dry (RCR 23)	Wet (16)/ Icy (8)	Wet (16)/ Icy(8)	

Table 1. Environmental Conditions.

Under current MOB Concept of Operations, these credible worst case conditions occur in

- North Arabian Sea in hot/humid conditions
  - characterized by high temperature, high pressure altitude, moist or wet runway

This may affect takeoff more than landing. The second case would be:

- Sea of Japan in cold/high precipitation/high sea state
  - characterized by low temperature, icy runway.

This may affect landing more than takeoff.

Takeoff Distance

Aircraft factors that will impact takeoff distance are:

- Thrust
- Total Weight
  - empty weight
  - fuel
  - stores/ordnance
- Aeronautical performance
  - Wing loading
    - Drag
    - Induced and parasite
- Rolling Friction
  - Tire
  - Tire Pressure

In takeoff, the most demanding requirement for runway length occurs with a maximum weight aborted takeoff. This combines speed (function of thrust, weight and aero performance) and braking (combines weight and rolling friction).

The difference in computation of takeoff distances between the USAF and U S Nave are that USAF doctrine requires computation of refusal distances to clear a 50' obstacle clearance at end of runway. USAF instructions also state that "no takeoff shall be planned that requires more than 80% of the available runway". US Navy doctrine for shipboard takeoffs include a goal of 5 or more knots of end speed at conclusion of catapult stroke. The Navy land based takeoff distance computation is similar to the USAF.

Specific takeoff distance computations have been made for one aircraft, the F-15 E. The credible worst case conditions can add anywhere from 15% to 50% to the takeoff distances. All figures are for 60,000 lb aircraft with full fuel (internal and tanks), but no ordnance (typical transshipment configuration). These distances are shown in the Table 2 below:

	Takeoff	Takeoff
F-15 E	0 Wind	10KT Head Wind
Standard	4400	2500
0DegF Dry	3100	2400
0DegWet	3620	
0DegF Icy	4900	
100Deg Dry	4800	4200

Table 2. F-15E Takeoff Distance in Feet

The credible worst case of an engine failure on takeoff (same aircraft conditions above) is characterized by the difference between two airspeeds. Based on a given runway lengths, this calculation will yield a series of airspeeds that distinguish between **the minimum go speed**, that speed at which aircraft can experience an engine failure and still fly and the **maximum abort speed**, the speed at which aircraft can abort its takeoff and stop on available runway. The minimum go speed for an F-15E at 60,000lb on a standard day is 130 KIAS. The maximum abort speed is indexed for various runway lengths:

- 5000' = 100KIAS
- 6000' = 110KIAS
- 8000' = 125KIAS

Note that in every case, the minimum go speed exceeds the maximum abort speed. Losing engine between these speeds could result in an extremis situation. The ideal case includes runway lengths for which the minimum go speed exceeds the maximum abort speed.

The conclusions of this study for takeoff lengths include

- Takeoff can be controlled somewhat by
  - management of aircraft weight/fuel/stores
  - timing of takeoff to avoid certain failures
  - pre-flight checks
- Environmental effects that are most critical occur with either
  - hot temperatures/high humidity
  - icy runway

The USAF requirement for 50' obstacle clearance needs to be examined with the recommendation that aircraft operate in aircraft carrier mode. Eliminating this would significantly reduce the required runway length. The critical failure mode is engine failure, yielding an area of uncertainty between minimum flying speed and maximum abort will exist for all proposed MOB length, however, ideally one would like to minimize the size of interval if possible.

Given previous efforts to determine the runway length for operation of the C-17, critical MOB runway length for takeoff may be determined not by tactical aircraft, but by various strategic lift aircraft.

Landing Distance

Aircraft factors that will impact takeoff distance are:

- Total Weight
  - empty weight
  - fuel remaining
  - stores/ordnance
- Aeronautical performance
  - Drag
  - Induced and parasite
- Glideslope
- Angle of Attack
  - Rolling Friction
  - Tire Pressure
  - Aerodynamic Braking Devices

The USAF and U S Navy have vastly different perspectives on landing. Aboard an aircraft carrier, an arrested landing is the normal mode of operation. The Navy also designs its aircraft and trains its aircrew with arrested landings in mind. On the other hand, the USAF aircraft are not built to withstand arrested landings on a routine basis, its pilots are not trained for arrested landings and an arrested landing is viewed as an emergency or last-ditch option. If only carrier-based aircraft operated off a MOB, use arresting gear on a routine basis would significantly decrease requirement for runway length due to landings. If USAF aircraft operate from MOB arresting gear would be for emergency situations only. The differences in doctrine are highlighted in Table 3.

	Total Dry R	Ldg Dist	Total Wet	Ldg Dist
	0 Kt HW	10Kt HW	0 Kt HW	10 Kt HW
F/A-18C	5050	4550	7150	6650
E-2C	3200	2950	3590	3280
EA-6B	5100	4600		
S-3	4900	4450		

Table 3. Doctrinal Differences for Landing.

The landing distances (shore-based operations) for U S Navy aircraft are shown in Table 4.

Defining Aircraft Operating Parameters	Items in Bold Affect RWY Length	USAF	USN
Landing	Threshold		None
	Obstacle Clearance	Flight Manuals plan for either 0' or	12' Hook-to-Ramp
	Landing Aids	VASI	ACLS/ILS/ Fresnel Lens

Table 4. Landing Distances for U. S. Navy Aircraft

The F-15E has been evaluated in a variety of circumstances to bound the credible worst case. The following considerations apply to the distances calculated.

- Glideslope
  - Normal = 2.5 deg
  - Minimum Run = 1.5-2 deg
- Approach Speed flown is commensurate with 20-22 Units AOA
- Normal Landing Occurs 500-1500 from the threshold
- Max Crosswind
  - Dry = 30 kts
  - Wet = 15 kts
- If arrested engagement, USAF SOP requires
  - Land 800 feet short of cable
  - Lower nose prior to engagement
  - Engage cable in center
  - Max engagement speed determined by cable type

Drawing on the previous analysis done by the Navy, the likely credible worst case landing would consist of a high landing weight coupled with a common flight control failure. The case that was chosen was a flap failure that would cause a no flap landing. This condition is well documented in a variety of aircraft weight and environmental conditions. The normal landing roll on a standard day for an F-15E is shown in Table 5. Additionally, Tables 6 and 7 detail the effects of other conditions on the landing distance of the F-15E. These tables (Tables 5, 6 & 7 are shown on the following page)

The conclusions of the landing section would include:

- Worst case for environmental factors is the same as for takeoff
- Operating a MOB under aircraft carrier would eliminate the 50' obstacle clearance and shorten USAF landing distances (even without using arresting gear)
- Credible worst case would involve:
  - heavy weight
  - control surface failure (e.g., no flaps)
  - hot/wet or cold/icy conditions
  - no wind
- For tactical aircraft such as F-15E, would result in landing distances of approximately 8,000' (dry runway)
  - wet runway would be greater

Gross Weight	Temperature	Approach Speed	Winds	Runway Condition	Landing Roll (0' Obst/2.5 deg GS)	Landing Roll (50' Obst/3 deg GS)
45,000	15 deg C 59 deg F	165	0	Dry	5100	6200

Table 5. Normal Landing Distance for F-15E.

The following charts show the effect of various other conditions on the landing distance of an F-15E.

Gross Weight	Temperature	Approach Speed	Winds	Runway Condition	Landing Roll (0' Obst/2.5 deg GS)	Landing Roll (50' Obst/3 deg GS)
50,000	40 deg C 100 deg F	175	10 kts Tail	Dry	7200	8300

Table 6. High Weight/Hot Temperature/Tailwind Landing Distance for F-15E.

Gross Weight	Temperature	Approach Speed	Winds	Runway Condition	Landing Roll (0' Obst/2.5 deg GS)	Landing Roll (50' Obst/3 deg GS)
50,000	40 deg C 100 deg F	180	Calm	Dry	7900	8900

Table 7. High Weight/No Flap/Hot Temperature Landing Distance of F-15E.

Conclusions

- The environmental conditions can be grouped into two "worst cases"
  - hot/humid and possibly wet
    - adversely affects pressure altitude and aircraft performance on takeoff
    - moisture affects takeoff and landing distances
  - cold and wet/icy
    - cold temperatures positively affect aircraft performance
    - moisture, particularly ice, significantly affects takeoff and landing distances, possibly by increasing by as much as 60%

- The takeoff "credible worst case" includes:
  - engine loss on takeoff
  - some interval between max abort and min flying speeds for MOB lengths up to 8000'
  - may have to accept possibility of long-field arrested landing
  - takeoff environment may be controllable for many other situations
  - does not account for urgency of mission
- USAF obstacle clearance requirement should be revisited for MOB operations
- would significantly shorten takeoff distances
- Orienting MOB into relative wind will always reduce takeoff (and landing) distances
  - no wind may be unavoidable, but tailwind and crosswind should be avoidable

- Landing "Credible Worst Case"
  - combination of aircraft weight and failure
    - high weight
    - flight control failure - no flaps/slats
  - Wind over the deck study shows that all cases are not recoverable
  - USAF has 50' obstacle clearance - should revisit
  - arrested landings on routine basis only suitable for Navy carrier-based aircraft

PROCEEDINGS OF THE THIRD INTERNATIONAL WORKSHOP ON VERY LARGE FLOATING STRUCTURES
(VLFS '99), VOL. I, EDS. R.C. ERTEKIN & J.W. KIM, 22-24 SEPTEMBER 1999, HONOLULU, HAWAII, USA

On the Global Response of a Mobile Offshore Base*

Suqin Wang and Balji Menon
American Bureau of Shipping[1]

ABSTRACT

A direct analysis approach based on first principles is necessary for the global response assessment of a Mobile Offshore Base (MOB) because of the lack of experience with this structure. The response assessment method for a proposed MOB concept is presented in this paper that focuses on the wave-induced responses. Emphasis is placed on the influence of environmental criteria on the motions of each module of a connected 5-module MOB, and the load effects for a single module. Results of the responses generated using different environmental criteria are compared and the probability of exceedance of motions and load effects over the 40-year life of the MOB are provided.

1. INTRODUCTION

A Mobile Offshore Base (MOB) with a 40-year life having the capability of conducting flight, maintenance, supply and other military support operations has been proposed [1]. The MOB, once built, will be the largest floating structure ever constructed. Hence there is no experience related to the design of such a structure. The classification rules developed for other floating structures and calibrated with years of experience do not appear to be applicable to the MOB. Therefore, a direct analysis approach based on first principles is necessary.

The direct analysis approach provides a better transparence between wave-induced load effects and the structural strength for the designer providing a high degree of confidence in the safety of the structure. However, the quality of the results from the direct analysis will depend much on the analysis methodology, numerical tools, etc. MOB Classification Guide (Draft) developed by American Bureau of Shipping [2] provides guidance for the quality assurance. It is required in the Guide that all the related uncertainties need to be taken into account in the assessment. The direct analysis method has the advantage that as long as the uncertainties are recognized, they can be dealt with in a systematic manner.

One of the most important aspects in the response assessment is the selection of environmental criteria, which varies from industries. The environmental criterion of 100-year wave [3] has been widely used in offshore industry, although 100-year wave may not induce the 100-year response. While the direct stochastic analysis method [2] and the environmental contour method (ECM) [4] are recommended for the response assessment of MOB [2]. The combination of environmental parameters determined from ECM, if the uncertainties are neglected, generate the response with a given probability of exceedance in the lifetime of the subject structure, but with certain assumptions. The direct stochastic analysis method is consistent with ECM without any limitations. It can also predict the lifetime response for a given return period of the environmental parameters. However, how comparable is the 100-year approach vis-à-vis the direct stochastic approach, has not been clear. Therefore it is important to provide guidance to the designer, for the four potential deploy sites, what difference it will make by using the two approaches. This paper provides comparative results obtained from the two approaches for the subject MOB at the North Atlantic Ocean site.

The response assessment involves the wave load, motion and load effect predictions. The subject MOB is a 5-module system linked together by hingers. The motions of the connected MOB and load effects on an unconnected single module are included.

The analysis methods may be characterized as viscous [5] or potential [6], rigid or hydroelastic [7], linear or non-linear [8], frequency or time domain, and

* The views expressed in this paper are those of the authors and not necessarily those of the American Bureau of Shipping.

[1] 16855 Northchase Dr., Houston, TX 77060, USA

deterministic or probabilistic [9]. The procedure used here is emphasized on the use of potential flow, rigid body, linear, frequency domain and probabilistic method. The focus is on the adequacy of procedure to meet safety and functionality requirements.

2. CHARACTERISTICS OF THE MOB

The subject MOB is the McDermott's concept [10] in which each single module (SBU) is a port/starboard and for/aft symmetric semi-submersible hull. The MOB system consists of five modules linked by hinges. The main particulars of the SBU are given in Table 1.

Table 1: Main particulars of one MOB module

Upper hull dimensions	280 x 150 x 24.6 m^3
Lower hull dimensions	260 x 38 x 16 m^3
Transverse spacing	100 m
Column dimensions	21 x 21 m^2
Operating draft	39 m
Displacement	337000 metric ton
LCG (from amidships)	0
TCG (from center plane)	0
VCG (from baseline)	26.87
Water plane area	3452 m^2
VCB (from baseline)	13.1
BMT	40.1
BML	66.0
Roll radius of gyration	55.8
Pitch radius of gyration	93.2
Yaw radius of gyration	97.1

3. RESPONSE ASSESSMENT PROCEDURE

The scheme of the global response assessment procedure is given in Figure 1. The procedure, intended to ensure the overall structural integrity in the design, is discussed stage by stage in following sections.

4. WAVE ENVIRONMENT

The wave environment can be represented in terms of wave spectra and wave scatter diagrams, from which the joint probability of the significant wave height and the characteristic period are found. These parameters should, at least, be obtained for the 40-year of lifetime of the MOB. If lifetime-long database is not available, the uncertainties in the database should be evaluated and taken into account in the functionality and strength assessment [11].

In this application, Walden wave data [5] for North Atlantic is used, which is one of the four possible deployment sites for the MOB. The corresponding wave scatter diagram is given in Table 2. This scatter diagram is employed in the direct stochastic analysis.

For the 100-year environmental criterion, the 100-year wave of 32 m of maximum wave height [12] is used. The corresponding significant wave height is 17.2 m. By using ratios of wave height to wave period, the parameters for a 100-year wave could be given as shown in Table 3 [13].

Table 3: Sea state data [13]

Hs m	12.0	13.5	14.8	17.2	17.2	17.2	17.2	17.2
Tp sec	14.0	15.4	16.8	18.2	19.6	21.0	22.4	23.8

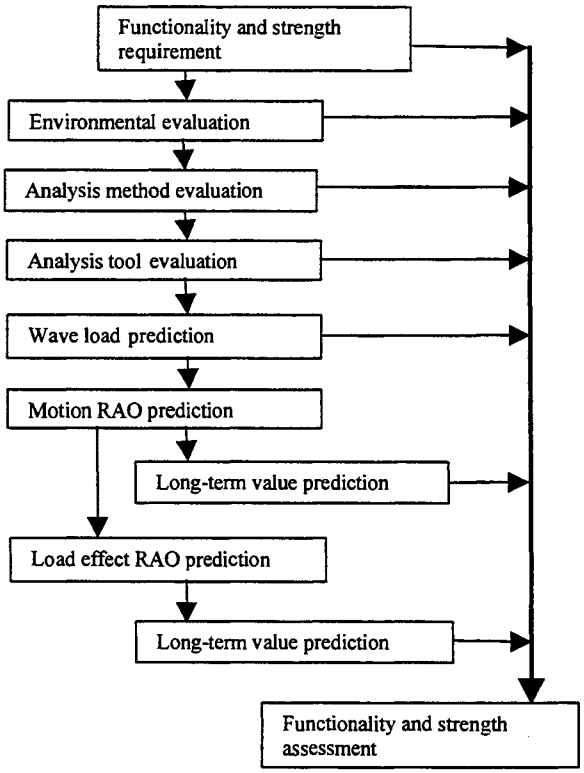

Figure 1: Global response assessment procedure

5. ANALYSIS METHOD

The MOB response has been characterized as stochastic, non-linear, hydro-elastic, dynamic and viscous. The uncertainties due to any simplification of the method should be considered in the final assessment.

In the present study, nonlinearality, hydro-elastic effects, viscous effects have been neglected, which will result in some bias and uncertainty in the response prediction. The investigation of these bias and uncertainties are not covered here, but they are very important in the response assessment.

Here, the stochastic analysis approach is employed in the response prediction. With in linear theory, the stochastic analysis includes the predictions of the Response Amplitude Operator (RAO), short-term

response and long-term response. In determining the RAOs, all possible wave headings and frequencies should be included. The frequency range should, in general, cover the entire wave energy range. The RAOs can be obtained from the solutions of equations of motions:

$$[M_s + M_a]\{\ddot{x}\} + [B]\{\dot{x}\} + [K]\{x\} = \{F\} \quad (1)$$

Where M_s and M_a are structural mass matrix and hydrodynamic inertial matrix, respectively, B is hydrodynamic damping, K is hydrodynamic stiffness and F is wave excitation.

Table 2: Wave scatter diagram [Walden (1964)]

	Wave period, T (second)								
H_s (m)	<5	5-7	7-9	9-11	11-13	13-15	15-17	>17	sum
<0.75	20.91	11.79	4.57	2.24	0.47	0.06	0.00	0.60	40.64
0.75-1.75	72.78	131.08	63.08	17.26	2.39	0.33	0.11	0.77	287.8
1.75-2.75	21.24	126.41	118.31	30.24	3.68	0.47	0.09	0.56	301.00
2.75-3.75	3.28	49.60	92.69	32.99	5.46	0.68	0.12	0.27	185.09
3.75-4.75	0.53	16.19	44.36	22.28	4.79	1.14	0.08	0.29	89.66
4.75-5.75	0.12	4.43	17.30	12.89	3.13	0.56	0.13	0.04	38.51
5.75-6.75	0.07	2.90	9.90	8.86	3.03	0.59	0.08	0.03	25.46
6.75-7.75	0.03	1.39	4.47	5.22	1.93	0.38	0.04	0.04	13.50
7.75-8.75	0.00	1.09	2.55	3.92	1.98	0.50	0.03	0.02	10.09
8.75-9.75	0.00	0.54	1.36	2.26	1.54	0.68	0.20	0.04	6.62
9.75-10.75	0.01	0.01	0.10	0.11	0.10	0.05	0.02	0.00	0.40
10.75-11.75	0.00	0.00	0.03	0.08	0.17	0.06		0.00	0.34
11.75-12.75		0.05	0.00	0.14	0.22	0.06	0.01		0.48
12.75-13.75		0.02		0.07	0.09	0.03		0.01	0.22
13.75-14.75				0.02	0.06	0.02	0.00	0.01	0.11
14.75-15.75	0.00	0.02	0.00	0.01	0.01	0.02	0.01	0.01	0.08
sum	118.97	345.43	358.72	138.59	29.05	5.63	0.92	2.69	1000.00

The short-term response can be expressed by

$$S_R = S_W(\omega)\left|RAO(\omega)\right|^2 \quad (2)$$

where $S_W(\omega)$ represents the wave spectral density function.

In order to compute the long-term extreme values of the response, the long-term wave height and wave period distribution must be known. The probability distribution could be in analytical form or a distribution table such as a scatter diagram (see Table 2).

The probability of excedance of the response ($x > x_0$) can be calculated by

$$P_r\{x > x_0\} = \sum_i \sum_j p_i(\alpha_i) p_j(w_j) \exp\left\{\frac{-x_0^2}{2(\sigma_{ij})^2}\right\} \quad (3)$$

where $p_i(\alpha_i)$ is the probability of the i-th heading angle α_i, $p_j(w_j)$ is the probability of the j-th pair of significant wave height and characteristic wave period, σ_{ij} is the root-mean square of the response obtained from short-term analysis.

The probability is related to the number of cycles in which the response is expected to exceed the value x_0 at least once during the MOB lifetime.

6. ANALYSIS TOOLS

The wave loads on the MOB, in general, can be predicted by use a numerical source-distribution method based on a diffraction/radiation theory. Many tools have been developed to this end and have been widely used in the marine industry. These tools can be adopted for MOB applications, but validation and benchmark studies are necessary.

Programs WAMIT and AQWA are used for the prediction of global response for a single module and the connected MOB, respectively. They are both linear-frequency-domain analysis programs, but AQWA does not take into account the hydrodynamic interaction between modules.

The validation study for program WAMIT has been conducted and the motion responses from WAMIT agree well with those from model tests [14]. Program AQWA has been benchmarked against WAMIT and the motion responses from the two compare very well [11].

7. GLOBAL RESPONSE OF A SINGLE MODULE

The global responses for one loading condition are presented here although all possible loading conditions need to be analyzed. The analysis was carried out using program WAMIT focusing primarily on the motions and load effects on the module. The panel model used for the analysis is depicted in Figure 2.

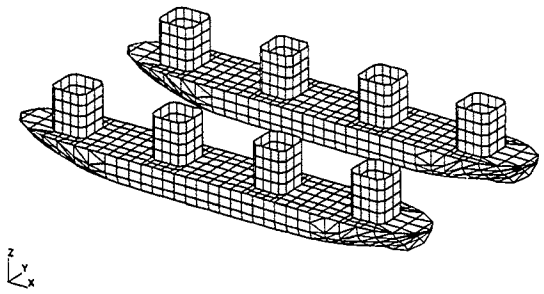

Figure 2: Single module panel model

The response RAOs ware determined for a wave period range of 6 to 30 seconds. All wave headings were considered with 15° interval. Since the module is port/starboard and fore/aft symmetric, only the results for headings from 0 to 90 are presented. Figures 3 to 5 are heave, roll and pitch RAOs.

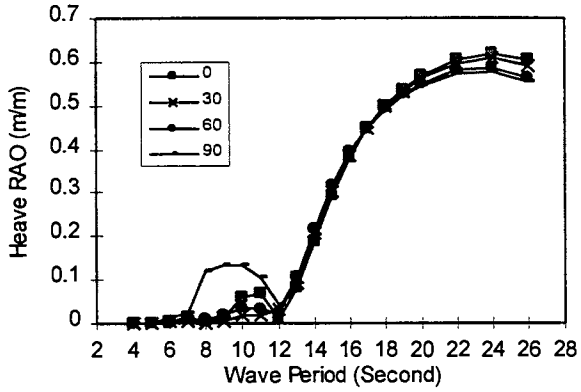

Figure 3: Single module heave RAOs

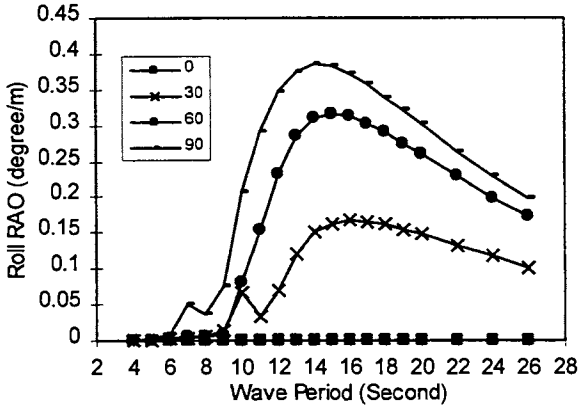

Figure 4: Single module roll RAOs

The longitudinal load effects, namely the vertical and horizontal bending moments and torsion at a transverse cross section, are presented for the middle section of the SBU, in Figures 6 to 8. The torsion is with respect to the waterline.

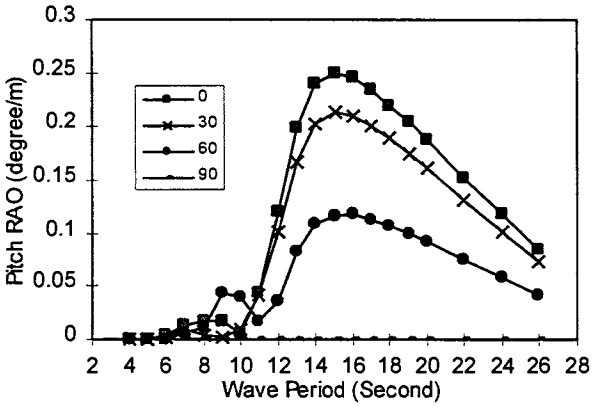

Figure 5: Signle module pitch RAOs

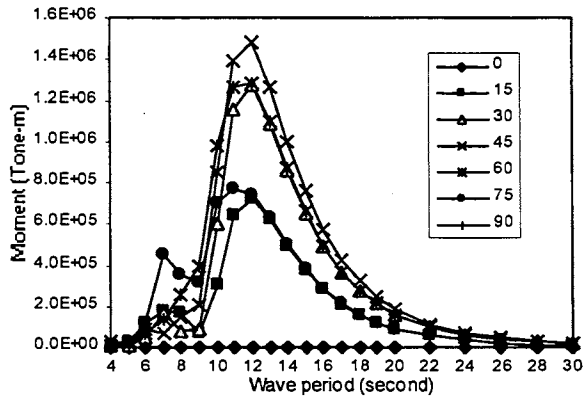

Figure 6: Single module vertical bending RAOs

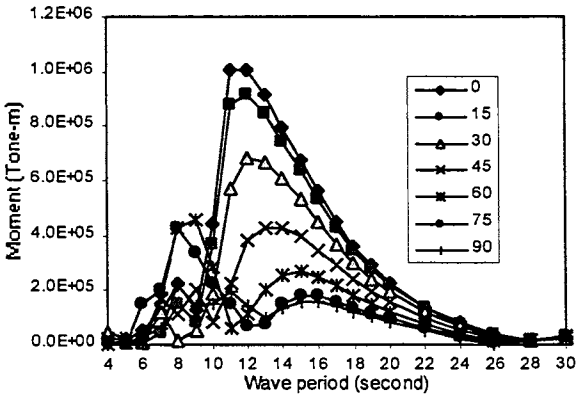

Figure 7: Single module torsion RAOs

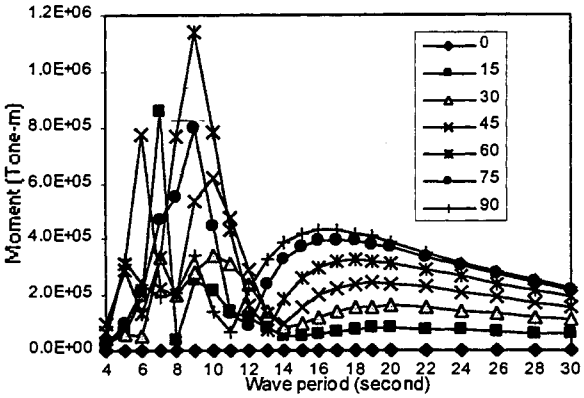

Figure 8: Single module horizontal bending RAOs

Similarly, the horizontal load effects are shear force, bending moment and torsion at a longitudinal cross section. These moments are usually called prying moment, yaw-splitting moment and pitch torsional moment, which are important parameters in the strength evaluation for a semisubmersible-type structure. For the subject MOB, these load effect RAOs are calculated at the cross section of the lower deck and columns and they are given in Figures 9 to 11.

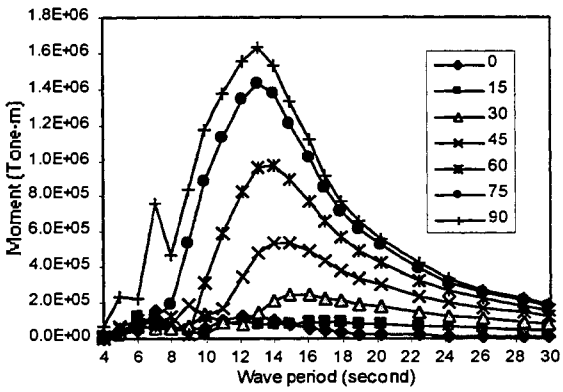

Figure 9: Prying moment RAOs

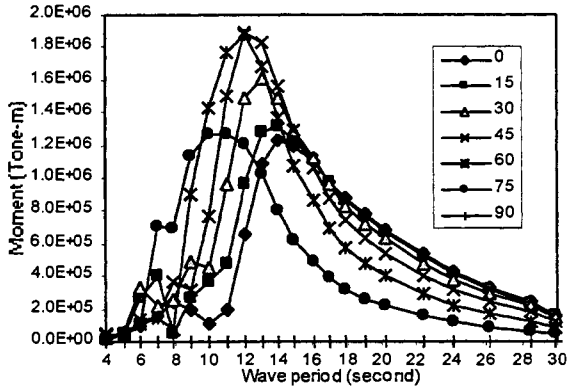

Figure 10: Pitch torsion RAOs

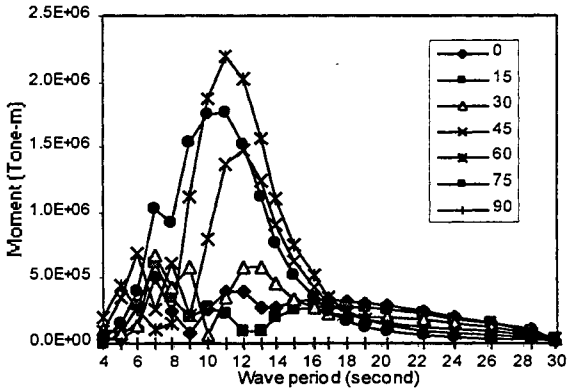

Figure 11: Yaw splitting moment RAOs

The scatter diagram and the 100-year wave data are used in the short term and long term response predictions. The short-term response is computed using Bretschneider spectrum and waves are assumed long crested.

For the long-term extreme value calculation, two methods are employed: 1) using equation (3) and the scatter diagram and 2) using spectra response for the 100-year wave and the 3-hour storm duration. Equal probability is applied to each wave heading.

Method (1) predicts the most probable extreme values of the responses over 40 years and also calculates the probabilities of excedance of the predicted responses based on the number weighted response cycles. Method (2) predicts the most probable extreme values of the response to a 100-year wave. There is no information of the probability of excedance.

For the subject SBU, the results from using methods (1) and (2) are given in Table 4.

Table 4: Most probable extreme values

	Heave (m)	Roll (deg)	Pitch (deg)
diagram	8.93	4.40	2.87
100-year	7.03	5.05	2.97
	VBM (t-m)	HBM (t-m)	Torsion (t-m)
diagram	8.50e6	5.65e6	1.14e7
100-year	4.14e6	5.42e6	4.86e6
	Prying-M (t-m)	Pitch-T (t-m)	Yaw-S (t-m)
diagram	1.53e7	1.69e7	1.53e7
100-year	8.75e6	9.26e6	6.09e6

8. GLOBAL RESPONSE OF CONNECTED MOB

The global response of the connected MOB for one loading condition given here focuses on the motions. The panel model used is same as that in the single module case. The distance between the center of gravity of two neighboring modules is 300 m and the modules are assumed to be hinged at deck level (see

Figure 12).

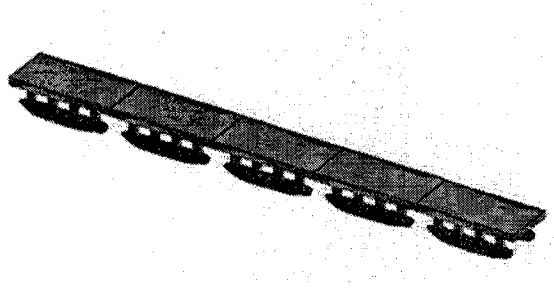

Figure 12: Sketch of the 5-module connected MOB

The motion RAOs are calculated for wave headings in the range of 0 to 90 degrees. The responses at other headings can be derived using symmetric and anti-symmetric properties. The maximum of the RAOs of each module (unit) in heave, roll and pitch at each heading are given in Figures 13 to 15, respectively. Note that 0 degree is following seas and unit 1 is the bow unit.

The extreme motion responses are computed through sea-state 7, since the MOB is designed to operate through that sea state. As the modules will be disconnected in worse environmental conditions, the scatter diagram is modified so that the probability of occurrence of the sea-state larger than 7 is set to zero.

Although several sea state definitions exist [2] that are not the same, in the present study, the upper limits of sea state 7 are taken, ie.: $H_s = 8.87m$ and $T_p = 15.1\,\text{sec}$.

The most probable extreme values for heave, roll and pitch motion in 40 years for operational environmental condition were calculated and they are listed in Table 5.

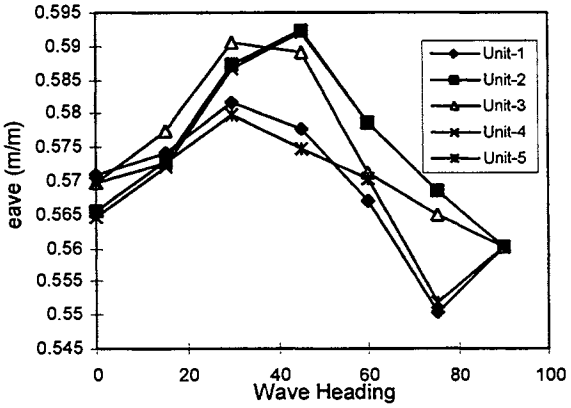

Figure 13: Maximum heave RAOs at CG of units

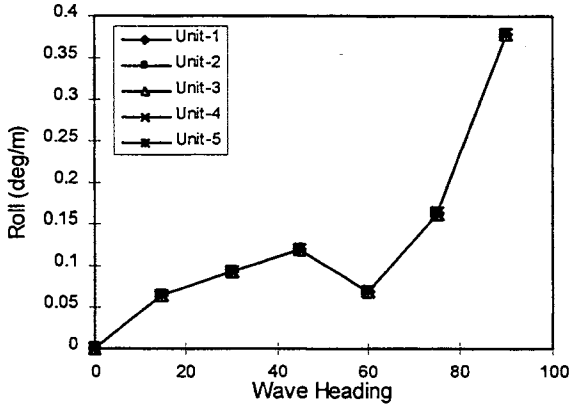

Figure 14: Maximum roll RAOs at CG of units

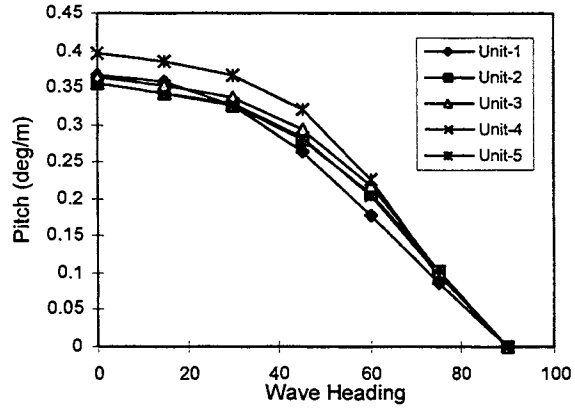

Figure 15: Maximum pitch RAOs at CG of units

Table 5: Most probable extreme motions of MOB

	Unit 1	Unit 2	Unit 3	Unit 4	Unit 5
Heave (m)	4.03	3.93	3.94	3.93	4.03
Roll (deg)	3.07	3.07	3.07	3.07	3.07
Pitch (deg)	2.62	2.05	2.04	2.05	2.62

It can be seen that the roll motions are the same for all 5 units and it is very close to that of the single module. Since the MOB is port/starboard and fore/aft symmetric, the maximum responses of unit 1 and unit 5, unit 2 and unit 4 are the same, respectively. Head seas generate the largest response for the bow unit (unit 1), while the following seas do so for unit 5. The maximum heave occurs when the seas are oblique.

9. CAPACITY ASSESSMENT

The capacity assessment here includes functionality and strength. It evaluates the response against the

requirements and the structure capacities. The structure is safe if

$$\varphi R \geq \gamma Q \tag{4}$$

where φ is the resistance factor that incorporates uncertainties associated with the capacity of the structure, R is the capacity of the structure, γ is the response factor that incorporates uncertainties associated with the response prediction, Q is the predicted response.

If it is assumed that the factors of φ and γ are as unity, this study suggested that the minimum allowable motions and the load effects should be as that given in Table 6. The corresponding probabilities of excedance in 40 years for the allowable values are between 10^{-8} and 10^{-9}. Figures 16 to 18 depict the plots of probability of excedance versa the motions and load effects, respectively.

Table 6: Minimum allowable values for the MOB

	Allowable values
Heave (m)	4.03
Roll (deg)	3.07
Pitch (deg)	2.62
VBM (t-m)	8.50e6
HBM (t-m)	5.65e6
Torsion (t-m)	1.14e7
Prying-M (t-m)	1.53e7
Pitch-T (t-m)	1.69e7
Yaw-S (t-m)	1.53e7

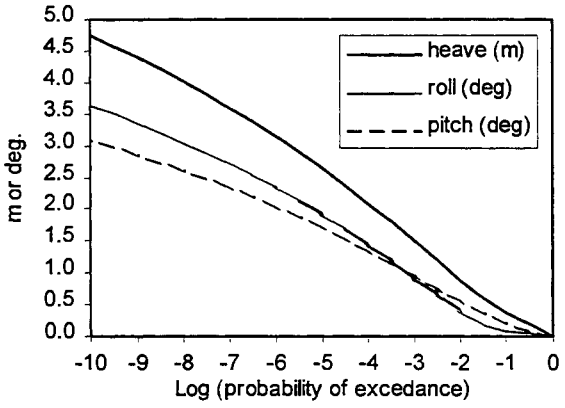

Figure 16: Probability of excedance of motions

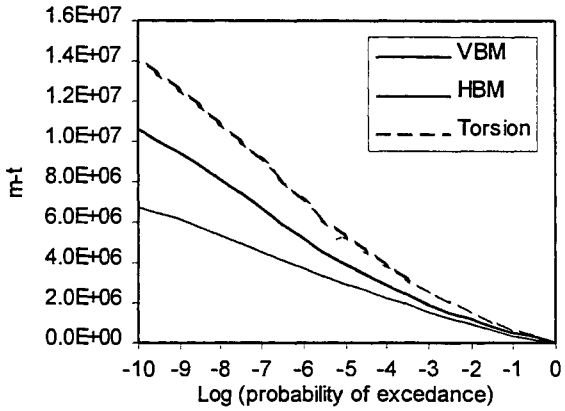

Figure 17: Probability excedance of longitudinal load effects

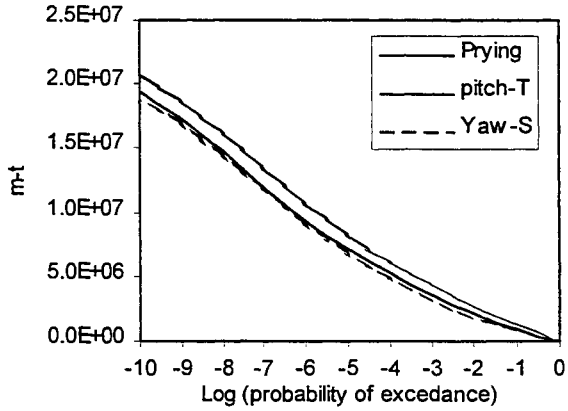

Figure 18: Probability excedance of transverse load effects

10. DISCUSSION AND CONCLUSION

A direct analysis method is applied to the global response assessment of a 5-module MOB concept. Emphasis is placed on the assessment procedure and on the motion responses of the hinged 5-module MOB and on the load effects of a single module. The single module is analyzed for the survival environmental condition while the connected MOB responses pertain to operation environmental condition. The scatter diagram approach and the 100-year wave approach are both considered for survival environmental condition and the results are compared.

The results from using 100-year wave and those from using scatter diagram do not show a consistent pattern. The extreme motion results are reasonably close while the load effects are quite different. Although this deserves more investigation, the 100-year wave

approach is not suggested for present use until many calibration studies have been carried out.

The load effects of torsion, prying moment, pitch torsion and yaw splitting moment are much higher than the vertical and horizontal bending moments. While for a semi-submersible structure, the section modulus to resist yaw splitting moment and pitch torsion are usually large, the section modulus for prying moment and torsion are small. Beam seas and quartering seas generate the highest prying moment and torsion, respectively, and the maximum prying moment occurs when the center-line spacing of the pontoons is close to half the wave length.

For the 5-module hinged MOB, the motion responses of each unit are in the same order as that of one single module except surge that reduces significantly. The units at the two ends have the largest motions in heave and pitch. The maximum roll motion is same for all the units. However it appears that the extreme roll motion is large and did not meet the preliminary motion criteria given in [2]. Therefore, increasing the roll damping is necessary for the proposed concept.

Acknowledgement: The authors wish to thank the Office of Naval Research for sponsoring the project the objective of which is the development of a MOB Classification Guide. Oversight of this project is provided by the MOB Standard & Criteria Working Group under the chairmanship of Dr. Theodore Shugar of Naval Facilities Engineering Service Center, Port Hueneme, California.

References

[1] Remmers, G., Zueck, R., Palo, P.and Tylor, R., "Mobile Offshore Base," *Proc. of the Eighth (1998) Int. Offshore and Polar Engineering Conference*, Montreal, Canada, pp. 1-5, May 24-29, 1998.

[2] "Draft MOB Classification Guide," American Bureau of Shipping, Houston, 1999.

[3] "Recommended Practice for Planning, Designing, and Constructing Tension Leg Platforms," API recommended practice 2T, August 1997.

[4] Niedzwecki, J. M., van de Lindt, J. W. and Yao, J. T. P., "Estimation Extreme Tendon Response Using Environmental Contours", *Engineering Structures*, Vol. 20, no. 7, pp. 601-607, 1998.

[5] Chakrabarti, S. K., Hydrodynamics of Offshore Structures, Computational Mechanics Publications, 1987.

[6] Faltinsen , O. M., and Michelsen, F., "Motions of Large Structures in Waves and Zero Frode Number," *Int. Symposium Dynamics of Marine Vehicles and Structures in Waves*, London, pp. 99-114, 1974.

[7] Newman, J. N.,"Wave Effect on Hinged Bodies" Part IV- Vertical Bending Modes, Sept. 11, 1998

[8] Engle, A., Lin, W. M., Salvesen, N. and Shin, Y. S., "Application of 3-D Nonlinear Wave-Load and Structural Response Simulations in Naval Ship Design," *Naval Engineers Journal*, Vol.109, N0.3, May 1997.

[9] Floating Structures: a Guide for Design and Analysis", OPL, 1998.

[10] "Preliminary Design Report, Vol. I, Structure and System," McDermott Shipbuilding Inc., September 1997

[11] "Commentary to MOB Classification Guide", American Bureau of Shipping, Houston, January 1999.

[12] Guidelines and Classification Notes , Vol. 2, Det Norske Veritas.

[13] "Hydrodynamic Motions & Loads Volume 2 & 3,". Kvaerner Maritime. December, 1998.

[14] "Preliminary Design Report, Vol. II, Connectors, Motions and Loads," McDermott Engineering Houston, LLC., September 1997.

PROCEEDINGS OF THE THIRD INTERNATIONAL WORKSHOP ON VERY LARGE FLOATING STRUCTURES
(VLFS '99), VOL. I, EDS. R.C. ERTEKIN & J.W. KIM, 22-24 SEPTEMBER 1999, HONOLULU, HAWAII, USA

Response of Ships Moored to a Mobile Offshore Base

David Raj and Michael J. Edwards
McDermott Technology Inc.*

ABSTRACT

McDermott Technology, Inc. (MTI) under the Navy contract "Design Technologies for Mobile Offshore Base", has developed a code for predicting the cargo transfer rates from a berthed ship to a Mobile Offshore Base (MOB). The input to the code is the time history of the relative motions between the ship and the MOB. This paper deals with the calculations of berthed ship response time histories in moderate sea states, which were performed in support of the cargo transfer rate study. The analyses are performed using a non-linear structural finite element program, ABAQUS (HKS Inc.). The hydrodynamic loads are obtained from the linear frequency domain hydrodynamic program HIPAN (MIT) and applied to the structure using MOB-HyLoads developed by MTI. The response of three different ships (SL7, CapeH, and LSD41) subjected to wave loads under sea states 3 to 5, and under different wave headings are presented.

1. INTRODUCTION

The transfer of cargo to a Mobile Offshore Base (MOB) from moored auxiliary ships is critical to operational effectiveness. It is anticipated that over 90% of all cargo required for a military deployment will arrive by ship. Traditional limits on cargo transfer based on maximum relative motions for a given sea state can be overly conservative. To provide a better estimate of cargo transfer between cargo ships and the MOB, McDermott Technology, Inc. under the Navy contract "Design Technologies for Mobile Offshore Base", has developed a code for predicting cargo transfer rates. The inputs to this code are the time histories of the relative motions between the ship and the MOB [1]. To exercise the cargo transfer rate code, accurate estimates of the time histories of the relative motions between the berthed ship and the MOB are needed.

Various MOB concepts have been proposed by a number of companies and agencies. However, all the concepts consist of multiple Single Base Units (SBUs) that are connected to form a mile long structure. The connections between the SBUs are critical to the survivability of the MOB under severe sea states. Significant effort has been expended to design connectors that will limit motions of the SBUs as well as limit connector loads to reasonable levels. Some of the connector designs are very sophisticated and extremely non-linear in their behavior. In addition to the non-linearity of the MOB connectors the behavior of the mooring lines and fenders used to berth the cargo ships to the MOB are also non-linear. Hence, the structural response analysis is highly non-linear and traditional frequency domain methods for calculating the ship/MOB motions cannot be used. However, the assumption of linear hydrodynamics for the calculation of the wave loads on large structures such as the MOB is reasonable.

McDermott Technology Inc. (MTI), under the Navy contract "Design Technologies for Mobile Offshore Base", has developed the methodology and software tools (MOB-HyLoads) to couple linear, frequency domain hydrodynamic analysis to non-linear, time-domain structural analysis. This methodology is therefore ideal for analyzing the motions of berthed ships where the wave loads are expected to be linear and the response of the structures non-linear. In this procedure, HIPAN is used for the hydrodynamic analyses, while ABAQUS is used for the non-linear, time-domain structural analyses (see [2] and [3]). MOB-HyLoads uses the HIPAN results to apply the hydrodynamic loads to the structural model as either

* 1562 Beeson Street, Alliance, OH 44601, U.S.A.
eMail: david.raj@mcdermott.com
mike.j.edwards@mcdermott.com

distributed loads along the structure, or as point forces at the centers of gravity (CG) of an N-Body problem. In this paper the berthed ship analysis is solved as an N-body problem where the hydrodynamic forces are applied as point forces at the CGs of the SBUs and the berthed ship.

Three different cargo ships are being investigated:
1. a 280 m container ship (SL7)
2. a 205 m Ro/Ro cargo ship (CapeH)
3. a 175 m dock landing ship (LSD41)

These ships represent the range of ships expected to be used for cargo transfer to the MOB. The mooring patterns for berthing these ships to the MOB are taken from the Seaworthy Systems Report on Cargo Ship Interfaces [4] and the NFESC Report on Concepts for Mooring U.S. Navy Ships at a MOB [5]. Only the wave loads were used in this analysis. The berthed ship relative motion time histories in moderate sea states and different wave headings were calculated. The results of these analyses are summarized here. The motion time histories were provided for the cargo transfer rate study

2. ANALYSIS PROCEDURE

A brief description of the methodology employed by MOB-HyLoads to apply the hydrodynamic loads to the structural model is presented in this section. More details can be found in [6]. Following the description of the methodology, the procedure that was followed for performing the berthed ship analysis using MOB-HyLoads is presented.

2.1 Methodology

The fundamental assumption in the development of MOB-HyLoads is that the hydrodynamic loads on a large structure are linear. Therefore, a frequency domain hydrodynamic program such as HIPAN can be used to calculate the diffraction forces and hydrodynamic coefficients. MOB-HyLoads uses the HIPAN results to calculate the hydrodynamic forces acting on a structure. The structural response is then calculated using a general-purpose non-linear finite element program such as ABAQUS. For each time step, equations of motion being solved by ABAQUS are:

$$[M]\{\ddot{x}\}+[C]\{\dot{x}\}+[K]\{x\}=\{F\} \quad (1)$$

where the forcing function, {F} is:

$$\underset{\text{Forcing Function}}{\{F\}} = \underset{\text{Diffraction}}{\{F_D\}} + \underset{\text{Radiation}}{\{F_R\}} \quad (2)$$

The diffraction force $\{F_D\}$ is known from the HIPAN diffraction solution for the different wave periods and wave headings for unit wave amplitudes. Scaling these forces with respect to the wave spectrum and spreading function simulates a sea state. The contributions from the different wave periods and headings are added with random phases to provide the time dependent diffraction forces.

The radiation force $\{F_R\}$ depends on the instantaneous displacement (and displacement history) of the structure and, hence, has to be calculated iteratively until a converged solution is obtained.

MTI has developed an ABAQUS user written element (UEL subroutine) which is used to apply the hydrodynamic loads. Input to this subroutine is supplied by MOB-HyLoads in the form of diffraction force time histories, infinite frequency added masses and impulse response functions. This data is used by the ABAQUS user subroutine to calculate and apply the motion dependent hydrodynamic forces to the structural model.

2.2 Analysis Procedure

The analysis procedure consists of the following steps:
1. Prepare the geometry file for the hydrodynamic analysis.
2. Perform the hydrodynamic analysis at the required number of periods and headings.
3. Define the sea state for the analysis and use MOB-HyLoads to calculate the necessary inputs for the ABAQUS UEL subroutine.
4. Generate the ABAQUS structural model.
5. Perform the structural analysis and extract the desired results from the ABAQUS results file.

2.2.1 Hydrodynamic model

The first step is to define the geometry for the hydrodynamic analysis. The hydrodynamic code HIPAN is a higher order panel method that requires the wetted surface to be defined using B-spline patches. Unlike linear panel methods where the surface is defined using faceted panels, the use of B-splines permits the surface to be defined as accurately as desired. The process of defining the surfaces using B-spline patches is, however, not trivial for complex geometries and MultiSurf (a program by AeroHydro – see [7]) is recommended for generating the geometry file. Any number of patches can be used to define the wetted surface, but since the solution is not continuous across patches, it is desirable to use as few patches as possible. For the berthed ship analysis, a 3-SBU MOB was assumed with the ship berthed to one of the SBUs. Since, the N-body option of HIPAN was used to generate the hydrodynamic forces and coefficients, all three SBUs and the ship had to be completely modeled.

HIPAN does not permit symmetry for the N-body option.

2.2.2 Hydrodynamic analysis

The hydrodynamic analysis is performed using the N-body option of HIPAN. A convergence study is performed to determine the analysis refinement required to obtain a desired accuracy. Next, the periods and headings for the analysis are selected. The periods selected for the analysis should cover the ranges required for the diffraction and radiation solutions. The headings are selected based on the wave headings and spreading selected for the analysis. The HIPAN results of interest are the diffraction forces and the hydrodynamic coefficients. For each period and heading, there are 6N diffraction forces, where N is the number of bodies in the N-body analysis. These forces are for unit amplitude waves and have to be scaled for the sea state being analyzed. In addition, there are 6Nx6N added mass and radiation damping terms for each analysis period. A separate HIPAN run is required to obtain the 6Nx6N infinite frequency added mass coefficients.

2.2.3 MOB-HyLoads analysis

MOB-HyLoads reads the HIPAN diffraction forces and hydrodynamic coefficients and stores the results in a random access database. Then, after the sea state is defined (wave spectrum and spreading), MOB-HyLoads scales the diffraction forces based on sea state and spreading and uses random phases to generate diffraction force time histories. The radiation damping results are then used to generate the impulse response functions (6Nx6N). The diffraction forces, infinite frequency added mass and the impulse response functions (IRF) are provided to the ABAQUS UEL subroutine for the calculation of the diffraction and radiation forces at each time step.

2.2.4 Structural model

The structural model is a lumped mass model with the structural mass of each body lumped at its center of gravity (CG). Beams are used to connect the CGs to the connectors, mooring line attachment points and the fender locations. The beams can be rigid or flexible. However, using flexible beams only introduces flexibility to the structural model. Hydro-elastic effects are not included since, the hydrodynamic analysis is performed assuming the bodies to be rigid. The connectors between the SBUs, the mooring lines and the fenders can be modeled in as much detail as desired using all the features provided by ABAQUS. The hydrostatic stiffness terms calculated by HIPAN are applied by using springs (JOINT element in ABAQUS) from the CG locations to ground. A special user element has to be defined using the CG nodes. This user element calculates and applies the diffraction and radiation forces at the CGs of each body. These forces are applied at each analysis time step.

2.2.5 Structural analysis

The structural analysis is performed using the DYNAMIC procedure in ABAQUS. The diffraction and radiation forces are ramped up over a period of 500 seconds. The CG motions and the desired forces (such as connector loads, mooring line tensions and fender forces) are extracted from the results file and post-processed as necessary.

3. MODEL DETAILS

A 3-SBU McDermott design MOB, as shown in Figure 1, was used for the analysis. The 3-SBU MOB configuration, instead of the standard 5-SBU configuration, was chosen to cut down on the HIPAN analysis time. Using only 3 SBUs is not expected to influence the berthed ship motions.

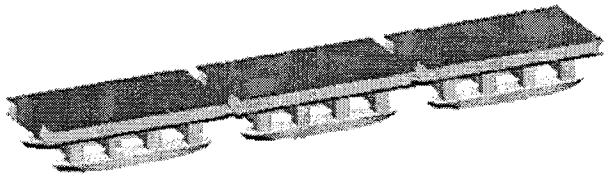

Figure 1. McDermott MOB Design

The connection between the SBUs is assumed to be with a ball joint amidships and non-linear wing connectors outboard, as shown in Figure 2. The wing connectors are assumed to have non-linear stiffness characteristics as shown in Figure 3.

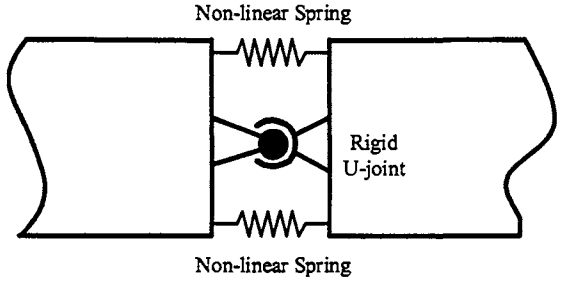

Figure 2. SBU Connectors – Plan View

3.1 Hydrodynamic Models

The hydrodynamic models required for HIPAN consist of the definition of the surface geometries of the wetted surfaces of the MOB SBU and the cargo ships. The wetted surfaces are divided into large patches, and each patch is defined using B-spline surfaces. The

program MultiSurf was used to generate the B-spline surfaces for all the bodies.

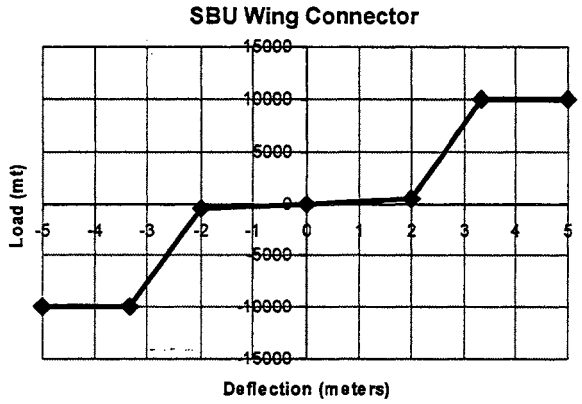

Figure 3. Wing Connector Spring Characteristics

3.1.1 MOB Single Base Unit

The HIPAN geometry model of the SBU is shown in Figure 4. A total of 62 patches were used to define the wetted surface. These patches include the 8 patches at the water surface that cap the columns. These patches are required by HIPAN to remove the effect of the irregular frequencies that are generated during the analysis. Convergence studies were performed on a single SBU to optimize the analysis refinement so that accurate results are obtained down to a period of 1 to 2 seconds. This resulted in a total of 1960 unknowns for each SBU.

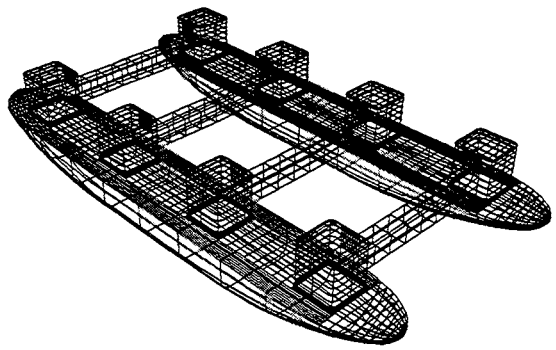

Figure 4. HIPAN Geometry of an SBU

3.1.2 SL7 Container Ship

The HIPAN geometry model of the SL7 container ship is shown in Figure 5. Three patches were used to define the wetted surface incluing the patch used to cap the model at the free water surface. Convergence studies were performed to optimize the analysis refinement (run time versus accuracy). For accurate results down to a period of 2 seconds, the selected analysis refinement resulted in 1196 unknowns.

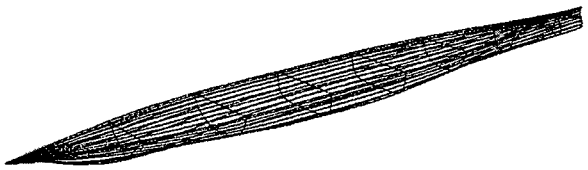

Figure 5. HIPAN Geometry of an SL7 Container Ship

3.1.3 CapeH RO/RO Cargo Ship

The HIPAN geometry model of the CapeH cargo ship is shown in Figure 6. This model consisted of a total of three patches and 1196 analysis unknowns.

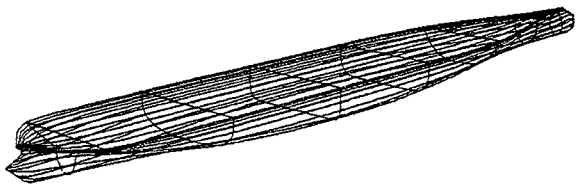

Figure 6. HIPAN Geometry of a CapeH RO/RO Ship

3.1.4 LSD41 Dock Landing Ship

The HIPAN geometry model of the LSD41 Dock Landing ship is shown in Figure 7. This model consisted of a total of four patches and 1232 analysis unknowns. [It should be noted that free surface patches used to cap the models must be removed while performing the infinite frequency calculations.]

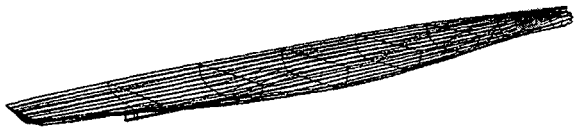

Figure 7. HIPAN Geometry of an LSD41 Ship

3.2 Hydrodynamic Analyses

The N-body option of HIPAN is used to perform the hydrodynamic analysis of the berthed ships. The assumption is that each SBU and the ships can be treated as rigid bodies. Four bodies are defined for each analysis – the 3 SBUs and the berthed ship. Four different configurations were analyzed:

1. SL7 berthed to SBU#2 (starboard side)
2. SL7 berthed to SBU#1 (starboard side)
3. CapeH berthed to SBU#1 (port side)
4. LSD41 berthed to SBU#2 (port side)

For each configuration, the analyses were performed at 192 separate periods and 25 different headings. In addition, the infinite frequency added mass coefficients were calculated. The output of interest are the 24 diffraction forces (4 bodies x 6 dof for each body) per period and heading and the radiation damping coefficients (24x24) for each period. All the forces are at the CGs of the bodies. The diffraction forces and the hydrodynamic forces are read by MOB-HyLoads for further processing.

3.3 MOB-HyLoads Analysis

For each configuration, MOB-HyLoads reads all the diffraction forces and hydrodynamic coefficients and stores the results in a database. The radiation damping coefficients are used to calculate the impulse response functions (24x24). The impulse response functions along with the infinite frequency added masses are stored in a file and provided to the ABAQUS UEL subroutine during the structural analysis.

3.3.1 Sea State Definition

The structural analyses are performed at three different sea states – 3, 4 and 5. For each sea state, the Bretschneider wave spectrum is assumed with significant wave heights and peak periods as listed in Table 1. The definition of a sea state along with the desired spectrum and spreading are provided to MOB-HyLoads. In all the results presented here, no spreading was assumed. Based on the desired sea state, the unit amplitude diffraction forces in the MOB-HyLoads database are scaled and combined with random phases and provided to the UEL subroutine.

Table 1. Sea State Description

Sea State	Hs (m)	Tp (sec)
3	0.88	7.5
4	1.88	8.8
5	3.25	9.7

3.3.2 Validity of Impulse Response Functions

The impulse response functions are calculated from the radiation damping coefficients. Since, it is difficult to know apriori how many periods are needed to accurately define the IRFs, some sample structural analysis runs were performed for the case where the bodies are assumed to be unconnected. The results of the time-domain structural analysis (RAOs) were compared with the results obtained directly from HIPAN. Since, the problem is linear, the frequency-domain results from HIPAN should be exactly the same as the time domain results obtained from the ABAQUS structural analysis. Figure 8 shows a comparison of the SL7 response predictions for 45-degree heading waves when the ship is not connected to the SBU. The plot shows excellent agreement between the HIPAN and ABAQUS results. The good agreement shows that the impulse response functions are accurate. It also shows that the number of periods used for the hydrodynamic analysis was adequate for calculating the IRFs.

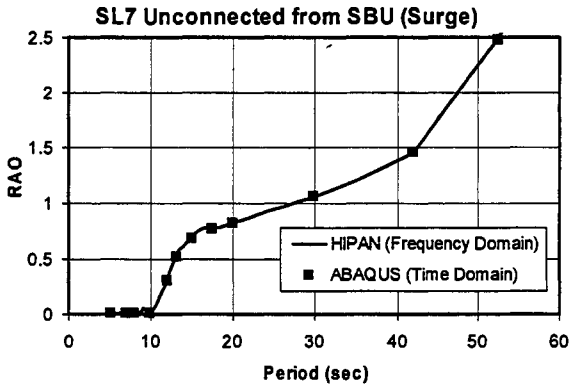

Figure 8. Surge Response of an unconnected SL7

3.4 Structural Model

The finite element program ABAQUS is used for structural modeling. The structural model consists of simplified lumped mass models of the three SBUs and the berthed ship. Rigid beams are used to connect the CGs of each body to the connector, mooring line and fender attachment points.

3.4.1 SBU Model

A plan view of a SBU model is presented in Figure 9. Three SBU models are strung together to form the MOB model. Each SBU is modeled with the mass lumped at its CG, with rigid beams attaching the connectors to the CG. Table 2 lists the structural mass properties of each SBU.

The hydrostatic stiffness, obtained from the HIPAN analysis, is modeled as springs between the CG and ground, using an ABAQUS JOINT element. The properties of these springs are presented in Table 3.

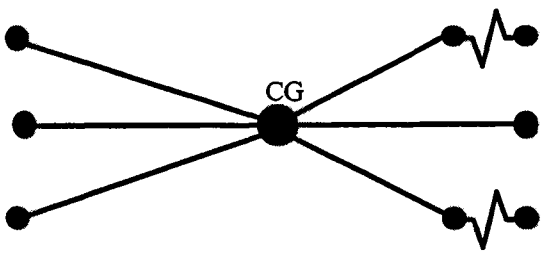

Figure 9. SBU Structural Model – Plan View

Table 2. SBU Mass Matrix

M11– Surge (Kg)	3.370E+8
M22 – Sway (Kg)	3.370E+8
M33 – Heave (Kg)	3.370E+8
M44 – Roll (Kg-m^2)	1.049E+12
M55 – Pitch (Kg-m^2)	2.927E+12
M66 – Yaw (Kg-m^2)	3.177E+12

Table 3. SBU Hydrostatic Stiffness

K11 – Surge (N/m)	0.000
K22 – Sway (N/m)	0.000
K33 – Heave (N/m)	3.390E+7
K44 – Roll (N-m)	4.008E+10
K55 – Pitch (N-m)	1.230E+11
K66 – Yaw (N-m)	0.000

In addition to the beams connecting the CG to the connectors, additional rigid beams are used to connect the CGs to the mooring line and fender attachment points. It is assumed that all mooring lines are attached to smart winches on the SBU with characteristics as shown in Figure 10. Since the stiffness of the mooring lines are much larger than that of the winches to which they are attached, all mooring line characteristics are the same, independent of their lengths. The fenders are attached to the SBU and have characteristics as shown in Figure 11.

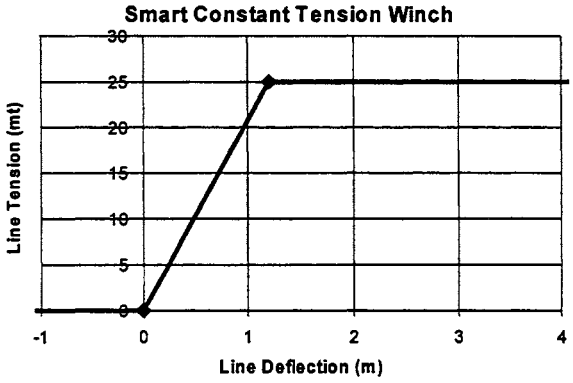

Figure 10 Smart Winch Characteristics

3.4.2 Container Ship – SL7

The SL7 is modeled as a lumped mass with structural mass and hydrodynamic stiffness properties as listed in Tables 4 and 5.

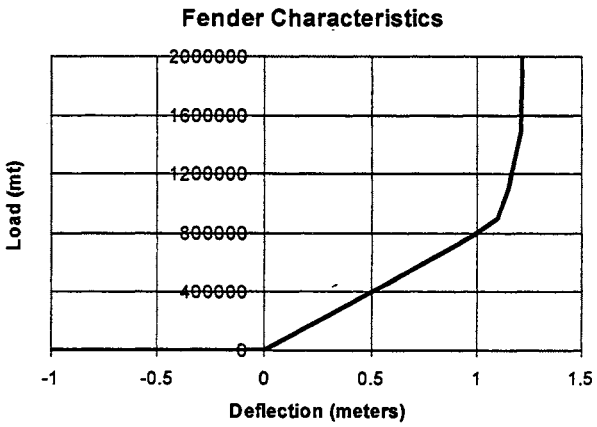

Figure 11 Fender Load-Deflection Characteristics

Table 4. SL7, CapeH and LSD41 Mass Matrix

	SL7	CapeH	LSD41
M11 (Kg)	5.122E+7	3.877E+7	1.599E+7
M22 (Kg)	5.122E+7	3.877E+7	1.599E+7
M33 (Kg)	5.122E+7	3.877E+7	1.599E+7
M44 (Kg-m^2)	6.529E+9	6.472E+9	1.965E+9
M55 (Kg-m^2)	2.55E+11	9.85E+10	2.97E+10
M66 (Kg-m^2)	2.55E+11	9.85E+10	2.97E+10

Table 5. SL7, CapeH and LSD41 Hydrostatic Stiffness

	SL7	CapeH	LSD41
K33 (N/m)	6.087E+7	5.261E+7	3.484E+7
K35 (N)	-3.922E+8	-1.940E+8	-3.488E+8
K44 (N-m)	8.778E+8	5.218E+8	4.968E+8
K55 (N-m)	2.21E+11	1.22E+11	6.44E+10

The SL7 was analyzed for two different mooring configurations:

1. SL7 berthed to SBU#2 (starboard side)
2. SL7 berthed to SBU#1 (starboard side)

The mooring arrangement used for the first configuration is shown in Figure 12. SBU#2 is shown in the figure. A total of 6 mooring lines and 4 fenders are used to berth the SL7 to the SBU. The mooring arrangement for configuration 2 is exactly the same as the first configuration, except that the SL7 is berthed to SBU#1 instead of SBU#2.

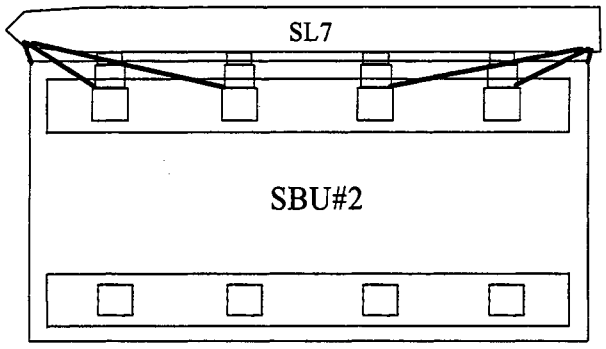

Figure 12 SL7 Mooring Arrangement (SBU#2)

3.4.3 RO/RO Ship -- CapeH

The CapeH is modeled as a lumped mass with structural mass and hydrodynamic stiffness properties as listed in Tables 4 and 5. The mooring configuration for the CapeH, from [4], is shown in Figure 13. Six mooring lines and 4 fenders are used.

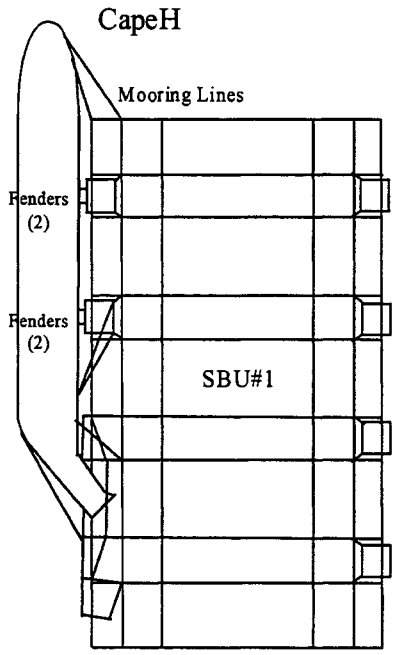

Figure 13 CapeH Mooring Arrangement (SBU#1)

3.4.4 Dock Landing Ship – LSD41

The LSD41 is also modeled as a lumped mass with structural mass and hydrodynamic stiffness properties as listed in Tables 4 and 5. The mooring configuration for the LSD41, from [4], is shown in Figure 14. Nine mooring lines and 7 fenders are used.

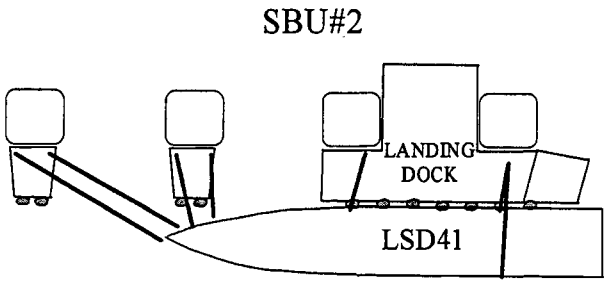

Figure 14 LSD41 Mooring Arrangement (SBU#2)

3.5 Structural Analysis

The structural analysis is performed using the DYNAMIC procedure of ABAQUS. The loads are applied by the user-defined element (UEL subroutine). These loads are gradually ramped on over 500 seconds. The drag damping is included using dashpots. For the base case, 5% damping was assumed. All the simulations are carried out over a period of one hour.

The CG motions and the forces in the mooring lines and fenders are saved at each time step of the analysis. These results are processed to get the relative velocities between the ship and the SBU that are required for the cargo transfer rate studies. The peak and rms values of the motions and forces are also calculated. In this paper, the CG motions of the ship are presented so that the effect of heading, berthing location and other variables can be evaluated. The goal here is to calculate the relative motions. The end goal, however, is to keep the relative motions between the SBU and the berthed ship to a minimum so that cargo transfer can take place under higher sea states.

4. RESULTS

The rms displacements of the berthed ship are calculated from the displacement time histories over a 2600-second duration (1000 to 3600 seconds).

4.1 Container Ship (SL7)

The results for the two different configurations analyzed are presented here.

4.1.1 Configuration 1

The displacements of the SL7 berthed to SBU#2 under sea state 4 for different wave headings are presented in Table 6. The motions of the SBU are significantly smaller than the ship motions for wave headings other than head seas, and are not shown in the table. In all the results presented, the surge, sway and yaw displacements are in meters and the roll, pitch and yaw rotations are in radians.

Table 6 SL7 rms Displacements in Sea State 4

Head.	Surge	Sway	Heave	Roll	Pitch	Yaw
-90.0	0.0381	0.3428	0.3664	0.00360	0.00074	0.00063
-75.0	0.0766	0.2335	0.2690	0.00564	0.00387	0.00239
-45.0	0.0472	0.0473	0.0805	0.00336	0.00296	0.00099
0.0	0.0219	0.0198	0.0367	0.00176	0.00108	0.00038
45.0	0.0551	0.0507	0.0648	0.00272	0.00232	0.00088
75.0	0.0619	0.1727	0.2629	0.00475	0.00434	0.00195
90.0	0.0384	0.2872	0.3872	0.00326	0.00085	0.00055

4.1.2 Configuration 2

The displacements of the SL7 berthed to SBU#1 under sea state 4 for different wave headings are presented in Table 7.

Table 7 SL7 rms Displacements in Sea State 4

Head.	Surge	Sway	Heave	Roll	Pitch	Yaw
-90.0	0.0608	0.3357	0.3702	0.00348	0.00080	0.00075
-75.0	0.1180	0.2266	0.2721	0.00614	0.00390	0.00254
-60.0	0.0861	0.0996	0.1398	0.00700	0.00371	0.00203
-45.0	0.0560	0.0474	0.0717	0.00453	0.00301	0.00108
-30.0	0.0377	0.0360	0.0717	0.00295	0.00180	0.00073
-15.0	0.0348	0.0350	0.0568	0.00202	0.00167	0.00066
0.0	0.0221	0.0305	0.0451	0.00126	0.00128	0.00051
15.0	0.0290	0.0289	0.0495	0.00133	0.00148	0.00048
30.0	0.0375	0.0342	0.0562	0.00260	0.00146	0.00061
45.0	0.0585	0.0544	0.0711	0.00296	0.00265	0.00102
60.0	0.0765	0.0835	0.1041	0.00375	0.00427	0.00156
75.0	0.0767	0.1581	0.2697	0.00492	0.00461	0.00220
90.0	0.0421	0.2841	0.3790	0.00291	0.00128	0.00057

The effect of damping on the ship motions was studied by decreasing the damping to 2% and then increasing it to 10%. The motions for these cases are presented in Tables 8 and 9, respectively.

Table 8 SL7 Displacements in SS 4 (2% Damping)

Head.	Surge	Sway	Heave	Roll	Pitch	Yaw
-90.0	0.1234	0.3637	0.4131	0.00396	0.00103	0.00112
-75.0	0.1711	0.2459	0.3043	0.00739	0.00438	0.00267
-45.0	0.0874	0.0560	0.0780	0.00480	0.00331	0.00123
0.0	0.0297	0.0327	0.0492	0.00132	0.00142	0.00054
45.0	0.0848	0.0645	0.0805	0.00340	0.00287	0.00111
75.0	0.0997	0.1636	0.2962	0.00567	0.00523	0.00232
90.0	0.0572	0.2912	0.4198	0.00313	0.00148	0.00065

Table 9 SL7 Displacements in SS 4 (10% Damping)

Head.	Surge	Sway	Heave	Roll	Pitch	Yaw
-90.0	0.0357	0.3107	0.3172	0.00319	0.00061	0.00066
-75.0	0.0787	0.2104	0.2340	0.00564	0.00329	0.00247
-45.0	0.0429	0.0421	0.0641	0.00437	0.00262	0.00099
0.0	0.0186	0.0281	0.0397	0.00122	0.00112	0.00049
45.0	0.0483	0.0496	0.0604	0.00281	0.00235	0.00098
75.0	0.0568	0.1538	0.2355	0.00466	0.00384	0.00213
90.0	0.0297	0.2695	0.3253	0.00274	0.00106	0.00053

A comparison of the results for different damping are presented in Figure 15 for the surge motion and in Figure 16 for the sway motion. Figure 16 shows that the sway motion is not significantly affected by damping. This is also true for the heave, roll, pitch and yaw motions. However, it is clear that the selected damping value affects the surge motion.

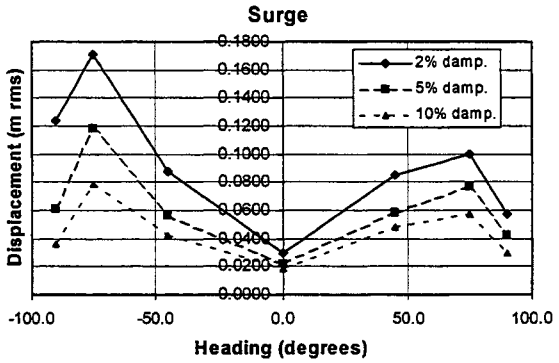

Figure 15 Effect of Damping on the Surge Motion

Figure 17 shows a time history of the ship surge motion. It is clear from the figure that a low frequency response is present. This is the surge resonance of the ship. However, it is not clear at this point why this resonance gets excited, especially since the wave spectrum does not contain energy at this frequency.

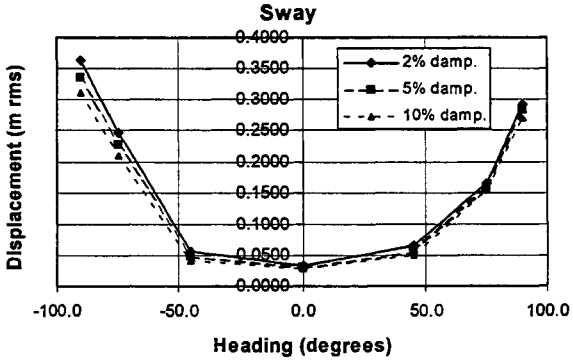

Figure 16 Effect of Damping on the Sway Motion

The SL7 motions for Sea States 3 and 5 were also calculated. These results are presented in Tables 10 and 11. Figure 18 compares the sway motions for the three different sea states.

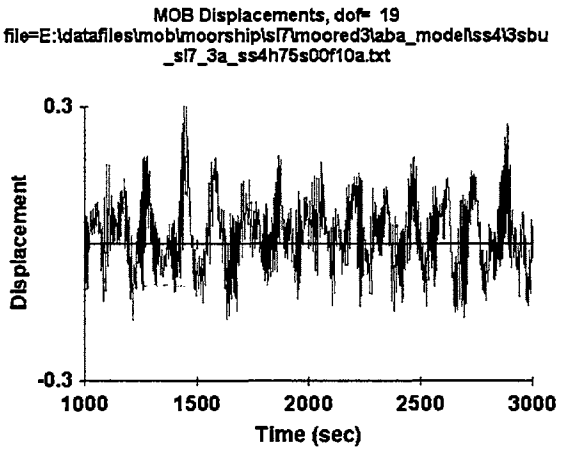

Figure 17 SL7 Surge Motion Time History

Table 10 SL7 Displacements in SS 3

Head.	Surge	Sway	Heave	Roll	Pitch	Yaw
-90.0	0.0205	0.1135	0.1491	0.00091	0.00049	0.00028
-75.0	0.0269	0.0664	0.0949	0.00253	0.00153	0.00099
-45.0	0.0142	0.0171	0.0240	0.00139	0.00089	0.00034
0.0	0.0110	0.0151	0.0185	0.00060	0.00048	0.00023
45.0	0.0116	0.0156	0.0246	0.00091	0.00067	0.00031
75.0	0.0273	0.0487	0.0907	0.00155	0.00180	0.00080
90.0	0.0168	0.1047	0.1434	0.00093	0.00043	0.00026

Table 11 SL7 Displacements in SS 5

Head.	Surge	Sway	Heave	Roll	Pitch	Yaw
-45.0	0.1591	0.1115	0.1833	0.01065	0.00636	0.00252
0.0	0.0615	0.0497	0.0922	0.00262	0.00287	0.00092
45.0	0.1605	0.1180	0.1474	0.00686	0.00611	0.00236

4.2 RO/RO Ship (CapeH)

The CapeH displacements for different headings under sea state 4 are presented in Table 12.

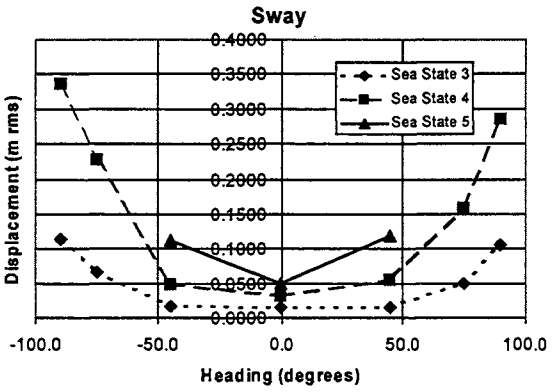

Figure 18 SL7 at Sea States 3, 4 and 5

Table 12 CapeH Displacements in Sea State 4

Head.	Surge	Sway	Heave	Roll	Pitch	Yaw
-90.0	0.1463	0.2642	0.3443	0.00261	0.00177	0.00216
-75.0	0.1244	0.1800	0.2497	0.00250	0.00489	0.00324
-45.0	0.0629	0.0501	0.1092	0.00280	0.00330	0.00145
0.0	0.0536	0.0492	0.0850	0.00138	0.00334	0.00093
45.0	0.0755	0.0735	0.1185	0.00292	0.00398	0.00197
75.0	0.1557	0.2341	0.2598	0.00468	0.00451	0.00366
90.0	0.1770	0.2970	0.3477	0.00246	0.00117	0.00259

4.3 Dock Landing Ship (LSD41)

The LSD41 displacements for different headings under sea state 4 are presented in Table 13.

Table 13 LSD41 Displacements in Sea State 4

Head.	Surge	Sway	Heave	Roll	Pitch	Yaw
-90.0	0.3328	0.5080	0.3502	0.01313	0.00222	0.00751
-75.0	0.2405	0.3375	0.3240	0.01065	0.00378	0.00540
-45.0	0.2126	0.2090	0.1238	0.00870	0.00460	0.00470
0.0	0.0810	0.0623	0.0512	0.00478	0.00187	0.00178
45.0	0.2304	0.1514	0.1455	0.01011	0.00523	0.00414
75.0	0.3031	0.4303	0.3064	0.01487	0.00495	0.00682
90.0	0.3442	0.6009	0.3835	0.01513	0.00173	0.00784

4.4 Comparison of Results

The ship motions for different headings are compared in Figures 19 to 21 for the surge, sway and roll motions respectively.

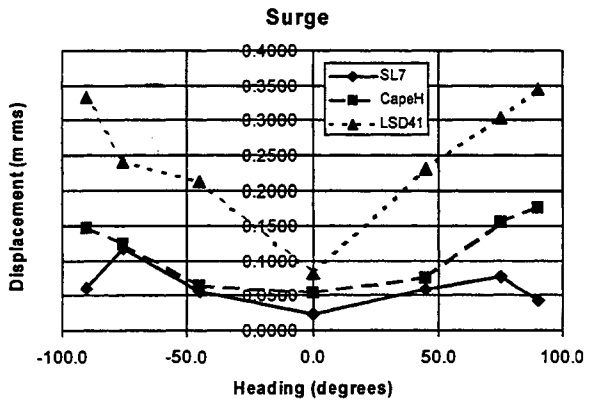

Figure 19 Comparison of Surge Motions

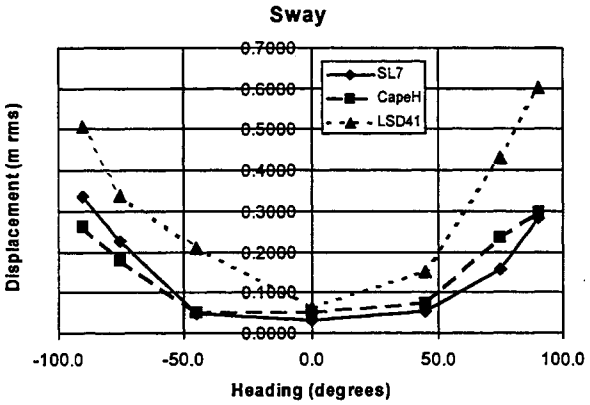

Figure 20 Comparison of Sway Motions

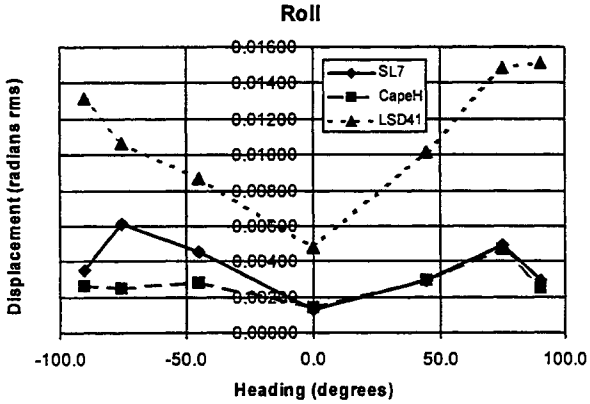

Figure 21 Comparison of Roll Motions

The figures show that the SL7 and CapeH motions are comparable, with the LSD41 motions much larger. This was an expected finding. The figures also show that the response curves are symmetric about the head sea case (0 degrees) indicating that the shielding effect of the SBU is not very significant. This observation was surprising, since the SBU was expected to provide shielding for berthed ships.

5. CONCLUSIONS

The first order wave motions for three different berthed ships are calculated using a non-linear, time domain structural finite element program coupled to a linear hydrodynamic frequency domain program. The results show the influence of heading and other parameters on the resulting motions. Very little shielding was observed. In addition, limiting the wave heading to +/- 45 degrees produced the least motions. The effects of wind and current have not been included in the analyses. Work is currently under way to study the importance of these effects for cargo transfer.

Acknowledgement: This material is based on work supported by the U.S. Office of Naval Research's MOB Program, ONR Contract N00014-97-C-0410, "Design Technologies for Mobile Offshore Base".

REFERENCES

[1] Cybulsky, M. K. and Currie, R., "Simulation as a Tool for Cargo Rate Determination," *Proc. of the 3rd Int. Workshop on Very Large Floating Structures*, VLFS '99, Honolulu, Hawaii, 1999.

[2] Lee, C.H. and Newman, J.N., HIPAN 2.0.2 User's Manual, "A Radiation-Diffraction Panel Program for Wave-Body Interactions", Massachusetts Institute of Technology, 1998.

[3] Hibbitt, Karlsson & Sorensen, Inc., ABAQUS User's Manual Version 5.8, Hibbitt, Karlsson & Sorensen, Inc., 1998

[4] Seaworthy Systems, Inc. Mobile Offshore Base (MOB) Preliminary Design Report, Volume III - Cargo Ship Interfaces, 30 Sep 1997.

[5] W. Seelig, Concepts for mooring U.S. Navy Ships at a Mobile Offshore Base (MOB), NFESC Report TR-6007-OCN, 1999 (draft).

[6] Edwards, M. J. and Raj, D., "Non-linear Time-domain Response of Connected Mobile Offshore Base Units Using Linear Frequency Domain Hydrodynamic Forces," *Proc. of the 3rd Int. Workshop on Very Large Floating Structures*, VLFS '99, Honolulu, Hawaii, 1999.

[7] MultiSurf, General Reference Version 4.0, AeroHydro Inc., December 1998.

PROCEEDINGS OF THE THIRD INTERNATIONAL WORKSHOP ON VERY LARGE FLOATING STRUCTURES
(VLFS '99), VOL. I, EDS. R.C. ERTEKIN & J.W. KIM, 22-24 SEPTEMBER 1999, HONOLULU, HAWAII, USA

MISSION REQUIREMENTS FOR THE MOBILE OFFSHORE BASE (MOB)

Philippe M. Lopez

SYNTEK Technologies Incorporated
4301 North Fairfax Drive, Suite 750
Arlington, VA 22203 – USA
E-mail: plopez@syntek.org

ABSTRACT

Since 1997, the Office of Naval Research (ONR) has assumed leadership for the Mobile Offshore Base (MOB) Science and Technology (S&T) program. This S&T effort focuses on the advancement of critical technologies required to reduce the technical, operational and financial risks associated with the design, construction, operation and maintenance of a MOB capable of meeting the needs of the U.S. Armed Forces in the 21st Century. The overall goal of the ONR S&T program is to establish the technical feasibility and affordability of such an asset. Although the requirements for an actual MOB would be developed as part of a formal system acquisition process, a meaningful set of mission-based functional requirements are mandatory to effectively bound the S&T effort. This paper describes the purpose, the system engineering process and the major products of the functional requirement derivation undertaken within the scope of the S&T program.

1. INTRODUCTION

Since the end of the Cold War, the face of the world has changed. Though potential confrontation between superpowers has decreased, regional instabilities have generated a multitude of crises. At the dawn of the 21st Century, the United States must adapt to a new geostrategic environment. Projecting military power remains a central element of U.S. defense strategy[1]. As a global power, the United States will continue to employ all available instruments of influence (i.e., diplomatic, political, economic, and military) to fulfill its obligations and protect its national interests as well as those of its allies. The ability to project combat force rapidly and virtually unimpeded to widespread areas of the globe remains the cornerstone of America's continued military preeminence. However, much of the U.S. power projection capability depends on sustained access to regions of concern. Unfortunately, U.S. Armed Forces long-term access to forward bases, to include air bases, ports and logistics facilities cannot be assumed in the near future. Any number of circumstances might compromise the U.S. forward presence, subsequently diminishing the ability to apply military pressure and, therefore, reducing U.S. military and political influence in key regions of the world. Moreover, U.S. Armed Forces may find themselves called upon to project power in areas where no substantial basing structure exists. The increasing uncertainty for U.S. forces to access forward bases in foreign countries created a need for a sovereign operational and sustaining basing capability in support of U.S. and allied forward-deployed forces. The recent crisis in the Persian Gulf, as well as the opposition to the U.S. military presence on Okinawa, have renewed the interest of Pentagon officials in the seabasing concept as a way to ensure U.S. military access to critical regions.

By serving as a sea-based conduit for logistics support, the Mobile Offshore Base (MOB) conceptually provides indefinite sustainment capabilities, allowing U.S. forces to conduct Combat Operations and Operations Other Than War (OOTW) in areas lacking adequate basing structure. The MOB would enable a continuous flow between bases located in the U.S. or overseas, and elements conducting operations ashore or at sea. In the recent past, small offshore bases have been successfully used in various temporary configurations to support joint operations in Vietnam (1967-72) and in the Persian Gulf (1987-89). While deployed at a lesser scale than the future MOB to support Special Operation Forces (SOF), they clearly demonstrated the advantage of establishing a sea-based conduit for logistics support in areas and under conditions which precluded development of adequate or timely basing ashore.

The MOB concept clearly represents an opportunity to provide an alternative to increasingly inaccessible,

[1] "A National Security Strategy for a New Century," The White House, October 1998.

vulnerable[2] and unaffordable forward land bases. In concept, a MOB is a very large floating structure, on the order of up to 1,500 meters long by 120 meters wide. MOB provides aircraft operations capabilities up to the C-17 cargo transport aircraft, cargo loading and offloading from military sealift and commercial cargo ships; provides internal cargo storage and handling facilities; and personnel support facilities for up to 20,000 personnel dependent upon the type of mission. Most concepts proposed to date within the scope of the MOB S&T program consist of multiple large semi-submersible modules, connected by various means to provide a functionally continuous platform.

2. OVERVIEW OF THE MOB S&T PROGRAM

Enabling technologies for the MOB were first investigated by the Defense Advanced Research Project Agency between 1993 and 1995, with the ultimate objective of conducting an Advanced Concept Technology Demonstration (ACTD) of the MOB. However, it was determined at the time that the unprecedented size and requirements of the MOB translated to unacceptably high risks using then state-of-the-art technology to design, construct and operate such a platform. Therefore, the Chief of Naval Operations directed the Office of Naval Research (ONR) to assume leadership of a Science and Technology (S&T) program focused on reducing these risks. The goal of the S&T program is to advance critical technologies required to reduce the technical, operational and financial risks of designing, constructing, operating, and maintaining a MOB capable of meeting mission requirements. The primary focus of the S&T program is to establish the technical feasibility and affordability of a MOB and consists of the following four general product areas: Mission Requirements and Performance Measures, Standards and Criteria, Design Tools, and Alternative Concepts. Each of these efforts is described briefly in the following paragraphs.

2.1 Mission Requirement and Performance Measure

The main objective of this effort is to define a set of mission-based functional requirements for a MOB, a rational procedure, and the necessary tools for evaluating alternative concepts on the basis of functional performance, operational availability, and total system life cycle cost. These data and tools provide a consistent basis for the development, refinement and evaluation of different MOB concepts. They also provide the means for ensuring that the S&T program remains focused on solving those technology issues most important to meeting critical mission requirements for the MOB. The major products resulting from these efforts include:

- Concepts of Operations (CONOPS), Operational Scenarios, System Capabilities Documents (SCD), Performance Requirement Documents (PRD), and Design Evaluation Criteria (DEC) derived from the existing Mission Need Statement (MNS);
- Hierarchical Database containing MOB system capability requirements and associated functional requirements;
- Operational Availability (Ao) Models used to assess the performance of any MOB concept relative to the mission-based requirements, and to evaluate the sensitivity of various performance parameters to changes in concept configuration and mission requirements;
- Cargo Transfer Rate Models for transfer of Lift-On/Lift-Off (LO/LO) and Roll-On/Roll-Off (RO/RO) cargo between the MOB and various ships and lighterages;
- Enhancement of existing ship design synthesis models; and,
- Constructability Risk Assessment and development of risk-based constructability guidelines.

2.2 Standards and Criteria

Under "Standards and Criteria," the objective is the development of a draft MOB *Classification Guide*, addressing structural safety and integrity of such very large floating structures. This effort includes the development of reliability-based design standards applicable to MOB-type structures and the definition of environmental and fatigue criteria. The *Classification Guide* is one of the primary technical deliverables of the MOB S&T program. This guide establishes a common design reference for both contractors and government to help ensure that each ongoing and future developed MOB concept is designed as accurately and realistically as possible relative to the functional requirements. The American Bureau of Shipping (ABS) is developing the *Classification Guide* by extending current offshore practices and standards to accommodate the MOB, and by integrating military standards where appropriate. This guide will help the offshore industry plan and execute the design of a MOB and serve as a reference for the certification process. In addition, the *Classification Guide* should also benefit the offshore industry and other commercial sectors in general, as it will be applicable to a broad variety of very large floating structures (e.g., offshore airports, processing plants, storage facilities, or habitations).

[2] Asymmetric warfare: U.S. Marine Corps headquarters in Beirut (1983), Khobar Towers in Saudi Arabia (1996).

2.3 Design Tools

The main objective of the Design Tools effort is to develop and validate a set of computer tools supporting the evaluation of hydrodynamic and structural behavior of MOB structures. The state-of-the-art in terms of hydroelastic models as defined at the beginning of the MOB S&T program did not allow adequate numerical analysis of structures on the scale of MOB modules (i.e., lack of accuracy of the models and unpractical computation time). The major products of the Design Tools effort include:

- Evaluation of existing analysis, design tools and models;
- Development of advanced hydroelastic models adequate to address structures on the scale of the MOB;
- Development of a "Load Generator" tool to provide a numerical interface between frequency domain hydrodynamic analysis and time domain structural dynamics methods; and,
- Generation of new physical model data to validate the design tools being developed.

2.4 Alternative Concepts

Alternative concepts for an overall MOB, as well as concepts for specific critical components such as connectors, are being studied under this product area to both advance existing technologies and identify additional technology gaps. By sponsoring the development of competing point designs for the MOB and some of its specific components, the shipyard and offshore industries help identify and fill their own technology gaps. The following four MOB system concepts are being developed through the preliminary design stage as part of this effort.

- *Hinged Semi-Submersible Module MOB*: Comprises up to five semi-submersible steel modules up to 300 meters long, connected with compliant hinge-type connectors (Figure 1).

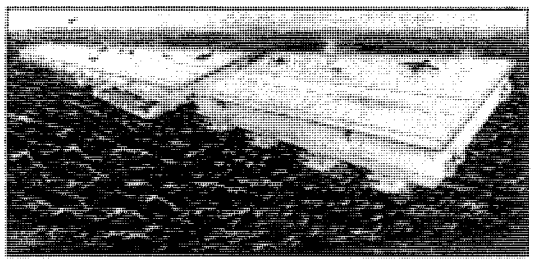

Figure 1. Hinged Semi-Submersible Module MOB (Courtesy of McDermott International Inc.)

- *Semi-Submersible Modules Connected by Flexible Bridges*: This concept consists of three semi-submersible steel modules, each about 235 meters long, connected by long (410 meters), full width flexible truss "bridges" that provide a continuous flight deck (Figure 2).

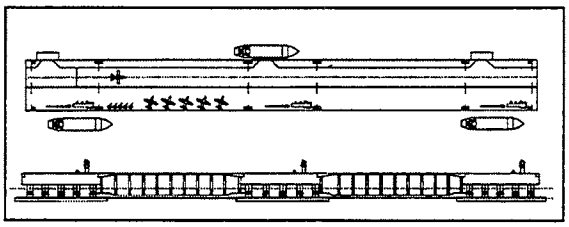

Figure 2. Semi-Submersible Modules with Flexible Bridges MOB – Plan and elevation views, respectively (Courtesy of Kvaerner Maritime)

- *Independent Semi-submersible Modules*: This concept is made up of three very large (490 meters) semi-submersible steel modules that are only functionally connected by drawbridges to span the gap between dynamically positioned modules providing a continuous airplane runway. This concept relies on dynamic positioning to maintain overall orientation and relative position between modules, instead of structural load-bearing connectors (Figure 3).

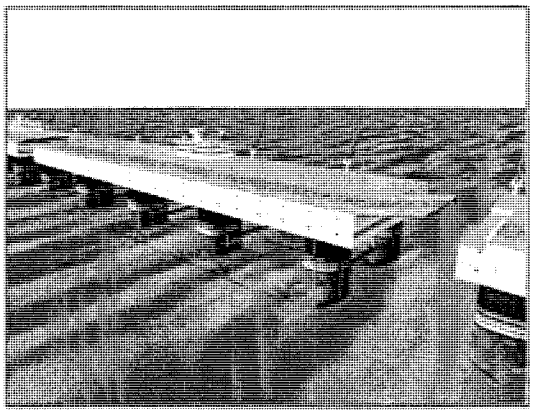

Figure 3. Independent Semi-Submersible Module MOB (Courtesy of Bechtel National Inc.)

- *Concrete and Steel Semi-submersible Modules*: This concept consists of 380 meters long semi-submersible modules connected with compliant elastomeric bearings, with a concrete hull and steel deck. A concrete hull may provide a longer life and require less maintenance (Figure 4).

In addition to these four primary concepts, a concept comprising steel semi-submersible modules connected with a rigid connector system was already fully developed to the preliminary design stage under the original DARPA program. While the initial work on this fifth concept is completed, all five concepts are evaluated as part of the S&T program.

The ship design synthesis models mentioned earlier are also utilized to develop conventional ultra-large "mono-hull" alternatives to meeting MOB mission requirements. While these "mono-hull" concepts are not capable of meeting all MOB mission requirements, they serve as a familiar point of departure and comparison of feasibility and cost of other MOB designs.

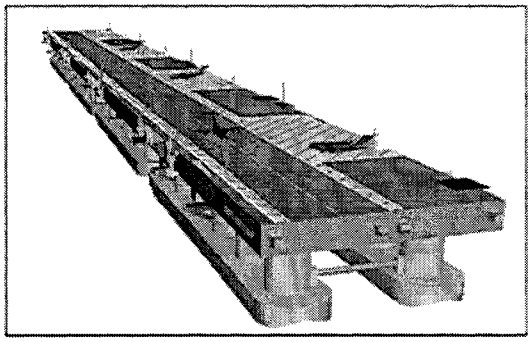

Figure 4. Concrete and Steel Semi-Submersible Module MOB (Courtesy of Aker Norwegian Contractors AS)

In addition to the system concepts described above, the following specific components are also being addressed within the Alternative Concepts product area:

- Connectors, including specific connector concepts not addressed in the system concepts described above, connector materials, and connection methods in general;
- Multi-module Dynamic Positioning (DP) systems;
- Lightweight decking materials;
- Cargo transfer systems;
- Pneumatic stabilization method for platforms; and,
- High capacity mooring lines and suction pile anchors.

3. MISSION REQUIREMENTS DEFINITION

The primary focus of the MOB S&T program described above is the advancement of critical technologies to reduce the technical, operational, and financial risks of designing, constructing and operating a MOB for an actual mission. Although the requirements for an actual MOB will be developed as part of a formal system acquisition process, it was realized that a consistent set of mission-based functional requirements was needed to help bound and guide the S&T program.

3.1 A Systems Engineering Approach

A Systems Engineering (SE) based process (Figure 5) was selected for deriving the specific mission-based functional requirements for the MOB. This process begins with the "Mission Need Statement (MNS) for the MOB," dated 15 September 1995, and methodically decomposes the broad-based MNS into multiple discrete missions for which a Concept of Operation (CONOPS) is developed. In turn, each CONOPS serves to establish the basis for a System Capabilities Document (SCD), which leads to the definition of specific physical and performance requirements associated with each capability. These physical requirements are the data of most value to designers establishing the design goals for a MOB. This derivation method also lends itself to documentation in a hierarchical database, linking specific mission requirements to system capabilities, each in turn linked to specific functional requirements.

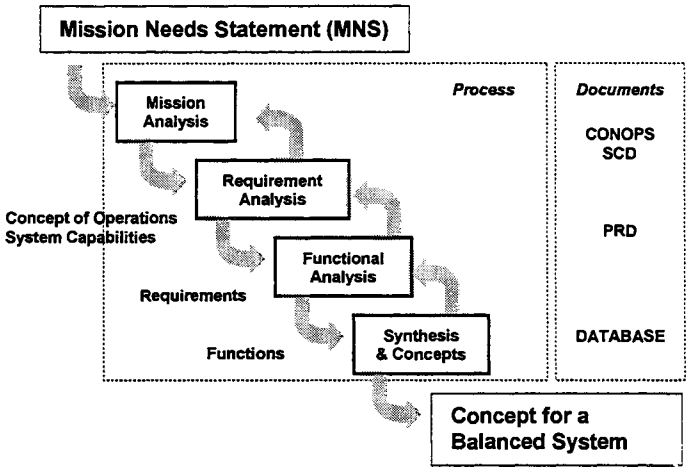

Figure 5. Systems Engineering Process – Conceptual Design Phase

3.2 Mission Definition

The basis for the derivation of functional requirements to support the MOB S&T program is the 1995 MNS. While this document has not gone through the required Joint Requirement Oversight Council (JROC) process, it is the only authoritative document available providing guidance towards the definition of requirements for an actual MOB and was therefore adopted as the starting point for the requirement

definition process. The major missions for the MOB included in the MNS are summarized below:

- Maintain continuous overseas presence and theater access complementary to, or independent of, allied or coalition support and infrastructure;
- Extend and maintain operational reach within a theater of operation;
- Conduct pre-planned and crisis-generated operations, at any level of engagement or conflict, in any area of the world. These operations include military-to-military contacts, humanitarian operations, security assistance, peace operations, counter-terrorism, special force operations, power projection, non-combatant evacuation operations, lesser and major regional contingencies;
- Stow, maintain and deliver selective and ready afloat pre-positioned equipment, fuel and water;
- Provide an advanced base from which air, land and naval expeditionary forces can conduct operations complementary to, or independently of, host-nation support;
- Provide an in-theater command and control (C2) center and operation facility directing and supporting air, sea and land systems and providing command, control, communications, computer, and intelligence (C4I) capabilities to a Joint Task Force (JTF);
- Provide a tactical aviation operations and support base for CTOL, STOL, VSTOL, and rotary wing aircraft;
- Provide a base capable of launching and recovering SOF missions employing SOF aircraft and maritime assets;
- Provide supplemental or alternative capability to land-based naval advanced logistic support sites and naval forward logistic sites, to include refueling and re-supply of military units;
- Provide supplemental or alternative mobile pre-positioning of military combat, combat service and combat service support equipment and supplies;
- Provide an inter-theater and intra-theater logistics node supporting movement of both pre-positioned and deployed equipment and supplies to required locations via both sealift and airlift assets including C-17;
- Provide a transportation node capable of supporting routine movement of combat and transportation assets, including current and future U.S. and allied commercial and military air and sea transportation and combat, surveillance aircraft and ships; and,
- Provide in-theater organizational, intermediate and selected depot maintenance and repair facility supporting deployed air, sea and land systems.

The statements above reflect the fact that MNS are intended as broad statements of general mission needs, making them open to wide differences in interpretations. Before meaningful functional requirements could be derived, the contents of the MNS needed to be further clarified and refined into a Concept of Operations (CONOPS). However, because the MOB could actually support each of several independent military missions, serving as a large logistics base, or as a smaller platform supporting special operations, for example, it was decided to break the MNS itself down into several discrete missions for which CONOPS would each be developed.

Six separate missions for the MOB were initially identified for which CONOPS would be developed. These included the MOB as a logistics base, as a special operations platform, in support of tactical aviation, for operations other than war, as a sea-base supporting Operational Maneuver From The Sea, and as a pre-positioned equipment storage site and platform for the marriage of troops with their prepositioned gear.

The identification of these missions was based in part on how each would drive the physical requirements for the MOB. For example, those missions requiring aircraft operations for conventional fixed-wing aircraft would require a full-length, functionally connected MOB. Other missions involving only vertical take-off and landing aircraft and more modest storage and operating spaces may only require one or two units of a full MOB. Similarly, some but not all missions may require specialized facilities such as lighterage loading and offloading. Although a single MOB system would still be required to fulfill all of these discreet missions at various times, dissecting the overall MNS in this way allows for the consideration of specialized MOB modules making up the full MOB. This in turns allows for maximizing the flexibility of the system while reducing unneeded and costly redundancy of systems.

After outlining the basic operations and required capabilities to support each of these missions, the MNS was revisited to ensure that every statement was covered by at least one of the six preliminary missions.

3.3 Concepts of Operations for MOB

The six missions identified and described in the previous paragraph were addressed in the development of CONOPS corresponding to each mission. The CONOPS developed for each mission describes the operational environment and the specific roles that the MOB plays in supporting operations. In addition to a general overview of the operations and how the MOB fits in, the CONOPS also describe operations involving or impacting the MOB during both the planning and execution phases of the operations. The execution

phases include deployment and reception as well as operation. Notional force lists are included as a means of estimating the numbers of personnel and amount and type of equipment and aircraft to be supported for that mission. A scenario describing a hypothetical operation in a specific geographic location also is included to illustrate how the MOB might support a real mission.

During the course of developing the draft CONOPS, it was determined that the Operations Other Than War (OOTW) mission and capabilities were already covered within other missions (both logistics and special forces operations). Similarly, the Operational Maneuver from the Sea (OMFTS) and Marine Prepositioned Force (MPF) missions could be effectively combined. CONOPS for the four resulting missions were developed.

3.3.1 Logistics

In this concept of operations the MOB serves as a sea borne forward base in an overall joint "hub and spoke" logistics architecture which provides an at-sea terminal area to receive, warehouse, assemble, and distribute equipment and supplies to sea, air and land forces. In addition, MOB has the capability to provide intermediate level maintenance and repairs for all assets used by Armed Forces operating in the area. MOB is employed across the full spectrum of operations including Combat Operations and Operations Other Than War (OOTW) where there is an absence of adequate support infrastructure or where operational concepts dictate using the sea as maneuver space.

3.3.2 Special Forces Operations (SOF)

A MOB providing or hosting operational level support for SOF accommodates the spectrum of sequential and concurrent tasks required to stand-up the Joint Special Operations Task Force (JSOTF), facilitate preparations for operations, conduct operations and support services during extended engagements. Functioning as an operational base, the MOB receives and accommodates strategic re-supply and replacement as well as regeneration of combat units in contact with enemy forces and repair of assets needed to maintain operational readiness.

3.3.3 Operational Maneuver From The Sea (OMFTS)

In this CONOPS MOB is part of the sea-basing concept envisioned in the Maritime Prepositioning Force of 2010 (MPF 2010) and Beyond. MOB serves as a sea base with accommodations for up to 20,000 embarked MPF Marine Air Ground Task Force (MAGTF) personnel, facilities for assembly and staging areas, and facilities to effect sea-based command and control of the MPF MAGTF operations. MAGTF forces operate using the concept of OMFTS and Ship to Objectives Maneuver (STOM). The forces committed ashore are indefinitely sustained from MOB. Finally, MOB is capable of in-theater reconstitution and redeployment.

3.3.4 Tactical Aircraft Support (TACAIRSUP)

This CONOPS addresses the MOB in a support role to other air-capable bases or ships and covers missions in which tactical aircraft are operated in and around the MOB. Because the MOB is in a supporting role only, no aircraft are assigned to the MOB as a permanent base. Instead, the MOB provides support activities that enhance the productivity and flexibility of the bases and ships it supports. Potential missions for the MOB in this context include its serving as a divert field for tactical aircraft, a transshipment point for planned transit of aircraft into or out of the theatre of operations, and as a base providing routine operational support for aircraft operations. Operational support includes Carrier Onboard Delivery (COD), Intelligence, Surveillance and Reconnaissance (ISR), Search and Rescue (SAR), tanking support, and Fuel Carrier Landing Practice (FCLP). Tactical aircraft addressed in those CONOPS include all U.S. Air Force tactical aircraft, U.S. Navy fixed-wing carrier-based aircraft, and U.S. Marine Corps fixed-wing aircraft, planned for operation in the 2010 time period and beyond.

3.4 System Capabilities Definition

Following definition of the CONOPS for each mission the specific capabilities required of the MOB to support that mission are defined and documented in a System Capabilities Document (SCD). The definition of system capabilities is the intermediate step between defining the concept of operations for a mission and deriving the physical requirements needed to meet that mission.

As an example, some of the top-level system capabilities required of the MOB to support the logistics mission include:

- Organic C4I capability to support sea-based logistics planning and information support, including Joint Total Asset Visibility and Global Combat Support System;
- Selective offload capability including automated storage systems, re-configurable internal stowage spaces for vehicles, aircraft and containerized cargo, climate controlled storage space, warehouse capability and services, areas for marshaling, staging and breakout of cargo and equipment, and

the capabilities needed to provide throughput of all classes of supply;
- Multiple vertical take-off and landing (VTOL) sites;
- Aircraft operations capability for fixed wing aircraft up to the C130 and C17, through seastate 6 conditions;
- Intermediate level maintenance, repair and battle damage repair on logistics aircraft, watercraft, and unit equipment;
- Aircraft hangaring facilities;
- Loading and unloading of commercial and naval ships, including LO/LO, RO/RO, oilers, lighterage and air cushioned vehicles through seastate 3;
- Fresh water production, distribution and storage;
- Ordnance and hazardous material handling, storage and transfer;
- Survivability against 21st century anti-ship missiles, torpedoes and mines; and,
- Personnel support facilities, including berthing, messing, medical and limited recreational facilities.

3.5 Functional Requirements Definition

To define the specific physical requirements for the MOB, each system capability requirement is analyzed to determine what physical requirements must be fulfilled to provide that capability. For example, if the System Capabilities Document requires personnel accommodations for 15,000 troops to satisfy a particular mission, the amount of physical space needed for berthing, messing and other personnel support facilities, is determined in this step. These requirements could then be provided to a concept developer as a design requirement for their version of the MOB. These requirements will also be used to evaluate the adequacy of existing concepts to meet these specific physical requirements.

The functional capabilities are based upon current practice and doctrine for Navy ships, where appropriate. For new missions such as landing strategic cargo aircraft on the MOB, new capabilities requirements have been identified as part of the requirement definition process.

The method of decomposing the various missions into specific functional requirements also serves as the basis for the development and contents of a hierarchical database established to serve as a tool in defining MOB functional requirements. This database serves as a repository for all currently envisioned mission elements as well as the associated capabilities and physical requirements. Each entry into the database is annotated with references and dates so that mission elements, capabilities and requirements can be updated as MOB applications and technology evolve.

The database is structured with mission elements at the top level, with each element linked to the system capabilities needed to meet that mission element. Each capability is in turn linked to the specific functional and physical requirements needed on the MOB to meet that capability. Since the top level of the database consists of individual *mission elements* instead of the four CONOPS representing an overall mission, it allows the user to build new missions from the list of elements and not be tied to the four missions selected for initial CONOPS development. This helps ensure that the database and the requirements documented will remain useful tools for the MOB program as missions and CONOPS for the MOB evolve with time.

3.6 Performance Requirements Definition

Within the scope of the MOB S&T Program, a Performance Requirements Document (PRD) was developed for each CONOPS and is considered as a legacy document to facilitate the transition to the Development Phase of a potential Defense Acquisition Program. The development of the PRD gave us the opportunity to better understand the overall problem. Each PRD defines the MOB in terms of functional and performance requirements without making any assumption relative to a specific design. Each PRD defines for a specific CONOPS "What" needs to be done and "How well" the total system has to perform. Each PRD synthesizes the first attempted iteration in the development of what a formal acquisition program would call the "Type-A" specification of a MOB. Each PRD is a stand-alone document addressing the following topics:

- *Applicable documents*: Government Specifications, Standards and Handbooks, Classification Guide (ABS), International Maritime Organization (IMO) Standards, American National Standards Institute (ANSI) and American Society for Testing and Materials (ASTM) Standards and Guidance Documents;
- *Mission Requirements*: Operational profiles, Embarked Personnel, Support of mission specific C4I, Terminal services for Vessels/Craft and Aircraft, Storage of Equipment and Supplies, Mobility, Maintenance, Personnel Support Services, and Prevention and Control Damage;
- *Operational Environment*: Threat and Natural Environments, Electromagnetic Environment Effects, and External and Fleet Interfaces;
- *Functional Requirements*: Design Goals, Principal Characteristics, Readiness, Survivability and Vulnerability, "Ship" Services, Organic C4I, and Statutory and Regulatory Requirements;

- *Arrangements*: Proximity Considerations, Mission Space Requirements, Access/Egress Requirements, Habitability, and Medical Spaces; and,
- *Verification and Preparation for Delivery*: Not fully addressed within the scope of the S&T Program.

4. LESSONS LEARNED

4.1 Major Design Drivers for MOB

In the course of deriving the physical requirements for the MOB, it became apparent that some mission elements and associated capabilities have a greater impact on the physical requirements than others. At this time, the following major mission elements are expected to be part of any future MOB mission, and to drive the physical requirements of the MOB:

- *Physical Operating Environment*: The weather and sea states that the MOB must withstand during transit and on station (in both connected and disconnected configurations) will influence structural, propulsion and station-keeping system requirements.
- *General Performance Requirements*: Transit speed, range and dynamic positioning (if any) will drive propulsion system requirements. Overall system operational availability requirements will drive all critical systems.
- *Aircraft Operations*: The requirements derived from Aircraft Operations are expected to drive the ultimate size of the MOB, as length requirements are tied to aircraft type, payload and fuel load required for a particular range and mission. The sortie rate for aircraft operations will impact width of the MOB in terms of taxiway and aircraft parking requirements. Identification of the type and number of aircraft requiring shelter at the MOB may drive topside space requirements for hangaring aircraft that may be too large to be sheltered below decks, and will drive below decks space requirements, as well as elevator or ramp requirements. Aircraft operations fuel requirements also will drive liquid cargo storage and distribution requirements on the MOB.
- *Personnel Accommodations*: The MOB must have the capability to provide personnel support facilities for the following categories of personnel:
  - MOB crew responsible for day-to-day operation and maintenance of the MOB platform and organic systems (permanent).
  - Unit personnel attached to organizations stationed at the MOB for the duration of a particular mission (long-term).
  - Unit personnel using the MOB as a temporary staging point to marry up with unit equipment in preparation for deployment to an objective site (short-term).
  - Non-military personnel, such as refugees or prisoners of war, requiring temporary personnel support facilities prior to relocation (mid-term).

  The type and extent of personnel support facilities requirements will differ for each category listed above. Facilities requirements will consist of berthing spaces, messing facilities, medical and dental facilities, recreational facilities, and quarantine or secured facilities for certain groups of personnel. These facilities in turn drive internal space requirements, arrangements and utility requirements.
- *Cargo Storage & Handling*: Requirements for storing and accessing vehicular, containerized, palletized, and liquid cargo will drive internal space requirements and arrangements.
- *Ordnance Facilities*: Special considerations for the amount and type of ordnance stowed, handled and transferred at the MOB will drive internal arrangements. Survivability against accidental detonation will impact structural requirements.
- *Cargo Transfer*: Cargo transfer operations between the MOB and sea-going vessels will dictate the number and type of berthing and/or mooring locations required at the MOB, and cargo handling system requirements. This is anticipated to include transfer of cargo to vessels ranging from lighterage to sealift support vessels, commercial containerships, and tankers, and include Lift-On/Lift-Off (LO/LO), Roll-On/Roll-Off, and liquid cargo transfer operations.
- *Assigned & Transient Unit Equipment and Facilities*: Space for equipment and operations of organizations assigned to the MOB will drive both topside and below decks space requirements and arrangements.
- *Survivability*: The physical requirements of the structure will be greatly impacted by the requirement to withstand attack from 21st century anti-ship missiles, torpedoes and mines.

4.2 MOB as a Joint National Asset

While developing the CONOPS derived from the initial MNS, it became clear that a MOB should be considered as a national asset. As such, MOB could enable joint capabilities (i.e., logistics and tactical support) for the Navy, Marine Corps, Army, Air Force, Coast Guard, as well as other federal and civilian agencies operating overseas (e.g., Department of State, U.S. Agency for International Assistance, and

commercial entities). MOB is by nature a multiple mission asset that could be primarily used by the U.S. armed services and multinational coalition forces conducting combat operations, Operations Other Than War (OOTW) and humanitarian operations in areas lacking adequate land bases. Figure 6 illustrates the context in which MOB would have to operate, as well as the different entities to interface with.

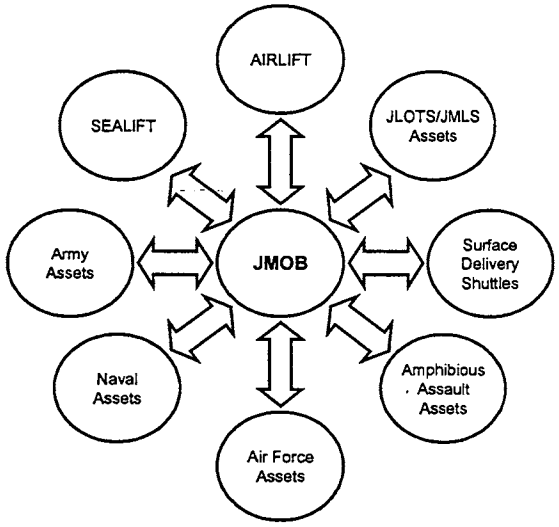

Figure 6. Context Diagram for a Joint MOB

The mission requirement effort undertaken within the scope of the ONR S&T Program for MOB provides a service-oriented perspective of the problem with a large emphasis on naval expeditionary operations. In addition, the CONOPS derived from the initial MNS are based on current and near-term doctrines and force structures.

The initial assessment of mission requirements is valuable and supports adequately the primary objectives of the S&T program. However, the full potential of a joint concept of operations for MOB remains to be thoroughly explored. One should now consider developing such a joint concept of operations and assess the military utility of a MOB beyond the single-service point of view and in the context of emerging technologies. In that case, it would be interesting to investigate the utility of MOB as an alternative forward basing capability. As shown in figure 7, deploying MOB in the theater of operations could be a flexible approach to solving the problem posed by increasingly inaccessible overseas facilities.

This assessment, somewhat beyond the scope of the current S&T program, is the next logical step in addressing the true value of a MOB and should be jointly conducted in a national security context by all U.S. armed services.

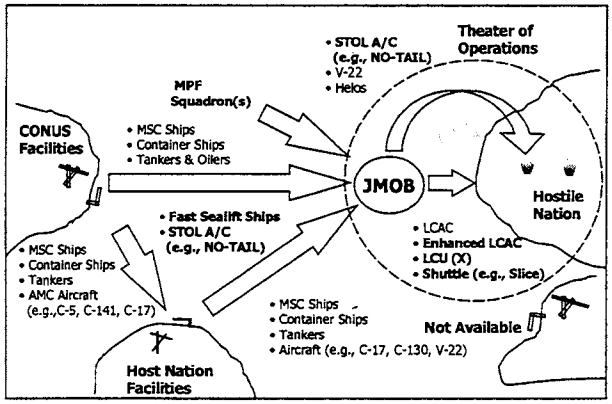

Figure 7. "End-to-End" Capability Approach for a Joint MOB

Such an assessment should (1) Identify candidate joint operating concepts; (2) Develop associated operational doctrines; and (3) Measure the joint operational value and utility of MOB.

5. CONCLUSION

The ultimate goal of the ONR S&T program for the MOB is to establish technical feasibility and affordability of a MOB capable of meeting mission-based requirements as broadly stated in the MNS of September 1995. Toward this end, efforts are well underway in the advancement of those technologies critical to reducing the technical, operational and financial risks of designing, constructing, operating, and maintaining a MOB.

As part of this effort, a requirements definition process and a baseline set of mission-based requirements were developed to help guide the development and refinement of MOB concepts, as well as to establish the basis for a consistent and fair evaluation of alternative concepts. This mission requirement effort has already successfully contributed to a better understanding of the total system and ensured that the S&T program focused its resources on those technology issues most critical to meeting mission needs for a MOB, therefore meeting the primary objectives of the overall effort.

Finally, it became clear in the course of the mission requirement effort that a MOB should be considered as a national asset, enabling joint logistics and tactical support capabilities for U.S. armed services and civilian agencies operating in forward areas lacking adequate land bases. The full potential of MOB as a true joint capability remains to be understood and warrants further evaluation.

ACKNOWLEDGEMENTS

The material is based upon work supported by the Office of Naval Research MOB S&T program. The author wishes to acknowledge the contribution of all members of the "Mission Requirements and Performance Measures" Working Group in developing the functional requirements and the design evaluation tools described in this paper.

BIBLIOGRAPHY

[1] "Mission Need Statement for the Mobile Offshore Base (MOB) - ACAT Level I," September 1995.

[2] "Mobile Offshore Base Science and Technology Program Plan," Office of Naval Research, November 1997.

[3] "Overview of Preliminary Requirement Documents and Requirement Derivation Process," Office of Naval Research, June 1998.

[4] "Logistics Concept of Operations for the Mobile Offshore Base," Revision 1.3, Syntek Technologies Inc., March 1999.

[5] "Special Forces Operations (SOF) Concept of Operations for the Mobile Offshore Base," Revision 1.3, Syntek Technologies Inc., March 1999.

[6] "Operational Maneuver From The Sea (OMFTS) Concept of Operations for the Mobile Offshore Base," Revision 1.3, Syntek Technologies Inc., March 1999.

[7] "Tactical Aircraft Support (TACAIRSUP) Concept of Operations for the Mobile Offshore Base," Whitney, Bradley and Brown, Inc., August 1998.

[8] "System Capabilities Document (SCD) for Logistics Concept of Operations - Mobile Offshore Base," Revision 1.3, Syntek Technologies Inc., March 1999.

[9] "System Capabilities Document (SCD) for Special Forces Operations (SOF) Concept of Operations - Mobile Offshore Base," Revision 1.3, Syntek Technologies Inc., March 1999.

[10] "System Capabilities Document (SCD) for Operational Maneuver From The Sea (OMFTS) Concept of Operations - Mobile Offshore Base," Revision 1.3, Syntek Technologies Inc., March 1999.

[11] "System Capabilities Document (SCD) for Tactical Aircraft Support (TACAIRSUP) Concept of Operations - Mobile Offshore Base," Revision 1.2, Syntek Inc., September 1998.

[12] "Operational Scenario for Logistics Concept of Operations - Mobile Offshore Base," Syntek Technologies Inc., July 1999.

[13] "Operational Scenario for Special Forces Operations (SOF) Concept of Operations - Mobile Offshore Base," Syntek Technologies Inc., July 1999.

[14] "Operational Scenario for Operational Maneuver From The Sea (OMFTS) Concept of Operations - Mobile Offshore Base," Syntek Technologies Inc., July 1999.

[15] "Operational Scenario for Tactical Aircraft Support (TACAIRSUP) Concept of Operations - Mobile Offshore Base," Syntek Inc., July 1999.

[16] "Operational Maneuver From The Sea (OMFTS) – A Concept for the Projection of Naval Power Ashore," Headquarters U.S. Marine Corps, January 1996.

[17] "A concept for Ship-To-Objective Maneuver (STOM)," Headquarters U.S. Marine Corps, July 1997.

[18] "Maritime Prepositioning Force (MPF) 2010 and Beyond," Headquarters U.S. Marine Corps, December 1997.

[19] "Seabased Logistics – A 21st Century Warfighting Concept," Marine Corps Combat Development Command, May 1998.

[20] "Naval Expeditionary Logistics – Enabling Operational Maneuver From The Sea," Naval Studies Board, National Research Council, 1999.

[21] "Joint Vision 2010," Chairman of the Joint Chiefs of Staff.

[22] "Universal Joint Task List," CJCSM 3500.04A, Office of the Joint Chiefs of Staff, September 1996.

[23] John J. Turner, Michele A. Murdoch, Daniel L. Wilkins, Philippe M. Lopez, "Functional Requirements Definition for a Mobile Offshore Base (MOB), Proceedings of the 1998 Naval Logistics Conference, Alexandria (VA), USA, pp.427-441, 1998.

Author Index

Volume I : 1 to 446 and Volume II : 447 to 919 pages

REPORT DOCUMENTATION PAGE

Form Approved
OMB No. 0704-0188

1. REPORT DATE *(DD-MM-YYYY)*	2. REPORT TYPE	3. DATES COVERED *(From - To)*
21-09-1999	Proceedings	July 1999 – December 1999

4. TITLE AND SUBTITLE

Proceedings of the Third International Workshop on Very Large Floating Structures, Volumes I and II, Honolulu, HI, September 22-24, 1999

5a. CONTRACT NUMBER

5b. GRANT NUMBER

N00014-99-1-0988

5c. PROGRAM ELEMENT NUMBER

MOB Project

6. AUTHOR(S)

Editors: Ertekin, R. Cengiz
Kim, Jang Whan

5d. PROJECT NUMBER

5e. TASK NUMBER

5f. WORK UNIT NUMBER

7. PERFORMING ORGANIZATION NAME(S) AND ADDRESS(ES)

University of Hawaii, SOEST
2540 Dole Street, Holmes Hall 402
Honolulu, HI 96822

8. PERFORMING ORGANIZATION REPORT NUMBER

9. SPONSORING/MONITORING AGENCY NAME(S) AND ADDRESS(ES)

Department of the Navy
Office of Naval Research, MOB Program
800 N. Quincy Street
Arlington, VA 22217-5660

10. SPONSOR/MONITOR'S ACRONYM(S)

ONR, MOB

11. SPONSOR/MONITOR'S REPORT NUMBER(S)

12. DISTRIBUTION/AVAILABILITY STATEMENT

Approved for public release; distribution is unlimited

13. SUPPLEMENTARY NOTES

The United States Government has a royalty-free license through out the world in all copyrightable material contained herein.

14. ABSTRACT

The Proceedings of the Third International Workshop on Very Large Floating Structures (VLFS'99) includes 110 written contributions by 241 authors on the Mobile Offshore Base Project of the U.S. and the Mega-Float Project of Japan, as well in the general areas related to the design and analysis of VLFS. The Workshop was held in September 22-24, 1999, Honolulu, and attended by more than 160 researchers from 10 countries.

15. SUBJECT TERMS

Very Large Floating Structures (VLFS), Mobile Offshore Base (MOB), Mega-Float Project of Japan

16. SECURITY CLASSIFICATION OF:			17. LIMITATION OF ABSTRACT	18. NUMBER OF PAGES	19a. NAME OF RESPONSIBLE PERSON
a. REPORT	b. ABSTRACT	c. THIS PAGE			R.C. Ertekin
U	U	U	UU		19b. TELEPHONE NUMBER *(Include area code)* (808) 956-6818